

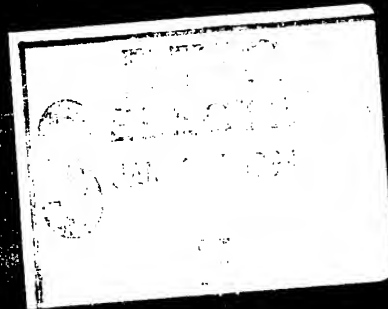
19950111139



**Fifth Symposium  
(International)**

on

**DETONATION**



**Pasadena, California**

**August 18-21, 1970**

This document has been approved  
for public release and sale; its  
distribution is unlimited.

~~000000~~ 007

**ACR-184**

**Office of Naval Research  
Department of the Navy**

PROCEEDINGS

Fifth Symposium

(International)

on

DETONATION

*Sponsored by the*  
U.S. NAVAL ORDNANCE LABORATORY  
*and the*  
OFFICE OF NAVAL RESEARCH



August 18-21, 1970  
Pasadena, California

19950111 139

DTIC QUALITY INSPECTED 3

UNANNOUNCED

Accession For	
NTIS CRA&I	<input checked="" type="checkbox"/>
DTIC TAB	<input type="checkbox"/>
Unannounced	<input type="checkbox"/>
Justification	
By	
Distribution/	
Availability Codes	
Dist	Avail and/or Special
A-1	

ACR-184

OFFICE OF NAVAL RESEARCH—DEPARTMENT OF THE NAVY  
Arlington, Virginia



## AVAILABILITY OF DETONATION SYMPOSIA PROCEEDINGS

The Detonation Symposia Proceedings have been printed as hardbound books since the Fourth Symposium. Motivated by suggestions from colleagues attending the Seventh and Eighth Symposia, the Organization Committee printed Proceedings of the First and Second (bound as one book), and Proceedings of the Third in hardbound editions. The Committee reprinted Proceedings of the Fourth Symposium in 1988. This reprint of the Proceedings of the Fifth Symposium was printed in 1989.

Copies of the Detonation Symposia Proceedings are available for sale. At the time this book was reprinted in 1989, the price of the Proceedings was \$50 per book. The seven volume set (including Proceedings of First through Eighth) is \$350.

The books are sold on a prepaid basis. To order copies, mail a request for copies, specifying which Proceedings and the number of copies, with a check or money order (not cash), payable to:

The Detonation Symposium  
Naval Surface Warfare Center  
Attn: Dr. James M. Short  
10901 New Hampshire Avenue  
Silver Spring, MD 20903-5000

JAMES M. SHORT  
WANDA J. OHM  
Naval Surface Warfare Center  
April 1989

## PREFACE

The Fifth Symposium (International) on Detonation is the fifth of a series of U. S. Navy sponsored symposia on condensed phase detonations and the second unclassified meeting on this subject in the United States having international participation. A listing of available documents of the previous symposia is to be found on the preceding page of these proceedings. The present meeting cosponsored by the Office of Naval Research and the Naval Ordnance Laboratory took place on 18-21 August 1970 at the Huntington-Sheraton Hotel, Pasadena, California. Of the 300 participants who attended there were about 60 representing foreign countries throughout the world.

These proceedings contain the complete and revised papers presented and discussed at the symposium. In a few instances, where the authors chose to publish elsewhere, we have given the abstract for their papers with reference to the outside publication when available at the time of printing. Written discussion has also been included.

We take note at this point that one of our active colleagues in detonation, Dr. Stuart R. Brinkley, Jr., died on Friday, 7 August 1970, at his summer home in South Bristol, Maine. He was preparing to attend this symposium and chair the first session on "Detonation and Related Flows". At the time of his death, Dr. Brinkley was associated with Combustion and Explosives Research, Inc., of Pittsburgh, Pennsylvania. He had been active in the field of detonation since 1942 and had written numerous theoretical papers on the subject.

We wish to take this opportunity to thank the Session Chairmen, whose names appear under the title for each session, for their assistance in conducting the programs at the meeting. We particularly wish to thank Dr. I. C. Skidmore for taking on the session intended for Dr. Brinkley and Dr. R. E. Duff for his last minute replacement for Dr. L. Deffet who was unable to attend because of illness. We also wish to recognize, with thanks, the efforts of the following who assisted in the logistics of the meeting: Dr. Donna Price of the Naval Ordnance Laboratory for her assistance in reviewing abstracts, selecting papers, and organizing the sessions make-up; Dr. Rudolph J. Markus of ONR, Pasadena, for his handling of local arrangements; Norman L. Rump, Harold J. Gryting, and C. Douglas Lind of the Naval Weapons Center for their assistance in the conduct of the symposium. The secretarial load was ably handled by Mrs. C. Y. Richtmyer and Mrs. P. J. Hodge of ONR, Washington, and Miss A. Damico of the Naval Weapons Center.

Past meetings sponsored abroad in this field worthy of mention include:

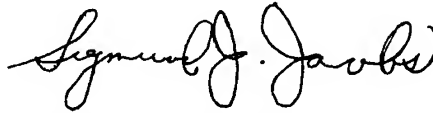
"A Discussion of the Initiation and Growth of Explosion in Solids," led by Professor F. P. Bowden in London on March 30, 1957 with papers published in the Proceedings of the Royal Society, A240, 145-297 (1958).

A symposium on "Les Ondes de Detonation" sponsored and published by the French National Center of Scientific Research and chaired by Professor G. Ribaud with the assistance of Dr. J. Berger at Gif-Sur-Yvette in the week of August 28, 1961.

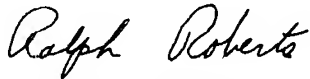
The "International Conference on Sensitivity and Hazards of Explosives," held in London on October 1, 2, 3, 1963 by G. K. Adams and E. G. Whitbread under sponsorship of the Explosives Research and Development Establishment, Waltham Abbey and the British Ministry of Aviation who financed publication of the proceedings.

The Symposium H. D. P. on "Behaviour of Dense Media under High Dynamic Pressures," sponsored by I. U. T. A. M. Paris, Sep. 1967 published by Dunod, Paris and Gordon and Breach, New York, 1968.

This volume was made possible through special funding by the Office of Naval Research. Details of the publication were ably handled by Mr. Irving Rudin of the Naval Research Laboratory.



SIGMUND J. JACOBS  
Naval Ordnance Laboratory



RALPH ROBERTS  
Office of Naval Research  
Cochairmen

## CONTENTS

<u>SESSION I - DETONATION AND RELATED FLOWS</u>	Page
FLASH X-RAY OBSERVATION OF MARKED MASS POINTS IN EXPLOSIVE PRODUCTS . . . . .	3
W. C. Rivard, D. Venable, W. Fickett, and W. C. Davis	
PRESSURE MEASUREMENTS FOR COMPOSITION B-3 . . . . .	13
W. C. Davis and Douglas Venable	
SHOCK VELOCITY MEASUREMENTS IN INERT MONITORS PLACED ON SEVERAL EXPLOSIVES . . . . .	23
R. L. Jameson and A. Hawkins	
DIVERGENT SPHERICAL DETONATION WAVES IN A SOLID EXPLOSIVE . . . . .	31
R. Chéret and G. Verdes	
A COMPARISON OF SPHERICAL, CYLINDRICAL AND PLANE DETONATION VELOCITIES IN SOME CONDENSED AND GASEOUS EXPLOSIVES . . . . .	41
C. Brochet, J. Brossard, N. Manson, R. Cheret, and G. Verdes	
DETONATION CHARACTERISTICS OF VERY LOW DENSITY EXPLOSIVE SYSTEMS . . . . .	47
James L. Austing, Allen J. Tulis, and Charles D. Johnson	
AN ANALYSIS OF THE "AQUARIUM TECHNIQUE" AS A PRECISION DETONATION PRESSURE MEASUREMENT GAGE . . . . .	59
J. K. Rigdon and I. B. Akst	
EFFECTS OF PRECOMPRESSION UPON THE DETONATION PROPERTIES OF LIQUID AND SOLID EXPLOSIVES . . . . .	67
W. H. Andersen, L. Zernow, A. L. Mottet, Jr., and R. R. Randall	
<u>SESSION II - UNSTEADY DETONATIONS AND DETONATION STRUCTURE</u>	
THE STABILITY OF LOW-VELOCITY DETONATION WAVES . . . . .	81
R. W. Watson, J. Ribovich, J. E. Hay, and R. W. Van Dolah	
FAILURE DIAMETER, SENSITIVITY AND WAVE STRUCTURE IN SOME BIS-DIFLUOROAMINO ALKANES . . . . .	89
L. B. Seely, Joseph G. Berke, Robert Shaw, Derek Tegg, and Marjorie Evans	
THE FAILURE DIAMETER THEORY OF DREMIN . . . . .	99
Julius W. Enig and Francis J. Petrone	
WALL TRACES OF DETONATION IN NITROMETHANE-ACETONE MIXTURES . . . . .	105
P. A. Urtiew and A. S. Kusubov	
A PHOTOGRAPHIC TECHNIQUE FOR MAPPING FAILURE WAVES AND OTHER INSTABILITY PHENOMENA IN LIQUID EXPLOSIVES DETONATION . . . . .	115
Per-Anders Persson and Gert Bjarnholt	

ON THE DYNAMICS OF SHOCK INTERSECTIONS . . . . .	119
A. K. Oppenheim, J. J. Smolen, D. Kwak, and P. A. Urtiew	
METAL ACCELERATION BY COMPOSITE EXPLOSIVES . . . . .	137
M. Finger, H. C. Hornig, E. L. Lee, and J. W. Kury	
LIGHT EMISSION DURING INITIATION OF LIQUID EXPLOSIVES . . . . .	153
Per-Anders Persson and T. Sjölin	
DARK WAVES IN LIQUID EXPLOSIVE SYSTEMS: THEIR ROLE IN DETONATION FAILURE . . . . .	169
Richard W. Watson	

### SESSION III - NON-STEADY REACTIVE SHOCKS

NUMERICAL CALCULATIONS OF DETONATION FAILURE AND SHOCK INITIATION . . . . .	177
Charles L. Mader	
THE ROLE OF THE MATRIX IN DETERMINING THE SHOCK INITIATION CHARACTERISTICS OF COMPOSITIONS CONTAINING 60% BY VOLUME OF HMX. .	185
W. W. Marshall	
EFFECT OF PULSE DURATION ON THE IMPACT SENSITIVITY OF SOLID EXPLOSIVES . . . . .	191
B. D. Trott and R. G. Jung	
SHOCK SENSITIVITY, A PROPERTY OF MANY ASPECTS . . . . .	207
Donna Price	
SHOCK SENSITIVITY AND SHOCK HUGONIOTS OF HIGH-DENSITY GRANULAR EXPLOSIVES . . . . .	219
Julius Roth	
EXPERIMENTAL STUDY OF THE TRANSITION FROM BURNING TO DETONATION . . . . .	231
J. Calzia and H. Carabin	
SHOCK INITIATION OF NITROMETHANE, METHYL NITRATE, AND SOME BIS DIFLUORAMINO ALKANES . . . . .	237
J. G. Berke, R. Shaw, D. Tegg, and L. B. Seely	
THE ROLE OF INTERSTITIAL GAS IN THE DETONATION BUILD-UP CHARACTERISTICS OF LOW DENSITY GRANULAR HMX . . . . .	247
W. W. Marshall	
THE SHOCK HUGONIOT OF UNREACTED EXPLOSIVES . . . . .	251
V. M. Boyle, W. G. Smothers, and L. H. Ervin	
EFFECT OF PARTICLE SIZE ON SHOCK INITIATION OF PETN, RDX, AND TETRYL . . . . .	259
Calvin L. Scott	
EXPLOSIVE BEHAVIOR OF METHYLNITRATE AND ITS MIXTURES WITH LIQUID DILUENTS . . . . .	267
M. Kusakabe and S. Fujiwara	

#### SESSION IV - MOSTLY INITIATION BY NON-SHOCK STIMULI

THE THERMAL INITIATION AND GROWTH OF REACTION IN SECONDARY EXPLOSIVES UNDER TRANSIENT CONFINEMENT . . . . .	279
K. Beedham, A. S. Dyer, and W. I. Holmes	
INITIATION OF DETONATION BY FRICTION ON A HIGH EXPLOSIVE CHARGE . . . . .	291
Alan S. Dyer and John Watson Taylor	
DEFLAGRATION IN SINGLE CRYSTALS OF LEAD AZIDE . . . . .	301
M. M. Chaudhri and J. E. Field	
THE INFLUENCE OF SURFACE MELTING OF CRYSTALS ON THE BURNING OF SOLID EXPLOSIVE UNDER RISING PRESSURE CONDITIONS . . . . .	311*
John Watson Taylor	
DEFORMATION OF A CYLINDER OF EXPLOSIVE MATERIAL IN UNCONFINED IMPACT . . . . .	313
H. S. Napadensky, T. V. Eichler, C. A. Kot and T. A. Zaker	
DECOMPOSITION OF A SHOCKED SOLID EXPLOSIVE . . . . .	321
B. G. Craig and E. F. Marshall	
THERMAL DECOMPOSITION OF HIGH EXPLOSIVES AT STATIC PRESSURES 10-50 KILOBARS . . . . .	331
E. L. Lee, R. H. Sanborn, and H. D. Stromberg	
EXPERIMENTAL OBSERVATIONS OF INITIATION OF PRIMARY EXPLOSIVES BY A HOT WIRE . . . . .	339
Howard S. Leopold	

#### SESSION V - EXPERIMENTAL TECHNIQUES

EQUATION-OF-STATE INVESTIGATION OF GRANULAR EXPLOSIVES USING A PULSED ELECTRON BEAM . . . . .	351
J. H. Shea, A. Mazzella, and Louis Avrami	
CREATION OF AN INTENSE SHOCK IN SOLID DEUTERIUM BY A PULSED LASER BEAM — REQUIREMENTS FOR HUGONIOT DATA MEASUREMENTS . . . . .	361
C. Fauquignon	
QUARTZ GAUGE TECHNIQUE FOR IMPACT EXPERIMENTS . . . . .	369
G. E. Ingram and R. A. Graham	
SHOCK-INDUCED ELECTRICAL SIGNALS FROM DIELECTRICS . . . . .	387
G. E. Hauver	
THE MECHANISM OF ELECTRICAL CONDUCTIVITY OF LIQUID DIELECTRICS IN SHOCK WAVES . . . . .	399
A. N. Dremin and V. V. Yakushev	
ELECTRICAL EFFECT OF BIMETALLIC AND METAL SEMICONDUCTOR JUNCTIONS UNDER SHOCK . . . . .	403
J. Jacquesson, J. P. Romain, M. Hallouin, and J. C. Desoyer	

\*Abstract Only

EXPERIMENTAL STUDY OF THE ELECTROMAGNETIC VELOCITY-GAGE TECHNIQUE . . . . .	413
Sigmund J. Jacobs and David J. Edwards	
DETERMINATION OF CONSTITUTIVE RELATIONSHIPS WITH MULTIPLE GAGES IN NON-DIVERGENT WAVES . . . . .	427*
M. Cowperthwaite and R. F. Williams	
SHOCK-INDUCED ELECTRICAL POLARIZATION OF A SOLID EXPLOSIVE . . . . .	429
J. Morvan and H. Pujols	
QUARTZ GAUGE STUDY OF UPSTREAM REACTION IN A SHOCKED EXPLOSIVE . . . . .	435
J. E. Kennedy	
MEASUREMENT OF MASS MOTION IN DETONATION PRODUCTS BY AN AXIALLY-SYMMETRIC ELECTROMAGNETIC TECHNIQUE . . . . .	447
B. Hayes and J. N. Fritz	
 <u>SESSION VI - FLOW DYNAMICS AND THERMODYNAMICS</u>	
EXPLOSIVE DEFLECTION OF A LINER AS A DIAGNOSTIC OF DETONATION FLOWS . . . . .	457
M. Défourneaux and L. Jacques	
ELASTIC-PLASTIC BEHAVIOUR OF POROUS BERYLLIUM . . . . .	467
G. Eden and C. P. M. Smith	
NUMERICAL ANALYSIS OF A DIVERGING SHOCK WAVE IN PLEXIGLAS CYLINDERS . . . . .	477
Minao Kamegai and John Erkman	
A CODE METHOD FOR CALCULATING HYDRODYNAMIC MOTIONS IN HE DETONATIONS . . . . .	487
Charles E. Needham	
A REALISTIC APPROACH FOR DESCRIBING THE EXPLOSION-GENERATED AXI-SYMMETRIC WAVE PROPAGATING IN A HALF-SPACE . . . . .	493
A. Sakurai	
THE COMPUTATION OF GENERAL PROBLEMS IN ONE DIMENSIONAL UNSTEADY FLOW BY THE METHOD OF CHARACTERISTICS . . . . .	501*
B. D. Lambourn and N. E. Hoskin	
EQUATION OF STATE OF DETONATION PRODUCTS . . . . .	503
H. C. Hornig, E. L. Lee, M. Finger, and J. E. Kurrle	
OPTICAL PROPERTIES OF DETONATION WAVES (OPTICS OF EXPLOSIVES) . . . . .	513
M. Busco	
HYDRODYNAMIC BEHAVIOR AND EQUATION OF STATE OF DETONATION PRODUCTS BELOW THE CHAPMAN-JOUGUET STATE . . . . .	523
L. A. Roslund and N. L. Coleburn	
SHOCKED STATES OF FOUR OVERDRIVEN EXPLOSIVES . . . . .	533
J. H. Kineke, Jr. and C. E. West, Jr.	

\* Abstract Only

SESSION VII - EXPERIMENTS ON SHOCKS AND FLOWS

VAPORIZING OF URANIUM AFTER SHOCK LOADING . . . . .	547
Ph. de Beaumont and J. Leygonie	
OBSERVATIONS OF DETONATION IN A HIGH VACUUM . . . . .	559
J. E. Hay, W. C. Peters, and R. W. Watson	
PLANE SPALLING OF COPPER . . . . .	567
F. David, J. Vacellier, F. Prouteau, J. Legrand, and R. Chéret	
SPALLING UNDER OBLIQUE IMPACT . . . . .	573
I. C. Skidmore and J. W. Lethaby	
INTERACTIONS OF SPHERICAL SHOCK WAVES IN WATER . . . . .	581
N. L. Coleburn and L. A. Roslund	
THE SPEED OF PROPAGATION OF RELEASE WAVES IN POLYMETHYL METHACRYLATE . . . . .	589
Karl W. Schuler	
ARTIFICIAL VISCOSITY METHOD CALCULATION OF AN UNDERWATER DETONATION . . . . .	597*
H. M. Sternberg and W. A. Walker	
SPHERICAL EXPLOSIONS IN WATER . . . . .	599
L. W. Hantel and W. C. Davis	
LIST OF ATTENDEES . . . . .	605
AUTHOR INDEX . . . . .	611

\*Abstract Only



## **Session I**

# **DETONATION AND RELATED FLOWS**

Chairman: I. C. Skidmore  
*Atomic Weapons Research Establishment*

# FLASH X-RAY OBSERVATION OF MARKED MASS POINTS IN EXPLOSIVE PRODUCTS

W. C. Rivard, D. Venable, W. Fickett, and W. C. Davis  
*University of California, Los Alamos Scientific Laboratory*  
*Los Alamos, New Mexico 87544*

## ABSTRACT

The flow behind a plane detonation wave in composition B-3 ( $\rho_0 = 1.730$  g/cc, 60/40 RDX/TNT) is examined by radiographically observing the motion of  $12.5 \mu\text{m}$  thick metal foils embedded in 10 cm cubes of explosive. The position  $x_f$  of each foil as a function of its initial position  $x_i$ , and time  $t$ , together with the detonation front position  $X(t)$  is sufficient to determine the density, particle velocity, pressure, and internal energy throughout the flow with no a priori assumption of an equation of state. A simple analytic representation of  $x_f(x_i, t)$  consistent with the classical Chapman Jouguet/Taylor wave model accurately describes all the data. The front pressure is found to be  $275 \pm 4$  kbar. An alternate model representing a slightly unsteady detonation wave describes the data equally well.

## INTRODUCTION

The PHERMEX flash x-ray machine at Los Alamos has given us for the first time a long-needed direct quantitative look at the one-dimensional flow behind a plane detonation wave in a large-diameter charge, and a new determination of the state at the front. A sequence of radiographs records at discrete times the position of the detonation front and of mass elements marked by tantalum foils embedded in the explosive. Electrical signals from the passage of the wave over the foils give a separate measurement of the detonation velocity. The experimental setup and a typical radiograph are shown in Fig. 1. The x-ray beam axis is perpendicular to the direction of detonation in a 10 cm cube of Composition B-3 explosive (the HE) which is initiated by a large diameter plane-wave lens. (Since the machine can be flashed only once during the passage of the detonation wave, the time sequence is obtained from repeated experiments with the HE as nearly identical as possible.) The range of front positions recorded is 5 to 10 cm.

The radiographs show an adequately large central region of one-dimensional flow not yet

affected by the incoming side rarefactions. We confine our attention to this region and treat the flow as one-dimensional and laminar. Thus all results are averages over any fine-scale structure due to transverse waves on the front or to the granular nature of the material.

A density profile is obtained directly from each radiograph. Least-squares fitting of a continuous function to the measured final foil positions  $x_f$  as a function of their initial positions  $x_i$  gives the density distribution by differentiation:

$$\rho_0/\rho = dx_f/dx_i. \quad (1)$$

Evaluation of the density at the front, together with the Rankine-Hugoniot relations and the measured front velocity, determines the pressure and particle velocity there. In practice, this requires an additional assumption, which will be made throughout. Since the reaction zone is much smaller than the foil spacing, the reaction is treated as instantaneously complete within the shock transition, and the final state to which the Rankine-Hugoniot equations apply is taken to be the equilibrium state at the end of the reaction zone. No evidence of a reaction

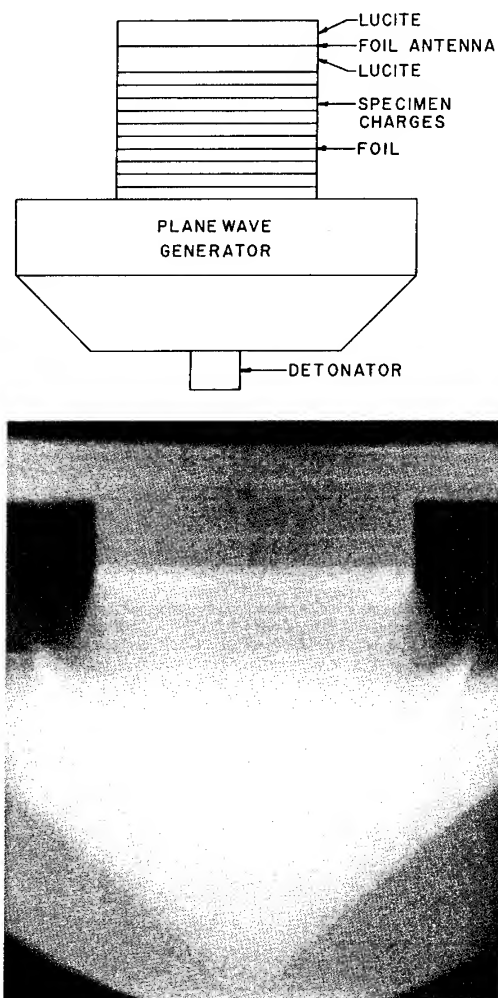


Fig. 1 - Experimental arrangement and radiograph

zone can be detected either in the analysis of the foil data or on the radiographs.

Additional information is obtained from the sequence of radiographs by fitting a function  $x_f(x_i, t)$  to the entire collection of data. Partial differentiation of this function with respect to  $t$  at constant  $x_i$  (that is, along a particle path) gives the particle velocity field. Finally, with one additional assumption, the pressure and internal energy in the interior can be determined by applying the equations for conservation of momentum and energy. The additional assumption, probably quite good for this flow, is that viscous forces and other transport processes can be neglected.

The classical detonation model consisting of a front moving at the constant Chapman-Jouguet

(CJ) velocity followed by a centered rarefaction (Taylor) wave is found to represent the data within experimental error. Figure 2 shows a portion of the flow in the  $x - t$  plane according to this model, together with the measured foil and front positions. The CJ pressure obtained here is significantly lower than that given by the conventional method of measuring the free-surface velocity of driven plates.

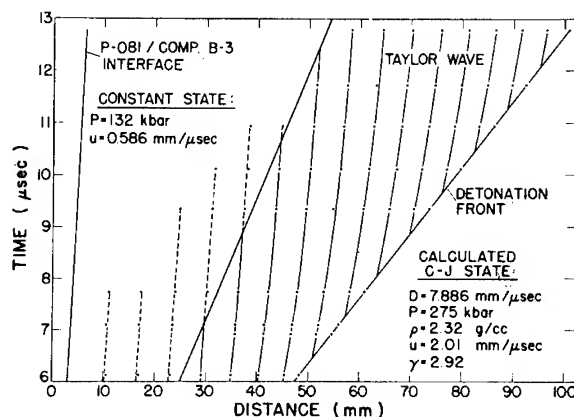


Fig. 2 - Measured foil and front positions in the  $x - t$  plane. The detonation wave crosses the lens/HE interface at  $x = t = 0$ . The curves connecting the points are from a fit to the data.

Details not included in this paper are given in a separate report (1).

## EXPERIMENT

A typical experimental assembly, represented schematically in Fig. 1, is made up of precisely machined blocks of explosive with tantalum foils between blocks. A plane-wave generator is used to initiate the detonation so that the wave is parallel to the plane of each foil. The HE slabs,  $10 \times 10 \times 0.635$  cm, are Composition B-3,  $60 \pm 1.5\%$  RDX,  $40 \pm 1.5\%$  TNT by weight, of density  $1.730 \pm 0.001$  g/cc. The slabs are held to a dimensional tolerance of  $\pm 0.005$  cm in parallelism,  $\pm 0.0125$  cm in thickness, and  $\pm 0.025$  cm in other dimensions. Individual pieces are selected and oriented for the assembly with respect to both dimensions and parallelism so that tolerance build-up is avoided. The assemblies are clamped and measured after clamping to be certain that no gaps are present. The plane-wave generators are 20 cm in diameter, with an inner charge of baratol. All generators are from the same production lot. The tantalum foils, all from the

same roll, are  $12.5 \mu\text{m}$  thick. The total mass of the tantalum is at most 2% of the mass of the HE. Thicker slabs of HE are used in the assembly (for economy) in the regions where foils cannot be observed satisfactorily. The data points plotted in Fig. 2 show the positions of the foils in the several shots.

The PHERMEX machine (2) produces a pulsed beam of electrons of 27 MeV energy and  $0.1 \mu\text{sec}$  duration, which is focused to a spot less than 1 mm diameter on a tungsten target. The x-rays produced in the target cast a sharp shadow of the assembly containing the embedded foils upon a photographic film. Radiation exposure of 25 R at 1 m is adequate to produce high-contrast images with source-to-object distance 3 m and source-to-film distance 3.75 m. The distances are carefully measured and controlled to give accurate magnification. The positions of the images of the foils on the developed films are measured with a comparator. The foils and the front can be located to  $\pm 0.1 \text{ mm}$ .

Since the foils are all parallel, and the x-rays are generated at a point, only one foil of the set can be in a plane which goes through that point. Therefore, only one foil can produce a sharp image, and all the others are slightly distorted because they are viewed at an angle. In practice, this limits the region over which useful measurements can be made, and makes it impossible to obtain information about the entire charge in one shot. The corrections to the measured positions are negligible in the region used.

Detonation wave velocity is measured using a method developed by Hayes (3), which detects the electrical signals generated when the detonation reaches a foil. The arrival times are determined to  $\pm 3 \text{ nsec}$ . No change of detonation velocity with distance can be detected in any shot. The measured velocities from eight shots have a range of  $\pm 1/2\%$  and a mean of  $7.886 \text{ mm}/\mu\text{sec}$  whose estimated standard deviation is  $\pm 0.1\%$ .

## THEORY

In this section we consider the implications of complete knowledge of the functions

$$x_f = x_f(x_i, t), \quad X = X(t) \quad (2)$$

where  $x_f$  is the position at time  $t$  of the fluid element initially at position  $x_i$ , and  $X$  is the position of the detonation front. Our experimental data are of course a discrete sample of these functions.

To get the conditions at the front we make use of the Rankine-Hugoniot equations across the front

$$\rho_0 D = \rho(D - u) = p/u = \sqrt{2(E - E_0)/(v_0 - v)}$$

$$D = dX/dt \quad (3)$$

with subscript 0 denoting the initial state, with neglect of  $p_0$ , and with velocities stated in the laboratory frame (that of the undisturbed material). For the interior flow we assume that the inviscid (Euler) equations apply:

$$x_h = \rho^{-1}, \quad x_t = u, \quad p_h = -u_t, \quad E_t = -pv_t \quad (4)$$

$$v = \rho^{-1}, \quad h = \rho_0 x_i, \quad x = x_f.$$

The subscript notation is used for partial differentiation. The independent variables are  $h$  and  $t$ , with  $h$  the material (Lagrangian) coordinate which labels a mass element. The calculation of  $\rho$  and  $u$  is direct and their values at the front used in the Rankine-Hugoniot relations furnish initial conditions for the  $p$  and  $E$  integration (the partial differentiations becoming ordinary differential equations along lines of constant  $t$  for  $p$ , and constant  $h$  for  $E$ ). The sound speed is given by

$$c^2 = (\partial p / \partial \rho)_h = p_t / \rho_t \quad (5)$$

If the classical detonation model with its self-similar rarefaction wave is correct, the analysis is simpler because there is only one independent variable  $x/t$ . The assumptions of this model are: (1) initiation to the constant CJ detonation velocity is instantaneous and the reaction zone thickness is negligible, and (2) the discontinuous front moves at the constant velocity given by the Chapman-Jouguet (CJ) hypothesis, which states that the flow immediately behind the front is sonic in a frame attached to the front, i.e.,  $D = u + c$ . In consequence, the flow is isentropic and (for back boundary velocity less than  $u_{CJ}$ ) a centered simple rarefaction wave (Taylor wave) is attached to the front. For constant back boundary (lens/HE interface) velocity the flow region following the tail of the rarefaction is a uniform constant state, and the entire flow depends on the single independent variable  $x/t$ . This is approximately the case in our experiment.

It is convenient to introduce the dimensionless variables

$$y = x_f/Dt \quad \text{and} \quad Y = x_i/Dt, \quad (6)$$

with  $D$  the constant detonation velocity. The given function  $x_f(x_i, t)$  then takes the form  $y(Y)$  and the given function  $X(t)$  becomes just  $Dt$ . The forward characteristics along which the flow state is constant are just rays of constant  $y$ . The flow equations are

$$\rho = \rho_0 (dy/dY)^{-1}, \quad c = (\rho_0/\rho) DY, \\ u = Dy - c, \quad dp/dY = c^2 d\rho/dY. \quad (7)$$

The second and third of these equations will be recognized as the equations of the forward characteristics in  $x-t$  and  $h-t$  space,  $dx/dt = u + c$  and  $dh/dt = \rho c$ . The analysis is straightforward:  $\rho$ ,  $c$ , and  $u$  are calculated directly, and  $p$  is calculated by integrating the last equation with the initial value at the shock obtained as before.

#### DATA ANALYSIS

The first step in analyzing the data is to choose one or more fitting forms. The simplest reasonable ones are those based on the classical model. With their single independent variable  $x/t$  or  $h/t$  and concomitant minimum number of adjustable parameters, they are the natural choice, provided they reproduce the data within experimental error. We want to test the classical model in any case, since it is so widely used with considerable practical success. We therefore employ it in the initial examination of the data.

The classical model requires that the detonation velocity be constant, the reaction zone thickness negligible, and the flow self-similar. As stated earlier, the measured detonation velocity is constant within experimental error in the experimental region. The reaction zone thickness of a small fraction of a millimeter estimated from other experiments (4) is consistent with our failure to detect it here, and is small enough to make its neglect a good approximation. The next step then is to plot the data with appropriate scaling to see if the flow appears to be self-similar and thus dependent on a single independent variable. This is done in Fig. 3. The curve is a two-piece fit to all of the data, described below. Although this is not the most sensitive test, it is clear that the classical model is at least approximately correct. We therefore proceed to apply and test it carefully. We first look to see if there is any significant trend with distance of run; none is found. We then try to fit the data with forms  $y(Y)$  consistent with the classical model. This is successful, with a number of different

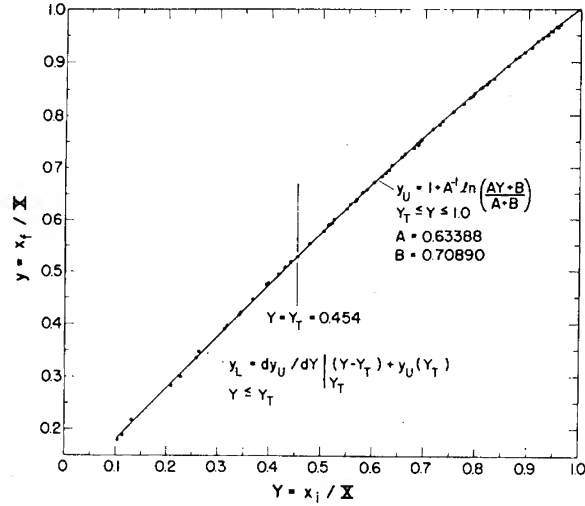


Fig. 3 - Final foil position  $x_f$  vs initial foil position  $x_i$ , both divided by  $X$ , the position of the front at the time of measurement of  $x_f$ . The points are the experimental data, the curve a fit.

choices reproducing the data within experimental error.

We begin by fitting the data for the individual shots (each being associated with a given length of run) and look for any trend with length of run. For convenience we use a fit of the form  $y(Y)$  but emphasize that in applying it to a single shot, we are freed completely from the assumptions of the classical model, for at a fixed time this is equivalent to  $x_f(x_i)$  which is sufficient to determine the density profile and thus the complete state at the front. Other flow variables cannot of course be determined in the interior without an additional assumption such as that of self-similar flow. We first provisionally pool the data from all shots and locate the tail characteristic of the rarefaction wave as described below. The points of each shot lying within the rarefaction wave are then fit with the form

$$y = 1 + A^{-1} \ln [(AY + B)/(A + B)], \\ \rho/\rho_0 = AY + B, \quad (8)$$

constructed to pass through the front at  $y = Y = 1$ . Figure 4 shows the front state as a function of run length. A linear fit of  $p(X)$  indicates a slight upward trend, with the pressure rising from 268 kbar at 50 mm to 282 kbar at 100 mm. Statistically, however, this increase does not differ significantly from zero, so we proceed with the analysis under the assumptions of the classical model, deferring further consideration of the possible increase until later.

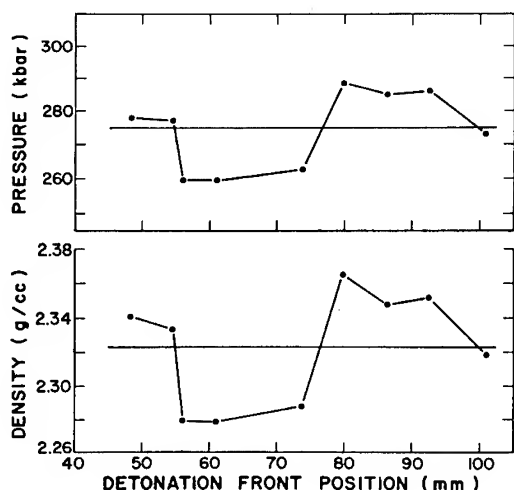


Fig. 4 - Front state vs run length from the foil data for individual shots

We now proceed to fit the pooled data for all of the shots with a  $y(Y)$  form. This must be constructed of two pieces,  $y_U$  and  $y_L$  in Fig. 3, with the changeover point  $Y_T$  the value of  $Y$  at the tail of the rarefaction where the first derivatives of the state variables are discontinuous. The form given by Eq. (8) is used for the rarefaction wave and a linear function for the approximately constant-state region behind it. The dividing point is found by examining a sequence of trial values of  $Y_T$  and choosing the one for which the densities at the tail given by the fits in the two regions agree. The constant state and  $Y_T$  are given in Figs. 2 and 3. The overall results are not sensitive to the value of  $Y_T$ . From here on we consider only the 53 foil-position data points (the total number from all nine shots) lying within the rarefaction wave.

The data points from the different shots are pooled and fit to the two-parameter functional form given by Eq. (8). This fit reproduces the data within experimental error. More precisely, the deviation of every data point but one from the fit is less than twice the estimated standard deviation of its reading error. The exception is about three standard deviations away.

Before proceeding to the discussion of error estimates and other possible choices for the fitting form, we digress briefly to consider possible alternatives to the CJ hypothesis. The CJ condition is incorporated into the analysis by placing the lead characteristic of the rarefaction wave in coincidence with the front. In

considering the alternatives, we continue to suppose that the reaction is essentially instantaneous so that the detonation Hugoniot curve for complete reaction exists but that the state point lies not at the CJ (tangent) point but either above it on the strong branch or below it on the weak branch. The strong point is rejected on the grounds that the expected decrease in pressure and velocity as the rarefaction wave overtakes the front is not observed. The possibility of a weak state is suggested by observations of gas detonations which show that the flow immediately behind the front, while not one-dimensional in the small, is on the average supersonic with Mach number 1.10 to 1.15 (5, 6). Possible mechanisms for steady reaction zone solutions which terminate at a weak point, with a constant velocity determined by details of the kinetics, have been described (7, 8). Finally, a constant velocity front with instantaneous transition to a weak state produces a flow which is self-similar with the exception of the constant-state region of increasing width which must be present between the front and the head of the rarefaction wave. To see how far the state point might be displaced along the weak branch, we have tried fitting the data assuming constant-state regions of varying width  $\Delta Y$  behind the front. For  $\Delta Y = 0.02$ , which places the rear edge of the constant-state region near the foil closest to the front, the Mach number is 1.03, the CJ pressure is reduced 3% below that for  $\Delta Y = 0$ , and the standard deviation of the fit (SDF), defined as

$$\text{SDF} = \left[ \frac{1}{51} \sum_{i=1}^{53} (y_c(Y_i) - y_e(Y_i))^2 \right]^{1/2} \quad (9)$$

with sub c and sub e for calculated and experimental points, is increased only trivially (less than 0.1%). For  $\Delta Y = 0.10$ , for which the constant-state region includes 13 foils, the Mach number is 1.15, the CJ pressure is decreased by 12%, and the SDF is increased by 13%. It is thus less likely that we have a weak detonation with Mach number this large, but a weak detonation with Mach number a few per cent larger than unity with corresponding lower front pressure cannot be excluded.

We now turn to the question of error estimates and the possible choices for the fitting form. To remove the bias inherent in the arbitrary choice of a single form and to provide additional information about the error, we have tried a total of 11 different two-parameter forms. Measured by the SDF, essentially the only criterion available, these are all equally good. For a single fitting form the SDF is 0.0017 and the estimated standard deviation

(SD) of the density at the front (computed from the fit) is  $\pm 0.4\%$ . The corresponding SD of the pressure, taking into account the small error in  $D$ , is about three times as large, or  $\pm 1.2\%$ . The percentage SD of the flow variables of interest varies little in passing from front to rear through the flow. The collection of values of density at the front given by the different fitting forms has a range of  $\pm 1.5\%$  (with corresponding pressure range of  $\pm 4.5\%$  or  $\pm 12$  kbar), and a mean value whose estimated SD is  $\pm 0.3\%$ . A related collection of three-parameter forms gives essentially the same mean value, with a larger estimated SD for a single fit and a smaller SD for the mean of the collection. But in every case, all elements of the matrix of correlation coefficients are near unit magnitude, indicating that a two-parameter form is adequate.

As our final result for the CJ state we give the state variables computed from the mean front density of the collection of two-parameter forms. The form given by Eq. (8) is centrally located in the collection, and is chosen as a compact representation of the flow. The errors quoted are estimated SD's arising from a combination of two approximately equal errors: that due to the scatter of the data as estimated by the SD of the density computed from a single fit, and that due to the uncertainty in the choice of fitting form as estimated by the computed SD of the mean of the densities given by the different forms. These are treated as independent, with the final SD for density of  $0.5\%$  given by the square root of the sum of the squares of these two. We are unable to arrive at any useful estimate of systematic errors.

Returning to the question of a possible trend with run length, we describe a limited study with more general fitting forms not subject to the restrictions of the classical model. For three of the two-parameter forms, we replace each coefficient by a linear function of time, thus converting these to four-parameter forms, and use the general analysis described earlier. The result is that the front pressure increases with run length by about the same amount found in fitting the individual shots, i.e., 14 kbar over 50 mm of run, with the mean value that given by the classical model. Again, the slope is not distinguished statistically from zero. Pressure is calculated from the indicated front density using a constant detonation velocity. Strictly speaking, this is inconsistent with our assumption of instantaneous reaction which confines the state point to the complete-reaction Hugoniot. But using any reasonable approximation to the Hugoniot to compute pressures from densities would give essentially the same result,

and (provided we are in the neighborhood of the CJ point) a corresponding variation in  $D$  of less than  $0.1\%$ , well within its experimental error.

## RESULTS

The classical CJ model of a detonation with a constant velocity lens/HE interface reproduces the results of the experiment within experimental error. The numerical values based on this model are summarized in Table 1. They are the central values from a collection of 11 different two-parameter forms, all of which fit the data equally well. They have the form  $y(Y)$ ;  $y = x_f/tD$ ,  $Y = x_i/tD$ , with  $x_i$  the initial position of a fluid element,  $x_f$  its position at time  $t$ , and  $tD (= X)$  the front position. The centrally located form given by Eq. (8) is presented in the table as an analytic representation of the flow. The errors are estimated standard deviations taking into account both experimental error and uncertainty in the choice of fitting form, as described above. There are 51 degrees of freedom in the data analysis, with the exception of  $D$  for which there are seven.

The data are fit equally well by several four-parameter forms not incorporating the assumptions of the classical model. The result from these is that the front pressure increases by 14 kbar over 50 to 100 mm of run, with the average value about the same as that given by the classical model analysis. The increase, however, is not statistically distinguished from zero.

All results presented are for explosive with embedded foils. For the same explosive without foils, the extrapolated infinite-medium detonation velocity is  $7.977$  mm/ $\mu$ sec, but a measurement by Hayes (9) on a system identical to that used here but with foils omitted gives  $7.915$  mm/ $\mu$ sec,  $0.4\%$  higher than the corresponding value with foils in Table 1. Pressure measurements made by the conventional driven-plate method on charges with and without foils give a pressure 1 to  $2\%$  higher without foils.

## COMPARISON WITH OTHER WORK

We compare our experimental results with those calculated from the isentropes of three widely used detonation-product equations of state calibrated to experimental data. These are the  $\gamma$ -law, as calibrated by Deal (10,11), the JWL (Jones-Wilkins-Lee) as calibrated by Lee, Hornig, and Kury (12), and the BKW-HOM, calibrated by Mader (13). These equations of state, particularly the latter two, are compact

HE:	Composition B-3, $\rho_0 = 1.730$ g/cc, RDX/TNT 60/40 weight %		
Front:	$D = 7.886 \pm 0.008$ mm/ $\mu$ sec	$\rho = 2.32 \pm 0.01$ g/cc	$c = 5.87 \pm 0.03$ mm/ $\mu$ sec
	$p = 275 \pm 4$ kbar	$u = 2.01 \pm 0.03$ mm/ $\mu$ sec	$\gamma = 2.92 \pm 0.05$
Fit:	<p>Given <math>y(Y)</math> ; <math>\rho_0/\rho = dy/dY</math> , <math>c/D = Y\rho_0/\rho</math> , <math>u/D = y - c/D</math> , <math>dp/dY = c^2 d\rho/dY</math></p> <p><math>y = 1 + A^{-1} \ln [(AY + B)/(A + B)]</math> , <math>\rho/\rho_0 = AY + B</math> ,</p> <p><math>p/\rho_0 D^2 = A^{-2} V^{-1} + 2BA^{-2} \ln V - B^2 A^{-2} V + 1 - 2A^{-1} + 2BA^{-2} \ln (A + B)</math> , <math>V = v/v_0</math></p> <p><math>A = 0.63388 \pm 0.019</math> , <math>B = 0.70890 \pm 0.015</math> , (<math>P_{CJ} = 275</math> kbar)</p>		

We have taken what we believe, after consultation with the originators, to be the best current values of the parameters. For the sake of uniformity in comparison, we have imposed a small adjustment of the parameters so that each equation of state passes through the CJ point defined by the initial density and detonation velocity of Table 1 and Deal's CJ pressure (11) of 292 kbar. The values of the parameters used are given in Table 2. Profiles in a number of

The differences between this work and the JWL and BKW-HOM equations of state are in no way due to any limitation of the analytic representation which they use. The analytic forms

Form	$a_1$ or $\gamma$	$a_2$	$a_3$	$a_4$	$a_5$	$a_6$	SDF $\times 10^3$	$P_{CJ}$
$\gamma$ -law	2.6848 (2.5980)	—	—	—	—	—	3.9 (3.6)	292 (299)
JWL	12.095 (92.815)	-1.34	5099.6 (43074.0)	-4.2 (-8.1024)	76.783	-1.10	7.6 (1.8)	292 (268)
BKW-HOM	3.4918 (4.4186)	-2.3316 (0.26037)	.25961 (2.0275)	.028355	-.012436	—	3.4 (1.8)	292 (267)

$\gamma$ -law  $p = P_{CJ}(v/v_{CJ})^{-\gamma}$ ;  $v_{CJ} = \gamma/(\gamma + 1) \rho_0$ ,  $P_{CJ} = \rho_0 D^2/(\gamma + 1)$

JWL  $p = a_1 V^{a_2} + a_3 e^{a_4 V} + a_5 e^{a_6 V}$ ;  $V = v/v_0$

BKW-HOM  $\ln p = a_1 + a_2 \ln v + a_3 (\ln v)^2 + a_4 (\ln v)^3 + a_5 (\ln v)^4$

Coefficients are for  $p$  in kbar,  $v$  in cc/g.

Values in parenthesis are from fitting these forms to our foil data.



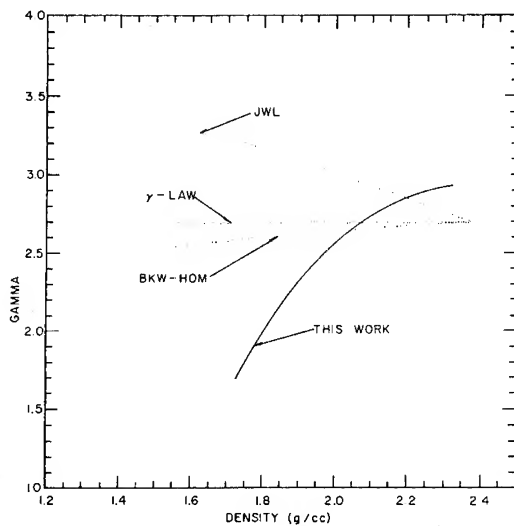
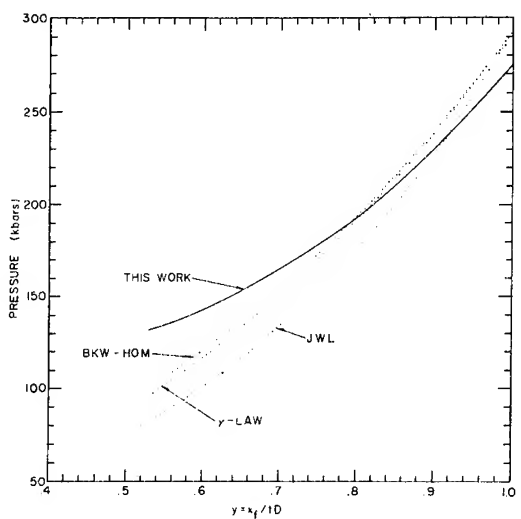
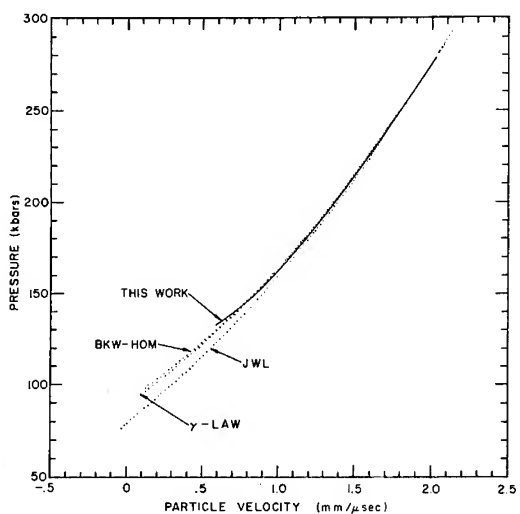
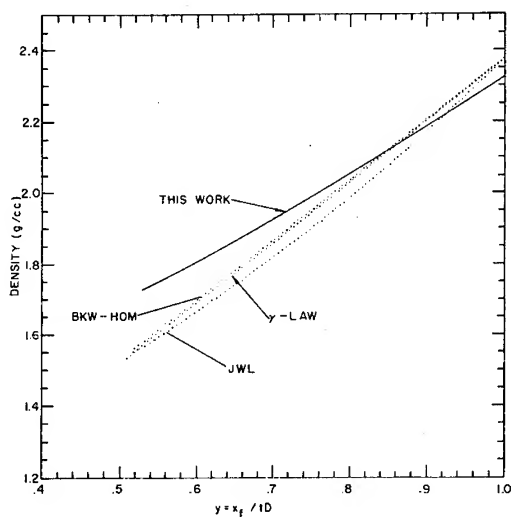
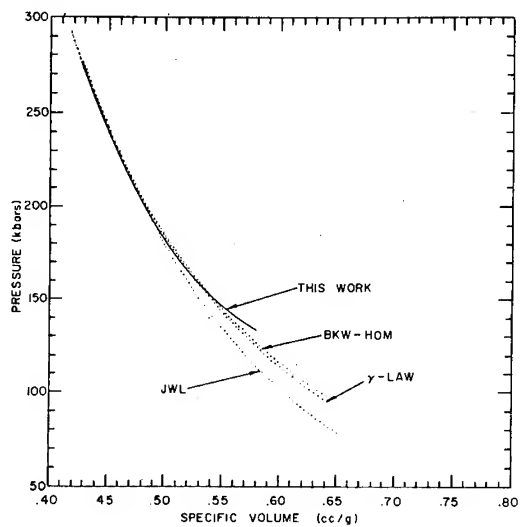
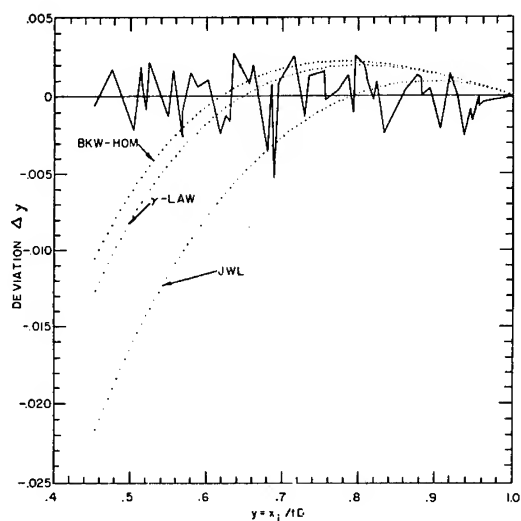


Fig. 5 - Comparison with previously calibrated equations of state

for their isentropes are in fact two members of our collection of two-parameter fitting forms referred to above. For this purpose two of the parameters of each are treated as independent adjustable parameters, a third is dependent on these two, and the rest are fixed at their previously calibrated values. Values of the constants so adjusted, the calculated  $p_{CJ}$ , and the corresponding SDF's, Eq. (9), are given in parenthesis in Table 2. Note that the  $\gamma$ -law form is too simple to represent our data within experimental error (with the single parameter  $\gamma$  treated as adjustable).

The CJ pressure obtained here from the analysis based on the classical model, 275 kbar, is significantly lower than the value 292 kbar reported by Deal (11). This difference is discussed in the following paper (14). Several questions remain unresolved. In the meantime, it should be remembered that the previously calibrated equations of state perform well in many practical calculations where the feature of principal interest is the motion of metal driven by the explosive. Recalibrating them to the present experiment without changing anything else would probably give poorer results.

#### REFERENCES

1. W. C. Rivard and D. Venable, Los Alamos Scientific Laboratory Report LA-4426 (1970).

2. D. Venable and T. Boyd, Fourth Symposium on Detonation (U. S. Government Printing Office, 1965), p. 639.
3. B. Hayes, J. Appl. Phys. 38, 507 (1967).
4. R. E. Duff and E. Houston, J. Chem. Phys. 23, 1268 (1955).
5. D. H. Edwards, T. G. Jones, and B. Price, J. Fluid Mech. 17, 21 (1963).
6. D. R. White, Phys. Fluids 4, 465 (1961).
7. W. W. Wood, Phys. Fluids 6, 1081 (1963).
8. J. J. Erpenbeck, Phys. Fluids 7, 1424 (1964).
9. B. Hayes, private communication.
10. W. E. Deal, Phys. Fluids 1, 523 (1958).
11. W. E. Deal, J. Chem. Phys. 27, 796 (1957).
12. E. L. Lee, H. C. Hornig, and J. W. Kury, Lawrence Radiation Laboratory Report UCRL-50422 (1968).
13. C. L. Mader, Los Alamos Scientific Laboratory Report LA-2900 (1963).
14. W. C. Davis and D. Venable, Fifth Symposium on Detonation, following paper.

#### DISCUSSION

Charles L. Mader  
Los Alamos Scientific Laboratory  
Los Alamos, New Mexico

One-dimensional numerical calculations have been performed using the SIN code\* to obtain an estimate of the effect of the Baratol lens on the rarefaction wave of the Composition B. Calculations for a system of 10.16 cm of Baratol and 9.928 cm of Composition B using the  $\gamma$  law or BKW equation of state indicated that the Baratol lens began to effect the rarefaction wave of the detonation products at a  $Y = X_1/tD$  of 0.7 and a pressure of 150 kbar. The calculations

including the effect of the Baratol lens resulted in improved agreement with the Phermex data.

ROBERT L. CONGER  
Abaris Co., 122 15th Street  
Del Mar, California

The experimental data indicates that the simple  $\gamma$  equation of state is as good as more complicated equations of state and that a  $\gamma$  decreasing from about 3 to about 1.4 would fit the experimental data well. Is that correct?

#### REPLY BY RIVARD

The answer to the first part of your question is no and to the second part, yes.

\*Charles L. Mader, Los Alamos Scientific Laboratory report LA-3720 (1967).

## PRESSURE MEASUREMENTS FOR COMPOSITION B-3

W. C. Davis and Douglas Venable  
*Los Alamos Scientific Laboratory*  
*University of California*  
*Los Alamos, New Mexico 87544*

### ABSTRACT

A new technique for measuring detonation pressure by using x-ray photography to trace the position of a rarefaction wave as a function of time is described. The pressure value obtained for Composition B-3 is compared with values obtained with other techniques. The values are  $\leq 268 \pm 6$  kbar with the new x-ray technique,  $275 \pm 4$  kbar using another new x-ray technique,  $292 \pm 5$  kbar using an old plate-push technique, and  $312 \pm 5$  kbar using a newer plate-push technique. No satisfactory explanation for the large range of values is presented. There seems to be no reason to choose one value as "correct" in preference to the others.

### INTRODUCTION

Measurements of detonation pressure in explosives have been of academic and practical interest for a long time. Most of these measurements have been made by using the explosive to drive an inert material and inferring the explosive pressure from the velocity of a surface of the driven inert. However, electromagnetic methods for determining the velocity of an embedded foil have been employed by some workers (1). The inverse method has also found favor by others (2). In the preceding paper a method for determining the motion of embedded foils with x-rays has been described. In this paper, we describe yet another x-ray method in which the measured quantity is the position of a rarefaction wave in the explosive products. This method, which apparently has not been used elsewhere, provides a measure of the particle velocity behind a detonation wave. We also collect measurements of detonation pressures for Composition B-3, and compare the values from different methods, finding a surprising range among the results.

With our new method, we trace the position of a rarefaction wave propagating into the explosive products. In a later section of this paper we describe how an upper limit of the detonation pressure can be inferred from the

rarefaction velocity. The value obtained by this method is  $268 \pm 6$  kbar.

In the preceding paper, Rivard et al (3) describe experiments in which thin metal foils embedded in the explosive serve to mark mass points so they can be seen by dynamic radiography. Each of these experiments gives uniquely the density of the explosive products throughout the flow, from which the pressure can be inferred. Here we are interested in only the pressure at the front. The value obtained is  $275 \pm 4$  kbar.

The flash gap technique used by Deal (4) to measure the free-surface velocity of driven inert plates has also been used to infer the detonation pressure in Composition B-3. The flash gaps are covered with a thin steel shim which is driven by the moving plate, and this shim compresses gas between it and a transparent plastic plate. The light flash from the hot gas is recorded with a smear camera. The value inferred by this method is  $292 \pm 5$  kbar.

Another technique, which we call the reflection-change flash-gap technique, has also been used to determine the velocity of driven plates. The arrival of the shock at the surface is detected by the change in reflectivity of the surface, and the time-of-flight through a known

distance by the flash produced as the plate hits a piece of plastic. This technique has also been applied both to Composition B-3 in large cross-section pieces, and to the same explosive with foils embedded between layers, exactly as used by Rivard et al (3). The foils have a small effect on the velocity of a driven plate. The pressure inferred by this method is  $312 \pm 5$  kbar.

The inverse method (2), using the measured variation of detonation velocity with initial density and a value of  $\alpha$  assumed as usual to be exactly  $1/4$ , gives a pressure of 289 kbar. There is no way to guess how accurate this value may be.

The differences among the values of detonation pressure inferred from these five methods are very disturbing. We have no explanation for their existence. Table 1 is a compilation of the measured values. It is observed that there is a disagreement between values obtained from similar techniques, and we note that the inferred pressures from free-surface velocity measurements are higher than those from the x-ray methods by 10 to 18%. Although it may be coincidence, it is interesting to recall that a similar difference was found by Davis, Craig, and Ramsay (5) when they compared the inverse method and the free-surface velocity method for nitromethane and TNT. They found the pressure from the free-surface velocity measurements was about 15% higher than that from the inverse method. They interpreted their result as showing a failure of the Chapman-Jouguet theory; perhaps the difficulty is really that we do not know how to make true pressure measurements.

TABLE 1  
Measured Pressure for  
Composition B-3

Technique	Pressure - kbar
Rarefaction velocity	$268 \pm 6$
Embedded foils	$275 \pm 4$
Protected flash gap	$292 \pm 5$
Reflection-change flash-gap	$312 \pm 5$

The new experimental method reported in this paper is attractive because, unlike most of the others, the presence of instrumentation, i.e., the x-ray quanta in this case, has a truly negligible effect on the phenomena being explored. This technique depends only upon the interpretation of the observable progress of a rarefaction wave that has moved into the reaction

products behind a detonation, having first passed through the shock and reaction zone at its front. Limitations of the precision of this technique so far preclude observations of the rarefaction's traverse through the narrow, still uncharted, nonequilibrium region between the shock front and a position postulated to be the end of the reaction zone of Composition B. The measured trajectory of this rarefaction wave is projected back to the front of the detonation wave, hence presumably to the end of the reaction zone by virtue of the assumption that this indirectly explored narrow region is negligibly thin. A similar situation exists with plate-push experiments where the effect of the shock (or rarefaction) reflected into this same narrow region is underdetermined and also neglected by argument of thinness.

#### X-RAY PHOTOGRAPHS OF RAREFACTION WAVES IN EXPLOSIVE PRODUCTS

The head of a rarefaction wave travels with the local velocity of sound in the medium. In explosive products, which are in forward motion, the velocity of the wave in the laboratory frame of reference is the difference between the velocity of sound  $c$  in the products and their particle velocity  $u$ . Thus, a measurement of the apparent rarefaction wave velocity gives  $c - u$  in the explosive products.

When a plane detonation wave impinges normally upon a plane boundary where it drives a low impedance material, a rarefaction wave is reflected into the explosive products. This wave is a pressure discontinuity when it starts, but becomes less steep as it runs. In flash x-ray photographs, the wave is very sharply defined in its early stages, and becomes less distinct as time goes on. Fortunately radiographic resolution is good enough that measurements of wave position made over the first centimeter or so of its run are valid to about 0.02 cm; this gives the wave velocity to about 2%.

As the rarefaction wave from the front propagates back into the products, these same products are also affected by the rarefaction wave from the rear (the Taylor wave) which reduces the pressure, and changes the properties of the material. The pressure falls by about 50 kbar at the head of the rarefaction wave during the time of measurement in these experiments. To estimate these effects on our measurements we take values of  $c$  and  $u$  from Rivard et al (3). The sound velocity falls about 10% and the particle velocity about 23%. Their

difference, however, falls only about 3%, so the fit to the data is not sharply curved and is easy to define with a few points.

Classical Chapman-Jouguet theory of detonation requires that, at the end of the reaction zone,

$$D = c + u,$$

where  $D$  is the detonation velocity. Refinements of the theory show that under some conditions, such as an exothermic reaction followed by a sufficiently strong endothermic reaction, a weak detonation can exist, with

$$D > c + u$$

at the end of the reaction zone. A strong detonation apparently can exist only in an overdriven detonation, which is not present in these experiments. If we subtract the measured quantity  $c - u$  from each side of the inequality or equality, we find

$$D - (c - u) \geq 2u.$$

Thus from a measurement of  $c - u$  at the end of the reaction zone we obtain an upper limit on the particle velocity there.

Plexiglas served as the mismatch material needed to create a rarefaction wave. The experiments were initiated by a plane wave lens 20 cm in diameter, and the explosive was 20 cm square and 10 cm thick. The explosive was Composition B-3, with density  $1.730 \pm 0.001$  g/cm<sup>3</sup> and composition RDX/TNT 60/40 by weight with less than  $\pm 1.5\%$  variation in the amount of RDX. The PHERMEX x-ray machine produces an electron beam of 27 MeV which strikes a tungsten target with a spot size less than 1 mm diameter. The radiographs were taken using a pulse length of  $0.1 \mu\text{sec}$ , which gave a radiation output of about 25 R at 1 m. The center line of the explosive was 305 cm from the x-ray target, and the film pack 68.6 cm beyond that, giving a magnification of 1.225. All distances were accurately controlled. With this geometry the effective source size becomes less than 0.2 mm. A more complete description of the radiographic techniques is given in the references in the preceding paper (3).

Images on the films were measured using a precision automatic comparator which determines film densities at precisely known spacing on the film. For these films, the densities were recorded on magnetic tape as twelve-bit numbers, and the measuring interval was  $10 \mu\text{m}$ . The instrument has been described by Steinhaus,

Engleman, and Fisher (6). The recorded densities were sorted and processed using a large computer; the effect of this treatment was as if the slit of the comparator had been increased from 2 mm long to 16 mm long, reducing the film noise. Other processing was investigated, but seemed of little value for the present problem. The measured  $x - t$  positions of the rarefaction head are shown plotted in Fig. 1, along with a straight line fitted to them and the curve found from the work of Rivard et al (3).

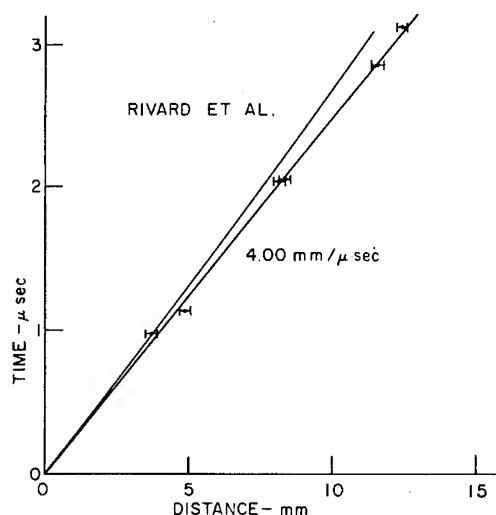


Fig. 1 - Plot of measured positions of head of rarefaction wave in Composition B-3 vs time. The lower curve is a linear fit to the data, and the upper curve is derived from the results of Rivard et al (3).

The value found for  $c - u$  is  $4.00 \pm 0.08$  mm/ $\mu\text{sec}$ . For this Composition B-3 the detonation velocity found by extrapolating the measured values for long sticks to infinite diameter is  $7.977$  mm/ $\mu\text{sec}$ . Measurements made by B. Hayes of this laboratory on a system much like the one used for these experiments showed that the velocity does not reach infinite-medium velocity in a short run, and is about  $7.915$  mm/ $\mu\text{sec}$  after 10 cm of travel. Using  $D = 7.977$  mm/ $\mu\text{sec}$  we get  $u \leq 1.99$  mm/ $\mu\text{sec}$  and  $p \leq 274$  kbar. It seems better to use the measured velocity for the distance of run; with  $D = 7.915$  mm/ $\mu\text{sec}$  we get  $u \leq 1.96$  mm/ $\mu\text{sec}$  and  $p \leq 268$  kbar. The standard deviation of the measured values of particle velocity and pressure is about 2%.

### X-RAY PHOTOGRAPHS OF EXPLOSIVES WITH EMBEDDED FOILS

Rivard et al (3) have discussed these measurements in the preceding paper, so there is no need for extensive comment here. The idea is that the mass of material between two foils before the detonation is still between them after the explosive has detonated. Therefore,

$$\rho_0 \Delta x_i = \bar{\rho} \Delta x_f,$$

where  $\rho_0$  and  $\bar{\rho}$  are initial density and the mean density at the time the photograph was taken, and  $\Delta x_i$  and  $\Delta x_f$  are the corresponding spacings between two adjacent foils. The set of final foil positions, measured behind the detonation wave, is fitted by a functional form

$$x_f = x_f(x_i) \quad (1)$$

where we have assumed that the flow is smooth. Equation (1) describes the final position of any mass point (not just a foil) as a function of its initial position. Thus the density is given by

$$\rho_0/\rho = (dx_f/dx_i)$$

which is obviously just the limit of the first density expression. To determine the detonation pressure, the detonation wave velocity  $D$ , and the density just behind and just ahead of the detonation wave are needed. The density behind the wave is obtained by extrapolating the functional form to the front position. A number of reasonable forms were tried, and all gave the same value of density with a standard deviation of about 1/3%. Application of the laws of conservation of mass and momentum across the detonation front gives the equation of the Rayleigh line

$$p - p_0 = \rho_0 D^2 (1 - \rho_0/\rho)$$

where  $p$  and  $p_0$  are detonation pressure and initial pressure. The initial pressure here is negligible compared with detonation pressure. Substitution of the density found from the fit to the x-ray film measurements gives the detonation pressure. The assumptions used here are very simple: the state at the front is near enough to steady (independent of time) for the jump form of the conservation laws to apply; the foils are a small perturbation to the flow of the explosive products; and the density is a sufficiently smooth function of distance that the extrapolation (for only 2 mm) is sensible. The pressure determined from these measurements is  $p = 275 \pm 4$  kbar.

### FLASH-GAP PRESSURE MEASUREMENTS

Pressure measurements on a slightly different explosive, Composition B, Grade A, which is RDX/TNT/wax 64/35/1 parts by weight with density  $1.713 \text{ g/cm}^3$ , have been reported by Deal (4). He used a Plexiglas flasher block providing 1.5–2.5 mm of plate motion, with 0.1 mm terminal argon gaps covered with 0.1 mm steel shim stock. The flashes from the gaps were recorded with a smear camera. He found a free-surface velocity of  $3.389 \text{ mm}/\mu\text{sec}$  for 24ST dural with density  $2.791 \text{ g/cm}^3$ , and inferred a detonation pressure of  $292.2 \pm 2.6$  kbar. First order corrections for density and composition changes can be made using values given by Deal (4). These suggest that the Composition B-3 used for all the other experiments described in this paper should give the same pressure as Deal found for Composition B, Grade A. A few shots fired using Deal's technique on Composition B-3 confirm this projection to within 2%. To allow for the additional uncertainty introduced by the difference in explosive, the pressure inferred with this technique is taken to be  $292 \pm 5$  kbar.

In a later paper, Deal (7) reported values of pressure induced in eleven materials by Composition B, Grade A, establishing the release isentrope and reflected shock Hugoniot curve, and inferred a pressure of  $290.4 \pm 2.9$  kbar. For our present purposes this value is not distinguished from that of the earlier work.

### REFLECTION-CHANGE FLASH-GAP PRESSURE MEASUREMENTS

Shots were fired especially to see whether there is a detectable effect of the embedded foils used in the x-ray experimental (3) on the way the explosive drives a plate. The charges consisted of a 20-cm diameter plane wave lens, one piece of Composition B-3 10 cm square and 5.1 cm thick, eight pieces of Composition B-3 10 cm square and 0.635 cm thick with  $12.5\text{-}\mu\text{m}$  thick tantalum foils between explosive pieces, and a plate of 6061 dural of density  $2.702 \text{ g/cm}^3$  driven by the system. The explosive and assembly technique were identical with those of Rivard et al (3). The free-surface velocity was measured with an optical technique: the shock arrival time was detected by the change of reflectivity of the metal, and the arrival of the plate across a 0.127 cm gap was detected by a plastic flasher. The times were measured with a high-resolution smear camera. This technique has been checked against the reflected edge or

wire technique of Davis and Craig (8), and found to give the same values.

These experiments give the free-surface velocity as a function of distance across the aluminum surface, as shown in Fig. 2. The value chosen from that curve is the central value,  $3.51 \text{ mm}/\mu\text{sec}$ . Data points from four experiments are shown in Fig. 3. A line through these points extrapolates to  $3.60 \text{ mm}/\mu\text{sec}$ , which corresponds to a detonation pressure of  $312 \pm 5 \text{ kbar}$ . The line which Deal fitted to his experimental results is also shown in Fig. 3, to show that the slope of the lines is the same.

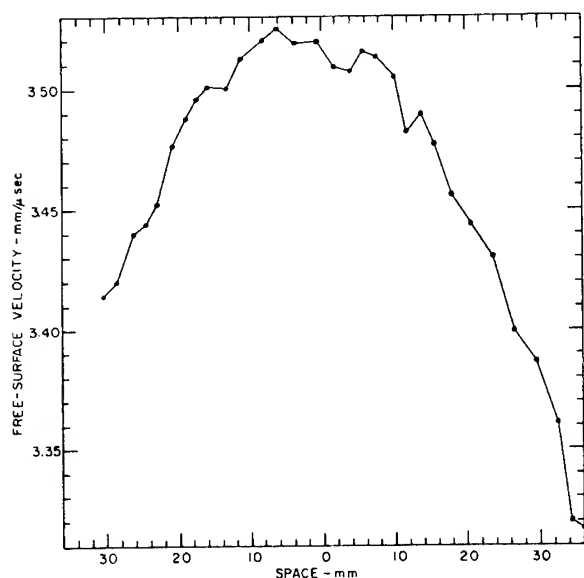


Fig. 2 - Plot of measured free-surface velocity of dural plate driven by Composition B-3 vs distance from the axis of the charge.

Another series of experiments with Composition B-3 20 cm diameter and 12.7 cm thick, using the same technique, gives a free-surface velocity of  $3.66 \text{ mm}/\mu\text{sec}$  by extrapolation. The experimental points are shown plotted in Fig. 3. The pressure is  $317 \pm 8 \text{ kbar}$ . It seems that the foils do not seriously affect the velocity of a driven plate.

Four experiments by Craig using the reflected wire technique (8) are also pertinent. Two charges were 5.1 cm diameter and two were 2.54 cm diameter; all were 16 diameters long. The driven plates were 2024 dural, one 2.07 mm thick and another 2.81 mm thick for each

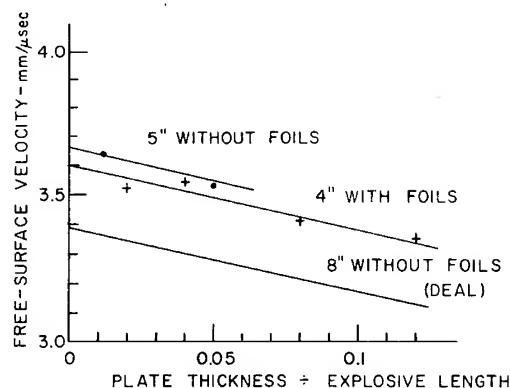


Fig. 3 - Plots of measured free-surface velocity vs plate thickness/charge length. Upper curve, charge of Composition B-3 127 mm long, without embedded foils. Center curve, charge of Composition B-3 100 mm long, containing embedded foils. Lower curve, charge of Grade A composition B 200 mm long, from experiments reported by Deal.

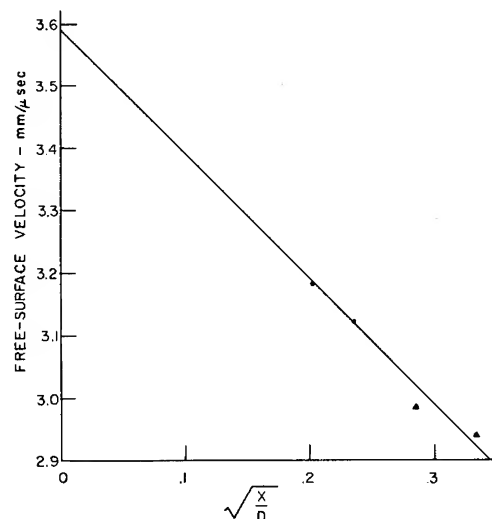


Fig. 4 - Plot of free-surface vs (plate thickness/charge diameter) $^{1/2}$ . The explosive was Composition B-3.

diameter. The data are shown plotted in Fig. 4, with the square root of the ratio of plate thickness to stick diameter as abscissa. The reason for using this plot is given in the discussion section. These data extrapolate to a value around  $3.60 \text{ mm}/\mu\text{sec}$ , in agreement with the plane wave measurements.

## DISCUSSION

The data presented here show a large range for the values of the detonation pressure obtained by different methods, and there is no obvious reason for choosing one rather than another. This lack of consistency is typical of results of pressure measurements. In their excellent review of all the available experimental pressure data, Kamlet and Dickenson (9) observe that "values ranging from 177 to 220 kbar have been quoted as experimental detonation pressures of TNT at 1.63-1.64 g/cc, and belief in both extreme values among different knowledgeable detonation hydrodynamicists is encountered by the authors." We do not know the reasons for the differences, but perhaps a review of some facts and ideas will eventually lead to more fruitful discussions of the spread in Composition B pressures reported in this paper.

The difference between the two types of free-surface velocity measurements may be attributed to the mechanisms of spalling. The metal plate is accelerated to full velocity very rapidly as the shock emerges from the surface. Then, since the material is cohesive, the free surface is decelerated by the rarefaction wave (the Taylor wave) which follows the front. The resulting tension increases until it reaches the strength of the plate material, and then the plate spalls. The subject has been reviewed by Veretennikov et al (10), who showed with some very nice experiments how spall affects these kinds of pressure measurements. The free-surface velocity needed for pressure measurements is the initial free-surface velocity, so the weaker the material the less the deceleration and the better the measurement. However, if the spall layer is very thin it may not be detected by the instrumentation, for example a flash gap protected by a steel shim. The flash will not appear until more material reaches the flasher, and the measured velocity will not be the initial free-surface velocity. The newer optical techniques, such as the reflected wire technique (8), allow direct observation of the surface and can detect very thin layers. Observation of dural surfaces with these techniques shows that even with the best time resolution available, there is no measurable deceleration of the surface, although with other materials it can be seen. This may indicate that a very thin layer is spalled off, but it is not clear how or why such spalling might occur. The explanation for the difference between the flash gap and reflection-change flash-gap measurements may be that one is sensitive to thin layers and the other is not. Even if this explanation is correct, it is still not certain that the higher velocity from the newer techniques

gives a better pressure measurement, because the Hugoniot curve for the dural was measured in similar fashion. The whole subject of free-surface velocity technique requires very careful reexamination to avoid persistent circular arguments.

Whether or not we understand why the two sets of free-surface velocity measurements do not agree, it is clear that the x-ray values are statistically meaningfully lower than either. Since the plate velocity methods have been studied and used for a long time and the x-ray methods are quite new, one must wonder if there may be some overlooked bias in the new methods. The embedded foils have to be accelerated by the explosive, and can be expected to have some effect. The free-surface velocity measurements show only a small effect, but they sense only a very short distance back into the products. It seems that the presence of the foils must reduce the particle velocity somewhat below that in explosive with no foils. On the other hand, the pressure obtained from the rarefaction velocity measurement is the lowest of all, and those charges contained no foils which might perturb the flow. At the present time, we do not know how much effect the foils might have. Another possibility is that the low values are the result of averaging over a larger volume of the charge. It is obvious from Fig. 2, for example, that the pressure falls off as we move away from the centerline. In the foil experiments, the positions were measured on the axis, and the values are representative of a region there. In the rarefaction measurements no such selection was possible, and the value is some sort of average through the whole 20 cm thickness. The foils might be responsible for the low value in the one case and the averaging responsible in the other.

If values from all the experiments are accepted as good values, they may imply that there is a high pressure region near the front. The plate velocity measurements sense back only about 0.2 cm, while the x-ray measurements sense only behind that region. Probably the x-ray data could be fitted just as well if a model were assumed with a narrow high pressure zone near the front but following the reaction zone. This has not been done, because there has been no reason, either theoretical or experimental, to believe that one exists. On the other hand there have been observations of such a structure, but in different charge arrangements, reported by Craig (11); this region of large pressure gradient has been referred to as a "decay zone," not identified with the reaction zone.



His interpretation has been questioned because his pressure drop seems to be what has been expected from the usual model of the reaction zone of a detonation wave. Petrone (12) on the basis of ad hoc assumptions about reaction kinetics, has made detailed calculations to show just how a reaction zone might affect plate velocities, and has been able to reproduce one of Craig's curves. Veretennikov et al (10) have suggested that deceleration before spalling could account for the rest of Craig's results. It seems worthwhile to go over these problems again.

Most of the measurements which Craig reported were made with long sticks of nitromethane driving dural plates. The data were presented as the graph in Fig. 5. The straight lines marked A, B, and C show how one might, using the usual model for plane detonations, interpret any one of the data sets to find the CJ pressure. Obviously the three sets do not give the same result. Craig's resolution of this discrepancy was to postulate a decay zone with a large pressure gradient behind the front, and to assume that the reaction zone could not be seen because it was too thin. As they are plotted in this plane it is difficult to extrapolate the data points in any satisfying way.

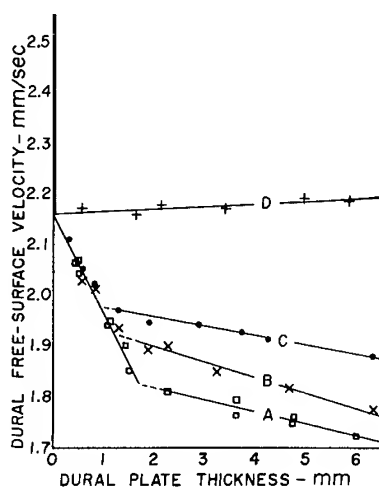


Fig. 5 - Plots of free-surface velocity vs dural plate thickness for long sticks (curves A, B, and C) and for short plane-wave charges (curve D) of nitromethane, as reported by Craig.

In detonation theory there is a model, Taylor's model of a spherical detonation (13), which has an infinite pressure gradient behind

the detonation front. Experimental work, for example that of Hantel and Davis (14), shows that there is in fact a very steep gradient behind a spherical detonation wave. From Taylor's model it is easy to show that if plate velocity measurements were made with a spherical driving wave, the plot of velocity vs (plate thickness)<sup>1/2</sup> would be a straight line.

If Craig's data are plotted in a reduced form appropriate to Taylor's model, using the square root of the ratio of plate thickness to stick diameter as abscissa, they all fit a single curve, as shown in Fig. 6. It can be made plausible that this fit is not accidental, because the decay zone can be avoided by using plane initiation of large diameter, short charges. Some data from shots of this kind, done by Craig, are plotted in Fig. 7. The abscissa is the ratio of plate thickness to charge length plus a constant; the constant apparently adjusts for the fact that the rarefaction wave is not exactly a centered simple wave. The data of curve D of Fig. 5 are the crosses in Fig. 7. The intercept of the long stick fit is 2.141 mm/ $\mu$ sec, and that of the plane wave fit is 2.189 mm/ $\mu$ sec. These values are in reasonable agreement. Since no reaction zone is apparent in the plot of plane wave data, it seems very unlikely that the large pressure gradient inferred from the long stick data is evidence of a reaction zone. Craig's interpretations of the data as showing that the reaction zone is too thin to be detected, and that there is a very steep pressure gradient behind the front in long sticks, seems justified. (The nitromethane pressure is  $134 \pm 4$  kbar at  $23^\circ\text{C}$ , or  $142 \pm 4$  kbar at  $4^\circ\text{C}$ .) The data in Fig. 4 for Composition B-3 show similar behavior, and the results for nitromethane show why we plotted them as we did.

Decay zones are not observed in large diameter, short, plane-wave charges such as those used to obtain the Composition B-3 results reported in this paper. Therefore the discrepancy in the results is not related to the decay zone described by Craig. Many other experiments have shown, however, that the values obtained from pressure measurements are affected by changes in the initiating systems, and by changes in charge dimensions and proportions. Some of the effects that have been seen are obviously caused by side rarefactions, but others are more subtle and have not been satisfactorily explained. The present discrepancy may be another manifestation of these effects.

We have demonstrated that a single group of experimenters using the same explosive for

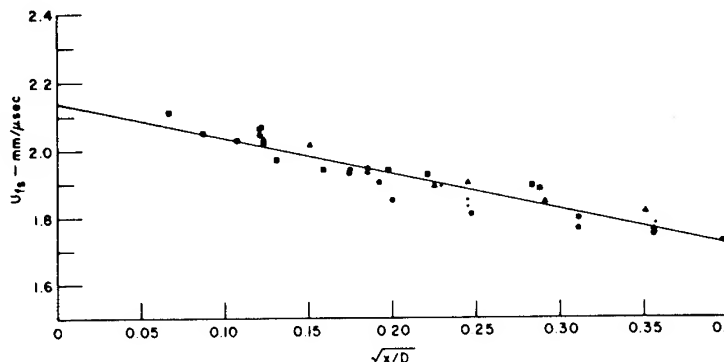


Fig. 6 - Plot of free-surface velocity vs (plate thickness / charge diameter)<sup>1/2</sup> for nitromethane. The points plotted here are those curves A, B, and C of Fig. 5.

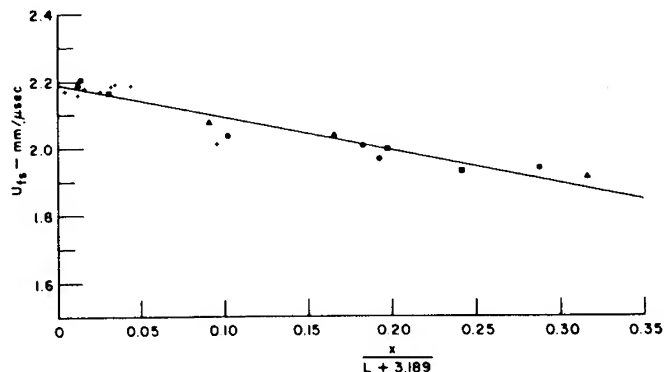


Fig. 7 - Plot of free-surface velocity vs plate thickness / [charge length + a constant (3.189 cm)] for short plane-wave charges of nitromethane. The points plotted as crosses are the points used for curve D of Fig. 5.

all experiments can obtain significantly different values for the detonation pressure by using different techniques. In the past it has been common to dismiss such differences in reported pressure values as being caused by (1) differences in the explosive used or (2) differences in the plate material or (3) the biases of observers. But now those easy excuses for avoiding the problem are gone, and something, perhaps more basic to the physics of the phenomena, is still wrong. Pressures are not measured directly in any of the experimental techniques; they must be inferred. It seems clear now that some or all of the inferential schemes are inadequate or incorrect, or that some of the underlying assumptions about the experiments are unjustified. More work will be needed to discover where the faults lie.

#### ACKNOWLEDGMENTS

We are indebted to B. G. Craig for ideas, and discussion, and for generously furnishing us some unpublished data. B. Hayes also allowed us to use some of his results. The computer processing of more than  $10^6$  density measurements to make them usable was directed by J. B. Ramsay. Many other members of the Los Alamos Scientific Laboratory also contributed to this work. All the work was done under the auspices of the United States Atomic Energy Commission.

#### REFERENCES

1. A. N. Dremin and P. F. Pokhil, Dokl. Akad. Nauk., USSR, 128, 899 (1959).

2. Y. Pujol and N. Manson, *Comp. Rend.* 254, 3173 (1962).
3. W. C. Rivard, D. Venable, W. Fickett, and W. C. Davis, preceding paper in this symposium, p. 3.
4. W. E. Deal, *J. Chem. Phys.* 27, 796 (1957).
5. W. C. Davis, B. G. Craig, and J. B. Ramsay, *Phys. Fluids* 8, 2169 (1965).
6. D. W. Steinhaus, R. Engleman, Jr., and K. J. Fisher, Los Alamos Scientific Laboratory Report LA-4117, 1969.
7. W. E. Deal, *Phys. Fluids* 1, 523 (1958).
8. W. C. Davis and B. G. Craig, *Rev. Sci. Instr.* 32, 579 (1961).
9. M. J. Kamlet and Charles Dickenson, *J. Chem. Phys.* 48, 43 (1968).
10. V. A. Veretennikov, A. N. Dremine, O. K. Rosanov, and K. K. Shvedov, *Fizika Gorenia i Vzryva* 3, 3 (1967). English translation, *Combustion, Explosion, and Shock Waves* 3, 1 (1967).
11. B. G. Craig, Tenth Symposium (International) on Combustion, The Combustion Institute, 1965, pp. 863-867.
12. F. J. Petrone, *Phys. Fluids* 11, 1473 (1968).
13. G. I. Taylor, credited by Courant and Friedrichs, *Supersonic Flow and Shock Waves*, Interscience Publishers, 1948, p. 429.
14. L. W. Hantel and W. C. Davis, this symposium, p. 599.

## DISCUSSION

R. DUFF  
Systems, Science, and Software  
P.O. Box 1620  
La Jolla, California 92037

Several possible sources of the disagreement between different measurements of detonation pressure were suggested by Dr. Davis.

He did not include the thought that the C-J relation itself may not hold precisely. In other words, perhaps  $D \neq u + c$ . It seems appropriate to keep this possibility in mind at least until a more satisfactory detonation theory which explicitly includes the known wave instability is developed.

# SHOCK VELOCITY MEASUREMENTS IN INERT MONITORS PLACED ON SEVERAL EXPLOSIVES

R. L. Jameson and A. Hawkins  
*Ballistic Research Laboratories  
Aberdeen Proving Ground, Maryland*

## ABSTRACT

Measurements of average shock velocity in inert monitors placed on the end of detonating solid phase explosives have been made. Brass, aluminum, magnesium and Plexiglas were used on TNT, and Plexiglas on Octol, Comp B, Pentolite and 9404. The reaction zone measurements were sensitive to the shock impedance of the monitor in relation to the impedance of the explosive. A value for the reaction zone length for TNT,  $a = 0.6 \pm 0.1$  mm, was calculated from the measurements with the four monitor materials. Von Neumann spike measurements were impractical due to the error that would occur from extrapolation. Chapman-Jouguet pressures were calculated and were as follows: TNT ( $P = 200 \pm 10$  kilobars), 50/50 Pentolite ( $P = 245 \pm 10$  kilobars), Comp B ( $P = 280 \pm 10$  kilobars), Octol ( $P = 305 \pm 10$  kilobars), and PBX 9404 ( $P = 345 \pm 10$  kilobars). These measurements were independent of the monitor material used.

## INTRODUCTION

The one dimensional steady detonation wave has been characterized by Zeldovich (1), von Neumann (2) and Doring (3), as a shock wave in the unreacted explosive followed by a reaction zone which ends at a region designated as the Chapman-Jouguet plane. An illustration of this model is shown as Fig. 1. There are several points of this model that are important to the physical understanding of the detonation process and its application. These points are the pressure in the shock wave, the reaction zone length and the pressure at the Chapman-Jouguet plane.

We have made measurements of the shock velocity in inert materials placed on the end of a detonating solid phase explosive. Five explosives of military interest were selected for this work: TNT, 60/40 Comp B, 50/50 Pentolite, 75/25 Octol, and PBX 9404. All were cast except 9404, which was pressed.

detonated, a shock wave followed by a rarefaction wave is transmitted into the inert material. If the inert material and the explosive have the same shock impedance  $\rho_0 U$ ,  $\rho_0$  the original density and  $U$  the shock velocity, all the energy of the shock wave will be transmitted into the inert monitor and there will be no reflected wave. If, however, the inert material is of lower shock impedance, a rarefaction wave will be reflected back into the explosive. Conversely, if the inert material is of higher shock impedance, a compression wave will be reflected back into the explosive. In their work with Composition B, Duff and Houston (4) assumed that the aluminum monitors and Composition B were of the same impedance, thus, no reflection took place. They developed an equation to calculate the reaction zone thickness from a knowledge of the free surface velocity of aluminum on Composition B versus the thickness of the aluminum and other characteristics of the explosive and the metal. The equation for reaction zone length "a"

## THEORY

When an inert material is placed in contact at the end of an explosive charge that is then

$$a = \frac{b [D_i(u_t + c_t - D_t)(1 - \alpha)]}{[D_t(u_t + c_t - \alpha D_i)]} \quad (1)$$

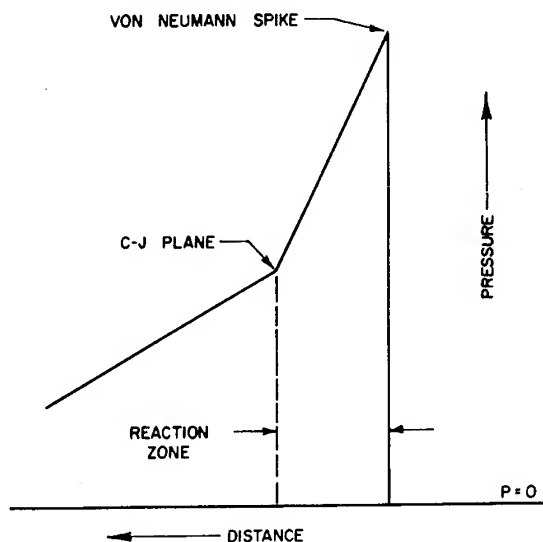


Fig. 1 - Model of a one-dimensional steady detonation wave as characterized in references (1), (2), and (3).

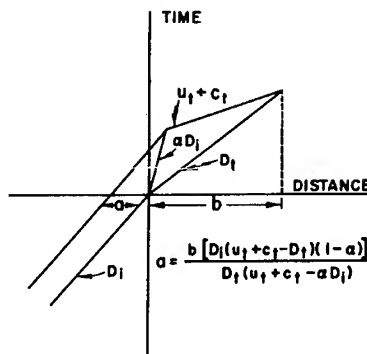


Fig. 2 - Distance-time diagram of a detonation striking an inert barrier for a condition in which there will be no reflected wave at the interface. (From Duff and Houston (4).)

was developed from an analysis of the geometric parameters of experiment that made use of the average shock velocities in the metal. A shock diagram for a detonation striking a barrier is shown as Fig. 2. The parameters are  $D_1$ , the detonation velocity;  $aD_1$ , the velocity of the interface through the reaction zone;  $D_2$ , the average shock velocity in the metal monitor (this is the same as  $\bar{U}$  used later in this paper);  $u_1 + c_1$ , the average velocity of the foot of the rarefaction wave and  $b$  the plate thickness at which the foot of the rarefaction wave overtakes the shock wave. As in reference (4) isentropic flow is assumed behind the shock wave and  $u_1 + c_1$  is dependent on pressure and is the value of the C-J state of the explosive as transmitted to the metal. This is determined by the extrapolation of the Taylor wave data to the interface in the manner used for the C-J calculations discussed later in this paper. The values of the local sound velocity  $c_1$  are calculated from the shock wave velocity in the monitor and the known linear  $U - u$  Hugoniot by the Jacobs approximation (5). This useful approximation uses only the linear  $U - u$  relation and the assumption that  $P - u$  curve of a Hugoniot also represents the isentrope. Checks of this approximation against data in the literature for aluminum indicate agreement to within 2%. The Jacobs approximation has been detailed by Allison in reference (6). The equation derived for the local sound velocity is

$$c = (U - u)(U + su)/U \quad (2)$$

where  $U$  and  $u$  are shock and particle velocity respectively, and  $s$  is the slope of the linear  $U - u$  Hugoniot. A more complete discussion of the derivation may be found in reference (4). We have applied this equation in calculation of a number, "a" the reaction zone length, for conditions in which reflection will take place. We calculated "a" for TNT with four impedance combinations. The other explosives were calculated with Plexiglas. We make the same assumption as reference (4) which might be better stated as assuming that the velocity of the C-J state is unaffected by the reflected wave from the interface and the reaction time is also unaffected.

Pressures were inferred from theoretical considerations using values of shock velocity taken from curves of shock velocity  $U$  versus distance of shock travel  $s$  in the monitor material. Calculations of an approximate pressure were made first from the interface equation

$$P_1 = \frac{P_2(\rho_2 U_2 + \rho_1 D_1)}{2\rho_2 U_2} \quad (3)$$

where  $\rho$ ,  $U$ ,  $P$ , and  $D$  are density, shock velocity, pressure, and detonation velocity, respectively, and 1 refers to the donor material and 2 the acceptor material. These pressures were refined using the approach of Coleburn (7) which employs an isentropic equation of state for the product gases

$$PV^k = A \quad (4)$$

where  $P$  is pressure,  $V$  volume, and  $k$  and  $A$  are constants. Coleburn derived the following two equations from which the pressures are calculated by an iteration

$$P_1 = P_2 \left[ 1 - \frac{(k^2 - 1)u_2 - (k - 1)D}{2kD} \right]^{-\frac{2k}{k-1}} \quad (5)$$

$$P_1 = \rho_0 D^2 / (k + 1) \quad (6)$$

where  $u_2$  is particle velocity in the monitor.

### EXPERIMENTAL PROCEDURE

Average shock velocities were measured in inert materials placed on the explosive samples. Four monitor materials were used in the TNT experiments and only Plexiglas on the other explosives. The materials and the Hugoniots used are listed below.

Aluminum (2024),  $\rho = 2.785 \text{ gm/cm}^3$   
 $U = 5.328 + 1.338 u$  Ref. (8)

Brass (271),  $\rho = 8.443 \text{ g/cm}^3$   
 $U = 3.802 + 1.418 u$  Ref. (9)

Magnesium (AZ31B),  $\rho = 1.776 \text{ g/cm}^3$  Ref. (10)  
 $U = 4.648 + 1.198 u$

Plexiglas (II UVA),  $\rho = 1.183 \text{ g/cm}^3$   
 $U = 2.695 + 1.538 u$  Ref. (11)

The monitors were placed on the surface of a 10-cm-diameter by 2.5-cm-thick test charge which was boosted by a 10-cm Comp B - TNT plane wave lens. The monitors were fabricated as disks whose flat surfaces were lapped and polished plane and parallel. The diameter was dictated by the thickness of the pellet to avoid side rarefactions. Disk thicknesses were measured to within  $\pm 2$  microns. The surface of the Plexiglas disks was to be in contact with the explosive was aluminized by vacuum evaporation. In order to observe the arrival of the shock wave at the surface of the explosive, Plexiglas disks were placed on the charge in the area between the opaque sample. The arrival of the detonation wave at the explosive surface and the shock wave at the top surface of the monitors was sensed by a change in the reflection at the monitor surfaces of the light from an argon flash bomb as viewed by a rotating mirror streak camera.

The shock travel times were determined by reading the streak camera record on an optical comparator. The cameras limit of time

resolution was 3 nanoseconds. Average shock velocities were calculated from these times and the disk thickness. Each point in Figs. 3-10 includes data from at least three experimental firings.

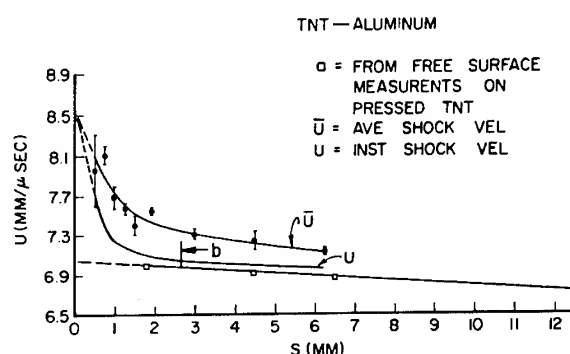


Fig. 3 - Shock velocity - shock travel distance plot for Aluminum monitors on TNT

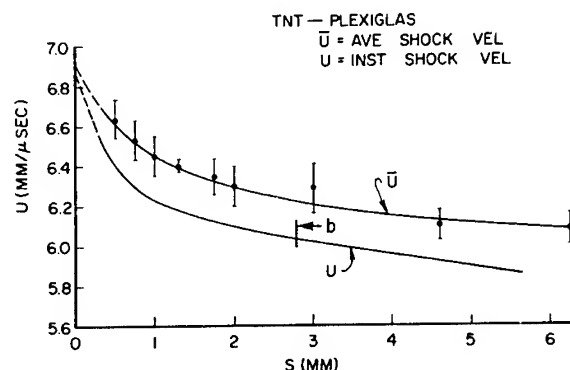


Fig. 4 - Shock velocity - shock travel distance plot for Plexiglas monitors on TNT

### RESULTS

The average shock velocities  $\bar{U}$  for each explosive were first plotted versus the shock travel distance  $S$  (monitor thickness). A "by eye" fit to the data is made and then this curve is related to the instantaneous shock velocity  $U$  by the relationship

$$U = \frac{\bar{U}}{1 - \frac{S}{\bar{U}} \frac{d\bar{U}}{dS}} \quad (7)$$

Slopes are calculated by numerical differentiation of the smooth data. The results of TNT with Al, Brass, Mg, and Plexiglas monitors and

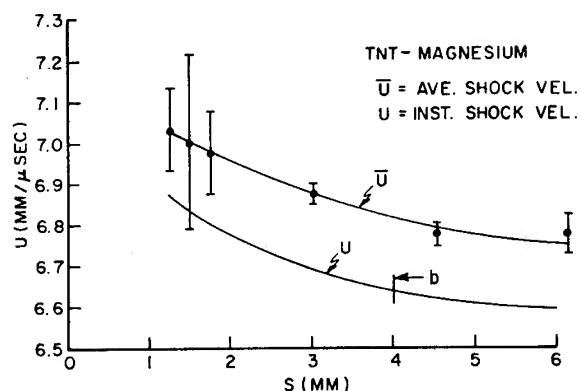


Fig. 5 - Shock velocity - shock travel distance plot of Magnesium monitors on TNT

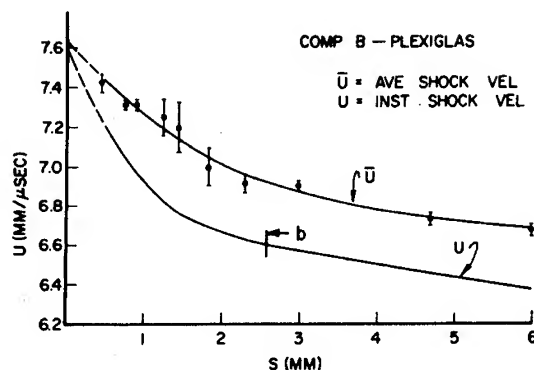


Fig. 7 - Shock velocity - shock travel distance plot for Plexiglas monitors on Composition B

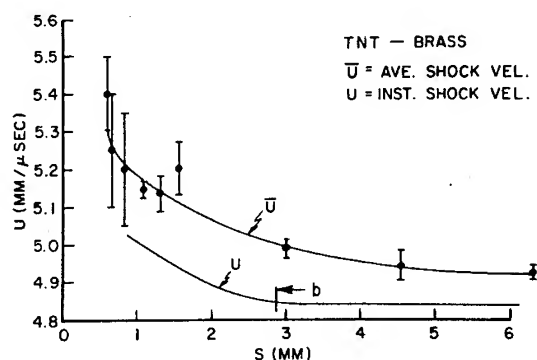


Fig. 6 - Shock velocity - shock travel distance plot for Brass Monitors on TNT

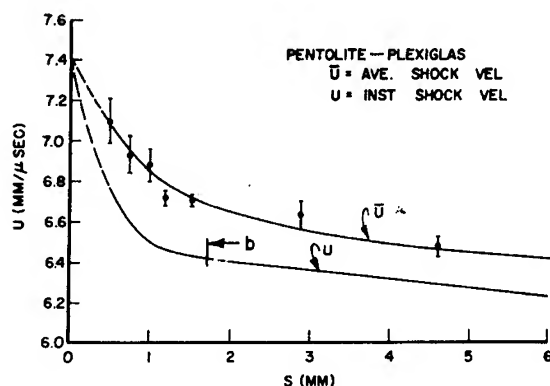


Fig. 8 - Shock velocity - shock travel distance plot for Plexiglas monitors on Pentolite

Pentolite, Comp B, Octol, and PBX 9404 with Plexiglas monitors are shown as Figs. 3-10. The curves display a rapidly changing shock velocity in the region of the thin monitors as would be expected from 1D model shown in Fig. 1. There is then a transition region followed by a slowly changing shock velocity in the region of thicker monitors. We have taken the end of the transition region to represent the image of the C-J plane and an indication of the end of the reaction zone. This is the point where the end of the rarefaction fan catches the shock wave in the monitor, the distance "b" in equation (1). This is in agreement with the transition zone mentioned by Petrone (12) and Craig (13). Using equation (1) we calculated an effective reaction zone length to the closest 0.1 mm from the data of Figs. 3-10. Analysis of the impedance relationship between explosive and monitor would indicate that the true, no reflection, reaction zone length would be  $a_0 = 0.6 \pm 0.1$  mm for TNT. The value calculated for the other explosives

with Plexiglas monitors would be slightly higher than the true  $a_0$  because a rarefaction wave would be reflected into the explosive in each case. In the case of a shock wave passing from TNT into a monitor material a compression wave would be reflected back into TNT from brass and aluminum, a rarefaction wave reflected from Plexiglas and a magnesium monitor is nearly a perfect match for solid TNT and there would be no reflection. The TNT results could indicate that the reaction was slowed as the pressure in the reaction zone was dropped by a rarefaction wave and conversely accelerated when the pressure was increased by a compression wave.

If the value of  $U$  (the shock velocity) at the end of the transition region is used to calculate the pressure in the explosive, this pressure will correspond to an aquarium type experiment (7)

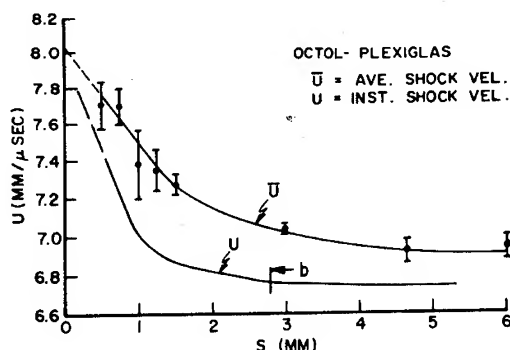


Fig. 9 - Shock velocity - shock travel distance plot for Plexiglas monitors on Octol

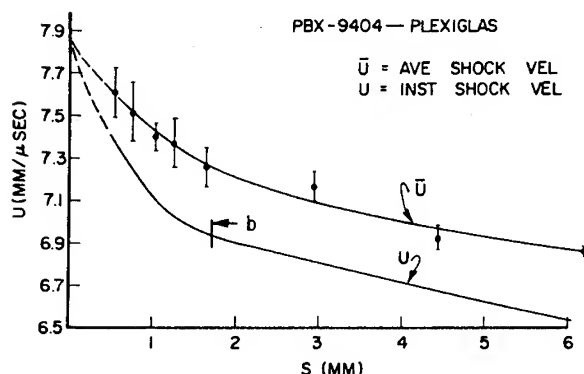


Fig. 10 - Shock velocity - shock travel distance plot for Plexiglas monitors on PBX 9404

TABLE 1  
Effective Reaction Zone Lengths

Explosive	Monitor	"a" in explosive
TNT	Plexiglas	0.7 mm
TNT	Magnesium	0.6 mm
TNT	Aluminum	0.3 mm
TNT	Brass	0.4 mm
Comp B	Plexiglas	0.7 mm
Pentolite	Plexiglas	0.5 mm
Octol	Plexiglas	0.8 mm
9404	Plexiglas	0.5 mm

which is insensitive to velocities within the spike affected area. When the Taylor wave region, the region following the C-J plane, is extrapolated to  $S = 0$  the value will be similar to the measurements of Cast, et al. (14) where an extrapolation technique was used. Table 2 gives pressures calculated in both ways. Pressures are limited both by preliminary estimate from the interface equation (3) and the Coleburn equation (5). Pressures were calculated with the TIGER Code (15-16) for each explosive as a comparison with the experimental results. The nonextrapolated values generally compared well with those measurements available in the Coleburn report (7), but the pressure for TNT in this work was slightly higher. The extrapolated values for TNT were 10 kilobars higher and 9404 was 29 kilobars lower than reported by Cast, et al. (14). We fired several pressed TNT shots with aluminum monitors on which free surface velocities were measured. The free surface velocities were converted to shock velocities and shown on Fig. 3. Pressure calculated from this data,  $\rho = 1.614 \text{ g/cm}^3$ , were 194 Kb by Coleburn's equation, 10 kilobars lower than the  $\rho = 1.63 \text{ g/cm}^3$  cast TNT with Al shock velocity monitors. A density correction would bring the results somewhat closer together for good agreement.

The extrapolation of the data which reflected the pressure of the spike to  $U$  at  $S = 0$  should indicate a spike pressure. However, the sensitivity of the calculation to changes in shock velocity require all the data in the thin monitor range to be of very high precision to yield a reliable result. With a limiting time resolution of 3 nsec the error in thin monitors becomes large. The authors would therefore refrain from extrapolation until higher precision equipment is available and velocities in thinner samples could be measured.

#### ACKNOWLEDGMENT

The authors would like to thank Miss Toni Taylor for making the TIGER calculations used in this work.

#### REFERENCES

1. Y. B. Zeldovich, J. Expth. Theoret, Phys. (USSR) 10, 542 (1940).
2. J. von Neumann, O.S.R.D. Report 549 (1942).
3. W. Doring, Ann. Physik, 43, 421 (1943).



TABLE 2  
Detonation Pressure Calculations

Explosive	Monitor Material	$\rho$ g/cm <sup>3</sup>	D mm/ $\mu$ S	P (no extrapolation)		k	P (extrapolation)		k
				Eq. (3) (kilobars)	Eq. (5) (kilobars)		Eq. (3) (kilobars)	Eq. (5) (kilobars)	
TNT	Al	1.63	6.860	198	195	2.927	204	202	2.806
TNT	Plex	1.63	6.860	197	195	2.926	211	210	2.657
TNT	Brass	1.63	6.860	196	186	3.122	196	186	3.122
TNT	Mg.	1.63	6.860	194	194	2.947	201	201	2.816
			average pressure P = 193			2.981		200	2.850
					$\pm 5$	$\pm 0.095$		$\pm 10$	$\pm 0.195$
TNT	*TIGER (13)	1.63						227	
50/50 Pentolite	Plex	1.66	7.448	242	240	2.859	248	246	2.750
50/50 Pentolite	*TIGER	1.66						266	
COMP B	Plex	1.692	7.840	269	266	2.910	284	281	2.698
COMP B	*TIGER	1.692						287	
75/25 Octol	Plex	1.800	8.550	309	304	3.335	310	305	3.315
75/25 Octol	*TIGER	1.800						335	
9404	Plex	1.845	8.835	337	331	3.355	353	346	3.160
9404	*TIGER	1.845						372	

\*TIGER is an equilibrium chemistry computer code.

- R. E. Duff and E. J. Houston, J. Chem. Phys. **23**, 1268, 1955.
- S. J. Jacobs (NOL) private communication.
- F. E. Allison, "Thermodynamic States for Aluminum and Polystyrene," BRL R 1294, July 1965.
- N. L. Coleburn, "Chapman-Jouguet Pressures of Several Pure and Mixed Explosives" NOLTR 64-58, 25 June 1964.
- J. N. Fritz, S. P. Marsh, W. J. Carter and R. G. McQueen, "The Hugoniot Equation of State of Sodium Chloride in Sodium Chloride Saturate," LA-DC-9989, 1968.
- R. G. McQueen and S. P. March, J. of Appl. Phys. **31**, 1253, 1960.
- M. Van Theil, editor, "Compendium of Shock Wave Data," UCRL 50108.
- G. Hauver, BRL private communication.
- F. J. Petrone, Phys. of Fluids, **11**, 1473, 1968.
- B. G. Craig, "Tenth Symposium (Int.) on Combustion," p. 863 (The Combustion Institute), Pittsburg, Pa., 1965.

14. J. C. Cast, H. C. Hornig, J. W. Kury, "Standard Test for Detonation Pressure Measurements," UCRL 50645.
15. W. E. Wiebenson, W. H. Zwisler, L. B. Seely and S. R. Brinkley, Jr., "TIGER Computer Program Documentation," Vol. I, II, III and IV (in publication).
16. S. R. Brinkley, Jr. and T. B. Seely, "Construction of the Hugoniot Curve and Calculation of the Chapman-Jouguet Points for General Equation of State," Combustion and Flame, V13, #5, Oct 1969.

## DISCUSSION

B. G. CRAIG

Los Alamos Scientific Laboratory  
Los Alamos, New Mexico

1. You state that you have taken the point where the end of the rarefaction fan catches the shock wave as the distance "b" for Eq. 1. I expect the effect of reflected shocks and rarefactions to be in the direction you indicate; however, I do not expect it to be as great as you indicate in Table 1. When I look at the data in Figs. 3-6 and consider the experimental error I tend to pick "b" as a number near 1 mm independent of the plate material. Your free-surface velocity data in Fig. 3 seem to support my choice for aluminum plates. Please elaborate on your basis of choice for "b".

2. Since you admittedly do not have enough precision to reliably extrapolate to the spike pressure, how did you deduce the appropriate velocities ( $\alpha D_i$  for example) required to calculate the reaction-zone length with the Duff and Houston equation?

3. What do the error flags in Figs. 3-10 represent?

gathered from experiments on pressed TNT which from the literature seems to have narrower reaction zones.

2. The values of  $\alpha D_i$  were average values between a point at the spike gotten by extrapolation and the value of the C-J plane. The reaction zone length calculation is not as sensitive to an error in  $\alpha D_i$  as the pressure would be in the shock velocity extrapolation for spike pressure.

3. The error flags in Figs. 3-10 represent  $\pm\sigma$ .

M. HELD

Bölon-Apparatebau  
8898 Schrobenehausen, Germany

Why would it not be possible to continuously record the shock wave by orienting the streak camera slit parallel to the wave propagation direction? This could be equally possible for opaque media by using the BRL developed technique.

## REPLY BY JAMESON

1. The value of "b" is taken as that point at which the V vs S plot, going from higher to lower S, first deviates from a linear or near linear trend. The data shown on Fig. 3 from free surface velocity measurements were

## REPLY BY JAMESON

The authors have found the measurements of average shock velocity to be more precise than observing rapidly changing velocities over a 1-2 mm path length. Observations near the monitor interface are often very difficult in either system you suggest.

# DIVERGENT SPHERICAL DETONATION WAVES IN A SOLID EXPLOSIVE

R. Chéret and G. Verdès  
*Commissariat à l'Energie Atomique  
Centre d'études de Vaujours  
93 Sevrans (France)*

## ABSTRACT

An initiation device has been achieved which induces a divergent spherical detonation wave in composition F.209; the relative space defect does not exceed 0.3% as soon as the wave radius  $x$  is beyond 75 mm. The detonation velocity is measured from  $x = 15$  to  $x = 140$  mm; it starts from values less than the "infinite diameter" velocity  $D_{\infty}^P$ , increases up to values greater than  $D_{\infty}^P$ , decreases, and finally keeps a constant value which significantly exceeds  $D_{\infty}^P$ . Moreover, up to  $x = 100$  mm, the material velocity field is graphically deduced from the 250-ns sampled radiographic record of thin gold foils carried along by the detonation products; it differs significantly from that of Taylor's self-similar flow in the vicinity of the wave front. Through theoretical considerations, the Chapman-Jouguet mechanical characteristics are directly deduced from the flow field measurements. These "experimental" values agree reasonably well with the "usual B.K.W. calculated" ones.

## INTRODUCTION

When the detonation phenomenon — a mechanical regime associated with the release of chemical energy that propagates through the medium at a speed of a few mm/ $\mu$ s — was first observed by Berthelot and Vieille, it appeared to have a remarkably constant velocity. Later, however, Jouguet put forward the hypothesis that, under some special circumstances, the propagation velocity of this wave may not be as uniform as it was believed to be from the early investigation. Since then experimental studies of nonsteady detonation waves received a good deal of attention and numerous observations of such phenomena have been reported with reference to a variety of reactive mixtures, various containers, and various initiation devices. In our opinion, it is of prime importance to make a clear distinction between those experiments where the "walls" have a definite influence upon the generation and propagation of the explosion (the so-called plane waves as well as the so-called cylindrical waves) and those where such effects are of lesser significance (the so-called spherical waves).

The above distinction is of particular significance to further progress of our knowledge in this field since today we are confronted with a choice between the well proven measuring techniques in the former case, when the quantitative results are strongly dependent on "wall" effects which are yet too little known to be theoretically taken into account, and the latter case which is still associated with great difficulties as far as experimental techniques are concerned, but whose results can be checked more readily with advanced theories.

Although theoretically, spherical detonations are quite simple, the proper generation poses great difficulties. From that point of view, to say the least, convergent waves must be dissociated from the divergent ones.

In the latter case, as far as we know, the available results only deal with detonation velocity measurements in gaseous explosives. Therefore, divergent spherical detonations in solid explosives are doubly interesting in so far as (i) velocity measurements give a basis of comparison (1) between solid and gaseous

explosives, and (ii) the X-ray measured flow field can be checked in a consistent manner with theory.

All the experiments reported herein have been performed with some composition F. 209 whose detonation velocity  $D_{\infty}^P$  m/s in "infinite diameter cartridges" varies with the initial density  $\rho_0$  g/cm<sup>3</sup> according to the law:  $D_{\infty}^P = 8193 + 3165 (\rho_0 - 1.720)$ . The density of every explosive piece is known within 1 mg/cm<sup>3</sup>; the overall mean density of the explosive structures is 1.720 g/cm<sup>3</sup>; any quantity which refers to the mean density will be underlined and called nominal.

## INITIATION DEVICE

The difficulties associated with experimental studies of spherical detonations are well known; they can be summarized as follows:

1. The necessity of initiating the process without disturbing the uniformity of the initial state or the spherical symmetry by means of a suitable device that would deposit a sufficient and reproducible amount of energy in the explosive medium.

2. The requirement for so large a sphere that an observable part of the travel of the detonation wave would take place in an unperturbed medium.

According to these remarks, the following process has been chosen.

One casts two identical hemispheres; on the plane surface of each, one mills two diametrically opposite hemicylindrical cavities whose diameter is 10 mm and whose bottom lies 4.5 mm from the center (Fig. 1). By proper assemblage of these hemispheres, one gets a round ball with two cylindrical cavities in each of which a detonator may be introduced. Thus the initiation area consists of two diametrically opposite circles whose common axis will be called the axis of initiation.

Let  $(\pi)$  be the diametrical plane of the sphere which is perpendicular to the axis of initiation. The emergence of the detonation from the free surface of the explosive has been observed in plane  $(\pi)$  with a streak camera. A perfect sphericity of the wave would imply a straight line on the film; in other words the sphericity defect is measured by the largest difference along the time axis. For spheres 75 mm in radius, the mean time defect has been found to be 30 ns, with which corresponds a

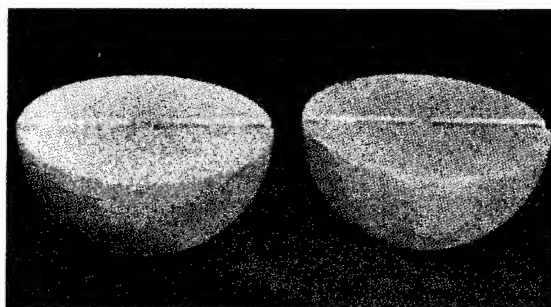


Fig. 1 - Explosive structure for detonation velocity measurements and sphericity analysis

space defect of 0.25 mm, i.e., a relative space defect of 0.3%. The same value was found for greater spheres, 100 and 150 mm in radius. As 0.3% is the order of magnitude that should be expected from the manufacturing and assembling allowances of such a material, one could not reasonably expect a better result. Figure 2 shows a typical streak camera record.

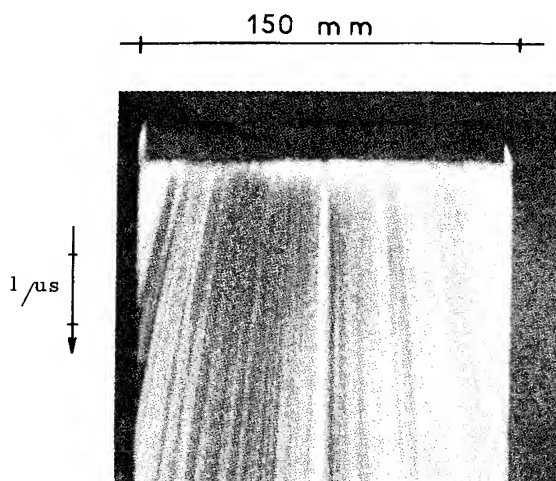


Fig. 2 - Sphericity analysis. Typical streak camera record.

## DETONATION VELOCITY MEASUREMENTS

The velocity of the thusly initiated spherical divergent detonation has been measured by means of an "air-chambers probe". Such a probe (Fig. 3) consists of a hollow lucite cylinder (6 mm in outside diameter, 4 mm in inside diameter) in which are inserted small cylindrical

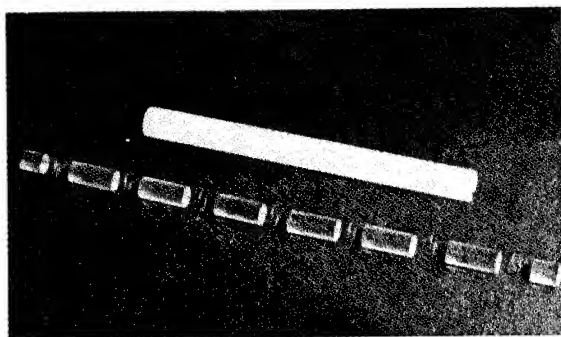


Fig. 3 - Air-chambers probe

sticks of polished lucite (4 mm in diameter, 10 or  $15 \pm 0.01$  mm in length) separated from one another by piano-string rings (0.1 mm thick) which define minute air chambers. The probe is introduced in a 6-mm-diameter cylindrical cavity bored along a ray of plane  $\pi$  down to 7.5 mm from the center. When the detonation wave reaches a chamber, the enclosed air is lighted up. These flashes are recorded on the film of a streak camera, provided the axis of the probe coincides with the optical axis of the camera. A typical streak camera record is shown in Fig. 4; it is worth noticing that the sphericity of the wave may be checked at each shot.

As a result of the above-mentioned measurements of the lucite sticks, the space resolution is  $10^{-3}$ . One has managed to get the same order of magnitude as for the time resolution by:

- Choosing a high rotational speed of the mirror ( $v \sim 4000$  t/s), so that the interval between two luminous tracks might be measured with a precision of  $3 \times 10^{-4}$ .

- Measuring the half-period  $T$  of mirror rotation during which the detonation takes place so that  $\Delta v/v \leq 4 \times 10^{-4}$ .

Moreover, one has systematically measured the intervals in the middle part of the film in order to get free of the variation of the inscription speed along "the time-axis" of the film. Consequently, it can be asserted that, in each interval, the mean detonation velocity  $D$  is measured with an experimental error less than 14 m/s.

The difference between  $1.720 \text{ g/cm}^3$  and the density of the sphere where  $D$  is measured is then taken into account according to the above-mentioned rate of variation of  $D_{\infty}^P$  with  $\rho_0$ . The nominal values  $\underline{D}$  of  $D$  are given in Table 1 and plotted on Fig. 5 as a function of the mean

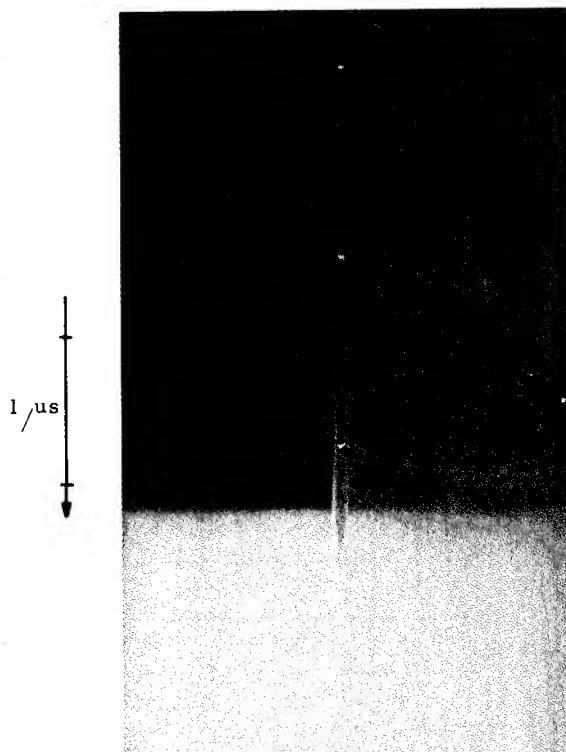


Fig. 4 - Detonation velocity measurements. Typical streak camera record.

radius  $x$  of the interval. When remembering that  $D_{\infty}^P = 8193 \text{ m/s}$ , one easily realises that  $\underline{D}(x)$  starts from values lower than  $D_{\infty}^P$ , increases up to values higher than  $D_{\infty}^P$ , then decreases and finally keeps a constant value  $D_{\infty}^s$  which is significantly higher than  $D_{\infty}^P$ .

This last result now raises a question: is  $D_{\infty}^s$  greater than  $D_{\infty}^P$  for any given density  $\rho_0$ ? According to Table 2, in which the  $\underline{D}(x \geq 110 \text{ mm})$  measurements are compared with steady detonation velocity measurements in  $d = 50 \text{ mm}$  — cartridges with adjusted density — it seems that the answer may reasonably be considered as positive.

## FLOW FIELD MEASUREMENTS

### Principles

The experimental technique is that previously used in the study of the flow behind the detonation front in a cylindrical charge (2,3). It consists in materializing parallel planes in the explosive ball by inserting 0.01-mm thick rectangular gold foils whose centers are lined up along a ray. As soon as reached by the

TABLE 1  
Ten Values of the Nominal Spherical Divergent Detonation Velocity  $\bar{D}(X)$

$\frac{x_1}{x_2}$	$\frac{7.5}{22.5}$	$\frac{22.5}{37.5}$	$\frac{37.5}{52.5}$	$\frac{52.5}{67.5}$	$\frac{67.5}{82.5}$	$\frac{82.5}{97.5}$	$\frac{105}{115}$	$\frac{115}{125}$	$\frac{125}{135}$	$\frac{135}{145}$
x mm	15	30	45	60	75	90	110	120	130	140
$\bar{D}$ m/s	8081	8110	8198	8230	8254	8279	8237	8228	8227	8227

TABLE 2  
Comparison of  $\bar{D}(x \geq 110 \text{ mm})$  and  $\bar{D}(d = 50 \text{ mm})$  for  $1.727 \leq \rho_0 \leq 1.728 \text{ g/cm}^3$

		X = 110 mm	X = 120 mm	X = 130 mm	X = 140 mm	d = 50 mm		
$\rho_0$		D	D	D	D	D	$\rho_0$	
1.727			8257	8255	8256	8219	1.727	
1.727				8240	8252	8197	1.727	
1.728		8276	8273	8248	8245	8207	1.728	
1.728		8246	8226	8263	8251	8229	1.728	
Average	1,7275	8261	8252	8251		8213	1.7275	Average

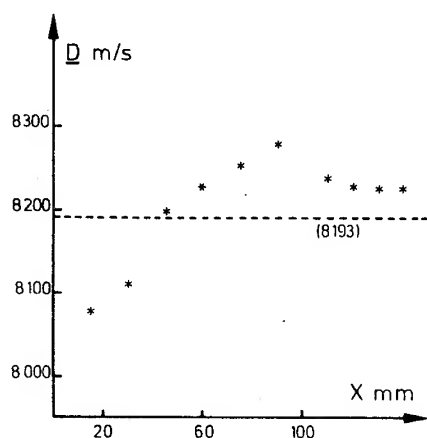


Fig. 5 - Nominal velocity  $\bar{D}$  v. wave radius x

wave, the foils are carried along by the detonation products. The radiographic record of their successive positions yields the movement of material surfaces behind the wave.

Such experiments are rather difficult. The generator need be strong enough so that the beam is not completely absorbed. As for the

X-ray tube, it must have an emissive focus small enough for the displacement measurements to remain meaningful in spite of the geometric blur. Finally, the release jitter must be very short, since otherwise shots should be numerous in order to make up for their irregular timing.

### Experiments

A 2.5-MV Francitron generator is used together with a CGR reflexion tube: the flash duration is 50 ns, the emissive focus diameter is 4 mm, and the release jitter is 50 ns.

The initiation device is that described above, and an idea of the explosive structure is given by Fig. 6. Because of the manufacturing and assembling constraints, the interval between foils is 10 mm; the first lies 20 mm, the last 90 mm, from the center. The side of the foils which is meant to be perpendicular to the beam is 50 mm large; the dimension of the other side is chosen so as to be approximately one-half of the penetrated explosive. Moreover, in order to avoid useless absorption of the beam, the diameter of the spheres is 150 mm when studying the early phases of the detonation ( $\approx 9 \mu\text{s}$ ), 200 mm afterwards.

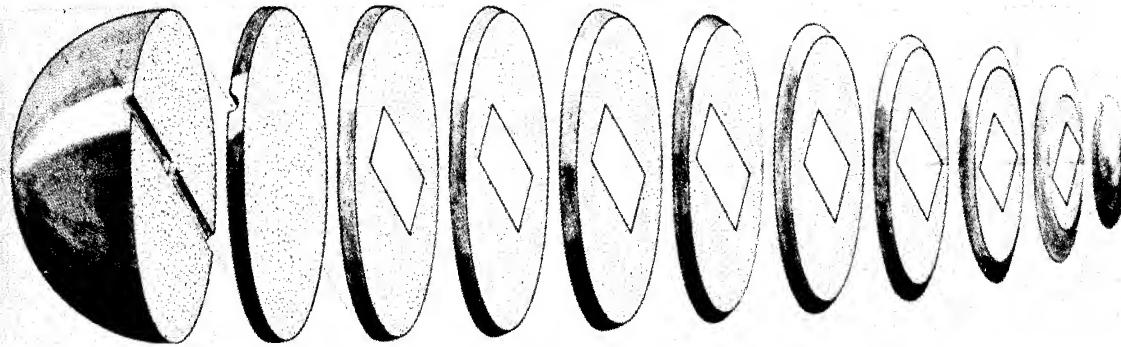


Fig. 6 - Explosive structure for flow field measurements

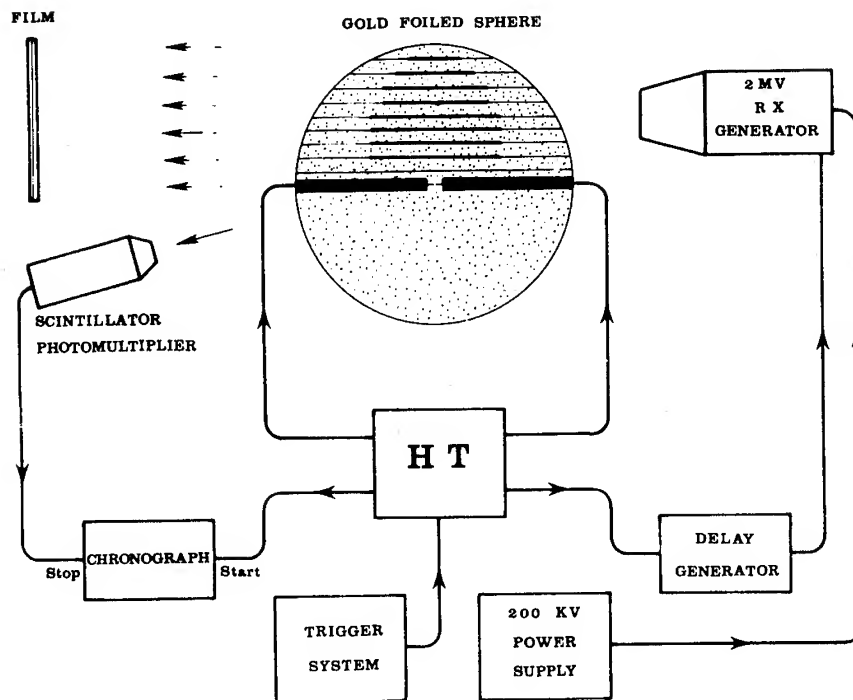


Fig. 7 - Experimental arrangement for flow field measurements

The time elapsed between the initiation time  $t_0$  and the recording time  $t_i$  ( $i = 1, 2, \dots$ ) is measured according to the experimental arrangement shown in Fig. 7. Times  $t_i$  are chosen so that  $t_1 - t_0 = 2.40 \mu\text{s}$  and  $t_{i+1} - t_i = 250 \text{ ns}$ . Figures 8 and 9 are reproduction of two of these radiographic records.

### Results

The  $i$ th record yields the position  $X_i$  of the detonation front and the position  $R_i$  of the center

of every foil whose initial abscissa  $R_0$  is less than  $X_i$ . Thus, from time measurements and X-ray pictures, one is able to construct the path of the center of a foil. Figure 10, where these results have been summarized, shows plausibly if not certainly, that the material velocity  $u$  never goes negative.

Let  $\tau(X)$  be the time when the wave front reaches radius  $X$ . With a view to studying the flow in the vicinity of the wave front, the arches  $R[R_0, \tau(R_0) < t < \tau(R_0 + 4.5 \mu\text{s})]$  are represented in the form  $R = a/3 t^3 - b/2 t^2 + ct + d$ .

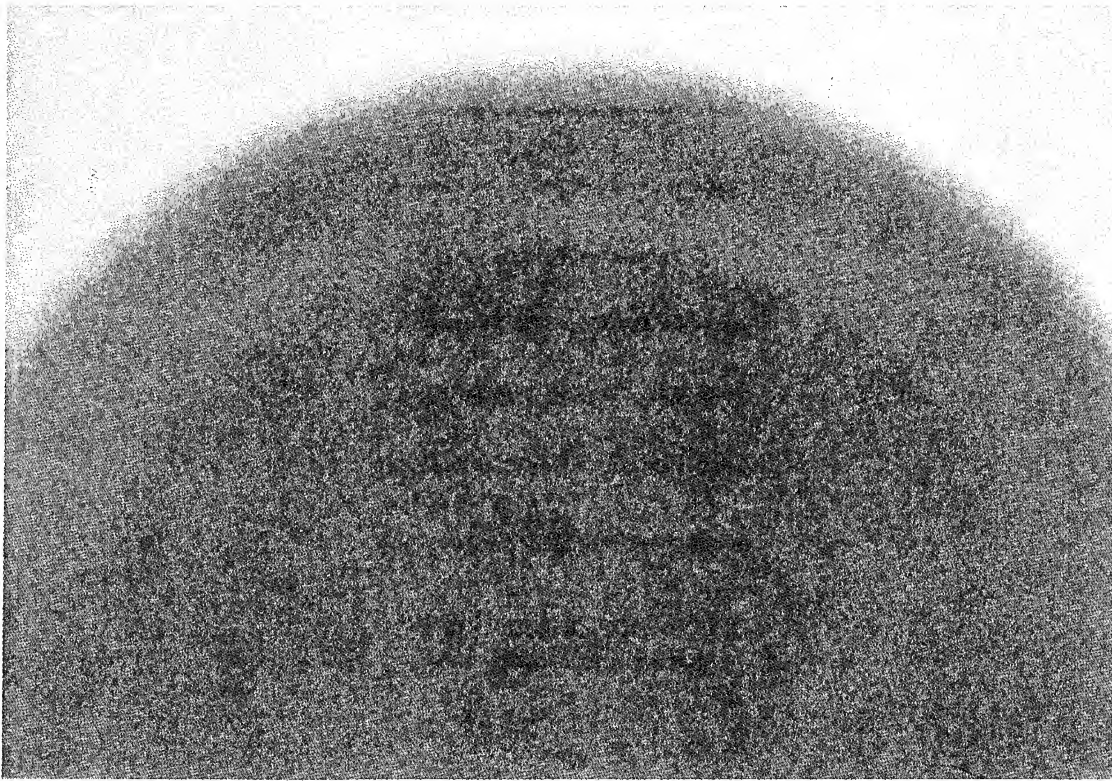


Fig. 8 - Dynamic radiograph at  $t_i = t_0 + 8.65 \mu s$

The values of  $a(R_0)$ ,  $b(R_0)$ ,  $c(R_0)$ ,  $d(R_0)$  are numerically deduced from the curves of Fig. 10, and given below.

$R_0$ mm	20	30	40	50	60	70
a	0.097	0.17	0.14	0.14	0.16	0.13
b	1.20	2.36	2.33	2.75	3.46	3.09
c	3.78	8.52	9.99	14.08	19.30	19.61
d	13.89	11.94	13.57	4.95	-9.31	-10.7

Let  $z$  be an Eulerian coordinate defined as the positive distance to the wave front. The flow field at  $\tau(X)$  may be parametrically defined by the equations

$$\begin{cases} z = X - R[R_0, \tau(X)] \\ u = u[R_0, \tau(X)] \end{cases}$$

The  $u(z, X)$  and  $u(z/X, X)$  curves —  $X = 55.75$  mm — are respectively given on Figs. 11a and 11b. The latter shows that the material velocity field differs significantly from that of Taylor's

self-similar model (4) in the vicinity of the wave front.

## THEORETICAL CONSIDERATIONS

Theoretical Approximation of  $u(z, X)$

Let us use the following notations:

$C_v$  = specific heat at constant volume

$C_p$  = specific heat at constant pressure

$\gamma$  = specific heats ratio

$\kappa$  = coefficient of heat conduction

$\omega$  = longitudinal Prandtl number

$v = \rho^{-1}$  massic volume

$p$  = pressure

$-a^2/v^2$  = first derivative of  $p$  vs  $v$  along a chemical equilibrium isentrope of the detonation products

$\ddot{p}$  = second derivative.



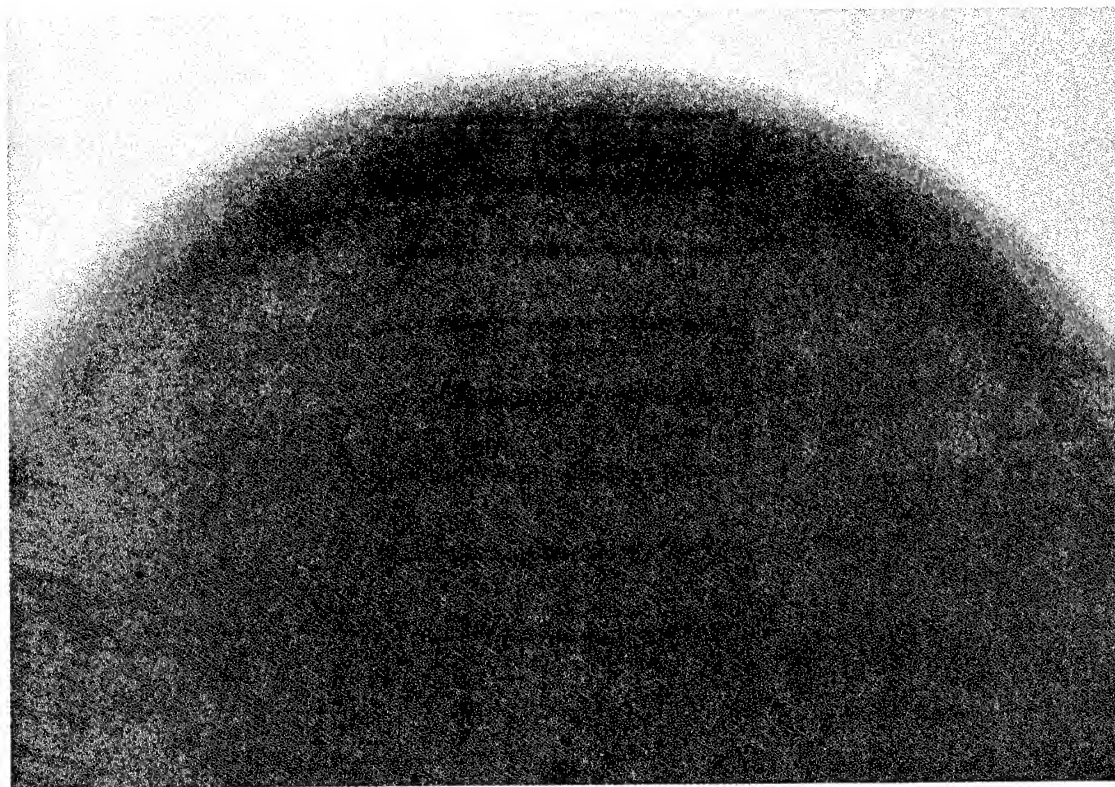


Fig. 9 - Dynamic radiograph at  $t_1 = t_0 + 10.81 \mu s$

Results.

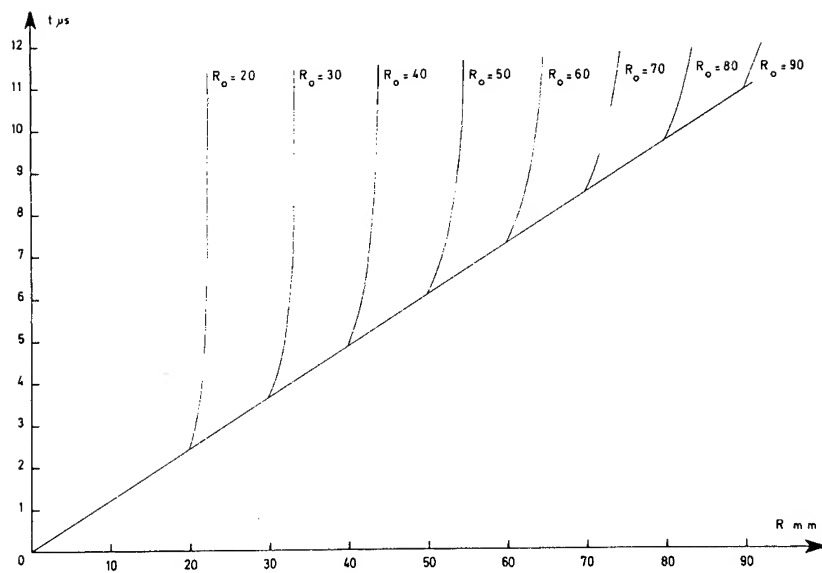
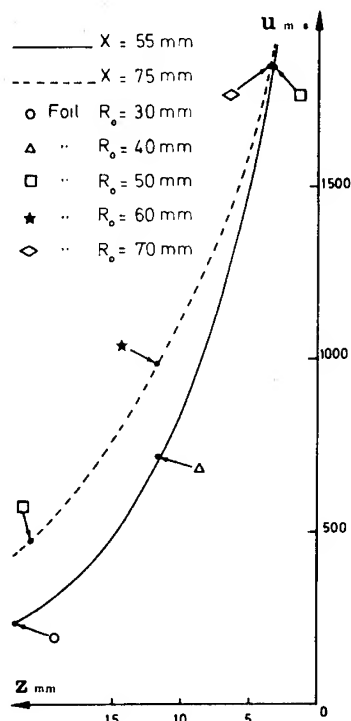
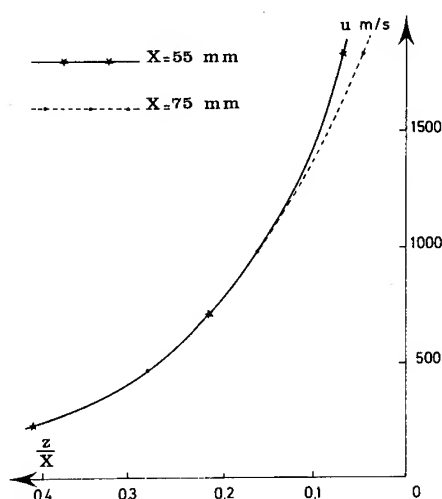


Fig. 10 - Movement of the gold foils --  $(R, t)$  diagram



(a)

FIG. 11. b. MATERIAL VELOCITY FIELD;  $u(z/X, X)$  DIAGRAM

(b)

Fig. 11 - (a) Material velocity field;  $u(z, x)$  diagram, and (b) material velocity field,  $u(z/X, X)$  diagram

$$\beta_* = \frac{(\rho_0 D_*)^3}{u_* \dot{P}_*}, \quad \ell_* = (\gamma_* + \omega_* - 1) \left( \frac{xv}{dC_p} \right).$$

It may be deduced from the theoretical results given references 5 and 6 that, in the vicinity of  $u_*$ , the function

$$u_* \left[ 1 + \beta_* \frac{\ell_*}{z} - 2 \sqrt{\beta_* \frac{z}{X}} \right] \quad (1)$$

is an approximation of  $u(z, X)$ .

#### Interpretation of the Experimental Results

Let  $\Gamma_*$  be defined as the difference  $(D_*/u_*) - 1$ . From the numerical study of the detonation products of a condensed explosive, it is well known that a very good approximation of  $\dot{p}_*$  is obtained by assuming that the C-J isentrope osculates the  $(P/P_*)(v/v_*)^{\Gamma_*} = 1$  curve. Owing to this remark, it is easily shown that  $\beta_* = \Gamma_*/(\Gamma_* + 1)$ , which enables to write equation (1) in the form

$$u_* \left[ 1 + \left( 1 - \frac{u_*}{D_*} \right) \frac{\ell_*}{z} - 2 \sqrt{\left( 1 - \frac{u_*}{D_*} \right) \frac{z}{X}} \right]. \quad (2)$$

The quantities  $u_*$  and  $\ell_*$ , when considered as parameters, may be sought so as to best represent the experimental curves  $u(z, X)$   $X = 55, 58, 65, 68, 75$ . When assigning to  $D_*$  the value  $D_{\infty}^s$ , one is led to the following values:

$$u_* = 2.04 \text{ mm}/\mu\text{s}$$

$$\ell_* = 3 \text{ mm}.$$

This value of  $u_*$  agrees reasonably with the "usual B.K.W. calculated" C-J value 2.12 mm/ $\mu$ s (by usual, one means that the calculations are performed with parameters  $\beta$  and  $\kappa$  adjusted so that the calculated C-J velocity equals the measured value  $D_{\infty}^D = 8193 \text{ m/s}$ ).

#### CONCLUSIONS

In view of a possible generalization to other solid explosives, three among the above-reported results seem worth emphasizing:

1. The spherical, divergent detonation velocity tends toward a limit which is significantly higher than that which is reached in a large-diameter cartridge;

Let the subscripts 0 and \* characterize respectively the initial state of the explosive and the C-J state of the detonation products. Let the number  $\beta_*$ , and the length  $\ell_*$ , be defined by

2. The material velocity field differs significantly from Taylor's self-similar flow in the vicinity of the wave front;

3. The theoretical considerations based upon the internal and external structures of zeroth order of the detonation wave give a direct way of determining the C-J mechanical characteristics from material velocity measurements.

## REFERENCES

1. C. Brochet, J. Brossard, R. Chéret, N. Nanson, and G. Verdès, 5th Symposium on Detonation.

2. C. Fauquignon, M. Prouteau, and G. Verdès, 4th Symposium on Detonation, Washington, 1965.

3. G. Verdès, F. David, F. Prouteau, and M. Dufresne, Symposium H.D.P., Paris, 1967.

4. G. I. Taylor, Proceedings, of the Royal Society, A, 200, 1950, p. 235.

5. R. Chéret, Comptes rendus, 269, série B, 1969, p. 603.

6. R. Chéret, Comptes rendus, 270, série B, 1970, p. 1517.

## DISCUSSION

M. COWPERTHWAIT  
Stanford Research Institute  
Menlo Park, California

I agree with Dr. Chéret that the flow near the shock front is not self-similar. For the

Z-N-D model for a spherical detonation wave it is easy to prove that the flow cannot be self-similar because of the reaction and the divergence.

# A COMPARISON OF SPHERICAL, CYLINDRICAL AND PLANE DETONATION VELOCITIES IN SOME CONDENSED AND GASEOUS EXPLOSIVES

C. Brochet, J. Brossard, and N. Manson  
*Laboratoire d'Energétique  
University of Poitiers*

and

R. Chéret, and G. Verdès  
*Commissariat à l'Energie Atomique  
Centre d'études de Vaujours  
93 Sevrans (France)*

## ABSTRACT

New experimental results, as well as previous ones, have been considered in view of comparing the plane ( $D_p$ ), divergent cylindrical ( $D_c$ ) and spherical ( $D_s$ ) detonation velocities of a solid explosive ( $\rho_0 = 1.720 \text{ g/cm}^3$ ), a liquid explosive (commercial grade nitromethane), a gaseous explosive ( $\text{C}_3\text{H}_8 + 5 \text{ O}_2$  mixture,  $p_0 = 1 \text{ bar}$ ,  $T_0 = 293^\circ\text{K}$ ).

Taking into account the values  $D_{p\infty}$ ,  $D_{c\infty}$ , and  $D_{s\infty}$  of the detonation velocity corresponding to infinite values of the geometrical parameters, as the charge diameter, the thickness of the cylindrical charge, the abscissa of the detonation front, it can be concluded that:

- (i) Only the velocity  $D_{s\infty}$  seems to characterize intrinsically the detonation process,
- (ii) The detonation velocity does depend on the rear flow and thus the Chapman-Jouguet theory appears as a first approximation.

## I - INTRODUCTION

I.1 - It is now well proved that the measured values of the detonation velocities  $D$  generally agree within a few percent (3 to 5%) with those  $D_{th}$  which are calculated through the usual Chapman-Jouguet equations. This agreement is more particularly obvious in the case of gaseous explosives, provided the heterogeneities of the wave front (1-4) do not perturb the velocity measurements, i.e., when the typical length of the multidimensional structure (5) of the front is negligible with respect to the distance over which the detonation is observed. For condensed explosives, such an agreement between  $D_{th}$  and  $D$  is obtained through a proper choice of thermodynamic data in a way which is generally thought to be satisfactory.

According to various considerations, the velocity  $D$  does not seem to be the most appropriate detonation parameter to ground a definite appreciation of Chapman-Jouguet theory. Nevertheless, it does remain that  $D$  is the only detonation characteristic which can be measured accurately (0.2%) whatever be the wave configuration, and that gathering and comparing numerous and accurate velocity measurements will help further progress in the field.

I.2 - The present paper summarizes the conclusions brought out by the results of some new experiments which have been achieved in view of completing the existent knowledge of plane, divergent cylindrical and spherical waves in gaseous and condensed explosives. In order to refer easily to previous measurements of

our own and to other authors' results, these experiments deal with usual explosives (composition F.209, commercial grade nitromethane,  $C_3H_8 + 5 O_2$  mixture) under usual pressure and temperature conditions.

It appears to be convenient to present and discuss the plane  $D_p$ , cylindrical  $D_c$ , spherical  $D_s$  velocity measurements according to the distance  $X$  covered by the wave and to a parameter  $d$  defined as follows:

(a) for a plane wave,  $d$  is hydraulic diameter of the charge;

(b) for a cylindrical wave in an  $h$ -high charge,  $d = 2h$  ( $2h$  is the limit of the hydraulic diameter when  $X$  goes to infinity);

(c) for a spherical wave,  $d = X$ .

The limits of  $D_p$ ,  $D_c$ ,  $D_s$  when  $d^{-1} = 0$  are respectively called  $D_{p\infty}$ ,  $D_{c\infty}$ ,  $D_{s\infty}$ .

Though small, the differences between the three above-defined limits are significant insofar as they appear systematically in such a way that, when accounted for in other experiments involving other explosives, they may be interpreted in terms of confinement effects on the movement of the detonation products.

## 2 - EXPERIMENTAL RESULTS

### 2.1 - Composition F.209 - (Fig. 1) -

#### 2.1.1. Plane detonations.

Dealing with bare cartridges ( $20 < d_{mm} < 100$ ,  $240 < X_{mm} < 440$ ) and using ionization probes, we have verified that, as it generally happens in solid high explosives, the detonation propagates at a constant velocity  $D_p$  when  $X > 3d$  and that the variation of  $D_p$  with  $d$  is less than 0.2% for the considered values of  $d$ . Therefore the measured value may be considered as the limit  $D_{p\infty}$ . According to our measurements,  $D_{p\infty}$  varies with  $\rho_0$  ( $1.710 < \rho_0 < 1.730$  g/cm<sup>3</sup>) according to the law  $D_{p\infty}(m/s) = 8193 + 3165(\rho_0 - 1.720)$ .

#### 2.1.2. Cylindrical detonations.

Cylindrical detonations have been generated (6) in 300-mm-diameter flat cylinders whose density  $\rho_0$  belongs to the range 1.712 to 1.725 with 1.720 as a mean value, and whose height  $h$  is 10, 20, or 30 mm. The initiation was obtained through the same device as that described in (7),

and the velocity  $D_c(X)$  has been measured, in the plane of symmetry, by means of air-chamber probes (cf. (7)). The difference between 1.720 and the density of each cylinder has been taken into account according to the above-mentioned rate of variation of  $D_{p\infty}$  with  $\rho_0$ . The thus normalized experimental results show that, for each of the three charge heights  $h$ ,  $D_c(X)$  reaches a constant value  $D_c$  when  $X > X(d)$ ; one notices that  $(X(d) - 1.5 d)$  is positive and decreases when  $d$  increases. These three  $D_c$  values are such that  $|D_c - D_{p\infty}|/D_{p\infty} = 0.2\%$ . Therefore one may consider that  $D_{c\infty}$  does not differ from  $D_{p\infty}$ .

#### 2.1.3. Spherical detonations.

Spherical, divergent detonations have been initiated under conditions described in (7), in explosive (150-mm diameter) spheres whose density  $\rho_0$  belong to the range 1.714 to 1.728 g/cm<sup>3</sup> with 1.720 as mean value. The velocity  $D_s(X)$  has been measured by means of air-chamber probes, along a ray normal to the axis of initiation. The measurements have been then referred to the density 1.720 according to the law  $D_{p\infty}(\rho_0)$ . The normalized velocity starts from values smaller than  $D_{p\infty} = 8193$  m/s, increases up to values higher than  $D_{p\infty}$ , then decreases slowly and finally keeps, when  $X > 120$  mm, a constant value  $D_s = 8227$  m/s. It may be emphasized that this later value identified with  $D_{s\infty}$  value exceeds  $D_{p\infty}$  by approximately 0.4% (cf. Fig. 1).

In order to remove the uncertainty which may originate from "normalization," experiments have been designed so that the measurements of  $D_s(X > 120 \text{ mm}) = 8251$  m/s only deal with spheres whose density is 1.727 or 1.728 g/cm<sup>3</sup> and can be directly compared to the  $D_{p\infty} = 8213$  m/s value measured in ( $d = 50$  mm) cartridges of the same  $\rho_0$  density. This comparison confirms that  $D_{s\infty} > D_{p\infty}$ .

### 2.2 - Commercial grade nitromethane -

#### 2.2.1. Plane detonations.

By means of ionization probes and chronographs, we have measured within 0.2% the velocity  $D_p$  in steel tubes (length 500 mm, internal diameter  $20 \leq d \leq 36$  mm, wall thickness  $2 \leq e \leq 9$  mm). In agreement with many other studies on nitromethane (8, 9) and on different liquid explosive (10, 11) we have found that  $D_p$  is a linear function of  $d^{-1}$  (cf. Fig. 2) (P curve).

Moreover it seems that the  $D_{p\infty}$  value does not depend on the nature of the confinement,

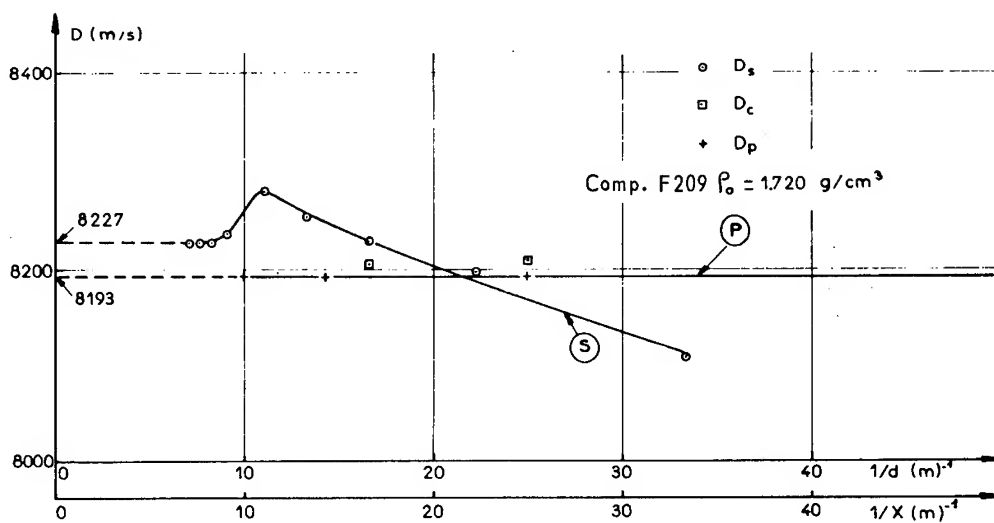


Figure 1

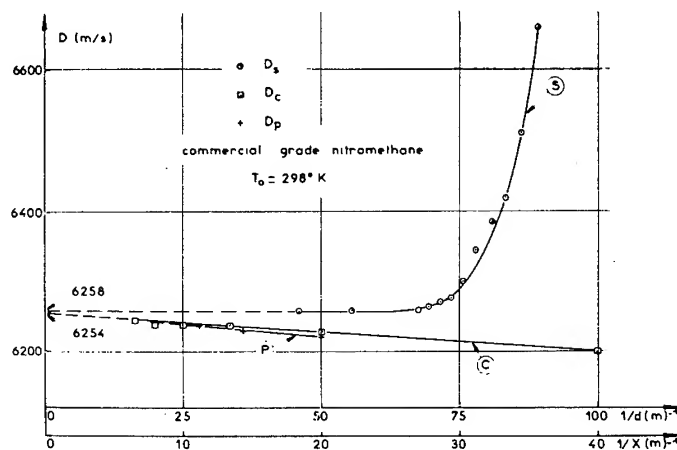


Figure 2

whereas the slope  $\Pi_p = |\partial D_p / \partial (d^{-1})|$  does vary with the mechanical properties and thickness of the tube.

### 2.2.2. Cylindrical detonations.

Owing to the above mentioned technique, the detonation velocity  $D_c$  of nitromethane ( $T_0 = 298 \pm 1^\circ\text{K}$ ) in cylindrical sectors ( $5 \leq h \leq 30$  mm,  $36^\circ \leq \alpha \leq 60^\circ$ , 1.2-mm thick steel walls) has been measured (12) within 0.3% over a distance of 200 mm (and sometimes 400 mm). When  $X > 50$  mm, it appears to keep a constant value which is a linear function of  $d^{-1}$  (cf. Fig. 2, C curve). The  $D_{c\infty}$  corresponding equals  $D_{p\infty}$  within experimental error.

### 2.2.3. Spherical detonations.

The spherical divergent detonation of commercial grade nitromethane ( $T_0 = 298 \pm 1^\circ\text{K}$ ) has been initiated (13) by the spherical divergent detonation of a 50-mm-diameter solid explosive ball, which is itself initiated as described in (7). The container is made of glass and is shaped as a cube whose side is 110 mm long. The velocity  $D_s$  has been measured within 0.2% by means of the argon flash technique and streak camera. It has been found that  $D_s$  decreases rapidly when  $(X - X_0)$  increases ( $X_0 =$  initiator radius = 25 mm) and keeps, when  $(X - X_0) > 12$  mm, a constant value  $D_{s\infty}$  which equals  $D_{p\infty}$  within 0.2% (cf. Fig. 2, S curve).

2.3 -  $C_3H_8 + 5 O_2$  Mixture -

## 2.3.1. Plane detonations.

In previous experiments (14) (15), plane self-sustained detonations of  $C_3H_8 + 5 O_2$  mixture ( $p_0 = 1$  bar,  $T_0 = 293 \pm 3^\circ K$ ) in circular tubes ( $14 \leq d_{mm} \leq 52$ ) have been investigated in such conditions that the velocity keeps a constant value of  $D_p$  over a distance  $x > 10$  m. It was then evidenced that the amplitude of the linear variation of  $D_p$  with  $d^{-1}$  depends on the internal surface roughness and nature of the tubes (cf. Fig. 3, curve P). More precisely, the stainless steel tubes involve a value of  $\Pi_p = |\partial D / \partial (d^{-1})|$  which is smaller than that involved by ordinary steel tubes which are rougher (15). However, the value of  $D_{p\infty}$  deduced from the first serie of tubes does not differ significantly from that deduced from the second. In that respect it is worth noticing that the investigation (16) of plane steady self-sustained detonations of various mixtures in rectangular tubes (length 15 m, cross section  $10 \times 23$ ,  $22 \times 48$ ,  $34 \times 72$  mm<sup>2</sup>) has shown that  $D_p$  still varies linearly with  $d^{-1}$  but that  $D_{p\infty}$  is significantly higher (about 1% in the case of  $C_3H_8 + 5 O_2$  mixture at  $0.3 \leq p_0 \leq 0.5$  bar) than that found in circular tubes.\*

It is also interesting to emphasize that the  $D_{p\infty}$  values generally are higher (0.5 to 1% in various mixtures including  $C_3H_8 + 5 O_2$ ,  $0.5 \leq p_0 \leq 3$  bars, and  $293 \leq T_0 \leq 430^\circ K$  (14) (15)) than the corresponding values of  $D_{th}$  calculated a priori from the Chapman-Jouguet theory.

## 2.3.2. Cylindrical detonations.

In a previous investigation (17) of the cylindrical divergent detonations of  $C_3H_8 + x O_2 + ZN_2$  mixtures ( $p_0 = 1$  bar,  $T_0 = 293 \pm 2^\circ K$ ) in cylindrical sectors ( $2 \leq h_{mm} \leq 14$ ,  $\alpha = 60^\circ$ , lucite walls), the velocity has been measured within 0.2% by means of ionization probes and chronographs. When  $150 \leq X_{mm} \leq 500$ , the velocity appears to keep a constant value  $D_c$  and in spite of a nonlinear variation of  $D_c$  vs  $d^{-1}$ , a conventional value  $D_{c\infty}$  has been defined which exceeds the corresponding  $D_{p\infty}$  by 1 to .15%.

But new experiments achieved in the same mixtures  $4.5 \leq x \leq 5.5$  and  $Z = 0$  with  $h = 25$  mm have shown that  $D_c(d^{-1})$  goes through a maximum, and consequently the previous extrapolation

mode leading to a conventional  $D_{c\infty}$  value must be reconsidered (cf. Fig. 3, curve C).

## 2.3.3. Spherical detonations.

The detailed investigations (18) (19) of the spherical divergent detonations of various mixtures ( $C_3H_8$  or  $H_2$  or  $C_2H_4$  or  $C_2H_2$  with  $O_2$ ;  $T_0 = 293 \pm 3^\circ K$ ,  $0.1 \leq p_0 \leq 2.8$  bar) in a 1-m-diameter steel container, have shown that in  $C_3H_8 + 5 O_2$  mixture, when  $x > 100$  mm, the detonation velocity, measured within 0.4% by the Doppler technique, keeps a constant value which may be considered as  $D_{s\infty}$  (cf. Fig. 3, curve S).

## 2.3.4. Remarks.

(i) In the range of initial pressure investigated, the  $D_{s\infty}$  values are generally smaller than the corresponding  $D_{th}$  values. For example in  $C_3H_8 + 5 O_2$  mixture,  $p_0 = 1$  bar and  $T_0 = 293^\circ K$ , this difference is about 1%.

(ii) One of us (J.B.) has noticed that the value of  $D_{s\infty}$  and the curve  $D_c(d^{-1})$  may lead (cf. Fig. 3) to think that  $D_{c\infty} = D_{s\infty}$  and that  $D_p(d^{-1})$  ceases to be linear for large values of  $d$ . The results of the first experiments, performed with  $C_3H_8 + 5 O_2 + ZN_2$  mixtures ( $0.1 \leq p_0 \leq 1.7$  bar,  $T_0 = 293^\circ K$ ) in 107-mm-diameter steel tubes 11 m long, seem to support this assumption.

## 3 - DISCUSSION AND CONCLUSIONS

The results which are summarized in Figs. 1, 2, and 3, together with a few others which have been quoted above, lead to the following conclusions:

## (1) In condensed explosives

- $D_{p\infty}$ ,  $D_{c\infty}$ ,  $D_{s\infty}$  may be defined without any ambiguity,
- $D_{c\infty}$  equals  $D_{p\infty}$  within experimental error,
- $D_{s\infty}$  exceeds  $D_{p\infty}$  in the case of a solid explosive, and equals  $D_{p\infty}$  in the case of a liquid explosive.

## (2) In gaseous explosives

- only  $D_{s\infty}$  may be defined unambiguously.

The first point is not really surprising insofar as the products of a spherical divergent

\*The  $\Pi_p$  value corresponding to the brass rectangular tubes is smaller than those observed in the case of stainless steel and steel circular tubes.

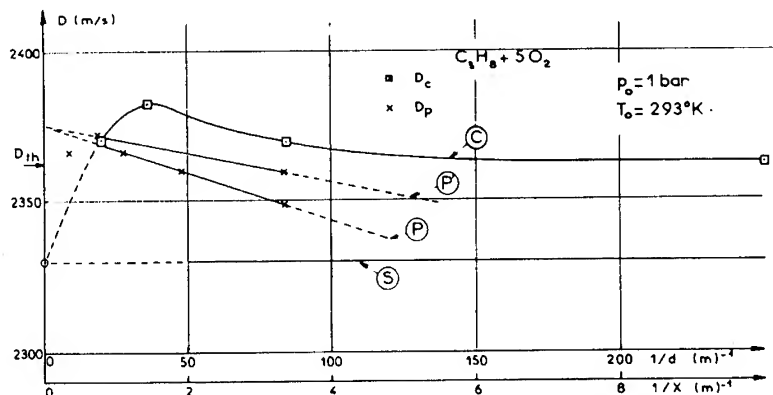


Figure 3

detonation are self-confined, whereas the confinement induces a lateral expansion wave in the products of a plane or divergent cylindrical detonation, and thus modifies the amount of chemical energy which is deposited in the flow and therefore the velocity of propagation (20, 21).

The interpretation of the second point is somewhat less obvious. However, one may notice that the range of detonability of a mixture (defined as a domain of the initial-parameters space) varies with the kind of the wave: it is narrower for a spherical wave than it is for a plane wave, and, in the latter case, it seems to be influenced by the nature of the walls. These facts, as those discussed previously in connection with the intrinsic instability of plane (1) and cylindrical (17) detonations, suggest that the walls do act in favour of a steady velocity. This stabilization effect of the walls on the wave does not contradict their well-known contribution to the decrease of  $D$  with decreasing  $d$ . The latter is all the more important as  $d$  is smaller; on the contrary, the former is appreciable only when  $d$  becomes large enough.

The available experimental results do not allow a more precise analysis of these phenomena. Nevertheless, when recalling the main features of the flow behind a plane detonation wave in a explosive and trying to conceive what can be the flow field in similar charges of gaseous explosives, it appears that:

(i) Among all the detonation parameters we are now able to measure with accuracy, only the velocity  $D_{s\infty}$  of the spherical detonation wave seems to characterize the detonation process by itself, the detonation products being self-confined in respect of the quasi-perfect symmetry of the flow field;

(ii) Contrary to the Chapman-Jouguet theory, the detonation velocity does depend, in higher-order approximation, on the rear flow of the detonation products.

#### REFERENCES

1. N. Manson, C. Brochet, J. Brossard and Y. Pujol, 9th Symp. Intern. on Combustion, pp. 461-469, Academic Press, New York, 1963.
2. J. H. Lee, B.H.K. Lee and J. Shanfield, 10th Symp. Intern. on Combustion, pp. 808-817, The Combustion Institute, Pittsburgh, 1965.
3. N. Manson and F. Ferrié, 4th Symp. Intern. on Combustion, pp. 486-494, Williams and Wilkins, Baltimore, 1953.
4. H. Freiwald and H. W. Koch, 9th Symp. Intern. on Combustion, pp. 275-281, Academic Press, New York, 1963.
5. D. H. Edwards, 12th Symp. Intern. on Combustion, pp. 819-828, The Combustion Institute, Pittsburgh, 1969.
6. R. Chéret and G. Verdès, Centre d'études de Vaujours, France, to be published.
7. R. Chéret and G. Verdès, Centre d'études de Vaujours, France, paper in this Symposium.
8. C. Brochet, Y. Guasson, Y. Pujol and N. Manson, C. R. Acad. Sc. Paris, 269, pp. 105-108, July 1969.



9. A. W. Campbell, M. E. Malin and T. E. Holland, 2nd O.N.R. Symp. on Detonation, pp. 336-359, Washington and White Oak, 1955.
10. E. A. Igel and L. B. Seely, Jr., 2nd O.N.R. Symp. on Detonation, pp. 321-335, Washington and White Oak, 1955.
11. J. Brossard, Y. Bernard, P. Claude and N. Manson, C. R. Acad. Sc. Paris, 263, pp. 1095-1098, Nov. 1966.  
C. Brochet, 2nd Colloquium on Gas-dynamics of explosions and reactive systems, Novosibirsk, Aug. 1969, *Astronautica Acta* 15, pp. 419-425, 1970.
12. C. Brochet, N. Manson and H. Presles, Lab. Energétique, Poitiers, to be published.
13. R. Chéret and G. Verdès, Centre d'études de Vaujours, France, to be published.
14. C. Brochet, these Doctorat ès Sciences, Poitiers, June 1966.
15. Y. Pujol, thèse Doctorat ès Sciences, Poitiers, Apr. 1968.
16. J. N. Boislevé, thèse Doctorat 3eme Cycle, Poitiers, 1970.
17. J. Brossard, N. Manson and M. Niollet, 11th Symp. Intern. on Combustion, pp. 623-633, The Combustion Institute, Pittsburgh, 1967.
18. J. Brossard, C.R. Acad. Sc. Paris, 268, pp. 2061-2064, June 1969.
19. J. Brossard, these Doctorat ès Sciences, Poitiers, 1970.
20. M. A. Cook, the science of high explosives, Reinhold Pub. Corp., New York, 1958.
21. J. Taylor, Detonation in condensed explosives, Clarendon Press, Oxford, 1952.

## DISCUSSION

Y. MANHEIMER-TIMNAT  
Technion, Israel Institute of Technology  
Haifa, Israel

What was the wavelength used in the microwave Doppler measurement? Did the air-chambers-probe cause any disturbance in the detonation wave? Was its accuracy compared with one of the other methods in a plane detonation and what were the results?

## REPLY BY CHÉRET

The microwave Doppler effect was obtained from a 9.135-MHz frequency klystron

generator (cf. C.R. Acad. Sc. PARIS, t 268, p. 2061, 1969).

In spite of the rather high writing speed (25 mm/ $\mu$ s), the streak camera record, which yields the detonation velocity and also checks the simultaneity of the emergence, does not show any sphericity defect of the wave in the vicinity of the probe.

We did not think of such a comparison since we did not know of any other method which could enable us to measure an unsteady detonation velocity inside the explosive within 0.4%.

# DETONATION CHARACTERISTICS OF VERY LOW DENSITY EXPLOSIVE SYSTEMS

James L. Austing and Allen J. Tulis  
*IIT Research Institute*  
*Chicago, Illinois 60616*

and

Charles D. Johnson  
*Honeywell, Inc.*  
*Ordnance Division*  
*Hopkins, Minnesota 55343*

## ABSTRACT

The detonation characteristics of very low density explosive systems such as nitrocellulose, foamed PETN, and foamed nitrocellulose/nitroglycerine at 0.25 g/cc and lower were studied. The foamed systems were of the urethane class, with PETN or nitrocellulose/nitroglycerine dispersed uniformly throughout the structure. At a diameter of 5.08 cm, foamed PETN exhibited an essentially constant detonation velocity of 1.0-1.2 mm/ $\mu$ sec over an explosive density range of approximately 0.06-0.13 g/cc. The detonation velocity of the nitrocellulose explosives varied linearly with density, and values from 2.07 to 2.74 mm/ $\mu$ sec over a density range 0.104-0.225 g/cc were obtained. A carbon resistor-polyethylene shock wave pressure gage mounted at the end of the charges was utilized to estimate the detonation pressure. The gage pressures, which were in the range of 2 to 9 kilobars, correlated with the explosive densities quoted above. Calculation of Chapman-Jouguet parameters for some of the systems utilizing the impedance mismatch equation yielded values that had no physical significance, because the calculated particle velocities exceeded the detonation velocities. It is concluded that utilization of relatively high density substances as witness materials will not permit accurate measurement of detonation pressure of very low density explosives.

## INTRODUCTION

The work described in this paper was one phase of an investigation on the utilization of very low density explosive systems. Particularly important observations that were made included evaluation of detonation stability and measurement of detonation pressure. The term very low density implies explosives of density 0.25 g/cc and lower. These values are considerably below the minimum densities that can be obtained from most pure powdered explosives, and charges at very low densities can be expected to have detonation pressures lower than those associated with powdered explosives.

Archibald (1) prepared very low density PETN charges by three different methods: (a) utilizing expandable polystyrene beads, (b) utilizing low density fillers, and (c) precipitating PETN in porous solids. In the present work, polyurethane foams were utilized; an explosive material incorporated in the urethane was dispersed throughout the given volume so as to yield a very low apparent explosive density. The systems that were studied extensively were foamed PETN over an explosive density range 0.022-0.185 g/cc, and foamed nitrocellulose/nitroglycerine over a range 0.057-0.191 g/cc. In addition, some work was performed on a commercial expanded nitrocellulose product

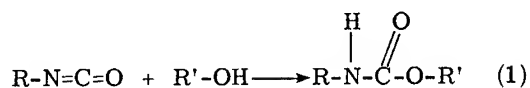
and on fibrous nitrocellulose with absorbed nitroglycerine.

The method used to measure detonation velocity consisted of monitoring the response of ion probes at selected intervals in the charge by means of cathode ray oscilloscopes equipped with Polaroid cameras. This method has been used extensively to measure explosive systems of densities higher than those of interest in the present work. Each charge also included a carbon resistor pressure gage that was utilized to estimate the detonation pressure. The low densities studied herein and the presence of inert foam caused the loss of some records; however enough data were obtained to indicate the trends of the performance.

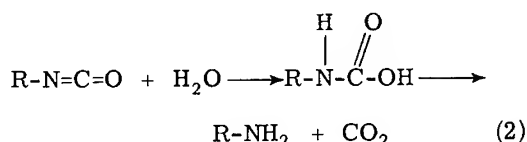
## CHARGE PREPARATION

### Polyurethane Foams

Polyurethane foams are produced by the reaction between two chemicals which expand and crosslink to form a cellular structure with a possible density range from below 0.02 g/cc to about 1.12 g/cc. The two chemicals are a polyol and an isocyanate or diisocyanate. The polyol component is a hydroxyl-terminated polyether or polyester. The chemical reaction between an isocyanate and a hydroxyl compound is

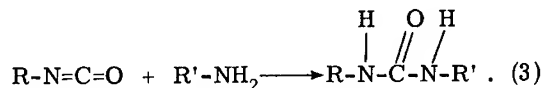


which is an urethane. This reaction will proceed when the two components are mixed. It is an exothermic reaction, and would result in a solid polymer if provision for foaming were not included. Foaming is achieved by incorporating either water or a low-boiling solvent such as Freon. The difference in these two techniques is as follows. The low-boiling solvent such as Freon does not enter into the chemical reaction but merely changes physical state from liquid to gas, due to the increased temperature of the exothermic reaction between the isocyanate and polyol. The use of water as a blowing agent involves a chemical reaction, as follows:



so that the products are an amine and  $\text{CO}_2$  gas, which acts as the blowing agent. Thus it should be noted that void spaces in Freon-blown foam

are filled with a Freon gas, and in water-blown foam are filled with  $\text{CO}_2$  gas. The amine that is formed in the case of water-blown foams will further react with the isocyanate to produce an urea:



The isocyanate can further react with the urea and the urethane of the primary reaction; however, this further reaction is of little consequence. Of concern was the possibility that an amine that might be formed would be incompatible with the explosive incorporated into the formulation; in retrospect, no such problems were encountered.

### Foamed PETN

The best procedure for preparing foamed PETN charges was to mix the required quantities of polyol, isocyanate, surfactant, explosive, and water (if used) quickly in a disposable beaker, and then to pour the entire mass into the confinement tube, in which the foaming subsequently occurred. After foaming had ceased, and the foam had cured, any excess material that had foamed out of the tube was evenly scraped from the end of the tube and weighed. The weight of material remaining in the tube was calculated by subtracting the weight of ingredients used in the initial formulation. The density of foamed explosive in the tube was calculated from the known internal volume of the tube, by assuming that all ingredients were evenly distributed in both the remaining material and excess material, and that no reaction had occurred between the PETN and foaming agents.

### Foamed Nitrocellulose/Nitroglycerine

The foaming of fibrous nitrocellulose (NC) of less than maximum nitration presents the advantage that the available hydroxyl groups will react with the isocyanate in much the same manner as the polyols; thus the nitrocellulose will contribute to the structural integrity of the system. However, the large difference in densities of fibrous nitrocellulose and the foaming agents precluded incorporation of sufficient nitrocellulose to result in a detonable foam. This problem was solved by foaming a nitrocellulose/nitroglycerine mixture containing approximately 50% absorbed nitroglycerine (NG) by weight.

The procedure utilized to prepare the NC/NG mixture was as follows. The appropriate quantities of wet fibrous nitrocellulose (13.45% N) and 10/90 nitroglycerine/ $\beta$ -lactose\* were mixed together. Then the  $\beta$ -lactose was dissolved with a large quantity of water, whereupon the nitrocellulose absorbed the nitroglycerine. The mixture was filtered on a Buechner funnel, with several water-washings to remove all the  $\beta$ -lactose. The major advantages of this procedure are that (a) the nitrocellulose need not be dried, and (b) handling of pure nitroglycerine is not required.

The foaming of the NC/NG was accomplished with essentially the same procedure that was utilized for the PETN systems. The principal blowing agent in the NC/NG foams was Freon. However, improved foaming occurred if the NC/NG mixture was wet; apparently the moisture reacted with the isocyanate to promote liberation of  $\text{CO}_2$  gas, which then complemented the blowing action of the Freon. Thus, it was not necessary to dry the NC/NG mixture after its preparation; hazards in the handling of dry explosive were eliminated.

#### Expanded Nitrocellulose

The expanded nitrocellulose† consists of generally spherically shaped granules of nitrocellulose in the range 1.6 to 2.4 mm in diameter. This product is available in three bulk densities of 0.10, 0.14, and 0.25 g/cc, respectively. In general, the two lower density explosives each had larger particles of about the same size; the highest density material consisted of both smaller particles and relatively fine particles.

#### Experimental Configuration

The experimental configuration showing the velocity probes and carbon resistor pressure gage is depicted in Fig. 1; this same arrangement was also utilized to study the nitrocellulose systems. The booster for all shots was a piece of DuPont A-4 "Detasheet" Sheet Explosive of diameter equal to the inside diameter of the confining tube. The booster in turn was initiated by a tetryl pellet and a No. 6 electric detonator. The ion probes were connected to condenser discharge circuits. Two of the probes were used for oscilloscope trigger. The eight probes for monitoring detonation were

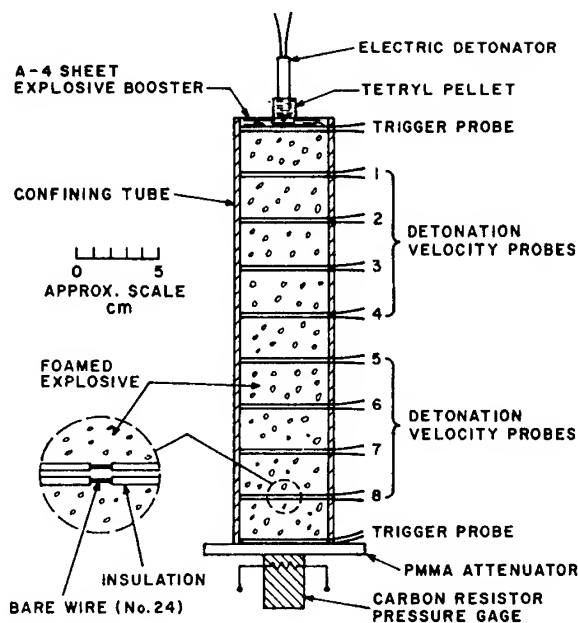


Fig. 1 - Experimental arrangement for studying detonation characteristics of foamed explosives. (PMMA is an abbreviation for polymethyl methacrylate.)

arranged in two sets, with voltage steps of 22-1/2 volts, 45 volts, 67-1/2 volts, and 90 volts, respectively. The advancing detonation progressively shorts out one probe at a time, and produces corresponding vertical deflections that relate the position of the detonation as a function of time.

#### RESULTS OF DETONATION VELOCITY MEASUREMENTS

Table 1 includes the results of the measurement of detonation velocity on all foamed PETN systems for which readable records were obtained. For each system, the entries are listed in order of decreasing explosive density, which is the amount of explosive material per unit volume of total system contained within the confining tube. The foam density is also included in the table, and the total system density is the sum of the explosive and foam densities.

The particle size of the PETN had a very noticeable effect on the detonation stability. Most of the data in Table 1 represent the results for foamed PETN made from a 10-12-micron PETN. This foamed system detonated stably at explosive densities in the range 0.09-0.13 g/cc, whereas foamed systems using very coarse PETN from Primacord or a very

\*Product of E. I. DuPont, Wilmington, Delaware.

†Marketed by Hercules, Inc., Wilmington, Delaware under the trade name "Shock-Gel."

TABLE 1  
Detonation Velocity of Low-Density Foamed PETN Charges

Test No.	Confinement		Type of PETN <sup>b</sup>	Weight Percent PETN	Foam Density, g/cc	Explosive Density, g/cc	Detonation Velocity, mm/μsec
	Type <sup>a</sup>	I.D., cm					
54	PMMA	5.71	Coarse	Unknown	Unknown	0.185	2.15
72	PMMA	5.08	Fine	56.3	0.136	.176	2.45
87	Steel	5.08	Fine	43.0	.175	.133	1.17
91	PMMA	5.08	Fine	43.8	.154	.120	1.14
60	Steel	5.08	Fine	47.4	.121	.109	1.12
88	Steel	5.08	Fine	39.8	.142	.094	.98
68	Aluminum	5.08	Fine	40.2	.087	.058	1.02
95	PMMA	7.62	Fine	30.9	.127	.057	Unstable
89	Steel	5.08	Fine	31.0	.124	.055	.78
92	PMMA	5.08	Fine	31.0	.124	.055	Unstable
96	Steel	5.08	Fine	30.7	.112	.049	.59
62	Steel	5.08	Fine	13.3	0.140	0.022	Unstable

<sup>a</sup>PMMA is an abbreviation for polymethyl methacrylate. Wall thicknesses were approximately 6 mm.

<sup>b</sup>Coarse PETN was obtained from Primacord; fine PETN has an average particle size of 10-12 microns.

fine\* PETN exhibited instability at these same densities.

Figure 2 presents a plot of the detonation velocity of foamed PETN as a function of explosive density. The figure shows that the foam has no effect on detonation propagation at densities in the neighborhood 0.18 g/cc. At densities appreciably below this, however, it appears that the foam retards the detonation, although the effect is essentially constant in the range 0.06-0.13 g/cc. Below 0.06 g/cc, type of confinement becomes more important, because the detonation is stable when the system is confined in metal, but unstable when confined in plastic. The curve drawn through points in Fig. 2 is a cubic equation of the detonation velocity of foamed PETN versus density, and is centered at 0.104 g/cc. A least squares fit of the rectified data reveals this equation to be:

$$D = 1.11 + 2515 (\rho_0 - 0.104)^3, \quad \rho_0 < 0.180 \text{ g/cc} \quad (4)$$

where

D is the detonation velocity in mm/μsec

$\rho_0$  is the initial explosive density in g/cc.

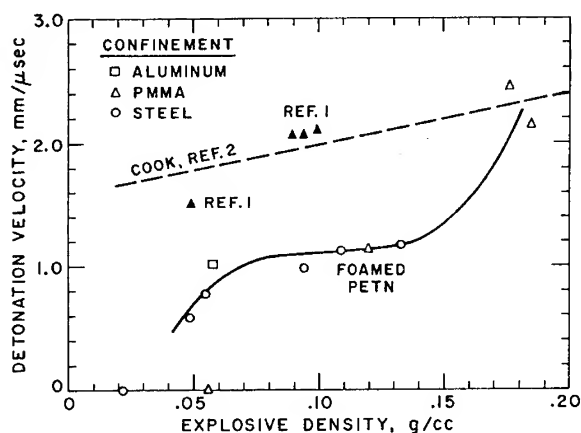


Fig. 2 - Detonation velocity of foamed PETN as function of density. (Darkened points represent Archibald's data.)

For purposes of comparison, the data of Archibald (1) are presented, as well as an extrapolation of the straight line equation of Cook that expresses detonation velocity as a function of density for high-density PETN (2).

Figure 3 shows detonation velocity of foamed PETN as a function of explosive content. The equation of the least squares curve through the points is given by

$$D = 0.16 - 1.843 w + 9.793 w^2 \quad (5)$$

\*Very fine PETN was prepared by precipitating one liter of a PETN-acetone solution (75 g/liter) in two liters of agitated ice water for two minutes.

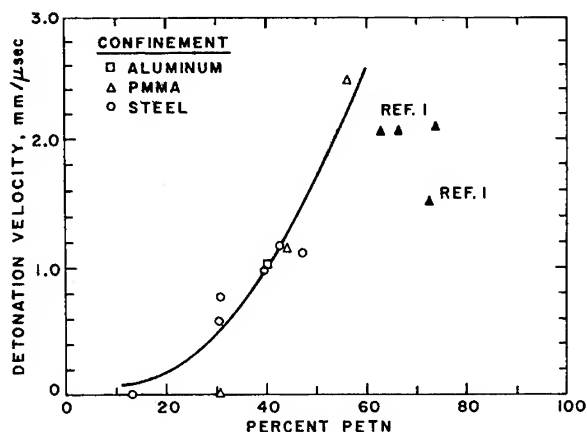


Fig. 3 - Detonation velocity of foamed PETN as function of weight percent PETN. (Darkened points represent Archibald's data.)

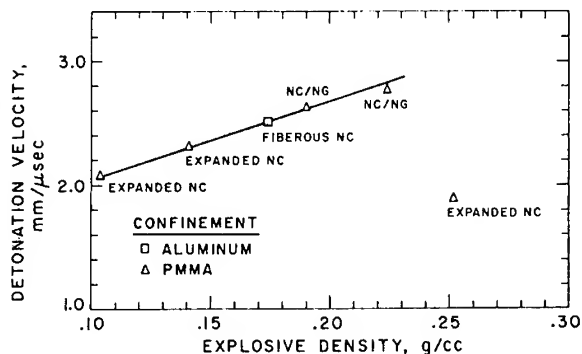


Fig. 4 - Detonation velocity of expanded and fibrous nitrocellulose and of nitrocellulose/nitroglycerine.

where  $w$  is the weight fraction of PETN. Again for purposes of comparison, the data of Archibald (1) is presented in Fig. 3.

The results of the detonation velocity measurements on foamed NC/NG and on other low-density nitrocellulose charges are summarized in Table 2. The explosive content for the foamed systems was in the range 30-48 percent by weight. It is seen that the detonation in foamed NC/NG confined in a 2.54-cm plastic tube is unstable. The data for the NC/NG mixtures and the nitrocellulose charges are plotted in Fig. 4. The equation of the straight line is given by

$$D = 1.42 + 6.29 \rho_0 \quad (6)$$

The detonation velocity of the expanded nitrocellulose charge at 0.252 g/cc is much lower

than the data for the other points would predict it to be. The possible explanation for this behavior is that this charge was composed of both large and fine granules, whereas the other two expanded nitrocellulose products each had much more uniform granules. Sadwin et al (3) point out the findings of Jacobs (4) wherein ammonium picrate charges composed of large particles detonated at lower velocities than those composed of small particles, but that charges composed of a mixture of large and small particles detonated at still lower velocities; these effects were most pronounced at small diameters and tended to disappear at sufficiently large diameters.

### DETONATION PRESSURE MEASUREMENT

Each shot in which a low density explosive was studied included a carbon resistor pressure gage on the bottom of the charge in order to estimate the detonation pressure. The oscilloscope that recorded the response of the gage was triggered by the lowermost ion probe in Fig. 1. This section describes the construction and operation of the gage, its calibration, and the problems in interpreting the detonation pressure from the gage records for some of the systems.

### Construction and Operation

In its construction and operation, the carbon resistor gage responds to an inert shock wave pressure that is related to the decrease in the resistance of the resistor. The inert shock pressure must then be converted to detonation pressure by using interface matching techniques or other appropriate mathematics. The basic gage system was similar to that described by Watson (5), and consisted of a 1/4-watt, 470-ohm carbon resistor mounted in a polyethylene or polystyrene cylinder 1.91-cm in diameter by 1.91-cm long. In the finished gage, the resistor was approximately 1-2 mm from the interface from which the shock wave to be measured would emerge. The 470-ohm resistors were selected from a lot of 5% tolerance resistors to be within  $\pm 2$  ohms of the specified value.

The procedure in constructing the gage was as follows. A 2.44-mm hole was drilled diametrically through a polyethylene cylinder near one of its bases. The carbon resistor was then inserted in the hole, the leads of the resistor were insulated with plastic spaghetti tubing and folded down, and the entire gage was wrapped

TABLE 2  
Detonation Velocity of Low-Density Nitrocellulose/Nitroglycerine Charges

System	Test No.	NC/NG Wt Ratio	Confinement		Foam Density, g/cc	Explosive Density, g/cc	Detonation Velocity, mm/ $\mu$ sec
			Type <sup>a</sup>	I.D., cm			
Foamed NC/NG	133	50/50	PMMA	2.54	0.255	0.191	Unstable
	147	50/50	Steel	5.08	.134	.121	0.68
	150	50/50	Steel	5.08	.173	.118	.42
	148	50/50	Steel	5.08	.108	.083	.62
	146	50/50	Steel	5.08	.103	.074	.72
	149	50/50	Steel	5.08	0.130	.057	.70 <sup>b</sup>
NC/NG Mixture	130	97/3	PMMA	2.54	-	.191	2.6
	131	87/13	PMMA	2.54	-	.191	2.6
	132	77/23	PMMA	2.54	-	.191	2.7
	138	60/40	PMMA	2.54	-	.225	2.74
Fibrous NC	84	100/0	Aluminum	7.62	-	.174	2.51
Expanded NC	106	100/0	PMMA	2.54	-	.252	1.88
	104	100/0	PMMA	2.54	-	.141	2.31
	105	100/0	PMMA	2.54	-	0.104	2.07

<sup>a</sup>PMMA is an abbreviation for polymethyl methacrylate. Wall thicknesses were approximately 6 mm.

<sup>b</sup>Average velocity over entire length of charge.

with plastic electrical tape. The end of the polyethylene cylinder was brought into contact with a small piece of hot glass lying on a hot-plate. This heat caused the polyethylene to flow, thereby sealing in the resistor and providing a smooth surface on the end of the polyethylene cylinder. Then the gage and piece of glass were quenched in water, and this facilitated a clean separation of the gage from the glass. The final step was to dry the gage under vacuum in a desiccator for several hours.

The circuit to monitor the gage resistance under shock loading is shown in Fig. 5. The decrease in resistance of the gage causes an increase in current flow through the circuit, which manifests itself as an increase in the voltage drop across the current sampling resistor,  $R_L$ . If  $E_p$  is the initial amplitude of the voltage pulse increase appearing across the resistor,  $R_L$ , the minimum gage resistance is given by:

$$R_{\min} = \frac{E_0 R_L R_0 - E_p (R_L + R_c + R_0) (R_L + R_c)}{E_0 R_L + E_p (R_L + R_c + R_0)} \quad (7)$$

where

$E_0$  is the battery potential,

$R_0$  is the initial gage resistance, = 470 ohms,

$R_c$  is the line resistance, = 1.14 ohms.

If the line resistance,  $R_c$ , is negligible, Eq. (7) easily reduces to the equation quoted by Watson (5). The oscilloscope records that were obtained were very similar to those shown by Ribovich et al (6).

#### Calibration of the Gage

The calibration of the carbon resistor pressure gage was accomplished by firing the experimental arrangements depicted in Fig. 6. The essential feature of these set-ups was that the Chapman-Jouguet (CJ) properties of the explosives and Hugoniot of the inert materials were well enough known that the pressure induced in polyethylene or polystyrene could be calculated reliably. The calibration shots including gage pressures and measured minimum gage resistances are summarized in Table 3 for the gages fabricated from polyethylene and in Table 4 for the gages fabricated from polystyrene. It is noted that the latter gage was calibrated only in the low pressure region.

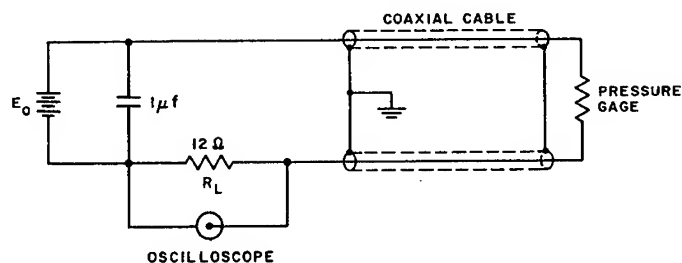


Fig. 5 - Circuit for monitoring gage resistance under shock loading

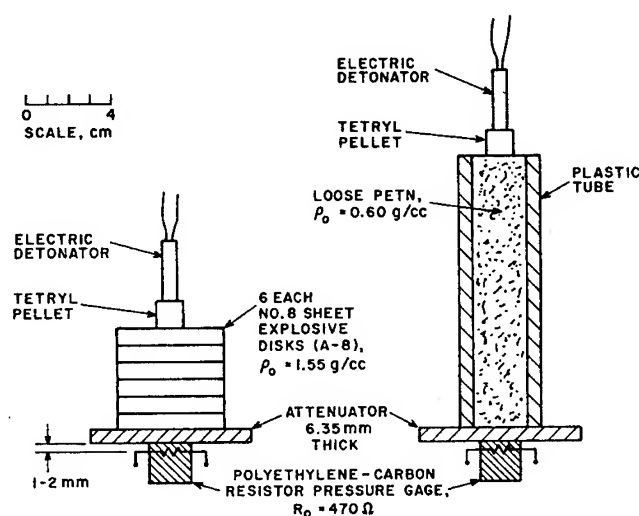


Fig. 6 - Experimental arrangements for calibration of the carbon resistor pressure gage

 TABLE 3  
 Calibration of Carbon Resistor-Polyethylene Pressure Gage

Explosive	Density g/cc	Attenuator	Gage Pressure, kilobars	Minimum Resistance, ohms	Reciprocal Resistance, (ohms) <sup>-1</sup>
A-8 "Detasheet"	1.55	PMMA	142.8	24.9	0.04016
A-8 "Detasheet"	1.55	Aluminum	111.1	29.3	.03413
A-8 "Detasheet"	1.55	Brass	65.0	37.3	.02681
Loose PETN	0.60	PMMA	33.1	47.2	.02119
Loose PETN	0.60	Aluminum	15.1	88.2	.01134
—	—	—	0	470	0.00213

Type A "Detasheet" contains 85% PETN. Independent verification of the detonation velocity of both this "Detasheet" and the loose PETN of 0.60 g/cc yielded values to within 2% of those predicted by Cook (2). The C-J pressure and

particle velocity of both densities were obtained from Cook (7), who presents extensive calculations of the detonation state of PETN. The gage pressures were calculated graphically by utilizing the hydrodynamic property that pressure and



TABLE 4  
Calibration of Carbon Resistor-Polystyrene Pressure Gage

Explosive	Density g/cc	Attenuator	Gage Pressure, kilobars	Minimum Resistance, ohms	Reciprocal Resistance, (ohms) <sup>-1</sup>
Loose PETN	0.60	PMMA	38.1	104.0	0.00962
—	—	—	0	465	0.00215

particle velocity are continuous across an interface over which a shock wave or detonation wave has passed. The curves for the reflected shock Hugoniot and isentrope of the explosive reaction products were plotted from the equations derived by Deal (8); the Hugoniots for brass and aluminum were obtained from Walsh et al (9); the Hugoniot of PMMA was obtained from Reynolds and Seay (10) and Liddiard (11); the Hugoniot of polyethylene was obtained from Bert et al (12); finally that for polystyrene was obtained from Rinehart (13) and a Sandia Laboratories drawing (14). The various cross-curves for the inert materials were drawn with the usual assumption that the cross-curve is a mirror image reflection around its Hugoniot.

The data for gage pressure as a function of gage minimum resistance fit two equations of the type

$$y = a + b/x.$$

This can be shown by rectifying the data, i.e., by plotting gage pressure versus reciprocal resistance from the data in Tables 3 and 4. This has been done in Fig. 7, and two slopes are evident for the polyethylene gages. Least squares analyses of the rectified data yield the following two relationships for the low resistance, high pressure and high resistance, low pressure regions, respectively, for polyethylene:

$$P = \frac{5848}{R_{\min}} - 90.8, \quad R_{\min} < 47.2 \text{ ohms} \quad (8)$$

$$P = \frac{1738}{R_{\min}} - 4.0, \quad R_{\min} \geq 47.2 \text{ ohms} \quad (9)$$

where

$P$  is the gage pressure in kilobars

$R_{\min}$  is in ohms.

For the polystyrene gages, the calibration equation in the low pressure region is:

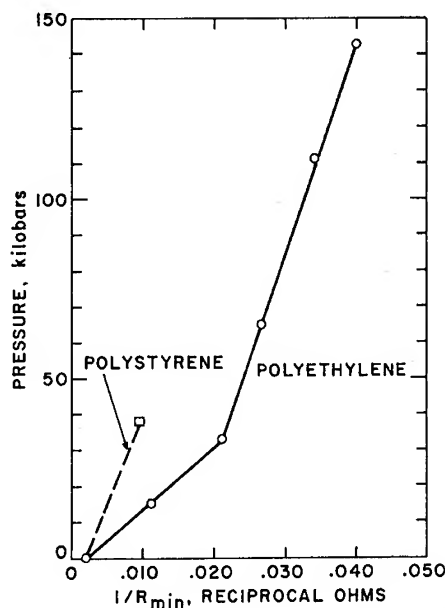


Fig. 7 - Rectified calibration data for the carbon resistor pressure gage.

$$P = \frac{5100}{R_{\min}} - 11.0, \quad R_{\min} \geq 104.0 \text{ ohms} \quad (10)$$

#### Calculation of Pressures for Low Density Charges

Table 5 presents the calculation of gage pressure, the pressure in the PMMA attenuator (Fig. 1), and the detonation pressure for those low density systems for which gage records were obtained. The gage pressures are plotted as a function of explosive density in Fig. 8. For the foamed PETN, the least squares equation of the gage pressure-density relationship is given by

$$P = -3.0 + 105.09 \rho_0 - 248.06 \rho_0^2 \quad (11)$$

TABLE 5  
Calculation of Detonation Pressure for Low-Density Explosive Systems

System	Test No.	Explosive Density, g/cc	Foam Density, g/cc	Minimum Gage Resistance, ohms	Gage Pressure, <sup>a</sup> kbars	PMMA Pressure, kbars	Detonation Pressure, kbars
Foamed PETN	72	0.176	0.136	274	7.6	8.0	4.8
Foamed PETN	87	.133	.175	282	7.1	7.5	-
	67	.101	.086	331	4.4	4.9	-
	68	.058	0.087	381	2.4	2.9	-
Expanded NC	106	.252	-	264	8.3	8.6	4.8
	104	.141	-	326	4.6	5.1	2.8
	105	.104	-	399	1.8	2.2	1.2
97/3 NC/NG	130	.191	-	94.5	14.4	18.2	-
87/13 NC/NG	131	.191	-	81.7	17.3	20.9	-
77/23 NC/NG	132	.191	-	87.8	15.8	19.5	-
60/40 NC/NG	138	0.225	-	74.0	19.5	23.4	-

<sup>a</sup>Gage pressure was calculated from Eqs. (9) or (10) in text.

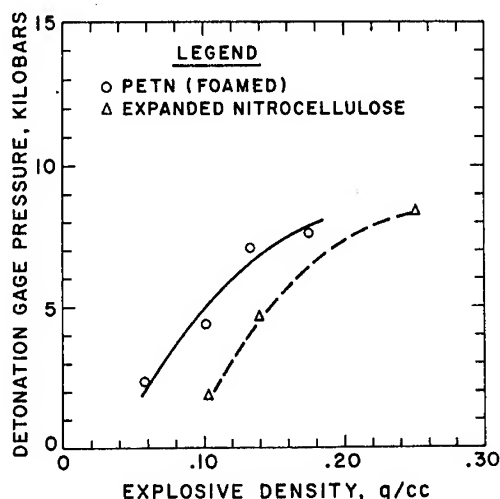


Fig. 8 - Gage pressures produced by detonation of foamed PETN and expanded nitrocellulose charges. (Gages were fabricated from polystyrene.)

$$P_{cj} = \frac{\rho_0 D + \rho_M U}{2 \rho_M U} P_M \quad (13)$$

where

$P_{cj}$  is the detonation or Chapman-Jouguet pressure,

$P_M$  is the pressure induced in the PMMA attenuator

$U$  is the shock velocity in the PMMA attenuator,

$D$  is the detonation velocity of the explosive,

$\rho_0$  is the initial density of the charge, here assumed to be the sum of explosive and foam densities,

$\rho_M$  is the initial density of the PMMA attenuator.

and for the expanded nitrocellulose the relationship is:

$$P = -10.3 + 145.95 \rho_0 - 286.10 \rho_0^2 \quad (12)$$

where  $P$  is in kilobars and  $\rho_0$  is in g/cc. The detonation pressures in Table 5 were calculated from the impedance mismatch equation:

No difficulty was encountered when Eq. (13) was applied to the data for the foamed PETN at 0.176 g/cc and for the expanded nitrocellulose charges. However, when this equation was applied to the foamed PETN at 0.133 g/cc and lower, solutions were obtained that have no physical reality; the predicted Chapman-Jouguet conditions by this method yielded particle velocities that were in excess of the measured

TABLE 6  
Summary of Calculated Chapman-Jouguet Conditions for  
Low Density Explosive Systems<sup>a</sup>

System	Shot No.	Initial Explosive Density, g/cc	Foam Density, g/cc	CJ Density, g/cc	CJ Pressure, kbars	Particle Velocity mm/ $\mu$ sec	$\gamma$
Foamed PETN	72	0.176	0.136	0.420	4.8	0.63	2.89
Expanded	106	.252	-	.550	4.8	1.02	.84
	104	.141	-	.223	2.8	.85	1.72
	105	0.104	-	0.141	1.2	0.54	2.84

<sup>a</sup>Detonation velocities are quoted in Tables 1 and 2.

detonation velocities. In the case of the NC/NG mixtures, the particle velocities did not exceed the detonation velocities, but were much too high to be believable.

The calculated Chapman-Jouguet (CJ) conditions are summarized in Table 6 for those systems that had realistic calculated values. The polytropic exponent  $\gamma$  was calculated from the relationship

$$\gamma = \frac{\rho_0 D^2}{P_{cj}} - 1$$

$$= \frac{D}{u_{cj}} - 1 \quad (14)$$

where  $u_{cj}$  is the Chapman-Jouguet particle velocity. The general conclusion that can be made is that the carbon resistor pressure gage and the impedance mismatch equation do not consistently provide realistic CJ values for very low density explosive systems. In the first place, the calculations require a rather large extrapolation from the conditions in a relatively dense medium (polyethylene) to those in the very low density explosives. Secondly, for the lighter foamed PETN systems the presence of the foam lowered the detonation velocity but caused higher-than-expected gage pressures; hence the impedance mismatch equation, which does not take into account effects of other nonexplosive constituents in a system, cannot and did not yield realistic answers for foamed PETN. Thirdly, we are unable to explain the high gage pressures recorded for the nitrocellulose/nitroglycerine mixtures.

A survey of the available Hugoniot data for other possible condensed phase witness materials that might be used in lieu of polyethylene revealed that all these have values of shock

impedance far in excess of  $0.025 \text{ g}/\mu\text{sec cm}^2$ , which is the approximate impedance of the low density foamed explosive. The goal, of course, is to utilize witness materials that have shock impedances of the same order of magnitude as those of the explosive being evaluated. It appears that a thorough study of the shock properties of polyurethane foams would provide the ultimate solution to the problem of determining the detonation pressure of low density explosives. By proper selection of densities, foamed systems having the desired values of shock impedance could be developed and utilized as witness materials.

#### ACKNOWLEDGMENTS

The authors are indebted to Messrs. R. S. Neumeister, Robert Gartner, and Richard Whiting of Honeywell, Inc., whose cooperation and direction made this work possible. The conscientious efforts of Messrs. James Daley and Douglas Baker of IIT Research Institute, who assisted in experiment portions of the detonation studies, are deeply appreciated.

#### REFERENCES

1. P. B. Archibald, "A Low Density, Low-Pressure Solid Explosive," Lawrence Radiation Laboratory Report UCRL-14186, May 25, 1965.
2. M. A. Cook, "The Science of High Explosives," Reinhold Publishing Corp., New York, 1958, page 45, Eq. 3.1.
3. L. D. Sadwin, R. H. Stresau, S. J. Porter, and J. Savitt, "Nonideal Detonation of Ammonium Nitrate-Fuel Mixtures," Proceedings, Third Symposium on Detonation, ONR Symposium Report ACR-52, Vol. 1, September 1960.

4. S. J. Jacobs, et al., OSRD Report No. 1755.
5. R. W. Watson, Rev. Sci. Inst., 38 978, 1967.
6. J. Ribovich, R. W. Watson, and F. C. Gibson, AIAA J., 6, 1260, 1968.
7. M. A. Cook, "The Science of High Explosives," Reinhold Publishing Corp., New York, 1958, Tables 12.12 through 12.14.
8. W. E. Deal, Phys. of Fluids, 1, 523, 1958.
9. J. M. Walsh, M. H. Rice, R. G. McQueen, and F. L. Yarger, Phys. Rev., 108, 196, 1957.
10. C. E. Reynolds and G. E. Seay, J. Appl. Phys., 33, 2234, 1962.
11. T. P. Liddiard, Jr., "The Compression of Polymethyl Methacrylate by Low Amplitude Shock Waves," Proceedings, Fourth Symposium (International) on Detonation, ONR Report ACR-126, October 12-15, 1965.
12. C. W. Bert, E. J. Mills, D. N. Gideon, and R. A. Stein, "Preliminary Survey on Hypervelocity-Impact Properties of Plastics and Plastic Laminates," Battelle Memorial Institute, ARPA Order 197, June 1963 (Defense Documentation Center, Cameron Station, Alexandria, Virginia, AD-408 386).
13. J. S. Rinehart, "Compilation of Dynamic Equation of State Data for Solids and Liquids," U. S. Naval Ordnance Test Station Report NOTS TP 3798, May 1965.
14. Sandia Laboratories Drawing N65093, "Hugoniot Data."

# AN ANALYSIS OF THE "AQUARIUM TECHNIQUE" AS A PRECISION DETONATION PRESSURE MEASUREMENT GAGE

J. K. Rigdon and I. B. Akst  
*Mason & Hanger - Silas Mason Co., Inc.*  
*Amarillo, Texas*

## ABSTRACT

Several analytical approaches have been applied to evaluate the experimental shock wave data obtained from "Aquarium Technique" experiments. Ten explosives were tested. The detonation pressure values obtained were in good agreement with those of explosively driven metal plate experiments, and serve to illustrate this method's relative simplicity, low cost, and precision. Detonation pressure as a function of charge length was apparently observed.

## INTRODUCTION

The experimental measurement of shock wave pressures characteristic of most detonating solid explosives is typically expensive, difficult, and generally problematical. Although there is currently a number of pressure measurement schemes which are considered to be state-of-the-art (1), these methods are often elaborate, sophisticated, and costly to a point that discourages widespread regular usage.

There is a continuing need, especially in the evaluation of new explosive formulations, for a relatively simple, comparatively inexpensive, yet dependable detonation pressure measurement gage. Recognizing this need, we have attempted to reevaluate one method which has already enjoyed long usage, but one which we feel has not had its full capabilities — and therefore its wider applicability — firmly established. This method is most commonly known as the aquarium technique (2-4).

The task of the user of the aquarium technique for detonation pressure measurements is the determination of — to the maximum degree of precision permitted by camera records — the velocity of the shock transmitted into the water immediately at the explosive/water interface. From this shock parameter, the magnitude of

the incident pressure or detonation pressure may be derived.

Aquarium test pressure values are very sensitive to errors in determining the transmitted shock velocity, and for that reason calculation of detonation pressure in this manner has tended to be less favorable than some other methods. Arguments against the technique appear to be the uncertainties involved in arriving at the initial transmitted shock wave velocity.

Probably the most precise method for detonation pressure measurement currently in use is the measurement of free surface velocity of metal plates (5). Analysis techniques for determining the free surface velocity of explosively driven, impedance matched, metal plates over short distances prove to be much less involved than the aquarium technique. The metal plate experiments are much more difficult to perform. Also, as is pointed out in Ref. (5), Wilkins (6), Lambourn and Hartley (7), and Petrone (8) have indicated there are some uncertainties associated with the free surface velocity technique or its interpretation, as have Veretennikov, Dremin, et al (9), and Craig (10).

Detonation pressures determined via the aquarium technique have characteristically been below the accepted published nominal values

from other methods, especially in the early development of the technique. To a large degree, this seems to relate primarily to the lack of adequate treatment of the space-time ( $R-t$ ) data, from the streak camera records, i.e., a sufficiently "good" analytical fit to the experimental data for differentiation and solution for interface velocity conditions. For this reason, one of our principal concerns has been the methods of numerical analysis by which the initial or "jump-off" velocity could best be deduced from aquarium test data, and from which reliable detonation pressure values could be generated from single (or small sample) shot experiments. We have, based on the exhaustive work of other investigators, implicitly assumed the validity and applicability of the impedance match method for calculation of detonation pressure.

## EXPERIMENTAL

The existence of a large quantity of accepted pressure data for most common explosives has given us the opportunity to better evaluate the several analytical approaches as well as the total experiment. PBX 9404, (94/3/3 HMX/nitrocellulose/tris- $\beta$ -chloroethyl phosphate) whose detonation pressure has been heavily researched (although there is still some disparity as to what its steady state pressure actually is) was chosen for "calibration" of the aquarium experiment. The detonation pressure,  $P_{det}$ , of PBX 9404 is nominally considered to be about  $372 \pm 5$  kbars.

The experiments consisted of aquarium testing ten explosives in right circular cylinder geometry. All specimens were 7.2 cm in diameter. The lengths tested were 1.27, 2.54, 5.08, and 11.4 cm for the PBX 9404 and 11.4 cm only for the remaining explosives tested.

Test samples were carefully prepared and assembled for firing as shown in Fig. 1. All shots were initiated with P-40 (~10 cm diameter) plane wave generators (output pressure ~140 kbars). This was done to maximize the one-dimensionality of the output waves and to avoid any overdriving of the detonation in the test samples.

The charges were immersed in distilled water in commercially available glass walled aquariums. Shadowgraphic backlighting was provided by exploding bridgewires in an atmosphere of liquid Freon (11). The Freon has the effect of improving the quantity of light as well as the useful life of the source. The EBW's were positioned at the focal point of a 12.7 cm

diameter, 19 cm focal length lens which was centered with the optical axis and the output surface of the test sample, and attached to the outside surface of the glass wall. This system resulted in significantly improved streak camera records as opposed to argon bomb light sources.

Considerable care was exercised in the alignment of the shots within the optical system. Tilted shots, i.e., shots whose cylindrical axis was not perpendicular to the optical system axis, produced a double trace effect which seriously changed the pressure results.

Alignment was accomplished by replacing the EBW light source with a mercury vapor point light source. The point source was located at the focal point of the condenser lens on the aquarium to produce a beam of parallel light. The entire aquarium was then adjusted such that the parallel beam was centered about the axis of the optical system. Final adjustment of the test sample — by three leveling screws — was then made until a straight shadowgraphic image of the output surface of the charge was observed on the streak camera slit plate. The position of the point source was noted; the EBW backlight source was then located at that point for the test.

The streak camera records obtained were generally of high quality. A typical sample is shown in Fig. 2. All shots were fired at magnification of about 1:1 and at camera writing rate of 5.0 mm/ $\mu$ sec.

## ANALYSIS AND RESULTS

The measurement of transmitted shock velocity into water permits one to ascertain, by use of the water Hugoniot equation-of-state, the associated particle velocity for the shock. There has been considerable work done to develop the shock properties for water (3, 12-14). We have used the Rice-Walsh equation because it is probably the most comprehensive effort and because Papetti and Fujisaki (15), in a separate theoretical study, thoroughly evaluated and further verified the Rice-Walsh  $p-v-e$  data for purposes of extrapolating it to higher pressures. The Rice-Walsh equation was reported (Ref. 12) in the form:

$$U_s - 1.483 = 25.306 \log_{10}(1 + U_p/5.190) .$$

Where  $U_s$  and  $U_p$  are shock and particle velocity respectively in km/sec. By doing a second order polynomial regression fit to their  $U_s - U_p$  data, a much more easily used functional

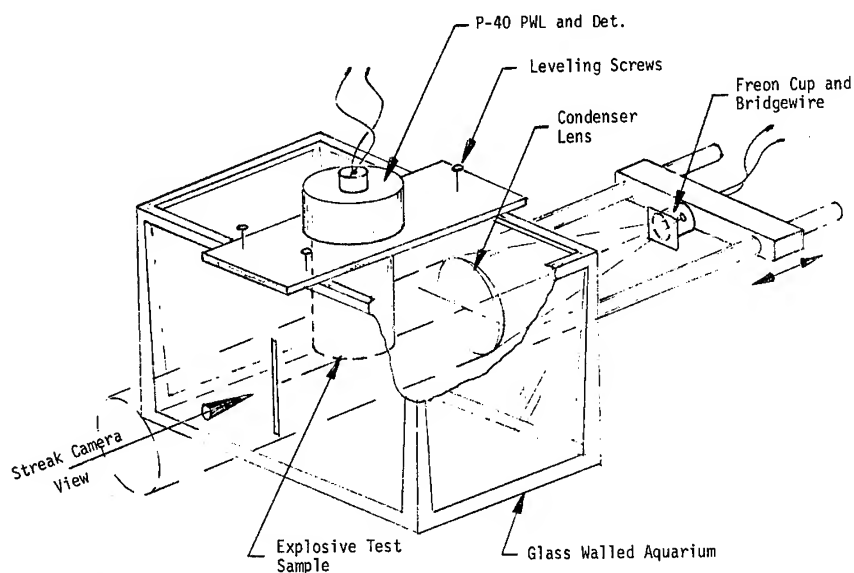


Fig. 1 - Typical aquarium test setup for measuring detonation pressure

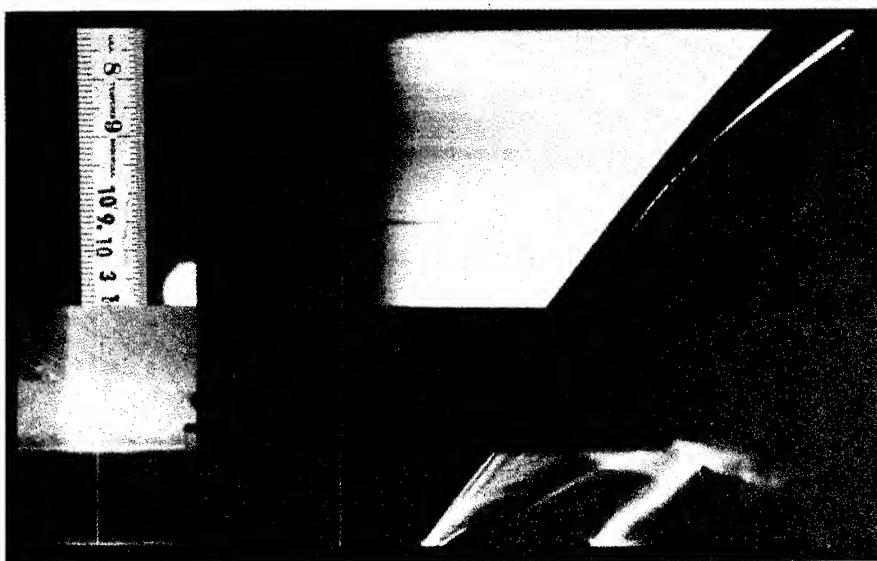


Fig. 2 - Typical streak camera trace illustrating type records used for detonation pressure measurement (camera writing rate = 5.0 mm/ $\mu$ sec, explosive - PBX 9404,  $d = 7.2$  cm,  $L = 11.4$  cm)

relationship was obtained. The quadratic representation is:

$$U_p = -.607 + .372 U_s + .0283 U_s^2.$$

Values computed via this form differ by less than 1/2% from the above Rice-Walsh equation over the range of interest.

Having determined values for shock and particle velocity, one may easily compute the transmitted pressure with the familiar conservation relation:

$$P_1 - P_0 = \rho_0 U_s U_p.$$

The impedance match equation was then used to calculate the incident or detonation pressure. The impedance equation is:

$$P_i = P_t \left[ \frac{\rho_0 U_s + \rho_{HE} D}{2 \rho_0 U_s} \right]$$

where

$P_i$  = incident or detonation pressure

$P_t$  = transmitted pressure

$\rho_0$  = initial density of the water

$D$  = detonation velocity

$U_s$  = transmitted shock velocity

$\rho_{HE}$  = initial density of the explosive.

#### ANALYTICAL CURVE FITS

Initially we attempted five separate methods to obtain the desired transmitted shock velocity. They were:

1. Graphical fits to the first few mm of trace motion by drawing straight lines on 40X photographic enlargements.
2. Polynomial regression fits from one through tenth degree to about 35-40 mm of trace motion.
3. Polynomial regression fits — degree one — to the first 2 mm of trace motion.
4. The combination of an exponential and linear function.
5. The combination of an arc tangent and linear function.

Each streak camera record was analyzed on a Grant comparator. The time, ( $t$ ), values were read and an IBM card punched for successive .025 mm increments in the space direction ( $R$ ) for a total of 2 mm. The process was then repeated for a total distance of about 35-40 mm in .250 mm increments.

Photographic enlargements (~40X) on paper were made of the jump-off region and graphically analyzed to determine the slope of the trace. Although the calculated results from this method were generally good, and therefore recommended for "quick" evaluations, the results were somewhat sensitive to the experience of the analyst. For this reason, we have not included these data in this paper.

The second method attempted — and probably the most commonly used — was one through tenth degrees polynomial regression fits. Polynomial best fits,  $R = f(t)$ , at first appeared to be ideal, e.g., easily differentiated and solved for  $t = 0$  to obtain the initial transmitted shock velocity. But in general, high order polynomials failed to yield good results. Table 1 serves to illustrate the point. Referring to Table 1, it can be seen that for the two shots presented, the "goodness of fit" to the  $R - t$  values improves with increasing degree of polynomial, as one would expect. This, however, does not insure better velocity results upon differentiation and solution at  $t = 0$ ; in fact, the opposite is usually the case. There was no obvious or reliable criterion for selecting the degree of polynomial which would yield the best results. An investigator using this approach would find it very difficult to decide which is the most nearly correct velocity value from tests of an unknown explosive. The tendency of polynomials, as the degree increases, to try to pass through all the read values, causes the derivatives to behave less and less like the actual physical decay of the shock with time. Quadratic fits to slowly decaying shocks such as occur with larger explosive charges produce reasonable results, but not without a potential for error larger than one is usually satisfied with.

The third approach taken was the least squares fitting of a straight line to the first 2 mm of shock travel. This method is of course based on the assumption that the shock velocity is constant over the 2 mm or the deceleration for that distance is zero. This assumption proved to be quite good, especially with the longer charges which produce more slowly decaying shock waves in the water. The use of the first 2 mm of shock travel for linear fits is easily the most expedient of all the methods attempted. The success of this method, however,



TABLE 1  
Velocity Pressure Data (Determined by Polynomial Regression Method for 1st Through 10th Degree Polynomials for TNT and LX-10)

De- gree Fit	$U_s$ (cm/ $\mu$ sec)	Correlation Coefficient	Stand- ard Error of Est.	$P_{det}$ (kbar)
TNT ( $P_{det} \sim 199$ kbar)				
1	.515	.99936655	.54065	168
2	.581	.99995576	.14320	213
3	.540	.99999778	.03216	184
4	.544	.99999790	.03136	187
5	.566	.99999925	.01881	202
6	.571	.99999928	.01851	206
7	.583	.99999938	.01724	214
8	.584	.99999938	.01728	214
9	.600	.99999943	.01651	227
10	.600	.99999943	.01660	227
LX-10 ( $P_{det} \sim 370$ kbar)				
1	.653	.99986350	.16939	347
2	.692	.99998572	.05492	388
3	.664	.99999695	.02546	358
4	.649	.99999793	.02106	343
5	.649	.99999793	.02113	343
6	.660	.99999803	.02079	354
7	.868	.99999826	.01952	381
8	.724	.99999883	.01769	422
9	.763	.99999877	.01653	466
10	.769	.99999877	.01656	473

is contingent upon very high quality streak camera results at the jump-off portion of the trace, and the early portion of streak camera records for this type test is often the most troublesome. This fact prompted us to examine other approaches which would allow use of an order of magnitude more of the streak trace by taking advantage of the improved shadow-graphic effect produced after the shock wave began to have some slight curvature. The one-dimensionality assumptions are increasingly affected as the system becomes more divergent; however, here we are only interested in matching an equation to the actual shock decay characteristics for purposes of solution for interface conditions.

On the assumption that the acceleration of the shock wave in the water decayed in some exponential manner with time, we proceeded to develop a curve fitting model with that characteristic behavior (16). If  $R''(t) = Ae^{-k^2t}$ ,

$R'(0) = N$  and  $R(0) = 0$ , then by successive integration,  $R = AK^{-4}(e^{-k^2t} - 1) + (N^2 + AK^{-2})t$ . Rewriting this equation and combining the constants, one gets the general form of what we have called curve fitting Model I, or:

$$R = A_1 + A_2t + A_3e^{A_4t}.$$

The constraint imposed by the above boundary conditions that the curve passes through the origin at  $t = 0$  has been removed in Model I by addition of the constant,  $A_1$  in order to further increase the versatility of the model.

The Model I equation was fitted to each of the  $R - t$  data sets. The  $A$ 's are constants determined by computer after force fitting the curves to three data points (first, middle, and last) followed by subsequent refinement through successive iterations until convergence to within the desired limits is attained. Shock velocity values are then computed by differentiation of the resulting equation for any desired  $t$  value within the range of the data.

The last of the above mentioned techniques was developed from observation of computer plots of  $R - t$  data sets. Examination of plots of incremental slopes as a function of time,  $\Delta R/\Delta t$  vs  $t$ , had behavior similar to a specialized form of a "Witch of Agnesi" curve. The characteristics of the larger shots, namely a very slow initial decay, followed by a region of faster decay, which subsequently leveled off to practically constant velocity, indicated that integration of a form:

$$R' = C + \frac{8A^2B}{t^2 + 4A}$$

would yield a general equation having properties similar to the  $R - t$  data. The constants  $A$  and  $B$ , are the major and minor axis of an ellipse, and  $C$  represents the almost constant value of velocity attained after the shock has propagated some distance.

Integration of this equation produced the Model III curve fit of the general form:

$$R = A_3t + 4A_1A_2 \tan^{-1}(t/2A_1).$$

Model III was fitted to each of the  $R - t$  data sets; the constants being determined in the same manner as with Model I.

Velocity-pressure values from the last three methods described above were the most

successful. These data are presented in Tables 2 and 3. Table 2 summarizes the PBX 9404 data. Referring to Table 2, the straight line fit appears to offer the best precision followed by the Model I, then the Model III. The straight line fit seems to show an effect of charge length on detonation pressure. Considering only the straight line fit averages, the 1.27 and 2.54 cm shots are 5.8% below the nominal; the 5.08 cm shots are 3% below, while the 11.4 cm values agree with the nominal within < 1%.

The mean pressures given in Table 2 are shown in Fig. 3 in a plot of the ratio of the measured pressure, to the nominal pressure as a function of charge length. A "best fit by eye" curve has been drawn through the data to roughly indicate the capabilities of the technique as determined by these experiments.

Table 3 includes the velocity-pressure data for the nine other explosives tested. Since the 11.4 cm PBX 9404 charges produced the best results — best agreement with nominal detonation pressure — that length was chosen as the standard for the remaining explosives. Where the data were available, the detonation pressure as determined by LRL's "Standard Test for Detonation Pressure Measurement" (5) are also presented for comparison. For the most part, there is very good agreement; when normalized

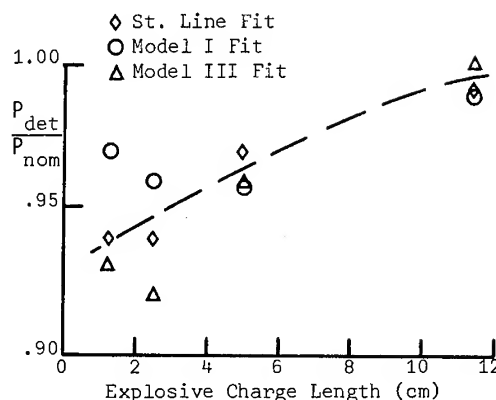


Fig. 3 - Ratio of experimentally measured pressure to nominal detonation pressure as a function of charge length

for density by  $\Delta P/\Delta \rho \sim 0.5$  kbar/mg/cc from  $P \sim \rho D^2/4$ , the straight line fit values are within 1% or less for all explosives for which there are comparative data, except for TNT and 50/50 Pentolite, where the differences are 4% and 2%, respectively. It should be noted here that an error of fixed size in the measurement of initial transmitted shock velocity will result in a proportionately greater error in  $P_{det}$  at lower pressures than at higher ones simply because

TABLE 2  
PBX 9404 Aquarium Test Results (All Charges  $d = 7.2$  cm)

Charge Length (cm)	Density (g/cc)	Det. Vel.* (cm/ $\mu$ sec)	Transmitted Shock Vel., $U_s$ (cm/ $\mu$ sec)			Measured Detonation Pressure, $P_{det}$ (kbar)			Average Detonation Pressure $P_{det}$ (kbar)		
			St. Line Fit 2 mm	Model I	Model III	St. Line Fit 2 mm	Model I	Model III	St. Line Fit 2 mm	Model I	Model III
1.27	1.846	.882	.657	.662	.645	349	355	338	350	360	346
1.27	1.845	.882	.659	.679	.660	351	364	353			
2.54	1.844	.881	.658	.671	.658	351	363	351	351	357	342
2.54	1.843	.881	.658	.657	.640	350	350	332			
5.08	1.844	.880	.669	.663	.659	360	355	350	361	357	357
5.08	1.843	.881	.672	.671	.685	364	364	377			
5.08	1.845	.882	.668	.658	.649	360	351	343			
11.4	1.844	.882	.677	.680	.694	370	373	384	370	369	377
11.4	1.844	.882	.676	.671	.677	369	364	370			

\*Detonation velocities calculated from  $D = .36 \rho + .2176$ .

$$\text{Model I: } R = A_1 + A_2 t + A_3 e^{A_4 t}$$

$$\text{Model III: } R = A_3 t + 4A_1 A_2 \tan^{-1}(t/2A_1)$$

TABLE 3  
Single Shot Results for Ten Explosives (All Charges d = 7.2 cm, L = 11.4 cm)

Explosive	Density (g/cc)	Det. Vel. (cm/ $\mu$ sec)	Transmitted Shock Vel., $U_s$ (cm/ $\mu$ sec)			Measured Detonation Pressure, $P_{det}$ (kbar)			LRL Values <sup>1</sup>		
			St. Line Fit 2 mm	Model I	Model III	St. Line Fit 2 mm	Model I	Model III	Density	Det. Vel.	$P_{det}$ $\pm 5$ (kbar)
PBX 9404 <sup>a</sup>	1.844	.881	.677	.676	.686	370	369	377	1.846	.882	375
TNT <sup>P</sup>	1.638	.692	.561	.553	*	201	195	*	1.632	.694	190
Pentolite <sup>2,P</sup>	1.644	.752	.618	.624	.630	257	262	250	1.644	.752	252
Comp. B <sup>3,c</sup>	1.729	.798	.641	.637	.647	297	294	302	1.733	.800	300
LX-04-1 <sup>4</sup>	1.858	.846	.654	.688	.660	338	372	344	1.867	.848	345
LX-07 <sup>5</sup>	1.850	.859	.694	.684	.694	381	370	381	-	-	-
LX-09 <sup>6</sup>	1.861	.882	.662	.682	.682	354	372	373	-	-	-
LX-10 <sup>7</sup>	1.841	.881	.679	.675	*	374	370	*	-	-	-
Cyclotol <sup>8,c</sup>	1.757	.830	.644	.659	.668	312	325	333	1.760	.830	316
RX-11-AY <sup>9</sup>	1.876	.625	.540	.639	.541	190	187	191	-	-	-

<sup>1</sup>Values determined by the LRL "Standard Test for Detonation Pressure Measurement" (Ref. 5)

<sup>2</sup>50/50 PETN/TNT average PETN particle size 10

<sup>3</sup>60/40 RDX/TNT

<sup>4</sup>85/15 HMX/Viton

<sup>5</sup>90/10 HMX/Viton

<sup>6</sup>93.3/4.2/2.5 HMX/DNPA/FEFO

<sup>7</sup>95/5 HMX/Viton

<sup>8</sup>72/25 RDX/TNT

<sup>9</sup>HMX/Potassium Perchlorate Formulation

$$\text{Model I: } R = A_1 + A_2 t + A_3 e^{A_4 t}$$

$$\text{Model III: } R = A_3 t + 4A_1 A_2 \tan^{-1}(t/2A_1)$$

<sup>a</sup>Average of two shots

<sup>P</sup>Pressed

\*Model III failed to converge to a solution

<sup>c</sup>Cast

it is a larger proportion of the absolute transmitted shock velocity.

## CONCLUSIONS

Clearly, the aquarium technique is capable of yielding good detonation pressure data. The experiments performed and the results obtained show that it is feasible to use the aquarium technique on a nonstatistical experimental basis.

The cost of a test was generally much lower than our cost for a metal plate free surface velocity experiment and the technique has the added potential of collecting useful shock data at distances from the HE/water interface.

Good agreement between nominal and measured pressure values was obtained for the 7.2 cm diameter, 11.4 cm long charges. The discrepancy in the results for the L = 1.27, 2.54,

and to some extent the 5.08 cm shots appears to be real but is not explained. The analytical precision seems to be somewhat enhanced when the records are produced by charges on the order of at least 10 cm long.

Aquarium test space-time streak camera shadowgraphs from explosive charges of this magnitude are well suited to the analysis schemes we have tested. For the numerical analysis techniques attempted, the following conclusions are made:

- Graphical fits to paper photographic enlargements of the streak camera records are recommended only for a first order analysis.
- One through tenth degree polynomial regression fits, although generally, a routine exercise in curve fitting, can produce erroneous results if one selects the degree to be used by the normal

"goodness of fit" criteria, i.e., correlation coefficient and standard error of estimate, etc.

- c. Straight line fits to about the first 2 mm of the shock travel produces good results with large charges providing the record quality in that region is very good and sufficiently large magnification is used in performance of the experiment.
- d. The alternate methods examined, while considerably more involved, take advantage of much more of the trace recorded in a typical aquarium type experiment. Velocity-pressure values derived by these methods were generally good; perhaps these or similar functions can eventually be made to more closely approximate the actual physical decay of the shock in water.

#### REFERENCES

1. A. A. Giardini and E. C. Lloyd, High Pressure Measurement, D. G. Doran, Measurement of Shock Pressures in Solids, pp. 59-84, Butterworths, Washington, 1963.
2. W. C. Holton, The Detonation Pressure in Explosives as Measured by Transmitted Shocks into Water, NAVORD Report 3968, Dec. 1, 1954.
3. M. A. Cook, R. T. Keyes, and W. O. Ursenbach, Measurement of Detonation Pressure, J. Appl. Phys. 33, p. 3413, 1962.
4. N. L. Coleburn, Chapman-Jouguet Pressures of Several Pure and Mixed Explosives, NOLTR Report 64-58, June 25, 1964.
5. J. C. Cast, H. C. Hornig, and J. W. Kury, Standard Test for Detonation Pressure Measurement, UCRL Report 50645, June 12, 1969.
6. M. L. Wilkins, The Use of One- and Two-Dimensional Hydrodynamic Machine Calculations in High Explosive Research, Proceedings of Fourth Symposium on Detonation, ACR-126, U. S. Government Printing Office, p. 519, 1965.
7. B. D. Lambourn and J. E. Hartley, The Calculation of the Hydrodynamic Behavior of Plane One-Dimensional Explosive/Metal Systems, Proceedings of Fourth Symposium on Detonation, ACR-126, U.S. Government Printing Office, p. 539, 1965.
8. F. J. Petrone, Validity of Classical Detonation Wave Structure for Condensed Explosives, Phys. Fluids 11, p. 1473, 1968.
9. V. A. Veretennikov, A. N. Dremin, O. K. Rozanov, and K. K. Shvedov, Applicability of Hydrodynamic Theory to the Detonation of Condensed Explosives, Combustion, Explosion, and Shock Waves, Vol. 3, No. 1, pp. 1-5, 1967.
10. B. G. Craig, Measurements of the Detonation-Front Structure in Condensed-Phase Explosives, Tenth Symposium (International) on Combustion, p. 863, 1965.
11. C. E. Canada, Modification of the Exploding Light Source, Paper to be presented at SMPTE Symposium, 1970.
12. M. H. Rice and J. M. Walsh, Equation of State of Water to 250 Kilobars, J. Chem. Phys. 26, p. 824, 1957.
13. M. van Thiel, Compendium of Shock Wave Data, UCRL Report 50108, Vol. 1, 1966.
14. H. G. Snay and J. H. Rosenbaum, NAVORD Report 2383, April 1952.
15. R. A. Papetti and M. Fugisaki, The Rice-Walsh Equation of State for Water: Discussion, Limitations, and Extensions, J. Appl. Phys. 39, p. 5412, 1968.
16. R. W. Ashcraft, Fitting Curves to HE Diagnostic Data, Internal R&D Report, Pantex AEC Plant, 1969.

# EFFECTS OF PRECOMPRESSION UPON THE DETONATION PROPERTIES OF LIQUID AND SOLID EXPLOSIVES

W. H. Andersen, L. Zernow, A. L. Mottet, Jr., and R. R. Randall  
*Shock Hydrodynamics Incorporated*  
*Sherman Oaks, California 91403*

## ABSTRACT

A derivation of the detonation equations that includes the ambient charge pressure is given, based on the Gruneisen state equation. The solution of these equations indicates that for relatively small ambient charge pressures, the detonation properties (e.g., detonation velocity) are essentially the same as if the explosive were merely initially at the charge density produced by the pressure. As the ambient charge pressure is increased sufficiently, however, the detonation velocity and pressure decrease from the values expected on the basis of charge density only. Experimental studies of the effects of ambient hydrostatic pressure on the detonation velocity of nitromethane, Composition C-3 and HBX explosives are described. Hydrostatic pressures up to 90,000 psi for nitromethane, and 60,000 psi for the solid explosives were employed. Charge densities were obtained from charge pressures using the Tait equation. The resulting detonation velocity vs charge density correlations for the various explosives were linear, indicating that the only apparent influence of charge pressure in this pressure range was in increasing charge density.

## INTRODUCTION

The experimental ideal detonation velocity of a solid explosive charge at atmospheric pressure usually increases linearly with increase in the loading density of the charge, up to the crystal density of the explosive. A study with liquid nitromethane in which the density was varied over a relatively small range by means of the ambient temperature also showed a linear relationship (1). The static prepressurization of an explosive prior to its detonation would increase the charge density above the crystal density of the explosive, and simultaneously store compressional (pressure-volume) energy in the explosive. If the prepressurization were conducted dynamically there would in addition be thermal energy imparted to the explosive, and possibly also kinetic (mass flow) energy, depending on the manner in which the explosive was dynamically precompressed.

The effects of ambient pressure on the detonation properties of a condensed explosive charge are of interest for a variety of reasons.

However, ambient pressure is not ordinarily included as a parameter in the hydrodynamic-thermodynamic equations that are used to describe the detonation properties.

In this paper a derivation of the detonation equations that includes the ambient pressure is first presented, based on the Gruneisen state equation. The equations are then solved in order to elucidate the general effects of the prepressurization of an explosive on its detonation properties. A comprehensive experimental investigation of the effects of hydrostatic pressure upon the detonation velocity of nitromethane and two solid explosives is then described, and the results discussed in terms of the derived theory.

## DERIVATION OF EQUATIONS

### State Equation

The Mie-Gruneisen equation for solids is used to describe the state properties of the detonation products, since at high densities all

molecular degrees of freedom become vibrational in nature. Early studies by Jones (2) indicated that this equation may give a valid description of the state properties of detonation gases at high densities, and studies in several laboratories over the past few years have demonstrated this approach to be valid. The Mie-Gruneisen equation is given by

$$P = GE_t/V - dU/dV \quad (1)$$

$P$ ,  $V$ ,  $E_t$  are pressure, molar volume and internal thermal energy of the detonation products, and  $G$  is the Gruneisen parameter. The potential energy  $U$  between the various vibrating molecular species is assumed to be given by the Morse potential, i.e.,

$$U = D_e \exp[-2a(R - R_e)] - 2D_e \exp[-a(R - R_e)] \quad (2)$$

$D_e$  is the average sublimation (dissociation) energy of the gaseous products at 0°K,  $a$  is the Morse potential parameter,  $R_e$  is the average internuclear distance between the gaseous detonation products at the minimum in the potential energy, and  $R$  is the average internuclear distance between the gaseous detonation products at any molar volume  $V$ , where

$$R = (V/NC)^{1/3} \quad (3)$$

$N$  is Avogadro's number,  $C$  is the lattice constant, and  $V = M/\rho$ , where  $M$  is the average molecular weight of the gaseous detonation products and  $\rho$  is the density of the gaseous products. Combining Eqs. (1) and (2), and replacing  $E_t$  by  $3R_g T$ , where  $T$  is absolute temperature and  $R_g$  is the gas constant, gives the state equation for the detonation products

$$P = 3G\rho M^{-1}R_g T - K\rho^{2/3}E(1 - E) \quad (4)$$

$$K = 2D_e a k / M^{2/3}; \quad k = [3(NC)^{1/3}]^{-1} \quad (5a)$$

$$E = \exp[-a(R - R_e)] \quad (5b)$$

#### Gruneisen Parameter

The expression used for  $G$  was obtained by using Eq. (2) with the Dugdale-MacDonald theory for  $G$  which gives (3)

$$G = \frac{aR}{6} \left[ \frac{4E - 1}{2E - 1} \right] \quad (6)$$

#### Rankine-Hugoniot Equation

The Rankine-Hugoniot (RH) equation is given in a completely general form by (4)

$$E_j - E_o = (E_j - E_j^*) - (E_o - E_o^*) - (E_o^* - E_j^*) \\ = \left( \frac{1}{2} \right) (P + P_o) (\rho_o^{-1} - \rho^{-1}) \quad (7)$$

The  $E$ 's are internal energies, the subscripts  $j$  and  $o$  denote the Chapman-Jouguet (CJ) state and the initial explosive charge conditions, respectively, and the superscript star  $*$  denotes a chosen standard state of pressure and temperature. Choose the standard state to be 1 atm pressure, and normal room temperature (293°K). Then  $(E_o^* - E_j^*) = Q$ , where  $Q$  is the normal (conventional) heat of detonation. The total internal energy  $E_i$  is the sum of the thermal energy and the molecular interaction potential energy, i.e.,

$$E_i = C_v T + U \quad (8)$$

$C_v$  is the constant-volume heat capacity at  $T$ . Note that Eqs. (4) and (8) satisfy the requirement for thermodynamic consistency, i.e.,

$$\left( \frac{\partial E_i}{\partial V} \right)_T = T^2 \frac{\partial (P/T) V}{\partial T} \quad (9)$$

Substituting Eq. (8) into Eq. (7) and recalling that  $U^* = 0$ , i.e., the potential energy of a low density gas is zero, gives

$$\bar{C}_v(T - 293) + U - [C_{vo}(T_o - 293) + (U_o - U_o^*)] = Q + \frac{1}{2} (P + P_o) \times (\rho_o^{-1} - \rho^{-1}) \quad (10)$$

$\bar{C}_v$  is the average heat capacity between  $T$  and 293°K. Equation (10) is valid for either zero or finite initial charge pressure, i.e., for either normal or compressed explosive charges. The terms in the brackets account for any deviation of the initial charge conditions (temperature or pressure) from the standard state conditions. For the detonation of a charge under normal (i.e., standard state) conditions the value of the terms in the brackets is zero. If the explosive is compressed dynamically, e.g., shocked before detonation, it will be both compressed and heated. In this case the terms in the brackets are equal to the Hugoniot energy of the unreacted explosive as determined from the Hugoniot curves, i.e.,

$$C_{vo}(T_o - 293) + (U_o - U_o^*) = \Delta E_o(\text{Hug}) \quad (11a)$$

$$\Delta E_o(\text{Hug}) = \frac{1}{2} P_o (\rho_1^{-1} - \rho_o^{-1}) = \frac{1}{2} u_o^2 \quad (11b)$$

where  $u$  is the particle (mass) velocity of the unreacted explosive, and the subscripts 1 and o indicates the initial and shocked state, respectively. Thus, the shocked state of the explosive defines the initial state for the detonation of a preshocked (dynamically precompressed) explosive.

### Chapman-Jouguet Equation

The CJ condition is

$$\left( \frac{\partial P}{\partial V} \right)_s = \frac{-(P - P_o)}{(V_o - V)} = \left( \frac{dP}{dV} \right)_{(\text{Hug})} \quad (12)$$

The subscript  $s$  indicate constant entropy, and Hug indicates along the Hugoniot.

Evaluating Eq. (12) along the Hugoniot gives the CJ equation, i.e.,

$$T = \frac{\frac{KE}{\bar{C}_v \rho^{1/3}} \left[ 1 - E - \frac{4M\bar{C}_v E(1-E)}{3R_g(4E-1)^2} - \frac{\bar{C}_v a k M^{4/3}(1-2E)}{3R_g G \rho^{1/3}} \right] + \frac{MP_o \rho_o}{3R_g G \rho(\rho - \rho_o)}}{\frac{4GE}{(4E-1)^2} + \frac{(5\rho_o - 2\rho)}{3(\rho - \rho_o)} - \frac{3R_g G}{M\bar{C}_v}} + \frac{MKE(1-E)}{3R_g G \rho^{1/3}} \quad (13)$$

### Velocity Equations

The detonation velocity,  $D$ , and the particle (mass) velocity,  $W$ , are obtained from the usual hydrodynamic equations, i.e.,

$$D = \left[ \frac{P - P_o}{\rho_o \left( 1 - \frac{\rho_o}{\rho} \right)} \right]^{1/2} + u_o \quad (14)$$

$$W = \frac{(\rho - \rho_o)}{\rho} D + u_o \quad (15)$$

### METHOD OF SOLUTION

The detailed solution of the preceding equations for a particular explosive requires that the detonation product composition (e.g.,  $H_2O$ ,  $N_2$ ,  $CO$ ,  $CO_2$ ,  $C$ , etc.) of the explosive be known. The average values of the various compositional parameters used in the above equations (e.g.,  $D_e$ ,  $a$ ,  $M$ ,  $R_g$ , etc.) can then be computed. If a solid such as free carbon is present, its compressed volume must be subtracted from the total volume to obtain the effective volume available to the gaseous products. This complication will not be considered here. The exact product composition is determined by the various temperature-dependent chemical equilibria that must be satisfied, and hence the product composition is also a variable quantity in the solution of the equations. The evaluation of the equilibrium compositions (at various charge densities) generally require electronic high speed computational techniques, due to the time-consuming iterative nature of the solution.

In order to illustrate the general nature of the solution of the preceding equations, it is not necessary to include the effects of an equilibrium product composition, although it is clear that this would be required for a detailed calculation of a specific explosive. For the present purposes the

computations have been carried out for RDX explosive assuming a fixed CJ product composition of water, nitrogen and carbon monoxide. The values used for  $D_0$  and  $a$  in Eq. (2) for the various detonation products were obtained by roughly fitting the Gruneisen equation with Morse potential to the experimental shock Hugoniot data of the detonation products. The appropriate equations are given in Ref. 3. Because the use of a fixed product composition is highly approximate (large amounts of  $\text{CO}_2$  and C are formed at high charge densities), and the Hugoniot fits were only rough, the results of the calculations should not be considered to apply in detail to RDX, but rather are illustrative of a typical condensed explosive.

Under conditions of an assumed fixed product composition, the preceding detonation equations are solved for a specified  $\rho_0$  by solving Eqs. (4), (6), (10) and (13) simultaneously to obtain the values of  $P$ ,  $T$ ,  $\rho$ , and  $G$ . The values of  $D$  and  $W$  are then obtained using Eqs. (14) and (15).

#### COMPUTATIONAL RESULTS

The equations were solved with an electronic computer. In performing the calculations the following values were used for the various parameters in the equations:  $M = 24.67$  gm/mole,  $\rho_e = 0.906$  gm/cc,  $Q = 1228$  cal/gm,  $a = 10^8$  cm<sup>-1</sup>,  $D_e = 8940$  cal/mole,  $c = 1$ , and  $\bar{C}_v = 0.4$  cal/gm<sup>o</sup>K. The computed results are summarized in Table 1, and the detonation velocity behavior is shown in detail in Fig. 1.

The top solid line in Fig. 1 is the computed detonation velocity as a function of charge density for the explosive charge, assuming no precompression of the charge, i.e.,  $P_0 = 0$ . The relationship is linear as is usually found experimentally. The broken line continuation of the solid line corresponds to an extrapolation of the linear curve above assumed crystal density (1.8 gm/cc) but the computed solution also gives this line for  $P_0 = 0$ .

The solid curve at chargedensities greater than crystal density corresponds to the computed detonation velocities when the explosive charge has been shock compressed to various densities greater than crystal density prior to its detonation. The charge therefore has finite values of  $P_0$  at the different densities. The curve identifies the pressure at three different charge densities. These values were obtained from the shock Hugoniot of RDX (5). However, the mass velocity of the compressed explosive  $u_0$ , in Eqs. (14) and (15) was taken to be zero in the computations in order to illustrate the effect of a finite value of  $P_0$  on the detonation velocity. It is apparent that compressing an explosive to some specified charge density greater than crystal density prior to its detonation decreases the detonation velocity below that which would be obtained at the corresponding charge density if the charge pressure  $P_0$  were considered to be zero. The same is likewise true of detonation pressure, as may be seen from Table 1, but the differences are less pronounced.

TABLE 1  
Computed Detonation Properties Using the Gruneisen Equation

$\rho_0$ (gm/cc)	$P_0$ (kbar)	$\rho$ (gm/cc)	$G$	$P$ (kbar)	$T$ (K <sup>o</sup> )	$D$ (m/sec)	$W$ (m/sec)
1.0	0	1.450	1.231	145	5209	6832	2121
1.2	0	1.704	1.126	188	4820	7282	2155
1.4	0	1.969	1.048	246	4373	7797	2254
1.6	0	2.242	0.986	318	3851	8327	2384
1.8	0	2.521	0.936	403	3253	8851	2530
2.0	0	2.804	0.895	502	2585	9357	2684
2.2	0	3.092	0.859	615	1854	9842	2839
2.4	0	3.383	0.828	740	1068	10300	2994
1.44	20*	1.987	1.043	253	4471	7685	2100
1.62	44*	2.190	0.997	313	4415	7998	2083
1.78	74*	2.371	0.962	374	4367	8235	2042
2.22	65†	3.024	0.867	593	2248	9457	2514
2.22	-65	3.216	0.845	673	1746	10360	3209
2.27	79†	3.078	0.861	620	2187	9502	2494
2.55	157†	3.387	0.828	764	1830	9795	2434
2.55	-157	3.795	0.792	962	697	11550	3805

\*Based on nitromethane Hugoniot.

†RDX Hugoniot.



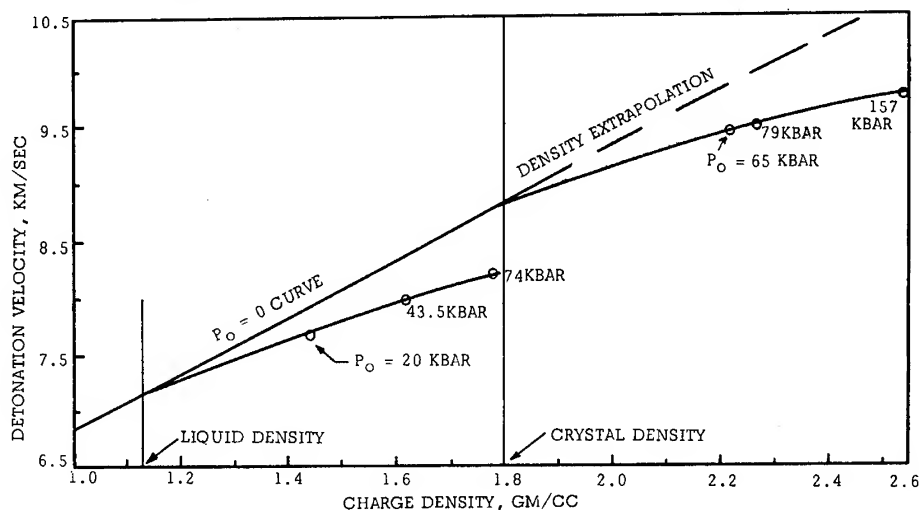


Fig. 1 - Computed detonation velocity as a function of charge density and charge pressure for a typical liquid and solid explosive

The preceding solution for  $P_0 = 0$  was also assumed to apply to a typical liquid explosive. Assuming liquid density to be 1.13 gm/cc, the effect of finite values of  $P_0$  on the detonation velocity was computed as before, and is shown by the lower curve above the liquid density point in Fig. 1. The values of  $P_0$  at various charge densities were obtained from the shock Hugoniot of nitromethane (5). As before, the effect of compressing a liquid explosive above its normal liquid density is to give a detonation velocity that is lower than what would be expected at the corresponding charge density if the ambient charge pressure was zero.

Two other effects of interest shown by the computations in Table 1 may be mentioned. Sample calculations were performed for the case of a precompressed charge having a negative initial pressure. This would correspond to a tensile wave following a precompression. It is seen that the resulting detonation velocity and pressure are both much greater than the density-extrapolation values. On the other hand, the temperature is much lower which may quench the decomposition reaction. The practical significance of these results is not clear since a negative (tensile) pressure would tend to reduce the loading density if the tensile wave were to become uncoupled from the detonation. The attainment of a steady detonation wave is thus doubtful. Nevertheless the effect may be related to certain nonsteady phenomena, and the concepts are intriguing.

## EXPERIMENTAL STUDIES

An experimental investigation of the effects of ambient hydrostatic pressure on the detonation velocity of nitromethane and solid HBX and Composition C-3 explosives was conducted concurrently with the preceding theoretical studies. Hydrostatic pressures up to 90,000 psi for nitromethane, and 60,000 psi for the solid explosives were employed. This investigation required the development of suitable techniques for conducting the studies, since studies of this nature had not previously been reported. Subsequent to this investigation, a study of the effects of pressure up to 9000 psi has been reported for nitromethane (6).

### Experimental Procedures, Apparatus and Monitoring Instruments

The experiments were conducted by placing the explosive in a two foot long section of precision steel tubing, pressurizing the explosive hydraulically, and then initiating it to detonation. The progress of the detonation was monitored by appropriate sensing probes.

For most measurements stainless steel tubing of 9/16" OD and either 3/16" or 5/16" ID was employed, although in the initial measurements SHELBY tubing of 0.569" OD and 0.325" ID was used. The tubes were sealed at one end with a high pressure closure fitting,

and the high pressure fitting at the other end was connected to the pressurization unit through a capillary tube. The pressurization system was a two stage system utilizing a compressed air pump capable of generating hydrostatic pressures up to 5000 psi and an intensifier with an area ratio of 24:1 to generate the final pressure. The pressurizing fluid in the intensifier unit was composed of equal parts of kerosine and motor oil. A rubber separating plug was used to prevent the mixing of the pressurization fluid with the explosive.

The explosive charge was initiated to detonation with A4 DuPont Deta sheet wrapped on the high pressure closure fitting, and a detonator. This system provided a converging shock into the explosive in the tubing. Detonation velocity was measured by means of electronic pin switches monitored by a raster oscilloscope. The pin switches were 2-56 machine screws sharpened to a point and supported by a semiflexible plastic strip. Each strip protruded about 3/32" and was firmly anchored in the strip by a 2-56 nut. The strips varied from 16" to 22" long and the pin switches were about 1.75" apart. About ten probes were used in each case. After being set in the plastic strip, a reference impression of the probe locations was made on an aluminum bar and measured.

The plastic strip holding the probes was attached to the stainless tubing with RTV silicone compound and then taped to insure a slight tension against the tubing. A strip of 1.5 mil mylar magnetic recording tape was then inserted between the switch and the tubing. A slight pull on the mylar revealed if the probe was in firm contact with the mylar. Also, electrical conduction was checked between the tube and probe. Therefore all the probes were within 1.5 mil of the stainless steel tube but not in electrical contact with it.

When a switch was closed by firing, a signal was sent to a 101 raster oscilloscope where a vertical deflection was produced in the beam. A time resolution of  $\pm 20 \times 10^{-9}$  sec was possible. A typical total transit time for the experiment was approximately 50  $\mu$ sec.

#### Experimental Measurements and Results

Experimental measurements were made on liquid nitromethane, and HBX and Composition C-3 solid explosive. The nitromethane was sensitized by the addition of 5% benzylamine by volume. The temperature increase of the nitromethane caused by pressurization was allowed

to equilibrate with the ambient temperature before firing the charge, and the ambient temperature noted.

Some fluctuation in velocity between the various probes generally occurred, and these fluctuations can result from a variety of factors. An analysis of the data indicated these fluctuations were reasonably random in nature, except in some cases for that of the first probe, for which the data was usually discarded. This implied that the system was in a steady state, and the data were consequently treated by means of least squares analysis. A summary of the reduced measurements are given in Table 2. A plot of this data for the various explosives shows that the detonation velocity is a non-linear function of the pressure, as would be expected since the pressure range is large.

#### Analysis of the Experimental Results

The experimental detonation velocities were correlated on the basis of charge density, which was obtained using charge pressure and the Tait equation, as modified by Nanda and Simha (7), i.e.,

$$1 - \rho_1/\rho_0 = C \ln (1 + P_0/B) \quad (16)$$

C and B are experimental constants,  $\rho_1$  is density at atmospheric pressure, and  $\rho_0$  is density at charge pressure  $P_0$ . The constants B and C were evaluated by assuming that the normal compressibility equation

$$\rho_0 = \rho_1 \exp (\beta P_0) \quad (17)$$

is valid at low pressure,  $\beta$  is the compressibility coefficient. Equation (17) was used by itself in reducing the data obtained using the SHELBY tubing.

The value of  $\beta$  for nitromethane is apparently not known, and was estimated theoretically by two different thermodynamic expressions

$$\beta = \frac{TV \alpha^2}{C_p - C_v} \approx \frac{TV \alpha}{\Delta H_v - RT} \quad (18)$$

T is absolute temperature, v is volume,  $\alpha$  is coefficient of thermal expansion,  $\Delta H_v$  is heat of vaporization, and  $C_p$  and  $C_v$  are heat capacity at constant pressure and constant volume. Using values of  $\alpha = 1.239 \times 10^{-3} \text{ } ^\circ\text{K}^{-1}$ ,  $\Delta H_v = 9100 \text{ cal/mole}$ ,  $C_p = 0.415 \text{ cal/gm}^\circ\text{K}$  and  $C_v = 0.242$  gives values of  $\beta$  of  $5.76 \times 10^{-11}$  and  $5.86 \times 10^{-11} \text{ cm}^2/\text{dyne}$  for pure nitromethane at  $90^\circ\text{F}$  by the above two equations, respectively, which

TABLE 2  
Measured Detonation Velocity of Pressurized Explosives

Explosive	Hydrostatic Pressure KPSI	Ambient Temperature °F	Detonation Velocity, m/sec		
			Measured Velocity	$\sigma^1$ m/sec	Velocity Corrected to 90°F
Nitromethane 5/16" ID Tubing	0	90	6,023	7.3	6,023
	0	100	5,999	5.5	6,019
	20	100	6,211	6.7	6,234
	20	90	6,254	6.1	6,254
	40	91	6,379	4.6	6,381
	60	87	6,495	6.1	6,489
Nitromethane 3/16" ID Tubing	0	91.5	5,997	7.3	6,000
	30	84	6,300	6.1	6,288
	62	94.5	6,500	16.5	6,510
	62	74	6,492	14.3	6,439
	88	94	6,596	4.6	6,550
Nitromethane SHELBY Tubing	0	64	6,099	14.6	6,095 <sup>2</sup>
	0	68	6,140	13.4	6,145
	10	66	6,221	11.3	6,221
	10	62	6,257	18.6	6,249
	20	65	6,315	4.9	6,313
	20	66	6,308	13.7	6,308
C-3 5/16" ID Tubing	0	40-50	7,844	6.1	
	20		7,941	6.1	
	36		8,042	6.1	
	41		8,033	6.1	
	56		8,054	9.1	
	60		8,045	6.1	
HBX 5/16" ID Tubing	0	40-50	7,285	11.0	
	37		7,598	6.7	
	54		7,670	10.7	

<sup>1</sup> $\sigma$  is the standard deviation obtained from the least squares fit to the experimental velocity data obtained from the probes.

<sup>2</sup>Data in this group (SHELBY Tubing) were corrected to 66°F.

are thus in excellent agreement with each other. These values include corrections for the benzylamine impurity. The corrected ambient charge density of nitromethane at 90°F was 1.114 gm/cc(1).

For the solid explosives, the composition of HBX was taken as 75% Composition B and 25% aluminum (by weight) for the computations; the compressibility of Composition B is  $2.81 \times 10^{-11}$  cm<sup>2</sup>/dyne. Aluminum was considered to be incompressible. The  $\beta$  of Composition B was also used for Composition C-3, since its  $\beta$  was not known.

The densities computed by the preceding equations for nitromethane at the various charge pressures are shown in Fig. 2 together with the corresponding detonation velocity. The data of Campbell et al (1) using 1.75" charges contained in 1.875" OD brass tubes are also shown. The present data show a linear dependence between detonation velocity and charge density. The data also show a slight dependence on the diameter (and possibly confinement) of the charge. This diameter dependence indicates that the charges were detonating slightly non-ideally. The detonation velocity of the 5/16" cased charges is given as a function of charge density by the empirical equation

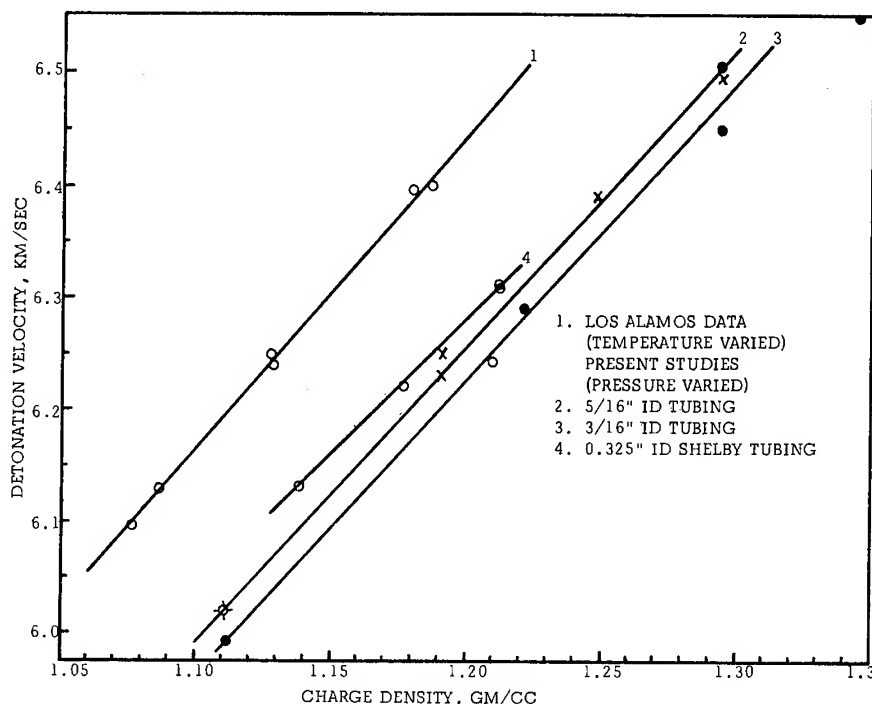


Fig. 2 - Comparison of experimental detonation velocity data for nitromethane

$$D = 6020 + 2695 (\rho_o - 1.114) \text{ m/sec} \quad (19)$$

The data of Campbell et al relating the ideal detonation velocity of nitromethane at various ambient temperatures were converted to a density basis, and are given by the equation

$$D = 6198 + 2855 (\rho_o - 1.114) \quad (20)$$

A comparison of Eqs. (19) and (20), as well as of the two lines in Fig. 2, indicates that the slope of  $D$  vs  $\rho_o$  of the present data is very near that obtained on the Los Alamos studies. There is, however, an absolute difference of the order of 180 m/sec in the detonation velocities. Analysis of the possible sources of error indicates that measurement or data reduction errors cannot be responsible for the differences observed. An analysis of the 3/16" and 5/16" charges with the curved front theory for moderately confined charges (8) suggests the ideal diameter is about 80 m/sec above that of the 5/16" charges, which is roughly half the observed differences. The (largely) dilution effects of benzylamine in the nitromethane can easily explain the remaining difference. Thus the absolute difference in the detonation velocity of the present studies from those of Los Alamos can be attributed to slight nonideality of the detonation and dilution of the nitromethane with the benzylamine.

Although the detonation velocity vs charge density correlations in the present studies are essentially linear, there is no reason to believe that they must necessarily be linear if the detonation is slightly nonideal. Moreover, if the correlation is linear the slope need not be that of the ideal detonation. The slope of the lines in Fig. 2 is slightly lower than that of the Los Alamos curve but it is not known whether this difference is real. It was found that the slope depended very slightly on the value of the pressures used to evaluate the constant in Eq. (16).

Therefore, to the accuracy inherent in the experimental data and the data reduction techniques, it can be said that the increase in detonation velocity with increase in ambient pressure of the nitromethane can be explained entirely by the increase in charge density resulting from the increase in pressure. This conclusion is thus in agreement with the theoretical conclusion discussed earlier, since the ambient pressures are too small to produce significant effects due to pressure only.

The detonation velocity vs charge density correlations obtained for the HBX and Composition C-3 charges are shown in Figs. 3 and 4. These data likewise show a linear correlation between detonation velocity and charge density. The data cannot be compared with the  $D$  vs  $\rho_o$

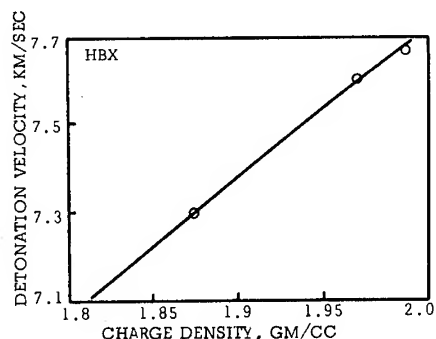


Fig. 3 - Detonation velocity of pressurized HBX

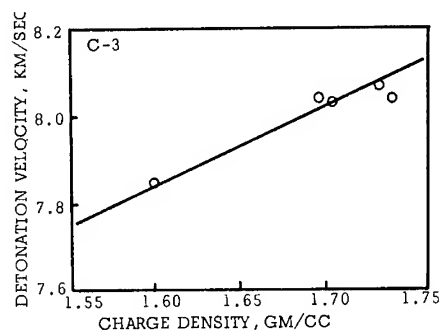


Fig. 4 - Detonation velocity of pressurized C-3

data at lower densities since this latter data was not known. It may thus be concluded, as with nitromethane, that the increase in detonation velocity with increase in ambient pressure of the solid explosives, over the relatively small pressure range employed in the studies, is explained entirely by the increase in the charge density resulting from the increase in charge pressure.

#### ACKNOWLEDGMENT

This work was supported by the Air Force Armament Laboratory, U. S. Air Force under Contracts AF08(635)-4829 and AF08 (635)-5852.

#### REFERENCES

1. A. W. Campbell, M. E. Malin and T. E. Holland, *J. App. Phys.* **27** 963 (1956).
2. H. Jones, "The Process of Detonation in Solid Explosives," British Report RC-166 (1941).
3. W. H. Andersen, "Evaluation of the Gruneisen Parameter for Compressed Substances. I. Metals," Preprints and Proceedings, Fourth Symposium on Detonation, U. S. Naval Ordnance Lab., White Oak, October 1965.
4. J. Taylor Detonation in Condensed Explosives, Clarendon Press, Oxford (1952).
5. V. S. Ilyukhin, P. F. Pokhil, D. K. Rozanov and N. S. Shvendova, *Dokl. Akad. Nauk* **131**, 793 (1960).
6. C. Brochet, Y. Guasson, Y. Pujol and N. Manson, *C. R. Acad. Sci. Paris. t. 269, Series B*, 150 (1969).
7. V. S. Nanda and R. Simha, *J. Chem. Phys.* **41**, 1884 (1964),
8. H. Eyring, R. E. Powell, G. H. Duffey and R. B. Parlin, *Chem. Rev.* **45**, 69 (1949).

#### DISCUSSION

W. C. DAVIS  
Los Alamos Scientific Laboratory  
Los Alamos, New Mexico

The authors have presented measurements of the variation of detonation velocity with initial pressure, and shown how these data can be used to test assumptions underlying a chosen equation of state. The data can also be used in an

extension of the inverse method to find a C-J pressure for the explosive.

A number of workers, including Jones (1), Stanyukovich (2), Manson (3), and Wood and Fickett (4), have shown that useful relationships among derivatives of detonation velocity with respect to any initial state quantity can be found by differentiating the Rayleigh line and Hugoniot

curve equations at the C-J point. Because the two are tangent at that point, the differentials containing pressure and volume enter in the same form in each expression, and can be eliminated, leaving only differentials containing initial state quantities. Using the notation of Wood and Fickett, the variation of detonation velocity is given by

$$\frac{dD}{D} = -A \frac{dv_o}{v_o} + B \frac{dE_o}{D^2} - (A+1) \frac{dp_o}{\rho_o D^2} \quad (1)$$

$$A = (\Gamma - 1 - \alpha)/(\alpha + 2) \quad (2)$$

$$B = \alpha(\Gamma + 1)^2/(\alpha + 2) \quad (3)$$

$$\Gamma = -(\partial \ln p / \partial \ln v)_S \quad (4)$$

$$\alpha = p(\partial v / \partial E)_p \quad (5)$$

Here  $D$  is the detonation velocity,  $v_o$  the initial specific volume,  $E_o$  the initial specific internal energy,  $p_o$  the initial pressure,  $\rho_o = 1/v_o$  the initial density,  $p$  the C-J pressure,  $v$  the C-J specific volume, and  $E$  the C-J specific internal energy.

Looking at Eq. (1) we see that substituting into it a measured value for the initial slope of the curve of detonation velocity versus any initial state parameter, say temperature or pressure, gives a linear equation in  $A$  or  $B$ . Two independent variations give two linear equations which can be solved for  $A$  and  $B$ . With  $A$  and  $B$  known, Eqs. (2) and (3) can be solved for  $\alpha$  and  $\Gamma$ , and these are values at the C-J point. The pressure can be found from the C-J relation

$$P_{CJ} = \rho_o D^2 / (\Gamma + 1) \quad (6)$$

For any particular variation the slope of the linear equation is determined by the thermodynamic derivatives at the initial state, and the measurement just determines the intercept.

Figure 1 is a plot in the  $A, B$  plane of the linear relationships determined by some experiments with nitromethane. The data in Table 2 of Andersen, et al., give a value of about 160 m/sec per kb for  $(\partial D / \partial p_o)_T$ . To use this derivative in Eq. (1) we need to determine the isothermal compressibility (Eq. 18 of Andersen, et al.) from, for example,

$$k = (\rho_o c^2)^{-1} + \frac{T \beta^2}{\rho_o C_p} = 6.69 \times 10^{-11} \text{ cm}^2/\text{dyn} \quad (7)$$

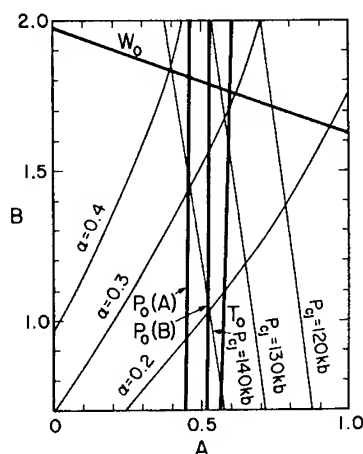


Fig. 1 - Plot in the  $A, B$  plane of the linear relationship between  $A$  and  $B$  determined by experiment. The curve labelled  $p_o(A)$  is from the detonation velocity vs initial pressure measurements of Andersen, et al.; that labelled  $p_o(B)$  is from those of Brochet, et al. The curve labelled  $T_o$  is from the detonation velocity vs initial temperature measurements of Campbell described by Davis, et al. The curve labelled  $w_o$  is from the measurements of detonation velocity vs dilution with Acenina of Davis, et al. Contours of constant pressure and of constant  $\alpha$  are shown as light lines.

where  $c = 1335$  m/sec is the sound velocity,  $T$  is the initial temperature,  $\beta = 1.158 \times 10^{-3} \text{ } ^\circ\text{C}^{-1}$  is the thermal expansion coefficient, and  $C_p = 0.414$  cal/g is the specific heat at constant pressure. We also need

$$(\partial E_o / \partial p_o)_T = (k p_o - T \beta) / \rho_o = -0.277 \text{ cm}^3/\text{g} \quad (8)$$

The nearly vertical line farthest to the left represents the relationship between  $A$  and  $B$  determined by the data of Andersen, et al. The parallel line just slightly to the right represents the relationship determined by the initial pressure variation measurements of Brochet, et al., (5), who found 197 m/sec per kb for nitromethane. To determine values for  $A$  and  $B$  an independent variation of initial state is required. The nearly vertical heavy line farthest to the right, not quite parallel to the pressure variation lines, represents the relationship between  $A$  and  $B$  determined by the measurements

made by Campbell, reported by Davis, et al., (6), on the variation of  $D$  with initial temperature. The value found for nitromethane is  $-3.964$  m/sec  $^{\circ}\text{C}$ . Obviously initial temperature and initial pressure are not a good pair to vary to determine  $A$  and  $B$ , because the lines are too nearly parallel. Another variation of the initial state of nitromethane has been reported by Davis, et al., (6). They mixed an explosive called Acenina which has the same atomic composition as nitromethane, with nitromethane, and evaluated the derivative  $\partial D/\partial w_0$  for pure nitromethane ( $w_0$  is the weight fraction of Acenina). The experiments determined another relationship between  $A$  and  $B$  which is represented by the nearly horizontal heavy line near the top of the graph. This line intersects the lines from the pressure and temperature variations nicely, and pressures can be determined from those intersections. The light lines with large negative slope are lines of constant pressure in the  $A, B$  plane. Combined with the  $w_0$  variation, the temperature variation experiments give a  $C$ - $J$  pressure of about 127 kb, the pressure variation work of Brochet, et al., gives 132 kb, and the pressure variation work of Andersen, et al., gives 137 kb. To agree with the temperature variation work, the pressure work would have to find a coefficient of 238 m/sec per kb.

The light, slightly curved, lines with positive slope are lines of constant  $\alpha$ . There is no accurate way to predict  $\alpha$ , and values over the range of intersections shown are all reasonable.

The indication seems to be that there is a real disagreement between measurements of  $\partial D/\partial T_0$  and of  $\partial D/\partial p_0$ . Careful study of the possible errors of all the experiments is necessary to decide whether the difference is significant. If it is, there are several possible reasons for a difference. The derivation of Eq. (1) depends upon the validity of the Chapman-Jouguet condition; if this condition is violated the equation does not hold, and agreement can not be expected. Another possibility is that the measured derivatives have a strong temperature dependence, and that the temperature corrections must be made.

## REFERENCES

1. H. Jones, in Third Symposium on Combustion, Flame and Explosion Phenomena, (Williams and Wilkins, Baltimore, 1949), p. 590.
2. K. P. Stanyukovich, "Nonstationary Flows in Continuous Media," (in Russian, State

Publishers of Technical-Theoretical Literature, Moscow, 1955) and (in English, Pergamon Press, London, 1960), p. 310.

3. N. Manson, *Compt. Rend.* **246**, 2860 (1958).
4. W. W. Wood and W. Fickett, *Phys. Fluids* **6**, 648 (1963).
5. C. Brochet and F. Fisson, *Explosifs* 1969, No. 4, p. 113; C. Brochet, Y. Guasson, Y. Pujol, and N. Manson, *Compt. Rend.* **269**, 105 (1969).
6. W. C. Davis, B. G. Craig, and J. B. Ramsay, *Phys. Fluids* **8**, 2169 (1965).

## REPLY BY W. H. ANDERSEN

The suggestion of Davis to use experimental detonation velocity versus initial charge pressure data in the inverse method to find the  $CJ$  pressure of an explosive is of interest, and may well have considerable potential since it is not necessary to employ large pressures in the studies. His lucid calculation using the data of our paper clearly illustrates the nature and some limitations of the method. However, it is not to be expected that this calculation would yield a highly accurate value of the  $CJ$  pressure or one in complete agreement with that calculated on the basis of the initial temperature. The basic equation of the inverse method (Eq. 1 of Davis) is based on ideal detonation, and the Los Alamos experiments in which the initial temperature was varied were conducted on relatively large diameter charges that detonated ideally. On the other hand charges of a relatively small diameter were used in our studies because of the very high pressure that was employed in some of the experiments. It was demonstrated experimentally that the detonation of these charges was slightly nonideal, i.e., the velocity depended weakly on both diameter and confinement. It is therefore to be expected that the computed  $CJ$  pressure will be only approximate in value, and in fact in view of the small uncertainty brought about by the slight nonideality of the detonation it would appear that the values based on initial temperature and on initial pressure are actually in reasonable agreement. It is evident that further studies on ideally detonating charges of pure nitromethane based on initial pressure are required before the agreement between measurements based on initial temperature and initial pressure can be fully assessed.

**SESSION II**

**UNSTEADY DETONATIONS  
AND DETONATION STRUCTURE**

Chairman: Tsutomu Hikita  
*University of Tokyo*



# THE STABILITY OF LOW-VELOCITY DETONATION WAVES

R. W. Watson, J. Ribovich, J. E. Hay, and R. W. Van Dolah  
*Pittsburgh Mining and Safety Research Center, Bureau of Mines*  
*U.S. Department of the Interior, Pittsburgh, Pennsylvania*

## ABSTRACT

Experimental studies of low-velocity detonation (LVD) in nitro-glycerin-ethylene glycol dinitrate (NG-EGDN) in cylindrical containers composed of a variety of materials are reported. Instrumentation consisted of expendable pressure transducers, strain gauges, continuous velocity probes, high-speed framing camera observation and/or flash radiography. Results are in accord with the cavitation model of LVD developed at this Center; steady LVD's are observed only for those container materials in which steady precursor cavitation is possible, i.e., in which the elastic wave velocity in the walls exceeds the sonic velocity of the explosive. In materials such as lead, in which the extensional velocity is less than the sonic velocity of the explosive, no elastic precursor is observed and the LVD while it appears to propagate indefinitely does so in a pulsating manner. Evidence is presented that the precursor wave responsible for the major part of the cavitation is not in all cases identifiable with the elastic precursor but may be attached to the reaction zone.

## INTRODUCTION

In a continuing effort to understand the phenomenology of LVD, a research program was conducted on the stability of LVD. Details of the LVD wave structure, which were in essential agreement with the earlier Bureau cavitation model for LVD (1), were presented in a recent paper (2); and mechanisms relevant to the initiation of reaction in the cavitated liquid were also discussed recently (3). This paper describes some experiments aimed at a better understanding of the factors governing the stability of LVD's with particular emphasis on studying the precursor wall waves and their interaction with the reaction zone.

## EXPERIMENTAL

The experiments were conducted using the experimental setup depicted in Fig. 1. It consisted of an acceptor container of either Plexiglas,\* aluminum, lead, polyethylene, or glass. The containers were 2.5 cm i.d. and had a

0.32-cm thick wall except for glass which had a 3.2-cm i.d. and a 0.32-cm wall thickness; container lengths varied from 40 cm to 3.05 m. The charges were instrumented with strain gauges and resistive pressure gauges (4) to monitor the precursor waves in the tube wall and the shock wave leading the reaction front. For the most part, the gauges were positioned at the midpoint of the tube or 6 inches from the downstream end of the tube. The explosive sample in all cases was a 50/50 mixture of NG-EGDN; water-control trials were also conducted to differentiate between the precursor waves generated by the initiating shock and those produced by the reacting explosive. Low-velocity detonations in the liquid explosive columns were initiated from shocks derived from a 4.1-cm diameter by 2.5-cm tetryl pellet coupled to a 4.1-cm diameter by 12.7-cm long Plexiglas attenuator.

The results, presented in Fig. 2, were obtained with a 1.37-m long water-filled aluminum tube and serve to illustrate the response of the strain gauge to the wall wave generated by the same shock donor used to initiate LVD in the liquid explosive trials. The strain gauge was mounted at the midpoint of the tube, 69 cm from the attenuator-water interface. The figure

\*Trade names are used for convenience and do not imply endorsement by the Bureau of Mines.

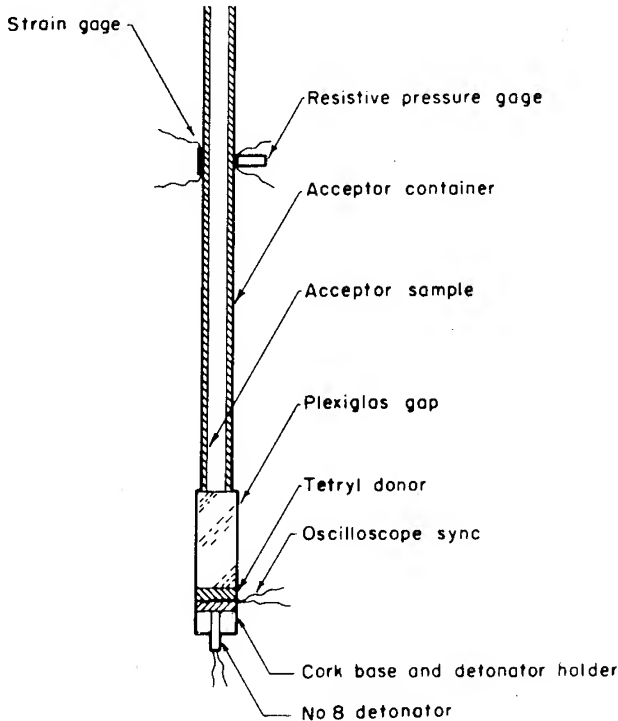


Fig. 1 - Experimental arrangement

shows the oscillographic record obtained in the trial and a distance-time plot deduced from the

record; corresponding points are labeled in both. The points labeled 1, 3 and 4 represent the gauge response to the elastic wave in the tube wall; this wave travels downstream and reflects from the open end of the tube and appears on the oscillogram below the baseline as the polarity reverses. The velocity of the wave was observed to be  $5.1 \text{ mm}/\mu\text{sec}$  which agrees well with the handbook value for the extensional wave velocity in aluminum which is  $5.0 \text{ mm}/\mu\text{sec}$  (5). The pulse, labeled 2 in the oscillogram, is identified with a weak pressure wave in the water which was observed to travel at  $1.3 \text{ mm}/\mu\text{sec}$ . This value is less than the velocity of sound in water and if experimentally significant may be attributable to fluid cavitation caused by the elastic wave in the wall.

Figure 3 shows the results obtained in a trial with an aluminum tube filled with NG-EGDN undergoing LVD. The tube was 1.98 m long; a strain gage and a resistive pressure gage were mounted on opposite sides of the tube 15 cm from the downstream end of the tube. Points labeled 4 on the oscillogram and the distance-time plot correspond to the arrival of the LVD wave front at the gauge stations. The detonation wave velocity was observed to be  $1.9 \text{ mm}/\mu\text{sec}$ . Pulses labeled 1, 2, and 3 are associated with a  $5.1 \text{ mm}/\mu\text{sec}$  elastic wall wave reflecting from the open downstream end of the tube and a discontinuity

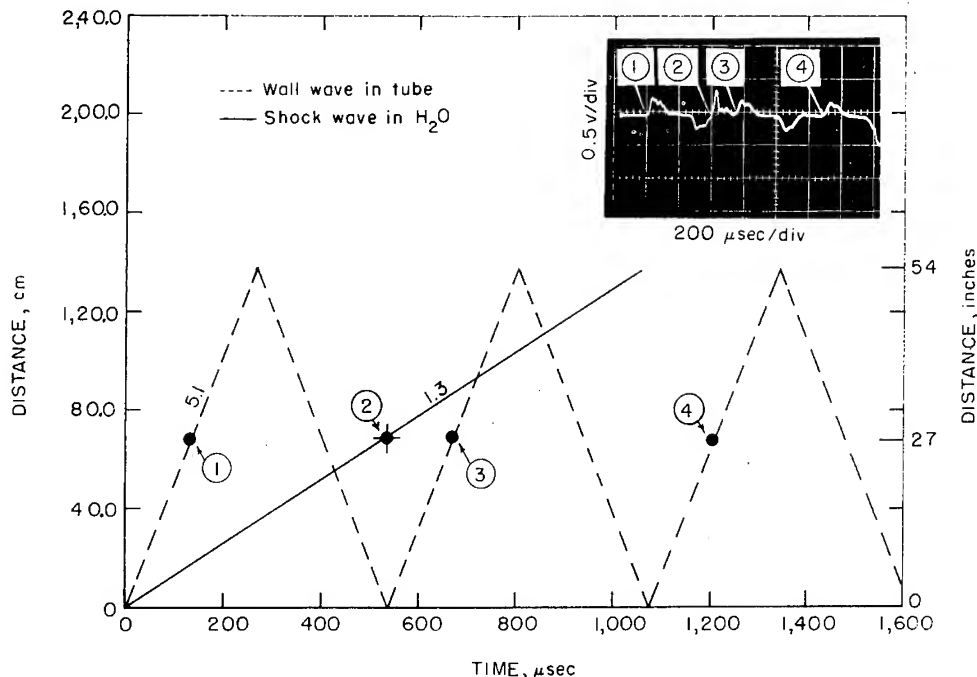


Fig. 2 - Wave velocities in water-filled aluminum tube; insert oscillogram shows strain gauge response

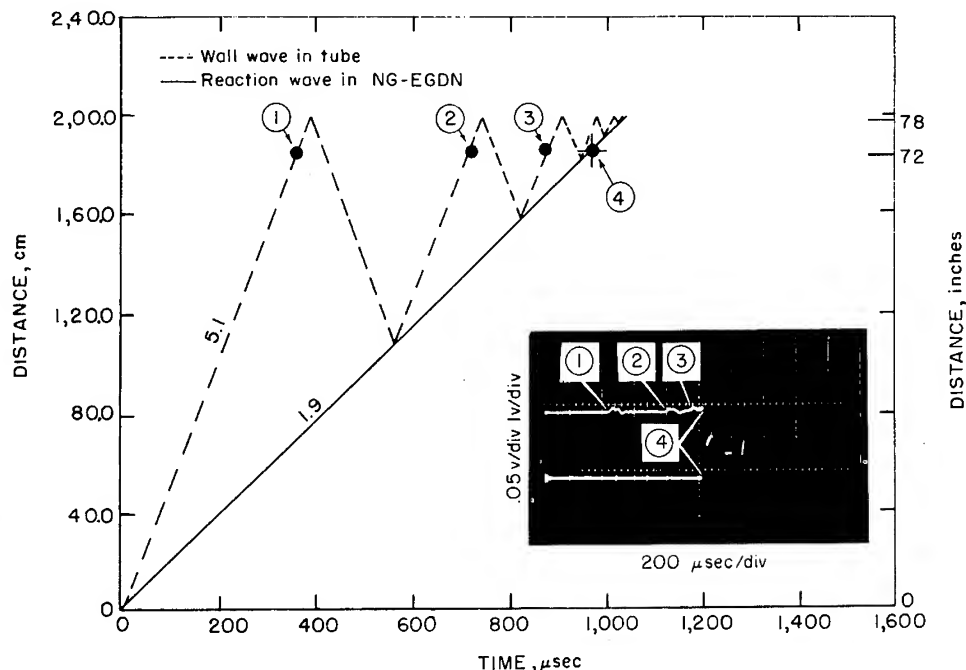


Fig. 3 - Wave velocities in detonating NG-EGDN in an aluminum tube; insert oscillogram shows strain (upper trace) and pressure (lower trace) gauge responses

linked with the advancing detonation wave front. This discontinuity is probably due to tube rupture at or near the detonation wave front. In the oscillogram of Fig. 3 the negative (tensile) portions of the elastic wave are not clearly evidenced as in Fig. 2; this is due to the low gain used (1 v/div for Fig. 3 compared to .5 v/div for Fig. 2) and the fact that the strain gauge was located only 15 cm from the free end of the tube allowing portions of the advancing compression wave to interfere with the reflected tension wave. The resistive pressure gauge was insensitive to the elastic wall wave and responded only to the much higher pressures associated with the reaction zone, approximately 10 kilobars.

Similar experiments were conducted with the other four tube materials; the results are summarized in Table 1. These results represent average values obtained in a number of trials using tubes of various lengths. Values of the elastic wall wave velocity,  $V_w$ , were observed to be the same in trials with tubes filled with NG-EGDN undergoing LVD and in control trials using water-filled containers. Except in the case of polyethylene the experimental values agree with handbook values for the extensional wave velocity for the five materials used. The precise reason for this discrepancy

is unclear but may be due to differences in the physical properties of different grades of polyethylene or to nonlinear strain properties in the polyethylene since the stress levels here are much greater than that of acoustic waves. The values of the detonation rate,  $U_d$ , are average velocities determined from distance-time relationship as, for example, in Fig. 3. In all cases with the exception of lead, the detonation velocities were subsonic relative to the measured elastic wave velocity in the confinement tubes.

In order to determine if the detonation in the various containers represented stable flow configuration, additional firings were conducted with tubes instrumented with continuous velocity probes (6). In all cases other than lead, the velocities were constant within the experimental error which is estimated to be less than 5 percent. The record obtained using lead confinement is shown in Fig. 4(a). The record gave evidence that the velocity was interrupted at regular intervals of about 60  $\mu$ sec; the corresponding spatial separation is approximately 10 cm based on an average propagation velocity of 1.7 mm/ $\mu$ sec along the tube length. It should be noted that the strain gauge record gives no indication of an elastic precursor wave ahead of the reaction in the lead container.

TABLE 1  
Observed Wave Velocities for NG-EGDN  
Undergoing Low-Velocity Detonation under  
Various Conditions of Confinement

Container	$V_w$	$U_d$	$V_{ext}$
Plexiglas	2.2	2.0	1.8
Aluminum	5.1	1.9	5.0
Lead	1.2	1.7	1.2
Polyethylene	1.9	1.4	0.9
Glass	5.0	1.6	5.2

NOTES: (1) All velocities in mm/ $\mu$ sec.  
(2)  $V_w$  measured elastic wall wave velocity.  
(3)  $U_d$  measured detonation rate.  
(4) Handbook values of extensional velocity.

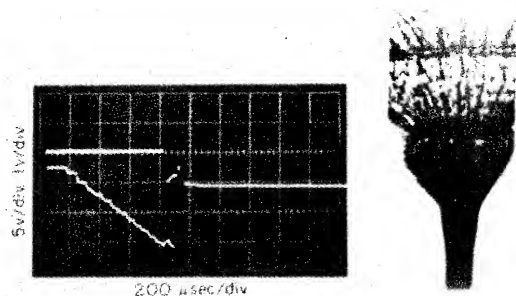


Fig. 4 - (a) Oscilloscope showing response of strain gauge (upper trace) and continuous velocity probe (lower trace) to pulsating low-velocity detonation in a lead tube; (b) expansion and breakup of lead tube containing NG-EGDN undergoing pulsating low-velocity detonation

In order to eliminate the possibility that the steplike appearance in the continuous velocity record of Fig. 4(a) was due to electronic or mechanical anomalies in the probe response, a series of flash radiographs were obtained of the expansion profiles of lead tubes containing NG-EGDN undergoing LVD. One of the radiographs is reproduced in Fig. 4(b). At the time the radiograph was taken the detonation wave had progressed to the end of the tube which was 94 cm long and had an inside diameter of 2.5 cm and a 0.32-cm thick wall. The radiograph gives distinct evidence of regular perturbations similar to those recorded by the continuous velocity probe; the two horizontal bands in the fragmentation pattern are approximately 10 cm apart which was the same spacing observed using the continuous velocity probe. In addition,

a bulge in the expansion profile is beginning to form 10 cm below the central band. These are believed to be associated with interruptions in the detonation wave. These pulsating detonations can be described on the basis of the previously developed cavitation model for LVD. In essence, the reaction wave, once initiated, consumes that portion of the fluid that has been cavitated by the precursor wave; this reaction is interrupted when the cavity field is consumed. However, the elastic precursor wave is able to propagate ahead and create another cavitated region. The residual pressure field is then capable of causing further reactive flow; this process then repeats itself in a remarkably reproducible way. The factors controlling the frequency of these pulsations are undoubtedly complex. The inherent reaction role of the fluid as well as the sound velocity of the container and the container dimensions are felt to be important.

Two other experiments bearing on the subject of stability were carried out using tube materials in which stable low-velocity detonations were produced.

In the first experiment, high-speed framing camera photographs were obtained of LVD's in glass tubes to determine if the elastic precursor wave was capable of causing fluid cavitation. Tubes having lengths up to 3 m were used. Though poorly defined, the leading edge of the cavitation field traveled at 5.0 mm/ $\mu$ sec, in phase with the elastic precursor, and continually outdistanced the reaction wave traveling at 1.6 mm/ $\mu$ sec. The cavitation population appeared to be much more dense near the reaction zone. The length of this dense cavitation zone was relatively constant, giving some evidence for a steady-state wave ahead of the reaction zone traveling at detonation velocity. The records obtained in the earlier trials with strain gauges located at various positions along the tube also gave some evidence for a steady-state wave but were often obscured by the elastic precursor wave traveling at the extensional wave velocity.

In the other series of experiments, resistive pressure gauges were positioned in the liquid column 15 cm from the downstream end of a 1.37-m long charge of NG-EGDN confined in an aluminum tube having a 2.5-cm i.d. and a 0.32-cm wall. The record, shown in Fig. 5, indicates that the gauge responded to a series of compression and rarefaction waves for a period of about 20  $\mu$ sec before the arrival of the low-velocity detonation wave front. Control trials using water-filled aluminum tubes showed that the pressure gauge would not

respond to waves generated by the elastic precursor when used in this manner. The gauge is not calibrated for the low kilobar pressure levels but the results of this experiment are not in disagreement with the results of Dubovik, et al., using the electromagnetic method for determining particle velocity (7). In experiments with nitroglycerin confined in Plexiglas tubes, they noted a 1.5 to 2.0 kilobar pressure wave followed by a pressure release wave to essentially zero pressure ahead of the reaction wave which had an amplitude of about 10 kilobars.

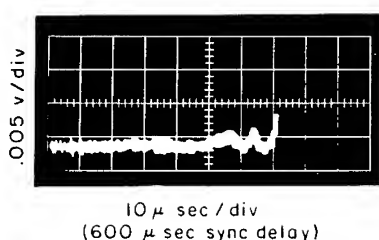


Fig. 5 - Resistive gauge response to pressure waves immediately ahead of the low-velocity reaction zone in NG-EGDN contained in an aluminum tube

## CONCLUSIONS

Experimental measurements of the sonic wave and detonation wave velocities in a variety of materials have demonstrated that a necessary condition for stability is that the detonation wave be subsonic relative to the wave velocity of the container material. If this condition is not met pulsating detonations will occur. The simple model for LVD previously postulated has been found to be complicated by the existence of an elastic precursor wave derived from the initiating shock which is capable of cavitating the fluid. If this were the only cavitating mechanism, then all LVD's would be inherently unsteady since the elastic precursor continually outdistances the reaction zone. Some evidence has been presented indicating the presence of a precursor pressure wave which was attached to the reaction zone. Additional experimental work is required to confirm

these points; however, the experimental work presented here in general supports the cavitation model for LVD.

## ACKNOWLEDGMENT

This work was supported by the Naval Ordnance Systems Command, Department of the Navy, under Contract 17-0-8000.

## REFERENCES

1. R. W. Watson, C. R. Summers, F. C. Gibson, and R. W. Van Dolah, "Detonations in Liquid Explosives—The Low-Velocity Regime," ONR Fourth Symposium (International) on Detonation, ACR-126, U.S. Naval Ordnance Laboratory, White Oak, Maryland, pp. 117-125, Oct. 1965.
2. R. W. Watson, "The Structure of Low-Velocity Detonation Waves," Reprinted from Twelfth Symposium (International) on Combustion, University of Poitiers, France, pp. 723-729, July 1968.
3. J. E. Hay and R. W. Watson, "Mechanisms Relevant to the Initiation of Low-Velocity Detonations," Reprinted from Annals of The New York Academy of Sciences, Vol. 152, Article 1, pp. 621-635, Oct. 1968.
4. R. W. Watson, "Gauge for Determining Shock Pressures," The Review of Scientific Instruments, Vol. 38, No. 7, pp. 978-980, July 1967.
5. American Institute of Physics Handbook, pp. 3-80, McGraw-Hill, New York, 1957.
6. J. Ribovich, R. W. Watson, and F. C. Gibson, "Instrumented Card-Gap Test," AIAA Journal, Vol. 6, No. 7, pp. 1260-1263, July 1968.
7. A. V. Dubovik, I. M. Voskoboinikov, and V. K. Bobolev, "Role of the Leading Shock in the Propagation of Low-Velocity Detonation in Liquid Nitroglycerin," Combustion, Explosion, and Shock Waves, Vol. 2, No. 4, pp. 105-110, 1966.

## DISCUSSION

A. N. DREMIN

Institute of Chemical Physics, USSR

The discovery of the existence of precursor wall waves ahead of the low-velocity reaction front and the change to an aggregative state of the liquid under the influence of the elastic waves are the main achievements of the recent years in the study of low-velocity detonation mechanism. Some attempts to explain the nature of low-velocity detonation have been made. But the following fundamental points of the phenomenon have not been developed so far.

(1) What determines the velocity of this process and (2) what is this velocity dependence on charge diameter?

To solve the problem it is necessary to answer the following questions. First—why does the heterogeneous state of a liquid appear before the reaction front and how does this state change as the reaction wave propagates; second—in what way does the exothermic reaction progress along this heterogeneous substance? The second question involves some knowledge of reaction origin. Exact solutions to these questions permit us to consider the stationarity of the process, its velocity, and structure of the reaction wave front.

I will speak only about some of our experimental data on this problem. I will be concerned primarily with the problem of stationarity of the process. If at some distance (no less than 70 mm) from the beginning of a glass tube filled with nitroglycerine an artificial crack is introduced, two low-velocity waves will propagate from this point in opposite directions at about 15  $\mu$ sec after the elastic wave in the glass has reached the crack. The velocities of these waves and the velocity of the first wave propagating from the beginning of the tube, with due regard to measurement precision, are equal. In addition we have found that the elastic wave attenuates rather slowly in glass-tube walls and is equal approximately to 10 kbars after it has traveled a distance of one meter. All this means that the elastic wave is not directly connected with the process of low-velocity detonation and therefore the stationarity of such detonations is open to discussion. Next, in what way does the cavitating in liquids occur under the influence of the elastic waves in the tube walls? As was shown experimentally, radial and longitudinal vibrations take place in steel tubes without liquids (Ref. 1). We have also observed vibrations behind elastic waves in

flat glass plates. It is obvious that the elastic wave in liquid-filled glass tubes produce vibrations which result in ultrasonic cavitations of the liquid.

It is of interest to relate qualitatively the vibration frequency of the tube with the number of cavities formed. It has been shown theoretically that the frequency of natural vibrations of a thick-walled tube depends on the ratio of the inner to outer radii and has a maximum at a ratio equal to 0.65 (Ref. 2). From cavitation theory (Ref. 3) it is known that the resonance size of gaseous cavities in liquids are determined by the frequency of the applied ultrasonic field. Here we have an approximately inverse dependence. Bubbles of a size larger than the wave length of resonance do not disappear. They vibrate intensively and increase in diameter under the influence of gases and vapors of the liquid. In addition, the bubble's diameter increases considerably due to coagulation. This implies that when the vibration frequency of a tube increases, the number of bubbles in a liquid explosive within also increases. We find indirect confirmation of this behavior in the results of photographic and radiographic observations of the appearance and progress of cavitation bubbles in liquid explosives after the elastic wave has passed. It was shown that the bubbles appear behind the elastic wave after a certain time and that their size increase up to the moment of meeting with the detonation front.

And now, let us consider the progress of reaction in a liquid explosive when the bubbles contain explosive vapor. Taking into account such facts as explosion of metallic wires in nitroglycerine; the possibility of propagation of both low and normal detonation after the first low-velocity wave; data concerning shock initiation of detonation in nitroglycerine, and other information; we conclude that under shock compression of bubbles the explosion of explosive vapor in the bubbles occurs. The explosion does not spread too far relative to the dimensions of the bubbles. The front of the low-velocity reaction wave does not represent a smooth surface. It is not stationary in time or in intensity distribution. From one bubble to the next spherical shock waves attenuate rapidly and consequently do not give rise to any considerable reaction in the bulk. The velocity of these waves will, in general, decrease down to the speed of sound of the liquid. This fact is obviously the reason that the velocities of

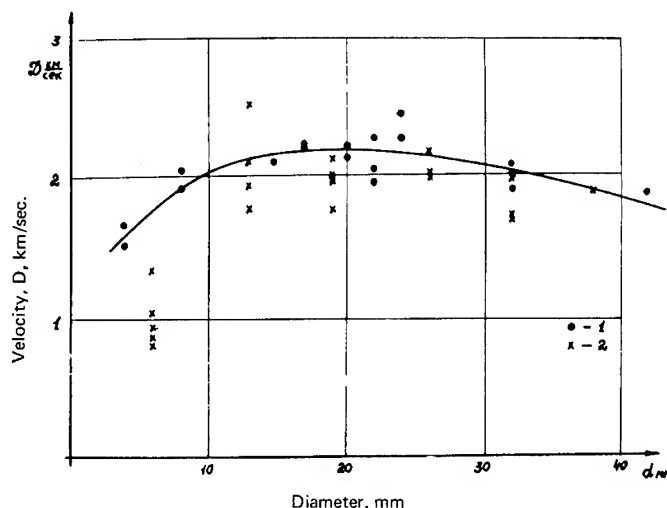


Fig. 1 - Reaction progress velocity, LVD, vs the inner diameter of a glass tube for nitroglycerine. Wall thickness is approximately 1.5 mm (see Ref. 1).

low-velocity waves in all known liquids are only a little larger than the sound velocity. In fact, the bubbles in liquid explosives supply energy to the wave and prevent its velocity from decreasing down to the second velocity. The highest limit of the velocity must be the detonation velocity of explosive vapors because when very many bubbles originate they will nearly touch each other.

Thus, there must be a dependence of the reaction progress velocity LVD on the number of bubbles in the liquid. To confirm this conclusion let us present the dependence of the reaction progress velocity on the inner diameter of a glass tube for nitroglycerine (Fig. 1). The tube wall thicknesses in all cases was about 1.5 mm. As you can see, the velocity has a maximum which agrees qualitatively with the dependence of the maximum frequency of natural vibrations in a gas-filled tube on the ratio of inner to outer diameter. In this figure the

ratio varies from 0.65 to 0.93. As previously pointed out, the number of bubbles increases with increasing frequency of the applied sound field.

#### REFERENCES

1. J. H. Heiman and H. Kolsky, *J. Mech. and Phys. Solids*, **4**, 3, 121 (1966).
2. J. F. Bird, R. W. Hart, and F. T. McClure, *J. Acoust. Soc. of Am.* **32**, 11, 1404 (1960).
3. L. K. Zarembo, V. A. Krasilnikov, *Vvedeniye v Nelineinuyu Akustiku*, Izd. Nauka, 262 (1966).
4. Y. Taylor, "Detonation in Condensed Explosives," Chap. X, Clarendon Press, Oxford (1952).

# FAILURE DIAMETER, SENSITIVITY AND WAVE STRUCTURE IN SOME BIS-DIFLUOROAMINO ALKANES

L. B. Seely,\* Joseph G. Berke, Robert Shaw,  
Derek Tegg, and Marjorie Evans†

*Stanford Research Institute  
Menlo Park, California 94025*

## ABSTRACT

Failure diameters and shock reaction times have been determined for all four bis(difluoroamino)propane isomers and some of the butanes, including two homologs. The difference between the failure diameters of the vicinal (for 1,2-DP; 1.6 mm) and geminate (for 2,2-DP; 4.0 mm) compounds presents a striking example of the dependence of a transient detonation characteristic on isomeric structure. Measured shock reaction times show a difference consistent with the failure-diameter difference on the basis of Dremine's mechanism for the dark-wave mode of failure and reinitiation. The reaction times for the difluoroamino butanes are indistinguishable from the homologous propanes, but the failure diameters are several times larger (IBA and 2,3-DB; 9.5 mm). Rotating mirror camera photographs of failure in the butanes and brass pressure indentation plates of failure in the propanes suggest strongly that failure for these compounds is always by the dark-wave mode. The pressure gradient in the dark wave, the magnitude of the pressure at failure, differences in heat of reaction, and differences in heat capacity all enter into determination of the failure diameter.

## INTRODUCTION

Equilibrium properties of detonations in condensed materials have for over twenty-five years been treated with considerable success according to the Chapman-Jouguet hypothesis. The details of the wave structure have been pictured according to the model of the steady wave proposed independently by von Neumann (1), Zel'dovich (2) and Doering (3) (NZD). The NZD theory has in turn suggested a model for the kinetic behavior of the wave which permits a plausible explanation for its transient behavior. However, this kinetic model is less satisfactory than the steady state model and has failed to explain several experimental facts that have been known for a long time. Perhaps the earliest sign of trouble was the discovery that glass-confined liquids failed at large diameters and furthermore failed at a velocity only

1% below the rate at infinite diameter (4,5). According to proposals made on the basis of the NZD model of the reaction zone, failure is the result of diameter effect carried to the extreme; divergence of flow prevents some of the late-released energy from supporting the wave. This produces a weakened preceding shock in the unreacted material, which in turn greatly slows the reaction, so that still less effective support is given, and the result is cumulative. This might explain why failure would be expected to occur rapidly once the diameter had been reduced sufficiently to have a noticeable effect on the velocity. But it does not explain why failure occurs at a velocity only 60 m/sec below the infinite-diameter rate. Presumably detonation velocity is controlled by divergence as proposed in the current diameter-effect theories. However, failure is not directly controlled by divergence; "dark waves" (5,6) seem

This work performed for the Office of Naval Research under Contract NONR 3760.

\*Present address: Menlo College, Menlo Park, California.

†Present address: Evans Associates, 14511 DeBell Drive, Los Altos Hills, California.



to be its cause, and, while dark waves must be affected by the degree of divergence, the direct effects of divergence are apparently not crucial in determining failure diameter.

#### DIFLUORAMINES FOR THE STUDY OF TRANSIENT DETONATION PROPERTIES

The availability of all four bis-difluoroamino propane isomers and several of the bis-difluoroamino butanes presents a unique opportunity to compare the transient detonation behavior of very similar explosives. The nature of the active groups and the number of active groups is the same in all these compounds. The differences lie in the arrangement of the active groups and hydrogen atoms on each carbon atom; among the propanes, the 2,2-difluoroamino compound has no hydrogen atoms on the fluoroamino-bearing carbon [ $\text{CH}_3\text{-C}(\text{NF}_2)_2\text{CH}_3$ , (2,2-DP)]; the 1,1 isomer has one hydrogen atom [ $\text{CH}(\text{NF}_2)_2\text{CH}_2\text{CH}_3$ , (1,1-DP)]; the 1,2 isomer has two fluoroamino-bearing carbons, one with one hydrogen and one with two [ $\text{CH}_2\text{NF}_2\text{CHNF}_2\text{CH}_3$  (1,2-DP)]; and the 1,3 isomer has two such carbon atoms, each with two hydrogens and a fluoroamino group [ $\text{CH}_2\text{NF}_2\text{CH}_2\text{CH}_2\text{NF}_2$  (1,3-DP)]. Some of the available butanes are exact isomers; namely, 1,2-bis-difluoroamino-n-butane and 2,2-bis-difluoroamino-n-butane. However, the most plentiful butane, and the one with which most of our experiments were done, called "isobutylene adduct" [ $(\text{CH}_3)_2\text{CNF}_2\text{CH}_2\text{NF}_2$  (IBA)], contains one fluoroamino-bearing carbon with no hydrogen and one with an active group and two hydrogens. Thus, these compounds should display the effects of isomeric structure and also the effect of "internal dilution"—a term used to designate the addition of the  $\text{CH}_2$  group to the propanes to form the homologous butanes.

The purity of our samples of difluoroamino propanes and butanes was checked by infrared spectroscopy and chromatographic analysis and estimated to be 99% or better.

All the propanes have very closely the same thermodynamic properties; the equilibrium detonation properties are expected to be indistinguishable. The physical properties such as density, expansion coefficient, and sound velocity are also nearly the same; therefore, the shock properties of all the propanes are similar. Some of the pertinent physical properties are given in Table 1. Transient detonation properties, i.e., those exhibited during approach to or departure from a steady state, may well depend on structure.

TABLE 1  
Some Physical Constants of  
Bis(difluoroamino)alkanes  
[J. Chem. Eng. Data, 15 140 (1970)]

Compound	Density $\rho$ g cm <sup>-3</sup>		Sound Velocity, c cm sec <sup>-1</sup>	Coefficient of Expansion $\alpha_{25}$
	5 deg C	40 deg C		deg <sup>-1</sup>
1,2-DP	1.296	1.241	$0.96 \times 10^5$	$1.26 \times 10^{-3}$
2,2-DP	1.287	1.245	$0.89 \times 10^5$	$1.34 \times 10^{-3}$
1,2-DB	1.245	1.202	$1.00 \times 10^5$	$1.18 \times 10^{-3}$
IBA	1.242	1.193	$0.90 \times 10^5$	$1.15 \times 10^{-3}$

Among the transient detonation properties, failure diameter is one of the easiest to define. Ideally, it is the smallest diameter at which a very long charge would continue to detonate. In practice, one must use relatively short charges, and consequently the booster size and the conditions of introduction of the wave into the liquid require careful control. Further practical considerations require the provision of a smooth confining wall and the absence of any foreign material within the body of the liquid.

For our tests very thick-walled lead confinement was used to reduce the size of the charges. Lead turned out to be a convenient material because a method of forming holes with mirror-smooth walls was found for lead. A smooth rod with a hemispherical end was forced through lead with an arbor press; the hole size was the size of the rod. Using this technique, holes over 64 diameters long could be produced 0.8 mm in diameter. At smaller diameters the rod was quite flexible and tended to wander.

Sensitivity is a particularly hard property to define and quantify. It is clear in general terms that the shock sensitivity of a material to detonation is related to the ease with which reaction can be started in the material, but it is not clear that ordinary chemical reactivities can be extrapolated to the conditions existing in initiating shocks. It has also been clear that sensitive compounds have small failure diameters, but the exact empirical relationship is not likely to be obvious from experimental data on a variety of compounds since many other factors affect conditions in the shock. For comparison, it is particularly valuable to have the bis(difluoroamino) propane isomers, since the difference in shock conditions may be expected to be minor and major differences in shock

sensitivity may be expected to arise mainly from differences in reactivity. To obtain a reactivity measurement under actual conditions in shocks and thus avoid many difficulties, we have measured the time to run-away reaction after shocks of various magnitude have been introduced.

Our measurements of reaction time were in gap-test-like geometry. Advantages are the good reproducibility and simplicity of gap tests. The disadvantage is that the measurement applies to a divergent flow field. Plane wave measurements are preferable insofar as the wave is truly plane, but in practice perturbations on the wave are often responsible for the reaction. Furthermore, divergent flow fields are encountered at failure diameter. It is perhaps no more difficult to use data from a flow field in which the divergence is not the correct value (but approaches it) than it is to use data from a field in which there is no divergence at all. In any case, our reaction times are for flow of unspecified but definite divergence. For those conditions the sensitivity is an asymptot to the measured reaction times.

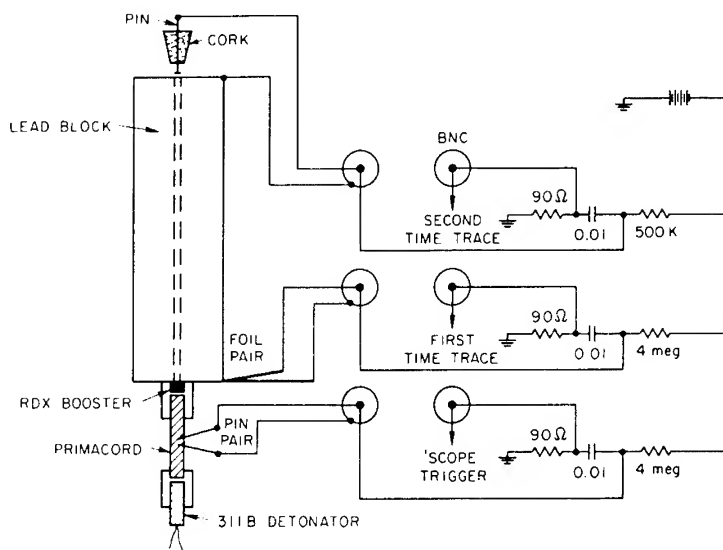
## FAILURE DIAMETER

Failure diameters for the difluoroamino propanes and butanes were determined in charges indicated in Fig. 1. Lead was chosen as the confinement material because of its low sound velocity and its high density (providing

"good" confinement). For purposes of this study, we were concerned with the failure of the high order wave, although for safety purposes one might wish to use a different criterion. It was noted that low-velocity waves exist below our failure diameter for all the difluoro-amino compounds tested.

The criterion of detonation was a velocity measurement which in reality was a transit-time measurement over the entire length of the column. There is good evidence to show that pins in the liquid or gauges mounted in the walls produce failures and thus distort the results. The first signal was taken from a pair of 1/2-mil copper foils between the booster and the 1/2-mil Tedlar (8) barrier that was cemented to the bottom of the lead block. The second signal came from a common pin held so that its head was positioned exactly at the top of the lead over the hole holding the liquid. The head was immersed because of the meniscus of the liquid.

Difluoroamino liquids are conductive enough to reduce the voltage between the pin and the lead block. The detonation products also do not produce clean signals at low voltages. A satisfactory system was developed using 300 volts and a rather large capacitor across the terminal pin. This resulted in deflection of the trace off scale at the end of the record, but the break in the trace was easy to read.



RA-4051-110

Fig. 1 - Failure-diameter charge. Failure of detonation was determined by the velocity calculated from the transit time measured between a pair of foils at the end of the booster and a pin at the end of the lead block.

The question arose as to whether the velocity calculated from two time signals was a measure of a relatively constant velocity or the average of perhaps two widely different velocities over different sections of the charge. In general it seems to represent a single velocity. However, very close to failure diameter intermediate velocities are calculated and here it seems likely part of the travel is at high velocity, part at low.

Below failure diameter of the C-J velocity the question of constant velocity for the low-velocity regime becomes very important. For this low velocity in 1,2-DP wave, tests were made at four different charge lengths: 16, 32, 64 and 96 diameters long. Except for a slightly higher velocity in the short tubes, the velocity was constant, in this case at about  $1.7 \text{ mm}/\mu\text{sec}$ . Although the experimental precision of these measurements is not very high the results seem

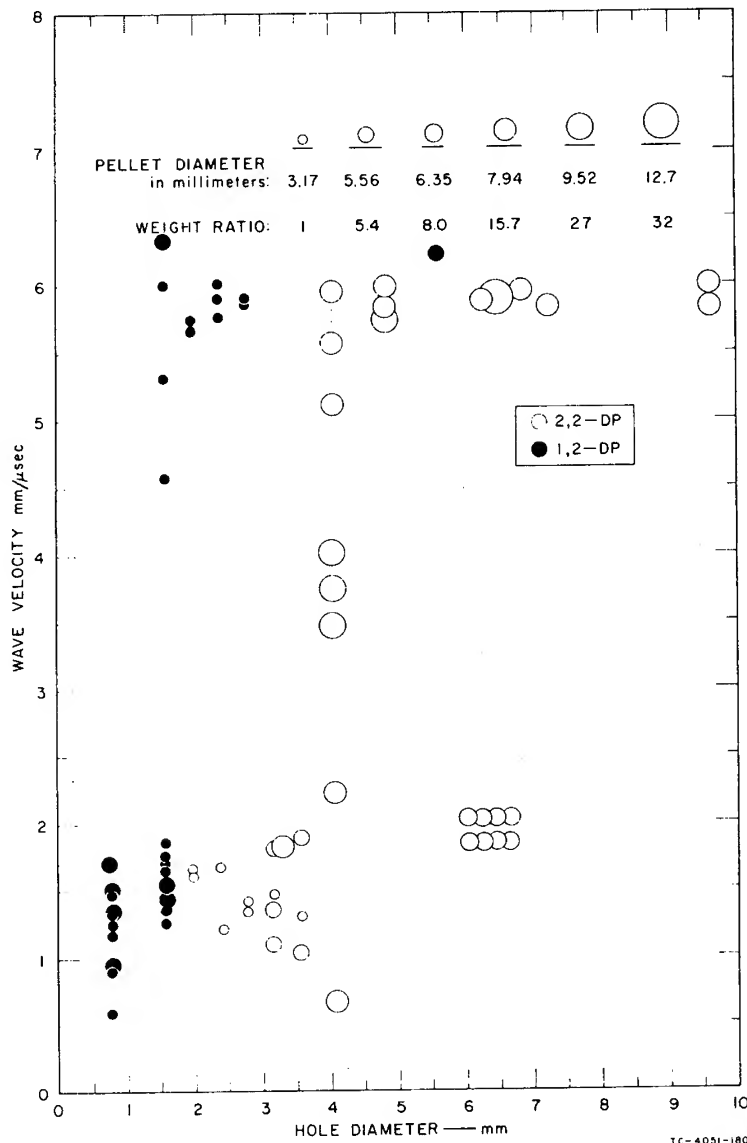


Fig. 2 - Failure diameters for 1,2-DP and 2,2-DP. The average velocity over the entire length of the lead block is plotted against the diameter of the liquid explosive. The failure diameter is indicated by the drop from C-J velocity ( $6 \text{ mm}/\mu\text{sec}$ ) to about one third this value.

to indicate a definite regime. The case of nitromethane is quite different; below failure diameter of the C-J wave no low-velocity wave is recorded.

As a result of much testing it was found that it was very important to have the diameter of the booster greater than the charge diameter and also that the mass of the booster should be larger than some minimum. Failures will result above the true failure diameter if both these requirements are not met. Proper determination of the failure diameter requires that the change from detonation to failure be due to diameter alone. In practice it is necessary to demonstrate that the same failure diameter is obtained over a range of booster strengths.

Otherwise, what are thought to be failure diameter tests may in fact be sensitivity tests.

Results of failure diameter tests are summarized in Figs. 2, 3 and 4. Tests run to determine the correct booster size have not all been included on the graphs.

Figure 2 shows the results of failure diameter tests on 1,2-DP. The wave velocity was calculated from the total length of the heavy-walled lead block and the transit time measured electronically; it thus represents an average velocity. An increase to a high-velocity wave occurred between 1.6 and 2.0 mm. The intermediate velocities recorded at 1.6 mm indicate that this is very close to the actual failure

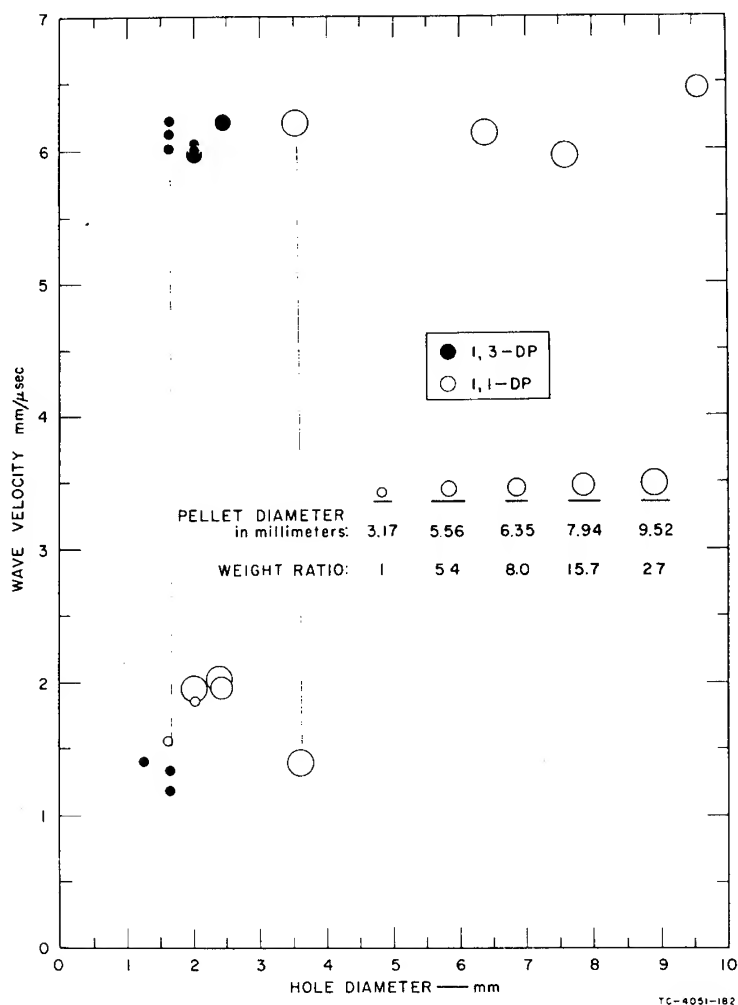


Fig. 3 - Failure diameters for 1,3-DP and 1,1-DP. The apparent slight difference between the failure diameters of 1,1-DP and 2,2-DP (Fig. 2) is consistent with the difference in structure, but may not be real.

diameter. The fact that the same failure diameter could be produced by two booster sizes indicates that the test is a true failure-diameter determination.

The results for 2,2-DP are also shown in Fig. 2. With this material many of the boosters were too small, apparently because the difference in sensitivity between 1,2-DP and 2,2-DP is emphasized at small diameter. The failure diameter at 4.0 mm was confirmed with two booster sizes. Twelve additional low-velocity results with small boosters at large diameters are not shown on the plot.

Although 1,1-DP is a relatively rare material, fifteen experiments were performed in 2-inch-diameter lead billets using RDX pellets of four different diameters. The results are shown in Fig. 3. It was necessary to use pellets 7.94×7.94 mm in diameter or greater to obtain high-velocity waves. At a hole diameter of 3.57 mm both slow and fast velocities were obtained. This suggests that the failure diameter is very close to 3.57 mm and may be different than the 4.0 mm displayed by 2,2-DP. However, with the small number of results for 1,1-DP we are probably not justified in distinguishing its failure diameter from that of 2,2-DP.

The 1,3 isomer is also a relatively scarce compound, and as a result the failure diameter was estimated with the small number of shots, also shown in Fig. 3. The failure diameter appears to be 1.6 mm as was the case for 1,2-DP.

Failure diameters were also measured for two difluoroamino butane compounds, 2,3-DB (a d,1-mixture) and IBA (the isobutylene adduct). The results for the two compounds are shown in Fig. 4. Both failure diameters are about 9.5 mm. It would require more extensive data to establish a difference between these two compounds.

The values for the failure diameters of the difluoroamino propanes are of particular significance because a very clear difference has been established between 1,2-DP and 2,2-DP. On the other hand, the physical properties of these two materials are very similar and calculations using a  $C_V(T)$  equation of state show almost identical shock temperatures (9). In other words, the difference in failure diameters is to be looked for in the reaction mechanism rather than the temperature effect on the rate constant.

Failure in IBA at about 1 cm diameter can be photographed with the smear camera; the geometry is sufficiently large to gather light

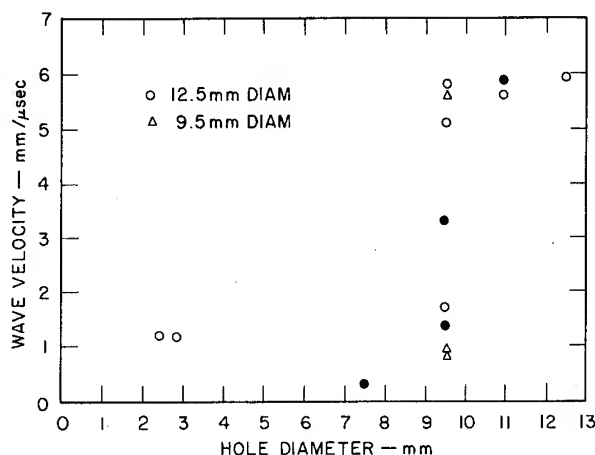


Fig. 4 - Failure diameters for IBA and 2,3-DB. The small number of tests on 2,3-DB in the failure region prevent us from distinguishing the failure diameters of the two compounds.

from within the tube, although vignetting is pronounced and the depth of field is small. It is significant that all the failures observed optically have been in the dark-wave mode even when all precautions were taken to avoid all extraneous conditions known to cause dark waves.

## REACTION TIMES

Because of the difficulty of calculating shock conditions in liquids and the added difficulty of using ordinary chemical reaction parameters at these conditions even if correctly calculated, we have measured the time to completion of reaction in shocked difluoroamino liquids.

The container, incorporating a jacket for temperature control, is shown in Fig. 5. The shock entered the liquid through the bottom of the box through a PBX 9404 pellet 2 inches long and 2 inches in diameter initiated centrally at one end (10). The density of this pellet was 1.82 g/cm<sup>3</sup>. To avoid wall reactions, the inside diameter of the box was 2-1/4 inches. Variation of peak pressure was provided by changing the thickness of an attenuator of CR-39 (11). The peak pressure generated by this system was determined by careful measurement of the transit times through various thicknesses of CR-39 together with a determination of the free surface velocity or, alternatively, by means of a manganin-wire or quartz pressure gauge. The system has the inherent difficulty that the

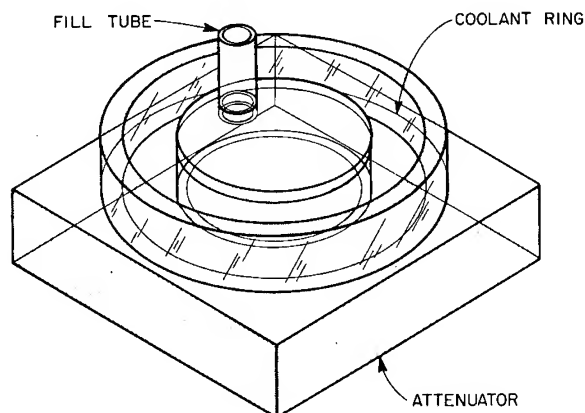


Fig. 5 - Container for determining shock reaction time. A rotating mirror camera viewed the charge end-on through the top. The reaction time was measured as the time from the entrance of the shock into the liquid to the first appearance of light. The peak pressures in the plastic were determined by both optical and gauge measurements.

two liquids of different acoustic impedances can never experience exactly the same pulse with this system. Nevertheless, for appreciable attenuator thicknesses it is useful to compare effects at the same pressure.

The reaction times for several difluoro-amino liquids have been reported in a paper preprinted for this symposium (7). Curves drawn to represent some of those data are shown in Fig. 6. The times are measured from the time of entrance of the shock into the liquid to the appearance of the detonation light at the attenuator-liquid interface. The overtake time—the time required for the overdriven wave to overtake the original shock—is a check that the initiation is proceeding according to the mechanism discovered by Campbell et al. (12). Variations in overtake time mean initiation is taking place at various positions in the shocked liquid, and are an indication that the reaction time under these particular conditions is not valid as a measurement.

In Fig. 6 it is clear that the reaction time for 2,2-DP is longer at a given pressure than the reaction time of 1,2-DP or, more directly, that a higher pressure is required to produce a given reaction time in 2,2-DP than in 1,2-DP.

shape of the pressure pulse is to some degree different at each attenuator thickness. Thus,

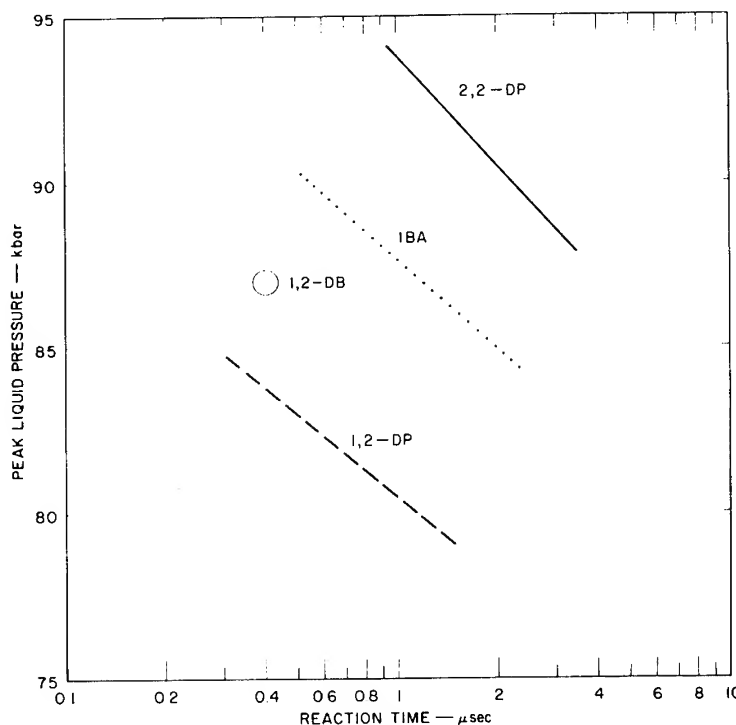


Fig. 6 - Shock reaction times. Curves represent data from Ref. 7 for 1,2-DP, 2,2-DP and IBA. A single result is shown for 1,2-DB.

Because of the magnitude of the difference, this qualitative fact is quite clear in spite of any qualifications we might wish to make because of the difference in divergence at the different attenuator thicknesses or because of the difference in shock conditions deriving from differences in physical properties of the isomers.

The data for IBA are clearly differentiated from both of the propane isomers although they more closely resemble the data for the vicinal compound. IBA is not an exact homolog but contains an active group that is identical in its position to one of the groups in 1,2-DP. This approximate resemblance and the similarity of reaction times stands in contrast to the great difference between the failure diameters of IBA and 1,2-DP.

Also included in Fig. 6 is one point for 1,2-DB, the exact homolog of 1,2-DP. This point indicates that the reaction times for the two compounds are indistinguishable. The failure diameter of 1,2-DB has not been determined, but from the failure-diameter experiments on IBA and 2,3-DB it would be expected to be close to 9.5 mm. Other reaction times of 1,2-DB (at a preshock temperature of 40°C) are given elsewhere (7), and these also indicate close similarity to 1,2-DP.

## KINETICS

On the basis of electronic structure the strength of the C-N bonds in 2,2-DP might well be expected to be weaker than those in 1,2-DP; in either case the C-N bond will be weaker than any other in the molecule. In fact, a pyrolysis experiment (13) at very low pressures, in which the decomposition occurred away from the influence of other molecules, showed the expected difference in strength. Thus, one would expect that 2,2-DP would be more sensitive than 1,2-DP—in our terms, that a lower pressure would be required to cause reaction time of a certain duration. This is the reverse of the actual situation in the liquid state in a shock; 1,2-DP reacts at a lower pressure than 2,2-DP.

A major part of the difficulty is thought to arise because we are dealing with the liquid state and even more so because the liquids are compressed beyond normal densities. Not only are reaction rates affected; entirely new reaction paths may become possible.

Rates for elimination of HF from difluoroamino compounds have been run in aqueous solution by Brauman and Hill (14) who find that HF will not split out of geminate difluoroamino

alkanes in basic solution whereas it splits out easily whenever the difluoroamino group and a hydrogen atom reside on the same carbon atom. While one cannot maintain that the experiments in aqueous solution at room temperature are pertinent to compressed pure liquid in the neighborhood of 1000°C, nevertheless it is regarded as plausible that the close proximity of polar molecules will facilitate dehydrofluorination. The existence of this reaction at carbon atoms holding hydrogen and an active group may explain the greater reactivity of the non-geminate compounds.

## WAVE STRUCTURE

Rotating mirror photographs were taken of detonation waves in IBA and 2,3-DB near failure diameter. In all cases in which failure occurred it was seen to occur in the dark-wave mode. Similar optical tests were quite difficult to make on the difluoroamino propanes because of the small size of the explosive column in the lead failure block. One method of testing the mode of failure in the difluoroamino propanes is by the brass pressure-writing technique using a wedge-shaped charge (15). The charge assembly is shown in Fig. 7. The experiment was pseudo two-dimensional—initiated with sheet explosive along the thick end of the wedge. For this length wedge, the width was not enough to make the effect truly two-dimensional, and the joints between face plates and side plates may have been the source of dark waves. However, failure occurred at an explosive thickness about twice the failure diameter in a cylindrical charge, as is to be expected from a comparison of the expressions for the divergence in three- and two-dimensions.

A wedge plate from a test with 1,2-DP is shown in Fig. 8. The general nature of the failure in the dark-wave mode can be seen. Thus, while we are not in a position to prove that other modes of failure are impossible, we have only been able to develop evidence for dark-wave failures. Tests in cylindrical geometry have recently supported this conclusion.

There are also other interesting points concerning the impressions left by the pressure in the detonation wave. The final broad dark waves that cause the failure develop from very finely structured lines that originate far up the charge. These fine lines are probably similar to the fine dark lines seen in mixtures of acetone and nitromethane. They develop into dark waves where the pressure is evidently low—at least, low relative to the regions of

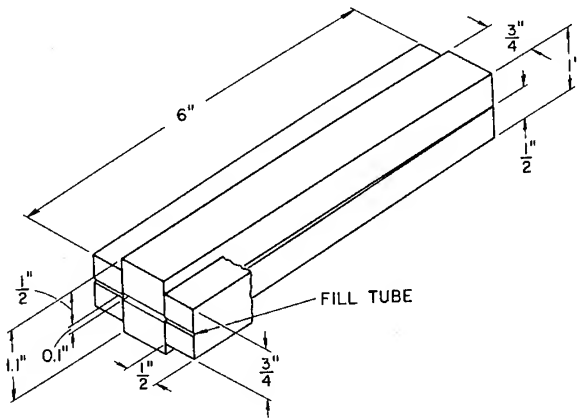


Fig. 7 - Wedge container. The wedge-shaped central cavity contained the liquid against polished brass faces so that pressure indentations were recorded at the failure thickness.

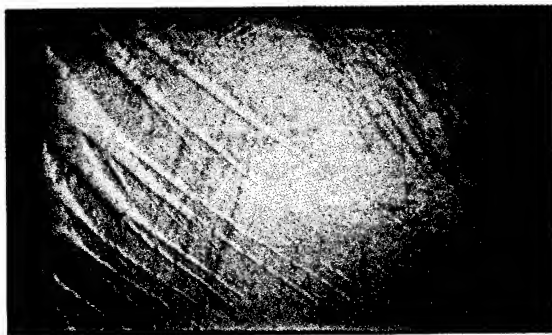


Fig. 8 - Dark-wave failure of 1,2-DP. The inside surface of a brass face plate recovered after a shot.

detonation around it. Thus these dark lines are not the primary transverse waves postulated by Dremine (6) to account for the reactivity in the detonation wave. Instead they are regions where transverse waves are absent and reinitiation occurs almost immediately.

The sharpness of the boundary at both edges of the dark waves almost certainly means that a similarly sharp discontinuity in pressure existed at this point on the brass surface at some instant during the time while the impression was being made. In terms of the advancing detonation front this means that the pressure suddenly fell to the pressure within the non-reactive shock wave. On reinitiation, the pressure suddenly rose again when the

overdriven detonation broke through the front of the low-velocity wave.

The failure theory built on the NZD theory (16,17) relies on calculation of the reaction time and its relationship to the shock-wave speed in unreacted explosive. Another relationship between reaction time and the velocity is given by diameter-effect theories. The smallest diameter at which both these relationships hold is the failure diameter. We thus implicitly rely on wave curvature to produce failures.

In Dremine's proposal for a failure theory (6), the reaction in a detonation wave occurs in the interactions between transverse waves. Failure is evidenced by cessation of chemical reaction because of the disappearance of transverse interactions. Failure diameter is determined not by the relationship between reaction and velocity in the detonation but by whether reinitiation can occur in the dark wave through smooth shock mechanism (which is much slower for a given average wave pressure than in the transverse interactions).

In Fig. 9 is an x-t plot of a dark wave at the edge of a charge of liquid explosive. The dark wave passes the point F and reaction in the wave ceases. The brass inscription tells us that the pressure is lowered suddenly, and,

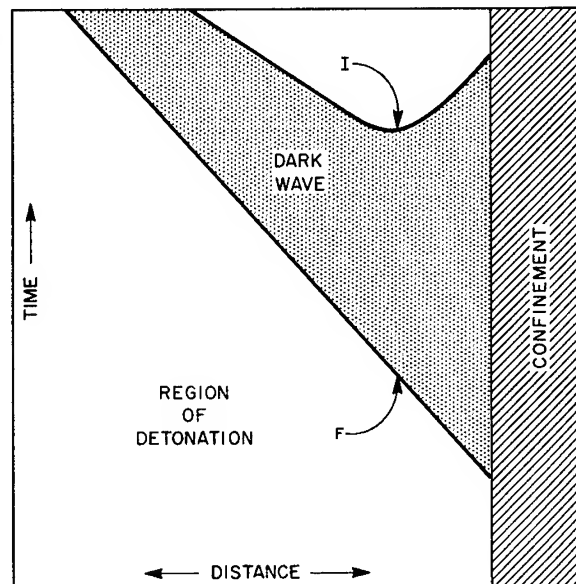


Fig. 9 - Reinitiation in a dark wave. A time-distance plot such as might be obtained in an end-on rotating-mirror photograph of a dark wave at the edge of a charge.



since the wave is now traveling in unreacted material, the velocity must drop noticeably. In order to satisfy the conservation equations another wave, of which no evidence is seen, must interact at point F. For similar reasons a reinitiation wave is called for in the reinitiation process that culminates in the overdrive at the point I.

The dark-wave reinitiation process resembles closely the initiation taking place in our reaction time test, but the divergence of flow in dark waves at failure diameters of the size we have investigated is greater than in the two-inch diameter reaction time test. Nevertheless, the reaction times are good indicators of the difficulty of reinitiation and for the difluoroamino propanes predict the failure diameters directly.

The failure diameters of the difluoroamino butanes are affected by several factors that need not be taken into account in a comparison among the propanes. Calculations with a  $C_v(T)$  equation of state have shown that the temperature in a given strength shock is very much the same in the butanes as for the propanes. The effect of the greater heat capacity is about balanced by the greater compressibility. The bigger failure diameter for the butanes, then, is accounted for by the lower pressure in the detonation wave and presumably also in the dark wave.

## CONCLUSION

The failure diameter of 2,2-DP has been found to be 2.5 times greater than that of 1,2-DP; that of IBA is still 2.5 times greater. Shock reaction times for these compounds are 2,2-DP > IBA > 1,2-DP and these very simply explain the failure diameters on the basis of Dremin's theory of failure diameter. It is apparently necessary to abandon the idea that the effect of diameter on detonation velocity enters into determining failure diameter.

## REFERENCES

1. J. von Neumann, Office of Scientific Research and Development Report 549 (1942).
2. Ya. B., Zel'dovich, *Zh. Eksp. Teor. Fiz.* **10**, 542 (1940).
3. W. Doering, *Ann. Phys.*, **43** (1943).
4. A. W. Campbell, M. Malin, and T. E. Holland, "Detonation in Homogeneous Explosives," 2nd ONR Symp. Detn. (U.S.: Dept. Navy, Washington, 1955).
5. E. A. Igel and L. B. Seely, 2nd ONR Symp. Detn. (U.S.: Dept. Navy, Washington, 1955).
6. A. N. Dremin, O. K. Rozanov, and V. S. Trofinov, *Combust. Flame*, **7**, 2 (1963).
7. J. G. Berke, L. B. Seely, R. Shaw, and D. Tegg, "Shock Initiation of Nitromethane, Methyl Nitrite and some Alkyl Bis Difluoroamines." This symposium, preprinted paper.
8. Tedlar is fluorinated polymer in sheet form manufactured by E. I. DuPont de Nemours and Co.
9. M. Cowperthwaite and R. E. Shaw, *J. Chem. Phys.*, **53**, to be published (1970).
10. PBX 9404 is a plastic-bonded explosive consisting of approximately 94% cyclotrimethylenetrinitramine, 3% tris ( $\beta$  chlor-ethyl) phosphate, and 3% nitrocotton.
11. CR-39 is a polymer of diethylene-glycolbisallyl carbonate obtainable from Homalite Corporation, Wilmington, Delaware.
12. A. W. Campbell, W. C. Davis, and J. R. Travis, *Phys. Fluids*, **7**, 498 (1961).
13. S. W. Benson and G. N. Spokes, *JACS* **89**, 252 (1967).
14. S. K. Brauman and M. E. Hill, *J.O.C.* **34**, 3381 (1969).
15. This technique was used at Los Alamos Scientific Laboratory by A. W. Campbell and Murray Malin about 1955 for recording failures in nitromethane.
16. H. Eyring, R. E. Powell, G. H. Duffey, and R. B. Parlin, *Chem. Revs.*, **45**, 69 (1949).
17. Marjorie W. Evans, *J. C. Phys.*, **36**, 193 (1962).

# THE FAILURE DIAMETER THEORY OF DREMIN

Julius W. Enig and Francis J. Petrone  
*U. S. Naval Ordnance Laboratory  
Silver Spring, Maryland 20910*

## ABSTRACT

Dremin's failure diameter theory has been used to calculate values of the "failure diameter,"  $d_f$ , as a function of initial temperature  $T_0$  for nitromethane. The latter, a very sensitive test of the theory, leads to predicted values of  $d_f$  in good agreement with the experimental values. It is shown that an important approximation in the theory can be removed, and that the experimental thermal explosion times used by Dremin and Trofimov as input for their calculations can be theoretically derived, a necessary condition for the practical application of the theory.

## INTRODUCTION

For every explosive, in any given state, there exists a critical diameter, called the "failure diameter,"  $d_f$ , below which propagation of a steady-state detonation in a cylindrical charge does not occur. Moreover,  $d_f$  depends on the confinement of the explosive by the surrounding walls.

Recently, Dremin (1) introduced a new theory of the failure diameter that was subsequently extended by Dremin and Trofimov (2,3); their application of this theory to unconfined nitromethane and liquid TNT, each at a single initial temperature, led to values (2,3) of  $d_f$  in good agreement with the experimental values.

The purpose of this paper is to remove an important approximation in their calculation, to show that the thermal explosion times used as input for their calculations can be theoretically derived, a necessary condition for the practical application of the theory, and to calculate for the first time values of  $d_f$  as a function of initial temperature  $T_0$  for nitromethane. The latter, a very sensitive test of the theory, leads to predicted values of  $d_f$  in good agreement with the experimental values. For completeness, a description of the theory that includes the pertinent theoretical flow analysis left out of the extremely condensed original article (2) is included.

## DETAILED THEORETICAL ANALYSIS

Their theory can be formulated in the following manner. Consider the passage of a detonation front with velocity  $D_0$  from a heavy-walled tube of inner diameter  $d < d_f$  (of the unconfined material) containing explosive into a region of explosive of diameter much larger than  $d_f$ . Starting at the edge of the tube, a wavefront on which reaction is quenched moves into the reaction zone with velocity  $v$  perpendicular to the direction of detonation propagation. One explanation of the nature of this wave is described elsewhere (1). Consider a coordinate system that moves along the locus  $OA$  of the intersection of this wavefront with the detonation front as shown in Fig. 1. Under the assumptions that the detonation reaction zone thickness is negligible and that the region behind the detonation front is a constant state, namely, the Chapman-Jouguet state, state (1), the flow is seen to contain, in addition, a centered rarefaction fan, region (R), an oblique shock front  $AB'$ , and a slip line  $AB$  separating two constant supersonic states, regions (2) and (3), of equal pressure which are terminated by the sonic signal  $BB'$  originating at the tube edge  $O$ . Regions (1), (R), and (2) consist of gas products; region (3) contains unreacted shocked explosive.

Let  $p$ ,  $\rho$ ,  $c$ ,  $u$ , and  $M = u/c$  be, respectively, the pressure, density, sound speed,

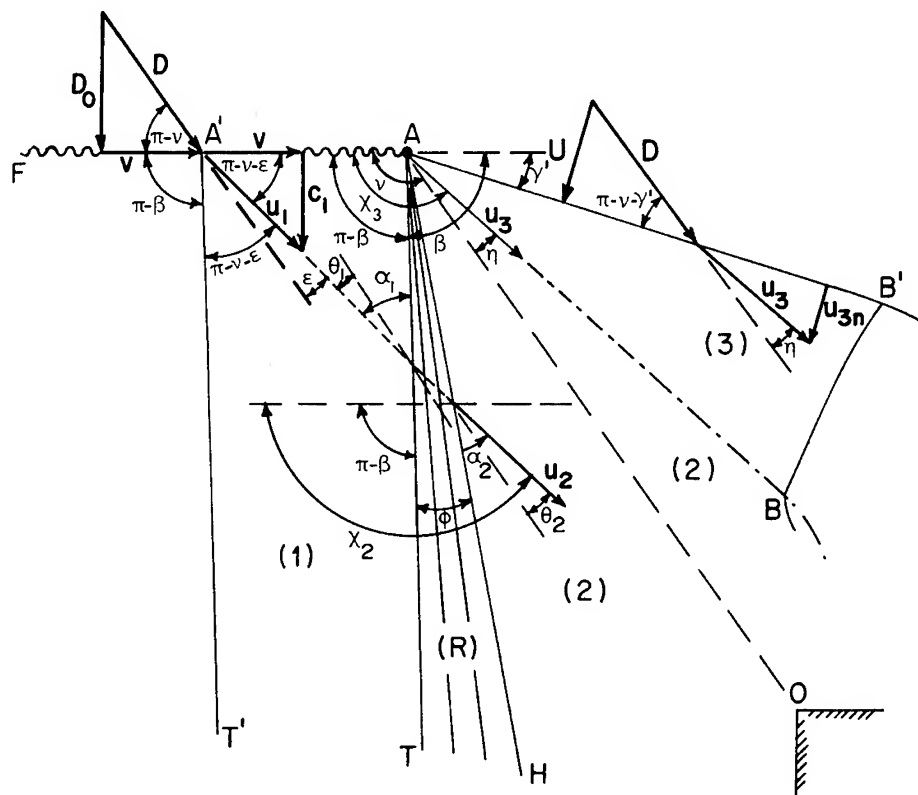


Fig. 1 - Flow field resulting from the passage of a detonation front from a tube into a much larger volume of explosive as seen in a coordinate system moving with the locus OA

particle velocity, and Mach number. In this coordinate system, the unreacted explosive in the initial state (0) crosses the detonation front FA with velocity

$$D = (D_0^2 + v^2)^{1/2}.$$

The products in region (1) travel with velocity

$$u_1 = (c_1^2 + v^2)^{1/2},$$

cross the centered rarefaction fan TAH into region (2), and then move with velocity  $u_2$  parallel to AB. The explosive that enters AB' with velocity D subsequently moves with velocity  $u_3$  parallel to AB.

For  $\gamma$ -law products, the Chapman-Jouguet condition yields

$$p_1 = \rho_0 D_0^2 / (\gamma + 1),$$

$$\rho_1 = (\gamma + 1) \rho_0 / \gamma,$$

and

$$c_1 = \gamma D_0 / (\gamma + 1).$$

From

$$v = \pi - \tan^{-1}(D_0/v)$$

and

$$c_1 = v \tan(\pi - v - \epsilon),$$

where  $\pi = 180^\circ$ , it follows that

$$\epsilon = \pi - v - \tan^{-1}[(\rho_0/\rho_1) \tan(\pi - v)]$$

is the deflection of the streamline on crossing the detonation front. Thus, state (1) is completely determined.

From the theory of two-dimensional steady-state potential flow (4), the angle  $\theta$  between the streamline and a line parallel to AO, the Mach angle  $\alpha$  between the streamline and the characteristic, and the particle velocity  $u$  in the Prandtl-Meyer expansion region (R) are related by the equations  $dp = -\rho u du$ ,  $\sin \alpha = c/u$ ,  $du = u \tan \alpha d\theta$ , and  $c^2 = dp/d\rho$ , which when

combined with  $M = u/c$  and the isentropic relation,  $p/p_1 = (\rho/\rho_1)^\gamma$ , yield

$$dM/d\theta = M \left[ 1 + \frac{1}{2} (\gamma - 1) M^2 \right] / (M^2 - 1)^{1/2}.$$

Integration between the limits  $\theta = \theta_1 = \epsilon$ ,  $M = M_1$  and  $\theta = \theta_2$ ,  $M = M_2$ , leads to

$$\theta_2 - \epsilon = F(M_2) - F(M_1) \quad (1)$$

connecting the head AH and the tail AT of the expansion fan, where

$$F(M) = \left( \frac{\gamma + 1}{\gamma - 1} \right)^{1/2} \tan^{-1} \left[ \frac{\gamma - 1}{\gamma + 1} (M^2 - 1) \right]^{1/2} - \cos^{-1} \frac{1}{M}. \quad (2)$$

Combination of the Bernoulli equation,

$$2\gamma p_2 + (\gamma - 1)\rho_2 u_2^2 = 2\gamma p_1 + (\gamma - 1)\rho_1 u_1^2,$$

with

$$(p_2/p_1) = (\rho_2/\rho_1)^\gamma,$$

$$M_2 = u_2/c_2,$$

and

$$c_2^2 = \gamma p_2/\rho_2,$$

yields

$$(p_2/p_1)^{(\gamma-1)/\gamma} = [(\gamma-1)M_1^2 + 2]/[(\gamma-1)M_2^2 + 2]. \quad (3)$$

Thus, Eqs. (1) and (3) relate  $\theta_2$  to  $p_2$ . Since

$$\alpha_1 = \sin^{-1}(1/M_1) = \pi - \nu - \epsilon,$$

and the characteristic A'T' must be parallel to AT, it follows that  $\beta = 2(\pi - \nu - \epsilon)$ . Thus,

$$\chi_2 = \pi - \beta + \alpha_1 + \theta_2 - \theta_1,$$

the obtuse angle between  $u_2$  and the detonation front, is an explicit function of  $p_2$  by Eqs. (1) and (3). The angle between the head and tail of the fan is  $\phi = \alpha_1 - \alpha_2 + \theta_2 - \theta_1$ . The above result,  $\chi_2(p_2)$ , reduces to Eq. (7) of Ref. 2 after some algebraic manipulation.

Let  $U = c'_0 + au$  be the shock velocity in a stationary explosive, where  $c'_0$  and  $a$  are constants. Then, by the Rankine-Hugoniot relations,

$$U = \frac{1}{2} c'_0 \left[ 1 + (1 + 4ap_3/\rho_0 c'^2_0)^{1/2} \right] \quad (4)$$

is the particle velocity into AB',

$$1/\rho_3 = 1/\rho_0 - p_3/\rho_0^2 U^2, \quad (5)$$

and

$$u_{3n} = \rho_0 U/\rho_3; \quad (6)$$

the continuity of tangential velocity yields

$$\eta = \pi - \nu - \gamma' - \tan^{-1} [(u_{3n}/U) \tan(\pi - \nu - \gamma')],$$

where

$$\gamma' = \frac{1}{2} \pi - \nu + \cos^{-1}(U/D).$$

Hence,  $\chi_3 = \nu + \eta$ , the obtuse angle between  $u_3$  and the detonation front, is an explicit function of  $p_3$ . Finally,

$$u_3^2 = u_{3n}^2 + D^2 - U^2$$

may be rewritten as

$$u_3 = \left[ D^2 + \frac{c'^2_0}{2a^2} - \frac{c'^2_0}{2a^2} \left( 1 + \frac{4ap_3}{\rho_0 c'^2_0} \right)^{1/2} - \left( 2 - \frac{1}{a} \right) \frac{p_3}{p_0} \right]^{1/2}, \quad (7)$$

the result of Dremin and Trofimov (2) by using Eqs. (4) - (6).

The intersection of the shock polars,  $\chi_2(p_2)$  and  $\chi_3(p_3)$ , in the streamline deflection-pressure plane yields the derived pressure,  $p_2 = p_3$ , and from that, states (2) and (3). Note that  $\eta = \theta_2$ .

An observer at the end of the tube at O sees the point A receding at velocity D and the head of the rarefaction wave BB', originating at O, also receding from O. Along AB, the distance between BB' and A increases with time.

To an observer traveling with A (as in Fig. 1), BB' is receding from A, along AB, with the smaller of the velocities,  $u_3 - c_3$  or  $u_2 - c_2$ . For nitromethane and liquid TNT, the equation of state of Enig and Petrone (5) gives  $c_3$ ; this leads to  $0 < u_3 - c_3 < u_2 - c_2$ . In the absence of an equation of state for unreacted explosive, Dremin and Trofimov (2) assumed that  $u_2 - c_2 < u_3 - c_3$ .

Consider an element of explosive entering region (3). Due to adiabatic heating it will explode after an induction time  $\tau_3$  which depends on  $p_3$  and the temperature  $T_3$ . At time  $t_1$  ( $>\tau_3$ ) after passage of the detonation front from the confined tube at O, thermal explosion will occur at B, a distance

$$u_3 \tau_3 = (u_3 - c_3) t_1 \quad (8)$$

from A. The detonation, initiated at B and traveling in all directions, will reach A in the time

$$t_2 = u_3 \tau_3 / (D_3 - u_3), \quad (9)$$

where  $D_3$  is the detonation velocity in region (3). "Failure" occurs when

$$d = 2v(t_1 + t_2), \quad (10)$$

i.e., when the detonation at B reaches A just as A reaches the axis of the explosive. By Eqs. (8) - (10), the failure diameter is (2,3)

$$d_f = 2u_3 v \tau_3 \left( \frac{1}{D_3 - u_3} + \frac{1}{u_3 - c_3} \right). \quad (11)$$

This failure diameter coincides with the failure diameter for an unconfined cylindrical charge, the failure mechanism being the same (1).

## CALCULATED RESULTS

The value of  $\tau_3$ , directly measured by Dremin and Trofimov (2,3), can be calculated theoretically from

$$\tau_3 \approx K T_3^2 \exp(E^\ddagger / RT_3), \quad (12)$$

where  $K$  is a constant depending on the explosive,  $R$  and  $E^\ddagger$  are the gas constant and activation energy, respectively, and  $T_3$  is calculated as described elsewhere (5). Although  $v$  must still be determined experimentally, it is independent of any failure diameter experiment.

The input parameters  $\rho_0$ ,  $D_0$ , and  $p_1$  (used to compute  $\gamma$ ) are functions of  $T_0$  (6) (as are  $c_{p,0}$  (7) and  $\alpha_0$  (8) which are needed to calculate  $T_3$ ). In the absence of more accurate data, it is assumed that  $v$ ,  $a$ ,  $c_0'$ ,  $E^\ddagger$ , and  $K$  are constants, and  $D_3$  is linear in  $\rho_3$ , for a given explosive (9). Also, constant  $\gamma$  in the range  $p_2 \leq p \leq p_1$  is an excellent approximation for fixed  $T_0$  (10).

The calculated values of  $d_f$  (using Eq. (11)) as a function of  $T_0$  for nitromethane are shown in Table 1. These are seen to be in good agreement with the experimental values  $d_f^{(expt)}$  (for glass confinement) of Campbell, Malin, and Holland (11) and, in fact, above  $T_0 = 273^\circ\text{K}$ , the results fall within the experimental error,  $\pm 2-3$  mm, of the latter.

The results of a sample calculation for nitromethane (drawn to scale in Fig. 1) are as follows:  $T_0 = 293.16$ ,  $T_3 = 1123.7^\circ\text{K}$ ;  $\rho_0 = 1.1370$ ,  $\rho_1 = 1.5896$ ,  $\rho_2 = 1.4327$ ,  $\rho_3 = 1.8840$  g/cm<sup>3</sup>;  $c_1 = 4.5139$ ,  $c_2 = 4.1727$ ,  $c_3 = 5.5745$ ,  $D = 7.8985$ ,  $D_0 = 6.3106$ ,  $D_3 = 8.6370$ ,  $U = 4.6930$ ,  $u_1 = 6.5527$ ,  $u_2 = 6.8453$ ,  $u_3 = 6.9558$ ,  $v = 4.75$  mm/ $\mu\text{sec}$ ;  $p_0 = 0$ ,  $p_1 = 128.91$ ,  $p_2 = p_3 = 99.29$  kbar;  $\tau_3 = 0.2080$ ,  $t_1 = 1.0474$ ,  $t_2 = 0.8606$   $\mu\text{sec}$ ;  $\alpha_1 = 43.54^\circ$ ,  $\alpha_2 = 37.56^\circ$ ,  $\beta = 87.08^\circ$ ,  $\gamma' = 16.58^\circ$ ,  $\epsilon = \theta_1 = 9.49^\circ$ ,  $\eta = \theta_2 = 12.43^\circ$ ,  $\nu = 126.97^\circ$ ,  $\phi = 8.92^\circ$ ,  $\chi_2 = \chi_3 = 139.39^\circ$ ;  $d_f = 18.13$  mm. With this value of  $c_3$ , had Eq. (11) been used, the calculated value of  $d_f$  by Dremin and Trofimov (2,3) would have been  $\approx 19.5$  mm instead of their 14.3 mm.

For liquid TNT initially at  $356^\circ\text{K}$ , the experimental value is  $\approx 68$  mm (2,3); the calculated  $d_f$  is 94.71 mm, where  $D_3$ ,  $u_3$ ,  $c_3$ ,  $u_2$ , and  $c_2$  are, respectively, 9.3140, 6.2134, 5.4555, 6.1117, and 4.2281 mm/ $\mu\text{sec}$ . With this value of  $c_3$ , had Eq. (11) been used, the calculated value of  $d_f$  in Refs. 2 and 3 would have been  $\approx 119$  mm instead of their 62 mm.

While the above analysis is based on steady-state oblique shock theory, an alternative method was considered by Mader (12) who calculated the failure of a nitromethane

TABLE 1  
Comparison of the Calculated Failure Diameters  $d_f$  with the Experimental Values (11)  $d_f^{(expt)}$  at Different Initial Temperatures  $T_0$  for Nitromethane

$T_0$ ( $^\circ\text{K}$ )	253.16	263.16	273.16	283.16	293.16	303.16	313.16
$p_3$ (kbar)	107.28	105.33	103.34	101.33	99.29	97.22	95.13
$T_3$ ( $^\circ\text{K}$ )	1079.0	1090.9	1102.3	1113.2	1123.7	1138.3	1154.1
$d_f$ (mm)	42.91	33.84	27.09	22.00	18.13	14.05	10.83
$d_f^{(expt)}$ (mm)	34.8	29.0	24.5	20.9	18.0	15.7	13.3

detonation resulting from a side rarefaction cooling the explosive inside its reaction zone with the aid of an unsteady two-dimensional Eulerian hydrodynamic code. This was an attempt to simulate the experimental work of Davis (13), who studied the failure of a supported nitromethane detonation wave traveling up a rectangular copper tube and then into a large container of nitromethane. Because of the extremely small calculated reaction zone thickness,  $0.24 \mu$ , the dimensions in Mader's calculations are out of scale by about three orders of magnitude. However, his "early time" calculations show qualitatively the flow configurations to be expected as the rarefaction wave comes in from the side. Using the  $3000^\circ\text{K}$  isotherm throughout the reaction zone, he obtains a rarefaction velocity of  $4.0 \pm 0.5 \text{ mm}/\mu\text{sec}$  which is compared with Davis' experimental "failure" waves that run across the front at about  $3.72 \text{ mm}/\mu\text{sec}$ . Since the calculations were not carried out to the point where re-ignition occurs, the critical failure diameter was not calculated, and, hence, it is not clear whether the rarefaction wave moving into a homogeneous reaction zone really represents the failure mechanism. On the contrary, Dremin believes that the reaction of a liquid explosive will be initiated first at sites where oblique waves collide, and that the "failure" wave is a function of these sites.

#### SENSITIVITY OF THE CALCULATED RESULTS

It should be noted that Dremin and Trofimov found  $v = 4.75 \text{ mm}/\mu\text{sec}$  and Davis found  $v = 3.72 \text{ mm}/\mu\text{sec}$ . Inasmuch as the former were working with axisymmetric and the latter with plane symmetric detonations, it would be expected that the value of  $v$  for the former case would be larger due to convergence. In order to check the effect of variation of the parameter  $v$ , the calculation in Table 1 for  $T_0 = 293.16^\circ\text{K}$  was repeated with different  $v$ . For  $v = 3.72, 4.275, 4.75, 5.225$ , and  $5.78 \text{ mm}/\mu\text{sec}$ , the resulting values of  $d_f$  are, respectively, 35.3, 23.0, 18.13, 16.09, and 16.5 mm.

By Eqs. (11) and (12), it is seen that  $d_f$  is most sensitive to errors in  $T_3$  and  $E^\ddagger$ . In particular, the relative error is given by

$$\frac{\Delta d_f}{d_f} = \frac{E^\ddagger}{RT_3} \frac{\Delta E^\ddagger}{E^\ddagger} \approx - \frac{E^\ddagger}{RT_3} \frac{\Delta T_3}{T_3},$$

where  $\Delta d_f$  is the error in  $d_f$ , etc., and  $E^\ddagger/RT_3 \approx 24$ . Thus, it is critical that values of  $E^\ddagger$  and the temperature equation of state be

known quite accurately. Arrhenius kinetic parameters such as  $E^\ddagger$  and the frequency factor (incorporated in  $K$ ) have not been measured at the elevated temperatures and pressures encountered here and it is doubtful that they will for some time to come. Hence, the present low-pressure low-temperature value of  $E^\ddagger = 53.6 \text{ kcal/mole}$  is the best that is available. As for the temperature calculations, an alternative method involves use of the Walsh and Christian method with the assumption that the specific heat at constant volume,  $c_v$ , is a constant (14). Here the shock temperature,  $T_3 \approx 1295^\circ\text{K}$ , leads to a value of  $d_f \approx 1.014 \text{ mm}$  which is much smaller than the experimental  $18.0 \text{ mm}$  (for  $T_0 = 293^\circ\text{K}$ ). If the equation of state of Cowperthwaite and Shaw (14) with variable  $c_v(T)$  is used, then  $T_3 \approx 966^\circ\text{K}$  and  $d_f \approx 681 \text{ mm}$ , a value much too large.

#### REFERENCES

1. A. N. Dremin, Dokl. Akad. Nauk SSSR 147, No. 4, 870 (1962) [English transl.: Doklady Physical Chemistry 147, 845 (1962)].
2. A. N. Dremin and V. S. Trofimov, Zhur. Prikl. Mek. i Tekh. Fiz., No. 1, 126 (1964) [English transl.: Clearinghouse for Federal Scientific and Technical Information, U.S. Dept. of Commerce, Report No. AD615211, pp. 205-216 (March 1965)]. Eq. (7) is misprinted and should read  $\text{tg } \frac{1}{2} \beta = n \{p_1/[\rho_0(n+1)]\}^{1/2}/v$  in both.
3. A. N. Dremin and V. S. Trofimov, Tenth Symposium (International on Combustion) (The Combustion Institute, Pittsburgh, Pennsylvania, 1965), p. 839. More details given in Ref. 2.
4. A. Ferri, Elements of Aerodynamics of Supersonic Flows (Macmillan Company, New York, 1949); see Chapter 2.
5. J. W. Enig and F. J. Petrone, Phys. Fluids 9, No. 2, 398 (1966).
6. For nitromethane: (a)  $\rho_0 = 1.1615 - 0.0011952 (T_0 - 273.16) - 1.553 \times 10^{-6} (T_0 - 273.16)^2 \text{ g/cm}^3$  for  $296 \leq T_0 \leq 473^\circ\text{K}$  is given by H. A. Berman and E. D. West, J. Chem. Eng. Data 12, 197 (1967), and the extrapolation,  $\rho_0 = 1.13065 - 0.0012728 (T_0 - 298.16) \text{ g/cm}^3$ , was used for  $T_0 < 298.16^\circ\text{K}$ ; (b)  $D_0 = 6.374 - 0.003964x (T_0 - 277.16) \text{ mm}/\mu\text{sec}$  (see W. C. Davis, B. G. Craig, and J. B. Ramsay, Phys. Fluids 8, 2169 (1965)); (c)  $p_1 = 128 + (T_0 - 296.16) \times dp_1/dT_0 \text{ kbar}$ , where

- $p_1 = 128$  kbar is the experimental value at  $T_0 = 296.16^\circ\text{K}$  (see F. J. Petrone, *Phys. Fluids* **11**, 1473 (1968), and  $dp_1/dT_0 = 0.30476$  kbar/ $^\circ\text{K}$ ,  $253 \leq T_0 \leq 313^\circ\text{K}$ , was determined by H. Hurwitz (private communication) from RUBY thermochemical calculations. For liquid TNT: (d)  $\rho_0 = 1.54463 - 0.0010156 (T - 273.16)$  g/cm<sup>3</sup> (see H. H. Cady and W. H. Rogers, Los Alamos Scientific Laboratory Report No. LA-2696 (July 1962)); (e)  $D_0 = 6.590 - 0.0035x (T_0 - 366.16)$  mm/ $\mu\text{sec}$  (see Ref. 6(b)); (f)  $p_1 \propto \rho_0^2$  (see C. H. Johansson and P. A. Persson, *Nature* **212**, 1230 (1966) and M. J. Kamlet and S. J. Jacobs, *J. Chem. Phys.* **48**, 23 (1968)), where  $p_1 = 171.8$  kbar at  $T_0 = 365.16^\circ\text{K}$  (see W. B. Garn, *J. Chem. Phys.* **32**, 653 (1960)).
7. For nitromethane,  $c_{p,0}$  is given by W. M. Jones and W. F. Giauque, *J. Am. Chem. Soc.* **69**, 983 (1947) for  $T \leq 303^\circ\text{K}$  and by H. A. Berman and E. D. West, *J. Chem. Eng. Data* **13**, 107 (1969) for  $T \geq 308^\circ\text{K}$ . For liquid TNT,  $c_{p,0} = 0.45023 - 0.00080182x (T_0 - 273.16)$  cal/g (see Ref. 6(d)).
  8.  $\alpha_0 = -(1/\rho_0) d\rho_0/dT_0$ , see Refs. 6(a) and (d).
  9. (a)  $v = 4.75$  mm/ $\mu\text{sec}$  for nitromethane (2) and  $2.76$  mm/ $\mu\text{sec}$  for liquid TNT (2). (b) The values of  $c'_0$ ,  $a$ , and  $E^\ddagger$  are given in Table I of Ref. 5. (c) For nitromethane ( $T_0 = 294^\circ\text{K}$ ) shocked to 86 kbar, the average experimental adiabatic explosion time  $\tau \approx 1.4 \mu\text{sec}$ , and calculated shock temperature,  $1034^\circ\text{K}$ , leads to  $K = 6.1977 \times 10^{-18}$  sec deg<sup>-2</sup> by Eq. (12); similarly,  $K = 1.83223 \times 10^{-13}$  for liquid TNT ( $T_0 = 358^\circ\text{K}$ ) shocked to 125 kbar and  $1166^\circ\text{K}$  with  $\tau \approx 0.7 \mu\text{sec}$ ; see A. W. Campbell, W. C. Davis, and J. R. Travis, *Phys. Fluids* **4**, 498 (1961). (d)  $D_3 = D_0 + (\rho_3 - \rho_0)(dD_0/dT_0)/(d\rho_0/dT_0)$  (for justification of this approximation, see Ref. 9(c)); see Refs. 6(a), (b), (d), and (e) for  $\rho_0(T_0)$  and  $D_0(T_0)$ .
  10. C. L. Mader, Los Alamos Scientific Laboratory Report No. LA-2900 (Feb. 1963).
  11. A. W. Campbell, M. E. Malin, and T. E. Holland, *J. Appl. Phys.* **27**, 963 (1956). More details given in *Second Office of Naval Research Symposium on Detonation* (Washington, D.C., 1955), p. 336.
  12. C. L. Mader, Los Alamos Scientific Laboratory Report No. LA-3771 (Nov. 1967).
  13. Private communication from W. C. Davis reported by C. L. Mader, Los Alamos Scientific Laboratory Report No. LA-3077 (June 1964).
  14. M. Cowperthwaite and R. Shaw, *J. Chem. Phys.* **53**, 555 (1970).

## WALL TRACES OF DETONATION IN NITROMETHANE-ACETONE MIXTURES

P. A. Urtiew and A. S. Kusubov  
*Lawrence Radiation Laboratory, University of California  
Livermore, California 94550*

### ABSTRACT

Wall traces of detonation in nitromethane-acetone mixtures are presented, and the technique of obtaining them is discussed. These records are compared to the carbon soot records of gaseous detonations, and the structure of the wave front is said to be similar in both phases of the explosive mixtures. Surface indentations found along the traces provide additional evidence that the traces were produced by localized peaks of pressure such as those associated with triple wave intersections. Complementary measurements of the wave velocity indicate that the process investigated is a full-scale detonation rather than a degenerate case of a low-velocity type.

### INTRODUCTION

Early studies of detonation in nitromethane and its mixtures with acetone, by Campbell, et al. (1) in the U.S. and Dremine and associates (2) in the U.S.S.R., have indicated that the detonation process in these explosives is nonuniform and basically unstable at the wavefront. Non-uniformities of the detonation wave are deduced from self-light streak photographs taken through slits at the side and back wall of an explosion container. The records clearly illustrate non-luminous streaks traveling from the edges toward the center of the tube. The pebbly structure of the wave in a nitromethane-acetone mixture has also been observed by Mallory (3) by an impedance mirror technique.

In a series of papers, Dremine (4) and collaborators have developed a theory that, in nitromethane-acetone mixtures, all nonuniformities of the wavefront that are seen as dark striations on the film are sites of no reaction, formed at the outside boundary of the explosive during impingement of the detonation front on the tube wall. However, the detonation products generating the shock wave into the unburned medium may cause reignition after a certain induction time that is characteristic of the

particular explosive mixture. In their theory, Dremine and associates have developed the concept of a critical diameter which sustains detonation without being extinguished by the radially convergent rarefaction waves. In trying to determine this critical diameter for other liquid explosives, Dremine (5) also has found that detonations through some of the liquids do not exhibit dark nonluminous striations and, therefore, must behave like classical one-dimensional detonations.

Using a framing camera, Mallory and Greene (6) have looked into the matter of interpreting streak records and resolving irregularities by this method. They find that the detonation process also yields large dark areas which form at the outside edge of the charge and move slowly around along the tube wall, never reaching the center of the charge. Demonstrating in a way that streak records alone are insufficient to complete the study of the detonation phenomenon, Mallory has confirmed the existence of nonuniform and irregular burning at the wavefront.

To provide a different insight into the phenomenon of detonation in liquid explosives and in particular to gain some direct analogy



between the processes taking place in liquid and gaseous mixtures, the authors (7) have developed a very simple but useful technique for recording traces of the detonation as it propagates along the walls. Independently, a similar wall-trace method has been devised by Howe (8). Wall-trace records are analogous to the carbon soot records which in the last decade have gained wide recognition in the field of gaseous explosives.

A similar technique has also been used in solid explosives (9). However, in this case, microscopic inhomogeneities of the original mixture probably contribute greatly to the observed pattern on recovered walls.

Although some of our wall-trace records of detonations in nitromethane-acetone mixtures have already been presented (7), the authors intend in this paper to show that these traces are the paths of the high-pressure points inherently associated with the wavefront. Furthermore, it is hoped that new trace records of detonations in various shapes and sizes of containers will stimulate further analytical investigations of this phenomenon similar to that being presented in a concurrent paper (10).

## EXPERIMENTAL

The experiments consisted of recovering side walls from tubes in which detonations had taken place. The best results were obtained when the detonation process was somewhat marginal; i.e., when various wave events, if any, were sufficiently far apart to allow visual interpretation of the records. A cross section of the experimental assembly is shown in Fig. 1.

All tubes were made of 1/4-in. metal plates bonded together by resin to form a square cross section of the desired dimension. Before assembly, the inner surfaces of the walls were machined flat and hydrohoned to a uniform matte surface of not more than 5-micron roughness. The bottom end of the tube was sealed by a 25-micron aluminum foil; the top was left open for filling. The tube housed a cylinder of C-4 solid explosive, which was fitted into an opening in the bottom plate so as to be in direct contact with the aluminum foil separating it from the liquid explosive.

To aid in recovery of the walls, the tube was imbedded in a layer of Wood's metal, acting as a momentum trap, protected the tube from extraneous deformation. The whole assembly was surrounded by lead bricks which acted as a barrier, preventing the separated

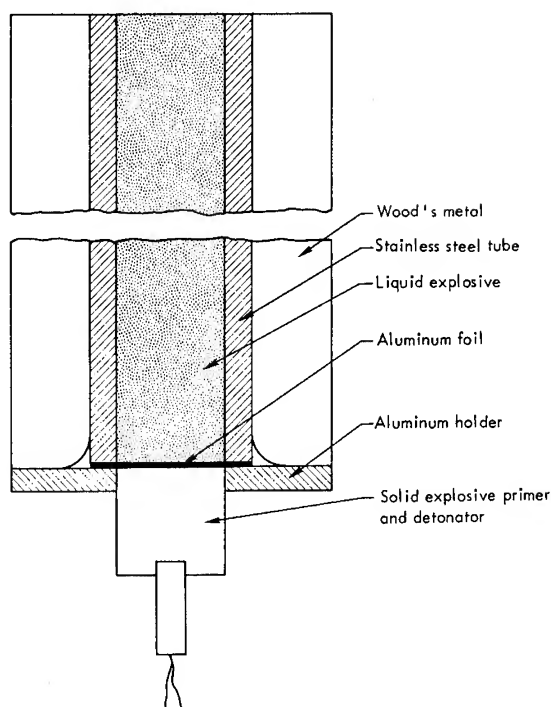


Fig. 1 - Cross section of the experimental assembly

wall plates from flying too far from the test point.

## DISCUSSION

To study the effects of various containers on the propagation of detonation in the liquid explosive, the experiments were performed in tubes of different sizes, shapes, and materials. Of the four materials tested, aluminum was the softest and underwent the most deformation, obscuring any traces that might have been produced during the process. Armco iron and stainless steel produced the most distinct white lines on the otherwise blackened background. Brass displayed a layer of carbon deposited in such a manner that the pattern was clearly visible. An important difference between the records on stainless steel and brass was that, on the former, the traces are impregnated into the metal and could not be washed away readily even with acetone, while on the latter the carbon layer could be wiped off easily.

Typical records of wall traces left in brass and stainless steel by a detonation wave propagating through a straight tube of  $2.5 \times 2.5 \text{ cm}^2$  cross section are presented in Fig. 2. In both cases, the detonable mixture was 80%

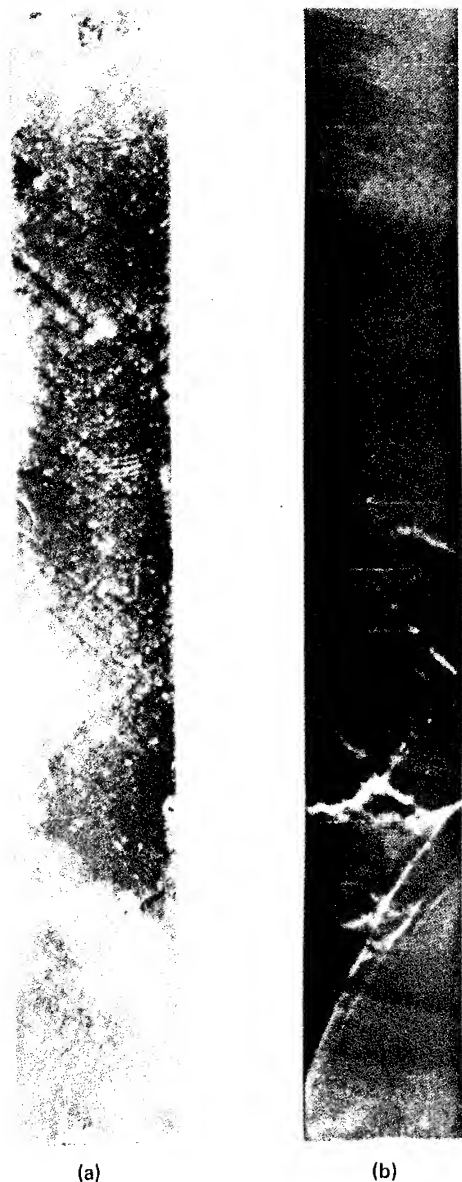


Fig. 2 - Typical records showing initial traces due to geometrical mismatch of the explosives and traces during the steady velocity propagation of the process; (a) brass walls, (b) stainless steel walls

nitromethane and 20% acetone by volume; and as expected, the pattern is of approximately the same mesh size.

Both records exhibit traces produced by two different modes of operation. The process in the first 8 cm of the tube is predominantly overdriven. The fine structure of the wave is

hardly visible. What appears to be a single-mode detonation has resulted from a geometrical mismatch during the transition of detonation from the solid explosive into the liquid test mixture; this will be discussed later.

Of primary interest here is the second region, where the wall exhibits a nonuniform but very regular pattern quite similar to that observed on the carbon soot records of gaseous detonations. The criss-cross pattern is characteristic of a "multiheaded" detonation which is cellular in structure and intrinsically unstable but as a whole travels at a constant detonation velocity near its theoretical C-J value.

To measure the velocity of detonation in a nitromethane-acetone mixture, experiments were performed in stainless steel tubes where barium titanate pins were imbedded into the side wall 1 cm apart over the entire length of the tube. The pins were so located that their tips were only 1 mm from the test mixture. Since the distance to the explosive, was controlled to within 5 microns, all pins reacted to the shock pressure with equal delay and gave out time-of-arrival signals with an estimated accuracy of 1%. The history of the processes taking place in two mixtures (80:20 and 75:25 nitromethane-acetone) in a  $2 \times 2$  cm<sup>2</sup> tube are represented on a space-time diagram, Fig. 3. This figure also shows the wall trace record actually recovered from the experiment with the 75:25 mixture.

With the slope of the line representing the velocity of the wave, one can easily see that in less than 2  $\mu$ sec and only 9 cm of travel the wave has reached an apparent steady state, propagating at a constant velocity of 5.65 and 5.46 mm/ $\mu$ sec in the rich and lean mixture, respectively. The high values of the constant velocity also indicate that the processes observed here and recorded on the walls are not of the degenerate, low-velocity type, but rather those of full-scale detonations.

The significance of the single-mode trace in the initial region is that it proves the traces to be those marked by the high-pressure points of the triple wave intersections. The geometrical mismatch between the two explosives is generated because the C-4 igniter was made as a cylinder 1 in. in diam while the internal cross section of the tube was  $2.5 \times 2.5$  cm<sup>2</sup>. The four corners of the tube thus were not originally in contact with the primer; and when the detonative process entered the test mixture, the corners were not affected. The traces in Fig. 2 emerging from the corners must, therefore, have been

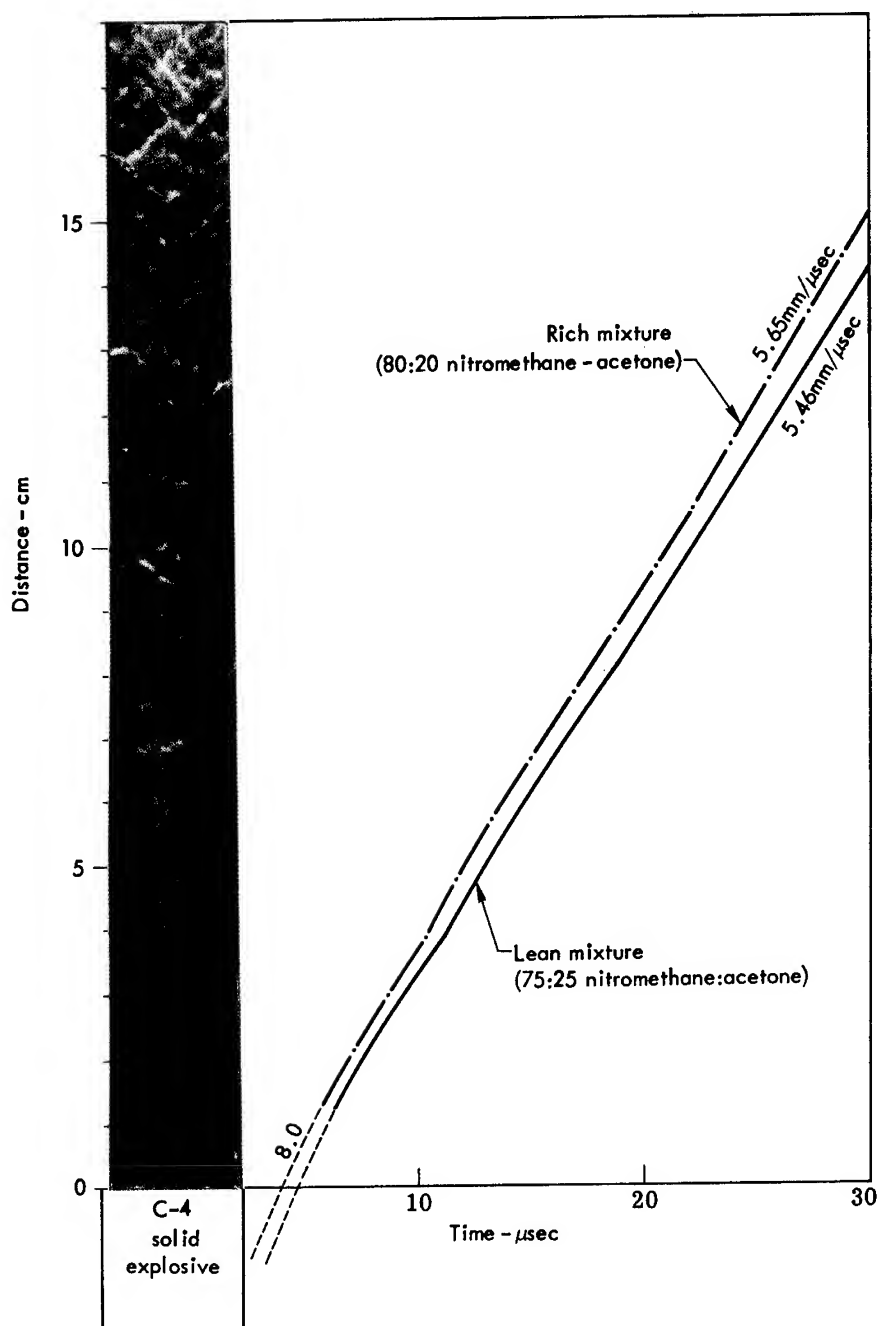


Fig. 3 - The space-time history of detonation waves propagating through 75:25 and 80:20 nitromethane-acetone mixtures in a  $2 \times 2$  cm<sup>2</sup> stainless steel tube. The numbers indicate the velocity in mm/ $\mu$ sec. The wall trace record along the ordinate is from the 75:25 mixture.

originated by some process that took place at a later time.

When this process is compared to gaseous processes that would occur under similar

conditions, the explanation becomes rather simple. As the detonation wave enters the test mixture from a solid explosive, it is at first highly overdriven, spreading radially into the corners. Converging onto the trapped unburned

mixture, the wave ignites this mixture, producing a sudden release of energy and creating a new center for a strong detonation wave that propagates along the edge of the tube and catches up with the original one. Both waves being of spherical form will intersect at an angle, thus producing a line of intersection which along the wall appears as a point. The corner wave, being stronger and faster than the already attenuating central wave, will force the point of intersection towards the center of the wall. This inscribes a trace which appears as a perfect replica of a single cell in gaseous detonations.

The main proof that the traces are produced by localized high pressure, such as those known to exist at Mach intersections, comes from the fact that some of the records exhibit a clear and visible-by-eye indentation along the trace and a large dented area where the two traces meet. This effect is illustrated in Fig. 4, which shows three surface profiles taken along the line indicated on the accompanying record. Although the measurement of the surface profile is fairly accurate, to within 5%, the actual pressures that caused such indentations have not yet been estimated.

A rather enlightening correlation between gaseous and liquid detonations and their unique nonuniform structure, consisting of triple wave intersections, is evidenced by the behavior of the process as it propagates through a tube and encounters a change in the cross sectional area. The experiments were performed with a rich mixture to ensure steady propagation of the wave through the initial cross section  $1.5 \times 1.5$  cm<sup>2</sup>. Figure 5 shows the transition of detonation into a  $1.5 \times 2.5$  cm<sup>2</sup> cross section through a relatively smooth area change where  $dA/dx = 0.15$  cm<sup>2</sup>/cm.

The mixture here is 80:20 nitromethane to acetone, and the structure is seen to change smoothly from a cell size of about 1 mm to that of about 2 mm.

Figure 6 illustrates the transition through a sudden area change  $dA/dx = \infty$  from a  $1.5 \times 1.5$  cm<sup>2</sup> cross section into a  $1.5 \times 2.5$  cm<sup>2</sup> cross section (a) and a  $1-1/2 \times 2$  cm<sup>2</sup> cross section (b). In both cases, the mixture is 85:15 nitromethane to acetone. The effect of the enlargement is quite evident. In our previous work (7), we had shown that larger tube sizes are more favorable to sustaining the process in a particular mixture, and yet here the process entering a larger tube undergoes extinction, in one case even dying out completely. This can be explained only on the basis of a complex triple

wave structure in which the process is carried on behind the transverse moving waves and sustained by continuous interactions and head-on collisions of such. During the transition into sudden enlargement of the area, unlike the highly overdriven case (Fig. 2b) where the detonation is easily bent around the corners, the normal and steady detonation wave suffers a momentary lack of reflections which locally attenuates the process to such an extent that it goes to extinction. This extinct region, where no reaction takes place, propagates toward the center of the tube with the velocity of sound corresponding to that behind the detonation wave, and as a result forms a triangular dome in the direction of motion.

If a wall of the larger tube is encountered before a certain state of attenuation is reached, the reflection off that wall reignites the mixture; but revival of the process over the whole cross section additionally depends on the width of the nonreactive zone, and also on whether the two reflected waves produce a sufficiently strong explosion center upon their collision.

The effect of the larger tube on the transition of detonation into a sudden change of area is clearly demonstrated by the two cases shown in Fig. 6. In (a), the walls were recessed 5 mm away; and although reignition did occur behind the reflected wave, the process did not survive. In (b), the larger tube walls were recessed only 2.5 mm; and they turned out to be sufficiently close to reignite the mixture, not only behind the reflection off the wall but also behind the collision of the two reflected waves at the center of the tube. In this particular case, the nonreacting zone persisted, continuing on for another cycle until the third reflection off the wall finally led to its elimination, letting the process go on unobstructed.

The same phenomenon is observed in gaseous detonations and is best described in Ref. 11. A similar phenomenon in liquid explosives was investigated by Dremine and Savrov (12) with streak self-light photography through a slit in the back wall of the larger tube. However, there the main object of the investigation was to establish the critical minimum diameter of the smaller tube from which detonation would pass unobstructed into a large volume with no limitations on the size of the larger tube. The present records demonstrate the importance of the walls after transition into the large tube and clearly illustrate the effect of a reflection on the propagation of detonation.

To further our study of the behavior of the detonation wave and its ability to reignite after

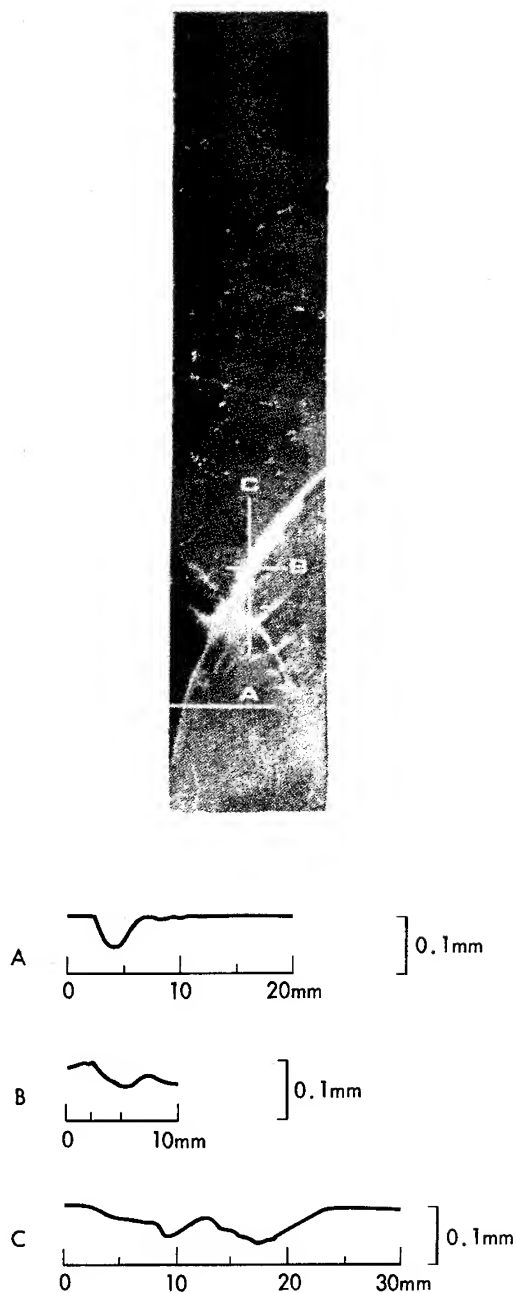


Fig. 4 - Surface profiles across the traces induced by a geometrical mismatch of the explosives during the ignition process. The mixture was 75:25 nitromethane-acetone in a  $2.5 \times 2.5 \text{ cm}^2$  stainless steel tube.

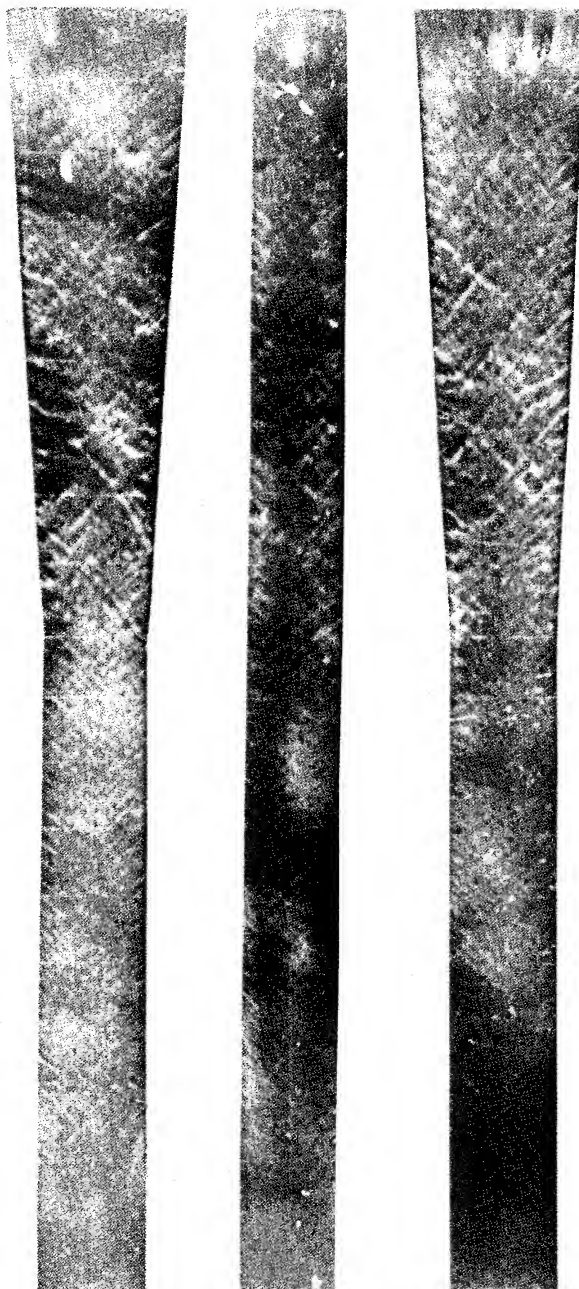


Fig. 5 - Wall trace records depicting the transition of detonation through a smooth enlargement of the cross section area from a  $1.5 \times 1.5 \text{ cm}^2$  into a  $1.5 \times 2.5 \text{ cm}^2$  stainless steel tube. The mixture was 80:20 nitromethane to acetone.

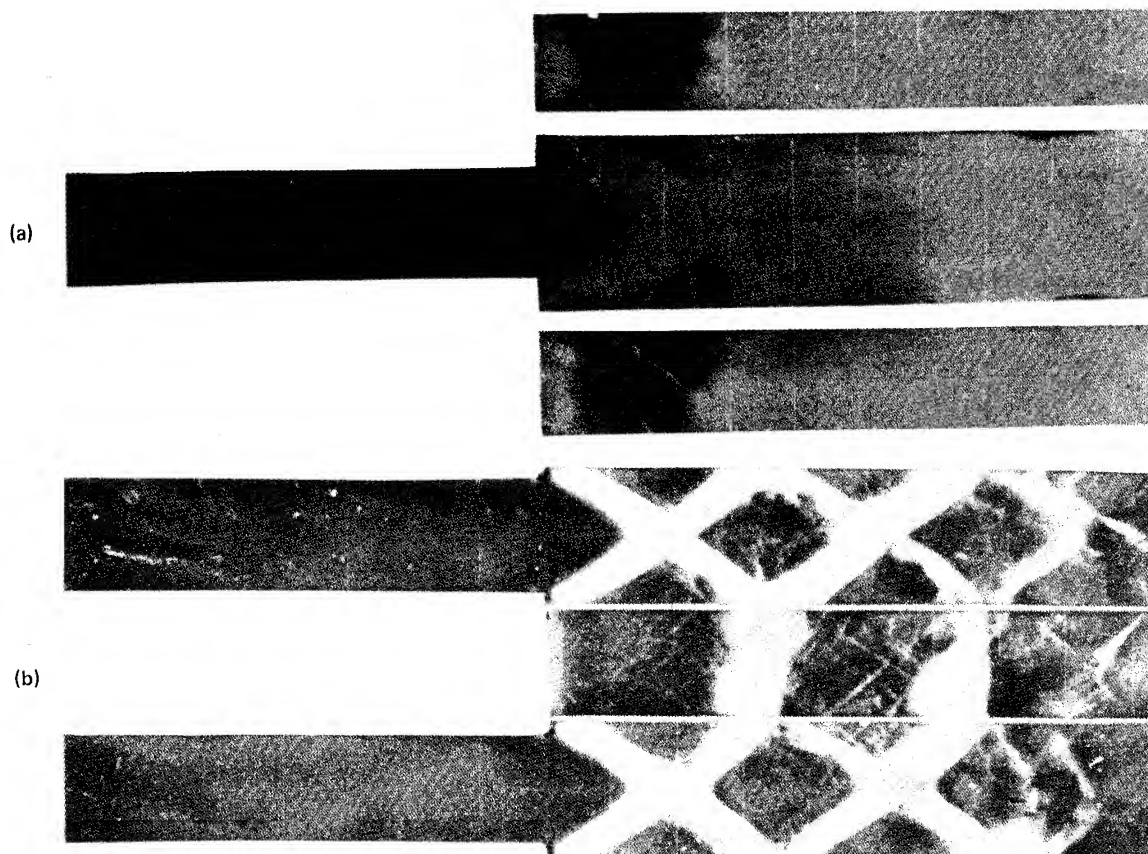


Fig. 6 - Wall trace records depicting the transition of detonation through a sudden enlargement of the tube cross section from a  $1.5 \times 1.5 \text{ cm}^2$  into (a)  $1.5 \times 2.5 \text{ cm}^2$  and (b)  $1.5 \times 2 \text{ cm}^2$ . The mixture in both cases is 85:15 nitromethane to acetone.

collisions, an experiment was performed in which a steady-state wave was split around a wedge and then brought back together with a head-on collision in a manner like that which takes place in each of the cells of gaseous detonations. The two colliding waves then produce a new explosion center, which creates a new detonation wave spreading out as a single cell. The record of such an experiment is shown in Fig. 7. Here the wedge was only 1 cm high in the tube that was originally  $2.5 \times 2.5 \text{ cm}^2$ . The mixture was 80:20 nitromethane to acetone.

In light of what happened to the detonation process with sudden expansion of the tube (Fig. 6), a wide white trace—the evidence of no reaction—appeared behind the wedge and proceeded towards the side walls. However, the nonreactive shock waves that propagated around the corners of the wedge collided head on and produced a locally intense pressure region which turned into a new explosion center, which

in turn generated a new detonation wave spreading out as a spherical wave and engulfing the whole cross section. The trace of the unreacted cone moved away from its origin behind the wedge and then propagated along the two side walls, reaching the fourth wall in a manner similar to the so-called slapping wave. While the nonreacting zone ultimately seems to have covered the whole cross section of the tube, the newly ignited detonation took over and continued the process to the end.

In a more dilute mixture, the collision of shock waves behind the wedge might be strong enough to generate a new explosion center which would reignite the mixture at that point, but it would not have sufficient strength to induce and sustain detonation over the whole cross section.

Failure to reestablish detonation occurred in a 75:25 nitromethane-acetone mixture, a record of which is shown in Fig. 8. The



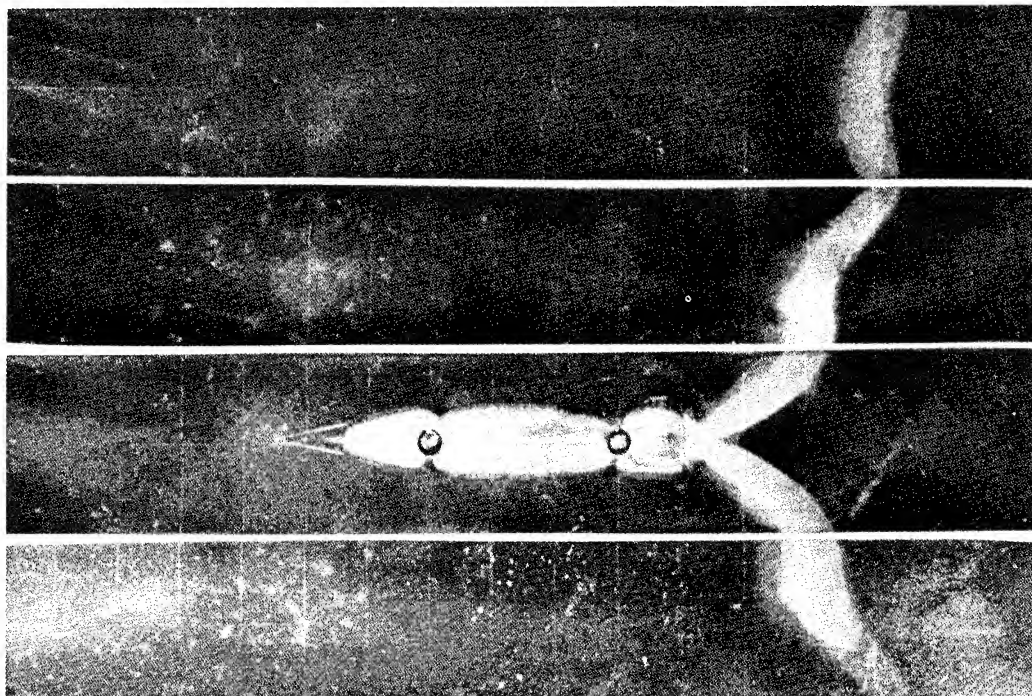


Fig. 7 - Wall trace records of detonation traveling past a wedge 1 cm high. The tube was  $2.5 \times 2.5$  cm<sup>2</sup> stainless steel and the mixture 80:20 nitro-methane to acetone.

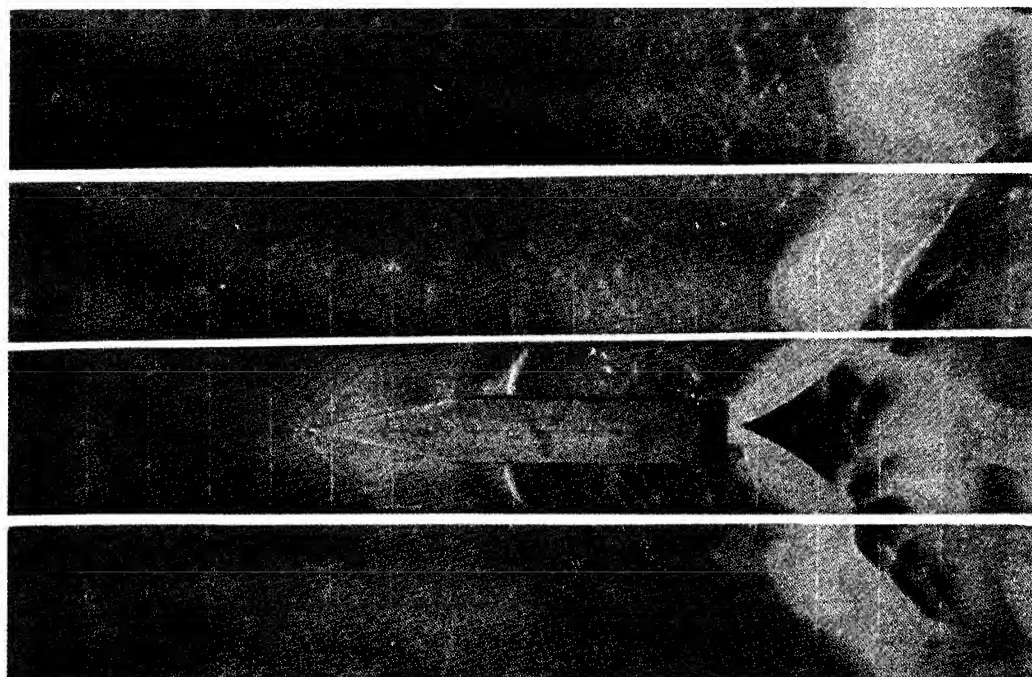


Fig. 8 - Wall trace records of detonation traveling past a wedge 1 cm high. The tube was  $2.5 \times 2.5$  cm<sup>2</sup> stainless steel and the mixture 75:25 nitro-methane to acetone.

weakness of the mixture, which in essence was the cause for the suppression of the detonation process, was also the reason for more details on the record before the wedge and in the narrow section of the tube. Of interest here is the pattern, which resembles the waveform usually obtained in a steady transonic flow around a wedge or airfoil. What this pattern represents is difficult to answer at this time; however, one could speculate that as the detonation wave passed the wedge, the flow behind it may have been locally transonic and steady long enough to impregnate the characteristic pattern. That the pattern is indeed impregnated into the plate and nearly 0.1mm deep is deduced from the surface profile which was scanned along the line parallel to the wedge and 2 mm away from it.

Thus, from all the evidence above, it is rather clear that the front of a detonation wave in a homogeneous nitromethane-acetone mixture is not one-dimensional but rather a complex three-dimensional structure consisting of pressure discontinuities. The traces being caused by high pressure peaks mark the paths of the triple wave intersections as they propagate in the transverse direction, colliding and enforcing each other.

The slope of the trace relative to the tube axis is in all cases near 45 deg, suggesting that the transverse velocity of the triple points is very close to the detonation velocity. In effect, this also indicates that instabilities of the wavefront are of the same order of magnitude in the direction of detonation as well as in the transverse direction.

## CONCLUSION

In conclusion, then, it is felt that the similarity is established between the processes that take place in gaseous and nitromethane-acetone mixtures, and that the cellular wavefront is an essential feature of the detonation process in these explosives. Whether the same is true for other homogeneous liquid explosives is not yet known. The authors intend to use this experimental technique on liquids which, on the basis of photographic records (5), seem to behave differently and produce uniform, stable, one-dimensional detonation fronts.

## ACKNOWLEDGMENTS

The authors wish to express their gratitude to R. E. Neatherland and C. H. Michel for their invaluable assistance in preparing and assembling the experimental shots.

## REFERENCES

1. A. W. Campbell, T. E. Holland, M. E. Malin, and T. P. Cotter, "Detonation Phenomena in Homogeneous Explosives," *Nature*, Vol. 178, pp. 38-39, July 7, 1956.
2. A. N. Dremin, O. K. Rozanov, and V. S. Trofimov, "On the Detonation in Nitromethane," *Combust. Flame*, Vol. 7, pp. 153-162, June 1963.
3. H. D. Mallory, "Turbulent Effects in Detonation Flow: Diluted Nitromethane," *J. Appl. Phys.*, Vol. 38, No. 13, pp. 5302-5306, Dec. 1967.
4. A. N. Dremin, "Critical Phenomena in the Detonation of Liquid Explosives," 12th Symp. (Int.) on Combust., pp. 691-699, The Combustion Institute, Pittsburgh, Pa., 1969.
5. A. N. Dremin and S. D. Savrov, "On the Stability of the Detonation Front in Liquid Explosives," *Fiz. Goreniya Vzryva*, No. 1, pp. 36-46, 1966.
6. H. D. Mallory and G. A. Greene, "Luminosity and Pressure Aberrations in Detonating Nitromethane Solutions," *J. Appl. Phys.*, Vol. 40, No. 12, pp. 4933-4938, Nov. 1969.
7. P. A. Urtiew, A. S. Kusubov, and R. E. Duff, "Cellular Structure of Detonation in Nitromethane," *Combust. Flame*, Vol. 14, No. 1, pp. 117-122, Feb. 1970.
8. P. M. Howe, "Transverse Waves in Detonating Liquids," *Appl. Phys. Lett.*, Vol. 15, No. 7, pp. 197-198, Oct. 1, 1969.
9. B. B. Dunn, "Transverse Wave Instability in a Solid Explosive," *Science*, Vol. 167, No. 3921, pp. 1124-1126, Feb. 20, 1970.
10. A. K. Oppenheim, J. J. Smolen, D. Kwak, and P. A. Urtiew, "On the Dynamics of Shock Intersections" (in this symposium).
11. B. V. Voitsekhovskiy, V. V. Mitrofanov, and M. E. Topchian, "Struktura Fronta Detonatsii v Gazakh," pp. 99-101, *Akad. Nauk SSSR*, Novosibirsk, 1963.
12. A. N. Dremin and S. D. Savrov, "Limiting Conditions of a Stable Propagation of Detonation with a One Dimensional Zone in Liquid Explosives," *Fiz. Goreniya Vzryva*, No. 4, pp. 75-84, 1966.



## DISCUSSION

MOSTAFA M. KAMEL

Gasdynamics Laboratory  
Division of Aeronautical Sciences  
University of California, Berkeley

At Berkeley, we passed a low mode detonation wave in equimolar  $C_2H_2 + O_2$  through a sudden enlargement of the cross section of a thin tube. Within a narrow range of pressure, the wave was either extinguished completely or was dramatically re-established upon the first intersection between the shock waves reflected from the wall. In your Fig. 6, the final re-establishment occurred at the third intersection, rather than the first. Since each intersection is, presumably, weaker than the preceding one, could this be due to non-homogeneous conditions? If not, could you account for this phenomenon?

REPLY BY P. A. URTIEW

Your comment is very well taken because it is indeed logical to expect the re-establishment of the process to take place right after the first intersection or not at all.

The record of Fig. 6 has puzzled us too and the only explanation we can offer at this time is the following: Between setting up the shot and firing we usually used 5-10 minutes of a hot summer day. During that time a small temperature or density gradient can have set in the mixture since the top of the tube was open and exposed to the atmosphere. The case must have been a truly marginal one and a slight gradual change in initial conditions could have caused such a struggle for survival.

F. E. WALKER

Lawrence Radiation Laboratory  
Livermore, California 94550

It appears from the patterns of the traces on the metal waves that the area of original

initiation to detonation is relatively smooth (no strong shock interactions) but that these interactions develop as a result of small pressure waves, from centers of higher levels of reaction within the detonation front, which then collide with or are reflected from the metal walls. The reflected shocks then appear to interact to form centers of higher pressure and temperature, and thus high levels of chemical reaction. The shock patterns also appear to vary with the tube width (or geometry) and the chemical composition of the explosive. Would you care to comment on the possibility that the shocks are initially a result of chemical reaction rather than a cause and that the wall traces are an artifact of the geometry rather than a necessary factor in the continuation in the progress of the detonation?

REPLY BY P. A. URTIEW

The absence of the wave pattern in the area of original initiation is due to the overdriven initiation of the NM acetone mixture by the solid explosive. As the wave attenuates its cellular structure becomes more pronounced and traces begin to appear on the walls. When the process reaches its "steady state" it acquires a structure whose cell size is characteristic to the particular chemical composition of the mixture and also the size of the tube.

As far as the shocks being the result of or the cause for the chemical reaction, we know from gaseous detonations that both statements are true. First the chemical reaction generates shock waves which then colliding with each other produce new centers for renewed chemical reaction.

The wall traces as such are of course not a necessary factor for the continuation of the detonation process but they are the result and the experimental evidence of the triple wave intersections in the wave front, which we believe are the main driving mechanism of the self-sustained detonation front.

# A PHOTOGRAPHIC TECHNIQUE FOR MAPPING FAILURE WAVES AND OTHER INSTABILITY PHENOMENA IN LIQUID EXPLOSIVES DETONATION

Per-Anders Persson and Gert Bjarnholt  
*Swedish Detonic Research Foundation*  
*Vinterviken, 117 48 Stockholm*

We have found the open-camera aquarium technique (Winning 1954, 1958, Johansson and Sternhoff 1959) to be a very powerful and simple instrument for making measurements of the failure waves and other instability phenomena in detonating liquid explosives. A charge of liquid explosive in a transparent casing such as a glass tube is immersed in water in an aquarium. In this way, and by placing the charge and camera in darkness, the only light that reaches the film of the open-shutter camera is that emitted from the very thin reaction zone when it sweeps through the charge. The record is a picture of the charge having the same outline as before detonation because very little gross motion takes place within the reaction zone. We have found that the variations of temperature and reaction time associated with failure waves in pure nitromethane are clearly visible as a pattern in such records.

Figure 1 shows the still picture (a), and reaction light recording (b) of a tubular charge of nitromethane in a 19.5/22-mm (internal/external diameter) glass tube, emerging into a wider tube, also filled with nitromethane. Initiation was done from below by the 84-mm-long and 29-mm-diameter pressed TNT booster through an 0.25-mm PVC barrier. The record shows a fine crisscross network of failure waves at the surface on the 19.5/22-mm glass tube. At the top is seen the integral picture of the light emitted from the complicated failure and reinitiation processes after the detonation emerges into the wider tube. Outside the main contour of the glass envelope of the charge, there is a faint halo-like light. We believe this to come from the reaction products during their relatively slow expansion behind the reaction zone.

Figure 2 shows a series of four separate records of four different shots of pure nitromethane in straight tubes of ca 150-mm length,

all initiated by the same booster system as in Fig. 1. In the record 2a the envelope was a 19.5/22-mm glass tube, in 2b and 2c (identical charges) 15.5/17.9-mm glass and in 2d 16-mm internal diameter (i.d.) 0.07-mm-thick Mylar.

Figure 2a shows, perhaps more distinctly than Fig. 1a, the crisscross pattern of intersecting failure waves. In Figs. 2b and 2c, with a diameter closer to the critical diameter, the wave pattern is coarser.

Figure 2d shows the pattern of detonation failure obtained when the tube wall was made of thin Mylar instead of glass.

On the basis of the patterns of Figs. 2a, b and c we suggest the following theory for the failure wave.

Assume that the detonation is most sensitive to slight disturbances at the wall. This is where the reacting explosive is most directly accessible to the effects of the lateral expansion. The paper by Persson and Sjölin in these proceedings shows very clearly how extremely sensitive the detonation reaction is to changes in front pressure. Thus, it appears likely that, given a slight local disturbance to the detonation at a point on the wall, the reaction will effectively stop at this point, to restart again only after a given initiation induction period has elapsed. The reaction failure will spread as an expansion wave along the detonation shock front so that a volume of the explosive within a conical surface will be left unreacted. The conical surface has its apex at the initial failure point and its axis in the direction of detonation. If the detonation front were a plane and perpendicular to the tube axis, the cone would be straight and its half-angle  $\alpha$  would be given by

$$\operatorname{tg} \alpha = (1/D) \sqrt{C_f^2 - (D - u_{pf})^2}, \quad (1)$$

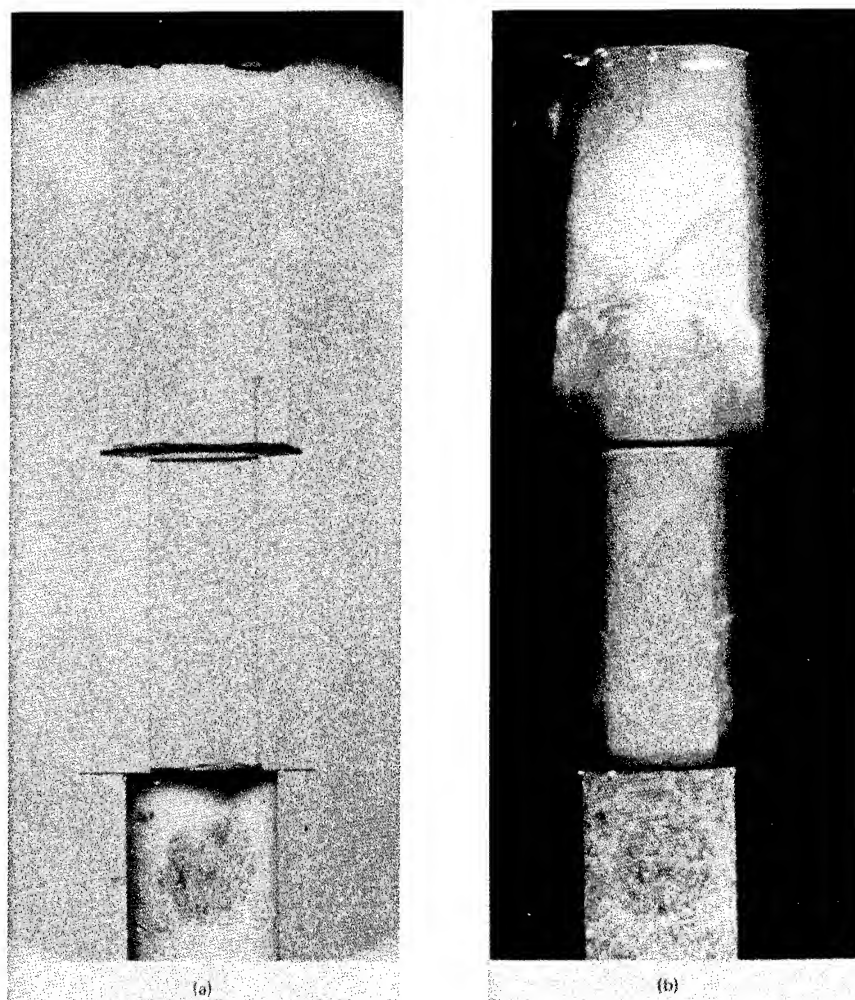


Fig. 1 - Still picture (a) and detonation light recording with open camera (b) of detonation in pure nitromethane emerging from a 19.5-mm i.d. glass tube into a 33-mm i.d. glass tube. TNT booster 84-mm long by 29-mm diameter.

where  $D$  is the detonation velocity,  $u_{pf}$  the detonation front particle velocity and  $C_f$  the sound velocity in the shock-compressed but unreacted explosive at the front of the steady detonation-reaction zone.

After the initiation induction period has elapsed, reinitiation takes place at the cone apex. A detonation wave will spread spherically out from this point through the shock-compressed, unreacted explosive within the cone and will eventually catch up with the shock front. Catch-up will occur first at the tube surface and later further in. The catch-up surface will be forward concave. Figure 3 shows a schematic of the process in two longitudinal and two perpendicular views of the tube.

Failure and reinitiation take place at the point A, failure spreading along the cone generator AC. B is the point of first and C (also D) that of last catch-up.

The intersection between the failure cone and the tube wall is the lines DAD, and that between the catch-up surface and the wall the line DBD. Thus, because the detonation in the pre-compressed material affected by the failure is less luminous than the ordinary detonation, the surface ADBDA will appear dark. Also, because of the higher than normal light intensity from the detonation immediately after catch-up, the surface BDCDB will appear lighter than the surrounding.

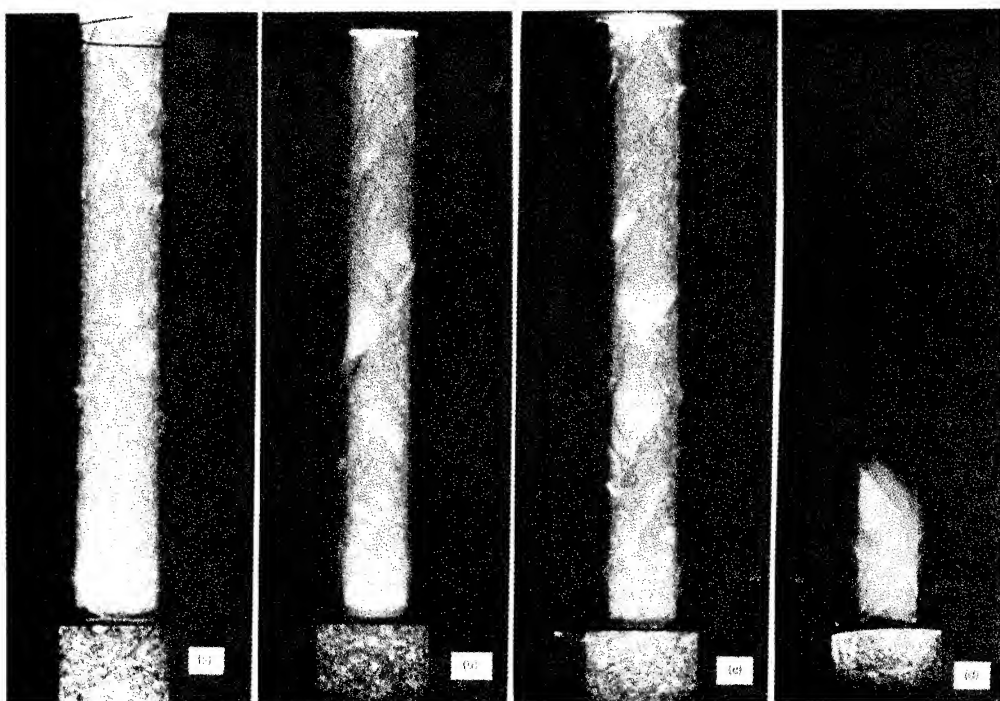


Fig. 2 - Open camera detonation light records of detonation in pure nitromethane in 150-mm-long tubes of diameter 19.5/22-mm glass (a), 15.5/17.9-mm glass (b) and (c), 16-mm, i.d., 0.07-mm-thick Mylar (d)

These features are modified by the curvature of the real detonation front and the interaction between a multitude of failure waves. Using the values  $D = 6.29$  km/sec,  $C_f = 5.05$  km/sec, and  $u_{pf} = 2.52$  km/sec, in Eq. (1) we arrive at the value  $\alpha = 27^\circ$ , which is in the range suggested by Figs. 2a, b and c.

In a perpendicular cross section of the tube, such as that seen by a camera looking down the tube, the zone of unreacted material would appear as a half-circular dark band or a half-circular dark surface depending upon whether or not catch-up has occurred. These are obviously the failure waves observed by

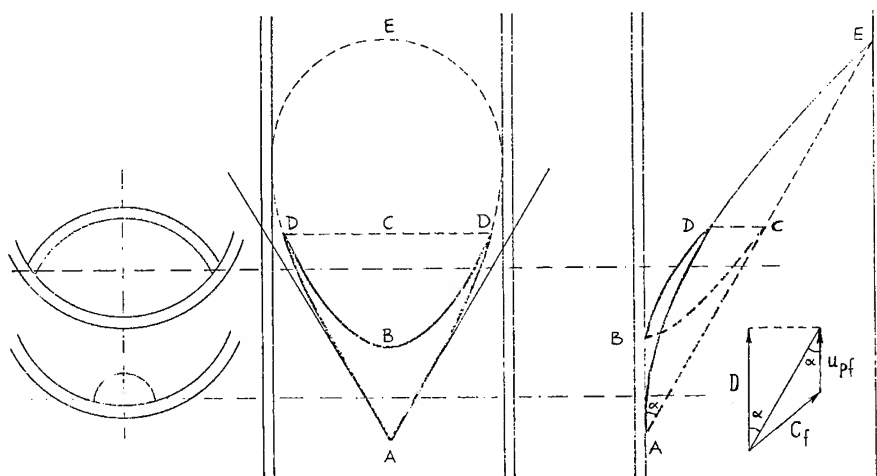


Fig. 3 - Schematic of the geometry of failure and reinitiation waves in a liquid explosive detonating in a tube

Watson (these proceedings) in framing camera pictures and by others in streak cameras with the slit across a diameter of the tube. In the latter records, the similarity with the cross-sectional, dashed-line surface ACBA is striking.

With the mechanism suggested, it would appear likely that the disturbance due to the initial failure at A spreads further along the cone surface than to the final catch-up DCD. We suggest that such "ripples," propagating sideways within the reaction zone and following for long distances the conical surface, are the origin of the detonation-wave fine structure first observed by Cotter (1956).

#### ACKNOWLEDGMENTS

The authors are grateful to Dr. Nils Lundborg for suggesting the use of the open-camera

technique for the present work. They also wish to acknowledge the economic support received from Nitro Nobel AB, Atlas Copco AB and the Swedish Technical Research Council.

#### REFERENCES

- Johansson, C. H. and Sternhoff, L. "Suppressed Light Emission of the Reaction Zone in Detonation". *Nature* **183**, 247 (1959).
- Winning, C. H., C.R. 27th Congr. Int. Chemie Industr., Bruxelles (1954), *Proc. Roy. Soc. A* **246**, 288 (1958).
- Campbell, A. W., Holland, T. E., Malin, M. E., and Cotter, T.P., Jun. "Detonation Phenomena in Homogeneous Explosives". *Nature* **178**, 38 (1956).

#### DISCUSSION

##### P. A. URTIEW

Lawrence Radiation Laboratory  
University of California  
Livermore, California

The records shown by Dr. Persson are indeed very interesting, but they represent a different phenomenon than that discussed in our paper. The main difference is in the way in which the experiments were conducted. While for his open-shutter photographs Dr. Persson used a thin glass tube immersed in a transparent medium (water), we were not concerned with the transparency of the surrounding but rather have put all our efforts toward containing the process in a heavy stainless steel tube surrounded by molten seraban and a layer of lead bricks. Dr. Persson has truly observed failure waves setting in at the boundaries due to the break up of the tube, but in our case we believe that we see traces of the triple wave intersections that play an important part in sustaining the detonation rather than extinguishing it.

##### P. A. PERSSON

Swedish Detonic Research Foundation  
Vinterviken, 117 48 Stockholm

Not always is a detonating liquid as well contained the thick, heavy, high shock impedance material as in Dr. Urtiew's experiments. Our results should sound a warning bell against drawing the parallel too far between gaseous and liquid media detonation.

For detonating liquids, in contrast to gases, the containing wall is less rigid. The region near the wall, therefore, is often the region of the liquid where failure waves will originate. And at the same time, effects similar to the wall reflections that occur so readily in gaseous detonation are more difficult to provoke.

That they can be provoked has been shown, very nicely, by Dr. Urtiew.

# ON THE DYNAMICS OF SHOCK INTERSECTIONS

A. K. Oppenheim, J. J. Smolen, D. Kwak  
*University of California  
Berkeley, California*

and

P. A. Urtiew  
*Lawrence Radiation Laboratory  
Livermore, California*

## ABSTRACT

Upon the recognition that collisions between shock intersections play a dominant role in the self-sustenance of detonations, an analysis of their dynamic properties is presented, covering a full scope of possible wave configurations in gaseous media as well as in condensed explosives. In both cases theoretical results and experimental records are shown to be in satisfactory agreement.

## INTRODUCTION

In the last decade our concepts of gaseous detonation waves have been completely revolutionized (1,2). Instead of the classical NDZ model of a plane shock followed by a steady-flow deflagration, it became evident that the self-sustaining wave is both nonsteady and non-homogeneous. The mechanism of wave propagation was revealed to be associated with the action of a set of concentrated explosions that generate blast waves whose fronts are, as a rule, nonplanar. The latter collide with each other, creating intersection points which, in turn, undergo mutual collisions producing new shock intersections that bring about new explosion centers, while for most of the time between collisions the wave system is in a state of decay. The overall steady state propagation is thus achieved as a result of a balance between the wave amplification due to new explosions and the wave decay during the remainder of the time.

As it is apparent from the above, shock intersections and their collisions play a dominant role in the self-sustenance of detonation waves.

Moreover, they provide simple diagnostic means for the study of the wave structure, since intersection points leave traces of their trajectories on the walls along which the detonation wave propagates, yielding an informative record of their dynamic behavior. The traces are produced as a result of the fact that shock intersections generate regions of high pressure and temperature which, as a consequence of rarefaction associated with the basic blast wave structure of the flow field, are localized in the immediate vicinity of the intersection points. These regions contain, moreover, concentrated vortices due to the action of the slip-line discontinuity that is concomitant to any asymmetric shock intersection. Thus the traces of the trajectories of the intersection points can be engraved on the walls by the sharp pressure peaks as well as by the twister action of the vortices. The latter is the prevailing mechanism producing the well-known smoke-foil records in gaseous detonations, while the former provides principal means for the attainment of similar records in condensed explosives.

The purpose of this paper is to present the dynamic properties of collisions between shock

---

This work was supported by the U.S. Air Force through the Air Force Office of Scientific Research under Grant AFOSR 129-67, by the National Aeronautics and Space Administration under Grant NsG-702/05-003-050, and by the National Science Foundation under Grant NSF GK-2156; it was carried out also, in part, under the auspices of the U.S. Atomic Energy Commission.

intersections in a gaseous medium as well as in a condensed phase explosive. While the analysis of shock intersections is textbook material (3,4), their collisions have received only sporadic attention (1,5). The basic features of these processes are, therefore, developed here from elementary concepts.

## SHOCK INTERSECTIONS

In a detonating medium shocks are generated in blast waves where they appear primarily as their fronts. They form intersections between each other as a result of either head-on or rear-end collisions, as illustrated in Fig. 1.

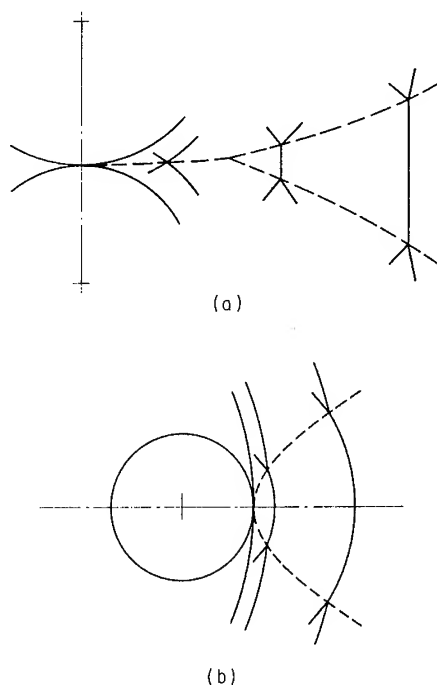


Fig. 1 - Illustration of the formation of shock intersections in an explosive medium: (a) head-on collision between blast waves; (b) rear-end collision between blast waves

In the case of a head-on collision, Fig. 1(a), at first the two fronts undergo, along the line of centers, a normal interaction producing a reflected shock (3,4,6). At the next instant quadruple shock intersections are formed on both sides of the line of centers. When the intersection angle acquires a certain critical value, the quadruple shock intersection can no longer

satisfy the dynamic compatibility conditions, and triple shock intersections set in.

The rear-end collision occurs, as illustrated in Fig. 1(b), when the second explosion is formed inside the blast wave of the first, or; what is of course equivalent, when an explosion occurs behind a plane shock. In this case, at first the two shock fronts merge along the line of centers, producing a transmitted shock and a reflected rarefaction fan. At the next instant, triple shock intersections are generated. The trajectories of these intersections, referred to simply as "triple points," are represented in Fig. 1 by broken lines.

If the shock fronts are sufficiently thin in comparison to the flow field treated by the analysis, which is usually the case with strong shocks, in the immediate vicinity of an intersection point the curvatures of the fronts can be neglected and the surrounding flow field considered to be essentially the same as in the case of plane fronts. The various wave configurations that are, under such circumstances, dynamically compatible are depicted in Fig. 2. Shown first is a quadruple shock intersection equivalent, in effect, to an asymmetric regular reflection (Fig. 2(a)). As the strength of one of the waves participating in the intersection is increased while the other is assumed to remain the same as before, the reflected shock behind the stronger wave becomes annihilated and one obtains an inverse Mach intersection, shown next (Fig. 2(b)). Then, for still higher strength of both incident waves, a normal Mach intersection is obtained (Fig. 2(c)). In this case the Mach stem is normal to the incident flow and the reflected shock is identical to that of a symmetric regular reflection. Following this, one gets the conventional Mach intersection (Fig. 2(d)). The limiting case for this configuration is attained when the reflected shock becomes normal to local flow (Fig. 2(e)). After that, one can have either a conventional (Fig. 2(f)) or a choked (Fig. 2(g)) "arrowhead" intersection—one in which all three shocks are of the same family (i.e., they turn the flow in the same sense), the latter being associated with a Prandtl-Meyer expansion while the flow behind the reflected shock is locally sonic.

The dynamic compatibility conditions which a wave intersection must satisfy stem from the requirement that each component has to obey the jump conditions for an oblique gasdynamic discontinuity, while the flow field generated by the intersection has to have uniform pressure and its particle velocities with respect to the intersection point must be mutually parallel.

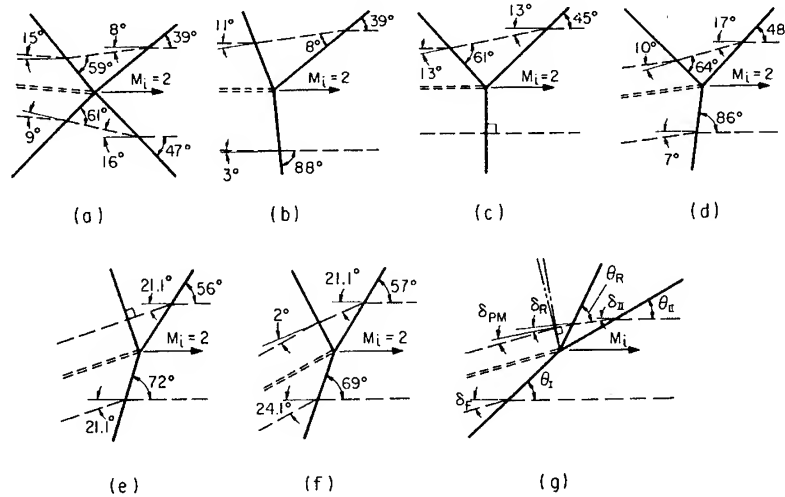


Fig. 2 - Typical shock intersection patterns: (a) quadruple intersection (equivalent to an asymmetric regular reflection); (b) inverse Mach intersection; (c) normal Mach intersection; (d) conventional Mach intersection; (e) limiting case of the conventional Mach intersection where reflected shock is normal to local flow; (f) conventional "arrowhead" intersection; (g) choked "arrowhead" intersection (sonic flow behind reflected shock)

It is the latter condition that gives rise to a slip-line discontinuity. For a given Mach number of incident flow,  $M_i$ , the jump conditions specify the angle of incidence,  $\theta$ , the flow deflection angle,  $\delta$ , and the downstream flow Mach number,  $M_j$ , as a function of the coordinates of a point on the Hugoniot curve.

In terms of nondimensional pressure ratio,  $P = p_j/p_i$ , specific volume ratio,  $\nu = v_j/v_i$ , and the local velocity of sound parameter,

$$\Gamma_k = \frac{a_k^2}{P_k \nu_k}, \quad (k = i, j) \quad (1)$$

these parameters can be expressed as follows (5):

$$\theta = \sin^{-1} \left( \frac{M_n}{M_i} \right), \quad (2)$$

$$\delta = \cot^{-1} \left[ \left( \frac{\Gamma_i M_i^2}{P - 1} - 1 \right) \tan \theta \right], \quad (3)$$

and

$$M_j^2 = \frac{\Gamma_i M_i^2 - (P - 1)(1 + \nu)}{\Gamma_j P \nu}, \quad (4)$$

where, with reference to Eq. (2),  $M_n$ , the Mach number of the normal component of incident flow, is related to the coordinates of the Hugoniot curve by the equation:

$$\Gamma_i M_n^2 = \frac{w_n^2}{P_i \nu_i} = \Gamma_i M_i^2 \sin^2 \theta = \frac{P - 1}{1 - \nu}. \quad (5)$$

Thus, for a given  $M_i$ , Eqs. (2), (3), and (4) become functions of the pressure ratio alone, if the specific volume ratio is eliminated by the use of the Hugoniot equation. The latter can be expressed most conveniently in the form of a rectangular hyperbola, which, for a shock front, represents the Rankine-Hugoniot curve passing through the point  $P = 1$  and  $\nu = 1$ . Its equation is then:

$$(P + \beta_P)(\nu - \beta_\nu) = (1 + \beta_P)(1 - \beta_\nu), \quad (6)$$

and it represents, indeed, an excellent approximation for most gaseous substances. In this case Eq. (5) becomes:

$$\Gamma_i M_n^2 = \frac{P + \beta_P}{1 - \beta_\nu}, \quad (7)$$

and, since  $M_n = 1$  as  $P = 1$ , the velocity of sound parameter becomes related to the asymptotes of the Rankine-Hugoniot hyperbola as follows:



$$\Gamma_i = - \left( \frac{\partial P}{\partial \nu} \right)_{H_i} = \frac{1 + \beta_P}{1 - \beta_\nu} \quad (8)$$

For a perfect gas with constant specific heats,  $\Gamma_k = \gamma$  while  $\beta_k = (\gamma - 1)/(\gamma + 1)$ ; ( $k = i, j$ ).

As a consequence of the fact that the compatibility conditions require the establishment of a regime of uniform pressure and flow direction immediately behind a wave intersection, the key to the solution of most problems in this domain is the relationship between the pressure and the flow deflection angle, known as the shock polar. Computer plots of such polars and of their auxiliary diagrams for the evaluation of the incidence angle,  $\theta$ , and the Mach number,  $M_j$ , based on Eqs. (1) through (8) for the case of a perfect gas with  $\gamma = 1.4$  (i.e.,  $\beta = 1/6$ ), are given in Plates 1, 2, and 3. With their use, the various intersections depicted in Fig. 2 (except for case (g)) were solved graphically (5), as shown in Fig. 3.

#### COLLISIONS BETWEEN INTERSECTIONS

As pointed out in the introduction, the most important events in the self-sustenance of detonations are collisions between shock intersections. Since, as it is evident from Fig. 1, any intersection pattern produced by explosions must evolve into a triple-point intersection, while in the most common case of shock-induced explosions represented by Fig. 1(b), such intersections are formed immediately at the outset, only this case need be thus considered.

##### Symmetric Collision

A symmetric collision between triple-point intersections is described schematically in

Fig. 4, showing the wave configurations immediately before and after this event. As a rule, the intersection point "consumes" the weaker incident shock, I. In order for a collision to occur, this shock, must be thus "consumed" from two sides, and the collision takes place then at the moment when it becomes annihilated. Immediately after this, the two stronger shocks, II, of the previous configuration acquire the role of the weaker shocks, I', while either a new stronger shock, II', is formed "pushing" the triple points away from the axis of symmetry, or a regular reflection is obtained, as that of Fig. 2(c), so that the resultant triple point "slides" along the axis of symmetry. In the latter case a Mach intersection will eventually be formed, as illustrated in Fig. 1(a). Of particular significance to the self-sustenance of detonations is here the fact that, as a result of this process, in both cases a high pressure and temperature region associated with a concentrated vortex is created in the immediate vicinity of the collision point.

##### Solutions

The wave system resulting from a symmetric collision is fully determined by the fact that the weaker incident shock after collision was the stronger shock before, while, due to symmetry, the newly formed stronger shock is perpendicular to the axis of symmetry. The process of collision has, therefore, two invariants: the pressure ratio,  $P$ , across the wave which remains unaffected by this process, and the angle between the two shock fronts,  $\Phi$ .

Exploiting the plane of collision invariants, one can thus construct a chart for the evaluation of the resultant wave system. Figure 5 represents such a chart for the case of a perfect gas with  $\gamma = 1.4$ . The wave systems that

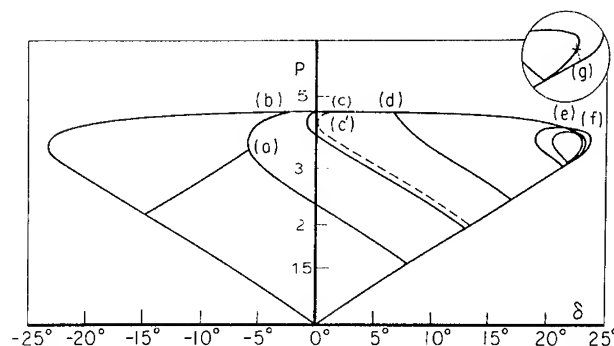


Fig. 3 - Shock polar solutions of the intersection processes represented in Fig. 2

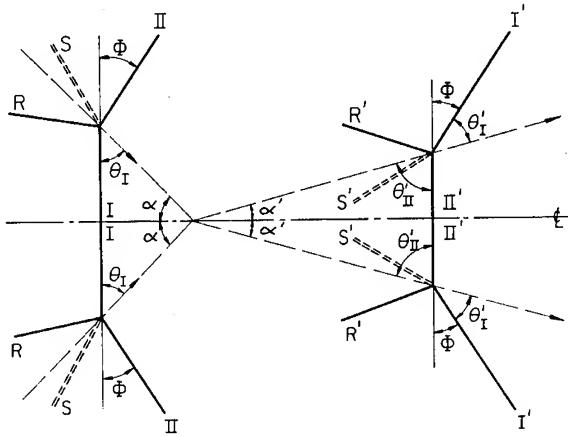


Fig. 4 - Schematic diagram of a symmetric collision between triple points

can be obtained after collision are represented there by continuous lines determined by taking for  $P$  the pressure ratio across the weaker incident shock. The corresponding wave systems before collision are represented by broken lines; these were obtained simply by taking for  $P$  the pressure ratio across the stronger shock of the same intersection. The chain-dotted lines denoted by  $\Phi'$  represent the loci of the normal reflected solutions (case (e) of Figs. 2 and 3), while those denoted by  $\Phi''$  are the regular reflection limits (case (c) of Figs. 2 and 3) beyond which the angle of reflection,  $\alpha' = 0$ .

On the  $P - \Phi$  plane of Fig. 5, each point of intersection between a continuous line and a broken line represents a solution of a collision process, specifying fully the wave systems immediately before and after this event. Once the solution in terms of  $P$  and  $M_i$  is known, the angles between the trajectories of the triple points can be determined from the auxiliary  $\theta = \theta(\delta)$  plot, Plate 2, as, by reference to Fig. 4,

$$\alpha = 90^\circ - \theta_I$$

while

$$\alpha' = 90^\circ - \theta'_{II} = 90^\circ - \Phi - \theta'_I.$$

(9)

Thus, making use of Fig. 5 and Plates 1 and 2, the angles between the trajectories of the triple-point intersections before and after symmetric collisions were evaluated for a set of incident flow Mach numbers, and the results are given in Figs. 6 and 7. From the latter one should note that  $\alpha - \alpha'$  becomes negligibly small as  $\Phi$  tends to zero which corresponds to

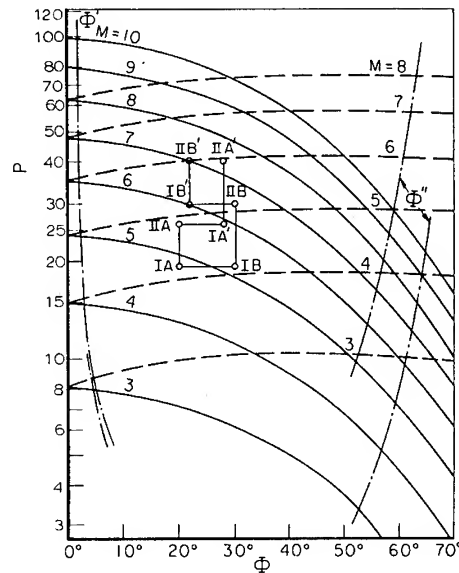


Fig. 5 - Solutions of collision processes between triple points on a plane of collision invariants (the case of a perfect gas with  $\gamma = 1.4$ )

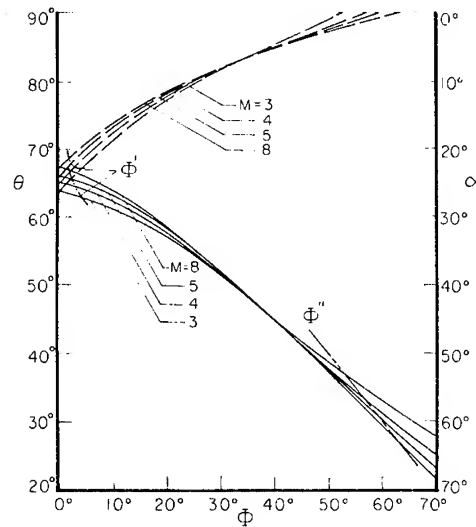


Fig. 6 - Solutions of collision processes corresponding to Fig. 5 expressed in terms of shock incidence angles

$M_j = 1$ , the condition which is attained when the reflected shock becomes reduced to a characteristic. Moreover, as it appears there, the relationship between  $\theta_I$  and  $\Phi$  is practically independent of the incident flow Mach number, especially if its value is high enough. Since

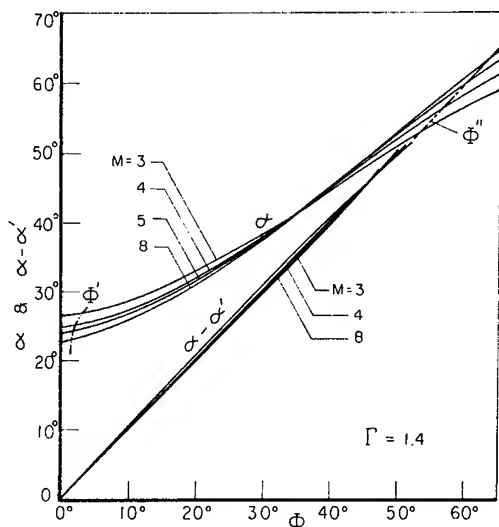


Fig. 7 - Solutions of collision processes corresponding to Fig. 5 expressed in terms of the triple-point trajectory angles

this means that in Eqs. (9)  $\theta_I = \theta'_I$ , one has therefore, in this case, quite a simple rule for estimating, with good approximation, the change in the angle between the trajectories of the triple points due to their collision, namely,

$$\alpha - \alpha' \approx \Phi. \quad (10)$$

#### Asymmetric Collision

An example of wave configurations associated with an asymmetric collision is represented by Fig. 8. The wave system before

collision shares the incident shock, so that  $P_{IA} = P_{IB}$ . The resultant wave system is determined by four conditions which are imposed by the requirement that the two stronger shocks of the initial wave system are unaffected by the collision, acquiring the roles of the weaker incident shocks after this event, while the newly formed stronger shock is common to both the resultant intersections  $A'$  and  $B'$ . One has, therefore,

$$(1) P_{IIA} = P_{IA'}$$

$$(2) P_{IIB} = P_{IB'}$$

$$(3) \Phi_A + \Phi_B = \Phi_{A'} + \Phi_{B'}$$

$$(4) P_{IIA'} = P_{IIB'}$$

The solution corresponding to Fig. 8 is one which satisfies these conditions in the case of two Mach intersections generated by an incident shock of Mach number  $M_i = 4.06$  ( $P_I = 19.5$  if  $\gamma = 1.4$ ) in a shock tube fitted with two wedges, one of a  $20^\circ$  and the other of a  $30^\circ$  apex angle. This is shown in Fig. 5, demonstrating how the numerical results given in Fig. 8 were obtained. As can be observed, the approximate rule of Eq. (10) applies here as well, since the difference between the values of  $2\alpha = 70^\circ$  and  $2\alpha' = 20.5^\circ$  is practically equal to  $\Phi_A + \Phi_B = 20^\circ + 30^\circ = 50^\circ$ .

#### Experimental Verification

The physical validity of the above theory has been demonstrated by comparison with a variety of experimental results obtained in the

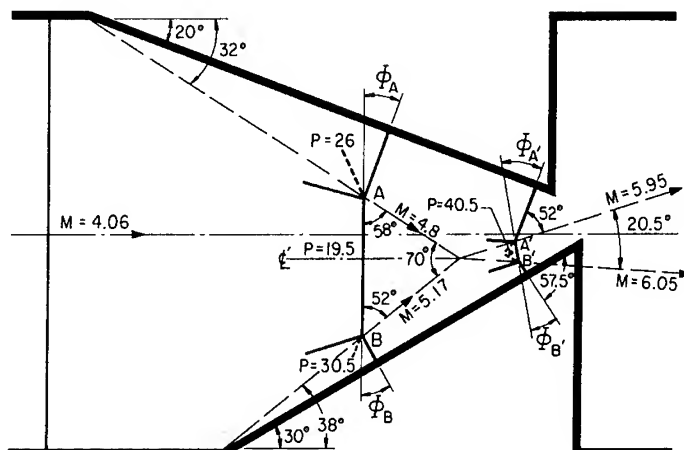


Fig. 8 - An example of an asymmetric collision between triple points

course of detonation processes (1) as well as with the use of inert gases where the shock intersections were generated by means of wedge walls in shock tubes as in the case of Fig. 8. Selected for illustration here were, in fact, the records corresponding to this case. They were obtained in a shock tube  $1\frac{3}{4} \times 1\frac{3}{4}$  in. in cross section filled initially with nitrogen at room temperature and a pressure of 5mm Hg—the conditions for which the assumption that the substance behaves as a perfect gas with  $\gamma = 1.4$  is indeed very good. Stroboscopic laser-schlieren records of the wave systems obtained when the incident shock Mach number was 4.06 are given in Fig. 9. The smoke-film traces of trajectories of the triple points are represented in Fig. 10. Their agreement with Fig. 8 is indeed most satisfactory.

#### THE CASE OF A CONDENSED EXPLOSIVE

Recently some records of condensed explosives resembling the smoke-film traces of gaseous detonations became available (7). The clearest evidence of such traces was obtained with nitromethane-acetone mixtures (8). These records were therefore adopted here as the test case for checking the applicability of our simple theory of collisions between triple points to wave phenomena in a condensed phase.

As a consequence of the dearth of available information on the thermodynamic properties of this medium at the high pressures achieved in detonation experiments, only a rough estimate of the Rankine-Hugoniot curves could be made at this time.

For incident shock fronts this is based on experimental records (9) according to which it appears that, in the regime of interest, the normal shock velocity,  $w_n$ , can be assumed to be linearly related to the induced particle velocity,  $u$ ; i.e.,

$$w_n = a_i + bu, \quad (11)$$

where  $a_i$ , the normal shock velocity corresponding to  $u = 0$ , is, of course, the measure of the local velocity of sound in the undisturbed medium.

As a consequence of Eq. (11), one obtains, by virtue of mechanical shock conditions,

$$\nu = \frac{w_n - u}{w_n} = 1 - \frac{1}{b} + \frac{1}{bM_n}, \quad (12)$$

and, with the use of Eq. (1),

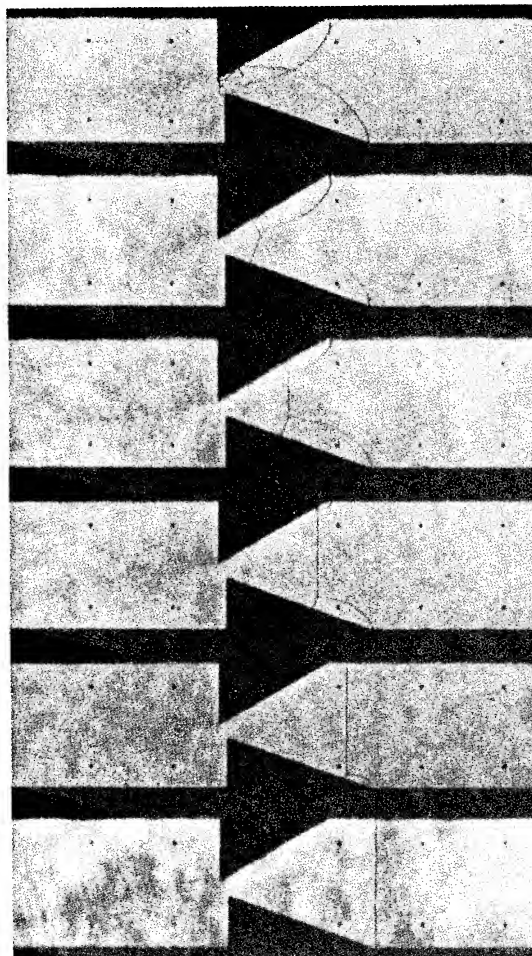


Fig. 9 - Stroboscopic laser-schlieren records of the generation of triple points by means of wedges in a shock tube and of an asymmetric collision between them

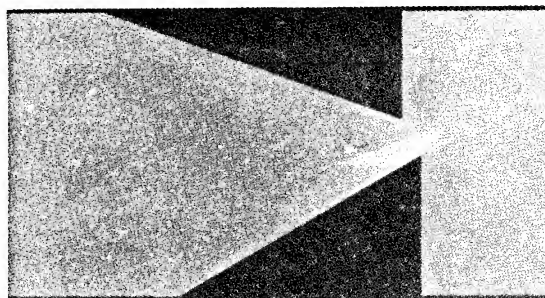


Fig. 10 - Smoke-film traces of the process recorded in Fig. 9

$$P = 1 + \frac{w_n u}{P_i v_i} = 1 + \frac{\Gamma_i}{b} M_n (M_n - 1). \quad (13)$$

Eliminating  $M_n$  from the above two equations, one gets the following expression for the Rankine-Hugoniot equation:

$$\frac{P-1}{1-\nu} [1 - b(1-\nu)]^2 = \Gamma_i \quad (14)$$

For  $\nu \leq 1$  the curve representing this equation on the  $P - \nu$  plane resembles a branch of a rectangular hyperbola. Its negative slope at  $\nu = 1$  is equal to  $\Gamma_i$ , similarly as in the case of the hyperbolic expression for the Rankine-Hugoniot curve, Eq. (6), while its asymptote at  $P = \infty$  is

$$\beta = 1 - \frac{1}{b} \quad (15)$$

For the evaluation of wave intersection processes one needs, in addition to the shock Hugoniot on the pressure-specific volume plane, information on the local velocity of sound in the shock compressed medium. Since, at present, there is no experimental evidence available in this connection, we could base our estimate at this juncture only on some general properties of condensed materials (6). From these we concluded that possibly the simplest expression for this purpose that is still compatible with the proper behavior of the substance is

$$a_j^2 = w_n^2 + cu^2 \quad (16)$$

where  $c$  is a constant. Noting that from mechanical shock conditions,

$$u^2 = (P-1)(1-\nu) p_i v_i \quad (17)$$

and taking advantage of Eqs. (1) and (5), Eq. (16) becomes

$$\Gamma_j = \frac{P-1}{P\nu(1-\nu)} + c \frac{(P-1)(1-\nu)}{P\nu} \quad (18)$$

whence, by virtue of Eq. (4) combined with Eqs. (5) and (9), one obtains

$$c = \frac{\sec^2 \alpha - M_i^2 - 1 + \nu^2}{(1-\nu)^2 M_j^2} \quad (19)$$

The value of  $c$  can be estimated from triple-point trajectories. A record of such trajectories, obtained with the use of a nitromethane-acetone mixture, is shown in Fig. 11, an enlargement of a segment of a record of Ref. 8. As they appear there, the traces of the triple points intersect each other at approximately right angles without a noticeable change in direction; i.e.,  $\alpha \cong \alpha' \cong 45^\circ$ . According to the observations made here in connection with Figs. 5 and 6, one can conclude from this that  $\Phi \cong 0$ , which means that the triple points are associated then with "arrowhead" intersections in the vicinity of  $M_j = 1$ . Under such circumstances Eq. (19) reduces to

$$c = \left( \frac{\nu}{1-\nu} \right)^2 \quad (20)$$

whence, as a consequence of Eq. (12), noting that  $M_n = M_i \cos \alpha$ ,

$$c = \left( \frac{b M_i}{M_i - \sec \alpha} - 1 \right)^2 \quad (21)$$

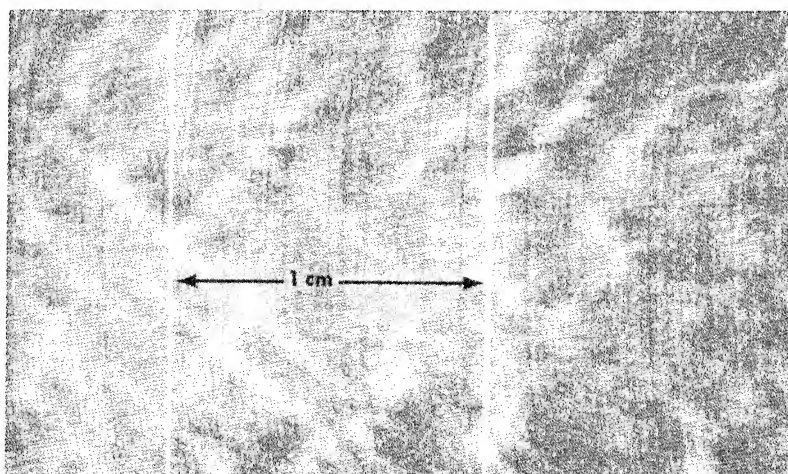


Fig. 11 - An enlargement of a segment of a record of Ref. 8 showing traces of triple-point trajectories in a nitromethane-acetone mixture

Now, for an 84:16 nitromethane-acetone mixture, a composition corresponding most closely to that used for experiments reported in Ref. 8,  $a_i = 1.89 \text{ mm}/\mu\text{sec}$  and  $b = 1.7$ , while the density at atmospheric pressure is  $\rho_0 = 1.081 \text{ g/cm}^3$  (9). From Eq. (1) it follows then that  $\Gamma_i = 38.4 \times 10^3$ , while according to Eq. (15),  $\beta = 0.412$ , and, assuming that, when the records were obtained from which it appeared that  $\alpha = 45^\circ$ , the triple points traveled, on the average, at a Mach number  $M_i = 4$ , one gets from Eq. (21)  $c = 2.655$ .

On the basis of these values, the shock polars and their auxiliary diagrams were computed as before, and the results are given in Plates 4, 5, and 6. Inserted in Plate 4 is a rarefaction polar and its auxiliary plots for  $\gamma = \Gamma = 7$ . The corresponding diagrams for the reflected shock are presented in the same scale in Plate 7. The latter corresponds to  $\Gamma = 7$ ,  $b = 1.7$  ( $\beta = 0.412$ ) and  $c = 2.655$ .

With the use of Plates 4-7, shock intersection processes which can occur in the medium under study can be now evaluated. Thus, similarly as before, one obtains a master diagram on the plane of collision invariants, Fig. 12, and the  $\theta = \theta(\Phi)$  plot, Fig. 13, which was deduced from Fig. 12 (with the help of Plates 4 and 5), yielding finally the trajectory angles  $\alpha = \alpha(\Phi)$  and their change due to collisions,  $\alpha - \alpha'$ , Fig. 14.

It should be noted in this connection that, as a consequence of the large difference in the value of  $\Gamma$  across the incident shock, all the solutions given in Figs. 12-14 correspond to choked "arrowhead" intersections, the pattern represented by case (g) in Figs. 2 and 3. (It is for this reason that one needs the rarefaction

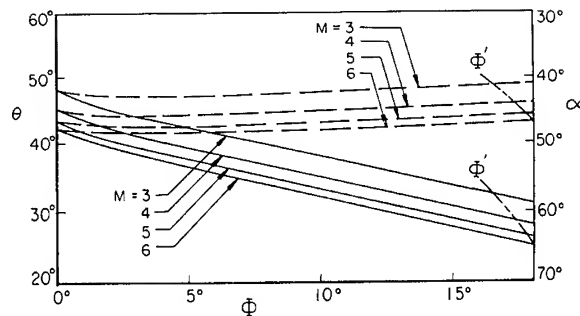


Fig. 13 - Solutions of collision processes corresponding to Fig. 12 expressed in terms of shock incidence angles

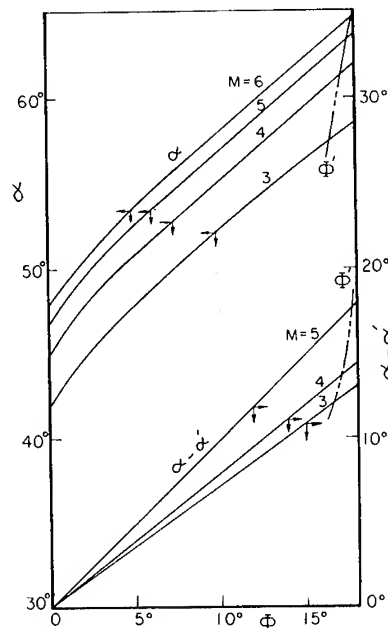


Fig. 14 - Solutions of collision processes corresponding to Fig. 12 expressed in terms of the triple-point trajectory angles

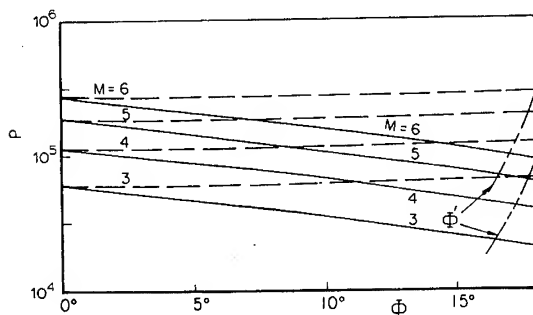


Fig. 12 - Solutions of collision processes between triple points on the plane of collision invariants for an 84:16 nitromethane-acetone mixture expressed in terms of  $\Gamma_i = 38.4 \times 10^3$ ,  $b = 1.7$  ( $\beta = 0.412$ ) and  $c = 2.655$

polars included in Plate 4.) The limit lines shown on these diagrams denote the first instant when the regular reflection can be also obtained, so that to the right of these lines there is a regime of ambiguity in that two types of dynamically compatible solutions are possible. Since, however, the regular reflection, corresponding in this case to solution (c') in Fig. 3, has at first a pressure behind the reflected shock higher than that behind the "arrowhead" intersection, the latter intersection is more likely to occur. This is due to the

fact that, in the course of detonation, shock waves appear as fronts of decaying blast waves, and these, as a rule, are associated with rarefaction, favoring thus the establishment of a wave pattern that corresponds to a lower pressure.

As it appears from Fig. 14, the approximate rule of Eq. (10) is not as good now as it was in the case of the perfect gas of Fig. 7. However in the vicinity of  $\phi = 0$ , one still has  $\alpha \approx \alpha'$ . Since the experimentally recorded traces are quite fuzzy, one cannot discern a 1 to 2° change in the direction of  $\alpha$ . Let us take for example  $\alpha - \alpha' = 1^\circ$  at  $M_1 = 4$ . The wave configurations immediately before and after triple-point collision, evaluated for these conditions from Figs. 12-14, are shown in Fig. 15. Denoted there are pressure levels in the various flow regimes. As it appears then, the concentrated vortices induced by the slip-line discontinuities are in regions where the pressure is about 2 kbar higher than behind the incident shock. Since, as it was pointed out in the introduction, this is followed by rarefaction due to the decaying blast wave structure of the flow field, the high pressures can exist only in the immediate vicinity of the triple point. One has thus pressure peaks of an order of 2 kbar concentrated at the triple-point trajectories—a phenomenon certainly of sufficient intensity to produce the recorded traces. This result can be considered as providing as good a proof as one can wish at this juncture of the essential correctness of our theory in its applicability to a condensed explosive.

## CONCLUSIONS

In a multiwave structure of a detonation wave, shock intersections form basic elements. Concomitant to this is the fact that collisions between intersection points play a dominant role in the dynamic aspects of the self-sustenance of detonations. Presented here was a simple theory of wave intersections and their collisions that applies to gaseous media as well as to condensed explosives, covering a full scope of possible wave configurations. It appears from this that the prevalent type of wave pattern in gaseous media is a Mach intersection, while in the condensed explosives it is the "arrowhead" intersection.

The theoretical results are in good agreement with experimental observations, suggesting that collisions between intersections should be recognized as valuable diagnostic means for the investigation of the structure and self-sustenance of detonations in condensed

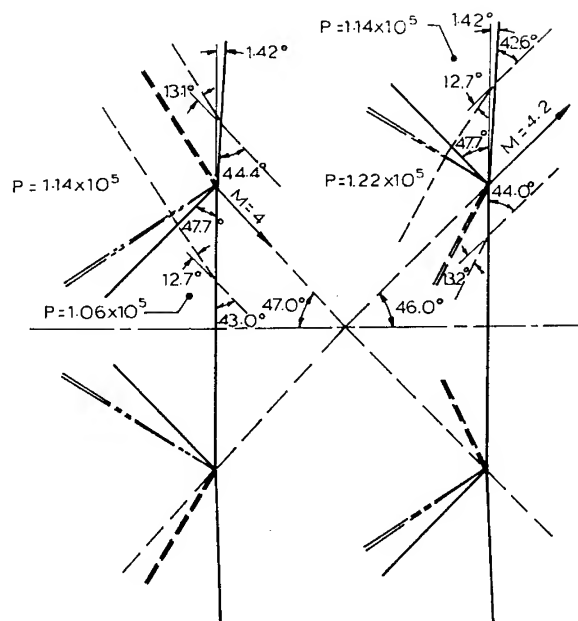


Fig. 15 - Estimated shock intersection patterns in a detonating nitromethane-acetone mixture

explosives, as much as these means have been already exploited in studies on gaseous detonations.

## REFERENCES

1. R. A. Strehlow, "Gas Phase Detonations: Recent Developments," *Combustion and Flame*, Vol. 12, No. 2, pp. 81-101, April 1968.
2. J. H. Lee, R. I. Soloukhin, and A. K. Oppenheim, "Current Views on Gaseous Detonations," *Astronautica Acta*, Vol. 14, No. 5, pp. 565-584, June 1969.
3. R. Courant and K. O. Friedrichs, *Supersonic Flow and Shock Waves*, p. 318, Interscience Publishers, Inc., New York, 1948.
4. A. H. Shapiro, *The Dynamics and Thermodynamics of Compressible Fluid Flow*, Vol. 1, p. 553, The Ronald Press Company, New York, 1953.
5. A. K. Oppenheim, J. J. Smolen, and L. J. Zajac, "Vector Polar Method for the Analysis of Wave Intersections," *Combustion and Flame*, Vol. 12, No. 1, pp. 63-76, Feb. 1968.

6. P. A. Urtiew, "Reflected Shock-Velocity Particle-Velocity Relationship in Solids," J. Applied Physics, Vol. 40, No. 10, pp. 3962-3967, Sept. 1969.
7. P. A. Urtiew, A. S. Kusubov, and R. E. Duff, "Cellular Structure of Detonation in Nitromethane," Combustion and Flame, Vol. 14, No. 1, pp. 117-122, Feb. 1970.
8. P. A. Urtiew and A. S. Kusubov, "Wall Traces of Detonation in Nitromethane-Acetone Mixtures," in this symposium.
9. A. N. Dremin and O. K. Rozanov, "Measurement of Shock Adiabats in Nitromethane-Acetone Mixtures," Bulletin of the USSR Academy of Sciences, Division of Chemical Sciences, No. 8, pp. 1417-1419, Aug. 1964.

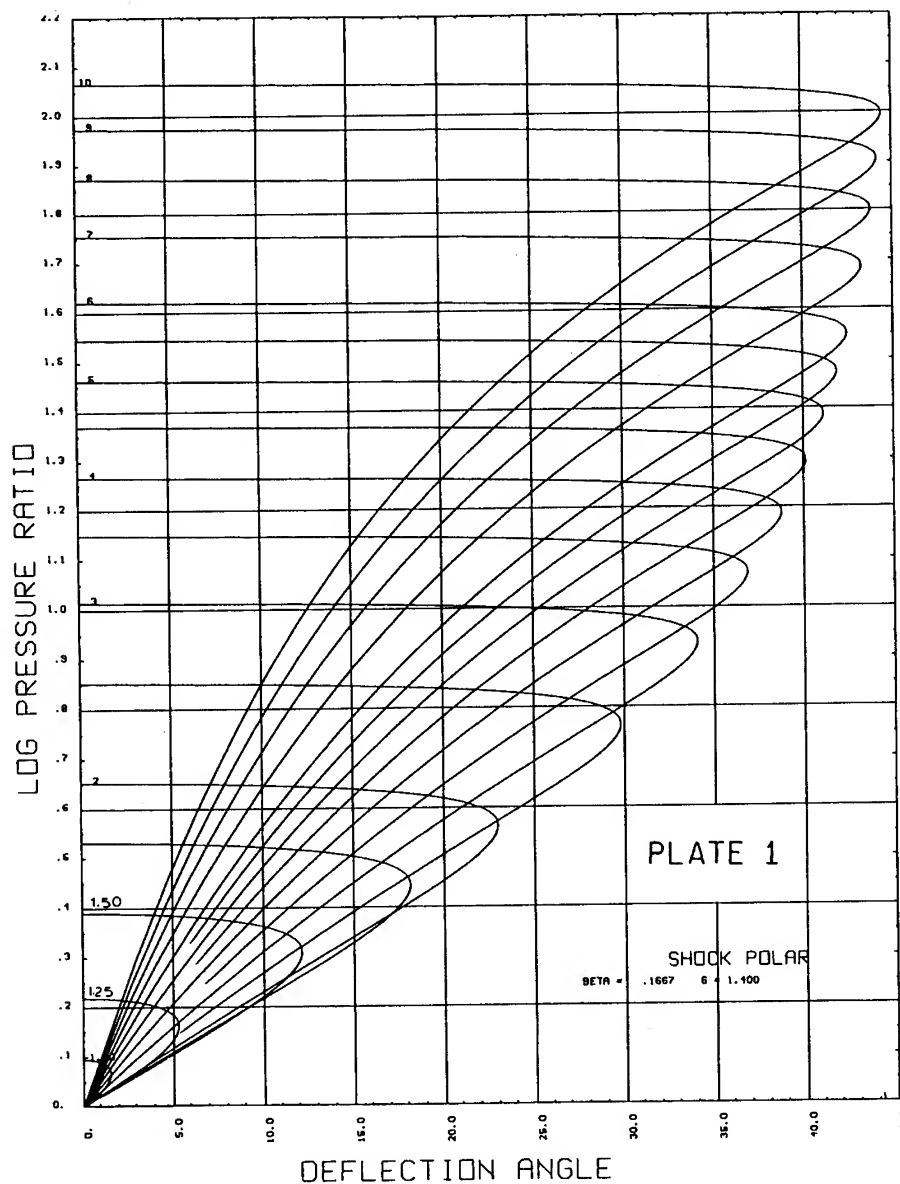
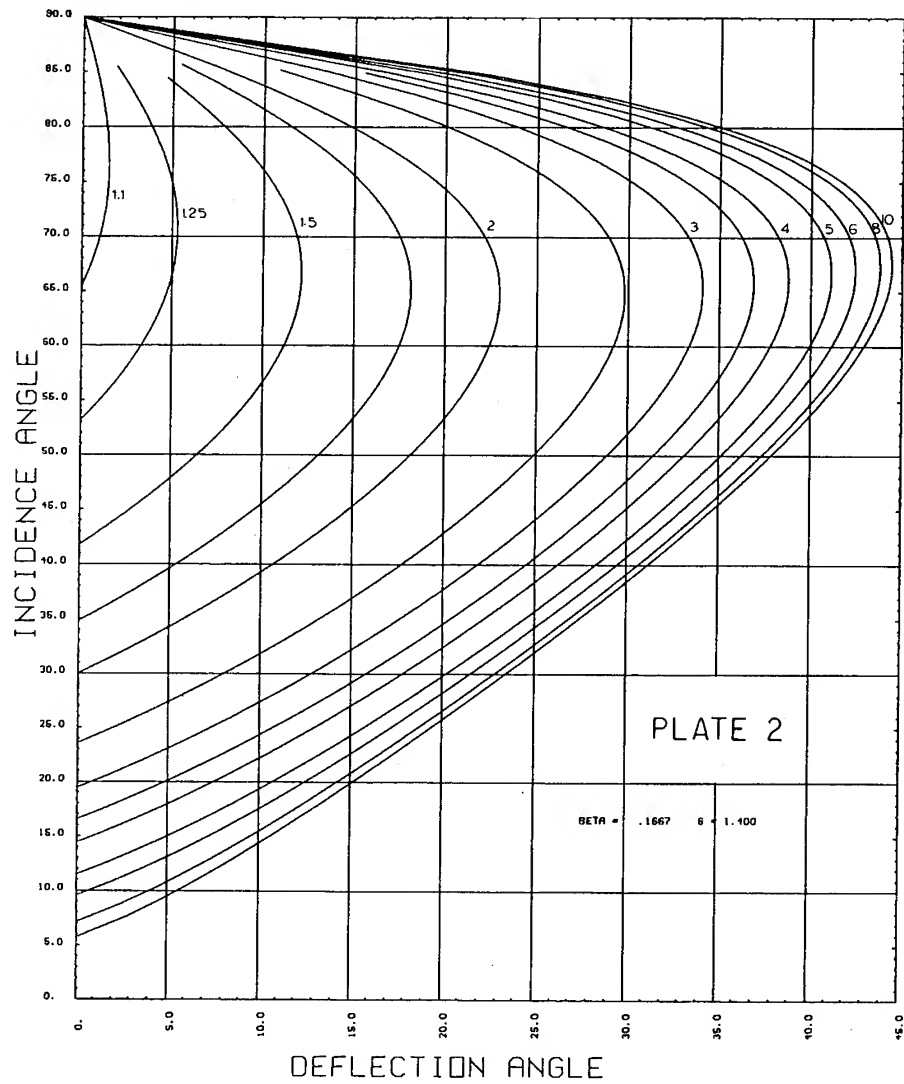
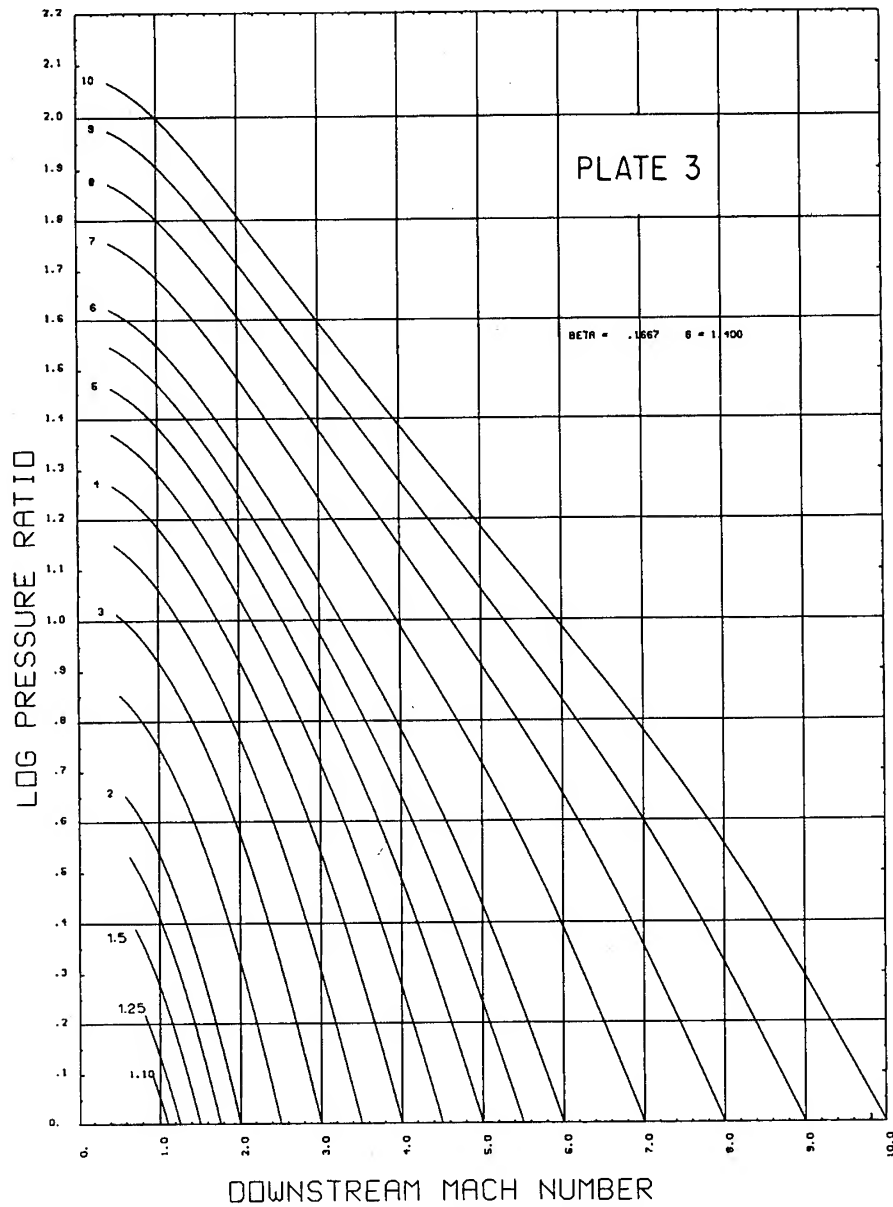


Plate 1 - Shock polars for the case of a perfect gas with  $\gamma = 1.4$



Plate 2 - Auxiliary  $\theta = \theta(\delta)$  plot for Plate 1

Plate 3 - Auxiliary  $M_j = M_j(P)$  plot for Plate 1

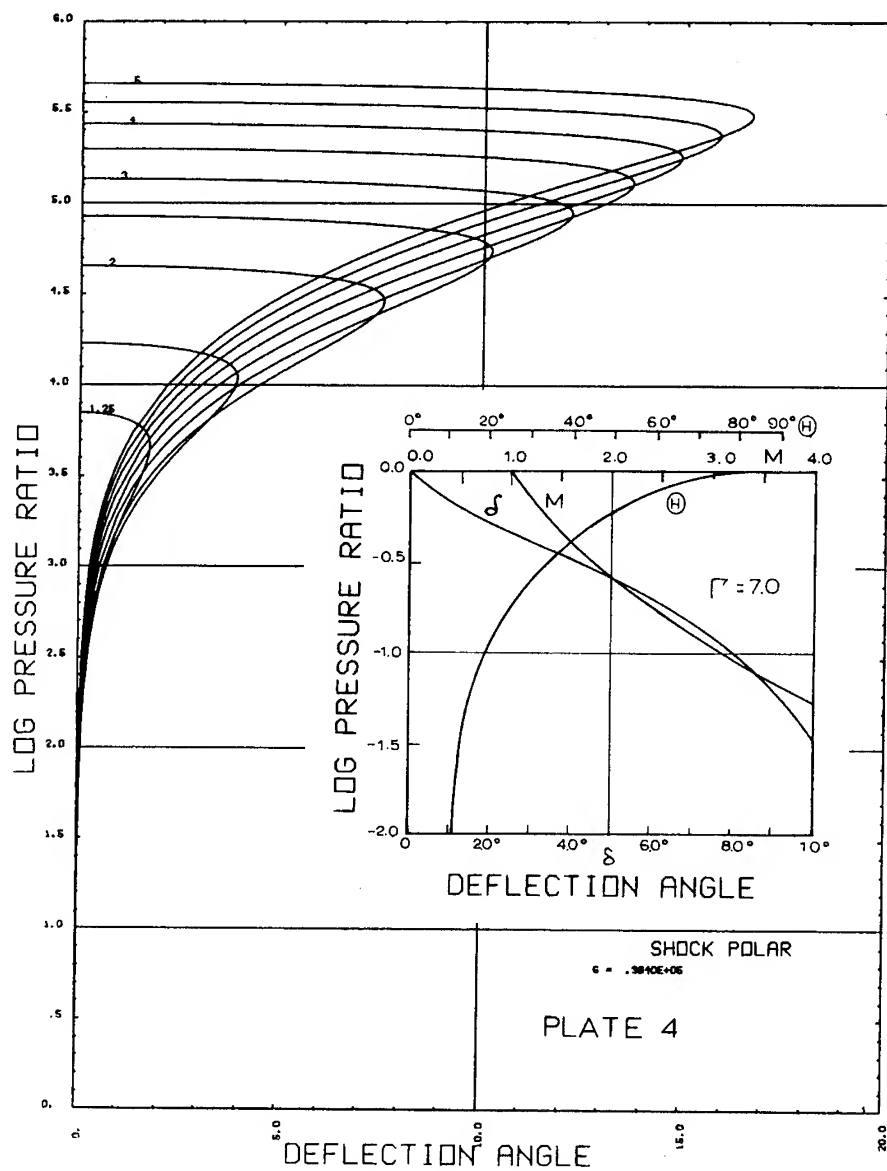
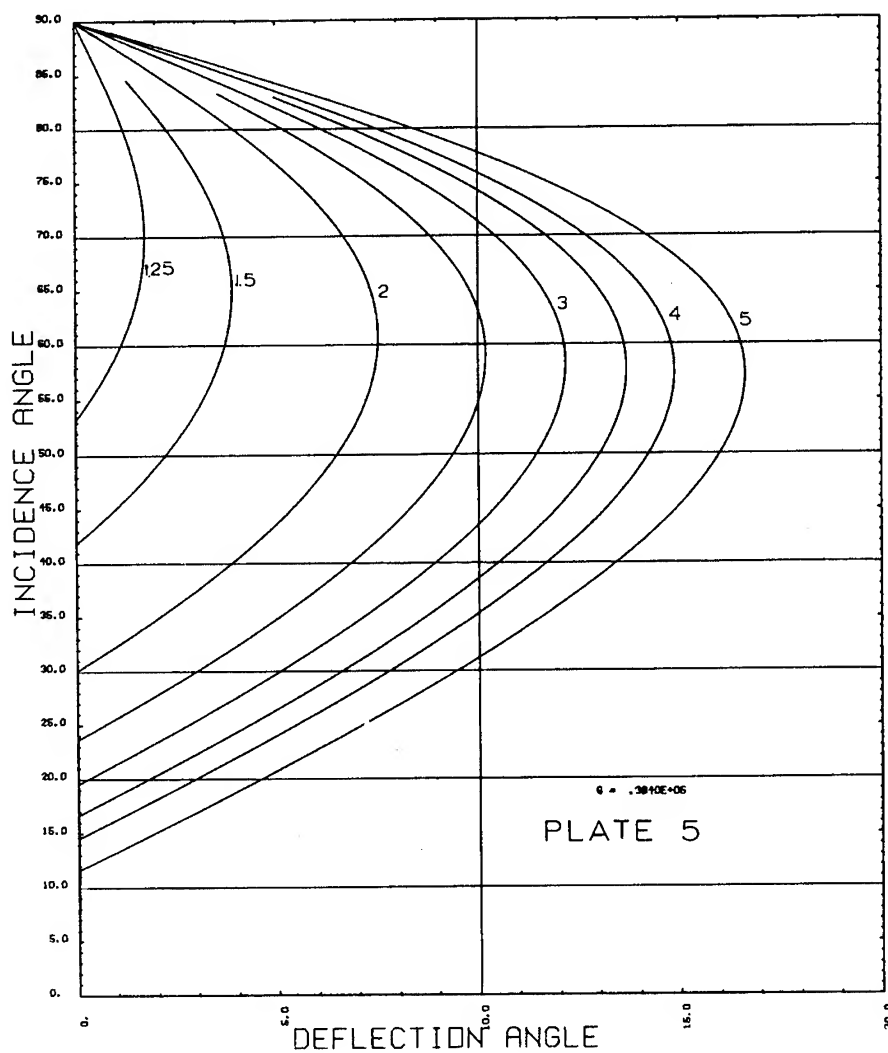
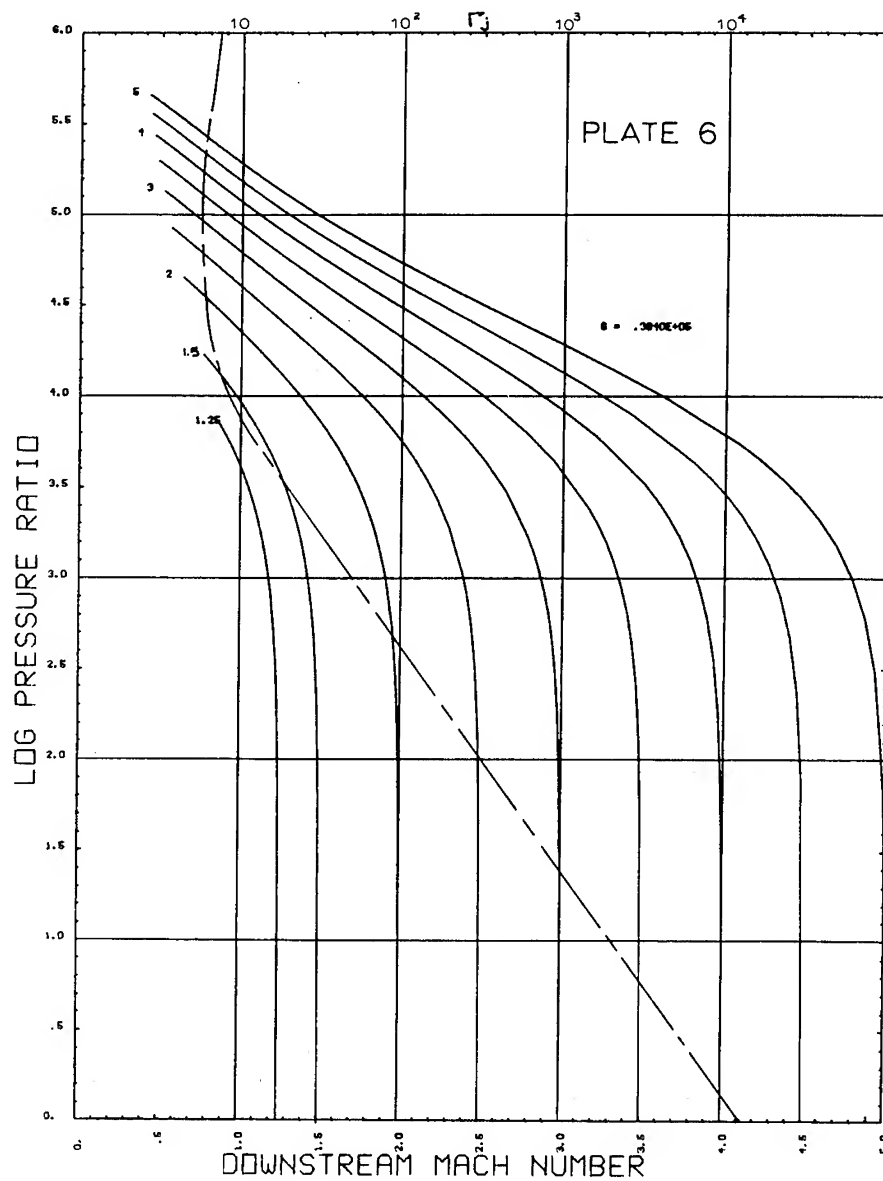


Plate 4 - Shock polars for the case of an 84:16 nitromethane-acetone mixture expressed in terms of  $\Gamma_i = 38.4 \times 10^3$ ,  $b = 1.7$  ( $\beta = 0.412$ ) and  $c = 2.655$ ; insert: rarefaction polar for  $\gamma = \Gamma = 7$

Plate 5 - Auxiliary  $\theta = \theta(\delta)$  plot for Plate 4

Plate 6 - Auxiliary  $M_j = M_j(P)$  plot for Plate 4

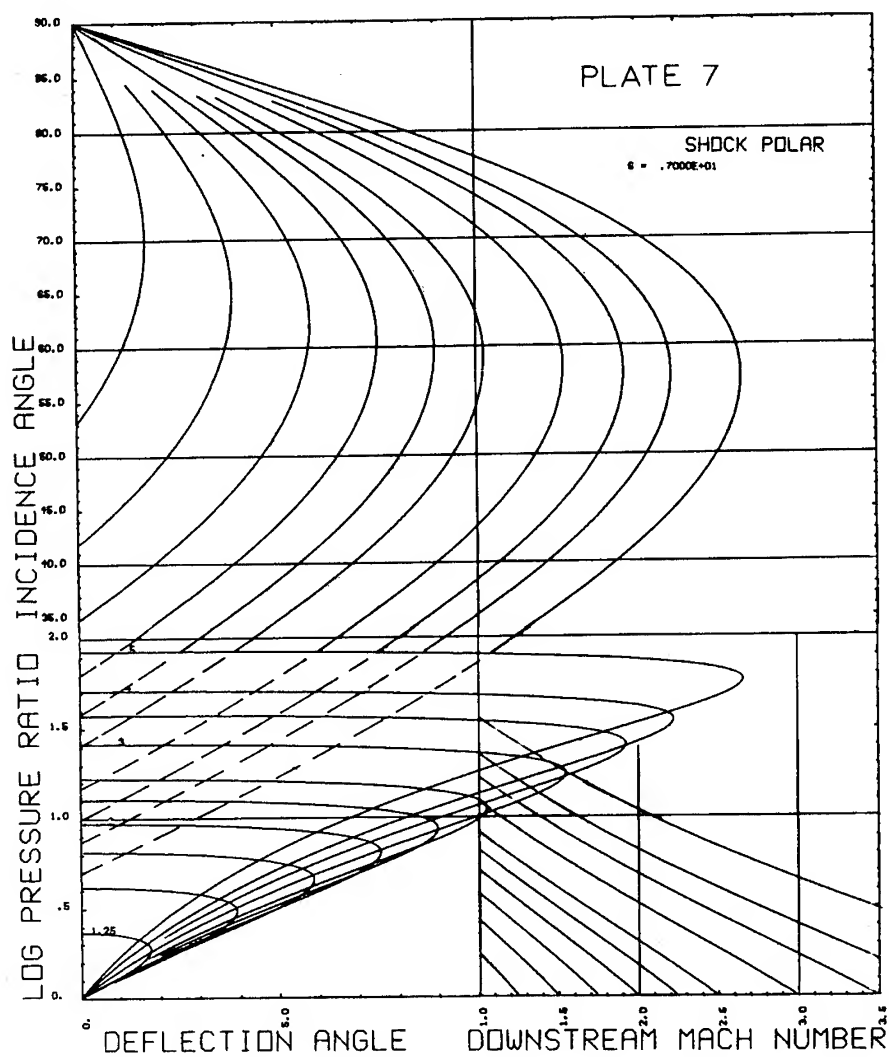


Plate 7 - Reflected shock polars and the auxiliary diagrams for the case of an 84:16 nitromethane-acetone mixture expressed in terms of  $\Gamma_1 = 7$ ,  $b = 1.7$  ( $\beta = 0.412$ ) and  $c = 2.655$

# METAL ACCELERATION BY COMPOSITE EXPLOSIVES

M. Finger, H. C. Hornig, E. L. Lee, J. W. Kury  
*Lawrence Radiation Laboratory, University of California  
Livermore, California 94550*

## ABSTRACT

The metal accelerating ability of plastic-bonded explosives (PBX) containing aluminum, inorganic oxidizers, or mixtures of the two has been investigated. These composite formulations were prepared by replacing a portion of the HMX in conventional PBX's with aluminum, ammonium perchlorate, or potassium perchlorate. Thermodynamic-hydrodynamic code calculations were used to model extremes in performance for these systems. Comparison with experimental results enabled us to infer rates and extent of reactions of the additives.

## INTRODUCTION

We have extended our previous work (1) on the metal accelerating ability of simple, fast reacting explosives to include a variety of composite explosives; that is, explosives containing inorganic oxidizers and fuels. Gordon (2) was the first to apply the term composite to such explosives. These metal- and oxidizer-containing formulations release their chemical energy over a much longer time scale than simple explosives, finding wide use as a result in air blast, underwater, and cratering applications. However, reaction rates of the composite explosives generally have been too slow for effective use in metal acceleration. In this paper we describe the calculated and experimental performance of plastic-bonded, HMX-based composites. Results indicate that these materials can be used advantageously for metal acceleration.

## MODEL FOR DETONATION OF COMPOSITE EXPLOSIVES

The generally accepted model for the physical and chemical processes occurring in the detonation of a composite explosive involves ignition followed by reaction between oxidizer and fuel. These steps produce heat, and gaseous and solid products at high pressure. Transfer of heat to the gas and expansion of the products

then results in useful work. For simple explosives such as HMX or Viton-bonded HMX, the chemical reactions are complete in less than a microsecond (3). For ammonium nitrate-aluminum-water slurry explosives, these reactions take many milliseconds (4,5). Adding HMX to a slow reacting composite formulation can decrease the reaction time to the range 1 to 100  $\mu$ sec. Figure 1 compares the approximate range of chemical reaction times for these systems with the maximum available time for various applications.

It is presently impossible to calculate the behavior of composite explosives. The complex nature of the calculation, for example of an HMX-ammonium perchlorate-aluminum-Viton composite, is best illustrated by considering the actual processes involved. These are (2, 6-10):

1. Shock ignition and reaction of HMX
2. Decomposition and reaction of ammonium perchlorate
3. Heating to ignition of aluminum
4. Diffusion and mixing of products
5. Oxidation of aluminum and HMX detonation products by any of several sources of oxygen, including excess oxygen from the ammonium perchlorate

---

This work performed under the auspices of the U.S. Atomic Energy Commission.

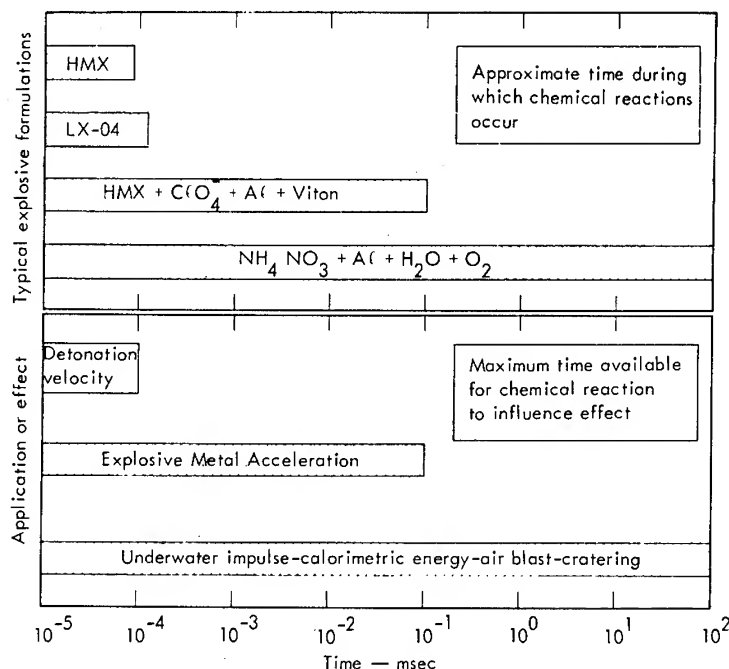


Fig. 1 - Approximate variation of reaction times for typical explosive formulations

6. Heat transfer from condensed products such as  $\text{Al}_2\text{O}_3$ , to the expanding gaseous detonation products.

Accurate P-V-T equations of state, diffusion coefficients, and kinetic data are unavailable for predicting and optimizing the performance of this system.

General considerations, however, do let us identify the major factors influencing the actual rates of reaction that determine performance. For instance, the smaller the particles of aluminum and ammonium perchlorate, the faster the reaction. (Practical formulations can be made with particles a few microns in size.) Also, the higher the initial detonation temperature, the faster the rate. This implies that a minimum amount of nonenergetic binder is desirable. It also means that a detonable additive like ammonium perchlorate should react faster than a metal perchlorate.

In addition to these obvious general guidelines, we have gained a semi-quantitative insight into the effect of possible reactions on performance by using the thermodynamic-hydrodynamic code RUBY (11). As previously shown, RUBY isentropic expansion calculations are erroneous on an absolute basis, but on a relative basis they accurately predict the behavior of simple explosives (1). Calculations

for explosives under test were thus compared to calculations for pure HMX, and the same relative comparison was also made for the experimental data. (See Ref. 1, page 11, for the procedure used.) We ran calculations allowing complete chemical reaction and others where all or part of an ingredient remained inert. In this way we were able to model the effect of partial reactions commonly occurring in composite explosives. Calculational results are presented in the discussion section, in terms of the fraction of additive reacted. The actual fractions were determined by experimental performance measurements.

## EXPERIMENTAL RESULTS

In all, 24 composite explosives were investigated. Detonation velocity and metal accelerating ability were measured in our standard cylinder test (1). Detonation pressures were determined (12) by using the technique developed by Davis and Craig (13). Table 1 summarizes the composition, density, detonation velocity, and detonation pressure data. Table 2 presents cylinder test results.

## DISCUSSION

### Aluminum-Containing Explosives

We investigated the effect of adding 5 $\mu$  aluminum to our standard HMX-Viton explosives:



TABLE 1  
Explosive Formulations and Properties

Explosive	Formulation			$\rho$ (g/cc)	Detonation Velocity (mm/ $\mu$ sec)		P (kbar)
	Wt %	Composition <sup>a</sup>	Vol %		1 in.	2 in.	
HMX <sup>b</sup>	100	HMX	99.6	1.894	9.11		
LX-10 <sup>b</sup>	95/5	HMX/Viton	93/5.2	1.862	8.82		
LX-07 <sup>b</sup>	90/10	HMX/Viton	88/10.2	1.860	8.65		
Aluminum Systems							
RX-04-DS	81.0/9.9/9.1	HMX/Al, 5 $\mu$ /Viton	83.1/7.1/9.8	1.918		8.52	350
LX-04 <sup>b</sup>	85/15	HMX/Viton	83.5/15.4	1.866	8.47	8.48 <sup>c</sup>	
RX-04-BM	81.6/4/14.4	HMX/Al, 5 $\mu$ /Viton	81/2.8/15	1.893	8.44		
RX-04-BN	79/6.6/14.3	HMX/Al, 5 $\mu$ /Viton	79.6/4.7/15	1.913	8.41		
HAV-10	74.7/10.6/14.7	HMX/Al, 5 $\mu$ /Viton	76/7.6/15.5	1.930	8.33		
RX-04-BO	72.7/13.3/14.0	HMX/Al, 5 $\mu$ /Viton	75/9.6/15	1.954	8.31		
HAV-20	65.7/18.9/15.4	HMX/Al, 5 $\mu$ /Viton	69/14/16.7	1.99	8.16		
RX-04-BT <sup>b</sup>	76/10/14	HMX/LiF/Viton	77/7.3/15.3	1.936	8.35		
LX-11 <sup>b</sup>	80/20	HMX/Viton	79/21	1.876	8.32		
Perchlorate Systems							
RX-22-AG	73.6/26.4	HMX/LP, 5 $\mu$	77/22	1.988	8.43		350
RX-11-BA	51/39/10	HMX/AP, 5 $\mu$ /Viton	51/38/10	1.89		8.12	
RX-04-AU <sup>b</sup>	92/8	HMX/PE	83.5/14.3	1.719	8.63		~325
RX-11-AF	52/43/5	HMX/KP, 3 $\mu$ /PE	55/34/11	1.994	7.63	7.76	
RX-11-AI	52/43/5	HMX/KP, 10 $\mu$ /PE	55/34/11	1.985		7.63	~305
RX-11-AJ	52/43/5	HMX/KP, 44 $\mu$ /PE	55/34/11	1.992	7.46	7.54	
RX-18-AH <sup>b</sup>	71/29	HMX/EDNP	62/37	1.66	7.77	7.69 <sup>d</sup>	270
RX-18-AB	51/20/29	HMX/AP, 5 $\mu$ /EDNP	45/17/38	1.67	7.45	7.31 <sup>d</sup>	~230
RX-18-AE	51/20/29	HMX/AP, 90 $\mu$ /EDNP	45/17/38	1.67	7.19	7.09 <sup>d</sup>	
RX-18-AG	51/20/29	HMX/AP, 200 $\mu$ /EDNP	45/17/38	1.67	7.15	7.03 <sup>d</sup>	235
RX-18-BA	31/45/24	HMX/KP, 3 $\mu$ /EDNP	30/35/35	1.87	6.66		
A-589 <sup>b</sup>	86/14	HMX/PB	75/25	1.66	8.26	8.29	275
A-590	80.3/5.9/13.8	HMX/AP, 6 $\mu$ /PB	70/5/25	1.66	8.19		275
A-591	69/17/14	HMX/AP, 6 $\mu$ /PB	60/15/25	1.67	7.96	8.05	~275
A-592	57/29/14	HMX/AP, 6 $\mu$ /PB	50/25/25	1.67	7.63	7.76	260
RX-18-AJ	52.6/34.7/12.7	HMX/KP, 15 $\mu$ /PB	50/25/25	1.82	7.00	7.13	~250
RX-11-AW	51/35/14	HMX/KP, 3 $\mu$ /PB	48/25/27	1.78	6.94	7.13	220
RX-11-AX	51/35/14	HMX/KP, 9 $\mu$ /PB	48/25/27	1.78		7.17	220
RX-11-AY	33.4/53.4/13.2	HMX/KP, 3 $\mu$ /PB	33/40/27	1.88		6.25	180
RX-11-AZ	33.4/53.4/13.2	HMX/KP, 9 $\mu$ /PB	33/40/27	1.88		6.11	165
Aluminum and Perchlorate System							
RX-25-AA	22/58/10/10	HMX/AP, 5 $\mu$ /Al, 5 $\mu$ /Viton	23/59/7.4/10.4	1.97		6.54	

<sup>a</sup>Compositions are as follows: AP =  $\text{NH}_4\text{ClO}_4$ ; KP =  $\text{KClO}_4$ ; LP =  $\text{LiClO}_4$ ; PE = polyethylene; EDNP = ethyl 4,4-dinitropentanoate with 1% Cab-O-Sil ( $\text{SiO}_2$ ) gelling agent; PB = hydroxy terminated polybutadiene; Viton = vinylidene fluoride-hexafluoropropylene copolymer.

<sup>b</sup>Reference formulation.

<sup>c</sup>For infinite diameter (not this work).

<sup>d</sup>For 0.55-in. diameter.

TABLE 2  
Cylinder Test Results for Explosive Formulations

Explosive	Test Diam <sup>a</sup> (in.)	Time ( $\mu$ sec) at $R - R_0$ (mm) =						Velocity (mm/ $\mu$ sec) at $R - R_0$ (mm) =					
		5	10	15	19	26	32	5	10	15	19	26	32
HMX <sup>b</sup>	1	3.75	6.66	9.41	11.57	15.28	18.40	1.63	1.77	1.84	1.87	1.91	1.93
LX-10 <sup>b</sup>	1	3.87	6.88	9.73	11.93	15.72	18.92	1.59	1.72	1.79	1.82	1.86	1.88
LX-07-1 <sup>b</sup>	1	3.99	7.09	10.02	12.30	16.20	19.48	1.53	1.67	1.74	1.77	1.82	1.84
Aluminum Systems													
RX-04-DS	1	4.09	7.18	10.09	12.33	16.15	—	1.52	1.68	1.76	1.80	1.85	—
	2	4.13	7.21	10.10	12.33	16.12	—	1.52	1.69	1.77	1.81	1.87	—
LX-04-1 <sup>b</sup>	1	4.12	7.30	10.32	12.67	16.71	20.12	1.52	1.62	1.68	1.72	1.76	1.78
	2	4.07	7.26	10.27	12.62	16.66	20.06	1.50	1.62	1.69	1.71	1.75	1.77
RX-04-BM	1	4.17	7.34	10.35	12.70	16.71	20.10	1.50	1.62	1.68	1.72	1.76	1.79
RX-04-BN	1	4.24	7.46	10.49	12.84	16.85	20.20	1.50	1.61	1.68	1.72	1.77	1.80
HAV-10	1	4.25	7.48	10.50	12.83	16.79	20.11	1.47	1.61	1.70	1.74	1.79	1.82
RX-04-BO	1	4.31	7.62	10.70	13.09	17.15	20.56	1.45	1.58	1.65	1.69	1.76	1.77
HAV-20	1	4.51	7.95	11.10	13.52	17.58	20.97	1.40	1.53	1.63	1.68	1.76	1.78
RX-04-BT <sup>b</sup>	1	4.28	7.70	10.93	13.46	17.80	21.46	1.43	1.51	1.57	1.59	1.63	1.65
LX-11 <sup>b</sup>	1	4.23	7.51	10.62	13.05	—	—	1.46	1.57	1.63	1.66	—	—
Perchlorate Systems													
RX-22-AG	1	3.86	6.86	9.67	11.85	15.57	18.71	1.57	1.74	1.81	1.86	1.90	1.93
RX-11-BA	1	4.10	7.24	10.22	12.53	16.48	19.81	1.48	1.65	1.71	1.75	1.79	1.81
	2	4.03	7.13	10.05	12.32	16.21	19.48	1.52	1.67	1.74	1.78	1.82	1.84
RX-04-AU <sup>b</sup>	1	4.27	7.57	10.67	13.08	17.22	20.70	1.43	1.58	1.64	1.67	1.71	1.73
RX-11-AF	1	4.25	7.47	10.49	12.82	—	—	1.50	1.61	1.69	1.73	—	—
	2	4.09	7.20	10.17	12.50	16.40	—	1.54	1.65	1.70	1.75	—	—
RX-11-AI	2	4.39	7.64	10.71	13.14	17.14	20.53	1.48	1.60	1.66	1.70	1.75	1.77
RX-11-AJ	1	4.65	8.26	11.57	14.13	—	—	1.35	1.46	1.54	1.58	—	—
	2	4.51	7.93	11.11	13.58	17.76	—	1.40	1.52	1.59	1.65	1.70	—
RX-18-AH <sup>b</sup>	1	4.63	8.18	11.52	14.10	18.52	22.24	1.33	1.46	1.53	1.57	1.61	1.62
RX-18-AB	1	4.52	8.03	11.35	13.91	18.29	21.99	1.39	1.47	1.54	1.58	1.61	1.63
RX-18-AE	1	4.85	8.50	11.86	14.48	18.97	22.73	1.28	1.43	1.51	1.54	1.58	1.61
RX-18-AG	1	5.15	8.98	12.53	15.26	19.94	23.86	1.22	1.36	1.44	1.48	1.52	1.54
RX-18-BA	1	4.85	8.46	11.80	14.36	18.78	22.47	1.29	1.45	1.53	1.57	1.61	1.63
A-589 <sup>b</sup>	1	4.55	8.03	11.31	13.85	18.18	21.83	1.36	1.49	1.56	1.59	1.64	1.65
	2	4.61	8.13	11.43	13.99	18.37	22.04	1.36	1.48	1.55	1.58	1.62	1.64
A-590	1	4.50	7.98	11.23	13.75	18.07	21.71	1.35	1.49	1.57	1.60	1.63	1.67
A-591	1	4.51	8.01	11.24	13.76	18.03	21.63	1.37	1.50	1.57	1.61	1.66	1.67
	2	4.35	7.70	10.81	13.22	17.34	—	1.44	1.56	1.64	1.68	1.71	—
A-592	1	4.60	8.09	11.34	13.85	18.15	—	1.36	1.49	1.57	1.60	1.65	—
	2	4.48	7.85	11.03	13.49	17.66	—	1.44	1.54	1.61	1.64	1.72	—
RX-18-AJ	1	5.29	9.36	13.13	16.05	21.00	—	1.16	1.29	1.35	1.39	1.44	—
	2	5.25	9.19	12.83	15.65	—	—	1.21	1.33	1.40	1.44	—	—
RX-11-AW	1	5.21	9.08	12.69	15.45	—	—	1.23	1.35	1.42	1.46	—	—
	2	4.98	8.66	12.08	14.74	19.24	—	1.23	1.41	1.48	1.52	1.58	—
RX-11-AX	2	5.02	8.73	12.17	14.83	—	—	1.24	1.41	1.48	1.53	—	—
RX-11-AY	2	5.30	9.08	12.58	15.28	19.88	—	1.22	1.39	1.46	1.50	1.55	—
RX-11-AZ	2	6.21	10.65	14.67	17.75	22.86	—	1.08	1.19	1.28	1.32	1.41	—
Aluminum and Perchlorate System													
RX-25-AA	1	5.66	9.42	12.81	15.39	19.70	—	1.22	1.42	1.52	1.58	1.65	—
	2	4.78	8.16	11.33	13.74	17.83	21.22	1.34	1.53	1.63	1.68	1.74	1.79

<sup>a</sup>2-in.-diam cylinder tests are normalized to 1-in.-diam by listing  $0.5 \times$  actual  $R - R_0$ ,  $0.5 \times$  actual time, and velocity unchanged.

<sup>b</sup>Reference formulation.

LX-04 and LX-07. Figure 2 summarizes the cylinder test performance of LX-04 with various amounts of aluminum added. The curves in this figure are relative RUBY calculations for the extremes—aluminum inert or completely reacted. A good check on the calculation for aluminum inert was obtained by testing a formulation containing LiF instead of aluminum. The RUBY calculations showed that with 10 vol % aluminum, the difference in energy between fully reacted and inert is almost 30%.

Experimental cylinder test points relative to HMX are shown in Fig. 2 at three stages in the expansion of the 1-in.-diam cylinder. From this figure, two observations are apparent. First, the optimum percentage of aluminum predicted by the calculation is approximately correct. This optimum results from a tradeoff between total heat of detonation and moles of gas available to do the work. Second, there is a definite time dependence to the energy release. At early expansion of the cylinder, the aluminum is almost inert. Later, progressively larger fractions of the aluminum have reacted. Assuming a linear relationship between the fraction of aluminum reacted and the increased performance, we obtained the results presented in Fig. 3. The formula used for computing the fraction reacted is:

$$\text{Fraction reacted} = \frac{E_R - E_{\min}}{E_{\max} - E_{\min}}$$

where

$E_R$  = Experimental relative energy (wall velocity of test)<sup>2</sup>/(wall velocity of HMX)<sup>2</sup> at the appropriate  $R - R_0$  (cylinder wall radius);

$E_{\max}$  = RUBY-calculated relative energy release for the maximum reaction at  $V/V_0$  appropriate to the above  $R - R_0$ ;

$E_{\min}$  = RUBY-calculated relative energy release for the minimum reaction at  $V/V_0$  appropriate to the above  $R - R_0$ ; and

$V/V_0$  = relative volume of detonation products.

RUBY calculations were also run for HMX-aluminum compositions containing only 10% Viton as binder. This system again showed a maximum performance in the range 7-12 vol % aluminum. We experimentally investigated a composition containing 7 vol % aluminum (RX-04-DS) in both 1-in.-diam and 2-in.-diam

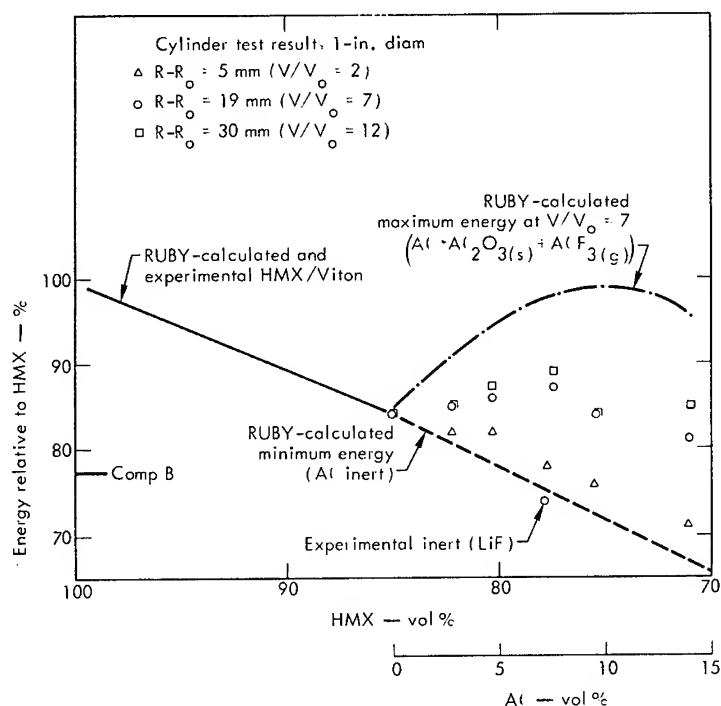


Fig. 2 - Performance of aluminized LX-04

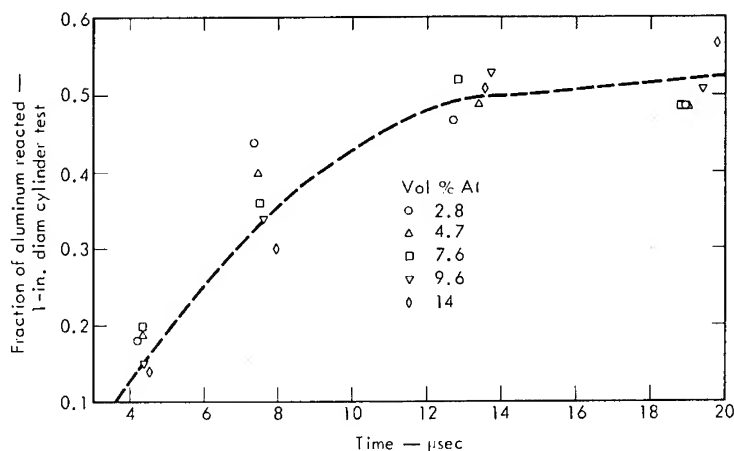


Fig. 3 - Rate of aluminum reaction in aluminized LX-04

scaled cylinder tests. The diameter effect was approximately 1% in wall velocity. The results listed in Table 2 show that ~75% of the aluminum reacted during the time of the 2-in.-diam experiment.

#### Perchlorate-Containing Explosives

Perchlorates, because of their high density and excess oxygen, have potential as additives in propellant and explosive formulations. The RUBY-calculated performance of HMX with lithium perchlorate (LP), ammonium perchlorate (AP), and potassium perchlorate (KP), Fig. 4, indicated that all these systems are potentially very energetic. As a result, we investigated their metal accelerating ability as functions of perchlorate particle size and amount of plastic binder. The results are discussed below. It should be noted that our choice of binders was somewhat limited because of stability and sensitivity considerations, and that in general all the formulations were fairly sensitive.

**HMX-Ammonium Perchlorate-Viton.** The explosive RX-11-BA containing 38 wt % 5μ perchlorate represents the most energetic ammonium perchlorate explosive tested. Figure 5 shows how the energy of this system, containing a minimum of binder, varies with composition. Figure 6 shows the actual wall velocities relative to HMX for scaled 1-in.-diam and 2-in.-diam cylinder tests, indicating a diameter effect of about 2% in wall velocity. This small diameter effect and the high performance level suggest that the excess oxygen from the perchlorate actually has reacted with the HMX detonation products in the time scale of our experiment.

#### HMX-Potassium Perchlorate-Polyethylene.

Figure 7 shows how the energy of potassium perchlorate formulations varies with composition. Our most energetic formulation, containing 34 vol % of 3μ potassium perchlorate, was fired in both cylinder and detonation pressure tests. The results indicate that this explosive delivered its maximum possible energy in the 2-in.-diam cylinder test. However, when formulations containing 10μ and 44μ potassium perchlorate were tested, considerably less than maximum performance was observed. Figure 8 shows the amount of perchlorate reacted as a function of time, based on a linear interpolation similar to that used with the aluminum-loaded explosive.

#### HMX-Ammonium Perchlorate-Polybutadiene.

To see what effect large amounts of a nonenergetic binder would have on the performance of ammonium perchlorate-HMX explosives, conventional propellant technology was used to fabricate a series of compositions containing 25 vol % polybutadiene. Charges containing 0, 5, 15 and 25 vol % 6μ ammonium perchlorate were fired in cylinder and detonation pressure tests. RUBY calculations and cylinder experimental results for these systems are presented in Fig. 9. The data indicate that maximum possible performance (i.e., complete reaction) was obtained even with this large amount of polybutadiene present.

#### HMX-Potassium Perchlorate-Polybutadiene.

The effect of large amounts of a nonenergetic binder on the performance of potassium perchlorate-HMX systems was also explored, using ~27 vol % polybutadiene. Formulations containing 25 vol % 3μ, 9μ, or 15μ potassium perchlorate and 40 vol % 3μ or 9μ potassium

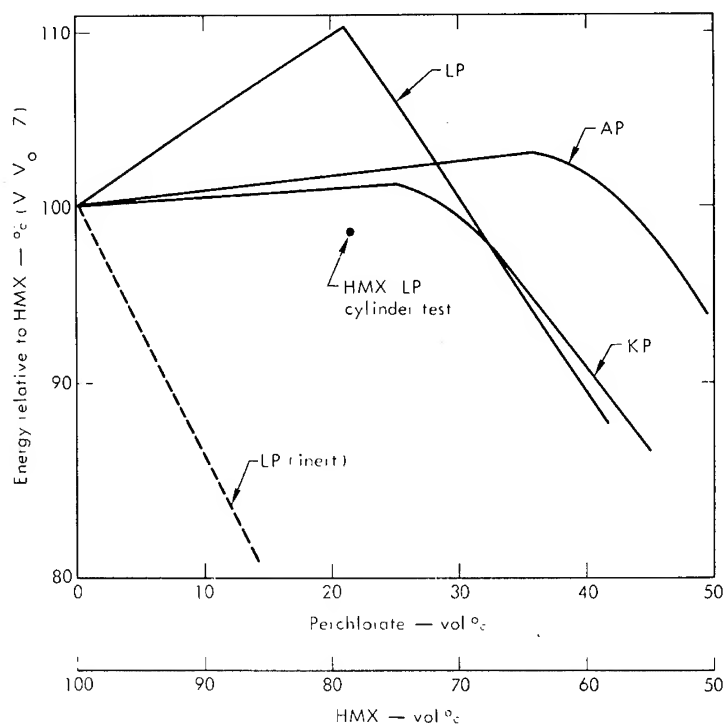


Fig. 4 - RUBY-calculated HMX-perchlorate performance assuming complete reaction

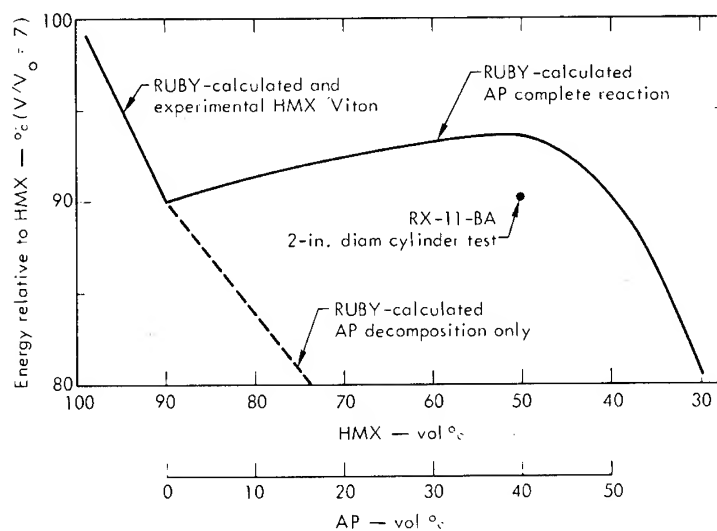


Fig. 5 - Performance of the most energetic ammonium perchlorate formulation

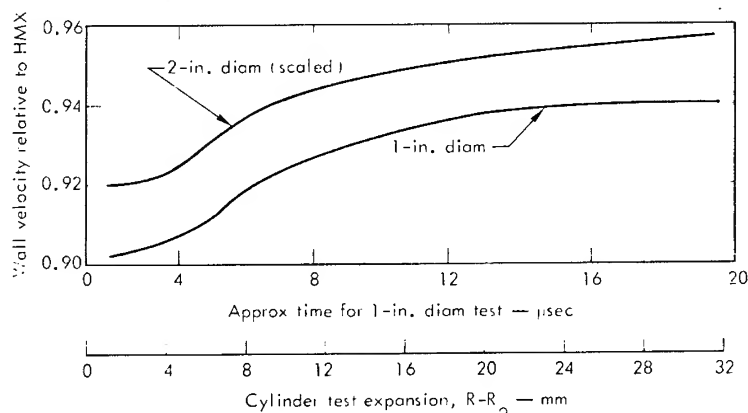


Fig. 6 - Diameter effect in cylinder tests using RX-11-BA

perchlorate were fired in cylinder and detonation pressure tests. Figure 10 presents RUBY calculations and cylinder test results for these explosives. In contrast to the higher energy, hotter formulation RX-11-AF, these explosives did not exhibit maximum possible performance.

Figure 11 presents the fraction of potassium perchlorate reacted as a function of time. Significant reaction takes place over a 30  $\mu$ sec time scale. Increasing the particle size from

3  $\mu$  to 15  $\mu$  decreases the amount of perchlorate reacted, as does increasing the concentration of 9  $\mu$  perchlorate from 25 to 40 vol %.

Also, comparison of the data for polybutadiene-ammonium perchlorate and polybutadiene-potassium perchlorate formulations indicates that the potassium systems deliver their energy more slowly. This is consistent with the fact that ammonium perchlorate contributes energy on its own, whereas

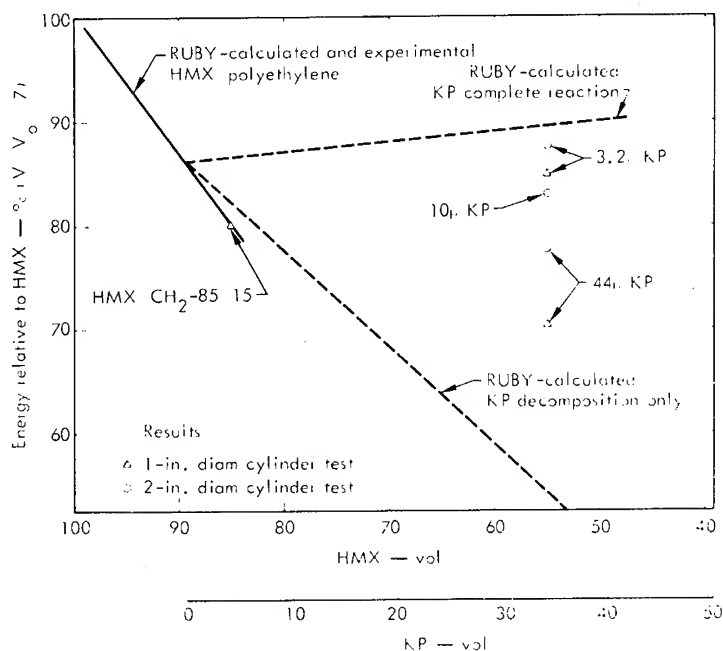


Fig. 7 - Performance of the most energetic potassium perchlorate formulation

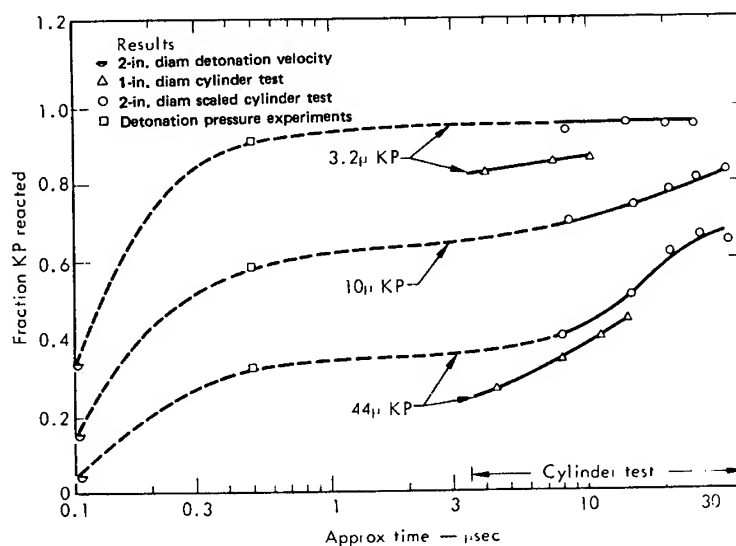


Fig. 8 - Rate of potassium perchlorate reaction as a function of particle size in polyethylene formulations

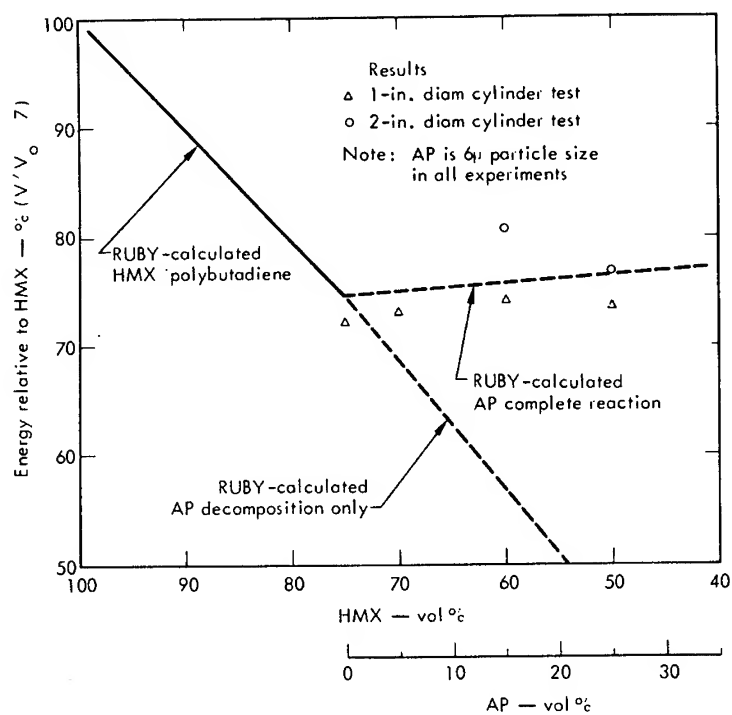


Fig. 9 - Performance of HMX-ammonium perchlorate with 25 vol % polybutadiene binder

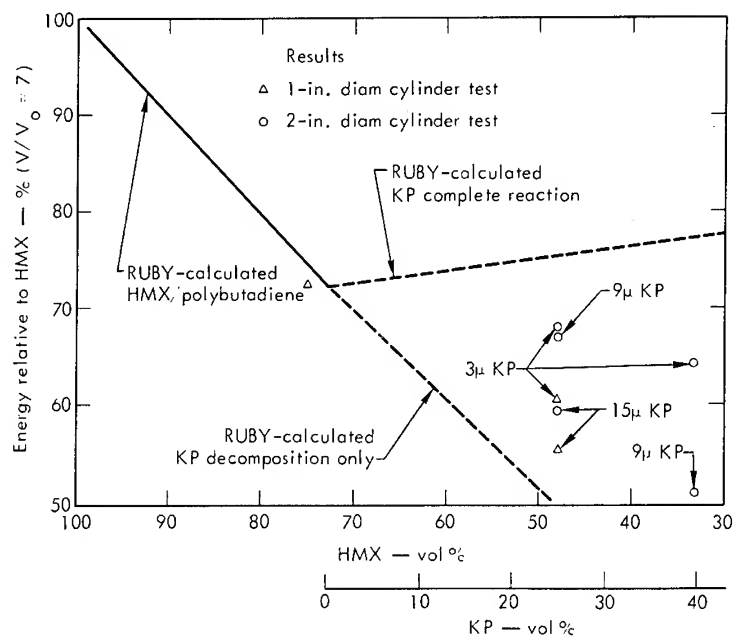


Fig. 10 - Performance of HMX-potassium perchlorate with 27 vol % polybutadiene binder

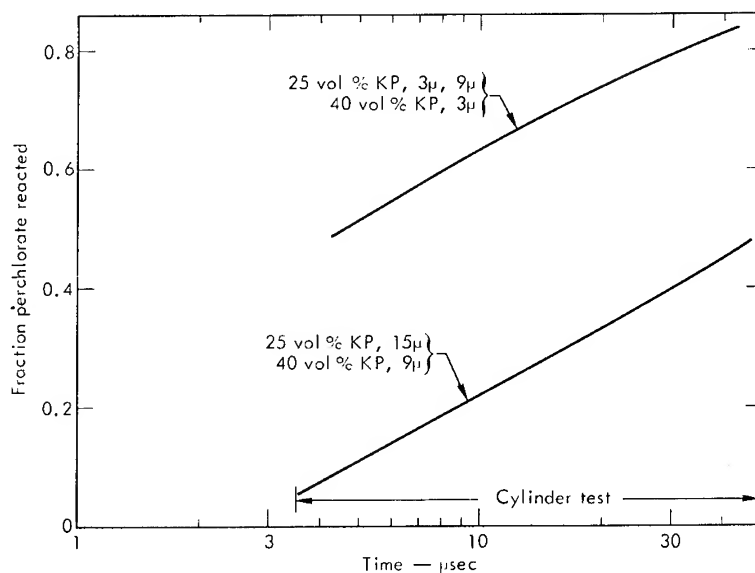


Fig. 11 - Rates of reaction for potassium perchlorate in HMX-27 vol % polybutadiene formulations



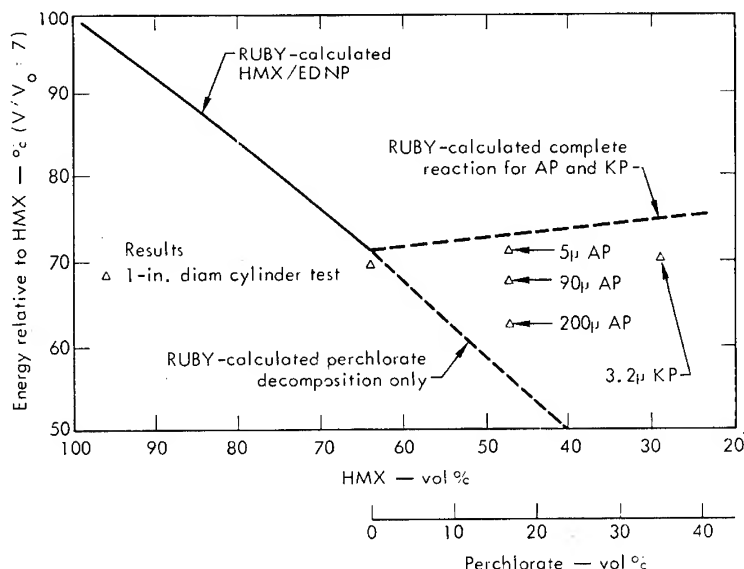


Fig. 12 - Performance of ammonium and potassium perchlorate in HMX-38 vol % EDNP slurries

potassium perchlorate must react with HMX products or the binder to release energy.

**Slurry System.** The performance of ammonium perchlorate and potassium perchlorate in HMX-slurry formulations was investigated. Slurries were found to be experimentally convenient for investigating the effect of oxidizer particle size. A low-energy liquid (ethyl-4, 4-dinitropentanoate with 1% Cab-O-Sil gelling agent) at a level of 36 vol % was used to suspend the solid ingredients. Charges containing 17 vol % of 5 $\mu$ , 90 $\mu$ , and 200 $\mu$  ammonium perchlorate and 35 vol % of 3 $\mu$  potassium perchlorate were fired in 1-in. and/or 2-in. cylinder tests. Both the 5 $\mu$  ammonium perchlorate and the 3 $\mu$  potassium perchlorate delivered nearly their maximum possible energy (see Fig. 12). However, the 90 $\mu$  and 200 $\mu$  ammonium perchlorate showed reaction over a 30  $\mu$ sec time scale (see Fig. 13).

**HMX-Lithium Perchlorate.** The most energetic system we tested contained 74 wt % HMX and 26 wt % lithium perchlorate (RX-22-AG). This composition has a measured calorimetric heat of detonation of 1.63 kcal/g compared to 1.48 kcal/g for HMX. Comparison of RUBY calculations with the experimental results (Fig. 4) shows that even in the 1-in.-diam cylinder test a major fraction of the

lithium perchlorate took part in the detonation reaction.

The RX-22-AG composite was prepared by mixing and pressing in a dry atmosphere. In general, this and related formulations are difficult to handle and are very sensitive. Extreme caution should be exercised in working with such formulations.

**HMX-Aluminum-Ammonium Perchlorate-Viton Explosive.** All the aluminum-loaded HMX systems discussed above are deficient in oxygen. RX-25-AA was formulated to see if adding ammonium perchlorate to improve oxygen balance would significantly increase performance. Small particle size (5 $\mu$ ) aluminum and ammonium perchlorate were used to maximize the possibility of fast reaction. Results from 1-in.-diam and 2-in.-diam scaled cylinder tests are presented in Fig. 14. The large diameter effect and steadily increasing relative cylinder wall velocity indicate a very nonideal detonation. Oxidizer-fuel reactions are taking place on a time scale as long as 40  $\mu$ sec (2-in.-diam test). Even so, the metal accelerating ability of this explosive in the 2-in.-diam test is about equal to cyclotol (1). This is an extreme example of an explosive for which performance predictions based on detonation pressure or detonation velocity measurements would be grossly in error.

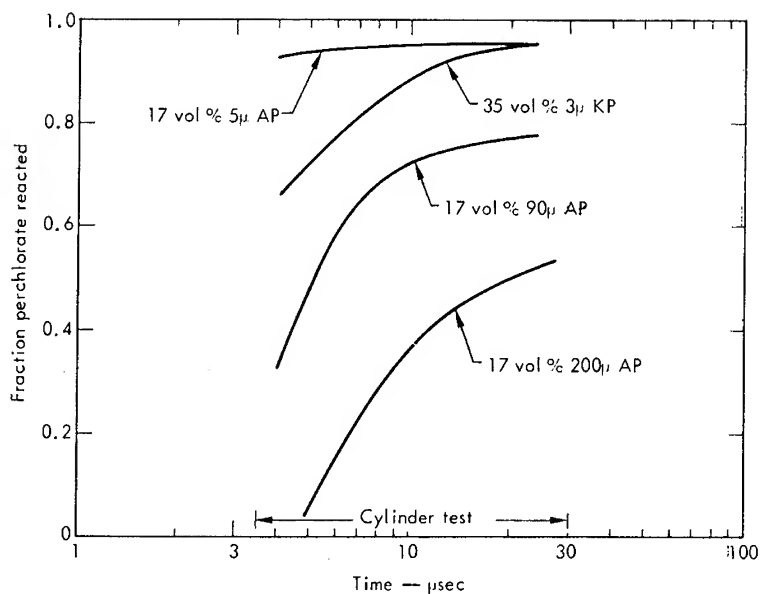


Fig. 13 - Rate of perchlorate reaction in HMX-38 vol % EDNP slurries

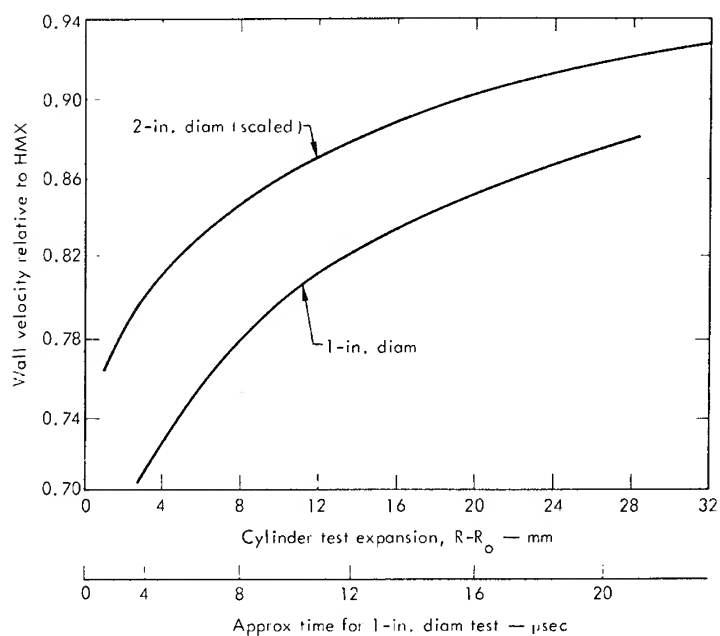


Fig. 14 - Cylinder test results for HMX-ammonium perchlorate-aluminum-Viton explosive, RX-25-AA

## SUMMARY AND CONCLUSIONS

The experiments discussed above show that aluminum and inorganic perchlorates can be used effectively in plastic-bonded HMX explosives to accelerate metal. In general, metal acceleration by these composites is no better than that of the simple explosives previously investigated (1). The rate of acceleration, however, is significantly slower and can be varied.

Our experiments have not yielded detailed mechanisms of transport and reaction in composite explosives. However, we have demonstrated that composite explosives using oxidants and fuels in selected particle sizes ( $3\mu$  to  $200\mu$ ) react in time short enough to influence the results of hydrodynamic experiments. The reaction time can be adjusted by changing the particle size, and furthermore the experimental results fall within the limits predicted by RUBY calculations. These results point the way to further experimental and theoretical studies of nonideal detonations.

## ACKNOWLEDGMENTS

The authors are grateful to the many members of the Organic Materials Section at LRL who cooperated in the code calculations, explosive formulation and fabrication, safety evaluations, chemical analyses, experimental measurements, and data reduction. Special acknowledgment is made of the contributions by R. R. Karpp (BRL visitor), B. M. McKinley, Capt. M. C. Purdy (USAF), K. J. Scribner, F. H. Helm, J. R. Humphrey, K. V. Fordyce, P. B. Archibald, J. E. Tash, D. L. Seaton, D. M. Coleman, A. J. Pane, W. Selig, G. L. Crossman, J. C. Cast, D. L. Ornellas, M. W. Jepson, B. M. Hilliker and the section head, E. James. We recognize the exceptionally fine detonation pressure and cylinder test measurements made on a number of the formulations by J. K. Rigdon and G. T. West of the Pantex AEC plant.

## REFERENCES

1. J. W. Kury, H. C. Hornig, E. L. Lee, J. L. McDonnell, D. L. Ornellas, M. Finger, F. M. Strange, and M. L. Wilkins, "Metal Acceleration of Chemical Explosives," Proc. Symp. Detonation, 4th, Office of Naval Research, Rept. ACR-126, pp. 3-13, U.S. Govt. Printing Office, Washington, D.C., 1965.
2. W. E. Gordon, "Detonation Limits on Composite Explosives," 10th Int. Symp. Combust., pp. 833-838, The Combustion Institute, Pittsburgh, Pa., 1965.
3. R. E. Duff and E. Houston, "Measurement of the Chapman-Jouguet Pressure and Reaction Zone Length in a Detonating High Explosive," J. Chem. Phys., Vol. 23, No. 7, p. 1268, July 1955.
4. M. A. Cook, "The Science of High Explosives," ACS Monograph No. 139, Reinhold, New York, 1958.
5. M. A. Cook and H. E. Farnam, U.S. Patent 2,930,685 (1960).
6. P. K. Salzman, O. R. Irwin, and W. H. Andersen, "Theoretical Detonation Characteristics of Solid Composite Propellants," AIAA J., Vol. 3, No. 12, pp. 2230-2238, 1965.
7. A. F. Belyaev and N. N. Bakhman, "Theory of Burning of Powders and Solid Rocket Propellants (Review)," Combust. Explos. Shock Waves, Vol. 2, No. 4, pp. 1-10 (Eng.), Winter 1966.
8. D. Price, J. O. Erkman, A. R. Clairmont, Jr., and D. J. Edwards, "Explosive Behavior of a Simple Composite Propellant Model," U.S. Naval Ordnance Laboratory, Rept. NOLTR 69-16, March 1969.
9. L. N. Akimova, L. N. Stesik, and A. Ya. Apin, "Detonability of Perchlorate Explosives," Combust. Explos. Shock Waves, Vol. 3, No. 3, pp. 235-239 (Eng.), Fall 1967.
10. A. Maček, "Fundamentals of Combustion of Single Aluminum and Beryllium Particles," 11th Int. Symp. Combust., pp. 203-217. The Combustion Institute, Pittsburgh, Pa., 1967.
11. H. B. Levine and R. E. Sharples, "Operator's Manual for RUBY," Lawrence Radiation Laboratory, Livermore, Rept. UCRL-6815, March 1962.
12. J. C. Cast, H. C. Hornig, and J. W. Kury, "Standard Test for Detonation Pressure Measurement," Lawrence Radiation Laboratory, Livermore, Rept. UCRL-50645, 1969.
13. W. C. Davis and B. G. Craig, "Smear Camera Technique for Free-Surface Velocity Measurement," Rev. Sci. Instr. 32, 579 (1961).

## DISCUSSION

CHARLES L. MADER

Los Alamos Scientific Laboratory  
Los Alamos, New Mexico

The authors have assumed that the velocity of a metal cylinder shocked by detonated interior explosive is related to the calculated BKW energy of the detonation products of that explosive when the specific volume of the products is seven times the initial specific volume of the explosive.

While their approximation might have some applications for determining the relative performance of explosives having similar detonation product isentropes, it is doubtful that the approximation will give good results for explosives with quite different detonation product isentropes such as HMX and an Al containing HMX mixture. As shown in LA-2900 the isentrope for Alex 20 (20% Al in Composition B) is considerably less steep than the isentrope for HMX or Composition B. For imparting energy to a metal cylinder one is interested in some complicated integral under the isentrope curve. With very different isentropes the energy at any fixed expansion volume cannot be expected to correlate with the energy delivered to the metal cylinders. The authors show in their reference (1) that for nitromethane their approximation is off by about 10%. Since the authors are reporting differences of that magnitude and since the basic approximation for relating the cylinder metal velocity to the energy of the explosive is questionable, it would seem one should not attempt to infer rates and extents of reactions of additives to explosives from such evidence.

The observations made by these authors that metal acceleration by these composites is no better than that of the usual HMX type of explosive is in agreement with the studies of this author described in the Third Symposium on Detonation, in LA-2613 and in various other reports. As described in these reports, there is no reason to assume that significant additional burning of the Al occurs at low expansion pressures for CHNOAl systems such as Alex 20, since the experimental evidence for these systems may be explained by permitting all of the Al to burn at the C-J plane. CHNOAl, BCHNO and CHNOF explosives have high C-J temperatures and low C-J pressures because of the large detonation product molecules present such as  $\text{Al}_2\text{O}_3$ ,  $\text{B}_2\text{O}_3$  and  $\text{CF}_4$ . The C-J performance of an explosive is a very sensitive function of the C-J particle density and the

particle density is low for these explosives. A decrease of the particle density results in an increase of the thermal energy at the expense of the intermolecular potential energy with resultant higher C-J temperatures and lower C-J pressures. The thermal energy is available only upon expansion of the detonation products to low pressures and results in a less steep isentrope than for the usual CHNO explosives.

## REPLY BY E. L. LEE

While it is certainly true that BKW does not correctly calculate the absolute value for the internal energy of detonation products and that the inclusion of various exotic products will further affect the accuracy of the calculations we have been careful to make all our comparisons on a relative basis. In particular we have compared calculations and experiments for systems where the only variable was the particle size of the perchlorate in the composite explosive. The resulting differences were well outside reasonable estimates of error.

The calculation of fraction reacted is, as we point out in our paper, only semi-quantitative but lacking other techniques seems to us to be an informative approach to the problem. That the experimental performance of formulations containing very coarse and very fine particle size additives coincides with the limits set by the "normalized" BKW calculation is reassuring in this regard.

It is inconceivable that the fuel and oxidizer particulates could be completely mixed and reacted within a microsecond of the passage of the detonation front and that the expansion behavior could thereby be described as merely a property of the fluid.

H. J. GRYTING

Naval Weapons Center  
China Lake, California

How do increases in cylinder diameter to 4 and 6 inches affect the results of Al addition to HMX-Viton systems?

How does diameter increase affect the contribution of fine particle AP?

## REPLY BY M. FINGER

Increasing the cylinder diameter from 1 to 2 inches increased the wall velocity about 1% in

the aluminized HMX-Viton system. We have no experimental results in 4- and 6-inch diameter. However, an increase in diameter should result in somewhat greater cylinder wall velocity.

There was no diameter effect noted in 1- and 2-inch-diameter experiments with fine particle AP (~6 micron). In the experiments the fine AP participated to its full potential. At diameters approaching the critical diameter, I would expect significantly lower energy contribution from the AP.

JAMES L. AUSTING  
IIT Research Institute  
Chicago, Illinois 60616

What does adding aluminum to the HMX-Viton do to the critical diameter of the charge?

REPLY BY M. FINGER

We do not have direct evidence of how aluminum affects the critical diameter of an HMX-Viton system. However, the experience of the blasting agents, manufacturers, has shown that the addition of fine aluminum has sensitized their ammonium nitrate compositions to the point of lowering failure diameters appreciably. Of course, the composition and confinement play an important role as well as the particle size of the aluminum on the failure diameter.

E. T. MOORE, JR.  
Physics International Co.  
San Leandro, California

How did you determine the fraction of perchlorate and aluminum reacted?

REPLY BY M. FINGER

RUBY code calculations were used to bound the minimum and maximum energy potential of the aluminized explosives. We were careful to compare the calculated results and the experimental results some distance down the isentrope from the C-J plane. We assumed a linear relationship between the fraction of aluminum reacted and the increased performance. Figure 3 in the text is essentially a direct interpolation of the results given in Fig. 2.

ROBERT L. CONGER  
Abaris Co.  
122 15th Street  
Del Mar, California 92014

Does the  $\text{Ba}(\text{NO}_3)_2$  in baratol function qualitatively like  $\text{NH}_4\text{ClO}_4$  in composite explosives? Is the  $\text{Ba}(\text{NO}_3)_2$  an effective oxidizer?

REPLY BY M. FINGER

I believe it does, although we have no direct experimental evidence. In fact, Dr. Défourneaux has reported in his paper at this Symposium direct evidence that  $\text{Ba}(\text{NO}_3)_2$  is an effective oxidizer.

# LIGHT EMISSION DURING INITIATION OF LIQUID EXPLOSIVES

Per-Anders Persson and T. Sjölin  
*Swedish Detonic Research Foundation  
Vinterviken, 117 48 Stockholm*

## ABSTRACT

A fast photomultiplier and oscilloscope have been used to study the rapid phenomena of transmission of detonation in liquid explosives through a barrier of 0.25-mm-thick plastic film in 30-mm cylindrical charges. The spectral distribution of the light and the temperature variation in the reinitiation process have been studied, as well as the influence of donor charge detonation pressure.

All explosives investigated, which included NG, EGDN, and NM, as well as mixtures between two of these and also solutions in either of these of RDX, PETN, TNT, DNT, MNT, toluene, and metanol, were found to have a common pattern of behaviour. This pattern was found to change with the initiating pressure level. Immediate reinitiation (within less than 5 nsec) occurred at shock pressures high above their own detonation pressure. Delayed initiation with shock catch-up and overshoot occurred at lower pressure. At the lowest pressures investigated, a previously unknown pattern similar to that common in pressed, inhomogeneous explosives was observed.

Differences between different explosives in their chemical reactivity appear to have only a small effect on the delay time before detonation occurs in initiation with intense shock from a given donor system. The shock compression temperature, which increases rapidly with decreasing shock impedance, appears to be the decisive factor.

## INTRODUCTION

The basic feature of the chemical reaction in initiation and detonation of high explosives is the rapid increase in reaction rate with temperature. This is most clearly illustrated by the temperature dependence of the slow decomposition of explosive compounds. In that temperature region, an increase in temperature of 10°C results in an increase in reaction rate by a factor of 10<sup>4</sup> or more. With increasing temperature, this factor becomes less, but even at a temperature of 1500°C, an extrapolation of the Arrhenius equation indicates that a 10°C temperature increase will increase the reaction rate by a factor of 1.25. This is the reason why the initiation and detonation behaviour of most inhomogeneous explosives is dominated by the reaction starting at points of locally increased temperature. Such hot spots are generated by the concentration of compressional energy at

inhomogeneities such as cavities or gas bubbles, grains of foreign material or grains of another explosive. They can also be generated by local frictional or viscous heating. (Bowden and coworkers 1947, Bowden and Yoffe 1952.)

In the absence of hot spots, secondary explosives as a rule require quite high shock pressures for initiation. A shock of a few kb will initiate reaction and detonation in nitroglycerine containing a sufficient number of air bubbles, whereas a shock of about 100 kb is required for reaction and detonation to occur in homogeneous, bubble-free nitroglycerine.

These differences between homogeneous explosives were clarified by Campbell, Davis and Travis (1961) and Campbell, Davis, Ramsay and Travis (1961). Homogeneous liquid explosives may be initiated by low-amplitude shocks, however, if the shock interaction with the

boundary results in cavitation. By the process of cavitation bubble generation, the homogeneous explosive is transformed to an inhomogeneous explosive, so that initiation occurs later in the shock reverberation process (Winning 1963). Van Dolah and coworkers (1965) have shown that the process of low-velocity detonation in liquid explosives in tubular containers is of a similar nature. The precursor shock in the tube wall material generates cavitation bubbles which will act as sensitive hot spots in the detonation reaction.

In homogeneous explosives, even a high-intensity shock wave will at first cause no measurable chemical reaction, and the explosive behaves like an inert liquid. After an induction period, the length of which is dependent upon the shock pressure, a high rate of reaction develops rapidly at or very close to the shock entry boundary. This reaction creates a detonation wave that propagates in the shock-compressed explosive and catches up with the shock front. Because this detonation is associated with a particle velocity higher than that in a normal one-step detonation, it will briefly overdrive the detonation after catch-up. The overdriven detonation then gradually decays into a normal steady state detonation. Those features were first observed by Campbell, Davis, and Travis (1961) in experiments with liquid explosives using a streak camera and initiating shock pressures equivalent to induction periods of the order of a microsecond. Single-crystal RDX and PETN were found by Cachia and Whitbread (1958) to behave in a similar way.

Using a donor-barrier-receptor charge arrangement with nitromethane charges and polyethylene barriers together with a fast photomultiplier recording system, Persson, Andersson and Ståhl (1963) found this reinitiation behaviour to prevail even with barriers as thin as 15  $\mu$ .

The present study was undertaken to investigate in some further detail the temperature involved in this process and also to make a survey of different explosives in an effort to find evidence for possible differences in reaction kinetics between different chemical compositions. We have used a rapid photomultiplier system similar to that used in the previous studies (Persson et al. 1963) to record the light emitted in the forward direction during initiation.

## EXPERIMENTAL

Figure 1 shows the standard charge arrangement used throughout the investigation.

The donor charge of length-to-diameter ratio 5 is contained in a 30-mm internal diameter, 2-mm wall thickness paper bakelite tube. It is initiated by a booster charge of length  $\times$  diameter equal to 48  $\times$  29 mm of pressed 96/4 RDX/wax of initial density 1.61 g/cm<sup>3</sup> or pressed 90/10 PETN/paraffin wax of initial density 1.54 g/cm<sup>3</sup>, in turn initiated by a pressed TNT cylinder of length  $\times$  diameter 25  $\times$  15 mm, containing a No. 8 electric blasting cap in a 20-mm-deep central hole.

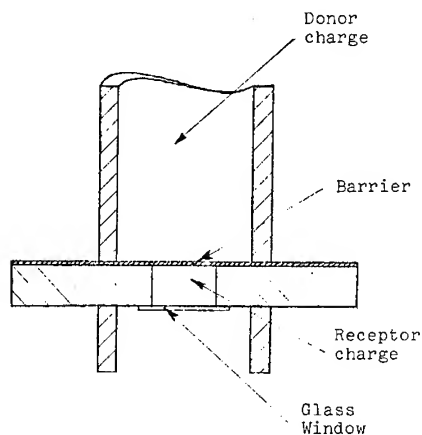


Fig. 1 - Standard charge arrangement

The receptor charge is contained in a central 15-mm-diameter cylindrical cavity in an 8-mm-thick plate of bakelite closed against the donor explosive by a black PVC (Kobex) barrier of normal thickness 0.25 mm, and closed towards the photomultiplier optical system with an 0.1-mm-thick cover glass window. The receptor charge cavity was filled using a hypodermic syringe inserted through a radial 1-mm-diameter hole. After being filled, the hole was blocked by a 1.2-mm brass screw, threaded into the hole. Great care was taken to remove all visible air bubbles from the cavity.

The charge arrangement was placed at the firing site in a vertical position with the short empty lower tube fitting into a hole through a wooden baseplate. This served as the bottom closure of a 0.5-m-edge cubic cover of black PVC. In this way, no detonation light except that emitted through the cover glass window was allowed to fall via the 45-degree mirror and bunker Perspex window into the photomultiplier optical system. Without the black PVC cover, minute scratches and specks of dust on the mirror, window or lens surface were found occasionally to transmit enough diffuse light

from the initiator and donor charge detonation to cause premature triggering of the signal-triggered Tektronics 519 oscilloscope used for recording.

In one series of experiments, narrow-bandwidth interference filters (100 Å half-width) were used to analyse the relative intensities of the light emitted from the initial detonation in the precompressed liquid, the overdriven detonation, and the final steady detonation as functions of wavelength.

In several series of further experiments, different liquid explosives, mixtures between these, and also mixtures between liquid explosives and different explosive or inert substances were used as the donor or receptor charge. All recordings in these further experiments were made without filters.

The optical system, photomultiplier, and oscilloscope arrangement has been described in detail in a previous paper (Persson et al. 1963). By a standard 400-mm objective with a built-in variable aperture, an end-on view of the acceptor charge is focussed on a pinhole diaphragm, so that light from a small central part of the acceptor along the charge axis is allowed to reach the multiplier cathode. With a pinhole diameter of 0.5 mm, an objective aperture setting of 1:22 and an object-to-lens distance of 1 m, the whole thickness of the acceptor charge is within the depth of focus, and the diameter of that part of the acceptor from which the light is recorded is 1 mm. For the series of experiments with narrowband interference filters, it was necessary to use larger pinholes, up to 2 mm diameter, and a greater aperture opening, up to 1:5.6. Even with these values, effects due to detonation front curvature and decreased depth of focus were negligible.

A considerable part of the experiments were made with an oscilloscope sweep rate of 50 nsec/cm. It would have been advantageous to have the oscilloscope triggered at the time when the donor charge detonation reached the barrier. The necessary accuracy in triggering would, however, have required a considerable complication in charge preparation. For the sake of simplicity, triggering was therefore made on the first light recorded. A 20-nsec delay cable was incorporated to delay the input voltage signal relative to the trigger input signal. Each record thus includes a sweep of 20 nsec before the time of triggering.

Figure 2 shows typical records of the initiation of nitromethane (NM) through barriers of 0.14-, 0.25-, and 0.75-mm black PVC, using

NM as a donor charge. All three records show the typical homogeneous explosive initiation behaviour. The first plateau is the light emission from the detonation in the shock-compressed material. At the end of the plateau, there is a rapid increase in emission when the detonation catches up with the shock front, followed by a slowly decaying overdriven detonation gradually approaching the emission of a steady normal detonation.

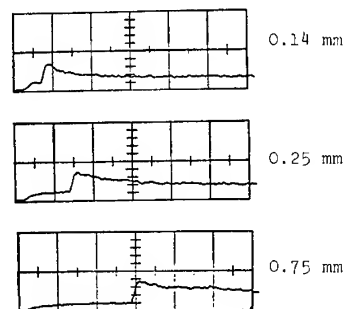


Fig. 2 - Light from initiation of NM with NM as a donor at three different PVC barrier thicknesses. Sweep speed 50 nsec/cm.

#### THE SPECTRAL DISTRIBUTION OF LIGHT AND ESTIMATION OF TEMPERATURES IN INITIATION

In a first series of experiments, narrow-bandwidth interference filters were used to analyse the spectral distribution of the light emitted. Ten filters were used, with peak emission wavelengths at 4000, 4330, 4660, 5000, etc., up to 7000 Å.

Figure 3 shows records of the total emission and that transmitted through a 4000- and a 6330-Å filter during reinitiation of a detonation in NM (NM in donor and acceptor charge) behind an 0.25-mm black PVC barrier. All three records show the same general features. It is seen that the short-wavelength light increases steadily up to the point of shock catch-up, whereas the longer wavelength light and the total light, which is dominated by the longer wavelengths, both show a marked plateau. A fairly large number of records were analysed. The sensitivity of the 56 AVP multiplier with an S11 phosphor at 6000-7000 Å is only a small fraction of its peak sensitivity at 4250 Å. This had to be compensated by changes in pinhole



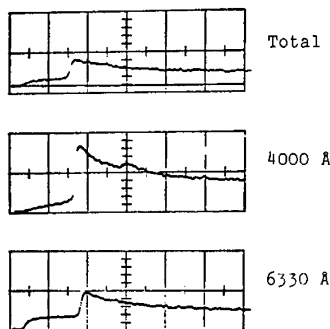


Fig. 3 - Total light emission and emission through narrow-band filters at 4000 and 6330 Å. Amplitudes not comparable. Sweep speed 50 nsec/cm. Nitromethane.

size and lens aperture settings. No effort was made to obtain an absolute calibration. Instead, the plateau detonation light intensity  $E_1$  and peak over-drive detonation light intensity  $E_2$  were measured relative to the steady detonation light intensity  $E_0$  for each record separately. Figure 4 shows these intensities plotted versus wavelength on the assumption that the steady state detonation emits blackbody radiation at a temperature of 3800°K. This is the steady state temperature obtained for NM by Gibson, Bowser, Summers, Scott, and Mason (1958). Mader (private communication, 1968) has reported somewhat lower temperatures obtained from calculations using the Becker-Kistiakowsky-Wilson equation of state. The steady state temperature was 3120°K, the precompressed detonation temperature was 2810°K, and the peak over-drive temperature 4300°K, all corresponding to an initial 85-kb shock, heating the NM to 1198°K. We find from the present results that the emission temperature is between 400 and 450°K higher for the over-drive detonation and between 250 and 300°K lower for the preshock detonation than the steady state detonation emission temperature. There is a tendency for the long wavelength points to fall above and the short wavelength points to fall below the best-fitting blackbody curve.

We find also that the rise time at catch-up is essentially independent of the wavelength but that it increases with increasing barrier thickness. The values for the thin barrier are only slightly greater than the multiplier rise time ( $\approx 2$  nsec).

The first-light rise time, on the other hand, increases considerably with decreasing wavelength from about 20 nsec at 7000 Å to

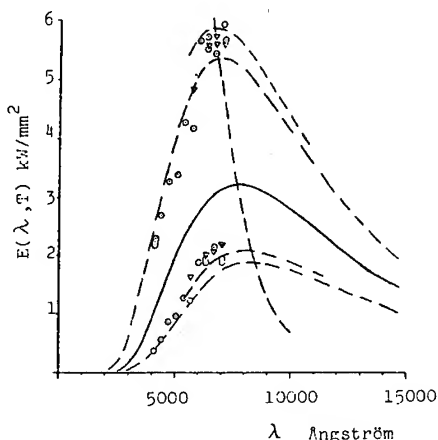


Fig. 4 - Spectral distribution of light emission during initiation of NM by a NM donor and different thicknesses of PVC barriers. Barrier thickness 0.25 (○), and 0.75 mm (▽). Upper set of points, peak amplitude, and lower set of points, amplitude of precompressed detonation; both relative to steady state level, assumed to be at a temperature of 3800°K (full line). Dashed lines represent best-fitting blackbody distribution curves at constant temperature--(a) 4250°K; (b) 4200°K; (c) 3500°K; and (d) 3400°K.

over 80 nsec at 4000 Å. We take this to indicate that the reaction products are slightly transparent to the short-wavelength light. The preshock detonation travels nearly 1 mm in the longest rise time recorded, 80 nsec.

#### EFFECTS OF INITIATING PRESSURE LEVEL

In a second series of experiments, we investigated the effects on the initiation process of varying the initiation pressure in NM and nitroglycerine (NG). Several liquid solutions of TNT in NG and of NM in NG were also investigated. To obtain different initiating pressures, we used a range of donor charges of different pure and mixed explosives.

Table 1 shows a representative selection of donor explosives used. The detonation pressures are the best available measured values for the pure explosives. For mixtures, pressures were estimated on a basis of linear extrapolation to the mixture ratio used.

Figure 5 shows the results for NG and NM. We find that the behaviour thought typical of liquid explosive initiation with a plateau such as those shown previously in this paper for NM is only one of a whole range of different processes. With a sufficiently high initiating pressure, detonation appears to start with a delay of less than 5 nsec, and no, or a very slowly decaying, overshoot. With decreasing pressure, the plateau begins to appear, accompanied by a more pronounced overshoot. With a further decrease in pressure, the plateau lengthens and becomes preceded by a region of faint, slowly increasing light. At the same time the sharp catch-up increase in light intensity disappears and is replaced by a more and more gradual increase. Finally at the lowest pressures

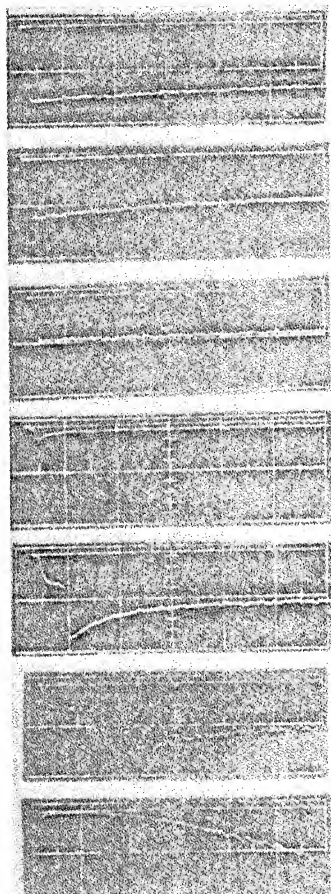


Fig. 5a - Light emission from initiation of NM with different donors. Barrier: 0.25-mm PVC. Time 200 nsec/cm. Amplitudes comparable except 42/58 NG/NM record.



Fig. 5b - Light emission from initiation of NG with different donors. Barrier: 0.25 mm PVC. Time: top 5 records, 100 nsec/cm; otherwise 200 nsec/cm.

TABLE 1  
Donor Charge Explosives

Explosive	Initial Density (g/cm <sup>3</sup> )	Detonation Pressure (kb)
59/41 HMX/NG	1.76	330
60/40 HMX/TNT	1.72	315
RDX	1.61	266
NG	1.60	238
70/30 NG/NM	1.42	202
40/60 NG/NM	1.28	170
20/60 NG/NM	1.20	148
NM	1.13	127
96/4 NM/MNT	1.13	

studied the plateau has completely disappeared, and the process is one of gradually increasing light emission up to a point where a change in slope occurs and a more rapid increase occurs up to a relatively steady niveau.

Before proceeding to discuss these results, it is worth noting the differences in the "steady" detonation light intensity level at the end of each recording. This level has a minimum when the donor has a detonation pressure considerably higher than that of the receptor, i.e., when the plateau and overdrive have disappeared. It is higher when an extremely strong initiation pressure is applied, such as when NM is initiated with a 59/41 HMX/NG donor, and also higher when a weaker initiation results in an initiation delay and subsequent overdrive when the precompressed detonation or reaction wave catches up with the shock front. Compared to the differences in measured temperatures between the precompressed detonation and overdrive detonation in NM these differences appear to be of the order of a few hundred degrees or at most 500°K.

The slowly increasing weak light recorded before the plateau develops, or, at even weaker initiation, the gradually increasing light intensity which grows up to a steady high intensity level are phenomena not previously experienced with homogeneous liquid explosives. They are similar to the initiation phenomena in inhomogeneous explosives such as pressed or cast solids. In these, in contrast to the initiation process in homogeneous explosives, the initial shock wave is gradually strengthened by reaction at numerous hot spots until it reaches the level of a steady detonation.

Previous studies of the initiation process of homogeneous explosives have been made with large, plane-wave-initiated charges. In the

present experiments, the initiation shock wave is a rapidly decaying wave in which the pressure behind the front has a steep gradient. It is possible that such a wave may, after it has traveled some distance into the explosive, cause initiation by slow reaction almost simultaneously within a greater volume of explosive at the barrier. This would delay or prevent the development of a sharp preshock detonation front, as the pressure increments from each part of the reaction zone would take longer to interact to form a sharp front. Consequently, a behaviour similar to that of inhomogeneous explosives might be expected. The tendency toward that type of behaviour would be more pronounced, the lower the shock temperature for a given pressure gradient.

It is difficult to calculate the shock temperature at a given shock pressure due to the lack of data on the p-v-T relation for unreacted explosives. Mader (1963) has calculated the temperature in NM shock compressed to 85 kb to be 1200°K, using the BKW equation of state for NM. Ilyukhin et al. (1960) measured the shock adiabat for NM up to pressures about 80 kb.

The shock adiabat can be described in the form of a linear relation between the shock wave velocity  $u_s$  and the particle velocity  $u_p$

$$u_s = 2.00 + 1.38 u_p \quad (1)$$

If we assume Mader's temperature to be correct, we may obtain from the shock adiabat an upper limit for the change in shock temperature with changing shock pressure by neglecting the change in the 0°K internal energy.

Let us write the increase in internal energy of the unreacted explosive

$$E - E_0 = E_c + \int_{T_0}^T c_v dT, \quad (2)$$

where  $E_0$  is the initial internal energy,  $E_c$  is the increase in internal energy obtained by compression at 0°K and the integral is the additional internal energy increase due to thermal motion.

The "cold" or "elastic" internal energy  $E_c$  is thus

$$E_c = \int_{v_0}^v (pdv)_{0^\circ K} \quad (3)$$

The error introduced by assuming that  $\Delta E_c$  is negligible compared to  $\Delta E_t$  is not great and will decrease with increasing shock pressure and temperature, as the ratio  $\Delta E_t/\Delta E_c$  increases considerably with increasing shock pressure.

When  $p \gg p_0$ , which is a condition valid for the present calculation, we have from the shock conservation relation

$$E - E_0 = \frac{1}{2} u_p^2 = \frac{1}{2} p(v_0 - v), \quad (4)$$

where  $u_p$  is the shock particle velocity, i.e., the increase in internal energy equals the increase in kinetic energy and also the surface under the Rayleigh line in the  $p-v$  plane.

An increase in shock pressure from  $p_1$  to  $p_2$  thus gives the increase in internal energy  $\Delta E$

$$\Delta E = \frac{1}{2} p_2(v_0 - v_2) - \frac{1}{2} p_1(v_0 - v_1) = \frac{1}{2} \Delta(u_p^2), \quad (5)$$

where  $v_1$  and  $v_2$  are the corresponding volumes on the shock adiabat.

The corresponding temperature difference is then approximately

$$\Delta T = \frac{\Delta E}{c_v} = \frac{1}{2} \frac{\Delta(u_p^2)}{c_v}. \quad (6)$$

Based on the shock state at 85 kb with  $T = 1200^\circ\text{K}$  and  $u_p = 1.8$  km/sec, and with  $c_v = 0.37$  cal/g  $^\circ\text{K}$ , the values of  $\Delta T$  after Eq. (6) are given in Table 2, together with the reaction half-life of NM, assuming an Arrhenius law decomposition with frequency factor  $1.26 \cdot 10^{12}$  and activation energy 39.7 kcal/mole  $^\circ\text{K}$ .

TABLE 2  
Estimated Shock Temperatures of NM

$p$ (kbar)	$u_p$ (km/s)	$\Delta T$ ( $^\circ\text{K}$ )	$T$ ( $^\circ\text{K}$ )	NM Half-Life ( $\mu\text{sec}$ )
69	1.5	-219	981	402
85	1.71	0	1200	9.82
92	1.8	100	1300	2.64
99	1.9	219	1419	0.720
108	2.0	345	1545	0.240
126	2.2	617	1617	0.126
144	2.4	915	2115	0.007
164	2.6	1235	2435	0.002

It is obvious from the approximate temperature values of Table 2, even allowing for a

considerable error in the temperature estimate, that a small change in shock pressure will make a considerable change in shock temperature and a quite decisive change in the rate of chemical reaction.

## EFFECTS OF EXPLOSIVE AND INERT ADMIXTURES

In the third series of experiments, different substances were dissolved in the NG or NM receptor charge in an effort to investigate the effects of chemically sensitizing additives. From drop-weight tests, for example, it is well known that additives such as TNT, DNT or MNT appreciably decrease the sensitivity of NG. Inert liquids such as metanol are often used in the explosive industry as solvents for NG to facilitate the safe removal or transport of the liquid explosive. All these additives are known also to increase the critical diameter of NG. Van Dolah and coworkers (1966) found a correlation between the sensitivity of NG mixtures and their overall oxygen balance. The greatest sensitivity was found to coincide with oxygen balance—increasing oxygen surplus or deficit was found to decrease sensitivity. Although very little is known of the details of the chemical reactions involved, it has long been considered that these effects are due to changes in the chemical reaction rate brought about by the additives.

Figure 6 shows the effect on the initiation process of NG containing increasing amounts of dissolved TNT. With a comparatively strong donor such as 70/30 NG/NM, the main difference appears to be a slightly decreasing light intensity with increasing TNT content. With weaker initiation, there is a clearly visible increase in reaction delay, and with the weakest donor, the process has transformed to that of a gradually increasing reaction.

Figure 7 shows the effect of adding toluene to the NG receptor. Contrary to what might have been expected, the initiation delay increases considerably with increasing toluene content. At the same time, the light intensity decreases.

The effects of adding metanol to NG are very similar to those of adding toluene (Fig. 8). Even at a 32% metanol content, reaction starts with a short delay using a 42/58 NG/NM donor, and the effect at weaker initiation with a 24/76 NG/NM donor is even more spectacular. Obviously, reaction starts the more rapidly, even with a weaker donor charge, the *greater* the metanol content. In this case, as in the case of

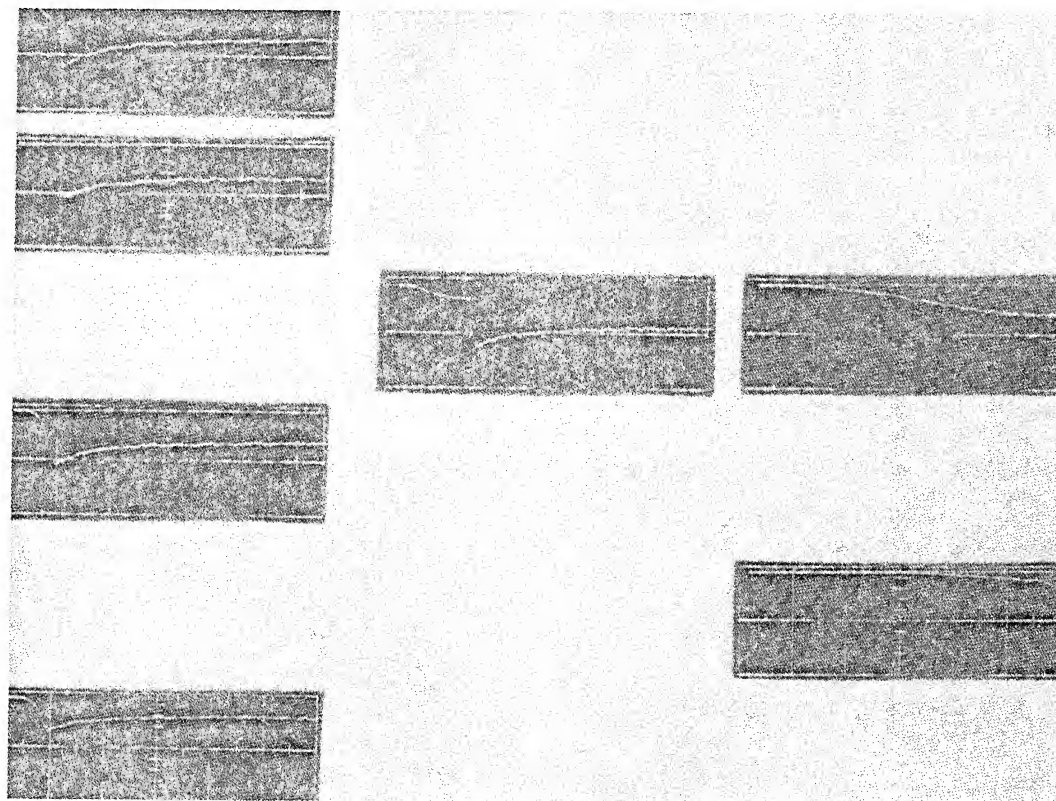


Fig. 6 - Effects of TNT added to NG. Time 100 nsec/cm. Comparable amplitudes.

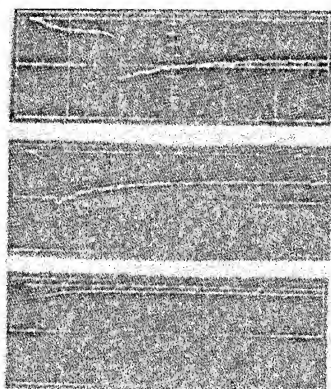


Fig. 7 - Effects of toluene added to NG. Donor charge 42/58 NG/NM. Time 100 nsec/cm. Comparable amplitudes.

shows the effect of adding 1% of TNT, PETN, or RDX to NG, pure NG being shown for comparison, at two different donor strengths. All three explosives act in a similar way, that is to very slightly increase the initiation delay. With the 38/62 NG/NM donor all three additives give rise to a changeover from the simple plateau and decaying overshoot behaviour of pure NG to the seemingly unstable overshoot behaviour typical of a weak initiation. Of the three, PETN appears to give a very slightly longer initiation delay than the others.

In a last attempt to investigate the effect of increasingly greater carbon excess, we studied the influence of adding 4% each of toluene, MNT, DNT or TNT to NG. The results are shown in Fig. 10, with pure NG for comparison, and with two different donor strengths. Of the four additives, toluene and MNT were found to give shorter delays, while DNT and TNT gave longer initiation delays than pure NG. In order of increasing initiation delay, the additives can be arranged as above.

the toluene additive, the light intensity decreases with increasing additive content.

The solubilities in NG of the solid explosives PETN and RDX are about 1%. Figure 9

Although the selection of additives in these series of experiments may not be the optimal



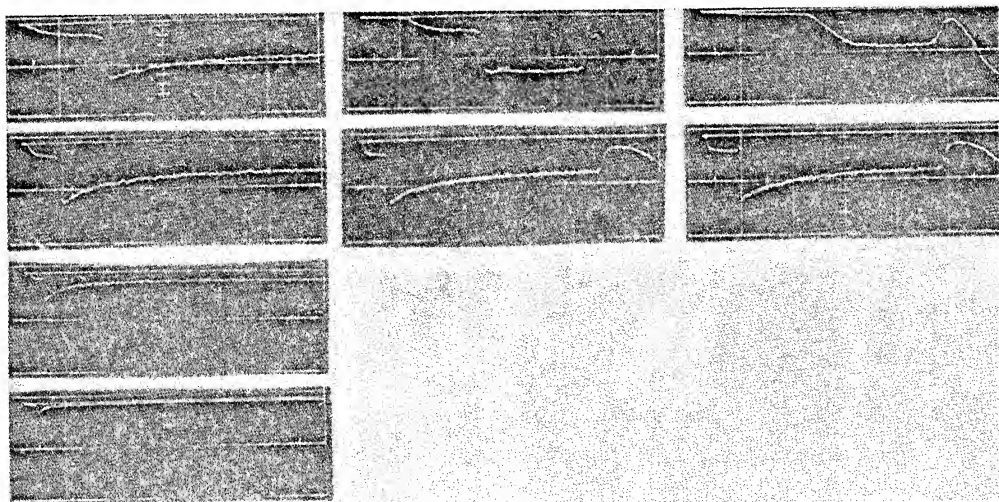


Fig. 8 - Effects of metanol added to NG. Time 100 nsec/cm. Comparable amplitudes.

one from a chemical point of view, it is sufficient to show beyond doubt that chemical activation or deactivation by additives plays a very inconsiderable part in determining the reaction delay in the initiation of NG with strong shock waves.

Other effects apparently are far more important. We would tentatively suggest that the most important effect is the change in initial density or shock impedance of the explosive caused by the additive. In Table 3, the explosives and additives used in this investigation

are arranged in order of decreasing density (top to bottom). We see that the explosives or additives with the lowest densities give the shortest reaction delays, those with higher densities give longer delays. TNT, which has a density very close to that of NG, gives the smallest effect in NG. Although this is not necessarily the case with all additives, the ones used in this investigation appear to give an increase in the density of their mixture with NG compared to that of pure NG if their own density is higher than that of pure NG and vice versa. From investigations of the shock

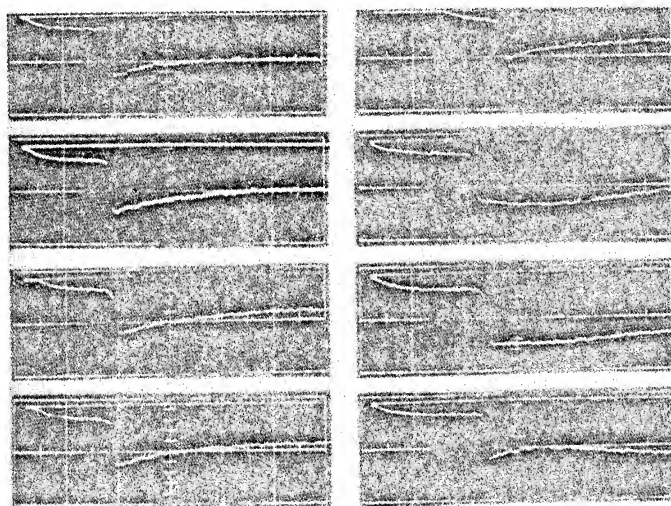


Fig. 9 - Effects of 1% RDX, TNT, or PETN in NG. Time 100 nsec/cm comparable amplitudes.

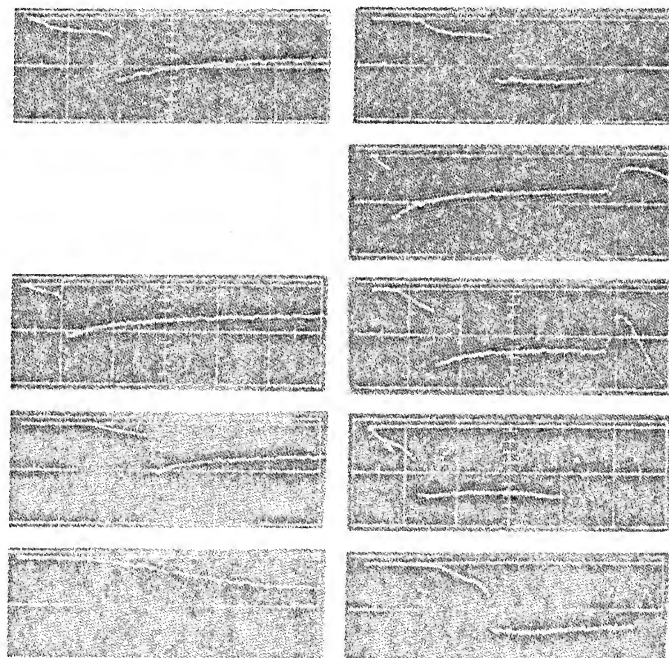


Fig. 10 - Effects of 4% toluene, MNT, DNT, or TNT in NG. Time 100 nsec/cm. Comparable amplitudes. Barrier: 0.25-mm PVC.

adiabats of various inert liquids, Walsh and Rice (1957) have shown that generally, the shock impedance ( $\rho c$ ) of most liquids is lower over the whole shock pressure region up to several hundred kb the lower their initial density. There are some notable exceptions.  $\text{CS}_2$ , for example, although having the relatively high initial density of 1.27, showed the lowest shock impedance of all the liquids investigated.

TABLE 3

Density of Explosives and Additives, Arranged After Increasing Initial Density. (Increasing from Top to Bottom.)

Additive or Explosive	Density at 18°C (g/cm <sup>3</sup> )	Additive or Explosive	Density at 18°C (g/cm <sup>3</sup> )
Metanol	0.793	EGDN	1.48
Toluene	0.89	NG	1.60
NM	1.13	TNT	1.64
MNT	1.16	PETN	1.67
DNT	1.28	RDX	1.80

The effect of a change in shock impedance on the pressure and particle velocity generated in a liquid by interaction with an incoming shock of given amplitude in a given barrier material is well understood. The lower the shock

impedance of the liquid, the lower will be the pressure and the higher the particle velocity in the resulting shock. For an inert shock, the increase in internal energy is given approximately by Eq. (4) and is seen to be proportional to the square of the shock particle velocity.

Clearly, the increase in internal energy will increase with decreasing shock impedance. We may safely assume that the additives have no decisive effect on the ratio between elastic and thermal internal energy or on the specific heat. Thus, as a first approximation, we may assume the resulting shock temperature to rise roughly in proportion to the increase in internal energy. Consequently, using the argument in the previous section (Table 2), we find that the effect of decreasing the density of the receptor charge will be to increase considerably the shock temperature and thereby to radically increase the rate of reaction.

In general, therefore, we may expect an explosive with a low shock impedance to show a shorter initiation delay for a given donor charge and barrier than one with a high shock impedance. Some results in this series of experiments show, however, that there are some exceptions to this. DNT has a density considerably lower than NG and might be expected to bring about a decrease of density when added to NG.

In fact 4% DNT added to NG gave an increased reaction delay compared to NG for a 42/58 NG/NM donor. TNT, with a density only 2.5% higher than NG, gave a very considerably increased reaction delay compared to pure NG when added in as small a percentage as 4. We conclude that these, and the very few other results conflicting with the shock impedance theory presented above, are evidence of chemical deactivation effects.

#### COMPARISON OF DIFFERENT PURE EXPLOSIVES

Figure 11 shows the initiation of the pure explosives NG, EGDN, and NM with a donor of 42/58 NG/NM. All three records are obtained with the same instrument setting and optical arrangement. We again note the increasing reaction delay with increasing density (compare Table 3). The total intensity of the steady detonation is also highest for NG, slightly lower for EGDN, and very much smaller for NM. The ratios of the intensities are 1:0.82:0.11. Qualitatively, they indicate that the characteristic temperature is highest for NG and lowest for NM. The ratios do, however, appreciably over-emphasize the real temperature differences because the sensitivity of the S11 phosphor of the 56 AVP photomultiplier is greatest close to the short-wavelength foot of the emission curve and very low at its peak for the range of detonation temperatures between 3000 and 4000°K likely for these explosives.

#### TRANSMISSION OF DETONATION THROUGH A BARRIER

Figure 12 shows the transmission of detonation of the three liquid explosives NM, 90/10

NM/TNT, and NG through barriers of thickness 0.25 and 0.75 mm. In each experiment, the same explosive was used in donor and acceptor. There are obvious differences between the explosives.

NM shows the longest initiation delay, NG the shortest. However, with increasing barrier thickness, we will undoubtedly find the same increasing plateau length in the two other explosives as with these thin barriers in NM.

#### QUENCHING OF THE DETONATION LIGHT UPON IMPACT ON TRANSPARENT BARRIERS

During the course of the experiments described above it was noted that the rate of

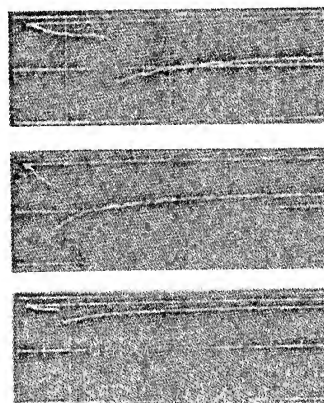


Fig. 11 - Comparison between different pure explosives. Donor charge 42/58 NG/NM. Time 50 nsec/cm. Comparable amplitudes. Barrier: 0.25-mm PVC.

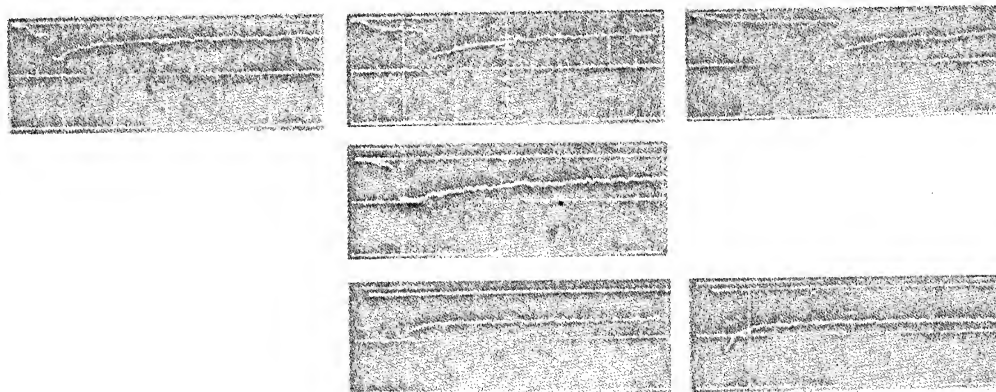


Fig. 12 - Transmission of detonation through barriers of different thickness. Same explosive in receptor and donor. Time 100 nsec/cm. Comparable amplitudes.



decrease of light intensity when the receptor charge detonation arrived at the cover glass window at the end of the receptor charge varied depending on the prehistory of the detonation. If the detonation had decayed over a sufficiently long distance after an overshoot initiation, the rate of decrease was small, and the intensity decreased typically to about half its steady value. If the detonation was still overdriven, for example, due to a long reaction delay, the rate of decrease was very much greater. A few exploratory experiments were made to investigate this further. Figure 13 shows the results of these, all with pure NG as receptor.

In record 13a, initiation was by a donor of 37,25/62,75 NG/NM, and the length of the receptor charge, 4.1 mm, was chosen so that the detonation arrived at the 2-mm-thick glass plate about 20 nsec after shock catch-up. The decrease in light intensity upon collision is rapid, and the intensity is approaching zero after about 11 nsec. In record 13b, with an identical charge and window arrangement, initiation was by a stronger shock wave from a pressed TNT charge of density  $1.56 \text{ g/cm}^3$ . The initial overshoot has decayed by the time the detonation arrives at the glass window, and we see the very gradual decrease in intensity to about 40% of the steady value, continuing for the full 300 nsec while the shock is traveling through the glass.

In record 13c, the measurements and initiation were identical to those of record 13b, with the exception that the glass window was replaced by a 15-mm-high column of water in

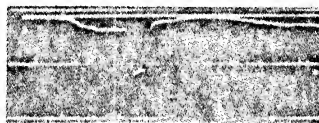
contact with the NG receptor end surface. (To do this experiment, the charge setup was turned upside down, with initiation from the bottom.) Except for a more rapid initial decrease in intensity, this record, too, shows the same features as 13b, the light intensity decreasing to about 40% of the steady detonation level, where it stays for the duration of the recording, about 350 nsec.

Figure 14 shows a series of double barrier shots, using 10/90 TNT/NM in both donor and receptor charges. The receptor charge was divided in two by the insertion of a second barrier of transparent PVC of the same thickness as the first, black PVC barrier.

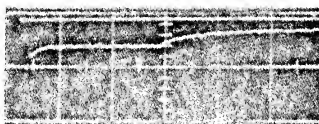
The numbers to the left of each record indicate the barrier thickness, the distance between the first and the second barrier and the cover glass window. Where only two numbers occur, the latter two distances were equal. The top record with 0.1-mm barrier thicknesses shows the normal double reinitiation, in which the overdrive detonation has decayed into a steady state before hitting the second barrier. As in Fig. 13a the light quenches slowly at the second barrier. The second record, with 0.25-mm barriers, is different. The overdrive detonation has not decayed sufficiently and in agreement with Fig. 13a the light then quenches suddenly. Reinitiation is then almost immediate. The time lag between quenching and reinitiation, 42 nsec, corresponds well with a shock-wave velocity of 6 km/sec through the barrier. There is no visible plateau, but a very brief overshoot of about 20-nsec duration.

#### DONOR CHARGE

a.  
37.75/62.25  
NG/NM



b.  
Pressed TNT



c.  
Pressed TNT



Fig. 13 - Effects of detonation amplitude on detonation light quenching at receptor end surface. (a) and (b) 2-mm glass window, (c) 15-mm water window. Sweep 100 nsec/cm. Comparable amplitudes. Barrier: 0.25-mm PVC.

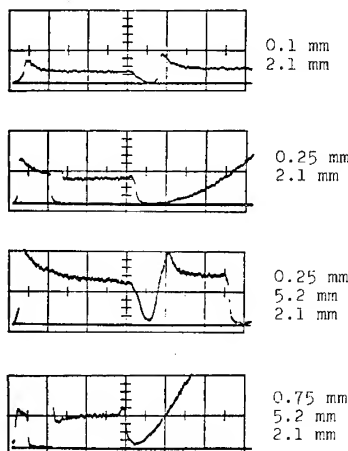


Fig. 14 - Initiation light and light quenching at second barrier in double barrier arrangements. Sweep speed top record 100 nsec/cm, others 200 nsec/cm.

The third record shows, again with 0.25-mm barriers, how the phenomenon of slow quenching reappears together with a slower rise and a longer overshoot when the barrier separation is doubled (5.2 mm instead of 2.1 mm). The fourth record shows the return of the rapid quenching and immediate reinitiation when the barrier thickness is made greater (0.75 mm) while keeping the 5.2-mm barrier separation.

Although these experiments give very little quantitative information about the structure of the reaction zone, there are some important qualitative conclusions to be drawn.

a. The region within the reaction zone that emits the highest temperature is closer to the detonation front, the higher the detonation pressure. The highest detonation pressure for a given explosive is that reached when the precompressed detonation catches up with the shock front in delayed plateau initiation. Relative to the shock front, this detonation travels with a velocity of at most 6 km/sec. The rise time of the light upon catch-up is between 2 and 11 nsec. Consequently, the high-temperature, forward-emitting region is less than  $60\ \mu$  and perhaps as little as  $10\ \mu$  behind the detonation front. This varies little between different explosives.

b. When an overdriven detonation collides with the surface of an inert material, the light quenches to zero or close to zero intensity, again within a time of about 10 nsec. Not even when the inert material has a higher shock impedance than the unreacted explosive is there an increase in light intensity.

Perhaps the most interesting observation in this respect is the small difference in initial quenching rate between that obtained at a glass surface and that at a water surface. Compared to the shock impedance of unreacted NG, the shock impedance of glass is higher and that of water is lower. The collision of the detonation in NG with the glass surface will therefore result in shock reflection which will initially increase the pressure in the NG close to the glass above that at the detonation front. The resulting shock in the glass will have a lower temperature than that of the shock-compressed NG at the glass surface just prior to collision. Collision of the detonation in NG with the water surface will bring the opposite effects, i.e., a rarefaction wave will initially travel back into the NG and the shock temperature of the water will be higher than the shock front temperature of the NG. This appears to rule out conduction cooling at the surface as

the mechanism for the rapid initial quenching of light at the water surface.

c. When the initially overdriven detonation has had a sufficient distance of propagation to decay back into what would appear to be a steady state detonation, the quenching of light at impact with an inert is far less rapid, typically of the order of 50 to 100 nsec. Similarly, when initiation is done with low pressure, the rise time of the light when the precompressed detonation catches up with the shock front increases to values of the same order.

d. A sufficiently thin barrier or a sufficiently high initiating pressure creates a detonation with a delay of less than 5 nsec and with no visible overshoot. This is again an indication that the light emitted in the forward direction from a steady or slightly overdriven detonation comes from a zone less than  $50\ \mu$  behind the front. Again, there are some differences between different explosives. NM appears to have the light-emitting zone appreciably closer to the front than does NG or TNT-mixed explosives.

e. Our final conclusion is that even pressures equal to or somewhat higher than those normally considered typical of the region behind the reaction zone are not sufficient to generate an immediate reaction in a liquid explosive. For NM, experiments aimed at measuring the Chapman-Jouguet pressures have given values varying between 115 and 140 kbar (Craig 1965, Persson 1969). To get immediate reinitiation we need pressures of the order of the detonation pressure of NG, that is, well above 200 kbar. These conclusions hold true even if we take into account the slight decrease in pressure caused by the impedance mismatch between the explosive and the barrier material.

For NM, we find an initiation delay of about 150 nsec at a pressure of about 120 kbar. Mader (1963) cites experiments where the initiation delay in NM was  $1.4\ \mu$ sec at a shock pressure of 85 kbar.

For NG, we similarly find an initiation delay of 450 nsec at an initiating pressure of about 175 kbar. At about 220 kbar (NG donor), the delay has decreased to some 100 nsec, but there is still a marked overshoot, indicating that this is a true reaction delay.

We conclude from this that an appreciably higher pressure than the Chapman-Jouguet pressure must exist at the front of the detonation. From the experiments with strong donor charges, we estimate these front pressures for

TABLE 4  
Rate Constants for Thermal Decomposition of Different Explosives

Explosive	Frequency Factor $\log Z$ ( $\text{sec}^{-1}$ )	Activation Energy (kcal/mole $^{\circ}\text{K}$ )	Temp for Expl After 1 Sec ( $^{\circ}\text{C}$ )	Reference
NM	12.1	39.7	220	Mader 1967
NG	18.64	43.7		Andreev & Beljaev 1964
NG	23.5	50		Bowden & Yoffe 1958
TNT	11.4	344-140		Cook 1959
TNT	12.3	41.1	255	Mader 1969
PETN	19.8	47		Bowden & Yoffe 1958
RDX	18.5	47.5		Cook 1958
Lead azide	(17.42)*	37-38	340	Bowden & Yoffe 1958

\*Based on 1 sec - 340 $^{\circ}\text{C}$ ,  $E = 37.5$  kcal/mole  $^{\circ}\text{K}$ .

steady detonation to be for NM about 230 kbar or more, and for NG about 330 kbar or more. Combined with shock velocities equal to the detonation velocities of 6.29 and 7.58 km/sec, respectively, we arrive at a conservative lower limit for the corresponding shock front particle velocities of 3.24 and 2.72 km/sec, respectively. Neglecting the contribution to the pressure from the 0 $^{\circ}\text{K}$  isotherm of either explosive, which is probably allowable, and assuming a specific heat for both explosives of 0.4 cal/g  $^{\circ}\text{K}$ , we arrive at an estimate of the shock front temperature increase of 3140 $^{\circ}\text{K}$  in NM and 2210 $^{\circ}\text{K}$  in NG.

#### ACKNOWLEDGMENTS

The work described in this paper was carried out at the Swedish Detonic Research Foundation with financial support from Nitro Nobel AB and the Swedish Technical Research Council. The work on the spectral distribution of light was carried out by Thomas Lindblad with the assistance of Miss Berit Alm. The authors gratefully acknowledge these contributions, without which the work had not been possible.

#### REFERENCES

1. F. P. Bowden, M. A. Stone, and G. K. Tudor, "Hot Spots on Rubbing Surfaces and the Detonation of Explosives by Friction", *Proc. Roy. Soc. A* **188**, 329 (1947).
2. F. P. Bowden, and A. D. Yoffe, "Initiation and Growth of Explosion in Liquids and Solids", Cambridge University Press, Cambridge, 1952.
3. A. W. Campbell, W. C. Davis, and J. R. Travis, "Shock Initiation of Detonation in Liquid Explosives", *Phys. Fluids* **4**, 498 (1961).
4. A. W. Campbell, W. C. Davis, J. B. Ramsay, and J. R. Travis, "Shock Initiation of Detonation of Solid Explosives", *Phys. Fluids* **4**, 511 (1961).
5. C. H. Winning, "Initiation of Nitroglycerine", *Explosivstoffe* **11**, 2 (1963).
6. R. W. Van Dolah, R. W. Watson, C. R. Summers, and F. C. Gibson, "Detonation in Liquid Explosives—The Low-Velocity Regime", *Proc. 4th Symp. Detonation*, Silver Spring, Maryland 1965, ACR-126 (1966).
7. S. P. Cachia, and E. G. Whitbread, "The Initiation of Explosives by Shock", *Proc. Roy. Soc. A* **246**, 268 (1958).
8. P. A. Persson, B. Andersson, and S. O. Ståhl, "A Technique for Detailed Time-Resolved Radiation Measurements in the Reaction Zone of Condensed Explosives", *Proc. 4th Symp. Detonation*, Silver Spring, Maryland 1965, ACR-126 (1966).
9. F. C. Gibson, M. L. Bowser, C. R. Summers, F. H. Scott, and C. M. Mason, "Use of an Electro-Optical Method to Determine Detonation Temperatures in High Explosives", *J. Appl. Phys.* **29**, 628 (1958).
10. V. S. Ilyukhin, P. E. Pokhil, D. K. Rozanov, and N. S. Shvedova, "Measurement of the Shock Adiabatic Curves for Cast TNT, Crystalline RDX, and Nitromethane", *Doklady Akad. Nauk USSR* **131**, 793 (1960).

- English translation in: Soviet Physics, Doklady, 5, 337 (1960).
11. J. M. Walsh, and M. H. Rice, "Dynamic Compression of Liquids from Measurements on Strong Shock Waves", J. Chem. Phys. 26, 815 (1957).
  12. C. L. Mader, "The Time-Dependent Reaction Zones of Ideal Gases, Nitromethane, and Liquid TNT", Los Alamos Scientific Laboratory Report LA 3764, 1967.
  13. B. G. Craig, "Measurements of the Detonation Front Structure in Condensed Phase Explosives", Proc. 10th Symp. on Combustion, Cambridge, 1964. Combustion Institute, Pittsburg (1965).
  14. P. A. Persson. Unpublished results (1969).
  15. A. A. Andreev, and A. F. Beljaev, "Theory of Explosives", Moskva 19, German translation by Sek. för Detonik och Förbränning, Svenska Nationalföreningen för Mekanik, Stockholm, 1964.
  16. F. P. Bowden, and A. D. Yoffe, "Fast Reactions in Solids", Butterworths, London, 1958.
  17. M. A. Cook, "The Science of High Explosives", Reinhold Publ. Co., New York, 1958.

## DISCUSSION

T. HIKITA  
University of Tokyo  
Tokyo, Japan

Some of the results you obtained are very interesting. What do you think about the fact that in the propagation stage of detonation, a higher density solvent can support the detonation of the mother liquid better? The results you obtained show that the inverse relation exists in the initiation stage.

## REPLY BY PERSSON

It is important to distinguish between the initiation delay, on the one hand, and the ability to propagate detonation, on the other. The delays we have measured and their variation with additive content, appear to be simply dependent upon shock temperature. With a given donor, the explosive with a low shock impedance will attain a high shock temperature and this usually means a short delay.

In propagating detonation, the detonation front pressure and the initial temperature are determined separately by the combination of the explosive's own initial density and the reaction product isentrope, essentially as required by the Rayleigh line tangency condition. We know that high-density explosives have a high detonation pressure and low-density explosives a low pressure. It appears not unlikely, under these conditions, and especially if we are

considering charges of equal diameter, that a high-density solvent may aid the detonation more than a low-density solvent.

F. E. WALKER  
Lawrence Radiation Laboratory  
Livermore, California 94550

As I understand the experiment you described, the light recorded passed through a port at the base of the system, and the detonation proceeded vertically from this port. How could you then determine that the initiation to detonation did occur first at the face of the sample liquid explosive that was first struck by the shock? (In a later viewing of some of Dr. Persson's photographs, it did appear that there was a relatively dark zone below the apparent initiation-to-detonation site.)

In the plot which showed temperature at the peak amplitude and at a plateau with relation to a standard temperature value, what did the peak amplitude and the plateau actually represent?

## REPLY BY PERSSON

In separate experiments using relatively thick barriers, we have found the photomultiplier records to be in complete harmony with the picture of the process of shock initiation in

liquids given almost 10 years ago by Campbell, Davis and Travis in their "Physics of Fluids" paper.

The plateau of relatively weak emission comes from the detonation in the shock-compressed liquid, the peak emission comes from the transient overdriven detonation when the catch-up occurs.

H. J. GRYTING

Naval Weapons Center  
China Lake, California

What is the effect on initiation delay of changes in specific heat without change in density?

REPLY BY PERSSON

We have not made any systematic study of the effect of changes in specific heat alone.

# DARK WAVES IN LIQUID EXPLOSIVE SYSTEMS: THEIR ROLE IN DETONATION FAILURE

Richard W. Watson

*Pittsburgh Mining and Safety Research Center, Bureau of Mines  
U.S. Department of the Interior, Pittsburgh, Pennsylvania*

## ABSTRACT

High-speed framing camera observations as well as flash radiographs were obtained on a number of widely different liquid explosive systems that exhibit dark wave structure. The effects of charge diameter, confinement material, and initial explosive temperature have been explored. The results of this investigation lead to the conclusion that the dark wave phenomenon may be common to all liquid explosive systems. The early explanations proffered appear to be correct in that the dark wave phenomena are associated with non-reactive regions in the explosive near the periphery of the charge. This paper's major contribution lies in the correlation between the apparent physical size of the area of the explosive charge effected by the dark waves and the minimum film thickness for detonation determined in independent trials using the wedge technique developed at this Center. The results lead to the conclusion that they are responsible for detonation failure and that while simple reaction kinetics may be used as a first basis for theoretical formulations of detonation failure models, two-dimensional reactive flow computations will be required even in the simplest description of this problem.

## INTRODUCTION

The subject of detonation failure in homogeneous explosives is one of continued interest. Early experimental work by Campbell (1) and his associates suggested that detonation failure was linked to the so-called dark waves observed in homogeneous explosive systems. The subject was then diligently pursued by Dremin (2,3). This latter work greatly elucidated the role of gross peripheral dark waves and fine wave structure at the detonation front in the propagation and failure of detonation in liquid explosive systems. Mallory's (4) recent work on turbulent effects in detonating liquids failed to show any gross dark waves even when the reaction waves were observed under failing conditions. However, his observations were limited to the central regions of the detonation wave front and he took this as slight evidence that such regions are edge effects. Recent experiments at the Lawrence Radiation Laboratory (5) have provided dramatic evidence supporting the concept that detonation in nitromethane is cellular in nature in support

of Shchelkin's hypothesis concerning the similarity between liquid and gaseous detonations (6).

Most of the experimental work in this area has been carried out using nitromethane mixed with various diluents. In our work at the Safety Research Center we have accumulated data relating to the limiting thickness for low- and high-velocity detonation failures in a large number of liquid explosive systems. The results are obtained using a technique involving a wedge-shaped charge and a velocity-monitoring probe (7). The data obtained in this fashion are valuable in assaying the relative sensitivity of liquid explosives but the technique fails to provide any information relating to the mechanisms of detonation failure for either the high- or low-velocity modes. The purpose of this paper is to describe the results of some recent observations of dark waves employing high-speed framing camera photography and flash radiography. The experimental results supplement the observations of the previous investigations. They indicate that the gross dark waves

are a feature of all liquid explosive systems and are intimately linked with detonation failure limits for high-velocity detonation.

#### EXPERIMENTAL DETAILS AND RESULTS

The experiments were carried out with various liquid explosives contained in 20.3-inch long Plexiglas or aluminum tubes. The Plexiglas tubes had inside diameters of 2.2 cm, 3.0 cm and 5.1 cm with corresponding wall thicknesses of 0.16, 0.32, and 0.32 cm. The aluminum tubes had an inside diameter of 2.54 cm and a wall thickness of .08 cm. The charges were initiated by means of a tetryl booster separated from the liquid by a thin polyethylene diaphragm stretched over the ends of the confinement tube. The boosters were all 2.54 cm long; a 2.54 cm diameter was employed with the 2.2 cm-diameter Plexiglas and 2.54-cm diameter aluminum tubes. For the two larger Plexiglas tube sizes the booster diameter was the same as the inside diameter of the tubes.

The framing camera observations were made at a fixed interframe time of  $1.0 \mu\text{sec}$  and an exposure time of  $0.16 \mu\text{sec}$ . The camera view was directed along the axis of the charge normal to the oncoming detonation wave front.

A pulsed X-ray system with a pulse duration of 30 nanoseconds was used in the flash radiographic studies. The exposures were made normal to the charge axis providing a profile view of the detonation wave front. The X-ray unit was operated at 300 kv with a discharge current of 1400 amp. Except where indicated, all of the firings were conducted at ambient temperatures, approximately  $20^\circ\text{C}$ .

Selected frames of detonating nitromethane in the three Plexiglas tube sizes are presented in Fig. 1. The views correspond to a position approximately 5.1 cm from the downstream end of the tube or 15.2 cm from the booster-liquid interface. Dark waves emanating from the periphery of the charges were observed for all three charge diameters. The size of the dark regions appears to decrease with increasing charge diameters. The structure observed in the 2.2-cm diameter charge is particularly interesting. The dark wave traversing the center of the charge originated at the charge periphery near the center of the second quadrant and took approximately  $3.0 \mu\text{sec}$  to cross the body of the charge. After this, the detonation continued and subsequent camera views were similar to that of Fig. 1(b). Besides the dark waves, regions in the explosive having higher luminosity than the detonation wave luminosity near the center of the charge were frequently observed. They were usually spike-shaped and extended from the charge periphery some distance into the body of the explosive. One of these is clearly visible on the left side of Fig. 1(b) and another near the bottom of Fig. 1(c). These were invariably observed after the disappearance of two neighboring dark regions and are probably due to shock wave convergence.

The results of an examination of some of the factors influencing the gross appearance of the dark waves are presented in Fig. 2. The firings depicted in Fig. 2(a), (b), and (c) were carried out in 3.8-cm diameter Plexiglas tubes while that of Fig. 2(d) was made in a 2.5-cm diameter aluminum tube. Fig. 2(a) shows the results obtained with neat nitromethane diluted with 5%, by weight, acetone, a desensitizing additive. The dark wave structure appears to be much coarser than that observed for neat

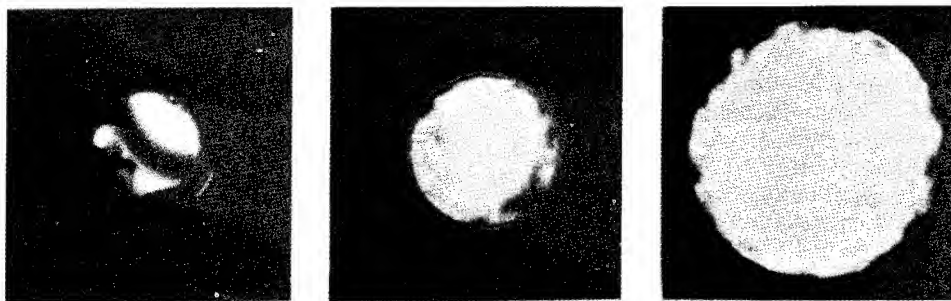


Fig. 1 - Framing camera views showing gross dark wave structure in detonating nitromethane in Plexiglas tubes of varying diameter: (a) 2.2 cm; (b) 3.0 cm; (c) 5.1 cm. Detonation front is advancing toward the observer.

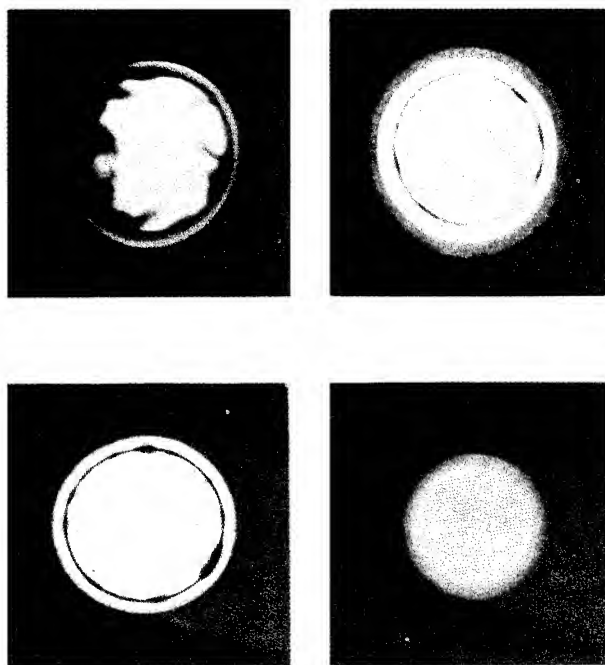


Fig. 2 - Framing camera views of the dark wave structure of detonating nitromethane. (a) Plexiglas tube: nitromethane + 5 wt percent acetone at 20°C; (b) Plexiglas tube: nitromethane + 3 wt percent tetranitromethane at 20°C; (c) Plexiglas tube: nitromethane at 50°C; (d) aluminum tube: nitromethane at 20°C.

nitromethane under the same experimental conditions (Fig. 1(b)). The addition of a sensitizing agent, 3% by weight tetranitromethane, almost totally eliminates the dark wave structure shown in Fig. 2(b). A nominal increase in the temperature produces nearly the same effect. This is shown in Fig. 2(c) which was obtained with neat nitromethane having an initial temperature of 50°C in the same tube geometry as Fig. 2(a). An effect of confinement tube material is shown in Fig. 2(d). This firing was conducted with neat nitromethane contained in a 2.5-cm inside diameter aluminum tube. In this case, dark waves were not observed.

Additional insight concerning the nature and origin of the dark waves was obtained from flash radiographs of the detonation wave in some of the explosive-container combinations. These are presented in Fig. 3. Fig. 3(a) shows the detonation wave in neat nitromethane contained in a 3.8-cm diameter Plexiglas container. It will be noted that the wave front has a pronounced curvature, especially at the charge periphery. The results of Fig. 3(b) were obtained with a similar charge containing

nitromethane diluted with 5% acetone. In this case the wave front is very irregular. The addition of 3% tetranitromethane appears to reduce the detonation wave curvature below that observed in neat nitromethane. This is shown in Fig. 3(c) which was also obtained with a 3.8-cm diameter Plexiglas tube. Neat nitromethane in the thin wall aluminum container (Fig. 3(d)) yielded an almost plane detonation wave front.

It has already been suggested that the gross dark waves observed in liquid explosives were associated with detonation failure; this coupled with the fact that the preponderance of experimental data was obtained with nitromethane-based explosives led to another series of trials involving explosives other than nitromethane. The explosives chosen for this purpose consisted of a mixture of 50/50 nitroglycerin-ethylene glycol dinitrate diluted with 22-1/2% acetone by weight and a casting solvent containing 80% TMETN, 19% TEGDN, and 1% NDPA. These two systems were chosen because in previous experiments, using the wedge technique, they had exhibited the same minimum



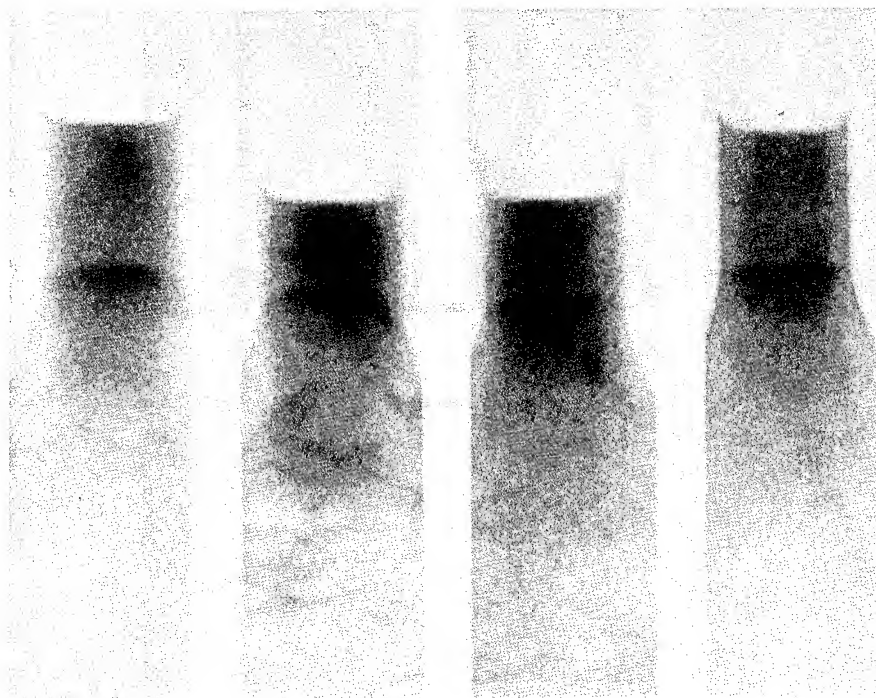


Fig. 3 - Flash radiographs of the wave front curvature of detonating nitromethane. (a) Plexiglas tube: neat nitromethane; (b) Plexiglas tube: nitromethane + 5 wt percent acetone; (c) Plexiglas tube: nitromethane + 3 wt percent tetranitromethane; (d) aluminum tube: neat nitromethane.

film thickness for the propagation of high-velocity detonation,  $0.25 \text{ inch} \pm 0.02 \text{ inch}$  (8). Framing camera views comparing the dark wave structure in these two explosive systems with that of neat nitromethane are presented in Fig. 4. Fig. 4(a) shows the results obtained with neat nitromethane; results of trials with the casting solvent and diluted nitroglycerin-ethylene glycol dinitrate are shown in Figs. 4(b) and 4(c) respectively. The explosives were contained in Plexiglas tubes having a 3.8 cm diameter. As will be noted, the dark wave structures in the three explosive systems are quite similar in terms of the distance that the dark waves penetrate into the body of the liquid. In Fig. 4(b) and (c), the dark waves appear to coalesce and form a dark irregular ring between the illuminated container top and the oncoming detonation front.

## DISCUSSION

The qualitative features of all of the foregoing results can be described in terms of the current understanding of homogeneous explosive systems. Using simple adiabatic explosion theory and assuming first order Arrhenius

reaction kinetics, we note a strong dependence of the induction time on the temperature which in turn is a function of the shock pressure. For example, the recent calculations of Enig and Petrone yielded a value of induction of  $2.31 \mu\text{sec}$  for nitromethane shocked to 86 kilobars and a corresponding temperature of  $1103^\circ\text{K}$  (9). Similar calculations for a shock pressure of 201 kilobars and a corresponding shock temperature of  $1662^\circ\text{K}$  yielded a value of  $0.00320 \mu\text{sec}$  for the induction time. In the radiographic experiments with neat nitromethane in Plexiglas containers, the detonation wave was noticeably curved at the charge periphery. It might be expected that the shock pressure near the charge periphery is considerably less than the pressure at the charge axis. Simple calculations based on oblique shock theory and rough measurements of the angle of wave incidence with the container wall yield a shock pressure of approximately 100 kilobars in this region. At this pressure, the corresponding induction time would be approximately  $1.0 \mu\text{sec}$ . This time would allow a rarefaction wave to penetrate approximately 0.5 cm into the body of the fluid; the dark waves are observed to penetrate to approximately the same depth in the 3.8-cm diameter firings with neat nitromethane. In the



Fig. 4 - Framing camera views showing similarity of dark wave structure in (a) nitromethane; (b) 50/50 NG-EGDN + 22-1/2 wt percent acetone; (c) 80/19/1 TMETN/TEGDN/NDPA casting solvent

case of the firing conducted in the aluminum containers, a shock wave is propagated back into the reacting fluid until the pressure is released at the external tube boundary. In this case the wave would be essentially planar and there would be no increase in induction time. The flash radiograph of Fig. 3(d) indicates that the wave front is nearly plane and there is a complete absence of dark wave structure in the end-on view of Fig. 2(d).

The effects of desensitizing and sensitizing additives as well as the effects of elevated temperature can be anticipated in the same way—increasing or decreasing the induction time. The effects produced by the addition of 3 wt percent TNM and by temperature elevation of only +30°C are consistent with this explanation.

Since the recent experiments at the Lawrence Radiation Laboratory (5) showed a relatively high degree of uniformity in the cellular structure of the detonation waves in acetone-nitromethane mixtures, an attempt was made to determine if there was any periodicity in the motion of the dark waves observed in our experiments. For this purpose a number of the 25-frame sequences showing well-defined dark wave structure were "animated" using a repeat-frame technique. While the motion picture strips obtained in this way did give some impression of detonation "spin," the overall changes in the dark wave pattern within the time resolution of the experiment set by the 1.0  $\mu$ sec interframe time were too great to completely resolve this point. In addition, it might be pointed out that the framing camera technique employed here was not adequate for resolving any fine detail in the structure of the detonation front such as those observed by Mallory using the impedance mirror method.

In conclusion, our framing camera and flash radiographic observations agree with the

results of other investigators. They add further weight to the contention that the peripheral dark waves correspond to unreacted regimes in the explosive are associated with lateral rarefactions and are common to all homogeneous explosive systems. In addition, these qualitative features appear to correlate with the failure thickness for detonation determined in independent experiments (7,8). Namely, liquids having the same failure thickness exhibit similar dark wave structure when detonated under the same conditions. This leads to the conclusion that any theory accounting for detonation failure in liquid explosives must take into account the complex flow configuration introduced by the dark waves as well as the kinetic parameters describing the explosive system.

#### REFERENCES

1. A. W. Campbell, T. E. Holland, M. E. Malin, and T. P. Cotter, Jun., "Detonation Phenomena in Homogeneous Explosives," *Nature*, Vol. 178, No. 4523, pp. 38-39, July 7, 1956.
2. A. N. Dremin, O. K. Rozanov, and V. S. Trofimov, "On the Detonation of Nitromethane," *Combustion and Flame*, Vol. 7, pp. 153-162, June 1963.
3. A. N. Dremin, "Critical Phenomena in the Detonation of Liquid Explosives," pre-printed for Twelfth Symposium (International) on Combustion, University of Poitiers, France, July 14-20, 1968.
4. H. Dean Mallory, "Turbulent Effects in Detonation Flow: Diluted Nitromethane," *J. of Applied Physics*, Vol. 38, No. 13, pp. 5302-5306, Dec. 1967.

5. P. A. Urtiew, A. S. Kusubov, and R. E. Duff, "Cellular Structure of Detonation in Nitromethane," UCRL Preprint 71479, June 6, 1969.
6. K. I. Shchelkin, "Two Cases of Unstable Detonation," Zh. E. T. F., 36, 600, 1959.
7. J. Ribovich, "A Wedge Technique for Evaluation of Detonation Hazards of Liquid Explosives," Annals of The New York Academy of Sciences, Vol. 152, Article 1, pp. 766-772, Oct. 28, 1968.
8. F. C. Gibson, R. W. Watson, J. E. Hay, C. R. Summers, J. Ribovich, and F. H. Scott, "Sensitivity of Propellant Systems," Bureau of Mines Quarterly Report Oct. 1 - Dec. 31, 1965.
9. J. W. Enig and F. J. Petrone, "Equation of State and Derived Shock Initiation Criticality Conditions for Liquid Explosives," Phys. Fluids, Vol. 9, No. 2, pp. 398-408, Feb. 1966.

NOTE: Reference to trade name "Plexiglas" is made to facilitate understanding and does not imply endorsement by the Bureau of Mines.

**SESSION III**  
**NON-STEADY REACTIVE SHOCKS**

Chairman: James E. Ablard  
*Naval Ordnance Laboratory*

# NUMERICAL CALCULATIONS OF DETONATION FAILURE AND SHOCK INITIATION

Charles L. Mader  
*Los Alamos Scientific Laboratory  
University of California  
Los Alamos, New Mexico*

## ABSTRACT

The failure of a nitromethane detonation resulting from a side rarefaction cooling the explosive inside its reaction zone has been calculated using an Eulerian, reactive, numerical, hydrodynamic code. The velocity of the rarefaction agrees with the experimental measurements of Davis. The formation of hot spots from the interaction of a shock in nitromethane with a cylindrical void, and the failure of the hot spot to initiate propagating detonation as a result of the rarefactions interacting with the reaction zone have been computed. The interaction of the hot spots formed from several voids has been computed. The basic two-dimensional processes involved in the shock initiation of heterogeneous explosives have been numerically described.

## INTRODUCTION

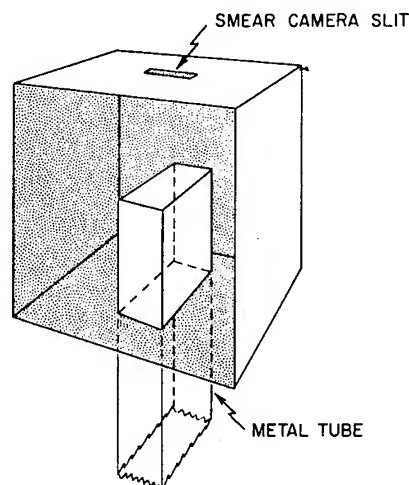
To increase our understanding of the basic processes involved in the shock initiation of inhomogeneous explosives, we have studied theoretically the formation of hot spots from shocks interacting with discontinuities of various densities. In reference (1) we described the hot spots formed when a shock in nitromethane interacts with a spherical, cylindrical, or conical void and with cylinders and spheres of aluminum. The PIC (particle-in-cell) method was used for numerically solving the hydrodynamics. It was concluded that the PIC type of numerical hydrodynamics could be used to compute the interaction of a shock with a density discontinuity, the formation of a hot spot, and buildup to propagating detonation. The failure of the resulting hot spot to initiate propagation detonation could be described in those cases in which the failure mechanism did not depend on the details of the structure of the reaction zone.

It was necessary to study the time-dependent reaction zone of homogeneous explosives before one could calculate cases that required resolved reaction zones. The stability of the reaction zone was studied in both one- and two-dimensional geometry. As described in reference (2), it was found that the amount of overdrive necessary to

stabilize the nitromethane and liquid TNT detonation decreases with decreasing activation energy and that nitromethane with an activation energy of 40 kcal/mole is stable to all perturbations at C-J velocity. Also described in reference (2) was the failure of a propagating detonation as a result of rarefactions from the rear cooling the explosive in the reaction zone. One of the major problems that had to be solved for further understanding of the basic processes involved in the shock initiation of explosives or in the failure diameter of explosives was that of failure of propagating detonation because of side rarefactions cooling the explosive inside the reaction zone. The Eulerian approach to solving the reactive hydrodynamic equations is suitable for such problems provided that only one component is present. Therefore, the Eulerian code called 2DE, described in reference (3), was written to solve these problems.

## FAILURE OF A NITROMETHANE DETONATION WAVE

Davis (4) has studied the failure of a supported nitromethane detonation wave traveling up a copper tube and then into a large container of nitromethane as shown below. He observed rarefaction or "failure" waves that ran across



the front at about  $0.37 \text{ cm}/\mu\text{sec}$  and that extinguished the detonation if the tube was a cm or less wide.

If the tube was larger, the detonation was not extinguished. A narrow failure or dark wave ran into the front, getting narrower as it progressed. This wave extinguished detonation at its front, but reignition occurred at the rear and caught up with the wave. Under these circumstances the explosive in the box would detonate. These experiments demonstrate the basic processes involved in the problems of the failure of detonation, of the failure diameter of explosives, and of the "sputtering" initiation observed for density discontinuities near the critical size.

The light observed by Davis is thermal radiation from the hot explosive. Only near the end of the reaction zone is material hot enough to produce enough light for a high speed camera to record. Some of the light emitted is absorbed in the partially reacted explosive ahead of it, and if the reaction zone is thick enough, no light is recorded. The apparent discontinuity in light intensity which Davis recorded corresponds to a sharp change in the distance from the shock front to the region hot enough to produce recordable light. Rather than present the complete analysis of emission and absorption here, we assume for illustration that no light is recorded when the distance from the shock front to the  $3000^\circ\text{K}$  isotherm becomes twice what it is for the high-order detonation. Fortunately, the change is so sudden and so large that the value obtained for the apparent velocity does not depend much upon the criterion chosen.

Figure 1 shows the calculated isobars and isotherms of the failure of a nitromethane

reaction zone resulting from side rarefactions, for an activation energy of  $53.6 \text{ kcal/mole}$ . Similar results were obtained for an activation energy of  $40 \text{ kcal/mole}$ . The reaction zone profiles for both activation energies vary only a few kilobars from the steady-state values during the time of interest in these calculations (2).

The experimental arrangement is approximated numerically by a steady-state reaction zone flowing through 150 of the 300 cells near the lower boundary to approximate the top of the metal tube. The cell is a square of  $40\text{-}\mu\text{m}$ . For a  $\gamma$  of 0.68, an activation energy of  $53.6 \text{ kcal/mole}$ , and a frequency factor of  $4 \times 10^8$ , the reaction zone of a C-J detonation of nitromethane occupies  $2400 \text{ }\mu\text{m}$ , or 60 of the 300 cells, along the half-slab left boundary. The von Neumann spike pressure is 212 kbar, and the C-J pressure is 130 kbar. The use of a  $300 \times 300$  mesh for a total of 90,000 cells is near the maximum resolution possible if one wishes to expend a reasonable amount ( $\sim 24$  hours for IBM 7030) of computer time.

Using the  $3000^\circ$  isotherms throughout the reaction zone, one obtains a rarefaction velocity of  $0.4 \pm 0.05 \text{ cm}/\mu\text{sec}$  which is in good agreement with that found experimentally by Davis.

The failure of a slab of nitromethane with a void on the outside is shown in Fig. 2 with  $300 \times 300$  cells. The radius of curvature is greater, and the rarefaction is stronger, for the nitromethane confined by a void than for nitromethane confined by nitromethane.

Similar studies were performed in cylindrical geometry and are described in reference (4).

Having demonstrated the failure of a detonation wave because of rarefactions from the side cooling the explosive inside the reaction zone, we now proceed to study the formation of hot spots and the initiation of an explosion which does not result in a propagating detonation.

#### THE INTERACTION OF A SHOCK WITH A CYLINDRICAL VOID

In reference (5) we described the interaction of an 85-kbar shock in nitromethane with a  $0.032\text{-cm}$ -radius,  $0.032\text{-cm}$ -high, cylindrical void, using the PIC code. The same system was computed using the Eulerian code and the results are shown in reference (4). The agreement between the two problems is sufficient to allow a semiquantitative study of the formation

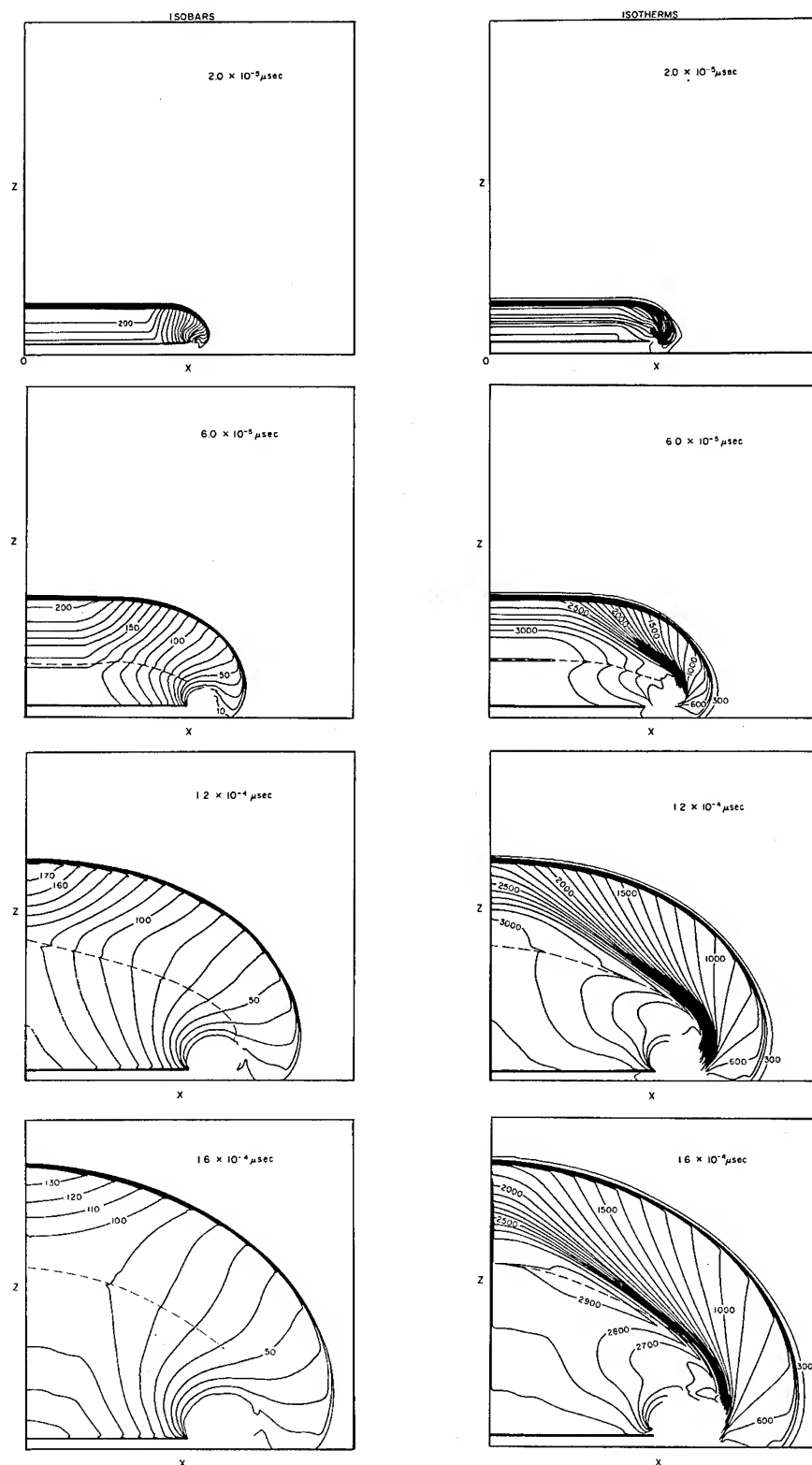


Fig. 1 - The computed isobars and isotherms for a supported slab nitromethane C-J detonation wave passing into a box of nitromethane. The interval between isobars is 10 kbar. The interval between isotherms is 100° Kelvin. The dashed line is the location of the end of the reaction zone. 300 x 300 40-A-square cells were used.

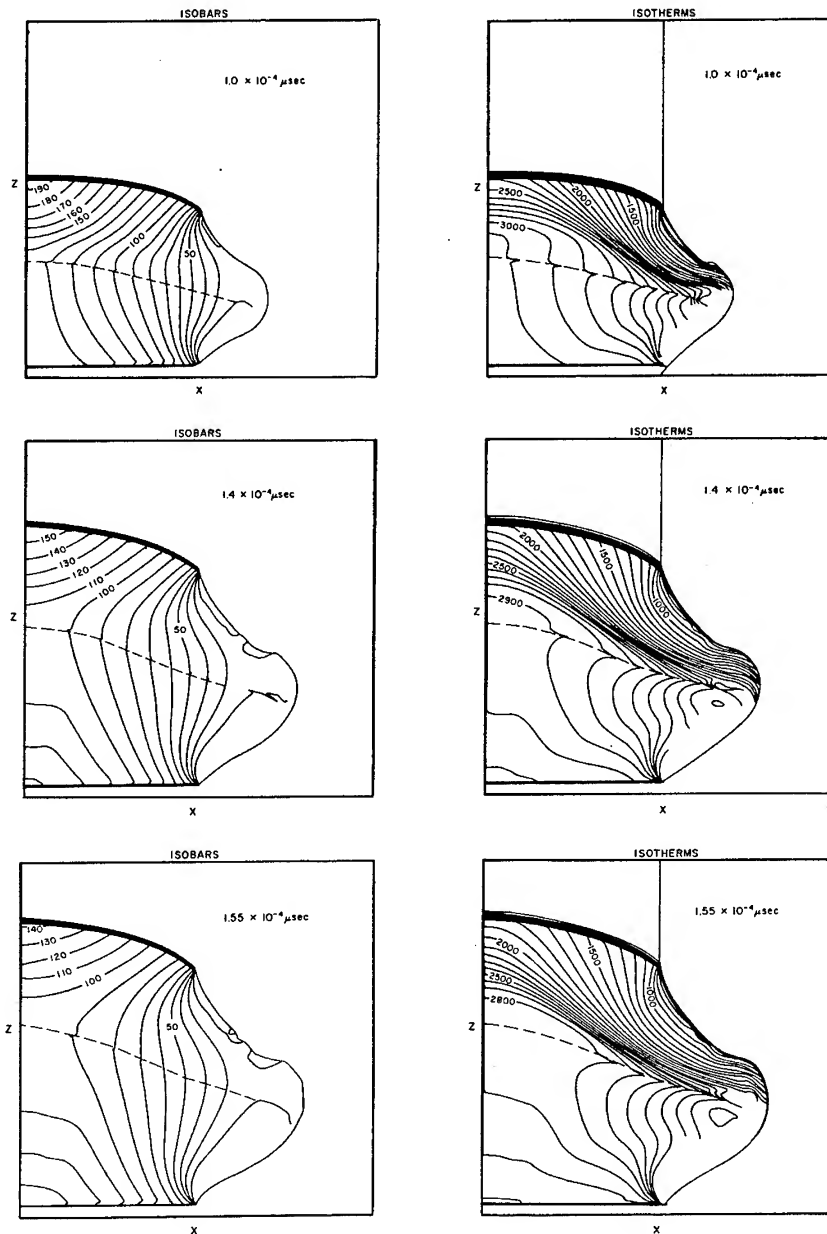


Fig. 2 - The computed isobars and isotherms for a supported slab nitromethane C-J detonation wave passing into a slab of nitromethane with a void on the right side of the slab. The dashed line is the location of the end of the reaction zone.  $300 \times 300$  40-A-square cells were used.

of hot spots, the resulting explosion, and failure to propagate.

Figure 3 shows the formation of a hot spot in nitromethane from an 85-kbar shock interacting with a  $2 \times 10^{-5}$ -cm-radius cylindrical void with chemical reaction permitted. The hot

spot explodes but fails to establish propagating detonation.

A  $3.2 \times 10^{-4}$ -cm-radius hole is the largest that will result in a resolved reaction zone and, hence, permit failure of an explosion to occur in a  $100 \times 100$  mesh of which the hole is  $20 \times 20$ .



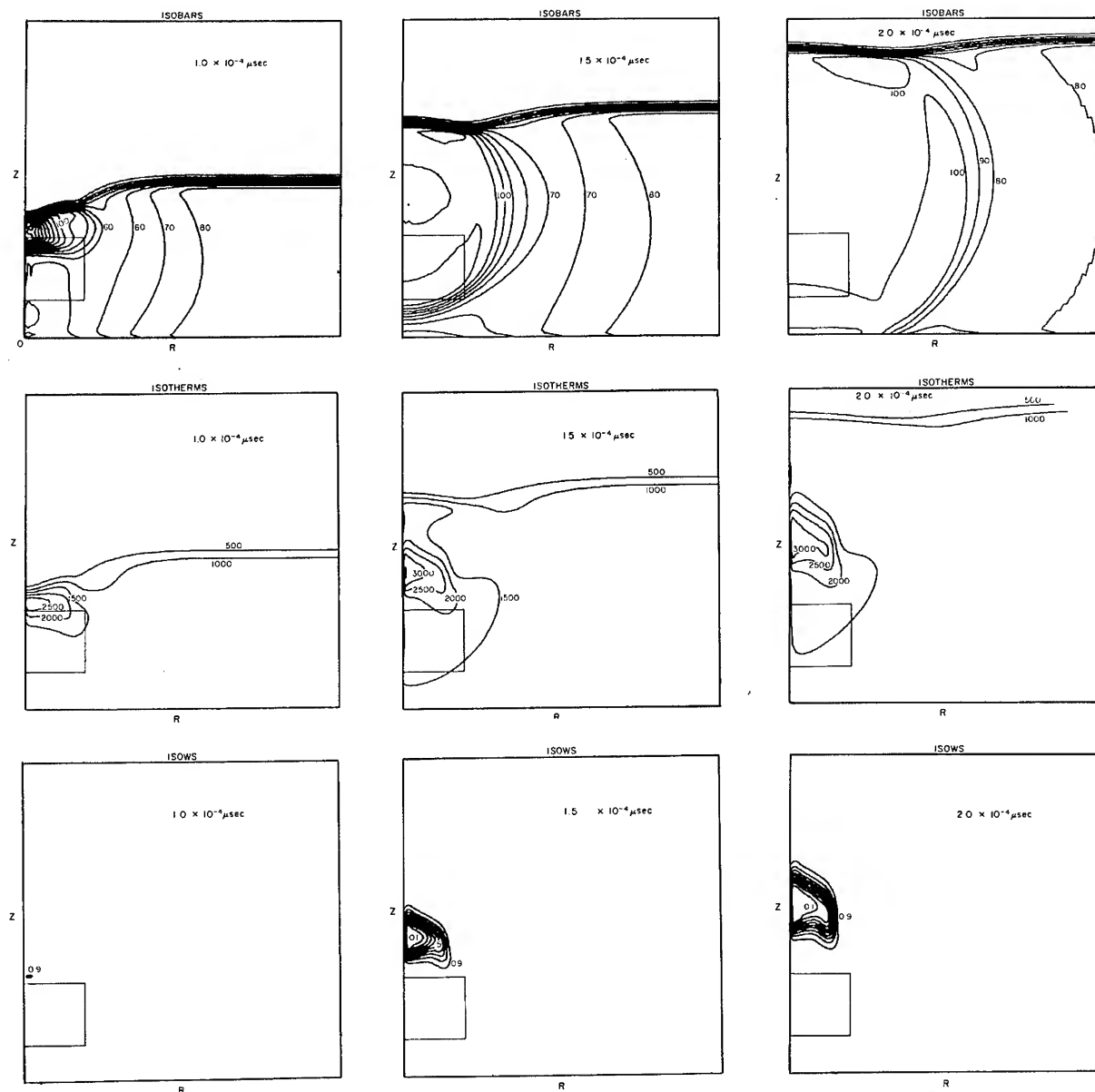


Fig. 3 - The computed isobars, isotherms, and isows of an 85-kbar shock interacting with a  $2 \times 10^{-5}$ -cm-high, cylindrical void in a  $1 \times 10^{-4}$ -cm-radius,  $1 \times 10^{-4}$ -cm-high cylinder of nitromethane. Chemical reaction is permitted. The interval between isobars is 10 kbar, that between isotherms is  $500^\circ$  Kelvin, and that between isows is 0.1 where  $w$  is mass fraction of undecomposed explosive. The original position of the void is shown.

This is two orders of magnitude smaller than the experimentally observed critical size. To obtain suitable resolution one would require a mesh of  $10,000 \times 10,000$ , or 100 million, cells. This is not a practical problem to solve with present computers.

We have demonstrated how a hot spot can explode but then fail to propagate because of

rarefactions cooling the reactive detonation wave.

#### THE INTERACTION OF A SHOCK WITH FOUR RECTANGULAR HOLES

The interaction of a shock with four rectangular voids, the bottom two with a half-width of

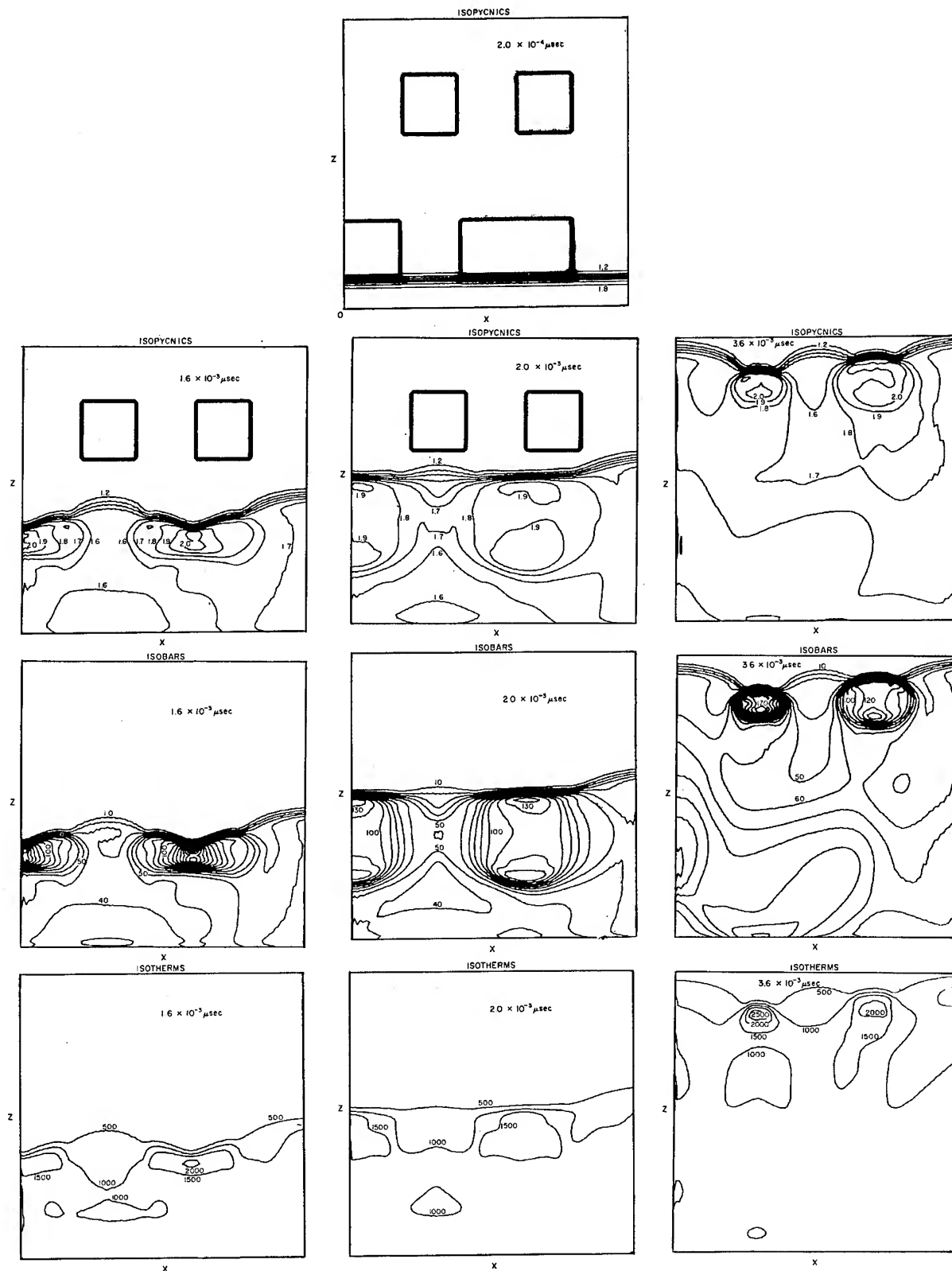


Fig. 4 - The interaction of an 85-kbar shock in a  $1.6 \times 10^{-3}$ -cm half-width,  $1.6 \times 10^{-3}$ -cm-high slab of nitromethane with four rectangular holes. Chemical reaction is not permitted. The interval between isopycnics is 0.1 cm/cc, that between isobars is 10 kbar, and that between isotherms is 500° Kelvin. The isopycnics show the hole geometry.

$3.2 \times 10^{-4}$  cm, and the top two with a width of  $3.2 \times 10^{-4}$  cm, is shown in Fig. 4 for nonre-active nitromethane. The same problem with chemical reaction included is shown in Fig. 5.

While propagating detonation does not occur when the shock interacts with the first two holes, the enhancement of the shock wave by chemical reaction does produce a hotter hot spot upon interaction with the upper two voids. The hot

spot is so hot that complete nitromethane decomposition occurs at the shock front. While a propagating detonation would not be expected to occur experimentally in this geometry of four holes (the computed detonation is the result of insufficient numerical resolution to resolve the reaction), the enhancement of the shock wave would be expected to occur experimentally. These calculations show the basic features of the shock initiation of heterogeneous explosives.

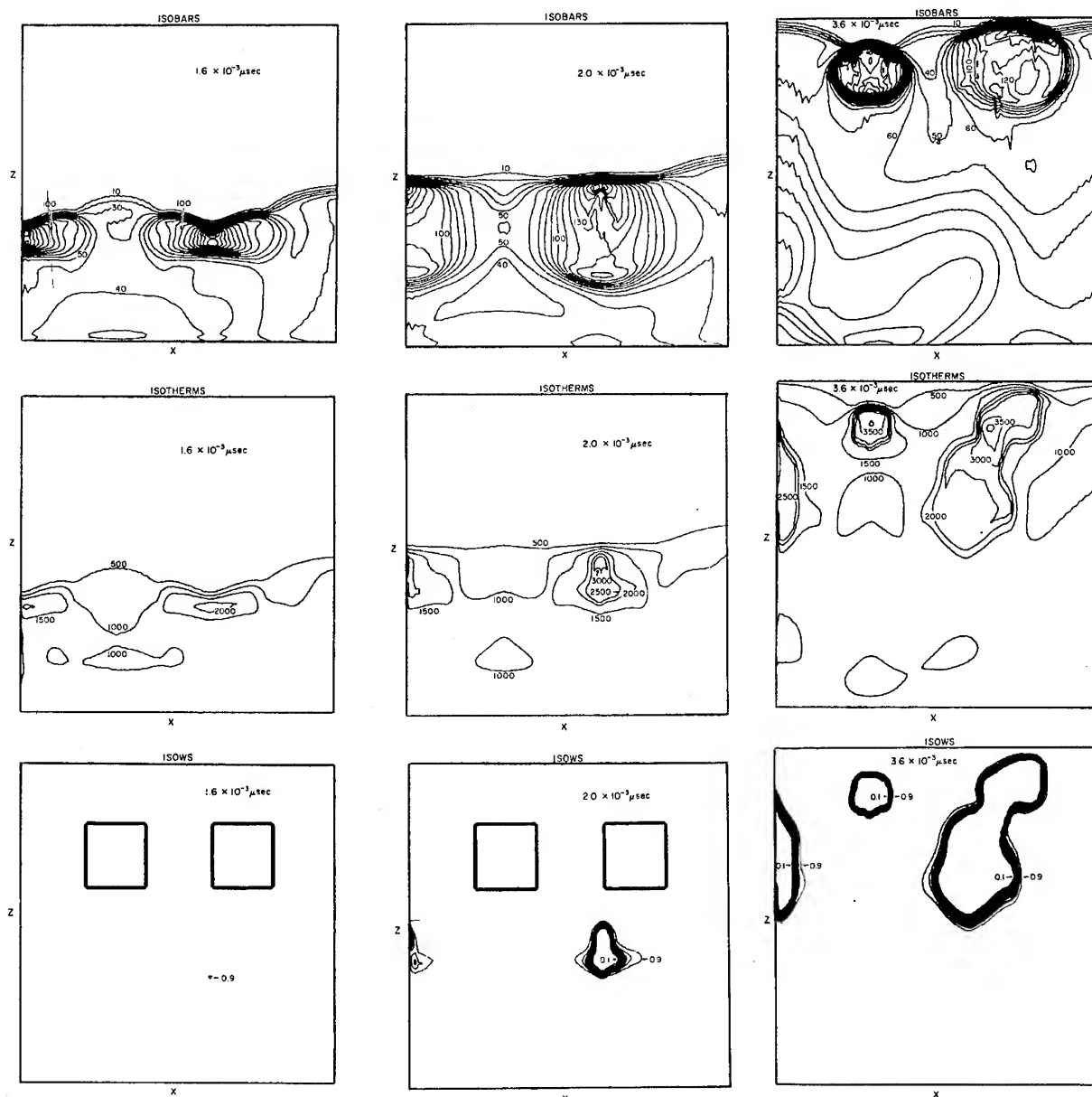


Fig. 5 - The interaction of an 85-kbar shock in a slab of nitromethane with four rectangular holes of the same dimensions as those in Fig. 4. Chemical reaction is permitted. The interval between iso-bars is 10 kbar, that between isotherms is 500° Kelvin, and that between isows is 0.1 where w is the mass fraction of undecomposed explosive.

A shock interacts with the density inhomogeneities, producing numerous local hot spots which explode but do not propagate, thereby liberating energy which strengthens the shock so that, when it interacts with additional inhomogeneities, hotter hot spots are formed and more of the explosive is decomposed. The shock wave grows stronger and stronger, releasing more and more energy, until it becomes strong enough to produce propagating detonation. Additional slow decomposition continues to occur behind the shock front which may be the source of the energy observed to be released from shocked-but-not-detonated explosive by Craig and Marshall (6).

## CONCLUSIONS

The failure of a nitromethane detonation resulting from side rarefactions cooling the explosive inside its reaction zone has been calculated. The velocity of the rarefaction agrees with the experimental measurements of Davis. The formation of hot spots from the interaction of a shock in nitromethane with a cylindrical hole, and the failure of the hot spot to initiate propagating detonation as a result of the rarefactions interacting with the reaction zone have been computed. The interaction of the hot spots formed from several holes has been computed.

The basic two-dimensional processes involved in the shock initiation of heterogeneous explosives have now been numerically described. The problem that remains is the study of the interaction of a shock with a matrix of holes in three-dimensional geometry. The basic two-dimensional processes involved in the failure of detonation, the failure diameter of explosives, and the "sputtering" initiation observed for density discontinuities near the critical size have been described. The three-dimensional study of the interaction of numerous failures and reignited detonations which is necessary for a complete numerical description of these problems must await new computing hardware.

## ACKNOWLEDGMENTS

The author gratefully acknowledges the assistance and contributions of W. C. Davis, W. Fickett, J. Travis, B. Craig, and L. C. Smith of GMX-Division; and R. Gentry, G. N. White, Jr., S. R. Orr, F. Harlow, and W. R. Gage, of T-Division, of the Los Alamos Scientific Laboratory. This work was performed under the auspices of the U. S. Atomic Energy Commission.

## REFERENCES

1. Charles L. Mader, "Initiation of Detonation by the Interaction of Shocks with Density Discontinuities," *Phys. Fluids*, Vol. 8, No. 10, pp. 1811-1816, Oct. 1965.
2. Charles L. Mader, "One- and Two-Dimensional Flow Calculations of the Reaction Zones of Ideal Gas, Nitromethane, and Liquid TNT Detonations," *Twelfth Symposium (International) on Combustion*, pp. 701-710, Williams and Wilkins, New York, 1968.
3. William R. Gage and Charles L. Mader, "2DE-A Two-Dimensional Eulerian Hydrodynamic Code for Computing One Component Reactive Hydrodynamic Problems," Los Alamos Scientific Laboratory LA-3629-MS, January 19, 1967.
4. Charles L. Mader, "The Two-Dimensional Hydrodynamic Hot Spot, Volume IV," Los Alamos Scientific Laboratory LA-3771, Nov. 22, 1967.
5. Charles L. Mader, "The Two-Dimensional Hydrodynamic Hot Spot, Volume II," Los Alamos Scientific Laboratory LA-3235, April 3, 1965.
6. B. G. Craig and E. F. Marshall, "Behavior of a Heterogeneous Explosive when Shocked but not Detonated," *Fifth Symposium (International) on Detonation*, 1970.

# THE ROLE OF THE MATRIX IN DETERMINING THE SHOCK INITIATION CHARACTERISTICS OF COMPOSITIONS CONTAINING 60% BY VOLUME OF HMX

W. W. Marshall

*Atomic Weapons Research Establishment  
Aldermaston, Berkshire, England*

## ABSTRACT

Card gap tests have been carried out at ambient temperature and at approximately 95°C on a number of compositions containing 60% by volume of HMX. The results show that the shock sensitivities increase markedly with temperature. At any one temperature the shock sensitivity depends almost entirely on the density or shock impedance of the matrix, and is probably independent of its specific heat, thermal conductivity, or heat of explosion. The presence of voids produced by the solidification of a matrix such as TNT may have a slight sensitizing effect. Using zinc chloride solution of various densities as a matrix, it has been found that the shock sensitivity rises to a maximum at a density of about 1.55 g.cm<sup>-3</sup> and then falls. No explanation has been found for this unexpected result.

## INTRODUCTION

Although cast TNT is very insensitive to initiation by shock HMX/TNT is considerably more shock sensitive than the corresponding HMX/water or HMX/wax. The work described in this note was undertaken to compare the shock sensitivities of a number of compositions each containing 60% by volume of a coarse granular HMX, and to determine which matrix properties were major factors in determining the shock sensitivity of the composition.

## EXPERIMENTAL

Thin walled brass cylinders 3-1/2 inches long, 3/4 inch ID sealed at one end with 0.006 inch brass shims were preheated to 100°C. A slurry of coarse granular HMX (particle size range 100-1,000 micron, mean 400 micron, tap density 60% of theoretical) and the matrix material was heated to 100°C, whilst granular HMX was heated separately. The cylinders were filled with the slurry and hot dry HMX was added until the tube was filled with sedimented HMX. The tubes were allowed to cool, excess material was removed from the tops and they

were then closed with mild steel witness plates. This method gave a constant HMX/matrix volume ratio of 60/40 which was confirmed by analysis throughout the programme. The shock sensitivities of the charges were determined for each series by a card gap test in which the donor was a one inch long by half inch square pellet of a pressed composition containing 95% HMX by weight. The "cards" were shim brass. The shock sensitivity was determined by a Bruceton procedure in which about twelve rounds were fired for each composition. The standard deviation of shock sensitivity in a batch was about 50% greater than is achieved with pieces machined from pressed charges, and this was regarded as acceptable. Some rounds were fired at a temperature of approximately 95°C. These were assembled, each placed in an expanded polystyrene flask in an oven for one hour, and were fired in the flasks as soon as possible after removing them from the oven. Separate experiments showed that this method ensured that the temperature of the round was 92 ± 3°C for the time required to complete the firing.

Initially, the shock sensitivity of HMX/TNT was compared with that of HMX/water, and

HMX/paraffin oil. A number of materials with melting points similar to TNT but with a range of heats of explosion was then selected to replace the TNT. A TNT/sodium chloride composition in which the sodium chloride had approximately the same bulk properties as the HMX was prepared and tested at 20°C. Finally, a series of HMX/zinc chloride solution compositions was prepared in which the density of the zinc chloride solution was varied from 1.1 g.cm<sup>-3</sup> to 1.85 g.cm<sup>-3</sup>. Three of these compositions were fired at 95°C as well as at ambient temperature.

## RESULTS AND DISCUSSION

The results are given in full in Table 1. The sodium chloride/TNT results shows that TNT is not sensitized by being dispersed around an inert crystalline material, and hence it is unlikely that in HMX/TNT, enhanced sensitivity is due to the dispersion of the TNT about the HMX.

It would be expected that in a simple explosive system the shock sensitivity would increase with increasing temperature, and this has been shown for nitromethane by Campbell et al (1). In the present series of experiments where there were no matrix phase changes between 20°C and 95°C, the shock sensitivities did indeed increase with temperature. With these compositions the density falls with rising temperature and as will be discussed later, this would be expected to reduce the rise in shock sensitivity due to temperature. Where there is a phase change in the matrix the accompanying large change in density may mask the effect of temperature.

Matrix properties which may affect the shock sensitivity of the charge include:

- (1) thermal properties
- (2) presence of discontinuities
- (3) heat of explosion
- (4) shock impedance

TABLE 1  
The Shock Sensitivities of HMX Based Compositions

Matrix Material	Density at 20°C (g.cm <sup>-3</sup> )	Shock Sensitivity at 20°C (mil. of brass)	Density at 95°C (g.cm <sup>-3</sup> )	Shock Sensitivity at 95°C
Water	0.99	86, 95	0.96	117
Paraffin oil	0.85	75	0.80	102
Naphthalene	1.15	130	0.93	112
4 MNT	1.29	151	1.13	126
2 : 4 DNT	1.52	177	1.33	168
2 : 4 : 6 TNT	1.65	221	1.45	215
Zinc chloride solution	1.10	110, 117		210
	1.25	133		
	1.40	182, 175		
	1.55	195		292
	1.65	183		
	1.70	183		
	1.75	173		
	1.80	174		
	1.85	170		188
NaCl/TNT		0		
Water at +3°C	1.0	90		
Ice at -3°C	0.89	84		

### 1. Thermal Properties

The most useful pair of results for comparison is naphthalene/HMX and water/HMX at 95°C where both matrices have approximately the same density, zero heat of explosion, and are liquid so that the effect of intergranular discontinuity is nil. HMX is slightly soluble in naphthalene, but this is probably of little consequence. The shock sensitivities are 117 (water) and 112 (naphthalene) which are not significantly different at the 99% level. As the specific heat of water is about three times greater than that of naphthalene, and the thermal conductivity about four times greater, the effect of these properties is judged to be small if not negligible. This is probably because the time constants of heat transfer processes between HMX and matrix are long compared with explosive reaction times.

### 2. The Occurrence of Discontinuities

There is a decrease in shock sensitivity on cooling HMX/water, HMX/zinc chloride solution, and HMX/paraffin compositions, from 95°C to 20°C, yet an increase in shock sensitivity for those systems where the matrix solidifies between these two temperatures. The solidification process is normally accompanied by an increase in density and this may well account for an increase in sensitivity large enough to more than counterbalance the decrease due to decreasing temperature. Figure 1, which is a graph of shock sensitivity at 20°C v density includes the points for MNT, DNT, TNT and naphthalene, and does not show that these compositions are all more sensitive than the zinc chloride solutions of the same density. The results for HMX/ice and HMX/water about 0°C where there is an expansion on solidification are consistent with the density change. It seems unlikely, therefore that the occurrence of discontinuities is a major factor in determining the shock sensitivity.

### 3. Heat of Explosion

The shock sensitivities of HMX/naphthalene, /MNT, /DNT and /TNT increase with increasing heat of explosion of the matrix material. However, the densities also increase in the same order. Figure 1 shows that the sensitivities of HMX/MNT/DNT and /TNT are not greatly different from the sensitivities of HMX/zinc chloride solution of the same densities. Heat of explosion of the matrix material would therefore appear to be relatively unimportant in determining the shock sensitivity of these compositions.

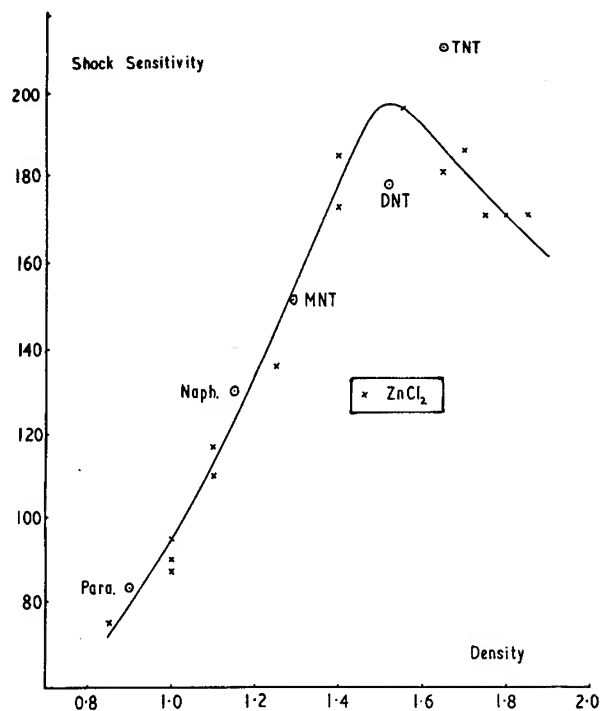


Fig. 1 - Shock sensitivity v density

### 4. Shock Impedance

In the absence of data on the shock velocity in the matrix materials, density has been taken as a measure of shock impedance. Shock sensitivity is plotted against density in Fig. 1 which includes all the experimental results at 20°C. This shows, firstly that the shock sensitivity of a composition depends to a great extent on the density of the matrix, and secondly, that the sensitivity rises to a maximum at a density of about 1.55 g.cm<sup>-3</sup>. This peculiar result is unexplained. The optimum transfer of energy between zinc chloride solution and HMX will occur when the respective pressure - particle velocity Hugoniots coincide at the pressure of the incident shock. This does not occur for the range of densities used, but the greater the density, the more nearly does the zinc chloride Hugoniot approach the HMX Hugoniot. Temperature, time-at-temperature and compression calculations for simple models of the experimental set-up have all failed to show anything other than a monotonic relationship between density and the property being calculated. A computer programme was set up to calculate the compressions in layers of zinc chloride solution 400 microns thick alternating with layers of HMX 600 microns thick. Results from this programme and several variations on it again showed that the more dense the zinc chloride

solution the greater should be the effect on the HMX.

It seems that the models chosen to represent the compositions in the mathematical treatments are too simple to explain what must be a quite complex situation.

The experiments and the conclusions drawn from them are based on compositions containing 60% by volume of a coarse granular HMX, and may not apply to other systems.

#### ACKNOWLEDGEMENT

Data on the Hugoniot of zinc chloride solutions was kindly supplied by Mr. J. Wackerle

of the Los Alamos Scientific Laboratory. The experiments were made by Messrs. Chick, Corby and Clinch under the general direction of Mr. H. Watts. Computations on model systems were carried out by Dr. N. Hoskin.

#### REFERENCE

1. A. W. Campbell, W. C. Davies and J. R. Travis, "Shock Initiation of Detonation in Liquid Explosives", *Phys. Fluids*, Vol. 4, pp. 498-510, 1961.

#### DISCUSSION

B. G. CRAIG

Los Alamos Scientific Laboratory  
Los Alamos, New Mexico

You observe that as the density of HMX/ $\text{ZnCl}_2$  solutions increases, the sensitivity increases, reaches a maximum near 1.5 g/cc, and then decreases. The decrease is counter to expectations. If the decrease is real, i.e., a property of the explosive rather than an artifact of the experimental arrangement, then this is an important observation, because it indicates a change in regime. The possibility that the decrease might be due to 2-D effects is one which you could check. However, have you eliminated the following possibilities: (1) That the lower density solutions may be entering microscopic defects in the HMX crystals and thereby partially "healing" these defects. The denser and more viscous solutions might not be able to enter the defects. (2) That the more viscous solutions might trap and hold bubbles which sensitize the mixture. (3) That different viscosities might result in some preferential particle-size separation which results in a less sensitive explosive for the more viscous mixtures?

#### REPLY BY MARSHALL

I think that Craig's points 1 and 2 are invalid in that neither prolonged evacuation of the HMX/solution mixture prior to filling the charge nor evacuation of the filled tubes affected the shock sensitivity. The third point might well be valid, and some experiments are being made in

which the HMX/solution mix is centrifuged in the brass tubes.

R. DUFF

Systems, Science and Software  
P.O. Box 1620  
La Jolla, California 92037

The "unexpected" maximum in sensitivity with variation of density of the matrix suggests a competition between two phenomena with opposite effects upon the initiation process. These phenomena may be: (1) The heterogeneity of the system when the density difference between explosive and matrix is large will tend to attenuate the primary shock and prevent initiation. (2) On the other hand, the heterogeneity tends to generate hot spots which promote initiation. The maximum in the sensitivity curve suggests that shock attenuation is relatively more important than hot spot generation at low density and that the loss of hot spot temperature differential is dominant as the impedance difference between the explosive and matrix decreases.

G. WACKERLE

Los Alamos Scientific Laboratory  
Los Alamos, New Mexico

I cannot agree with Dr. Marshall's conclusion regarding the unimportance of density



discontinuities in shock sensitivity but would rather regard them as essential to the generation of the hot spots and would consider requisite to the initiation of heterogeneous explosives. I would suggest that the decrease in gap thickness with zinc chloride solutions above 1.55 g/cc density results merely from the synthesis of a more homogeneous mixture as the shock properties of matrix solution more closely match those of HMX... an effect which overwhelms that of better coupling between the donor and the acceptor sample. The inference is that were the data extended with still higher density interstitial liquids, that the curves in Fig. 1 would turn upward again.

#### REPLY BY MARSHALL

This is an interesting idea. We intend to extend the work to higher matrix densities, probably by using solutions of other zinc halides. I did not intend to imply that density discontinuities were unimportant in shock sensitivity in general, but that in my particular system, the discontinuities produced by the solidification of (say) a TNT matrix did not produce an appreciable effect, as the sensitivities of those systems with such voids were not significantly different from liquid systems without voids. Whilst the idea that the increasing homogeneity of the charge reduces the sensitivity is interesting, it seems quantitatively unlikely. The difference in sensitivity between systems of zinc chloride solution density 1.55, and 1.85, is similar to the difference between pressed TNT of 71.5% theoretical density and 98% theoretical density as shown in Dr. Price's paper. It seems unlikely that the relatively small inhomogeneity differences between the zinc chloride and the HMX would produce such large effects.

C. L. MADER

Los Alamos Scientific Laboratory  
Los Alamos, New Mexico

The hydrodynamic hot spot theory would predict that the sensitivity of the mixture should decrease as the density of the zinc chloride increased and approached a good pressure match to HMX and then increase as the density got higher and the pressure match was poorer. (See LA-3450) Unfortunately, this is just the

reverse of what you report having observed. Your experimental arrangement is multi-dimensional and for the same attenuator you have increasing shock pressures as the density of the HMX-ZnCl<sub>2</sub> mixture increases. This will make the material appear "more sensitive" and is probably dominant over the hydrodynamic hot spot effect. This is why you see apparent "increasing sensitivity" as the density of the material increases. The actual mixture, however, is probably actually less sensitive and the Pop plot distance of run to propagating detonation is probably increasing. Such an increase is important in two-dimensional experiments as one reaches a state where the side failure waves can extinguish the detonation. You then must increase the initial shock pressure to maintain a detonation which would look like the explosive was "less sensitive." So one can easily postulate reasonable models for the behavior you have observed.

To determine what is actually occurring you would need to do a few plane wave shots and determine the "Pop plots" for several different HMX-ZnCl<sub>2</sub> mixtures.

#### REPLY BY MARSHALL

Experiments are to be made to follow up Dr. Mader's suggestions.

JACOB SAVITT

Explosiform, Inc.  
P.O. Box 36  
Belvedere, California

Card gap tests\* carried out on 2-inch-diameter cardboard — confined charges of nitroguanidine have shown that the shock sensitivity of the nitroguanidine depends upon the density of the matrix in the same way as shown in Fig. 1 of this paper. The sensitivity increases with increasing density in the region between 0.16 and 0.45 gm/cc but decreases with increasing density in the region between 0.45 and 1.00 gm/cc.

\*J. Savitt, Detonation Sensitivity of Very Low Density Pressings of Nitroguanidine, Paper No. 68-31, Western States Section, 1968, Combustion Institute Fall Meeting.

## EFFECT OF PULSE DURATION ON THE IMPACT SENSITIVITY OF SOLID EXPLOSIVES

B. D. Trott and R. G. Jung  
*Battelle Memorial Institute*  
*Columbus Laboratories*  
*505 King Avenue*  
*Columbus, Ohio 43201*

### ABSTRACT

The response of Comp B-Grade A, Comp B-3, and PBX-9404 explosives to impact of aluminum flyer plates was experimentally investigated in the pressure range 30 to 110 kilobars and the pulse duration range 0.05 to 1.70 microseconds. The flyer plates were launched from brass or copper buffer plates utilizing the impedance mismatch technique and explosive plane wave drivers. The shock front was followed through the explosive samples using a split-charge, transparent channel technique. A one-dimensional Lagrangian, computer code was also developed to compute the response of explosives to such impact. The burning model used for nonhomogeneous explosives assumes grain boundary initiation and a burning rate which depends on pressure raised to a power and an Arrhenius gas temperature relation. An analytical method of relating the unknown burning rate parameters to the pressure exponent was also developed. The pressure exponent was determined by comparison of computed run distances with the run distance measured for a single well-chosen experiment. Computed and experimental data for Comp B-Grade A are in good agreement. They exhibit thick pulse response in agreement with the data of Ramsay and Popolato. The thin pulse response data shows a more rapid increase in run distance with decreasing pressure than the thick pulse data. Comp B-3 and PBX-9404 experimental data show a similar response with, however, an appreciable detonation overshoot measured in PBX-9404 for very thin pulses.

### INTRODUCTION

Considerable experimental and theoretical work associated with the impact initiations of explosives has been conducted. The work of Gittings (1) showed the pulse length dependence on impact initiation in a preliminary way for PBX-9404. The present work extends experimental investigations of the pulse length dependence of impact initiation to longer pulse durations for PBX-9404 and to Comp B-3 and Comp B-Grade A as well. In conjunction with the experimental work, a finite difference Lagrangian computer code was developed which demonstrates good agreement with the experimental findings for Comp B-Grade A.

### EXPERIMENTAL PROCEDURE

The experimental technique used was a combination of the flyer-launching technique by impedance mismatch as employed by Gittings (1), with the split-charge technique employed by Boyle and Ervin (2) to allow continuous observation of the planar shock progress through the explosive charge. The experimental arrangement used to gather the most recent data reported here is shown schematically in Fig. 1.

A simultaneous streak and framing camera (Beckman and Whitley Model 200) equipped with an auxiliary telephoto lens was arranged so that its optical axis was parallel with the 5-mil

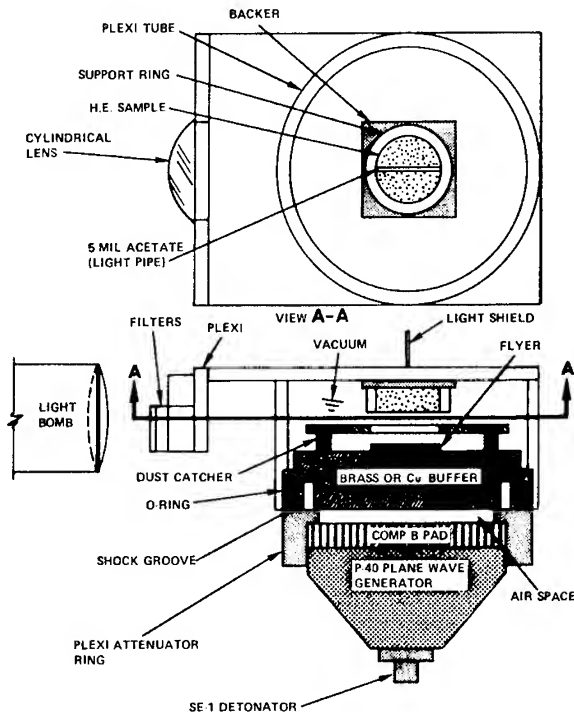


Fig. 1 - Arrangements for experiments in vacuum

acetate light pipe and the streak line was coincident with its edge. The field of camera view extended across the thickness of the explosive sample and the free flight distance of the flyer, making possible the measurement of the flyer velocity and explosive shock response from a single film.

The experiments were back-lighted using a roughly collimated light from an explosive driven argon flash bomb consisting of a 5.5-in.-diameter heavy-walled cardboard tube and expendable collimating lens formed from a pair of water-filled, 6-in.-diameter watch glasses. Collimation of the light source was necessary to enable adequate lighting of both the acetate strip and free-flight zone. This was achieved by the provision of a cylindrical lens segment to focus a strip of light on the acetate strip, and filters to reduce the light intensity across the free-flight zone. It is estimated that the light requirement of these two zones differ by a factor of  $\sim 100$ .

The initial fourteen experiments were conducted for experimental convenience in a methane atmosphere to prevent self luminous air shocks from obscuring the image. The presence of a visible shock wave in the methane preceding the flyer which gave rise to a visible

precursor traveling at sonic velocity in the explosive sample in some experiments raised some doubt as to the effect of the methane on the results obtained. Although Gittings (1) work had shown that the differences between methane and vacuum were relatively small, and indeed indistinguishable if plotted on a pressure versus pulse duration plot as we have done, all later experiments were conducted in a vacuum chamber approximately as shown in Fig. 1, although several minor changes were made from time to time. A vacuum of  $\sim 100\mu$  in the sample chamber was found to eliminate all visible traces of air shock and was used for the vacuum experiments. This vacuum level at the chamber was found to correspond to a value of  $10\text{--}15\mu$  at the vacuum pump when pumping through the necessary length of vacuum line to protect the pump from damage. Our methane and vacuum data were also found to be indistinguishable and have not been differentiated in the presentation of data.

The explosive driver was a 4-in. plane wave generator topped by a  $1/2$  in. Comp B-3 pad to improve the planarity of impulse imparted to the buffer plate. Both copper and brass buffer plates were used, in thicknesses from  $1/2$  to 1 in., the thickness being varied as a secondary velocity control. The primary means of velocity control employed was a variable air gap, edge supported by a thick lucite ring. This attenuation method proved to be highly satisfactory for small adjustments in flyer velocity. The variation in flyer velocity  $V$  (in mm/ $\mu$ sec) with air gap  $G$  (in mm) is well described by the liner relation:

$$V = 1.362 - 0.062 G$$

for air gaps from one to ten millimeters.

The flyer material employed throughout was heat annealed 1100 aluminum. The free-flight distance of the flyer ranged from 7.01 to 8.66 mm. Approximate analyses showed that the copper or brass to aluminum impedance mismatch would provide from  $\sim 2.5$  to  $\sim 5 \mu$ sec of free time between the impact of the flyer on the explosive and that of the buffer plate, over the range of flyer velocities from  $\sim 1.8$  to  $1.0$  mm/ $\mu$ sec, respectively. Analysis of the streak photographs obtained showed that this free time was sufficient to prevent influence of the buffer plate on the explosive response during times of interest.

The degree of flyer planarity was established in a series of four shots using the standard driver and buffer plate, in which the impact surface of the explosive sample was replaced

by the silvered surface of a mirror, viewed from above. The reflectivity change in the mirror upon flyer impact was monitored by the streak and framing camera, and the planarity determined quantitatively from the resulting streak records. Two shots each of 0.2 and 1.02-mm thick flyers were fired. In each case, the central portion of the flyer was nearly planar and impacted first with the outer edges trailing slightly behind. The average deviation from impact simultaneity over region of explosive impact was ~44 nsec for the 1.02-mm flyer and ~73 nsec for the 0.2-mm flyer with a maximum of 81 nsec. Using a flyer velocity of 1.45 mm/ $\mu$ sec as measured for several other shots using this configuration the maximum deviation from flyer planarity at impact is ~0.12 mm. In terms of deviation from a planar shock in the sample explosive this amounts to ~0.4 mm, which, due to the form of the observed deviation should not invalidate the assumption of one dimensionality.

To establish the limits of flyer thickness versus flyer velocity which could be launched without spallation of the flyer using this driver system a series of 16 tests were performed. The presence of flyer spallation was detected by means of edge-on flash X-radiographs taken after the flyer had traveled several inches in air. Cases of complete spalling, edge spalling of oversized flyers, and no spalling were observed. Since the tendency for flyer spallation increases with increasing flyer velocity and thickness, and was observed to increase with increasing flyer diameter, the following approximate upper limits for nonspallation of 50.8-mm flyers with this driver technique were established.

Buffer Plate Thickness	Maximum Flyer Thickness	Typical Flyer Velocity
12.7 mm	2.03 mm	1.65 mm/ $\mu$ sec
25.4 mm	3.18 mm	1.45 mm/ $\mu$ sec
19.03 + 3.81-mm air gap	4.75 mm	1.15 mm/ $\mu$ sec

All results reported here lie within these limits. It may be noted in passing that the first of these limits appears to be in contradiction to the recovery experiments of Curran (3), who used flyers extending closer to the edge of his plane wave generator. We also noted spallation occurring in portions of the flyer launched from areas further from the center of the plane wave generator than one inch in this case, apparently caused by an increased slope of the following rarefaction wave, near the edge of the generator. Apparently the fragments he recovered

were obtained from portions away from the center of the generator.

The major source of experimental difficulty encountered was the presence of micro jetting from the plane surfaces of the buffer and flyer plate and Pujols (4) jetting from the discontinuity at the edge of the flyer plate. This jetted material moved at velocities well in excess of the flyer plate velocity and started at the same time as the shock emergence from the free surface. It appeared as an irregular cloud in the frame photographs similar to the early stages of an explosion under some earth. Extreme care in smoothing the free surfaces, slight undercutting of the edges of flyer plates, and installation of the dust catcher shown in Fig. 1 were found to be effective in minimizing this difficulty, although occasionally the exact time of impact of the flyer and the initial shock velocity in the explosive were still obscured. This phenomenon was generally distinguishable from the flyer and shock in the explosive by its blurred appearance and apparently rapid deceleration on the streak photographs.

#### Explosives Investigated

The three explosives investigated in this study were: PBX-9404-3, as described in Ref. (5), density as tested 1.830 to 1.836 gm/cc; cast Comp B-3, per specification MIL-C-45113A (MU), density as tested 1.724 to 1.730 gm/cc; and cast Comp B-Grade A, per specification MIL-C-401C, density as tested 1.711 to 1.717. All explosive shapes used were manufactured to a uniform high standard by Mason and Hanger-Silas Mason Company, Inc., Burlington, Iowa. The density of each piece was measured, it was determined to be radiographically sound and passed complete dimensional inspection.

#### Data Obtained

The quantitative data were obtained from streak photographs, supported by the high-speed frame photographs taken simultaneously. Data obtained from the streak records include the flyer velocity, initial and final shock velocity in the explosive samples, and in the samples which detonate, the run distance and run time.

The flyer velocity was determined from the measured flight time from takeoff to impact on the streak record, and accurately determined preassembly measurements of the flight distance. Flyer velocities are generally accurate to  $\pm 2\%$ , except in certain cases where the

impact of the flyer was obscured by Pujols debris or the film record quality was poor for other reasons. Experience gained with the air-gap velocity control feature allows assignment of a probable error in these cases of about  $\pm 5\%$ .

Shock velocities in the explosive sample were determined from slope measurements on the streak records. Often the shock velocity was changing continuously and only short lengths of the initial or final shock wave velocity were available for measurement. An average accuracy for these measurements is probably about  $\pm 10\%$ , although some variation exists from shot to shot.

#### Data Reduction

The results of these experiments were analyzed using standard analytic procedures to calculate the pressures created by flyer impact with the explosive samples. For these analyses it was assumed that the shock velocity could be expressed in the form

$$U_s = C_0 + S U_p$$

where  $U_s$  is the shock velocity,  $C_0$  is the hydrodynamic sound speed,  $S$  is a material constant, and  $U_p$  is the particle velocity. The values used for these parameters are shown below; with the initial density  $\rho_0$  for each material.

Material	$\rho_0$	$C_0$	$S$	Reference
Al	2.70	5.27	1.37	6
PBX-9404	1.834	2.5	2.5	7
Comp B-3	1.727	2.71	1.86	8
Comp B-Gr. A	1.715	2.71	1.86	8

#### Results for PBX-9404

The results obtained from the experiments on PBX-9404 are shown plotted on Fig. 2 as flyer velocity or impact pressure versus pulse duration  $\tau$  calculated as  $\tau = 2t/U_s$  where  $t$  is the flyer thickness and  $U_s$  is the shock velocity in the flyer appropriate to the impact pressure calculated. Also shown on Fig. 2 is the line separating initiation and noninitiation areas for the earlier data of Gittings (1) for extremely short pulse durations. Our new data are shown to be a reasonable extension of her data for longer pulse durations.

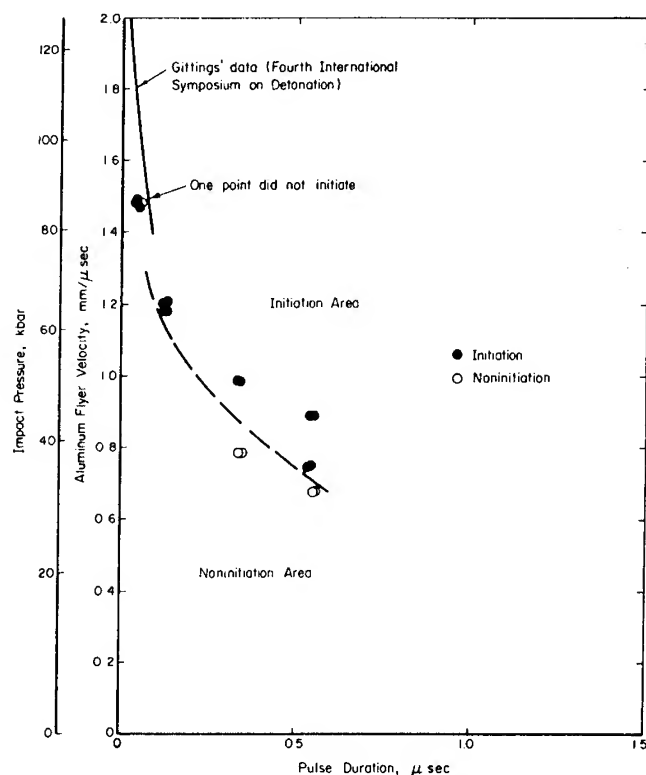


Fig. 2 - Effect of pressure and pulse duration on initiation of PBX-9404

The initiation behavior of PBX-9404 under the conditions in which we observed it showed strong evidence of detonation overshoot similar to that expected for a homogeneous explosive, when thin pulse conditions were present, except that from the point of initiation there was also evidence for a retonation or retrograde detonation wave progressing back into the material through which the shock wave had already passed. Sections of the streak photos showing this behavior are shown in Fig. 3 together with other pertinent data. Apparently the retonation wave is self-luminous and the acetate light pipe was not sufficiently destroyed by the shock passage to prevent the escape of some of this light. A measure of the thinness of pulse is given in Fig. 3, which shows the ratio of the initial pulse duration to the run time to detonation. This ratio is similar to the ratio Gittings used for

plotting her data, except in the denominator she used the run time to detonation expected for long pulses. Hence, corresponding values for our ratio would be expected to be somewhat smaller than hers. The very small values of the ratio obtained, suggest strongly that thin initiating pulse effects are present. It appears from this admittedly meager data that the tendency for detonation overshoot increases with decreasing values of the time ratio. Other shots with larger values of the ratio showed no identifiable detonation velocity overshoot. Further analytical work on this HMX-based explosive will be required to achieve a complete understanding of these phenomena. Other treatments of this PBX-9404 data will appear in the discussion section for convenience of comparing it with the results obtained for the other explosives.

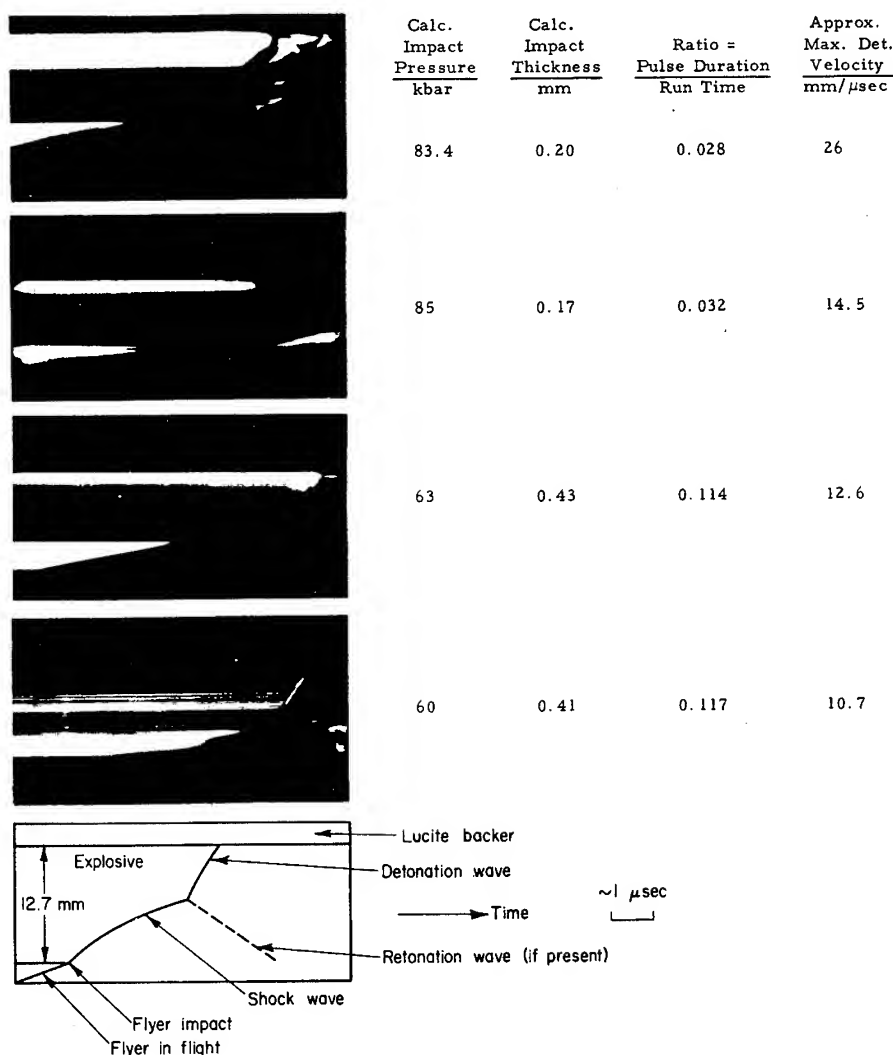


Fig. 3 - Variation in the initiation behavior observed for PBX-9404. These experiments were conducted in a methane atmosphere.

### Results for Comp B-3

The results obtained from the experiments on Comp B-3 are shown plotted on Fig. 4 as flyer velocity or impact pressure versus pulse duration. Figure 4 shows the trend toward lower impact pressure requirements for detonation with longer pulse durations.

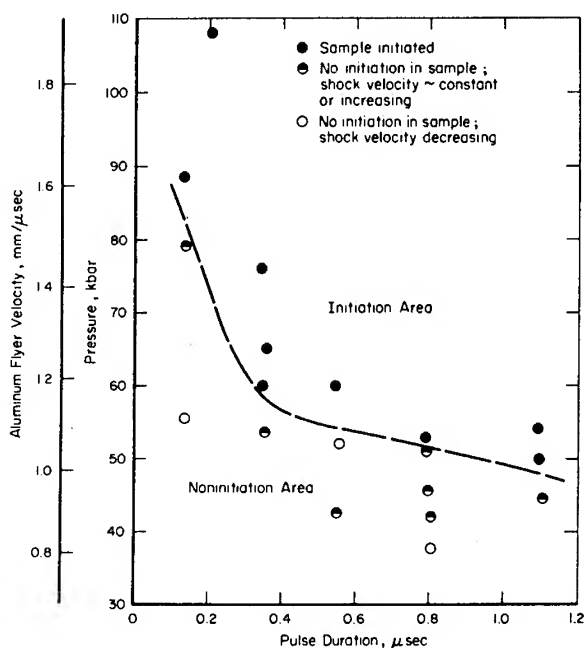


Fig. 4 - Effect of impact pressure and pulse duration on initiation of Comp B-3

The initiation behavior of Comp B-3 was observed to follow the usual pattern of increasing shock velocity to detonation. Qualitatively, the transition from shock to detonation appeared to occur a little more sharply than in Comp B-Grade A but no definite evidence for detonation overshoot was obtained. Further treatment of this Comp B-3 data will appear in the discussion section where comparisons with the performance of the other explosives is more convenient.

### Results for Comp B-Grade A

In order to obtain a more complete understanding of the initiation behavior of one of the explosives investigated, Comp B-Grade A was studied more intensively. These data are shown plotted on Fig. 5 as flyer velocity or impact

pressure versus pulse duration. The initiation behavior of Comp B-Grade A is quite similar to that of Comp B-3, when examined in this way. Comparisons of Figs. 4 and 5 shows that the Comp B-Grade A is slightly less sensitive to initiation than Comp B-3. The similarities in the two Comp B formulations make these results what one might expect. Further treatment of the Comp B-Grade A data will appear in the discussion section.

### ANALYTICAL STUDY

A one-dimensional Lagrangian computer code HIEX was written during this study to calculate the response of explosives to short-duration pressure pulses. The code uses a special equation of state for reactive materials which allows mixtures of unburned material and gaseous reaction products to coexist. For the unburned material a Mie-Gruneisen equation of state was used with the measured Hugoniot as the reference. For the burned gas products the Fickett and Wood beta equation of state was used. The reference curve used was the isentrope through the measured Chapman-Jouguet pressure as calculated by Mader (9) using the Becker-Kistiakowsky-Wilson equation of state. For a mixture of solid and gas products pressure equilibrium was assumed and the equations

$$V_{\text{mixture}} = f V_{\text{gas}} + (1 - f) V_{\text{solid}}, \quad (1)$$

and

$$E_{\text{mixture}} = f E_{\text{gas}} + (1 - f) E_{\text{solid}}, \quad (2)$$

were assumed to hold,  $f$  being the mass fraction of the explosive which has been burned. The code is written to calculate the response of both homogeneous and nonhomogeneous explosives (although in what follows here only the nonhomogeneous case will be considered). Up to ten materials, either reactive or nonreactive, may be used in a problem. As many as three energy sources may be used to irradiate the materials, a left-hand constant velocity piston may be activated for an arbitrary time duration, and flyer-plate impact may be simulated.

The burning model used in HIEX for nonhomogeneous explosives is based on the assumption that the burning explosive mixture consists of solid spherical grains of unburned explosive surrounded by hot gaseous burned products. It is also assumed that the energy of detonation resides with the newly created gas and that no heat transfer occurs between the burned gas and the unburned solid. Pressure

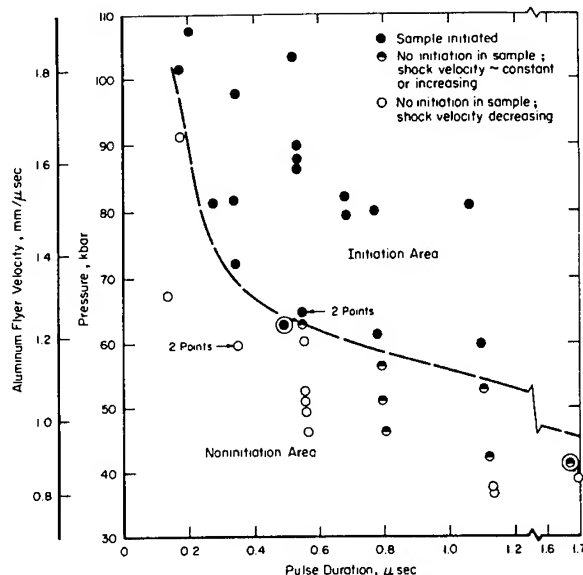


Fig. 5 - Effect of impact pressure and pulse duration on initiation of Comp B-Grade A

equilibrium of the phases is assumed to exist. The burning rate is assumed to depend on the surface area of the burning grains, on the burning pressure raised to some power, and on an Arrhenius temperature term. This model was first suggested by F. J. Warner (10) and can be expressed as:

$$\frac{df}{dt} = k P^n (1-f)^{2/3} \exp \left[ -E_a / RT_{gas} \right] \quad (3)$$

where

$f$  = the mass fraction of the explosive which has been burned

$t$  = time

$k$  = a scaling factor in time

$P$  = pressure

$n$  = a constant of the explosive

$E_a$  = the activation energy of the controlling rate process

$T_{gas}$  = the temperature of the burned gas products.

A method for finding a relationship between the burning-rate parameters  $k$  and  $n$  was

developed during this study. It is integration of the burning rate equation over the reaction zone which exists during steady-state detonation of the explosive. The calculation requires that the solid Hugoniot, the gas product isentrope through the measured Chapman-Jouguet pressure (including gas temperature), the detonation velocity, and the reaction zone length be known. The solid Hugoniot, the gas product isentrope, and Eq. (1) are used to calculate the P-V relationships for partially burned states. The steady-state character for the detonation wave then requires that the burning process occurs along a straight line in the P-V plane. This determines the burn fraction as a function of pressure. A slide-rule calculation of the gas product energy as the burning progresses, making use of Eq. (2) and the gas temperatures on the reference isentrope determines the gas product temperature as a function of pressure. This method of finding burn fraction and gas temperature as a function of pressure is only approximate since unloading of the solid occurs along the isentrope through the spike pressure and since the newly burned gas fractions do not lie exactly on the Chapman-Jouguet isentrope. However, these more exact results which can be found by a trial and error method have been found to agree with the approximate results to within a few percent. This is because, as will be shown, most of the burning occurs at pressures near the spike pressure. The burning



time of the explosive is calculated by dividing the reaction zone length by the detonation velocity minus the particle velocity at the spike point. The burning rate equation can now be systematically integrated over the reaction time for an assumed value of pressure exponent  $n$  to give a uniquely determined value of the time scaling factor  $k$  and a required pressure-time history of burning. This is a three-step process. In the first step it is assumed that each of a chosen number of equal  $\Delta t$  intervals requires an equal burning time which is calculated from the total burning time of the explosive as found above and the number of intervals chosen. The constant  $k$  is considered to be unknown. Using the values of pressure and gas product temperature at the midpoint of each  $\Delta t$  interval,  $\Delta t$  is calculated for each of the intervals using Eq. (3). These  $\Delta t$ 's are then summed and set equal to 1.0 giving an initial estimate of  $k$ . In the second step the  $\Delta t$  in each interval is evaluated using the initial estimate of  $k$ . It is not, in general, equal to the  $\Delta t$  assumed initially for the interval. Therefore, the time of burning in each interval is adjusted so that the assumed and calculated  $\Delta t$  agree. These adjusted burning times are summed. In the third step the initial estimate of  $k$  is multiplied by the ratio of the above summed time to the true burning time to give the true value of  $k$ , and the burning times in the  $\Delta t$  intervals are divided by this ratio to give the true burning times of the  $\Delta t$  intervals.

In the case of Composition B-Grade A (59.5/39.5/1.0/RDX/TNT/wax) these calculations were done using the solid Hugoniot of Coleburn and Liddiard for Comp B-3 (60/40/RDX/TNT) (8), and the detonation velocity of 7.95 mm/ $\mu$ sec. found by them, the gas product isentrope for Comp B (64/36/RDX/TNT) as calculated by Mader (9) through a Chapman-Jouguet pressure of 284 kilobars, a reaction zone length of 0.13 mm as measured by Duff and Houston (11) for Comp B (63/37/RDX/TNT), and an activation energy of 43.4 kilocalories per mole as given by Cook (12) for TNT. A representative reaction zone profile found by the above method is shown in Fig. 6. The pressure exponent assumed for this calculation was  $n = 3.00$  and the resulting scaling factor is  $k = 1.04 \times 10^7 \mu\text{sec}^{-1} \text{ mbar}^{-3}$ . As can be seen from the profile, 50 percent of the explosive is burned in the first 15 percent of the reaction zone and between the spike pressure of 382 kilobars and a lower pressure of 355 kilobars. Other values of pressure exponent  $n$  and the scaling factors  $k$  which resulted are  $n = 2.11, 2.41, 2.81, 2.96, 3.03,$  and  $3.11$  with  $k = 4.15 \times 10^6, 5.70 \times 10^6, 8.60 \times 10^6, 1.01 \times 10^7, 1.07 \times 10^7,$  and  $1.20 \times 10^7$ .

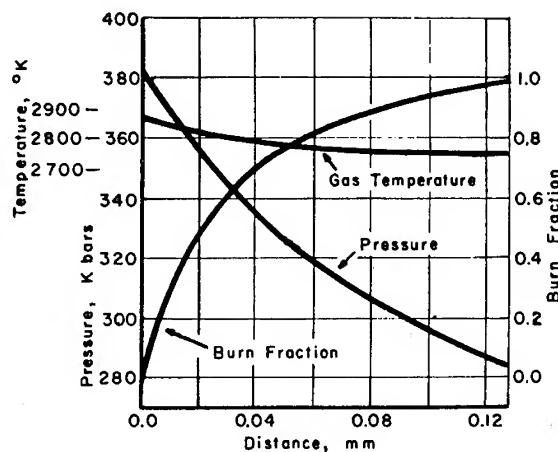


Fig. 6 - Reaction zone profile determined for Comp B-Grade A burning calculation ( $n = 3.00$ ,  $k = 1.04 \times 10^7 \mu\text{sec}^{-1} \text{ mbar}^{-3}$ )

Selection of the appropriate value of the pressure exponent  $n$  to be used for Comp B-Grade A was made by comparing the run distance to detonation measured in the laboratory for a chosen impact condition with the run distances to detonation computed by the code for various assumed values of  $n$  and associated  $k$ . The impact condition chosen was a 40-mil aluminum flyer at a velocity of 1.44 mm/ $\mu$ sec. and impact pressure of 75 kilobars. Computed run distances as a function of  $n$  are shown in Fig. 7. The results of several experiments suggested that the measured run distance for this impact condition is about 8 millimeters. Therefore, the value of  $n$  selected for further use was 3.0 and the associate  $k$  was  $1.04 \times 10^7 \mu\text{sec}^{-1} \text{ mbar}^{-3}$ . The initiating pressure pulse was from a 1.02-mm aluminum flyer impacting at 1.44 mm/ $\mu$ sec.

## ANALYTICAL RESULTS

The output of the code is much too voluminous to present here even for a single run. However, to illustrate the code results, plots of pressure and burn fraction as a function of pulse travel into Comp B-Grade A are shown in Fig. 8 for the case where the left-hand piston moved at 1.87 mm/ $\mu$ sec for a time duration of 0.14  $\mu$ sec. This resulted in a pressure front of 200 kilobars initially in the explosive. Six selected problem times are shown in the figure. From these, one may note the following things:

- (1) The pressure at the shock front increases continuously with pulse travel into the explosive and increased from

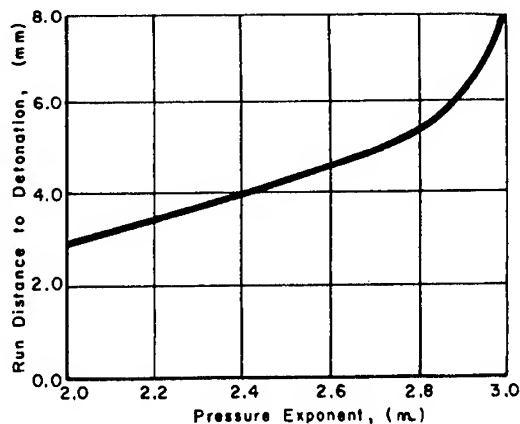


Fig. 7 - Computed effect of variation of the burning-rate pressure exponent on the run distance to detonation in Comp B-Grade A

200 kbars to 350 kbars during the 0.14  $\mu$ sec the piston was moving.

- (2) Up until the time that the pressure pulse becomes a fully developed detonation wave, about 0.158  $\mu$ sec, the burning is spread over a large reaction zone behind the front.
- (3) The burning rate at the pressure front becomes progressively larger and larger until the detonation wave is fully developed.
- (4) The peak pressure computed at the spike of the detonation wave and the reaction zone length as computed by the code are in close agreement with those used in the evaluation of the burning-rate parameters  $k$  and  $n$ .

It should also be mentioned here that the gas product temperatures as calculated by the code for the fully developed detonation are also in agreement with those assumed in the parameter evaluation.

A number of flyer plate impact computations have been made with HIEX. Some of these results are shown in Fig. 9 along with applicable experimental data. As can be seen, the computed and experimental results are usually in very good agreement. The results show that when an explosive is impacted by a flyer of a given thickness, take 40 mils as an example, the response is as follows. When the impact pressure is large, greater than about 90 kilobar for the case of the example, the explosive

responds as though the initiating pressure pulse is sustained. This type of response can be called thick-pulse response and run distance would remain the same even if the flyer were made thicker. As the impact pressure is decreased, there is reached a point at which the response of the explosive is no longer thick-pulse response, for instance about 80 kilobar for the 40 mil example. At this point, the run distance to detonation is larger than would be found if a thicker flyer impacted at the same pressure. This type of response can be called thin-pulse response. The impact pressure at which the response changes from thick-pulse to thin pulse is a function of the thickness of the flyer, and, of course, of the explosive being impacted. In Fig. 9 thick-pulse response is drawn as a solid line. The thin-pulse response to 25 mil, 40 mil, and 63 mil aluminum foils are shown as dashed lines.

Figure 10 shows the differences in the thick-pulse and thin-pulse response of Comp B-Grade A. For the thick-pulse cases, 63 mil flyer at 100 kilobar and 25 mil flyer at 120 kilobar, the rise of pressure at the front is at a continually increasing rate. For the thin-pulse case, 25 mil flyer at 100 kilobar, the pressure at the front rises immediately after impact and continues to do so for some length of time exactly as in the thick-pulse case. However, at some later time the rate of pressure increase at the front drops off for some period of time after which the pulse accelerates to detonation conditions.

Figure 11 has been included here to show that thin-pulse response as calculated by HIEX is very much dependent on the value of burning-rate parameter  $n$  whereas thick-pulse response is not nearly so dependent on this parameter. This would indicate that if thick-pulse response of an explosive is all that is desired the value of burning-rate parameter  $n$  is not so critical as when both types of response are to be determined.

## DISCUSSION

As shown in Fig. 9, good agreement between calculated and experimental results for Comp B-Grade A was achieved for both thick flyers and thin flyers. Figure 10 shows that pressure buildup as a function of run in the explosive for thin flyers is identical to that for a thick flyer in the initial portion of the buildup curve. The thin flyer buildup curve then levels off for a distance at an intermediate pressure during an "incubation stage" before finally building up to the steady state detonation

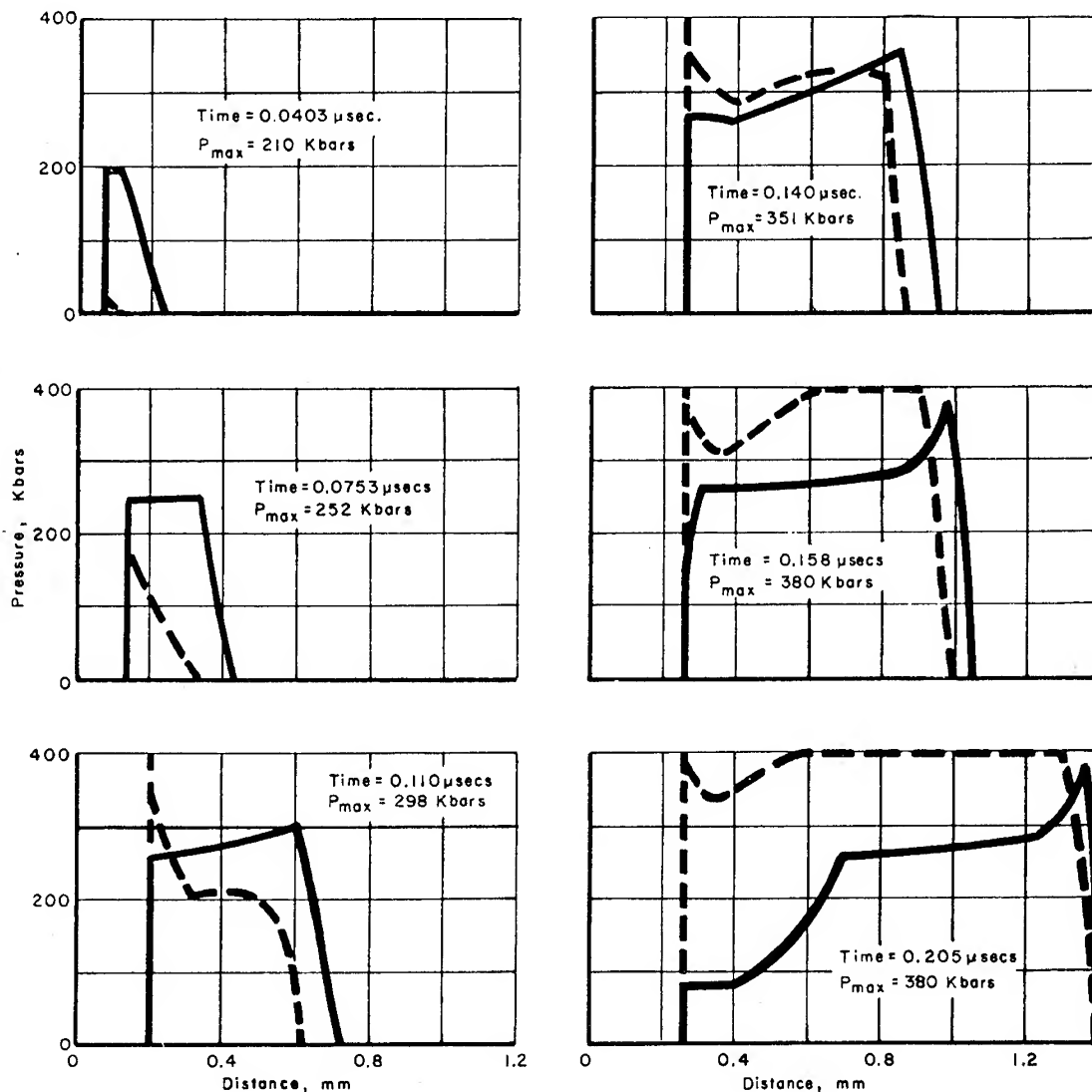


Fig. 8 - Computed buildup to detonation on Comp B-Grade A. A constant velocity piston moving at 1.87 mm/ $\mu$ sec was applied to the left-hand boundary for 0.14  $\mu$ sec resulting in an initial pressure front of 200 kbars.

pressure. Some attenuation of the pressure at the shock front can even occur during this incubation stage, see Fig. 10, before the burning occurring behind the front can communicate sufficient energy to the front to again produce a pressure buildup at the front. This result, found analytically, correlates well with behavior observed in the explosive. This attenuation effect preceding final pressure buildup has been observed in all of the explosives studied experimentally but the effect is shown in a most pronounced manner in PBX-9404, as shown in Fig. 3. Particularly in the cases of the thinnest flyers where values of the ratio of pressure

pulse duration to time to detonation were very small, a very significant shock velocity attenuation was observed before detonation occurred. Burning apparently continuing to occur behind the shock front eventually develops a pressure buildup at the front sufficient to produce a significant detonation overshoot. These effects could probably be better understood through computer studies of this explosive as well, although they have not yet been attempted.

In view of the calculated and observed behavior for Comp B-Grade A it is tempting to examine the rather meager data obtained for

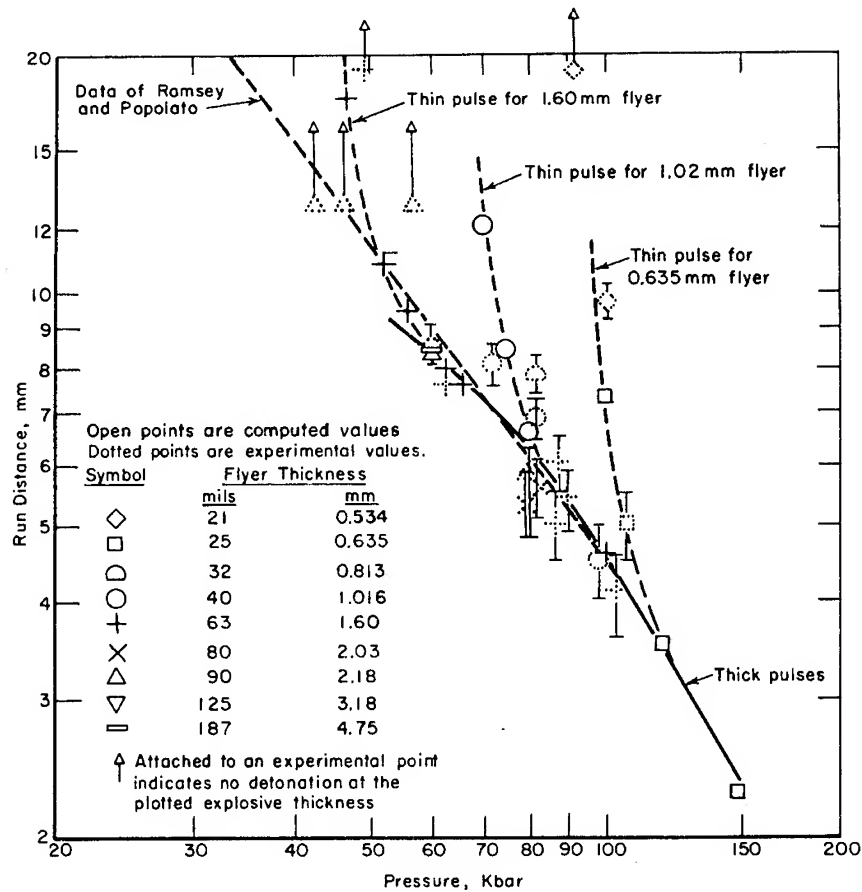


Fig. 9 - Effect of impact pressure and flyer thickness on rundistance, Comp B-Grade A explosive calculated and experimental results

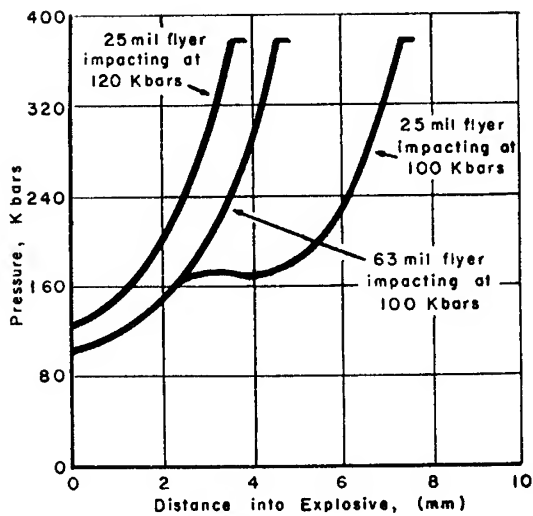


Fig. 10 - Computed effort of flyer thickness and impact pressure on pressure buildup at the shock front

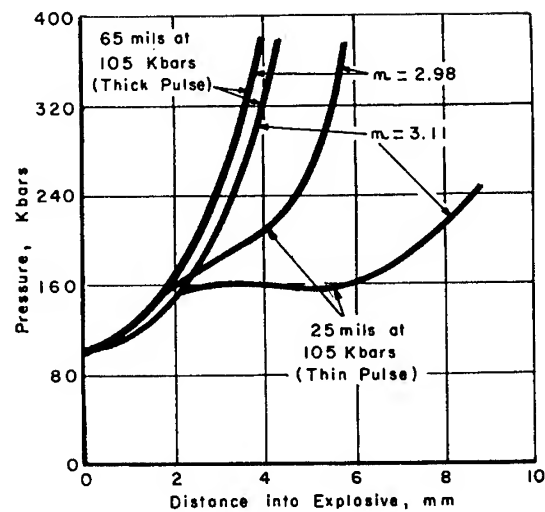


Fig. 11 - Computed thick-pulse and thin-pulse peak pressure response variation with burning rate parameter  $n$

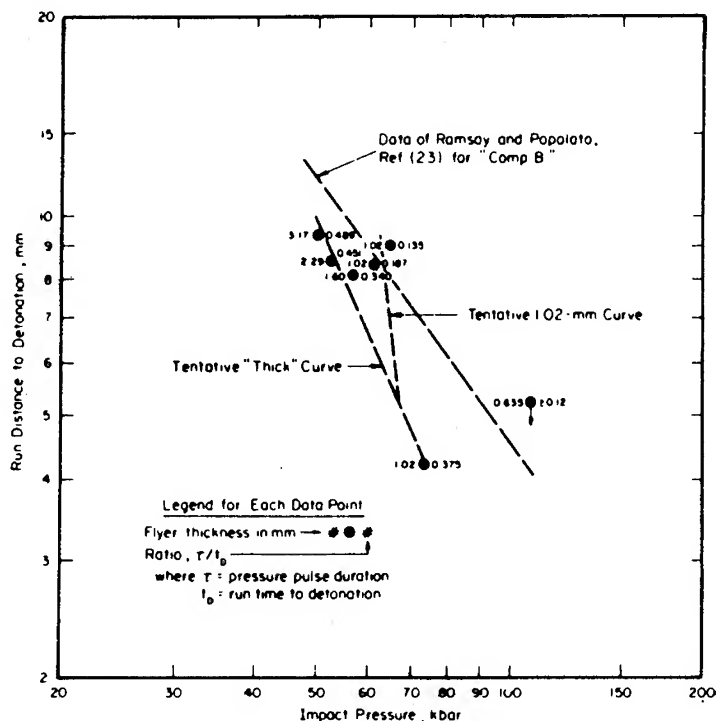


Fig. 12 - Effect of impact pressure and flyer thickness on run distance, Comp B-3 explosive experimental results

Comp B-3 and PBX-9404 in this way. Shown plotted on Figs. 12 and 13 are the detonation data for Comp B-3 and PBX-9404 respectively.

For Comp B-3, several of the data points have large enough ratios that they should lie on the thick pulse curve, which appears to lie close to but at lower pressures than the Comp B-Grade A curve. A slightly greater slope is suggested as well. The two data points having ratios  $<0.2$  appear to describe the beginning of the thin pulse branch for 1.02-mm thick aluminum flyers.

For PBX-9404, only one of the data points has a ratio great enough to qualify as a thick-pulse. This point lies squarely on the thick-pulse curve as previously determined for PBX-9404 by Ramsay and Popolato (7). Since the objective of this program was primarily to examine thin-pulse effects, the other data points all lie in the region of thin pulses. Dashed lines are shown on Fig. 13 to indicate the probable locations of the thin pulse curves of detonation for aluminum flyer thicknesses near 0.18 and 0.42 mm.

Although these results for Comp B-3 and PBX-9404 should be regarded as tentative, the

concept of a thick-pulse, pressure-run distance curve from which a family of thin-pulse curves branch off at successively lower pressures for successively longer pulse durations does appear to apply to the explosives investigated.

The fact that pressure attenuation at the advancing shock front can occur prior to development of a detonation wave necessarily restricts the validity of the experimentally determined, no detonation points to explosives no thicker than the samples investigated. Some credence for a lower limit to the impact pressure capable of producing a detonation in explosives of any thickness for a given flyer thickness is provided by both the experimental and analytical results which show that run distance to detonation begins to increase very rapidly as pressure is reduced. This is shown on Fig. 9 for the three flyer thicknesses, which were examined in some detail.

For the thickest thin flyer, studied, 1.60 mm thick, there appears to be a slight discrepancy between the calculated and experimental results, although there is not enough data to verify the cause of this discrepancy.

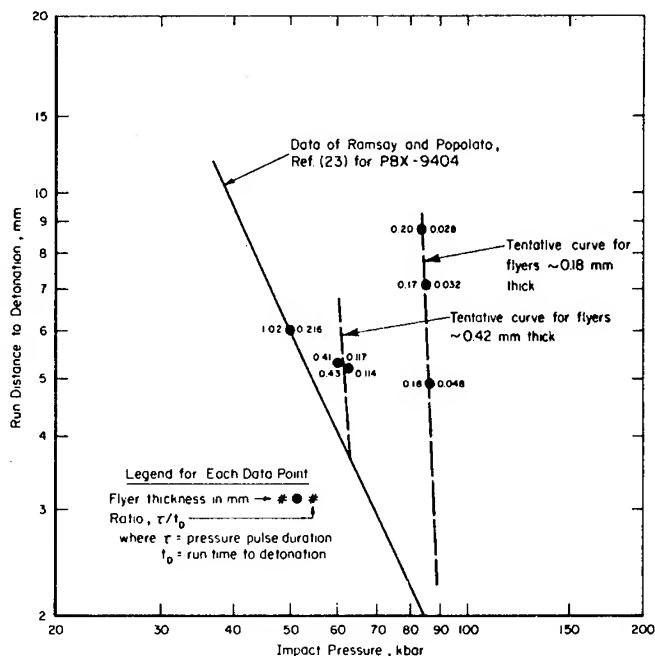


Fig. 13 - Effect of impact pressure and flyer thickness on run distance, PBX-9404 explosive experimental results

## SUMMARY

During the course of this study, quantitative data on the effect of pressure pulse duration on the initiation behavior of three different explosives have been obtained. Two experimental techniques were combined to obtain these data. The recently developed split-charge technique applied here for the first time to the study of short duration initiating pulses has proven to be a powerful tool for the study of phenomena of this type.

One of the three explosives, Comp B-Grade A, was studied fairly intensively. A total of 40 experimental data points were obtained. These show the variation in initiation behavior of this explosive with impact pressure in the range of ~40 kbar to ~100 kbar, and with pressure pulse duration in the range of ~0.17 to 1.1  $\mu\text{sec}$ .

Concurrent with the experimental effort, analyses of the known initiation behavior of explosives and of previous efforts to calculate the initiation behavior of explosives were conducted and burning models for both homogeneous (liquid and single crystal) explosives and inhomogeneous (solid) explosives were selected. A computer code, HIEX was written to implement these burning models. In order to treat the

explosive-reaction product equations of state properly for partially burned explosive mixtures, a mixture equation of state was written into the code. HIEX carries with it considerable flexibility for the study of a wide variety of shock propagation problems as well as the capability to treat the initiation of either homogeneous or inhomogeneous explosives.

Application of the inhomogeneous burning model to Comp B-Grade A was made. Through application of this burning model to the fully developed detonation and utilization of the measured reaction zone length in Comp B, the adjustable burning parameters were reduced to a single constant, the pressure exponent, which required experimental data for its determination.

Parametric studies showed that the predicted run distance is much more sensitive to the choice of pressure exponent for thin pressure pulses than for thick pressure pulses. Hence, the pressure exponent was established based on a thin-pulse experiment. Further code runs using the selected constant showed good fits with the experimental run distance and run time data on Comp B-Grade A for both thick and thin initiating pulses over the range of variables investigated. Furthermore, the code calculates correctly the von Neumann spike pressure, the Chapman-Jouguet pressure, and the detonation velocity.

It was shown that the response of Comp B-Grade A can be characterized by a single curve of impact pressure versus run distance to detonation for all sufficiently long pulse durations. Along this curve, all sufficiently long pulse durations at a given pressure will produce the same run distance. A family of curves for thin-pulse response also exists, one for each flyer thickness, which exhibit a rapid increase in run distance for small pressure decreases, and join smoothly into the thick curve for higher pressures. Short pulse durations produce a thin-pulse response which separates from the thick-pulse response at higher pressures than do longer pulse durations.

The other two explosives investigated in preliminary experiments were Comp B-3 and PBX-9404. Comp B-3, chemically very similar to Comp B-Grade A, shows a similar response with slightly shorter run distances than Comp B-Grade A for similar pressures, as expected due to its slightly greater sensitivity. PBX-9404 is appreciably more sensitive to impact initiation than either of the other two explosives investigated. For very thin pulse conditions, detonation overshoot or superdetonation at the transition from reactive shock to detonation was observed. Nevertheless, the experimental run distance-pulse duration-impact pressure obtained appears to fit the same type of thick-pulse, thin-pulse model previously described and suggests that this behavior pattern may be characteristic of many solid explosives.

#### ACKNOWLEDGMENT

This work was supported by the Advanced Research Projects Agency through the Naval Research Laboratory. Thanks are due to Mr. Stanley Goddard who conducted most of the experimental work and contributed the design of the lighting scheme employed, and for many helpful discussions with Mr. Edward G. Bodine and Dr. Robert A. Stein all of Battelle Memorial Institute and Mr. Walter Atkins of the Naval Research Laboratory.

#### REFERENCES

1. E. F. Gittings, "Initiation of a Solid Explosive by a Short Duration Shock," Proceedings of the Fourth International Detonation Symposium, Naval Ordnance Laboratory, White Oak, Maryland, p. 373 (October 12-15, 1965).
2. V. M. Boyle, and L. H. Ervin, "Hugoniot Relationships in Opaque Media Determined Optically Through the Use of a Transparent Channel Technique," BRL Memorandum Report 1814 (January, 1967).
3. D. R. Curran, "Nonhydrodynamic Attenuation of Shock Waves in Aluminum," *J. Appl. Phys.*, **34**, 2677 (1963).
4. H. Pujols, "Application de la Cinematographic Ultra-Rapide et de la Radiographic Eclair a l'Etude des Phenomenes de Jets et Fragmentation de Plagues Metalliques Projetees au Moyen d' Explosifs Puissants," VII. International Congress on High Speed Photography, Zurich, p. 383 (1965).
5. UCRL High Explosive Handbook Vol. I, Rev. I, 1967 (UCRL-6759).
6. S. P. Marsh, private communication in "Compendium of Shock Wave Data," M. van Thiel, ed., UCRL-50108 (Vol. I), Lawrence Radiation Laboratory, June, 1966.
7. J. B. Ramsay, and A. Popolato, "Analysis of Shock Wave and Initiation Data for Solid Explosives," Fourth Detonation Symposium, Naval Ordnance Laboratory, 233-238 (1965).
8. N. L. Coleburn, and T. P. Liddiard, Jr., "The Unreacted Hugoniot Equation of State of Several Explosives," U. S. Naval Ordnance Laboratory, White Oak, Maryland, in *Journal of Chemical Physics*, **44**, p. 1929 (1966).
9. C. L. Mader, "Detonation Properties of Condensed Explosives Computed Using the Becker-Kistiakowsky-Wilson Equation of State," Los Alamos Scientific Laboratory Report LA-2900 (July, 1963).
10. F. J. Warner, "The Initiation of Detonation in Solid Explosives," *Ninth Symposium on Combustion*, Academic Press, p. 536 (1963).
11. R. E. Duff, and E. Houston, "Measurement of the Chapman-Jouguet Pressure and Reaction Zone Length in a Detonating High Explosive," *The Journal of Chemical Physics*, **23** (17), 1,268 (July, 1955).
12. M. A. Cook, *The Science of High Explosives*, Reinhold Publishing Corporation, New York (1966).

## DISCUSSION

B. G. CRAIG

Los Alamos Scientific Laboratory  
Los Alamos, New Mexico

The detonation velocity of 26 mm/ $\mu$ sec given in Fig. 3 is ridiculously high even for a super detonation in PBX-9404. The advance of the shock as shown in Fig. 3 cannot be correct for the interpretation given. The shock front should first accelerate in the PBX, as for a conventional explosive/attenuator driver system. After there has been time for a rear

rarefaction to form and overtake the shock front, the shock front can decelerate. The smear-camera records shown have many characteristics in common with those obtained when one simply views the outside of a charge; these include the "retonation" light, the "apparent" overshoot due to a high phase velocity, and the immediate deceleration of the shock front. This suggests that your recording system is sensing, at least on occasion, some perturbed part of the charge.

B. D. TROTT

(February 22, 1972)

The interpretation of results obtained for PBX-9404 is admittedly open to some question, and further verification of the behavior of this explosive under the influence of very thin initiating pulses is needed to clarify the situation. The split charge experimental technique shows the maximum forward progress of any shock disturbance of sufficient magnitude to disrupt the functioning of the acetate sheet as a light pipe, thus interrupting the light transmitted through the sheet. This probably occurs first near the center of the charge, leaving areas of the sheet away from center portion relatively unaffected, due to the gradual inward progress of a lateral rarefaction wave, with forward motion of a thin shock wave. These outer areas of the sheet can still act as a light pipe for self-generated light, such as observed in the retonation waves, and thus the lateral location (central or near the surface) of the observed retonation waves is open to some question. It may be noted however, that retonation waves were not observed for the Comp B type explosives investigated.

The high observed velocities of detonation overshoot may be explainable on the basis of the perturbation in the planar shock front produced by the presence of the more compressible acetate light pipe sheet, so that the observed velocity is, in fact, a closing phase velocity of the shock with the light pipe material. This explanation of the thin pulse shots for the PBX-9404 raises doubts as to the validity of the data for the other explosives investigated. However, in about 100 other shots on the other explosives investigated, for both thick and thin pulse conditions, no detonation overshoot was observed, and measured initial shock velocities and detonation velocities agreed with Hugoniot predictions and published values within experimental error, as did the experimental results on PBX-9404 for thick pulse initiating conditions. It appears that the perturbing effects of the light transmitting sheet, if indeed this is the cause for the observed results, become noticeable only for the combination of thin initiating pulses which have a very small ratio of thick pulse run time to thin pulse run time and a significant Hugoniot mismatch between the explosive and light pipe sheet material.



## SHOCK SENSITIVITY, A PROPERTY OF MANY ASPECTS

Donna Price  
*U. S. Naval Ordnance Laboratory  
White Oak, Silver Spring, Maryland*

### ABSTRACT

Shock sensitivity of an explosive includes its threshold for propagation of steady state detonation at the critical diameter ( $d_c$ ) as well as its numerous thresholds for initiation of detonation under different transient conditions. Data for TNT charges of differing degrees of homogeneity are used to show a continuous variation of  $d_c$  with the initiating pressure ( $P_i$ ) measured with the NOL large scale gap test. An example of a critical curve is constructed in the pressure-time plane; it runs from the threshold conditions at  $d_c$  through those at  $P_i$ . It is suggested that all other initiating pressures measured for the same charge would also fall on this curve which illustrates the relationship between the different threshold values.

The "shock sensitivity" of an explosive cannot be described by a single valued parameter. Shock sensitivity encompasses all of the complex reactions of the explosive to many different shock conditions. Such reactions are manifested by the phenomenon of failure diameter for propagation of detonation as well as by the critical initiation pressures for shock to detonation transition observed in the numerous gap, booster, projectile, and wedge experiments. A complete description of an explosive's sensitivity to shock should encompass therefore not only the thresholds for initiation under transient conditions but also the threshold for propagation under steady state conditions. Moreover, it should account for the large effect of the physical state of the explosive on both thresholds.

The relationships between these many aspects of shock sensitivity are complex and cannot be simply stated. This situation has led to a general confusion about the meaning of different measurements. It is the purpose of this paper to clarify the situation by describing the relationships between the conditions at the critical diameter and those at the critical initiating pressures (gap test) and then, by using measured values for one explosive in a number of different physical states, to demonstrate the trends observed in both critical diameter and critical initiating pressure with increasing charge homogeneity. TNT was chosen for the present work because it has been so widely

studied that more data are available for it than for any other pure explosive. Moreover, it is a castable material and hence can provide an almost continuous range of physical heterogeneity between the highly compacted porous charge and the perfect single crystal.

### THRESHOLD FOR SHOCK-TO-DETONATION TRANSITION

The critical initiating pressure is defined as the minimum pressure ( $P_i$ ) required to initiate detonation of the explosive. It defines a threshold for the initiation of detonation under transient conditions. The value of  $P_i$  measured in any given test is determined not only by the chemical composition of the test material and its physical state but also, in large part, by the physical dimensions of the test. These dimensions control the times at which rear and lateral rarefactions can arrive at the shock front and relieve the pressure. Thus each test devised to measure  $P_i$  is apt to use a different pressure pulse (pressure-time profile) to excite reaction of the explosive. Different profiles can be obtained by varying the composition and shape of donor explosives in the gap, booster, wedge tests and by varying projectile material, shape, and velocity in the projectile impact and wedge experiments. They are also obtained by varying the diameter of the acceptor explosive. The explosive response differs as the stimulus differs, and hence gives

different  $P_i$  values in different tests. In other words, not only  $P_i$  but also  $P_i$  vs time ( $t$ ) should be specified in each test.

Eleven years ago it was shown theoretically (1) that a limiting pressure-time ( $P-t$ ) curve exists for a 50% chance of build-up to detonation in homogeneous explosives; the limiting curve divides the impulse plane into a detonation region and a failure region. Brown and Whitbread (2) demonstrated by impact of cylindrical projectiles on two physically heterogeneous explosives that the  $P_i$  determined must have a minimum duration for detonation to occur. They also showed qualitatively that, at  $P > P_i$  and a duration shorter than that required at the critical pressure level, detonation could also be initiated. Since then there has been rather general agreement that initiation of detonation must be the result of the pressure-time history of the initiating shock, and that a critical limit curve in the  $P-t$  plane must exist for each explosive.

In many cases of explosive loading (e.g., a gap test), maximum shock pressure can be determined much more readily than the pressure-time profile. Hence many of the shock sensitivity measurements have been restricted to pressure measurements only. However, Walker and Wasley (3) have recently combined some plate projectile impact data (for which pulse duration can be computed from plate thickness) with gap test measurements about which some information on the pressure-time profile was available. These data appear to define a critical ignition energy from which a critical pressure-time limit curve for ignition can be derived.

Some of the gap test data used in the above work (3) were obtained with the calibrated NOL large scale gap test (LSGT) (4). Because it will be used for data in this work, its important characteristics will be briefly reviewed. It is a conventional gap test with a 5 cm diam  $\times$  5 cm long, 1.51 g/cc tetryl donor and an attenuator gap of polymethyl methacrylate (PMMA) or its equivalent. The acceptor explosive can be tested unconfined or in the moderate confinement of a steel sleeve (3.65 cm ID, 4.76 OD). A mild steel witness plate is used in both cases, and the gap length is varied until the 50% value is found, that is, the attenuation at which a hole is punched in the witness plate in 50% of the trials. The system donor/gap has been calibrated (5) to give shock pressure as a function of gap length. This 50% pressure ( $P_g$ ) at the end of the gap can be converted to the initiating pressure ( $P_i$ ) transmitted to the explosive by

use of the Hugoniot of the gap material (5) and that of the explosive, e.g., cast TNT (6).

The standard donor of the LSGT is approximately point initiated; hence the detonation from the donor is spherical and the hydrodynamic flow in the gap and in the acceptor is divergent. The transmitted pressure falls off rapidly. From optical observations of the tetryl/PMMA system, the shock pressure decreases to half its initial amplitude in about one  $\mu$ sec (7). Walker and Wasley (3) estimated that such a pulse was equivalent to a square pulse of an amplitude of  $0.9 P_i$  and 1.6  $\mu$ sec duration. Although a one-dimensional hydrodynamic flow computation on the tetryl/PMMA system produced a half-width of 4  $\mu$ sec (7), analogous two-dimensional computations (8) indicate values of 1.1 to 1.7  $\mu$ sec, in fair agreement with the original estimate from experimental work.

Like all such tests, the LSGT exhibits a diameter effect. Inasmuch as doubling the length of the standard booster does not affect the measured pressure (9), rear rarefactions play no part in the attenuation. Thus the observed, as well as the computed, pulse shape can be attributed to the effect of lateral rarefactions on the initial pulse. Because confinement of the charge delays the arrival of lateral rarefactions at the charge axis we find, for the same measured  $P_i$ , that the diameter of the unconfined charge is approximately twice the core diameter of the confined charge, i.e., 76 mm (10). This value of the equivalent diameter ( $d_e$ ) seems applicable to a number of different explosives, but the size of the change in measured  $P_i$  with confinement depends on the shock sensitivity of the explosive. The change is greatest for the least sensitive materials (10).

Both pressed and cast TNT exhibit the usual sensitivity phenomena of shocked solid heterogeneous explosives (11, 12): a critical initiating pressure ( $P_i$ ) for detonation, break-out of detonation downstream from the shocked boundary, and a consistent decrease of both the run distance and delay time to steady-state detonation with increased amplitude of the applied shock. The run distance is the distance from the plane of shock entry into the explosive to the plane in which steady-state detonation is first established. The delay time is the total time from the moment of shock entry to the time at which steady-state detonation begins.

Liquid TNT and presumably single crystal TNT behave as shocked homogeneous explosives (13). They too exhibit a critical initiation

pressure, but detonation occurs, after a delay (induction) time, at the plane of shock entry. The detonation wave travels through shocked explosive to overtake the shock wave. There is subsequently a short period of overdrive of the unshocked explosive. The measured induction time decreases with increasing pressure of the initiating shock. Special cases which require destruction of material homogeneity (14) or shock interaction with the confinement (15, 16) before initiation will not be considered.

The LSGT shock sensitivity values for pressed TNT have been reported in previous work (17) as  $P_g$  vs percent theoretical maximum density (% TMD). The trend was the usual one of increasing  $P_g$  with increasing compaction. The average particle size of the TNT used for that work was about 150  $\mu$  with a maximum particle size of 600  $\mu$ . Subsequent tests on charges made from 100  $\mu$  and 200  $\mu$  TNT showed the same  $P_g$  values at 80% TMD (10). Although TNT in the LSGT shows no particle size effect on  $P_g$ , the less sensitive nitroguanidine (18) does. So too do tetryl and PETN (19) when tested at smaller  $d_c$  than that of the LSGT. In both cases, the measured effect is small and disappears at high compactions.

The LSGT measurements on TNT have been collected in Table 1.  $P_g$  values have been converted to  $P_i$  values by using the Hugoniot of PMMA (5) and of cast TNT (6) except for the low density charge. In that case an interpolation was made between the Hugoniot for TNT ( $\rho_0 = 1$  g/cc) (20) and that at higher density (6).  $P_i$  values at  $d_c \geq 3 d_c$  (the critical diameter) and hence approximating the infinite diameter value are given for each charge. A single TNT crystal has not been tested, but liquid TNT has been (13) and supplies the limiting value of 125 kbar. Computations using Hugoniot of solid (6) and liquid (21) TNT show that the energy and temperature jump across the shock front is much less for the solid than for the liquid.

Values for the two cold pressed charges of Table 1 are smoothed values from previous work (17). The values for the confined charges of two of the castings have been deduced from measurements on bare charges, as described in Ref. (10). All values have been arranged in order of increasing physical homogeneity of the charge, judged from a knowledge of its method of preparation. Thus, a rapid cooling and solidification of TNT results in a casting containing many small crystals; it should be the most heterogeneous of the castings although more homogeneous than any pressed charge. A vacuum casting should be more homogeneous than a creamed casting both because of the evacuation

of any trapped air and because cooling under vacuum would be somewhat slower than the air cooling of the creamed casting. Casting No. 4 was obtained with a heated mold and steam fingers which supplied some heat to the interior of the casting throughout the solidification process. The charges so prepared contained a number of large TNT crystals and most closely approximated the case of the single crystal.

The data of Table 1 show two things very clearly: (1) there is a continuous variation in  $P_i$  values from the most to the least heterogeneous charge, and (2) the required initiating pressure increases monotonically with increasing physical homogeneity of the charge. Although a smooth trend in the range of cold pressed charges is commonly found, earlier work (17) suggested a discontinuity between the initiating pressure required for the highest density pressed charge and that for a single crystal (RDX or PETN). If the values for the cast charges were omitted from Table 1, a similar apparent jump in  $P_i$  would occur for TNT. A castable material can be handled to produce charges of homogeneity bridging the difference between that of the highest density pressed charge and of the perfect crystal. A comparable treatment for non-castable explosives such as RDX would involve the use of a solvent, i.e., solution in place of melting. In both cases, a continuous variation in homogeneity and hence in  $P_i$  can probably be obtained.

#### THRESHOLD FOR PROPAGATION OF DETONATION

The failure or critical diameter ( $d_c$ ) determines the charge size at which there exists a threshold for the propagation of detonation under steady state conditions. By definition,  $d_c$  is that diameter at or above which detonation propagates and below which it fails. The existence of a failure diameter is the result of two dimensional effects. In accord with this and with the shock-to-detonation transitions discussed in the previous section,  $d_c$  defines that charge size at which the steady-state detonation wave has been attenuated from its infinite diameter value by lateral rarefactions until it is just critical for initiation. In other words, at  $d_c$  the pressure pulse between the von Neumann shock front and the C-J plane is just critical for initiating detonation after a run length equal to the reaction zone length and a total delay time equal to the reaction time. Thus at  $d_c$  the transient initiation phenomena just fit into the reaction zone at the threshold of steady-state propagation. This is the rather complex relationship between the explosive behavior at

TABLE 1  
LSGT Shock Sensitivity Data for Various Forms of TNT

Form of Charges	$\rho_0$ g/cc	% TMD	Unconfined (d = 3.81 cm)			Confined ( $d_e \sim 7.6$ cm)					
			50% Point			50% Point					
			Gap (mm)	$P_g$ (kbar)	$P_i$ (kbar)	Gap (mm)	$P_g$ (kbar)	$P_i$ (kbar)	$\frac{d_e}{d_c}$		
<u>Pressed at 25°C</u>	1.18	71.5	(50.3	18	13) <sup>b</sup>	63.7	11	8	10		
	1.62	98.0	(29.7	43	49) <sup>b</sup>	45.2	22	25	35		
Castings											
	<u>Poured</u>	<u>Cooling Rate</u>									
1	Clear	Rapid	1.57	95.0	24.9	50	61	(40.2	28	32) <sup>b</sup>	5
2	Creamed	Moderate	1.615	97.75	18.5	62	74	34.3	37	43	3
3	Clear <sup>a</sup>	Moderate	1.62	98.0	9.7 <sup>c</sup>	87.5 <sup>c</sup>	104 <sup>c</sup>	(20.6	58	69) <sup>b</sup>	3
4	Clear	Very slow	1.61	97.5	Subcritical <sup>d</sup>			>0 <sup>e</sup>			
<u>Perfect Single Crystal</u>			1.65	100	-	-	-	>125 <sup>f</sup>		3	

<sup>a</sup>Vacuum cast. <sup>b</sup>Values in parentheses were not measured. See Ref. (10). <sup>c</sup>Tested at d = 5.08 cm because  $d_c = 3.81$  cm. <sup>d</sup>Entering shock at zero gap induced fading reaction. Front traveled at 6.8 mm/ $\mu$ sec for 5 to 6 cm, and then at 4.7 mm/ $\mu$ sec for next 9 to 10 cm. <sup>e</sup>Only one shot at zero gap; measured detonation velocity was 6.9 mm/ $\mu$ sec. <sup>f</sup>Estimate - see text.

these different thresholds, each of which is a different facet of shock sensitivity. A quantitative illustration of this proposed relationship will be given later.

#### Available Data on $d_c$ of TNT

In the range of cold pressed charges, the variation of the critical diameter with the charge porosity has served as the basis of a convenient classification of explosives into two groups (17). Group 1, typified by TNT, exhibits decreasing  $d_c$  with increasing compaction (increasing % TMD). Group 2, typified by ammonium perchlorate (AP), exhibits the reverse trend. As a result of the different failure behavior, the two groups also exhibit differences in their detonation velocity ( $D$ ) vs  $\rho_0$  curves at finite diameters. Members of Group 1 have linear  $D$  vs  $\rho_0$  curves whereas those of Group 2 can exhibit  $D$  vs  $\rho_0$  curves with a maximum in  $D$ . In later work (18) we found that the division between the two groups was not as sharp as we first thought, that some materials, e.g., nitroguanidine, have a U-shaped  $d_c$  vs  $\rho_0$  curve and exhibit Group 1 patterns at lower % TMD, Group 2 patterns at higher % TMD. It is probable that

any pressed explosive can behave in this way provided the necessary range in degree of compaction can be achieved experimentally.

Most of the  $d_c$  measurements on pressed TNT (porous, granular compacts) have been made by Russian investigators. Figure 1 shows some of these data plotted  $d_c$  vs  $\rho_0$ . The two solid lines are values reported by Bobolev (22) for fine and coarse TNT. These curves show the Group 1 behavior described above and also demonstrate the effect of particle size on critical diameter. In the  $\rho_0$  range of 0.85 to 1.23 g/cc,  $d_c$  is decreased by a factor of 2 to 3 for a decrease in the initial average particle diameter (increase in surface area) of about a factor of 4. It should be noted, however, that the curve for the fine TNT ends at 75%, probably because of pressing difficulties. If experimental data could be obtained to extend that curve, it should approach the curve for the initially coarser TNT even as the two  $P_i$  vs  $\rho_0$  curves become coincident at high compactions. That this is probably the case is indicated by a recent determination (23) on fine (20-70  $\mu$ ) TNT at 97% TMD. In this work a critical slab thickness ( $h$ ) was measured; it and the approximate  $d_c \approx 2h$  are plotted as crosses in Fig. 1. Either value

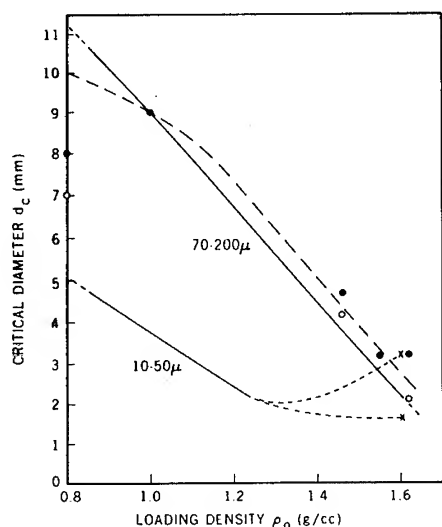


Fig. 1 - Failure limit curves for TNT in diameter-density plane

(—) Ref. 22; x Ref. 23;  
 • Detonation; o Failure, Ref. 26;  
 - - Curve chosen for Ref. 26 data;  
 . . . Interpolation)

indicates that the fine TNT critical value will approach or go through a minimum and that at high compaction there will be no significant difference in  $d_c$  of the initially fine and initially coarse TNT.

Although there is only one set of data for the fine TNT, there are several for the coarser material. Dremin et al (24) quote limit data from Apin and Stesik (25) for 100  $\mu$  TNT. That failure limit curve, not shown in Fig. 1, lies 0.8 to 0.2 mm below Bobolev's curve for 70 - 200  $\mu$  TNT, about where it should be for a small decrease in the average particle size. The most recent data are those of Stesik and Akimova (26); their limiting shots for failure and detonation are plotted in Fig. 1. Over the range 1.0 to 1.62 g/cc they agree quite well with the data of Ref. (22); at 0.8 g/cc there is a large disagreement. The close agreement at higher densities makes the size of the discrepancy between the most porous charges seem improbable. Examination of the  $D$  vs reciprocal diameter ( $d^{-1}$ ) curve (26) for the charges at  $\rho_0 = 0.8$  g/cc shows a sharp change in slope at  $d = 10$  mm. For this reason,  $d_c$  (0.8 g/cc) = 10 mm is used here instead of the lower value selected in Ref. (26). (At  $d < d_c$ , it is often difficult to distinguish an overdriven shock from a steady-state detonation in a low density charge of moderate length.) With this change, the Ref. (26) data are in for better agreement with data

from both Ref. (25) and Ref. (22), as shown in Fig. 1.

The possible forms of the lower curve of Fig. 1 at higher density strongly suggests that TNT can be put in a physical state in which it will exhibit a U-shaped  $d_c$  vs  $\rho_0$  curve. This possibility has been recently confirmed with measurements on hot pressed (72° - 76°C) TNT. In the narrow range of 1.60 to 1.65 g/cc in  $\rho_0$  and 8 to 13 mm in  $d$ , these charges exhibit Group 2 patterns for both  $D$  vs  $\rho_0$  and  $d_c$  vs  $\rho_0$  curves (27) i.e., a maximum  $D$  in the  $D$  vs  $\rho_0$  curve and  $d_c$  increasing with increasing  $\rho_0$ .

The above measurements on pressed charges are summarized in Table 2 which also includes available data for cast TNT. The data have been arranged in order of increasing physical homogeneity of the charge, as were those of Table 1. As in the case of  $P_i$ , there is a continuous variation in  $d_c$  from the most to the least heterogeneous charge. The gap between the values for the highest density pressed charge and the single crystal (with  $d_c$  greater than that of Casting 4) is smoothly bridged by charges produced by the different methods of preparation. Similarly, the gap between the cold pressings (heterogeneous and permeable to fluids) and the castings (approximately homogeneous and impermeable) can be bridged by hot pressing. Pure TNT melts at 81°C; hence pressing at 72 - 76°C will cause some local melting and flow so that the charges contain both permeable and impermeable regions. In the region of cold pressed charges,  $d_c$  decreases with increasing degree of homogeneity (a Group 1 pattern), but this trend is reversed in the region of hot pressing. Thereafter  $d_c$  like  $P_i$  increases with increasing homogeneity. The overall trend strongly suggests that permeability permitting convective heat transfer by flow of hot gas products has a role in the initiation and propagation of detonation. Finally the data of Table 2 show that the effect of the initial particle size on  $d_c$  is appreciable at low % TMD and negligible at high % TMD, as it was for  $P_i$ .

#### Other Information about Critical Conditions

More information can be obtained about the failure conditions if other measurements are made in addition to  $d_c$ . In particular, from the detonation velocity at  $d_c$  ( $D_c$ ), an estimate of the detonation pressure at critical conditions is

$$P_{jc} \cong \rho_0 D_c^2 / 4 \quad (1)$$

TABLE 2  
Critical Diameters of Various Forms of TNT

Form of Charges	$\rho_0$ g/cc	% TMD	$d_c$ mm	Reference
<u>Pressed at 25°C</u>				
ca. 140 $\mu$	1.18	71.5	7.5, 6.4, 7.0	22, 25, 26
	1.62	98.0	2.0, 1.8, 2.5	22, 25, 26
ca. 30 $\mu$	1.18	71.5	2.5	22
	1.60	97.0	ca. 2.5	23
<u>Pressed at 72 - 76°C</u>	1.64	99.2	7.8	27
<u>Castings</u>				
<u>Poured</u> <u>Cooling Rate</u>				
1 Clear      Rapid	1.62	98.0	14	26
2 Creamed      Moderate	1.61	97.5	24, 27	28, 29
3 <sup>a</sup> Clear      Moderate	1.62	98.0	38	30
4 Clear      Very slow	1.61	97.5	>38	30
<u>Perfect Single Crystal</u>	1.65	100	-	

<sup>a</sup>Vacuum cast.

A measure of the reaction zone length ( $x$ ) leads to an estimate of reaction time ( $\tau$ ). Since  $x = (D - \bar{u})\tau$  where  $\bar{u}$  is the average particle velocity in the reaction zone, the estimate  $\bar{u} = 1.2 u_j$  leads to  $x_i = f(\gamma)D_i\tau_i$  where  $f(\gamma)$  is a slowly varying function of the adiabatic exponent  $\gamma$ ;  $f(\gamma)$  can be approximated, as in Ref. (31), by 2/3 to give

$$\tau_i = 1.5x_i/D_i \quad (2)$$

Equation (2) gives the approximate value for the ideal or infinite diameter detonation reaction time because measurements or estimates of  $x$  are made at conditions approaching ideal. For near voidless materials, however,  $D_c \approx D_i$  and  $\tau_i$  should be a good approximation for  $\tau_c$ . Finally an estimate of the energy required for propagation at  $d_c$  can be obtained from

$$E (\text{cal/cm}^2) = P^2 \tau / \rho_0 U \quad (3)$$

where  $U$  is the shock velocity of amplitude  $P$  in the unreacting explosive. Walker and Wasley (3) derived Eq. (3) for a square pressure pulse of amplitude  $P$  and duration  $\tau$  created by high velocity impact of an explosive projectile against an explosive target. If  $P$ ,  $\tau$ ,  $\rho_0$ , and  $U$  are in units of kbar,  $\mu\text{sec}$ ,  $\text{g/cm}^3$  and  $\text{mm}/\mu\text{sec}$ ,

respectively, the conversion factor is 0.239. With the hydrodynamic relation,  $P = \rho_0 U u$ , Eq. (3) can be converted to

$$E = P u \tau \quad (4)$$

where  $u$  is particle velocity. For the units of kbar,  $\mu\text{sec}$  and  $\text{mm}/\mu\text{sec}$ , a factor of 2.39 gives  $E$  in  $\text{cal/cm}^2$ . To obtain the energy value at  $d_c$ , where  $U = D_c$ , we approximate  $P \approx P_{jc}$  and  $\tau_c = \tau_i$ . The result is a low estimate because the square pressure pulse equivalent to the pulse between the von Neumann and C-J planes should have an amplitude greater than  $P_{jc}$  ( $\tau_i$  is probably less than  $\tau_c$  as well).

Stesik and Akimova (26) reported, in addition to the  $d_c$  values already used, a number of  $D$  vs  $d$  measurements and also derived reaction zone length data. Their data and results computed from them with Eqs. 1 to 4 are summarized in Table 3. All the critical parameters of the pressed charges show a smooth variation with  $\rho_0$  or % TMD, but the only linear curves are  $d_c$  vs % TMD and  $\log P_{jc}$  vs % TMD. The rest are, like  $(D_c/D_i)$  vs % TMD, concave upward. The tabulated values of  $(D_c/D_i)$  show the low values (ca. 0.6) typical of loose powder charges and the high values (ca. 0.95) typical of

TABLE 3  
Additional Data for TNT in Several Different Forms

$\rho_0$ g/cc	% TMD	Parameters at Failure Conditions					Ideal Reaction Zone			Energy at $d_c$
		$d_c$ mm	$D_c$ mm/ $\mu$ sec	$P_{jc}$ kbar	$\frac{D_c}{D_i}$	$\frac{P_c}{P_i}$	$x$ mm	$\tau$ $\mu$ sec	$t$ $\mu$ sec	$E$ cal/cm <sup>2</sup>
		(a)	(a)	Eq. 1	(a)	Eq. 1	(b)	Eq. 2	(a)	Eq. 3
Pressed Charges										
0.80	48.5	10 <sup>c</sup>	2.80 <sup>c</sup>	16	0.64 <sup>c</sup>	0.44	4.0	1.4	0.56	38
1.00	60.6	9.0	3.44	30	0.69	0.48	2.4	0.72	0.40	44
1.46	88.5	4.3	5.77	121	0.88	0.74	0.30	0.069	0.095	28
1.55	94.0	3.3	6.34	156	0.93	0.86	0.23	0.050	0.051	29
1.62	98.2	2.5	6.63	178	0.95	0.90	0.21	0.045	0.034	32
Cast Charge (rapidly cooled)										
1.62	98.2	15.0	6.61	177	0.94	0.88	0.9	0.19	0.15	133

<sup>a</sup>Ref. (26).

<sup>b</sup>From  $x = d(1 - D/D_i)$ , Ref. (32). See Ref. (33) for these specific values.

<sup>c</sup>Changed from Ref. (26) values as shown in Fig. 1.

cast or pressed charges at 95% or more of their voidless density.

There is at present some confusion about measuring detonation reaction zone length and reaction time. Table 3 gives reaction zone lengths ( $x_i$ ) and reaction time ( $\tau_i$ ) computed from Eyring's curved front theory. Stesik and Akimova (26) obtained an experimental value of the zone length on the basis of calibrating their system with one series of free surface velocity measurements on explosively driven plates of different thicknesses. They also computed from these results a detonation reaction time ( $t_i$ ) which is presented for comparison in Table 3. The times  $\tau$  were chosen for the present treatment because they produce a linear curve,  $\log \tau$  vs % TMD, which is also a fairly good approximation to the Ref. (26) data. Both  $\tau$  and  $t$  are of the same order of magnitude as the more recently reported direct measurements of reaction time (34).

The last column of Table 3 contains the values of energy per unit area ( $E$ ) delivered to the explosive to sustain propagation at the critical conditions. In view of the approximations used,  $E$  might be constant over the range of the pressed charges but it is certainly lower than

the value required for a cast charge. It should be noted that if Eq. (3) is converted to energy per gram instead of energy per unit area, it is equal to  $u_{jc}^2$  and shows a smooth variation with % TMD as do the other detonation parameters at  $d = d_c$ . Finally, the data of Table 3 can be used to construct a limit curve in the pressure-time plane for pressed TNT charges. This is shown in Fig. 2 where the curve divides the plane into a super- and a sub-critical region.

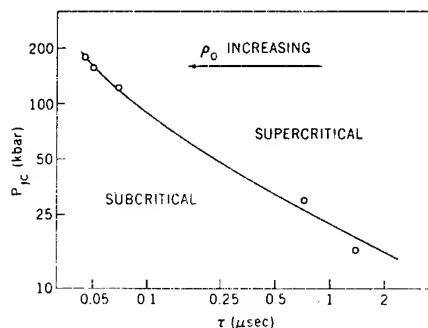


Fig. 2 - Critical curve for propagation in pressure-time plane for pressed TNT charges

## DISCUSSION

The data gathered for TNT have shown that both the critical initiating pressure  $P_i$  and the critical diameter  $d_c$  are determined in large part by the degree of physical homogeneity of the charge. It is to be expected therefore that these two threshold values will be related to each other, and the plot of  $d_c$  vs  $P_i$  shown in Fig. 3 affirms such a relationship by showing a smooth curve over the entire experimental range. This curve also serves as a graphic summary of much of our present information on the critical behavior of an organic explosive.

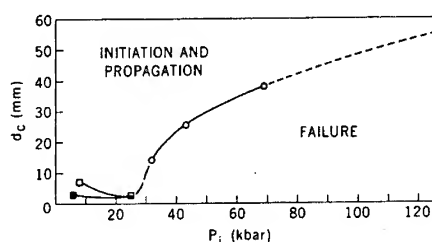


Fig. 3 - Variation of critical diameter with critical initiating pressure for several forms of TNT

(Cold pressed charges:  $\square$  Coarse;  $\blacksquare$  Fine; Hot pressed charges — —; Cast charges  $\circ$ ; Extrapolation ---)

Although there is no quantitative measure of the degree of physical homogeneity, we know that it varies from very low at the extreme left of Fig. 3 (high porosity, cold pressed charges) to very high at the extreme right (100% when the extrapolated curve reaches the perfect single crystal). Between these extremes,  $P_i$  shows a monotonic increase with increasing homogeneity and no particle size effect in the range of cold pressed charges. At the extreme right (single crystal) ignition and initiation must be by a homogeneous mechanism since no other is available. At the extreme left, it is generally agreed that initiation must be by a hot spot mechanism, i.e., surface reaction at areas of energy concentration. This heterogeneous mechanism is accepted because the measured initiating pressure is far too low to effect by shock compression a significant temperature rise throughout the bulk of the material. As the charges are changed from heterogeneous to homogeneous, the ignition mechanism also changes; it follows that, in some intermediate region, initiation must be by both heterogeneous and homogeneous mechanisms acting simultaneously. The effect of degree of homogeneity on  $P_i$  is attributed to

its reflection of the concentration, distribution and size of hot spot sites.

In the region of cold pressed charges, a particle size effect on  $d_c$  has been indicated. The Group 1 behavior of decreasing  $d_c$  with increasing % TMD, shown by the coarse TNT, was previously attributed to increasing domination of the heterogeneous reaction by the homogeneous (17). Thus, at higher density and higher reaction pressure, the dominance of bulk over surface reaction could result in shorter reaction times and reaction zone lengths which, in turn, would result in lower  $d_c$  values. This still seems a reasonable suggestion because detonation pressures of 120-180 kbar (Table 3 and Fig. 3) are quite high enough to cause appreciable bulk heating during shock compression. But the apparent reversal in trend shown by the fine TNT and the obvious reversal in trend ( $d_c$  vs  $P_i$  or  $d_c$  vs degree of homogeneity) in the hot pressed charge range, as compared to the cold-pressed, suggests that another factor should be considered. Because the behavior of the hot pressed charges bridges that of the cold-pressed and cast which are, respectively, permeable and impermeable, the new factor might well be the flow of detonation products through the charge. If so, convective heat transfer from such flow must play a role such that initiation is easier to achieve when the flow is optimum in permeable charges.

This suggestion is strengthened by the apparent importance of permeability in the transition from burning to detonation in granular compacts (35). Although permeability was not the only factor affecting the ease of transition (for example, surface to volume ratio of the individual particles and energy produced by chemical reaction were also considered), Griffiths and Grocock (35) found it a very important one. They proposed that the high velocity combustion necessary for transition was possible because of a convective transfer of energy from hot reaction gases to solid unreacted particles. A shock-to-detonation transition is a very rapid burning to detonation transition in which experimental time resolution is difficult. Mechanisms operative in more easily resolved transitions (35) may also be operative here.

In this connection, it should be noted that the phenomenon of "overshoot" observed in the shock initiation of detonation in cold pressed charges (11, 36, 37) is not observed in hot pressed charges (38) or in cast charges (11). The extent of overshoot in cold pressed charges is greatest for the most porous and least for the most compact (11). Permeability of the charge may be responsible for the appearance of overshoot.



Figure 3 summarized the large effects of the physical homogeneity on the propagation and initiation thresholds of a pure, chemically homogeneous explosive. Its complexity illustrates the impossibility of creating a single satisfactory model for a theoretical treatment of either failure or shock-to-detonation transition over the entire range of variation in initial physical state. At the same time, however, Fig. 3 shows that there are no discontinuous changes in the threshold values when preparation can be varied to give charges of different degrees of homogeneity so that they bridge the rather large gap between the highest density pressed charge and the perfect single crystal.

Although Fig. 3 demonstrates the continuum of threshold values, it does not provide a quantitative example of the relationship between conditions at these two types of threshold, i.e., the conditions of transient initiation and those at  $d_c$ . We can do this in two ways: (a) plot the two sets of pressure-time data (those at  $d_c$  and those from the LSGT) on a log-log scale, as suggested by Fig. 2, and approximate the limit curve by a straight line or (b) use the concept of a critical energy for initiation of detonation, compute that energy from the measurements at  $d_c$  with Eq. (3) and use it in Eq. (4) to define the limit curve. In either case, we must know the Hugoniot ( $P$  vs  $u$ ) of the non-reacting explosive or approximate it in some way. There are several Hugoniots for high density TNT which can be used for the near voidless TNT, pressed or cast, but there is only one for a very porous (1.0 g/cc) TNT (20). There is some question about the possibility of shocking such as porous material without inducing reaction, i.e., the Hugoniot data may be those of a partially reacting material rather than the desired data for the non-reacting material. Moreover, this very porous charge is in the region where the effect of the initial particle size is greatest (see Fig. 3) and where we lack the necessary critical data on charges prepared from fine TNT. For both of these reasons, we chose to use pressed TNT of  $\rho_0 = 1.62$  g/cc.

Table 3 shows that the "critical energy" for initiation of the high density compact is 32 cal/cm<sup>2</sup>. This is remarkably and probably fortuitously close to the energy limit of 33 cal/cm<sup>2</sup> Walker and Wasley report for ignition of pressed TNT at 1.64 g/cc. Our value is low because of approximating the critical pressure pulse with a square one of amplitude  $P_{jc}$  (a minimum rather than average value) but it does seem to be of the right order of magnitude. It is combined with the Hugoniot data (6) in Eq. (4) to generate the limit curve of Fig. 4. The curve is slightly concave upward, but can be fairly

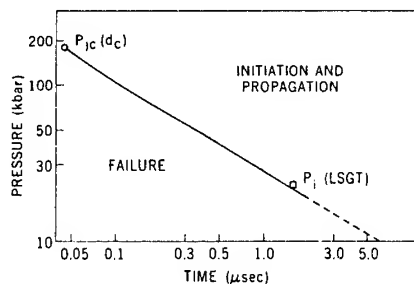


Fig. 4 - Critical curve through threshold values for pressed TNT ( $\rho_0 = 1.62$  g/cm<sup>3</sup>,  $E = 32$  cal/cm<sup>2</sup>)

well approximated by a straight line. Moreover the estimated square pulse equivalent of the initiating pulse used in the LSGT (0.9  $P_i$ , 1.6  $\mu$ sec) falls on the limit curve as shown, well within errors to be expected from those introduced experimentally as well as by the approximations used. The limit curve divides the  $P-t$  plane into a possible initiation and a failure region (above and below the curve, respectively). The curve originates at the  $P-t$  conditions found at the critical diameter threshold and runs through the continuum of ( $P$ ,  $t$ ) values which includes all the threshold values for initiation measured in the various gap, wedge, projectile, and booster tests. The conditions for the large scale gap test fall on the curve toward its lower end; the curve probably terminates shortly beyond that point since there is probably an upper time limit in which the critical energy must be delivered in order to initiate detonation. This particular example provides, therefore, a consistent and satisfying illustration of the conceptual relationship between conditions at the threshold for propagation and the numerous thresholds for initiation. It also supports the concept of a critical energy of initiation, but further tests with improved data should certainly be made.

In principle, a limit curve analogous to that for the pressed TNT can be constructed for the cast TNT. In fact, energies computed for the cast charge (rapidly cooled) of Table 3 from critical diameter data and from comparable  $P_i$  data (Table 1) differ by a factor of about two. This discrepancy is attributed to error in the reaction time used for the cast TNT. If we assume that the highest density pressed charge and all the castings have the same values  $D_c$  and  $P_{jc}$ , as the Table 3 data suggest, we can estimate critical energies and reaction times from Eq. (3) and the  $P_i$  data of Table 1. With LSGT conditions of  $P = 0.9 P_i$ ,  $t = 1.6 \mu$ sec, Eq. (3) indicates relative reaction times at  $d_c$

of 1, 1.6, 2.6, and 5.9, respectively, for the pressed, rapidly cooled cast, creamed cast, and vacuum cast charges. This is a reasonable trend and gives an increase in critical energy from the high density compact to Casting 1 of 1.6 instead of 4.1 times as shown in Table 3.

## SUMMARY

The various aspects of shock sensitivity have been illustrated with data obtained for TNT charges of varying degrees of physical homogeneity. Both the critical diameter for the propagation of detonation ( $d_c$ ) and the critical initiating pressure measured with the LSGT ( $P_i$ ) show continuous change with charge homogeneity.  $P_i$  increases (ease of initiation decreases) monotonically with increasing charge homogeneity. The same trend was observed for  $d_c$  in the region of cast charges, but the reverse trend occurs in the region of cold pressed charges. The reversal occurs in the region of hot pressed charges which bridges the cold-pressed, permeable charges and the cast, impermeable ones. The reversal is associated with the effect of permeability on the process of initiating detonation.

It is proposed that any charge will exhibit a critical curve in the pressure-time plane and that such a curve will start at a point corresponding to the detonation pressure and reaction time at  $d_c$ . The limit curve will then run through a continuum of ( $P$ ,  $t$ ) values corresponding to the various gap, booster, wedge, and projectile test values for shock sensitivity. In an example for pressed TNT at  $\rho_0 = 1.62$  g/cc,  $P_i$  from the LSGT fell on such a curve computed from a critical energy of initiation; the energy was evaluated from data obtained at  $d_c$ . This example supports the proposed model in which the transient initiation phenomena occur within the reaction zone at the threshold of steady state propagation. It also supports the concept of critical energy for initiation of detonation. Further tests of both concepts should be made with improved data.

## REFERENCES

1. H. W. Hubbard and M. H. Johnson, *J. Appl. Phys.* **30**, 765 (1959).
2. S. M. Brown and E. G. Whitbread, *Les Ondes de Detonation*, Edition du Centre National de la Recherche Scientifique, Paris, 1962, pp. 69-80.
3. F. E. Walker and R. J. Wasley, *Explosivstoffe* **1969**, 17(1), 9-13. See also Univ. Cal. Lawrence Radiation Laboratory, Preprint UCRL-70891, Jan. 26, 1968.
4. D. Price, and I. Jaffe, *ARS Journal* **31**, 595 (1961).
5. D. Price, I. Jaffe and G. E. Roberson, *Ind. Chim. Belge* **1967**, 32 (Special No.), pp. 506-510.
6. N. L. Coleburn and T. P. Liddiard, Jr., *J. Chem. Phys.* **44**, 1929 (1966).
7. I. Jaffe, J. Toscano, and D. Price, *Naval Ord. Lab. Rept.*, NOLTR 64-66 (1964).
8. M. Kamegai and J. O. Erkman, "Numerical Analysis of a Diverging Shock Wave in Plexiglas Cylinders," page 477 of this volume.
9. I. Jaffe and A. R. Clairmont, *Naval Ord. Lab. Rept.*, NOLTR 65-33 (1965).
10. D. Price, *Naval Ord. Lab. Rept.*, NOLTR 70-73, (1970).
11. S. J. Jacobs, T. P. Liddiard, and B. E. Drimmer, *Ninth Symposium (International) on Combustion*, pp. 517-529, Academic Press, New York, 1963.
12. D. Price and F. J. Petrone, *J. Appl. Phys.* **35**, 710 (1964).
13. A. W. Campbell, W. C. Davis, and J. R. Travis, *Phys. Fluids* **4**, 498 (1961).
14. G. K. Adams, J. R. Holden, and E. G. Whitbread, *Ind. Chim. Belge* **2**, (Suppl), 216-221 (1959).
15. L. B. Seely, J. G. Berke, and M. W. Evans, *AIAA Journal*, **5**, 2179 (1967).
16. A. N. Dremin, O. K. Rozanov, S. D. Savrov, and V. V. Yakushev, *Combustion, Explosion and Shock Waves*, **3**, 6 (1967).
17. D. Price, *Eleventh Symposium (International) on Combustion*, pp. 693-702, The Combustion Institute, Pittsburgh, 1967.
18. D. Price and A. R. Clairmont, Jr., *Twelfth Symposium (International) on Combustion* pp. 761-770. The Combustion Institute, Pittsburgh 1969.

19. L. B. Seely, Proc. Fourth Electric Initiator Symposium at Franklin Inst., Phila., 1963. Paper 27 of Rept. EIS-A2353.
20. V. A. Vasil'yev, L. G. Bolkhovitinov, and K. D. Khristoforov, Fizika goreniya i vzryva, 3, 604 (1967).
21. J. W. Enig and F. J. Petrone, Phys. Fluids 9, 398 (1966).
22. V. K. Bobolev, Dokl. Akad. Nauk SSSR 57, 789 (1947). Translated by U. S. Joint Publications Res. Service, JPRS:4026.
23. A. F. Belyaev and M. K. Sukoyan, Combustion, Explosion, and Shock Waves, 3(1) 11 (1967).
24. A. N. Dremin, V. M. Zaitzev, V. S. Ilyukin, and P. F. Pokhil, Eighth Symposium (International) on Combustion, pp. 611-619, Williams and Wilkins, Baltimore, 1962.
25. A. Ya. Apin and L. S. Stesik, Sbornik "Fizika Vzryva" No. 3, 1955 USSR Acad. Sci. Through Ref. (24).
26. L. N. Stesik and L. N. Akimova, Russ. J. Phys. Chem 33, 148 (1959).
27. G. G. Rempel, Zh. Prikl. Mekh. Tekh. Fiz. 1969, (2), 83-86.
28. W. B. Cybulski, W. Payman, and D. W. Woodhead, Proc. Roy. Soc. (London) 197A, 51 (1949).
29. I. Jaffe and D. Price, ARS Journal 32, 1060 (1962).
30. D. Price and A. R. Clairmont, Jr., unreported data.
31. M. J. Urizar, E. James, Jr., and L. C. Smith, Phys. Fluids 4, 262 (1961).
32. H. Eyring, R. E. Powell, G. H. Duffy and R. B. Parlin, Chem. Rev. 45, 69 (1949).
33. W. E. Gordon, Fourth Symposium (International) on Detonation, pp. 179-197, ACR-126, U. S. Gov. Print. Office, Washington, 1967.
34. A. N. Dremin and K. K. Shvedov, Zh. Prikl. Mekh. Tekh. Fiz. 1964(2), 154.
35. N. Griffiths and J. M. Groocock, J. Chem. Soc., 1960, 4154.
36. H. Bernier, J. M. Lezard, and F. Prouteau, Ind. Chim. Belge 1967, 32 (Special No.), pp. 582-586.
37. C. Fauquignon and R. Cheret, Twelfth Symposium (International) on Combustion, pp. 745-751, The Combustion Institute, Pittsburgh, 1969.
38. A. W. Campbell, W. C. Davis, J. B. Ramsey, and J. R. Travis, Phys. Fluids 4, 511 (1961).

# SHOCK SENSITIVITY AND SHOCK HUGONIOTS OF HIGH-DENSITY GRANULAR EXPLOSIVES

Julius Roth  
Stanford Research Institute  
Menlo Park, California

## ABSTRACT

Shock initiation thresholds and shock Hugoniots have been obtained for five granular explosives at initial loading densities of about 0.8 to 0.9 of voidless density. These data were obtained at ambient temperature and at least one elevated temperature. All five explosives were examined in divergent shock geometry (gap test). Two of the five, HNS and PBX 9404, were also subjected to plane-wave shocks. HNS, NONA, RDX, and PETN were found to be more shock sensitive at elevated temperature than at room temperature. PBX 9404 exhibits the same shock sensitivity at 25° and 150°C for divergent shocks (gap test), but when subjected to planar shocks it is more sensitive at the higher temperature. Shock pressure vs explosive thickness curves obtained with pressure transducers mounted on thin wafers of test explosive indicate that chemical reactions leading to initiation cannot occur solely at the shock front. On the other hand a few of the shock Hugoniots suggest some degree of reaction near the shock front. The implications of these apparently contradictory effects, as well as the effects of pre-heating and packing density, have been used to suggest a model of the initiation process.

## INTRODUCTION

This study examines the shock sensitivity of unconfined granular explosives pressed into pellets having a packing density of around 80 to 90% of voidless density. In all cases the initiating shock is produced by a donor explosive charge and enters the test explosive through an inert barrier. The main experimental determinations are the shock amplitude required to produce 50% initiations of the test explosive when the entering shock is divergent, and the variation of the distance from the shock entry face to the point at which steady detonation first occurs, as a function of the amplitude of the input shock.

An understanding of the behavior of shock-loaded explosives is of fundamental importance for the safe use and proper design of explosive devices. Shock initiation is also a great challenge to the theoretician who is attempting to

develop models of the initiation process. Consequently it is not surprising that the shock initiation of explosives has been the subject of numerous investigations. References particularly pertinent to the present study are Refs. (1-6). In spite of all this effort the mechanism of the shock initiation of granular explosives remains unclear. A systematic study of the many factors controlling shock initiation should contribute greatly to elucidating the shock initiation mechanism. It is hoped that the present investigation is a step in that direction.

## List of Symbols

- $c_0$  = sound velocity in unshocked explosive pellet
- $D$  = detonation velocity
- $h$  = thickness of unshocked explosive pellet
- $P_0$  = pressure in the explosive at the explosive barrier interface

Most of this work was sponsored by the Sandia Corporation. The preliminary study of particle size effects was sponsored by the Honeywell Corporation.

- $t_B$  = time of shock travel through inert barrier (see Fig. 1)  
 $t_t$  = time from pin signal to shocked air-gap flash signal (see Fig. 1)  
 $T_0$  = temperature of unshocked explosive pellet  
 $u$  = particle velocity in the explosive at the explosive/barrier interface  
 $U_0$  = shock velocity in the explosive at the explosive/barrier interface  
 $V$  = specific volume of the explosive at the explosive/barrier interface  
 $x_i$  = distance from explosive/barrier interface at which steady detonation begins  
 $\rho_0$  = density of unshocked explosive pellet

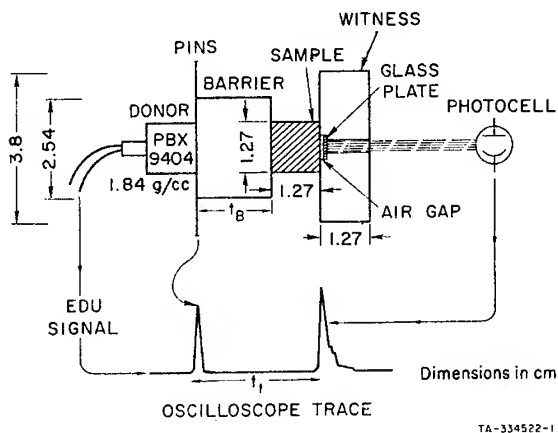


Fig. 1 - Schematic cross section of the gap test

## EXPERIMENTAL TECHNIQUES

### Apparatus and Procedures

A quantitative shock initiation experiment requires the generation of a controlled shock in the test explosive and the observation of the effects of this shock. The input shock may be divergent (gap test) or planar (wedge shot). A schematic diagram of the gap test is shown in Fig. 1. Reproducible PBX 9404 donor charges are used and shock amplitude is varied by varying the barrier length. A steel witness plate is used to determine whether the trial was a shot or a failure. Additionally a photocell views a thin air gap at the end of the test explosive. If the test explosive detonates it compresses air in the air gap to produce a bright flash which the photocell records. As shown in Fig. 1 this arrangement enables us to obtain the time  $t_t$  for every "go" trial. Data for obtaining the 50% initiation threshold were gathered in the Bruceton manner (7).

In several test series we desired to determine the effect of preheating the explosive sample. In these series the sample attached to the witness plate was heated in a temperature-controlled hot air stream and then quickly brought up against the room temperature donor/barrier system by remote means. These shots were fired within 10 sec of the preheated sample leaving the hot air stream. In other test series we wished to determine the shock transit time through thin wafers of test explosive. For these the witness plate was replaced by a pressure transducer acting as a time-of-arrival gage. Usually these gages were quartz and occasionally manganin. These data give an average shock velocity  $\bar{U}$  through the explosive.  $\bar{U} \rightarrow U_0$  if the explosive is thin.

Figure 2 illustrates the procedure used and the results obtained in plane-wave wedge shots. These shots were designed and many of them fired and analyzed by J. H. Blackburn, formerly of our laboratories. Preheating of the sample, if desired, was obtained by a small electric oven built into the shot. The explosive drivers were a P-80 plane-wave lens, and, depending on the input pressure desired, 1-inch-thick cylinders of loose TNT, RDX, or Baratol pads. All shots were illuminated with an argon flash bomb.

### Explosives

Properties of the explosive pellets used in this study and the initial conditions of the tests to which they were subjected are described in Table 1. The explosives used and their particle size distributions as determined with a Fischer Subsize Sizer are given in Table 2. Explosive pellets were made by pressing loose powder in a die, without the addition of any binder material (except for PBX 9404 pellets which were obtained in pellet form from Mason-Hanger Corp.). Wedges for plane-wave shots were machined (remotely) from cylindrical pressings.

Details of test techniques as well as sample preparation are given in Refs. (8, 9).

## RESULTS

### Shock Hugoniot

A quantitative treatment of the initiation of explosives by shocks introduced into the explosive through an inert barrier requires the use of the shock Hugoniot of the barrier and the explosive. In our work the barriers were

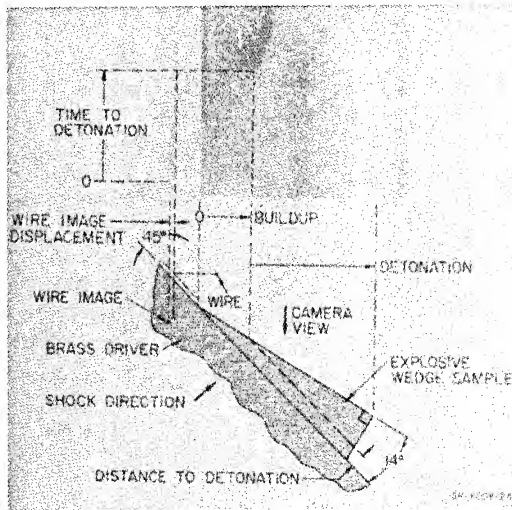


Fig. 2 - Streak camera record from wedge shot. Schematic drawing shows relationship between wedge geometry and camera record.

TABLE 1  
Initial Conditions of Explosive Pellets

Explosive	$\rho_0$ (g/cc)	$T_0$ (°C)	$c_0$ (mm/ $\mu$ sec)	Designation for Tables
RDX (A)	1.64	25	2.80	I
RDX (A)	1.58	180	2.45	I-H
RDX (B)	1.54	25	2.3	I-B
RDX (C)	1.54	25	1.0	I-C
RDX (D)	1.54	25	1.4	I-D
PETN	1.59	25	2.45	II
PETN	1.55	110	2.25	II-H
HNS	1.57	25	1.00	III
HNS	1.38	25	-	III-A
HNS	1.46	260	-	III-H
NONA	1.60	25	1.00	IV
NONA	1.49	250	-	IV-H
PBX 9404	1.84	25	2.60	V
PBX 9404	1.77	150	-	V-H

polymethylmethacrylate (PMMA) in the gap test and brass in the wedge shots. The shock Hugoniots of both of these materials are well known. The shock Hugoniots of our test explosives were unknown and had to be determined. Before presenting our shock Hugoniot data, it must be pointed out that defining shock parameters for heterogeneous pellets consisting of

explosive granules and air pockets present conceptual difficulties. At best the shock Hugoniots for such materials are useful only for describing the gross hydrodynamic behavior of granular explosives. It cannot be expected that the methods of continuum hydrodynamics applied to discontinuous media will yield any information on the fine structure of the state variables of the shocked explosive. Moreover, chemical reaction in or near the shock front can cause additional complications. Nevertheless, without further apology, we will use these macroscopic Hugoniots not only in establishing quantitative shock initiation thresholds but also for detecting the presence of chemical reaction at or near the shock front.

To construct shock Hugoniots one needs to determine any two of the state variables  $P$ ,  $V$ ,  $U$ , and  $u$ . Usually it is convenient to measure  $U$ . For wedge shots the only other measurement required is the brass free-surface velocity. Using the known Hugoniot for brass and the impedance mismatch method one then obtains all the other state variables. For gap test geometry one needs a calibration curve which gives the pressure in the PMMA barrier as function of barrier thickness. For the system shown in Fig. 1 optical measurements of  $U$  and  $u$ , or pressure transducer measurements of  $P$ , at the end of barrier are well represented by the following polynomial fit:

$$P = 227.1 - 28.42\ell + 1.246\ell^2 - 0.01840\ell^3 \quad (1)$$

where  $\ell$  is the thickness of the barrier in mm, and  $P$  is in kilobars. The standard error for this fit is  $\pm 0.88$  kbars, and the region over which data were obtained is for  $6 \text{ mm} \leq \ell \leq 25 \text{ mm}$ . These same data also give  $t_B$ , the shock transit time through the barrier, as a function of  $\ell$ . A good fit for this transit time in micro-seconds is

$$\ell = 8.41(1 - e^{-0.424t_B}) + 2.71t_B \quad (2)$$

The usual equations for constructing the Hugoniot curves hold rigorously only for plane-wave shocks. Optical observations indicate the shock on-axis of the PMMA barrier is nearly planar. Thus it is reasonable to use gap-test geometry to obtain Hugoniot data.

Wherever possible we will summarize our Hugoniot data in the convenient form of

$$U_0 = A + Bu \quad (3)$$

where  $A$  and  $B$  are constants. Least-square fits to this equation are shown in Table 3. Ideally the constant  $A$  should be  $c_0$ , the sound

TABLE 2  
Chemical Names and Particle Size Distribution of Explosives Used

Explosive	Chemical Name	Average Particle Size ( $\mu$ )		Average Specific Surface ( $\text{cm}^2/\text{g}$ )	
		Powder	Pellet	Powder	Pellet
RDX (A)	Cyclotrimethylenetrinitramine ↓	~25	17	--	1970
RDX (B)		8	5	4520	5800 (5100-6500)
RDX (C)		54	18	601	1800 (1450-2160)
RDX (D)		330	60	100	550 (400-790)
PETN	Pentaerythritoltetranitrate	$10 \times 100$	--	3350	--
HNS	Hexanitrostilbene	15	--	2700	--
NONA	Nonanitroterphenyl	~30	--	--	--
PBX 9404	94/3/3 Cyclotetramethylene tetranitramine/nitrocellulose/binder	"coarse"	--	--	--

TABLE 3  
Explosives Hugoniot Data in the Form of  $U_0 = A + Bu$

Explosive (See Table 1)	$U_0^*$ (mm/ $\mu\text{sec}$ )	$u$ Validity Range (mm/ $\mu\text{sec}$ )
III	$1.00 \pm 0.05 + (3.21 \pm 0.10)u$	0.00 - 0.68
IV	$1.00 \pm 0.05 + (3.21 \pm 0.10)u$	0.00 - 0.51
III-A	$0.61 \pm 0.29 + (2.77 \pm 1.09)u$	0.30 - 0.50
V	$2.45 \pm 0.21 + (2.48 \pm 0.11)u^\dagger$	0.00 - 1.45
V-H	$1.85 \pm 0.54 + (3.47 \pm 0.81)u$	0.00 - 0.77
I	$1.93 \pm 0.05 + (0.666 \pm 0.168)u$	0.11 - 0.35
I	$0.70 \pm 0.18 + (4.11 \pm 0.37)u$	0.35 - 0.47
I-H	$0.71 \pm 0.24 + (4.22 \pm 0.42)u$	0.25 - 0.32
II	$1.33 \pm 0.08 + (2.18 \pm 0.27)u$	0.03-0.37
II	$0.64 \pm 0.24 + (4.19 \pm 0.61)u$	0.29 - 0.48
II-H	$-0.59 \pm 0.46 + (8.66 \pm 1.74)u$	0.24 - 0.29

\* $\pm$  values are twice the standard deviation.

$^\dagger$ Private communication from J. B. Ramsay of LASL; the five data points we obtained agree closely with this fit.

velocity through the sample. Comparison of Tables 3 and 1 shows that  $A \approx c_0$  only for HNS, NONA, and PBX 9404. RDX and PETN data cannot be fitted by a single straight line; the break in the linear fit is presumably a manifestation of chemical reaction in the shock front. For these explosives  $c_0 > A$  even for the linear fit at small  $u$ . With the exception of PBX 9404, pre-heated explosives appear to exhibit some chemical reaction even at low shock levels

( $A$  is negative for hot PETN, suggesting that  $B$  is considerably smaller at lower  $u$  than shown in Table 3). The data for pre-heated HNS and 1.54 g/cc RDX could not be fitted to the linear form of Eq. 3 and are shown separately in Table 4. It is noteworthy that all the RDX data of Table 4 can be plotted on one  $P-u$  or even one  $P-V$  curve. Thus the particle size of the RDX does not appear to affect its gross hydrodynamic behavior. This is in contrast to the

TABLE 4  
Hugoniot Data for HNS and RDX

Explosive (See Table 1)	P <sub>0</sub> (kbar)	U <sub>0</sub> (mm/μsec)	u (mm/μsec)	v (cc/g)
III-H	11.9	2.16	0.368	0.560
III-H	13.4	2.21	0.417	0.548
III-H	14.0	2.25	0.420	0.552
III-H	32.0	4.00	0.540	0.586
III-H	52	5.2	0.68	0.59
I-D	6.6	1.70	0.250	0.553
I-C	7.9	1.75	0.292	0.538
I-C	9.0	1.73	0.335	0.523
I-B	9.2	1.90	0.323	0.541
I-D	10.9	1.92	0.377	0.522
I-C	11.0	1.90	0.380	0.521
I-D	11.0	1.93	0.375	0.523
I-B	11.1	1.88	0.380	0.518
I-B	17.0	2.39	0.475	0.522
I-B	17.4	2.38	0.483	0.517
I-C	18.1	~2.4	0.486	~0.52
I-B	22.7	2.80	0.586	0.528

data shown in Table 1 which indicate that sound velocities in RDX are influenced by the RDX particle size.

#### Initiation Thresholds

The raw data for determining the shock amplitudes for 50% initiation of the test explosive are the barrier thicknesses for which 1/2 the trials are shots and 1/2 are failures. With Eq. 1 and the Hugoniot data of Table 3 or 4 these barrier thicknesses are converted into pressure in the explosive at the barrier/acceptor interface. These initiation threshold pressures are shown in the second column of Table 5. Since these data include the effects of pre-heating, packing density, and particle size of the explosive, we will briefly comment on each of these effects.

The bar graphs of Fig. 3 show that pre-heating reduces the threshold pressure in four of the five explosives studied. The case of PBX 9404 which shows no sensitization due to pre-heating will be considered later. Kilmer (10) also observed that pre-heating sensitizes explosives to shock.

HNS and RDX are more shock sensitive at the lower packing densities than at higher packing densities. The same packing density effect has been reported by Price et al. (1) for a number of explosives.

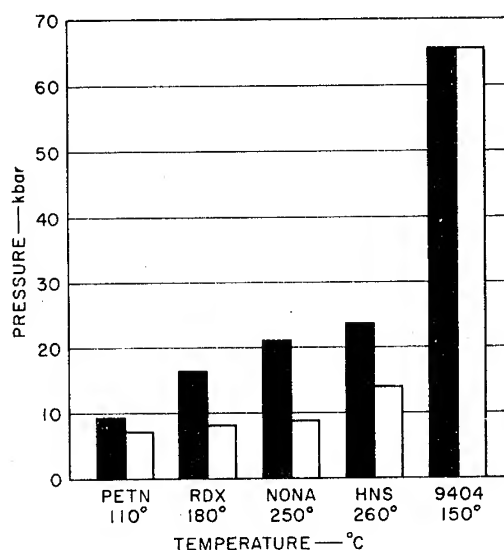


Fig. 3 - Shock sensitivity of five explosives. 50% thresholds are given as pressures in the explosive at the barrier/explosive interface. Dark-colored bars are for 25°C and light-colored bars are for the temperatures shown.

Since pre-heating reduces the packing density, one should consider whether the sensitizing action of pre-heating is primarily a packing density effect. Figure 4 shows that HNS at the



TABLE 5  
50% Initiation Threshold and Initiation Distance as  $\bar{x}_i = AP_0^B$

Explosive (See Table 1)	50% Threshold		Fit Constants			Data Points	Maximum Deviation of Data from Fit (%)
	$P_0$ (kbar)	$\bar{x}_i$ (mm)	A	B	$P_0$ (kbar)		
II	9.1	8.5	$6.13 \times 10^2$	-2.05	9.1 - 34.0	14	-16 to + 29
II-H	6.7	8.0	$3.39 \times 10^5$	-5.68	6.7 - 7.2	6	-10 to + 16
I	15.2	7.6	$6.94 \times 10^3$	-2.52	15.2 - 29.5	17	-18 to + 26
I-H	7.8	9.3	$1.87 \times 10^3$	-2.73	7.8 - 12.2	7	-14 to + 21
I-B	15.0	9.5	$1.72 \times 10^4$	-2.87	15.0 - 31.2	5	-18 to + 32
I-C	8.8	6.5	$4.75 \times 10^1$	0.969	9.1 - 31.1	7	-20 to + 12
I-D	9.0	12.5*	$3.65 \times 10^1$	0.637	9.1 - 30.4	12	-23 to + 41
III	23.2	7.5	$1.27 \times 10^3$	-1.69	23.2 - 140	11	-15 to + 27
III†	~19	5.6	$1.09 \times 10^5$	-3.24	21.5 - 32.0	4	± 2
III-H	13.2	11.0	$2.07 \times 10^4$	-3.01	13.2 - 22.2	11	-16 to + 43
III-H†	~9	7.4	$1.18 \times 10^2$	-1.27	11.5 - 52.2	6	-16 to + 43
III-H† and III-A‡	~9	7.4	$1.65 \times 10^2$	-1.38	9.4 - 52.5	10	-18 to + 32
IV	~19.5	6.3	$6.14 \times 10^4$	-3.09	20.2 - 22.5	7	-15 to + 17
IV-H	8.8	10.0	$7.73 \times 10^6$	-6.32	8.8 - 9.2	6	-24 to + 41
V and V-H	64.5	10.5*	$1.58 \times 10^8$	-4.01	64.5 - 119	12	-42 to + 24
V†	~15	20.2	$3.58 \times 10^3$	-1.73	18 - 159	23	-30 to + 21
V-H†	~15	8.7	$4.95 \times 10^3$	-1.92	28 - 59	6	± 3

\*Two pellets of 12.7 and 12.7 mm height stacked together.

†Plane wave experiments; threshold is assumed to be  $P_0$  at which  $\bar{x}_i$  becomes very large and  $\bar{x}_i$  value shown is the highest observed.

‡All but 5 of these data points are from Ref. (4).

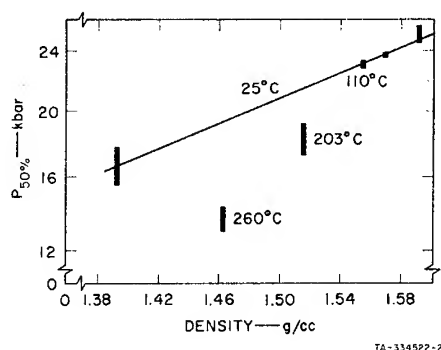


Fig. 4 - Effect of initial density and initial temperature on the 50% threshold of HNS

conclusion that pre-heating per se sensitizes explosives.

Seely (11) has observed a curious effect of particle size on the shock sensitivity of tetryl. Coarse tetryl was found to have a lower initiation threshold than fine tetryl. Our results (Tables 5 and 2) show that RDX behaves similarly. A very fine-grain RDX is less sensitive than a very coarse or an intermediate grain size which are about equally sensitive. Our comparison was made at  $\rho_0 = 1.54$  g/cc. This packing density represents a compromise between pellets of sufficient physical strength for handling and pellets in which grain crushing is not too excessive during pellet preparation.

#### Initiation Distance

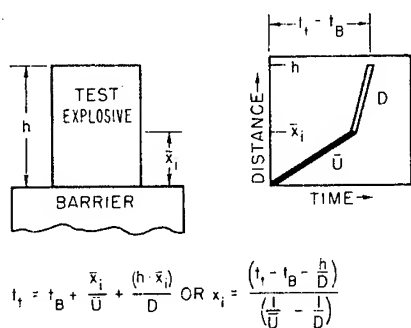
The distance from the shock entry face to the appearance of steady detonation is an

higher pre-heat temperatures is appreciably more shock sensitive than would be expected solely on the basis of reduced packing density. Our observations on RDX also lead to the

important parameter in the study of shock initiations. Figure 2 shows that this distance is obtained directly from a wedge shot record. Our instrumented gap test will also provide initiation distance data, as shown schematically in Fig. 5, if the assumption is made that a steady shock velocity changes abruptly into a steady detonation velocity. This assumption is justified by most wedge shot observations, e.g., that of Fig. 2, except in cases where  $\bar{x}_i$  is small. Initiation distance data are difficult to present. Following the suggestion of Ramsay and Popolato (4) we have fitted our data to an equation of the form:

$$\bar{x}_i = AP_0^B. \quad (4)$$

but with indifferent success as shown in Table 5. Most of deviation of observed  $\bar{x}_i$  from  $\bar{x}_i$  computed by Eq. 4 occurs near the initiation threshold. Consequently in Table 5 we have also listed the observed  $\bar{x}_i$  values nearest to the initiation threshold. The  $\bar{x}_i - P_0$  data of Table 5 may be used as a supplementary measure of the shock sensitivity of an explosive. Thus explosive A is more "sensitive" than explosive B if  $(\bar{x}_i)_A < (\bar{x}_i)_B$  at a fixed  $P_0$ . However, this criterion of shock sensitivity should be used with caution since we have observed crossovers for  $\bar{x}_i$  vs  $P_0$  plots. Because it is difficult to draw conclusions about the results shown in Table 5 without actually plotting  $\bar{x}_i$  vs  $P_0$  curves, a qualitative summary of these data is presented below:



TA-334522-4

Fig. 5 - Schematic representation of method of obtaining initiation distance,  $\bar{x}_i$ , in gap test

1. At "large" values of  $P_0$ , the  $\bar{x}_i$  values for a given explosive of a given particle size appear to be independent of initial conditions, i.e.,  $\rho_0$ ,  $T_0$ , or whether the shock is plane or divergent. For a "sensitive" explosive like PETN "large" means  $P_0 \geq 20$  kbar. For an

insensitive material like PBX 9404 "large" means  $P_0 \geq 80$  kbar.

2. Preliminary results with RDX pellets of different particle sizes indicate cross-overs of  $\bar{x}_i$  vs  $P_0$  plots. The coarsest grade (Type D, Table 2) in particular exhibits a much slower decrease of  $\bar{x}_i$  with increasing  $P_0$  than the other grades.

3. At low  $P_0$ , the  $\bar{x}_i$  values change very abruptly with changes in  $P_0$  in the gap test and less abruptly in the plane-wave shots. However, it is still possible to estimate a low-pressure asymptote for the latter.

#### Pressure-Distance Data

In a preceding section we mentioned the use of pressure transducers as time-of-arrival gages for shocks through thin explosive wafers. These experiments provide not only  $\bar{U}$  but also the pressure in the explosive at the explosive/transducer interface. By varying the thickness  $h$  of the explosive wafer this technique can be employed to obtain pressure-distance histories in shocked explosives. Figure 6, which gives the pressure-distance history in 1.59 g/cc PETN, illustrates the results obtained. The pressure at  $h = 0$  is  $P_0$ . The pressures at  $h > 0$  are the observed peak pressures in the transducer converted into pressures in the explosive at the explosive/transducer interface. The bottom curve of Fig. 6, for which the threshold  $P_{50\%} > P_0$ , shows continuous pressure decay with increasing  $h$ . Note that the early portion of this decay is indistinguishable from that observed with an inert  $(\text{NH}_4)_2\text{SO}_4$  wafer. The curve with  $P_0 = P_{50\%}$  parallels the bottom curve for  $h < 4$  mm, but for  $h > 5$  mm the pressure begins to increase although it is still below  $P_0$ . Beyond the data point at  $h = 6.3$  mm, the curve is drawn to approach asymptotically the  $\bar{x}_i$  for  $P_0 = 9.1$  kbar (Table 5). The initial slope of the curve for  $P_0 = 11.8$  kbar is estimated to be steeper than the slope for the PMMA barrier of the same initial pressure and about equivalent to the slope for  $(\text{NH}_4)_2\text{SO}_4$  at a slightly higher initial pressure. The curve for  $P_0 = 14.6$  kbar shows little or no pressure decay. Note, however, that the times of arrival for the four data points of this curve, including the wafer that detonated, lead to the same  $\bar{U}$ . This suggests that the first pressure pulse through all four wafers is a nonreactive or weakly reactive shock, and that additional pressure pulses were generated by reactions somewhere behind the shock front. Pressure-distance curves obtained for RDX and HNS show trends similar to those observed for PTEN. (8, 9)

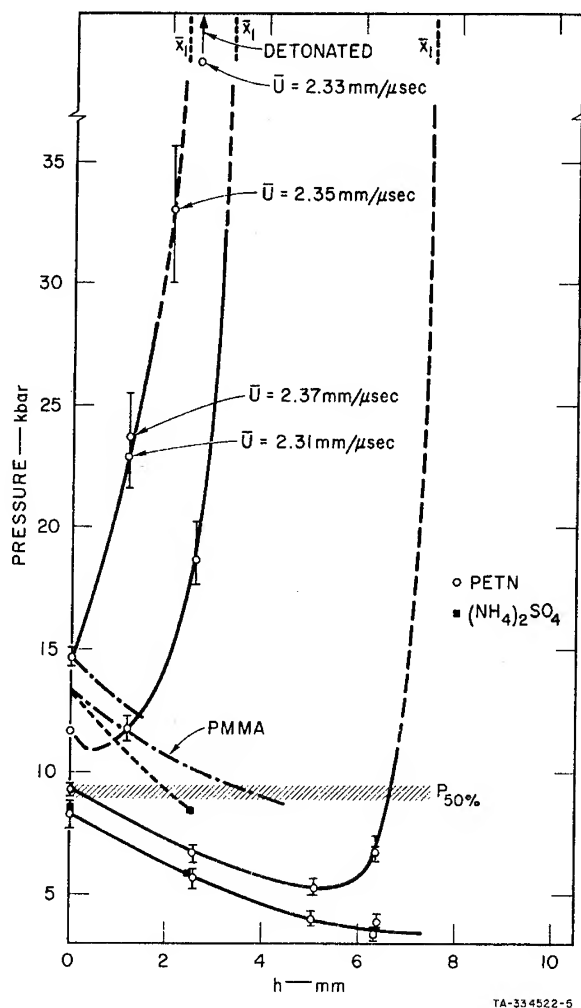


Fig. 6 - Pressure-distance history  
in 1.59 g/cc PETN

A preliminary test in which PBX 9404 wafers with manganin transducers were subjected to a planar shock also suggests a delayed reaction in the explosive. The record for a 1-mm-thick wafer shows an initial pressure rise of about 70 kbar, which is the expected  $P_0$  for the particular driver used if there is no reaction in the PBX 9404. This initial pulse is almost immediately followed by an additional pressure rise that reaches a peak of about  $3P_0/2$  in about  $0.3 \mu\text{sec}$ . Although the initial part of the pressure record for a 2-mm-thick wafer was lost, the peak pressure for this wafer was about  $2P_0$  and the peak was followed by a rapid decay. A 4-mm-thick wafer in this same shot detonated as determined from pressure and streak camera records. Its peak pressure was about 350 kbar. Unfortunately the early portion of this pressure record was again obscured. In

most of our pressure measurements for divergent gap test shots we also observed "hesitations" in those pressure-time records for which the peak pressure exceeded  $P_0$ . Often, though not always, this "hesitation" occurred at pressure levels about equal to  $P_0$ .

## DISCUSSION

There is quite general agreement that the shock initiation of explosives is basically a thermal process. Campbell et al. (5) have demonstrated satisfactory agreement between observed initiation delays in shocked liquid nitromethane and delays calculated on the basis of thermal explosion theory using the "low"-temperature kinetic parameters for nitromethane. The starting temperature for thermal explosion was shown to be adequately represented by

$$T = T_0 + \Delta T = T_0 + u^2/2c_v \quad (5)$$

with the specific heat,  $c_v$ , assumed to be constant. The above method of calculating  $\Delta T$  for porous solids is fairly inaccurate and gives only an upper limit estimate. Nevertheless it is instructive to make this simple calculation for shocks known to initiate porous solid explosives. Consider for example the data for RDX given in Table 4. For  $P_0 = 17$  kbar, which is above the initiation threshold of all the grades of RDX tested,  $u = 0.522$  mm/ $\mu\text{sec}$ , which gives an upper limit  $\Delta T = 110^\circ\text{C}$  and  $T_{\text{max}} = \Delta T + T_0 = 135^\circ\text{C}$ . RDX is quite stable at  $135^\circ\text{C}$ . Thus it is obvious that shock energies known to initiate RDX cannot produce sufficient bulk heating of the RDX pellet to cause even slow decomposition. The above example is typical of all the solid explosive compacts that we have studied. Clearly the input shock in these materials must produce localized regions of high temperature at which chemical reactions can proceed rapidly. How such hot spots are produced and how chemical decomposition at the hot spot sites leads to initiation of detonation is still a controversial question which the writer will now consider in terms of his own prejudices.

Although we have just shown that the level of homogeneous shock heating in a porous explosive is much too small for any thermal initiation process, it is still tempting to try to relate the input shock energy to the occurrence and magnitude of localized hot spots. For a fixed test geometry one might expect the formation of hot spots to control the level of the initiation threshold and since Hugoniot energy is proportional to  $u^2$  we might examine whether defining an

initiation threshold in terms of a critical particle velocity  $u_c$  (or  $u_c^2$ ), rather than the customary  $P_0$ , presents any advantages. This is done in Table 6, using our data as well as data from NOL and LASL. It is apparent from these results that a single  $u_c$  can represent initiation thresholds over an appreciable range of  $\rho_0$ . As expected this critical particle velocity may change with test conditions such as plane-wave vs divergent shock, charge diameter, confinement, and explosive particle size. Also  $u_c$  increases as  $\rho_0 \rightarrow \rho_{\text{crystal}}$ . Nevertheless it appears that the concept of a critical particle velocity, aside from any theoretical merits, simplifies the presentation of shock sensitivity data.

TABLE 6  
Critical Particle Velocity

Explosive	$\rho_0$ (g/cc)	Test	Initiation Threshold*	
			$P_0$ (kbar)	$u_c$ (mm/ $\mu$ sec)
RDX	1.64	(a)†	15.2	0.40
RDX	1.54	(a)	12.5	0.41
RDX	1.63	(b)	10.8	0.31
RDX	1.56	(b)	8.2	0.30
PETN	1.59	(a)	9.1	0.30
PETN	1.00	(c)	$\approx 2.5$	$\approx 0.3$
HNS	1.59	(a)	$\sim 25$	$\sim 0.56$
HNS	1.57	(a)	23.5	0.55
HNS	1.39	(a)	$\sim 16$	$\sim 0.54$
HNS	1.57	(d)	$\sim 17$	$\sim 0.44$
HNS	1.39	(d)	$\sim 9$	$\sim 0.40$
Tetryl	1.69	(b)	$\sim 19.7$	$\sim 0.40$
Tetryl	1.66	(b)	$\sim 18.5$	$\sim 0.40$
Tetryl	1.62	(b)	$\sim 13.5$	$\sim 0.35$
Tetryl	1.54	(b)	$\sim 8.6$	$\sim 0.32$
Tetryl	1.50	(b)	8.7	0.34
Tetryl	1.43	(b)	7.0	0.33
Tetryl	1.42	(b)	6.9	0.33
Tetryl	1.70	(e)	$\sim 21$	$\sim 0.41$
Tetryl	1.60	(e)	9.5	0.30
Tetryl	1.50	(e)	5.5	0.27
Tetryl	1.40	(e)	4.5	0.27
Tetryl	1.30	(e)	3.0	0.26

\*For wedge shots the threshold is estimated from  $\bar{x}_i$  vs  $P_0$  plots.

†Tests:

- (a) Gap tests, this paper.
- (b) NOL's "small scale gap test" (1).
- (c) Plane-wave wedge shots (12).
- (d) Plane-wave wedge shots, this paper.
- (e) Plane-wave wedge shots, (3).

In a porous explosive hot spots can be formed all along the shock path. With sufficiently strong shocks, and/or sufficiently reactive explosive, these hot spots can cause localized chemical decomposition rapid enough to contribute energy to the shock and continuously increase its intensity. Such shock front reactions certainly do occur as evidenced for example by P-V Hugoniots of positive slope or positive breaks in U-u Hugoniots. However near the initiation threshold, and possibly even considerably above the threshold, these shock front reactions do not appear to be the controlling reactions for the following reasons:

1. The observed shock velocities are steady, and change-over to detonation occurs rather abruptly.
2. The observed peak pressure, as a function of distance from shock entry often drop considerably below input levels, yet initiation is observed for sufficiently thick samples.
3. The first pressure pulse through an explosive wafer travels at a velocity characteristic of an "inert" shock even though the recorded peak pressure at the end of the wafer is greatly above the input pressure.
4. Pressure transducer records obtained with thin explosive wafers indicate a "slow" pressure increase after the abrupt pressure rise characteristic of the input shock.

These observations suggest that near the initiation threshold the controlling chemical reactions are occurring some distance behind the original shock front. A similar conclusion was reached by Liddiard and Jacobs (2). It is not unreasonable to expect that these reactions can grow into thermal explosions that send out new pressure pulses that overtake the original shock. There is an important difference between this point of view and the one suggested by Campbell et al. (5) for homogeneous explosives. In heterogeneous explosives reactions are expected to occur mostly in small localized regions, and consequently only a fraction of the total available chemical energy is liberated. Even if the shocklets produced by localized thermal explosions coalesce into a new pressure wave that catches up with the original shock, this pressure wave could still be too weak to initiate steady detonation in the unshocked explosive. However, the new pressure wave travels through a reacting medium before it overtakes the original shock. Consequently it can build up in intensity by receiving energy all along its travel path. Such "snow-balling" could produce a shock intense enough to initiate

bulk detonation in the unshocked explosive. It is probably an oversimplification to speak of a single pressure wave generated at some distance behind the shock front and eventually overtaking it. Considering the heterogeneity of the system a whole spectrum of pressure waves seems to be more plausible than a single wave, at least for conditions close to the initiation threshold. These waves may arrive at a transducer over a period of time because of differences in the chemical induction times for different hot spots and also because the travel times from the hot spot to the transducer will vary with the hot spot location. Thus the transducer may be expected to see a more or less continuously increasing pressure rather than an abrupt pressure change. As previously mentioned, we have obtained this type of pressure record with manganin pressure gages on plane-wave loaded PBX 9404. These records may also give an indication of the "snow-balling" effect since the 2-mm-thick PBX 9404 wafer shows a higher peak pressure and a faster pressure rise than the 1-mm-thick wafer.

Our view of the shock initiation of granular explosives bears considerable resemblance to the model proposed for the shock initiation of homogeneous explosives (5). It is interesting to examine whether some of the quantitative deductions of the homogeneous initiation model are also applicable to our model. If we apply simple geometric considerations to a space-time diagram similar to that presented for homogeneous initiations (Fig. 8 of Ref. (5)) we obtain the following expression of the chemical induction time  $\tau$

$$\tau = \bar{x}_i / \bar{U} [1 - \bar{U}/\bar{U}_t] / [1 - u/\bar{U}_t] \quad (6)$$

provided that we assume that all velocities are constant and that  $\bar{U}_t$  represents some average velocity of all the combined shocklets formed by localized thermal explosions. We expect that  $u/\bar{U}_t \ll 1$  so that it is justifiable to neglect  $u/\bar{U}_t$  in the denominator of Eq. 6. Our model requires that  $\bar{U}_t > \bar{U}$ . The model postulates incomplete chemical reaction in the region of  $x < \bar{x}_i$  and this suggests that  $D > \bar{U}_t$ . Consequently a plausible estimate for  $\bar{U}/\bar{U}_t$  is  $1/2$ ; i.e.,  $1 > \bar{U}/\bar{U}_t > \bar{U}/D \sim 1/4$ . For thermal explosion theory

$$\tau = [T^2 R_c / ZEQ] \exp(E/RT) \quad (7)$$

where  $Z$  and  $E$  are the Arrhenius parameters of the explosive and  $Q$  is its heat of reaction. For the problem that we are considering  $T$  represent a hot spot temperature and for simplicity we assume that it is steady and does not vary

from hot spot to hot spot. The data of Table 6 suggest that hot spot temperature is a function of  $u$ . Consequently we assume that  $T$  depends on the input shock according to

$$T = T_0 + Cu \quad (8)$$

where  $C$  is a constant characteristic of the explosive. A posteriori we find that the form of Eq. 8 gives better internal consistency than similar forms based on  $P_0$  or  $\bar{U}$  rather than  $u$ . Also  $u$  is a much better choice than  $u^2$ . We can now solve Eq. 6 for  $\tau$  using the data of Tables 3, 4, and 5 for  $u$ ,  $U_0 \approx \bar{U}$ , and  $\bar{x}_i$ , and assuming that  $\bar{U}/\bar{U}_t = 1/2$ . These values of  $\tau$  are then used in Eqs. 7 and 8 to get  $T$  and  $C$ . To normalize the data, the  $C$ 's are averaged and  $\tau$  is recomputed by Eq. 7 using the average  $C$  for the particular explosive. The results of these computations for PETN and RDX are presented in Table 7.

Obviously this treatment contains some drastic simplification. Nevertheless the fairly good agreement between  $\tau$ 's obtained from geometric considerations and  $\tau$ 's computed from thermal explosion theory tends to support the plausibility of the suggested model. Incidentally the choice of  $\bar{U}/\bar{U}_t$  has no other effect than to change the empirical constant  $C$  of Eq. 8. A small decrease in the  $E$  used for RDX would lead to much better agreement between  $\tau$ 's.

At present we can offer no theoretical justification for the apparent correlation between hot spot  $\Delta T$  and input  $u$  suggested by Eq. 8. This simple relationship does not indicate any particle size effect on hot spot temperature. That such particle size effects do exist is suggested by the work of Blackburn and Seely (15). It seems logical to attribute the observed decrease in the initiation threshold of coarse RDX (Table 5) and coarse Teteryl (Ref. (11)) to hotter and larger hot spots in coarse-grain than in fine-grain materials.

Now that we have some basis for expecting that pre-heating a granular explosive should always sensitize it to a subsequent shock, let us briefly examine why this expectation is not realized with PBX 9404 (see Fig. 3). For wedge shots with planar shocks we have found (9) that pre-heated PBX 9404, as expected, is more shock sensitive than room-temperature PBX 9404. However we also found that rarefactions travel faster in hot than in cold PBX 9404. Thus the observed equivalence of gap test initiation thresholds for hot and cold PBX 9404 appears to be a trade-off between sensitization by pre-heating and quenching by peripheral rarefactions.

TABLE 7  
Test of Thermal Explosion Model

Explosive (See Table 1)	$u$ (mm/ $\mu$ sec)	$\bar{u}$ (mm/ $\mu$ sec)	$x_i/2U^*$ ( $\mu$ sec)	$\Delta T^\dagger$ ( $^\circ$ K)	$\tau^\ddagger$ ( $\mu$ sec)
II	0.300	1.70	2.4	472	3.0
II	0.328	2.00	1.0	516	1.1
II	0.352	2.16	0.75	553	0.57
II-H	0.259	1.66	2.3	407	2.0
II-H	0.268	1.74	1.4	422	1.4
II-H	0.284	1.90	0.87	446	0.87
I	0.403	2.15	1.7	475	2.6
I	0.416	2.27	1.3	490	1.6
I	0.440	2.45	1.0	518	0.67
I-H	0.278	1.84	1.6	328	2.1
I-H	0.293	1.92	1.0	345	1.3
I-H	0.311	2.00	0.75	367	0.67

\*See Eq. 6.

$^\dagger \Delta T = Cu$  (see Eq. 8); for the data shown,  $C = 1571$  (1530 to 1604)  $^\circ$ K  $\mu$ sec/mm for PETN and  $C = 1179$  (1148 to 1210)  $^\circ$ K  $\mu$ sec/mm for RDX.

$^\ddagger$  From Eq. 7 with  $\tau = T_0 + Cu$ ; for PETN  $z = 10^{12}$   $\text{sec}^{-1}$  and  $E = 30 \times 10^3$  cal/mole (13) and for RDX  $z = 10^{15}$   $\text{sec}^{-1}$  and  $E = 41 \times 10^3$  cal/mole (14).

#### ACKNOWLEDGMENTS

In addition to developing our wedge shot techniques and supervising the firing and analysis of all our HNS wedge shots, Mr. J. H. Blackburn developed most of the method of analyzing the effects of peripheral rarefactions. He also contributed many helpful discussions on analyzing and presenting shock Hugoniot data. Mr. R. W. Gates performed most of the gap test experiments and Mr. B. O. Reese carried out all the plane-wave shots.

#### REFERENCES

- Donna Price and T. P. Liddiard, Jr., "The Small Scale Gap Test: Calibration and Comparison With the Large Scale Gap Test," NOLTR 66-87, July 1966.
- T. P. Liddiard, Jr., and S. J. Jacobs, "Initiation of Reaction in Explosives by Shocks," NOLTR 64-53, October 1965.
- I. E. Lindstrom, "Planar Shock Initiation of Porous Tetryl," J. Appl. Phys., Vol. 41, p. 337, Jan. 1970.
- J. B. Ramsay and A. Popolato, "Analysis of Shock Wave and Initiation Data for Solid Explosives," Proc. Fourth Symposium on Detonation, p. 233, Oct. 12-15, 1965.
- A. W. Campbell, W. C. Davis, and J. R. Travis, "Shock Initiation of Detonation in Liquid Explosives," Phys. Fluids, Vol. 4, p. 498, 1961.
- A. W. Campbell, W. C. Davis, J. B. Ramsay, and J. R. Travis, "Shocks Initiation of Solid Explosives," *ibid.*, p. 511.
- M. G. Natrella, "Experimental Statistics," pp. 10-22, NBS Handbook 91, August 1963.
- J. Roth and J. H. Blackburn, "Effect of Initial Temperature on the Shock Sensitivity of Granular Explosives," Final Report, Stanford Research Institute, Contract 58-1348, Aug. 1967.
- J. Roth and B. O. Reese, "Plane-Wave Shock Sensitivity of PBX 9404," Final Report, Stanford Research Institute, Contract 58-4926, June 1969.
- E. F. Kilmer, "Heat-Resistant Explosives for Space Applications," J. Spacecraft, Vol. 5, p. 1216, Oct. 1968.
- L. B. Seely, Jr., "A Proposed Mechanism for Shock Initiation of Low Density Granular Explosives," Paper 27, Proc. of Fourth Electric Initiator Symposium, Franklin Institute, Phila., 1963.
- G. E. Seay and L. B. Seely, Jr., "Initiation of a Low Density PETN Pressing by a

- Plane Shock Wave," J. Appl. Phys., Vol. 32, p. 1092, 1961.
13. J. Roth, "The Thermal Decomposition of PETN," p. 41, Addendum to Bulletin of 6th Army-Navy Solid Propellant Meeting, Michigan, 20-21 April 1950.
  14. A. J. B. Robertson, "Thermal Decomposition of RDX and HMX," Trans. Faraday Soc., Vol. 45, p. 85, 1949.
  15. J. H. Blackburn and L. B. Seely, Jr., "Detonation Light in Granular Explosives," Trans. Faraday Soc., Vol. 61, p. 537, 1965.

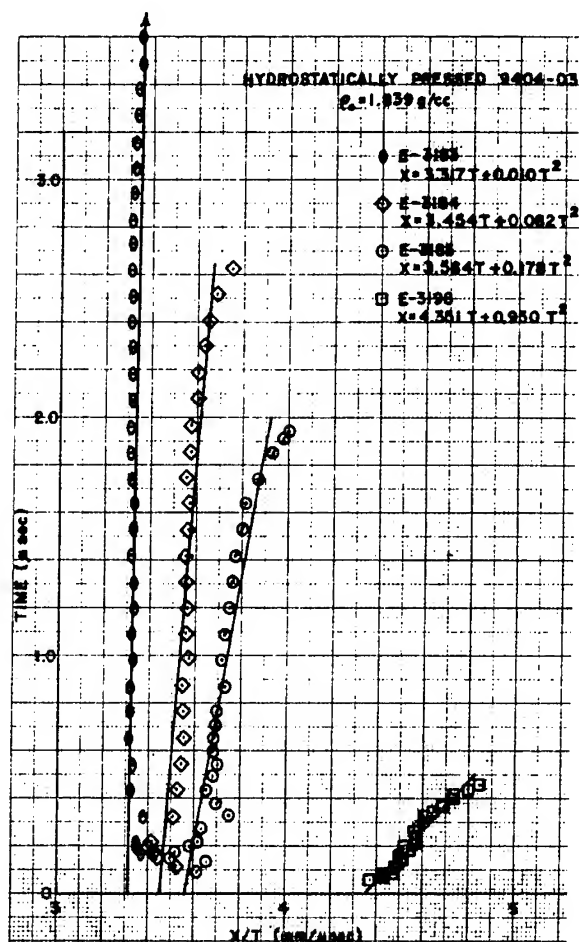
## DISCUSSION

B. G. CRAIG

Los Alamos Scientific Laboratory  
Los Alamos, New Mexico

You assume that a steady shock velocity changes abruptly into a steady detonation, and you cite some wedge shots as evidence of justification for this assumption. We have studied the shock velocity in several dense explosives. All of our experiments have been with large

plane-wave boosters. We find that dense explosives such as TNT, RDX, and HMX do not exhibit steady shock velocities except under very limited conditions. The shock front's progress is well described by the equation  $x = u_0 t \pm (1/2)bt^2$ , where  $x$  is the distance the shock has advanced in the time  $t$ , and  $u_0$  is the initial shock velocity. This is illustrated in the attached figure.



# EXPERIMENTAL STUDY OF THE TRANSITION FROM BURNING TO DETONATION

J. Calzia and H. Carabin  
*Poudaerie et Laboratoires*  
93 Sevran, France

## ABSTRACT

A study of the transition from burning to detonation in explosives has been initiated. Two measuring techniques were used:

(a) The continuous recording of the detonation velocity of the explosive by measuring the change in electrical resistance of a conducting wire probe.

(b) Streak camera photography.

The experiments clearly demonstrated the following:

1. The detonation first appeared within the explosive at a distance ahead of the burning surface.

2. The initial detonation velocity was much greater than the stable detonation velocity. This initial "strong detonation" persists for some time, after which the velocity progressively decreases to that of the stable detonation.

3. A "retonation" wave forms in the regions where the detonation appears and propagates back to the burning surface.

## INTRODUCTION

The study of the transition from burning to detonation is very important, especially for problems of safety. Fissures or a large porosity in the interior of a propellant grain can cause an acceleration of the deflagration to a detonation. The burning of a large quantity of an explosive can lead to its detonation; this has been the cause of serious accidents.

According to a number of important gas phase experiments, especially by Oppenheim (1) and Zeldovich (2), it was observed that the detonation appears at some distance up-stream from the flame.

With condensed explosives, this transition is more difficult to observe, for fortunately,

when an explosive burns, it generally does so without detonation. The latter is obtained only under heavy confinement or when the quantity of explosive is large; this is often difficult to realize in a laboratory. The first experiments were made by A. Macek and R. W. Gipson (3) using a continuous measurement of the detonation velocity. Following this, streak camera photography was carried out by N. Griffiths and J. M. Grocock (4), D. Price and J. F. Wehner (5), A. V. Obmenine and A. I. Korotkov (6). These studies were conducted with either powdered explosives (RDX, HMX, pentolite, tetryl) or with cast explosive (pentolite, DINA).

In all these cases (gaseous, powdered, or cast explosives), the process appears to be the following: The acceleration of the combustion of the explosive medium under confinement

NOTE: This paper was translated from the original by R. Roberts, Office of Naval Research, Department of the Navy.



entails the formation of compression waves which proceed in the intact explosives. Then, at a certain distance, these waves overlap to create a shock wave; finally this shock, if it is of sufficient intensity, generates a chemical reaction and transforms into a detonation. Andreev and his collaborators (7) have proposed a slightly different mechanism for mine explosives. They are of the opinion that the transition is due to the increase in surface during combustion. If this increase is sufficiently large, the equilibrium between gas formation and the flow of the gas is unstable and the pressure increases rapidly leading to the formation of a shock wave.

There follows a description of our experiments.

## 1. CONTINUOUS OSCILLOSCOPE RECORDING OF THE VELOCITY

### 1.1 Description of the Method

This classic method consists of recording on an oscilloscope the variation of the resistance of a probe carrying constant current placed longitudinally in the charge. The probe that we used consisted of a nichrome wire coiled on an enameled copper wire. This was coated with a thin film of nylon and placed inside a small tube. This type of probe has the advantage of functioning to all detonation velocities (8).

A second probe of the same type but having the ends insulated was placed either perpendicular at the beginning of the charge or axially. The generation of a short circuit then tripped the oscilloscope sweep.

### 1.2 Results

In order to observe the transition from deflagration to detonation, the explosive was placed under transparent confinement. The confining material must exhibit a high mechanical resistance (especially resistant to the shock due to the pressure produced by the initiator). Thick tubes obtained by the molding of a polyester resin, Rhodester 1108 CPSL, were selected. The coloration of this resin is practically nil even for large thicknesses (index of refraction  $n = 1.54 =$  index of glass). This product presents the advantage of gelling at ambient temperature without the need of degassing.

The dimensions of the tube were:

Diam. interior = 40 mm  
Diam. exterior = 120 mm  
Length = 200 mm  
(occasionally 400 mm)

The tube was clamped between two steel plates supported by threaded rods. The two plates were pierced with holes, the one placed on the side of the initiator is 16 mm in diameter in order to prevent the premature bursting of the tube; the other has a 3-mm-diameter hole in order to permit the insertion of the measuring probes (Fig. 1).

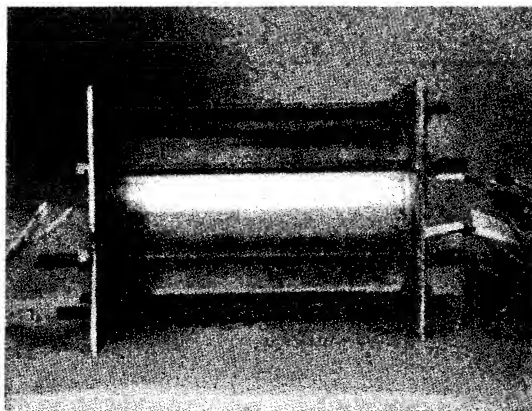


Fig. 1 - Experimental arrangement

The explosive used was RDX which was loaded in the tube without compression. An initiating charge of 10 g of powder (MI9) and a Gevelot P53 squib in a small cardboard tube closed by a sheet of polyethylene was placed at one end of the tube.

Reproduced below (Fig. 2) are the recordings which were obtained with RDX-CH (particle size 13 microns) loaded at a density of 1.0 g/cc - and with RDX-B (particle size 45 microns) loaded at a density of 1.15 g/cc.

From the traces, one is able to deduce the following points:

In the case of RDX-CH, the detonation appeared about 27 mm ahead of the initiator; its velocity initially was between 7200 m/s and 8000 m/s decreasing to a stable velocity of

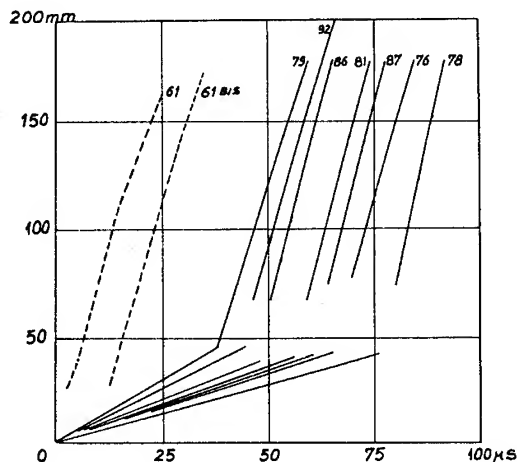


Fig. 2 - Recordings obtained with RDX-CH (dotted lines) and RDX-B (continuous lines)

6000 m/s at about 115 mm. The latter corresponds to the stable detonation velocity of RDX under the conditions of density, diameter, and confinement used.

In the case of RDX-B, it was noted that one first observed the curve corresponding to the deflagration regime. This curve was not obtained in the experiments with RDX-CH; this difference was probably due to an increase in the sensitivity of the recording probe. The deflagration propagates at a velocity within the range of 550 to 1180 m/s; the detonation appears a distance between 20 and 32 mm from the burning zone at a distance between 67 and 77 mm from the initiating face of the explosives.

In the shot in which the velocity of deflagration was the largest (shot no. 79), a discontinuity between deflagration and detonation was not recorded. The detonation appears in contact with the burning zone.

The average velocity of detonation was, in all cases, between 6400 and 7400 m/s. It appeared on the plate to be a little stronger at the beginning than at the end; the velocity was approximately in the neighborhood of 7500 m/s at the beginning tending toward 6000 m/s at the end.

## 2. RECORDING WITH AN ULTRAFAST CAMERA

### 2.1 Equipment Used

To determine the equipment requirements, the characteristics of the shot were considered.

First, the total time — that is, the time between initiation and detonation — is constant and rather long compared to the time of the detonation itself. Thus, in recording with a framing camera the time span between two frames may well be greater than the duration of the transition. On the other hand, the time before the explosive ignites is very uncertain and one cannot deduct this time from the total duration of the process.

To take account of this, two cinematographic methods were considered to be most suitable:

- (1) Either a rotating-mirror camera with a film long enough to record the whole process, while maintaining sufficient accuracy during the transition phase,
- (2) Or a camera with an image converter. With this type of camera which has an extremely short response time (a few ns), the camera can be started with an optical or electrical probe.

In these studies we used:

- (1) The CF 1 camera of the Central Laboratory for Armaments. It was a camera of the first type with a total recording length of 1674 mm.
- (2) The TRW model 1.D image converter camera. It was a double camera which can be used as a streak or a framing camera by a simple change of an electronic circuit.

In case 2, the light gain is greater than 50. This is a great advantage compared with a classical camera (gain < 1) and permits the recording of phenomena with low luminosity.

### 2.2 Results obtained with the Streak Camera CF 1

The experimental arrangement was the same as that described in section 1: tube of Rhodester diameter 40/120 with a length of 200 mm. The explosive was initiated with a squib, Gevelot P 53, and a charge of 10 g of MI9 powder.

The record obtained from one of the films is reproduced (Fig. 3). The explosive in this case was RDX-CH with an average grain size of 13 microns.

The analysis of the Fig. 3 is the following:

Streak (1) - this corresponds to the combustion of the MI9 powder.

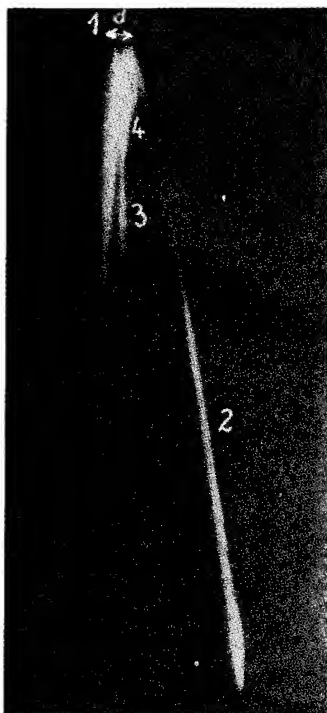


Fig. 3 - Recording with the streak camera CF 1

Streak (2) - this corresponds to a velocity of detonation which was equal to 7500 m/s during the first several centimeters and decreasing to 6800 m/s, then to 6000 m/s (the velocity reached after about 120 mm).

Streak (3) - this must be due to the bursting of the Rhodester tube. Moreover, at this place the lead plate on which the tube was placed showed a very sharp lateral spreading of the impression.

Streak (4) - this broad streak is explained by hypothesizing that it was due to a retonation which was initiated in the zone where the detonation appeared and which propagated until reaching the burning surface. The speed of this retonation was about 2300 m/s. Distance (d) is the one at which the detonation appears, approximately 38 mm.

### 2.3 Results Obtained with the TRW Camera in the "Streak" Version

In order to try to obtain on the same strip the propagation of the deflagration, the detonation, and the details of the transition zone, we have carried out a series of complementary

experiments with the TRW image converter camera provided with the circuit permitting its functioning as a streak camera. The light gain which one can obtain with this camera permits a very fine streak and, if necessary, phenomena of low luminosity to be recorded.

The shots were the same as those of section 1. However, in a number of cases recordings on the oscilloscope and on the camera were not obtained because one of the two instruments disengaged each time.

The curves obtained are reproduced in Fig. 4 and two streaks are given in Figs. 5 and 6.

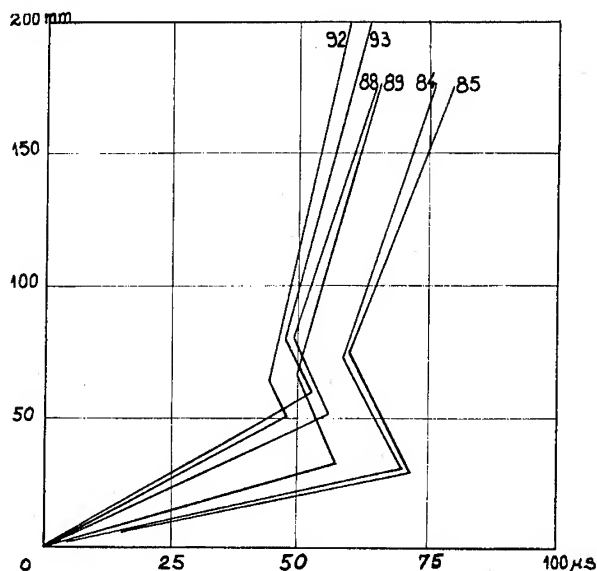


Fig. 4 - Streak recordings with the camera TRW

The speed of deflagration is in the range between 400 and 1150 m/s. The detonation appears at a distance between 18 and 50 mm ahead of the deflagration zone and at a distance of between 65 and 80 mm from the initiation face of the explosive. The average velocity, which is difficult to read, varies from 6200 to 8000 m/s. In addition, a retonation was observed. This was initiated in the zone where the detonation appeared and which propagated until it reached the combustion front. The speed of this retonation is in the neighborhood of 4000 m/s.

It was also observed, in shot 89 (Fig. 6), that a shock wave resulting from the retonation wave propagated at the interior of the

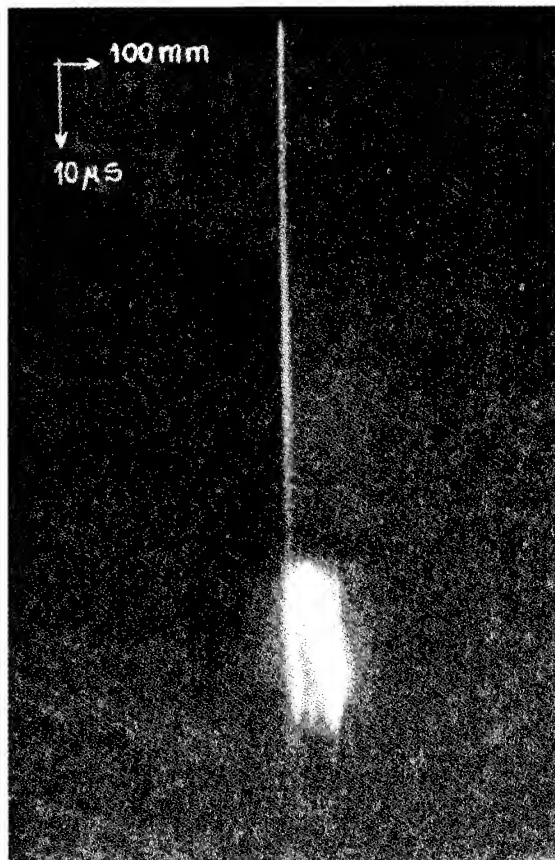


Fig. 5 - Shot No. 85

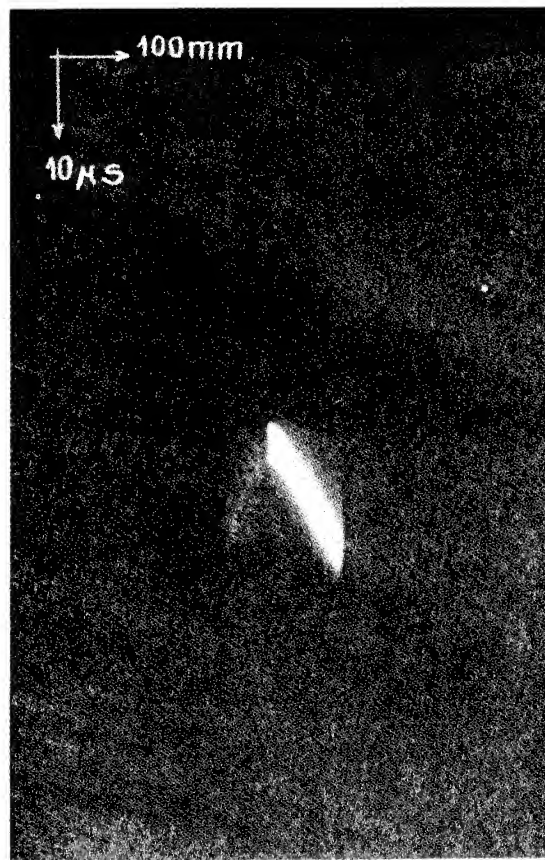


Fig. 6 - Shot No. 89

decomposition products as the result of the deflagration. This shock wave diminished in proportion to its propagation.

### CONCLUSION

The various results presented well confirm that the detonation begins in advance of the deflagration. Moreover, it was shown that this detonation had, at its initiation, a velocity in excess of the steady detonation velocity. It propagated in the explosive which had been compressed and it tended toward a stable detonation only after some time elapsed.

At the same moment that this detonation appeared a retonation occurred which propagated toward the rear to cause the detonation of the unreacted explosive.

Finally, the results of the two types of RDX are compared. In the case of RDX-B, the distance from the initiating face of the explosive to

where the detonation appeared was between 6 and 8 cm. In the case of RDX-CH, this distance was approximately 3 cm. Accordingly, it is verified that when the size of the explosive grain was decreased, the distance at which the detonation appeared was decreased.

In addition, if the processes found for mine explosives are different from those encountered here, it is doubtlessly because of the large viscosity of these explosives which leads to the poor transmittal of mechanical energy. The pressure signal emitted by the flame front no longer propagates and is immediately transformed into heat. The combustion is thus going to operate in a warmer medium, thus proceeding more rapidly. In addition, the combustion gases infiltrate the regions which are porous and cause an increase in the extent of the burning surface, thus causing an increase in the pressure of the burnt gases. The speed of reaction and pressure continue to increase until a detonation is attained and this is produced in the same zone as the combustion.

The authors wish to express their thanks to Professor Manson of the University of Poitiers who has been kind enough to follow this work and who has frequently guided it with his valuable advice.

## REFERENCES

1. A. J. Laderman, P. A. Urtiew and A. K. Oppenheim, "Generation of a shock wave by flame in an explosive gas", 9th Symp. on Combustion, pp. 265-274, 1963.
2. I. B. Zeldovich and A. S. Kompaneets, "Theory of detonation", Academic Press, New York, 1960.
3. A. Macek and R. W. Gipson, "Flame fronts and compression waves during transition from deflagration to detonation in solids", 8th Symp. on Combustion, pp. 847-854, 1962.
4. N. Griffiths and J. M. Groocock, "The burning to detonation of solid explosives", J. Chem. Soc., pp. 4154-4162, 1960.
5. D. Price and J. F. Wehner, "The transition from burning to detonation in cast explosives", Combustion and flame, G. B., 9, no. 1, pp. 73-80, 1965.
6. A. W. Obmenine, A. I. Korotkov et al, "Propagation of deflagration in burning porous explosives", Fizika Goreniyai Vzryva, Vol. 5, no. 4, pp. 461-470, 1969.
7. K. K. Andreev and V. V. Gorbunov, "On the transition of the burning of explosives to explosion", Russ. J. Phys. Chem 37, no. 9, pp. 1061-1065, 1963.
8. J. Calzia, "Experimental study of the transition deflagration-detonation", Powder Plant and Laboratory of Sevrans, note no. 2026, 1969. See also, F. C. Gibson, M. L. Bowser, and C. M. Mason, Rev. Sci. Instr. 30, 916, 1959.

# SHOCK INITIATION OF NITROMETHANE, METHYL NITRITE, AND SOME BIS DIFLUORAMINO ALKANES

J. G. Berke, R. Shaw and D. Tegg  
*Stanford Research Institute, Menlo Park, California*

and

L. B. Seely  
*Menlo College, Menlo Park, California*

## ABSTRACT

Reaction times for shock initiation were measured for some liquid explosives using a high speed smear camera and a modified gap-test. In all cases the reaction times decreased as the initiating shock pressure increased in the range 70 to 130 kbar, and as the pre-shock temperature was raised in the range 5° to 40°C. For constant shock pressure, the reaction time for liquid methyl nitrite is significantly less than the reaction time for nitromethane. This is consistent with thermal explosion theory, because the  $\text{CH}_3\text{O}-\text{NO}$  bond strength is more than 20 kcal/mole weaker than the  $\text{CH}_3-\text{NO}_2$  bond. For constant shock pressure, the reaction time of 1,2-bis(difluoramino)propane was significantly less than the reaction time for 2,2-bis(difluoramino)propane. Similarly, the reaction time for 1,2-bis(difluoramino)butane was significantly less than that for 2,2-bis(difluoramino)butane. We propose that the vicinal compounds decompose faster than the geminate compounds because the vicinal compounds can undergo a low activation energy, exothermic elimination of HF, via a four-center transition state  $-\text{CH}(\text{NF}_2)- \rightarrow -\text{C}(\text{NF})- + \text{HF}$ .

## GLOSSARY OF COMPOUNDS

Code Name	Structure	Chemical Name
NM	$\text{CH}_3\text{NO}_2$	nitromethane
	$\text{CH}_3\text{ONO}$	methyl nitrite
1,2-DP	$\begin{array}{c} \text{CH}_2-\text{CH}-\text{CH}_3 \\   \quad   \\ \text{NF}_2 \quad \text{NF}_2 \end{array}$	1,2-bis(difluoramino)propane
2,2-DP	$\text{CH}_3\text{C}(\text{NF}_2)_2\text{CH}_3$	2,2-bis(difluoramino)propane
1,2-DB	$\begin{array}{c} \text{CH}_2-\text{CH}-\text{CH}_2-\text{CH}_3 \\   \quad   \\ \text{NF}_2 \quad \text{NF}_2 \end{array}$	1,2-bis(difluoramino)butane
2,2-DB	$\text{CH}_3\text{C}(\text{NF}_2)_2\text{CH}_2\text{CH}_3$	2,2-bis(difluoramino)butane
IBA	$\begin{array}{c} \text{CH}_3 \\   \\ \text{CH}_2-\text{C}-\text{CH}_3 \\   \quad   \\ \text{NF}_2 \quad \text{NF}_2 \end{array}$	1,2-bis(difluoramino)-2-methylpropane (isobutylene adduct)

This work was supported by the Office of Naval Research under Contract Nonr 3760(00).

## INTRODUCTION

The main purpose of this paper is to supplement the work on the detonation failure of NF liquids (1). By dividing the work into two subjects — detonation failure and shock initiation — the results can be presented in greater detail. This seems worthwhile because in addition to its relevance to failure, shock initiation is of some intrinsic interest, and is clearly important to our understanding of shock sensitivity and gap testing. The ultimate goal of research on shock initiation is to develop the theory to the point where the shock sensitivity of a compound can be predicted from its chemical structure.

Research previously reported (2) has shown that in the JANAF gap test, initiation may occur at the walls of the container rather than at the charge axis. Since the object of the present work was to study the reactions occurring homogeneously in the liquid phase, particular care was taken to avoid wall initiation. Early in the research it was decided to use the divergent wave geometry of the gap test rather than plane waves. This decision was based on the good reproducibility and the low cost of the initiating explosive.

In their classic work on the shock initiation of liquid nitromethane, Campbell, Davis and Travis (3) showed that their results could be interpreted using homogeneous thermal explosion theory. The most important parameters in homogeneous thermal explosion theory are shock temperature and the chemical kinetics of the heat releasing reactions. Part of the underlying philosophy for this research was the assumption that isomers such as 1,2-DP and 2,2-DP would have similar physical properties when shocked and would therefore also have similar shock temperatures. Differences in initiation behavior would therefore be attributable to differences in heat release kinetics.

Nitromethane, because it is one of the most studied liquid explosives, and is also inexpensive, was used mainly to test our experimental procedure. A few experiments were conducted on its isomer, methyl nitrite. The main emphasis of the research however was on the NF liquids.

## EXPERIMENTAL

The source and purity of the Spectroquality nitromethane and of the NF liquids have been described earlier (4). A 200 ml batch of nitromethane was further purified by preparative

gas chromatography to reduce impurities from 2.5% to .5%. Methyl nitrite was prepared as follows (5, 6). Methanol (Allied Chemical) was run dropwise into isopentyl nitrite (Eastman Organic) in a 3-necked flask which was gently heated. The flask was fitted with a water-cooled condenser. The methyl nitrite was carried by a stream of nitrogen through a calcium chloride tube to remove unreacted methanol. The methyl nitrite was collected at  $-196^{\circ}\text{C}$  and distilled from bulb to bulb. The identity of the methyl nitrite was confirmed by infrared analysis (7) using 100 torr sample pressurized to 400 torr with nitrogen in a 9 cm gas cell and a Perkin-Elmer 237B grating spectrometer. Methanol has a strong peak at  $2.7\mu$  and isopentyl nitrite has a strong peak at  $14.6\mu$ . Neither impurity could be detected and their concentration was estimated to be less than 1%. The methyl nitrite was stored at  $-80^{\circ}\text{C}$ .

The shot set-up was very similar to that described earlier (see Fig. 4 of Ref. 2) except that the initiating charge was a 5.08 cm right cylinder of PBX instead of tetryl, and the chamber containing the explosive liquid was 5.08 cm in diameter and 1.25 cm long. In a few shots (see Table 1), the chamber was 1.9 cm long. The cell containing the liquid was made of optical grade Homalite plastic (8), and the pre-shock temperature of the liquid was controlled by a hot or cold liquid jacket and was measured by a thermocouple. The peak pressure in the liquid was varied from shot to shot in the range 70 to 130 kbar by varying the thickness of the Homalite attenuator. The peak pressure in the liquid was calculated from the known Hugoniot of the Homalite (8), and from a calculated Hugoniot of liquid using impedance matching (9).

The emission of light as a function of time was observed by a Beckman and Whitley model 770 rotating-mirror streak camera, operating at 600 revs per sec with an 80" lens and either 0.1 mm or 0.2 mm slit. A typical writing speed was 2 mm/ $\mu\text{sec}$ . In most of the experiments 70 mm Kodak Royal X film was used, but towards the end of the series, Kodak #2475 was substituted. The films were read on a Tele-readex with a resolution of 141 counts/mm. The systematic error in the variable, time, due to error in film reading is considered to be negligible.

## RESULTS AND DISCUSSION

A typical camera record for nitromethane is in Fig. 1. Three shots of 1,2-DP at successively lower shock pressures are shown in Figs. 2 to 4. The films were interpreted as in

TABLE 1  
Shot Analysis

Sample	Initial Temp	Attenuator Thickness	Transit Time	Net Time			Peak Liquid Pressure
	°C	mm	μsec	Reaction μsec	Over Take μsec	End μsec	kbar
Spectro quality Nitromethane	40	16.69	2.89	.40	.51	2.31	94
	40	18.67	3.21	.49	.65	2.68	88
	40	19.05	3.29	.58	.79	2.57	87
	40	19.74	3.42	.64	.86	2.80	85
	40	19.81	3.43	.61	.86	2.73	85
	40	20.83	3.63	.64	.92	3.25	82*
	40	21.36	3.74	.96	1.35	2.92	80
	40	21.84	3.83	.74	1.01	3.20	79
	40	22.30	3.93	1.67	2.43	3.51	78
	40	22.40	3.95	1.90	2.75	3.19	78
	40	23.16		fail			76
	22	15.88	2.69	0	.07	2.11	98
	21	15.88	2.69	.09	.09	2.22	98
	21	16.66	2.83	.15	.29	2.30	95
	23	19.05	3.29	.19	.34	2.26	87
	18	19.05	3.29	.28	.45	2.31	87
	25	19.27	3.33	.58	.83	2.63	87
	25	19.74	3.42	.66	.93	2.69	85
	22	19.84	3.44	.43	.63	2.29	85
	16	19.84	3.44	.48	.72	2.34	85
	26	19.86	3.44	.82	1.17	2.81	85
	25	20.47	3.56	1.17	1.67	2.94	83
							Fig. 1
	25	21.36	3.74	1.48	2.12	3.13	80
	25	21.59	3.78	2.34	3.34	3.62	80
	24	22.28		fail			78
	25	23.16		fail			76
Gas Chromatographically Purified Nitromethane	25	18.97	3.27	.55	.76	2.66	88
	25	19.81	3.43	.78	1.11	2.84	85
	25	20.66	3.60	1.40	2.05	3.18	82
	25	21.11	3.69	1.58	2.28	3.18	81
Spectro quality Nitromethane	6	17.88	3.06	.62	.90	2.60	91
	6	18.87	3.25	1.02	1.50	2.76	88
	6	19.05	3.29	1.14	1.68	2.74	87
	4	19.74	3.42	1.51	2.17	3.11	85
	4	20.47	3.56	2.84	—	4.17	83
	4	21.01		fail			81
	6	21.16		fail			81
	~-25	18.29		fail			90
	~-25	17.53		fail			92
	~-25	15.39	2.60	.57	.81	2.48	100
Methyl nitrite	~-50	19.05	3.29	.32	.37	2.44	87
	~-50	20.65	3.60	.73	.84	2.51	82
	~-50	22.23	3.91	1.11	1.32	2.76	78
	~-50	24.13	4.30	1.63	2.12	3.13	73

(Table continues)

\*In this shot, the depth of the liquid was 1.9 cm instead of the usual 1.25 cm.



TABLE 1  
Shot Analysis—Continued

Sample	Initial Temp	Attenuator Thickness	Transit Time	Net Time			Peak Liquid Pressure
	°C	mm	μsec	Reaction μsec	Over Take μsec	End μsec	kbar
1,2-bis(difluor-amino)propane (1,2-DP)	40	17.67	3.02	.22	.27	2.27	92
	40	18.82	3.24	.28	.37	2.58	88
	40	19.84	3.44	.45	.58	2.78	85
	40	20.65	3.60	.86	1.10	3.02	82
	41	22.05	3.88	.90	1.11	3.00	78
	41	23.16	4.10	1.23	1.52	3.14	Fig. 2 76
	40	23.44	4.16	2.07	2.60	3.60	Fig. 3 75
	40	24.03		fail			Fig. 4 73
	0	18.77	3.23	.14	.43	3.18	88
	4	20.22	3.51	.36	.68	3.20	84
	6	21.36	3.74	1.31	1.82	3.65	80
	3	22.29		fail			78
Spectro quality Nitromethane with 1% water added	25	20.57	3.58	.93	1.31	2.82	83
1,2-DP/Cyclohexane (20/3.1 by volume)	4	19.02	3.28	.23	.23	3.46	87
	4	20.09	3.49	.21	.34	3.40	84
	4	21.03	3.67	.29	.45	3.46	81
2,2-bis(difluor-amino)propane (2,2-DP)	37	16.81	2.86	.29	.39	2.63	95
	40	17.55	3.00	.47	.65	2.74	92
	40	18.75	3.23	.68	.93	2.67	88
	40	19.81	3.43	1.61	2.20	3.09	85
	40	20.55	3.58	1.77	2.45	3.18	83
	40	21.34	3.73	3.86			80
	40	21.44	3.75	1.78	2.48	3.50	80
	40	22.20		fail			78
	4	12.85	2.14	.22	.22	2.33	109
	4	15.19	2.56	.37	.57	3.15	100
	4	16.91	2.88	.94	1.35	2.69	94
	5	17.84	3.06	1.75	2.42	2.94	91
	5	18.75		fail			88
	4	18.80	3.24	3.16			88
	4	19.78		fail			85
1,2-bis(difluor-amino)-2-methyl propane (IBA)	40	17.65	3.02	.38	.52	2.85	92
	37	19.67	3.41	.40	.64	2.69	85
	41	19.74	3.42	.79	1.13	2.99	85
	40	20.90	3.65	1.49	2.84	3.38	82
	40	21.59	3.78	1.74	2.54	3.48	80
	40	21.65	3.80	2.02	2.97	3.57	80
	40	22.43		fail			77
	8	9.14	1.49	0.04	0.04	2.12	125
	7	12.60	2.09	.11	.11	2.21	110

(Table continues)

TABLE 1  
Shot Analysis—Continued

Sample	Initial Temp	Attenuator Thickness	Transit Time	Net Time			Peak Liquid Pressure
	°C	mm	$\mu$ sec	Reaction $\mu$ sec	Over Take $\mu$ sec	End $\mu$ sec	kbar
1,2-bis(difluor-amino)-2-methyl propane (IBA)—Continued	5	16.40	2.78	.35	.50	3.44	96*
	4	17.57	3.00	.39	.61	3.13	92*
	4	17.65	3.02	.55	.88	3.42	92*
	4	18.58	3.20	.63	.99	2.24	89
	10	18.67	3.21	.52	.74	2.32	88
	4	18.69	3.22	.64	1.25	3.55	88*
	4	18.80	3.24	.77	1.19	2.52	88
	4	19.18	3.30	1.07	1.61	3.56	87
	4	19.28		fail			87
	4	19.55	3.38	2.11	2.78	4.06	86*
	5	20.08	3.49	1.82	2.66	3.01	84
	4	20.21		fail			84
1,2-bis(difluor-amino)butane	38	20.57	3.58	.64	.90	2.94	83
	41	22.15	3.90	1.30	1.84	3.19	78
	40	23.22	4.11	1.22	1.75	3.20	75
	4	19.13	3.30	.41	.66	2.38	87
	4	20.93		fail			82
2,3-bis(difluor-amino)butane	40	22.38		fail			78
	10	20.40		fail			83
2,2-bis(difluor-amino)butane	40	19.05	3.28	3.74		4.94	87
	4	17.78		fail			91

\*In this shot, the depth of the liquid was 1.9 cm instead of the usual 1.25 cm.



Fig. 1 - Streak camera photograph of shock initiation of nitromethane at 83 kbar. For experimental conditions see Table 1.



Fig. 2 - Streak camera photograph of shock initiation of 1,2-DP at 78 kbar. For experimental conditions see Table 1.

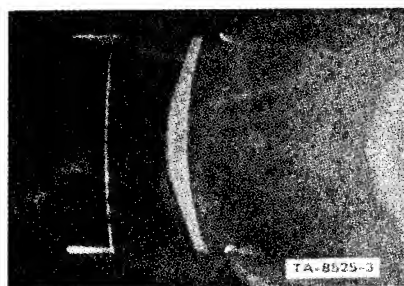


Fig. 3 - Streak camera photograph of shock initiation of 1,2-DP at 76 kbar. For experimental conditions see Table 1.

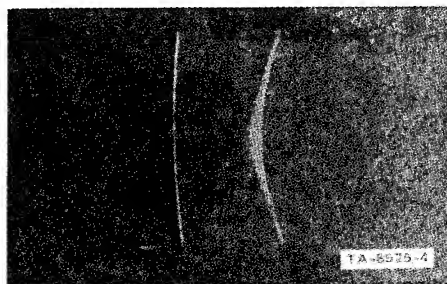


Fig. 4 - Streak camera photograph of shock initiation of 1,2-DP at 75 kbar. For experimental conditions see Table 1.

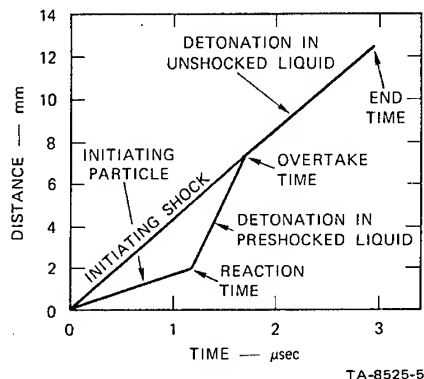


Fig. 5 - An x-t diagram corresponding to Fig. 1

is calculated from Fig. 5 to be  $4.1 \text{ mm}/\mu\text{sec}$  compared with the observed (11) value of  $6.4 \text{ mm}/\mu\text{sec}$ . The calculated detonation velocity is therefore less than what it should be, and this is consistent with the initiating pressure decreasing with time.

Although the pressure/time profile is probably complex, the reaction times for nitromethane observed in this work are in fair agreement with those observed by other workers (3, 12). For example, at 86 kbar, Campbell, Davis and Travis found that the reaction time was  $2.26 \mu\text{sec}$ , whereas in the present work at the same shock pressure of 86 kbar the reaction time is  $0.7 \mu\text{sec}$ . The effects of varying the shock pressure and varying the preshock temperature on the reaction time were also in agreement with earlier findings (Fig. 6). However, it was interesting to find that reducing the impurities in the nitromethane from around 3% to less than 0.5% had no effect on the reaction time (Fig. 7). Similarly, it was somewhat surprising to find that saturating the nitromethane with water had no effect on the reaction time (Fig. 7).

Methyl nitrite is an isomer of nitromethane, and as such, may be expected to have a similar shock temperature for the same shock pressure. We have found that reaction times for methyl nitrite are significantly less than those for nitromethane (Table 1). This provides some support for homogeneous thermal explosion theory because the weakest bond in methyl nitrite,  $\text{CH}_3\text{O}-\text{NO}$ , is some 20 kcal/mole weaker than the weakest bond in nitromethane  $\text{CH}_3-\text{NO}_2$ .

The availability of the bis-difluoramino alkane isomers and homologs provided an excellent opportunity to test the effects of

Fig. 5 of Ref. 2. The results of all the experiments are in Table 1. No experimental results were discarded.

Since in the present experiments the initiating charge was not a plane-wave generator the pressure along the axis of the liquid is probably decreasing with time. However, for the time being let us assume that the initiating charge was a piston of constant velocity. The nitromethane shot in Fig. 1 can then be analyzed (3, 10) as an x-t diagram (Fig. 5) which is drawn to scale. The pressure of the shock entering the liquid was 83 kbar, which from the Hugoniot, corresponds to a particle velocity of  $1.67 \text{ mm}/\mu\text{sec}$ , a shock velocity of  $4.39 \text{ mm}/\mu\text{sec}$  and a density of  $1.824 \text{ g/cc}$ . From the experiment, the reaction time was  $1.17 \mu\text{sec}$  and the overtake time  $1.67 \mu\text{sec}$ . From Fig. 5 the velocity of the detonation through the preshocked nitromethane is therefore  $10.6 \text{ mm}/\mu\text{sec}$ , compared with a value of  $9.9 \text{ mm}/\mu\text{sec}$  calculated by extrapolating the detonation velocity as a function of density (10). The detonation velocity in the unshocked nitromethane

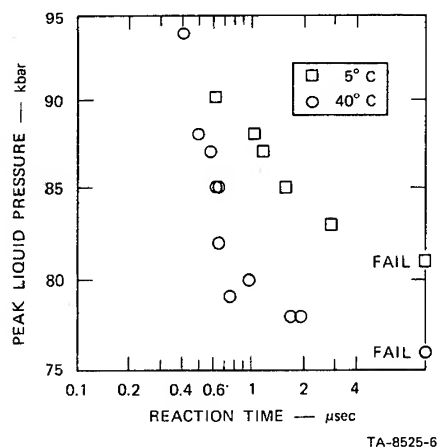


Fig. 6 - Effect of preshock temperature on the reaction time of 97% pure nitromethane

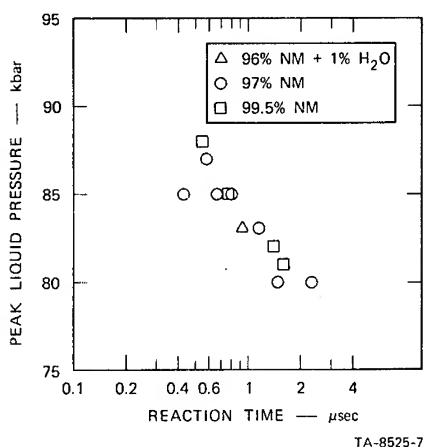


Fig. 7 - Effect of purity of nitromethane on its reaction time at preshock temperature of 25°C

difference in chemical structure on shock sensitivity with the minimum of physical effects. Reaction times were measured as a function of peak shock pressure, and of pre-shock temperature for 1,2-DP, 2,2-DP, 1,2-DB, 2,2-DB, and IBA. For each liquid the reaction time decreased with increasing shock pressure and increasing pre-shock temperature as expected. However, homogeneous thermal explosion theory together with subatmospheric rate data predicted that 2,2-DP would have a shorter reaction time than 1,2-DP, because the weakest C-NF<sub>2</sub> bond in 2,2-DP is significantly weaker than the weakest C-NF<sub>2</sub> in 1,2-DP (13). The observed results were exactly opposite from the expected (Fig. 8). That is, 1,2-DP had a significantly shorter reaction time than 2,2-DP

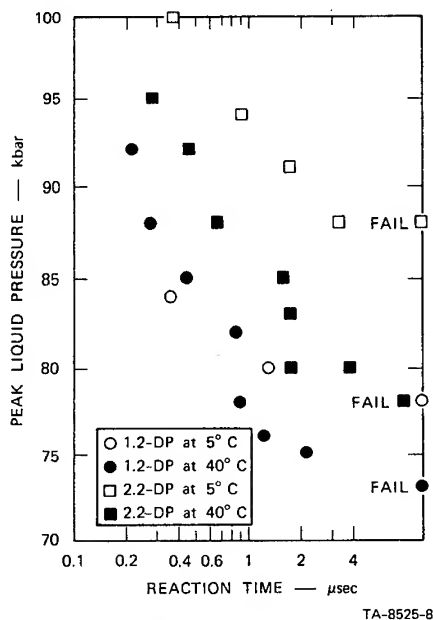


Fig. 8 - Effect of preshock temperature on the reaction time of 1,2-DP and 2,2-DP

for the same shock pressure. We have postulated that this result is caused by a different rate controlling mechanism at pressures of the order of 100 kbar than at subatmospheric pressures. In NF compounds which have the group CHNF<sub>2</sub>, there exists the possibility of a very exothermic four-center elimination of HF, CHNF<sub>2</sub> → CNF + HF. Under laboratory conditions, this mechanism may not be observed because it has a tight transition state and therefore a low Arrhenius A factor. However, at high pressure the equilibrium for the HF elimination is far over on the side of products, whereas for the C-N bond split the equilibrium is close to the undissociated reactant resulting in negligible net reaction and little heat release. Geminate compounds with the structure R<sub>2</sub>C(NF<sub>2</sub>)<sub>2</sub> where R ≠ H cannot undergo four center elimination and must therefore decompose by a mechanism which will require a higher activation energy. The above postulate has received support in several ways.

The reaction time results show that varying the preshock temperature has a much bigger effect on 2,2-DP than on 1,2-DP (Fig. 8). This implies that the reaction time for 2,2-DP is more sensitive than the reaction time for 1,2-DP to variation in shock temperature. This in turn implies that the activation energy for decomposition for 2,2-DP is greater than that for 1,2-DP.

In the laboratory, using  $\text{CH}_3\text{NF}_2$  as a model compound, David S. Ross (13) has demonstrated the feasibility of the HF elimination by preparing  $\text{CH}_3\text{NF}_2$  in a chemically activated state by combining  $\text{CH}_3$  radicals with  $\text{NF}_2$  radicals, and observing the production of HCN and HF.

Another area of support comes from the reaction time measurements for the butane isomers (Fig. 9). There was only enough 2,2-DB for two shots, but it is clear that the reaction time for 1,2-DB was significantly less than that for 2,2-DB. In addition, the results for IBA were intermediate between 1,2-DB and 2,2-DB. It seems possible that this is because the ordering of the total number of molecules of HF which can be eliminated by the four-center mechanism is 1,2-DB: IBA: 2,2-DB = 3:2:0. An interesting feature of the results is that 1,2-DP and 1,2-DB have similar reaction times (Fig. 10). This is consistent with homogeneous thermal explosion theory because the Arrhenius parameters must be similar and the shock temperature calculations showed that they have very similar shock temperatures (13). Dilution of 1,2-DP with about 6% cyclohexane so that the mixture had the same C:H:N:F ratio as 1,2-DB had little effect on the reaction time, suggesting that overall thermochemistry, i.e., heat of detonation, was less important than reaction mechanism.

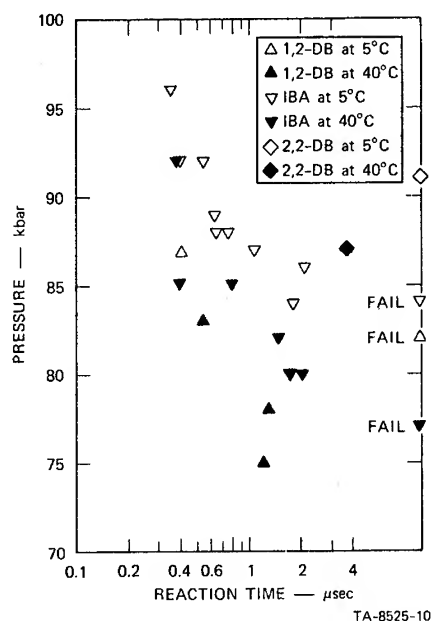
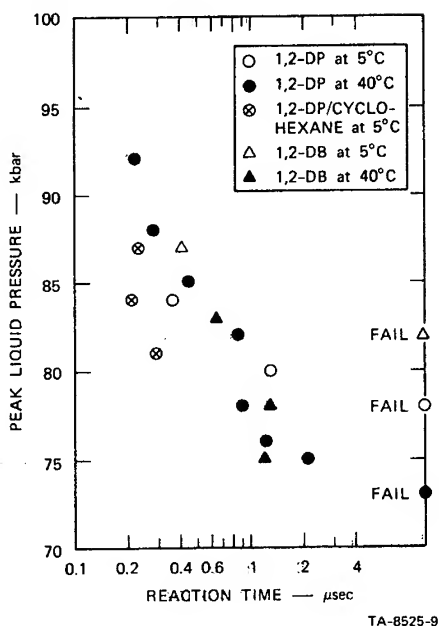


Fig. 9 - Effect of preshock temperature on the reaction time of the NF butanes



C. M. Benson for making and firing the shots; and J. R. Harmon and V. Klein for preparing the manuscript.

## REFERENCES

1. L. B. Seely, J. G. Berke, R. Shaw, D. Tegg, and M. W. Evans, "Failure Diameter, Sensitivity and Wave Structure in Some Bis-difluoramino Alkanes," Fifth Symposium on Detonation.
2. L. B. Seely, J. G. Berke, and M. W. Evans, "Initiation of Detonation During Gap Testing of Liquids," AIAA Journal 5, 2179 (1967).
3. A. W. Campbell, W. C. Davis, and J. R. Travis, "Shock Initiation of Detonation in Liquid Explosives," Phys. Fluids 4, 498 (1961).
4. B. O. Reese, L. B. Seely, R. Shaw and D. Tegg, "Coefficient of Thermal Expansion of, and Sound Speed Through, Nitromethane and Four Bis(difluoramino)Alkanes," J. Chem. Eng. Data 15, 140 (1970).
5. L. Phillips, "The Pyrolysis of Methyl Nitrite," J. Chem. Soc. 1961, 3082.
6. Personal communication from L. Phillips.
7. P. Tarte, "Rotational Isomerism as a General Property of Alkyl Nitrites," J. Chem. Phys. 10, 1570 (1952).
8. J. Berke and L. B. Seely, "Equation of State of Polydiethylene Glycol-Bis-Allyl Carbonate," AIAA Journal 7, 985 (1969).
9. L. B. Seely, R. Shaw, J. G. Berke, and D. Tegg, "Sensitivity Fundamentals," Stanford Research Institute Semiannual Technical Progress Report 68-2, Project 4051, 15 November 1968.
10. R. F. Chaiken, "Eighth Symposium (International) on Combustion," p. 759, Waverly Press, Inc., Baltimore, Maryland.
11. A. W. Campbell, M. E. Malin and T. E. Holland, "Detonation in Homogeneous Explosives," Second ONR Symposium on Detonation, p. 336, Washington, D. C., February 9-11, 1955.
12. I. M. Voskoboinkov, V. M. Bogomolov, A. D. Margolin, and A. Ya. Apin, "Determination of the Decomposition Times of Explosive Materials in Shock Wave," Dokl. Phys. Chem. 167, 167 (1966) English Translation.
13. M. E. Hill, D. S. Ross, R. Shaw, R. W. Woolfolk, T. Mill, and L. B. Seely, "Sensitivity Fundamentals," Standord Research Institute Final Report, Project 4051, May 1970.

# THE ROLE OF INTERSTITIAL GAS IN THE DETONATION BUILD-UP CHARACTERISTICS OF LOW DENSITY GRANULAR HMX

W. W. Marshall

*Atomic Weapons Research Establishment  
Aldermaston, Berkshire, England*

## ABSTRACT

The shock sensitivities (card gap test) and times to build-up to stable detonation have been determined for charges consisting of coarse HMX loose filled to a density of  $1.14 \text{ g.cm}^{-3}$  (60 volume %). The interstices in the charges were filled with nitrogen or methane at various pressures up to 1,000 psi.

In a series of experiments, the output from the standard gap test donor explosive was attenuated by brass shims placed between the donor and the HMX charge. A range of shim thicknesses, up to 90% of the gap test critical thickness was used. It has previously been reported (1) that the shock sensitivity is dependent on the nature and pressure of the interstitial gas; the present work shows that the initiation delay time is independent of the nature of the gas or its pressure, and is determined by the incident shock parameters (which are governed by the donor charge and the thickness of the attenuator shim).

## INTRODUCTION

This paper is an extension of M. C. Chick's work on the effect of interstitial gas on the shock sensitivity of coarse, granular, low density HMX charges (1) where it was shown that the shock sensitivity depended on the pressure and nature of the interstitial gas in a way which suggested that heat transfer mechanisms played an important role. This work has been extended to measure the initiation delay times using nitrogen and methane at a range of pressures, and various degrees of attenuation of the donor shock.

## EXPERIMENTAL

An assembled round consisted of a 3.5 inch length of 0.75 inch ID thin walled brass tube, closed at one end by a 0.006 inch thick brass shim, soldered in place. Probes consisting of 29 SWG enamelled copper wire inside 0.028 inch OD hypodermic needle tubing were soldered diametrically across the brass tube at 0.5 or 1.0 cm intervals from the shim. The tube was filled with coarse granular HMX (particle size

range 100 to 1,000  $\mu$ , median 400  $\mu$ ) by vibrating to a density of  $1.14 \text{ g.cm}^{-3}$ , and was closed with a mild steel witness block held in position by adhesive tape. The donor was a PETN pellet 0.23 inch diameter, 0.2 inch long, initiated by an EBW detonator. For each experiment the required attenuator shim was placed between the donor and the filled tube, with a probe between donor and shim. This probe was made from very thin copper/polyester laminate, and served to provide a fiducial signal to start the recording sequence. The assembly was taped together, placed in the firing vessel and connections made to the firing and recording apparatus. The vessel was sealed, pressurised with the appropriate gas, vented and repressurised before firing.

In a preliminary series of experiments, the thickness of shim for which the probability of detonation was 50% (called the critical value) was determined for each set of conditions. For these experiments the probes were in the tubes, although they were not used, as their presence had been found to have a small effect on the critical value.

The main series of rounds was then fired with a range of attenuating shim thicknesses up to and including 90% of the critical values. The times of closure of the foil probes and the hypodermic needle probes were recorded with a multi-channel oscilloscope. The first few probes were found to give somewhat variable results, probably because the shock pressure and velocity were too low for the correct functioning of this type of probe.

## RESULTS AND DISCUSSION

A typical space-time plot (Fig. 1) shows a normal build-up to stable detonation. The straight line part of the graph was extrapolated both graphically and mathematically to zero distance. The time at zero distance includes the time through the shim; this was calculated assuming a shock velocity of  $4.6 \text{ mm}/\mu\text{s}$  through

the shim and subtracted to give the initiation delay, or lost time.

The results (Table 1) confirm Chick's work and show that shock sensitivity is markedly dependent on the nature and the pressure of the interstitial gas. The lost times for all the experimental conditions have been plotted as a function of shim thickness in Fig. 2 where it can be seen that the lost time is independent of the nature and pressure of the gas, and depends only on the parameters of the initiating shock as determined by the thickness of the attenuation shim.

These results may be explained if it is postulated that two quite different mechanisms operate. The first of these, which determines whether the round will detonate or fail, is strongly affected by the nature and pressure of the interstitial gas, and therefore probably involves heat transfer. It is of short duration compared with the lost time. The second

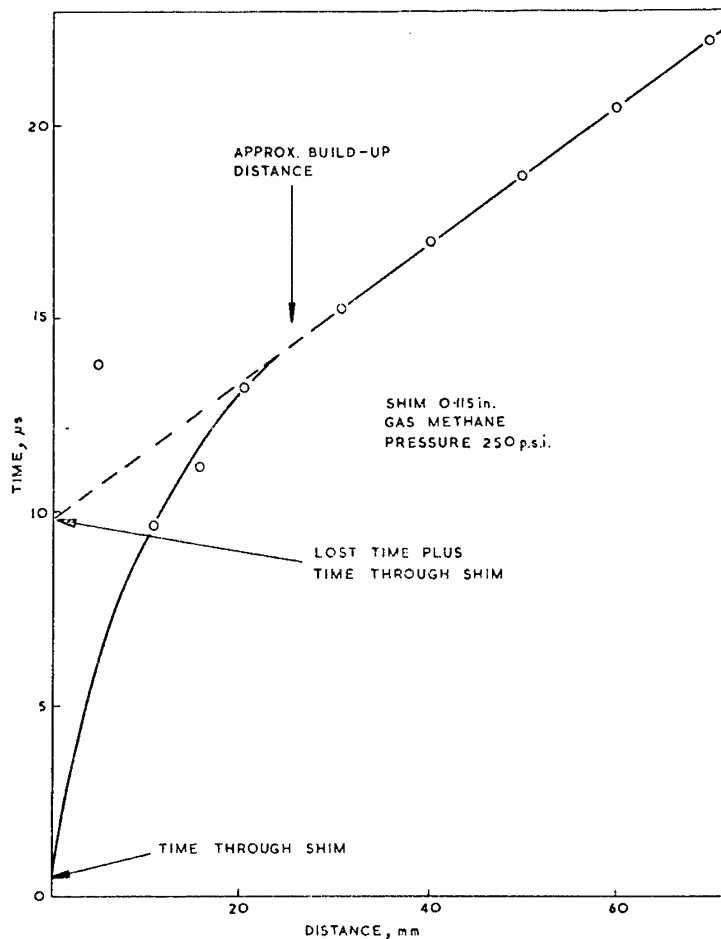


Fig. 1 - Typical space-time plot



TABLE 1  
Results of Multiprobe Detonation Build-up Experiments

Pressure (psi) and gas	Shim thickness (mil)	Extrapolated linear regression time at zero distance ( $\mu$ s)	Lost time ( $\mu$ s)	Shock sensitivity (mil. of brass)
15 N <sub>2</sub>	208	23.16	21.01	231
500 N <sub>2</sub>	126	12.29	11.60	196
1000 N <sub>2</sub>	66	10.29	10.56	134
15 N <sub>2</sub>	143	16.43	15.64	231
1000 N <sub>2</sub>	6	1.10	1.10	134
500 N <sub>2</sub>	70	7.53	7.14	196
1000 CH <sub>4</sub>	21	5.54	5.42	28
250 CH <sub>4</sub>	115	10.03	9.39	135
100 CH <sub>4</sub>	121	11.25	10.58	187
100 CH <sub>4</sub>	6	0.71	0.70	187

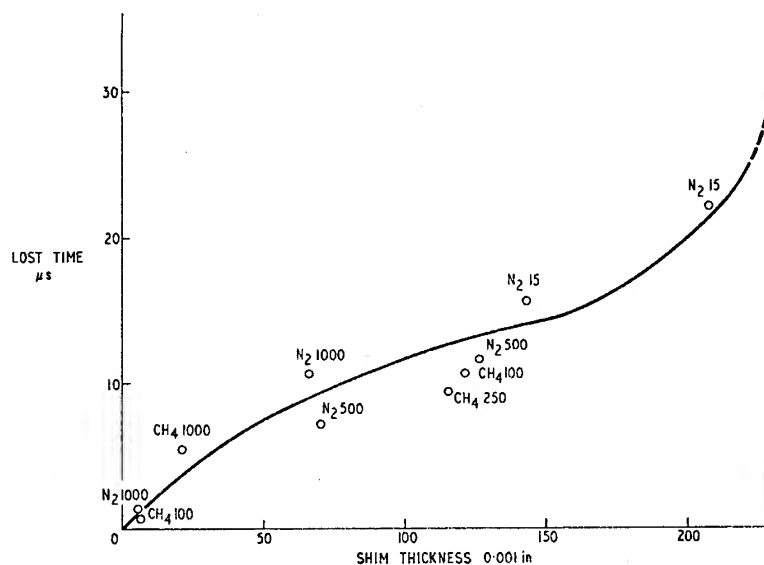


Fig. 2 - Lost time v shim thickness

mechanism operates during the build-up phase after stable detonation has been initiated but not yet achieved, and gives rise to substantially all of the lost time. This process is independent of the interstitial gas or its pressure, and therefore probably does not depend on mechanisms of heat transfer across the interstices.

#### REFERENCE

1. M. C. Chick, "The Effect of Interstitial Gas on the Shock Sensitivity of Low Density Explosive Compacts," Proceedings of the Fourth Symposium (International) on Detonation 1965, pp. 349-358.

# THE SHOCK HUGONIOT OF UNREACTED EXPLOSIVES

V. M. Boyle, W. G. Smothers, L. H. Ervin  
*USA Ballistic Research Laboratories  
Aberdeen Proving Ground, Maryland*

## ABSTRACT

Hugoniot data were obtained for three cast explosives; TNT, Tritonal, H-6, and for two pressed explosives; PBX 9404 and Tritonal. The explosive samples were shocked through a buffer plate attached to a 10 cm diameter plane wave lens. A streak camera was used to measure the shock velocity in the explosive sample and in a Plexiglas monitor in contact with the buffer plate. The impedance match technique was used to determine the particle velocity in the explosive. In the same experiment a Plexiglas overlay was placed on the explosive sample and the shock velocity in it was measured. The interface equation was then used to determine the particle velocity in the explosive sample. If the explosive remained unreacted both particle velocity determinations gave essentially the same value. Divergence of the particle velocities indicated that explosive reaction had occurred during the time of shock transit through the sample. This time was approximately one microsecond.

## INTRODUCTION

When a sufficiently strong shock wave traverses a solid polycrystalline explosive, the small local discontinuities characteristic of the material, cause small local convergences of the shock wave and its associated mass flow. This gives rise to local high temperature sources and consequent reaction sites (1). The energy released by the reacting explosive increases the pressure and velocity of the original shock wave and represents a source of error in the typical experiment designed to determine Hugoniot data for unreacted explosive. This paper describes an experiment designed to obtain Hugoniot data of unreacted explosive and to indicate when the data are affected by explosive reaction.

## EXPERIMENT

The basic experimental arrangement is shown in Fig. 1. A 10 cm diameter plane wave lens and attached base pad are detonated to provide a shock wave arrival at the buffer which is plane to within  $.03 \mu\text{sec}$  over the central 7.6 cm. The impedance mismatch presented by the metal buffer plate decreases the energy and pressure transmitted to the sample. The buffer plates were machined to size and sanded, the top surface was polished to improve

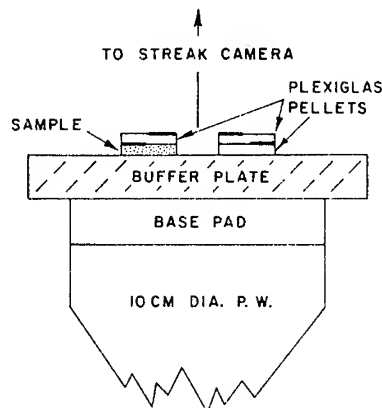


Fig. 1 - System for shocking explosive samples

its reflectivity and to enhance intimate contact between it and the pellets which were cemented to it with epoxy. All pellets were a nominal 1.9 cm diameter; they were polished and measured for thickness (0.3 cm). The Plexiglas pellets were aluminized in an evaporative coater to provide mirror surfaces over the areas indicated by heavy dark lines in the figure. During assembly a two-kilogram weight was placed on each set of pellets to prevent epoxy from flowing between the surfaces and causing a

separation. The centers of all pellets were located within 1.27 cm of the center of the buffer plate to minimize pressure gradients caused by rarefactions from the charge boundary.

A range of pressures in the sample was obtained by varying the base pad (TNT, Comp B), the buffer plate material (brass, aluminum, Plexiglas) and by using buffer systems composed of layers of mismatched materials as, e.g., brass-hexane-brass, brass-Plexiglas-brass, etc. One surface of the base pad was machined at a  $5^\circ$  angle as indicated in Fig. 2. This produced a slightly oblique shock wave (with negligible effect on the results) which improved detection of the wave at the various surfaces of interest; upon shock arrival the surface is tilted through a slight angle which for a given material is a function of the pressure, and a previously aligned, collimated light beam is reflected out of the field of view of the camera objective lens causing a sharp extinction of the reflected light. The light source consisted of an explosive pad in contact with argon gas in a cardboard container. The face of the container was covered by a thin transparent plastic, Saran Wrap, which was blacked out except for a long, narrow region (1 cm  $\times$  15 cm) parallel to the streak camera slit; this served as a linear source of roughly collimated light. The light source was positioned about 2.5 meters from the plane wave lens.

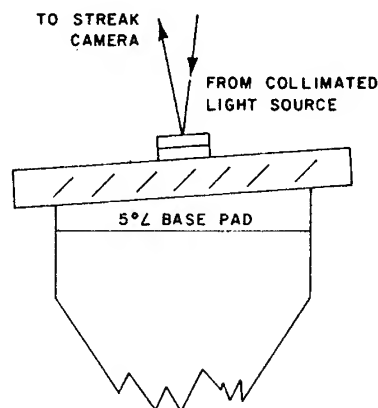


Fig. 2 - Another view of Fig. 1 revealing angled base pad

A streak camera, recording at 3.28 mm/ $\mu$ sec was used to obtain the shock transit time through the sample pellet, the overlay pellet (refers to the Plexiglas pellet on the sample), and the two Plexiglas monitor pellets. This transit time and the measured pellet thickness

gave the average shock velocity in each pellet. An approximate correction factor for shock velocity decay was obtained from the average shock velocity in each of the monitor pellets. All velocities were corrected back to a time equal to half the sample pellet thickness divided by the average sample shock velocity which needed no correction. Typical measurements indicated the shock velocity in the monitor pellets decreased by 2% per  $\mu$ sec of shock travel time when a TNT base pad was used in conjunction with the plane wave lens which had a TNT core and 6% per  $\mu$ sec when a Comp. B pad was used. Because of this, TNT pads were used in practically all of the firings. In practice, it was found easier to refer to existing Manganin gauge records (2) showing the pressure decay for typical buffer systems as a function of time and compute approximate correction factors.

The Hugoniot of the materials used in the experiment can be represented by the material density,  $\rho$ , in gm/cm<sup>3</sup> and the linear relationship,

$$U = a + bu$$

where

$U$  = shock velocity in mm/ $\mu$ sec.

$u$  = particle velocity in mm/ $\mu$ sec.

$a$ ,  $b$  = constants for each material.

An occasional  $x$  and  $p$  subscript refer respectively to explosive and Plexiglas.

$$\text{Brass, 271: } \rho = 8.443, U = 3.802 + 1.418u \quad (3)$$

$$\begin{aligned} \text{Aluminum, 2024: } \rho &= 2.785, \\ U &= 5.328 + 1.338u \end{aligned} \quad (4)$$

$$\begin{aligned} \text{Magnesium, AZ31B: } \rho &= 1.773, \\ U &= 4.65 + 1.20u \end{aligned} \quad (5)$$

$$\begin{aligned} \text{Plexiglas II UVA: } \rho &= 1.183, \\ U &= 2.695 + 1.538u \text{ from} \\ &\quad 25 \text{ to } 240 \text{ kilobars} \end{aligned} \quad (6)$$

An experimental determination of the Plexiglas Hugoniot was made for the low pressure region since available data (7) indicated some disagreement. The impedance match technique was used with brass as the standard material.

$$\begin{aligned} \text{Plexiglas II UVA: } \rho &= 1.183, \\ U &= 2.938 + 1.284u \\ \sigma(U) &= .035 \text{ mm}/\mu\text{sec} \\ \text{for } 3.3 < U < 4.0 \text{ mm}/\mu\text{sec}. \end{aligned}$$

## IMPEDANCE MATCH SOLUTION

Once the shock velocity in the monitor pellets was known the impedance match solution (4) was used to infer the pressure in the buffer plate. To determine the particle velocity in the explosive sample corresponding to a measured shock velocity in that sample, a further application of the impedance match solution was made as shown in Fig. 3. The shock pressure in the buffer and the Hugoniot curve of the buffer are known and a release isentrope from the pressure-particle velocity point was approximated by constructing a mirror image of the buffer Hugoniot about a constant particle velocity line through that point. The intersection of this isentrope with the line of slope  $\rho_x u_x$  determines the pressure and particle velocity at the common interface of the buffer and the explosive sample. If the shocked explosive reacts the chemical energy liberated will increase the pressure and velocity of the initial shock giving an increased slope  $\rho_x u'_x$  as indicated by the dashed line in Fig. 3. The intersection of the buffer isentrope with the line of slope  $\rho_x u'_x$  formally gives a particle velocity which is lower than the initial, correct particle velocity in the explosive sample. The particle velocity determined for this reactive shock should be regarded as an indicator of reaction occurring rather than a correct value of particle velocity. The right half of Fig. 3 is an analytical expression showing that the computed particle velocity decreases as the shock velocity in the sample increases. It can be obtained by writing the expression for the mirror image buffer Hugoniot and differentiating at the point of intersection with the line slope  $\rho_x u_x$ .

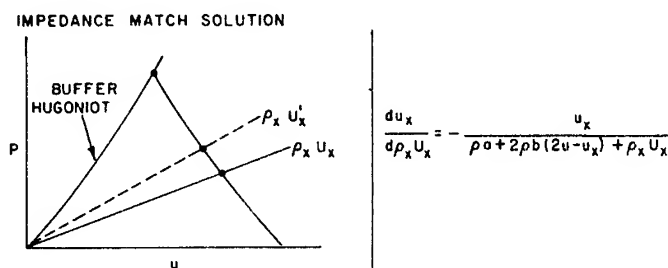


Fig. 3 - Graphical representation of impedance match solution. An increase in explosive shock velocity yields a lowered particle velocity solution.

## INTERFACE EQUATION SOLUTION

The average shock velocity in the explosive sample and in the Plexiglas overlay are

used in the interface equation solution (8) to determine the particle velocity in the explosive at the common interface of the explosive and the Plexiglas overlay. The Plexiglas Hugoniot is known and the particle velocity  $u_x$ , in the explosive can be obtained from the equation shown in the right half of Fig. 4. The interface equation is strictly valid at low pressures but has been shown to be a good approximation at higher pressures. The left half of Fig. 4 illustrates graphically the interface equation solution. The unreacted explosive line of slope  $\rho_x u_x$  is shown; the reacting explosive line of slope  $\rho_x u'_x$  is also shown. In the interface equation construction a line having the negative of the slope of the  $\rho_x u_x$  line is constructed from the pressure-particle velocity point representative of shock conditions in the Plexiglas overlay. The intersection of this line with the  $\rho_x u_x$  line of the unreacted explosive determines the pressure and particle velocity in the explosive sample. As can be seen from the construction, an increase in shock velocity in the sample leads to an increased pressure in the Plexiglas overlay, an increase in the line slope, and the calculation of a particle velocity in the explosive sample increased from the initial value in the unreacted explosive. The right half of Fig. 4 indicates that the calculated particle velocity is directly proportional to the square of the shock velocity in the Plexiglas overlay and inversely proportional to the shock velocity in the explosive sample. When the explosive sample reacts the calculated particle velocity is increased above the initial, correct particle velocity in the sample and serves as an indicator of explosive reaction under shock loading. By employing both techniques; impedance match and interface

$$\frac{du_x}{d\rho_x u_x} = -\frac{u_x}{\rho_0 + 2\rho_b(2u - u_x) + \rho_x u_x}$$

equation, in a single experiment, Hugoniot data for unreacted explosive were obtained and the occurrence of reaction was indicated by a divergence of the calculated particle velocity pairs.

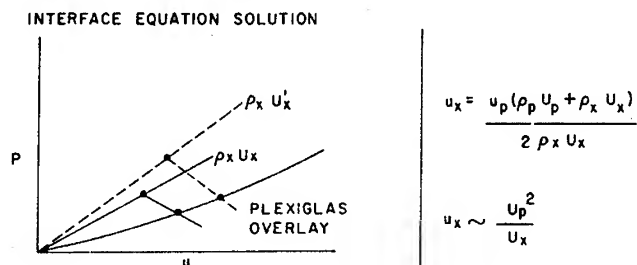


Fig. 4 - Graphical representation of interface equation solution. An increase in explosive shock velocity yields an increased particle velocity solution.

In order to gain some confidence in the validity of the experiment an inert material, Magnesium alloy AZ31B,  $\rho = 1.771 \text{ gm/cm}^3$  was used as the sample and subjected to a range of shock pressures. The results are indicated in Fig. 5 where shock velocity is plotted against particle velocity in the sample. The black dots ( $\cdot$ ) represent impedance match solutions and the crosses (+) represent interface equation solutions. A least squares fit of the data gave,

$$U = 4.723 + 1.115u$$

$$\sigma(U) = .063 \text{ mm}/\mu\text{sec}$$

This can be compared with a well determined Hugoniot for this alloy (5) represented by,

$$U = 4.65 + 1.20u$$

$$\sigma(U) = .02 \text{ mm}/\mu\text{sec}$$

The agreement is felt to be satisfactory since most of the data were gathered during the early stages of this experiment when the technique was still being refined.

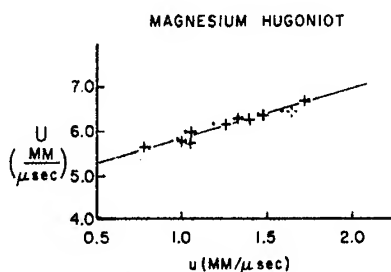


Fig. 5 - Magnesium Hugoniot in the shock velocity-particle velocity plane. In this and the following figures the black dots refer to impedance match data and the crosses refer to interface equation data

## RESULTS

Hugoniot data for unreacted explosive in the shock velocity-particle velocity plane are summarized for five explosives.  $D$  = detonation velocity in  $\text{mm}/\mu\text{sec}$ ,  $\rho$  = density in  $\text{gm/cm}^3$  and  $U_B$  = bulk sound velocity in  $\text{mm}/\mu\text{sec}$ .

cast TNT,  $\rho = 1.62$ ,  $D = 6.80$

$$U = 2.274 + 2.652u \text{ for } U < 3.7 \text{ mm}/\mu\text{sec}$$

$$\sigma(U) = .065 \text{ mm}/\mu\text{sec}$$

$$U = 2.987 + 1.363u \text{ for } U > 3.7 \text{ mm}/\mu\text{sec}$$

$$\sigma(U) = .124 \text{ mm}/\mu\text{sec}$$

$$U_B = 2.297 \text{ mm}/\mu\text{sec} \quad (9)$$

PBX 9404,  $\rho = 1.84$ ,  $D = 8.835$

$$U = 2.310 + 2.767u \text{ for } U < 3.2 \text{ mm}/\mu\text{sec}$$

$$U_B = 2.310 \text{ mm}/\mu\text{sec} \quad (10)$$

cast Tritonal,  $\rho = 1.73$ ,  $D = 6.70$

$$U = 2.313 + 2.769u \text{ for } U < 3.8 \text{ mm}/\mu\text{sec}$$

$$\sigma(U) = .073 \text{ mm}/\mu\text{sec}$$

cast H-6,  $\rho = 1.76$ ,  $D = 7.40$

$$U = 2.654 + 1.984u \text{ for } U < 3.7 \text{ mm}/\mu\text{sec}$$

$$\sigma(U) = .095 \text{ mm}/\mu\text{sec}$$

pressed Tritonal,  $\rho = 1.66$ ,  $D = 6.52 \quad (11)$

(insufficient data for a fit)

The cast tritonal consisted of 80% TNT, 20% aluminum, but radiographs of the finished

pellets indicated some separation of the components had occurred. The same situation prevailed with H-6 which consisted of 45% RDX, 30% TNT, 20% AL and 5% wax. Pressed Tritonal sample charges were made in order to get homogeneity but their shock sensitivity prevented the acquisition of sufficient data to make a fit.

The Hugoniot data for cast TNT are shown in Fig. 6. Several points are of interest here. First, it appears that the Hugoniot can be represented by two distinct straight lines in the shock velocity-particle velocity plane. The question of whether this represents a phase change in TNT cannot be answered here. An extrapolation of an estimate of the bulk temperature of shocked TNT (9) gives a temperature of around 100°C for TNT shocked to a pressure of 32 kbars, the approximate intersection point of the two lines representing the TNT Hugoniot data. A more sophisticated analysis would be needed to determine what conditions of temperature and pressure would produce a phase change in shocked TNT. For purposes of comparison the Hugoniot of liquid TNT (7) which represents unreacted material, is also drawn in Fig. 6. This data can be represented by

$$U = 2.14 + 1.57u, \quad T = 81^\circ\text{C},$$

$$\rho = 1.472 \text{ gm/cm}^3, \quad \sigma(u) = .06 \text{ mm}/\mu\text{sec}$$

The dashed lines represent extrapolation of the data to the detonation velocity. The cast TNT Hugoniot extrapolates to a particle velocity of 2.80 mm/ $\mu\text{sec}$ . An estimate of this spike particle velocity, i.e., the particle velocity in the shocked but unreacted explosive at the head of the detonation wave (12), gives approximately the same value. At the lower pressure end, the data extrapolate close to the bulk sound velocity

at zero particle velocity, the bulk sound velocity not having been included in the least squares fit; it has been shown (3) for a large number of solid inorganic materials that the zero particle velocity intercept is the bulk sound velocity. Using the detonation pressure point indicated in the figure (13) and assuming the validity of the rather large extrapolation to the detonation velocity the spike pressure is calculated to be 157% of the detonation pressure.

The particle velocity pairs in Fig. 6 exhibited a greater divergence as the intensity of the initial shock pressure increased. However, as can be seen, this divergence was not very rapid and so it was assumed, in this case, that a least squares fit of the particle velocity pairs would give a fair representation of unreacted explosive. The lowest pressure where the particle velocities indicate divergence is about 30 kilobars. One outlying low pressure point was not included in the data reduction; it is included in the figure to suggest the possibility, if it is not an experimental error, that explosive reaction may occur at much lower pressures.

The low pressure Hugoniot points for TNT are plotted on a larger scale in Fig. 7. The isothermal (18°C) compressibility of TNT, density = 1.63 gm/cm<sup>3</sup>, was determined hydrostatically up to a pressure of 21 kilobars (14). This isotherm has been transformed to the shock velocity-particle velocity plane by treating the isothermal pressure-compression points as Hugoniot data. It can be seen that both curves are in satisfactory agreement. A straight line fit to the isotherm gave,

$$U = 2.199 + 2.596u.$$

Figure 8 shows the Hugoniot data for PBX 9404. In this case, the bulk sound velocity was used in estimating a linear fit to the rather

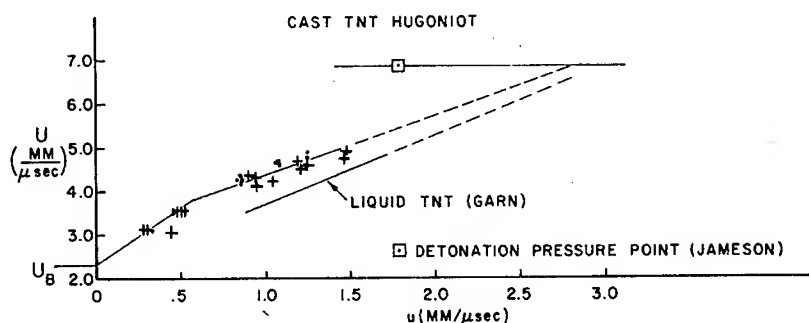


Fig. 6 - Cast TNT Hugoniot data. Dashed line here and in the following figures represents extrapolation to the detonation velocity. Liquid TNT Hugoniot added for comparison.

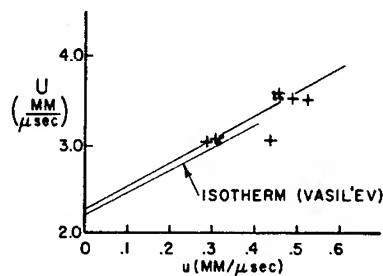


Fig. 7 - Enlarged view of low pressure points for cast TNT. Isotherm ( $18^\circ\text{C}$ ) of hydrostatically compressed TNT.

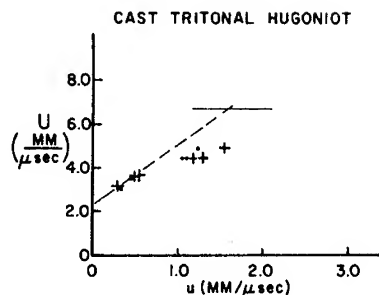


Fig. 9 - Cast Tritonal Hugoniot data

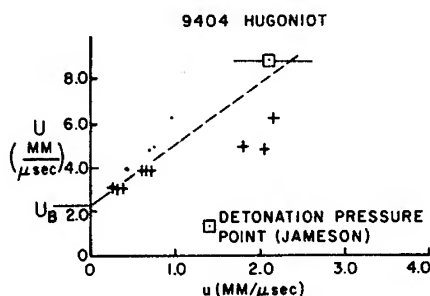


Fig. 8 - PBX-9404 Hugoniot data

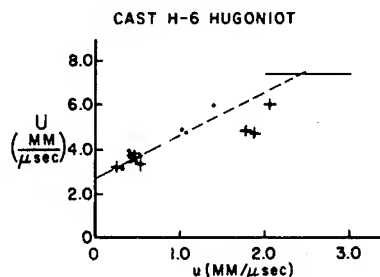


Fig. 10 - Cast H-6 Hugoniot data

meager unreacted Hugoniot data. The particle velocities, in contrast to TNT, exhibit a large divergence. The lowest measured points correspond to a pressure of 17 kilobars. A long extrapolation is made up to the detonation velocity strictly for illustrative purposes. The spike particle velocity estimate for 9404 (12) was about  $3.5 \text{ mm}/\mu\text{sec}$ . The detonation pressure point (13) is also shown in the figure.

Figures 9 and 10 show Hugoniot data for cast Tritonal and cast H-6 respectively. The H-6, being more sensitive, indicates a greater divergence of the particle velocities. Only the lower pressure unreacted points were used to determine a least squares fit to the data.

Figure 11 is a good illustration of the sensitivity of pressed Tritonal. Even at pressures as low as 13 kilobars reaction occurred.

## CONCLUSION

Since the energy liberated by reaction in a shocked explosive produces an accelerating shock wave, the average shock velocity in the explosive sample is high with respect to the

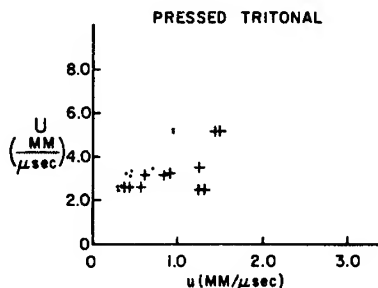


Fig. 11 - Pressed Tritonal Hugoniot data

initial velocity at the buffer-sample interface and low with respect to the final velocity at the sample-monitor interface. The use of the average shock velocity, therefore, in impedance match and interface equation solutions for the particle velocity in the shocked explosive yields values which are too low and too high respectively. The combination of both techniques in a single experiment can indicate when Hugoniot data of unreacted explosive are being perturbed by chemical reaction of the explosive under shock loading.

## REFERENCES

1. A. W. Campbell, W. C. Davis, J. B. Ramsay and J. R. Travis, *Phys. Fluids*, 4, 511, (1961).
2. A. Melani, BRL, private communication.
3. R. G. McQueen and S. P. Marsh, *J. Appl. Phys.*, 31, 1253, 1960.
4. M. H. Rice, R. G. McQueen and J. M. Walsh, "Solid State Physics, Advances in Research and Application." Academic Press Inc., New York (1958), Vol. 6, p. 1.
5. UCRL-50108, Vol. 1, Compendium of Shock Wave Data.
6. G. E. Hauver, BRL, private communication.
7. UCRL-50108, Vol. 2, Compendium of Shock Wave Data.
8. R. E. Duff and E. Houston, *J. Chem. Phys.* 23, 1268 (1955).
9. R. J. Wasley and J. F. O'Brien, "Low Pressure Hugoniots of Solid Explosives." Fourth Symposium on Detonation, Oct. 1965. Preprints Vol. 1.
10. UCRL-14592, "Properties of Chemical Explosives", Dec. 1965.
11. OSRD 5611, Jan..15, 1946, "The Rate of Detonation of Various Explosive Compounds and Mixtures.
12. J. B. Ramsay and A. Popolato, "Analysis of Shock Wave and Initiation Data for Solid Explosives." Fourth Symposium on Detonation, Oct. 1965.
13. R. L. Jameson and A. Hawkins, "Shock Velocity Measurements in Inert Monitors Placed on Several Explosives. This Symposium.
14. M. Ya. Vasil'ev, D. B. Balashov and L. N. Mokrousov, *Russian Jour. of Phys. Chem.* (English translation), 34, 1159 (1960).

## DISCUSSION

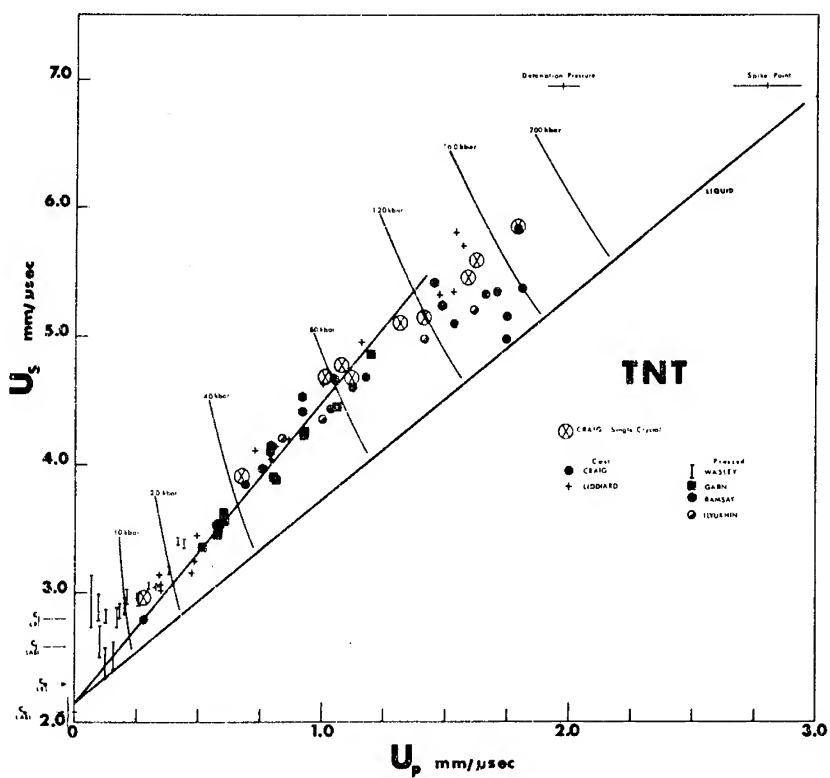
B. G. CRAIG

Los Alamos Scientific Laboratory  
Los Alamos, New Mexico

There is confirmation of your observation that the  $U_s - U_p$  curve for TNT deviates from linearity. In the oral presentation of your reference 12, J. B. Ramsay presented data for pressed, for cast, and for single-crystal TNT. That data showed an abrupt deviation from linearity as does your current data for TNT. The deviation in Ramsay's data occurred at a higher pressure (ca. 80 kb) than you observe but the TNT was of a higher density. One explanation

of the deviation from linearity proposed at that time was that of melting. Ramsay cited some calculations by J. N. Fritz of L.A.S.L. which showed that a shock-induced phase change from solid to liquid TNT might occur near the observed deviation. However, the exact location of the transition predicted by Fritz's calculations was strongly dependent on the input parameters; it could not be demonstrated from existing independent data that a solid-to-liquid phase change was in fact responsible for the non-linearity of the  $U_s - U_p$  data. For comparison purposes I have submitted a reproduction of the TNT data presented by Ramsay.





$U_s$  vs  $U_p$  for TNT

## EFFECT OF PARTICLE SIZE ON SHOCK INITIATION OF PETN, RDX, AND TETRYL

Calvin L. Scott  
*U. S. Naval Ordnance Laboratory, White Oak  
Silver Spring, Maryland*

### ABSTRACT

The effect of particle size on shock sensitivity was determined for PETN, RDX, and tetryl in a modified small scale gap test. Generally, for each explosive, sensitivity increased with increasing particle size. The transmitted shock pressure over which the study was made ranged from approximately 5.0 to 18.5 kilobars.

### INTRODUCTION

The effect of particle size on shock initiation of explosives has been of considerable interest in the attempts to explain the mechanisms of explosive reactions. In a review of the literature concerning shock sensitivity, Eadie (1) noted that there was an apparent inconsistency relative to the effects of particle size. Some investigators (2) have reported that shock sensitivity increases with decreasing particle size while others (3, 4) infer the opposite from their work.

Dimmock, Hampton and Starr (5) in their study of propagation of detonation between small confined explosive charges found that the sensitivity of tetryl to initiation was greater for smaller particle sizes than for the less finely divided explosive. On the other hand Price and Liddiard (6) indicate that at atmospheric pressure, shock sensitivity increases with increasing particle size.

In the tests of Dimmock, Hampton and Starr and those of Price and Liddiard the criterion used for a successful fire was the production of a large dent or a hole in a steel plate on which the acceptor charge rests. For such to occur the elastic limit of the steel must be exceeded. This requires a pressure in excess of 100,000 psi. The production of such high pressures requires vigorous reaction in the explosive; most likely detonation reactions or reactions so vigorous that they border on detonation. The nature of these tests then is such

that initiation will not be detected unless the reaction initiated grows to such an intensity that the associated pressure can do mechanical damage to a steel witness plate.

In all of the above studies, interpretation of the results was based on determining a shock pressure just sufficient to initiate an acceptor explosive to high order detonation 50 percent of the time. The studies did not attempt to investigate reactions in the acceptor explosive that did not build to detonation.

The 50 percent point is just one of three significant parts of the distribution curve representing an acceptor explosive's response to a shock. If one is interested in applying the results to reliability measures, then the values approaching 99.9 percent fires might be better. If one is interested in safety considerations, values around the 0.1 percent fire point would be more significant.

In an investigation by Savitt (7) it was stated, "... it is possible to differentiate between various levels of TETRYL growth reaction by observing the depth of the dent produced in the steel block in contact with the TETRYL provided that a level of reaction below that of the high order stable detonation is close enough to the steel to be recorded by the dent produced in it. An explosive system for the observation of the effect of initiation vigor upon the growth of detonation in one inch long columns of highly confined TETRYL as measured by the depth of dent produced in a steel block is shown...".

This report likewise deals with varying the vigor of a transmitted shock to an acceptor explosive but here the idea was to determine input conditions needed for starting vigorous reaction (burning, deflagration) rather than detonation. Whether or not vigorous reaction occurred was decided on the basis of any production of a dent on a steel witness block in contact with the acceptor explosive. Input stimuli were varied to the point where detonation finally did occur in the acceptor explosive. The experimental results were plotted as the depth of dent produced in the steel block as a function of the input stimulus. Curves of the type shown in Fig. 1 were thus obtained. By obtaining a number of distribution curves of an explosive for different particle size ranges, the sensitiveness of the explosive as a function of particle size could be compared for certain observed reactions of the explosive column.

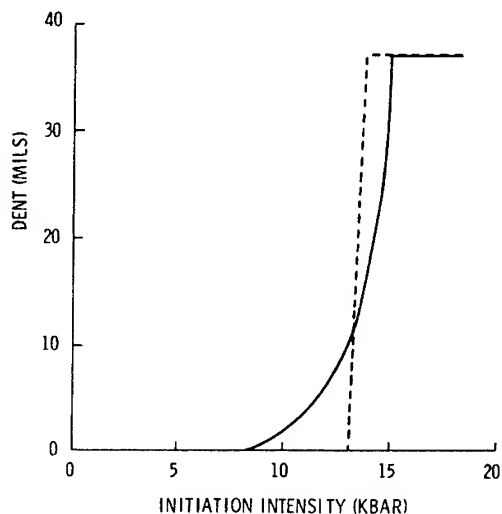


Fig. 1 - Typical curves of dent vs. input stimulus for different particle sizes of an explosive

## EXPERIMENTAL

The gap test arrangement shown in Fig. 2 was used to obtain the sensitivity and the output of the explosives. The polymethyl methacrylate (PMMA) barrier formed a very critical part of the test arrangement. The PMMA barrier thickness governed the shock pressure that was applied to the acceptor charges.

The PMMA barrier thicknesses were designated by the "decibang unit" (dbg) which was the same as that used in NAVWEPS Report 7342 (8). The decibang is defined as

$$\text{dbg} = 30 - 10 \log (\text{gap thickness in mils})$$

Note that the barrier thickness (Table 1) increases as the "decibang unit" decreases.

TABLE 1  
Decibang (Dbg) vs  
PMMA Thickness (mil)\*

Dbg	Mils
6.00	251.2
6.25	237.1
6.50	223.9
7.00	199.5
7.25	188.4
7.50	177.8
7.75	167.9
8.00	158.5
8.25	149.6
8.50	141.3
9.00	125.9
9.50	112.2
10.00	100.0
10.50	89.1
11.00	79.4
11.50	70.8
12.00	63.1

\*Dbg =  $30.00 - 10 \log$  PMMA thickness (mils).

The barrier thickness in terms of "decibangs" is quantitative in pressure units only when calibrated for standard donors. Since a non-standard donor was used, a new calibration or a correlation of the new donor - PMMA barrier combination had to be made. See Fig. 3. The experimental donor (explosive and PMMA gap) was correlated to a standard RDX donor (explosive and PMMA gap that had been calibrated in terms of shock pressure applied at the PMMA-acceptor explosive interface). Teteryl (40/60) was the acceptor explosive. The average densities of the teteryl were  $1.513 \pm 0.011$  g/cc and  $1.512 \pm 0.014$  g/cc used respectively with the experimental and the standard donor.

The output (dent in a steel block) and the lowest stimulus for an observed reaction was determined for the two groups of acceptors. The results are shown in Fig. 4.

A smooth curve was drawn through the points obtained for each acceptor group. The variation in displacement of the curves is due to different thickness of the PMMA gap as it relates to the strength of the donor. At the maximum and minimum points of the curves, the output is constant and is similar for both.

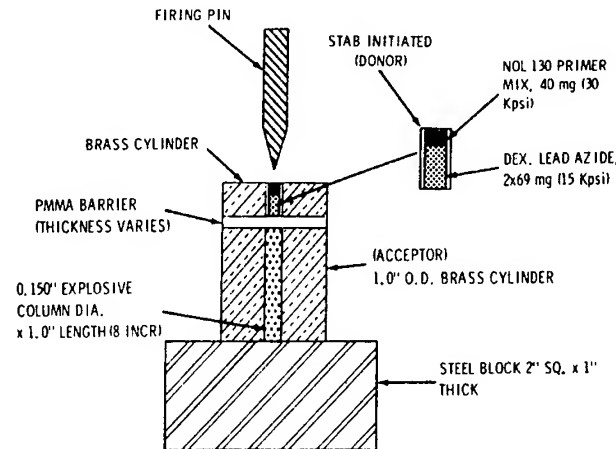


Fig. 2 - Experimental assembly for obtaining sensitivity to initiation and output of the explosives

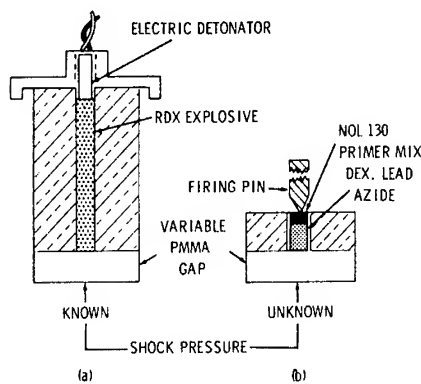


Fig. 3 - Standard donor (a) and experimental donor (b) for small scale gap tests correlation

Using the standard donor and gap, shock pressures (6) are known for the points along the standard curve. By relating points on the standard curve to the points on the experimental curve at which identical dents (identical explosive action) were obtained, the shock pressures are then known for the experimental donor and its gap. Figure 5 shows this relationship. Table 2 was then compiled to show the shock pressures from the experimental donor.

Also helpful in evaluating the two different curves of Fig. 4 was to compare corresponding points in an area where acceptor response was sensitive (the central region of that portion of the curve having a very steep slope). For the calibrated donor and the experimental donor, these points, shock (dbg), marked by X's in

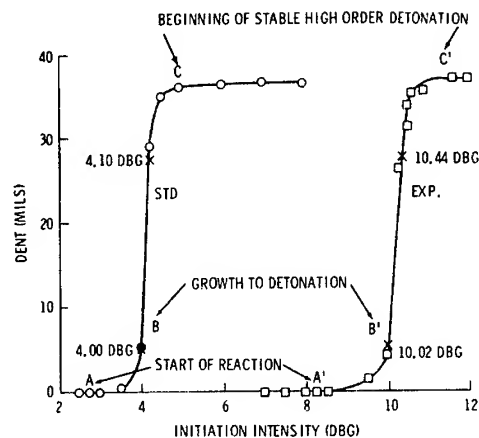


Fig. 4 - Output curves of tetryl acceptors from standard donor or experimental donor initiation intensities

Fig. 4 and their corresponding PMMA gap thickness, were respectively:

Calibrated		Experimental	
Shock (Dbg)	Gap (Mils)	Shock (Dbg)	Gap (Mils)
4.00	398.1	10.02	99.5
4.10	389.0	10.44	90.4
	9.1		9.1

In each case the same reduction in thickness of the PMMA gap was required to effect the change from a small dent to a significantly larger dent.

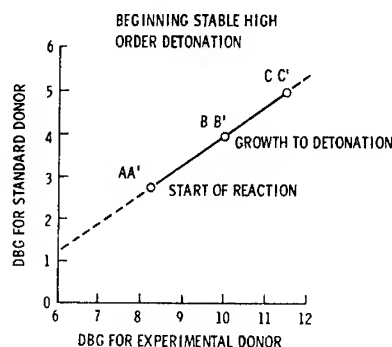


Fig. 5 - Correlation of acceptor reaction for experimental donor and standard donor

#### EXPLOSIVE MATERIAL STUDIED

Different particle sizes of tetryl, RDX, and PETN were confined as acceptor charges (0.150-inch diameter  $\times$  1.0-inch length). The various particle size ranges of tetryl, RDX, and PETN were obtained by sieving the service grade lots of these materials. The sieve cuts are shown in Table 3. In Figs. 6-8, photomicrographs show the explosive particles. Tetryl crystals are shown in 35X magnification; PETN and RDX crystals are shown in 100X magnification.

#### RESULTS AND DISCUSSION

An explanation as to just what is meant by initiation is presented here as a clarification for interpreting the findings of this study. When the explosives of this study were subjected to shock stimulus, three distinct events happened according to the intensity of the shock. The explosives either:

- melted or showed no reaction at the PMMA barrier — explosive interface,
- reacted either completely or only in a portion of the confining brass cylinder with no dent in the steel witness block, or
- reacted vigorously enough to register a dent in the steel block.

A shock pressure at which item (b) is the observed characteristic was taken to be the first manifestation of initiation. This shock pressure was then used as an index of sensitivity for the explosive. When the item (c)

TABLE 2  
Determination of Shock Stimulus in  
Terms of Pressure (kbar)

Experi- mental Donor	Standard Donor	Standard Donor
Shock (Dbg)	Shock (Dbg)	Pressure (kbar)
--	1.25	5.00
6.00	1.29	5.06
--	1.40	5.25
6.25	1.46	5.35
--	1.50	5.42
--	1.55	5.50
6.50	1.62	5.63
--	1.69	5.75
6.75	1.80	5.97
--	1.82	6.00
7.00	1.96	6.28
--	2.00	6.36
--	2.07	6.50
--	2.25	6.90
7.50	2.28	6.97
--	2.30	7.00
--	2.50	7.48
--	2.51	7.50
8.00	2.63	7.80
--	2.71	8.00
--	2.75	8.10
--	2.90	8.50
8.50	2.96	8.67
--	3.00	8.79
--	3.08	9.00
--	3.24	9.50
9.00	3.30	9.68
--	3.40	10.00
--	3.50	10.32
9.50	3.64	10.80
--	3.70	11.00
10.00	3.97	12.00
--	4.00	12.13
--	4.10	12.52
--	4.22	13.00
10.50	4.31	13.40
--	4.45	14.00
--	4.50	14.25
11.00	4.64	14.91
--	4.66	15.00
--	4.86	16.00
11.50	4.98	16.63
--	5.00	16.74
--	5.05	17.00
--	5.22	18.00
12.00	5.31	18.50
--	5.39	19.00

TABLE 3  
Sieve Cuts of the Explosives

Sieve Cut	Particle Size (mm)	Explosive
10/20*	2.00 to 0.84	tetryl†
40/60	0.42 to 0.25	tetryl
60/80	0.25 to 0.177	RDX
120/200	0.125 to 0.074	tetryl†
120/200	0.125 to 0.074	RDX
120/200	0.125 to 0.074	PETN
200/270	0.074 to 0.053	PETN
325/pan	0.044 and smaller	tetryl
325/pan	0.044 and smaller	RDX
325/pan	0.044 and smaller	PETN

\*Read 10/20 as: through Sieve No. 10 and retained on Sieve No. 20.

†Used to obtain the typical curves of Fig. 1.

characteristic was observed, it represented low or high order detonation of the explosive at a later stage of the development of the reaction.

Each explosive of interest was tested at a minimum of two different particle sizes at approximately the same loading density. The output dent was determined as a function of the

intensity of the initiation stimulus. Also, the initiation stimulus was recorded for the explosives which did not react vigorously enough to produce a dent. The results were plotted as curves as shown in Figs. 9 through 13. Each point of the curves represents only one trial.

The figures show curves for at least two different particle sizes for each of the explosives, PETN, RDX, and tetryl. The shift with particle size is apparent. PETN is seen to be more sensitive than RDX. RDX, in the same manner, is more sensitive than tetryl. In the test as run, the initiation intensity needed for dents to just be produced is about 7 kbar for PETN, 7.5-11 kbar for RDX, and 10-15 kbar for tetryl. As the stimulus increases the curves go to a constant dent, characteristic of the maximum output possible from the acceptor. These characteristic dents were approximately 37 mils for tetryl, 41 mils for PETN, and 43 mils for RDX. The transition from zero dent to maximum dent was usually very sharp, occurring within a 1 to 2 kbar stimulus interval. Obviously, the usual 50 percent firing point also falls within that same interval. Further examinations were made of the effects of variation in particle size and density.

Figure 9 shows the results for particle sizes for tetryl of 10/20, 40/60, and 325/pan at about a density of 1.505 gm/cc. There is no significant difference in the maximum output

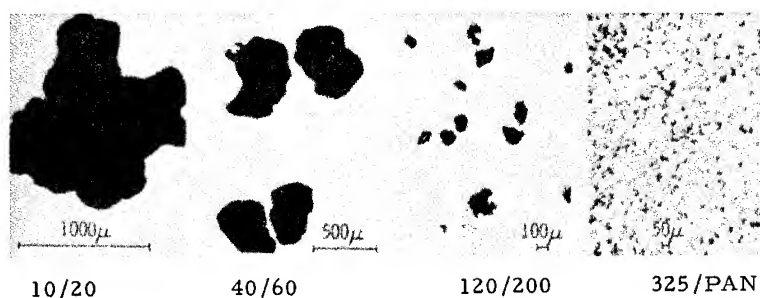


Fig. 6 - Tetryl crystals, 35X

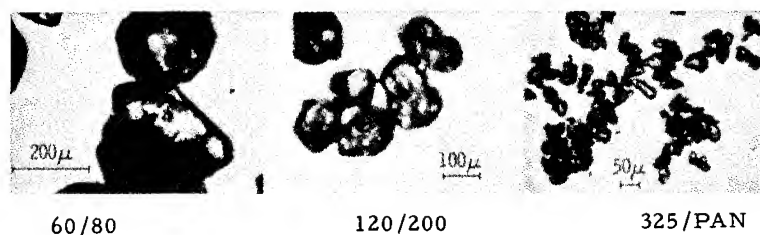


Fig. 7 - RDX crystals, 100X

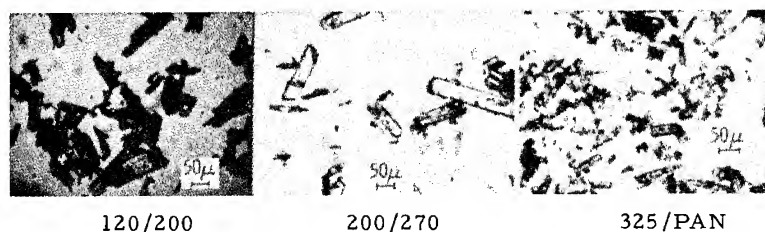


Fig. 8 - PETN crystals, 100X

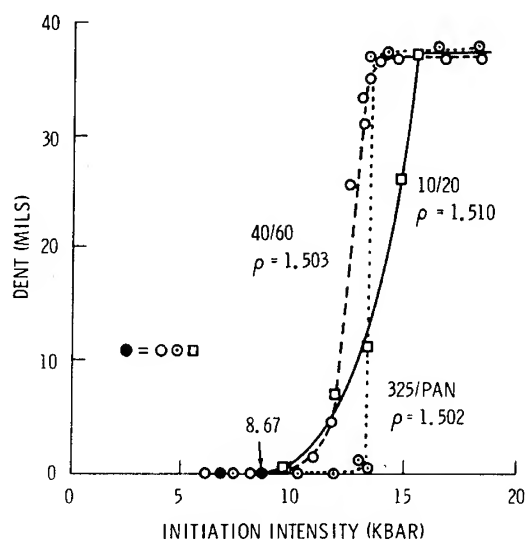
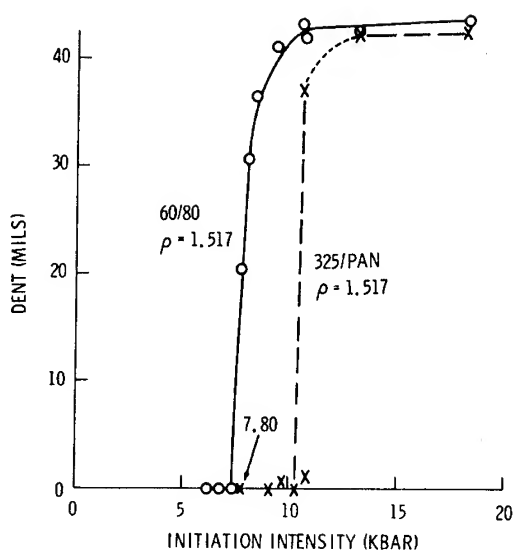
Fig. 9 - Output of tetryl particle sizes (10/20, 40/60, and 325/pan).  $\rho$  = density in gm/cc.

Fig. 11 - Output of RDX particle sizes (60/80 and 325/pan)

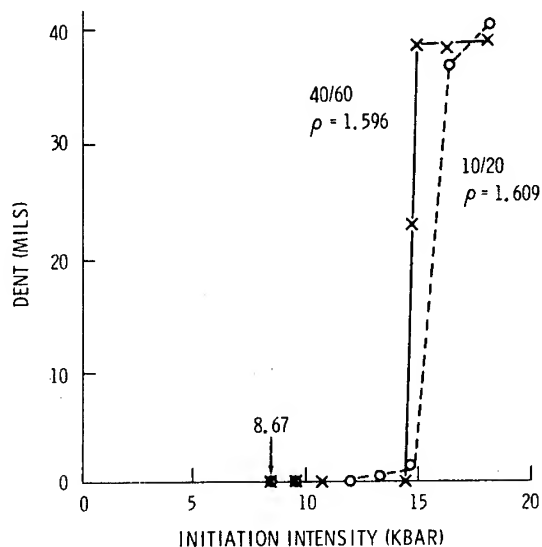


Fig. 10 - Output of tetryl particle sizes (10/20 and 40/60)

once a steady state detonation has been attained in the acceptor. In these cases, the 10/20 and 40/60 particle sizes, however, did not show the transition from zero dent to maximum dent as the usual sharp transition. Very definite points shown on the transition part of the curve show the intermediate level of reaction below stable high order detonation. A combination of large particle size and density effects was assumed to have caused an increase in reaction zone length; thereby, the full vigorous reaction was not attained in the 1.0-inch long explosive column. Seely (9) states, "... In general it is not satisfactory to use this large a particle size in the small scale test, apparently because the growth to detonation becomes the critical stage of the overall initiation process for some densities, whereas in the large-scale test the ignition stage is critical under all conditions." Small scale gap test data are presented here because of the correspondence of dimensions

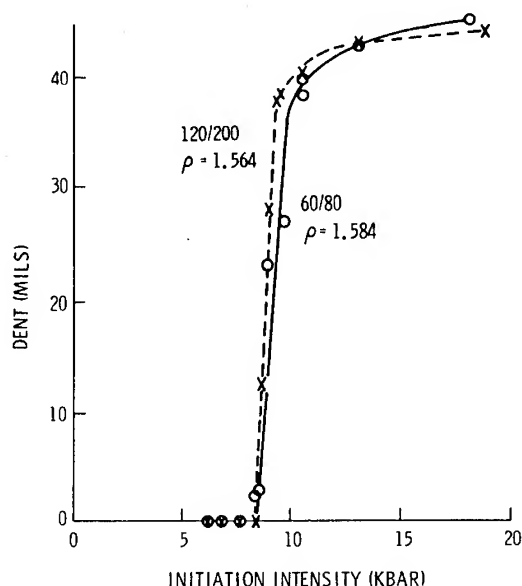


Fig. 12 - Output of RDX particle sizes (60/80 and 120/200)

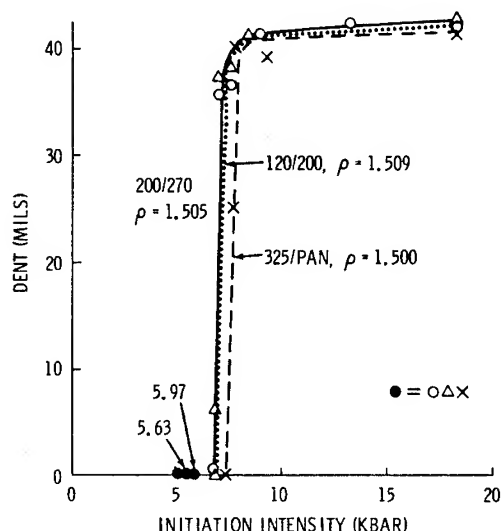


Fig. 13 - Output for different particle sizes of PETN

to those typical of explosive components dimensions.

The analysis of Figs. 9 and 10 (10/20 and 40/60 tetryl, about 1.60 gm/cc) leads to the fact that larger particles are more sensitive than smaller particles since a comparison was made of their manifestation of initiation by a reaction in the confining brass cylinder. The comparison for sensitivity of the various particle sizes was made at 8.7 kbar and 12 kbar. At

8.7 kbar of shock pressure, both 10/20 and both 40/60 particle sizes of tetryl reacted, but not quite vigorously enough to produce a dent in the steel block. The 325/pan particle size showed an appearance of melting or no reaction at all. When the shock stimulus was 12 kbar, 10/20 and 40/60 tetryl at the higher density (Fig. 10) reacted but failed to produce a dent. The 325/pan tetryl (Fig. 9) reacted but failed to support the initiating shock wave; 3/4 of the explosive remained.

Seely (9) points out, "One set of circumstances in shock initiation of granular explosives might result in the ignition stage of the process being the critical one. This would mean that the question of whether the stagnation hot spot could grow or not would determine whether the explosive detonated. The chances for growth of the hot spot would depend on the size of interstitial spaces. This in turn depends at a given density on the size of the particles. We thus come to the conclusion that when the initial growth of the hot spots is in question, a granular explosive composed of large particles would be more sensitive than the same explosive composed of small particles."

Larger particles of RDX are more sensitive to shock stimulus than smaller particles (see Figs. 11 and 12). The comparison was made at a shock stimulus of 7.8 kbar. RDX at 60/80, 1.517 g/cc density reacted vigorously enough to produce a steel dent. RDX 60/80, 1.584 gm/cc density reacted less vigorously and produced no dent in the steel. Three-fourths of the 120/200 RDX 1.562 gm/cc density, remained. No reaction was observed for the 325/pan RDX 1.517 gm/cc density. Incidentally, the curves for the three largest particle sizes show points on the transition curve that are representative of the extent or final vigor of the reaction for corresponding initiating stimuli.

For PETN it was difficult to show a significant difference in the required shock stimulus to produce dents or full detonation for all particle sizes and densities tested since the particles in each group were about the same size. See Fig. 13, however, for an analysis of the data. At a shock stimulus of 5.63 kbar, all particle size groups of PETN showed no reaction. At 5.97 kbar, all particle size groups reacted vigorously but produced no dent in the steel block. At 6.97 kbar only the 120/200 particle size gave an indication of initiation by the production of a very slight dent in a steel block. For a 7.43 kbar stimulus, 120/200 particle size produced a 35.5 mil dent; the 200/270 particle size at 7.33 kbar stimulus produced a dent of



36.8 mils; and the 325/pan particle size at 7.38 kbar stimulus produced no dent. The data indicates the larger particles of PETN are more sensitive to initiation than are the smaller particles.

## CONCLUSIONS

The study of the effect of particle sizes of PETN, RDX, and tetryl on their shock sensitivities indicates that larger particles are more sensitive than are smaller particles.

Although smaller particles are less sensitive than larger particles, smaller particles once initiated more readily reach a stable high order detonation.

## REFERENCES

1. John Eadie, "The Effect of Wax on the Shock Sensitivity of Explosives Compacts," The Fourth Symposium on Detonation, White Oak, Silver Spring, Md., October 12-15, 1965, Preprints Vol. II, C-143.
2. A. W. Campbell, W. C. Davis, J. B. Ramsay, and J. R. Travis, "Shock Initiation of Solid Explosives," Phys. Fluid 4, 511 (1961).
3. N. Griffiths, and J. M. Grocock, "The Burning to Detonation of Solid Explosives," J. Chem. Soc., 4154 Part IV (1960).
4. R. H. Dinegar, R. H. Rochester, and M. S. Millican, "Effect of Specific Surface on the Shock Sensitivity of Pressed Granular PETN," Explosivstoffe, 188, Nr. 9/1963.
5. W. E. Dimmock, L. D. Hampton and L. E. Starr, "Investigation of the Propagation of Detonation Between Small Confined Explosive Charges Progress Report," Navord Report 2385 (1 April 1952).
6. D. Price and T. Liddiard, "The Small Scale Gap Test: Calibration and Comparison with the Large Scale Gap Test," NOLTR 66-87 (7 July 1966).
7. J. Savitt, "Some Observation on the Growth of Detonation," NAVWEPS Report 3753 (25 August 1954).
8. J. N. Ayres, "Standardization of the Small Scale Gap Test Used to Measure the Sensitivity of Explosives," NAVWEPS Report 7342 (16 January 1961).
9. L. B. Seely, "A Proposed Mechanism for Shock Initiation of Low-Density Granular Explosives," Proceedings of Electric Initiator Symposium, The Franklin Institute, Philadelphia, Pa., 1-2 October 1963, 27-1.

## DISCUSSION

### R. STRESAU

R. Stresau Labs.  
Star Route  
Spoonerville, Wisconsin 54801

A number of explosives have been used as acceptors in gap tests in which the donor charge diameters were about 0.8 mm in diameter. Donor column lengths of RDX or PETN were about 8 mm or longer. Gaps were aluminum. Acceptors were 2.5 mm diameter by 6.25 mm long and contained in Delrin. For most explosives tested, including RDX, Tetryl, and HNS,

the materials tested were more sensitive as the particle size of the acceptor explosive became finer. In the case of HNS, this trend was monotonic for four lots of HNS (two of HNS-I and two of HNS-II) each of which had a significantly different particle size than any other. Most explosives tend to have "optimum" densities for greatest sensitivity. For HNS-II, a very sharp "optimum" was observed at a density of 1.65 gm/cc (which may be compared with lower "optimum" densities usually observed in NOL Small Scale Gap Tests).

## EXPLOSIVE BEHAVIOR OF METHYLNITRATE AND ITS MIXTURES WITH LIQUID DILUENTS

M. Kusakabe and S. Fujiwara  
*The Government Chemical Industrial Research  
Institute, Tokyo, Division 7  
Hiratsuka-City, Kanagawa, Japan*

### ABSTRACT

Methylnitrate in a glass tube had three modes of propagation of reaction wave: HVD, stable LVD and unstable LVD whose velocities were 6700 m/sec, 2540 m/sec and 2140 m/sec, respectively. Charge diameter and strength of initiation had some effect in the mode selection. In the streak photographs of LVD and of transition from LVD to HVD, a kind of blur was observed which was caused probably by the bubbles located ahead of detonation front. In aluminum and copper tubes, an extraordinarily low-velocity-reaction wave was observed and the velocities were less than one-tenth of the Chapman-Jouguet detonation velocity. In lead tubes, LVD with periodical structure was observed. Mixtures of methylnitrate with seven inert liquids were also tested for their detonabilities. The order of quenching abilities of the liquids for LVD conformed to the inverse order of the shock impedance of the liquids.

### INTRODUCTION

Methylnitrate is a colorless liquid with a boiling point of 65 to 66°C. It is volatile and inviscid and has a specific gravity of 1.217 at 15°C. The liquid has long been known as a powerful explosive and some experimental works on its explosive properties has been done, but our knowledge of its explosive behavior is still poor compared with those of the other useful nitric esters such as nitroglycerine (NG), nitroglycol and pentaerythritoltetranitrate (PETN). In the text of T. Urbansky (1), the detonation velocity of methylnitrate is cited from the previous literature as having widely scattered values of 1500 to 8000 m/sec. The value suggests so-called low-velocity detonation in this liquid, which has a propagation velocity much less than the Chapman-Jouguet velocity. But the conditions of its occurrence are not clear and are yet to be studied.

The mechanism of such a low-velocity reaction wave in liquid explosives was studied by several workers. Watson et al. (3) proposed a model in which cavitation plays an important role in the propagation. In the model proposed

by Amster et al. (4), "Mach disc" leads the propagation. We investigated this phenomena in methylnitrate which is one of the simplest nitric esters.

Liquid explosives are simpler in the theoretical treatment of their explosive behaviors than solid explosives, because of their homogeneity and isotropic nature. Working out the explosive behavior of methylnitrate will present some clues for making clearer the propagation mechanism of detonation in condensed explosives

### EXPERIMENTAL PROCEDURE

Methylnitrate (MN) was prepared, washed with alkali and water, and dried with anhydrous sodium sulphate.

Inert liquids used to mix with MN are of extra-pure grade. The mixing ratio is measured in volume by using a mess cylinder or burettes, within the accuracy of  $\pm 1$  percent in volume. When the amount of a component is weighed by chemical balance, the accuracy is enhanced within the error of  $\pm 0.3$  percent in volume.

Sample liquids were put into tubes of various inner diameters and of several materials. The tubes were hung vertically and initiated at the top of the liquid charges. The camera was not equipped with an image slit, in order to take a still photograph on the same film before the shot. This enabled us to catch the original shape of the charge in the streak photograph. The accuracy of the velocity obtained was within  $\pm 1.5$  percent for our typical experimental dimension of tube length of 250 mm and for high-velocity detonation. To obtain more accurate values, long tubes of 400-mm length were used.

Propagation velocities of MN and the mixtures depend on tube diameter, on tube material and also on the strength of initiation. A No. 6 detonating cap was used in weak initiation, and in strong initiation, 1.7 to 3 grams of P-30 (a plastic high explosive containing PETN as a main component; specific gravity, 1.40; detonation velocity, 7200 m/sec) was used as a booster. PETN detonating fuses were used in several shots.

#### EXPLOSIVE PROPERTIES OF METHYLNITRATE

Impact sensitivity was measured by the falling hammer test. A drop of MN was placed in a copper cup with an inner diameter of 10 mm and a depth of ca. 3 mm. One of two steel cylinders of roller bearings with 10-mm diameter and 10-mm height was fitted to the cup, and another was placed under the cup. This sample assembly was set on an anvil and struck by a falling hammer of 5 kg.

The ballistic mortar test was also carried out. Ten grams of MN was put into a small rubber tube with a rubber lid, and initiated with a No. 6 detonating cap. For comparison, we shot PETN charges in the same containers. The results are shown in Table 1 together with the other explosive properties of MN (1). They show that MN is one of the most powerful explosives, and has a relatively low impact sensitivity.

#### EXPLOSION OF METHYLNITRATE IN GLASS TUBE

Explosion of MN in glass tube can be divided into three modes, the Chapman-Jouguet high-velocity detonation (HVD) which propagates in a velocity of 6700 m/sec, "stable" low-velocity detonation (stable LVD) with a velocity of 2540 m/sec and "unstable" low-velocity detonation (unstable LVD) with a propagation velocity of ca. 2140 m/sec. What may occur among

TABLE 1  
Explosive Properties of Methylnitrate (MN)

Ignition point: 150°C			
Fall Hammer Test (5-kg Hammer):			
MN	2/3	at	30 cm
	0/3	at	20 cm
NG	2/2	at	10 cm
	0/2	at	5 cm
Ballistic Mortar Test: MN=129 (PETN=100)			
*Linear Burning Velocity: $U=0.010+0.133P$ :			
	P(kg/cm)	U(cm/sec)	
*Trauzl Test: 520 ml with a No. 1 detonator			
		(NG: 190 c.c.)	
615 ml with a No. 8 detonator			
		(NG: 590 c.c.)	
Detonation Velocity: HVD: 6700 m/sec			
(in glass tube) LVD: 2500 m/sec			

\*Cited from (1).

them depends mainly on the tube diameter. Figure 1 shows the propagation velocity of the reaction wave in MN against inner diameter of a hard glass tube.

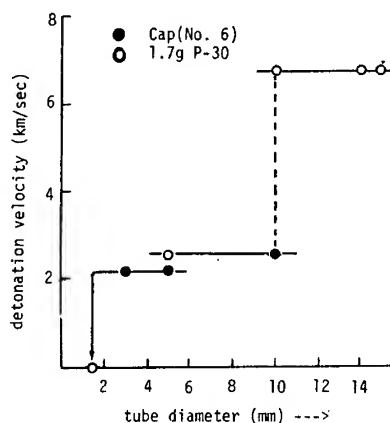
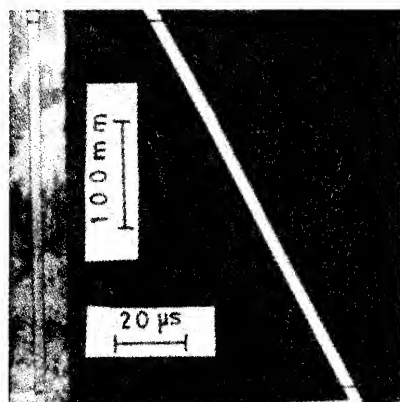
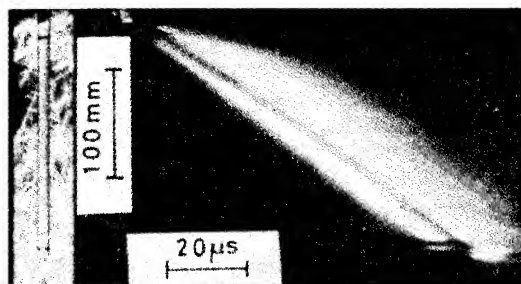


Fig. 1 - Detonation velocities of MN in glass tubes of varied diameters

Thick tubes with inner diameters larger than or equal to 12.7 mm always gave HVD. In tubes with inner diameters of 10 mm, strong initiation resulted in HVD and weak ones did in stable LVD. In tubes with diameters of 5 mm,



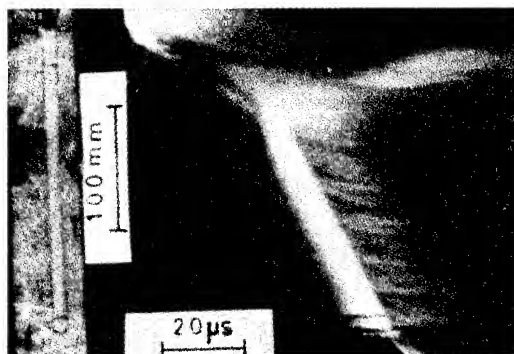
(a) High-velocity detonation  
 $\phi = 10$  mm, boosted with 1.7 g P-30



(b) Stable low-velocity detonation  
 $\phi = 10$  mm, initiated with a No. 6 cap



(c) Unstable low-velocity detonation  
 $\phi = 5$  mm, initiated with a No. 6 cap



(d) Transition to HVD from LVD  
 $\phi = 10$  mm, boosted with 1.7 g P-30

Fig. 2 - Typical streak photographs of detonation of MN in glass tubes

both modes of LVD occurred, that is, stable LVD in strong initiation and unstable ones in weak initiation. Thin tubes of 3-mm diameter always gave unstable LVD, and 1.6-mm tubes failed to transmit any reaction wave.

Figure 2a, b, and c are typical examples of streak photographs for HVD, stable LVD and unstable LVD respectively, in glass tubes. In the photographs, direction of motion is downward, and time elapses from left to right. At the left of each picture is attached a still picture of the charge taken immediately before the shot.

Figure 2a shows HVD of MN in a tube of 10-mm inner diameter and 400-mm length, initiated by a 1.7-g booster. The luminous trace is straight and well defined. There appears a bright light by the booster at the top and a horizontal (timewise) bright line which is caused by illumination of a glass plate at the bottom of the tube. Stable LVD in Fig. 2b is initiated with a No. 6 detonating cap in a tube of the same diameter. The trace of the reaction is separated into two blurred bright loci between which is a narrow dark zone. The blur ahead of the trace

may be considered to appear due to scattering of light by numerous tiny bubbles caused by cavitation. This supports the cavitation theory on the mechanism of LVD propagation proposed by Watson et al. (3). The preceding locus is straight throughout the length of the charge and its width is increasing. The increase may be caused by the lengthening of the cavitated column of the charge and/or by the increase of reaction light. From this point of view, we estimated the propagation velocity of LVD from the inclination of the trailing edge of the preceding locus. The unstable LVD of (c) was initiated with a No. 6 detonating cap in a 5-mm tube. The preceding locus is not as stable as that of (b). The bright regime and faint regime appear alternately. Propagation velocity in the bright regime is the same as that in (b), and that in the faint regime is slower. Luminous reaction decelerates and then accelerates. The interval between the two regimes and the entire structure is constant among all the unstable LVD including those in tubes of 3-mm diameter. As a result, the mean propagation velocity over the entire tube length becomes lower than that of stable LVD, and remains constant, shot by shot.

Transitions from LVD to HVD were occasionally observed. Figure 2d shows an example of such transition in a glass tube with an inner diameter of 10 mm. As clearly seen in the photograph, the transition occurs abruptly and after that the velocity of the HVD is constant throughout the remaining length of the tube. In the HVD regime, we can see a straight and well-defined border line of the charge. The other border line (preceding side) is, however, not clear; it is covered with a blur. It is clear from the location of the blur relative to the border line and to a luminous spurt at the bottom of the charge that the blur appears before the arrival of the detonation front. There is a straight and well-defined shadow of the black mark on the glass tube. This means that the light came from interior of the tube. These facts all prove the existence of cavitations or bubbles ahead of the detonation front. The velocity of these HVD's transferred from LVD's is generally higher than the intrinsic one of MN due to precompression of the charge by a precursor wave transmitted through the tube wall. The velocities of these HVD's with overshoot were different shot by shot.

#### EXPLOSION OF METHYLNITRATE IN METAL TUBES

Propagation velocities of reaction waves in tubes of aluminum, steel, copper, and lead were determined. The results are shown in Table 2.

A slit in 1 mm width or a series of holes (1 mm diameter) with intervals of 20 mm was opened in the side wall in parallel to the tube axis, and was covered with transparent adhesive cellophane tape. These openings are for photographic observation of the reaction waves.

Thickness of walls were 0.5 mm in lead tubes and 1 mm in the other tubes.

Thick tubes again gave HVD. Traces in streak photographs were clear and straight like that shown in Fig. 2a. In an aluminum tube of 6-mm inner diameter and in a copper tube of 5.5-mm diameter, extraordinarily low-velocity waves were observed which had velocities of 504 m/sec and 604 m/sec, respectively. These were observed in tubes with holes. In an aluminum tube with a slit of the same 6-mm diameter, the reaction proceeded with a velocity of 1030 m/sec. Figure 3a shows this extraordinarily low-velocity reaction in a copper tube of 5.5 mm diameter.

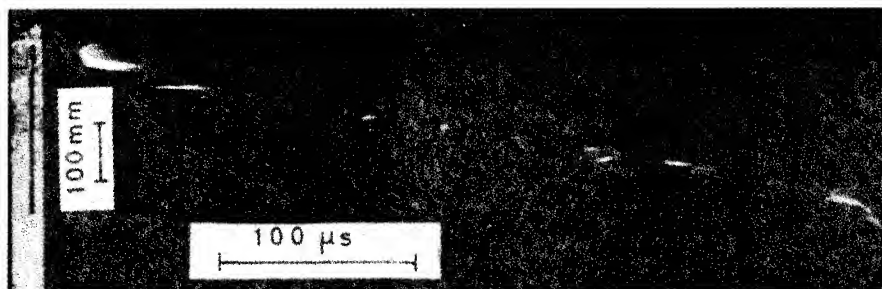
Traces of these extraordinarily low-velocity reactions were faint and irregular. In a tube with a slit, the trace in the streak photograph was intermittent, and it appears as if the photograph was taken with a shot in a tube with holes. The difference in velocities observed in tubes with slits and holes suggests that interaction of the wave with those openings may have some role in the mechanism of wave propagation.

All the four shots in lead tubes gave traces which undulated periodically in their streak photographs. Among them, three had nearly the same velocity of 1422 to 1460 m/sec, and the pitch of the undulation was ca. 13  $\mu$ sec or 18 mm. One of the shots in 6-mm lead tubes made a transition to HVD. The pitch of the undulation increased gradually to about two-thirds of the original value and then transferred abruptly to HVD. The HVD trace was as continuous and solid as the other HVD traces. This overshooted HVD was estimated to have a detonation velocity of 7320 m/sec. Figure 3b is a streak photograph of the shot in 6-mm-diameter lead tube. The reaction proceeds with the velocity of 1450

TABLE 2  
Detonation Velocities of Methylnitrate in Tubes of Various Materials

Material	Density (g/ml)	Sound Velocity (m/sec)	Inner Diameter (mm)	LVD (m/sec)	HVD (m/sec)	Remark
Aluminum	2.70	6420	6	504		Hole
Aluminum	2.70	6420	6	1030		Slit
Steel	7.83	4982	7		6840	Slit
Copper	8.92	3666	5.5	604	6890	Hole
Copper	8.92	3666	8		6730	Hole
Lead	11.33	1320	4	1427		Slit
Lead	11.33	1320	6	1460		Slit
Lead	11.33	1320	6	1600*	7320*	Slit

\*A case of transition to HVD from LVD.



(a) Extraordinarily low-velocity propagation in copper tube  
 $\phi = 5.5$  mm, initiated with detonating fuse;  $D = 604$  m/sec.



(b) Undulating propagation in a lead tube  
 $\phi = 6$  mm, initiated with a No. 6 cap;  $D = 1460$  m/sec.

Fig. 3 - Explosion of MN in metal tubes

m/sec in the regime of undulation with the decreasing pitch. Transition to HVD is seen very near the tube end. These undulations suggest a spinning of the reaction wave front (2).

#### EFFECTS OF DILUENTS ON EXPLOSION OF METHYLNITRATE

Seven kinds of inert liquids were mixed with MN. All the mixtures were shot in hard glass tubes with inner diameters of 10 mm, and their explosions were observed with the streak camera. As in the case of pure MN, HVD and stable LVD were observed and transition from LVD to HVD also happened occasionally, but unstable LVD did not occur.

The detonation velocity of a mixture generally decreases as the content of the diluent increases, and further increase of the diluent over a certain critical mixing ratio (a quenching limit) results in a failure of propagation. Figures 4 and 5 show the variation of detonation velocities with contents in volume percent of the diluents, for the mixture with chloroform and for that with carbon tetrachloride, respectively.

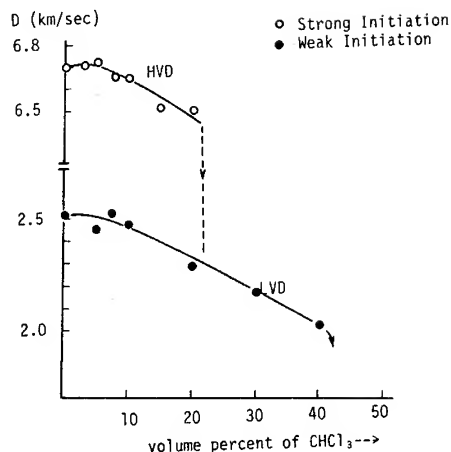


Fig. 4 - Detonation velocities of HVD and LVD in MN-chloroform mixtures

As the diluent increases, the velocities of HVD and LVD in the mixture with carbon tetrachloride linearly decrease from the values for

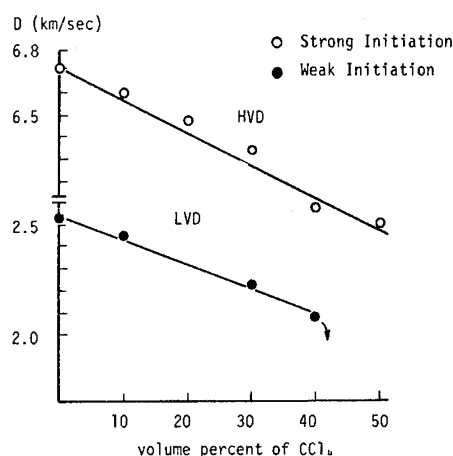


Fig. 5 - Detonation velocities of HVD and LVD in MN-carbon tetrachloride mixtures

pure MN; on the other hand for the mixture with chloroform, either curve has a hunch near 5 percent.

Quenching limits of the two mixtures for LVD are nearly the same, but those for HVD are different. These limits depend not only on the kind of the diluents but also on the charge diameter. The bigger the charge, the larger is the value of quenching limit. The charge diameter of 10 mm is suitable to discriminate the differences in quenching effects of inert liquids. Quenching limits of the other five liquids were also obtained. Table 3 shows the results for LVD in volume percent as well as in weight percent.

The order of these limits agrees with the order of densities and also with the order of

shock impedances at 50 kbar. The value changes from ca. 10 percent in weight for the light cyclohexane to ca. 50 percent for the dense carbon tetrachloride. Shock impedances are calculated from the shock Hugoniot data for these liquids obtained by Walsh and Rice (5). This order is well explained by assuming that the mixture consists of many microphases of MN and of diluent and that any diluent behaves merely as a shock transmitter between active MN phases (6, 7).

The order of the quenching limits for HVD did not always conform to the order of the shock impedances of these diluents, similarly with the mixtures of nitromethane and inert diluents. In those mixtures of nitromethane and inert diluents, polar inert liquids such as chloroform revealed a high quenching ability (6). Though not marked as in the case of nitromethane, the difference between quenching limits of the two liquids is larger than that presumed from the difference between their shock impedances. A mixture containing nonpolar carbon tetrachloride can transmit HVD even in a large content of diluent more than half the weight of the mixture, and the quenching limit for HVD exceeds that for LVD. HVD is more apt to initiate than LVD in high diluent content. However, for mixtures with chloroform, LVD is easier to propagate than HVD in high-diluent content.

To make sure of the shape near the hunch in the HVD velocity curve of Fig. 4, we estimated detonation velocities of HVD accurately in the range of 0 to 10 percent in volume at intervals of 2.5 percent. Mixtures were prepared within the error in mixing ratio of  $\pm 0.3$  percent in volume, and were shot in long tubes. Each point near 5 percent on the HVD curve shows the mean of values for 2 to 3 shots. It assures the existence of a hunch on the HVD curve, and

TABLE 3  
Critical Mixing Percents of Inert Liquids

Liquid	Density (g/ml)	Shock Impedance at 50 kbar ( $\times 10^5$ CGS)	Quenching Limit			
			Vol.	%	Weight	%
Cyclohexane	0.778	3.184	10	15	7	10
Ethyl alcohol	0.785	3.247	15	20	10	14
Benzene	0.874	3.571	15	20	11	15
Monochlorobenzene	1.101	4.058	20	22.5	18	20
Nitrobenzene	1.198	4.385	20	22.5	20	22
Chloroform	1.480	4.587	35	40	40	45
Carbon tetrachloride	1.589	4.789	40	45	47	52

suggests the existence of such a hunch also on the LVD curve. There may be a correlation between this hunch and the strong quenching effect of chloroform.

#### ACKNOWLEDGMENT

The authors express their profound thanks to Professor Hikita for his guidance and discussion and to Dr. K. Shiino for his kindness in preparing methylnitrate for our experiment.

#### REFERENCES

1. T. Urbansky, "Chemistry and Technology of Explosives," Vol. II, pp. 160-163, Pergamon Press, New York, 1965.
2. V. V. Mikhailov and M. E. Topchiyan, "Study of Continuous Detonation in an Annular Channel," Combustion, Explosion and Shock Waves, Vol. 1, No. 4, pp. 12-14, 1967.
3. R. W. Watson, C. R. Summers, F. Gibson, and V. K. Bobolev, "Detonations in Liquid Explosives — The Low Velocity Regime," The Fourth Symposium on Detonation, N.O.L., pp. 117-125, 1965.
4. A. B. Amster, D. M. MoPachern, and Z. Pressman, "Detonation on Nitromethane-Tetranitromethane Mixtures: Low and High Velocity Waves," Fourth Symposium on Detonation, N.O.L., p. 126, 1965.
5. J. M. Walsh, and M. H. Rice, "Dynamic Compression of Liquids from Measurements on Strong Shock Waves," J. C. P., Vol. 26, No. 4, pp. 815-823, April 1957.
6. S. Fujiwara, M. Kusakabe, and T. Hikita, "Study of Detonation in Multi-Components Condensed Phase. II. On Solutions of Nitromethane and Inert Solvents," J. Ind. Expl. Soc. Japan(Kogyo Kayaku), Vol. 30, No. 2, pp. 77-80, 1969.
7. T. Hikita, S. Fujiwara, and M. Kusakabe, "Two-Phase Model of Detonation Propagation in Condensed Explosives with Inert Diluents," unpublished.



## GENERAL DISCUSSION

R. Duff, Systems Science and Software  
P.O. Box 1620, La Jolla, California 92037

Perhaps it is possible to recognize a unifying thread which relates several of the papers presented at this session. Dr. Price suggests that both homogeneous and heterogeneous initiation mechanisms will be involved in explosives of intermediate density. Drs. Roth and Wackerle

have discussed wedge records which indicate homogeneous initiation waves originating at the input surface of the charge. Dr. Roth and Marshall have shown pressure data which indicates heterogeneous initiation processes are occurring. It may well be that both mechanisms occur simultaneously. What is observed may be governed in large part by what one looks for.

## **Session IV**

### **MOSTLY INITIATION BY NON-SHOCK STIMULI**

Chairman: N. Manson  
*Université de Poitiers*

# THE THERMAL INITIATION AND GROWTH OF REACTION IN SECONDARY EXPLOSIVES UNDER TRANSIENT CONFINEMENT

K. Beedham, A. S. Dyer, and W. I. Holmes  
*Atomic Weapons Research Establishment  
Aldermaston, Berks, England*

## ABSTRACT

Explosive events have been obtained by dropping 1/3-oz charges of secondary explosives in a weighted holder onto a heated metal plate. The impact pressure pulse was arranged to correspond to that experienced in the AWRE oblique impact test where a 45 lb hemispherical charge is dropped from a few feet onto a hard target. Heating occurred during the time of impact, while the explosive surface was under transient confinement. A number of explosive compositions were tested over a range of temperatures and for each an estimate was made of the temperature at which the incidence of explosive events was 50%. Explosions were also obtained when charges were impacted onto a hot wire. The results have been compared with the calculated response of a simple thermal model of the system in which the rate of thermal decomposition of the explosive followed an Arrhenius function. It has also been shown that extent of explosive reaction in the charge is affected by the impact pressure and the presence of cracks in the charge. Conditions which lead to loss of confinement near the initial reaction site result in less violent explosive events.

## INTRODUCTION

Previous work has shown that secondary explosives can be initiated under accidental impact conditions when special features are present which lead to conversion of a significant amount of the available mechanical energy into heat at the surface of the explosive charge. This role is played by the abrasive surface in the AWRE Oblique Impact Test (1) and by the air gap between the metal spigot and the explosive charge in the AWRE Spigot Test (a modified version of the LASL Spigot Test (2)). In the Oblique Impact Test, where a 45 lb charge is dropped from a few feet onto a hard target, impact pressures of 15,000 to 30,000 lbf in.<sup>-2</sup> can occur, depending on the drop height and strength of the explosive, with impact times of 1-2 ms. The mechanical energy at impact, however, is insufficient to raise the temperature of the bulk explosive, due to simple compression, by more than a few degrees and it is the concentration of thermal energy at a surface which is responsible for the initiation of the explosive charge.

The aim of the work reported here was to study the initiation of secondary explosives by

conduction from hot surfaces under high pressure pulse conditions appropriate to accidental impact situations. Thus the phase of the impact in which mechanical energy would be converted into heat at an interface would be simulated in a controlled way.

## EXPERIMENTAL METHOD AND EQUIPMENT

### Hot Plate Test

The test conditions were achieved by dropping the suitably mounted explosive sample onto a relatively massive electrically preheated metal plate. The equipment was designed to give peak impact pressures up to 80,000 lbf in.<sup>-2</sup> with durations of 1 to 2 ms.

The explosive sample mounted in a dense laminated wood (Jabroc) holder was attached to the bottom of a 50 lb steel weight which was allowed to fall down a guide tube so that the sample impacted squarely onto the hot plate.

The 3/8-in.-thick hot plate was made of a nickel alloy (Nimonic 105) and was attached

to the top of an electrical heater unit encased in the same alloy. Nimonic 105 was chosen despite the difficulty of fabrication because it has considerable strength at temperatures up to 1,000°C.

The temperature of the hot plate was monitored by a thermocouple near the top surface and the current flow in the heater was adjusted manually so that a steady temperature at the hot plate surface was obtained before impact of the explosive sample.

The heater assembly was mounted on top of a load cell but thermally insulated from it to keep the load cell at a safe working temperature. The output from the load cell was displayed as a function of time on an oscilloscope which was triggered by the falling weight passing a photoelectric device. In the absence of explosive reaction a fairly smooth pressure pulse was obtained although there was some mechanical resonance of the heater/load cell assembly. When an explosive event occurred a pressure spike appeared on the load cell record and this indicated the time to explosion. A high-speed cine film of the impact was taken so that the response of the explosive could be studied and compared with the pressure records.

After the initial impact a remote manually operated winch was used to raise the explosive sample clear of the hot plate so that the effect of the primary impact on the sample could be studied and unnecessary damage to the equipment, by subsequent explosive reaction, could be avoided.

After the drop height of the weight had been adjusted to obtain the required pressure pulse, tests were carried out on each explosive composition over a range of temperatures using a 10°C increment. The test sequence was arranged so that an estimate could be made of the temperature at which there was 50% probability of explosive events,  $T_{50\%}$ .

#### Hot Wire Test

The test procedure was modified so that the effect of the geometry of the hot surface could be studied. A 0.006-in. constantan wire was sandwiched between two explosive samples mounted as before in Jabroc holders. The impact pulse was generated by dropping the 50 lb steel weight down the guide tube onto the explosive assembly mounted on top of the load cell. At the peak of the pressure pulse a 16  $\mu$ F capacitor bank, at a selected voltage between 400 V and 600 V, was discharged through the wire. The trigger signal for the discharge was

provided by a piezo-crystal underneath the explosive assembly. The discharge current was determined by monitoring the voltage drop across a low resistance in series with the constantan bridgewire, and this enabled the energy deposited per unit length of the bridgewire  $E_c$  to be calculated from

$$E_c = R_c \int I^2 dt$$

where  $R_c$  is the resistance per unit length of bridgewire which is effectively constant over the range of temperatures of interest. The discharge was completed in approximately 80  $\mu$ s. The temperature rise  $T_c$  in the wire then follows from

$$T_c = \frac{E_c}{C \times M}$$

where

$C$  = average specific heat, and

$M$  = mass per unit length of wire.

After the drop height of the weight had been adjusted to obtain the required pressure pulse, tests were carried out over a range of wire temperatures by adjusting the voltage on the capacitor bank.

#### PREPARATION OF THE EXPLOSIVE SAMPLES

Information about the explosives tested is given in Table 1.

TABLE 1  
Test Explosives

Explosive	Composition (parts by weight)	Manu- facture
PETN		Pressed
RDX		Pressed
HMX		Pressed
DATB		Pressed
TNT		Cast
Octol-A	HMX/TNT/Wax 80/20/1	Pressed
Octol-B	HMX/TNT/Wax 70/30/1	Pressed
HW4	HMX/Wax 95/5	Pressed
PBX 9404	HMX/NC/TCEP 94/3/3	Pressed
HV4	HMX/Viton 85/15	Pressed
Comp B3	RDX/TNT 60/40	Cast
Comp B3 (waxed)	RDX/TNT/Wax 60/40/1	Cast

The samples of the explosive compositions and TNT were prepared by machining discs 1.125-in. diameter by 0.33-in. thick from charges manufactured by pressing or casting as appropriate for each composition. The explosive discs were bonded into a recess in a Jabroc holder and the exposed surface of the explosive was machined to a constant height of 0.062 in. above the face and parallel to the back of the holder (Fig. 1). Thus on impact, a good machined surface was presented squarely to the hot plate surface with similar confinement on all compositions. The finished sample was 0.3-in. thick and weighed approximately 0.3 oz.

The pure explosive samples of PETN, HMX, RDX, and DATB were prepared by hot pressing and were between 98% and 99% crystal density. These pressed compacts were made

1-in. diameter  $\times$  0.3-in. thick and mounted in the Jabroc holders without machining.

## RESULTS OF HOT PLATE TESTS

### Effect of Hot Plate Temperature on the Incidence of Explosive Events

All the explosives tested, except TNT, were subjected to similar pressure pulses, the peak pressures lying in the range 13,000 to 18,000 lbf in.<sup>-2</sup> and the pulse durations varying between 1.6 and 2.0 ms. To keep within this range the drop height was adjusted for each explosive. Tables 2 and 3 show the effect of hot plate temperature on the incidence of events for a variety of explosive compositions and Table 4 gives a detailed description of the damage criteria to the explosive sample and to

TABLE 2  
Effect of Temperature on Explosive Reaction

Explosive Composition	Drop† Height (in.)	Hot Plate Temperature °C									
		340 -350	360 -370	380 -390	400 -410	420 -430	440	450	460	470	480
Octol-A	6							NNN	NNp	<u>PP</u>	
Octol-B	6			N	<u>PN</u>	N		NNN	NNP	<u>PPP</u>	pPP
			N	N	N			NPP	<u>P</u>	<u>Pp</u>	<u>Pp</u>
HW-4	6							NNN	Npp p	p	
PBX 9404	6				N			N	NN	<u>PE</u>	
HV-4	6				N		NNN	ppp	p		
Comp B3	10						NNN	<u>PPP</u>	<u>P</u>		
Comp B3 + 1% Beeswax	10					NNN	NPP	NP	<u>P</u>	p	
HMX	6							N*NN	N*	<u>P*</u>	
RDX	6					E* <u>P*</u>		E			
PETN	9	N*E* H	NE NE	NP E	<u>P</u>						

\*Hot plate was made of EN58B instead of Nimonic 105.

†Yielding a nominal peak pressure of 13,000 to 18,000 lbf in.<sup>-2</sup>.



Fig. 1 - Explosive disc mounted in Jabroc holder

TABLE 3  
Effect of Temperature on Explosive Reaction of TNT and DATB

Temp (°C)	Nominal Peak Pressure (lbf in. <sup>-2</sup> )	
	18-in. Drop 19,400-28,500	12-in. Drop 16,700-21,800
	TNT	DATB
600	N	N* p†
610		p† p†
620		p†
630		p†
640	N	p†
650	NNN p	p†*
660		
670	N p	p†*

\*Hot plate made of EN58B instead of Nimonic 105.

†Very small events, very difficult to detect.

the holder which was used to classify the nature of the events observed.

All the HMX and RDX compositions gave explosive reactions in the temperature range 400°C to 470°C, whereas PETN gave explosions at temperatures above 350°C.

#### Nature of the Explosive Events

A considerable variation from explosive to explosive was observed in the violence of the events obtained as shown by damage to the

TABLE 4  
Classification of Size of Explosion

Symbol	Group	Description
N	Fail	No event on the first impact.
p	Small partial	10% or less of HE consumed. Slight flaking of Jabroc holder. Small cloud or puff of flame seen on cine film.
<u>P</u>	Large partial	Up to 90% of HE consumed. Large pieces of Jabroc removed flush with base of HE sample.
E	Explosion	All HE consumed. Holder split. Jabroc broken into small pieces to base of HE sample. Damage to hotplate heat shield and tufnol base.
H	High Order Explosion	All HE consumed. Hotplate dented and fixing screws broken. All Jabroc broken into powder. Severe damage to tufnol base plate.

explosive and its mounting. Thus HW4 and HV4 gave events which were typically classified as small partials (p). A sample which failed to give an explosive reaction was dyed and showed some surface cracking caused by impact on the hot plate.

Octol-B and the waxed version of Composition B3 tended to give a mixture of small and large partials. Explosives which gave events which were typically classified as large partials (P) included Octol-A and Composition B3 (unwaxed). The events with PBX 9404 tended to be more violent and were classified as explosions (E), and in one test a high order explosion (H) was observed. PETN and RDX also gave very violent explosions.

#### Behaviour of TNT and DATB in the Hot Plate Test

TNT and DATB were included in the test programme because they have markedly

different kinetic parameters from the other explosives tested. In fact it was necessary to raise the hot plate temperature above 600°C for explosive reactions to be observed (see Table 3). It was difficult to obtain a satisfactory pressure pulse similar to that used on the other HE. For TNT a wide range of drop heights up to 18 in. were tried giving pulses with peaks varying from 6,000 to 33,000 lbf in.<sup>-2</sup> and durations of 2.0 to 2.8 msec. The explanation of the large positive fluctuations of pressure which were observed on the leading edge of the main pressure pulse was that on contacting the hot plate the TNT melted leaving a thin film of liquid which was ejected out round the edges of the sample uncovering fresh unmelted TNT. This process was repeated until the peak pressure of the main impact had occurred. The examination of the cine film agreed with this mechanism and showed a jet of material radiating out from the contact region. The recovered samples, also showed a crystallised layer of TNT on their surfaces.

DATB with 12-in. drops, in contrast to TNT, showed no clear signs of melting, but similar pulse effects giving rise to pressure peaks in the range 16,000 to 21,000 lbf in.<sup>-2</sup> and durations of 2.1 and 2.3 msec were observed. The only evidence for ignition with DATB came from an examination of the cine film when puffs of gas were seen although there was no sign of a pressure spike on the load cell record.

Two explosive events were obtained with TNT each being clearly identified by the damage caused and the presence of pressure spikes on the load cell records.

#### Effect of Impact Pressure on the Behaviour of Octol-B on the Hot Plate

In order to assess what effect varying the pressure pulse had on  $T_{50\%}$  a series of tests

were made on Octol-B. The impact pressure was varied by altering the drop height of the sample. Five drop heights were used with hot plate temperatures between 450°C and 490°C and the results are given in Table 5. The peak impact pressures ranged from 6,000 to 26,000 lbf in.<sup>-2</sup> and the durations of the pulses from 2 ms to 1.6 ms respectively.

#### Effect of Cracks on the Behaviour of Octol-B on the Hot Plate

The results of drop tests on a hot plate at 480°C using cracked discs of Octol-B are compared with those on uncracked samples in Table 6. The tests were made at three drop heights. The artificial crack was introduced into the sample in the following way: the disc was cut into two segments along a diameter and the two halves were then bonded into the recess in the Jabroc holder to form a plane crack normal to the face of the disc. The surfaces of the crack were in contact to form a crack of nominally zero width.

The large partial explosions were similar in both cracked and uncracked samples. In the small partial explosions there was evidence of propagation of reaction down the crack.

#### Effect of Secondary Impacts on the Hot Plate

Ideally the hot plate test should permit only one impact by the explosive sample at a known pressure and duration of contact; this, however, is mechanically difficult to arrange and a series of subsequent impacts usually followed when no initiation occurred on the first impact. Examination of the cine record showed that explosive reactions or fires were obtained from some compositions on subsequent impacts

TABLE 5  
Effect of Pressure on the Explosive Reaction of Octol-B

Drop Height (in.)	Nominal Peak Pressure (lbf in. <sup>-2</sup> )	Hot Plate Temperature				
		450°C	460°C	470°C	480°C	490°C
1	6,000		N	NNp	pppp	ppp
2	9,000			NNp		
4	14,000			NNN		
6	16,000	NNNNPP	NNPP	pPPPP	pppPPP	
9	20,000	NPP				
18	26,000	NNP			PP	

TABLE 6  
Effect of Cracks on the Behaviour of Octol-B  
on the Hot Plate Test at 480°C

Drop Height (in.)	Uncracked Disc	Cracked Disc
1	pppp	N
6	ppp <u>PPP</u>	pp
18	<u>PP</u>	<u>Pp</u>

at the  $T_{50}$  temperature and at temperatures above and below  $T_{50}$ . For example, with Octol-B explosive reactions were observed in second or third impacts at hot plate temperatures down to 30°C below  $T_{50}$  and fires down to 80°C below  $T_{50}$ . With PETN fails and events were obtained over a 40°C temperature range on the first impact but only fires were observed on subsequent impacts of the failed samples. HV-4 and DATB were the only compositions to show neither explosive events nor fires on subsequent impacts.

The occurrence of explosive reaction on secondary impacts is probably due to some pre-heating of the surface of the explosive sample by the primary impact and also to the higher temperatures reached by any explosive dust remaining on the hot plate surface while the sample is rebounding.

#### Effect of Dead Weight Loading on the Behaviour of Explosives in the Hot Plate Test

Tests have been carried out with HMX and Octol-B to observe the behaviour under dead weight loading. The explosive sample mounted on the 50 lb weight in the usual way was lowered onto the hot plate preheated to 500°C and the sequence of events recorded on a cine camera framing at 32 fps. Smoke was emitted from both HMX and Octol-B within one frame of contact with the hot plate and became most copious in the case of Octol-B. Ignition occurred with HMX after 5 frames (150 ms) and with Octol-B after 13 frames (400 ms). In both cases the explosive samples burned fairly smoothly until the explosive was consumed.

#### RESULTS OF HOT WIRE TESTS

##### Effect of Hot Wire Temperature on the Incidence of Explosive Events for Octol-B

The results of a series of tests on Octol-B are summarised in Table 7. To achieve

pressure pulses with a peak value in the range 13,000 to 18,000 lbf in.<sup>-2</sup> the 50 lb weight was dropped from 12 in. The duration of the pulse was between 1.5 and 2.0 ms. The variations in wire temperature, calculated as described in Section 2.2, were obtained by varying the voltage on the 16  $\mu$ F capacitor bank between 450 and 500 V. The nature of the explosive events was classified by noting the extent of damage and amount of explosive consumed in each sample in accordance with Table 4. From the load cell records the time to ignition from the capacitor discharge to the explosion pressure spike was less than 0.2 ms.

TABLE 7  
Effect of Hot Wire Temperature on the  
Behaviour of Octol-B  
(Peak Impact Pressure 13,000-18,000 lbf in.<sup>-2</sup>)

Hot Wire Temp (deg C)	Explosive Reaction
532	<u>PP</u>
515	<u>P</u>
505	<u>P</u>
495	<u>P</u>
483	N
473	N
465	N
455	N

#### Nature of the Explosive Events for Octol-A, Octol-B and HW-4

Table 8 compares the violence of the characteristic events for three explosive compositions, Octol-A, Octol-B, and HW-4, when impacted on a hot wire with temperatures in the range 450 to 550°C. The 50 lb weight was dropped from 12 in. in each case.

In addition to the classification of event size by inspection of the damage and amount of explosive remaining, the peak of the explosion pressure spike on the load cell record may be used to assess the violence of the explosion, and the average value has been included in Table 8.

The damage to the top and bottom samples of the sandwich was found to be very similar in all tests. The extent of the damage was in general greater than that observed when the three compositions were impacted on the hot plate. The damage to the Jabroc holders places HW-4 in the same category as Octol-B (i.e., large



TABLE 8  
Behaviour of Octol-A, Octol-B, and HW-4  
in the Hot Wire Test  
(Peak Impact Pressure 13,000-18,000 lbf in.<sup>-2</sup>)

Explosive	Octol-A	Octol-B	HW-4
Hot Wire Temp °C	530-540	495-532	445-530
Typical Explosive Reaction	E	<u>P</u>	<u>P</u>
Pressure Peak of Explosion (lbf in. <sup>-2</sup> )	55,000	46,000	24,000

partial explosion). However, for HW-4 considerably more explosive was left in the holder and the explosion pressure spike was much less than Octol-B.

#### Effect of Pressure and Cracks on the Behaviour of Octol-B

Table 9 summarises the results of tests on cracked and uncracked samples of Octol-B. The cracked samples were prepared in the same way as for the hot plate tests. The explosive assembly was arranged so that the cracks in the top and bottom samples were in line. The constantan wire was laid across a diameter at right angles to the cracks.

Tests were made under two impact conditions, with the weight dropped from 12 in. and 3 in., using a hot wire temperature of 525°C ( $\pm 15^\circ\text{C}$ ). The pressure records showed that for the 12-in. drops the impact pressure for the cracked charge assembly was significantly smaller than for an assembly with uncracked charges. The same effect was noticeable but to

a lesser extent with the 3-in. drops. In addition to the visual assessment a quantitative measure of the violence of the reaction was obtained from the explosion pressure spike and these results are included in Table 9.

The violence of the reaction was found to be considerably smaller when the samples had cracks in them. Some propagation of reaction had occurred along the crack and has been enhanced at the point where the crack met the Jabroc mount. Reaction had also occurred at the edges of the disc where the hot wire had emerged from the sandwich.

Attempts to carry out tests with more severe impacts giving peak pressures of 25,000 lbf in.<sup>2</sup> have so far been unsuccessful due to failure of the bridgewire. Tests have however been made with uncracked samples under a 50 lb dead load. Even with a 600 V discharge giving an estimated wire temperature of 850°C no explosion or ignition occurred with Octol-B, and the only sign of reaction was a brown line where the wire had been in contact with the explosive.

#### A THERMAL MODEL OF THE HOT PLATE TEST

Some computer calculations of the temperature rise in the explosive have been made on a thermal model of the hot plate test in order to estimate the time to explosion. A digital code which solves the temperature distribution in a thermal model for a sequence of finite time steps was used after it had been modified to include decomposition of a reactive material. Two assumptions were made:

1. That the decomposition of the explosive conformed to zero order kinetics (i.e., the rate of reaction is independent of loss of reactant) with a rate defined by the Arrhenius function  $Ae^{-E/RT}$ .

TABLE 9  
Effect of Pressure and Cracks on the Behaviour of Octol-B in the Hot Wire Test  
(Wire Temperature 510°C-540°C)

Drop Height (in.)	Sample Disc	Peak Impact Pressure (lbf in. <sup>-2</sup> )	Explosive Reaction	Pressure Peak of Explosion (lbf in. <sup>-2</sup> )
12	Uncracked	18,000	<u>PP</u>	46,000
	Cracked	13,000	pp	13,000
3	Uncracked	7,000	pp	16,000
	Cracked	6,000	pp	8,000

2. That the temperature used to calculate the reaction rate from the Arrhenius function was constant during each time step of the calculation.

The code did not include thermal effects due to phase changes nor heat generated by impulsive loading of the explosive.

The thermal model of the hot plate test consisted of a simple mesh comprising two series of elements representing the hot plate and explosive respectively, i.e., one-dimensional heat flow from the hot plate to the explosive with no surface resistance. The mesh was surrounded by insulating boundaries at sufficient distance from the hot plate/explosive interface for the model to appear thermally infinite during the experimental time of contact (not more than 2 ms).

The size of the elements in the mesh at the hot plate/explosive interface were adjusted in proportion to the square root of the thermal diffusivities of the materials. The computer calculations predicted an immediate drop in the hot plate surface temperature on contact with the cold explosive sample. In the absence of exothermic decomposition the calculation indicated that this interface temperature remained essentially constant in agreement with the analytical solutions. It was verified that the computer calculations were independent of the arbitrary choice of mesh size by changing the fineness of the mesh near the interface and the size of the time steps in repeat runs of the computer programme. The estimated time to explosion when the self-heating term was included was also not significantly affected by these changes. The thermal and kinetic parameters (based on decomposition of the explosives

in the liquid phase between 200°C and 300°C) used in the computation of the thermal explosion times for the explosive compositions tested practically are listed in Table 10. For the pure explosives the values used in the computations were taken directly from Table 10. For the explosive compositions such as Octol-B and Composition B3 the value used for  $Q$  was factored in proportion to the percentage composition by weight of the most reactive constituents HMX and/or RDX and the exothermic contribution from the TNT, which would start to decompose at a higher temperature, was ignored.

Figure 2 shows a plot of time to explosion for Octol-B relative to the hot plate contact temperature. The contact temperature was calculated to be 40–50°C lower than the temperature of the hot plate surface before the impact by the explosive sample. The experimental results at the appropriate reduced temperatures are superimposed on the curve at the measured times to ignition from the start of the pressure pulse. Other compositions based on HMX gave

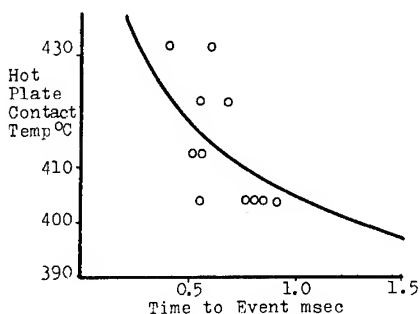


Fig. 2 - Time to explosion for Octol-B, computed curve and experimental results (o)

TABLE 10  
Thermal and Kinetic Parameters Used in Thermal Model Calculations

	Density $\rho$ (g/cc)	Specific Heat $C$ (cal/g/°C)	Thermal Conductivity $K$ (cal/s/cm/°C)	Heat of Decom- position $q$ (cal/g)	Activation Energy $E$ (kcal/mole)	Frequency Factor $\log A$
Nimonic alloy	7.99	0.11	$3.8 \times 10^{-2}$	—	—	—
Constantan	8.4	0.10	$6.4 \times 10^{-2}$	—	—	—
RDX	1.8	0.35	$6 \times 10^{-4}$	1020	45.81	17.87
HMX	1.9	0.35	$10 \times 10^{-4}$	1080	52.70	19.70
TNT	1.55 (cast)	0.35	$5 \times 10^{-4}$	860	47.90	15.33
PETN	1.75	0.35	$6 \times 10^{-4}$	1100	47.63	20.06

almost identical computed curves and the computed curve for RDX/TNT (Comp B3) was also very close. Table 11 gives a comparison between experimental and calculated temperature-time conditions for ignition. The experimental 50% explosion temperatures estimated from the results in Tables 2 and 3 closely follow those computed from the times to explosion. The computed temperature/time curve for TNT predicted initiation temperatures in the range where explosions were obtained practically and within similar times.

#### A THERMAL MODEL OF THE HOT WIRE TEST

The thermal model of the hot wire test consisted of a simple mesh comprising two series of radial elements representing the wire and explosive respectively, i.e., one-dimensional radial flow assuming no temperature gradients along the wire. The explosive mesh was surrounded by an insulating boundary at sufficient distance from the wire for the model to appear thermally infinite during the time of the impact pulse.

The boundary conditions were arranged so that the wire was heated at a rate proportional to the square of the discharge current using a typical profile from the current monitor. The computer calculations showed that the centre line temperature of the wire was largely unaffected by conductive flow from the wire surface during the time of the current discharge (80  $\mu$ s).

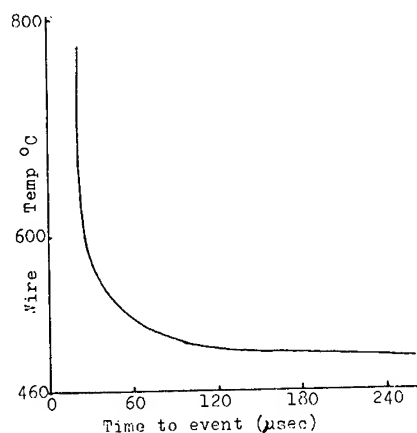


Fig. 3 - Time to explosion of Octol-B as a function of maximum wire temp

The maximum temperature rise in the wire as a function of time to explosion for Octol-B using the thermal constants in Table 10 is shown in Fig. 3. For ignition times below 80  $\mu$ s the Octol-B ignites before the discharge is complete and before the maximum wire temperature is attained. The calculated cut-off temperature is 480-490°C which is in good agreement with the experimental values for Octol-B in Table 7 which also indicate a cut-off temperature between 483°C and 495°C. At the cut-off temperature the energy deposited in the constantan wire was 1.25  $\text{Jin}^{-1}$ .

TABLE 11  
Comparison Between Experimental and Calculated Conditions for Ignition

HE	Experimental		Calculated	
	T <sub>50%</sub> Hotplate	Time to Explosion t <sub>e</sub> ms	Temp °C for Explosion in t <sub>e</sub> ms	
			Hot Plate	HE Surface
Octol-A	460	1.27	446	400
Octol-B	460	0.53	464	417
HW-4	460	0.68	452	406
Comp B3	450	0.96	424	390
Comp B3 + wax	440	0.87	426	392
PETN	340	0.66	357	326
TNT	650	0.7	623	576
HMX	470	NA	—	—
RDX	< 420	0.58	430	397

## DISCUSSION

There is a good correlation between the temperatures found experimentally at which the compositions tested show a 50% probability of explosive reaction and the temperatures predicted for thermal initiation in the observed time to explosion. Thus the sensitiveness to thermal initiation can be predicted by a simple thermal model using kinetic parameters for the explosive compositions, although these have been derived from decomposition studies at lower temperatures. Since the thermal model takes no account of the effect of pressure yet compares well with experimental results, it can be assumed that the main effect of pressure is to provide confinement. This prevents the heat losses which would otherwise occur by the escape of hot gases from the surface of the explosive and maintains good thermal coupling between the hot surface and the explosive. This is well illustrated by the test on a hot wire under a static load of 50 lb where no explosion was obtained.

Confinement would be particularly important (if rapid decomposition occurred in the gas phase rather than in the solid explosive) by preventing escape of gases in the early stages of initiation. This could be an important distinguishing feature between secondary and primary explosives. For primary explosives where thermal decomposition can occur rapidly in the solid phase, confinement would not be expected to be so important. The thermal sensitivity of primary explosives is defined by their decomposition kinetics largely independent of the presence or absence of confinement. However, for secondary explosives prediction of thermal sensitivity is possible from simple kinetics only when the confinement is such that the site of reaction is maintained close to the explosive surface and this condition can arise during impact. At the test temperature the explosive surface will be molten and the rate determining step is likely to be the formation of a reactive vapour. Reaction in the vapour phase would then proceed very rapidly under the test pressures. Under the impact pressure there will be a tendency for the thin melt layer to flow and distort the heat flow conditions at the interface. However for the range of pressures investigated the effect is believed to be small except for TNT where the ejection of melt was observed.

A comparison of the thermal sensitivity of the explosives tested on the hot plate shows that HMX is thermally more stable than RDX and this is also reflected in the relative sensitivity of HMX- and RDX-containing compositions.

PETN is considerably more sensitive than the other explosives tested whereas TNT and DATB are much less sensitive.

The influence of confinement on the magnitude of the events produced in Octol-B may be assessed from the results in Tables 5 and 9 relating to the effect of impact pressure. There is some indication that the likelihood of explosive events on the hot plate is reduced by a reduction in impact pressure and clear evidence that the violence of event is reduced in the hot wire test. This could be an important factor in the behaviour of explosive charges in, for example, the oblique impact test since the impact pressure will be dependent on the mechanical strength of the explosive composition.

The presence of cracks in the explosive sample does not lead to any enhancement of explosive reaction in Octol-B on the hot plate and in fact in the tests with a hot wire there is a marked decrease in the violence of the explosive event. Although this may be partly due to the lower impact pressure obtained with the equivalent drop on the cracked samples the nature of the explosive reaction suggests that it is the loss of confinement due to the presence of the crack, allowing escape of gases from the region of the hot wire, that is responsible for the reduced reaction.

## CONCLUSIONS

A test has been devised which can be used to examine initiation of secondary explosives by conduction from a hot plate or hot wire under impact conditions. Impact tests on a hot plate show that the thermal stability of organic explosives has the following ranking



The temperature conditions for initiation can be predicted reasonably well from a thermal model which takes account of the decomposition kinetics as a function of temperature. The impact provides confinement in the early stages of initiation. This prevents heat losses from the explosive surface which would arise through escape of hot gaseous reagents and decomposition products and maintains good thermal coupling between the hot surface and the explosive.

There is evidence that the extent of explosive reaction, which depends on the explosive tested, is also affected by the impact pressure and the presence of cracks. Conditions which lead to loss of confinement near the reaction

site result in a less extensive and less violent reaction.

however, necessarily represent the official views of AWRE.

#### ACKNOWLEDGMENTS

The thermal computer code used for the digital calculations was developed by Mr. R. J. Miller (AWRE, Aldermaston).

Thanks are due to the Director, AWRE, for permission to publish; the paper does not,

#### REFERENCES

1. SCC No. 3 Explosives Hazard Assessment, Manual of Tests, ERDE, September 1968.
2. Proceedings of the International Conference on Sensitivity and Hazards of Explosives, London 1963. ERDE, Waltham Abbey.

# INITIATION OF DETONATION BY FRICTION ON A HIGH EXPLOSIVE CHARGE

Alan S. Dyer and John Watson Taylor\*  
*Atomic Weapons Research Establishment  
Aldermaston, Berkshire, England*

## ABSTRACT

The initiation of explosion of small blocks of high explosive, a few centimetres in size, has been produced by sliding a flat face of the explosive along suitable surfaces. A specially designed apparatus produced a constant sliding velocity which was imposed from rest in a fraction of a millisecond. The pressure of the sample against the surface was held constant. Initiation was obtained only when grit was present on the surface. From experiments using arrays of isolated grit particles it is concluded that initiation is caused by a co-operative effect of many grit-to-grit contacts. This co-operative effect is considered to arise from the gas produced by slight decomposition around individual grit contacts, and the consequent confining action on the innermost gas-producing regions of the sliding area, leading to easier growth of reaction in these regions. The effect thus involves many 'warm spots' acting simultaneously. In most real situations it would swamp the classical process of growth from a single 'hot spot'.

Separate experiments were carried out using explosive charges with a few tens of centimetres typical dimension. A more complex frictional stimulus was applied in this case by allowing the charge to fall onto a horizontal surface at an oblique angle of incidence. Various degrees of explosive response were observed, depending upon the composition. Detonation resulted in some cases. These findings are compared with those which were obtained with the friction apparatus. It is concluded that the same mechanism of initiation is involved.

## 1.0 INTRODUCTION

It has long been recognised that accidental initiation of an explosive mass nearly always originates from chemical reaction in some very small region of it, with reaction then spreading to the main mass of explosive. It is therefore natural that a very small quantity of high explosive has often been considered sufficient for a test designed to assess the safety of an explosive.

Experience with such tests led to the recognition that with secondary explosives initiation by friction or by impact is relatively difficult. Secondary (solid) explosives were therefore regarded as being relatively free

from handling hazards. Such hazards as might be present were considered to be associated with powdered explosive, which appeared to be required before a significant explosion could develop. Consequently, secondary explosive in charge form was in no way regarded as likely to explode in day-to-day handling.

Occasional accidents with bare charges have subsequently shown the need to qualify this simple view, and have led to the introduction of new tests involving explosive in charge form.

The present paper is concerned with explosive in this form. Firstly it describes a friction apparatus which has been used to

\*Present address: Dept. of Fuel and Combustion Science, The University, Leeds, England.

elucidate the mechanism of frictional initiation, and which may also be used as a convenient safety test. Secondly it summarises the main features of, and results from, a useful large charge test in which frictional initiation is involved. Thirdly it discusses the growth of explosion which follows the frictional initiation process, and which leads to detonation in some cases.

## 2.0 CHARGE FRICTION APPARATUS

The most promising way to study the frictional initiation was thought to be to press a stationary friction surface against a stationary explosive surface, and then suddenly to cause the former to slide on the explosive at constant velocity. This is the basis of the charge friction apparatus. One important consideration was, of course, the need to operate the apparatus safely and this requirement determined several of the features of the design described below.

A high explosive (H.E.) charge sample, usually a 25.4 mm cube, was incorporated into a high-density laminated wooden surround (Jabroc), leaving one flat face of the explosive just protruding from the lower side (Fig. 1). The Jabroc was firmly bolted to the underside of a massive steel block which was constrained to move in a vertical direction only. A piston rested on the steel block making a total mass of (usually) 22.7 kg above the H.E. surface. The whole mass could be pressed downwards by means of compressed air acting on the piston. Remote operation of the apparatus involved a steel table (rotated on a radius of 0.98 m) being slowly raised by a hydraulic jack to the horizontal position when it lifted the

22.7 kg test-assembly off shoulders on which the assembly was supported during attachment of the H.E. The flat face of the H.E. was then resting on a friction surface which in turn rested on the steel table supported from underneath by a strong support-arm. A 45.4 kg weight was also raised remotely. In an experiment the friction surface was jerked in a horizontal direction via a series of linkages which moved suddenly following a suitable impact from the weight. The latter fell from a bomb release down a guide-pole. A high-speed cine photograph was taken through a port in the wall of the firing chamber, and this, together with visual and/or microscopic examination of the abraded or fragmented test sample, constituted the evidence which was obtained from each experiment.

For investigation of the processes occurring at the sample, a relatively sensitive composition, 98/2 HMX/TNT, was used unless otherwise stated.

### 2.1 Further Experimental Details

#### (a) Friction Surfaces

A standard sand/epoxy resin/steel friction surface was prepared by coating a sand-blasted 16 swg mild steel strip with epoxy resin using a roller to obtain an even film. A sieved fraction of British Drug Houses sand (251-295  $\mu$ ) was shaken over the surface of the epoxy film, then the excess sand was shaken off and the resin baked in an oven. The other friction surfaces were prepared by bonding sheet glass, slab H.E. (38 mm wide, 3.2 mm thick) or a thin metal file onto the steel strip in place of

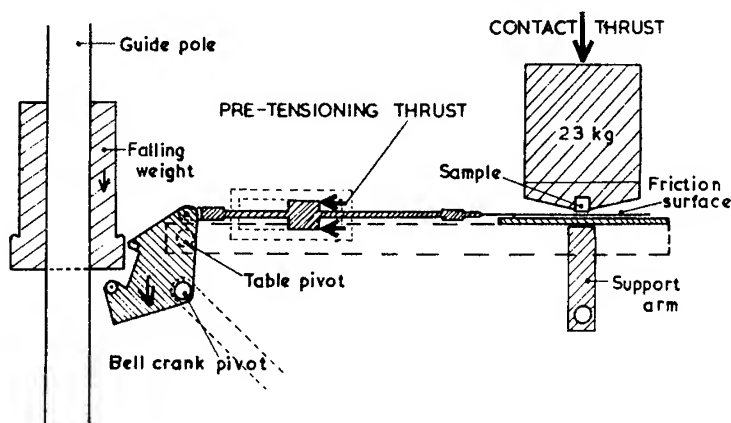


Fig. 1 - Charge friction apparatus (schematic sectional view)

the grit. The single grit particles used in some of the later experiments were approximately  $300\ \mu$  diameter sand particles, fairly rounded particles being selected, using a microscope.

A strip of PTFE  $76\ \mu$  film was interposed between the underside of the friction surface and the steel table to reduce unwanted friction.

#### (b) Constancy of Sliding Velocity

It was found with some H.E. compositions that, at the higher contact pressures, the falling weight could not always overcome the high frictional force. The friction surface tended to decelerate markedly. This effect does not seriously affect the results reported here. In the later experiments it was eliminated by inserting a pretensioning piston/cylinder system into the series of linkages and so providing a horizontal force to balance the sliding friction.

The friction surface accelerated very rapidly from rest, a steady velocity being achieved within 0.3 msec. The velocity remained approximately constant for 10 msec.

#### (c) Action of Falling Weight

The friction surface was linked through the pre-tensioning piston to a bell-crank which converted the impact of the falling weight into horizontal movement of the friction surface. The axle of the bell-crank was given strong support to prevent gross vibration under the impact loading.

#### (d) Self-Protecting Bell-Crank

The pre-tensioning system applied considerable horizontal force to the linkages which were restrained by the friction force between H.E. and sand before and after the friction surface started to slide. This frictional force would vanish in the event of an explosion and the bell-crank would then accelerate away from the falling weight with a self-damaging effect. This eventuality was guarded against by designing a three-armed bell-crank to engage with the falling weight. Then loss of frictional resistance would cause the bell-crank to slightly accelerate the falling weight towards the ground. The falling weight only disengaged from the crank when the crank and linkages had less than 6 mm of travel to a buffer. The weight then continued to fall. It landed on sandbags on a steel plate which acted as a load spreader to more sandbags laid on the concrete floor.

#### (e) Frictional Force Measurement

The frictional force acting between the H.E. and the friction surface was estimated via strain gauges bonded to the 16 swg steel plate.

#### (f) Alignment and Calibration

To ensure that the pressure acting on the H.E. surface was uniform a dummy assembly with a steel block substituted in place of the H.E. was used to check the alignment of the apparatus. The pressurizing cylinder, piston and test assembly were adjusted with shims until the thrust acted normally to the table on which the friction surface slides. When adjustment was complete (i) there was no gap between the steel block and the table before pressurising, and (ii) pressurisation produced an even compression of a lead disc squeezed between the block and the table.

The total thrust acting on a sample was established by calibration at various gas pressures of the vertical loading system, using a proving ring.

To prevent tilting of the H.E. sample assembly during friction on the sliding surface, steel rollers were fitted fore and aft of the 22.7 kg mass.

### 3.0 INITIATION OF EXPLOSION IN THE FRICTION APPARATUS

#### 3.1 High Pressure is Required

The first experiments were carried out with the weight of a 45.4 kg mass as the only source of pressure between the explosive surface and the friction surface. The contact pressure was therefore  $7.0\ \text{kg/cm}^2$ . In addition to the standard friction surface, various patterns and dispositions of the grit were used, such as loose grit on steel, loose grit on bonded grit, and grit bonded in a pattern of spots, but in none of these experiments was explosion observed. Likewise no explosion was detected when normal red match-head composition was placed between the explosive and the friction surface, although in this case occasional puffs of smoke could be seen on the cine film.

For subsequent experiments, compressed nitrogen on the piston was used to press the 22.7 kg test-assembly onto the friction surface, and so provide a greatly increased contact pressure between the explosive and this surface.



TABLE 1  
Frictional Initiation of Various Explosives  
Approximately 600 cm/sec  
(For symbols, see Appendix)

Contact Pressure (kg/cm <sup>-2</sup> )	Explosive, 25.4 mm Cube			
	98/2 HMX/TNT	PBX 9404	60/40 RDX/TNT	60/40/1 RDX/TNT/Wax
513			<u>P</u>	<u>P</u> <u>P</u> p E
432			<u>P</u> <u>P</u> N	N N N
346		<u>P</u>	N N N	
264		<u>P</u>	N	
180		<u>P</u> N		
85.7	E E E E	N N		
64.6	N N N N			
45.0	N			
23.9	N			

Explosions were then observed above a certain minimum contact pressure. Table 1 presents typical results and shows that the contact pressure required to initiate explosion varied considerably with the composition. As might be expected for frictional initiation, a higher sliding velocity facilitated initiation to some extent, so that for such a case initiation was observed at a contact pressure which was lower than that needed at low sliding speeds, see Table 2.

### 3.2 Grit-to-Grit Contacts are Required

In order to throw light on the mechanism of initiation, several other friction surfaces

were investigated. The attempt was made to choose surfaces which would perform only one of the main roles played by the standard grit surface. Thus, sheet glass was chosen to represent the role of a poor conductor, an H.E. slab to represent the embedded smear of H.E. which arises with the standard surface, and a metal file to represent the cutting action which a grit bed produces. None of these surfaces produced initiation under stringent conditions (600 cm/sec, 513 kg/cm<sup>2</sup>). This indicates that the characteristics which they represented are not the essential features which lead to the easy initiation on the grit surface. In a subsidiary experiment involving sand sprinkled on the file,

TABLE 2  
Effect of Sliding Velocity on Frictional Initiation  
98/2 HMX/TNT (25.4 mm cube)  
(For symbols, see Appendix)

Contact Pressure (kg/cm <sup>-2</sup> )	Approximate Sliding Velocity (cm/sec <sup>-1</sup> )		
	150	300	600
180	E E E E E		
138	N N E N		
85.7	N N N N	E E E N	E E E E
64.6		N N N E	N N N N
45.0		N N N N	N
23.9			N

initiation was easily obtained, thus confirming that the high thermal conductivity of the file surface would have been unlikely to have prevented initiation had a cutting action been the essential initiating mechanism. With these possibilities fairly well ruled out, the only remaining possibility of any real consequence concerns the action of grit-to-grit contacts. In several experiments a single grit particle was placed on a glass surface similar to that mentioned above. The glass constituted, of course, a planar, high melting (i.e., 'grit') surface. The particle was positioned under the centre of the explosive sample. An explosion was found to occur soon after sliding commenced. It can thus be concluded, that of all the characteristics of the standard surface, that which is most likely to be responsible for initiation is the characteristic that a source of grit-to-grit contacts is provided. This conclusion is consistent with the well known fact that grit particles may often facilitate ignition of explosives because the high melting point of such particles allows high temperatures at their surface, whereas in the absence of grit, mechanically attainable temperatures tend to be limited to the melting point of the explosive (Ref. 1).

### 3.3 Grit Particles Act Co-operatively

To enable more detailed conclusions to be drawn regarding the action of grit particles in

the standard grit surface, the effect of using several isolated particles on the glass was investigated. They were placed in a regularly-spaced symmetrical pattern on a 15 mm square, 5 or 16 particles being used.

The results of these experiments are given in Table 3. Before discussing them it is important to consider how many grit-to-grit contacts might be involved. The contact pressure usually crushes each grit particle so that many fragments are produced and become embedded in the H.E. By inspection of scratches on the glass plate after a slide with no explosion, these fragments were seen to have been distributed over a radius of 0.3 to 3 mm with occasional minute fragments at up to 6 mm radius. The fragment positions probably become displaced during an experiment, but only in relation to the typical slide distance prior to explosion, and this distance was found here to be not greater than 3 mm. Now, the initial position of a particle in the 5-membered array is no nearer than 10 mm to another particle, or 15 mm in the slide direction. It is therefore clear that fragments from different particles have almost no chance of coming into contact to produce more grit-to-grit contacts than would be expected from five completely isolated crushed particles. In the 16-particle case there might be a small percentage increase in the number of grit-to-grit contacts over the number to be expected from 16 isolated

TABLE 3  
Effect of Grit on Frictional Initiation  
98/2 HMX/TNT (25.4 mm Cube)  
300  $\mu$  sand particles (5 and 16 were in (15 mm)<sup>2</sup>)  
Approximately 600 cm/sec  
(For symbols, see Appendix)

Contact Pressure (kg/cm <sup>-2</sup> )	Friction 'Surface'				
	Glass	Grit on Glass (Number of Isolated Grit Particles)			Grit (Continuous Layer Bonded onto Epoxy Resin)
		1	5	16	
513	N N N	E E E*			
432		N N N			
346		N	E E E E		
264			N N N	E† E E	
180	N	N		E† N N	E E E
138					E E
85.7					E E E E
64.6					N N N

\*Approximately 200 cm/sec.

†16 particles plus one in the centre.

particles, but nevertheless the above conclusion will be approximately valid in this case also.

It can be seen from the results that the contact pressure needed for initiation was significantly lower when additional grit particles were present. Such a co-operative action of isolated grit particles cannot arise from additional grit-to-grit contacts, as we have seen. It must therefore be due to the influence of product gas from the micro-region around one crushed particle, on the processes occurring in the micro-region of another crushed particle. An influence of this kind would act by the gas from one micro-region hindering the escape of gas from a neighbouring micro-region and so allowing the pressure to rise higher than otherwise. This would enable reaction (especially at the innermost grit particle(s)), to develop to a greater extent towards full ignition.

This picture can be extended to the case of a continuous layer of grit particles such as was present on the standard friction surface. Ignition would then be expected to be achieved at an applied pressure which would be very much lower than that needed for initiation by a single grit particle. The last column of Table 3 shows that this is the case. The effect of a single grit particle would be completely insignificant at this lower stimulus level. However, with the layer of particles, the weak generation of gas at many micro-regions, i.e., 'warm spots', over the area of the explosive, would have a mutually amplifying effect. This would operate by the escape of gas near the centre of the area being severely hindered as referred to above for the grit-on-glass experiments. Initiation at the lower stimulus level is thus explained.

The standard surface had, of course, several features which were not simple extrapolations of the grit-on-glass system. For example

the grit layer was bonded in place. It was also several particles deep and so perhaps to some extent 'porous'. However these are minor features which do not seem to form a basis for invalidating the argument.

There seems little doubt that the co-operative mechanism under discussion will be equally relevant to other secondary explosives than the 98/2 HMX/TNT with which it has been investigated. Likewise, the picture can be extended with some confidence to certain other friction surfaces, including those which have practical importance such as bare concrete.

#### 4.0 OBLIQUE IMPACT OF LARGE CHARGES

The experiments which have been described above involved charges of a few centimetres typical dimension. This relatively small size would be likely to limit the intensity of explosive reaction which could develop. There is essentially no such limitation in the work which is summarised below. It involved charges which had a few tens of centimetres typical dimension.

A bare charge was allowed to impact a horizontal surface at an oblique angle of incidence, usually  $45^\circ$ . A frictional stimulus of some kind was therefore produced at the same time as a high (impact-derived) contact pressure. Hemispheres of H.E. weighing 11.3 kg or more were used. They were swung on long thin wires to strike a sand/epoxy surface (or occasionally another surface) at the desired angle (Fig. 2). Very low drop heights sometimes resulted in explosion, and in some cases detonation (see Table 4). By contrast initiation by vertical drop required at least an order of magnitude greater drop height, e.g., one experimental composition detonated after 0.3 m

TABLE 4  
Oblique Impact of Large Charges  
22.7 kg nominal

(For symbols, see Appendix)

Drop Height (metres)	Explosive			
	PBX 9404	Baratol	60/40 RDX/TNT	60/40/1 RDX/TNT/Wax
3.0				N N N p
1.5	H	<u>P</u>	<u>P</u> <u>P</u>	N
0.9	H N	p	N N p	
0.6	N			

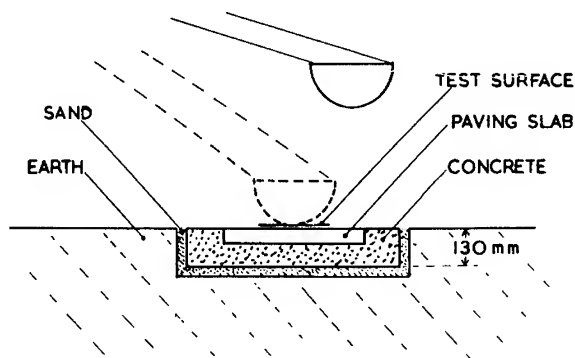


Fig. 2 - Oblique impact of large charges

drop and  $45^\circ$  incidence, but only after a 3.0 metre drop vertically. Investigation of the mechanism of initiation was directed towards deciding whether it was frictional and whether the position of initiation was at the charge surface.

#### 4.1 A Frictional Mechanism

As we have seen, impact initiation was greatly facilitated if an oblique angle of incidence was used. This effect is very difficult to explain other than by assuming that friction on the surface was the primary cause of initiation. Other confirmatory evidence was obtained:

(i) Water was poured over a concrete target slab prior to the experiments. In the absence of water, initiation would have been produced easily. However no initiation was observed, as might be expected by water providing lubrication and thus reducing friction, and/or providing heat sink effects.

(ii) Epoxy-resin/steel was compared with the standard sand/epoxy-resin/steel surface. Initiation only occurred on the latter, as might be expected for a frictional mechanism, since much higher temperatures can arise at grit-to-grit contacts.

#### 4.2 Initiation is at the Charge Surface

In a series of experiments small amounts of water were used to lightly wet the standard friction surface. In no case was initiation prevented, but in four out of six experiments the explosive event was markedly less powerful than with a dry grit surface. Such a controlling influence of the surface conditions could hardly occur if the point of initiation were some

distance inside the charge, and hence it is clear that the event initiates at the charge surface.

#### 4.3 Initiation Compares with that in Friction Apparatus

The initiation is thus a surface frictional effect which is greatly facilitated by the presence of grit, and which occurs whilst there is a high contact pressure produced by the impact. These surface conditions are clearly very similar to those which are present when initiation occurs on the friction apparatus. With the large charges, the frictional stimulus is somewhat more complex, in that sliding occurs under a contact pressure which rises to a peak and then may fall to zero. However this would not be expected to alter the essential nature of the process. We therefore conclude that the same initiation mechanism applies in the two cases.

### 5.0 GROWTH TOWARDS DETONATION

#### 5.1 Explosion Magnitudes

The effects following initiation varied greatly from explosive to explosive. Thus it was found that with some explosives there might be little more than a puff of gas produced, whilst with other explosives a very intense explosion would result. This was the case with both the small samples of the friction apparatus and the large charges of the impact experiments.

These effects were most marked and require further study. It will merely be noted here that they are clearly very relevant to the subject of explosion hazard. The empirical characteristic which is involved may be referred to as the 'explosiveness' of the system, and should be considered along with 'sensitivity' in any comprehensive assessment of explosion hazard.

Only a limited correlation was found between the 'explosiveness' in the small scale and that in the large scale experiments, as might be expected from the very different environments which the two systems provide for the growing reaction. Thus, factors such as area of contact, pressure of contact, strength of adjacent medium, etc., probably have an effect. Tables 1 and 4 give an indication of the types of explosion which were observed. Detonation is considered to have been attained in the case of the high order explosions of the large charges (Table 4), whilst with the friction

apparatus the detonation stage was never reached.

## 5.2 Principal Stages of Growth

These observations as a whole, appear to be explicable in terms of variation in the extent of occurrence of a sequence of processes rather than differences in their essential nature. The study of one particular composition is thus regarded as throwing light on the behaviour of secondary explosive charges in general. Whilst lacking positive proof as to the mechanism of growth subsequent to frictionally induced gas generation, the principal stages appear to be as follows:

(i) an ignition at the confined (contact) surface of the charge, leading to violent gas evolution;

(ii) a resulting pressure build-up which breaks up the charge, often with a violent crushing action;

(iii) consequent gas penetration to the internal surface, which therefore becomes ignited and gives a still more rapid gas production.

The extent of occurrence of any of these processes would depend upon the details of the system, especially upon its confinement, since the latter controls the pressure release.

An example of the way in which a small variation of the effective confinement of the reaction, may affect the magnitude of the explosion, is provided by results obtained with the friction apparatus using smaller samples of explosive. Thus, 12.7-mm cubes of 98/2 HMX/TNT were used instead of the usual 25.4 mm cube samples, so that the area in contact with the grit was only 12.7 mm x 12.7 mm. In contrast to the powerful explosions which usually occur with this composition, initiation led to quite mild explosions, considerable amounts of explosive often remaining unconsumed, see Table 5.

One supplementary experiment with a 25.4-mm cube sample but with a 6.3 mm x 25.4-mm contact area (achieved by a grit-coated 6.3-mm-width steel bar attached to the friction plate) also gave a very weak explosion. With the smaller confined area which was present in these experiments, the gas pressure would rise more slowly, and correspondingly less internal surface area of explosive would be exposed by the disruptive effect before the pressure release occurred. This would lead to an explosion of smaller magnitude, as observed.

TABLE 5  
Frictional Initiation of Small Samples  
98/2 HMX/TNT (12.7 mm cube)  
Approximately 600 cm/sec  
(For symbols, see Appendix)

Contact Pressure (kg/cm <sup>-2</sup> )	Result
148	<u>P</u> p
96.3	N N p <u>P</u>

## 6.0 FURTHER DISCUSSION OF INITIATION MECHANISM

### 6.1 Background Frictional Heating

From microscopic inspection of the glass plate after a sample has failed to initiate, traces of explosive were seen adhering to parts of the glass in a thin layer, with unmistakable signs of previous melting. In addition the sample surface had all the appearance of having been molten over the whole area and had a high polish. Likewise, from examination of the smear of embedded H.E. which remained after sliding on the standard surface, further clear indication of substantial melting was obtained.

Sliding on glass and sliding on the standard grit surface therefore both involve extensive melting of the explosive over most of the area of the sample. This indicates considerable heating over the surface as a whole, quite apart from the above mentioned gas generation processes occurring at individual grit particles. The heating on the standard surface can be assessed from approximate frictional force measurements which indicated a coefficient of friction in the region of 0.4. This value corresponds to a total heat generation in the range 5-25 cal cm<sup>-2</sup> during the 10 msec test interval. From these facts it seems likely that the gas-generating (and hence initiating) effect of individual grit particles will be facilitated to some extent by the background heating which occurs.

### 6.2 Time Delay to Initiation

The time required for initiation on the friction apparatus was estimated from the cine film record. In the case of a grit-on-glass surface, the time was usually less than one inter-frame time (~0.5 msec). When the standard sand/epoxy/steel surface was used the delay time tended to be slightly larger than with grit-on-glass for the same contact pressure. It decreased with increase of contact pressure,

TABLE 6

Contact Pressure (kg/cm <sup>-2</sup> )	Friction 'Surface'								
	Glass	Grit on Glass (Number of Isolated Grit Particles)						Grit (Continuous Layer Bonded onto Epoxy Resin)	
		1		5		16			
513	N N N	<0.5	<0.5						
432									
346				~0.5 <0.5 ~0.9					
264						<0.5	<0.5		
180							<0.5	2.5	1    1.5
138								7	3.5
85.7								7.5	~8    7    8
64.6									

### 6.3 Overall Frictional Initiation Mechanism

Some of the delay times can be seen to be relatively quite large. This fact requires a different explanation. These delays correspond to the sample having moved a significant distance which would place it outside the initial contact area before explosion occurs, approximately 4 msec being required to move one sample width.

some extent despite the smear of explosive which is continuously deposited on the grit layer. The heat loss rate from the contact area should therefore decrease as the slide continues. In other words the co-operative gas generation process at the grit-to-grit contacts should experience a progressively slower heat-loss to the matrix, until the former becomes manifest as an explosive event.

(i) gas generation by micro-decomposition at many transient grit-to-grit contacts;

(ii) a co-operative action of these which causes the innermost contacts to lose gas more slowly than otherwise, and hence to become more akin to classical 'hot spots';

(iii) a background heating, superposed on the whole, and which in time produces a much slower loss of heat from these 'hot spots'.

After some delay time, such features would favour a runaway reaction (ignition). The latter would arise at those innermost grit-to-grit contacts which happened to be rubbing together at that time.

## 7.0 ACKNOWLEDGMENTS

It is a pleasure to thank Mr. G.P. Cachia for helpful discussion. The large charge experiments were organised in a most notably

efficient way by Mr. R. Owen and Mr. D. Clarke at A.W.R.E. Foulness. The friction apparatus experiments were performed at A.W.R.E. Aldermaston where Mr. J.D. Butterworth assisted considerably in overcoming some of the early difficulties. The authors are grateful to the Director of A.W.R.E. for permission to publish this work, which however does not necessarily represent that Establishment's views.

#### APPENDIX

##### Symbols for Explosion Magnitude

Relative categories, one experiment type:

H  $\equiv$  High order explosion;

E  $\equiv$  Explosion;

P  $\equiv$  Partial explosion;

p  $\equiv$  Small partial explosion;

N  $\equiv$  No explosive event.

#### REFERENCE

1. F.P. Bowden and A.D. Yoffe, "Initiation and Growth of Explosion in Liquids and Solids", Cambridge (1952).

## DEFLAGRATION IN SINGLE CRYSTALS OF LEAD AZIDE

M. M. Chaudhri and J. E. Field  
*Surface Physics, Cavendish Laboratory*  
*University of Cambridge, England*

### ABSTRACT

A study has been made of the initiation and propagation of fast chemical reaction in single crystals of lead azide using high speed framing photography. It is shown that sufficiently thin crystals of lead azide deflagrate with a velocity of propagation which depends on the minimum dimension of the crystal: the velocity increasing with crystal thickness. However, above 215 microns and up to the largest size studied (670 microns) the propagation velocity remains approximately constant at about 2,900 m/sec. A high magnification examination of deflagrating crystals sustaining a reaction has shown that stress waves and fractures can travel ahead of the reaction zone. In some situations fracture ahead of the front affects the growth of the fast decomposition; however, initiation of fresh reaction sites was not observed. The shocks produced by the fast decomposition were not strong enough to sustain reaction. It is suggested that the energy from the decomposing layers is transmitted to neighbouring undecomposed layers by conduction of heat. This means that the upper limit of the propagation velocity should be equal to the velocity of sound in the crystal. The experimental results support this model.

### INTRODUCTION

If chemical reaction is initiated at a point in an explosive by a small thermal stimulus, under suitable conditions fast decomposition may propagate throughout the explosive. Initiation of fast decomposition produces pressure waves, which travel through the explosive at a velocity at least equal to its velocity of sound. If the propagation of fast decomposition is subsonic, then the pressure waves will interact with the undecomposed explosive ahead of the reaction front, and may cause either a non-uniform rate of growth or initiation of decomposition at points distant from the advancing front, as has been observed in granular and cast explosives (1,2).

Using a one-dimensional equation of conduction of heat, Griffiths and Grocock (1) predicted that the maximum rate of combustion in granular high explosives should be about 1 m/sec. This value is very low compared with measured values of the order of 1 km/sec. To explain this discrepancy they suggested that

permeation of gaseous reaction products through the interstices was important (see also (3)). However, this theory is clearly not applicable to a single crystal. The object of this present work was an investigation of the mechanism of propagation of reaction in single crystals.

A high speed photographic study of combustion and deflagration is a suitable approach to the problem. Evans and Yoffe (4) were able to follow the combustion of single crystals of some of the primary explosives with a high speed camera. They found that the combustion velocity depended upon the thickness and the nature of the crystal. Velocities for the crystals they studied were only of the order of a few m/sec. It is believed by several workers (3,5) that the primary explosive lead azide detonates immediately after being ignited and that a burning regime is absent. However, our experiments show that this idea needs modification.

The amount of work on the measurement of the propagation velocity of fast decomposition



in lead azide is very little. There is also no published work regarding the mode of propagation in lead azide single crystals. Bowden and McLaren (6) measured the detonation velocity in pressed unconfined sheets of lead azide of different thickness and successfully explained the results using Jones (7) theory. The only reported work on single crystals of lead azide is that of Strömsoe (8); however, the single crystals he used were very non-uniform and it seems possible that this affected the results in an unknown manner.

The high-speed framing camera investigation described here shows that in sufficiently thin lead azide crystals burning does occur. The propagation velocity increases with the thickness of the crystal, but becomes constant for crystal thickness in the range 215–670  $\mu\text{m}$ . In a deflagrating crystal the fast reaction progresses continuously with no new initiation sites produced ahead of the front. A qualitative model, based on heat conduction, is suggested to explain these observations.

## EXPERIMENTAL

Single crystals of lead azide ( $\alpha$  and  $\beta$ ) were prepared by a diffusion method (9). The crystals were identified using X-ray methods. The lead azide crystals used for the propagation studies were of the  $\beta$  form for thicknesses up to 70  $\mu\text{m}$  and the  $\alpha$  form for the thicker sizes. It was found difficult to grow suitably long  $\alpha$  crystals with thickness less than about 100  $\mu\text{m}$ : with the diffusion method used long crystals were invariably also thick. Single crystals of silver azide were prepared by recrystallizing silver azide from an ammonical solution.

Bowden and McLaren (6) and Strömsoe (8) measured the propagation velocity in lead azide with a drum camera. In this study a framing camera was used for the following reasons. Firstly, when an unconfined single crystal is deflagrating at about 2000 m/sec, then products of decomposition go ahead of the reaction zone (see (10)). It is clear that the trace on a drum camera film may not be an accurate position-time record of the flame front. Secondly, phenomena such as the formation and propagation of cracks can take place ahead of the reaction front. An examination of their influence on the growth of burning is best made by framing photography. The rotating mirror framing camera used was a Beckman and Whitley model 189 camera, capable of photographing at a rate of 4 million frames/sec with a total number of frames of 25. The event was illuminated

externally by discharging a bank of condensers charged to a potential of 2.5 kv through a Mullard F.A.5 xenon-filled tube, the total energy discharged being 150 Joules. The duration of the light flash from the discharge tube was sufficiently small so that double exposure of the film did not occur even at the maximum rotation speed of the mirror.

The needle-shaped crystals were placed on microscope glass slides and held in place by adhesive. A 50  $\mu\text{m}$  diameter platinum wire was laid across the crystal near the glued end, and also glued to the glass slide such that it made good contact with the crystal. A schematic diagram of this arrangement is shown in Fig. 1(a). A high-energy electrical pulse was discharged through the platinum wire causing the ignition of the crystal and allowing synchronization of the event with the camera.

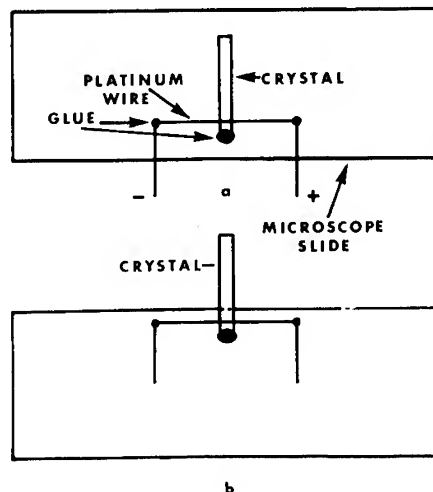


Fig. 1 - The schematic arrangement for the mounting and ignition of the crystal

In the arrangement shown in Fig. 1(a) it is possible that the stress waves in the glass (velocity of stress waves in glass > velocity of stress waves in lead azide) may cause fractures in the crystal ahead of the decomposition front and thus make the interpretation of the results difficult. This disadvantage was removed by using the arrangement shown in Fig. 1(b). Most of the measurements were made using this form of mounting.

It was observed that the decomposition front for crystals up to 70  $\mu\text{m}$  in thickness was fairly distinct. However, for thicker crystals

the decomposition front was obscured by reaction products. In order to hold back the products of reaction, crystals of thickness  $> 100 \mu\text{m}$  were confined by water. To minimise any hydrolysis of the crystals, the crystals were left in water for as short a time as possible before making the experiment. The crystals were ignited under water in the way described above.

Propagation of reaction in crystals at  $100^\circ\text{C}$  (in air) was also studied. A special furnace was used for this purpose. It consisted of a ceramic tube 0.15 m long and 0.1 m in diameter with 2 flat glass windows radially opposite to each other so that the combustion of the crystal could be photographed with back lighting. A piece of nichrome wire wound uniformly round the tube was the heating element. The mounted crystal was first placed inside the furnace and then electric current passed through the wire. The time taken to reach  $100^\circ\text{C}$  inside the furnace was only 5-6 minutes. It was assumed that during this time only a very small amount of decomposition of the crystal took place.

A photographic examination at a high magnification ( $\times 10$  on the film) was made of a region just ahead of the decomposition zone of a deflagrating crystal. The high magnifications were achieved by using a projection microscope in conjunction with the camera. However, it was found necessary to confine the crystal by a transparent fluid (we used water) to get distinct photographs. The working distance of the microscope was about 30 mm and therefore a small transparent cell of 'perspex' (lucite) was used in which the crystal was exploded under water and the mode of propagation of reaction photographed.

The crystals used in the experiments were typically 10 mm long, were reasonably transparent and those chosen were free of any macroscopic defects. In the high magnification studies the field of view of the camera was only a few mm. The region of the crystal chosen for observation was about 2 mm from the platinum wire, which was at one end of the crystal and out of the field of view of the camera. This arrangement ensured that reflected tension waves from the far end did not reach the region under observation until after the burning front.

## EXPERIMENTAL RESULTS

Fig. 2 shows the initiation and propagation of fast decomposition in a  $\beta$ -lead azide crystal. The crystal was mounted as shown in Fig. 1(a). Its dimensions are  $16.7 \times 0.175 \times 0.022 \text{ mm}^3$ .

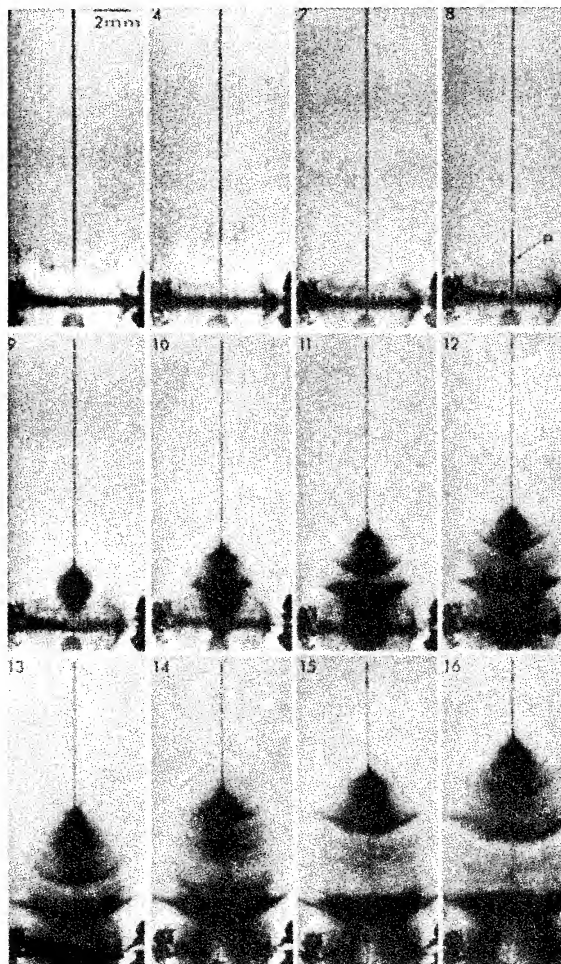


Fig. 2 - The propagation of fast reaction in a thin  $\beta$ -lead azide crystal in air, mounted as in Fig. 1(a).  $1.0 \mu\text{sec}$  between consecutive frames.

Except for the point of initiation (see frame 8), which is about 2.2 mm from the exploding wire, this sequence shows typically the propagation of a fast decomposition in thin (less than  $70 \mu\text{m}$ )  $\beta$ -lead azide crystals mounted in the manner shown in Fig. 1(a). It is believed that even though the point of initiation of fast decomposition in this crystal is not located under the wire, initiation is still thermal in origin. Frame 1 shows the crystal and the exploding wire (the wire started burning rapidly 2-3  $\mu\text{sec}$  before frame 1). It can be seen that the crystal is fairly uniform. It is very likely that as the hot vapours of the wire spread over the crystal they heat its surface to a sufficiently high temperature. In frame 8 a black spot has appeared on the crystal at P about 2.2 mm from the wire. By comparing frame 8 with frame 4, it is clear

that the hot vapours of the exploding wire had reached P before the crystal ignited at this point. The remaining frames then show the propagation of explosion on both sides of P. It will be noted that the front of the reaction zone is reasonably distinct. The velocity of propagation in this crystal is uniform, with a value of 1000-1100 m/sec. Two other interesting observations can be made from this sequence. Firstly, that in frame No. 16 the crystal seems to have developed deformation ahead of the flame, and secondly, that after reaction has passed a mark is left on the glass slide which is almost equal in width to that of the crystal (see frame 16). It was found by examining this mark under an optical microscope that it was due to very small particles of lead.

Other results showed that the velocity of propagation increased with crystal thickness (i.e., the minimum dimension). Variations in width did not produce noticeable changes in velocity if the thickness of the crystal was greater than 20  $\mu\text{m}$ .

Table 1 gives the average propagation velocity for crystals of different thicknesses under different conditions. Some results for silver azide single crystals are also presented. A few measurements given in this table are for crystals which were initiated under water by mild shocks (a few kbars) and this is indicated in the table; all other observations were on crystals ignited by exploding platinum wires.

TABLE 1

The Average Propagation Velocity for Lead Azide and Silver Azide Single Crystals of Different Thicknesses Under Various Conditions. The Uncertainty in the Velocity Measurements is  $\pm 100$  m/sec.

Thickness of Crystal Microns ( $\mu\text{m}$ )	Velocity (m/sec)			Initial Velocity of the Water Shock (m/sec)	Strength of Initial Water Shock (kbars)
	In Air At Room Temp	Under Water	At 100°C		
$\beta$ -lead azide (mean of 4 observations)					
18	980	—	—	—	—
22	1070	—	—	—	—
28	1110	—	—	—	—
34	1320	1030	—	—	—
39	1300	1100	1770	—	—
45	1210	—	—	—	—
50	1740	—	—	—	—
56	—	1000	—	—	—
61	1620	—	—	—	—
$\alpha$ -lead azide (individual observations)					
168	—	1200 (initiated by shock)	—	—	—
215	—	2800 (initiated by shock)	—	—	—
280	—	2850 (initiated by shock)	—	1670	1.3
310	—	2500	—	1670	1.3
560	—	2900	—	1720	2.0
670	—	2620	—	1900	3.5
Silver azide (mean of 4 observations)					
67	880	—	—	—	—
168	1040	—	—	—	—
185	—	780	—	—	—

Table 1 shows that the average propagation velocity of unconfined  $\beta$ -lead azide crystals (i.e., in air) rises gradually from 980 m/sec for 18- $\mu$ m-thick crystals to 1600-1700 m/sec for crystals 50-60  $\mu$ m in thickness. The effect of confining the crystals by water is to reduce the propagation rate. This effect is more pronounced on relatively thick crystals: a 56- $\mu$ m-thick crystal which deflagrates at about 1700 m/sec in air slows to 1000 m/sec in water. On the other hand, initial high temperature of the crystal increases the velocity from 1300 m/sec at room temperature to 1770 m/sec at 100°C for 39- $\mu$ m-thick crystals. These observations suggest that the heat losses from a deflagrating crystal influence its propagation velocity considerably. It will also be noted that a 60- $\mu$ m-thick  $\beta$ -lead azide crystal reacts at almost twice the rate with which a silver azide crystal of similar thickness reacts. Thicker crystals ( $\alpha$ -lead azide) give more striking results. A 168- $\mu$ m-thick crystal deflagrates at 1200 m/sec (in water) but a 215- $\mu$ m crystal reacts at 2800 m/sec. With further increase in the thickness of the crystal the propagation velocity does not increase and remains constant at 2500-2900 m/sec. This is so for crystals up to 670  $\mu$ m in thickness. It is interesting that even 'aged' crystals (aged in dark up to 14 months) gave the same propagation rates as fresh crystals (up to 3 days old). The experiments made under water also allowed measurements of the velocity of the shock transmitted from the deflagrating crystal to water.  $\alpha$ -lead azide crystals which deflagrate at a constant rate transmit shocks to the water with an intensity which depends upon the thickness of the crystal. For example, crystals 280-310  $\mu$ m in thickness transmit shocks of about 1.3 kbars to the water, whereas a 670- $\mu$ m-diameter crystal transmits 3.5 kbar shocks.

Figure 3 shows a sequence of photographs of a crystal deflagrating under water. The crystal, C, is held in position under water by the platinum wire, W (see frame 1). The crystal is 6 mm long and 670  $\mu$ m in diameter except for the final 1 mm which has a diameter of 450  $\mu$ m. Frames 2-4 show the start of the explosion of the wire and in frame 5 the crystal ignites at A. The next 3 frames show a uniform rate of growth of deflagration in the crystal at 2620 m/sec. The shock produced is quite strong and stress waves travelling in the supporting 'perspex', P, can be seen in frames 7 and 8. These waves produce fracture (frame 8). The production of fractures in solids by explosive loading has been examined in earlier work (11).

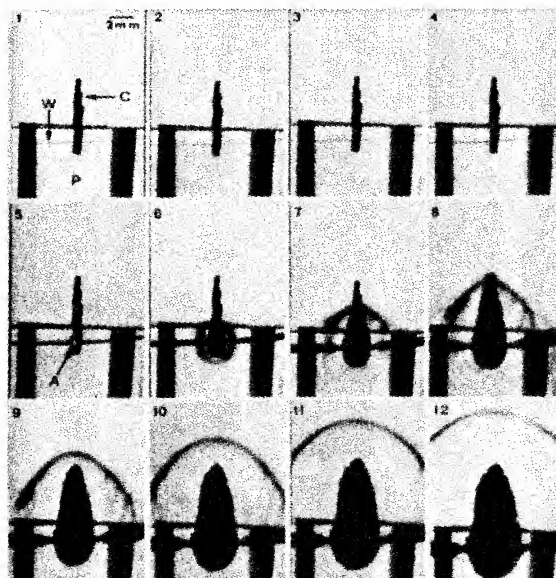


Fig. 3 - Propagation of fast reaction in a thick  $\alpha$ -lead azide crystal under water. Frame interval 0.7  $\mu$ sec.

#### THE STOPPING OF A PROPAGATING REACTION

It was found that in deflagrating  $\beta$ -lead azide crystals cracks can be produced ahead of the reaction front, and that these cracks can then influence the development of the chemical reaction. This effect was most pronounced for thicknesses less than 20  $\mu$ m. Figure 4 shows a sequence for a crystal of dimensions  $8.9 \times (0.45 - 0.25) \times 0.017$  mm<sup>3</sup>, mounted as in Fig. 1(b). Rapid heating of the wire, W, starts in frame 2 which leads to initiation of fast reaction in the crystal, C, in frame 4. The fast reaction propagates at a speed of  $\sim 1000$  m/sec (frames 4 and 5). However, in frame 5, a crack is formed across the width of the crystal at F (1.2 mm from the edge of the glass slide). By comparing frame 4 with frame 5, it is clear that the crack formed between these frames. The chemical reaction then travels up to this crack, but does not go further (frames 6 and 7). The later frames show the 'spalling' and break-up of the far end of the crystal.

If a crystal, besides being 17  $\mu$ m or less in thickness, is about 90  $\mu$ m or less in width then fast decomposition may not travel the whole length of the crystal. For thicknesses as low as 10  $\mu$ m reaction fails for widths less than 60  $\mu$ m. To find the possible reasons for the

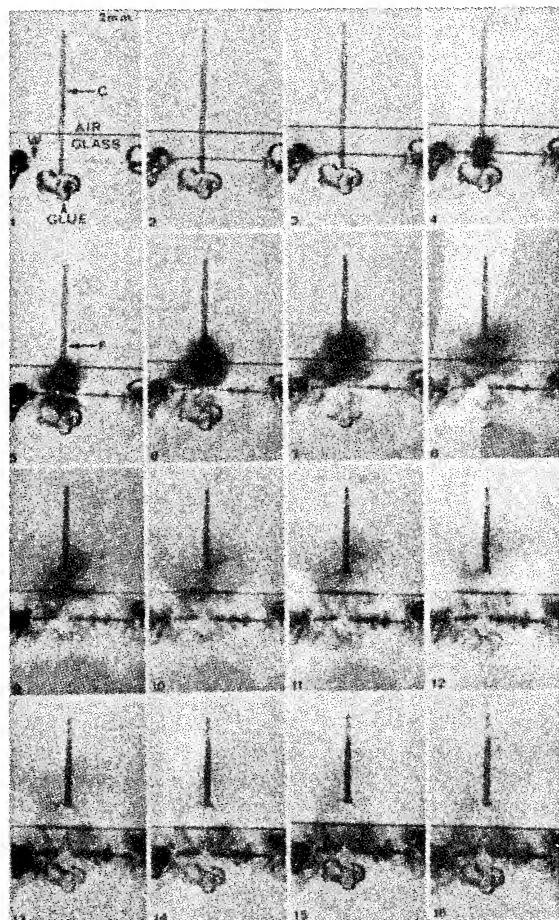


Fig. 4 - A thin  $\beta$ -lead azide crystal. The deflagration stops at a crack formed ahead of the reaction front. Frame interval 1.0  $\mu$ sec.

failure of propagation of reaction, experiments were performed on crystals which gradually reduced in thickness and width from sizes greater than the critical dimensions mentioned above. A typical sequence showing propagation

in such a crystal is shown in Fig. 5. The thickness of the crystal under the platinum wire is 14  $\mu$ m and its width is 112  $\mu$ m; the crystal is 5.3 mm long. The first 3 frames show the rapid heating of the wire. Fast decomposition starts between frames 3 and 4; the propagation velocity as measured from frames 4 and 5 is 1000 m/sec. In frame 5 the crystal seems to have deformed near the free end. This deformation becomes more pronounced in the next frame. The reaction fails at P where the crystal dimensions are 0.08 x 0.017 mm<sup>2</sup>. The last few frames show the fragmentation of the crystal. In two other such experiments the dimensions of the crystals where the reaction stopped were 0.084 x 0.017 mm<sup>2</sup> and 0.072 x 0.017 mm<sup>2</sup>. In all these experiments the crystals used were geometrically 'good', and each was about 5 mm long. After reaction initiated under the exploding wire in these crystals, it propagated for about 3  $\mu$ sec. During this time the stress waves travelling at the velocity of sound would have reflected as tension waves from the far end. It is possible that the interaction of these reflected waves may have helped in fracturing the crystal, and thus produced conditions under which the propagation of the reaction was difficult.

To show that the failure of propagation in very thin needles is not related to the method of initiation (i.e., exploding wire), experiments were undertaken with very thin but geometrically 'good' and uniform crystals: initiation of reaction was achieved by a red hot wire rather than by an exploding wire. In these experiments a thin  $\beta$ -lead azide crystal 10.0 x 0.056 x 0.012 mm<sup>3</sup> was placed on a microscope slide so that about 0.5 mm of its length projected outside the slide. Another slide was placed on the first with spacers between them. The crystal was ignited on the end projecting from the slides by touching with a red hot, gauge 30, nichrome wire. However, the whole of the crystal was not consumed. In fact, a part of the crystal was broken into many fragments of which most were

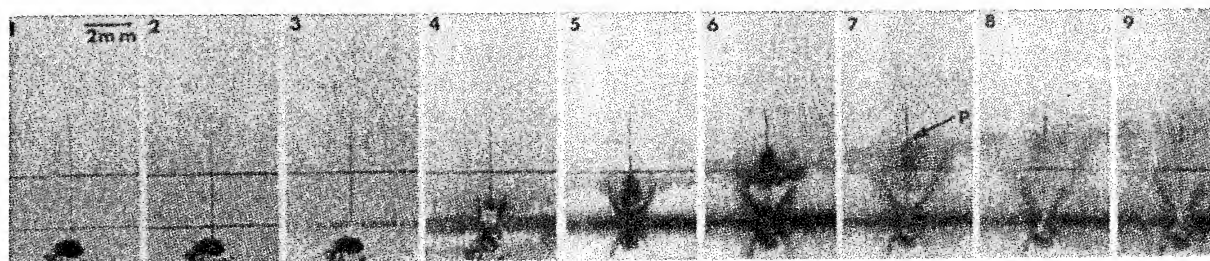


Fig. 5 - A typical sequence showing the failure of propagation of reaction in a thin tapered  $\beta$ -lead azide crystal. Frame interval 1.0  $\mu$ sec.



undecomposed. The dimensions of the fragments were measured and the results of two such experiments are given in Table 2.

TABLE 2

Original Size (mm)	Length of Fragments (mm)	Combined Lengths (mm)
10.0x0.056x0.012	3.4, 1.4, 1.3 1.2, 0.2, 0.2	7.7
7.1x0.062x0.012	3.9, 0.5, 0.4	4.8

It is obvious that the explosion could have travelled only in the unrecovered part of the crystals, that is, the original length minus the combined length of recovered fragments. If we assume that fast reaction in these thin crystals travelled at a speed of 1000 m/sec then in both these crystals the reaction propagated for at most 2-3  $\mu$ sec. During this time the stress wave waves, produced at the instant of initiation of reaction, could not have reached the free end of the crystals. This indicates strongly that the failure of propagation of fast reaction in very thin crystals is most likely attributable to the outgoing stress waves, produced by the initiation of reaction.

#### HIGH MAGNIFICATION STUDIES

The examination of deflagrating crystals at high magnification showed various interesting features. The dimensions of the  $\beta$ -lead azide crystal shown in Fig. 6 are 7.1x0.291x0.034 mm<sup>3</sup>, but only a 2.75-mm-long region appears in the field of view. The platinum wire is 2.8 mm outside the frame to the right. The whole of the crystal including the exploding wire is under water. Frames 1-3 show the crystal before the wire exploded. About 3  $\mu$ sec before frame 11 fast reaction was initiated in the crystal. In frame 11 the reaction is just entering the field of view from the right-hand side. Many cracks can be seen ahead of the flame, but no fast reaction initiates at these cracks. A black spot at P can also be seen but it does not appear that fast decomposition starts here, and the shape of the expanding reaction products supports this view. It is difficult to find in these pictures the points from where the cracks initiate. (That is, whether from the surface away from the flame or at the products/crystal interface.) Frame 12 shows that these cracks move in the direction of propagation of the reaction. Some of these cracks appear to move at about 360 m/sec. It seems that in the next frame the flame overtakes the cracks, and then continues to propagate into the uncracked region. The velocity of propagation as

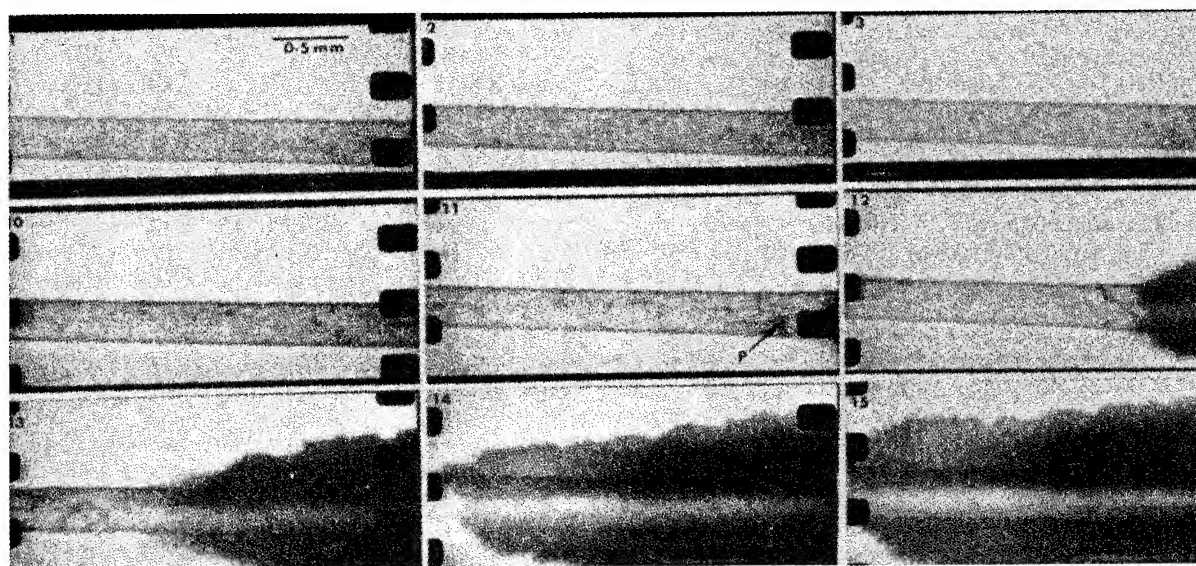


Fig. 6 - High magnification sequence of a  $\beta$ -lead azide crystal deflagrating under water. Fractures occur ahead of the front. Frame interval 1.0  $\mu$ sec.

measured from frames 12, 13 and 14 is 900 m/sec.

Another point of interest concerning the mode of propagation of reaction (see frames 12-15) is that as the reaction progresses, it leaves behind an 'object' which has a sharp boundary and whose width is 1.12 x the original width of the crystal. This boundary does not expand during the 4-5  $\mu$ sec after frame 12, it is not known what happens to it afterwards since the products of decomposition completely cover the field of view and nothing remains distinct in the later frames. It appears unlikely that this boundary shows the partially decomposed crystal because if it were so, we would have observed its further decomposition with time. It appears to be completely inert and it is possible that this boundary is due to lead particles produced during the decomposition (c.f. Fig. 2). This boundary starts at the reaction products/crystal interface (frame 12). These observations suggest that the decomposition of the crystal is complete very close to the reaction front.

Examination of enlargements of frame 12 revealed no evidence for permeation of gaseous products through the cracks and it thus seems unlikely that this process is important here.

## DISCUSSION

It is possible from these experiments to draw a number of conclusions. It has been shown that in thin  $\beta$ -lead azide crystals the velocity of propagation of reaction is smaller than the velocity of the longitudinal stress waves in these crystals. The reaction process is therefore a deflagration and not a detonation. An interesting consequence of this is that the stress waves can produce fractures in the crystal ahead of the reaction zone. The fracturing of deflagrating crystals can have various effects on the subsequent propagation of reaction. In very thin crystals reaction does not propagate below certain critical dimensions. In Fig. 4 there was clear experimental evidence that a fracture formed ahead of the flame could stop reaction. It is suggested that the failure of propagation of reaction in very thin  $\beta$ -lead azide crystals is most probably because of the formation of fractures ahead of the flame by stress waves caused by the reaction. The heat transfer from the reaction zone to the undecomposed part of the crystal across the crack will be much reduced. This then results in the cessation of the self-sustaining reaction.

The deflagration velocity increased with the thickness of the crystal (see Table 1). This

may be explained on the basis of thermal losses to the surroundings. The increase in the propagation speed when the crystal ambient temperature is increased to 100°C supports this.

It is interesting to compare our measurements with those of Bowden and McLaren (6) in compressed sheets, and those by Strömsoe (8) in single crystals (the morphology of Strömsoe's crystals was not given). Our values are the lowest for almost all thicknesses. The velocity in the present experiments rises gradually with thickness, but for thickness in the range 215-670  $\mu$ m it becomes constant and this value is in the range 2500-2900 m/sec. On the other hand Strömsoe obtained a velocity of 3300 m/sec for a crystal 332  $\mu$ m in thickness and Bowden and McLaren obtained a value of 5500 m/sec for a film thickness of 500  $\mu$ m. Strömsoe attempted to explain his experimental results on the theories of Jones (7) and Eyring et al. (12), but did not get an agreement between theory and experiment. He suggested that the mechanism of propagation must take into account the formation of reaction centres ahead of the flame. However, it should be emphasized that the Jones and Eyring theories can only be applied to those cases in which the non-ideal detonation velocity is not very different from the ideal detonation velocity.

The fact that the velocity of propagation in our experiments seems to be constant for crystals of thickness in the range 215-670  $\mu$ m does not mean that this is an ideal detonation velocity. The experiments with water confinement showed that relatively weak water shocks were produced (3.5 and 1.3 kbars for 670- and 280- $\mu$ m-thick crystals respectively). This suggests that the pressure in the reaction front is well below the shock pressure required to detonate a homogeneous single crystal. In pressed sheets of lead azide, however, shocks of the order of a few kbar can possibly cause initiation of reaction by compressing the gas spaces present in between the grains and in this manner sustain fast reaction. A different mechanism is required to explain our values.

In other experiments (9) it has been found that the velocity of longitudinal stress waves in a  $\beta$ -lead azide is in the range 1850-2450 m/sec. If we assume that it is approximately the same for  $\alpha$ -lead azide crystals, then a reaction speed of 2500-2900 m/sec is close to the stress wave speed for these crystals.

The question remains as to how deflagration in single crystals of lead azide travels at speeds in the range 1000 to 2900 m/sec. Bowden and Yoffe (5) proposed that in single crystals such

high-velocity reactions can be explained if shock waves travelling ahead of the flame front produce centres of reaction at defects and voids in the crystals. The high magnification photographs (Fig. 6) clearly show the zone just ahead of the flame front of deflagrating crystals. The crystal breaks and the cracks move at high speeds, but there is no initiation of reaction at these cracks: neither are there any reaction centres ahead of the flame. The theory of fracturing of lead azide giving rise to initiation of fast reaction has been put forward a number of times (13,14). The work presented here shows that fracture in a lead azide crystal does not cause initiation of fast reaction. In recent work in this laboratory (9) fracture experiments with lead azide, silver azide, and P.E.T.N. have shown that fracture velocities of several 100 m/s can be reached, and extensive mechanical break-up caused, without initiation of fast reaction occurring. Many investigators believe that the propagation of a low-velocity detonation in liquids takes place by the formation of reaction centres ahead of the reaction zone. It is therefore natural to think of a similar mechanism for homogeneous single crystals (as indeed Bowden and Yoffe (5) and Strömsoe (8) did). However, as we have shown photographically, such reaction centres do not exist in lead azide single crystals sustaining deflagration up to at least 2900 m/sec (the limit of our observations). The explosion of a crystal of lead azide results in the formation of reaction products and the emission of light. It would be expected that if the products of reaction take part in the mechanism of propagation of reaction and if in some way (for example, by exploding the crystal in a high-pressure atmosphere or confining the crystal by a liquid) the products of explosion are confined in the vicinity of the exploding crystal then the propagation rate would be higher than when the products are not confined (i.e., when exploding in air). On the other hand, our observations are that if the products are confined by water, the propagation rate drops (Table 1). This suggests that even if active nitrogen and free radicals are present as products they do not seem to play a significant role in the propagation of the fast reaction. Although light can bring about the explosion of lead azide, Courtney-Pratt and Rogers (15) believe that the light produced by the explosion of lead azide is insufficient to sustain the growth of fast reaction. The observation shown in Fig. 4 supports this because if light was sustaining the fast reaction then the propagation of fast reaction should not have stopped at the crack. Another piece of evidence is that in very thin crystals the reaction does not propagate through the whole length.

The following qualitative model for the propagation of fast decomposition (speeds up to 2900 m/sec) of single crystals of lead azide is now proposed. When a thin wire in contact with a crystal explodes, the part of the crystal in contact with the wire rapidly heats up to a sufficiently high temperature for thermal reaction. In a short time after initiation an equilibrium temperature is reached on the undecomposed crystal/reaction products interface. The value of this temperature will depend upon the rate of production of heat due to decomposition and the rate of loss of heat to the surroundings. It is clear that the value of this interface temperature will be higher for a thicker crystal. If we consider that the mechanism of decomposition of the crystal at these high temperatures is the same as at low temperatures (slow decomposition regime), then evidently the propagation of fast decomposition will be faster in thicker crystals. This is what we have observed. In this model, energy is transmitted from decomposing layers to neighbouring undecomposed layers by 'conduction'. This process will give an upper limit for the velocity of propagation since there is a maximum speed with which lattice vibrations of a crystal transport energy. The value of this maximum speed is the speed of sound in the lattice and this should be the maximum speed for propagation of reaction in the single crystal. Our observations support this model.

It should be emphasized here that the strength of the shock associated with the fast decomposition of crystals reacting at 2500-2900 m/sec is only a few kbar. This shock is too small to alter the speed of lattice waves appreciably.

It has also been shown that the intensity of the shocks produced by the fast decomposition also increases with the diameter of the crystal. When the diameter of the crystal is sufficiently large to produce shocks of enough strength to be able to compress the undecomposed crystal to the temperature required for the initiation of fast decomposition, the propagation will then be in the regime of the hydrodynamic theory of detonation. The propagation velocity will then be determined by this theory.

#### ACKNOWLEDGMENTS

This work was sponsored in part by the Air Force Office of Scientific Research, O.A.R. (70-0076), through the European Office of Aerospace Research U.S.A.F. and by A.W.R.E., Aldermaston.



## REFERENCES

1. N. Griffiths and J.M. Grocock, *J. Chem. Soc.*, 4154, 1960.
2. D. Price and J.F. Wehner, *Combustion and Flame*, 9, 73, 1965.
3. K.K. Andreev, *Combustion and Flame*, 7, 175, 1963.
4. B.L. Evans and A.D. Yoffe, *Proc. Roy. Soc. A238*, 325, 1956.
5. F.P. Bowden and A.D. Yoffe, "Fast Reactions in Solids", Butterworths Scientific Publications, London, 1958.
6. F.P. Bowden and A.C. McLaren, *Nature* 175, 631, 1955.
7. H. Jones, *Proc. Roy. Soc. A189*, 415, 1947.
8. E. Strömsoe, *Research* 13, 101, 1960.
9. M.M. Chaudhri, Ph.D. Thesis, Cambridge University, England, 1969.
10. T. Boddington, *Proc. 6th Int. Cong. High-Speed Photography*, The Hague, p. 508, 1963.
11. F.P. Bowden and J.E. Field, *Proc. Roy. Soc. A282*, 331, 1964.
12. H. Eyring, R.E. Powell, G.H. Duffey, and R.B. Parlin, *Chem. Rev.* 45, 69, 1949.
13. J.L. Copp, S.E. Napier, T. Nash, W.J. Powell, H. Skelly, A.R. Ubbelohde, and P. Woodward, *Phil. Trans. Roy. Soc. A241*, 197, 1948.
14. A.R. Ubbelohde, *Research* 3-5, 207, 1950.
15. J.S. Courtney-Pratt and G.T. Rogers, *Nature* 175, 632, 1955.

# THE INFLUENCE OF SURFACE MELTING OF CRYSTALS ON THE BURNING OF SOLID EXPLOSIVE UNDER RISING PRESSURE CONDITIONS\*

John Watson Taylor  
*Department of Fuel and Combustion Science  
University of Leeds, Leeds, England*

## ABSTRACT

A coalescence phenomenon has been found which limits the violence of explosive burning of HMX powder. It depends upon the surface melting of crystals and is related to a previously reported effect which limits the change from quiescent to explosive burning. The HMX powder was burned as a column in a tube in a strand burner. A gas pressure differential acted on the column. A small differential sufficed to cause flame to penetrate through the powder. If the absolute pressure was above a certain transition value, the powder was completely consumed. Below this pressure, the powder substantially survived the first passage of flame through it and was either consumed in a slow afterburn or remained as a congealed residue. It is concluded that this phenomenon would lead to there being a much greater chance of severe explosion in a (damaged) explosive charge, if the pressure developed during the initial phases of some reaction, reached the transition pressure of the local solid system as it then existed.

---

\*Paper submitted for publication elsewhere.

## DEFORMATION OF A CYLINDER OF EXPLOSIVE MATERIAL IN UNCONFINED IMPACT

H. S. Napadensky, T. V. Eichler, C. A. Kot and T. A. Zaker  
*IIT Research Institute  
Chicago, Illinois*

### ABSTRACT

Large deformations characterize the mechanical response of solid explosive materials prior to initiation in realistic accidental impact situations and in low-velocity unconfined impact experiments. To determine the mechanisms responsible for the initiation of detonation in low-speed impact, a two-dimensional Lagrangian tensor computer code has been developed. The code is an application and extension of a computational method formulated by Wilkins (1) and others. The code is applied to calculations of the mechanical response of a cylinder of TNT in normal end-on impact against a rigid ground surface. At an impact velocity of 690 fps, the axial normal stress behind the initial shock driven into the material is 10 kilobars. This shock stress is relieved by unloading waves originating from the stress-free lateral surface of the cylinder. The dynamic response of the cylinder is calculated prior to the initiation of reaction. Estimates are made of the transient temperature field in the TNT cylinder.

### INTRODUCTION

Large deformations characterize the mechanical response of solid explosives and propellant materials prior to initiation in realistic accidental impact situations and in low-velocity unconfined impact experiments. Unconfined impact produces complicated flow phenomena originating from the stress-free lateral periphery of the explosive. The stress and velocity gradients in the material may be responsible for mechanical energy conversion by dissipative mechanisms to thermal energy, causing local temperature increases sufficient to cause initiation of a deflagration or detonation. For these reasons the mechanical processes of unconfined impact are being investigated in some detail. To determine the mechanisms responsible for ignition in low-speed impact requires an understanding of material flow and energy conversion processes. Except for certain cases of one-dimensional wave propagation, unsteady flows with finite deformation cannot be attacked

analytically. Numerical methods using high-speed computing equipment are essential to the solution of these problems.

We have developed a two-dimensional Lagrangian code in Fortran IV for numerical analysis of cylinder and plane-strain impact problems with material strength (rigidity) effects. The code is based on a finite-difference formulation due to Wilkins (1). We drew upon several literature sources for, or worked out originally, the details of the computational procedure for greatest utility in applications of impact of solids with internal heat release. An understanding of mechanisms of ignition and subsequent detonation of solid explosive materials is essential to the development of methods to reduce their sensitivity during manufacturing and handling, with minimum compromise of performance. In addition, the extent of degradation of the explosive may be evaluated for situations where the impact stimulus is insufficient to cause an explosive reaction.

This research was supported by the U.S. Air Force Office of Scientific Research under Contract No. AF 44-620-67-C-0081.

## FIELD EQUATIONS

The motion is referred to cylindrical coordinates with  $x$  the radial coordinate,  $y$  the angular coordinate, and  $z$  the axial coordinate. With cylindrical symmetry the motion is confined to the  $x$  and  $z$  directions in each meridian plane, and is independent of the angular coordinate  $y$ . The formulation is such that problems of plane strain can also be treated, in which case  $y$  represents a rectilinear coordinate in the direction perpendicular to the plane of motion.

The nonzero stress components are the normal stresses  $\sigma_{xx}$ ,  $\sigma_{yy}$ ,  $\sigma_{zz}$ , and the shear stress  $\sigma_{xz}$ . The corresponding normal strain rates are

$$\frac{\partial u_x}{\partial x}, (\alpha - 1) \frac{u_x}{x},$$

and

$$\partial u_z / \partial z;$$

where  $\alpha = 1$  or  $2$  for plane or cylindrical symmetry, and  $u_x$  and  $u_z$  are the velocity components. The shear strain rate in the plane of motion is

$$(\partial u_x / \partial z + \partial u_z / \partial x) / 2.$$

## Mass Conservation

The differential equation of mass conservation is

$$\frac{\dot{\rho}}{\rho} + \frac{\partial u_x}{\partial x} + (\alpha - 1) \frac{u_x}{x} + \frac{\partial u_z}{\partial z} = 0 \quad (1)$$

where  $\rho$  is the current value of the density, and the dot denotes the time derivative following the motion. Mass conservation is expressed in integrated form by

$$\rho J = \rho^0 \quad (2)$$

where  $\rho^0$  is the initial density and  $J$  is the limit of the ratio of a differential element of current volume to that occupied by the same mass element initially.

## Momentum

The differential equations of momentum conservation are

$$\rho \dot{u}_x = \frac{\partial \sigma_{xx}}{\partial x} + \frac{\partial \sigma_{xz}}{\partial z} + (\alpha - 1) \frac{\sigma_{xx} - \sigma_{yy}}{x} \quad (3)$$

$$\rho \dot{u}_z = \frac{\partial \sigma_{xz}}{\partial x} + \frac{\partial \sigma_{zz}}{\partial z} + (\alpha - 1) \frac{\sigma_{xz}}{x}.$$

These express the accelerations in terms of the stress components and their derivatives with respect to the current coordinates.

## Energy Conservation

The energy equation is

$$\dot{e} = \frac{p}{\rho} \frac{\dot{\rho}}{\rho} + \dot{e}_d + h \quad (4)$$

where the pressure  $p$  is defined as the negative average normal stress,  $e$  is the internal energy,  $e_d$  is the strain energy of distortion, and  $h$  is the rate of local energy addition by heat release within the material. The rate of increase of distortional energy is given by the rate of work of the deviatoric (nonhydrostatic) stress components acting in the current strain-rate field.

## Equation of State

A wide choice of constitutive relations can be specified for the material. The stress and strain-rate tensors are split into isotropic (hydrostatic) and antisymmetric (deviatoric) parts. The pressure, defined as the negative average normal stress, is assumed to be a function of density and internal energy of the form

$$p = A + Be \quad (5)$$

where  $A$  and  $B$  are functions of density only.

The deviatoric stress components may be related to the corresponding strain components through elastic-plastic relations satisfying appropriate flow laws, through viscous stress-strain rate relations, or a combination of these. This type of behavior introduces irreversibility and the degradation of mechanical energy to heat.

The constitutive relations must be independent of any rigid-body component of motion. Each element of the material engages in instantaneous rigid rotation at the rate

$$(\partial u_z / \partial x - \partial u_x / \partial z) / 2,$$

and it is necessary to account for this effect in calculating the deviatoric stress components. Thus the equations of motion (3) relate accelerations to derivatives of stress components referred to fixed coordinates, while the constitutive equations relate the rotation-independent (objective) deviatoric stresses to deformation.

## CODE DESCRIPTION

The numerical method is based on integration of difference equivalents of the foregoing equations so as to follow the motion of a mesh of finite zones that moves with the material.

### Mass Zoning

The meridian section of the cylinder (or the plane of motion in the case of plane strain) is subdivided into initially rectangular zones, each of which contains a fixed mass of material for all times. For a cylinder the zone mass is that contained in the volume generated by revolving the zone about the cylinder axis in the initial state.

At some time during the motion the initially rectangular mesh is deformed into a set of quadrilaterals formed by straight lines joining the nodes whose motion represents that of material points.

In all problems of this type the lateral surface of the cylinder is free of stress. The upper and lower faces may be stress-free, or may be constrained to move parallel to rigid surfaces of contact, with a prescribed degree of velocity-related slip. Thus cases of dynamic compression between rigid plates with friction can be represented.

### Discrete Variables

The current values of the acceleration, velocity, and displacement components are defined at the nodes of the mesh, while state properties such as the stress, density, and internal energy are associated with the zones themselves. The node indices are discrete Lagrangian variables, since they identify mass points during the motion.

The acceleration, displacement, and all intensive properties are defined at the end of each time step, while the velocity is considered to be defined at the center of the time step. The acceleration, computed from the equations of motion at the beginning of each time step, is

used to obtain the velocity at mid-step. The displacement at the end of the step is obtained by integrating the velocity at mid-step.

### Difference Approximations

To compute the acceleration from derivatives of the stress requires expressing these derivatives in finite-difference form. For this purpose an integral definition of partial derivatives is used.

The gradient of any function  $F$  in a plane can be defined in terms of the limit of a line integral of the function around a closed circuit in the plane, divided by the enclosed area. This line integral is approximated in finite form to obtain approximations to the partial derivatives  $\partial F/\partial x$  and  $\partial F/\partial z$ .

To obtain the derivatives at a node, the line integrals are evaluated on a circuit passing through the four adjacent quadrilaterals. Edge nodes are treated by setting up fictitious edge zones with properties that satisfy the actual boundary conditions.

### Order of Computation

The initial rectangular mesh is set up and the zone masses are calculated. Initial velocities and stresses are prescribed. In an impact problem such as that considered here, the stress is initially zero throughout,  $u_x = \dot{x} = 0$ , and  $u_z = \dot{z} = -v_0$  except at the lower edge nodes, where  $\dot{z} = 0$ .

Initial node accelerations are computed from the equations of motion (3), and the velocities and displacements are obtained by integrating over one time step.

New zone volumes are calculated and the densities are obtained from the fixed zone masses. This is equivalent to application of mass conservation according to Eq. (2) in finite-difference form.

The internal energy and the stresses are obtained by solving the energy equation (4) simultaneously with the equation of state. Time is then advanced, and the process is repeated starting with the calculation of new accelerations from the equations of motion.

### Stability

An artificial viscous stress is added to the pressure in regions of compression ( $\dot{\rho}/\rho > 0$ ).

This artificial viscosity consists of two terms, one proportional to the relative compression rate  $\dot{\rho}/\rho$  and to the local sound speed, and the other proportional to the square of the relative compression rate. These have the effect of spreading shock transitions over two or three zone widths to preserve the continuous formulation of the problem, and suppressing extraneous oscillations that may develop in the solution.

The integration time step is chosen on the basis of the Courant stability criterion that the time interval be no larger than that required for a signal to traverse the smallest current mesh dimension. When the artificial viscosity is operative, the criterion is made somewhat more stringent by using a higher effective signal speed.

#### Equation of State for TNT

The equation used was that given by Enig and Metcalf (see Ref. 2). The form of the equation for solid TNT is

$$e = e_o + [(p+B)/\rho - (p_o+B)/\rho_o]/(\gamma-1) \quad (6)$$

Here  $p$ ,  $\rho$ , and  $e$  are pressure, density and specific internal energy respectively. The subscript  $o$  refers to ambient conditions,  $\gamma$  is a constant for the material.

$$B = \rho_o c_o^2 \quad (7)$$

where  $c_o$  is the ambient sound velocity. The equation relating energy, density and temperature is of the form

$$e = e_o + c_v T + \left[ A \left( \frac{1}{\rho} \right)^{1-\gamma} + \frac{\gamma-1}{\gamma} \frac{B}{\rho} - \frac{p_o+B}{\rho_o} \right] / (\gamma-1) \quad (8)$$

Here  $T$  is the absolute temperature,  $c_v$  is the specific heat at constant volume and

$$A = \left( \frac{1}{\rho_o} \right)^\gamma [p_o + B/\gamma - (\gamma-1) c_v T_o \rho_o] \quad (9)$$

The value of the ambient energy of the solid TNT is obtained from the detonation energy  $Q$  and the ambient state of the product gases, i.e.,

$$e_o = Q + c_{v,g} T_o \quad (10)$$

Here  $c_{v,g}$  is the specific heat at constant volume for the gas.

The constants reported by Enig are:

$\rho_o = 1.58 \text{ gm/cc}$	$p_o = 1 \text{ bar}$
$c_o = 227 \text{ cm/msec}$	$B = 81.4 \text{ kbar}$
$c_v = 0.5 \text{ cal/gm}$ (solid)	$T_o = 300^\circ\text{K}$
$c_{v,g} = 0.32 \text{ cal/gm (gas)}$	$\gamma = 6.68$
	$Q = 984 \text{ cal/gm}$

For computational purposes the equation of state was rearranged to give the form of Eq. (5)

$$p = A_o + A_1 e$$

where  $A_o$  and  $A_1$  are functions of density, namely

$$A_o = A_{o0} + A_{o1}(\eta-1) \quad (11)$$

$$A_1 = A_{10} + A_{11}(\eta-1) \quad (12)$$

The variable  $\eta = \rho/\rho_o$ , and the  $A_{ij}$ 's are constants.

For solid TNT these are

$$A_{o0} = -405.72 \text{ kbars}$$

$$A_{o1} = -324.32 \text{ kbars}$$

$$A_{10} = 8.9744 \text{ gm/cc}$$

$$A_{11} = 8.9744 \text{ gm/cc}$$

The temperature equation was written to give

$$T = B_1 e + B_2 \eta^{(\gamma-1)} + B_3 \frac{1}{\eta} + B_4 \quad (13)$$

The values of the constants are

$$B_1 = 4.77783 \times 10^{-4} \text{ kg } ^\circ\text{K/joule}$$

$$B_2 = 2.35118 \times 10^2 \text{ } ^\circ\text{K}$$

$$B_3 = -3.68846 \times 10^2 \text{ } ^\circ\text{K}$$

$$B_4 = -1.72663 \times 10^3 \text{ } ^\circ\text{K}$$

#### Application

The code is applied to calculation of the mechanical response of a laterally unconfined

cylinder of pressed TNT during end-on impact against a rigid lubricated surface. This problem simulates one type of sensitivity test for high explosives. The TNT billet is initially 5 cm in radius and 5 cm thick. The radius and thickness dimensions are resolved with 30 zones in an initially rectangular mesh. The initial velocity was 21 cm/msec, and calculations were carried out for 240 time steps, representing 23 microseconds of problem time. During this time the impact shock amplitude of 10.2 kilobars is relieved by rarefaction waves originating from the free surface and from the lateral periphery of the cylinder.

Figure 1 shows an undeformed grid whose nodal points are followed throughout the selected computations shown in Figs. 2, 3, 4 and 5. An additional horizontal line is shown in Figs. 2, 3 and 4 which represents the location of the shock front. In Fig. 2, 7.83  $\mu$ sec after impact the shock front has progressed through one-third of the length of the billet. In Figs. 3 and 4, the shock front has not yet reached the rear surface of the billet after 17.4  $\mu$ sec. In Fig. 5 the one-dimensional region has vanished and the peak pressure is 9.6 kilobars.

The variation of the maximum excess temperature with time is shown in Fig. 6. A rapid initial increase is followed by a nearly constant excess temperature. Finally a rapid decay of temperature occurs. The decay is caused by the equally rapid relief of pressure due to the interaction of strong rarefactions coming from the free surfaces. The location of the maximum temperature excesses is pictured in Fig. 7. Initially the highest temperatures occur in the center of the impact surface. As time progresses the maxima move up into the impacted material and towards its centerline. The maximum temperature continues to move upwards

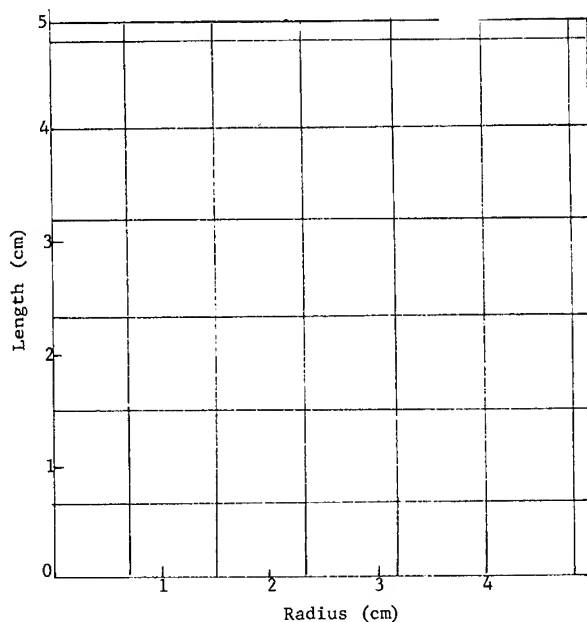


Fig. 1 - Initial geometry of TNT billet showing undeformed grid

along the centerline until the rarefaction waves relieve the pressure throughout the impacted billet.

#### REFERENCES

1. M. L. Wilkins, "Calculation of Elastic-Plastic Flow," *Methods in Computational Physics* 3, 211-263, Academic Press, Inc., New York (1964).
2. J. W. Enig and F. T. Metcalf, "Theoretical Calculations on the Shock Initiation of Solid Explosives," NOLTR 62-160, 24 Aug. 1962.

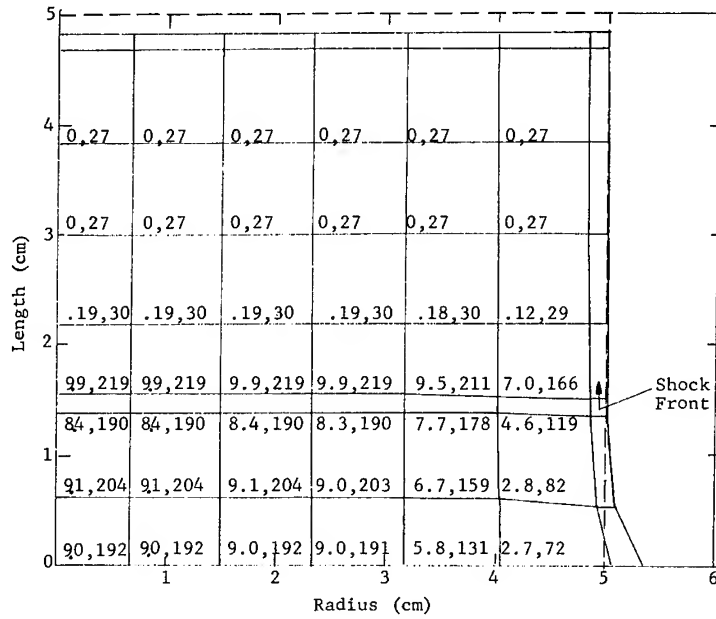


Fig. 2 - TNT cylinder impacting rigid target at 21 cm/msec: computation cycle 60; time = 7.83  $\mu$ sec after impact; time step = 0.121  $\mu$ sec; pair of numbers at nodes represent pressure in kilobars and temperature in degrees centigrade

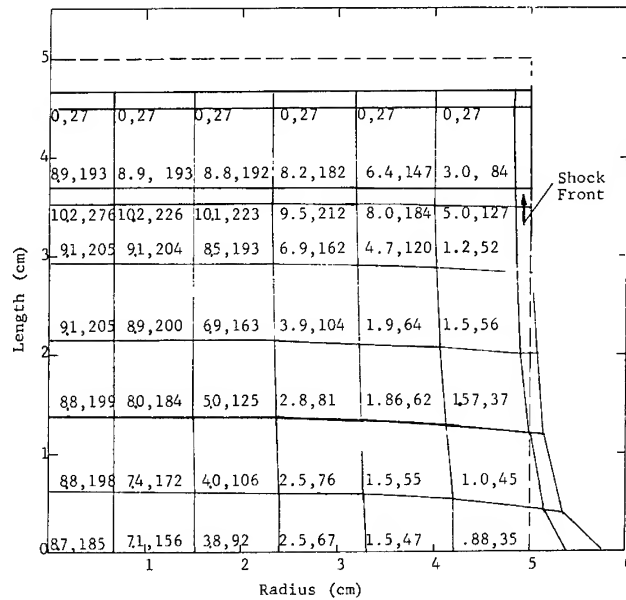


Fig. 3 - TNT cylinder impacting rigid target at 21 cm/msec: computation cycle 140; time = 15.7  $\mu$ sec after impact; time step = 0.085  $\mu$ sec; pair of numbers at nodes represent pressure in kilobars and temperature in degrees centigrade



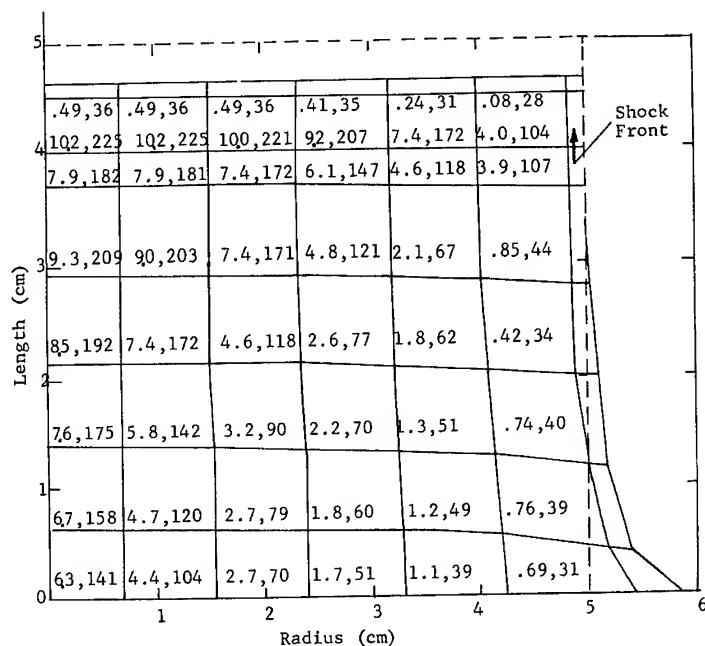


Fig. 4 - TNT cylinder impacting rigid target at 21 cm/msec: computation cycle 160; time = 17.4  $\mu$ sec after impact; time step = 0.079  $\mu$ sec; pair of numbers at nodes represent pressure in kilo-bars and temperature in degrees centigrade

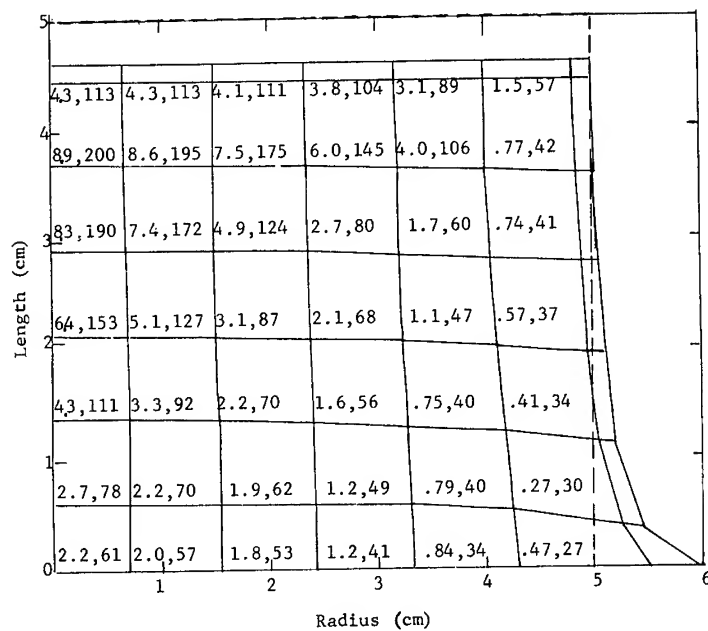


Fig. 5 - TNT cylinder impacting rigid target at 21 cm/msec: computation cycle 180; time = 18.9  $\mu$ sec after impact; time step = 0.075  $\mu$ sec; pair of numbers at nodes represent pressure in kilo-bars and temperature in degrees centigrade

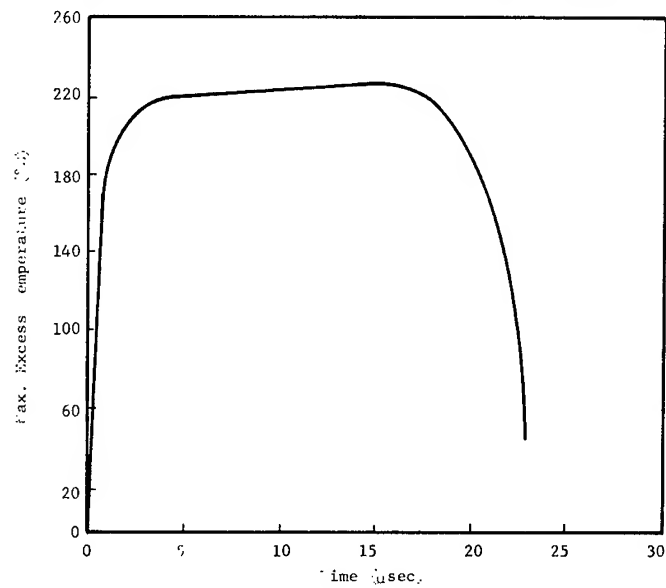


Fig. 6 - Maximum excess temperature as a function of time for a TNT cylinder impacting a rigid target at 21 cm/msec

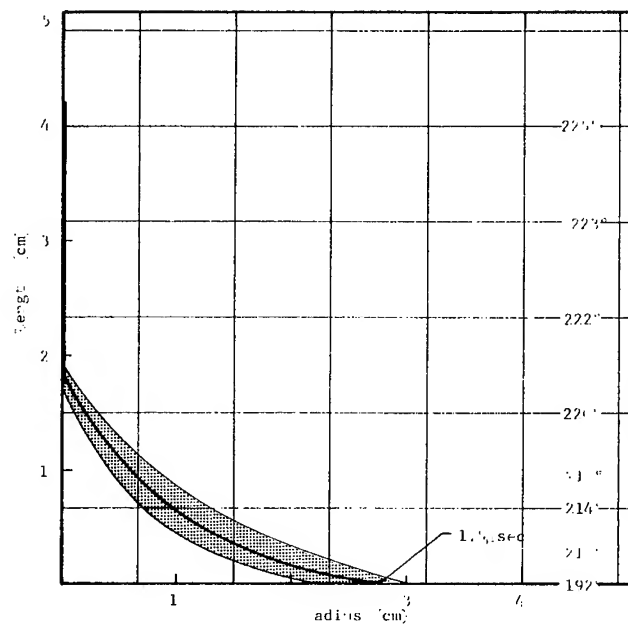


Fig. 7 - Location of maximum excess temperature in TNT cylinder impacting a rigid target at 21 cm/msec

## DECOMPOSITION OF A SHOCKED SOLID EXPLOSIVE

B. G. Craig and E. F. Marshall

*University of California, Los Alamos Scientific Laboratory  
Los Alamos, New Mexico*

### ABSTRACT

Samples of the plastic bonded HMX explosive PBX-9404 were subjected to plane shock waves with pressures which would not cause detonation within the thickness of the samples. A significant fraction of the PBX decomposed when the initial shock was of adequate pressure. Decomposition of the PBX was detected by increases in the free-surface velocity of the PBX and of driven Plexiglas plates. In response to an initial shock of 23 kb some decomposition occurs near the shock front, and when the sample is at least 5 mm thinner than the run to high-order detonation significantly more decomposition occurs at times greater than 1  $\mu$ sec after the shock front has passed. The late decomposition generates a slow-rising pressure pulse rather than a sharp-fronted detonation. The PBX located within about 5 mm of the transition to high-order detonation reacts essentially completely within much less than 1  $\mu$ sec after the shock front has passed.

### INTRODUCTION

It is generally agreed that shock initiation in homogeneous explosives, such as nitromethane, results from thermal explosion of the shock-heated explosive (1). Shock initiation in a heterogeneous explosive, such as the plastic bonded HMX explosive PBX-9404, is more complicated. The typical shock pressure required to initiate detonation is about 30 kb. The temperature rise associated with homogeneous compression alone for a 30 kb shock is about 100°C. This temperature rise alone is too small to initiate detonation. Detonation is initiated because hot spots are formed when the shock encounters density discontinuities. The explosive in the hot spots reacts and liberates energy which increases the shock pressure so that, when the shock encounters additional density discontinuities, larger hot spots are formed and more of the explosive reacts. The shock front accelerates as its pressure increases. In time, the shock pressure increases sufficiently that shock heating initiates detonation. The reader is referred to Refs. 2-4, for a more complete discussion of the sequence of events, and to Refs. 5 and 6 for a discussion of hot spots.

The usual plane-wave initiation experiments with heterogeneous explosives show what happens at the shock front, but these experiments are not informative about what happens behind the shock front. It seems obvious that some explosive in the hot spots reacts, but how much and on what time scale? Do the pressure pulses generated by individual hot spots interact to create new hot spots where additional reaction occurs (7)? The published experiments (8-12) with shocked-but-not-detonated explosive are complicated by two-dimensional flow. In this paper we describe experiments which were performed with large charges and plane shock waves.

The experiments reported below show that, if the initial shock in PBX-9404 is of adequate pressure, there is significant reaction near the front. The amount of early reaction increases with the initial pressure of the shock and with the distance which the shock has traveled in the explosive. Under appropriate conditions there is a rarefaction following the shock front which, in turn, is followed by another pressure pulse. The second pressure pulse is interpreted as evidence of decomposition occurring well after the shock front passes. The second pulse is a

slow-rising pulse. The peak pressure inferred is always equal to or less than that of detonating PBX-9404, which indicates phenomena different from those in a homogeneous explosive.

#### EXPERIMENTAL ARRANGEMENT

Our scheme was to observe how a shock wave changed as it advanced through a sample of explosive, then to deduce how much reaction occurred from the changes in the shock wave. Changes in the shock wave were detected by changes which it caused in the free-surface velocity of Plexiglas plates, which were driven by the shock wave after it had passed through various thicknesses of test explosive. The initial free-surface velocity as a function of the plate thickness and the instantaneous free-surface velocity of each plate as a function of time were measured. Representative data from both types of measurements are given.

The explosive studied was PBX-9404 with an initial density of  $1.840 \pm 0.003$  g/cc. The nominal composition by weight was 94 parts HMX and 6 parts plastic. About 1.4% of the volume was voids.

The experimental arrangement and technique for measuring the velocity of a driven plate were chosen so that: (a) Plane shock waves with sharply rising fronts and relatively small following rarefactions were induced into the PBX. (b) All measurements were made before the shock waves were affected by edge effects or by successive shocks from the booster. (c) The apparatus used for measurements introduced only trivial perturbations and responded meaningfully to a wide range of pressures.

A typical experimental charge consisted of a plane-wave booster system, a slab of PBX with a thickness less than the run to high-order detonation, and an inert plate. Sometimes the plate was omitted and the free surface of the PBX was observed directly.

The experimental parameters varied were the booster system and thereby the initial pressure and the run to high-order detonation in the PBX, the thickness of the PBX, and the thickness of the driven plate.

An investigation was made of the effect due to the type of material used as the driven plate. A driven-plate material which reflects a strong shock back into the PBX apparently modifies the decomposition time, presumably by additional shock heating. A plate material which

reflects a strong rarefaction (in the extreme case, no plate) presumably also modifies the decomposition by rarefaction cooling. Effects due to rarefaction cooling seem to be relatively small.

Plexiglas\* is a relatively good shock impedance match to PBX. It reflects a small rarefaction; consequently, neither additional shock heating nor major rarefaction cooling occurs to complicate the decomposition when Plexiglas is used as the driven plate. Most of the data given here were obtained from experiments in which the driven plate was made of Plexiglas.

#### TECHNIQUE AND ANALYSIS

In selected experiments electrical switches and an electronic chronograph were used to measure the free-surface velocities of the driven plates. However, most of the measurements were made with a modification of the optical technique described by Davis and Craig (13). The modification used "tagged" plates rather than an image. The free-surface of PBX showed sufficient difference between the reflectivity of grains of HMX and the plastic/fine-powder matrix to yield adequate records without tagging. The optical technique gave a continuous record of the position of the free surface as a function of time.

Much of the qualitative behavior of the free surface can be seen directly from the smear-camera records. Two typical records, obtained with bare PBX, are reproduced as Figs. 1 and 2 so that the reader can see the qualitative change in behavior. The important difference in the experiments from which these records were obtained was the thickness of the PBX. The space and time scales for both figures are essentially identical. The shock arrival at the free surface is marked by an abrupt change in reflectivity. The white streaks were formed by light reflected from the larger HMX crystals. The white vertical line is a superimposed image of the slit. The slope of the streaks is a measure of the velocity; the curvature of the streaks is a measure of the acceleration.

For quantitative purposes six readings, each consisting of about 100 position-time data points, were taken of each record. Results given in this paper (except those obtained with pins) were obtained by fitting the data from

\*Polymethylmethacrylate manufactured by Rohm and Haas, Inc.

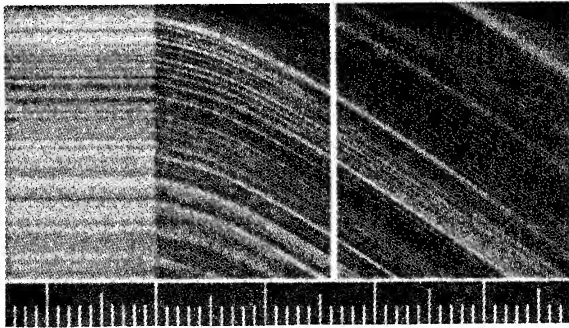


Fig. 1 - Reproduction of a smear-camera record of the free-surface motion of PBX. The thickness of the PBX was 6.3 mm. Time increases from left to right; each marker corresponds to  $0.10 \mu\text{sec}$ . The vertical field of view represents 11 mm of motion.

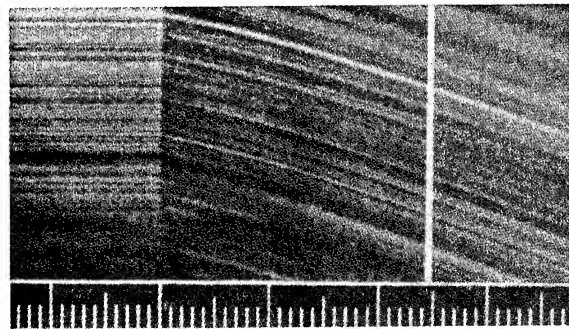


Fig. 2 - Reproduction of a smear-camera record of the free-surface motion of PBX. The thickness of the PBX was 2.5 mm. Time increases from left to right; each marker corresponds to  $0.10 \mu\text{sec}$ . The vertical field of view represents 11 mm of motion.

each record with a Fourier analysis and synthesis technique. This is a numerical technique for smoothing data in the velocity-time plane by use of time series analysis and statistical communication theory (14). The Fourier transform of each reading is taken. Transfer functions, which minimize the differences in time shifts and magnitudes, are computed. The spectral coherency among all readings is computed for each frequency component and a composite transform is computed. The inverse of the composite transform is taken as the smoothed function. The main advantage of this particular technique is that a predetermined form for the fit is not required so the smoothing is less arbitrary than it is in most other techniques. Several other smoothing schemes were also tried; none resulted in a significantly different final result. All of the important features of the smoothed data may be seen directly from a plot of the raw data.

The technique used does not completely smooth the data with only six readings. Some short time excursions introduced by reading errors remain. The trends are significant; the short time excursions are to be ignored.

#### EXPERIMENTAL DATA

A description of the booster systems is given as Table 1. The slabs of PBX placed on these boosters were of the thickness specified in each figure and were at least 100 mm in diameter. The Plexiglas plates placed on the PBX were at least 50 mm in diameter.

Some results obtained when slabs of PBX were initially shocked to 40 and 58 kb are shown in Fig. 3. The figure displays the fits to the free-surface velocity of a 5-mm thick Plexiglas driven plate as a function of time. Increasing the thickness of the PBX results in a higher initial free-surface velocity. The observed decelerations of the free surface are consistent with the initial free-surface velocities observed in other shots in which the only change was the use of thinner plates of Plexiglas.

As the amplitude of the initial shock in the PBX is decreased, the character of the free-surface velocity time curves changes. This may be seen by comparing Fig. 3 with Fig. 4. The initial pressure in the PBX samples of Fig. 4 was 29.5 kb. Data are plotted for two thicknesses of driven Plexiglas (5 and 2 mm), various thicknesses of PBX, and two treatments of the PBX interfaces. The free-surface velocity increases as a function of time for the first 1 to  $2 \mu\text{sec}$  in most of the experiments. The acceleration is relatively constant and does not show large discontinuities typical of successive shocks and detonations.

Those data identified with the letter G following the numeral which represents the PBX thickness were obtained with charges assembled in the following way. The components were cleaned and measured. A puddle of Eastman 910 adhesive was placed near the center of each piece. The appropriate components were quickly pressed together between flats so that excess adhesive flowed out all around. After the adhesive had set, the pressure was removed,

TABLE 1  
Description of Booster Systems  
(except as noted all components were at least 203-mm diam)

Type Lens	Explosive		Attenuator I		Attenuator II		Attenuator III	
	Thick-ness (mm)	Material	Thick-ness (mm)	Material	Thick-ness (mm)	Material	Thick-ness (mm)	Material
P-120	50.8	Boracitol	12.7	Brass	12.7	Dural <sup>a</sup>		
P-081	25.4	Baratol	24.1	Brass	15.0	Acrylite <sup>b</sup>		
P-081	25.4	Baratol	17.8	Polyethylene	11.4	SS-304 <sup>c</sup>	10.9	Acrylite
P-081	25.4	Baratol	17.8	Polyethylene	11.4	SS-304	10.9	Water
P-081	25.4	Baratol	17.8	Polyurethane <sup>d</sup>	11.4	SS-304	10.9	Acrylite
P-058 <sup>e</sup>	33.8	NQ <sup>f</sup>	11.4	SS-304	10.9	Acrylite		

<sup>a</sup>2024 T4 Dural.

<sup>b</sup>Polymethylmethacrylate manufactured by American Cyanamid, Inc.

<sup>c</sup>Stainless steel Type 304.

<sup>d</sup>Foamed plastic,  $\rho_0 = 0.48$  g/cc.

<sup>e</sup>147-mm diam, 68-mm thick. Lens made of nitroguanidine with an initial density of 0.4 g/cc and with PBX-9404 (2.54-mm thick) as the high-velocity component.

<sup>f</sup>Nitroguanidine,  $\rho_0 = 0.4$  g/cc. 147-mm diam confined in brass.

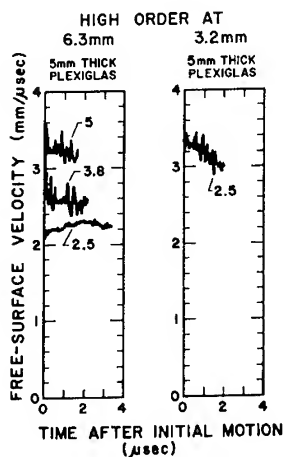


Fig. 3 - Free-surface velocity as a function of time for 5-mm thick Plexiglas plates when driven by slabs of PBX-9404 which are thinner than the run to high-order detonation. Time starts when the free surface begins to move. Data from two booster systems are given—one which would cause a 6.3-mm run to high-order detonation (initial pressure = 40 kb) and another which would cause 3.2-mm run to high-order detonation (initial pressure = 58 kb) if the PBX were sufficiently thick. The numbers 2.5, 3.8, and 5 refer to the thickness in millimeters of the PBX driving the Plexiglas plates.

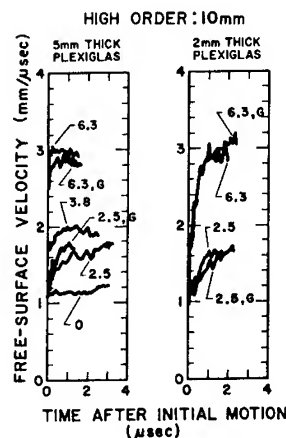


Fig. 4 - Free-surface velocity as a function of time for 5- and 2-mm thick Plexiglas plates when driven by shocked-but-not-detonated PBX-9404 initially shocked to 29.5 kb. The numbers 0, 2.5, 3.8, and 6.3 refer to the thickness in millimeters of the PBX driving the Plexiglas plates. The letter G indicates that both interfaces of the PBX were glued as discussed in the text.

the combined thickness was measured, and the thickness of the glue joint was calculated. The process was repeated as each piece was added. The thickness of the glue layer did not exceed 0.02 mm anywhere. Those data not identified with the letter G were obtained with charges assembled dry. The separation between components assembled dry did not exceed 0.03 mm. As may be seen from Fig. 4 these two treatments of the interfaces resulted in the same behavior of the PBX. Similar results were also obtained when the terminal plate of the booster was lapped plane. By contrast, sufficient roughening of the surface of the terminal plate in the booster did have an effect.

Data obtained when the PBX was shocked to a lower pressure (ca. 25 kb) are given in Fig. 5. The booster differed from that used in the above series of experiments in that the terminal booster layer was changed from a solid to a liquid ( $H_2O$ ). The experiments were arranged so that no visible bubbles were present in the water or at either of its interfaces. The PBX-Plexiglas interface was filled with adhesive in the fashion previously described.

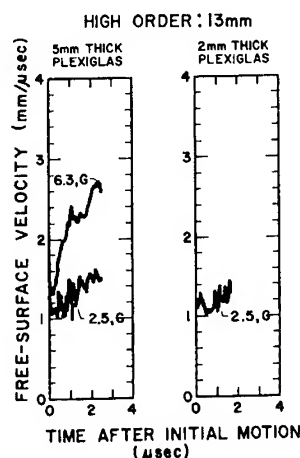


Fig. 5 - Free-surface velocity as a function of time for experiments with a water/explosive interface. The initial pressure induced into the PBX-9404 was about 25 kb. The numbers 2.5 and 6.3 refer to the thickness in millimeters of the PBX driving the Plexiglas plates. The letter G indicates the explosive assembly was glued as described in the text.

When the pressure of the initial shock induced into the PBX was reduced to 23 kb the data of Fig. 6 were obtained. These velocity

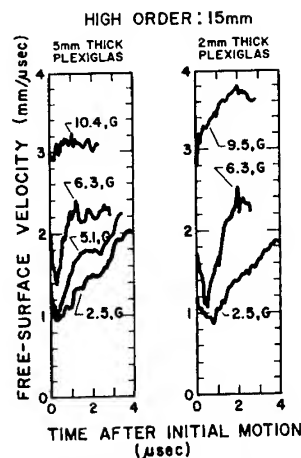


Fig. 6 - Free-surface velocity as a function of time for 5- and 2-mm thick Plexiglas plates when driven by PBX-9404 initially shocked to 23 kb. The numbers 2.5, 5.1, 6.3, 9.5 and 10.4 refer to the thickness in millimeters of the PBX driving the Plexiglas plates. Velocities for the shot with 2-mm thick Plexiglas and 9.5-mm thick PBX appear to be inconsistently high except at  $t = 0$ .

curves are significantly different from those of Fig. 4. In most cases the initial free-surface velocity is followed by a deceleration and then the slow acceleration noted in previous figures. This is indicative of a shock wave in which the initial front is followed by a rarefaction which is succeeded by a regime of rising pressure. The spike near the front may correspond to the energy released near the front by hot spots. The late pressure pulse indicates decomposition of PBX well after the shock front has passed.

The data of Fig. 7 reveal the behavior of PBX-9404 after it was shocked with an initial pressure near 8.5 kb. The initial motion of a 5-mm-thick driven Plexiglas plate was essentially the same for slabs of PBX which were 12.7 to 25.4 mm thick. The free-surface velocity did not increase significantly as a function of time. Auxiliary experiments with wedges of PBX showed that the shock velocity decreased as the shock advanced through the PBX. Apparently the initial pressure was so low that the mechanisms involved in this study would not initiate high-order detonation.

The data of Fig. 8 are given to illustrate the free-surface velocity of the PBX itself. Data obtained with two different booster systems are given. Two of the smear-camera records from which some of these data were obtained were given in Figs. 1 and 2. The

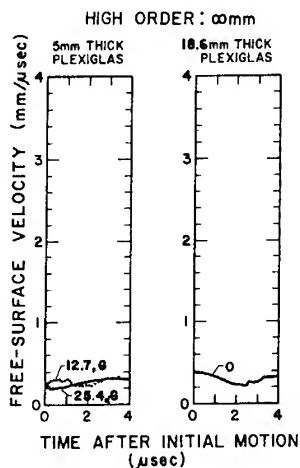


Fig. 7 - Free-surface velocity of Plexiglas when driven by PBX-9404 shocked to about 8.5 kb and when additional Plexiglas was substituted for the PBX. The numbers 0, 12.7, and 25.4 indicate the thickness in millimeters of the PBX. These data are subject to edge effects after 3 and 0.7  $\mu\text{sec}$ , respectively, for the 12.7- and 25.4-mm thick slabs of PBX.

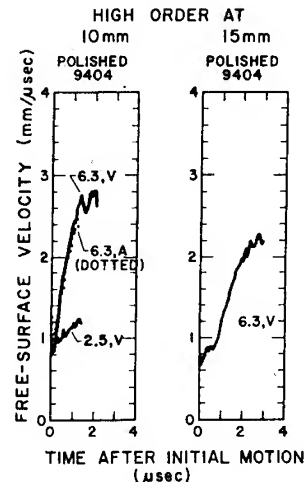


Fig. 8 - Free-surface velocity of shocked-but-not-detonated PBX-9404 as a function of time. Data are given for two sets of initial conditions: initial pressures of 29.5 and 23 kb. The numbers 2.5 and 6.3 refer to the thickness in millimeters of the PBX used to obtain the curves. The letters V and A indicate respectively that the free surface moved into a vacuum (nominally 0.012 torr) and into air at atmospheric pressure.

absence of definitive evidence of a pressure spike due to energy release by hot spots at the front is noted. It is not known if a narrow pressure spike could be detected in these experiments.

#### AUXILIARY EXPERIMENTS

Numerous experiments were performed to provide auxiliary data and to ascertain that the experiments were under control. These included measurement of the run to high-order detonation and of the initial pressure induced in the test explosive by a given booster system. The position of the shock front was measured as a function of time and these data were fitted with a second degree polynomial from which the instantaneous velocity can be calculated. These experiments were wedge-type experiments. They were repeated at least three times to establish reproducibility and error estimates. The uniformity of initiation (ca. 0.05  $\mu\text{sec}$  or less maximum spread over the central 76 mm) was established by measuring the arrival trace with multiple slits when the front was about 2 mm beyond the plane of transition to high-order detonation.

It was demonstrated that for the times of interest the experiments were indeed free of

edge effects and free of successive shocks originating within the boosters. Effects due to the type of material used as the terminal plate in the booster were found to be trivial.

Extra gaps or voids are likely to be present at an interface and might affect the behavior of an explosive sample. An investigation was made of possible effects due to the quality of the interfaces between the explosive samples and the other components. The effects appear to be minimized by requiring that the surfaces involved be reasonably plane (0.0002 cm/cm diam), well finished (30  $\mu\text{in.}$  or better), and in good contact. All data presented here are from experiments in which effects due to interfaces were apparently minimized. They include experiments in which the rear interface was (a) left dry, (b) filled with excess adhesive, or (c) wet with bubble-free water.\*

\*The dry and the excess-adhesive methods of assembly were not adequate to eliminate effects when additional interfaces were introduced within the explosive sample.



## CALCULATIONS

No one-dimensional model which quantitatively reproduces all of the experimental data has been found; however, it is informative to compare some of the data with calculations which assume that the PBX detonated high order without any low-order run. The solid curve in Fig. 9 represents the initial free-surface velocity calculated for a 5-mm thick Plexiglas plate when driven by various thicknesses of PBX-9404. In the calculation shown the PBX was made to detonate without any delay and the rear boundary was supported with the booster system which is used to obtain a 3.2-mm run to high-order detonation. The arrows extending down from the solid curve represent the calculated deceleration of the free surface during a time approximately equal to the time for measurement of the data obtained with the pin technique. It was assumed that the Plexiglas did not spall during this time. The solid circle represents the initial velocity as measured with the optical technique (see Fig. 3 for details of the motion). Under these experimental conditions shocked-but-not-detonated PBX drives a plate essentially as if the PBX had all detonated high order.

Curves very similar to that shown were obtained for other calculations in which the only change was the rear boundary support, i.e., the booster system. All calculated curves start at the appropriate free-surface velocity and approach the solid curve shown while the PBX is still relatively thin. The deviation of the experimental data from the corresponding calculation, which assumes detonation, increases as the experimental run to high-order detonation is increased.

The progress of an initiating shock in PBX can be closely approximated with a one-dimensional code originated by Mader of this laboratory. The model for this code assumes that partial reaction occurs near and only near the shock front. This model predicts a curve which in the plane of Fig. 9 starts at the appropriate free-surface velocity, rises slightly until it is near the thickness corresponding to that of the experimental high-order detonation, curves sharply upward, and then rises with a slope similar to that of the solid curve in Fig. 9, which assumes immediate detonation. Experimental data fall above the curves calculated with this model. Failure of this model is even more apparent when one compares the velocity of the Plexiglas at a time later than that represented in Fig. 9. It is apparent that much more decomposition occurs than is predicted by this model.

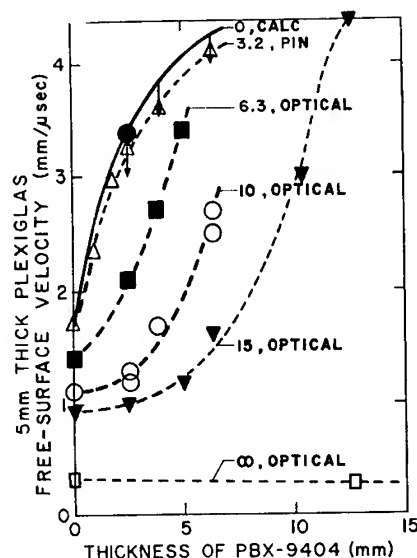


Fig. 9 - Free-surface velocity of a 5-mm thick Plexiglas plate as a function of the thickness of shocked-but-not-detonated PBX for several booster systems. Average velocities for the measuring time interval are given for those data obtained with pins; initial velocities are given for data obtained with the optical technique. The numerals 0, 3.2, 6.3, 10, and 15 indicate the run in millimeters to high-order detonation. The words--pin, and optical--indicate the technique used to obtain the data.

## DISCUSSION

Data have been given which show how shock waves with various initial pressures change as they advance through PBX-9404. These data have been compared with calculations which assume immediate high-order detonation and also with calculations which assume that partial reaction occurs near and only near the shock front. The data indicate that decomposition in shocked-but-not-detonated PBX-9404 is rather complicated. In addition to the partial reaction near the shock front there is significant decomposition occurring well behind the front.

In one experiment, when the run to high-order detonation was 3.2 mm, the early energy released was sufficient to drive a plate essentially as fast as the plate would have been driven if all of the PBX had detonated. In another experiment, when the run to high-order detonation was 6.3 mm, the early energy

released was only slightly below that expected if all of the PBX had detonated. Apparently about 5 mm of PBX adjacent to the high-order level reacted completely on a time scale which was relatively short. Part of the energy from this layer was released early enough to influence the initial shock front.

In other experiments the most significant energy release occurred well after the initial shock had passed. This late release of energy did not form a sharp-fronted super detonation of the type observed in the initiation of homogeneous explosives, but resulted in a relatively slow-rising pressure pulse. The amplitude of this pulse changed with time, and it depended on the initial pressure and the distance which the shock had run in PBX-9404.

In still other experiments, when the initial pressure was about 8.5 kb, no significant energy release was observed. The implication is that this pressure is below a threshold required to initiate detonation or even significant decomposition by the mechanisms involved in this study.

The evidence suggests that the explosive releases energy as a function of time at local sites distributed throughout the bulk of the shocked PBX. Two hypothetical mechanisms are burning at hot spots and reaction at secondary hot spots (15). Secondary hot spots are those caused by the interaction of pressure pulses from the initial hot spots. A quantitative model which accounts for the late energy release has not been found.

#### ACKNOWLEDGMENTS

The authors are especially grateful to Charles L. Mader for calculations as well as for much stimulating discussion. Group GMX-3 supplied the explosive which was of exceptional quality. J. E. LaBerge, J. R. Barnes, and R. E. Faudree assembled the charges, fired them, and assisted in reducing the data. A. W. Campbell, E. L. Peterson, W. C. Davis, and J. R. Travis provided criticism and encouragement. J. B. Ramsay and W. Rice developed the computer code used to smooth the data. J. E. Kennedy of Sandia Laboratories graciously shared preliminary results from related experiments. This work was performed under the auspices of the U.S. Atomic Energy Commission.

#### REFERENCES

1. A. W. Campbell, W. C. Davis, and J. R. Travis, *Phys. Fluids* **4**, 498 (1961).
2. A. W. Campbell, W. C. Davis, J. B. Ramsay, and J. R. Travis, *Phys. Fluids* **4**, 511 (1961).
3. S. J. Jacobs, T. P. Liddiard, and B. E. Drimmer, "The Shock-to-Detonation Transition in Solid Explosives," in *Ninth Symposium (International) on Combustion*, Cornell, 1962, p. 517.
4. G. P. Cachia and E. G. Whitbread, *Proc. Roy. Soc. A* **246**, 268 (1958).
5. C. L. Mader, *Phys. Fluids* **6**, 375 (1963).
6. C. L. Mader, *Phys. Fluids* **8**, 1811 (1965).
7. I. C. Skidmore, "A Semi-Quantitative Model of Shock Initiation in Heterogeneous Explosives," in *Proceedings of the International Conference on Sensitivity and Hazards of Explosives*, London, 1963.
8. U. Berg and P. A. Persson, "Some Recent Shock Initiation Experiments Using the Multiple Flash-Gap Technique," in *Proceedings of the International Conference on Sensitivity and Hazards of Explosives*, London, 1963.
9. Marjorie W. Evans, B. O. Reese, L. B. Seely, and E. L. Lee, "Shock Initiation of Low-Density Pressings of Ammonium Perchlorate," in *Fourth Symposium (International) on Detonation*, White Oak, 1965, p. 359.
10. J. Favier and C. Fanquignon, "Initiation de la Detonation par Choc dans les Explosifs Solides," in *Les Ondes de Detonation*, Gif-sur-Yvette, 1961, p. 59.
11. V. M. Boyle, R. L. Jameson, and F. E. Allison, "Pressure Measurements During Shock Initiation of Composition B," in *Tenth Symposium (International) on Combustion*, Cambridge, 1964, p. 855.
12. A. N. Dremin and S. A. Koldunov, *Vzryvnoye delo* **63**, 37 (1967), Translation by Clearinghouse, PB 188 145 T.

13. W. C. Davis and B. G. Craig, Rev. Sci. Instr. 32, 579 (1961).
14. E. A. Robinson, Statistical Communication and Detection (Hafner Publishing Co., New York, 1957) pp. 58-63.
15. C. L. Mader, "Numerical Calculations of Detonation Failure and Shock Initiation," in Fifth Symposium (International) on Detonation, Pasadena, 1970.

# THERMAL DECOMPOSITION OF HIGH EXPLOSIVES AT STATIC PRESSURES 10-50 KILOBARS

E. L. Lee, R. H. Sanborn, and H. D. Stromberg  
*Lawrence Radiation Laboratory, University of California  
Livermore, California 94550*

## ABSTRACT

We have measured the time to explosion of five high explosives (TNT, PETN, HMX, nitromethane, and 2,2-dinitropropane) under static pressures up to 50 kbar at various temperatures. The behavior of PETN and HMX indicates the suppression of gaseous intermediates by the high pressure and a corresponding reduction in the rate of decomposition. This is supported by observation that pressure does not affect TNT decomposition where it is known that the formation of solid intermediates is the important step. Nitromethane, on the other hand, exhibits an increase in rate with increase in pressure. Measurements of the infrared spectra of nitromethane at pressures up to 50 kbar reveal increasing intensity of the methyl group vibrations and a consequent shift in dipole moment related to associations in the liquid phase. Another nitro aliphatic with a different type of structure, 2,2-dinitropropane, exhibits a "normal" decrease in rate at high pressure.

## INTRODUCTION

Although some work has been published on the effect of pressure on high explosive decomposition (1), most papers dealing with thermal decomposition have neglected such effects. Experiments under shock conditions or "heavily" confined static experiments could be strongly influenced by such effects. Nevertheless, theoretical treatments of both static and dynamic experiments have generally assumed first order Arrhenius kinetics independent of pressure.

We have developed techniques for measuring time to explosion under very high pressure static loading, and have examined four major classes of homogeneous high explosives: an aliphatic nitrate ester, a cyclic nitramine, an aromatic nitro compound, and two aliphatic nitro compounds. (See Table 1.) Our experiments reveal a significant pressure dependence in all but one of these five representative explosives (TNT). This work, and that reported by others, casts doubt on the applicability of first order kinetics (2,3).

We have also applied high pressure infrared techniques to study nitromethane whose decomposition behavior is strongly affected by pressure. Although the results do not resolve the decomposition mechanism, they do provide important information.

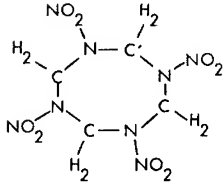
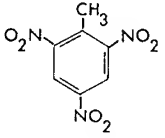
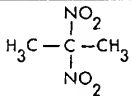
## EXPERIMENTAL

### Time to Explosions Measurement

In order to contain both liquid and solid high explosives under extreme pressure, we developed a sample container machined out of gold. The experimental configuration is shown in Fig. 1. When placed in the high pressure heater and compressed, the container forms a seal effectively containing liquids and even preventing the escape of gases as long as the gas pressure is lower than the applied pressure. We observed a "pressure cooker" effect on most of our runs; that is, the capsule retained nearly its original shape even though the solid or liquid high explosive within decomposed, producing gases in the sample container.

This work performed under the auspices of the U.S. Atomic Energy Commission.

TABLE 1  
High Explosives Examined

Explosive	Formula	Source, specifications, purity
PETN	$\begin{array}{c} \text{H}_2\text{C}-\text{O}-\text{NO}_2 \\   \\ \text{NO}_2-\text{O}-\text{H}_2\text{C}-\text{C}-\text{CH}_2-\text{O}-\text{NO}_2 \\   \\ \text{H}_2\text{C}-\text{O}-\text{NO}_2 \end{array}$	Trojan Powder Co.  Mil Spec 387 mp 140.0 °C
HMX		Recrystallized 99.9% HMX
TNT		Lone Star Ordnance Co. Flake type I  Mil Spec MIL-T-248A mp 80.2 °C
Nitromethane	Normal form $\text{H}_3\text{C}-\text{NO}_2$ aci-form $\text{H}_2\text{C}=\text{N}-\text{OH}$	Commercial Solvents Corp.
2,2-dinitropropane		mp 53 °C

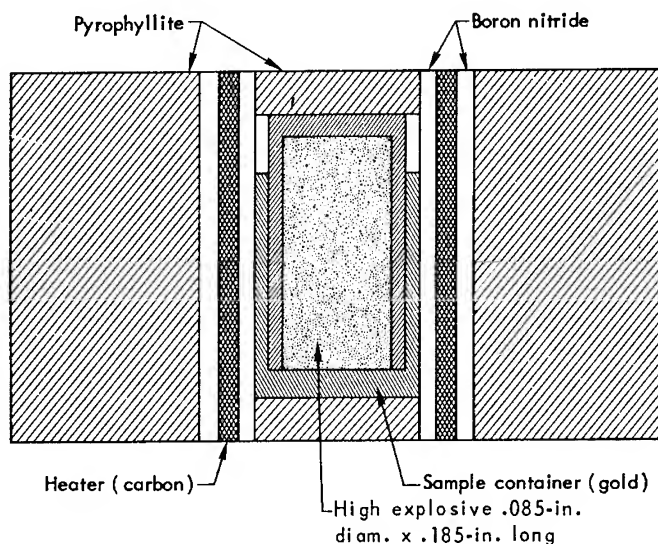


Fig. 1 - Experimental configuration  
for high pressure decomposition

Methods for measuring pressure are described extensively in the literature (4). We use the resistance change of Bi, Yb, and Ba at their phase transitions (Fig. 2) for pressure calibration of the system. The temperature is determined by measuring the power input to the

heater. Calibration of the power input measurement (Fig. 3) is accomplished by placing a Mo-Re thermocouple in the sample container through a special die with a small hole in its center. We also have placed materials with known melting points in the sample area. The

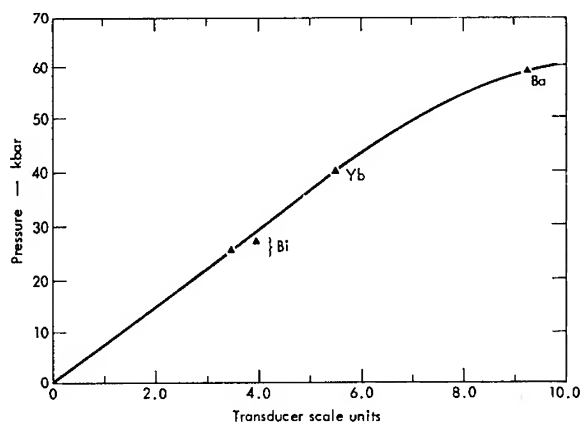


Fig. 2 - Pressure calibration data

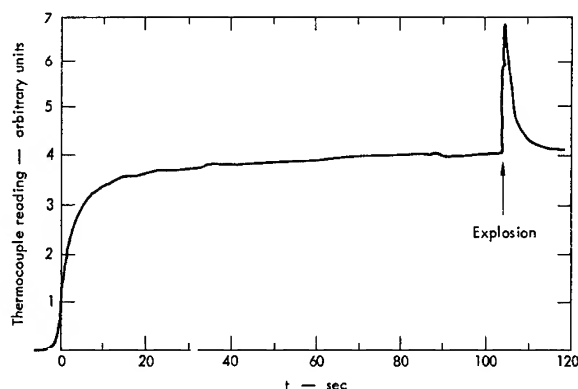


Fig. 4 - Thermocouple record of thermal decomposition of PETN at 50 kbar

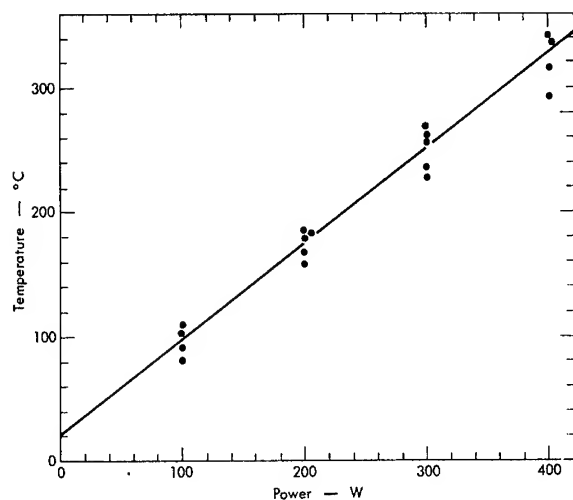


Fig. 3 - Power/temperature calibration data

two methods correspond to within  $15^{\circ}\text{C}$ . We are unable to fix the temperature/power calibration more precisely since, apparently, the condition of the heater varies slightly from one run to the next. Nevertheless, the reproducibility is such that with measurements at extreme pressure values we can unequivocally distinguish the pressure dependence.

In a typical run, the sample container is pressurized to either 10 or 50 kbar, and power is applied in a single step. The temperature external to the heater is measured by the Mo-Re thermocouple, whose output is read by a recorder. When the sample explodes, a sharp rise in temperature registers the time to explosion, as shown in a sample run for PETN (Fig. 4).

### High Pressure Infrared Studies

We used a diamond high-pressure IR cell (High Pressure Diamond Optics) with a range to 50 kbar for an infrared studies. A series of nickel gaskets 5, 1, and 0.35 mil thick, with a 0.015-in.-diam hole, was employed to contain liquid samples between the diamond anvils. MCB spectroquality nitromethane and nitroethane were used without further purification.

The cell was loaded by partially forming the gasket at low pressure, flooding the gasket and hole with the sample and, after reinsertion of the large anvil, quickly taking the cell to 40 kbar; nitromethane remains liquid at this pressure. A low power microscope was used to make sure that no bubbles were present and the gasket material had not extruded into the hole. The loaded cell was placed in a  $4\times$  beam condenser mounted in a Beckman IR-9 infrared spectrophotometer.

Since the light flux through the high pressure cell was extremely small, the reference beam had to be severely attenuated, and wide slits and high gain had to be used. The resulting resolution was from 5 to  $9\text{ cm}^{-1}$ .

The diamonds are quite transparent from 1700 to  $400\text{ cm}^{-1}$ , but have moderate absorption from 4000 to  $2600\text{ cm}^{-1}$  and strong absorption between these two regions. It was found that the background diamond absorption could be adequately subtracted out, in the high frequency region.

### RESULTS AND DISCUSSION

In Figs. 5 through 9 we show the times to explosion on an Arrhenius plot for the five high

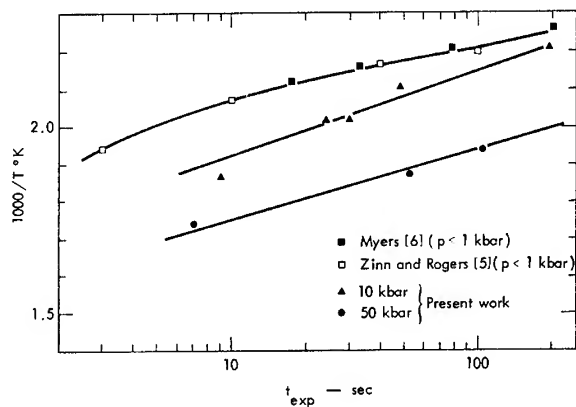


Fig. 5 - Time to explosion for PETN

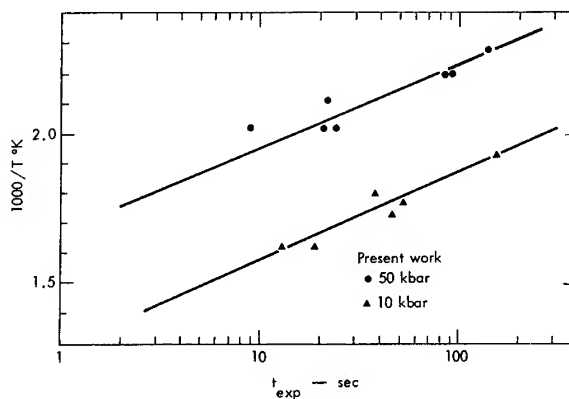


Fig. 8 - Time to explosion for nitromethane

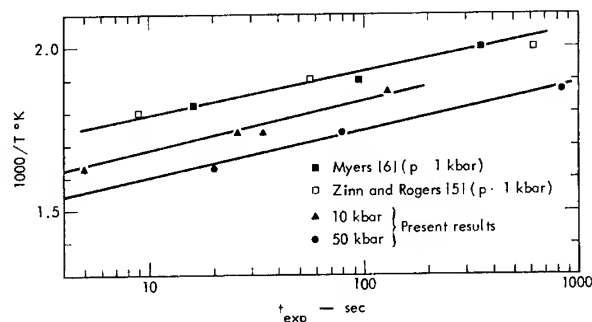


Fig. 6 - Time to explosion for HMX

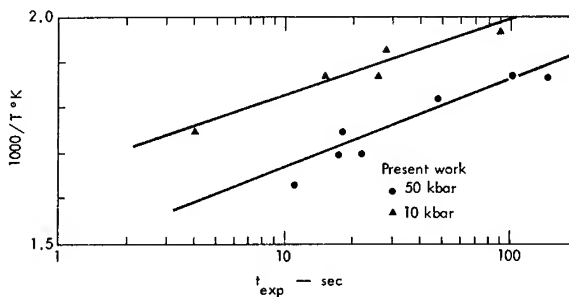


Fig. 9 - Time to explosion for 2,2-dinitropropane

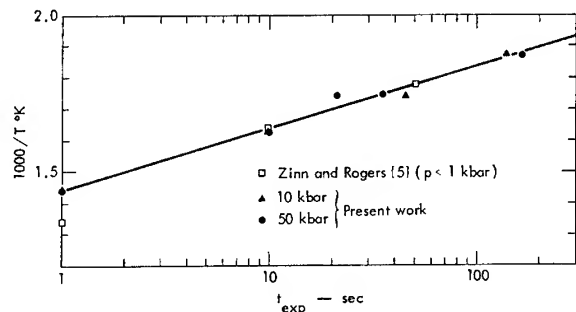


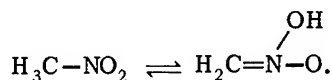
Fig. 7 - Time to explosion for TNT

explosives listed in Table 1. Work by Zinn and Rogers (5) and Myers (6) on PETN, HMX, and TNT at much lower containment pressure but in similar geometry exhibits the same slope as our data at 10 and 50 kbar. Moreover, their data are consistent with the trend in pressure behavior we find for PETN and HMX. Also, for TNT, where the 10- and 50-kbar curves coincide, the lower pressure data of Zinn and Rogers likewise coincides. We have interpreted

this behavior to mean that for PETN and HMX a rate-controlling step involving the formation of gaseous products can be suppressed by applying high pressure. It follows that for TNT the rate-controlling step does not involve gaseous products. Careful decomposition studies by Dacons, Adolph, and Kamlet (2) have demonstrated that the intermediate products are composed of a mixture of various aromatic compounds plus a "coke" which apparently has some catalytic properties. Very little gaseous material was found. Nitromethane is an exception to this "normal" behavior of high explosives. As can be seen in Fig. 6, the pressure dependence of nitromethane is the reverse of HMX and PETN and also the reverse of 2,2-dinitropropane. However, just as for the other explosives measured, no change in slope is evident in going from 10 to 50 kbar. The slopes of the curves for these explosives are apparently independent of pressure. This implies that the  $\Delta E$  (activation energy) and therefore the reaction mechanism may very well be unaffected by pressure. We have advanced a hypothesis to explain the behavior of

nitromethane, but our own confirmatory experiments force us to leave the question open.

Nitromethane has an aci-form also known as nitronic acid



It is known that the addition of amines which promote the aci-form sensitizes nitromethane (7,8). It is also known that nitromethane is highly associated in solution (9). As mentioned above, our experiments indicate that the mechanism of reaction does not change since the slopes of the curves are not altered by pressure. The rate is evidently increased through the formation of larger concentrations of the rate-controlling species. Two experiments were performed to see whether the rate-controlling species might be the aci-form of nitromethane.

Because of its structure, 2,2-dinitropropane does not possess an aci-form. Therefore, its behavior should be "normal" even though it is in the same general class as nitromethane. Its behavior was in fact found to be "normal," as illustrated in Fig. 9.

Infrared spectra of nitromethane at high pressure were taken to determine whether changes in spectra corresponding to the N—O or CH frequencies would confirm our notion about the chemical nature of nitromethane at high pressure. Figure 10 shows one such spectrum of liquid nitromethane with a 5-mil nickel gasket at high and low pressures in the region 4000 to 2600  $\text{cm}^{-1}$ . The three main infrared bands in the low pressure spectrum are the asymmetric methyl stretch at 3050  $\text{cm}^{-1}$ , the symmetric methyl stretch at 2960  $\text{cm}^{-1}$ , and the overtone of the symmetric methyl deformation at 2805  $\text{cm}^{-1}$ . The application of high pressure is seen to shift all three bands to higher frequencies, indicating a shortening of the C—H bonds. The intensity changes are not dramatic, but there appears to be increased absorption in the region above 3000  $\text{cm}^{-1}$ . Whether or not part of this absorption is in fact caused by the presence of some of the aci-form of nitromethane cannot be determined from this region. Hydrogen bonding between the methyl group of one molecule and a nitro group from another is a second explanation. That there is hydrogen bonding is shown by the increased intensity of the asymmetric methyl stretch relative to the symmetric stretch at the higher pressure. This band is very weak in the

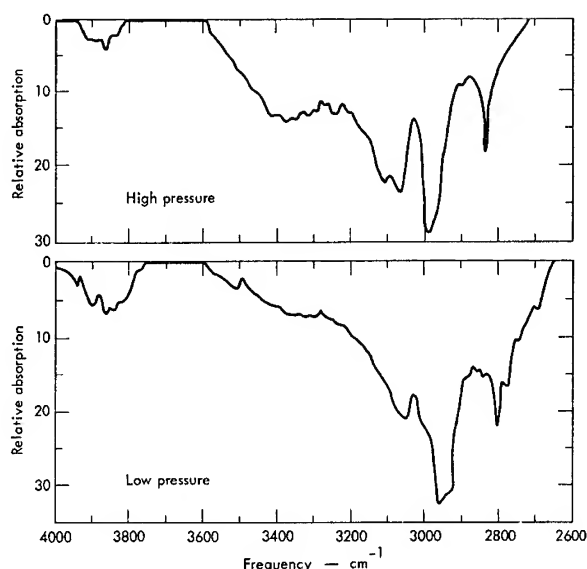


Fig. 10 - Nitromethane infrared spectra (4000 to 2600  $\text{cm}^{-1}$ )

gas phase spectrum but there the rotational lines are spread out by the Coriolis effect.

The lower frequency range of interest is shown in Fig. 11 for the low and high pressures, respectively, using a 0.35-mil nickel gasket. Table 2 lists the assignments for the two spectra. The weak band at 1430  $\text{cm}^{-1}$  in the low pressure spectrum is not resolved at high pressure, but it should be shifted similarly to the other bands. The two nitro bands are shifted higher by high pressure but undergo little change in intensity. The methyl bending vibrational (MBV) bands, however, are strongly

TABLE 2  
Infrared Spectrum of Nitromethane  
from 1700 to 1000  $\text{cm}^{-1}$

Infrared Band ( $\text{cm}^{-1}$ )		Assignment
Low Pressure	High Pressure	
1568	1583	Asymmetric $\text{NO}_2$ stretch
1430	?	Asymmetric $\text{CH}_3$ deformation
1408	1430	Symmetric $\text{CH}_3$ deformation
1090	1112	$\text{CH}_3$ rock



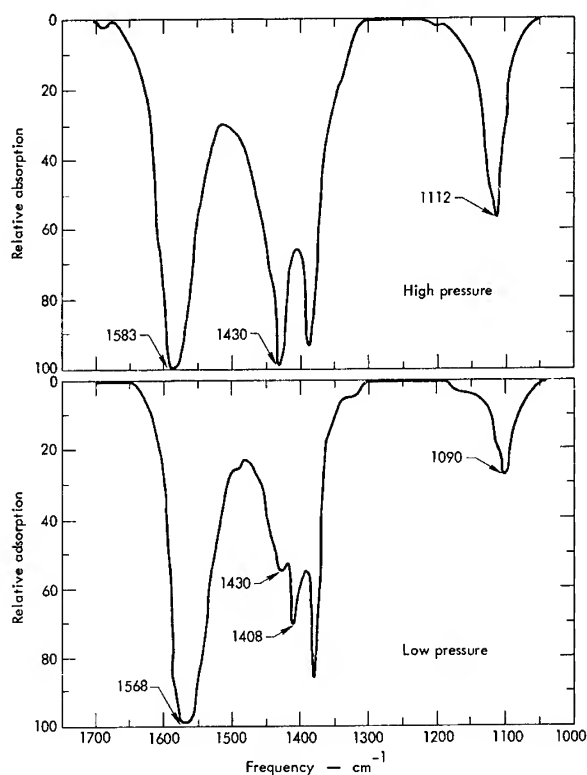


Fig. 11 - Nitromethane infrared spectra (1700 to 1000  $\text{cm}^{-1}$ )

influenced by the application of high pressure, becoming much more intense and shifting 22  $\text{cm}^{-1}$  to higher frequencies. No new features are observed in the spectrum at high pressure that could be ascribed to the *aci*-form of nitromethane. The observed shift to higher frequencies is caused by shorter C—H bonds at high pressure, but the increased intensity results from stronger hydrogen bonds. The region from 1000 to 500  $\text{cm}^{-1}$  produced some minor shifts in frequency and changes in intensity, but no new features at high pressure.

Changes in the infrared spectrum of liquid nitromethane produced by the application of high pressure can be explained adequately by the formation of stronger hydrogen bonds between the methyl group and neighboring nitro groups, and by a shortening of bond lengths. Spectra for nitroethane do not exhibit intensity increase in the MBV band under high pressure. We have not examined 2,2-dinitropropane.

It is evident that nitromethane exhibits intramolecular and intermolecular effects (not necessary isomerism) at high pressure. Further studies will be required before any

conclusions can be drawn about the decomposition mechanism of nitromethane.

Quantitative measurement of the time to explosion dependence on pressure has been severely limited by the precision of our data. We carried out an extensive series of runs on PETN in attempting to establish the pressure and temperature dependence. Measurements were made at 1, 7, and 50 kbar. The trend of our data is illustrated in Fig. 12, where lines are drawn to aid in analysis of the findings. The curves, including that for Myers' data, are roughly parallel.

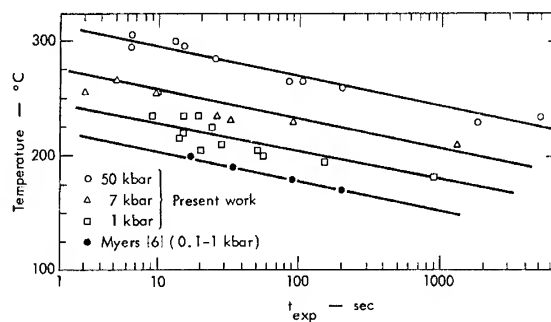


Fig. 12 - Decomposition of PETN at high pressure

Another series was run at a single power setting (230 W) to measure the pressure dependence alone. The combined results are shown in Fig. 13.

At any given temperature, the dependence can be expressed as

$$t_{\text{exp}} = C(T)P^N,$$

$$C(T) = Ae^{\frac{\Delta E}{T}}$$

where  $2.0 > N > 1.5$ . Thus it seems likely that the reactions are higher than first order. An alternative explanation is that the decomposition is diffusion-controlled and that pressure slows the diffusion process. If the reaction process were diffusion-controlled, we would expect a dependence of the form (10)

$$1/t_{\text{exp}} \sim D = A(T)e^{-bP}$$

where  $D$  is the diffusion constant. However, we find that this expression does not describe the results in Fig. 13. Thus it seems most likely

that reversible reactions yielding gaseous intermediates are rate-controlling at least for PETN, HMX, and 2,2-dinitropropane.

## CONCLUSION

The information we have obtained in confined systems under measured pressures has pointed out some important features in the thermal decomposition of high explosives, the most important being the possibility of either decreasing or enhancing the rate of decomposition by increasing the pressure. It seems likely that many of the questions raised in this work might be answered with improvements in temperature measurement and control, and by extension to other compounds. We hope to gain further information by quenching and chemical analysis, and by further infrared work.

We hope that this paper will encourage others to investigate some of the phenomena noted here.

## ACKNOWLEDGMENT

We would like to thank Don Ornellas, Milt Finger, and Don Seaton for supplying materials and suggestions.

## REFERENCES

1. F. P. Bowden, B. L. Evans, A. D. Yoffe, and A. M. Yuill, *Discuss. Faraday Soc.* **22**, 182 (1956).
2. J. C. Dacons, H. G. Adolph, and M. J. Kamlet, "Some Novel Observations Concerning the Thermal Decomposition of 2,4,6-trinitrotoluene," *J. Phys. Chem.* **74**, 3035 (1970).
3. A. G. Strunina, V. G. Abramov, and A. G. Merzhanov, *Combust. Explos. Shock Waves* **2**, 1 (1966).
4. H. D. Stromberg and D. R. Stephens, "Effects of Pressure on the Electrical Resistance of Certain Metals," Univ. of California, Lawrence Radiation Laboratory, Livermore, Rept. UCRL-7536 (1963).
5. J. Zinn and R. W. Rogers, *J. Phys. Chem.* **66**, 2646 (1962).
6. L. Myers (private communication).
7. "Storage and Handling of Nitromethane," Commercial Solvents Corp., Nitroparaffin Data Sheet, NP Series TDS **2** (1961).
8. D. R. Forshey, J. C. Cooper, and W. J. Dayak, *Explosivstoffe* **6**, 125 (1969).
9. M. S. Smith, Jr. and P. A. D. deMaine, *J. Miss. Acad. Sci.* **12**, 97 (1966).
10. P. G. Shewman, *Diffusion in Solids*, New York, McGraw-Hill, 1963.

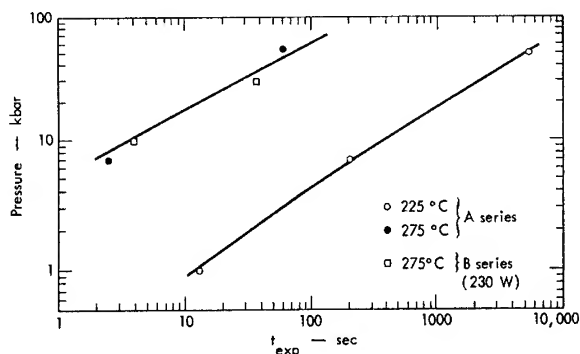


Fig. 13 - Rate dependence on pressure for PETN

## EXPERIMENTAL OBSERVATIONS OF INITIATION OF PRIMARY EXPLOSIVES BY A HOT WIRE

Howard S. Leopold  
*U.S. Naval Ordnance Laboratory, White Oak  
Silver Spring, Maryland*

### ABSTRACT

A technique has been developed for sensing the initial reaction of primary explosives initiated with a hot wire. A light pipe situated at the wire/explosive interface transmits the radiation emitted from the decomposing explosive to a photomultiplier detector tube. The photomultiplier tube output can then be correlated with the electrical input signal that heats the wire. The technique has been applied to the examination of the hot wire initiation of styphnates and azides when the wire is heated by a capacitor discharge. When the emission of visible light is used as a criterion of initiation, both styphnates and azides give a definite signal. When an infrared sensitive photomultiplier tube is used as the detector, non-propagating initiations of silver azide and dextrinated lead azide can be detected. The technique shows that initiations can occur not only during the wire temperature rise, but also on the cooling curve of the wire well after the maximum wire temperature.

### INTRODUCTION

The time interval required to heat a wire in contact with a primary explosive to a condition sufficient to cause fast explosive decomposition is referred to by such terms as "initiation lag time" or "ignition delay time." Available experimental techniques for determining the initiation or ignition lag time are limited. For example, Mallory and Goss (1) have described a technique for measuring the ignition time when using a constant current input to the wire as the electrical activation signal. The wire itself is used as the sensing element. On ignition, the explosive becomes a source of heat which is conducted into the wire. This heat produces a rapid change in the wire resistance as evidenced by the voltage drop across the wire and this voltage inflection is considered as the time of ignition. Shaw (2), using a capacitor discharge to heat a detonator bridgewire (colloidal lead azide spot on bridgewire) noticed a current inflection which was indicative of the creation of an electrically conductive path of much lower resistance than existed through the bridgewire. The beginning of the current surge correlated well with the total functioning time of the detonator and hence

was believed to be indicative of the beginning of detonation within the detonator.

A technique for sensing the initiation or ignition time and correlating this time with the electrical input signal to the wire has been developed. Initial experiments were performed using a capacitor discharge to heat the wire. In the past, a capacitor discharge has proven the most difficult electrical signal with which to correlate. The technique is also readily adaptable to other types of electrical input signals. Examples of possible uses of the technique include studying energy coupling from the wire to the explosive, making fundamental studies of initiation, studying effects of particle size and density upon initiation times, and checking assumptions upon which theoretical calculations are based.

### EXPERIMENTAL

Visible region and infrared detectors are used with an oscilloscope to detect, amplify, and display the light and heat signals emanating from the wire and the explosive when a firing pulse is delivered to the wire. A light pipe

situated at the wire/explosive interface is used to transmit the radiation to the detector without disturbance of the explosive confinement. The essential parts of the experimental apparatus are as follows:

**Firing Circuit** - The firing circuit is a simple capacitor discharge circuit with a mercury switch and can be considered to be a series RLC circuit. (See Fig. 1.) A coaxial current shunt is inserted in the circuit to measure the current waveform to the bridge-wire. The circuit parameters are:

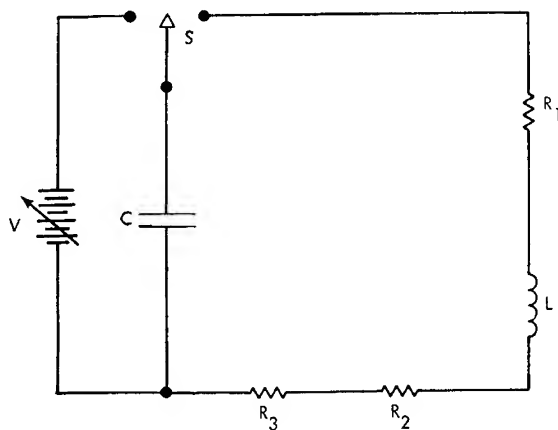
$$C = 1.0 \text{ microfarad}$$

$$R = 0.32 \text{ ohm}$$

$$L = 1.56 \text{ microhenries}$$

$$V = \text{variable (volts)}.$$

The circuit before insertion of the bridgewire is underdamped since  $R < 2\sqrt{L/C}$ . The bridgewire used in this investigation has a resistance range of 2.5-4.0 ohms and when incorporated into the circuit increases the resistance to a minimum of 2.82 ohms. Since  $R_{\text{MIN}} > 2\sqrt{L/C}$  with the bridgewire inserted, an overdamped current pulse is delivered to the bridgewire.



- C - CAPACITOR - 1.0 MICROFARAD  
 S - SWITCH - MERCURY  
 L - CIRCUIT INDUCTANCE - 1.56 MICROHENRIES  
 R<sub>1</sub> - CIRCUIT RESISTANCE - 0.31 OHM  
 R<sub>2</sub> - COAXIAL CURRENT SHUNT - 0.010 OHM  
 R<sub>3</sub> - BRIDGEWIRE - 2.5 TO 4 OHMS

Fig. 1 - Firing circuit

**Initiator Plug** - A specially prepared standard two pin phenolic initiator plug was used to observe the initial reaction of the

explosive. A hole was drilled axially through the initiator plug between the two pins and a light pipe was potted in this hole with transparent epoxy cement. (See Fig. 2.) The excess cement and light pipe fibers were trimmed flush on the plug surface with a razor blade and a 1-mil diameter nichrome wire soldered in place. An aluminum charge holder to contain the explosive material was then force-fitted on the plug.

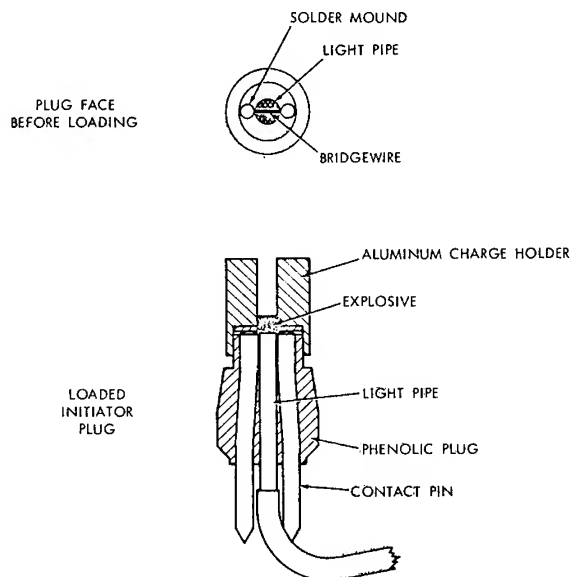


Fig. 2 - Modified initiator plug

**Light Pipe** - The light pipe used is flexible 16-fiber "Crofon" light guide developed by E. I. DuPont de Nemours & Co., Inc. The fibers are plastic and transmit wave lengths from 3100 to 11,100 Å. The outer protective jacket is peeled off the section inserted into the initiator plug and the light pipe views practically the entire bridgewire length between the contact pins. The length of the light pipe is kept as short as possible in the experimental setup (less than 50 cm) since there is a 9% loss of light each 30 cm.

**Detectors** - The radiation transmitted by the light pipe is detected by a photomultiplier tube with a high frequency response. An RCA-931A photomultiplier tube with a maximum response at 4000 Å was used to detect in the visible region and an RCA-7102 photomultiplier tube with a maximum response at 8000 Å was used to detect in the near infrared region. The relative quantum efficiencies and responses of the two detector tubes are shown in Fig. 3. The

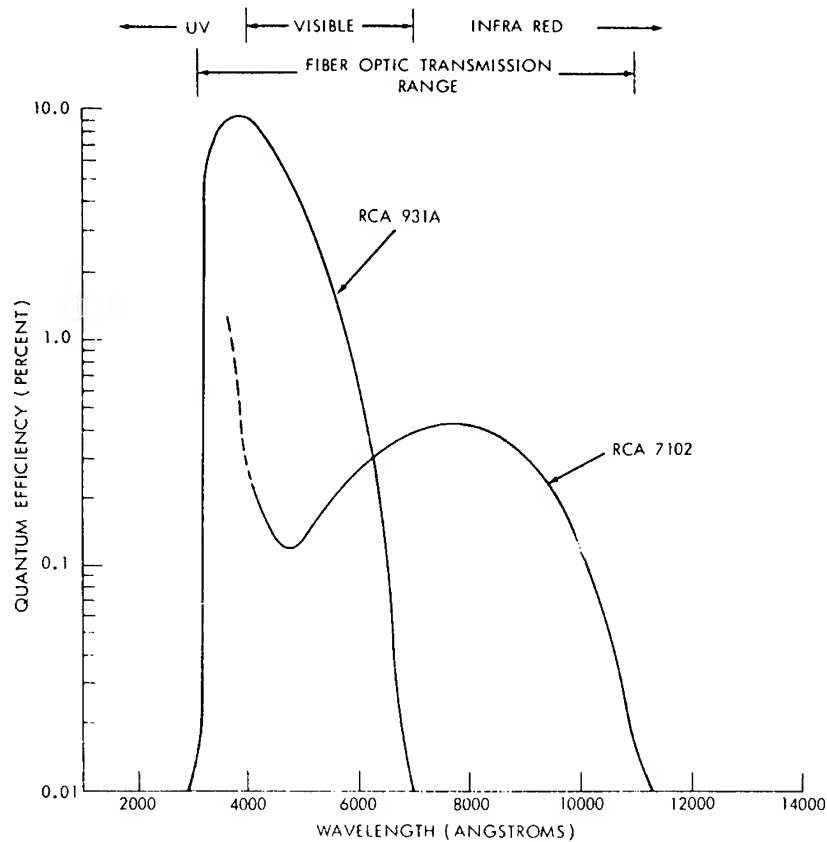


Fig. 3 - Quantum efficiency of detector tubes as a function of wavelength

RCA-7102 tube has a spurious response in the UV region which can be eliminated by the use of sharp cut yellow or red filters.

**Recorder** - A Tektronix 555 dual-beam oscilloscope with two fast rise Type K pre-amplifiers was used to observe the current and photomultiplier tube signals. The oscilloscope is triggered by the current signals and the photomultiplier tube is used to observe the light or heat emitted at the bridgewire/explosive interface (depending upon which tube is employed). A block diagram of the experimental arrangement is shown in Fig. 4.

## EXPERIMENTAL RESULTS

Initial exploratory experiments were performed using the RCA-931A photomultiplier tube as the detector with various primary explosives. Shots were first made using capacitor voltages just over the 50% firing voltage of the

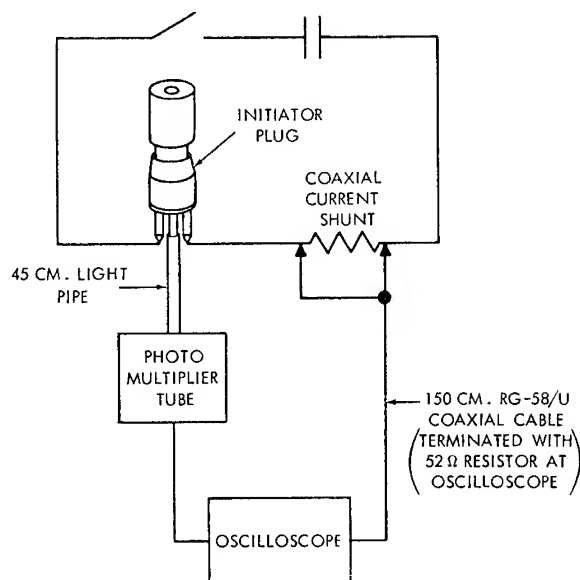


Fig. 4 - Test arrangement

test primary explosive and then at higher voltages to determine the effect upon initiation. The variation of firing response with voltage for the test explosives is shown in Table 1.

**Dextrinated Lead Azide** - Typical records obtained from the initiation of milled dextrinated lead azide are shown in Fig. 5. Figures 5A and 5B show initiations under the same conditions when the capacitor is charged to 66.1 volts. Figure 5A shows the overdamped type of capacitor discharge with the initiation occurring at 14.5 microseconds, close to the completion of the discharge. A definite light signal emitted from the explosive as detected by the photomultiplier tube is used as the criterion of initiation. Figure 5B shows a faster initiation occurring at 4.7 microseconds with the same charging voltage. A small perturbation of the current pulse can be observed approximately 0.5 microsecond after initiation. Figure 5C shows initiation of the lead azide when the capacitor is charged to 150 volts. Initiation occurs at 2.0 microseconds with a large perturbation of the current pulse occurring 0.4 microsecond after initiation. The current perturbation or surge is indicative of the creation of an electrically conductive path of much lower resistance than had existed through the bridge-wire. The lower resistance value momentarily underdamps the circuit. Measurements on 12 shots in which the lead azide affected the current pulse showed that the current perturbation lagged the initiation by 0.3 to 1.0 microsecond. It can readily be seen that, though the time lag variation of the perturbation is small, large percentage errors can evolve in comparison to short initiation times if the perturbation is used as an indication of initiation time for dextrinated lead azide.

**Silver Azide** - Typical records obtained from the initiation of silver azide are shown in Fig. 6. Figure 6A shows initiation occurring at 26 microseconds, well after completion of the current pulse to the wire. Figure 6B shows initiation occurring at 4.4 microseconds. The current perturbation occurs simultaneously with initiation. Measurement of 15 shots in which silver azide affected the current pulse all show simultaneous or at most a 0.1 microsecond delay in the development of the underdamped waveform indicating that the perturbation is a good indication of initiation time with silver azide. The almost immediate effect on the current waveform with silver azide indicates the rapidity with which ionization occurs in comparison to dextrinated lead azide. One might assume from the prolonged effect upon the current waveform that more intense ionization also occurs.

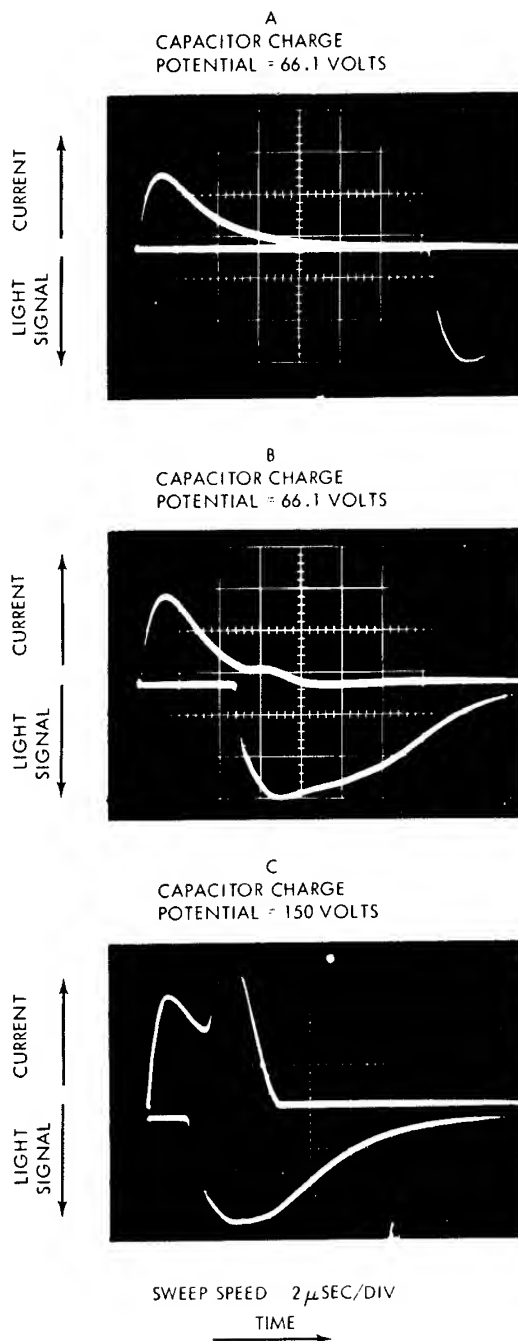


Fig. 5 - Lead azide records

**Basic Lead Styphnate** - Typical records obtained from the ignition of basic lead styphnate are shown in Fig. 7. Figure 7A shows ignition when the capacitor is charged to 60.6 volts. The basic lead styphnate ignites well after cessation of the current pulse with an ignition time of 77 microseconds. Much higher voltages ( $\geq 150$  volts) are necessary to effect

TABLE 1  
Calculated Percentile Firing Voltages\* for Test  
Primary Explosives†

Percentile Firing (%)	Basic Lead Styphnate (volts)	Normal Lead Styphnate (volts)	Silver Azide (volts)	Lead Azide (volts)
50	54.0	56.1	60.0	63.8
75	55.1	57.4	61.5	66.1
99.9	59.4	62.2	67.2	74.6

\*With 1 microfarad capacitor.

†All explosives milled and loaded at 10,000 psi in experimental initiator plug.

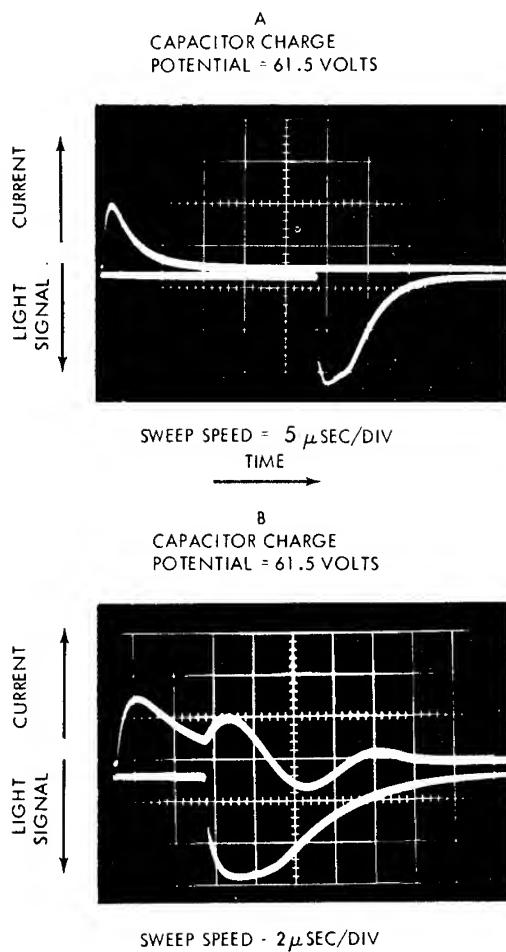


Fig. 6 - Silver azide records

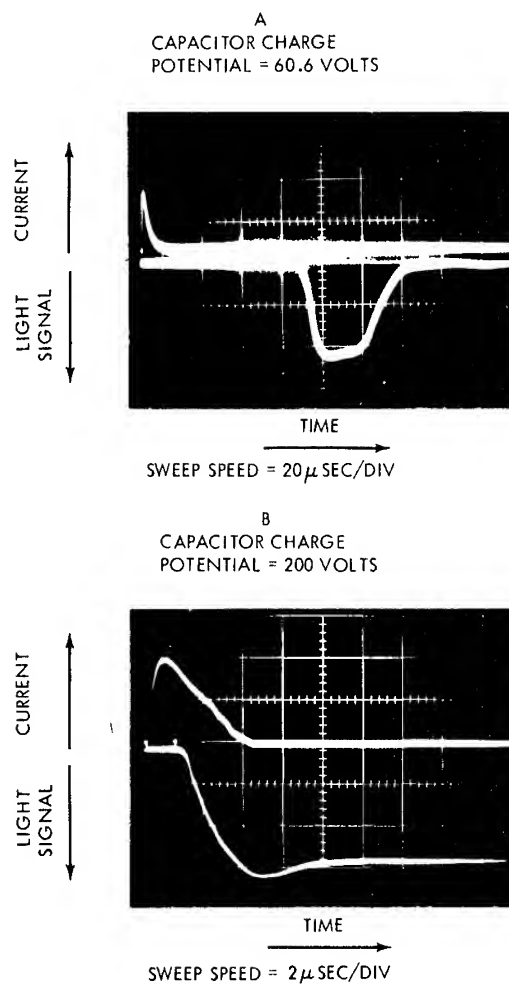


Fig. 7 - Basic lead styphnate records

ignition during the current pulse. Figure 7B shows ignition when the capacitor is charged to 200 volts (enough energy to weakly explode the bridgewire). Very little distortion of the current pulse is observed when basic lead styphnate is ignited during the current pulse. This is expected, since deflagration produces only a small amount of ionization in comparison to detonation.

**Normal Lead Styphnate** - Typical records obtained from the ignition of normal lead styphnate are shown in Fig. 8. The records are very similar to those obtained with basic lead styphnate. Figure 8A shows ignition well after cessation of the current pulse at 63 microseconds. The capacitor was charged to 63.6 volts. Figure 8B shows an ignition near the end of the current pulse when the capacitor was charged to 100 volts. No effect on the current pulse is seen since a deflagration of normal lead styphnate typically starts from a hot or weakly exploded wire.

It can be seen from these typical records that the technique can provide a definite indication of the time of initiation (criterion-detection of visible light emitted by the explosive). Even deflagrating type reactions give fairly sharp indications of ignition. One of the more interesting observations is that the initiation or ignition of the explosive can occur well after cessation of the energy input into the wire.

To determine if further information could be obtained about the induction period, an infrared detector (RCA-7102) was substituted for the RCA-931A photomultiplier originally employed. The RCA-7102 is not as sensitive as the RCA-931A (see Fig. 3) and it was found that a capacitor charge voltage of at least 70 volts was necessary to observe the heating produced in the bridgewire. Heating of the bridgewire while attached to initiator plug but before loading of the explosive was first examined. Oscillograms were made using four different sweep speeds to examine the bridgewire heating. (See Fig. 9.) With the experimental conditions used and at the fast sweep speeds, wire heating can be detected at 3 microseconds. The wire reaches its maximum temperature at 12 microseconds near the end of the capacitor discharge, remains at that value for a short period, and then starts the comparatively long cooling cycle. A comparative shot run with the RCA-931A tube detects no radiation. (See Fig. 10.)

Unfortunately, the sensitivity level of the RCA-7102 is usually not sufficient to detect the wire heating at voltages below 75 volts when explosive is loaded on the bridgewire. Many of

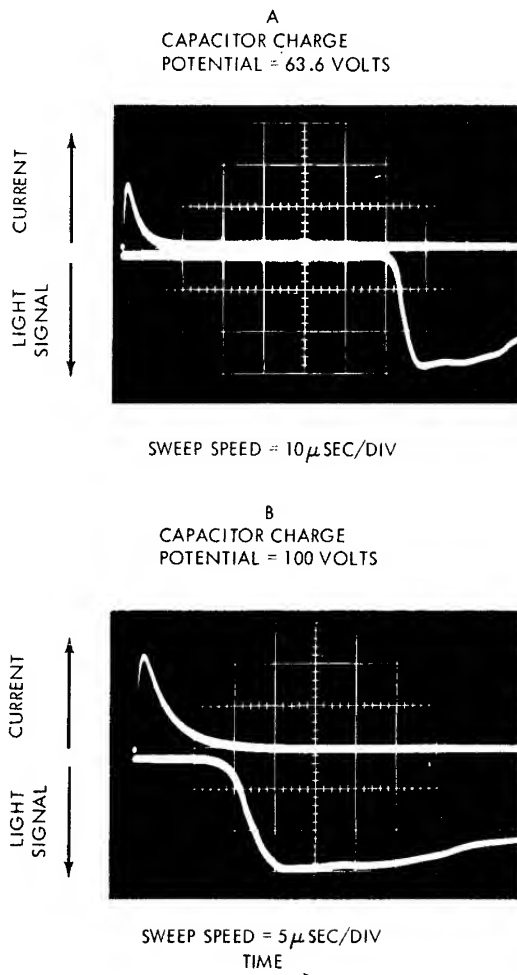


Fig. 8 - Normal lead styphnate records

the delayed initiations occur with capacitor potentials well below 75 volts when explosive is loaded on the bridgewire. However, many interesting events can still be observed. Figure 11 shows a shot in which partial initiation of silver azide occurred, but which failed to propagate. The RCA-7102 is not sensitive enough to detect wire heating at the energy level employed. However, a burst of heat from the silver azide is observed at 6.1 microseconds which undergoes an exponential decay. There is no effect upon the current waveform. Similar heat bursts have been observed with dextrinated lead azide in shots which failed to propagate.

All test shots previously described had the explosive loaded at 10,000 psi, a value often used in loading ordnance hardware. It has been observed that the energy necessary for hot wire initiation of lead azide increases with



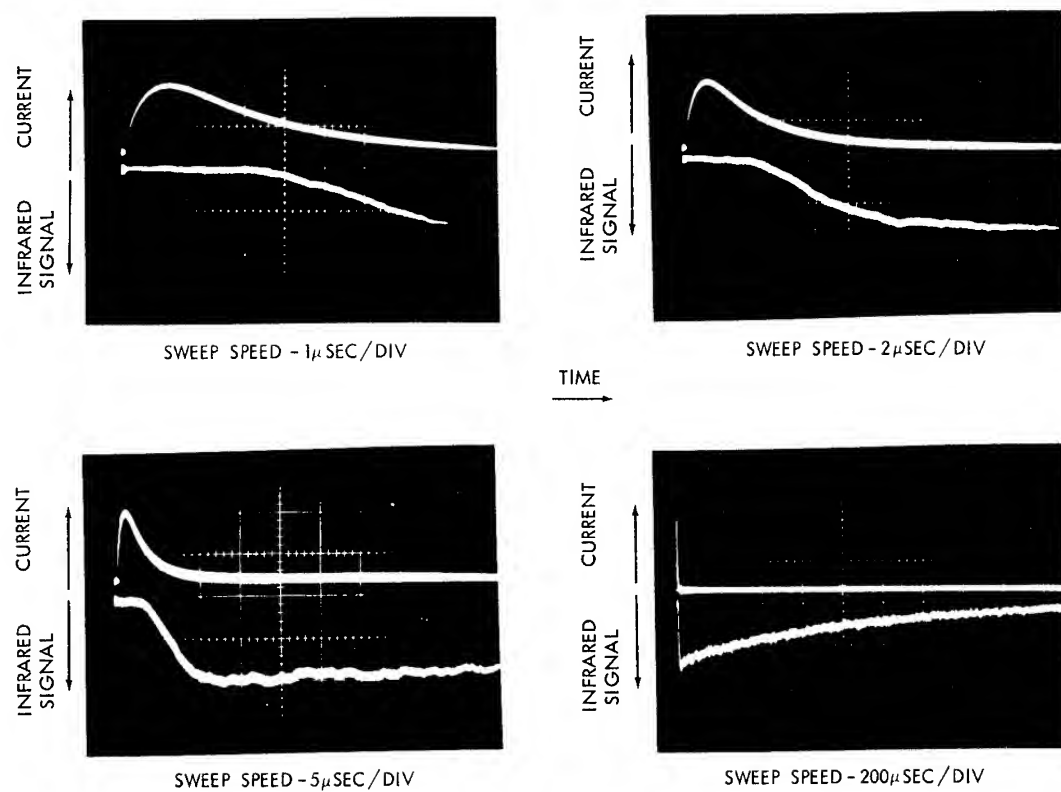


Fig. 9 - Heating of bare bridgewire

CAPACITOR CHARGE POTENTIAL = 70 VOLTS

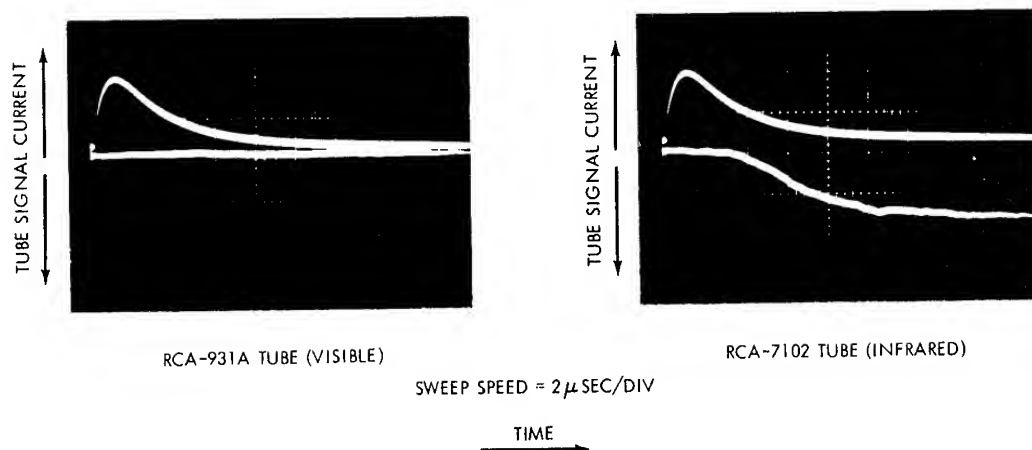


Fig. 10 - Comparison of detector tube responses to sense bare bridgewire heating

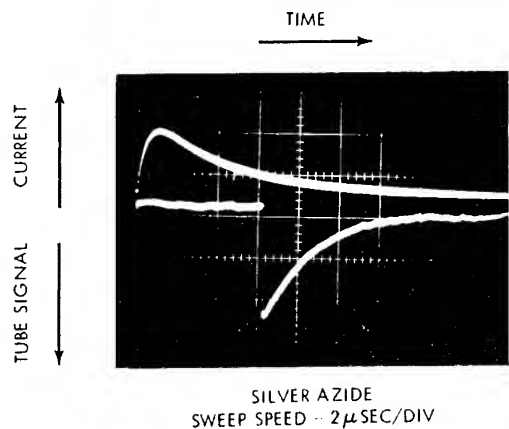


Fig. 11 - RCA-7102 detector tube record showing partial initiation of silver azide

decreasing loading pressure (3). At a loading pressure of 2,500 psi, the increased energy necessary for initiation is sufficient to show wire heating and yet still produce delayed initiations. See Fig. 12 which shows the initiation of lead azide occurring on the cooling curve well after cessation of the capacitor discharge.

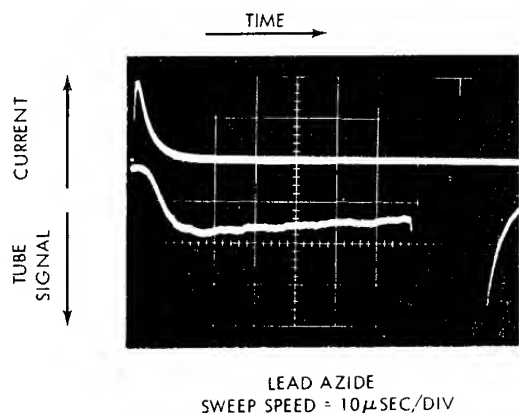


Fig. 12 - RCA-7102 detector tube record showing initiation of lead azide on cooling curve

## DISCUSSION

As can be seen by the oscillogram records, the light pipe technique using either the RCA-931A or the RCA-7102 photomultiplier tubes as detectors can successfully sense the initial reaction of primary explosives initiated by hot wires. Examination of the hot wire sensitivity

of explosives in the past has usually been confined to a determination of energy levels such as the "50% firing level" or the "99.9% firing level." The light pipe technique can prove a useful adjunct for examining the time of reaction at the various energy levels.

Theoretical calculations for hot wire initiations are frequently based on the assumption that the explosive is initiated during the period when the wire is being heated. Figure 12 with the infrared detection tube definitely proves that initiation can occur on the cooling curves. One can also surmise from the exploratory shots with the styphnates that the observed delayed ignitions can occur only on the cooling curve.

Occasionally, one uncovers reports where the investigator, on examining EED's that failed, is surprised to find "charred azide" next to the bridgewire. It can be seen in Fig. 11, and has been observed in other shots, that both silver and dextrinated lead azide can partially react producing small heat bursts without propagation occurring. One of the exploratory oscillograms obtained with silver azide showed two of these bursts occurring before a propagating initiation started. A definite time interval was observed between each event. (See Fig. 13.) The propagating initiation was missed because of the fast sweep speed used for this record but can be said to occur at least 7 microseconds after the second observed heat burst.

In the experimental system used, the bridgewire usually remains intact when voltages of less than 90 volts are used for initiation. Disruption of the bridgewire occurs when the

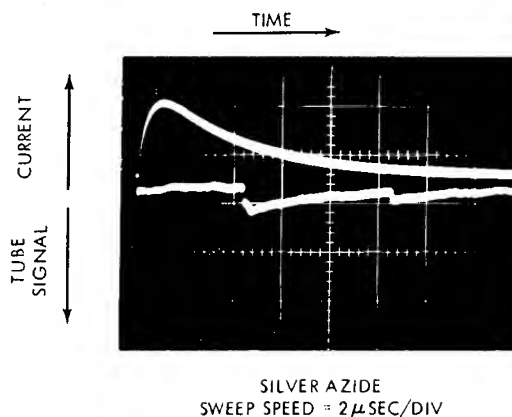


Fig. 13 - RCA-7102 detector tube record showing preinitiation heat bursts

initiator plug is destroyed by the explosive. Under these conditions when initiation occurs during the electrical signal input, the current perturbation caused by intense ionization in the vicinity of the bridgewire will provide a good indication of the time of initiation of silver azide and only a fair indication of the time of initiation of dextrinated lead azide.

## REFERENCES

1. H. D. Mallory and F. A. Goss, "A New Method for the Measurement of Initiation Times in Hot Wire Ignitions," in the Gilbert B. L. Smith Memorial Conference on Explosive Sensitivity, NAVORD Report 5746, June 1958.
2. D. N. Shaw, "The Electrical Input and Functioning Characteristics of Low Energy Wire Bridge Detonators," in Proceedings of 1957 Electric Initiator Symposium, Franklin Institute, Philadelphia, Pa., September 1957.
3. R. Stresau and M. H. Rowe, "Observations of the Effects of Loading Density on the Initiation and Growth of Detonation in Azides," in Proceedings of 1960 Electric Initiator Symposium, Franklin Institute, Philadelphia, Pa., November 1960.

**Session V**  
**EXPERIMENTAL TECHNIQUES**

Chairman: Russell Duff  
*Systems Science and Software*

# EQUATION-OF-STATE INVESTIGATION OF GRANULAR EXPLOSIVES USING A PULSED ELECTRON BEAM

J. H. Shea and A. Mazzella  
*Physics International Company*  
*San Leandro, California*

and

Louis Avrami  
*Feltman Research Laboratories, Picatinny Arsenal*  
*Dover, New Jersey*

## ABSTRACT

The effective Gruneisen coefficient has been measured for fine grain PETN, pressed to densities of 1.47, 1.54, 1.59 and 1.67 gm/cm<sup>3</sup>. A pulsed electron beam was used to produce sudden in-depth heating of the samples. A quartz transducer located adjacent to the heated region recorded the resulting stress pulse. Linear material response calculations, based upon the energy deposition profile and the measured sound velocity, were used to infer the pressure induced by the sudden heating. Values of the Gruneisen coefficient were found to range from about 0.7 for the 1.47 gm/cm<sup>3</sup> material to 1.2 for a 1.67 gm/cm<sup>3</sup> sample. The results confirm the predicted sensitivity of the coefficient to comparatively small changes in porosity.

## INTRODUCTION

Granular explosives represent a particularly interesting class of materials to study using pulsed electron beam techniques. High intensity, high voltage, pulsed beams can be used to produce a sudden increase in energy (and pressure) throughout a substantial volume of a solid, without shock compression. One then avoids questions associated with the local thermal non-equilibrium aspects of shock loading of granular explosives. Furthermore, the states attained by sudden volume heating are well removed from the Hugoniot, thus affording the opportunity to evaluate the adequacy of equation-of-state models under conditions not associated with shock loading.

## BACKGROUND FOR THE EXPERIMENT

In order to characterize the state of a material following constant volume heating, the

pressure-energy coupling relationship must be known. This relationship is determined through the Gruneisen coefficient,  $\Gamma$ , of the material. This parameter appears in the Mie-Gruneisen equation of state (1) and can be written in the form

$$P = f(V) + \frac{\Gamma E}{V} \quad (1)$$

where  $P$  is the pressure,  $v$  is the specific volume, and  $E$  is the specific internal energy.

The Mie-Gruneisen equation of state is generally employed in the finite difference computer codes that are currently used to calculate dynamic response of homogeneous material (2). However, when materials with porosity are encountered, one cannot continue to consider them as homogeneous media. On the other hand, the convenience of the finite difference computer codes is such that it is desirable to define constitutive relationships in such a way that they are treated as if they were

homogeneous, and average values for pressure, volume and energy are given correctly. Such formulations have been developed by Hermann (3) and Seaman and Linde (4).

An effective Gruneisen coefficient can be defined for solid materials, including porous substances such as granular explosives, by

$$\Gamma = v \left( \frac{\partial P}{\partial E} \right)_v \quad (2)$$

where the volume is considered in a macroscopic sense, i.e., bulk material plus any voids. The coefficient thus defined is expected to be energy dependent for porous materials, since internal pressure relief (still at constant volume) can occur due to the collapse of voids, especially as the shear strength of the material generally decreases with increasing temperature.

If the pressure in a substance is determined as a function of energy under constant volume conditions, the value of the Gruneisen coefficient can be obtained as a function of energy by differentiation, Eq. (2).

High intensity pulsed electron beams are well suited for producing sudden volume heating, so that the Gruneisen coefficient can be evaluated (5-8). When the irradiated sample (slab geometry) is thick enough to absorb all the incident electrons, a compressive stress wave propagates from the heated high pressure region toward the rear (away from the source) of the sample. A transducer, such as piezoelectric material or manganin gauge, located just beyond the deposition depth, can be used to record the stress pulse. Alternatively, the displacement or velocity of the rear surface may be observed using optical techniques. A relatively straight-forward procedure involving material response calculations can be used to infer the initial pressure distribution from the experimentally measured stress history provided the constitutive relation is reasonably well known. A knowledge of the energy deposition profile is then sufficient to determine the Gruneisen coefficient.

By locating the transducer just beyond the deposition region, the effects of uncertainties in the Hugoniot, dispersion, or attenuation are minimized. Moreover, since the entire stress profile is obtained, serious errors in the constitutive relation will be detected.

#### EXPERIMENTAL DESIGN

The materials studied in the present investigation were PETN, KDNBF, and RDX

explosives. The PETN wafers were pressed from a very fine grain powder (Diam  $\approx 0.003$  mm) to densities of  $1.47 \text{ gm/cm}^3$  to  $1.67 \text{ gm/cm}^3$ . A photomicrograph of the PETN powder is shown in Fig. 1. The RDX and KDNBF wafers were pressed from coarser grain (MIL SPEC) powders to densities of  $1.62 \text{ gm/cm}^3$  to  $1.65 \text{ gm/cm}^3$ . A photomicrograph of the RDX powder is shown in Fig. 2; a typical grain size of  $0.25 \text{ mm}$  diam is observed.

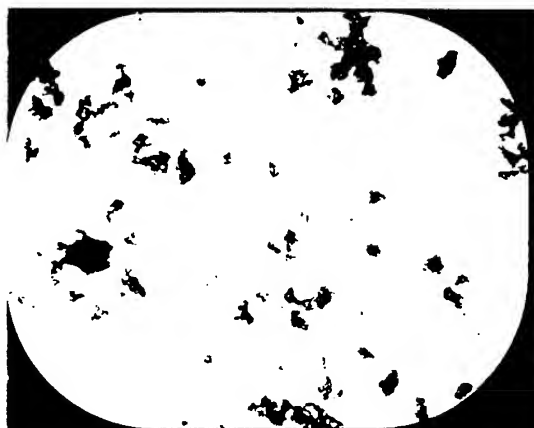


Fig. 1 - Photomicrograph of PETN powder (135X)



Fig. 2 - Photomicrograph of RDX powder (75X)

Quartz gauges were bonded to the rear surface of the wafers to measure the transmitted stresses. The gauges were Valpey Corporation Type QHJA which have a nominal  $0.5 \mu\text{sec}$  recording time. Eastman 910 was used as the bonding agent for the RDX and PETN samples, and ethyl cellulose was used for the

KDNBF samples. The bond thicknesses were less than one mil thick in order to insure a proper coupling of the transmitted stress from the wafers to the gauge. The explosive wafers were 3/4 in. diam; this size is sufficient to insure a one-dimensional strain geometry over the entire quartz gauge area.

The pulsed electron beam from the Physics International Model 312 Pulserad was used in the experiments. The sample irradiations were performed in an electron beam chamber that was evacuated to a pressure of 0.75 torr of air. This was necessary to produce a stable divergent electron beam. The wafers were covered with a one mil aluminum foil to provide a good ground plane for the electron beam and to contain any powder that spalled off the front surface.

The selection of the electron energy spectrum was based upon two major constraints. First, it is desirable to avoid large variations in the dose over dimensions comparable to the distance a stress wave can propagate during the energy deposition time. The pulse duration for the Model 312 Pulserad is approximately 25 nsec; stress waves in PETN can travel approximately 0.006 cm in this time. Based upon this alone the highest energy beam available would be used. However, the time duration of the subsequent stress pulse is determined by the depth of the heated region and in order to observe the complete compressive stress pulse in a 0.5  $\mu$ sec quartz transducer, the depth of heating must not exceed 0.12 cm (PETN). Based upon these considerations a nominal 0.4 MeV mean electron energy spectrum was selected.

In order to determine the spatial distribution of specific energy that is deposited in a target material from an electron beam, two characterizations of the beam are required: (1) the electron beam energy spectrum or a normalized deposition profile in depth in the target material, and (2) the incident fluence (the time integrated energy flux of the electron beam).

A measurement of the deposition profile was obtained utilizing an aluminum depth dosimeter. This dosimeter consists of a closely spaced stack of thin aluminum foils that are thermally isolated. The electron beam impinges normal to the foils. Iron-constantan thermocouples spot welded to each foil indicate the temperature rise, and consequently the dose deposited, in each of the foils.

The deposition profile normalized to an incident fluence of 1 cal/cm<sup>2</sup>, obtained from a

number of experiments using the aluminum depth dosimeters is plotted in Fig. 3. To determine the deposition profile in the explosive samples, the spatial coordinate of the aluminum deposition profile was scaled by the ratio of the density of aluminum to the density of the explosive. This was justified by a Monte Carlo electron transport calculation which indicated that differences in the scaled deposition profiles between aluminum and the explosives were less than the experimental error.

Current and voltage monitors were used to determine the characteristic functioning of the pulser on each shot. The data from these monitors were used to indicate any changes in the spectrum, and consequently the deposition profile, that might occur on subsequent shots.

In order to determine the fluence incident on a sample, use was made of total absorbing graphite calorimeters that were placed around the sample. In addition, thin bare thermocouples were placed around the perimeter of the explosive wafer. This setup is shown schematically in Fig. 4. Preliminary experiments were required to calibrate the output of the bare thermocouples in terms of the incident fluence. This was accomplished by a series of experiments in which the bare thermocouples were placed immediately in front of an array of graphite calorimeter blocks. A calibration curve from a number of shots is shown in Fig. 5.

On a given explosive sample experiment the fluence over the sample area was obtained by interpolating the data from surrounding calorimeter blocks and also by the output readings of the bare thermocouples. It was thus possible to determine fairly accurately any variation in fluence over the sample region of interest. The fluences determined by the two methods were in generally good agreement.

In order to check the experimental configuration, a preliminary experiment was conducted with a quartz gauge bonded to an aluminum sample. The equation of state of aluminum is quite well known, and consequently a well designed experiment should yield a good comparison between the calculated and measured stresses. Figure 6 is an oscillogram record of the response of a quartz gauge bonded to the rear surface of an aluminum sample irradiated with the pulsed electron beam. Figure 7 shows the comparison of the calculated and measured stress. It is seen that the agreement between the calculated and measured stresses is within 5%.

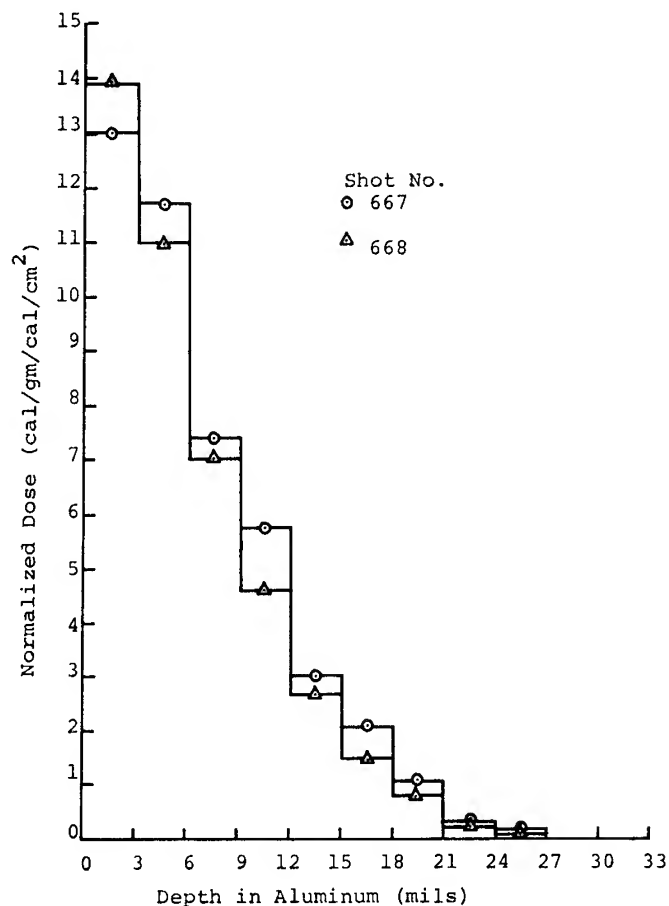


Fig. 3 - Measured energy deposition profiles in aluminum

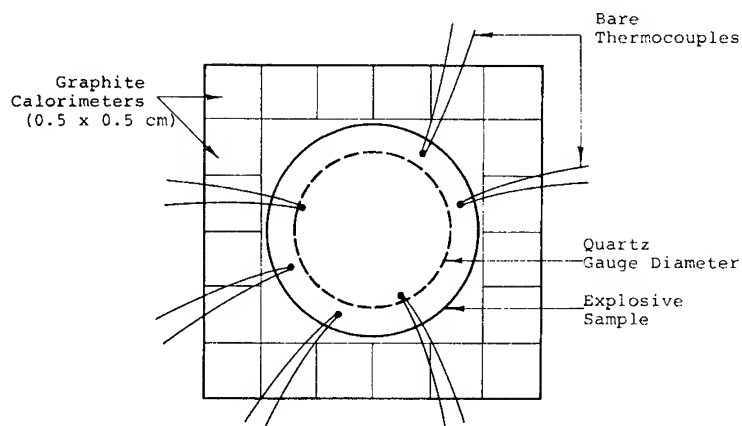


Fig. 4 - Sample configuration

## RESULTS AND DISCUSSION

A quartz transducer record obtained for the pressed PETN is shown in Fig. 8. The first

signal is a short pulse due to electron Bremsstrahlung radiation incident upon the cables for the transducer. This provides a precise fiducial point for the energy deposition. The



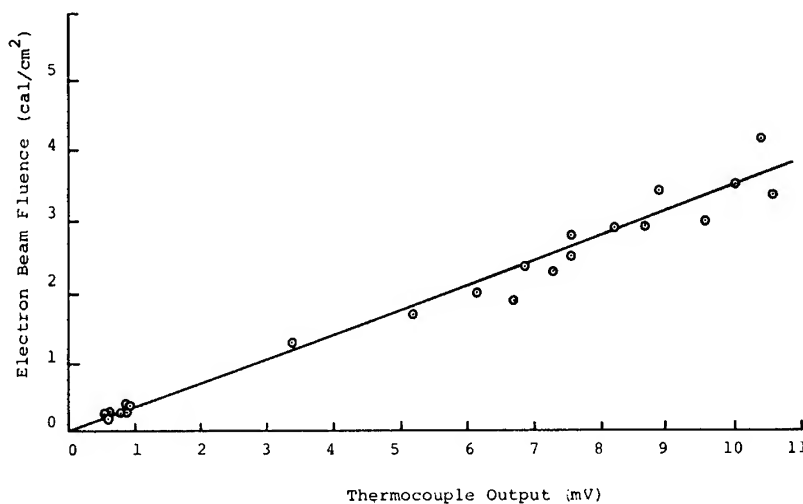


Fig. 5 - Bare thermocouple calibration curve for 0.4 MeV pulsed electron beam

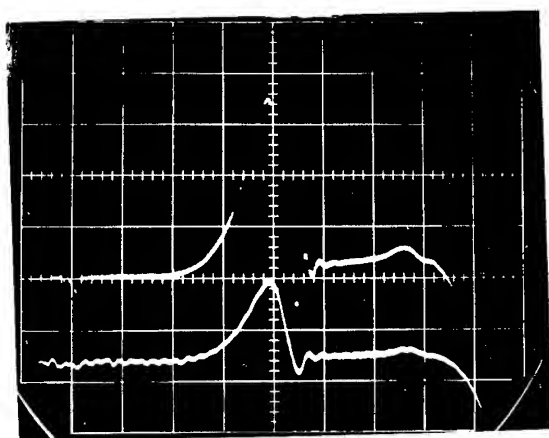


Fig. 6 - Quartz gauge record obtained for an aluminum sample, shot 614. Upper trace: 2 V/major division; lower trace: 5 V/major division; sweep speed: 0.1  $\mu$ sec per major division.

compressive stress pulse arrives shortly thereafter, and is completely recorded well within the 0.5  $\mu$ sec reading time of the transducer. Note that a measurement of the sound speed in the material can be obtained for each shot, when the sample thickness and deposition profile are known.

The recorded stress levels were comparatively low; further, a consequence of the Seaman and Linde model (4) is that the propagated stress pulse resulting from energy deposition in a porous solid will not exceed half the crush strength provided the voids are not filled and

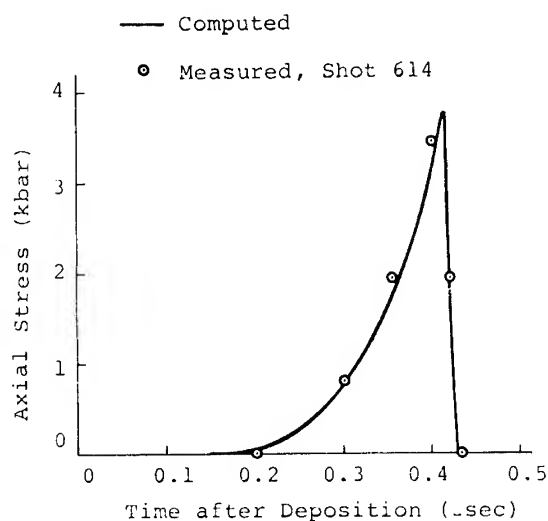


Fig. 7 - Computed and measured stress profiles for aluminum

no vaporization takes place. Therefore, linear equations were used to compute the material response. The effect of the source duration was included, although in this particular instance, the variation of the dose depth was such that it had only a minor effect upon the stress pulse.

A comparison of the measured stress profile with a computed stress profile based upon the energy deposition profile, a sound speed of 0.24 cm/ $\mu$ sec, and an assumed value for the Grüneisen coefficient of 0.51 is shown in Fig. 9. The agreement is quite satisfactory and is

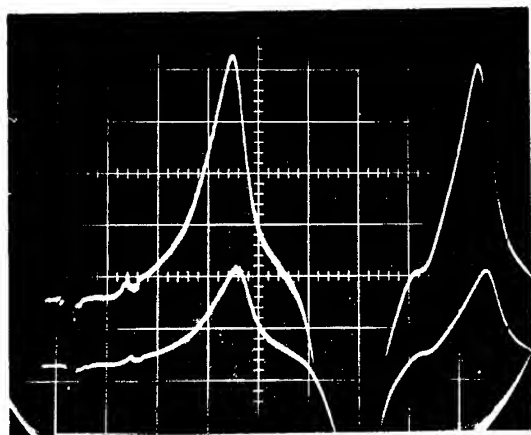


Fig. 8 - Quartz gauge record obtained for a PETN sample with a density of  $1.60 \text{ gm/cm}^3$ , shot 683. Upper trace:  $0.2 \text{ V/major division}$ ; lower trace:  $0.5 \text{ V/major division}$ ; sweep speed:  $0.2 \text{ μsec per major division}$ .

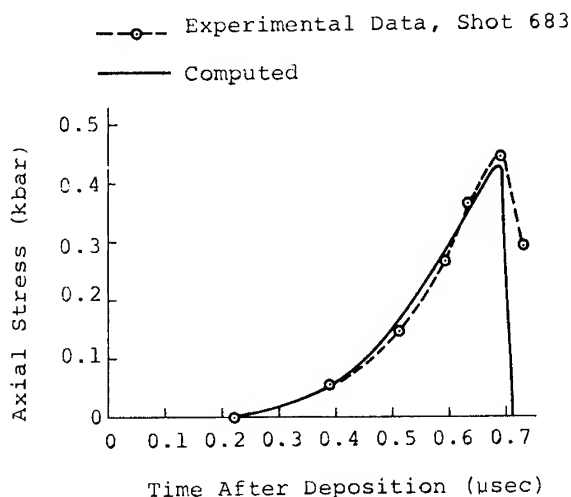


Fig. 9 - Computed and measured stress records for PETN sample

comparable to the agreement achieved for aluminum.

The results for all the PETN samples are summarized in Fig. 10 where the peak initial pressure inferred from the measured stress is shown as a function of peak dose. Linear relationships are found for samples with densities of  $1.59 \pm 0.01 \text{ gm/cm}^3$  and  $1.54 \pm 0.01 \text{ gm/cm}^3$ . The Gruneisen coefficients for these materials are computed from Equation (2) to be 0.51 and 0.15, respectively. Greater uncertainties are associated with the data of the low density samples,  $1.47 \text{ gm/cm}^3$  and  $1.54 \text{ gm/cm}^3$ . This is

a result of the lower densities and sound velocities producing stress pulses that slightly exceeded the nominal readtime of the quartz gauges and so an extrapolation of the records was necessary.

The pressure that was observed from the  $1.47 \text{ gm/cm}^3$  dense sample exposed to a dose of  $16 \text{ cal/gm}$ , falls within an expected region. The other  $1.47 \text{ gm/cm}^3$  dense sample however, produced a pressure that is higher than anticipated. It falls slightly above the data for the  $1.54 \text{ gm/cm}^3$  dense samples. This discrepancy was not resolved.

The datum point for material with a density of  $1.67 \text{ gm/cm}^3$  indicates a value for the Gruneisen coefficient of  $1.2 \pm 0.2$  which is considerably higher than that of the lower density materials. The Gruneisen coefficient is expected to be quite sensitive to density as crystalline density is approached, so this result is anticipated.

The sound speeds obtained from the oscilloscope traces for the  $1.59 \text{ gm/cm}^3$  and  $1.54 \text{ gm/cm}^3$  samples were found to be  $2.4 \pm 0.1 \text{ mm/μsec}$  and  $1.8 \pm 0.3 \text{ mm/μsec}$ , respectively. These agree with data reported by Roth and Blackburn (9) for PETN in the same density ranges. The measured sound speeds for the  $1.47 \text{ gm/cm}^3$  and the  $1.67 \text{ gm/cm}^3$  samples were  $1.7 \pm 0.3 \text{ mm/μsec}$  and  $2.8 \text{ mm/μsec}$ , respectively.

An estimate of the Gruneisen coefficient for fully dense PETN can be obtained from the relationship:

$$\Gamma = \frac{\beta k}{\rho c_p} \quad (3)$$

where  $\beta$  is the volume expansion coefficient,  $k$  is the adiabatic bulk modulus, and  $c_p$  is the specific heat at constant pressure. Using values of  $1.77 \text{ gm/cm}^3$  (fully dense) for the density,  $0.26 \text{ cal/gm-}^\circ\text{C}$  for the specific heat,  $46 \text{ kbar}$  for the bulk modulus (10), and a value of  $12 \times 10^{-5} \text{ cm/cm-}^\circ\text{C}$  for the linear expansion coefficient, which was obtained for PETN pressed to a density of 1.60 (11), Equation (3) predicts a value of 0.8 for  $\Gamma$ . The uncertainty in these parameters used in Equation (3) is not documented, but assuming that the last significant figure is uncertain only by one digit, a total uncertainty of  $\pm 20\%$  results. Moreover, the actual uncertainty using some of these values may be considerably larger.

Using the relationship between the bulk modulus and the dilatational sound speed,  $c_o$ ,

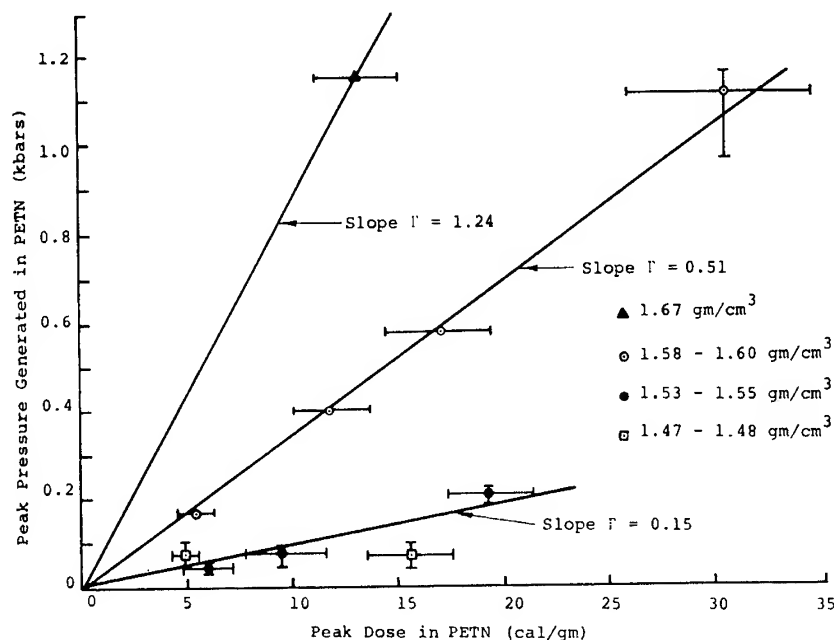


Fig. 10 - Peak generated pressure versus peak dose in PETN

$$k = \frac{\rho c_o^2}{3} \left( \frac{1 + \nu}{1 - \nu} \right) \quad (4)$$

where  $\nu$  is Poisson's ratio, it is possible to bound the bulk modulus. Since Poisson's ratio lies between zero and  $1/2$ ,

$$\frac{\rho c_o^2}{3} \leq k \leq \rho c_o^2 \quad (5)$$

Using the theoretical density of 1.77, and the sound speed measured for the highest density sample,  $k$  is bounded between 46 kbar and 140 kbar. It is unlikely that Poisson's ratio is zero, so the bulk modulus must exceed 46 kbar. Moreover, the sound velocity apparently increases with density, so the bounding values used here are also probably low. Consequently, the value for Gruneisen coefficient computed for fully dense PETN with Eq. (3) is probably too small, which is supported by the measured datum.

The peak dose achieved during these experiments was on the order of 30 cal/gm. This corresponds to a maximum temperature increase of approximately 115 C-deg (or less since the specific heat generally tends to increase with temperature). Since the samples were initially at room temperature, the final temperature is below the melting point, 141°C (10). Moreover, the volume expansion for this

dose will be approximately 4%, which is insufficient to fill the void volume, even if no external expansion occurs.

The linear relationship observed between the pressure and dose for the 1.59 gm/cm<sup>3</sup> PETN probably indicates that no significant loss in the shear strength is occurring at the dose levels and time scales of the experiments. As the melt enthalpy is reached, however, a rapid drop in the pressure with increased dose is anticipated up to the point where either thermal expansion completely fills the voids or initiation occurs.

The oscilloscope traces obtained for KDNEF and RDX are shown in Figs. 11 and 12. The contrast of these records with those obtained for PETN is striking. The difference in response is attributed to the initial particle sizes of the explosive grains before pressing. Since the stress pulses encountered are low amplitude (less than half a kilobar), the stress pulse reaching the quartz transducer through the coarse grain material is evidently non-planar, and substantial dispersion must have occurred. Consequently, attempts to obtain measurements on the coarse grain materials were abandoned.

The qualitative comparison of these results for materials with different grain sizes also raises questions as to whether or not meaningful observations can be made for an elastic precursor in coarse grain materials.

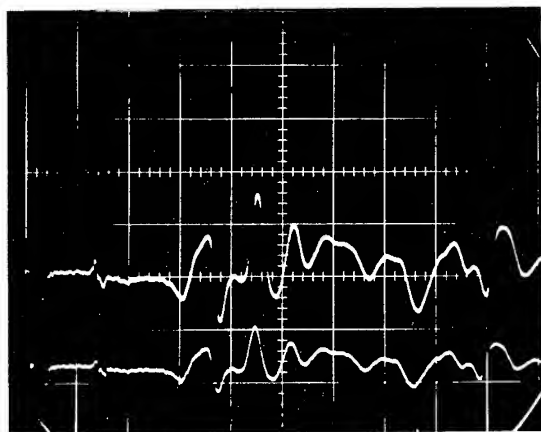


Fig. 11 - Quartz gauge record obtained for KDNBF sample. Upper trace: 0.1 V/major division; lower trace: 0.2 V/major division; sweep speed: 0.2  $\mu$ sec/major division.

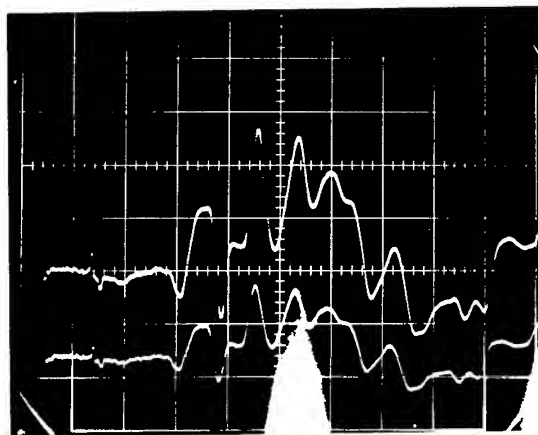


Fig. 12 - Quartz gauge record obtained for RDX sample. Upper trace: 0.1 V/major division; lower trace: 0.2 V/major division; sweep speed: 0.2  $\mu$ sec/major division.

## SUMMARY AND CONCLUSIONS

Table 1 summarizes the data obtained for fine grain PETN using pulsed electron beam techniques. The effective Gruneisen coefficient was found to be strongly dependent on the porosity of the samples; effective values ranged from 1.2 to 0.1 for samples of density 1.67 gm/cm<sup>3</sup> to 1.48 gm/cm<sup>3</sup> (5.5% to 16.5% porosity).

The effective Gruneisen coefficient for fine grain PETN pressed to a density of 1.59 gm/cm<sup>3</sup> has been determined to be 0.51, constant for dose levels up to 30 cal/gm. For samples pressed to a density of 1.54 gm/cm<sup>3</sup>, the effective Gruneisen coefficient was found to be 0.15, constant for dose levels up to 20 cal/gm. The experimental uncertainty associated with these measurements is estimated as  $\pm 15\%$ .

The elastic sound velocities were obtained concurrently for the samples of various densities. The values ranged from 1.7 mm/ $\mu$ sec to 2.8 mm/ $\mu$ sec.

A linear relationship between peak dose and pressure was observed over the range of the experimental conditions obtained for the 1.59 gm/cm<sup>3</sup> and 1.54 gm/cm<sup>3</sup> PETN. Consequently, additional data must be obtained at higher dose levels in order to provide an adequate test of the applicability of the Seaman and Linde model to granular explosives.

Finally, it appears that with some modifications in technique, it may be possible to extend the range of the measurement of the constant volume pressure-energy relationship into regions where significant reactivity of the explosive is encountered.

## ACKNOWLEDGMENTS

The assistance of H. Pollard, Physics International Company, and H. Jackson, Picatinny Arsenal, in the preparation of the explosive samples is gratefully appreciated. G. Harvey is thanked for his assistance in the performance of the experiments.

TABLE 1  
Summary of Results for PETN

Density (gm/cm <sup>3</sup> )	Relative Density, $\rho/\rho_0$ (Percent)	Sound Speed (mm/ $\mu$ sec)	$\Gamma$
1.67	94.5	2.8 $\pm$ 0.1	1.2
1.59	90.0	2.4 $\pm$ 0.1	0.51
1.54	87.0	1.8 $\pm$ 0.3	0.15
1.48	83.5	1.7 $\pm$ 0.3	(0.07 to 0.23)

## REFERENCES

1. M. H. Rice, R. G. McQueen and J. M. Walsh, *Solid State Physics*, Vol. 6, 1958.
2. L. H. Bakken and P. D. Anderson, "An Equation of State Handbook," Rept. SCL-DR-68-123, 1969, Sandia Corporation, Livermore, Calif.
3. W. Hermann, "Constitutive Equation for the Dynamic Compaction of Ductile Porous Materials," *J. Appl. Phys.*, Vol. 40, p. 2490, 1969.
4. L. Seaman and R. K. Linde, "Distended Materials Model Development," AFWL-TR-68-143, Vol. 1, Air Force Weapons Laboratory, Albuquerque, New Mexico, May 1969.
5. R. A. Graham and R. E. Hutchinson, "Thermoelastic Stress Pulses Resulting from Pulsed Electron Beams," *Appl. Phys. Letters*, Vol. 11, p. 69, 1967.
6. R. B. Oswald, Jr., D. R. Schallhorn, H. A. Eisen, and F. B. McLean, Jr., *Appl. Phys. Letters*, Vol. 13, p. 279, 1968.
7. A. Goodman, "The Direct Measurement of the Gruneisen Parameter," Rept. SC-TM-67-13, Sandia Corporation, Albuquerque, New Mexico.
8. P. W. Spence, G. Yonas, and D. K. Dean, "Shock Generation in S-200 Beryllium Using a Pulsed Electron Beam," *Bull. Am. Phys. Soc.*, Vol. 14, p. 1164, 1969.
9. J. Roth and J. Blackburn, "Effect of Initial Temperature on the Shock Sensitivity of Granular Explosives," Rept. SC-CR-67-2805, Sandia Corporation, Albuquerque, New Mexico, August 1967.
10. "Properties of Explosives of Military Interest," Army Materiel Command Pamphlet No. 706-177, March 1967.
11. Personal communication — J. Roth, Stanford Research Institute.

# CREATION OF AN INTENSE SHOCK IN SOLID DEUTERIUM BY A PULSED LASER BEAM

## REQUIREMENTS FOR HUGONOT DATA MEASUREMENTS

C. Fauquignon

*Commissariat à l'Energie Atomique, Centre d'Etudes de Limeil  
Limeil-Brévannes, France*

### ABSTRACT

The generation of a shock is a normal occurrence when heating a solid by an intense laser pulse. For pulse duration longer than about 1 nsec the hydrodynamics is correctly represented by a light-driven deflagration initiated at the free surface of the material facing the laser. In the case of  $10^{-10}$  - to  $10^{-12}$ -sec laser pulses the energy spreads into the solid through a thermal wave and the hydrodynamics develops only after the switch-off of the laser. It is shown that the hydrodynamic shock-tube model can be applied to this situation. By using both models shock pressures are estimated in the case of a neodymium glass laser impinging deuterium ice. Results of early experiments concerning deuterium and polyethylene irradiated by a 35-nsec pulse are presented.

### INTRODUCTION

When a laser beam impinges an absorbing medium the local electrons are accelerated by an inverse Bremsstrahlung process, then the energy is shared with the other particles through collisions. In the present paper we shall assume that the equipartition times are much shorter than that corresponding to the macroscopic motions of the matter; consequently the absorption zone is simply considered as a thermal source.

The thermal energy spreads in the surrounding material by heat diffusion and by hydrodynamical motions.

The relative importance of the two processes depends on both the temperature (then on the laser power) and the pulse duration. Indeed heat diffusion develops more rapidly than hydrodynamical motions, and in the case of a very short laser pulse is the only process during the time of the illumination.

Nevertheless it will be shown that in all cases, the heating of a solid by a giant laser pulse produces a shock wave which is initiated

during the illumination (light-driven deflagration) or after it by degeneration of a thermal wave.

Simple theoretical models have been established for both cases and are used to estimate the shock pressure.

The validity of the light-driven deflagration has been checked experimentally for solid deuterium by means of plasma temperature and shock-wave velocity measurements. Some other early experiments on polyethylene aiming at defining optimum conditions for accurate Hugoniot measurements are presented.

The laser used is a neodymium glass laser ( $\lambda = 1.06 \mu\text{m}$ ),  $10^9$  -  $10^{10}$  watts,  $5 \times 10^{-9}$  to  $3.5 \times 10^{-8}$  sec.

### SPECIFIC HYDRODYNAMIC BEHAVIOR OF A SOLID UNDER LASER HEATING

The absorption of the laser flux by a transparent material is explained by a preionization due to a multiphoton effect (1). The degree of

ionization is just adequate to make the material opaque to the laser frequency; higher frequencies can still propagate. The light intensity at which this effect appears depends on the material under consideration; a value of about  $10^{10} \text{ W} \times \text{cm}^{-2}$  has been found in the case of deuterium. The thermodynamic state after the preionization is unknown; however, for a rough estimate of the energy spent for it let us think that the enthalpy has not significantly increased. In the calculations which are presented it has been assumed further that we are still at the standard conditions.

The fundamental difference with regard to the behavior of gaseous and solid materials appears as we consider the limiting condition for the light to propagate in an ionized medium. This condition is given by:  $\omega_p/\omega < 1$ , where  $\omega_p$  is the plasma frequency and  $\omega$  is the laser frequency. As  $\omega_p$  is proportional to the square root of the electron density, it is found that an infrared light cannot enter a material at a density equal to that of a solid.

Let us first recall briefly the flow pattern associated with the heating of a gas: the light heats directly the gas at its standard density or, even, at a higher density in the case of a preloading by shock. The analogy between the absorption zone and the reaction zone of an explosive has led to the establishment of a light-driven-detonation model. This model, in which the Chapman-Jouguet conditions are assumed to be valid, has been successfully experienced (2), (3).

It is also to be noticed that the detonation wave develops outward from the focus toward the laser and in the opposite direction.

When a pulsed laser beam impinges a transparent solid target located in a vacuum, at first the ionization travels from the focus toward the laser and gradually rejects the light at the free surface. The further penetration of the light is only possible following an erosion of the material.

The density at the top of the absorption zone is called the cut-off density; its value corresponds to the equality  $\omega_p = \omega$ . In the case of deuterium ice irradiated by a  $1.06\text{-}\mu\text{m}$  wavelength light, the maximum density in the absorption zone is fifty times lower than the standard density. The heating occurs during the release of the material into a vacuum. Under such conditions, the behavior of a solid should be correctly represented by a light-driven deflagration which propagates in toward the target.

It is obvious that the same model can be applied to an opaque material, for instance a metal. If the target is located in gas at a pressure high enough for the multiple breakdown to occur (that is to say a pressure of some tens of Torr in air), a detonation wave and a deflagration wave will be initiated at the free surface and will propagate in opposite directions.

#### INTEREST IN THE LASER AS A SHOCK GENERATOR

The possibility that the laser flux will drive a deflagration leads us to compare it with a chemical explosive. From this point of view, the laser presents three main advantages:

(a) A radiant flux power per unit surface of  $10^{13} \text{ W} \times \text{cm}^{-2}$  is readily obtained in the present state of the art. The equivalent power delivered by an explosive is given by

$$P = E \times D \times \rho,$$

where

$E$ , specific energy  $\approx 5 \text{ KJ} \times \text{g}^{-1}$

$D$ , detonation velocity  $\approx 8 \times 10^3 \text{ m} \times \text{sec}^{-1}$

$\rho$ , mass density  $\approx 1.7 \text{ g} \times \text{cm}^{-3}$

Let us find numerically  $P \approx 10^{10} \text{ W} \times \text{cm}^{-2}$ .

(b) The radiation-driven deflagration can be initiated directly in the material the behavior of which we want to study under shock loading. This property is mainly interesting in the case of low-density materials which are severely mismatched with the classical shock generators.

(c) Due to the large speed of the light associated with the thinness of the absorption zone, shocks of a quasi-perfect planarity are obtained. Preliminary experiments on polyethylene show that the planarity of a shock propagating about  $150 \mu\text{m}$  in front of the deflagration wave is quite perfect over a diameter equal to 0.9 times that of the laser beam.

The former advantages are mainly due to the specific property of the laser to concentrate in space and time a relatively small energy. As an offset to this quality the highly loaded region has small dimensions and there the flow is strongly unstationary. To take an effective benefit of this new tool in the field of high-pressure Hugoniot data, measurements have to be done near the maximum of the pressure

spike, that is to say at the beginning of the fall of the laser pulse.

Rough hydrodynamic calculations applied to the heating of deuterium by the 35-nsec pulse considered in (8) show that the maximum shock pressure drops to about 10 percent along a path of  $3 \times 10^{-2}$  cm run by the shock in  $5 \times 10^{-9}$  sec.

The most recent experiments which will be described further aim at a smoothing of the pressure decay by delaying the instant when the absorption zone passes through the optical focus relative to that of maximum laser output power.

Nevertheless, the most severe limitations in the use of the high pressures generated by laser action concern the accuracy of the velocity measurements. A nanosecond time resolution is needed for the recording means.

If we are satisfied with lower pressures the measurements are to be done at the end of a relatively thick target: at a far enough region of that where the deflagration took place the pressure profile is smooth and conventional recording methods can be used (11).

#### RADIATION-DRIVEN DEFLAGRATION

As we have seen before, the laser flux energy is deposited and converted in a thermal form in a narrow region close to the free surface of the solid. If the laser pulse duration is long enough the plasma generated in the absorption zone has time to blow off into the vacuum and the so-called radiation-driven deflagration appears as a result of the momentum conservation law (4), (5). Another condition for its existence is that the thermal wave which may have been created at the origin of the interaction has become subsonic (6).

Figure 1 represents in a laser flux density-pulse duration diagram the frontier between the deflagration and the purely thermal regimes.

A deflagration process associated with a thermal conductivity spreading the energy from the absorption zone into the shock-loaded material is the usual situation in the neighbourhood of the dividing line of Fig. 1. The solution of such a problem requires the use of a large computer (7).

If heat diffusion is neglected and by putting a set of assumptions which will be presented later, an analytical solution for the flow can be found: any quantity can be expressed relatively to the unique laser flux.

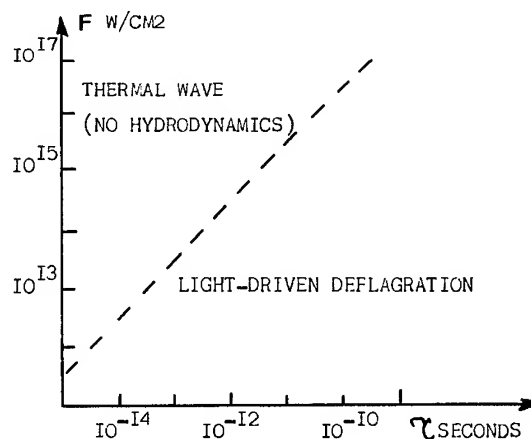


Fig. 1 - Domains of validity for hydrodynamic and thermoconduction models

Such a model has been described in (8) and will be used here to evaluate the pressure of the shock which propagates in front of the deflagration wave. Figure 2 gives a schema of the flow (a) and of the density and temperature profiles (b). The main assumptions used in the model (8) are:

- The flow is a one-dimensional one.
- The discontinuity in the deflagration wave (R) is the result of a surface absorption process.
- The centered rarefaction (E) is an isothermal one. The density at the head of the fan is equal to the "cut-off" density  $\rho_R$ .
- The deuterium is described by a perfect gas law; diatomic gas ( $\beta = 1.4$ ) in front of the deflagration and monoatomic ( $\gamma = 1.67$ ) behind it.

When the radiation in the plasma, which represents 5 percent of the total energy, is neglected, the different parameters of the flow are found proportional to a certain power of the incident laser flux  $F$ . In particular, the shock velocity  $D_s$  is given by

$$D_s = F^{1/3} \times \left[ \frac{(\beta + 1) \rho_R}{\rho_o} \right]^{1/2} \times \left[ \frac{\rho_R}{2} \left( \frac{7\gamma - 5}{\gamma - 1} - \frac{4\rho_R}{(\beta + 1)\rho_o} \right) \right]^{-1/3} \quad (1)$$



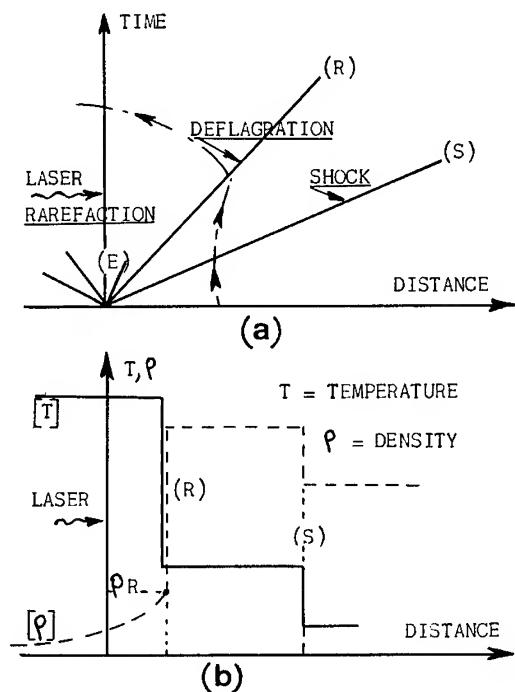


Fig. 2 - The laser-driven deflagration model

where

$$\rho_o = \text{initial density} = 0.17 \text{ g cm}^{-3}$$

$$\rho_R = \text{"cut-off" density} = 3.4 \times 10^{-3} \text{ g cm}^{-3}$$

for deuterium radiated by a neodymium glass laser.

Numerically,

$$D_s = 0.84 \times F^{1/3} \text{ cm sec}^{-1}$$

when  $F$  is expressed in  $\text{ergs cm}^{-2} \text{ sec}^{-1}$ .

The shock pressure is given by

$$p_s = \frac{2\rho_o}{\beta + 1} D_s^2$$

Numerically,

$$p_{s_{kb}} = 10^{-10} \times F^{2/3}; \quad F \text{ in C.G.S. units.} \quad (2)$$

Until now, only plasma temperatures and shock wave velocities have been measured. It will be shown later (see Fig. 5) that the

agreement with the corresponding calculated values is quite good. Consequently the equation (2) should give a reasonably correct estimation of the pressure which can be induced by laser action in the region of the  $F, \tau$  diagram (see Fig. 1) where the model is valid.

As an example, a 100-J,  $10^{-9}$ -sec laser beam impinging a deuterium speck on a  $1\text{-mm}^2$  area should induce a shock pressure of 2.10 Mb.

It must be noted, Eq. (2), that for a constant flux power the pressure varies as  $S^{-2/3}$  where  $S$  is the radiated area. With the former standard pulse,

$$p_s = 450 \text{ kb} \quad \text{when } S = 10 \text{ mm}^2 \text{ and}$$

$$p_s = 90 \text{ kb} \quad \text{when } S = 1 \text{ cm}^2.$$

When the energy balance is calculated it is found that 10 percent of the absorbed light intensity is used to supply the shock (8).

#### SHOCK GENERATION BY ULTRASHORT LASER PULSE

For high flux densities and very short laser pulses (left part of Fig. 1) the energy transfer occurs by thermal conductivity only.

Assuming a constant flux density  $F$ , the position  $X_i$  of the thermal wave relative to the solid deuterium free surface and the temperature  $T_i$  are given at time  $t_i$  by (6):

$$X_i = 3.8 \times 10^{10} \times F^{5/9} \times \left( \frac{t_i}{n_i} \right)^{7/9} \quad (3)$$

$$T_i = 6.3 \times 10^4 \times F^{4/9} \times \left( \frac{t_i}{n_i} \right)^{2/9}, \quad (4)$$

all quantities in C.G.S. units and  $n_i = 5 \times 10^{22} \text{ ions cm}^{-3}$  (constant volume heating).

At time  $t_i$  the conduction zone is a reservoir of length  $X_i$ , temperature  $T_i$  and pressure  $p_i = 2n_i k T_i$ , the fluid being at rest.

From now on  $t_i$  will represent the end of the laser pulse. If  $t_i$  exceeds the time at which the thermal wave becomes subsonic, a radiation-driven deflagration would be established after an ill-defined transition phase.

Figure 3 represents the history in a space versus time diagram; the hatching correspond to the hot region.

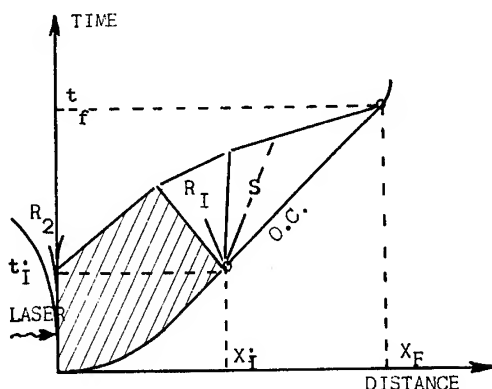


Fig. 3 - The thermal wave model and the hydrodynamic transition

At the end of the laser pulse the velocity of the thermal wave, which is no longer fed, vanishes rapidly and the thermal energy is transferred to the surrounding material by hydrodynamical motions (Fig. 3):

- Plasma ejection into vacuum ( $R_2$ )
- Shock wave (o.c.) in solid deuterium
- Reflected rarefaction fan ( $R_1$ ) in the heated region.

Such a schema is similar to that of the hydrodynamic shock tube; in this comparison time  $t_i$  corresponds to the breaking of the diaphragm.

The shock wave will be weakened when caught up by release waves  $R_2$  refracted through  $R_1$ . Let us call  $X_f$ ,  $t_f$  the coordinates of the end of the pressure plateau; a rough numerical calculation using a perfect gas law as an equation of state shows that  $X_f - X_i$ , which corresponds to the stationary region of the flow, is of the order of  $100 \mu\text{m}$  for a  $100\text{-J } 10^{-11}\text{-sec}$  laser pulse irradiating a  $1\text{-mm}^2$  area.

#### CALCULATION OF THE SHOCK PRESSURE

The shock tube similarity allows the use of well-known relations established in considering the continuity of the flow on both sides of the interface S (Fig. 3). We shall use the classical implicit relation between pressures and sound velocities:

$$\frac{p_i}{p_o} = \pi \left[ 1 - \frac{a_o}{a_i} (\gamma - 1) \right] \times \frac{\pi - 1}{2\beta[(\beta + 1)\pi + \beta - 1]} \left( \frac{2\gamma}{1 - \gamma} \right)^{\frac{2\gamma}{1 - \gamma}} \quad (5)$$

where

$a_o$ ,  $a_i$  are the sound velocities in the regions (0) and (1)

$\pi = \frac{p_c}{p_o}$  with  $p_c$  = shock pressure

$\beta = 1.4$ , the polytropic coefficient of cold deuterium

$\gamma = 1.67$ , the polytropic coefficient of hot deuterium

It should be noticed in the present case that the reservoir is heated at constant mass density and then  $p_i = 2n_i k T_i$ , the particle number being doubled by ionization.

We have also:

$$a_i = \left( \frac{R'}{M_i} \times T_i \right)^{1/2} = 6.45 \times 10^3 (T_i)^{1/2} \text{ cm sec}^{-1},$$

$$p_o = 10^6 \text{ baryes},$$

$$a_o = 2 \times 10^5 \text{ cm sec}^{-1}. \quad (9)$$

Assuming  $\pi \gg 1$ , Eq. (5) becomes the following implicit relation between  $T_i$  and  $p_c$ :

$$A \left( \frac{T_i}{p_c} \right) = \left[ 1 - \frac{B}{C} \times \frac{p_c}{T_i} \right]^{-5} \quad (6)$$

with

$$\left. \begin{aligned} A &= 2n_i k = 1.38 \times 10^7 \\ B &= \frac{a_o(\gamma - 1)}{[2\beta p_o(\beta + 1)]^{1/2}} = 49.6 \\ C &= 6.45 \times 10^3 \end{aligned} \right\} \text{ C.G.S. units}$$

From the symmetry played by  $T_i$  and  $p_c$  in Eq. (6) one draws a simple linear relation. The

coefficient of proportionality is determined at the limit  $T_i = T_o = 4^\circ\text{K}$  where  $p_c = p_o = 10^6$  baryes.

Then, we get

$$p_{c_{kb}} = 2.5 \times 10^{-4} T_i \text{ } ^\circ\text{K}.$$

Finally, by taking account of Eq. (4),

$$p_{c_{kb}} = 1.44 \times 10^{-4} F^{4/9} t_i^{2/9}, \quad (7)$$

where  $F$  and  $t_i$  are in C.G.S. units.

Remarks:

(a) In the former equations  $F$  represents the light intensity which has been effectively absorbed. When ultrashort pulses are considered a large fraction of the incident light is reflected due to the steep density gradient at the free surface which has no time to release. Consequently the efficiency of the heating is lowered.

(b) The assumption of a one fluid flow is no longer valid when the pulse duration becomes of the order of the time necessary for electrons to exchange energy with ions. At the solid density this time is about  $10^{-12}$  sec.

To illustrate the capability of the laser to produce intense shock waves, we have considered a 100-J rectangular pulse irradiating a 1-mm<sup>2</sup> area of deuterium ice, the duration of the pulse being the variable  $\tau$  and all the light intensity being assumed to be absorbed. Figure 4 represents the shock pressure  $p_c$  in terms of  $\tau$ ; the dotted line is an extrapolation of both models in the central region where heat diffusion and hydrodynamics are present.

## EXPERIMENTS AND RESULTS

The first set of experiments which is described here has been undertaken with regard to the study of the production of very hot deuterium plasmas by laser heating. The measurements of plasma temperature and shock wave velocity are aimed at checking the laser-driven-deflagration model.

In order to increase the efficiency of the laser action, the beam was focused on a very small area (0.1-mm in diameter) inside the deuterium ice; such experimental conditions are not fit for the measurements of Hugoniot parameters.

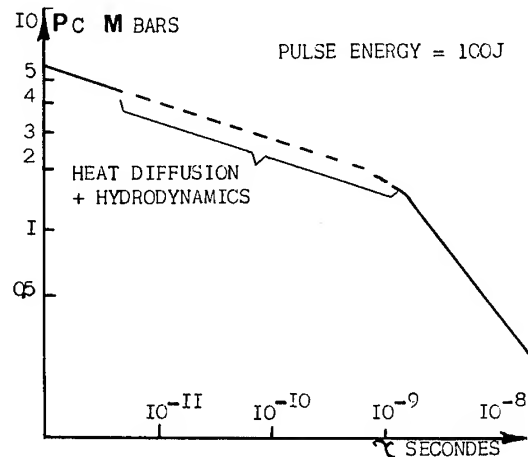


Fig. 4 - Calculated shock pressure in both models

More recent experiments have been performed in order to investigate in greater detail the shock-loaded region and the emergence of the shock at the free surface. For convenience a polyethylene target has been used up to now. The experimental setup remains the same with the exception of the focusing lens.

We use a Q-switched neodymium glass laser with five amplifier stages (5). The overall exit aperture is 45 mm in diameter.

The beam is focused onto the target either by means of a specially devised aspherical single lens (10) when sharp focusing is wanted (the focal spot can be moved  $\pm 2$  mm with respect to the target surface) or by a 600-mm focal length objective when a smoothly converging beam is needed to get a practically constant cross-sectional flow.

A 90° off-axis illumination of the target is obtained by a multiple breakdown in air. This is caused by focusing a part of the main laser beam which has been split in front of the interaction chamber (Fig. 5).

**Deuterium target:** the deuterium ice is obtained by condensation of gaseous deuterium inside a copper extruder chilled by liquid helium. The ice is a few millimeters long and has a 1- or 2-mm-thick square cross section.

**Polyethylene target:** it is a commercial strip of a given thickness (from 100 to 500  $\mu\text{m}$ ). It has been found that its behavior during the preionization phase was not identical to that of deuterium and the initiation of the deflagration

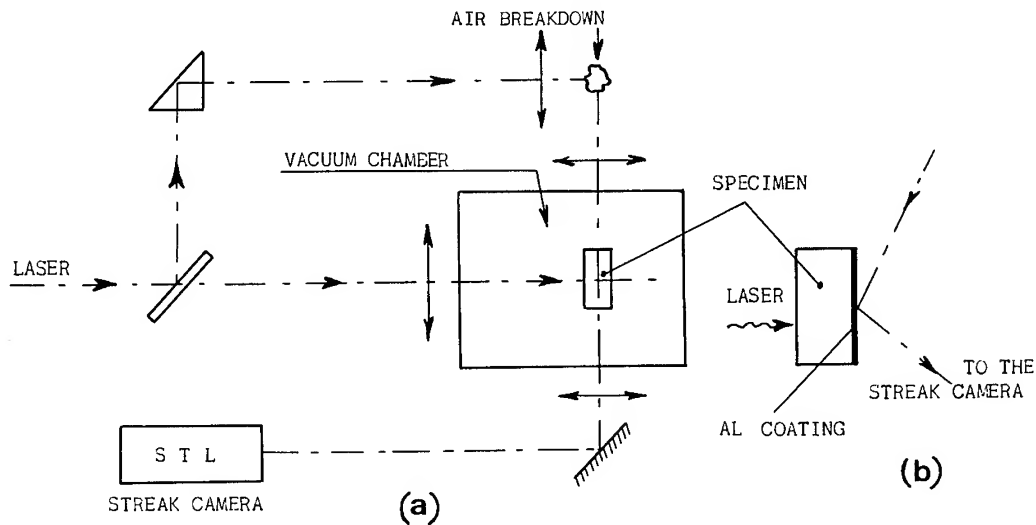


Fig. 5 - Experimental setup

has to be favoured by blackening (black ink) the free surface facing the laser.

### MEASUREMENTS AND RESULTS

In order to check the laser-driven-deflagration model, plasma temperature and shock wave velocity measurements have been performed on deuterium ice. The shock velocities have been calculated by a derivation of the path versus time recording of a STL streak camera. The mass density gradient associated with the shock is used to locate it in a Schlieren system.

Earlier measurements (8) had been performed by recording the self-luminosity of the event and it remained an uncertainty on the origin of the recorded trace (deflagration or shock wave).

Let us recall now that the light intensity is given by:

$$F = \frac{P}{s},$$

where  $P$  is the laser output power and  $s$  is the cross section of the absorbing layer.

For a given laser pulse, optimum performances are obtained if the deflagration front passes through the focal area at the time when the laser output power is maximum.

Figure 6 represents the maximum shock velocities which have been measured when this condition was fulfilled.

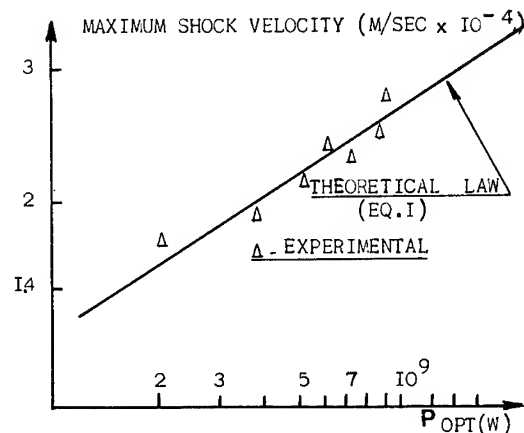


Fig. 6 - Experimental maximum shock velocity versus laser optimal power

It is obvious that if the focal area is passed by the deflagration front after the maximum output power has been reached, the shock pressure is lower but the flow is less unstationary. Consequently, focusing conditions can be used to govern the time dependence on the light intensity for a given output power.

The present experiments on polyethylene with respect to this possibility of smoothing the pressure decay and focusing conditions are varied in order to get reasonably constant shock velocities. The targets have different thicknesses ranging from 0.1 to 0.5 mm and the Schlieren method as presented before is used

to measure successively the shock and the free surface velocities.

On the other hand, a comparison between the shock-front diameter and that of the illuminated area is performed by using the setup of Fig. 5b. It has been found that the planearity of the shock front is quite perfect over a diameter of 0.9 mm when the absorbing layer which is 0.15 mm behind it has a diameter of 1 mm.

## CONCLUSION

The capability of the laser to generate very high pressures has been established with the assistance of simple theoretical models. At the present time the light-driven-deflagration model has been successfully checked.

The high pressures vanish rapidly after the laser switch-off and to take a real advantage of the laser, it appears that shock parameter measurements must be performed during or at the end of the illumination. A nanosecond time resolution is needed for the recording techniques to be used under such conditions.

An interesting behavior of the laser shock generator is the regulation of the flow by an action on the focusing conditions for a given waveform of the laser pulse. This mean has been found as a solution to approach the suitable pressure plateau which is needed for accurate Hugoniot data measurements.

## REFERENCES

1. R. G. Meyerand, A. F. Haught, "Gas Breakdown at optical frequencies", *Comptes Rendus de la 6ème Conférence Internationale sur les Phénomènes d'Ionisation dans les Gaz*, Paris, juillet 1963, S.E.R.M.A., Paris, pp. 479-490, 1963.
2. S. A. Ramsden, P. Savic, "A Radiative Detonation Model for the Development of a Laser Induced Spark in Air", *Nature*, Vol. 203, no. 4951, pp. 1217-1219, Sep. 1964.
3. J. L. Champetier, "Interprétation théorique de l'évolution du plasma créé par focalisation d'un faisceau laser dans l'air", *C.R. Aca. Sc., Paris*, t. 261, pp. 3954-3957, Nov. 1965.
4. R. E. Kidder, "Application of Lasers to the Production of High Temperature and High-Pressure Plasma", *Nuclear Fusion*, Vol. 8, no. 1, pp. 3-12, 1968.
5. J. L. Bobin, F. Delobea, G. de Giovanni, C. Fauquignon, F. Floux, "Temperature in Laser Created Deuterium Plasmas", *Nuclear Fusion*, Vol. 9, no. 2, pp. 115-120, 1969.
6. J. P. Babuel-Peyrissac, C. Fauquignon, F. Floux, "Effect of Powerful Laser Pulse on Low Z Solid Material", *Physics Letters*, Vol. 30 A, no. 5, pp. 290-291, Nov. 1969.
7. R. E. Kidder, W. S. Barnes, "Wazer-A One Dimensional, Two-temperature, Hydrodynamic Code", *Rept. U.C.R.L. 50583*, Jan. 31, 1969.
8. C. Fauquignon, F. Floux, "Hydrodynamic Behavior of Solid Deuterium Under Laser Heating", *Physics of Fluids*, Vol. 13, pp. 386-391, Feb. 1970.
9. P. A. Bezuglyi, R. H. Minyafaev, "Velocity of Sound and Elastic Properties of Normal Polycrystalline Deuterium", *Soviet Physics Solid State*, Vol. 9, no. 12, pp. 2854-2855, 1968.
10. J. L. Champetier, J. P. Marioge, J. de Metz, F. Millet, A. Terneaud, "Utilisation de lentilles asphériques pour l'obtention d'éclairements élevés", *C.R. Acad. Sc., Paris*, t. 266, no. 13, série B, pp. 838-841, 25 mars 1968.
11. A. J. Palmer, J. F. Asmus, "A Study of Homogenization and Dispersion of Laser Induced Stress Waves", *J. Applied Physics*, Vol. 9, no. 1, pp. 227-228, 1970.

# QUARTZ GAUGE TECHNIQUE FOR IMPACT EXPERIMENTS

G. E. Ingram and R. A. Graham  
*Sandia Laboratories*  
*Albuquerque, New Mexico 87115*

## ABSTRACT

The experimental techniques and construction processes involved in performing gun experiments to determine the mechanical properties of solids with the Sandia quartz gauge are described. The experimental configurations described include the sample-target gauge configuration, the projectile gauge configuration and the combination of both of these configurations. Methods of constructing quartz gauges are outlined. The delay circuitry employed to achieve accurate shock-velocity measurements is described along with the techniques employed in controlling alignment between the projectile and target. Typical instrumentation and calibration procedures are detailed.

## INTRODUCTION

Planar impact experiments in which flat-faced projectiles are accelerated to pre-selected velocities in compressed gas or propellant guns and impacted, with precise alignment control, upon a target sample have become a routine and widely used technique to study the properties of solids under shock compression. Likewise, the Sandia quartz gauge has become a widely used shock profile detector which, when combined with impact techniques, has proven particularly effective for studying the mechanical properties of solids. The widespread interest in both the impact experiment and the quartz gauge has prompted this detailed account of the experimental techniques which are presently employed in the Sandia 27 meter compressed gas gun (1). Measurements of the physical properties of solids with impact experiments have previously been summarized (2).

After a brief background description of general features of the planar impact experiment and the quartz gauge, typical experimental configurations will be described, followed by details of gauge construction, timing circuitry, instrumentation, and methods of alignment control.

## BACKGROUND

### The Planar Impact Gun Experiment

The techniques which have evolved into the presently employed gun experiments developed from several independent sources during the late 1950s. Although compressed gas and propellant guns had been used to accelerate large projectiles for many years, the planar experiment required the additional development of techniques to achieve precise alignment control between the projectile and the target. The first reported planar impact experiments (Hughes, et al. (3), 1957; Lundergan (4), 1960; Graham (5), 1960; and Brody (6), 1961), were originally thought to be significant principally because the gun provided a convenient method for achieving shock stresses less than 100 kbar. As techniques for achieving better control of alignment between the impacting surfaces were developed, it became apparent that the gun experiment offered experimental capabilities and characteristics not provided by other shock loading techniques. This has now become widely recognized (e.g., 7-20), and the number of guns nominally capable of planar impact has grown from less than ten in 1965 to more than 30 today. The recent development of multiple stage light gas

---

This work is supported by the U.S. Atomic Energy Commission.

guns (21) capable of planar impacts now permits pressures of several megabars to be achieved.

The principal elements of a gun experiment are shown in Fig. 1. The projectile is accelerated down the evacuated barrel to a preselected velocity, past the velocity pins, and into the target. Precise control of the alignment between the impactor and the target is maintained. Various experimental options for the impactor include facings chosen to produce a nominal stress value, sample materials to be studied, quartz projectile gauges, or thin fliers. Various target configurations include sample materials, quartz gauges, and reverberation plates. Experiments can be conducted at temperatures from  $-222^{\circ}\text{C}$  to  $1000^{\circ}\text{C}$ .

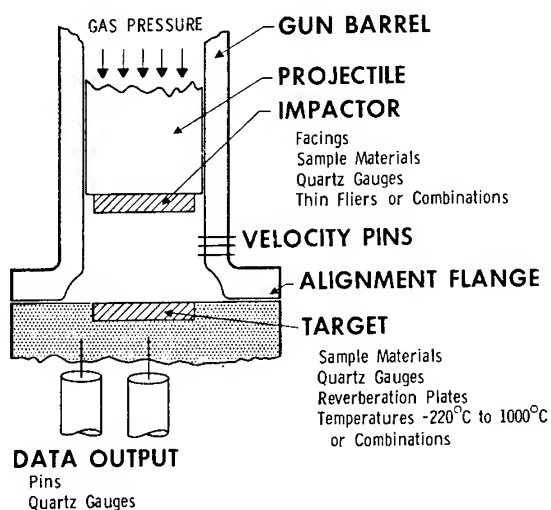


Fig. 1 - Experimental configurations for an impact experiment utilizing quartz gauges. The experimenter has a choice of a number of different impactors and target configurations. The principal experimental problem is to achieve precise alignment between the impacting surfaces.

An unusually well-defined state of stress and loading conditions is produced in the samples by planar impact in that both the impactor and sample are loaded directly in uniaxial compression. Because the magnitudes of the stress and particle velocities at the impact interface are equal, it follows that:

$$\sigma_T = \sigma_I, \quad (1)$$

$$u_I = u_o - u_T, \quad (2)$$

and

$$u_T = \left[ (Z_I(\sigma)) / (Z_I(\sigma) + Z_T(\sigma)) \right] u_o \quad (3)$$

where  $\sigma_T$  and  $\sigma_I$  are the stress values in the shock propagation directions in the target and impactor respectively,  $u_T$  and  $u_I$  are the particle velocity magnitudes imparted by the impact in the target and impactor, respectively;  $u_o$  is the impact velocity;  $Z_I$  and  $Z_T$  are the shock impedances ( $\rho_o U$ ) of the impactor and target, respectively;  $\rho_o$  is the initial density; and  $U$  is the shock velocity. Thus, if the impact Hugoniot ( $\sigma$  vs  $u$ ) of the impactor and target are known, the instantaneous magnitude of the stress and particle velocity imparted to the impactor and target can be calculated directly from Eqs. 1-3. For a given projectile velocity the error in stress or particle velocity depends upon the accuracy of the impact velocity measurement and the reproducibility of the impact Hugoniot. The nominal stress vs particle velocity Hugoniot of typical materials show variations of about  $\pm 5\%$ . The impact Hugoniot of several useful materials are shown in Fig. 2. The data shown were all obtained in direct impact experiments.

The symmetrical impact configuration is the best defined loading condition for shock compression experiments. If identical materials are impacted upon each other the loading is symmetrical across the impact interface and

$$u_T = u_I = u_o/2. \quad (4)$$

With this configuration the magnitude of the particle velocity imparted by the impact is exactly one-half the impact velocity regardless of the materials involved. Thus the particle velocity imparted to the sample is known to the accuracy of the impact velocity measurement. This accuracy is  $\pm 0.1\%$  on our gun.

The gun experiment also provides a convenient method of varying the impact velocity in small increments such that small increments of stress may be applied to the samples. Furthermore, the gas gun causes minimal noise and safety hazards; hence, it is easily incorporated into conventional laboratory facilities. The low electromagnetic noise levels around the gun experiment are advantageous in many instances.

The principal measures of the capability of a gun to perform the impact experiment are: (1) the "tilt" (the angular misalignment between the impacting surfaces), (2) the velocity range,

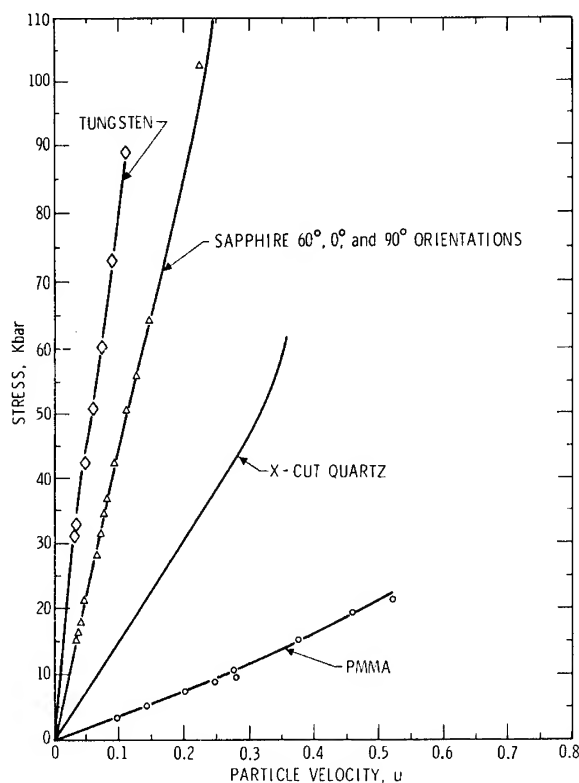


Fig. 2 - Stress vs particle velocity relations measured at the impact surface for facing materials which have convenient impedance values for various impact experiments. The polymethyl methacrylate (PMMA) is especially useful for experiments at stress values less than 10 kbar. A sapphire faced quartz gauge impactor combination will result in a stress in the quartz gauge with a value of about half the impact surface value, while a tungsten/quartz impactor will result in a quartz stress of one-third the impact surface value. The various stress-particle velocity relations are: PMMA (22),  $\rho_0 = 1.178 \text{ g/cm}^3$ ,  $\sigma = 31.4u + 23.6u^2$   $\sigma < 20 \text{ kbar}$ ; X-cut quartz (23),  $\rho_0 = 2.650 \text{ g/cm}^3$ ,  $\sigma = 151.6u$   $0 < \sigma < 25 \text{ kbar}$ ,  $\sigma = 147.3u + 28.6u^2$   $25 < \sigma < 60 \text{ kbar}$ ; sapphire (24),  $\rho_0 = 3.986 \text{ g/cm}^3$ ,  $\sigma = 444u + 13.6u^2$ ; tungsten (25),  $\rho_0 = 19.12 \text{ g/cm}^3$ ,  $\sigma = 998u$   $0 < \sigma < 32 \text{ kbar}$ ,  $\sigma = 13.2 + 596u + 730u^2$ ,  $32 < \sigma < 90 \text{ kbar}$ .

(3) the accuracy of the impact velocity measurements, and (4) the bore dimension of the gun. For our gas gun these figures are respectively 200-300  $\mu\text{rad}$ , 0.03 to 1.5 mm/ $\mu\text{sec}$ ,  $\pm 0.1\%$  and 6.35 cm.

#### The Sandia Quartz Gauge

The Sandia quartz gauge is basically a disk of X-cut synthetic quartz with a configuration

such that the short-circuited piezoelectric current response mode is employed to give accurate time-resolved measure of stress. Piezoelectric gauges existing before the invention of the Sandia quartz gauge operated in the charge mode which gives a measure of the average stress through the thickness of the disk. The two gauges utilize basically different physical principles which should be explicitly recognized. In this paper only the Sandia quartz gauge will be described and frequently referred to as a quartz gauge. The basic features of a guard-ring gauge are shown in Fig. 3. They include inner and outer plated electrodes with leads attached, and an insulating gap in addition to the X-cut quartz disk itself.

The short-circuited piezoelectric current can be related directly to the instantaneous value of the stress at the input electrode through analysis based on electrostatic theory (23, 26, 27). The analysis is based on a completely arbitrary waveshape and shows that the instantaneous value of the current,  $i$ , is

$$i = (kA/t_0) \sigma(t), \quad 0 < t < t_0, \quad (5)$$

where  $k$  is the piezoelectric current coefficient,\*  $A$  is the electrode area,  $t_0$  is the shock transit time through the gauge at a velocity of 5.72 mm/ $\mu\text{sec}$ , and  $\sigma(t)$  is the stress history at the input electrode. According to Eq. 5, the gauge requires no calibration, is not frequency response limited, is direct reading, self-powered, will respond equally well to any wave profile, and produces a large current which is relatively easy to measure. (For example, a 6.3 mm thick gauge with a 1.25 cm<sup>2</sup> area produces a current of 0.24 amp at 10 kbar.) Because of these advantageous features, the gauge has become the most widely used shock profile detector.

The generality of Eq. 5 to any waveshape is a consequence of severely limiting restrictions imposed on the mechanical and physical properties of the gauge material. Exceptions to the linear theory of Eq. 5 (23, 28-32) are caused by: (1) dielectric constant change, (2) electromechanical coupling, (3) finite strain, (4) insulating gap effects, (5) full electrode effects, (6) variable wave speed effect, (7) minus  $x$  orientation conductivity, (8) the unloading conductivity, (9) the stress relaxation effects, (10) plus  $x$  conductivity, and (11) Three-Zone Model (32) effects.

\*The data given in Ref. 23 can be fit by a linear relation  $k = [2.011 \times 10^{-8} + 1.07 \times 10^{-10} \sigma]$  coul cm<sup>-2</sup> kbar<sup>-1</sup>.



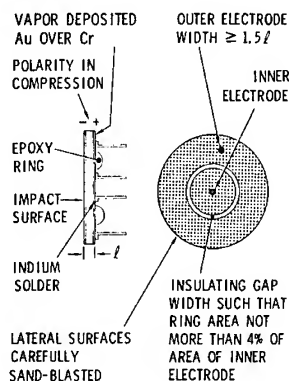


Fig. 3 - Basic Sandia Quartz Gauge with sand-blasted insulating gap and lead wires attached to positive surface electrode. The output of the gauge from the inner electrode is measured across resistive current shunts. A shunt is also used to balance the voltage on the outer electrode. The resistor on the inner electrode is chosen to have a value which gives a convenient signal level consistent with obtaining an RC time constant short compared to the desired rise time. For voltage balance the resistive load on the outer electrode is chosen to have a value equal to the resistive load on the inner electrode multiplied by the ratio of the inner electrode area to the outer electrode area.

Although this list of exceptions is formidable the conditions under which the gauge responds accurately are well documented and many of the effects are negligible. Thus, a plus x orientation disk can be used as a time-resolving gauge to an accuracy of  $\pm 2.5\%$  to a maximum loading stress of 25 kbar. Studies currently in progress indicate that the accuracy can be improved to  $\pm 1-2\%$ . Furthermore, studies at stresses greater than 25 kbar are in progress (31) and promise to enable the gauge to be used accurately at higher stresses, when a new nonlinear theory is developed.

## TYPICAL EXPERIMENTAL CONFIGURATIONS

Impact experiments utilizing the quartz gauge are performed on four basic configurations: (1) the sample-target gauge configuration, (2) the projectile-gauge configuration, (3) the target gauge configuration, and (4) combinations of these configurations. The quartz reverberation plate configuration recently described by Lysne, et al. (33) will not be described in this paper.

### Sample-Target Gauge Configuration

In many experiments the mechanical properties of a sample are obtained by measurements of stress vs time profiles at positions remote from the impact surface (e.g., 16, 34-37). The sample is shock loaded with a symmetric impactor or an impactor facing having a known stress vs particle velocity response. If the unloading response of the sample is desired, the impactor may be thin relative to the sample thickness. The impact velocity is routinely measured in all experiments. The quartz gauge mounted on the rear surface gives a time-resolved signal proportional to the stress at the quartz-sample interface. The wave transit times are obtained by applying precisely delayed fiducial signals to the quartz gauge record.

The measured stress at the quartz-sample interface is related to the incident stress by recognizing that the stresses and particle velocities at the interface are equal. If the shock impedance of the sample is constant for the stress levels encountered in the experiment

$$\sigma_i = \left[ (Z_Q + Z_S) / 2Z_Q \right] \sigma_Q, \quad (6)$$

where  $\sigma_Q$  is the stress at the sample-quartz interface,  $\sigma_i$  is the incident stress in the sample,  $Z_Q$  is the impedance of the quartz, and  $Z_S$  is the impedance of the sample. If the stress pulse is a single shock with stress-dependent impedance the method of solution described by Halpin, et al. (22), may be employed. Wave profiles with slowly rising shapes may be approximated by a series of small steps in stress. All of these methods of data reduction require that the arrival times of the stress pulses be measured along with the quartz gauge measurements.

These time measurements are accomplished as shown schematically in the target gauge portion of Fig. 4. A pair of flush trigger pins which will be described later are mounted on the plane of the sample impact face and detects the arrival of the surface of the impactor. Since the quartz gauge signal is also used to indicate wave arrival times, the trigger pulse must be accurately delayed and a timing fiducial applied to the signal. The trigger pulse is directed to various delay generators through the trigger fanout circuit. The trigger pulse is delayed by a preselected time to an accuracy of  $\pm 10$  nsec and the output from the delay generator triggers the oscilloscope just prior to the expected arrival time of the stress pulse. The delayed output from a second delay generator is then fed through a fiducial shaper and applied to the oscilloscope through a modification of the preamplifier. The time difference between impact time and fiducial time is registered on a one nanosecond counter. With cable lengths matched to  $\pm 1$  nsec, the time accuracy is limited by the arrival time reading from the quartz gauge record (which typically sweeps at 100 nsec/cm) and the time errors introduced by tilt.

With the alignment techniques to be described in the following sections the tilt time can be held to less than a preselected value and a wave velocity measurement of  $\pm 1\%$  can usually be accomplished. A tilt time correction can conveniently be obtained by measuring the signals from both the outer and inner electrode of the gauge. The nonplanarity and tilt of the wave-front at the gauge is indicated by the difference in arrival time between the inner and outer electrode signals. A tilt angle can then be calculated as this time difference multiplied by the wave velocity divided by the width of the outer electrodes.

#### Projectile Gauge Configuration

The mechanical properties of a sample can also be obtained by impacting the sample directly with a quartz gauge (11, 16, 22, 25, 34). The most versatile method for accomplishing this is the projectile gauge configuration in which the gauge is mounted as an impactor on the projectile. From Eqs. 1 and 2 it is apparent that a measurement of the gauge signal and the impact velocity gives a stress-particle velocity point directly on the impact Hugoniot. These data are obtained directly and unlike measurements on propagated wave profiles do not require steady wave propagation assumptions to be used in the data analysis. This projectile gauge measurement is particularly useful

for heterogeneous, porous, or highly rate sensitive materials whose propagated wave profiles show nonsteady behavior. Additionally, the projectile gauge configuration allows the target sample to be heated or cooled without affecting the instrumentation since the gauge does not contact the sample until impact. Rohde (25) and Towne (38) have performed experiments by this technique at  $1000^\circ\text{C}$  while Jones (39) has conducted experiments at liquid nitrogen temperatures.

As indicated in Fig. 4 this experiment does not involve the delay circuitry. The trigger pin pair is advanced above the sample impact surface a preselected distance to give an appropriate trigger advance. The tilt is indicated directly from the rise time of the gauge signal.

The principal limitation to wide use of the projectile gauge configuration is the upper stress limit to which the quartz can be used. For measuring the first current jump response accurately the stress should be limited to 40 kbar. The stress limit of the impact experiment can be appreciably increased by facing the projectile gauge with sapphire or tungsten. Because of the impedance mismatch between these materials and the quartz, the stress in the projectile gauge is approximately one-half the stress value at the impact interface for a sapphire facing and one-third the interface stress for a tungsten facing. Thus, the upper stress limit of the projectile gauge experiment is 120 kbar with a tungsten facing. When sapphire is used as a facing the maximum stress is 80 kbar which is well below the Hugoniot elastic limit of 120 kbar (40). Although the maximum stresses in the tungsten facings are well above the Hugoniot elastic limit of 40 kbar (25) dispersion of the wave as it propagates through the facing is not severe.

#### Target Gauge Configuration

An impact surface experiment can be accomplished without using the projectile gauge configuration. This is done by mounting the sample to be studied as an impactor on the projectile (11, 22). A target quartz gauge is constructed such that the front electrode of the gauge is exposed as the impact face of the target. As was the case with the projectile gauge no delay circuitry is required. When the impactor is an X-cut quartz disk this configuration is used to study the properties of the quartz gauge (8, 23, 30, 31).

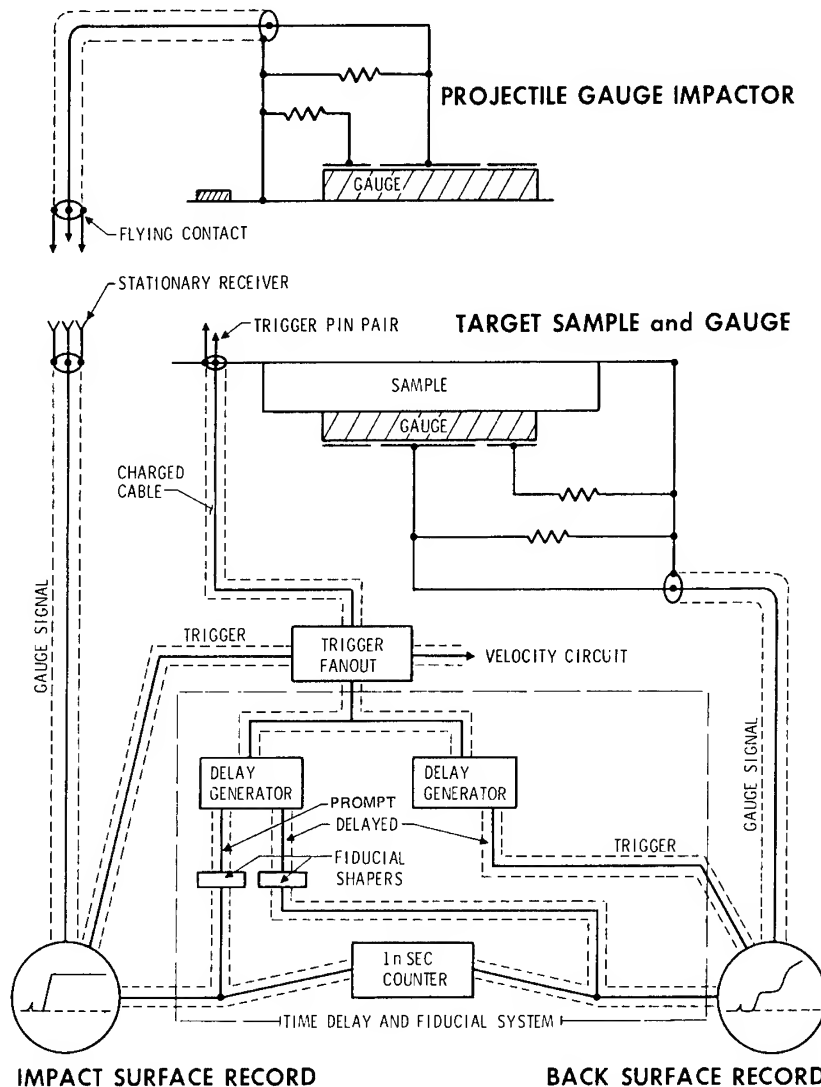


Fig. 4 - Block diagram of the circuitry involved in the simultaneous projectile gauge sample-target gauge experiment. In this experiment the sample is impacted by a quartz gauge mounted on the projectile. The signal from this gauge and the impact velocity measurement give stress-particle velocity data directly. The stress propagating in the sample is detected by the target gauge. This gauge also gives arrival time data for the various stress amplitudes which when combined with the impact surface record and the precise time delay circuitry gives precise shock velocity data. The delay generators are TRW Model 46A. The 1 nsec counter is Eldorado Model 796.

#### Combined Sample Target-Gauge and Projectile-Gauge Configuration

Although somewhat more difficult to perform, the most powerful of the techniques employs a configuration combining the projectile gauge experiment with the sample-target gauge configuration (11, 19, 22, 34). This experiment gives two independent measurements of the

mechanical response; the impact surface response and the propagated wave profile. In addition the effect of tilt on timing measurements is cancelled if the detection areas of both gauges are the same diameter.

The entire experimental set-up shown in Fig. 4 is used in this "front-back" experiment. In addition to the delay circuitry used in the

sample-target gauge configuration, a fiducial must be applied to the projectile gauge signal. The time difference between the two fiducials is indicated to  $\pm 1$  nsec by the counter. This technique will provide wave transit times accurate to a few nanoseconds.

### CONSTRUCTION TECHNIQUES

The quartz gauge has three basic configurations: the guard ring (23), the shorted guard ring (41, 42) and the full electrode (27). Since the guard ring gauge is the most universally used, the present paper will concentrate on methods of fabricating this gauge. The construction techniques are designed to produce a highly reliable response free from spurious signals. The most difficult problem in this regard is to insulate the gauge against the very high electric fields ( $\sim 10^6$  volt/cm at 20 kbar) which exist in the disk, along the sides of the disk, and in the insulating ring (28).

#### Quartz Gauge Preparation

The quartz gauge may be purchased from the manufacturer in various stages of completion. It is available as a bare transparent disk of quartz with both surfaces polished to a plate glass finish and a grind finish perimeter. It is optically flat and parallel to within 3 fringes of monochromatic helium light and its surfaces are oriented and cut perpendicular to the crystallographic X axis within 1 degree. It may be obtained with an electrode of vapor deposited gold over chromium applied to one or possibly both of the disk surfaces. When only one surface is plated the plating is deposited on the positive polarity surface. The polarity is identified with the aid of either an electrometer or a polarity detector (43) (Esprit Enterprises model PD 2709). Certain manufacturers are capable of sandblasting the insulating gap, described later, through the positive surface plating to form the guard ring configuration. Additional electroding on the perimeter and negative surface produces a shorted guard ring.

The quartz disk, when received from the manufacturer, is thoroughly inspected before it is assembled into a gauge assembly. The quartz interior is carefully examined for acmite inclusions, seedveils, bubbles, twinning and cracks so as to avoid later difficulties with questionable records. The more stringent the environment on the quartz gauge, such as measurements above 20 kbars and short duration pulse measurements at stresses greater than 10 kbars, the more important it becomes to obtain flaw-free crystals.

Surface imperfections which influence quartz gauges are: inadequate chromium plating, inadequate or poorly adhering gold plating, gold blobs rising above the electrode surfaces, and warped or distorted surfaces. Other surface problems are: wide guard ring gaps, high resistance solder joints, and microscopic cracks beneath overheated solder joints. Surface contamination leads to the most severe problem, that of electrical breakdown along the crystal perimeter and across the insulating gap.

The internal flaws and solder joints are best observed through the transparent surface of the quartz opposite to the guard ring electrode. Prior to encapsulation, a vapor deposited electrode is generally not required on the negative face since this surface can either be electroded after encapsulation or it will be faced with a conductive sample which provides the electrode. Likewise, the impactor quartz gauge need not be electroded before assembly since it will require additional electroding after assembly. The visibility of internal flaws is enhanced by edge lighting the disk with a strong light source.

If the crystal has been purchased with an electrode on the negative surface, the gold can be removed with aqua regia. The underlying chromium is stripped with hydrochloric acid. Occasionally, chemical action has to be initiated by scratching the chrome surface beneath the acid with a metal scribe. A dam is formed to contain the acids by wrapping the quartz perimeter with teflon adhesive tape (Mystik Tape Inc., No. 7504).

After the thickness of the crystal is measured with a 0.0001 inch indicating micrometer, the insulating gap is sandblasted through the positive surface plating by one of two methods. Diameters smaller than 1 cm are cut with the aid of a concentric masking disk and washer. A more uniform gap is cut on diameters larger than 1 cm by rotating the crystal in a jeweler's lathe while sandblasting with a  $0.003 \times 0.020$  inch rectangular nozzle. (The nozzle #351-1937, 27 micron alumina abrasive and the abrasive blasting unit was obtained from S. W. White, Inc.) Immediately after cutting the gap, measurements are made of the gap OD and ID at various positions using a 400 power depth measuring microscope with a 0.0001 in. resolution micrometer stage. The gap is cut into the quartz a depth of about 0.0005 inch. To prevent the gap from becoming contaminated, it is immediately painted with an artist's brush using 10 parts epoxy resin mixed with one part N-Hep hardener (described later), and then evacuated at  $< 5$  mm Hg for three minutes. Cure is accelerated under a heat lamp.

The electrical leads are attached to the vapor plating with a low temperature soldering technique using indium metal which melts at 150°C. Leads are formed from #22 tinned copper wire 5 cm in length with a 2 mm 90° bend on one end. The bend is "tinned" with indium solder which forms a small ball. A 230°C controlled temperature 20 watt pencil iron (Weller #W-TCP-2) is dipped, while hot, into a paste flux containing zinc chloride (Blue Seal Chemical Co.); then it is coated with indium. After redipping in flux, the indium coated iron is immediately pressed against the wire bend on the gold surface until the indium wets the surface, whereupon the iron is withdrawn. This technique transfers a thin film of flux which is adequate but does not contaminate the surface. Two leads are attached to the inner area and two to the outer. This allows electrical continuity to be tested after potting. Overheated indium solder joints are observed as slight discolorations in the chromium layer when viewed through the negative surface of the quartz. Since indium is very soft, it will deform slightly when the crystal is encapsulated, thus reducing lead stresses on the crystal. The four wires can now be used as a handle to support the crystal in future operations. To prevent strain on the solder connection, the coaxial cable is not attached until after the unit is potted.

The perimeter of the crystal is thoroughly sandblasted with alumina abrasive to remove pencil marks, vapor plating and finger prints. The surfaces are protected during this operation by being sandwiched between two flat lucite washers having inside diameters slightly smaller than the crystal. To maintain strict cleanliness the virgin crystal perimeter is not touched after the sandblasting.

Table 1 summarizes the characteristics of a well constructed guard ring gauge.

#### Sample-Target Gauge Assembly

The sample-target gauge unit is shown in Fig. 5. The unit is prepared against a removable assembly plate to maintain flatness of the sample and insure parallelism with the target cup flange. The assembly plate and holder permits the target cup, sample, gauge, ground connections and trigger pins to be firmly held in place while the entire assembly is encapsulated with epoxy potting. The surface of the assembly plate is coated with a Teflon mold release so that when the epoxy has hardened the entire target assembly can be removed from the plate. The assembled unit as it comes from the plate

TABLE 1  
Characteristics of a Well-Constructed  
Guard Ring Quartz Gauge

1. The X-cut quartz disk has low acmite content, is free of seedveils and twins, and is accurately dimensioned.
2. The vapor plating adheres well to the flat surfaces of the disk and is clean and free of plating lumps.
3. The lateral surfaces are sandblasted clean.
4. The outer electrode is equal to or greater than 1.5 times the thickness of the gauge (23).
5. The area of the insulating gap is not more than 4% of the inner area (23).
6. The insulating ring is narrow (about 0.0035 in.), free of conducting material, and has well-defined edges.
7. The thermal shock produced when the connection is made to the vapor plating has not cracked the quartz surface.
8. The connections to the coaxial electrical leads are short and do not stress the solder joint.
9. The insulating ring and lateral surfaces are well-insulated with low shrinkage epoxy with high dielectric strength which adheres well to the surface.
10. Intimate contact is achieved between the sample and the gauge.

is usually parallel to the holding flange of the target cup to within  $1 \times 10^{-4}$  radian. The quartz gauge may be assembled behind the target sample for transmitted wave measurements or it may be assembled directly against the assembly plate for impact surface measurements. The assembly plate technique is followed for either configuration.

Assembly plate preparation commences with machine lapping of the surface to remove previously deposited mold release and epoxy. To achieve good adhesion with the mold release the surface should not be polished. After spraying and drying the first heavy coat of mold release, the surface is burnished by vigorous rubbing with paper wipers. The surface is then resprayed with two more light coats. Viewing

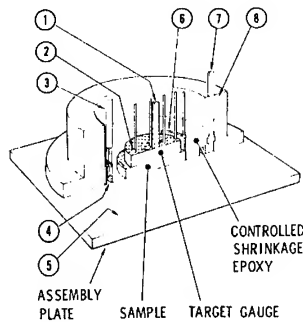


Fig. 5 - Cutaway view of sample target gauge assembly mounted on the flat assembly plate. The entire unit is held in place against the plate and encapsulated with epoxy potting. The quartz crystal and target material are held in intimate surface contact during epoxy encapsulation and cure procedure. After the epoxy has cured, the entire target assembly is removed from the plate. The individual parts shown are: (1) Nylon Rod, used to press target gauge and sample against assembly plate. Numerous rods may be used for thinner gauges as well as nylon disks for gauges of thinner than 0.15 inches. (2) Indium Soldered Lead Wires. These short wires are later connected to coaxial cables and load resistors after potting. (3) Cable, Raychem Corp. type 22-174, 1 ft. Conducts impactor gauge signal from contact subtending a 95° arc to air dielectric cable. (4) 95° Center and Ground Contacts. Couples signal from one of four flying contacts on projectile gauge. (5) Mold Release surface coating. Miller-Stephenson Chemical Co., type MS122. (6) Signal Ground Ring. Provides connection to negative quartz surfaces. Prevents shock reverberation from causing contact bounce. (7) Trigger Cable and Connector. (8) Flanged Lucite Container. Machines easily for tilt control and contains epoxy during cure.

this coating at a low angle may disclose minute lumps which must be removed.

Sample surfaces are prepared by lapping previously machined disks on a 12 inch Lap-master machine to a flatness of one to two fringes (11.6  $\mu$ in) as indicated with an optical flat and monochromatic light. Parallelism between surfaces is achieved by shifting a weighting disc to the high (thickest) side of the sample during lapping.

One of the most important considerations during assembly is the interface between the gauge and target. In order to prevent a perturbation to the stress profile at the interface, abrasives, thick electrodes, gold blobs, dust particles or any other foreign matter larger than a few microinches will be eliminated. After a thorough final cleaning of these surfaces with 200 proof ethyl alcohol on lintless tissue they are dried with pressurized filtered air. The surfaces are checked for contamination with a well-cleaned optical flat. A total fringe count of less than 5 fringes is acceptable. Ideally, one or two of these fringes form concentric circles if no foreign material is present. The gauge and target surfaces are then quickly wrung together before they become contaminated. A test may be performed for intimate interface conditions by tilting the assembled sample and gauge about 25 degrees from horizontal. If the materials adhere to each other for 3 to 5 seconds without sliding, good interface conditions exist.

The mated target and gauge are placed against the coated assembly plate, the flanged container placed down around it, and the two made concentric by means of three nylon rods distributed in the annular space and later removed. The mated pieces are then held in place with expendable non-conductive rods which eliminate additional capacitive coupling between electrodes caused by metal rods. Gauges thinner than 0.15 inches are held with a nylon disk to prevent warpage. Concentricity of target disks and container is maintained within 0.005 in. to minimize the influence of potting shrinkage on tilt and to enable accurate concentricity between target and impactor.

Prior to assembly interior surfaces of lucite cups and metal containers which form the outer shell of assembled targets and projectile gauges are sandblasted to improve epoxy adhesion. Ground connections are formed to the quartz gauge by one of three methods: (1) if the sample is electrically conductive, a

signal-ground ring is connected to it, as shown in Fig. 5; or (2) in the exposed target gauge configuration a vapor deposited metal such as aluminum, having a resistance of  $0.1\Omega/\text{square}$ , is placed across the entire impact surface connecting the ground ring to the gauge, or (3) when measurements are made on a non-conductive sample the sample surface is vapor coated and assembled as in method 1. This latter case is a situation where the shorted-guard-ring may be simpler to construct. The length of the signal ground ring in the shock direction exceeds the length of the quartz thus preventing shock reverberations from causing contact bounce with a subsequent loss of signal or noisy records.

Controlled-shrinkage doubly-evacuated transparent epoxy resin\* is used to encapsulate the target assembly inside the cup. The 2% volumetric reduction causes the cured epoxy to shrink away from the plane of impact about 0.005 inches. This prevents shocks from being initiated within the epoxy prior to those in the target sample. The 6% shrinkage of many epoxies will deform samples and crystals. The use of transparent epoxy permits the inspection of the gauge epoxy interfaces after encapsulation for good adhesion. Filled epoxies are generally not transparent and some actually swell after cure, possibly opening a gap between the quartz and sample. Tests indicate that our epoxy formulation flows into the microinch gap between the quartz and sample forming a bond between them. This bond contains no large foreign matter that is so difficult to filter from uncured epoxies and hardeners. This is a crucial role of the evacuation process.

After the cured assembly has been held in the assembly plate holding apparatus for about 24 hours it is removed. A thin layer of cured epoxy now remains on impact surface which is

removed with methylene chloride. This solvent is held in place with an automotive body putty dam (3M Co. #1167) surrounding the crystal or target. Hand polishing with 1 micron alumina on an alcohol wet rag produces a radius on sharp corners, cleans the surface for subsequent vapor coating, and polishes it for in-depth inspection. An optical flat placed on the impact surface and illuminated with monochromatic light permits detection of any bowing, wrinkling or undesirable particles that may be present.

After measuring the flatness and parallelism, the load resistors and coaxial cables are soldered to the lead wires. Vapor coating the impact surface, if necessary, finalizes the unit for the experiment.

#### Projectile Gauge

The quartz projectile-gauge is a separate and complete assembly that is attached to the projectile with screws as shown in Fig. 6. It is a versatile unit which may be attached to any weight or any length projectile. The assembly is constructed with various diameter and thickness crystals for off-the-shelf type of selection. During mounting, the assembly can be adjusted to compensate for any lack of perpendicularity between the gauge surface and the projectile sides by sanding the surface which is attached to the projectile.

The quartz gauge crystal is encapsulated within an aluminum ring which also contains the flying contactors, load resistor, and electrical connections and forms a complete gauge unit. The crystal preparation and assembly techniques are identical to those used in preparing the target assembly previously described.

Electrical signal connections are made to the unit just prior to impact. There are four equally spaced flying contactors extending ahead of the unit, one of which must impinge within the  $95^\circ$  arc segment of the center contact (the remaining contactors enter the receiver groove surrounding the target sample which prevents the introduction of a stress wave within the epoxy). Thus, a signal path is established independent of the angular orientation of the projectile within the barrel. The flying contactor length is adjusted, by means of a lead tin solder buildup, to complete the connection 0.003 inches prior to impact. Stationary signal ground contacts, which are also  $95^\circ$  arc segments, are placed on each side of the center contact. Solder buildup on the four corners of these segments complete connection 0.005 inches prior to impact. A short length of 22-174 Raychem

\*Epoxy is formulated, evacuated and cured as follows: (A) Pour together 100 parts by weight Epon 828 or Hysol 2038 and 6 parts Hydroxyethyl Piperazine hardener from Union Carbide Co. (B) Stir and heat to  $175-180^\circ\text{F}$ . (C) Maintain temperature for 5 minutes during exothermic reaction. Cool slightly as necessary when mixing large batches. (D) Cool to  $120^\circ\text{F}$  in "double boiler" containing icewater. (E) Evacuate mixture for 5 minutes at 3 mm Hg. (F) Pour into sample container to a depth only slightly covering the quartz positive surface or nylon disk top when assembling targets. Pour to cover resistors in the projectile gauge assembly. (G) Evacuate completed assembly for 5 minutes at 3 mm Hg. (H) Place uncured assembly in oven adjusted to  $105^\circ \pm 5^\circ$  for 28 to 36 hours. (I) Cool the cured assembly and let it stand for 24 hours before removing assembly surface plate.

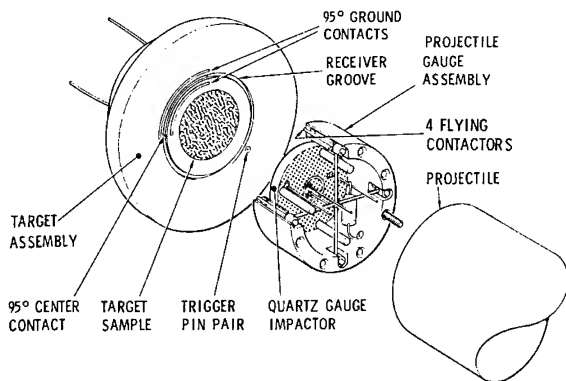


Fig. 6 - Cutaway view of projectile gauge assembly mounted on a projectile. Since the gauge impacts directly on the target sample this configuration gives the stress particle velocity response of the sample directly. Current-time signals from the quartz gauge are conducted through flying contacts to the recording instrument.

Corp. coaxial cable is attached to the three 95° segments and extends away from the target assembly to larger cable.

## TIMING CIRCUITS

### Fiducial Timing

In order to obtain nanosecond timing for the fiducial and delay system previously mentioned, a fiducial shaper and oscilloscope adaptation is employed. The delay generators do not have suitable output wave shapes for presentation on oscilloscopes operating at sweep rates faster than 200 nsec/cm. Therefore, the wave forms are reconstructed by fiducial shapers, shown in Fig. 7, which generate spikes of less than 2 nsec rise and fall times. Trigger threshold settings within the nanosecond counter become relatively unimportant when the inputs are presented wave forms of this character. The fiducial display on the scope trace damps to zero in a few nanoseconds to prevent interference with the quartz record.

Due to uncertainties in the propagation times of signals through preamplifiers, distributed amplifiers and delay lines among the various oscilloscopes, a method was devised to introduce the fiducial pulse into the scope input follower stage where input signal delay times of less than 1 nsec exist. Attempts at signal

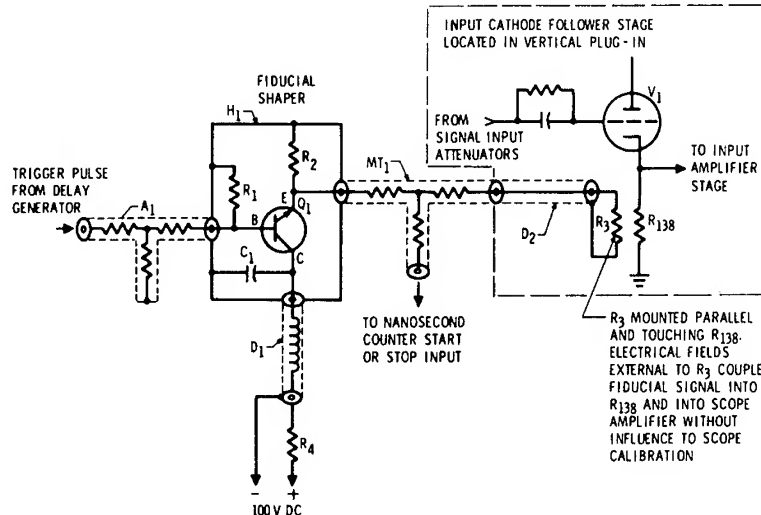


Fig. 7 - Complete schematic diagram of fiducial shaper and fiducial input modification to the Tektronix type 585 oscilloscope. The pulse from the delay generator is regenerated into a sharp spike by the avalanche transistor and the capacitor before it is injected into oscilloscope input follower stage. The individual parts shown are:  $A_1$  - Attenuator, coaxial 5X, Tektronix type 011-0060-01.  $C_1$  - Capacitor, 30 pf mica.  $D_1$  - Delay Cable, 5 ft, 5  $\mu$ sec, Columbia Technical Type HH-4000.  $D_2$  - Delay Cable, 1 ft miniature 50 $\Omega$ .  $H_1$  - Housing, Tektronix type 011-0081-00 modified with additional BNC connector.  $MT_1$  - Matching Tee Power Divider, General Radio type 874-TPD.  $R_1$  - Resistor, 51 $\Omega$  1/2 W.  $R_2$  - Resistor 1K $\Omega$  1/2 W.  $R_3$  - Resistor, 51 $\Omega$  1/4 W.  $R_4$  - Resistor, 150K $\Omega$  1 Q.  $R_{138}$  - Resistor, existing 750 $\Omega$ .  $Q_1$  - Transistor, NS1110.  $V_1$  - Vacuum Tube, existing 7586.



mixing, at positions near or before the scope input, caused undesirable attenuation and multiple reflections along the signal cable. The fiducial signal is injected into the cathode circuit of the follower stage which acts as a buffer to isolate input attenuators and input cable circuits. This easily added circuit, composed of a short length of 50 ohm cable  $D_2$ , and a 50 ohm terminating resistor  $R_3$ , has a 20 volt/cm sensitivity. A 4 volt peak fiducial pulse produces a satisfactory amplitude on the scope trace.

The fiducial shaper output exceeds 20 volts, hence coaxial attenuators are necessary although some attenuation is derived from the matching tee,  $MT_1$ , which divides the pulse between the scope input and counter inputs. The shaper incorporates an avalanche transistor with a charged capacitor that discharges with a short time constant. Collector bias and capacitor charging current is supplied through a 5 microsecond delay line,  $D_1$ , to prevent multifiducial pulsing during one sweep interval. Attenuator  $A_1$  prevents base overdriving from the delay generator output. The absolute time interval between gauge wave forms is derived from the interval between fiducial time marks and the remaining interval on the scope time-base. This timebase is calibrated from a 50 MHz standard crystal oscillator.

#### Impact Timing with Trigger Pin Pairs

The application of charged coaxial cables to the measurement of impact timing and projectile velocity has been previously described (44). An improved version of these circuits is shown in Fig. 8. The impact timing or trigger circuit is seen at the left side of the illustration. Within a few nanoseconds prior to impact, the trigger pin pair is contacted by metal on the impactor which connects the outer (shield) conductor of a charged coaxial cable to the center conductor. The total electrical path length external to the cable is only a few thousandths of an inch which minimizes the effect of open wire inductance and radio frequency radiation into surrounding circuits. The shield pin is advanced 0.001 inch ahead of the center pin to establish the important ground path first. When the center contact is made, a 50 volt discharging pulse with less than 3 nsec rise time is induced in the trigger cable. Cable lengths are cut to achieve  $\pm 1$  nsec simultaneity at the termination points.

#### Projectile Timing with Velocity Pins

At the right side of Fig. 8, a block diagram of the velocity circuit is shown which in most

respects is identical to the impact timing circuit. The velocity pins protrude 1 mm into the bore through the side of the barrel with either 1 or 2 cm separation. They are alternately charged positively and negatively. The projectile occasionally floats within the barrel and thus may become a charged capacitor when it contacts a charged pin. Alternate pin polarity insures that a current flow will be established in the cables with each projectile contact. Pins which are placed in direct alignment along the barrel will successively deform the projectile surface with each impact which changes the effective distance of projectile travel. This problem is eliminated by staggering the placement of each velocity pin by 1.5 mm so that it may impact on a fresh projectile surface.

The exact location of each velocity pin contact, along the axis of the barrel, is adjusted and measured with the aid of a mechanical device shaped like a fine-pitched screw. The device, called a velocity pin spacer and indicator, is inserted into the barrel with its flattened surface oriented to prevent pin bending. When the flat-sided helical grooves are rotated in the barrel they contact the pins in the same manner as the projectile. The zero position on the spacer indicator shoulder is aligned with a position mark on the end of the barrel. The pins are thus bent to a known position relative to the end of the barrel, and are measured with the same instrument by reengagement of the indicator shoulders and observation of the mils graduation where the neons NE-51 extinguish. The spacer-indicator was previously calibrated to an accuracy of  $\pm 50 \times 10^{-6}$  inches so that it may be used with confidence to measure the location of the pins to within  $\pm 0.0002$  inch. Times between successive pin closures are measured to within  $\pm 10$  ns. Thus, three average-velocity determinations are made during each shot with 0.1% consistency.

#### QUARTZ GAUGE SIGNAL TRANSMISSION AND RECORDING

The time resolution of absolute values of stress as detected by the quartz gauge is system limited by the rise time capabilities of the signal transmission and the recording systems. For this reason care should be exercised in selecting coaxial cables, connectors, terminators and oscilloscopes with rise time capabilities suitable for detecting the rapid change ( $< 10$  nsec) in stress amplitudes encountered in shock experiments.

Perhaps the most critical and most overlooked element is the coaxial cable. Properties of some typically used coaxial cables are shown

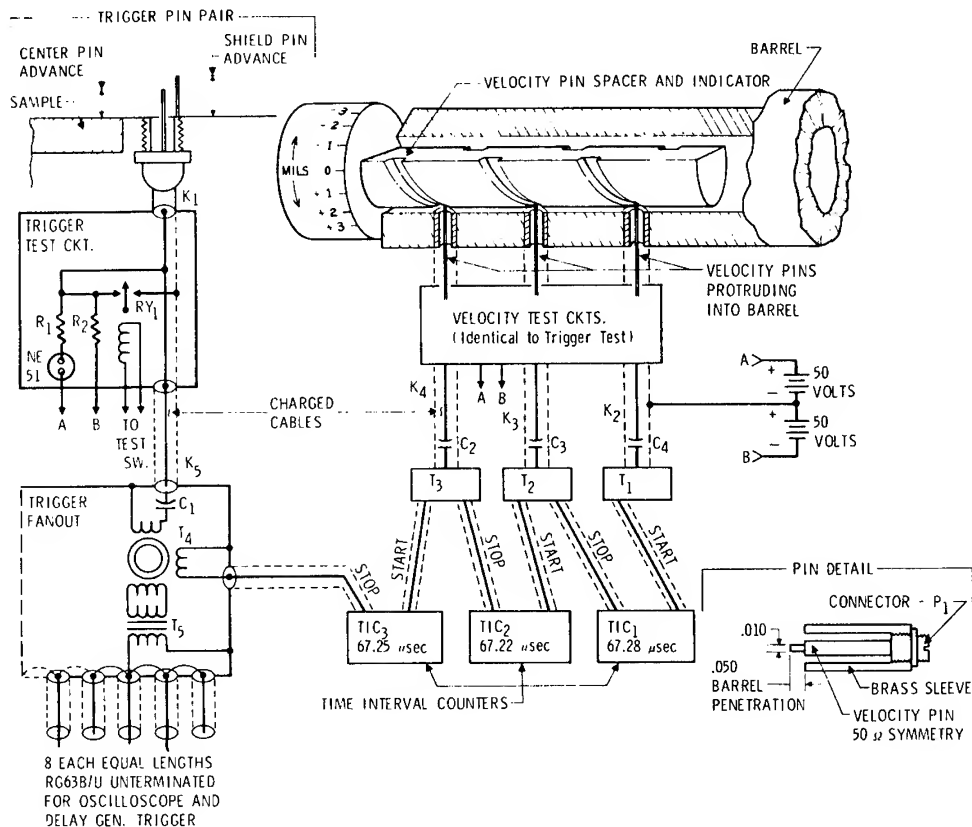


Fig. 8 - Circuit and block diagram of charged coaxial cable system for event timing and velocity measurements. Nanosecond timing pulses are generated by discharging the cables with contacts at one end. The location of the velocity pins is established in place in the barrel to within  $\pm 0.0002$  inch with the pin adjuster and pin location indicator. The individual parts shown are:  $C_1$ ,  $C_2$ ,  $C_3$  and  $C_4$  -- Capacitor 500 pf mica, in General Radio Insertion Unit 874X.  $K_1$  -- Connector type 031-0050 with Microdot 50 $\Omega$ , Mininoise cable.  $K_2$ ,  $K_3$ ,  $K_4$  and  $K_5$  -- Coaxial cable, 50 $\Omega$ , 1/2 in. dia., foamed dielectric.  $P_1$  -- Connector, 031-0050 Microdot.  $R_1$  -- Resistor, 220K $\Omega$  1/4 W.  $R_2$  -- Resistor, 3K $\Omega$  5 W.  $RY_1$  -- Relay, mercury reed, make before break, C.P. Clare type HGSM.  $T_1$ ,  $T_2$ ,  $T_3$  and  $T_4$  -- Transformer, pulse, Tektronix type 017-012.  $T_5$  -- Transformer, pulse, Pulse Engineering type EF 71-2432 housed in insertion unit.  $TIC_1$ ,  $TIC_2$ , and  $TIC_3$  -- Time Interval Counter, 10 nsec, Hewlett Packard type 5275A. NE51 -- Neon Lamp. The mercury relays are used for pre-shot testing of all circuits.

in Table 2. A typical experimental cable length of fifty feet has been chosen for a basis of comparison of the cables.

It is immediately obvious that severe rise time limitations are imposed on recording the gauge response unless air dielectric cable is employed. Furthermore, the use of RG 58 cable limits the time-resolution of the system to such an extent that it should not ordinarily be used for accurate time-resolved measurements. Our compressed gas gun facility uses 45.0 feet of RG 269 A/U with a 6.0 foot jumper of Andrew Superflex Type FSJ 4-50 and a one foot length

of Raychem 22-174 for connection to the gauge. For best signal fidelity it is good practice to avoid signal delay cables.

After installation of the cables and connectors the transmission and cable termination system is checked for absolute value of impedance and uniformity of impedance with a time domain reflectometer, Hewlett Packard model 1415A. A resistive terminator is selected with the time domain reflectometer which precisely matches the cable impedance.

Characteristics of several high frequency oscilloscopes that are compatible with many

TABLE 2  
Rise Times of Typical Coaxial Cables\*

Cable	Impedance $\Omega$	0-95% Rise Time (cable length 50 ft) nsec
RG 58	50	50
RG 71	93	10
RG 213	50	10
RG 269	50	0.23
A/U (7/8" Air Helix)		

\*These rise time data are calculated with 1 GHz attenuation from the analysis presented in the Lawrence Radiation Lab Counting Handbook, UCRL-3307 (Rev. 2) June 1964. Analysis and experiments for ramp-rising inputs is contained in R. L. Wigington and N. S. Nahman, "Transient Analysis of Coaxial Cables Considering Skin Effect," Proc. IRE, Vol. 45, 166 (1957).

quartz gauge signals are shown in Table 3. Depending upon the experiment our installation uses Tektronix 585, 454, or direct deflected Tektronix 517 oscilloscopes. To minimize the effect of capacitive loading upon signal rise-times, separate signal cables are used for each oscilloscope.

TABLE 3  
Oscilloscope Characteristics

	Band Pass mHz	Input Capaci- tance pf	10-90% Rise Time nsec
Tektronix 545 with 53/54L pre amp	45	20	12
Tektronix 585 with Type 86 pre amp	85	15	4.0
Tektronix 454	150	20	2.4
Tektronix 517 direct deflection	—	5	2.5
Hewlett Packard 183	250	—	1.5

#### A STANDARD PULSE VOLTAGE GENERATING SYSTEM

The absolute accuracy and repeatability of the output current from a quartz gauge exceeds the nominal accuracy of oscilloscopes and

standard pulse calibrators. Thus, special calibration procedures are required to determine the response of the entire current measuring system, composed of distributed amplifier type oscilloscopes, cables, connectors, and terminators. To accomplish this, the entire recording system is calibrated by means of a pulse voltage standard and the system is frequently checked for repeatability with a result that a system accuracy of about  $\pm 0.5\%$  is achieved. This pulse calibration signal is supplemented with a 1 kc standard accurate to  $\pm 0.5\%$ .

The single-shot pulse standard produces a voltage pulse, which rises (0-99+%)  $< 50$  nsec, with an amplitude accuracy of  $\pm 0.5\%$ , while driving a time-variable 45 to 55 ohm load. This new system (45) was developed for our laboratory by the National Bureau of Standards' Boulder Laboratories.\* The pulse-voltage generating system incorporates a Velonex Model 380 pulse generator, adjusted to a 400 volt peak output, to drive a two stage Unitrode Zener diode clipper circuit shown in Fig. 9. The clipper is submersed in liquid nitrogen to reduce temperature coefficient changes in Zener reverse characteristics. The divider and clipper output is stabilized at 6.54 volts for the particular Zener diodes used. The brass enclosure surrounding the circuit improves rise time performance. Other clipper units are being constructed for lower and higher voltage levels. The voltage output from each unit is calibrated using a slideback voltmeter constructed by the Bureau of Standards.

#### TILT CONTROL

The target and projectile gauge assemblies are designed to achieve flatness and perpendicularity, but there are a number of other factors which can affect the alignment of the impacting surfaces during the experiment. All of the alignments must be controlled to achieve a low "tilt." Some investigators align the experiment in place by adjusting the target assembly to the impacting surface of the projectile. The procedure used on the present facility is to rigidly and precisely control all the tolerances which enter into misalignment. Each of these tolerances is measured on each experiment so that there is a known upper limit on the tilt. The median value of tilt which is achieved with this procedure is 200 to 300  $\mu$ rad.

\*The standard was modified and constructed to meet our specifications by Mr. Stanley Booker of the Sandia Laboratories Standard Department.

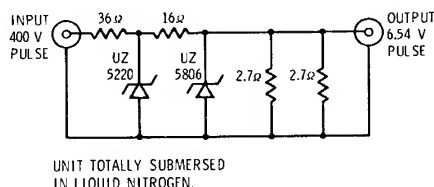


Fig. 9 - Schematic diagram of liquid nitrogen stabilized Zener diode peak clipping circuit. The 400 volt pulse from the Velonex generator is clipped in two stages, using resistive dividers and Unitrode Zeners, to a 6.54 volt  $\pm$  0.5% pulse. This low internal impedance calibrator accepts a 50 ohm load, and thus provides a complete system amplitude calibration of cables, connectors, terminators, attenuators and oscilloscopes after each experiment.

The surface from which the target face and the projectile face alignment is referenced is the target mounting flange. If this surface is perpendicular to the bore axis and the sample is parallel to the mounting flange the target surface is perpendicular to the axis of the bore. The projectile is then assembled such that the impacting face is perpendicular to the projectile sides. The chosen projectile diameter fits tightly to the gun bore and the projectile length of 28 cm minimizes the cocking of projectile in the bore.

Methods for assembling and measuring the targets, projectiles, and target mounting flange are shown in Figs. 10a through 10d.

The projectiles are ground and machined such that the impacting surface is perpendicular to the sides to within 100  $\mu$ rad. The impactor is glued to the projectile face in an alignment fixture shown in Fig. 10a which holds the impact surface perpendicular to the sides of the projectile to 50  $\mu$ rad. The epoxy glue joint thus served to allow for the final minor realignment. After the epoxy has cured the same fixture serves as a holder in which the perpendicularity is measured to 100  $\mu$ rad as shown in Fig. 10b with an electronic micrometer.

The target mounting flange is lapped flat and perpendicular to the axis of the gun bore with the lapping fixture shown in Fig. 10c. The rod is fit to the bore diameter to 0.0003." With a length of 28 cm this insures a maximum angular looseness of 20  $\mu$ rad. As the fixture is rotated the lapping compound on the cast iron disk laps the mounting flange. The mounting

flange may be lapped perpendicular to the bore to 20  $\mu$ rad with this technique. The surface is then hand polished with a 600 grit sandpaper.

The final alignment factor is the parallelism of the sample to the mounting surface of the target cup. After assembly, as described in the previous section, the parallelism is measured in the fixture shown in Fig. 10d. This parallelism is typically 100-200  $\mu$ rad. In the event that the sample assembly is defective and not parallel within this tolerance, the holding surface of the target cup is machined while indicating the alignment from the sample surface.

The target assembly is then mounted on the barrel flange after cleaning both surfaces with 200 proof alcohol. The surfaces are wrung together with no "O" ring seal or vacuum grease on the surfaces. The two lapped and "wrung" surfaces provide an excellent vacuum seal while atmospheric pressure holds the target assembly to the barrel.

## SUMMARY

This paper has summarized the basic features of impact experiments which utilize the Sandia quartz gauge to measure the mechanical properties of shock loaded solids. In addition, the circuitry involved in impact velocity, time of arrival, and time delay measurements have been described. Methods used in tilt control and sample preparation have also been discussed. The particular techniques and sample construction methods used are designed to achieve flexibility and to take maximum advantage of the unique features of impact surface measurements. These techniques have proven very useful in the study of the mechanical properties of solids under shock wave compression.

## ACKNOWLEDGMENT

The authors would like to thank their numerous Sandia Laboratory colleagues for their continuing dialogue which has provided a stimulating environment for this work.

## REFERENCES

1. S. Thunborg, Jr., G. E. Ingram and R. A. Graham, "Compressed Gas Gun for Controlled Planar Impacts over a wide Velocity Range," Rev. Sci. Instr. Vol. 35, pp. 11-14, 1964.

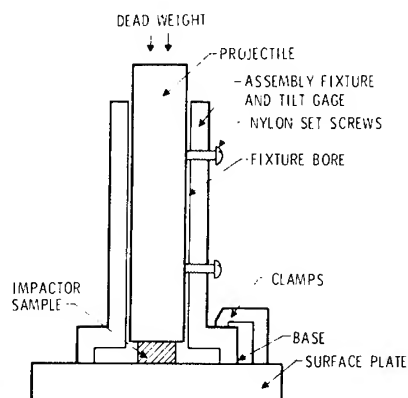


Fig. 10a

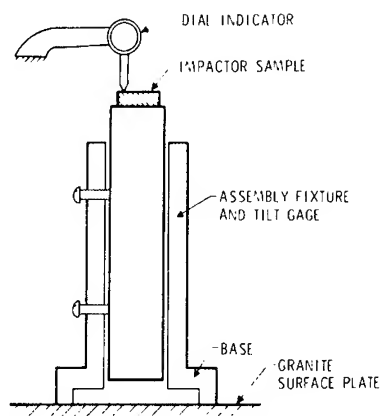


Fig. 10b

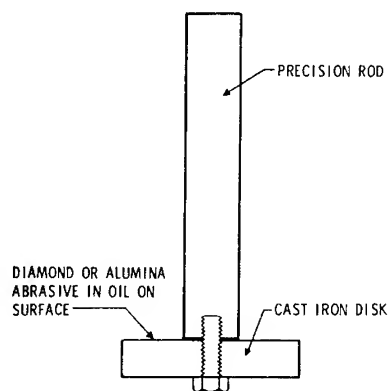


Fig. 10c

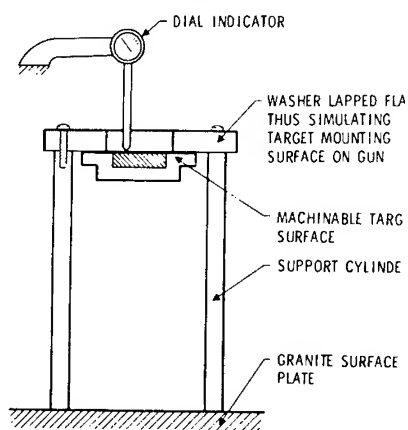


Fig. 10d

Fig. 10 - Cutaway drawings of the various schemes for adjusting and measuring the parameters contributing to angular misalignment of impacting surfaces. Uncontrolled rotation of the projectile in the long gun barrel prevents the use of an adjustable target. In Fig. 10a, a wedge of epoxy cures between the projectile and impactor interface while they are held in alignment with an assembly fixture and a surface plate. In Fig. 10b, the impactor sample is checked for alignment while the assembly fixture and tilt gage in which it is held is rotated. A dial indicator with 0.0001 inch resolution determines the acceptability for a particular experiment. Fig. 10c shows a 28 cm long rod that fits in the barrel with a 0.0003 inch difference in diameters. Attached to the rod, with a 5  $\mu$ rad control on perpendicularity, is a flat cast iron disk that is coated with 6 micron lapping compound. When inserted and rotated within the barrel, this device will produce a flat surface on the barrel alignment flange which is perpendicular to the bore to 20  $\mu$ rad. In Fig. 10d, the parallelism of the target assembly is checked with a fixture composed of a lapped washer to which is attached a support cylinder with its ends lapped parallel to 5  $\mu$ rad. A machinable flange on the target permits parallelism adjustments to be made on the target assembly to 100  $\mu$ rad. The target is held in place against the lapped washer with wooden dowels which penetrate the support cylinder.

2. R. A. Graham, "Impact Techniques for the Study of Physical Properties of Solids Under Shock-Wave Loading," J. Basic Engr. Vol. 89, pp. 911-918, 1967.
3. D. S. Hughes, W. M. Otto, E. B. Blankenship, Mary F. Gourley and L. E. Gourley, "Shock-Waves in Metals Generated by Projectile Impacts," Bull. Am. Phys. Soc. Series II, Vol. 2, p. 214, 1957.
4. D. Lundergan, "A Method of Measuring (1) The Parameters of Impact Between Two Plane Surfaces and (2) The Properties of the Plane Shock-Waves Produced," Sandia Corporation Research Report SC-4421 (RR), Nov. 1960.
5. R. A. Graham, "Piezoelectric Behavior of Impacted Quartz," Bull. Am. Phys. Soc. Series II, Vol. 5, p. 511, 1960.

6. P. S. Brody and R. H. Wittekindt, "Ratio of Dielectric Constant across a Shock Front in Barium Titanate," *Bull. Am. Phys. Soc.* 6, 42, 1961.
7. D. S. Hughes, L. E. Gourley and Mary F. Gourley, "Shock-Wave Compression of Iron and Bismuth," *J. Appl. Phys.* Vol. 32, pp. 624-629, 1961.
8. R. A. Graham, "A Technique for Studying Piezoelectricity Under Transient High Stress Conditions," *Rev. Sci. Instr.* Vol. 32, pp. 1308-1313, 1961.
9. John W. Taylor and Melvin H. Rice, "Elastic-Plastic Properties of Iron," *J. Appl. Phys.* Vol. 34, pp. 364-371, 1963.
10. C. D. Lundergan and Walter Herrmann, "Equation of State of 6061-T6 Aluminum at Low Pressures," *J. Appl. Phys.* Vol. 34, pp. 2046-2052, 1963.
11. W. J. Halpin, O. E. Jones and R. A. Graham, "A Submicrosecond Technique for Simultaneous Observation of Input and Propagated Impact Stresses" in *Dynamic Behavior of Materials ASTM Special Technical Publication No. 336*, 1963.
12. L. M. Barker and R. E. Hollenbach, "System for Measuring the Dynamic Properties of Materials," *Rev. Sci. Instr.* Vol. 35, pp. 742-746, 1964.
13. Richard J. Wasley and Joseph F. O'Brien, "Low Pressure Hugoniot of Solid Explosives," abstract in *Fourth Symposium on Detonation. Office of Naval Research Report ACR-126*, 1965.
14. Ronald K. Linde and David N. Schmidt, "Measuring the Submicrosecond Response of Shock-Loaded Materials," *Rev. Sci. Instr.* Vol. 37, pp. 1-7, 1966.
15. Charles H. Karnes, "The Plate Impact Configuration for Determining Mechanical Properties of Materials at High Strain Rates," in *Mechanical Behavior of Materials Under Dynamic Loads*, Edited by U. S. Lindholm, Springer-Verlag, New York, 1968.
16. N. H. Froula, "Hugoniot Equation of State of S-200 Beryllium and 6061-T6 Aluminum to 800°K and 50 kbar," *Bull. Am. Phys. Soc. Series II Vol. 13*, p. 1679, 1968.
17. G. R. Fowles, G. E. Duvall, P. Bellamy, F. Feistmann, M. H. Miles, J. Habberstad, R. Manvi, P. Holton, T. Michaels, R. Mitchell, D. Grady and R. White, "Gas Gun for Impact Studies," *Bull. Am. Phys. Soc. Series II Vol. 13*, p. 1680, 1968.
18. John H. Lower and Thomas J. Ahrens, "Shock Compression Experiments with a High Performance Propellant Gun," *Bull. Am. Phys. Soc. Series II, Vol. 14*, p. 1163, 1969.
19. J. E. Kennedy, this symposium.
20. J. Wackerle and J. O. Johnson have performed shock initiation experiments with gun impact and quartz gauge techniques. Private communication, 1970.
21. A. H. Jones, W. M. Isbell and C. J. Maiden, "Measurement of the Very-High Pressure Properties of Material using a Light Gas Gun," *J. Appl. Phys.* Vol. 37, pp. 3493-3499, 1966.
22. W. J. Halpin and R. A. Graham, "Shock-Wave Compression of Plexiglas from 3 to 20 kbars," in *Fourth Symposium on Detonation, Office of Naval Research Report ACR-126*, 1965.
23. R. A. Graham, F. W. Neilson and W. B. Benedick, "Piezoelectric Current from Shock Loaded Quartz - A Submicrosecond Stress Gauge," *J. Appl. Phys.* Vol. 36, pp. 1775-1783, 1965.
24. R. A. Graham and W. P. Brooks, "Shock-Wave Compression of Sapphire," *Trans. Am. Geophys. Union Vol. 50*, p. 673, 1969.
25. R. W. Rohde, "Equation of State of Shock-Loaded Tungsten at 950°C," *J. Appl. Phys.* Vol. 40, pp. 2988-2993, 1969.
26. F. W. Neilson, W. B. Benedick, W. P. Brooks, R. A. Graham and G. W. Anderson, "Electrical and Optical Effects of Shock-Waves in Crystalline Quartz," in *Les Ondes de Detonation, Editions du Centre National de la Recherche Scientifique*, Paris, 1962.
27. O. E. Jones, F. W. Neilson and W. B. Benedick, "Dynamic Yield Behavior of Explosively Loaded Metals Determined by a Quartz Transducer Technique," *J. Appl. Phys.* Vol. 33, pp. 3224-3232, 1962.

28. J. R. Freeman, "Field Fringing Around the Insulating Gap in Guard Ring Quartz Gauges," Sandia Laboratories Research Report SC-RR-69-55, Jan. 1969.
29. R. A. Graham and W. J. Halpin, "Dielectric Breakdown and Recovery of X-cut Quartz under Shock-Wave Compression," J. Appl. Phys. Vol. 39, pp. 5077-5082, 1968.
30. R. A. Graham and G. E. Ingram, "Anomalous Response from Quartz Gauges Subjected to Short Duration Stress Pulses," Bull. Am. Phys. Soc. Series II, Vol. 13, p. 1660, 1968.
31. R. A. Graham and G. E. Ingram, "Piezoelectric Current from X-Cut Quartz Shock Loaded from 25 to 70 kbar," Bull. Am. Phys. Soc. Series II Vol. 14, p. 1163, 1969.
32. F. W. Neilson and W. B. Benedick, "Piezoelectric Response of Quartz Beyond Its Hugoniot Elastic Limit," Bull. Am. Phys. Soc. Series II Vol. 5, p. 511, 1960.
33. P. C. Lysne, R. R. Boade, C. M. Percival and O. E. Jones, "Determination of Release Adiabats and Recentered Hugoniot Curves by Shock Reverberation Techniques," J. Appl. Phys. Vol. 40, pp. 3786-3795, 1969.
34. R. A. Graham, D. H. Anderson and J. R. Holland, "Shock-Wave Compression of 30% Ni-70% Fe Alloys: The Pressure-Induced Magnetic Transition," J. Appl. Magnetic Transition," J. Appl. Phys. Vol. 38, pp. 223-229, 1967.
35. L. M. Barker, B. M. Butcher, and C. H. Karnes, "Yield Point Phenomenon in Impact-Loaded 1060 Aluminum," J. Appl. Phys. Vol. 37, pp. 1989-1991, 1966.
36. J. R. Asay, G. E. Duvall and M. H. Miles, "Elastic Precursor Decay in LiF," Bull. Am. Phys. Soc. Series, II, Vol. 14, p. 1170, 1969.
37. T. E. Michaels and G. E. Duvall, "Elastic Precursor-Decay in Single Crystal Tungsten," Bull. Am. Phys. Soc. Series II, Vol. 14, p. 1170, 1969.
38. T. L. Towne, "High Temperature Fixtures for Use in Impact Stress Studies on Gas Gun Facilities," Sandia Laboratories Research Report, SC-RR-68-831, Nov. 1968, also Rev. Sci. Instr. Vol. 41, pp. 290-291, 1970.
39. O. E. Jones, "Piezoelectric and Mechanical Behavior of X-Cut Quartz Shock Loaded at 79°K," Rev. Sci. Instr. Vol. 38, pp. 253-256, 1967.
40. W. P. Brooks and R. A. Graham, "Shock-Wave Compression of Sapphire," Bull. Am. Phys. Soc. Series II, Vol. 11, p. 414, 1966.
41. G. A. Jones, "The Shorted Guard-Ring Quartz Gauge," Sandia Laboratories Research Report SC-RR-67-568, August 1967.
42. G. A. Jones and W. J. Halpin, "Shorted Guard-Ring Quartz Gauge," Rev. Sci. Instr. Vol. 39, pp. 258-259, 1968.
43. G. E. Ingram, "The Thumpatron, An Instrument for Determining the Direction of Polarization of Fragile Piezoelectric Samples," Report SC-DR-67-494, Clearinghouse, U. S. Dept. of Commerce, Springfield, Va. 22151
44. G. E. Ingram, "Application of Charged Coaxial Cables to the Measurement of Projectile Velocity and Impact Time in a Compressed Gas Gun," Rev. Sci. Instr. Vol. 36, pp. 458-460, 1965.
45. A. R. Ondrejka and P. A. Hudson, "Measurement Standards for Low and Medium Peak Pulse Voltages," J. Res. Natl. Bur. Std., C. Engineering and Instrumentation, Vol. 70C, No. 1, Jan.-March, pp. 13-18, 1966.

# SHOCK-INDUCED ELECTRICAL SIGNALS FROM DIELECTRICS

G. E. Hauver  
USA Ballistic Research Laboratories  
Aberdeen Proving Ground, Maryland

## ABSTRACT

Shock-induced electrical signals from linear polyethylene and o-nitroanisole have been analyzed within the framework of the Allison polarization theory. Hugoniot and dielectric constant data for the analyses were obtained in separate series of experiments. Analyses showed that signals from both materials are composed of more than one component. There is experimental evidence that components of the polyethylene signal relate to dipolar structures in the polyethylene. A similar conclusion may be drawn for o-nitroanisole, although an alternate interpretation is also offered. At high pressures, the profile of the polarization signal from o-nitroanisole is gradually modified by shock-induced electrical conductivity and the growth of chemical reaction. It was inferred that detonation electric signals might represent the final signal modification produced under conditions of stable detonation.

## I. INTRODUCTION

Most dielectric materials produce electrical signals during shock compression. There is a general tendency for weakly polar dielectrics to produce small signals and for strongly polar dielectrics to produce large signals. Experimental and analytical procedures for studying these signals were refined in an investigation of linear polyethylene, which is weakly polar, and were applied with certain necessary modifications in a study of o-nitroanisole,  $C_6H_4OCH_3NO_2$  (hereafter referred to as ONA). ONA is a metastable liquid dielectric with relatively large dipole moment of  $1.61 \times 10^{-29} \text{ Cm}$  (4.83 Debye units). The shock-induced electrical signals from these dielectrics exhibit complex profiles which have been found to contain more than one signal component. These signals have been interpreted within the framework of the Allison polarization theory (1). The paper briefly reviews the essential elements of the theory, describes the various experimental and analytical procedures used in polarization and ancillary investigations, and presents results and interpretations.

## II. THEORY

The parallel-plate configuration, commonly used to study shock-induced electrical signals, is shown schematically in Fig. 1. The polarization portion of the signal begins when a plane shock wave enters the dielectric from the first electrode. Allison (1) assumed that polarization is induced at the shock front and decays with a characteristic relaxation time  $\tau$ . If the RC time constant of the circuit is much less than the shock wave transit time (RC is commonly one nanosecond or less), the load may be considered to be a short circuit, and displacement current is given by the expression,

$$I = [C_1 Q + I_0 X_0 \exp(-t/\tau)] / (X_0 - C_1 t) ,$$

where,

$$Q = Q^* t^* I_0 X_0 \tau [1 - \exp(-t/\tau)] / (C_2 t + Q^* t^* X_0) ,$$

$$C_1 = U - (k_o/k)(U - u) ,$$

$$C_2 = I_0 X_0 \tau [1 - \exp(-t^*/\tau)] - Q^* t^* U ,$$



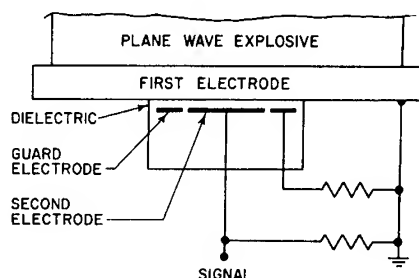


Fig. 1 - Experimental arrangement for polarization tests

#### List of Symbols

$I$	current
$I_0$	initial current
$Q$	electric charge on the electrodes
$Q^*$	electric charge at time $t^*$
$U$	shock velocity
$X_0$	initial thickness of the dielectric
$k$	dielectric constant of shock-compressed dielectric
$k_0$	dielectric constant of unshocked dielectric
$t$	time
$t^*$	time of shock arrival at the second electrode
$u$	particle velocity
$\tau$	relaxation time

and

$$I_0 = Q^* k_0 (U - u) / \{ \tau k U [1 - \exp(-t^*/\tau)] \} ,$$

Polarization induced at the shock front is given by the expression

$$P_s^0 = Q^* t^* / A \tau [1 - \exp(-t^*/\tau)] ,$$

where  $A$  is the electrode area.

If polarization is induced only in the vicinity of the shock front, then no additional polarization is induced in the interelectrode volume

after the shock front arrives at the second electrode. This assumes that the shock impedance of the second electrode is the same as that of the dielectric so that neither a shock nor rarefaction return into the interelectrode dielectric from the interface. It then follows from the Allison theory that the charge  $Q^*$ , which is on the electrodes at time  $t^*$ , decays with the characteristic relaxation time. The current in the relaxation portion of the signal, which occurs after the shock front arrives at the second electrode, is given by the expression

$$I = (-Q^*/\tau) \exp[-(t - t^*)/\tau] ,$$

where  $t \geq t^*$ . Yakushev, Rozanov, and Dremi (2) have reported this same relationship for the current in the relaxation signal.

In order to apply the Allison theory, it is necessary to know the shock-propagation characteristics, the dielectric constant under shock compression, and the relaxation time. In the study of linear polyethylene and ONA, ancillary experiments were performed to establish the Hugoniot and obtain information about the dielectric constant under shock compression. Relaxation times were obtained by analyzing the relaxation signal.

### III. POLYETHYLENE (3)

#### A. Introduction

Linear polyethylene was selected for several reasons. First, the shock-induced electrical signal is small and exhibits interesting behavior. It is negative at low pressures, begins to change polarity above 25 or 30 kbar, and is entirely positive by 70 kbar. Also, it was anticipated that dipolar structures might produce the electrical signal. If correct, the dipolar content could be modified by irradiation, possibly permitting signal sources to be identified. Second, Keeler and Mitchell (4) reported that polyethylene remains a reasonably good insulator to shock pressures well above 500 kbar. Their result was confirmed for this study by a conductivity test performed at 246 kbar. No conductivity was detected, and the sensitivity of the measurement imposed an upper limit of  $1.6 \times 10^{-5}$  mho/m. Third, the dielectric constant of polyethylene is essentially unchanged from DC to microwave frequencies (5), and it is unlikely that sites which produce the shock-induced electrical signal make a significant contribution to the dielectric constant. Furthermore, the small size of the shock-induced electrical signal tends to minimize its influence on the dielectric constant measurements.

### B. Experimental Arrangement for Polarization Tests

The experimental arrangement used for the study of shock-induced electrical signals from polyethylene was basically the arrangement shown schematically in Fig. 1. However, the test assembly was built coaxially onto a coaxial connector. The second electrode and its guard were formed by scribing a circular gap in a thin metal film deposited by vacuum evaporation on a thick polyethylene substrate. The interelectrode polyethylene was bonded to the second electrode and its guard with room-temperature setting epoxy, using a bond thickness which did not exceed 0.0025 mm. The second electrode was 13 mm in diameter, and the interelectrode polyethylene was approximately 1.0 mm thick. A thin metal film was used as the second electrode in an effort to minimize its influence on the shock wave and permit the relaxation signal to be recorded with optimum fidelity. Signals were recorded by an oscilloscope with a bandwidth of 150 MHz.

### C. Hugoniot

Hugoniot data were obtained for several linear polyethylenes, although only one (referred to as Brand X) was used for the tests reported in this paper. Brand X had an unknown origin and a density of  $0.960 \pm 0.002$  g/cc. The other polyethylenes were antioxidant-free Marlex 6002 with a density of  $0.960 \pm 0.002$  g/cc, and Alathon 7050 with a density of  $0.963 \pm 0.001$  g/cc. The Hugoniot data were obtained in plane shock wave experiments using the impedance matching technique (6). The shock velocity through polyethylene specimens was measured electrically, using the shock-induced polarization signal (7), or the signal obtained using an applied voltage (see Section III-D). Hugoniot data for the base plate metals were obtained from Ref. (6), or updated values were obtained from Ref. (8). The release isentropes needed for impedance calculations were generated assuming a constant  $\gamma\rho$ , where  $\gamma$  is the Gruneisen parameter and  $\rho$  is the density. The Hugoniot for both Brand X and AO-free Marlex 6002, in the pressure range from 16 to 246 kbar, is represented by the relationship  $U = 2695 + 1.570 u$ . (Velocity units are m/sec, here, and throughout the paper.) The standard deviation of  $U$  is 62. The Hugoniot for Alathon 7050 in the pressure range from 16 to 180 kbar is represented by the relationship  $U = 3064 + 1.557 u$ . These Hugoniots lie between the theoretical limiting Hugoniots calculated by Pastine (9). They parallel the theoretical Hugoniots at high pressures, but deviate slightly at low

pressures where the theoretical curves bend downward.

### D. Dielectric Constant under Shock Compression

The experimental arrangement for dielectric constant measurements is shown in Fig. 2. The polyethylene assembly was similar to the assembly used in the polarization tests. Approximately 500 volts was applied across the assembly and the series resistor  $R_T$ . The parallel capacitor  $C$  was three orders of magnitude larger than the other circuit capacitance and stabilized the voltage during a test. Shock pressures up to 173 kbar were produced by detonating an explosive in contact with the metal plate which served as the first electrode. Higher pressure was produced by impacting an explosively accelerated plate.

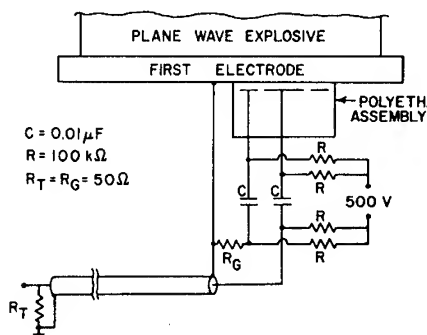


Fig. 2 - Experimental arrangement for dielectric constant measurements on polyethylene

When a plane shock wave entered the interelectrode dielectric, the capacitance increased as a result of compression and an increase in the dielectric constant of the shocked material. The associated charging current was recorded with an oscilloscope as the voltage drop across  $R_T$ . It may be shown that the charge on the polyethylene capacitor is given by the expression

$$Q = \frac{V \epsilon_0 k_0 A}{X_0 + [(k_0/k)(U - u) - U] t},$$

while the profile of the current signal is given by the expression

$$I = \frac{V \epsilon_0 k_0 A [U - (k_0/k)(U - u)]}{\{X_0 - [U - (k_0/k)(U - u)] t\}^2},$$

where  $V$  is the applied voltage and  $\epsilon_0$  is the permittivity of free space. Prior to shock compression, the charge on the polyethylene capacitor is

$$Q_1 = V k_0 \epsilon_0 A / X_0.$$

When the shock wave arrives at the second electrode,  $t = t^* = X_0/U$ , and the charge associated with the applied voltage is

$$Q_2 = V k \epsilon_0 AU / X_0 (U - u).$$

However, the charge on the electrodes at time  $t^*$  also includes the charge  $Q_p$  associated with the shock-induced polarization signal, so that

$$Q^* = Q_2 + Q_p.$$

During the transit time of the shock wave, the measured charge is

$$Q_m = Q^* - Q_1.$$

Substituting and solving for the dielectric constant,

$$k = \frac{U - u}{U} \left[ \frac{X_0 (Q_m - Q_p)}{V \epsilon_0 A} + k_0 \right].$$

The expression for  $k$  neglects any change in stray capacitance. The stray capacitance changed during a test, but except at 173 kbar where the change in stray capacitance represented almost 0.5 percent of  $Q_m$ , no correction was introduced. The polarization charge  $Q_p$  was evaluated in two ways as a check. It was evaluated directly with no applied voltage, and in tests with each polarity of the applied voltage so that  $Q_p = [Q_m(+)+Q_m(-)]/2$ . The dielectric constant of unshocked Brand X linear polyethylene was measured in a simple two-terminal system (10) and was found to be  $2.360 \pm 0.007$ .

Results of the dielectric constant measurements are plotted in Fig. 3 as  $(k-1)/\rho$  versus  $\rho$ , with individual test pressures indicated at the top. At 16 and 20 kbar, there was evidence that the applied voltage might have influenced the polarization signal. The exact extent of any influence could not be determined, so limits were set. The upper values at 16 and 20 kbar result if no influence is assumed; the lower values result if the polarization signal becomes zero when opposed by the applied voltage. From 36 to 246 kbar, there was no evidence of a voltage effect, and the dielectric behavior followed the Drude equation, assuming constant polarizability, with  $k-1 = 1.47 \rho$ .

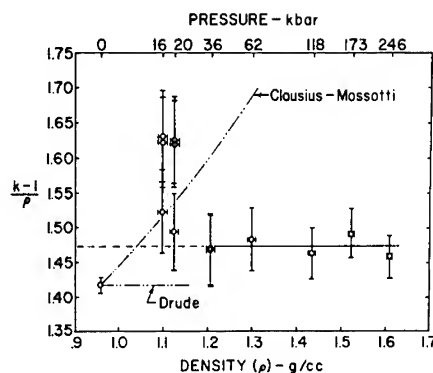


Fig. 3 - Dielectric constant data for polyethylene under shock compression

Gibbs and Jarman (11) measured the dielectric constant of polyethylene during static compression in the pressure range below three kilobars and found only one percent deviation from change predicted by the Clausius-Mossotti equation, assuming constant polarizability. Figure 3 suggests that the dielectric constant at low shock pressures also varies according to the Clausius-Mossotti prediction. The pressure at which dielectric behavior begins to follow the Drude equation is not firmly established, but is probably located between 20 and 36 kbar. The change in behavior may be associated with a phase transition. The Hugoniot measurements, and static measurements by Bridgman (12), give no indication of a transition below 36 kbar. However, Van Valkenburg and Powers (13) found evidence of a low pressure transition during static compression of polyethylene between diamond anvils. The transition was observed optically, was accompanied by an irreversible decrease in thickness, and post-test analysis suggested the presence of a triclinic cell. However, no transition pressure was reported. Cleron, Coston, and Drickamer (14) reported NMR data on polyethylene in the pressure range below 25 kbar. The width of the  $^1\text{H}$  resonance line showed no measurable change until a pressure of 5 kbar. A rapid increase in linewidth occurred above 5 kbar and leveled off near 22 kbar. The sudden increase in linewidth was not attributed to a phase transition, but the motion of the polyethylene chains suddenly became severely restricted and it was noted that polytetrafluoroethylene displayed similar NMR behavior at identified transition pressures.

The Drude equation results when the applied field is the effective polarizing field. Calculations by Brodsky and Burstein (15) and Gill and Bloembergen (16) have shown that the

effective field for electronic polarization is the macroscopic applied field when the electrons are delocalized. Royce (17), in considering the dielectric constant data for polymethylmethacrylate reported in Ref. (7), suggested that electrons may have become delocalized as a result of shock compression. This suggestion would also provide an appropriate explanation for the dielectric behavior of shock compressed polyethylene.

### E. Shock-Induced Electrical Signals

Some insight into the nature of shock-induced electrical signals from linear polyethylene can be gained by examining three signals produced near 50 kbar, which is at the midpoint of the pressure range where a polarity change occurs. One of the signals was produced by normal Brand X linear polyethylene, while the other two were produced by specimens of the same material which were first irradiated by a cobalt-60 gamma source.

Figure 4 presents the analysis of the signal produced by normal polyethylene at 47 kbar. The solid curve represents the observed signal. Its basic features include the initial positive portion, the slow risetime of the negative portion, and the slow decay of the relaxation signal back toward zero. The analysis reveals three major components: S1, S2, and S3. These components are identified by their relaxation times, which are listed in Table 1 along with the associated polarizations. The circular points in Fig. 4 represent the algebraic addition of the components. These points are in reasonable overall agreement with the observed signal, with the greatest departure occurring just after shock arrival at the second electrode. Here, a positive jog occurs and the observed signal lies above the calculated signal for an interval of about 30 nanoseconds. This departure may indicate a perturbation produced by the mismatched electrode film, although it is more strongly suspected to be thermoelectric. The electrode metal and lead wire were different in this test, producing a bimetallic junction at the center of the second electrode. It is evident that the fast-relaxing component S3 is primarily responsible for the initial positive portion of the observed signal and for the slow risetime of the negative portion, while the slow decay of the relaxation signal results from the relative relaxations of components S1 and S2. The polyethylene signal undergoes a polarity change because component S1 predominates at low pressures, while the positive components increase in magnitude and predominate at high pressures.

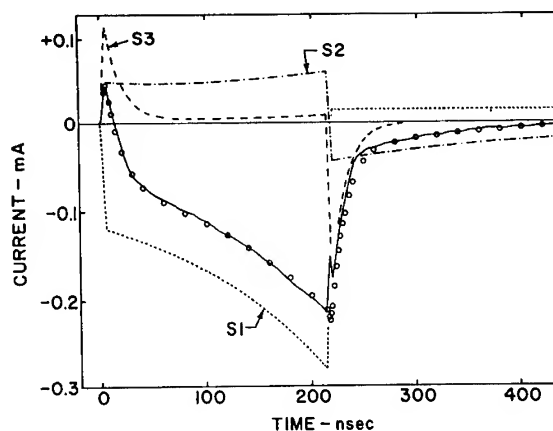


Fig. 4 - Analysis of the shock-induced electrical signal from normal polyethylene

TABLE 1  
Data for Signal Components

Material	Component	$\tau$ - $\mu$ sec	$P_s^0$ - $\mu$ C/m <sup>2</sup>
Normal Linear Polyethylene	S1	2.6	-0.32
	S2	0.24	+0.13
	S3	0.014	+0.37
Irradiated Without Air (30 Megarads)	S1	2.6	-0.13
	S3	0.014	+0.22
	S4	0.12	+0.15
Irradiated in Air (30 Megarads)	S1	2.6	-0.38
	S3	0.014	+0.42
	S4	0.12	+0.82

Polyethylene for a second test was prepared by irradiating a 25-mm thick block in a cobalt-60 cell. The dose rate was approximately 0.5 megarad per hour, and the total dose was 39 megarads. The block was then annealed above the crystalline melting point to eliminate radicals trapped in the crystallites. The oxidized surfaces were removed, a specimen was prepared from the core of the irradiated block, and a shock experiment was performed at 46 kbar. The shock-induced electrical signal was analyzed, and data for the signal components are listed in Table 1. The magnitudes of components S1 and S3 have decreased, component S2 is missing, and a new component S4 has appeared. At first inspection, component S4 may appear to be component S2 with the relaxation time reduced by one-half. This is doubtful. Relaxation times are presently believed to be characteristic of a particular source of polarization and serve as a means for identification.

Polyethylene for a third test was prepared by milling a block into 0.025-mm thick fluff which was oxidized by gamma irradiation in air, receiving a total dose of 30 megarads at a dose rate of 0.3 megarad per hour. The irradiated fluff was refabricated into a cylindrical form from which a test specimen was prepared. A control specimen, prepared from refabricated unirradiated fluff, produced a shock-induced electrical signal identical to the signal from original material. The shock-induced signal from oxidized polyethylene is shown in Fig. 5 and data for the components are listed in Table 1. The components produced by the specimen irradiated without air are again present, and are identified by their relaxation times. However, each component is larger. Component S4 underwent the most significant increase, becoming over five times larger. In Fig. 5, the calculated relaxation signal does not closely follow the observed signal. This is attributed to an impedance mismatch between the oxidized specimen and the unoxidized substrate of the second electrode. However, the test pressure increased to only 50 kbar, indicating a slight mismatch. Dielectric constant data for normal polyethylene were used to calculate the profile of the polarization signal. The dielectric constant data for oxidized material may be different, but the polyethylene signal was found to be extremely insensitive to the value of  $k_0/k$ . This was not thoroughly investigated, but was believed to result from the presence of signal components with opposing polarities.

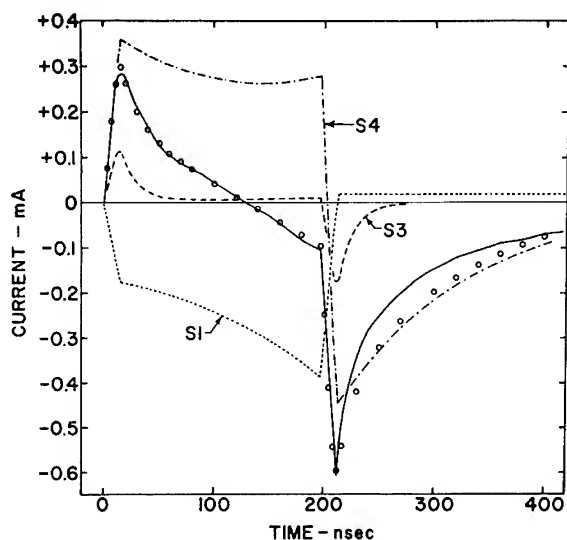


Fig. 5 - Analysis of the shock-induced electrical signal from oxidized polyethylene

The signal components are assumed to be produced by dipolar structures present in the polyethylene. Conklin (18) has considered the primary dipolar structures in linear polyethylene, and the changes which result from gamma irradiation. The primary dipolar structure inherent in linear polyethylene is vinyl unsaturation,  $-\text{CH}=\text{CH}_2$ . This structure decays rapidly with dose, and 30 to 40 megarads should reduce the vinyl content to less than ten percent of the initial value. Impurity dipolar structures are also present. These result from oxygen introduced by contact with air during manufacture and subsequent processing, and consist of various combination of carbon, hydrogen and oxygen. However, the carbonyl structure is dominant, and during gamma irradiation its concentration increases more rapidly than the hydroxyl structure, for example (19).

Signal component S2 is tentatively attributed to vinyl unsaturation. The 39 megarad dose, without air, probably reduced component S2 to a size not readily detected by the profile analysis. At the same time, the carbonyl concentration increased and was detected as signal component S4. The oxidized specimen showed a large increase in the magnitude of S4, more strongly associating this component with the carbonyl structure. The reduced magnitudes of components S1 and S3, in the signal from polyethylene irradiated without air, may be related to the increase of normal and pseudo cross linking which restrict motion in the shock wave. Conversely, the increased magnitudes of components S1 and S3 in the signal from oxidized polyethylene may indicate an influence by oxidation scission. However, S1 and S3 are not identified and their behavior may indicate an increase in the concentration of dipolar impurity structures other than carbonyl.

#### IV. O-NITROANISOLE (ONA)

##### A. Introduction

ONA was also selected for several reasons. First, it is a metastable liquid. Although insensitive, a confined column of ONA was initiated and observed to propagate a self-sustained shock wave at a velocity of approximately 5100 m/sec. Second, ONA produced the largest shock-induced electrical signal of all organic liquids tested. This is assumed to be associated with its large dipole moment. A large signal size permits the use of wide bandwidth instrumentation which cannot be used as effectively with smaller signals that require

amplification. Third, ONA remains a satisfactory insulator at shock pressures up to 70 kbar. The criterion for a satisfactory insulator is assumed to be  $\tau_c = k\epsilon_0/\sigma \gg X_0/U$ , where  $\tau_c$  is the relaxation time of free charge in a homogeneous conductor and  $\sigma$  is the conductivity.

### B. Shock-Induced Conductivity

Shock-induced electrical conductivity is a primary consideration in the study of shock-induced electrical signals. The shock-induced conductivity of ONA was measured using the experimental arrangement shown in Fig. 6. The ONA was laterally confined by a polyethylene well with an inside diameter of 7 mm. Conductivity was measured through a 0.5 mm initial thickness of ONA contained between the metal plate and a thin metal film deposited by vacuum evaporation on the end of a cylinder of C7 epoxy (Armstrong Products Company, Warsaw, Indiana). C7 epoxy was selected for its close match to the shock impedance of ONA. The conductivity circuits were slightly modified versions of the basic circuit attributed to Reimers (20). The major experimental uncertainty came from two sources: a weak rarefaction which propagated into the shock compressed ONA from the polyethylene, and the presence of a large relaxation signal. Uncertainty in the measured conductivity values was estimated to be from 30 to 35 percent in most tests.

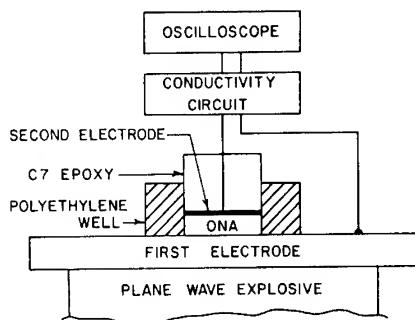


Fig. 6 - Experimental arrangement for conductivity measurements of o-nitroanisole

Conductivity data are presented in Fig. 7. At approximately 70 kbar, the electrical conductivity increases rapidly from values less than  $10^{-5}$  mho/m to a value between  $10^{-3}$  and  $10^{-2}$  mho/m. From 80 to 140 kbar, the conductivity remains at a plateau-like level, increasing by less than an order of magnitude. After a delay, or induction time, the conductivity

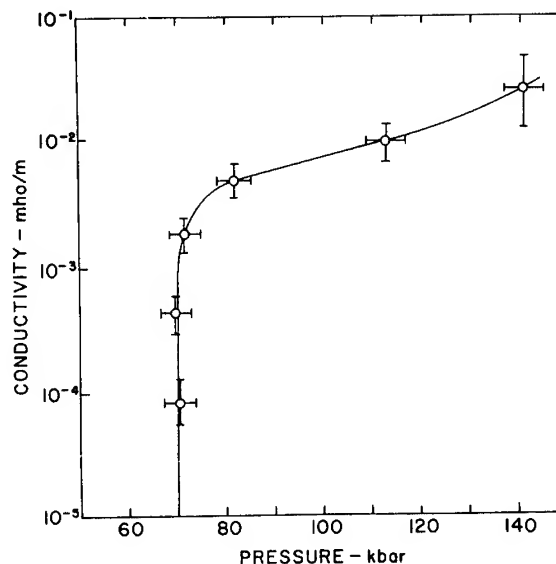


Fig. 7 - Shock-induced electrical conductivity in o-nitroanisole

was found to increase abruptly from the plateau value. At 115 kbar, the induction time was approximately 600 nsec; at 140 kbar, it had decreased to about 40 nsec. This phenomenon is assumed to be initiation and growth to detonation, but was not investigated in detail.

### C. Experimental Arrangement for Polarization Tests

The experimental arrangement used for the study of shock-induced electrical signals from ONA was basically the arrangement shown schematically in Fig. 1. Like the polyethylene assembly, the ONA assembly was built coaxially onto a coaxial connector. C7 epoxy was used as the substrate for the electrode film which was deposited by vacuum evaporation. A gap was scribed to divide the deposited film into the second electrode and its guard. The second electrode diameter was reduced to 2.5 mm in order to reduce the influence of shock wave nonplanarity. Interelectrode distances ranged from 0.2 to 0.3 mm in the different tests. A micrometer syringe was used to introduce ONA into the interelectrode volume through a small opening in the side of the coaxial assembly. Shock-induced electrical signals were recorded by an oscilloscope with a bandwidth of one GHz.

### D. Hugoniot

Hugoniot data for ONA ( $\rho_0 = 1.255$  g/cc) were obtained in plane shock wave experiments

using the impedance matching technique. The Hugoniot is represented by the relationship  $U = 2240 + 1.51 u$ , with a standard deviation (of  $U$ ) of 90 m/sec. It is based on 25 data points in the pressure range from 20 to 185 kbar. With the exception of three measurements, all shock velocities were obtained by measuring shock-induced electrical signals recorded in the polarization experiments described in Section IV-C. The ONA thickness of only 0.2 to 0.3 mm accounts for the large standard deviation. However, the small thickness and short transit time minimized the influence of chemical reaction on shock velocities measured at the higher pressures.

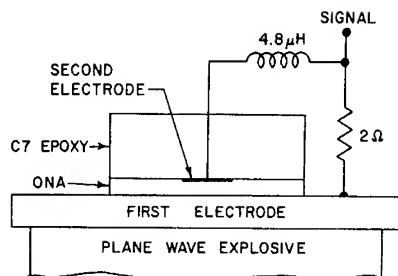


Fig. 8 - Experimental arrangement for dielectric constant measurements on o-nitroanisole

#### E. Dielectric Constant under Shock Compression

The applied voltage technique, used successfully for measurements on polyethylene, failed completely in tests with ONA. Failure could not be related to shock-induced conductivity, and is believed to have been related to the influence of applied voltage on the shock-induced polarization signal. Consequently, an alternate technique was introduced. The experimental arrangement is shown schematically in Fig. 8. This is a simple parallel-plate configuration for a polarization test, with inductance added to the circuit and the load resistance reduced to two ohms. C7 epoxy was used as the substrate for the second electrode because of its close match to the shock impedance of ONA. The second electrode was a thin vapor deposited aluminum film, 12 mm in diameter. The ONA diameter was semi-infinite and its initial thickness was adjusted to provide a shock-compressed thickness within the range from 1.27 to 2.01 mm.

When a plane shock wave enters the ONA from the first electrode, a shock-induced electrical signal results. The circuit oscillates at the resonant frequency and a damped oscillation is superimposed on the signal profile. The period of oscillation changes during shock transit through the ONA, but becomes essentially constant after shock arrival at the second electrode. The constant period is evaluated and related to the capacitance and dielectric constant of shock-compressed ONA. There are several problems, however. First there is field fringing and stray capacitance. These were taken into account by calibrating with reference dielectrics in a duplicate physical arrangement. The reference materials were air, polystyrene, sodium chloride, lithium fluoride, n-propyl alcohol, and nitrobenzene. With each material as the interelectrode dielectric, the

circuit was set into oscillation and the natural period was measured. Tests were performed with four dielectric thicknesses that ranged from 1.27 to 2.01 mm. The calibration consisted of a  $(P, \sqrt{k_o})$  relationship for each thickness, where  $P$  is the period and  $k_o$  is the dielectric constant. The period of oscillation from an ONA experiment was referred to this calibration which yielded four values of  $(k_o, X)$ , where  $X$  is the thickness. The dielectric constant of shock compressed ONA was evaluated from the  $(k_o, X)$  relationship at the shock-compressed thickness. A second problem arises because this is the complex dielectric constant, the real part is needed, and the loss is not determined. However, the circuit will not oscillate if the loss is high. In the tests with ONA, it was concluded that the complex value usually could not exceed the real part by more than five percent. A third problem is the actual error, which is greater than five percent and in the opposite direction, with the real part of the dielectric constant exceeding the measured value. This technique has been applied for measurements on a number of dielectrics, and with one possible exception, the measured values were obviously low. In an evaluation test with linear polyethylene, the measured value was approximately 30 percent low. Nevertheless, the measured values provide a rough guide to the dielectric behavior of ONA, and offer an initial value which may be refined in a polarization analysis.

Figure 9 shows the results of the measurements. At approximately 10 MHz, the dielectric constant is in the order of 46. There is a slight increase at 6 kbar, followed by a precipitous decrease at slightly higher pressures. Loss was very high during the rapid decrease and the circuit would oscillate for only a few cycles. Above 30 kbar, where the measured value was approximately 5, the loss was less and the circuit oscillated more freely. The

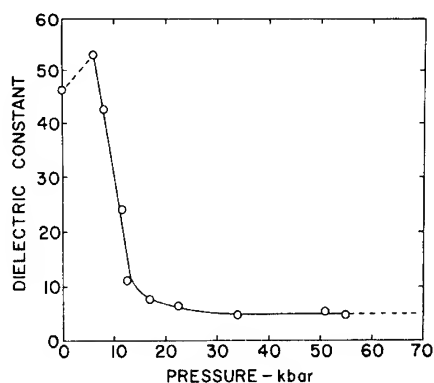


Fig. 9 - Dielectric constant data for o-nitroanisole

behavior of the dielectric constant suggests hindered rotation that may result from freezing under shock compression.

#### F. Shock-Induced Electrical Signals

The magnitude of shock-induced electrical signals from ONA increases rapidly with increasing pressure over the range from 20 to 70 kbar, but features of the profile remain essentially unchanged. Figure 10 shows a signal at 67 kbar. The solid curve in Fig. 10 represents the observed signal. The decrease in dielectric constant under shock compression is a dominant factor in the general appearance of the signal. An analysis shows that the signal is composed of two major components: S1 with a relaxation time of 424 nsec and a polarization of  $600 \mu\text{C}/\text{m}^2$ , and S2 with a relaxation time of 5 nsec and a polarization of  $333 \mu\text{C}/\text{m}^2$ . These signal components are about three orders of magnitude larger than the components of the polyethylene signal. A third component was considered at one point in the analysis, but was later rejected. The general rule has been to limit the number of components to the minimum required to achieve reasonable overall agreement with the observed signal. The circular points in Fig. 10 represent the algebraic addition of the two components. There is some discrepancy between the calculated and observed signals, but two components were judged to give reasonable agreement. Fortunately, the components have the same polarity and the analysis was found to be sensitive to the value of  $k_0/k$ . Although the analysis started with  $k \approx 5$ , the final analysis yielded  $k \approx 10$ , indicating that the measured value was about 50 percent low. This is consistent with the result of the evaluation test with polyethylene, which

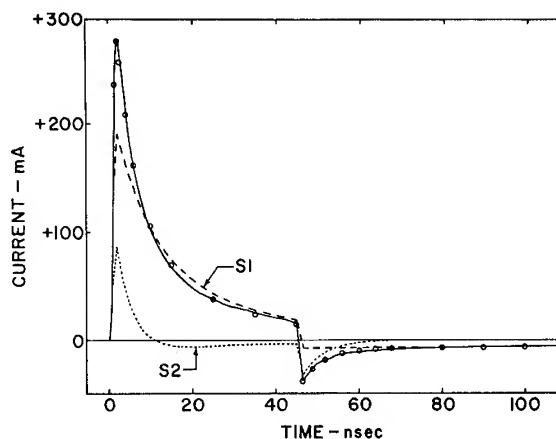


Fig. 10 - Analysis of the shock-induced electrical signal from o-nitroanisole

gave a value that was 30 percent low. An analysis can be long, and the analysis of all signals in the pressure range below 70 kbar was not carried to final state of the analysis shown in Fig. 10. However, the sensitivity to  $k_0/k$  suggested that profile analysis might provide improved values for the dielectric constant under shock compression.

Above 70 kbar, signal profiles are modified by electrical conductivity. This modification is implied by the data presented in Fig. 11, which shows  $Q^*/A$  versus shock pressure. This presentation of data actually has marginal quantitative significance, since

$$Q^*/A = P_s^0 \tau [1 - \exp(-t^*/\tau)]/t^*.$$

The quantity  $Q^*/A$  is dependent on  $t^*$ , and a smooth curve results only because all specimen thicknesses were approximately the same. Below 70 kbar,  $Q^*/A$  increases rapidly with pressure. When conductivity begins,  $Q^*/A$  drops abruptly to a plateau-like level and from 70 to 140 kbar decreases in a manner which mirrors the increase of electrical conductivity shown in Fig. 7. Above 150 kbar,  $Q^*/A$  again increases with pressure. This increase is assumed to be associated with the rapid growth of chemical reaction near the first electrode. The high electrical conductivity within the reaction may behave as an extension of the first electrode, rapidly increasing the capacitance. Unfortunately, ONA is very insensitive to initiation, and this series of tests did not extend to a pressure where detonation occurs "instantaneously" at the surface of the first electrode. Based on the observed trend, it might be



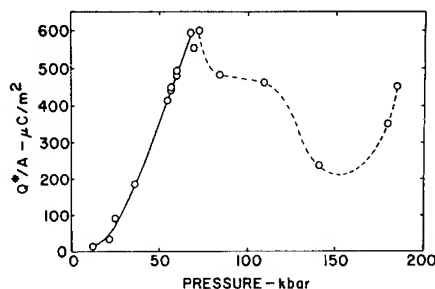


Fig. 11 - Dependence of the measured charge on shock pressure

inferred that the detonation electric effect (21) represents the final modification of the polarization signal which results from stable detonation. However, this would seem to require a thin residual volume of shock-induced polarization between the foot of the advancing shock wave and the region of high electrical conductivity associated with the detonation.

## V. DISCUSSION

Since polar groups apparently contribute to the shock-induced electrical signal from polyethylene, it might be concluded that polar groups on the ONA molecule contribute to its signal. However, it may be well to consider a possible alternative. The signal analysis reported in this paper has assumed that the Allison polarization theory provides a valid macroscopic description of the polarization process. This theory assumes that the dielectric coefficient is indeed constant under the conditions of shock compression. In the case of polyethylene, this seems to be a reasonably valid assumption. The sites which produce the shock-induced electrical signal probably do not make a significant contribution to the dielectric constant. In the case of ONA, the assumption of a constant dielectric coefficient cannot be accepted with the same assurance. Rice (22) has treated the case in which the dielectric coefficient is assumed to have a relaxing component. If the signal shown in Fig. 10 is analyzed by this approach, the profile of the polarization signal can be reproduced by assuming only one relaxing source of polarization. However, the set of constants for the polarization signal do not result in a completely satisfactory relaxation signal. Unfortunately, the constants cannot be readily evaluated by independent experiments. At the present time, the Allison theory with the assumption of two polarization sources seems to provide the better overall description of the observed signals from ONA.

## REFERENCES

1. F. E. Allison, "Shock-Induced Polarization in Plastics. I. Theory," *J. Appl. Phys.*, Vol. 36, No. 7, pp. 2111-2113, July 1965.
2. V. V. Yakushev, O. K. Rozanov, and A. N. Dremin, "On the Measurement of the Polarization Relaxation Time in a Shock Wave," *Soviet Phys. -JETP*, Vol. 27, No. 2, pp. 213-215, Aug. 1968.
3. Part of the results included in this section were reported at the Winter Meeting of the Am. Phys. Soc. in Los Angeles, 29-31 Dec. 1969. (G. E. Hauver, "Shock-Induced Electrical Signals from Polyethylene", *Bull. Am. Phys. Soc.*, Series II, Vol. 14, No. 12, p. 1163, Dec. 1969.)
4. R. N. Keeler and A. C. Mitchell, "Electrical Conductivity of Shock-Compressed Insulators," *Bull. Am. Phys. Soc.*, Series II, Vol. 12, No. 8, p. 1128, Dec. 1967.
5. A. von Hippel, *Dielectric Materials and Applications*, pp. 327-328, Technology Press, Cambridge, Mass., 1954.
6. M. H. Rice, R. G. McQueen, and J. M. Walsh, *Solid State Physics*, Vol. 6, pp. 1-63, Academic Press, New York, 1958.
7. G. E. Hauver, "Shock-Induced Polarization in Plastics. II. Experimental Study of Plexiglas and Polystyrene," *J. Appl. Phys.*, Vol. 36, No. 7, pp. 2113-2118, July 1965.
8. W. C. Carter, S. P. Marsh, J. N. Fritz and R. G. McQueen, "The Equation of State of Selected Materials for High Pressure Standards," *Symposium on the Accurate Characterization of the High Pressure Environment*, U. S. Dept. of Commerce, National Bureau of Standards, Gaithersburg, Maryland, October 14-18, 1968.
9. D. J. Pastine, "Theory of Polymer Behavior under Shock Attack," *Bull. Am. Phys. Soc.*, Series II, Vol. 14, No. 12, p. 1164, Dec. 1969.
10. A. H. Sharbaugh and S. Roberts, *Methods of Experimental Physics*, Vol. 6, Part B, pp. 1-31, Academic Press, New York, 1959.
11. D. F. Gibbs and M. Jarman, "The Permittivity of Hydrostatically Stressed Dielectrics," *Phil. Mag. (GB)*, Vol. 7, pp. 663-670.

12. P. W. Bridgman, "Rough Compression of 177 Substances to 40,000 Kg/cm<sup>2</sup>," Proc. Am. Acad. Arts Sci., Vol. 76, p. 72, 1948.
13. A. Van Valkenburg and J. Powers, "Optical Observation of Pressure Induced Transitions in Polymers," J. Appl. Phys., Vol. 34, No. 8, pp. 2433-2434, Aug. 1963.
14. V. Cleron, C. J. Coston, and H. G. Drickamer, "Apparatus for NMR Studies at High Pressures," Rev. Sci. Inst., Vol. 37, No. 1, pp. 68-72, Jan. 1966.
15. M. H. Brodsky and E. Burstein, "Relation Between Static and Optical Dielectric Constants in III-V Compounds," Bull. Am. Phys. Soc., Series II, Vol. 7, No. 3, p. 214, March 1962.
16. D. Gill and N. Bloembergen, "Linear Stark Splitting of Nuclear Spin Levels in GaAs," Phys. Rev., Vol. 129, No. 6, pp. 2398-2403, 15 March 1963.
17. Private communication from Dr. E. B. Royce, Lawrence Radiation Laboratory, Livermore, California, 17 May 1965.
18. G. E. Conklin, "Reduction of Dielectric Loss in Polyethylene," J. Appl. Phys., Vol. 35, No. 11, pp. 3228-3235, Nov. 1964.
19. J. A. Swisher and A. D. Coates, "A Study of the Dosimetric Properties of Low Density Polyethylene," BRL Memorandum Rept. 1336, March 1961.
20. L. V. Al'tshuler, L. V. Kuleshova, and M. N. Pavlovskii, "The Dynamic Compressibility, Equation of State, and Electrical Conductivity of Sodium Chloride at High Pressures," Sov. Phys. -JETP, Vol. 12, No. 1, pp. 10-15, Jan. 1961.
21. B. Hayes, "The Detonation Electric Effect," J. Appl. Phys., Vol. 38, No. 2, pp. 507-511, Feb. 1967.
22. Private communication from Dr. M. H. Rice, Physics Dept., University of South Dakota, Vermillion, South Dakota, Aug. 1969.

## THE MECHANISM OF ELECTRICAL CONDUCTIVITY OF LIQUID DIELECTRICS IN SHOCK WAVES

A. N. Dremin and V. V. Yakushev  
*Institute of Chemical Physics  
USSR Academy of Sciences  
Moscow, U.S.S.R.*

### ABSTRACT

Electrical signals resulting from a shock wave in a dielectric medium were observed through the use of various metal electrodes. The sign of the generated potential was a function of the metals used. It was concluded that the source of the electrical signal observed was electrochemical. Further evidence was obtained using an aluminum screen and either copper or magnesium counter electrodes with liquids of varying dielectric constant. The signals were observed only above a threshold pressure with saturation occurring at high pressures, 150,000 atm. in the case of carbon tetrachloride. These observations confirmed the ionic nature of the phenomena.

It has been found in studying polarization of liquid dielectrics in shock waves, that liquids involving polar molecules, such as water (1), acetone, chlorobenzene, bromobenzene, iodobenzene, nitrobenzene, and others give polarization signals. When shock waves are propagated over nonpolar liquids such as benzene, carbon tetrachloride, etc., no polarization signals appear (2). In this connection, an assumption arose that with decomposition of nonpolar molecules of a liquid behind the front of a shock wave into polar fragments, a polarization signal may be obtained from propagation of a second reflected shock wave over a shock-compressed substance (2). Carbon tetrachloride was the liquid used. A schematic view of the experimental device for observation of polarization signals is given in Fig. 1.

A flat shock front passed through a grounded metallic screen and entered substance 2 which was a dielectric of a flat-parallel condenser formed by the screen and electrode 3. The electrical signals were recorded by an oscillograph with input resistance  $R_e$ .

When the direct shock wave reached the electrode, a reflected wave was propagated back over the compressed substance (medium). In order to vary the reflected shock wave

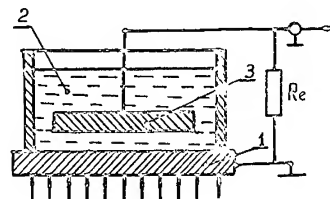


Fig. 1 - Experimental set-up for observing polarization signals in liquids. 1 - Screen (driver plate), 2 - Dielectric, 3 - Electrode.

amplitude electrodes were prepared from metals with different shock impedance. Electrical signals were actually recorded. The following features were observed. A signal appears when the shock is reflected only at a certain minimum initial pressure. With increasing initial pressure, the signal increases in amplitude up to a maximum and does not change with further increase in pressure. The signal was about one volt for various electrodes. The signal sign did not depend on the direction of wave propagation but was determined instead by the nature of the screen or electrode metal. For instance, when the aluminum screen was replaced by

magnesium with a zinc electrode; the signal sign changed. Generally speaking, electrical signals can be produced by polarization of a liquid at the shock wave front within the medium, as well as by thermoelectrical and electrochemical phenomena at metal-substance interfaces of shock-compressed states (2-3). However, for a general case, the signal sign will change with the direction of shock-wave propagation for either polarization in the bulk or appearance of thermoelectromotive force at the interface. Dependence of a signal sign on the nature of the electrode metal also indicates that this is a signal from a galvanic cell, rather than that of polarization. In this case, the voltage recorded will be

$$U = \frac{E}{1 + \alpha}$$

where  $\alpha = R_i/R_e$ ,  $E$  is the electromotive force of a cell,  $R_i$  its internal resistance and  $R_e$  the input resistance of the recording device. Hence it is evident that a distinct signal will be recorded at fairly low values of internal resistance of element  $R_i$ . Indeed, in the case of carbon tetrachloride, the signal appears at pressures corresponding to sufficiently high conductivity. In our experiments with carbon tetrachloride at a pressure of 180,000 atm,  $\alpha$  was about  $10^{-2}$ , and we therefore recorded, in fact, the electromotive force of the cell. To calculate  $\alpha$ , we made use of the data on conductivity of carbon tetrachloride, obtained by Mitchell and Keller (4).

Non-equilibrium processes occur on electrodes of the galvanic cell upon shock compression (in particular, since the liquid contains no ions of the given metals) and therefore no consistency of the value and sign of signals with the electromotive series of metals is to be expected. It is of interest to note that the signal signs in our shock wave experiments coincided with those obtained when immersing the same electrode pair into a solution of sodium chloride.

The results obtained and the conclusion that electrical signals arising on shock compression of non-polar dielectrics are of an electrochemical nature permit proposing two types of experiments for elucidating the nature of conductivity (5) in both polar and non-polar dielectrics (Figs. 2a and 2b). The device in Fig. 2a differed from that commonly used for observing polarization in that the electrode represented was a thin metal foil tape oriented normal to the shock front. Experiments with this set-up involved successive shock loading of the screen and of the electrode. In a symmetric device (Fig. 2b) the front of a shock wave reached two electrodes practically at the

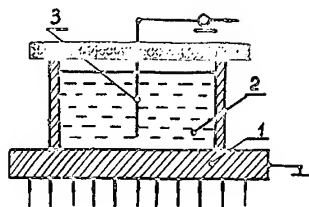


Fig. 2a - One electrode test set-up for study.  
1 - Aluminum screen,  
2 - Liquid dielectric,  
3 - Foil electrode.

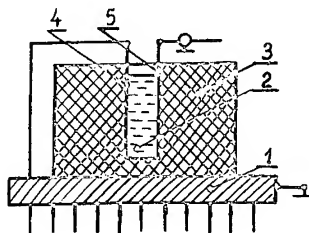
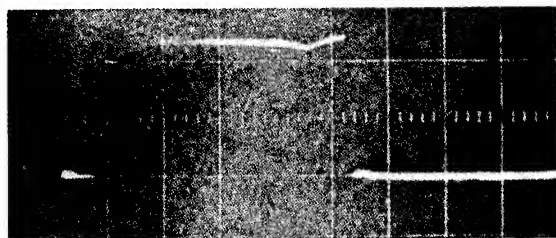


Fig. 2b - Two electrode symmetric test set-up for study. 3 is a Teflon container, 4 and 5 are parallel foil electrodes.

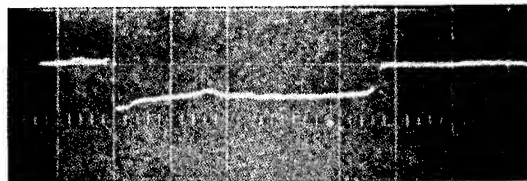
same time. Teflon was used for the cell bottom and walls. Eichelberger and Hauver (1) have shown that teflon does not polarize on shock compression and, according to Alder and Christian (6), it will remain a fairly good insulator at the pressures used.

These devices practically exclude the effect of polarization signals on the signal recorded and, thereby, permit investigating both polar and non-polar substances. Moreover, the formation of reflected shock waves is eliminated due to the electrodes geometry. A number of liquids such as water, methanol, acetone, dichloroethane, carbon tetrachloride, silicon tetrachloride, tin tetrachloride and methyl methacrylate was studied. In all the experiments the screen was made of aluminum, and the electrodes of copper or of magnesium.

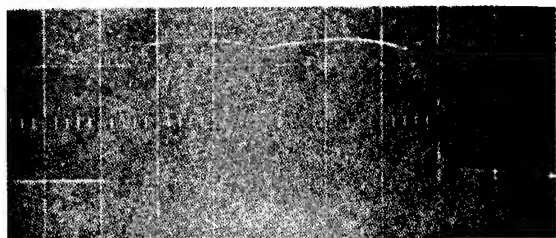
Figs. 3a to 3f are some oscillograms obtained with: water, copper electrode (Fig. 3a); water, magnesium electrode (Fig. 3b); tin tetrachloride, copper electrode (Fig. 3c); tin tetrachloride, magnesium electrode (Fig. 3d); methanol, copper electrode (Fig. 3e); methanol, magnesium electrode (Fig. 3f). The vertical jump occurs at the time of shock arrival at the electrode.



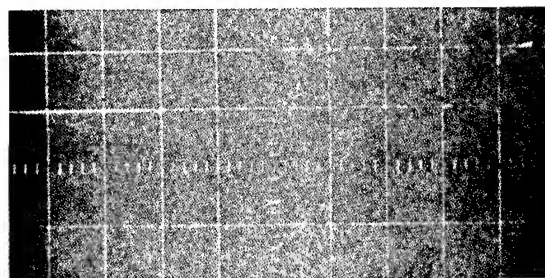
(a) Water, copper electrode



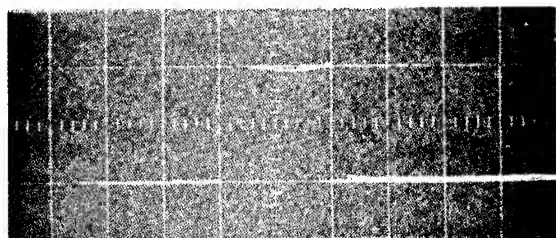
(b) Water, magnesium electrode



(c) Tin tetrachloride, copper electrode



(d) Tin tetrachloride, magnesium electrode



(e) Methanol, copper electrode



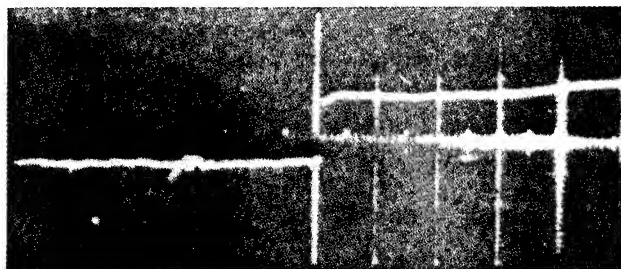
(f) Methanol, magnesium electrode

Fig. 3 - Oscillograms obtained with set-up scale of Fig. 2a. Vertical scale is 0.5 volts/div, horizontal scale is  $0.65 \mu\text{sec/div}$ .

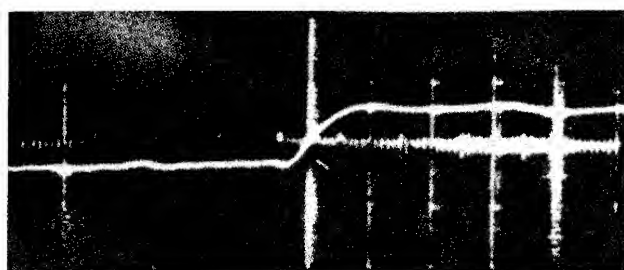
It can be seen that with a copper electrode the signal is positive, while with a magnesium electrode it is negative.

It is of interest that a signal also arises when the screen and electrode are made of the same metal, for example aluminum. The nature of these signals seems to be related to different conditions for electrochemical processes on the screen and on the electrode, since no signals are observed with the symmetric device (Fig. 2b) having identical electrodes. If these electrodes are made of different metals (copper and magnesium), stable electrical signals are recorded. Oscillograms obtained for dichloroethane and methyl methacrylate are given in Figs. 4a and b, respectively.

All the characteristic properties of signals which were observed in preliminary experiments with carbon tetrachloride, were found also in the experiments using various liquids, in particular, the signal for any liquid appears only at a certain threshold pressure, then it reaches the maximum and remains almost unchanged with further increase in pressure. The values of the pressures are defined not only by the properties of a liquid, but also by geometry of the experiment and by the value of input resistance of the recording device. In our experiments, saturation was achieved at a pressure of 150,000 atm. The oscillograms given in Figs. 3a-f and 4a-b were obtained at pressures above that for saturation.



(a) Dichloroethane



(b) Methyl methacrylate

Fig. 4 - Results with symmetric device of Fig. 2b, copper and magnesium electrodes. Vertical scale is 1.0 volts/div, horizontal scale is 0.5  $\mu$ sec/div.

The electrochemical nature of signals observed for all liquids studied is evidence that the electric conductivity arising on shock compression is of an ionic nature. Hamann and co-workers (6-9) came to the same conclusion when studying the conductivity of water, methanol and acetone in shock waves.

The persistence of transparency on shock compression of water, methanol and dichloroethane within the range of pressures corresponding to good conductivity (5, 10) is another evidence in favour of the ionic nature of these liquids under the given conditions.

#### REFERENCES

1. R. J. Eichelberger, G. E. Hauver, *Les Ondes de Détonation*, Paris, 1962, p. 363.
2. V. V. Yakushev, O. K. Rozanov, A. N. Dremin, *JETP, Letters*, **7**, 165, 1968.
3. A. N. Dremin, O. K. Rozanov, V. V. Yakushev, *Zh. prikl. Mekh. tekhn. Fiz.*, **5**, 53, 1968.
4. A. C. Mitchell, R. N. Keeler, *Rev. Sci. Instrum.*, **39**, 513, 1968.
5. V. V. Yakushev, A. N. Dremin, *Zh. fiz. Khim.*, (in press).
6. H. G. David, S. D. Hamann, *Trans. Faraday Soc.*, **55**, 72, 1959.
7. H. G. David, S. D. Hamann, *Trans. Faraday Soc.*, **56**, 1043, 1960.
8. S. D. Hamann, M. Linton, *Trans. Faraday Soc.*, **62**, 1, 1966.
9. S. D. Hamann, *Effects of Intense Shock Waves in Advances in High Pressure Research 1*, ed. by R. S. Bradley, Academic press, L. and N. Y., 1966.
10. Ya. B. Zel'dovich, S. B. Kormer, M. B. Sinitsin, K. B. Yushko, *Dokl. Akad. Nauk SSSR*, **138**, 1333, 1961.

## ELECTRICAL EFFECT OF BIMETALLIC AND METAL SEMICONDUCTOR JUNCTIONS UNDER SHOCK

J. Jacquesson, J. P. Romain, M. Hallouin  
*Ecole Nationale Supérieure de Mécanique et Aérotechnique*  
*Université de Poitiers, Poitiers, France*

and

J. C. Desoyer  
*Faculté des Sciences*  
*Université de Poitiers, Poitiers, France*

### ABSTRACT

When a shock wave crosses the junction of two metals an e.m.f. appears between the two noncompressed parts of the metals. The voltage-generator character of the junction under shock attack is first studied experimentally with a Cu-CTE junction perpendicular to the shock front. Then copper semiconductor junctions are studied: n and p type PbTe, monocrystalline intrinsic n and p type Ge in the [111] orientation, intrinsic Ge in the [100] orientation and polycrystalline intrinsic Ge. Tested pressure range (in Cu) is 80-420 kb. Polarity, which appears when the shock front crosses the junction, is related to the majority carriers' polarity in the semiconductor.

Chronometrical property of the junction effect is used to study, in Ge and Bi, the complex wave structure resulting from dynamic elastic limit and phase transitions. Some of the results in Ge could be explained by a dynamic transition very close to the metallic transition known to take place at 140 kb. Such a transition could be the cubic-to-tetragonal transition previously noticed under static compression but not under shock compression. In Bi, complex wave structure is also recorded and the first front is clearly identified as the 25-kb first-phase transition.

### INTRODUCTION

Previous shock wave compression experiments (1-5) on metal-metal junctions has shown that an e.m.f. appears between the non-compressed ends of the two metals when the shock crosses the junction. This e.m.f. is similar to a thermoelectrical effect where temperature is replaced by pressure.

The measured voltage is generally higher than the one expected from calculated equilibrium temperature, just behind the shock front, and normal thermoelectric effect. So this effect was called previously "anomalous" thermoelectric effect (5). Its characteristics were presented at the 4th Symposium on Detonation in 1965 (5); they were obtained principally from the Cu-CTE (constantan) junction:

1. This effect acts as a voltage-generator with very small internal resistance.

2. Voltage and polarity are functions of pressure. Polarity is generally the same as in a thermoelectrical effect, at least a low shock pressure. Voltage  $V$  versus pressure  $P$  has been observed to follow a linear empirical law,

$$V(\text{mV}) = 0.45P(\text{kb}) + 11.$$

3. In a chain with several junctions, swept by a shock wave which compresses some of the metals and junctions to the same pressure, the e.m.f. obtained between the ends of the chain is only dependent on the nature of the two metals where the shock wave limits the compressed part of the chain.

4. With a plane shock wave parallel to a junction, the electrical rise time of the response of the junction seems to be able to approach the true rise time of the pressure in the shock front.

Some theoretical attempts were made (6), (7), (8) to explain this effect but assumptions made are very restrictive. A. Migault (8) succeeds in solving coupled linearized Boltzmann equations for phonon and electron distribution functions in a metal with nonuniform and time dependent stress distribution; he gets for a shock compression through a junction an electrical effect superimposed to the normal thermoelectric effect. The proposed law agrees with polarity and order of magnitude of experimental results for pressures ranging up to 400 kb.

#### CU-CTE JUNCTIONS PERPENDICULAR TO THE SHOCK FRONT\*

The theory is grounded principally on the voltage-generator character of the junction effect (8); this was shown in two ways:

(a) Voltage amplitude is independent of junction surface and external load resistance (5),

(b) A plane junction attacked by a spherical wave generates an electrical signal as soon as the wave reaches the center of the junction, although the noncompressed part of this junction shortens the active compressed one (6).

Similar effect can be obtained with a junction perpendicular to the incident shock wave. Experiments in this way were performed on Cu-CTE junctions. Sketch of experimental device is given in Fig. 1.

A shock wave sweeping the junction divides it into two parts:

- One compressed part which generates the electrical effect,
- One noncompressed part which acts as a short-circuit for the previous active part.

A typical record is given in Fig. 2. The voltage rises with the wave sweeping the cylindrical junction and comes to a maximum when the whole junction is compressed. This result is different from the Conze et al. results (6),

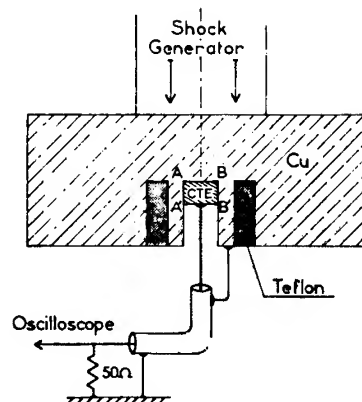


Fig. 1 - Sketch of experimental device with CU-CTE junction perpendicular to incident shock wave

AA'-BB': Cylindrical junction perpendicular to the shock (from 1 to 5 mm)  
AB: Plane junction parallel to the shock (6-mm diameter).

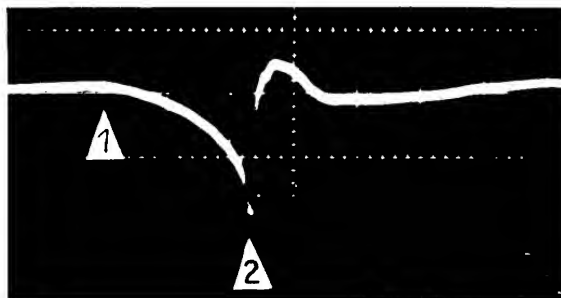


Fig. 2 - Typical record of Fig. 1 configuration

AA' = 5 mm pressure: 175 kb in Cu  
(1) Arrival of the shock on the AB plane junction  
(2) Arrival of the shock on the A' B' face  
scale: horizontal 0.5  $\mu$ s/div.  
vertical 50 mV/div.

where a plane junction is attacked by a spherical shock wave.

As no voltage appears when the shock wave overtakes the plane part AB of the junction (in (1) of Fig. 2), we may think that the resistance of the noncompressed cylindrical AA'-BB' part of the junction is much smaller than the internal resistance of the plane-compressed part acting as a generator. When the wave sweeps

\*With collaboration of the Commissariat à l'Energie Atomique.



the cylindrical part, the resistance of this junction increases as its surface decreases. Taking account of the  $50\text{-}\Omega$  external load resistance, if we assume that the junction resistance varies inversely with the magnitude of the surface, the record is well interpreted. Decrease of the internal resistance of the compressed active part of the junction may also be taken into account. Qualitative form of the oscillograms is well interpreted if this internal resistance also decreases inversely with the surface area.

From these results it may be expected that the voltage given by an usual plane junction will decrease with the surface area of the junction. Indeed this is observed with Cu-CTE junctions, surfaces of which are smaller than  $1\text{ mm}^2$ . For example, at 170 kb the mean voltage is 35 mV with a  $27\text{ mm}^2$  surface and becomes 20 mV with  $0.2\text{ mm}^2$ .

#### METAL SEMICONDUCTOR JUNCTIONS

Analogy with thermoelectric effect leads to study junctions with semiconductors, the thermoelectric power of which may be high. Also intrinsic, n- or p-doped materials make it possible to study the correlation of junction effect with the nature of the majority carriers. Furthermore, metallic phase transitions existing at high pressure may be expected to influence junction behaviour.

A sketch of the experimental device is represented in Fig. 3. The shock generator is either a plane wave generator, or for pressure below 250 kb, a standard small mass of high explosive. Pressure at the junction depends on the copper plate thickness  $h$  and was experimentally predetermined.

Always O.F.H.C. Cu is the first of the two materials of the first junction. The lateral dimension  $\phi$  of the second material A is small enough ( $\phi < 4.5\text{ mm}$ ) so that the acting part of the wave may be considered as a plane. Sample A thickness  $e$  is small ( $e < 3\text{ mm}$ ), so the induced shock pressure may be considered as constant during the time the wave is propagating through the sample disk. This sample is kept by a cylindrical copper made piece B, the diameter of which is generally smaller than sample diameter, so that, in spite of lateral expansion, part of the wave crossing the second junction (A-B) is still rather plane. In B the shock wave propagates again through O.F.H.C. copper. Then the two serial junctions (Cu-A) and (A-B) act and contribute to the output voltage, first by pressure effect (studied here) but

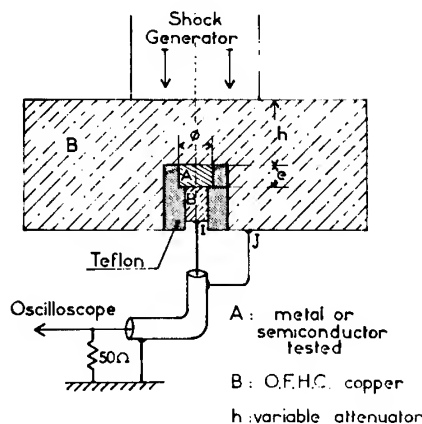


Fig. 3 - Sketch of experimental configuration (plane junctions parallel to the shock front)

also by normal thermoelectrical effect. If pressure is constant behind the shock front both junctions are at same pressure (and thermodynamical state), and we may expect the voltage between I and J to come back to zero, if the upper copper plate is maintained at ground potential. Voltage-time measurements are recorded with a Tektronix 555 oscilloscope with 13-ns rise time. If the sample resistance  $R$  is not negligible versus external load resistance ( $50\text{ }\Omega$ ), it must be taken into account and voltage has to be corrected by a  $R + 50/50$  factor.

#### Copper-Telluride of Lead Junctions (n- and p-type PbTe)

Junctions with O.F.H.C. copper and polycrystalline n- and p-type PbTe were tested. Sample thicknesses were between 2.40 and 3.05 mm and resistance was always smaller than  $0.15\text{ }\Omega$ , negligible versus  $50\text{ }\Omega$  external load. Measurements were made with shock pressure range from 100 to 230 kb in copper.

With n-type PbTe of nominal  $1.3\text{ to }2.5 \times 10^{-3}\text{ }\Omega\text{ cm}$  resistivity the oscillograms recorded, with Fig. 3 configuration, are similar to those that could be expected from a well-known Cu-CTE-Cu chain. The response from the CuPbTe (n) junction is the first electrical front. Front voltage appears to be negative and insensitive to the pressure, its value remaining between 30 and 40 mV for the studied pressure range (Fig. 4). Behind the electrical front, the voltage remains constant (Fig. 5) until the shock crosses the second junction, then as expected it comes back to the zero through a new

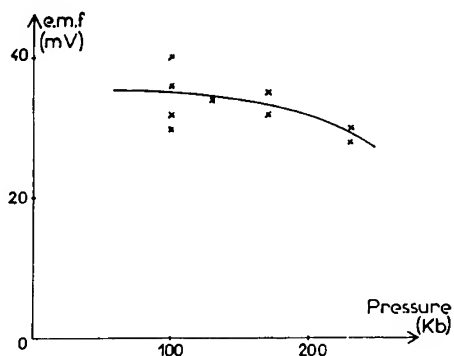


Fig. 4 - e.m.f. versus pressure in Cu for a Cu-PbTe (n) junction

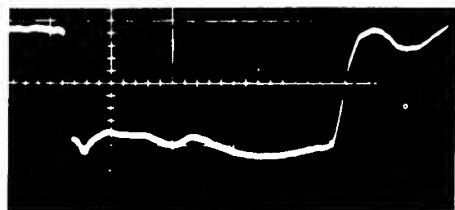


Fig. 5 - Typical record for a Cu-PbTe (n)-Cu chain in Fig. 3 configuration

PbTe sample thickness: 2.4 mm  
Pressure in Cu: 100 kb  
scale: horizontal: 0.2 s/div.  
vertical: 20 mV/div.

electrical front. Rise time of this "back" front is often longer than the one of the first front, due to the wave deformation by lateral expansion. Nevertheless, the time of propagation of a shock wave in sample PbTe can be precisely measured and so the average shock velocity can be determined. By the usual mismatching impedance method, pressure can be deduced. Results are reported in Table 1.

With a Cu p-type PbTe junction, the shock wave has a positive and small-amplitude electrical front (Fig. 6). Behind this front, voltage decreases and becomes negative as in previous experiments, and then voltage tends toward zero when the shock wave overtakes the second junction and comes again in copper.

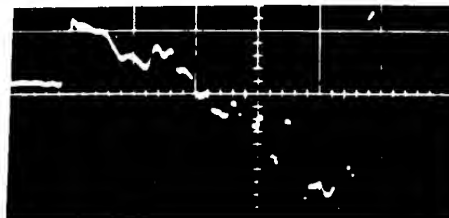


Fig. 6 - Typical record for a Cu-PbTe (p type) Cu chain in Fig. 3 configuration

PbTe sample thickness: 3 mm  
Pressure in Cu: 230 kb

scale: horizontal: 0.2 s/div.  
vertical: 10 mV/div.

#### Copper-Germanium Junctions\*

Specimens tested were a polycrystalline intrinsic Ge, single-crystal intrinsic Ge with a [100] then a [111] plane parallel to the shock wave, and n-type and p-type single-crystal Ge with a [111] plane parallel to the shock wave. Shock pressure range was from 80 to 420 kb in copper.

Previous experiments on Ge (9 - 11) have revealed, for high enough pressure, a complex

\*With collaboration of the Commissariat à l'Energie Atomique.

TABLE 1  
Experimental Results for PbTe (n)

Number of Shots	$P_{Cu}$ (kb)	$P_{PbTe}$ (kb)	$D$ (mm/ $\mu$ s)	$U_p$ (mm/ $\mu$ s)	$V_{Cu/PbTe (n)}$ (mV)
2	230	170	3.1	0.665	29
1	130	82	2.7	0.415	34
5	100	75	2.8	0.32	35

$$\rho_o = 8.25 \text{ g/cm}^3$$

wave structure which should result from a 44-kb Hugoniot elastic limit and a phase transition to metallic state at 140 kb under dynamical compression. Mismatching impedance requires an incident shock pressure of 190 kb in copper to induce this transition pressure in Ge.

With our standard experimental configuration (Fig. 3), we record again an electrical front when the shock wave crosses the Cu-Ge junction. Records obtained with a plane wave generator and a 330-kb pressure in copper at the junction are presented, Fig. 7. As previously noticed, the output voltage has to be corrected for Ge sample and contact resistances.

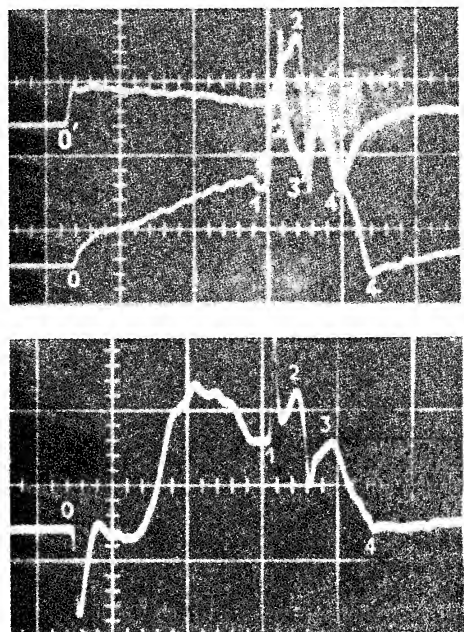


Fig. 7 - Typical records for Cu-Ge-Cu chain in Fig. 3 configuration. Pressure in Cu: 330 kb.

- (a) Polycrystalline intrinsic Ge, sample thickness 2.9 mm
- (b) p-type Ge, sample thickness 3 mm
- (c) n-type Ge, sample thickness 3 mm

horizontal (a, b, c) 0.2  $\mu$ s/div.  
scale: vertical (a, b) 50 mV/div.  
vertical (c) 100 mV/div.

When the shock wave attacks the first junction, the contact resistance of this junction may be modified. But this contact resistance is only a fraction of  $R$ , so if  $R$  is smaller than the 50- $\Omega$  external load resistance, we may neglect this variation, and a correction will be made with  $R$  value as measured before the

shot. This approximation is only valid for the first electrical front. The correction was made with n-type Ge in the [111] orientation, where  $R$  measurements give value smaller than 30  $\Omega$ . In experiments with the n-type Ge, the first electrical front is always negative (Fig. 7); corrected front amplitude versus shock pressure is reported in Fig. 8. Dispersion takes place in these experiments at about 140 kb, the phase transition pressure in germanium. We notice that the response of the junction is a pulse with the n-type Ge, so the amplitude might be also dependent upon the oscilloscope rise time. The pulse duration is about 50 ns; that should agree with the order of magnitude of 100 ns proposed as the relaxation time for carriers' equilibrium in Ge by R. A. Graham et al. (10). With intrinsic and p-type Ge the electrical front, when the shock enters the Ge sample, is always positive with a rather constant voltage between 20 and 40 mV, in the range of studied pressures.

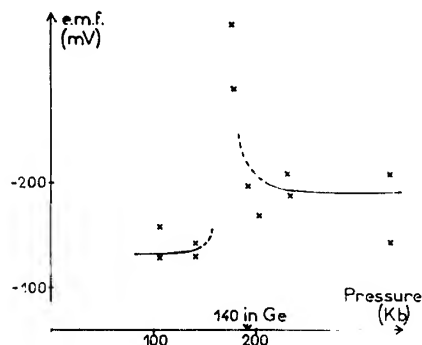


Fig. 8 - e.m.f. versus pressure in Cu for a Cu-Ge (n) junction

It must be noticed again that the normal thermoelectrical effect is included in the recorded voltage, and this effect may not be negligible. A rough estimation made for n-type Ge with normal pressure and temperature characteristics would give a thermoelectrical contribution of about 40 mV at 160°C, which is the calculated temperature at 140 kb in Ge (10). As the whole corrected voltage for n-type Ge is 140 to 190 mV (Fig. 8), the contribution of the thermoelectrical effect, which moreover is also a function of pressure and temperature, may be important.

### Conclusion

From the results obtained with doped Ge and PbTe samples we may conclude that the

electrical front voltage given by a Cu semiconductor junction attacked by a shock wave has the same polarity as majority carriers. Behind the front, for a given semiconductor, electrical behaviour seems to become similar whatever doping may be.

#### APPLICATION OF INVESTIGATION TO COMPLEX STRUCTURE WAVES IN Ge AND Bi

##### Germanium

When incident pressure is over 190 kb in copper, the induced shock pressure in Ge is over 140 kb and at this pressure the phase transition to metallic state (10 - 15) takes place. Taking account of an assumed elastic 44-kb wave (10, 11) the shock front propagating in a Ge sample is expected to present a triple wave structure. First junction being kept at the upper incident pressure, the second junction (Ge-Cu) will be successively hit by the 44-kb first wave, the 140-kb wave, then the upper pressure wave. Each wave abruptly changes the Ge state at the second junction, and a junction effect may be expected. Furthermore, the resistance  $R$  of the chain is modified by the phase transition to the metallic state. When the 140-kb transition wave propagates through the Ge sample,  $R$  is a linear function with time and, for a constant junction e.m.f., the recorded voltage should also be linear with time. So the correction factor and true e.m.f. amplitude is difficult to determine from the records.

Nevertheless, the time of arrival of waves can be correlated with the voltage fronts which can be seen clearly and read precisely on the oscillograms. In Fig. 7, with an incident plane shock wave of 330 kb (in Cu) and behind the

front 0 corresponding to the shock wave at the first junction, we observe four fronts (except in polycrystalline intrinsic Ge where front 1 does not appear). Transit times of the associated waves in samples of known thicknesses are given on Table 2, for experiments at 330 kb (in Cu). Corresponding velocities are given on Table 3. The R. A. Graham et al. (10) and Pavlovski (11) results are reported with our results on a space-time diagram in Fig. 9.

Time of arrival of successive fronts are indicated as 1, 2, 3, 4, as on Fig. 7. Point 4 on the record is the time when voltage comes back to zero value, and is correlated to the maximum pressure arrival on the Ge-Cu junction. Indeed the two junctions are then in the same state.

Our results agree with these of R. A. Graham et al. (10) for the fronts 1 and 3 which are identified as a 44-kb elastic wave and a 140-kb phase transition wave. Front 4 also agrees with calculated wave velocity from ref. (12).

It must be noticed that front 1 does not appear in intrinsic polycrystalline Ge. But in intrinsic [100] Ge this front again clearly appears with the same velocity of 5.75 mm/ $\mu$ s; although elastic [100] velocity is 4.92 mm/ $\mu$ s (13). So the elastic nature of the wave with a 5.75-mm/ $\mu$ s velocity may be a matter of conjecture.

No wave is reported, either by R. A. Graham et al. (10) or Pavlovski (11), which explains the front 2. Such a wave would have a velocity of 5 mm/ $\mu$ s. But it may be pointed out that time of arrival of this front coincides with the time when a reflected "elastic" wave interferes with the phase transition wave (Fig. 9); but reflected wave amplitude is small (about 4 kb), and also there is no reason to associate

TABLE 2  
Chronometry of Electrical Fronts (Pressure in Copper: 330 kb)

Type Ge :	[111] n		[111] p		Polycryst. Intrinsic	
Thickness :	3 mm		3 mm		2.9 mm	
Experiment no.:	CG 11 a	CG 12 a	CG 11 b	CG 12 b	CG 11 c	CG 12 c
Marks (cf. Figs. 7 and 9)						
1	.52 $\mu$ s	.52 $\mu$ s	.50 $\mu$ s	.52 $\mu$ s	—	—
2	.60	.60	.60	.60	600 ns	570 ns
3	.70	.70	.65	.68	680	690
4	.80	.82	.80	.80	no clear front	

TABLE 3  
Velocities of Different Parts of the Wave Induced in Ge (n or p Monocrystalline and Intrinsic Polycrystalline Ge) by a 330-kb (in Cu) Shock

Fronts no. (cf. Fig. 7)	Velocities in mm/ $\mu$ s			Dynamic Pressure in kb	Observations
	R. A. Graham and al. (10)	M. N. Pavlovski (11)	This work		
1 $D_1 =$	5.7	4.7	$5.75 \pm 0.2^*$	44 (10) (11)	- Elastic Front (?) - *[111] n et p Ge only
2 $D =$	—	—	$5.0 \pm 0.2$		
3 $D_2 =$	4.26	3.96	$4.3 \pm 0.2$	140 (10) (11)	- Metallic transition
4 $D_3 =$	—	—	$3.8^{**} \pm 0.2$	200	- ** Calculated velocity from (12) is 3.87 mm/ $\mu$ s

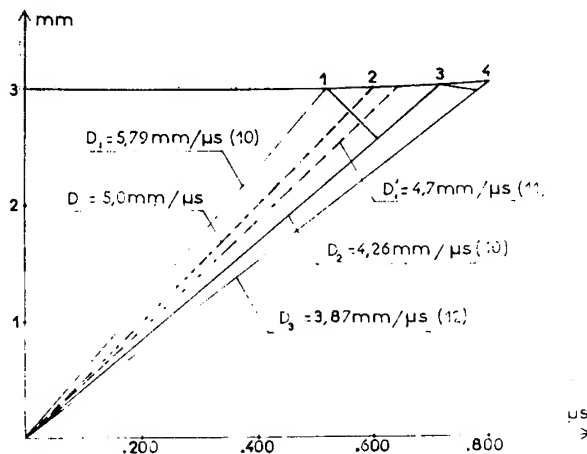


Fig. 9 - Space-time diagram (laboratory coordinates) showing successive wave arrivals on the terminal face (Ge-Cu junction) of Ge sample

- Ge sample thickness: 3 mm
- Pressure in Cu: 330 kb (corresponding pressure in Ge: about 200 kb)
- 1, 2, 3, 4: Positions of successive electrical fronts detected on Fig. 7 records
- Reflected shock wave velocities are calculated from (10) and (12)

electrical pulse with interference of this wave with the transition wave.

Another explanation may be proposed.

Polymorphic transition from cubic to tetragonal form, with 10 to 11% higher density, was reported by F. P. Bundy and J. E. Kasper in (14) (15). This transition takes place at lower

pressure than the metallic transition pressure. Cubic and tetragonal forms are both semiconducting with nearly the same resistivity. So the transition from one to the other form may not be revealed by resistance measurements such as those in the R. A. Graham et al. (10) experiments.

If this transition exists under shock compression, a new wave may be generated. Such a wave could explain the front 2 of our records (Fig. 7). In this assumption front 3 must be association with a transition wave from tetragonal to metallic phase. With a measured velocity of 5 mm/ $\mu$ s and a density of 5.86 g/cm<sup>3</sup>, the lowest value reported by F. P. Bundy and J. S. Kasper, the dynamic transition from cubic to tetragonal form would take place at 133 kb. Metallic transition takes place at 140 kb with a density of 6.02 g/cm<sup>3</sup> (14 - 15) so the two transitions are very close to one another.

Authors are conscious how frail is the assumption made about this phase transition in Ge which is studied here with the junction effect, the origin of which is in fact not well understood. So it seems necessary to study a junction effect signal given by a metal with a better-known phase transition such as bismuth.

#### Bismuth

At room temperature, bismuth has several forms according to the pressure, so a complex-structure wave must be expected. Previous works with various technics have clearly revealed Bi I  $\rightarrow$  II transition at 25 kb (17 - 19). As for Ge, we use here the chronometrical property of the junction effect. The metallic

chain is Cu-Bi-CTE, according to the Fig. 3 configuration where the lower B part is made of CTE. Bi used is high purity (99.999%).

A first electrical front is generated by the arrival of the shock at the Cu-Bi junction. The transmitted pressure profile in bismuth, in the tested pressure range of 40 kb to 170 kb, is composed of one or several successive waves according to possible induced phase transformations. It may be expected that each wave generates an electrical signal when crossing the Bi-CTE junction. Records of the junction response show effectively one or several electrical fronts, according to the pressure.

Chronometry of the different fronts makes it possible to calculate the velocity of wave correlated to each electrical front.

Typical records obtained from Cu-Bi-CTE chains at various pressures are presented in Fig. 10. Wave velocities versus pressure in bismuth are given in Fig. 11.

attributed to the arrival of the transmitted shock wave in bismuth at the Bi-CTE junction. Origin of front 1' is not clearly determined. It might be created by a reflected shock wave.

(2) 40-70 kb pressure range in bismuth: examples of records are given in Fig. 10a and 10c. The observed decomposition of electrical front 1 is interpreted as a complex structure wave front. This assumption is consistent with the fact that, for pressures lower than 70 kb, the 25-kb wave velocity ( $2.05 \text{ mm}/\mu\text{s}$ ) (12) is larger than velocities of higher pressure waves. Thus front 1 must be attributed to this 25-kb shock wave. Our results show indeed that the associated wave velocity becomes constant within the experimental error; and the measured average value of  $2.1 \text{ mm}/\mu\text{s}$  agrees with the 25-kb wave velocity. So this result confirms that the electrical front 1 is the 25-kb shock wave. The very first electrical front *e* of low amplitude observed on some records may be attributed to the elastic wave in bismuth (velocity  $2.18 \text{ mm}/\mu\text{s}$ ) (12).

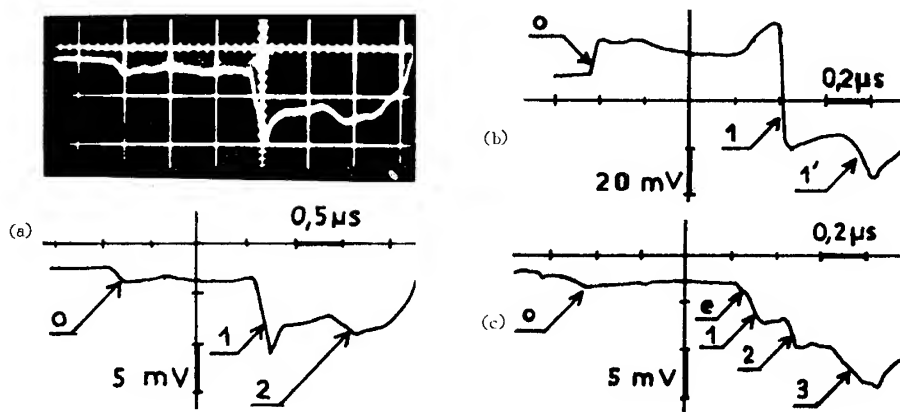


Fig. 10 - Typical records with a Cu-Bi-CTE chain

- Bi pressure: a: 50 kb, b: 170 kb, c: 60 kb
- Bi sample thickness: a: 3.2 mm, b: 2.12 mm, c: 1.9 mm
- 0 Shock arrival at the Cu-Bi junction
- e, 1, 2, 3: Bi-CTE signals respectively from elastic wave, 1st shock wave, 2nd shock wave and 3rd shock wave
- 1' signal presumably due to a reflected wave

(1) 70-170 kb pressure range in bismuth: A record at 170 kb is given in Fig. 10b. Front 0 indicates the arrival of the incident shock wave at the Cu-Bi interface. Referring to previous data on the Hugoniot of bismuth (12), the pressure profile should present a single front in this pressure range. However, on each record we may observe two electrical fronts, 1 and 1', behind the front 0. Front 1 has to be

Second- and third-wave velocities correlated with electrical fronts 2 and 3 decrease together with pressure. Values reported in Fig. 11 are Lagrangian velocities. In laboratory coordinates mass velocity due to precedent waves must be taken into account for determining absolute velocities of waves 2 and 3. For instance, the second wave has an absolute velocity of  $0.12 \text{ mm}/\mu\text{s}$  larger than reported values in Fig. 11.

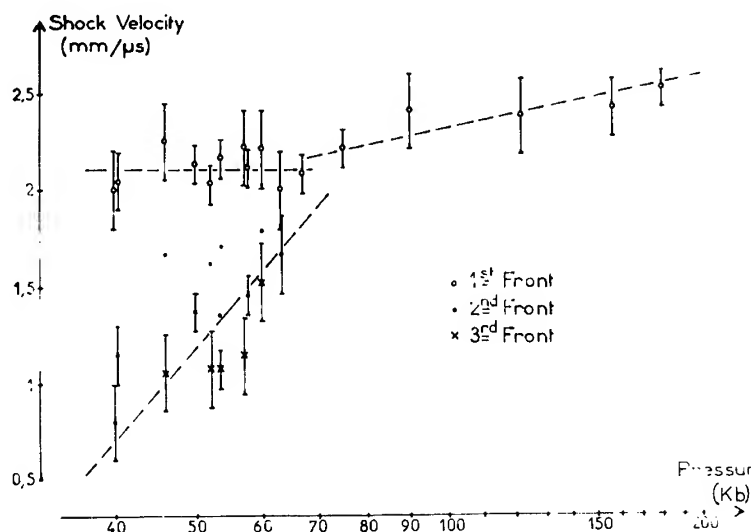


Fig. 11 - Velocity correlated with successive electrical fronts versus incident wave pressure in Bismuth

## CONCLUSION

In conclusion, it can be seen as well in Ge as in Bi that electrical effect, the origin of which is still uncertain, seems to be nevertheless very useful to study shock wave velocities and shock front decompositions.

## REFERENCES

1. J. Jacquesson, "analyse des contraintes", Vol. IV, no. 4, pp. 33-35, 1959; Vol. VI, No. 4, pp. 9-14, 1961.
2. J. Jacquesson, "Etude du profil des ondes de choc dans quelques metaux", "Les ondes de Detonation", International Symposium of C.N.R.S., 28 Aout - 2 Sept. 1961, pp. 415-422, CNRS edit, Paris 1962.
3. V. S. Il'yukhin and V. N. Kologrivov, Zhur. Fiz. No. 5, p. 175, Sept., Oct. 1962.
4. E. P. Palmer and G. H. Turner, J. Appl. Phys., Vol. 35, pp. 3055, 1964.
5. J. Crosnier, J. Jacquesson, A. Migault, "Fourth Symposium on Detonation", pp. 627-638, Office of Naval Research, Washington, D. C., 1965.
6. H. Conze, J. Crosnier, C. Bernard, "Behaviour of Dense Media Under High Dynamic Pressure", Symposium I.U.T.A.M., pp. 441-452, Gordon and Breach, New York, 1968.
7. A. Migault and J. Jacquesson, "Behaviour of Dense Media Under High Dynamic Pressure", Symposium I.U.T.A.M., pp. 431-440, Gordon and Breach, New York, 1968.
8. A. Migault, Contribution à l'étude de l'effet électrique créé dans une chaîne métallique par le passage d'une onde de choc," Theses no. 106, Poitiers, C.N.R.S. no. A.O. 3727, Paris mai 1970.
9. R. G. McQueen, S. P. Marsh, and J. Wackerle, Bull. Am. Phys. Soc., Vol. 7, p. 447, 1962.
10. R. A. Graham, O. E. Jones and J. R. Holland, J. Phys. Chem. Solids., Vol. 27, pp. 1519-1529, 1966.
11. M. N. Pavlovskii, Fiz. Tverdogo Tela., Vol. 9, No. 11, pp. 3192-3197, 1967. Sov. Phys. Solid. State., Vol. 9, No. 11, pp. 2514-2519, May 1968.
12. "Shock Wave Data", Lawrence Radiation Laboratory, Vol. 1, Sect A.1.
13. W. P. Mason, Physical Acoustics and the Properties of Solids. D. Van Nostrand, N. Y. (1958).
14. F. P. Bundy, J. E. Kasper, Sciences, Vol. 139, p. 338 (1963).
15. F. P. Bundy, J. Chem. Phys., Vol. 41, No. 12, pp. 3809-3279.

16. J. C. Jamieson, *Science*, Vol. 139, p. 762 (1963).
17. R. E. Duff and F. S. Minshall, *Physical Review*, Vol. 108, No. 5, p. 1207 (1957).
18. D. S. Hughes, L. E. Gourley and M. F. Gourley, *J. Appl. Phys.*, Vol. 32, No. 4, pp. 624-629, 1961.
19. D. B. Larson, *J. Appl. Phys.*, Vol. 38, No. 4, pp. 1541-1546 (1967).



## EXPERIMENTAL STUDY OF THE ELECTROMAGNETIC VELOCITY-GAGE TECHNIQUE

Sigmund J. Jacobs and David J. Edwards  
*U.S. Naval Ordnance Laboratory  
White Oak, Silver Spring, Maryland 20910*

### ABSTRACT

The electromagnetic method has been used to study the particle velocity in (a) polymethylmethacrylate PMMA in the set-up of the NOL gap test and (b) in several explosive charges. Factors which influence recording response are assessed and steps taken to improve the records are described. Under favorable conditions the response time is found to be as good as 20 to 30 nanoseconds. Preliminary values for detonation pressures and reaction times in cast and pressed TNT and in pressed tetryl are found to be in good agreement with results reported by Dremin and his co-workers.

### INTRODUCTION

About 10 years ago a promising technique, the electromagnetic method for measuring particle velocity in non-conducting or weakly conducting dense media was introduced into the Russian literature by Zaitsev, Pokhil, and Shvedov (1). The method has since been widely exploited by Dremin and other Russian workers (2-9) for measuring particle velocity in detonations and in media shocked by detonation wave impact. It has been used only to a limited extent in this country (10-13) chiefly for measurements in mildly shocked solids. The interesting results reported by the Dremin group on particle velocity through the reaction zone in detonations of solid and liquid explosives prompted us to undertake an exploratory study program to answer questions about details of the method not fully discussed in the Russian works. Our initial studies were with the simple donor-gap set-up of the large scale gap test, LSGT, used at NOL to assess the shock sensitivity of explosives. Particle velocity was measured in the polymethylmethacrylate (PMMA) gap material near the axis of the experimental set-up at various distances from the donor explosive (HE). These studies, primarily carried out to learn what we could about the method, produced some positive results about the way the shock wave attenuates in PMMA. We also learned the hard way about a

few instrumentation problems; noise in the records produced by the detonating explosive or its air shock and the effect of poor instrument response to the flow. Both problems were fairly adequately solved. A few experiments to measure particle velocity in detonating explosives were then undertaken. We will only highlight here the results of those efforts. The PMMA investigation is fully discussed in a laboratory report (14). The explosives work will be reported later (15). We conclude from our study that (a) particle velocity can be measured to an accuracy of about 2% provided the medium does not have a conductivity much greater than 10 mho per centimeter; (b) that time in the records can be resolved to about 50 nanoseconds or better under favorable conditions; (c) that some care must be exercised to eliminate noise; and (d) that the CJ particle velocity cannot always be sharply located by a distinct break in the particle velocity-time record.

Our inability to see a distinct change in the slope of the particle velocity-time curves in detonating explosives may be due, in part, to the small size of our explosive sample and to the close proximity of the gage to the plane wave booster. The results suggest, however, that there may not be a sharp break in slope of the  $u-t$  curve for many explosives near their maximum density. This possibility is considered in the discussion section. Within the space

limitations of this report both good and bad recorded results are shown.

### THE EMV GAGE METHOD

The principle of the electromagnetic velocity EMV gage is a simple adaptation of Faraday's law of electromagnetic induction. A rectangular "loop" of wire or foil is embedded in the non-conducting medium to be studied. The base of the loop of length,  $\ell$ , is the sensing element. It connects to the arms in the shape of a squared letter U, see Fig. 1. The loop is connected to a coaxial line either directly or with a resistance  $R_1$  in series. The coaxial line, terminated by its characteristic impedance, is connected to a recording oscillograph (scope). For a magnetic field,  $H$ , and a loop enclosing area,  $A$ , the induced voltage in the loop is proportional to the time rate of change of flux  $d(H \cdot A)/dt$  within the loop. When the field is normal to the area and the change in flux is due only to the motion of the base normal to the field the induced EMF is given by

$$V = H \times u \times \ell \times 10^{-4} \text{ (volts)} \quad (1)$$

where the velocity of the base is in mm/ $\mu$ sec,  $\ell$  in mm, and  $H$  in gauss. If the base were a foil of the order of 20 microns thick, its velocity would be the same as the medium soon (a few nanoseconds) after passage of a shock. Thus, except for response delays, the observed voltage will be a direct measure of the particle velocity of the medium; the EMV gage is therefore an absolute measuring transducer. The time rate of change of flux has been brought up to make it clear that motion of the arms which could change the loop area or change in flux

due to stray fields would introduce errors in the recorded voltage. For maximum precision the shock wave should therefore be plane and stray fields should be minimized.

With present day scopes, adequate output voltage is possible with field strengths as low as 300 gauss; we have generally used about 1000 gauss to increase the signal to noise ratio. Practical gages would have a base length of 5 to 10 mm, foil thicknesses between 10 and 80 microns and foil widths of 1 to 5 mm. Aluminum is a good foil material because of its moderately low shock impedance and high conductivity. It is simply folded about a squared off section of the sample to form the squared U shape. Silver or copper would be comparably good conductors. They may be better than aluminum in studies within detonating explosives where there is a possible danger that aluminum could react with the explosion products thereby reducing the conduction of the base. For optimum recording the rise time of the oscillograph should be small relative to the time required to shock the foil up to the particle velocity in the medium under study. (Rise time is customarily defined in electronics as the time for the response to a square step input to rise from 10 to 90% of the steady value.) We have used scopes of 2.4, 7.0, and 26 ns rise time. The last was found to give relatively poor records.

### EXPERIMENTAL SET-UP FOR PMMA STUDIES

Figure 1 shows schematically the set-up for studying the particle velocity in a plastic or an explosive. In the studies with PMMA the set-up used was that of the donor-gap configuration of the NOL LSGT (16). Referring to

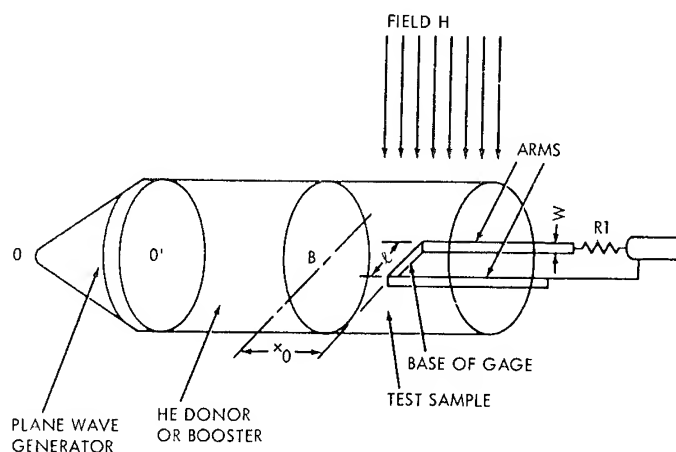


Fig. 1 - Schematic drawing for EMV gage measurements

Fig. 1, this consisted of a pressed tetryl donor of density  $1.51 \pm 0.01$  g/cc. The donor had a diameter of 5.08 cm and an equal length. It has a reported detonation velocity of  $7.2$  mm/ $\mu$ sec. Tentatively the Chapman-Jouguet, CJ, detonation pressure can be taken to be  $\sim 195$  kbars. The explosive is point initiated by a 30 cm primacord lead at point 0'. The detonator for the primacord was of the Exploding Bridgewire EBW type to increase safety in the presence of magnetic fields. The plane wave booster, PWB, shown in Fig. 1 for later discussion is absent. The PMMA samples were machined from Plexiglas rods having a density of  $1.18 \pm 0.01$  g/cc. The diameter was 5.08 cm. The EMV gage was made of a foil of aluminum usually 2 mm wide; thickness  $\delta$ , 13 microns (0.5 mils); and base length either 5 or 10 mm. The gage and gap assembly was formed by wrapping the foil about a block of PMMA of appropriate width; cementing on side blocks with the aid of chloroform as a solvent to form a cylinder; and finally cementing to a cylindrical block of length  $x_0$  to form the gap between the donor and the base of the gage. Care was taken to eliminate air bubbles. The total length of PMMA was  $x_0 + 12.7$  mm. For future reference the shock vs particle velocity relation for the PMMA was assumed to be (17)

$$U = 2.56 + 1.61 u \text{ (mm}/\mu\text{sec)} \quad (2a)$$

in the particle velocity range of interest. With the above stated dimensions the Hugoniot pressure, in kilobars, is given by the equation

$$P = 10 \times U \times u \times \rho_0, \quad (2b)$$

in which  $\rho_0$  = initial density in g/cc.

The gage arms were 32 to 44 mm long, including  $R_1$  when it was used. In the first experiments no series resistor was present. Later it was found, when using a fast response scope, that a value of  $R_1$  of about the characteristic impedance of the coaxial line reduced ringing in the recorded signal. The exact value of  $R_1$  was determined by measurement with a reflectometer to find the value for minimum signal reflection. The coaxial line was an RG 58 C/U, 50 ohm nominal impedance, 5 meters long. It was terminated at the scope with a 50 ohm terminator.

The magnetic field was obtained by the use of Helmholtz coils or an iron core magnetic. The former had mean coil diameters of 38 cm spaced 19 cm apart to maximize the uniformity of the field near the gage base. This gave a usable working gap of about 4 cm. The latter had square pole faces of 10.2 cm on a side

spaced 8.9 cm apart. For this magnet the field was uniform to within 0.6% in the space required for a measurement. The iron core magnet faces were covered with 6 mm of wood to protect them and to prevent the generation of stray signals observed when the air shock was allowed to hit the conducting face.

A sheet aluminum baffle reaching from the periphery of the charge to the poles of the magnet was located in the plane of the HE-PMMA interface. When grounded to a coaxial trigger line it was effective in reducing one source of noise to an acceptably low level. The grounding was essential.

Several oscillographs and combinations thereof were used in this study. These are outlined below for later reference by letter.

- A. Two Hewlett-Packard Mod 160 scopes in parallel with 60 cm of RG 58 C/U between, terminated at the end. Scope rise time of 26 ns.
- B. A single H-P Mod 160 scope, line terminated at scope.
- C. A single Tektronix Mod 454, rise time 2.4 ns, terminated at scope.  $R_1$  of about 50 ohms introduced on most shots to eliminate ringing.
- D. A Tektronix Mod 454 and a H-P 175 (rise time, 7 ns) connected by an impedance matching  $\gamma$  terminator to the coaxial line. (Not used for PMMA.)

After performing a number of experiments with the A set-up it was found that the method of connecting the scopes was detrimental to response rise time. The set-up was then abandoned. Our troubles in getting acceptably fast rise in the recorded signal with the B set-up led to the use of the faster scopes. An analysis of the theoretical response of a recording system was undertaken to get a better idea of what we could expect. This is described in the next section.

## FACTORS INFLUENCING RESPONSE

Rise Time Estimate. In the HE-PMMA system there are four factors which can influence the recorded signal response time. These are: the finite time for a curved shock front to intercept the entire gage base after first contact; the finite time to accelerate the base to the particle velocity of the medium under study; inherent response time of the oscillograph; and,

a time lag due to the offset initiation or tilt of the shock front. It is convenient to treat the first three in the spirit of the overall response of three electronic circuit elements in tandem. We therefore assign a mechanical rise time to the first two factors;  $T_1$  being defined as the time factor for 90% of the base to be intercepted by the wave,  $T_2$  being the time for the base to acquire 90% of the particle velocity of the medium when the shock is a square step, and  $T_3$  being the oscillograph rise time. The effect of tilt of the shock cannot be predetermined. A simple approximation to the overall rise time (for electronic circuits) can be found in elementary texts on oscillography. It is

$$T_0 = (\sum T_i^2)^{1/2} . \quad (3)$$

In the present application  $T_0$  is taken to be an estimate of the time to 90% of maximum signal response for a square step shock. The time  $T_1$  for 90% of the base length to be set in motion by a shock with a radius of curvature  $r_0$  and velocity  $U$  is acceptably approximated by the equation

$$T_1 = (0.9\ell)^2 / (8 \times r_0 \times U) . \quad (4)$$

A graphical analysis of the velocity attained by an aluminum foil shocked by PMMA shows that two double transits, shock followed by rarefaction, in the aluminum are sufficient to reach 90% or greater of the particle velocity of the PMMA.  $T_2$  is therefore assumed to be  $4 \times \delta / \bar{U}$ ,  $\delta$  being the thickness of the foil and  $\bar{U}$  the average wave speed in the metal.

For purposes of estimate in our experiments we assumed the nominal values  $r_0 = 55$  mm,  $U = 5.5$  mm/ $\mu$ sec, and  $\bar{U} = 5.8$  mm/ $\mu$ sec leading to a  $T_1$  of 32 ns when  $\ell$  is 10 mm and 8 ns when  $\ell$  is 5 mm. The value of  $T_2/\delta$  is 0.7 ns/micron;  $T_2$  is then 9 ns for the 13 micron foil. When the gage is used in explosives the value of  $\delta$  ranged from 25 to 125 microns;  $\bar{U}$  is somewhat higher than 5.8 because of the higher pressures involved. We therefore estimate  $T_2$  to range from 16 to 80 ns in that application. When the shock is plane the term  $T_1$  is absent. If the oscilloscope has a rise time of 10 ns or less the overall rise time for a plane shock in HE will usually be dominated by the transit time in the foil unless a significant amount of shock wave tilt is present.  $T_0$  gives us information about the response which can be expected when the shock is a square step. The question we also want to answer is, "What is the response to the decaying particle velocity behavior generally encountered?"

**Response Prediction.** In typical shock wave problems the particle velocity jumps to a maximum value and then decays. The initial decay is either approximately linear in slope or an approximately linear slope followed by an abrupt or gradual change to a lesser slope. The response to a jump to  $u_0$  followed by a linear slope is a curve which rises to a maximum value less than  $u_0$  at a finite time after shock arrival,  $T_{\max}$ , a rounding off; and then, after a time  $T_{lin}$ , an approximately linear decay. To illustrate the response and estimate the relation between  $T_0$  and  $T_{\max}$  or  $T_{lin}$  the electro-mechanical response of the measuring system may be approximated by the response of an RC, resistance-capacitance, circuit to a driving voltage which has a linear decay following a step jump in the input. In the problem the input voltage is given by the equation

$$Z_0 = e_0/e_{00} = 1 - a \times t = 1 - a \times \theta \times \tau \quad (5)$$

where  $e_0$  is the input voltage,  $e_{00}$  its initial value,  $t$  is the time,  $\theta = t/\tau$  is a dimensionless time, and  $\tau = RC$  is the time constant of the circuit. The rise time  $T$  for the RC circuit (10 to 90% response) is readily shown to be  $2.2\tau$ . It is assumed to represent the rise time  $T_0$  of the gage measuring system. The response of the RC circuit to the above driving function when the output is connected across the capacitance is

$$Z = e/e_{00} = 1 - a\tau\theta \times (a\tau + 1) \exp(-\theta) + a\tau . \quad (6)$$

A graphical comparison of Eqs. (5) and (6) for several values of the slope,  $a \times \tau$ , shows the time to maximum in the response curves to vary from 2.5 to 4  $\tau$ . A value of  $T_{\max}$  of about 1.5  $T_0$  is a reasonable mean. The output very nearly parallels the input at a time of about 4.5  $\tau$ ;  $T_{lin}$  can then be taken as about 2  $T_0$ . These values provide a means of estimating the rise time of the system when the oscillograms resemble the result of Eq. (6).

To answer the question, "What is the rise time needed to detect a change in slope which occurs shortly after the initial jump?", a problem allowing for two linear slopes in the input was set up and solved. The input in this case is normalized to a time  $t_1$ ; i.e.,

$$e_0/e_{01} = 1 - k_j(t/t_1 - 1) \quad (7)$$

where  $t_1$  is the time at which the input changes from slope  $k_0$  to  $k_1$ . The input voltage is  $e_{01}$  at time  $t_1$ . It is convenient to make the problem dimensionless by introducing the variables

$y = t/t_1$ ,  $\phi = \tau/t_1$ ,  $Z_i = e_i/e_{01}$ . The input is then

$$Z_0 = 1 - k_j(y-1) \quad (8)$$

The equation for the output is

$$Z = Z_0 - A_j \exp(-y/\phi) + k_j \phi \quad (9)$$

The values of  $A_0$  and  $A_1$  are found to be

$$A_0 = 1 + k_0 + k_0 \phi,$$

and

$$A_1 = A_0 - (k_0 - k_1) \times \phi \times \exp(1/\phi) \quad (10)$$

Equations (8) through (10) define the dimensionless input and output; for  $y \lesssim 1$ ,  $j = 0$ ; for  $y \gtrsim 1$ ,  $j = 1$ . The solutions of these equations for  $k_1 = 0.1$ ,  $k_0 = 1$ , and  $\phi$  varying from 0.1 to 2 are shown in Fig. 2. These parameters have given sufficient information to draw the general conclusions desired regarding rise time requirements. Other values of the  $k_j$ 's can be tried if the reader desires. We note in Fig. 2 that the inflection is not seen in the response when  $\phi$  is of the order of 0.8 or greater; is barely discernible when  $\phi$  is 0.4; and is quite distinct when  $\phi$  is 0.2. The initial slope is fairly close to the input when  $\phi$  is 0.2 or less. The conclusion is that the overall rise time of the electromechanical system should be less than half the time to a break in the input particle velocity if it is desired to define the particle velocity at early times as well as an abrupt change in slope with any degree of precision. The equations are derived and discussed in detail in reference (14).

**Electrical Conduction of the Medium.** The motion of a conducting medium surrounding the arms of the EMV gage will generate a voltage in the same way that the base motion produces a voltage (18). If the mean "plasma" velocity is identical to the base velocity no error would be recorded. But if the particle velocity in the medium is changing on a particle path the plasma velocity will not be the same and generated voltage across the arms will differ from that of the gage base. The extent to which this difference will affect the recorded signal will depend on the average resistance and velocity of the plasma as seen by the arms relative to the resistance and velocity of the base itself. The problem of plasma conduction is most likely to occur in measurements within a detonating explosive. An estimate of the greatest deviation of plasma velocity from base velocity would be a number of the order of  $\pm 50\%$ . For a plasma resistance of 50 times the base

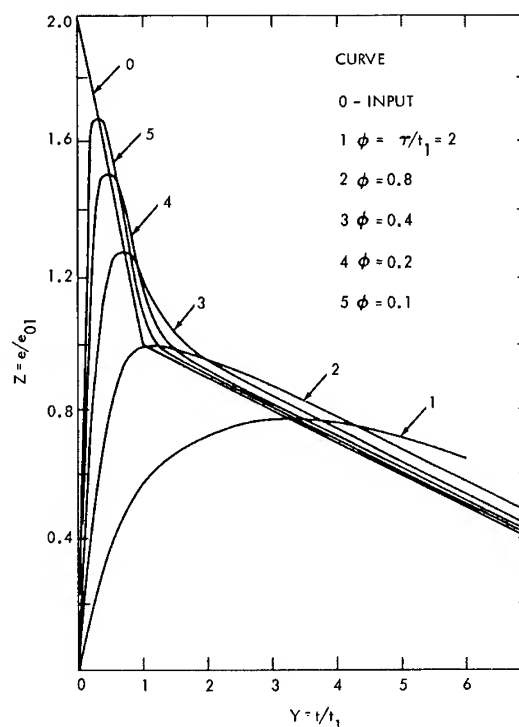


Fig. 2 - Dual slope input and response for an RC circuit

resistance, or greater, a 50% deviation in plasma velocity would affect the precision of a measurement by no more than 1%. Without going into great detail about our estimates we have concluded that for measurements with 50 micron aluminum or copper foils the medium resistivity could be as low as 0.1 ohm-cm without adversely affecting the measurement of particle velocity by the gage. The influence of plasma conduction can be reduced by thickening the base foil and possibly by appropriate insulation of the base and arms. Reported resistivities for several explosives (18 - 21) give evidence that the mean plasma resistance will usually be high enough and therefore not troublesome. If an aluminum foil were eroded or reacted with the explosive, measurements could depart from the real particle flow with increase of time after the initial shock arrival.

**Results of the PMMA Experiments.** Approximately 45 experiments were conducted with PMMA in the donor-gap set-up. The kinds of records obtained with different recording systems will first be discussed. The findings on  $u$  vs  $t$  and the initial value of  $u$  vs  $x_0$  will then be briefly mentioned. About a third of the experiments were rejected; 9 for excessive

ringing, 5 for loss of record or calibration. None of the poor records could be attributed to foil break in the gage. A better percentage of successes is now expected because of the experience gained in eliminating the ringing problem.

A summary of the experiments is shown in Table 1. It can be seen that the extrapolated initial particle velocity becomes independent of the system rise time when the gap distance  $x_0$  is 4 mm or greater. This is a consequence of the absence of a steep decay in the particle velocity following the shock at the greater distances. Table 2 shows the predicted and observed times to the maximum of the response for the several recording set-ups. Figure 3 is one of the records obtained with set-up A, the poor response system. Though the record looks pretty good the time to maximum is bad, about 300 ns. The break in the curve at  $t \sim 2.5 \mu\text{sec}$  is due to the arrival of the shock at the free boundary of the PMMA. Figure 4 shows a better record taken with the B set-up and a 5 mm gage base length. The time to maximum is about 80 ns, about as predicted. Figure 5, taken with the fastest oscillograph arrangement shows a rise to maximum in 54 ns. The total sweep time in this record is not much greater than the rise time in Fig. 3. The ringing observed at about 315 ns was probably excited by a sharp change in slope of the particle velocity.

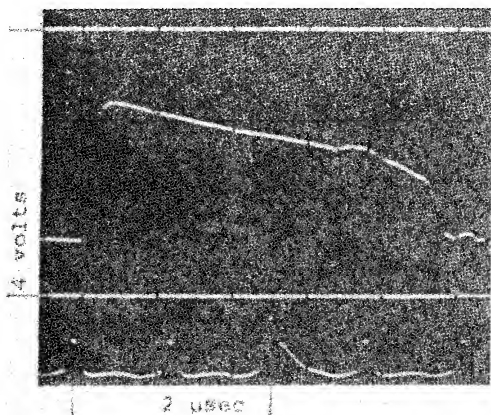


Fig. 3 - Record obtained with set-up A (Shot No. 44)

Some pertinent information about the reproducibility of detail has been found in a series of experiments taken at the same gap distance, 0.86 mm. The recording conditions varied from shot to shot. Two of our bad records, Figs. 6 and 7 were originally rejected because of ringing as well as a poor calibration

TABLE 1  
Data and Peak Velocity for PMMA

$x_0$ , mm	Shot No.	$l$ , mm	H, gauss	$u_0$ mm/ $\mu\text{sec}$
System A				
0.25	46	10.0	1410	2.06
0.25	51	5.0	1250	2.01
0.86	49	5.0	1190	1.90
1.0	52	5.0	1225	1.90
1.5	54	5.0	1275	1.83
1.5	55	5.0	1230	1.84
2.0	56	5.0	1160	1.78
2.0	53	5.0	1275	1.77
2.7	43	10.0	1100	1.70
2.8	45	10.0	1455	1.71
4.4	40	10.0	1180	1.65
4.6	44	10.0	1250	1.63
6.9	42	10.0	1240	1.52
7.1	39	10.0	1300	1.53
10.0	41	10.0	1305	1.43
10.0	38	10.0	1355	1.42
20.0	24	10.0	535	1.11
20.0	25	10.0	920	1.15
25.0	27	5.0	980	1.03
25.0	28	5.0	980	1.01
System B				
2.2	87	5.0	1200	1.89
4.8	88	5.0	1350	1.60
System C				
0.25	118	5.0	770	2.26
0.25	120	5.0	700	2.27
0.86	108	10.0	980	2.25
0.86	183	5.0	779	2.22
2.0	119	5.0	748	2.05
3.0	117	5.0	790	1.88
4.0	116	5.0	790	1.61
20.0	121	5.0	725	1.14

in the latter. For comparison a new shot with our best set-up was added at the end of the series. This experiment, read-outs from Figs. 6 and 7, and two other records are traced in Fig. 8. The ordinates have been displaced to assist in comparison. The plots are unsmoothed; when ringing occurs the plot is represented by a dashed line or a wavy line. Times at which related changes in slope occur are labelled A to D. What originally caught our eye in Figs. 6 and 7 was a related flattening, 3C and 4C, followed by a steepening at 3D and 4D. Traces that had been obtained at greater distances from the HE interface had shown this type of behavior at earlier times following the shock arrival. The result appeared to be

TABLE 2  
Oscilloscope Response Estimates and  
Observations, Nanoseconds

Set-up	A or B		C	
Gage Base	10 mm	5 mm	10 mm	5 mm
Estimated				
$T_1$	32	8	32	8
$T_2$	9	9	9	9
$T_3$	25	25	2.4	2.4
$T_0$	42	33	33	11.5
$T_{max}$	63	50	50	17
$T_{lin}$	85	66	66	23
Observed				
$T_{max}$	200 to 400	~140	50 to 64	20 to 31

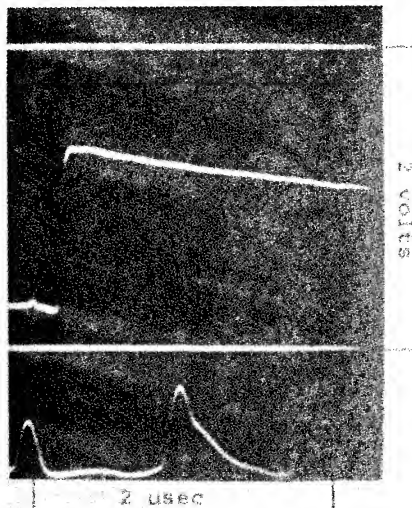


Fig. 4 - Record obtained with  
set-up B (Shot No. 88)

spurious until this detail was found in the previously rejected oscillograms. Curve 1 confirms the breaks in the curves albeit the timing is not in perfect agreement. The corresponding values of  $u$  are in fairly good agreement if we allow the assumption that the calibration in curve 4 is about 10% too low.

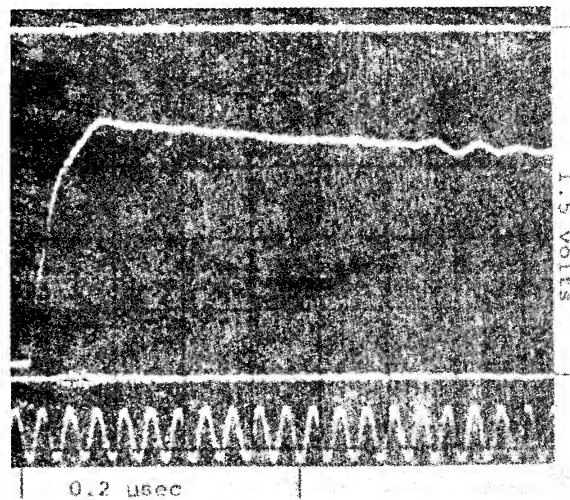


Fig. 5 - Record obtained with set-up C  
(Shot No. 108)

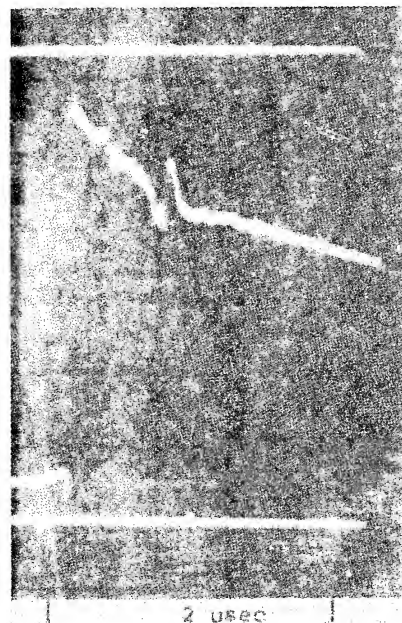


Fig. 6 - Noisy record which  
showed  $u$  vs  $t$  detail of in-  
terest (Shot No. 92)

Curves 1, 2, and 3 show related detail at time A, and curves 1, 3, and 4 show related detail at B; again not precisely at the same times. In curve 5, the poor response has washed out all of the early detail. It shows only one inflection in slope. This clearly relates to point C in



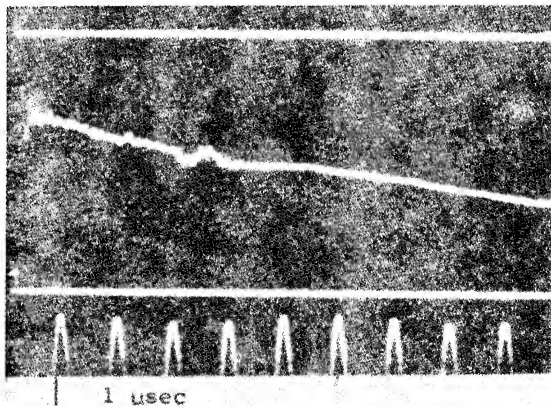


Fig. 7 - Noisy record with conditions as in Fig. 6 except for a change in scope (Shot No. 97)

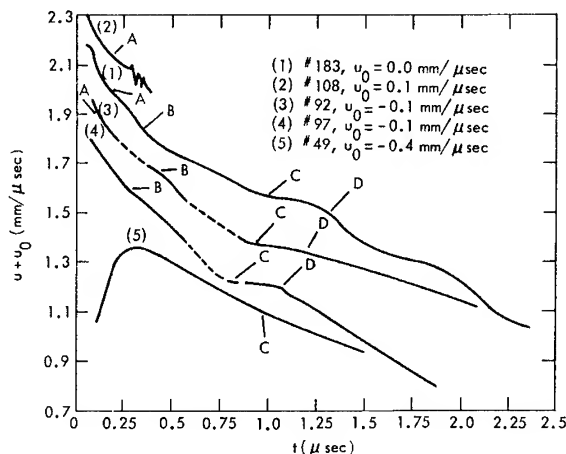


Fig. 8 - Comparison of 4 gage response for PMMA. Gage at 0.86 mm from HE interface.

curve 1. It is evident in comparing curves 5 and 1 that extrapolation of curve 5 from C back to shock arrival time gives an incorrect initial particle velocity. It is equivalent to extrapolating curve 1 from C through B to zero time. It is unfortunate that we do not have any two curves which correspond exactly. We have done better in some of the work in which the gage is embedded in an explosive. What is shown here is that the EMV method shows promise for extracting detailed information about the flow. We, as yet, have not fully realized the promise. As things now stand we find fairly good agreement in curves 1 through 4 for the first 500 nanoseconds. For PMMA in the LSGT, initial particle velocities with an accuracy of the order of 2% have been obtained by

extrapolating the best records to shock arrival times.

Figure 9 is a plot of these initial particle velocity vs gap distance. Data for  $x_0$  less than 4.4 mm are from records taken with set-up C. When  $x_0$  is greater than 4.4 mm all oscilloscope systems gave about the same results. Five points taken from the work of Liddiard and Price (16) are shown for comparison. The agreement at the selected points with the previous work is 0 to 4%. Figure 10 is a peak pressure-distance curve computed from the data of Fig. 9 using Eqs. (2a) and (2b). For comparison the earlier calibration curve of (16) is included. The significant difference in the two curves (for  $x_0$  less than 10 mm) suggests that the older curve was extrapolated with insufficient information to properly define the curve. Although we are not fully satisfied with the present result, we consider it to be an improvement.

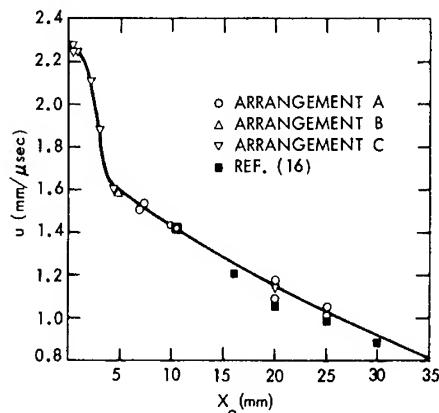


Fig. 9 - Initial particle velocity in PMMA vs distance from HE interface

**Studies in Solid Explosives.** Particle velocity curves were obtained for pressed TNT ( $\rho_0 = 1.60$  g/cc), cast TNT ( $\rho_0 = 1.62$  g/cc), and tetryl ( $\rho_0 = 1.51$  g/cc) as the test sample in a plane wave initiated system. Also studied were the flows for point initiated tetryl at various radii and two velocities where the gage was located at the interface between pressed TNT or tetryl in contact with PMMA. All measurements were made in cylinders of 50.8 mm diameter. The EMV gage base had a length of 10 mm, a width of 5 mm, and a thickness of 130 microns (5 mils) except as noted. The field strength was usually about 800 gauss but fields as low as 250 gauss have been used successfully. Noisy records were somewhat less of a



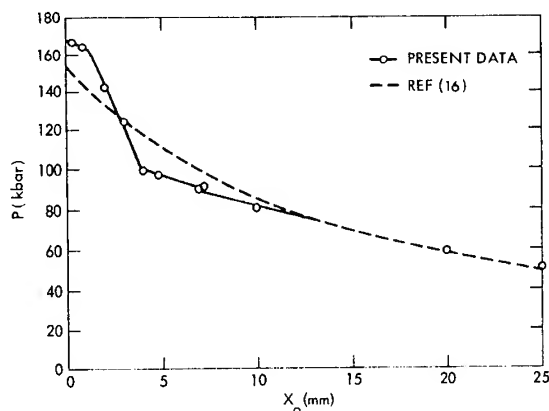


Fig. 10 - Initial peak pressure in PMMA vs distance from HE interface

problem than for PMMA; however, it was found desirable to continue the use of a grounded baffle. The baffle was placed at the interface with the PWB in the case of pressed TNT. The cast TNT was initiated by a pressed TNT charge following the PWB with the baffle located at the boundary between these two charges. The PWB was primacord initiated at 0 in Fig. 1.

Figure 11 shows the results of three good experiments and one bad with pressed TNT. The poor response in the bad record has washed out the typical reaction zone velocities yet the recorded particle velocities after reaching maximum are still of the right order of magnitude. The PWB-gage distance was 25.4 mm. The expected time to maximum is about 100 to 125 ns, in agreement with the 3 good records. The break in slope at about  $190 \pm 10$  ns is interpreted as giving the reaction zone time for pressed TNT. A best estimate of the corresponding CJ particle velocity is  $1.63 \text{ mm}/\mu\text{sec}$ . An experiment with the EMV gage located at the interface between pressed TNT and PMMA, shown in Fig. 12, gives a reaction time of about 150 ns. The CJ particle velocity computed from the record is  $1.67 \text{ mm}/\mu\text{sec}$ . This result is somewhat higher than the previous result as well as that found by Dremine (22) for a pressed density of 1.59.

Cast TNT has been studied at gage to PWB distances from 12.7 to 76 mm. (Distance includes a 12.7 mm pressed\* TNT booster to assure reliable detonation.) One result, typical of the observation for a gage distance of 25.4 mm is compared with a pressed TNT record in

\*6.35 mm pressed TNT was used for the 12.7 mm distance.

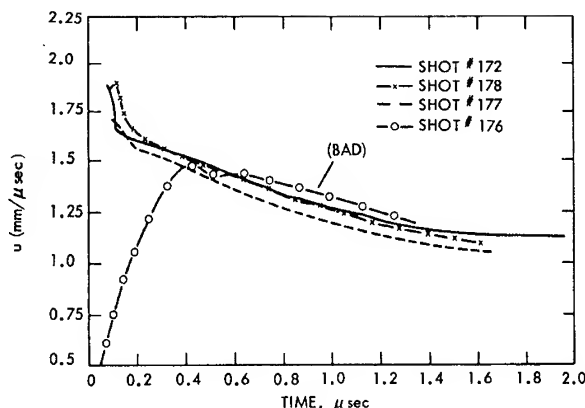


Fig. 11 - EMV gage records in pressed TNT at 25.4 mm from plane wave booster

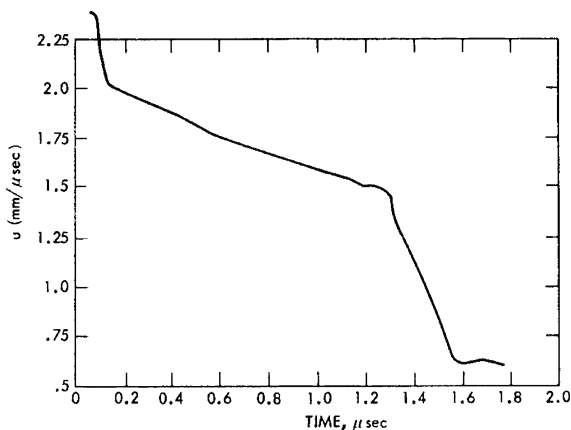


Fig. 12 - Record obtained at interface between pressed TNT and PMMA, at 25.4 mm from plane wave booster

Fig. 13. This and several other shots (see Fig. 14) suggest a reaction time in cast TNT of about 300 ns, the value obtained by Dremine (5). Our best estimate for the CJ particle velocity is  $1.60 \text{ mm}/\mu\text{sec}$ , in good agreement with Dremine.

Figure 15 shows a few selected results for the pressed tetryl; three were initiated at a point, the fourth on a plane at 50.8 mm from the gage. We note that all of the particle velocities come together at a time of about 70 to 100 ns. Our best estimate of the CJ particle velocity is  $1.75 \text{ mm}/\mu\text{sec}$ . An experiment with the gage at the interface between tetryl and PMMA, plane wave initiation, gives a value of  $u_{CJ}$  of  $1.70 \text{ mm}/\mu\text{sec}$  and a break time of about 200 ns. The aluminum foil gage thickness was 25 microns in the tetryl experiments. Check shots with 130 micron foils gave results in agreement

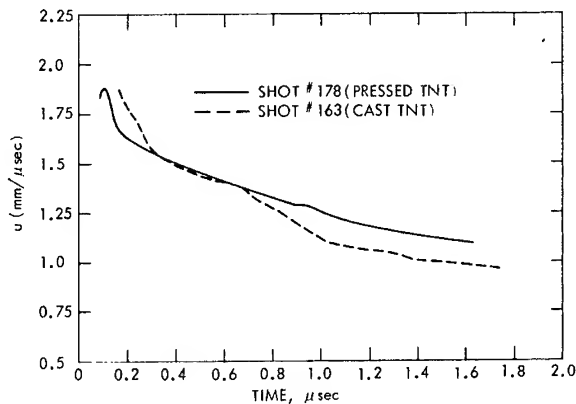


Fig. 13 - Comparison of results for cast and pressed TNT at 25.4 mm from PWB. (Cast TNT initiated by 12.7 mm of pressed TNT following PWB.)

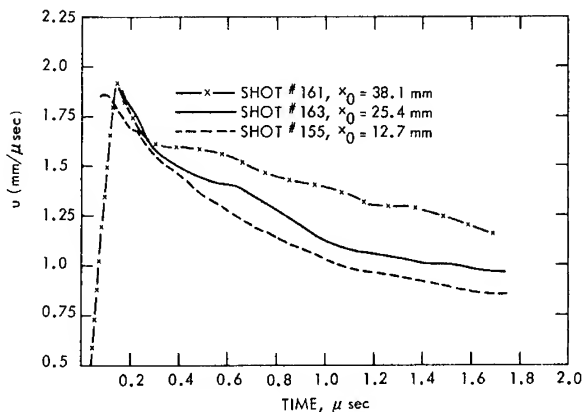


Fig. 14 - Effect of gage distance from PWB on particle velocities for cast TNT

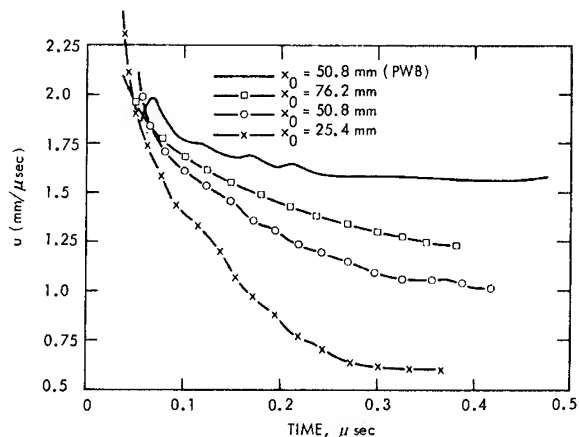


Fig. 15 - Gage records for pressed tetryl, both point and plane initiation

with the thinner foil except at early times after shock arrival. An increasing error in particle velocity with time is possible for the point initiated charges due to diverging motion of the arms. It is expected that the error from this source would be small in the first 100 to 200 ns.

## DISCUSSION

Based on our present experience with the EMV method, we cannot as yet endorse it as a one shot method for obtaining reliable data. This is no great criticism since there are very few experimental methods for the study of strong shocks and detonations which can qualify as single experiment tests. In repeat EMV experiments it is generally found that most of the  $u$ - $t$  curves will agree to about  $\pm 2\%$  in particle velocity at a given time. We have already seen quantitative reproduction of detailed structure in a few instances. This is important because the ultimate utility of the method will be greatly enhanced when one can use it for defining details of the flows in shocks and detonations. With present day oscilloscopes having rise times of 10 nanoseconds and less the experiment rise time is found to be limited by the transit time of the initial shocks in the base of the gage itself. In detonation experiments the need for using 25 to 125 micron foils sets rise time limits of between 20 and 100 ns on the recording system. In this regard a properly conducted free surface velocity experiment may be able to obtain somewhat better initial particle velocities than the EMV gage. By the use of "splitting off" foils (22), a free surface measurement can be made in a time which is long enough to assure a good velocity measurement. This advantage is, however, offset to a great extent by the need for many repeat experiments to outline a  $u$ - $t$  curve for an explosive and the need for the equation of state of the sensing plate. Improvements in the insulation of the gage from the medium could make it possible to improve the experimental rise time of the EMV gage. This requires further investigation.

The determination of a CJ particle velocity and a reaction zone time by the EMV gage has required judgment to select the point on the curves which one would associate with the "termination" of the reaction. This is not always a simple matter. In our pressed TNT records there was little choice but to take the time at which the  $u$ - $t$  curve levels off as the CJ value. This leads to a moderately reproducible particle velocity but a fairly wide spread in the selected reaction time. It is unlikely that the time spread is real; the explosive is likely to be fairly reproducible from shot to shot except

for an occasional bad experiment. Part of our time error can be attributed to the fact that the initial time of break from the baseline is more difficult to pinpoint than are relative times after the initial shock has passed. A zero error of 20 to 40 ns is not unlikely. This is about the error in the time we associate with the reaction. The cast TNT results are far less clear for defining the CJ point. Dremin has stated a reaction time of 300 ns. We see consistent but not too sharp changes in slope at this time. Note however, that in Fig. 14 there is a second slope change at about 600 ns in the records for gage distances of 25 and 38 mm. This break has been seen repeatedly. It could be due to lateral rarefaction. It might be the end of the reaction zone but this is doubtful because of the low particle velocity. There is a hint in the fact that the particle velocity does not follow the pressed TNT curve below 1.6 mm/ $\mu$ sec, that the reaction may not be terminating abruptly at about 300 ns, but, in fact, continues well beyond that time. One possible explanation for what we are seeing is that the reaction in cast TNT near the end of the reaction zone is homogeneous and of order 1 or higher.

Sternberg (23) in a theoretical analysis of the reaction zone for a laminar flow model has shown that the detonation for a homogeneous first order reaction never becomes truly steady. An examination of his Fig. 6, a 1-D computer run with fine zoning, shows that the time at which  $(u+c)/D$  equals 1 increases with run distance. At run distances corresponding to our experiments the reaction may be 99+% complete yet the wave shape continues to change with run distance. What this says, in effect, is that there is no sharp termination of the reaction for the homogeneous first order reaction and the best one can do is to approximate an effective reaction time and CJ pressure. It is generally agreed that the reaction for cast or pressed explosives is initiated by a hot spot mechanism even in a steady detonation. It has been the fashion to assume that the heterogeneous reaction persists all the way to the CJ point in the case of steady detonation. When one considers the fact that the entire body of a high density explosive is compression heated once the detonation is established, the need for assuming heterogeneous reaction throughout the zone vanishes. Single crystals of TNT will detonate by a relatively homogeneous reaction, so why not cast solids or even pressed solids near their theoretical maximum density? We may state further that if less than 1% residual energy is sufficient in an idealized problem to markedly alter the shape of a detonation wave near the end of reaction, there is good reason

to expect a similar influence in the real explosive. Equilibrium shifts in the real reaction will continue to alter the energy term throughout the reaction and rarefaction and the magnitude of the energy change could easily amount to more than 1%. In addition, the unstable wave structure of the type seen in nitromethane detonations is certainly present in all detonations of polycrystalline explosives. The frequency of these fluctuations is probably too high to be observed by the gage because of response limitations. The average which is observed is still subject to equilibration both spatial and chemical. It is suggested that the net result appears more like the effect of a homogeneous first order reaction than of a heterogeneous reaction.

In closing, we are strongly of the opinion that the electromagnetic velocity method is inherently a good technique which will be of considerable value as a tool for unravelling the complex problems of detonation waves and shocks in condensed media.

#### ACKNOWLEDGMENTS

The writers are happy to acknowledge the helpful discussions they have had with Donna Price, D. John Pastine, and J. O. Erkman. Experiments were conducted with the assistance of Carl Groves and Leon Markulis.

#### REFERENCES

1. V. M. Zaitsev, P. F. Pokhil, and K. K. Shvedov, "The Electromagnetic Method for the Measurement of Velocities of Detonation Products", *Doklady Acad. Sci. USSR*, **132**, 6, p. 1339 (1960).
2. A. N. Dremin, P. F. Pokhil, "Investigation of the Reaction Zone of TNT", *Zh. Fiz. Khim.*, **34**, p. 11 (1960).
3. A. N. Dremin and E. A. Karpukhin, "Shock Adiabats of Paraffin", *J. Appl. Mech. and Tech. Phys.*, **3**, p. 184 (1960).
4. A. N. Dremin, V. M. Zaitsev, V. S. Ilyukhin, and P. F. Pokhil, "Detonation Parameters", 8th Symp. on Comb., Williams and Wilkins Co., Balto., Md., p. 610 (1962).
5. A. N. Dremin and K. K. Shvedov, "The Determination of the Chapman-Jouguet Pressure and the Duration of Reaction in the Detonation Wave of High Explosives", *J. Appl. Mech. and Tech. Phys.*, **2**, p. 154 (1964).

6. V. A. Veretennikov, A. N. Dremine, and K. K. Shvedov, "Determination of the Detonation Parameters of Condensed Explosives", *Comb., Explo. and Shock Waves*, 1, 3, p. 1 (1965).
7. A. N. Dremine, S. V. Pershin, and V. F. Pogorelov, "Structure of Shock Waves in KCl and KBr Under Dynamic Compression to 200,000 Atm", *Comb., Explo. and Shock Waves*, 1, p. 4 (1965).
8. For details of the EMV method as used by the Dremine group see: (a) A. N. Dremine, K. K. Shvedov, and V. A. Veretennikov, "Research into the Detonation of Ammonite PZhV-20 and Certain Other Explosives", *Vzrynoye Delo*, 52, 9, p. 10 (1963). English translation in PB 188 144T, U. S. Dept. of Commerce Clearing House (Nov. 1969). (b) A. N. Dremine and S. A. Koldunov, "Initiation of Detonation by Shock Waves in Cast and Pelletized TNT", *Ibid*, 63, 20, p. 37 (1967). Translated in PB 188 145T, U. S. Dept. of Commerce Clearing House (Nov. 1969).
9. L. G. Bokhovitinov, V. A. Vasiljev, and V. N. Rodinov, "Initiation of Detonation in Low Density TNT by Air Shock", 12th Symp. on Comb., Poitiers, France, The Comb. Inst., Pittsburgh, Pa., p. 771 (1969).
10. S. T. Frazier, "Hypervelocity Impact Studies in Wax", BRL Rept. No. 1124 (Feb. 1961).
11. E. A. Ripperger and L. M. Yeakley, "Measurement of Particle Velocities Associated with Waves Propagating in Bars", paper presented at Annual Mtg. of ASME, New York (Nov. 1964).
12. J. T. Frasier and B. G. Karpov, "The Transient Response of Wax Target Subjected to Hypervelocity Impacts", *Exper. Mech.*, pp. 305-312 (Sep. 1965).
13. E. G. Johnson, "An Electromagnetic Technique for Measuring Particle Velocity in Shock Waves", Rohm and Haas Tech. Rept. S-118 (Feb. 1969).
14. D. J. Edwards, J. O. Erkman, and S. J. Jacobs, "The Electromagnetic Velocity Gage and Applications to the Measurement of Particle Velocity in PMMA", NOLTR 70-79 (1970).
15. D. J. Edwards and J. O. Erkman, NOLTR 71-19, (June 1971).
16. T. P. Liddiard and D. Price, "Recalibration of the Standard Card Gap Test", NOLTR 65-43 (1965).
17. D. Price and T. P. Liddiard, "The Small Scale Gap Test: Calibration and Comparison with the Large Scale Gap Test", NOLTR 66-87 (1966).
18. F. E. Allison, "Detonation Studies in Electric and Magnetic Fields", 3rd Symp. on Det., ONR Symp. Rept. ACR-52, p. 112 (1960).
19. R. L. Jameson, S. J. Kilasik, and B. J. Pernik, "Electrical Resistivity Measurements in Detonating Composition B and Pentolite", *J. Appl. Phys.*, 35, p. 1962 (1964).
20. B. Hayes, "Electrical Measurements in Reaction Zones of High Explosives", 10th Symp. on Comb., p. 860, The Comb. Inst. (1965); also 4th Symp. on Det., NOL-ONR, p. 412 (1965).
21. M. A. Cook, "The Science of High Explosives", Reinhold Pub. Co., N. Y., p. 145 (1958).
22. V. A. Vertennikov, A. N. Dremine, O. K. Rozanov, and K. K. Shvedov, "Applicability of Hydrodynamic Theory to the Detonation of Condensed Explosives", *Comb., Explo., and Shock Waves*, 3, p. 1-5 (1967).
23. H. M. Sternberg, "On the Mathematical Theory of the Chapman-Jouguet State", *Int. Colloqu. on Gasdynamics of Explosions*, Novosibirsk (Aug. 1969), *Astronautica Acta*, 15, p. 359 (1970).

## DISCUSSION

R. Chéret

Commissariat à l'énergie atomique  
Centre d'études de Vaujours  
B. P. No. 7, 93 Sevrans, France

It happens that Zavoiski's electromagnetic method for measuring particle velocity has also been developed in our labs. Figure 1 compares our experimental set-up to NOL's. At present time, only a small number of results are available for two explosives:

1. Some kind of RDX/TNT mixture (labeled 209 on Fig. 2)

2. HMX plastic bonded explosive (labeled 426 on Fig. 2). The main feature of these records is mentioned on Fig. 3. The maximum particle velocity  $v_M$  is approximately one half of the detonation velocity  $D$ . This brings out some experimental evidence on Von Neumann's spike.

		S. J. JACOBS AND D. J. EDWARDS N. O. L.	CENTRE D'ETUDES DE VAUJOURS C. E. A.
GAGE	NATURE	ALUMINIUM	COPPER
	LENGTH	5 or 10 mm	10 mm
	WIDTH	5 mm	1 mm
	THICKNESS	25 or 125 $\mu\text{m}$	30 $\mu\text{m}$
DIAMETER OF THE CARTRIDGE		50 mm	100 mm
MAGNETIC SET - UP	MEAN COIL DIAMETER	380 mm or 102 mm	100 mm
	COIL SPACING	190 mm or 89 mm	105 mm
	MAGNETIC FIELD	800 gauss	12 000 gauss
COAXIAL LINE	QUALITY	58 C/U ( $Z_c = 50 \Omega$ )	KX 4 ( $Z_c = 50 \Omega$ )
	LENGTH	5 m	25 m
OSCILLOGRAPH	MODE	TEKTRONIX 454 (AT BEST)	TEKTRONIX 519
	RISE TIME	2.4 ns	0.35 ns
	SWEEP SPEED	20 ns/DIVISION	20 ns/DIVISION

Figure 1

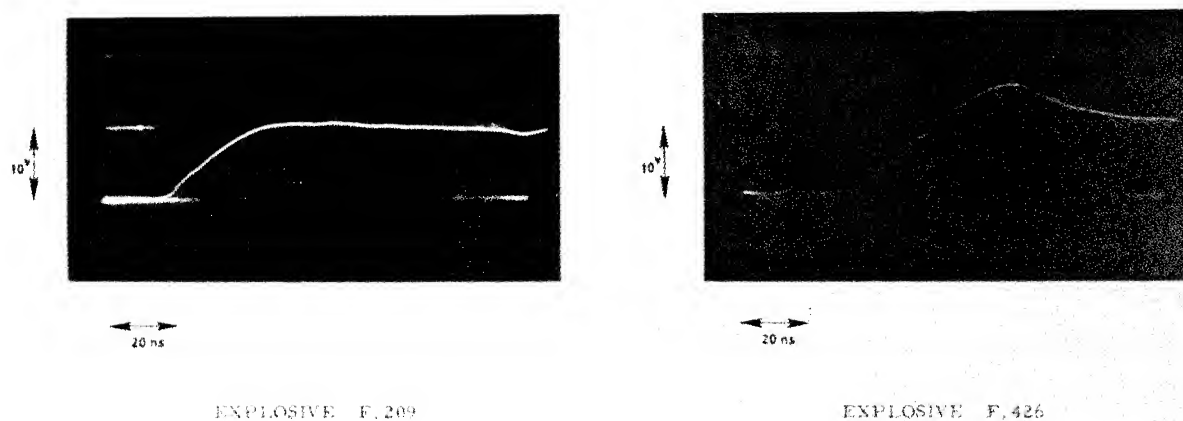


Fig. 2 - Typical experimental results

		F. 209	F. 426
INFINITE DIAMETER CARTRIDGE DETONATION VELOCITY	$D_{\infty}^p$ m/s	8 190	8 715
B. K. W. CALCULATED C. J. VELOCITY :	$U_{*}$ m/s	2 120	2 214
MAXIMUM VALUE OF THE MATERIAL VELOCITY : (AVERAGE OVER THREE SHOTS)	$U_M$ m/s	4 500	4 670
RISE TIME UP TO THE MAXIMUM : (AVERAGE OVER THREE SHOTS)	$\tau_{ns}$	49	42
B. K. W. CALCULATED C. J. CARBON CONCENTRATION :	$(c)_{*}$ g/cm <sup>3</sup>	0.328	0.253

Figure 3

## DETERMINATION OF CONSTITUTIVE RELATIONSHIPS WITH MULTIPLE GAGES IN NON-DIVERGENT WAVES

M. Cowperthwaite and R. F. Williams  
*Stanford Research Institute*  
*Menlo Park, California 94025*

### ABSTRACT

Constitutive relationships are calculated from multiple Lagrangian gage records obtained in one-dimensional wave experiments by integrating the flow equations expressing conservation of mass and momentum along a particle path. Specifically for flow adjacent to a constant state, particle velocity-stress relationships are calculated from multiple stress-time profiles by integrating the combined mass and momentum equations, and specific volume-particle velocity relationships are calculated from multiple particle velocity-time profiles by integrating the continuity equation; but these relationships are in general approximate because the material derivatives required to perform the integrations are generated from gages separated by finite distances. Steady-state, simple-isentropic, and simple nonisentropic waves are shown to be the only flows that allow constitutive relationships among stress, particle velocity, and specific volume to be determined exactly with either a pair of stress gages or a pair of particle velocity gages. Procedures are formulated for using three gages to test for these special types of flow and determine constitutive relationships when the flow is more complicated.

Note: This paper appears in its entirety in J. Appl. Phys. 42, 456 (1971).

4

# SHOCK-INDUCED ELECTRICAL POLARIZATION OF A SOLID EXPLOSIVE

J. Morvan and H. Pujols  
*Commissariat à l'Energie Atomique*  
*B.P. 2, 33 - Le Barp - France*

## ABSTRACT

An electrical polarization of explosive molecules is observed when a shock wave initiates the detonation in a solid explosive. Experimentally, the explosive (hexolite 80/20), placed between two electrodes connected through a resistance, generates an electrical signal characterizing the transition and detonation zones: (i) as long as the studied explosive is only submitted to the reactive shock wave, the emitted signal is similar in shape to that of a shock-induced polarization of an inert dielectric; (ii) when the explosive is thick enough for the detonation to be initiated, the signal consists of two successive parts, one being imputed to the explosive in process of initiation, the second one to the detonated explosive. Initial pressure varied between 40 and 130 kbar. Optical methods have confirmed the interpretation of obtained signals. The transition zone thickness may be deduced from the measured times. The phenomenon is attributed to a molecular polarization due to the reactive shock preceding the detonation.

## INTRODUCTION

When a heterogeneous explosive is submitted to a shock wave, a reactive shock expands, which can initiate the detonation in a very short time. The chemical reaction begins immediately at the interface and accelerates the shock front by supplying more and more energy till the steady detonation mode is reached.

The experimental study of detonation initiation usually consists in observing the reactive shock wave motion on the surface of a sample by means of high-speed cinematography standard techniques. It follows that the collected results can only account for the dynamics of the phenomenon.

An alternative procedure is to use electrical signals produced by the reactive shock and the detonation. A method of obtaining such signals was described by J. Travis in the Fourth Symposium (1). Significant results were obtained only with liquid explosives. Records from the polarization of solid explosives were reported by B. Hayes (2), with emphasis on

interface signals obtained between states of explosives.

The method consists in placing the studied explosive between two metallic electrodes connected through a resistance and in observing the voltage drop which results from the electrical polarization of explosive molecules; the signal evolution is typical of the reactive shock and detonation wave. In the present work, the amplitude and quality of the signals were sufficient for an analysis of the influence of various parameters.

This phenomenon which we think is a consequence of the change in the dipole moment of explosive molecules, behind the shock front and preceding the reaction zone, could offer a new field for the microscopic study of detonation.

## EXPERIMENTATION

A disk of solid explosive (hexolite 80/20) 50-mm diameter by  $h$  thick ( $1 \leq h \leq 10$  mm) is placed between two electrodes (Fig. 1). The electrode at ground potential is a disk 200 mm



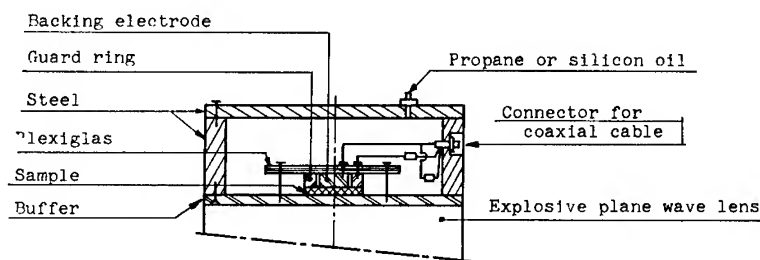


Fig. 1 - Experimental arrangement

in diameter placed in direct contact with an explosive plane wave lens; its nature and thickness are variable in order to change the intensity of the pressure pulse in the explosive sample. The backing electrode is a copper disk 30 mm in diameter with a guard ring 30 mm i.e., 50 mm o.d., which reduces the curvature effects of the shock wave in the sample and also those of electric current lines. The whole is mounted in a tight metallic box filled with propane or silicon oil, which becomes a screening cage against the electrical outside effects. The signal is measured at the terminals of a 60- $\Omega$  equivalent resistance with Tektronix 555 and 556 oscilloscopes. The resistance  $R_G$  which connects the guard electrode with the ground is such that the time constant of the measured circuit is equal to that of the guard circuit.

## EXPERIMENTAL RESULTS

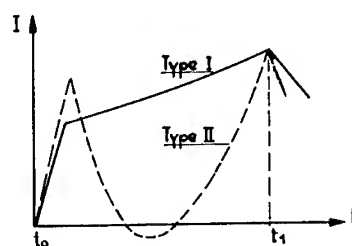
### A. Records

The electrical signals observed with this device are of two shapes, according as the steady regime of detonation is or not initiated in the thickness  $h$  of explosive.

$h_t$  being the thickness of the transition zone (explosive thickness in which the reactive shock expands) at the initiating pressure  $P$ , if  $h \leq h_t$ , the detonation cannot originate in the sample and the signal is only due to the reactive shock. In this case, it looks like that emitted by a plastic or ionic material, types I and II of Fig. 2 (2).

The shock enters into the explosive at time  $t_0$  and leaves at time  $t_1$ . The interval  $t_1 - t_0$  corresponds to the transit time of the reactive shock, which is used to determine directly its average velocity.

The rise time of the signal exceeding the rise time of the recording instruments can be

Fig. 2 - Schematic polarization signals for  $h \leq h_t$ 

due to the curvature or obliquity of the initiating shock wave. If  $h > h_t$ , the detonation begins in the sample and produces signals of types III and IV (Fig. 3). The reactive shock wave travels the specimen in the time  $t_1 - t_0$  and generates a signal shape similar to those of Fig. 2. The detonation begins at time  $t_1$  and reaches the backing electrode at time  $t_2$ . Its typical signal is always a sharp negative pulse followed by a positive rise. The records of Travis (1) in liquid explosives show equivalent shapes.

The explosive thickness  $h_d$  traversed by the detonation wave is given by the equations

$$h_d = D(t_2 - t_1),$$

$$h_t = h - h_d,$$

where  $D$  is the detonation velocity of the studied hexolite (8.1 mm/ $\mu$ s).

The average velocity of the reactive shock  $U_a = h_t/t_1 - t_0$  (or  $h/t_1 - t_0$ , when  $h \leq h_t$ ) permits us to calculate an average value of the initiating pressure in the explosive from the linear relation (3):  $U = 2.4 + 1.66 u$  (mm/ $\mu$ s). These values are in agreement with those determined by the shock polars ( $P, u$ ) for the shock generating system.

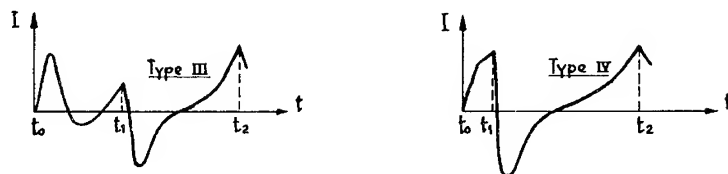
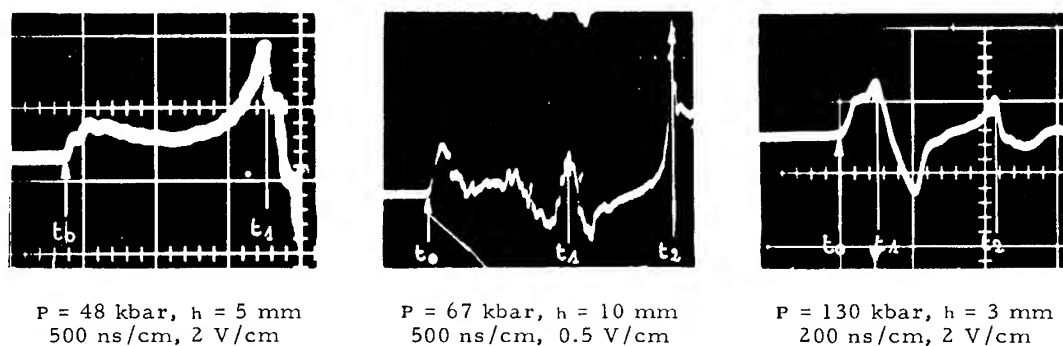
Fig. 3 - Schematic polarization signals for  $h > h_t$ 

Fig. 4 - Typical oscillograms

Different types of oscillograms are shown in Fig. 4.

This analysis of polarization signals was confirmed by simultaneous optical and electronic observations.

In this case an explosive plate 5 mm thick with a  $20^\circ$  wedge took the place of the explosive disk. The electronic measurements were obtained by means of a 30 mm diam. electrode without a guard ring, the optical observation by means of the reflectivity change of an aluminized Mylar layer covering the wedge and illuminated by an argon flash.

Such records are shown in Fig. 5. The change in slope observed by optical means at the beginning of the detonation corresponds to the appearance of the negative peak on the oscillogram, as mentioned in the preceding paragraph. The thickness of the transition zone measured by both methods generally agrees to less than 0.2-mm accuracy.

## B. Results

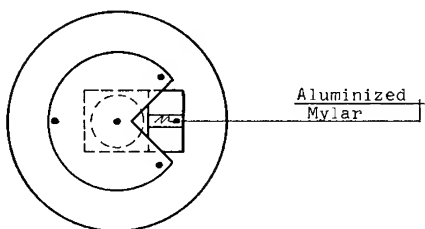
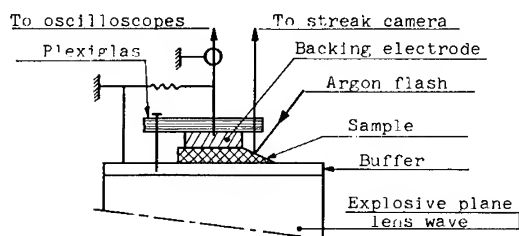
The experimental results are listed in Table 1. The shock pressure, the characteristics of specimens, the type of signal, the transition and detonation times, and the thickness of the transition zone are indicated with the

average value of the reactive shock velocity and the initial amplitude of the polarization current, extrapolated to time  $t_0$  by idealizing signals with zero rise time. The last column gives the amplitude of the initial current relative to a sample of 3 mm constant thickness, calculated by taking into account that the initial current is proportional to the area/thickness ratio of the sample (4). These last values permit a comparison of obtained signals at varied pressures. However, their evolution is rather irregular.

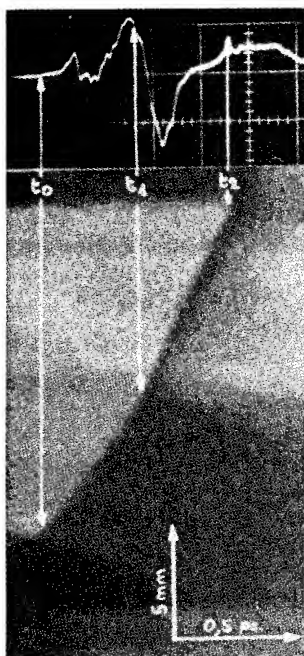
## INTERPRETATION OF RESULTS

Though we do not know the microscopic mechanism of the shock-induced polarization of a solid explosive, we can nevertheless localize its origin. Thus the importance of the initial value of the dipole moment relative to the compressed molecule about 16 Debyes, deduced from the analysis (4) of the recorded signal for a sample 5-mm thick submitted to a 60-kbar shock, leads us to think that this polarization is likely of molecular origin (permanent moment value of hexogen molecule: 5.79 Debyes).

The disappearance of dipoles produced previously under the action of deformation gradient at the shock front proceeds, on the contrary, from a plastic relaxation of the crystalline lattice. The dislocation should rearrange



(a)



(b)

Fig. 5 - (a) Experimental arrangement for coupled measurements; (b) Oscilloscope and streak camera records (oscillogram: 200 ns/cm, 1 V/cm)

This plastic relaxation of the solid behind the shock front might be the cause of the ultra-rapid thermal decomposition of the dynamically compressed molecules. The interactions of dislocations at high speeds should be responsible for this effect behind a strong-amplitude shock wave which precedes the reaction zone of the detonation, as well as behind a shock wave initiating the detonation.

However, at weak shock pressures (some tens of kbar) the thermal decomposition will take place at the outside of grains near zones, where the dislocation sources are easily created (pores, cracks, rugged zones of grains) and strongly excited against those few mobile of the Frank network. At stronger pressures (some hundreds of kbar) greater numbers of the internal dislocation sources will be in their turn excited, generating a considerable number of intragranular sources of thermal decomposition. In this case, those dislocations which interact with velocities greater than some critical value  $v_c$  (corresponding to a critical strength  $\sigma_c$ ) will produce the local thermal decomposition of the molecules. In other words, the interaction of dislocations will produce enough energy to reach locally the thermal decomposition temperature.

Hence, two relaxation modes of dipoles created in the shock front could appear inside the explosive. One, which corresponds to the plastic relaxation of the lattice, should predominate at low pressure. The other, corresponding to the thermal decomposition of molecules in connection with the dissipation of energy during plastic deformation, should be produced at high shock pressure. Consequently, relaxation times of relatively long duration, of the order of one microsecond, will be found at low shock pressure (type I signals), whereas relaxation times about ten times shorter will be determined at high pressure (type IV signals).

The analysis of polarization signals of type II is difficult; however, it seems that the negative part of signal preceding the pulse of same sign typical of the detonation issues from the start of the TNT detonation contained in the hexolite. These sign changes of the signal should result from the decrease of the polarization in the detonation front of TNT and hexogen. This phenomenon has also been found by Travis in liquid explosives. The type IV signals do not inverse before the mixture detonation. In this case, the initiating pressure being stronger, the TNT and hexogen detonations are almost simultaneous and consequently inseparable on the oscillograms. For the type III and IV signals, we observe before the start of

the lattice from uniaxial deformation state to a more stable configuration, which corresponds to an almost hydrostatic compression state.

TABLE 1  
Experimental Results

P kbar	h mm	Type of signal	$t_t$ $\mu s$	$t_d$ $\mu s$	$h_t$ mm	$U_p$ mm/ $\mu s$	$I_0$ m A	$I_0$ relative to a sample 3 mm thick
35	5	I	1.450	0	$\geq 5$	3.41	7.4	12.3
37	2	I	0.580	0	$\geq 2$	3.45	11.0	7.3
40	5	I	1.325	0	$\geq 5$	3.78	10.1	16.8
42	2	I	0.560	0	$\geq 2$	3.55	15.3	10.2
42	3	I	0.840	0	$\geq 3$	3.58	9.2	9.2
44	3	I	0.830	0	$\geq 3$	3.61	21.3	21.3
48	5	I	1.380	0	$\geq 5$	3.68	7.9	13.2
48	5	I	1.360	0	$\geq 5$	3.67	6.7	11.2
52	3	I	0.800	0	$\geq 3$	3.76	33.9	33.9
55	5	I	1.300	0	$\geq 5$	3.83	18.0	30.0
62	5	III	0.640	0.31	2.51	3.92	22.1	36.8
65	10	III	0.960	0.73	4.09	4.28	3.9	13.0
67	10	III	0.990	0.81	3.43	3.45	5.6	18.9
70	10	III	0.680	0.88	2.87	4.25	- 3.9 + 3.3	-13.0 +11.0
70	3	II	0.675	0	$\geq 3$	4.45	7.9	7.9
72	5	III	0.700	0.27	2.86	4.09	9.7	16.2
75	10	III	0.585	0.93	2.45	4.19	2.2	7.3
75	3	II	0.645	0	$\geq 3$	4.65	2.3	2.3
75	10	III	0.435	1.02	1.72	3.96	4.3	14.3
110	3	III	0.215	0.25	1.01	4.70	-12.0 +25.7	-12.0 +25.7
110	2	III	0.260	0.11	1.12	4.30	-13.4 +34.7	- 8.8 +23.1
130	2	IV	0.100	0.20	0.38	3.80	39.2	26.1
130	3	IV	0.105	0.32	0.39	3.71	17.5	17.5

hexogen detonation a sharp rise of the signal to a higher level than the first pulse. A rapid rise of the shock pressure in the hexogen grains up to the critical pressure threshold should be responsible for this effect.

## CONCLUSION

Although we have briefly localized, at the molecules, the origin of the shock-induced electrical polarization of a granular explosive, whatever the amplitude of the shock, the discovery of the molecular mechanism of this dynamic polarization remains. It is clear that

the comprehension of this phenomenon should give precious information on the process of thermal decomposition of explosive molecules.

A test of the qualitative interpretation of the various recorded signals has been formulated by means of a microscopic model of the detonation briefly discussed here, resulting from the release of heat during plastic deformation behind a shock front. Accounting for a phenomenon which expands inside the granular explosive, without supplying outside perturbations, this experimental method should conversely, permit us to test the validity of the presented microscopic model.

## REFERENCES

1. J. R. Travis, "Electrical transducer studies of initiation of liquid explosives," The fourth symposium on detonation, preprints, vol. II, D-61, Oct. 1965.
2. B. Hayes, "The Detonation Electrical Effect," J. Appl. Phys. 38, 2, 507, Feb. 1967.
3. These signals must be compared with that shown for TNT by A. G. Ivanov, et al., Soviet Physics, J.E.T.P., 27, 1, 153, Jul. 1968.
4. C. Fauquignon, thèse d'ingénieur-docteur, Faculté des Sciences de Paris, Apr. 1961.
5. F. E. Allison, "Shock-induced polarization in plastics: I. theory," J. Appl. Phys. 36, 7, 2111, Jul. 1965.

## QUARTZ GAUGE STUDY OF UPSTREAM REACTION IN A SHOCKED EXPLOSIVE

J. E. Kennedy  
*Sandia Laboratories*  
*Albuquerque, New Mexico*

### ABSTRACT

Shock initiation experiments on PBX-9404 explosive have been conducted by impacting gun-driven quartz stress gauges into explosive samples backed by Plexiglas buffer discs and quartz gauges. In each case the explosive sample thickness was insufficient for the reaction to grow to high order detonation. Stress histories were measured both at the impact face of the explosive and at the opposite face (the "downstream" face of the explosive) for time periods up to 1.6  $\mu$ sec. A substantial delayed stress excursion was observed to occur at a given face of the explosive sample whenever the initial shock stress at that face exceeded 30 kbars. These stress excursions were interpreted to indicate chemical energy release. It appears that this reaction occurring well behind the shock front may be in the nature of a thermal explosion.

### INTRODUCTION

Shock initiation experiments on solid and liquid high explosives have, until quite recently, been conducted primarily with photographic and electronic instrumentation methods designed to observe only the front of a shock moving through the explosive. This paper reports results of shock initiation experiments on PBX-9404 which were conducted utilizing Sandia quartz stress gauges (1) and gas gun planar impact techniques. The experiments used projectile-mounted impact gauges which measured the stress history at the impact face of the explosive sample, and target gauges downstream of the samples from which stress histories at the downstream face of the explosive could be derived.

Initial stress into the impact face of the PBX-9404 was varied from 15 to 30 kbars. In each experiment the thickness of the explosive was insufficient to permit growth of the reaction to high order detonation; this was done so that the stress history of the reaction could be monitored at the downstream surface of the explosive sample at some intermediate stage of reaction growth.

When the initial stress at a given face of the PBX-9404 was above 30 kbars, either at an impact face or at a downstream face after some buildup had occurred in the run through the sample thickness, a large compressive stress excursion was observed well behind the initial shock front (i.e., upstream of the shock front). These excursions were greater in amplitude and followed more closely behind the shock front when the initial shock strength was further increased. These excursions are interpreted as delayed chemical energy release.

The model of a delayed detonation wave, generated behind the shock front and eventually overtaking it, has been advanced for shock initiation of homogeneous explosives based upon experimental work of Campbell et al., (2) and computer calculations of Hubbard and Johnson (3), Mader (4), and others. Several years ago it was thought that all important reaction growth in shock-initiated heterogeneous explosives occurred at the shock front alone (5). However, Dremine and Koldunov (6) have reported important delayed reaction well behind the front in shocked TNT. In addition, separate pieces of photographic evidence recently published (7) and presented at this symposium (8),

\*This work was supported by the U.S. Atomic Energy Commission.

and stress histories measured here show that strong reaction may occur well behind the shock front in heterogeneous explosives. This new evidence indicates a need for development of a new model for initiation of heterogeneous explosives which will account for substantial chemical reaction occurring well behind the shock front and which may contain aspects of the model for homogeneous explosives.

This paper presents first the experimental configuration employed in this work. Quartz gauge performance and limitations, and the methods of treating gauge data to determine shock states are described next. Features of stress histories thus determined for the impact face and for the downstream face of PBX-9404 are then discussed. A correlation is drawn between the observed stress excursions and a parameter representing severity of shock loading of the explosive. Finally, implications of the observations and the correlation upon our picture of processes in reaction growth are discussed.

## EXPERIMENTAL ARRANGEMENT

The experimental components and techniques used in these one-dimensional strain (9) impact experiments were variations of those described in detail by Ingram and Graham (10) in this symposium. The gun and quartz gauge techniques have been developed over an extended period by many investigators at Sandia (1, 11 - 14). Experiments were performed using the Sandia 27-meter compressed gas gun with an evacuated barrel of 6.35 cm. nominal bore, in which projectiles can be driven by air or helium to velocities as high as  $1.5 \text{ mm}/\mu\text{sec}$  (15). Each projectile was faced with a quartz impact gauge from which the output signal was received by connection through the target assembly during the time of impact. As shown in Fig. 1, the target assembly was a laminate consisting of a PBX-9404 disk backed by a 3 mm thick Plexiglas II, type UVA disk (16) which was in turn backed by a quartz gauge. The PBX-9404 was bonded to the Plexiglas with Aron Alpha (16) and the Plexiglas-quartz bonding agent was an epoxy resin (16); each bond was 0.01 mm or less in thickness. The PBX-9404 initial density was  $1.830 \pm 0.006 \text{ g/cm}^3$ .

The arrangement thus provided two quartz gauges, an "impact gauge" which monitored the stress history at the impact and a "target gauge" which monitored the stress history transmitted through the Plexiglas buffer from the downstream face of the explosive sample. The intent in interposing an unreactive buffer

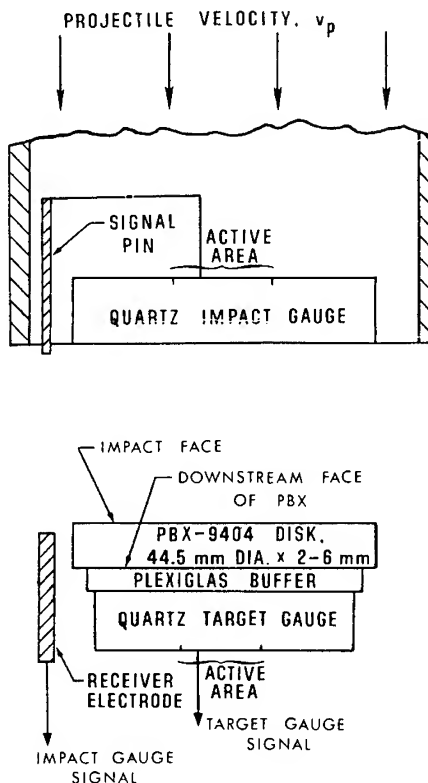


Fig. 1 - Projectile gauge and target assembly

material between the PBX-9404 and the downstream quartz was to provide "acoustic storage" of the shock wave in order that significant disturbances would not be reflected or transmitted back into the PBX during the duration of the experiment. Measurements of the "stored" wave profile were then made at the Plexiglas target gauge interface. Plexiglas was chosen as the buffer material because its shock impedance, although slightly lower, very nearly matches that of PBX-9404. Any reflections from the PBX-9404 - Plexiglas interface back into the PBX hence would be rarefactive rather than compressive and presumably would tend to quench rather than enhance reaction occurring behind the shock front. Recent work by Schuler (17) has shown that even though Plexiglas II-UVA has rate-dependent mechanical properties, the effects of these are negligible in our experiments. Our standard buffer thickness (3 mm) was the minimum value that would preclude a double transit in the buffer by the shock reflected from the Plexiglas-quartz interface during the target gauge recording time of  $1.66 \mu\text{sec}$ .

In preparing the experiments, care was taken to obtain minimum deviation from flatness

and parallelism between faces of each component and within the projectile assembly and target assembly so that a planar input shock wave could be achieved and maintained through the sample. Imprecise alignment of the projectile with the sample or misalignment within the target laminate results in "tilt" of the wave front relative to the sample face and reduces time resolution of the stress-time history. Tilt may be estimated by the apparent risetime of the stress jump on the trace. Each explosive sample was set in the bottom of a cup to provide separation from the gun muzzle and minimize the possibility of damage to the muzzle. Further, the cup was surrounded by an evacuated steel pipe to absorb blast and fragments, and to localize any unreacted powder. By adjusting three pairs of differential mounting screws set in the base of the cup, the target assembly within the cup was aligned parallel to the mounting face of the cup usually within 0.005 mm over the surface of the 44.5-mm diameter PBX-9404 sample. Typical tilts occurring in these experiments were about 1 milliradian, which resulted in oscilloscope trace risetimes of .01 to .04  $\mu$ sec.

Ramsay and Popolato (18) have published curves showing run distance to detonation in PBX-9404 as a function of transit time and of shock pressure. These curves proved to be a helpful guide in choosing experimental conditions and in selecting vertical oscilloscope gains and time delays between impact gauge and target gauge oscilloscopes.

## EXPERIMENTAL RESULTS

### Quartz Gauge Response

Many of our experiments utilized quartz gauges at stress levels beyond those previously thought to be the useful upper limit. Hence, it is pertinent to mention limitations of the quartz gauge which affect our interpretation of output current waveforms. Deviation from the basic proportionality between time-resolved current and stress below 26 kbar is small and is principally due to variation of the piezoelectric current coefficient (1, 19) and to finite strain imposed on the gauge during wave passage. Corrections were made for these deviations in our data reduction.

For the impact gauges, equal stresses are driven into the gauge and into the impacted explosive sample, so the gauge reading directly indicates stress history at the impact face of the explosive. With the exception of portions of two shots, all of our impact gauge records

indicate stresses below 26 kbars at all times. The gauge results are accurate to within  $\pm 2.5\%$  in this stress region.

Because of shock impedance mismatches, stress driven into the target gauge is higher than that incident upon the downstream face of the explosive, even without chemical reaction in the explosive. Our target gauges thus were subjected to stress levels from 25 to 80 kbars, which is beyond the linear response region of quartz. However, we are able to interpret our data in this stress region on the basis of Graham's (19) recent unpublished studies of the response of quartz in this stress range. For stresses up to 40 kbar our calculated stress values, which ignore the high stress nonlinear effects, are probably low by about 5%. These data are shown in Table 1 preceded by ">" to indicate the direction of correction.

For stresses greater than 40 kbar Graham's results indicate more complex nonlinear effects which probably cause our calculated stress values to be low by as much as 10%. Since the high stress response of quartz is complex, different stress profiles will cause different characteristic responses. Even though our particular calculated values are lower than actual stresses, other situations may be encountered in which the calculated values would be higher than actual stresses (20).

### Gauge Data Treatment

Impact gauge data and target gauge data were treated in different ways in order to infer incident stresses at the appropriate PBX-9404 faces. Regarding impact gauge output, the measured velocity of the quartz-faced projectile was used in conjunction with the directly measured stress at the impact interface to determine an instantaneous stress-particle velocity ( $\sigma_i$ ,  $u_p$ ) state in the impacted material (in this case PBX-9404), as depicted graphically in Fig. 2. The quantities  $\sigma_e$  and  $\sigma_u$  also shown in Fig. 2 are PBX-9404 impact face stresses calculated for the given impact conditions, assuming the PBX to have the "experimental" or "unreacted" Hugoniot (18), respectively. Values of  $\sigma_e$  and  $\sigma_u$  were calculated for each experiment to permit comparison with our impact gauge results. As implied in Fig. 2, our impact gauge stresses  $\sigma_i$  were usually lower than both  $\sigma_e$  and  $\sigma_u$ . These results will be discussed in the next subsection.

For all calculations quartz was assumed to behave elastically with a wave velocity of 5.72 mm/ $\mu$ sec and initial density of 2.65 g/cm<sup>3</sup> (1);



TABLE 1  
Stress Histories in Shocked PBX-9404

Shot No.	PBX-9404 Thickness h (mm)	Impact Velocity (mm/ $\mu$ sec)	Transit Time <sup>a</sup> ( $\mu$ sec)	Impact Face of PBX-9404				Downstream Face of PBX-9404					$x_i^f$ (mm)	$x_d^f$ (mm)
				Meas'd Stress History $\sigma_i(t)$			Calc'd Stress (kbar)	$t$ ( $\mu$ sec) <sup>b</sup>	Target Gauge $\sigma_i(t)$ (kbar)	PBX-9404 <sup>e</sup> $\sigma_d(t)$ (kbar)	Calc'd $\sigma_d(x_d)^g$ (kbar)			
				$\tau$ ( $\mu$ sec) <sup>b</sup>	$\sigma_i(t)$ (kbar)	$\sigma_c^c$								
												$\sigma_u^d$		
641	2	0.707	1.68	.037 .161 .919j	22.9 29.2 (2nd jump) 37.3	32.9	30.8	.040 .171 .339j	>40. >47. >63.	>31. >37. >50.	39	8.7	6.7	
658	4	0.661	2.08	.040 .134 .688 1.069j	19.7 23.9 (2nd jump) 27.9 29.0	30.3	28.4	.016 .114 .236j	>35. >41. >44.	>27. >32. >34.	42	9.8	5.8	
647	4	0.633	--	.011 .046 .059	16.2 21.7 24.7	28.8	27.0	.030 .335 .608j	>31. >46. >63.	>24. >36. >50.	39	10.7	6.7	
644	2	0.620	1.48	.064 .137 .362	22.0 21.1 23.4	28.1	26.4	.025 .330 .986j	>27. >34. >54.	>20. >26. >42.	32	11.1	9.1	
645	4	0.595	2.00	.024 .064 .134	20.6 21.2 22.4	26.7	25.2	.023 .314 .87j	>29. >40. >80.	>21. >31. >66.	35	12.0	8.0	
615	2	0.565	--	.056 .070 .440 1.159	22.7 23.7 18.9 25.5	25.1	23.7		Not measured			13.2	11.2	
648	6	0.510	2.98	.018 .126 .318	17.7 18.8 17.5	22.3	21.1	.026 .132 .540 1.126j	17. 25. >30. >62.	12. 19. >23. >49.	30	16.0	10.0	
656	2	0.525	1.82	.035 .105 .309	17.7 18.6 18.9	23.0	21.8	.022 .126 .545	22. >28. >29.	17. >21. >22.	25	15.1	13.1	
659	2 <sup>h</sup>	0.506	0.60	.017 .059 .118 1.168	19.4 18.2 17.3 29.9 (reflected shock)	22.1	20.9	.028 .037 .147 .555	25. 26. >32. >35.	16. 17. >21. >23.	24	16.2	14.2	
643	6	0.451	2.78	.021 .047 .306 .860	13.2 15.9 13.7 19.0	19.3	18.3	.018 .054 .292 .816	14. 19. 23. 26.	10. 14. 17. 20.	24	20.0	14.0	
614	2	0.394	--	.059 .099 .410 .833	16.3 17.9 15.2 18.2	16.5	15.7		Not measured			25.6	23.6	

<sup>a</sup>Through explosive sample plus buffer (if present).

<sup>b</sup>First time value indicates trace rise time, limited by tilt.

<sup>c</sup>Calculated from quartz impact against PBX-9404 with "experimental" Hugoniot (18).

<sup>d</sup>Calculated from quartz impact against PBX-9404 with "unreacted" Hugoniot (18).

<sup>e</sup>Calculated by Hugoniot reflection method and subject to quartz gauge performance limitations discussed in text.

<sup>f</sup> $x$  (mm) = Run distance to detonation in PBX-9404.  $x = X(\sigma)$  according to Eqs. (1) to (3) and Fig. 6.  $x_i = X(\sigma_i)$  pertains to impact face.

<sup>g</sup>Anticipated stress incident at PBX-9404 downstream face based on calculated run distance to detonation at that face.

<sup>h</sup>No Plexiglas buffer used.

<sup>j</sup>Premature end of gauge record.

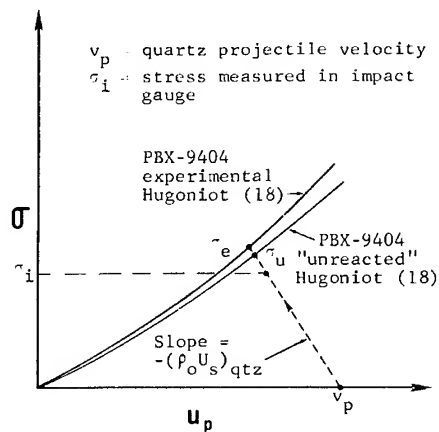


Fig. 2 - Determination of  $\sigma - u_p$  state from impact gauge output, and anticipated stresses from literature Hugoniot (18)

since the Hugoniot elastic limit of quartz is 62 kbars (19), this assumption is justified.

Estimation of the incident stress in PBX-9404 at its downstream surface from a target gauge stress reading requires treatment of the shock interactions which occurred at the buffer-quartz interface and at the explosive-buffer interface. Interactions at interfaces between dissimilar materials were treated by reflecting the Hugoniot of the upstream material about the  $u_p$  value of its incident state in the  $\sigma - u_p$  plane to represent a path for its unloading or further shock compression. This graphical method is illustrated in Fig. 3.

Because this explosive has low porosity and the stresses are low relative to its bulk modulus, it is believed that this procedure is justified whenever chemical reaction is negligible. When a substantial amount of delayed chemical reaction occurs, stress in the PBX-9404 will be increased above that indicated by the experimental Hugoniot (18) for a given value of  $u_p$ , and the unloading isentrope will have a lower slope in the  $\sigma - u_p$  plane due to the gaseous nature of the reaction products. These two adjustments to the PBX loading and unloading loci would have opposite effects upon the values of PBX-9404 stresses calculated from target gauge data, and thus tend to offset each other. Therefore, it cannot be categorically determined whether chemical reaction causes actual stress to be greater or less than the stress calculated simply by use of the experimental PBX-9404 Hugoniot (18) and its reflection for loading and unloading, respectively.

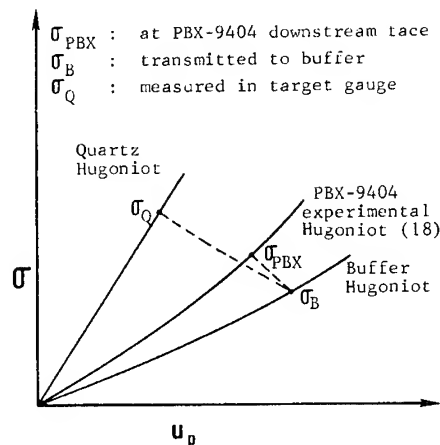


Fig. 3 - Determination of state at downstream face of PBX-9404 from target gauge data by reflected Hugoniot method

However, errors due to this source will be small (probably  $< 10\%$ ) because of the small difference in impedance between the Plexiglas buffer and PBX-9404.

The experimental PBX-9404 Hugoniot of Ramsay and Popolato (18) was used in these calculations because it pertains to propagated waves and because the presence of a buffer layer between the explosive and our target gauge slightly compromised the directness of our propagated wave measurements. For polymethyl methacrylate (PMMA), the composite Hugoniot given by Deal (21) was used. Calculated stress in the PBX-9404 was found to be insensitive to the choice of PMMA Hugoniot.

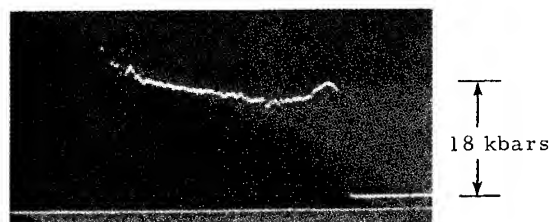
The time-resolved nature of quartz gauge results introduces the problem of concisely presenting the large amount of information they contain. Both the impact gauges and target gauges indicated significant variations in stress with time — mainly at very early times for impact gauges and at later times for target gauges. Table 1 presents data selected to represent the most interesting stress variations with time in each record. Table 1 also contains some values calculated from relations for PBX-9404 given in Ref. 18, to allow comparison and interpretation of our data.

#### Impact Gauge Results

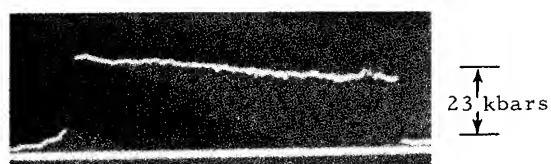
Stress at the impact face of the PBX-9404 sample depended markedly on time at early times. At impact velocities below  $0.6 \text{ mm}/\mu\text{sec}$

the initial stress jump usually was followed by relaxation in stress, as illustrated in Fig. 4(a), of as much as 20%. Samples exhibiting this relaxation also usually exhibited a recovery or slight increase in stress after about 1  $\mu\text{sec}$ . This delayed increase is believed to represent mechanical stiffening of the material rather than chemical reaction, since the corresponding target gauge records for the most part gave no evidence of significant early reaction which might be felt by the impact gauge.

The oscillogram in Fig. 4(b) is an example of an experiment in the lower velocity range in which stress remained sensibly constant over the entire gauge lifetime.



(a) Shot 614,  $v_p = .394 \text{ mm}/\mu\text{sec}$   
 $x_i = 25.6 \text{ mm}$



1  $\mu\text{sec}$   
(for both traces)

(b) Shot 645,  $v_p = .595 \text{ mm}/\mu\text{sec}$   
 $x_i = 12.0 \text{ mm}$

Fig. 4 - Quartz gauge oscillograms indicating PBX-9404 impact face stress histories

At velocities above  $0.63 \text{ mm}/\mu\text{sec}$ , a very early increase in stress was observed, which may be due to some chemical energy release almost immediately behind the input shock front, or may be a manifestation of strain-rate dependent stress behavior as was observed for TNT by Wasley and Walker (22) using quartz gauges at low stresses. For an impact velocity of  $0.707 \text{ mm}/\mu\text{sec}$  (shot 641), chemical reaction appears to be the very likely cause of the

extended stress rise observed on the impact gauge; reaction may also be responsible for the milder excursion at the impact face at an impact velocity of  $0.661 \text{ mm}/\mu\text{sec}$  (Shot 658).

Comparison of Table 1 of impact gauge results with calculated stresses  $\sigma_e$  and  $\sigma_u$  shows that a PBX-9404 "Hugoniot" taken from our impact gauge results would lie distinctly below both Hugoniots of Ramsay and Popolato (18). However, the selection of a single stress value to represent a given experiment seems inappropriate in view of the time dependence of the sample response. The true time dependence of the early shock response appears to be on a shorter scale than our tilt or sample reproducibility will allow us to resolve, since our impact gauge data exhibit scatter in the magnitude of time dependent effects among shots at similar impact velocity.

Regarding the differences in stress-particle velocity states as determined from our gauge observations and the PBX-9404 Hugoniots reported by Ramsay and Popolato, we suggest that over the stress range reported our impact gauge method is probably a more direct method of determining these data. The unsteady behavior which we observe can cause difficulties in the analysis of propagated profile measurements.

In Shot 659 no buffer was used between the PBX-9404 and the target gauge. A compression wave therefore was reflected into the PBX-9404 from the interface with the target quartz gauge, and was subsequently recorded by the impact face gauge. This indicates the feasibility of studying reflected wave behavior in explosives by a quartz gauge method.

#### Target Gauge Results

Target gauge output was analyzed as illustrated in Fig. 3 to estimate stress as a function of time at the downstream face of the PBX-9404 explosive. This steady wave analysis was used even though nonsteady effects have been indicated by the impact gauge. It should serve as a first order estimate to show the magnitude of the growth of the stress. A complete treatment would require information on the time-dependent response functions of the buffer and the unreacted explosive, and chemical reaction considerations including shock loading and unloading behavior of the partially reacted explosive.

Stresses observed in the gauge at each of several times, and the corresponding stresses calculated in the PBX, are listed in Table 1 for

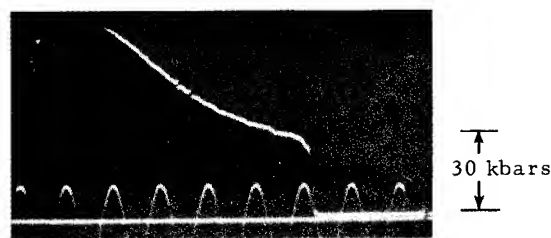
each experiment. In contrast to the impact gauge records, the target gauge records have more rounded initial jumps and did not exhibit large relaxations in stress with time. The buffer layer apparently caused the rounding. Time-resolved measurements by Halpin and Graham (23) of stress histories in Plexiglas at the impact interface and propagated to an interface 5 mm downstream showed (1) a relaxation in stress of 4% in 1.1  $\mu\text{sec}$  at a 15-kbar level, and (2) the propagated stress was about 10% less than impact stress. Dremine, et al., (24) estimated that each millimeter of PMMA buffer reduced the transmitted shock velocity by 0.5% which corresponds to reducing transmitted stress by about 2%/mm, roughly in agreement with Halpin and Graham's observation. Our 3 mm buffer then might reduce transmitted stress signals by ~6%. We have not yet determined a transfer function for our buffer which would allow us to attempt correction for the attenuating effects in wave propagation through Plexiglas.

Target gauge records for Shots 641 through 648 as listed in Table 1 showed stress excursions interpreted to represent clear evidence of substantial reaction occurring 0.2 to 1.1  $\mu\text{sec}$  behind the shock front. Examples of these traces are presented in Fig. 5. The gauge output, and accordingly the incident stress at the downstream face of the PBX-9404, grew in some cases to more than twice the value at the shock front. This increase occurred at sufficiently early times relative to normal gauge recording time that it was clear that the stress growth was real and not an anomaly in quartz response at the higher stress levels.

#### ANALYSIS OF DATA

Ramsay and Popolato (18) have shown that for each level of input stress, there is a corresponding propagation distance to reach detonation in PBX-9404. This correlation is given in a log-log plot in Fig. 6. The method of evaluating parameters discussed below is also demonstrated in Fig. 6.

Let us denote the run distance required to reach detonation as  $X$ , and note that  $X$  is a function of input stress, i.e.,  $X(\sigma)$ . We have used this run distance to detonate in PBX-9404 as a correlation factor for our data. A value of  $X$  pertaining to conditions at the impact face, denoted  $X_i$ , can be calculated from knowledge of the impact stress. In order that our calculations of  $X_i$  would be consistent with the basis of Ramsay and Popolato's correlation, we evaluated impact stress by utilizing our observed



(a) Shot 645,  $v_p = .595 \text{ mm}/\mu\text{sec}$   
 $x_d = 8.0 \text{ mm}$



1  $\mu\text{sec}$   
(for both traces)

(b) Shot 647,  $v_p = .633 \text{ mm}/\mu\text{sec}$   
 $x_d = 6.7 \text{ mm}$

Fig. 5 - Quartz gauge oscillograms indicating PBX-9404 downstream face stress histories

impact velocity and their experimental PBX-9404 Hugoniot (18); values of impact stress thus calculated,  $\sigma_e$ , are listed in Table 1. Values of  $X_i$  for all impact experiments are also given in Table 1. They were calculated from an algebraic expression of the function  $X(\sigma)$  shown in Fig. 6,

$$\ln X_i = 7.638722 - 1.568639 \ln \sigma_e, \quad (1)$$

where  $X_i$  is in mm and  $\sigma_e$  is in kbar.

As mentioned previously, each of our experiments was performed with a sample of thickness,  $h$ , less than the run distance required to reach detonation, i.e.,  $h < X_i$ . Knowing  $X_i$  at the impact face and the sample thickness  $h$ , it was simple to compute a value of  $x_d$ , defined as the remaining run distance to detonation for the disturbance reaching the downstream face of the explosive.

$$x_d = X_i - h. \quad (2)$$

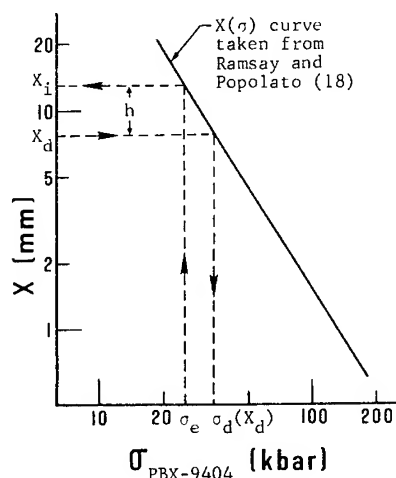


Fig. 6 - Run distance to detonation,  $X$ , in  $1.83 \text{ g/cm}^3$  PBX-9404 as function  $X(\sigma_{\text{PBX-9404}})$  (18). Dotted lines demonstrate evaluation of  $X$  at impact face ( $X_i$ ) and downstream face ( $X_d$ ) of PBX-9404 sample, and anticipated initial stress at  $X_d$ ,  $\sigma_d(X_d)$ .  $h$  = PBX-9404 sample thickness.

Values of  $X_d$  are also tabulated in Table 1 for each experiment.

Since the downstream face of each sample may be considered to be "along the way" in reaction growth toward detonation, it is of interest to examine whether the  $X(\sigma)$  curve is followed in the buildup process in a given explosive sample. That is, as the detonation plane is approached by travel through the sample, the value of  $X$  may be expected to decrease because of the reaction growth. The question we wish to examine is: does the stress in the PBX grow in accordance with this decrease in  $X$ , according to the relation  $\sigma(X)$  derived by inverting the given function  $X(\sigma)$ ? Let us define a stress  $\sigma_d(X_d)$  calculated from the value of  $X_d$  at the downstream face of the PBX-9494 sample according to an inverted form of Eq. (1),

$$\ln \sigma_d(X_d) = 4.869649 - 0.637495 \ln X_d, \quad (3)$$

and compare these stress values with the measured downstream PBX-9404 stress profiles  $\sigma_d(t)$ . As shown in Table 1, the initial measured stresses  $\sigma_d(t)$  are significantly lower than the corresponding calculated values  $\sigma_d(X_d)$ . Agreement improves at high input stress levels.

Study of Table 1 reveals that in each case where reaction appeared within a microsecond,

the value of  $X$  was 10 mm or less. This pertains for the impact stress profiles of Shots 641 and 658, and for the downstream stress profiles of Shots 641 through 648 as listed in the table. Stress growth appeared to occur more rapidly and closer to the shock front as  $X$  was decreased.

Each record showing distinct reaction was observed to have terminated prematurely (i.e., at less than normal gauge lifetime). While in some cases the gauges may have been driven gradually out of their stress range and in other cases mechanical failure of the gauge may have occurred, it was hypothesized that record termination in each case was due to occurrence of a strong reaction which abruptly drove the signals off scale. Figure 7 shows the time of record termination (denoted as an "induction time") for each gauge monitoring an explosive face where  $X < 10$  mm, as a function of  $X$ .

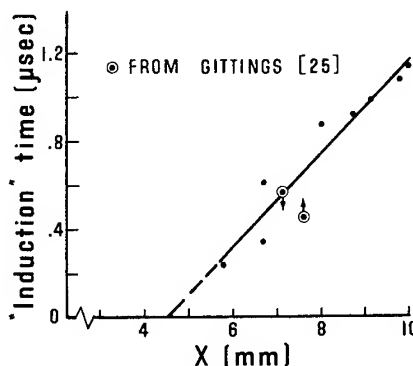


Fig. 7 - Time delay to "runaway" reaction

Two results obtained by Gittings (25) bracketing the impact pulse duration necessary to accomplish initiation of PBX-9404 are also plotted in Fig. 7. She reported the impact of PBX-9404 samples by Dural of 4915 mil thickness at  $0.75 \text{ mm}/\mu\text{sec}$  (resulting in failure to initiate detonation) and of 62.5 mil thickness at  $0.78 \text{ mm}/\mu\text{sec}$  (resulting in detonation). For each set of conditions we calculated impact stress (using data from Ref. 18 and 26), associated run distance to detonation (18), and loading pulse duration. Gitting's data (marked with arrows in Fig. 7 to show direction to initiation threshold) then correlate nicely with ours. In plotting her data in this way, the inference is that if a delayed release of explosive energy at the impact were crucial for initiation at the shock levels of her experiments, the energy release could not be lagging the front by more than the duration of the pulse, or failure to initiate would result.

A straight line appears to be a reasonable fit to the data, which show surprisingly little scatter. The line extrapolates to  $x \approx 4.5$  mm when the "induction" time or lag of the hypothesized strong reaction intercepts zero, i.e., when the strong reaction would be expected to occur very close behind the shock front. Craig and Marshall (8) also estimate that a strong reaction in PBX-9404, initially well behind the shock front, occurs very shortly behind the front when  $x = 5-6$  mm. In this vicinity the shock front stress  $\sigma(x)$  in PBX-9404 is 40 to 50 kbars, according to Eq. (3).

The apparent common correlation in Fig. 7 of time lag to occurrence of strong reaction at impact faces and at downstream faces further suggests that the delay time is independent of the neighborhood, that each element independently experiences a delay probably determined by the strength of the slowly growing shock front which first excited it.

## DISCUSSION AND CONCLUSIONS

Wackerle and Johnson (27) have also performed front-back quartz gauge measurements with a gun technique on PETN pressings in a manner analogous to that reported in this paper. Their observations of stress waveforms at the impact interface and those emerging from target explosive samples corresponded in form to our observations with PBX-9404 except that the excursions were more vigorous at similar input stress levels, due to the higher sensitivity of PETN.

Delayed stress excursions which may be interpreted as substantial reaction well behind the shock front have also been observed in recent photographic studies on PBX-9404 by Craig and Marshall (8) and on PETN pressings by Stirpe, Johnson, and Wackerle (7). The "ionization pulse" observed well behind the shock front in Composition B by Clay, et al., (28) may also be interpreted as due to delayed reaction.

## Reaction Growth

Growth of reaction at the shock front in heterogeneous explosives has been attributed to microscopic reaction sites at points of shock interaction in a rough shock front (5). The newly-observed development of substantial reaction well behind the front, however, is viewed as a form of thermal explosion. When the shock stress is sufficiently high to cause the time lag for the thermal explosion to be very

small, the contributions from interactions and from thermal runaway will be indistinguishable in time, and the maximum stress may be expected to occur at the shock front.

We have not attempted to experimentally examine conditions in PBX-9404 at  $x < 5$  mm, because we are already in an uncomfortably high stress environment for quartz gauge utilization. The data of Craig and Marshall (8), however, at  $x < 5$  mm appear to indicate a shock front with no strong stress excursions following the front. This indicates that transition to growth at the shock front may be present for PBX-9404 at a position near the estimated value of  $x = 5$  mm.

Overshoots in detonation velocity have been noted (2) for shock-initiated homogeneous explosives and have been ascribed to the overtaking of the essentially unreactive shock front by a strong reaction wave (actually a superdetonation). The model of growth at the shock front alone in heterogeneous explosives (5) does not admit detonation overshoot. There are several reported observations of overshoot with heterogeneous explosives, however, including pressed PETN (7), pressed TNT (29), and pentolite, tetryl, and cyclotol (30). To account for these overshoots in heterogeneous explosives it would appear that the reaction occurring behind the front would have to have a "wave" character, in which energy release from one element would increase the pressure in the forward neighboring element in time to enhance its reaction.

The chemical reaction rate expression of a mathematical model suggested by Bernier (31) for initiation of granular explosive compacts contains a factor linear in pressure as well as an exponential (Arrhenius) factor. This model appears capable of describing slow growth at the shock front, an excursion in pressure behind the front, and abrupt explosion after some delay time following shock passage. It deserves attention in view of these recent observations.

## ACKNOWLEDGMENTS

It is a pleasure to acknowledge the help of many persons at Sandia and Los Alamos who contributed to this study. The problem and experimental approach were suggested by O. E. Jones and C. L. Mader. B. G. Craig suggested the use of a buffer and made available preliminary results on his related initiation study, as did J. Wackerle. A. Popolato provided explosive material. G. E. Ingram advised us on gun and quartz gauge methods and R. A. Graham

provided quartz gauge record interpretations. The experiments were prepared and conducted in excellent fashion by O. B. Crump, Jr. and D. L. Allensworth.

# REFERENCES

1. R. A. Graham, F. W. Neilson, and W. B. Benedick, "Piezoelectric Current from Shock-Loaded Quarts — a Submicrosecond Stress Gauge," *J. Appl. Phys.* **36**, 1775-1783 (1965).
2. A. W. Campbell, W. C. Davis, and J. R. Travis, "Shock Initiation of Detonation in Liquid Explosives," *Phys. Fluids* **4**, 498-510 (1961).
3. H. W. Hubbard and M. H. Johnson, "Initiation of Detonation," *J. Appl. Phys.* **30**, 765-769 (1959).
4. C. L. Mader, "Shock and Hot Spot Initiation of Homogeneous Explosives," *Phys. Fluids* **6**, 375-381 (1963).
5. A. W. Campbell, W. C. Davis, J. B. Ramsay, and J. R. Travis, "Shock Initiation of Solid Explosives," *Phys. Fluids* **4**, 511-520 (1961).
6. A. N. Dremin and S. A. Koldunov, "Initiation of Detonation by Shock Waves in Cast and Pelletized TNT," UCRL-Translation-10408 from Vzryvnoye delo **63**, 37-50 (1967).
7. D. Stirpe, J. O. Johnson, and J. Wackerle, "Shock Initiation of XTX-8003 and Pressed PETN," LASL Rept. LA-DC-10970 (1969).
8. B. G. Craig and E. F. Marshall, "Decomposition of a Heterogeneous Explosive when Shocked but Not Detonated," Fifth Symp. on Detonation (1970).
9. Because PBX-9404 is microscopically heterogeneous, true uniaxial strain cannot be imposed. The term "one-dimensional" was used to indicate that no lateral rarefactions could reach the monitored region (the active area of the gauge) during the period of observations.
10. G. E. Ingram and R. A. Graham, "Quartz Gauge Technique for Impact Experiments," Fifth Symp. on Detonation (1970).
11. F. W. Neilson, W. B. Benedick, W. P. Brooks, R. A. Graham, and G. W. Anderson, "Electrical and Optical Effects of Shock Waves in Crystalline Quartz," in *Les Ondes de Detonation*, Editions. du Centre National de la Recherche Scientifique, 391-414, Paris (1962).
12. R. A. Graham, "A Technique for Studying Piezoelectricity Under Transient High Stress Conditions," *Rev. Sci. Instr.* **32**, 1308-1313 (1961).
13. O. E. Jones, F. W. Neilson, and W. B. Benedick, "Dynamic Yield Behavior of Explosively Loaded Metals Determined by a Quartz Transducer Technique," *J. Appl. Phys.* **33**, 3224-3232 (1962).
14. W. S. Halpin, O. E. Jones, and R. A. Graham, "A Submicrosecond Technique for Simultaneous Observation of Input and Propagated Impact Stresses," in *Dynamic Behavior of Materials*, ASTM Special Tech. Publ. No. 336 (1963).
15. S. Thunborg, G. E. Ingram and R. A. Graham, "Compressed Gas Gun for Controlled Planar Impacts over a Wide Velocity Range," *Rev. Sci. Instr.* **35**, 11-14 (1964).
16. Plexiglas is trade name for polymethyl methacrylate produced by Rohm and Haas Co. Aron Alpha, manufactured by Toacosei Chemical Industry Co., Ltd., contains alpha cyanoacrylate. Epoxy resin 602 was used with hardener H2-3490.
17. K. W. Schuler, "Propagation of Steady Waves in Polymethyl Methacrylate," *J. Mech. Phys. Solids* **18**, 277-293 (1970).
18. J. B. Ramsay and A. Popolato, "Analysis of Shock Wave and Initiation Data for Solid Explosives," Fourth Symp. on Det'n, ONR ACR-126, 233-238 (1965).
19. R. A. Graham and G. E. Ingram, "Piezoelectric Current from X-Cut Quartz Shock Loaded from 25 to 70 kbar," *Bull. Am. Phys. Soc. Series II*, Vol. 14, 1163 (1969).
20. Work is actively underway at Sandia Laboratories to define the effects of the various deviations from linear behavior of the gauge over a wide range of stresses and other operating variables, but it not yet completed.
21. W. E. Deal, "Shock Wave Research on Inert Solids," Fourth Symp. on Det'n, ONR ACR-126, 321-345 (1965).

22. R. J. Wasley and F. E. Walker, "Dynamic Compressive Behavior of a Strain Rate Sensitive Polycrystalline, Organic Solid," *J. Appl. Phys.* 40, 2639-2648 (1969).
23. W. J. Halpin and R. A. Graham, "Shock Wave Compression of Plexiglas from 3 to 20 Kilobars," Fourth Symp. on Det'n, ONR ACR-126, 222-232 (1965).
24. A. N. Dremin, O. K. Rozanov, S. D. Savrov, and V. V. Yakishev, "Shock Initiation of Detonation in Nitroglycerin," *Fizika Gor-niya i Vzryva* 3, No. 1, 11-18 (1967).
25. E. F. Gittings, "Initiation of a Solid Explosive by a Short-Duration Shock," Fourth Symp. on Det'n, ONR ACR-126, 373-380 (1965).
26. J. M. Walsh, M. H. Rice, R. G. McQueen, and F. L. Yarger, "Shock Wave Compressions of Twenty-Seven Metals," *Phys. Rev.* 108, No. 2, 196-216 (Oct. 15, 1957).
27. J. Wackerle and J. O. Johnson, private communication (1970).
28. R. B. Clay, M. A. Cook, R. T. Keyes, O. K. Shupe, and L. L. Udy, "Ionization in the Shock Initiation of Detonation," Third Symp. on Det'n, ONR ACR-52, Vol. 1, 150 (1960).
29. S. J. Jacobs, T. P. Liddiard, Jr., and B. E. Drimmer, "The Shock-to-Detonation Transition in Solid Explosives," *NOLTR* 62-197 (April 1963).
30. R. J. Eichelberger and M. Sultanoff, "Sympathetic Detonation and Initiation by Impact," *Proc. Roy. Soc.* A246, 274-281 (1958).
31. H. Bernier, Contribution to the Study of the Initiation of Detonation Produced by Impact on an Explosive, Thesis, U. of Paris (1964).



# MEASUREMENT OF MASS MOTION IN DETONATION PRODUCTS BY AN AXIALLY-SYMMETRIC ELECTROMAGNETIC TECHNIQUE

B. Hayes and J. N. Fritz

*University of California, Los Alamos Scientific Laboratory  
Los Alamos, New Mexico 87544*

## ABSTRACT

A new electromagnetic technique for measuring mass velocity is described in this report. Time-varying magnetic fields from eddy currents in a foil moving in a nonuniform steady field produce a signal in an external coil that is almost proportional to the velocity of the foil. Large noise-free signals are obtainable and one-dimensional flow can be maintained in the experiment. Data reduction is numerically more complicated than in the older electromagnetic techniques but is easily accomplished with the aid of modern computers. Some initial experiments where the technique is applied to a study of detonation product motion are described.

## INTRODUCTION

The Zavoiskii method of measuring mass flow velocity as used by Dremine, et al. (1), and Jacobs and Edwards (2), uses the motion of a small embedded conducting ribbon in a transverse magnetic field to generate a voltage which is delivered to an external circuit by direct connections through the shocked material. In this note a different electromagnetic technique is described. Instead of obtaining a voltage by a direct connection to a moving ribbon, a time-varying magnetic field produced by eddy currents in a moving foil induces a secondary current in a pickup coil located outside of the shocked material. The pickup coil acts as an electromotive force generator across the impedance of a transmission line used to carry signal voltages to recording devices.

This new technique, suggested and partially developed by R. S. Caird of this Laboratory to study shock-wave behavior in inert materials (unpublished work), was adapted to explosive product experiments when it was learned that the conductivity of detonation products did not affect eddy current generation in

high-conductivity foils. Stacked disks of explosive can be used that avoid longitudinal cuts which might cause perturbations and jetting. The moving conductor is usually a very thin metal foil sandwiched between layers of explosive. Although the detonation is probably quenched by the foil and must be reinitiated, no non-one-dimensional perturbations are introduced into the flow.

Some disadvantages of the conceptually simple Zavoiskii method are assembly difficulties, the uncertainty of circuit integrity throughout the observation time, and the problems associated with obtaining a proper transverse magnetic field. Either a proper field occupies a large volume and is homogeneous, so that early motions of conductors do not cause the flux in the embedded loop to change, or it is in a volume small enough to be unaffected by other moving conductors before and during the time of measurement. By contrast, the magnetic field employed for the pickup coil method is the near field from a current driven circular loop or a cylindrical bar magnet. The important quantity now is the radial magnetic component  $B_p$  of the field at the moving foil.

This work performed under the auspices of the U.S. Atomic Energy Commission.

Ideally, the foil should have zero thickness and infinite conductivity. The magnetic lines of force would then be effectively pinned to the foil surface. The motion of the foil is then transmitted to a motion of the lines of force as they adjust to a minimum energy configuration. From this point of view the projection of the pickup coil along the lines of force onto the foil is the effective area under observation. To a certain extent, the circumference of this projected image is equivalent to the cross length of the Zavoiskii probe and some effective  $B_p$  is equivalent to the transverse field. However, the simple Lorentz magnetohydrodynamic expression obtained by this analogy which relates the output voltage directly to the particle velocity, effective foil length, and the magnitude of the transverse field is not sufficiently accurate.

To obtain velocity-time records with the axial magnetic probe,  $B_p$  in the volume swept out by the moving foil must be known. The problem of calibrating and mounting permanent magnets in order to obtain a known field at the foil is under study and development. Also under development is a numerical code that utilizes  $B_p$  and the output voltage to calculate mass velocity. The general method being used is to treat all conductors as finite circular elements, each of which is an inductance-resistance circuit, and each of which is inductively coupled to all other elements. In the interim, an exact solution to the following somewhat idealized problem has been obtained. A source current loop produces a magnetic field and a foil of zero thickness and finite surface conductivity has a step function velocity profile applied to it. For these conditions the voltage response in a single pickup coil located on the axis has been calculated. Since the fields are linear, with the possible exception of the back reaction of the eddy current field on the permanent magnet, which could be shielded, one can add sources and pickup loops for the same velocity to approximate the response of a given experimental configuration. Of course, even without calibration, relative velocities are immediately obtained from the output voltage for geometries that have a relatively constant sensitivity function. This sensitivity function, defined as volts/velocity (v/mm/ $\mu$ sec) vs time or distance following a step function increase in the velocity, will depend on the instantaneous geometry and the past diffusion of the fields. For a wide range of experimental conditions the sensitivity function can be nearly constant so that the output voltage of a pickup coil will be directly proportional to foil velocity.

## THE IDEALIZED PROBLEM

The magnetic fields produced by the eddy currents in a thin foil of large lateral extent undergoing a general motion in the Z-direction can be represented by a succession of image sources located at suitable distances behind the plane of the foil. Let the  $Z = 0$  plane of a coordinate system be the original plane of the foil, the source be located at  $Z_s$  and the pickup coil at  $Z_c$ . The motion of the foil is represented by  $Z_f(t)$ , and  $U_p(t)$  is the time derivative of this function. Without loss of generality we can let the source be a single-turn current loop with current  $I_0$ . One image that is always present is the "optically reflected" one. The distance from the pickup coil to this image source,  $Z_1$ , is given by

$$Z_1 = Z_c - Z_f(t) + Z_s - Z_f(t) ,$$

and the current by

$$I_1 = -I_0 U_p(t) / [U_i + U_p(t)] .$$

The quantity  $U_i$  is the recession velocity of the other images due to diffusion of the original field through the foil. It is obtained from the relation:

$$U_i = 2/\sigma_s \mu_0 ,$$

where  $\sigma_s$  is the surface conductivity of the foil and

$$\mu_0 = 4\pi \times 10^{-7} \text{ h/m} .$$

Each interval of acceleration of the foil from

$$t^- \text{ to } t^+$$

[where

$$Z_f(t^+) - Z_f(t^-)$$

is small compared to the distance of the imaged source to the pickup coil] spawns another image source. The distance of this image from the pickup coil is given by

$$Z_2 = Z_c - Z_f(t) + Z_s - Z_f(t^+) + U_i(t - t^+)$$

and it has a current amplitude

$$I_2 = I_0 U_i (U_p^+ - U_p^-) / [(U_i + U_p^+)(U_i + U_p^-)] .$$

This single image is an approximation to a continuous succession of images created by velocity changes. Clearly a variable velocity can be approximated as closely as one pleases by choosing finer intervals and more images. For a step function in the velocity there are only two images. Proofs of these assertions will be left to a later, more detailed report.

For a step function in the velocity

$$[U_p(t > 0) = U_p, \quad \text{a constant}] ,$$

the induced voltage,  $V_i$ , in the pickup loop is given by the negative time derivative of the flux produced in the loop by the two images of the source. Since the currents in the images are constant for this case, the entire time dependence is contained in the coefficients of mutual inductance between the source images and coil. We have

$$\phi = L_{c1} I_1 + L_{c2} I_2$$

$$L_{ci} = \mu_0 \sqrt{\frac{4\rho_c \rho_s}{k_i^2}} \left[ \left(1 - \frac{1}{2} k_i^2\right) K(k_i) - E(k_i) \right]$$

$$k_i^2 = 4\rho_c \rho_s / [(\rho_c + \rho_s)^2 + Z_i^2]$$

$$-dL_{ci}/dt = \mu_0 Z_i [dZ_i/dt] f(k_i) / \sqrt{4\rho_c \rho_s}$$

$$f(k) = k \left[ \frac{1 - \frac{1}{2} k^2}{1 - k^2} E(k) - K(k) \right]$$

$$I_1 = -I_0 U_p / (U_i + U_p) \quad I_2 = I_0 U_p / (U_i + U_p)$$

$$Z_1 = Z_c + Z_s - 2U_p t \quad Z_2 = Z_c + Z_s - U_p t + U_i t$$

$$dZ_1/dt = -2U_p \quad dZ_2/dt = -U_p + U_i$$

In these equations  $\rho_c$  and  $\rho_s$  are the radii of the pickup and source loop respectively, the expression for  $L_{ci}$  is the coefficient of mutual inductance between coaxial current loops, and  $K(k)$  and  $E(k)$  are the complete elliptic integrals of the first and second kind. From the relation,  $V_i = -d\phi/dt$ , the following expression is obtained for the voltage induced on a single turn of the pickup coil due to a current loop in the source:

$$V_i/\text{turn} = \mu_0 I_0 U_p \frac{2Z_1 f(k_1) - (1 - U_i/U_p) Z_2 f(k_2)}{(1 + U_i/U_p) \sqrt{4\rho_c \rho_s}}$$

A surface current sheath can be used to approximate the right circular permanent magnet used as a source. This sheath can in turn

be approximated by  $N$  current loops. The radius, length and strength of this current sheath can be varied to obtain a best fit to measurements of  $B_z$  along the axis of the magnet. Although a fit of  $B_c$  at the foil surface would be preferable, a precise fit of  $B_z$  along the axis guarantees a correct  $B_c/\rho$  near the axis through the divergence equation for  $B$ . This method of mocking up the source was chosen because of the simplicity of the expression for  $B_z$  along the axis:

$$B_z = \frac{\mu_0 J}{2} \left[ \frac{Z + L/2}{[(Z + L/2)^2 + \rho_s^2]^{1/2}} - \frac{Z - L/2}{[(Z - L/2)^2 + \rho_s^2]^{1/2}} \right]$$

In this expression  $Z$  is measured from the mid-point of the magnet,  $L$  is the total length of the current sheath,  $\rho_c$  is its radius and  $J$  is the magnitude of the surface current. Clearly  $I_0 = JL/N$  and the rings are spaced  $L/N$  apart and centered on the mid-point of the magnet.

## AN EXPERIMENTAL SYSTEM

The experimental arrangement of components and equipment used in the present study is shown in Fig. 1. With this setup, the motion of the metal foil embedded in the test explosive is observed by recording the voltage which is derived from a current induced in the external pickup coil. The magnetic probe consists of the metal foil, the pickup coil, and the permanent cylindrical magnet. The explosive booster, 20 cm in diam, consisted of a planewave lens, a PBX-9404 driver explosive pad, 50.4 mm thick, and a lead attenuator plate 5.59 mm thick. The purpose of the lead is to provide a nearly rigid rear boundary for distance-time graphs whose slopes are detonation velocity and particle velocity.

For the present shots 1-mil copper foil was laid between pads of fine-grained PBX-9404 explosive. The test explosive consisted of a stack of three disks, each 74-mm diam by 2.54 mm thick. The high conductivity foil was between the second and third disks. A printed-circuit spiral pickup coil of the kind shown in Fig. 2 was placed on the upper explosive surface and a cylindrical bar magnet was mounted with its north pole 12.7 mm above the coil. The axis of the magnet and the coil were coincident with the explosive charge axis to achieve axial symmetry. Surrounding the test explosive was a mineral oil bath to suppress extraneous electrical noise and provide some degree of confinement.

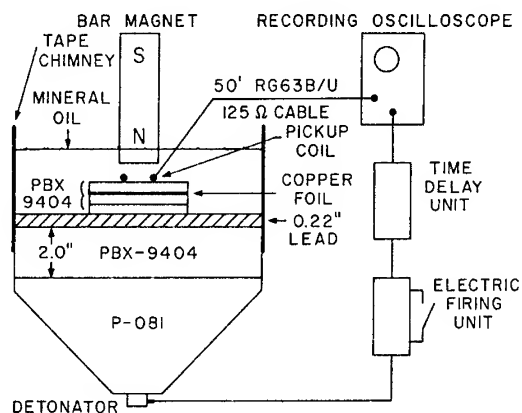


Fig. 1 - Schematic diagram of a magnetic probe experiment. The motion of the embedded copper foil in the nonuniform magnetic field induces a current in the pickup coil. The voltage developed across the impedance of the terminated transmission line is displayed on a high speed oscilloscope.

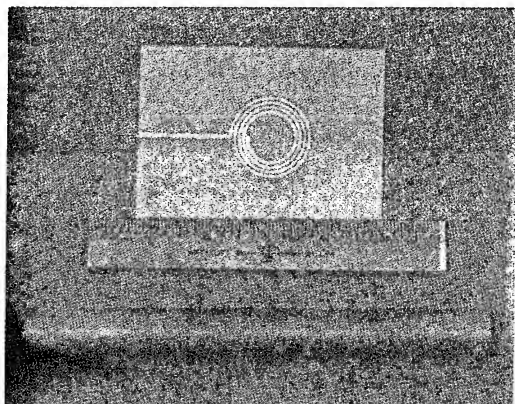


Fig. 2 - Printed-circuit pickup coil and bar magnet. Connection to the interior end of the coil is made through a hole in the phenoxy substrate. With the coil mounted face up on the explosive and the center conductor of the signal lead connected to the interior end of the coil, a positive signal is generated when the foil moves toward the north pole of the magnet. The magnet is an Arnold Engineering Company Alnico-5 Type 5C58A bar magnet.

The pickup coil was connected via a 125-ohm signal cable to the input of a 125-ohm Tektronix Type 519 traveling wave cathode ray tube oscilloscope. The coil was constructed to have a 5-nsec rise time response and to operate in an over-damped mode to prevent ringing. Coils with faster response are practical and are being

considered for future work. Coil response expressions are given in the Appendix.

After the interruption of the detonation wave by the foil, and the subsequent reestablishment of detonation downstream from the foil, it is assumed that the embedded foil moves with the particle velocity of the explosive detonation products after the subsidence of transients resulting from shock reverberations in the foil. It is known from many experiments that these events are present, but to what extent they affect gross results have not been established (3).

An oscilloscope trace obtained from the shot sketched in Fig. 1 is shown in Fig. 3. The upper and lower timing marks are superimposed before and after the shot record and consist of 10- and 100-nsec time calibration intervals. The interpretation of the waveform shown is as follows. The shock wave from the lead enters the test explosive at time  $t_A$ , and shortly thereafter at  $t_B$  the reactive shock run in the test explosive becomes a detonation as indicated by the flat horizontal portion of the trace. At time  $t_C$  the detonation wave arrives at the interface between the first and second explosive disks as indicated by the small interfacial electric signal. Steady state detonation resumes after the wave crosses the interface until the detonation wave contacts the embedded foil at time  $t_D$ . The small negative pulse on the wave trace is generated by the deposition of charge from the detonation front on the embedded foil. This small signal is followed by the magnetic probe signal, which starts as a rapidly rising positive voltage resulting from the forward motion of the foil.

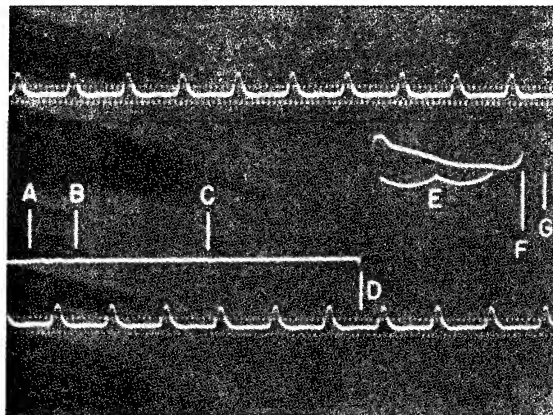


Fig. 3 - The voltage waveform from a magnetic probe showing event time signals as well as mass motion. See text for a complete explanation.

The structure of the wave trace over the region designated  $t_E$  includes the details of the initial motion of the foil and the effects of reverberation of shocks in the foil, all smeared by the finite pickup coil response. An unambiguous interpretation of this initial rise is prevented by the uncertainty of the existence of similar reaction products on either side of the foil. Nevertheless, qualitative features of the flow do appear. There appears to be a steady state region which lasts 20 to 30 nsec. The succeeding, decaying part of the record corresponds to the expected decreasing mass velocity. The break in the middle of the  $t_E$  region may be the end of the Taylor wave caused by the back boundary piston. At time  $t_F$  there is an upward swing to the signal produced as the detonation wave approaches the pickup coil. Finally, the sharply rising detonation electric effect signal appears on the coil followed by coil destruction at time  $t_G$ . Detailed structure of the foil-motion portion of the wave trace is provided by operating two oscilloscopes in tandem with different delay and sweep speed settings. A fast sweep record of this same shot is shown in Fig. 4, where the marker period is 5 nsec. All the features previously discussed are visible. The clarity of the record is due in part to the high signal-to-noise ratio (the peak amplitude of the voltage is approximately 10 v) and the avoidance of direct contact with detonation waves by signal conductors.

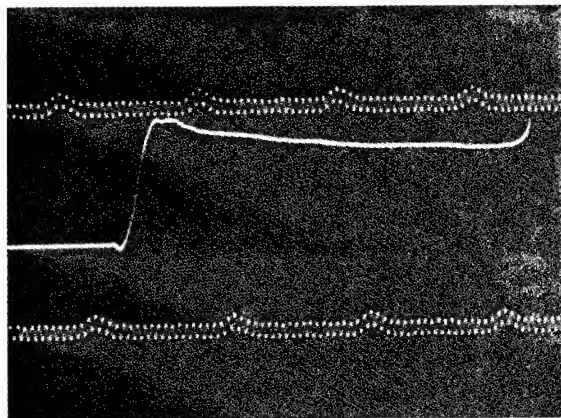


Fig. 4 - Expanded sweep record of Fig. 3

Another record of a magnetic probe experiment is shown in Fig. 5. For this record the shot geometry of Fig. 1 was again used, but the pickup coil was a 4-turn helix wound on a 12.7-mm diam polystyrene rod. In addition, the magnet was turned over to determine the

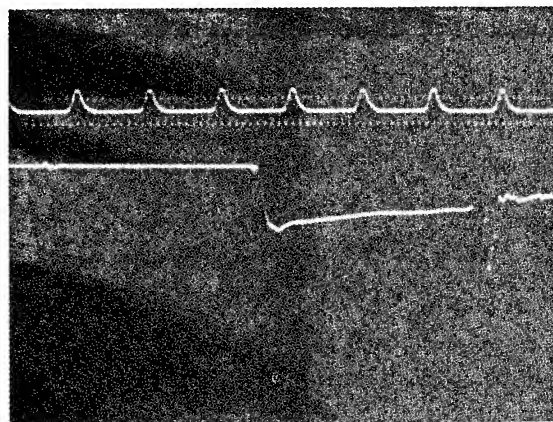


Fig. 5 - A magnetic probe record using a 4-turn helical pickup coil. The time marks are separated by 10 and 100 nsec.

effect of detonation electric signal response. Again, the same overall qualitative response is present. The initial negative pulse is evident, and the final positive upswing to the wave trace is present. In addition, the general shape of the magnetic probe signal after the initial rise corresponds closely to the response of the printed circuit coil. The main difference between the two shots appears to be the initial transient overshoot, which at present is being attributed to coil response.

Particle velocity profiles for the experiments discussed above have not been constructed because calibrated magnets were not used and the sensitivity function for the geometric configuration employed was not determined. The sensitivity function for a particular geometry can be experimentally obtained by using the constant velocity from the free surface of a metal plate to generate a magnetic probe voltage as a function of time. The wave trace obtained in this manner can be used to transform other wave traces to particle motion profiles when using similar geometric configurations.

An example of an experimental trace together with a calculated trace for the boundary conditions of the experiment is shown in Fig. 6. For this record the setup shown in Fig. 1 was employed with the lead and test explosive replaced by a 25-mm thick aluminum plate, 200-mm diam. A spiral coil was mounted 3 mm above the aluminum and a cylindrical bar magnet having a pole face strength of 1340 G was mounted 15 mm above the coil. The dots above the wave trace are the predicted output voltage using a free surface velocity of 3.16

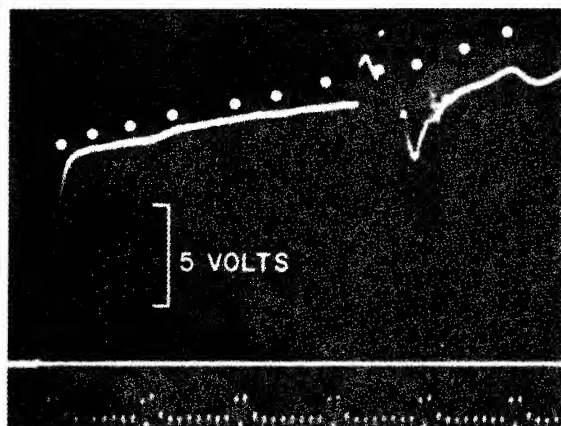


Fig. 6 - Comparison of a calculated trace (dots) with an experiment (solid curve) using an aluminum free surface as a constant velocity exciter for a magnetic probe. Time mark calibrations are separated by 10 nsec.

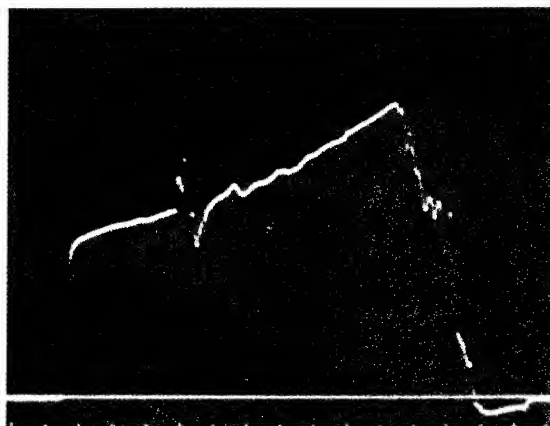


Fig. 7 - An overall record of an aluminum free surface exciting a magnetic probe. Time marks are spaced 100 nsec apart. Air shock causes the central portion of the record to be distorted. The peak signal represents the time for the aluminum to cross a 3-mm gap. For the geometry employed the initial sensitivity coefficient is about 3-V/mm/ $\mu$ sec.

mm/ $\mu$ sec for the aluminum.\* Part of the discrepancy between the predicted values and the observed values is attributed to cable loss which amounts to a few percent for 50-ft lengths. The large pulse in the middle of the record is caused by air shock contacting the coil. This disruption in the record persists until the coil is destroyed by the free surface contacting the coil. The time from the beginning of the magnet probe record to coil destruction can be used to determine the average free surface velocity. The calculated velocity in turn can be used to determine an initial vertical sensitivity factor. In this manner dynamic calibration factors are determined. An overall record for the experiment just described is shown in Fig. 7.

## CONCLUSIONS

A system for measuring the mass flow in detonation products has been developed, which differs from the Zavoiskii technique by using an external coil as part of the sensing device instead of conductors embedded parallel to the particle stream. The chief advantage of the system is that the signal line to recording equipment does not encounter the electrified detonation front of the explosive, the interaction potential associated with detonation products, or shock voltages from dynamic compressions

of nonreactive components. The signal-to-noise ratio is usually high because of the long effective coil length and the relatively low conductivity of the detonation products compared to the foil conductivity. Better signal waveforms are being sought through improvement in the embedded foil where the electrical and material properties interact to distort true fluid motion during the interaction time. For best results, coil time constants and reverberation times on the order of a nanosecond seem desirable in order to achieve spatial resolution of a few micrometers.

The principal drawback to this magnetic probe technique lies in data reduction. There is no simple procedure, either static or dynamic, to convert signal voltages to absolute velocity values. Even relative velocity measurements can be in error if the sensitivity function is not a constant. Magnet size, foil conductivity and size, and other geometric factors influence the sensitivity function. However, these numerical complications have been overcome with the aid of modern computers, and precise measurements of the  $B_0$  field permit the absolute determination of particle velocities.

## APPENDIX I

### Pickup Coil Design

Magnetic probe resolution and signal amplitude are determined in part by the pickup

\*Measurements of  $B_z$  along the axis for this magnet were used to determine parameters for the equivalent current sheath used in calculating this output voltage.

coil. To insure proper pickup coil response, parameters must be selected to maximize signal bandwidth. The coil can be visualized as a four-terminal network connecting an input voltage to a load. Lumped parameters can represent the network provided no physical dimensions exceed approximately 1/16 the wavelength of the highest frequency of interest. The equivalent circuit is then an inductor  $L$  in series with a resistor  $R$  shunted by a capacitance  $C$  and the impedance  $Z$  of a transmission line. For this arrangement the transfer expression is a second order, constant coefficient, inhomogeneous differential equation which can be written

$$A \frac{d^2V}{dt^2} + B \frac{dV}{dt} + V = DV_i \quad (I.1)$$

where  $A = LCD$ ,  $B = (RC + L/Z)D$ ,  $D = (1 + R/Z)^{-1}$ ,  $V$  is the output voltage, and  $V_i$  is the induced emf from magnetic flux linkage.

A perfect coil would be one with the coefficients  $A$  and  $B$  equal to zero and  $D$  having a value of unity. This condition can be approached in a coil having a very small capacitance, a moderate inductance, a small series resistance, and a large load impedance. For the practical case assume  $V_i$  to be a step function,

then the closed form solution of Equation (I.1) can be written\*

$$V = D \left[ 1 - \frac{ae^{-t/a} - be^{-t/b}}{a - b} \right] V_i \quad (I.2)$$

where

$$a = (1/2)B[1 - (1 - 4A/B^2)^{1/2}] \quad (I.3)$$

$$b = (1/2)B[1 + (1 - 4A/B^2)^{1/2}]$$

From the above expressions it is apparent that the quantity  $4A/B^2$  must be less than unity for the coil to operate in an overdamped mode free from self-oscillation. The parameters for the two different coil types used in the present experiments are given in Table 1. The major differences in the coils are the values of the inductance and capacitance. The resistance values are similar since they represent high frequency surface resistance of copper at 50 MHz: the approximate operating frequency of the test equipment.

\*G. Doetsch, "Anleitung Zum Praktischen Gebrauch Der Laplace-Transformation," R. Oldenbourg Munchen, 1956, p. 141, No. 38.

TABLE 1  
Pickup Coil Parameters

Quantity	Printed Circuit Coil <sup>a</sup>	4-Turn Helical Coil <sup>b</sup>
$L$	673 nH	519 nH
$R$	737 MΩ	719 MΩ
$C$	2.82 pF	7.66 pF
$Z^c$	125 Ω	125 Ω
$A$	$1.886 \times 10^{-18} \text{ sec}^2$	$3.952 \times 10^{-18} \text{ sec}^2$
$B$	$5.354 \times 10^{-9} \text{ sec}$	$4.158 \times 10^{-9} \text{ sec}$
$D$	0.994	0.994
$4A/B^2$	0.263	0.914
$a$	0.38 nsec	1.47 nsec
$b$	4.97 nsec	2.69 nsec
$V_0/V_i$ @ 5 nsec	60%	69%

<sup>a</sup>As shown in Fig. 2. The coil constants were measured on a Boonton Type 160-A Q-meter.

<sup>b</sup>The helical coil was closely wound from No. 12 Formvar-covered copper wire on a 0.5-in. diam polystyrene rod.

<sup>c</sup>125 Ω corresponds to the nominal input impedance of Type RG-63B/U coaxial cable.

In order to assess the response of the two coils, it is necessary to compare the voltage ratio from each of them at some particular time. Thus, at  $t = 5$  nsec the output of the printed circuit system has reached 60% of the final value while that of the helical system has reached 69%. It should be noted, however, that the magnitude of the output signal will be approximately 23% greater from the printed circuit coil than from the helical coil for the same excitation due to the higher initial inductance of the printed circuit coil. Thus, for nearly the same bandwidth the efficiency of the printed circuit coil is considerably better than that of the helical coil. At present the coil limits the rise time of the system. To match the 0.4-nsec

rise time of the oscilloscope system a coil with approximately 50 nH would be required.

#### REFERENCES

1. A. N. Dremin, "Structure of Shock Waves in KCl and KBr under Dynamic Compression at 200,000 atm," *Combustion, Explosion and Shock Waves*, 1, No. 4, pp. 3-9 (1965).
2. S. J. Jacobs and D. Edwards, this symposium.
3. B. Hayes, "The Detonation Electric Effect," *J. Appl. Phys.*, 38, pp. 507-511 (1967).



**Session VI**  
**FLOW DYNAMICS AND THERMODYNAMICS**

Chairman: Mark L. Wilkins  
*Lawrence Radiation Laboratory*

# EXPLOSIVE DEFLECTION OF A LINER AS A DIAGNOSTIC OF DETONATION FLOWS

M. Defourneaux and L. Jacques  
*French-German Research Institute  
of Saint-Louis (France)*

## ABSTRACT

The observation of the flow boundaries on both sides of an explosive slab, detonating parallel to its surface and coated on one side by a liner, provides important information on the detonation and the flow behind it. The polytropic exponent, the chemical energy released in the detonation and the maximum fraction of this energy which can be transferred to the liner are calculated for a certain number of RDX/TNT and similar compositions, under different loading densities. The behavior of various additives -- inert components, oxydizers and fuels -- is also investigated, and some general rules are established.

## PRINCIPLE OF THE METHOD

The behavior of condensed media under detonation loading is classically investigated through velocity measurements, especially free-surface velocity and final velocity  $v$  reached by a liner coating an explosive mass. In the second case, the liner mass constitutes an available parameter to be related with  $v$ , so this method provides a great deal of information on the detonation and the flow. This is why it has been used by several authors (1, 2, 3) in order to calculate the parameters of some equations of state for the detonation gas, and also in the present work, whose initial aim was to classify high explosives on the basis of the maximum kinetic energy they are able to transfer to a liner in the lateral projection geometry -- i.e., when the liner is a plane sheet coating one of the faces of a plane explosive slab detonating parallel to its surface (Fig. 1) -- in order to optimize shaped charges (4 - 5).

Now, when very simple equations of state are used, involving only one experimental parameter, for instance the polytropic exponent  $\Gamma$ , it is not even necessary to investigate the dependence of  $v$  on the liner mass: measuring the limiting velocity of the flow without any liner can provide the value of this parameter.

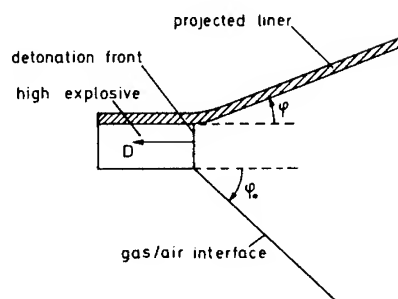


Fig. 1 - Flow behind a plane detonation wave with lateral confinement

Let us consider the geometry described in Fig. 1. Assuming all dimensions of both the explosive slab and the liner -- except their thicknesses -- to be infinite, the flow is two-dimensional and steady when studied in a coordinate system moving with the detonation, and its boundary is a surface associated with the detonation front. Combining the polytropic theory with a C-J detonation shows that, in vacuum, it is a plane whose inclination  $\phi_0$  on the slab is given by:

$$\phi_0 = \frac{\pi}{2} \left( \sqrt{\frac{\Gamma + 1}{\Gamma - 1}} - 1 \right). \quad (1)$$

Thus, by measuring only  $\phi_0$ , the value of  $\Gamma$  can be calculated. This enables the computation of important parameters such as the detonation pressure,

$$p_{cJ} = \frac{\rho_e D^2}{\Gamma + 1} \quad (2)$$

$$\times 10 \quad \text{if} \quad \begin{cases} p_{cJ} \text{ in kbar} \\ \rho_e \text{ in g/cc} \\ D \text{ in mm}/\mu\text{s} \end{cases},$$

and the chemical energy  $E_c$  of the high explosive

$$E_c = \frac{D^2}{2(\Gamma^2 - 1)}, \quad (3)$$

where  $\rho_e$  is the explosive density and  $D$  its detonation rate.

Now, the polytropic theory is only an approximation, so that the value of  $\Gamma$  is an averaged one, unfortunately different for each of the equations above, and depending on the pressure range considered in the experiments. When  $\Gamma$  is determined from free-surface velocities in a metal, its average value is calculated between pressures  $p_{cJ}$  and  $p_s$ , respectively, in the detonation front and in the material behind the shock wave. When  $\Gamma$  is induced from measurements of  $\phi_0$ , through Eq. 1, its average value is calculated between pressures  $p_{cJ}$  and  $p_a$ ,  $p_a$  being the pressure of the shock wave which precedes the gas-air interface when the experiments are carried out in air (see following paragraphs).

A mere continuity argument shows that

$$\Gamma \equiv \left( \frac{\partial H}{\partial E} \right)_s \rightarrow \gamma \equiv \frac{c_p}{c_v} \quad \text{when} \quad p \rightarrow 0, \quad (4)$$

$\gamma$  being the classical ratio of specific heats in the perfect gas. This means that  $\Gamma$  decreases with pressure, a result which can be more precisely induced from computations (6).

Since normally  $p_a \ll p_s$ , it can be guessed that the values of  $\Gamma$  induced from measurements of  $\phi_0$  will be smaller than those induced from shock-wave measurements in condensed media. This will be actually seen in the following results.

Then, calculating  $p_{cJ}$  through Eq. 2 using this low value of  $\Gamma$  will lead to overestimated detonation pressures, but on the contrary, the corresponding value of  $E_c$  should be rather valuable since Eq. 3 is derived from an integration from pressure  $p_{cJ}$  to vacuum. Unfortunately, this calculation is rather unprecise, since  $\Gamma$  is strongly dependent on  $\phi_0$ .

## BALLISTIC PROPERTIES OF HIGH EXPLOSIVES

Although the value of  $\Gamma$  should be sufficient to characterize the whole flow, and in particular to calculate energy transfers to a liner either in the experimental geometry of this work (3) or in a one-dimensional and unsteady one (7), direct measurements of this transfer were carried out. When one of the sides of the explosive slab is coated by a liner, indeed, the angle of deflection  $\phi$  of this liner must be smaller than  $\phi_0$  (Fig. 1), and a decreasing function of mass ratio  $\mu$  defined as follows:

$$\mu = \frac{\text{mass of liner per surface coated}}{\text{mass of explosive per surface coated}}. \quad (5)$$

The velocity  $v$  reached by this liner can be easily calculated:

$$v = 2D \sin \frac{\phi}{2} \approx D \cdot \phi, \quad (6)$$

and  $\phi$  can be experimentally measured by means of flash radiography. The relationship between  $\phi$  and  $\mu$  has already been studied (8, 9). Plotting  $1/\phi$  vs.  $\mu$  gives a curve which can be practically identified with its asymptote, except for very low values of  $\mu$  (Fig. 2), so that:

- The momentum  $I = \mu v$  of the liner per mass of high explosive increases with  $\mu$  and tends toward an asymptote  $I_\infty$  when  $\mu \rightarrow \infty$ ;
- Its kinetic energy  $E = 1/2 \mu v^2$  per mass of high explosive tends toward 0 when  $\mu \rightarrow \infty$ , and goes through a maximum  $E_m$  for a certain value of  $\mu$ .

$I_\infty$  is identical to the specific impulse classically defined for propellants, and  $E_m$  is a very important parameter called "ballistic coefficient."  $I_\infty/D$  and  $E_m/D^2$  are only functions of  $\Gamma$ , as well as the ratio  $E_m/E_c$ . This dimensionless ratio is the maximum amount of chemical energy the high explosive can transfer to the liner as kinetic energy; it was called its "ballistic efficiency" RB.

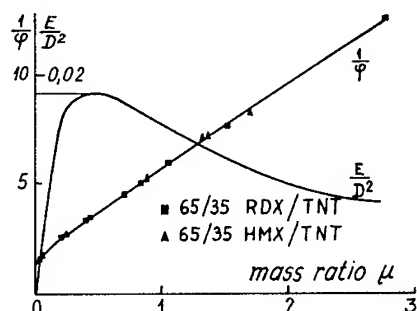


Fig. 2 - Variations of  $1/\phi$  and  $E_m/D^2$  vs. mass ratio for 65/35 RDX/TNT and HMX/TNT

The ballistic coefficient  $E_m$  was taken as the basis of the aforementioned classification of high explosives. Other geometries can of course be taken for the same purpose, including the shaped charge itself (10). The cylindrical geometry, in fact, has often been used (2, 11, 12). Its advantage over the present charge is to avoid edge effects, but its results depend somewhat on the nature of the casing used. Besides, applying Gurney's approximation (11) to this geometry shows that there is neither a maximum for  $E$  nor an asymptote for  $I$ :  $I \rightarrow \infty$  when  $\mu \rightarrow \infty$ , and  $E$  tends monotonically toward an asymptotic value  $E_\infty$ . The existence of the intrinsic values  $I_\infty$  and  $E_m$  constitutes the theoretical advantage of the present geometry, the simplicity of its experimental arrangement being the practical one. Now the real flow, experimentally studied, is rather different from the idealized theoretical one, since none of the dimensions involved is infinite. They were even very small in our experiments:

-  $130 \times 45 \times 10$  mm for the explosive slab;

-  $130 \times 35 \times \epsilon$  mm for the liner

$$(0.3 \leq \epsilon \leq 10) .$$

The reason for taking such small dimensions was the aforementioned ballistic classification of high explosives, which remained the first aim of this study. This classification did not allow very large-scale experiments, due to the large number of samples to be tested, but on the contrary it admitted the imprecision of small-scale ones, since only relative values were looked for, at least in its first phase. This is the reason why, in the following discussions, the values found for  $\Gamma$ ,  $E_m$  and  $RB$  will not be taken as absolute ones, but rather used in comparisons between different high explosives arranged in series and studied in identical conditions.

#### DETERMINATION OF THE POLYTROPIC EXPONENT $\Gamma$

The values calculated for  $\Gamma$  in a low range of pressures are expected to be lower than those calculated in higher ranges. This does not matter as long as no extrapolation is made from one range to the other, and this low-pressure average of  $\Gamma$  is in fact very valuable for the ballistic properties of high explosives, i.e., when detonation products are used to accelerate a liner in air.

Now, calculating  $\Gamma$  directly from the value of  $\phi_0$  measured in air would lead to a strong mistake. This angle, indeed, is smaller in air than in vacuum, since the expansion of the gases is limited by the pressure  $p_a$  behind the shock wave which precedes the gas-air interface (Fig. 3a). An order of magnitude can be given for this pressure: its value  $p_a = 500$  bar for 65/35 RDX/TNT at normal density. This is enough to create a difference of several degrees between the measured value  $\phi'_0$  in air and the theoretical one  $\phi_0$  in vacuum.

This difference can be easily calculated when the shock wave is attached to the detonation (Fig. 3a), but the calculation is much more difficult when it gets detached from it, because in that case, besides the intrinsic complexity of the mathematical problem, the shock wave is no longer straight (Fig. 3b). The existence of this embarrassing configuration is due to the fact that the shock polar for air, corresponding to the Mach number  $M$  of the interface, does not intersect the detonation gas adiabat (Fig. 3c). The limiting value between both configurations depends on  $\Gamma$  and  $M$ . For usual explosives, it was found to be about  $45^\circ$ .

In order to avoid all these corrections, the question might be asked: why not make the experiments directly in vacuum?

The first answer is that it makes the experimental arrangement much more complicated, but besides, such experiments have already been carried out (13) and they have given very surprising results: the value found for  $\phi_0$ , indeed, was considerably higher than expected, sometimes higher than  $90^\circ$ . This shows that the real limiting velocity  $w_\infty$  in vacuum is much higher than the calculated value, a result which had already been found by other authors (14) in frontal expansion.

The origin of this very important discrepancy might be the failure of the  $\Gamma$ -law since, according to Eq. 6, this assumption becomes absurd for expansions down to zero pressure,

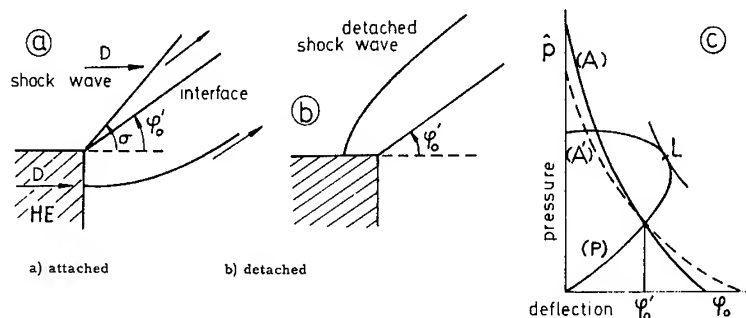


Fig. 3 - Shock wave in air induced by a lateral detonation: (a) attached, (b) detached, and (c) principle of calculations: (A) theoretical adiabat of detonation products ( $\Gamma$  assumed constant); (A') real adiabat (variable  $\Gamma$ ); (P) shock polar for air.

and the averaged value of  $\Gamma$  becomes much smaller in that case than when the expansion is limited to the shock pressure in air: this can explain why  $w_\infty$  and  $\phi_0$  become so unexpectedly high in vacuum.

The consequence of this discussion is rather paradoxical: since the  $\Gamma$ -law becomes absurd in vacuum,  $\phi_0$  must not be measured directly in vacuum, but rather in air, and then corrected to its value in vacuum.

In fact, the real adiabat in Fig. 3c is represented by (A') (dotted line): for the same experimental value of  $\phi_0'$ , it leads to a higher value of  $\phi_0$  than the constant- $\Gamma$  assumption, as experimentally established, and to a lower value of  $p_{cJ}$ . Now, the fact we have contented ourselves with the average- $\Gamma$  approximation does not mean the present method cannot provide something more precise with other equations of state:  $\phi_0'$ , indeed, is a particular point of the real adiabat (A').

#### EXPERIMENTAL ARRANGEMENT

The explosive slabs and the liners previously described were stuck together with very thin straps, and the explosives initiated through line wave generators. A thin strap of adhesive tape ( $\mu \approx 0.01$ ) was stuck on the unconfined side of the slab in order to visualize the boundary: this tape was found to behave much better than metal foils of equivalent weight (Fig. 4).

Except for this tape, liners were cut out of mild steel sheets of constant thickness. No appreciable surface break-up was found in most experiments, and no spalling for liner-to-explosive/thickness ratios lower than 0.8.

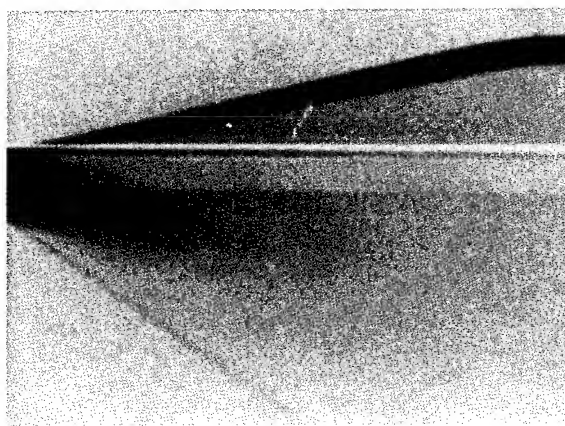


Fig. 4 - Typical radiograph of a liner before (below white line) and during projection

Liner and explosive masses were measured with milligram precision.

For each composition, four or six slabs were cast at a time, together with two  $\phi$  30-mm cylinders on which the detonation rate was measured separately.

The flash radiographic device (400-kV, 40-ns time exposure) was homemade (15). Thanks to its very thin anode, it provided very sharp radiographs (Fig. 4), allowing precise measurements of the deflection angles. Since, besides, much care was taken of the position of the slab in order to avoid parallax, the results were reproducible at less than  $\pm 10'$  of angle. This error was quite satisfactory for angles close to  $\phi_0'$ , but it became too important for small angles; this is why most experiments were carried out with  $\phi \geq 6^\circ$ .

Yet, for all the compositions studied, the very regular position of the experimental points (Fig. 2) showed that the precision of each individual measurement of  $\phi$  was quite satisfactory.  $\phi'_0$  was normally obtained by extrapolating the experimental  $1/\phi$  vs.  $\mu$  curve from the strap of adhesive tape to  $\mu = 0$ . The correction thus obtained was about  $2^\circ$ . In some cases, a direct measurement of  $\phi'_0$  was obtained by means of a Kerr cell. This method was not very accurate for the angle  $\phi'_0$  itself, but it provided an easy measurement of the shock-wave inclination and therefore a possibility of verification of the correction calculated from  $\phi'_0$  to  $\phi_0$  (Fig. 5).

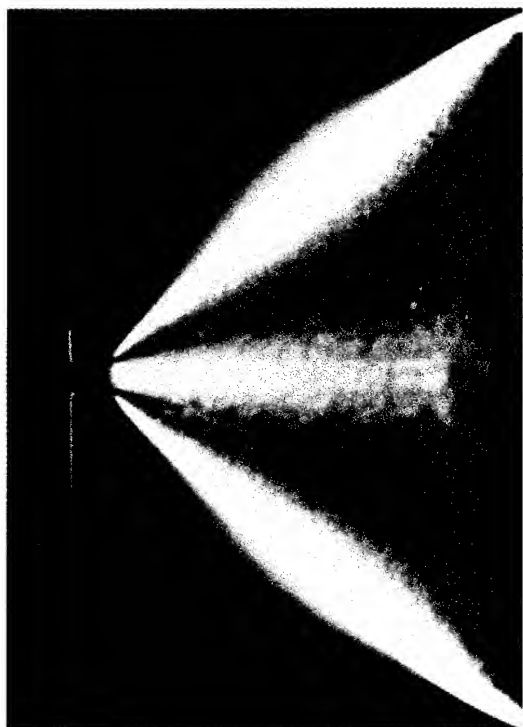


Fig. 5 - Typical photograph of the flow boundary and the shock wave in air (pressure and temperature behind the shock wave: approximately 500 bars and 7000°K)

#### EXPERIMENTAL RESULTS FOR TNT-BONDED COMPOSITIONS

The experimental results are presented in Table 1 for a wide range of compositions. Due to the imprecision of the values calculated for  $E_c$  and to the difference between real and idealized geometries and equations of state, the relationship expected between RB and  $\Gamma$  turned out experimentally to be a mere correlation.

RB increases slightly with  $\Gamma$ , a result which had already been found by other authors (7) in head-on projection. Very roughly, the following correlation was found:

$$RB \% \approx 28 + 18 (\Gamma - 3) , \quad (7)$$

with values of  $\Gamma$  varying from 2.19 to 3.13.

Several RDX/TNT compositions were studied, with rates of RDX varying from  $r = 40\%$  per mass (lower limit without sedimentation) to 89% (obtained by centrifugal sedimentation, Bölkow method). 1.4% nitrocellulose had to be added to the 70/30 composition in order to avoid sedimentation. Pure TNT and the 4/96 RDX/TNT eutectic were also studied, but the results for the former were very dependent on density and very badly reproducible, so no attention was paid to these results and the lowest value considered for  $r$  was 4%. The values corresponding to pure RDX were extrapolated from an isostatically pressed composition containing 98.8% RDX and 1.2% plastic binder. Except for this pressed composition, the densities of the slabs were those normally attained by casting in evacuated moulds. Both  $\rho_e$  and  $D$  showed a practically linear dependence on  $r$  (16). A small correction was made on the measured values of  $\Gamma$  to take into account the slight deviations from this linear relationship (Fig. 6).

As foreseen, the values given for  $\Gamma$  are generally smaller than those found by other authors on the same compositions with approximately the same densities. Now, after elimination of some high values of  $\Gamma$  (up to 2.88) found in some cases, with no understandable reason, for high-density pure TNT, the shape of the curve representing  $\Gamma$  vs  $r$  was found to be intermediate between those given by two other experimental works (17, 18) based on free-surface velocity measurements in aluminum and that given by computations using a BKW equation of state (6): the former suggested the existence of a minimum for  $\Gamma$ , whereas the latter indicated a monotonic variation. In the present work,  $\Gamma$  was found to decrease from pure RDX to 50/50 RDX/TNT, and then remain constant about  $\Gamma = 2.63$ .

The origin of the discrepancy in pure TNT between different methods is probably originated in the bad reproducibility of experimental results and, as far as theory is concerned, in the considerable dependence of the chemical energy  $E_c$  of TNT on the assumptions made on the chemical reactions in the detonation flow. According to the assumption chosen (19),  $E_c$  varies between 619 and 1282 cal/g.

TABLE 1  
Experimental Results for Explosives Without Additives

Composition	$\varphi'_0$	$\rho_e$ (g/cc)	D (mm/ $\mu$ s)	$\Gamma$	$E_c$ (cal/g)	$E_m$ (J/g)	RB (%)
RDX + 1.2% binder	36° 30'	1.746	8.480	2.75	1311	1310	23
RDX (extrapolated)	—	1.800	8.754	2.88	1395	—	—
89/11 RDX/TNT	36° 00'	1.765	8.500	2.78	1278	1319	24
75/25 RDX/TNT	37° 40'	1.745	8.240	2.67	1321	1254	22
65/35 RDX/TNT	38° 15'	1.730	8.020	2.63	1296	1160	21
65/35 RDX/TNT	39° 30'	1.665	7.750	2.55	1301	1099	20
65/35 RDX/TNT	40° 55'	1.55	7.350	2.47	1269	1110	20
65/35 RDX/TNT	43° 30'	1.46	7.050	2.33	1345	1090	19
65/35 RDX/TNT	46° 30'	1.29	6.320	2.19	1315	913	17
50/50 RDX/TNT	38° 30'	1.682	7.700	2.61	1213	1076	21
41.5/58.5 RDX/TNT	38° 20'	1.702	7.490	2.63	1133	1014	21
40/60 RDX/TNT	38° 15'	1.686	7.455	2.63	1123	990	21
30/58.6/1.4 RDX/TNT/NC	38° 15'	1.666	7.315	2.62	1089	1003	22
4/96 RDX/TNT	38° 25'	1.602	6.180	2.62	790	—	—
TNT	34° 30'	1.660	6.950	2.88	790	—	—
HMX + 1.2% binder	34° 30'	1.844	8.840	2.90	1263	1447	27
85/15 HMX/TNT	36° 30'	1.846	8.560	2.75	1334	1371	24
65/35 HMX/TNT	38° 30'	1.798	8.140	2.62	1348	1253	22
50/50 HMX/TNT	38° 15'	1.766	7.800	2.64	1220	1127	22
65/35 PETN/TNT	39° 00'	1.710	7.745	2.58	1258	1147	22

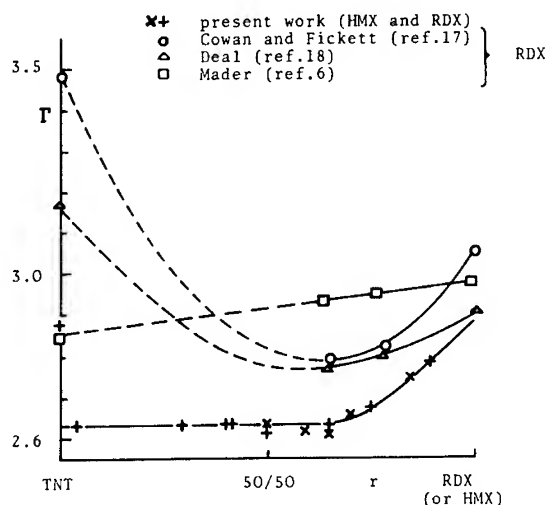


Fig. 6 - Variation of  $\Gamma$  vs. rate of RDX in TNT (density corrections made for the curve below)

Our values for  $\Gamma$ , being smaller than usual, lead to higher values for  $E_c$ . These values, in fact, are in better agreement with the calculated range than those obtained using a value of  $\Gamma$  corresponding to a higher pressure average. They seem to increase parabolically with  $r$ , the variation being slower toward pure RDX (Fig. 7).

The extreme values are:

$E_c = 1395$  cal/g for RDX ( $\rho_e = 1.800$ );  
calculated range = 1204/1481,

$E_c = 790$  cal/g for TNT ( $\rho_e = 1.660$ );  
calculated range = 619/1282.

As for the maximum kinetic energy  $E_m$ , it increases approximately linearly with  $r$  in the narrow range where measurements were carried out (Fig. 7).

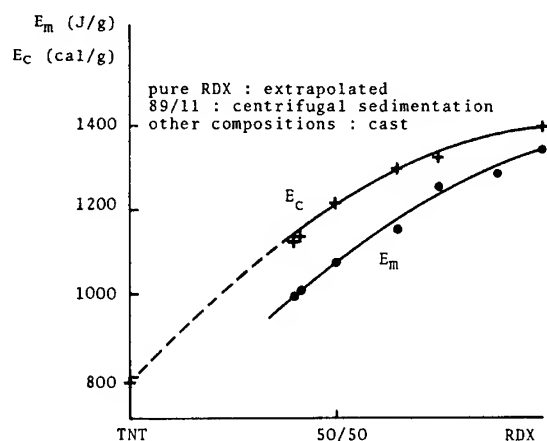


Fig. 7 - Variation of  $E_c$  and  $E_m$  vs. rate of RDX

A comparison between HMX, RDX and PETN was made, based on the values of  $E_m$ ; it classifies these explosives, as expected, in the order  $HMX > RDX > PETN$ . It must be noticed that the heats of explosion measured in a calorimeter for HMX and RDX are practically identical, whereas they are quite different in the above calculations. The advantage of HMX comes from its higher density, and its corresponding higher detonation rate. This strong influence of density on the detonation rate and detonation pressure has been investigated by several authors, and two rules have been established for a given composition used with different loading densities (20):

- a linear dependence of  $D$  on  $\rho_e$ ;

$$D = A \Phi^{1/2} (1 + B \rho_e) , \quad (8)$$

- a quadratic dependence of  $P_{cJ}$  on  $\rho_e$ ;

$$P_{cJ} = K \rho_e^2 \Phi . \quad (9)$$

$A$ ,  $B$  and  $K$  are numerical constants and  $\Phi$  a parameter depending on the composition studied. Eqs. 2, 8 and 9 yield

$$\frac{D^2}{(\Gamma + 1) \rho_e \Phi} = \frac{A^2 (1 + B \rho_e)^2}{(\Gamma + 1) \rho_e} = K . \quad (10)$$

A verification of these equations was made on 65/35 RDX/TNT, either cast ( $\rho_e \geq 1.70$ ) or sintered (down to  $\rho_e = 1.27$ ). Thermal cycles were used to lower the density of a cast sample

down to 1.665. Eq. 8 was well verified, except for the lightest samples which gave a lower detonation rate (Fig. 8). This slight discrepancy is quite understandable, since  $D$  was measured under a thickness of 20 mm, a value which probably became too close to the critical one for the lowest densities. This influence of thickness might perhaps also explain why the coefficients found for Eq. 8 are different from those given by Ref. 17 and 20,  $dD/d\rho_e$  being however very close:

$$D = 2.080 (1 + 1.635 \rho_e) , \quad (11)$$

$D$  being expressed in mm/ $\mu s$  and  $\rho_e$  in g/cc.

$\rho = 1.73$  and  $1.70$  : cast  
 $\rho = 1.665$  : cast with thermal cycles  
 $\rho = 1.55$  : sintered

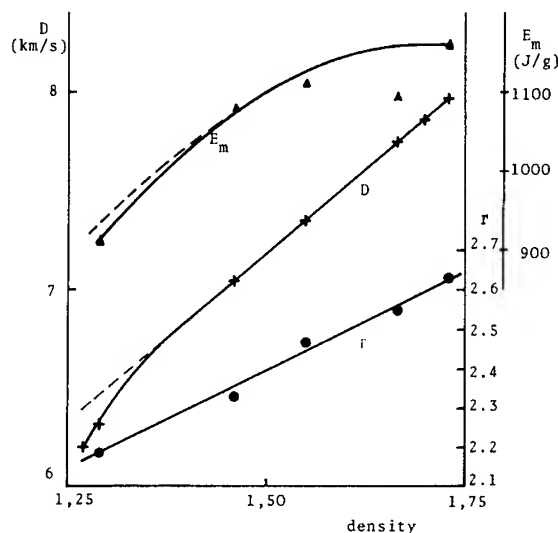


Fig. 8 - Variation of  $\Gamma$ ,  $D$  and  $E_m$  vs. loading density in 65/35 RDX/TNT

$\Gamma$  could not be exactly calculated by the normal method for the lightest sample, since the shock configuration of Fig. 3b (detached shock wave in air) was obtained. The correction from  $\phi'_0$  to  $\phi_0$  was extrapolated from higher densities.

A good agreement was not expected for Eq. 10, since it seemed difficult to extrapolate our low values of  $\Gamma$  to the detonation pressure. Yet the result was surprisingly good, since the calculated values of  $K\Phi$  stayed practically constant for different values of  $\rho_e$ :



$\rho_e$	1.723	1.665	1.55	1.46	1.29
$K\Phi$	10.19	10.18	10.05	10.22	9.7* 10.20†

\*Using the measured value of  $D$ .

†Using the value of  $D$  linearly extrapolated through Eq. 11.

This average value of  $K\Phi$  is quite consistent with the value given in Ref. 20 for 64/36 RDX/TNT (10.32).

$E_c$  appeared to be rather insensitive to small changes in density. As a consequence of Eqs. 3 and 10, it should go through a maximum for a particular value of  $\rho_e$ , equal to 1.385 g/cc with our experimental values. In spite of a certain dispersion of the values found for  $E_c$ , probably due to an imprecise determination of  $\Gamma$  for  $\rho_e = 1.55$ , this maximum was experimentally found.

$E_m$ , on the contrary, decreases monotonically with  $\rho_e$ , except for  $\rho_e = 1.665$  (thermal cycles), but its variation seems to be negligible for high loading densities (Fig. 8). This would mean that the maximum kinetic energy transmitted to a liner by a given mass of high explosive is not substantially modified by a low porosity.

## INFLUENCE OF ADDITIVES

The following results have been established using relatively few experimental results in comparison with the number of parameters involved, so that they should be used with a certain care.

When inert components were added to a high explosive, its chemical energy  $E_c$  and its ballistic coefficient  $E_m$  were found to decrease. The detonation rate was also found to decrease, but generally not substantially. Now, it seemed interesting to calculate  $E_c$  and  $E_m$  in relation not with the total mass of the slab, but with its partial mass of explosive, say  $E'_c$  and  $E'_m$ :

$$\frac{E'_c}{E_c} = \frac{E'_m}{E_m} = \frac{\text{total mass of the explosive slab}}{\text{partial mass of high explosive}} \quad (12)$$

The results presented in Table 2 showed that  $E'_c$  was always higher than the value of  $E_c$  determined for the pure explosive, but that  $E'_m$  was equal to the value of  $E_m$  for the pure explosive, at least up to 25% additive. This means that  $E'_m$  is a much better parameter than

$E_c$  to define high explosive efficiency, since its value does not depend on the amount of inert components, at least in the range where experiments were carried out.

In fact, these inert media were added to explosives as a reference for identical proportions of oxydizers and fuels of identical densities, in order to determine how these compositions behaved in the detonation and behind it: this method was also used by other authors in this Symposium (12). Yet, these identical proportions and densities of the additives did not always lead to identical densities for the explosive slabs, and this introduced some difficulty in the interpretation of certain results. These results are as follows for the comparison of inert media with aluminum powder and inorganic nitrates:

- Whatever the additive, the detonation rate is decreased, but its value seems to be much more dependent on the final density of the slab than on the nature of the additive. This tends to prove that none of these additives reacts in the detonation zone, a result which has already been pointed out for a long time for aluminum under certain conditions (21).

- Whatever the additive, too,  $E_c$  and  $E_m$  are decreased. This is very disappointing for explosives containing aluminum, since this additive normally increases the heat of explosion  $Q$  measured in a calorimeter. This result is due to the fact that the conditions of pressure, temperature and mainly time of reaction are quite different in a detonation and in a combustion.

Now, contrarily to  $D$ , the values of  $\Gamma$ ,  $E_c$  and  $E_m$  depend on the nature of the additive. This means that, if they all behave as inert components in the detonation zone, they behave differently in the expansion flow, and this behavior can be studied thanks to the aforementioned rule according to which  $E'_m$  keeps constant with inert additives. Of course, these post-detonation reactions involve chemical kinetics, so they are dependent on the dimensions of the explosive samples, which are particularly small in our experiments. This is why the following results, presented in Table 2, should be considered as qualitative:

- Adding aluminum increases  $E'_m$ : aluminum does react behind the detonation, but not very exothermally (10% increment with 25% aluminum). Micronizing aluminum powder does not modify  $E'_m$ , which might prove that the reaction has been completed, but it seems to increase  $D$  which might indicate that if sufficiently

TABLE 2  
Experimental Results for RDX/TNT Composition Containing Additives

RDX/TNT	Additive			$\rho_e$ (g/cc)	D (mm/ $\mu$ s)	$\Gamma$	Chemical Energy		Kinetic Energy		RB
	Nature	Density	%				$E_c$	$E'_c$	$E_m$	$E'_m$	
65/35	—	—	—	1.730	8.020	2.63	1296	1296	1160	1160	21
	Asbestos	2.85	10	1.800	7.885	2.72	1164	1295	1044	1160	21
	Asbestos	2.85	20	1.878	7.670	2.74	1080	1350	926	1155	20
	Al <sub>2</sub> O <sub>3</sub>	3.9	20	1.970	7.625	2.59	1217	1520	926	1155	18
	Pb O (red)	8.0	20	2.060	7.320	2.54	1173	1465	972	1215	19
	Ox. A*	3.9	20	2.050	7.755	2.66	1186	1485	1064	1330	21
50/50	—	—	—	1.682	7.700	2.61	1213	1213	1076	1076	21
	Asbestos	2.85	30	1.928	7.218	2.90	839	1225	712	1040	20
	NH <sub>4</sub> NO <sub>3</sub>	1.65	10	1.655	7.425	2.58	1162	1290	1073	1190	22
	NH <sub>4</sub> NO <sub>3</sub>	1.65	20	1.631	7.190	2.56	1112	1390	991	1240	21
42.7/57.3	—	—	—	1.700	7.500	2.63	1145	1145	1020	1020	21
	Na <sub>2</sub> SO <sub>4</sub>	2.7	25	1.860	7.220	2.72	973	1300	775	1030	19
	Al (50 $\mu$ )	2.7	25	1.855	7.180	2.61	1055	1405	867	1140	19
	Al ( 3 $\mu$ )	2.7	25	1.880	7.380	2.81	946	1260	865	1140	21
	Ox. B†	2.7	25	1.850	7.170	2.44	1244	1660	931	1240	17

\*Oxydizer A: 58/42 Pb nitrate/Ba nitrate (same density as Al<sub>2</sub>O<sub>3</sub>)

†Oxydizer B: 50/50 Ba nitrate/K nitrate (same density as Al and Na<sub>2</sub>SO<sub>4</sub>)

small sized, aluminum is able to react within the detonation zone.

•  $E'_m$  is also increased by inorganic nitrates, in a larger proportion than by aluminum (16% average increment with 20% oxydizer). This could be expected, and a direct evidence of such a reaction was obtained with Baratol (40% baryum nitrate/60% TNT), i.e., adding a strong proportion of an oxydizer to a strongly oxygen-deficient explosive: with this composition, indeed, it was impossible to measure  $\Gamma$  since the normally straight boundary of the flow showed in that particular case a strong curvature,  $\phi'_0$  varying from 20° to 36° within a few cm. On the other hand, the result obtained with PbO gave evidence of its decomposition behind the detonation.

Other fuels and oxydizers have been studied, but many more experiments will be necessary before quantitative rules can be established concerning all possible additives. Yet the present method seems a good one for that purpose.

#### CONCLUSION

Although used in very small-scale experiments, the present method has given a certain number of interesting results concerning RDX/TNT and similar compositions, under different loading densities, in good agreement with those obtained by other methods, taking into account the difference in the pressure averages. Besides, it shows how a systematic study of the

influence of inert and active additives might be carried out, and it provides a few preliminary results concerning this problem.

#### ACKNOWLEDGMENTS

The authors wish to thank Mrs. M. O. Rigaut and Mr. A. Légier for their contribution to this work, and Mr. W. Kegler for the way he solved all the problems related with high-explosive technology.

#### REFERENCES

1. M. L. Wilkins, B. Squier and B. Halperin: "The equation of state of PBX 9404 and LX 04-01", UCRL Rept. 7797, April 1964.
2. J. W. Kury, et al.: "Metal acceleration by chemical explosives", IVth Symposium on Detonation, Vol. 1, sec. A, pp. 109-120, Oct. 1965.
3. N. E. Hoskin, et al.: "The motion of plates and cylinders driven by detonation waves at tangential incidence," IVth Symposium on Detonation, Vol. 1, sec. A, pp. 5-15, Oct. 1965.
4. M. Défourneaux: "Optimisation de l'emploi balistique des explosifs", Explosifs, No. 4/69, pp. 121-139, Oct.-Dec. 1969.
5. M. Défourneaux and L. Jacques: "Etude théorique et expérimentale de la propulsion par explosif, et application à une classification balistique des explosifs", Mémoire de l'Artillerie Française, No. 3/69, pp. 515-543, July-Sept. 1969.
6. C. L. Mader: "Detonation properties of condensed explosives computed using the Becker-Kistiakowski-Wilson equation of state", LA 2900 Rept., July 1963.
7. A. K. Aziz, H. Hurwitz and H. M. Sternberg: "Energy transfer to a rigid piston under detonation loading", Phys. of Fluids, Vol. 4, No. 3, pp. 380-384, March 1961.
8. R. Schall: "Recherches expérimentales sur la balistique des explosifs brisants", ISL Rept. 39/46, Nov. 1946.
9. H. Richter: "Sur la théorie des charges creuses: Mouvement de revêtements minces en matériau plastique à la surface d'un explosif plan", ISL Rept. 42/46, Dec. 1946.
10. D. Price: "Dependence of damage effects upon detonation parameters of organic high explosives", Chem. Revs., Vol. 59, pp. 801-825, 1959.
11. R. W. Gurney: "The initial velocity of fragments from bombs, shells and grenades", BRL Rept. 405, Sept. 1943.
12. M. Finger, H. C. Hornig, E. L. Lee and J. W. Kury: "Metal acceleration by composite explosives", present Symposium, Aug. 1970.
13. H. Bernier: private communication.
14. C. H. Johansson and S. Ljungberg: "Influence of air pressure on the velocity of ejected explosion gases", Arkiv für Fysik, Vol. 6, No. 35, pp. 369-373, March 1953.
15. G. Thomer: "Röntgenblitztechnik", Kurzzeitphysik, pp. 328-366, Springer-Verlag, Wien & New York, 1967.
16. W. Kegler: "Vergleichende Untersuchungen über die Detonationseigenschaften von TNT/Hexogen- und TNT/Oktogen-Mischungen", ISL-Rept. T 24/68, June 1968.
17. R. D. Cowan and W. Fickett: "Calculation of the detonation properties of solid explosives with the Kistiakowski-Wilson equation of state", J. Chem. Phys., Vol. 24, No. 5, pp. 932-939, May 1956.
18. W. E. Deal: "Measurement of Chapman-Jouguet pressure for explosives", J. Chem. Phys., Vol. 27, No. 3, pp. 796-800, Sept. 1957.
19. M. J. Kamlet and J. E. Ablard: "Chemistry of detonations. II. Buffered equilibria", J. Chem. Phys., Vol. 48, No. 1, pp. 36-42, Jan. 1969.
20. M. J. Kamlet, S. J. Jacobs: "Chemistry of detonations. I. A simple method for calculating detonation properties of C-H-N-O explosives", J. Chem. Phys., Vol. 48, No. 1, pp. 23-35, Jan. 1969.
21. J. Berger, A. Cachin and J. Viard: "Vitesse de détonation dans un explosif renfermant de la poudre d'aluminium", C.R. Acad. Sci., Vol. 245, No. 1, pp. 139-141, July 1957.

# ELASTIC-PLASTIC BEHAVIOUR OF POROUS BERYLLIUM

G. Eden and C. P. M. Smith  
*United Kingdom Atomic Energy Authority  
Aldermaston, Reading*

## ABSTRACT

Studies of the elastic precursor to plastic waves have been found useful in constructing theoretical models of elastoplasticity in porous media. For a given plastic pressure in non-porous material, separation of these waves is governed by the rigidity modulus  $\mu$  of the medium. A metal with a particularly high value of  $\mu$ , beryllium, was chosen for experiments in which a plane shock wave was passed into specimens of up to 30% porosity. A standard shock system generated 100 Kbars in solid material and wave and free surface velocities were measured by optical methods, one of which was capable of resolving surface motion over the first 10  $\mu\text{m}$  travel. An elastic limit associated with the initial amplitude of the elastic wave is shown to fall by a factor of four over this range of densities. Agreement between plastic wave velocities and a purely hydrodynamic calculation indicates that this wave produced total pore compaction, and an estimate is made of the initial slopes of the plastic compression curves. These slopes fall by a factor of 100 over the density range.

## 1. INTRODUCTION

Simple elastoplastic behaviour is exhibited in solid material as a two wave structure when an applied shock pressure is great enough to exceed the dynamic yield strength and low enough to produce a plastic wave velocity less than the longitudinal sound speed. The plastic wave velocity increases with pressure from a minimum value of  $(K/\rho)^{1/2}$  and the elastic velocity of a plane wave is  $[(K + 4\mu/3)/\rho]^{1/2}$ , where  $K, \mu$  are the bulk and shear moduli of elasticity and  $\rho$  the density. The shear modulus clearly governs the rate of separation of the waves.

In porous materials, the physical structure of the medium reduces the amplitude and velocity of both waves and it may also produce multiple wave structure according to the type of porosity present. For example, a proposed explanation by Boade (1) for the second precursor wave which he observed in porous copper and tungsten, is that it may be due to the finite shear strength of the bond between granules produced by the sintering process which both metals had undergone.

Beryllium was chosen for these experiments for its particularly high  $\mu$  value (approximately

$1.5 \times 10^{12}$  dyne  $\text{cm}^{-2}$ ) and also because it can be produced in porous form by sintering.

## 2. METHOD

### 2.1 Materials Used

(a) Brush Beryllium Co. S200 D. powder: a "-200 mesh" powder, i.e., all particle sizes up to 74  $\mu\text{m}$ .

(b) Brush Beryllium Co. I400 powder: no specification of particle size but it has an average grain size of approximately 4  $1/2$   $\mu\text{m}$ .

The bulk material was produced by hot pressing and sintering. Specimens were cut from billets so that the normal to the wave front was parallel to the direction of pressing. Machining and polishing porous beryllium almost certainly caused some degree of flow in the surface layer producing some small depth of differing density. This would be thin enough to have no effect on the wave velocity measurements. Its effect is more likely to be seen in surface velocity measurements but as it is virtually a thin layer of higher impedance material, its motion represents that of the main

body of the specimen provided it remains attached.

## 2.2 Experimental Techniques

An explosive system was used to generate a plane shock in the beryllium specimens. The shock pressure was adjusted to approximately 100 kilobars in solid beryllium by inserting inert plates of differing impedance between the explosive and the specimen. Sufficient thicknesses of these plates were chosen to prevent a second shock reflected between layers from interfering with the observations.

Once established, the same shock generating system was used in all shots.

The experiments were of two types.

Type 1 — A streak camera technique for the accurate measurement of the motion of a free surface, based on the extinction of total reflection from a transparent block inclined at an angle to the surface, Ref. (2).

In order to record the motion due to the small amplitude elastic waves the technique was refined progressively until flight distances of the order of 10  $\mu\text{m}$  were used. With these small flights special care was required during the manufacture and assembly of the shots.

The beryllium specimens were prepared to a mirror finish and flat within one wavelength of light over the area to be monitored.

Examination and measurement of the angle between the specimen free surface and the base of the transparent velocity measuring prism was made using the interference pattern produced by a monochromatic source of light. The prism was adjusted until, when clamped down with a foil spacer under one end, the interference pattern consisted of the usual bright and dark bands parallel to the line of contact. The spacing of these fringes was measured with a microscope to give the angle between the prism and specimen. To check that the lower edge of the prism was truly in optical contact, the white light fringe pattern was viewed through the top face of the block and frustration of total reflection at that edge was observed via a vertical glass face. Care was taken to avoid placing the prism over any small polishing scratches or surface porosity defects which were revealed by any irregularities in the fringe pattern.

The assembly was not accepted for firing until the fringe pattern was as nearly perfect as possible.

The experiments recorded: —

(a) The shock contour as it emerged from the pressure reducing layer, using the loss in reflectivity of 0.1  $\mu\text{m}$  of gold leaf placed on the free surface. Axial symmetry is generally a feature of the wave shape produced by the shock system so the slit measuring this contour was placed parallel to the slit across the specimen, with both slits equidistant from the axis.

(b) The shock contour at two discrete points on each side of the beryllium specimen, using total reflection, to provide correlation with the contour (a) above.

(c) The free surface motion using frustration of total reflection at the inclined collision block (see Fig. 1). Some, but not all, experiments measured the motion due to both elastic and plastic waves on the same specimen.

(d) After the surface velocity had been recorded, with low angled blocks, and the metal was presumably in optical contact with the glass, a low level of light intensity persisted. This light was cut off later in a well defined but ragged trace. This final cut off was checked to coincide with the sharp acceleration of the free surface, due to the plastic wave arrival measured on an adjacent longer flight distance block. It is thought to represent the final complete compaction of the pores, since the effect has not been seen on solid specimens.

Type 2 — An optical lever type method, Ref. (3, 4).

A high speed rotating mirror streak camera was used to record the displacement of the image of a fixed grid, reflected in the specimen's polished surface, caused by the arrival of a plane wave inclined to the free surface. The accuracy of measurement is greater for wave velocity than for surface velocity, but the sensitivity of the method was varied by adjusting the distance between grid and specimen.

## 2.3 Analysis of Data

Velocities were obtained from wedge and inclined block surface traces by measuring at least 100 coordinate points on each streak camera record, using a computer programme

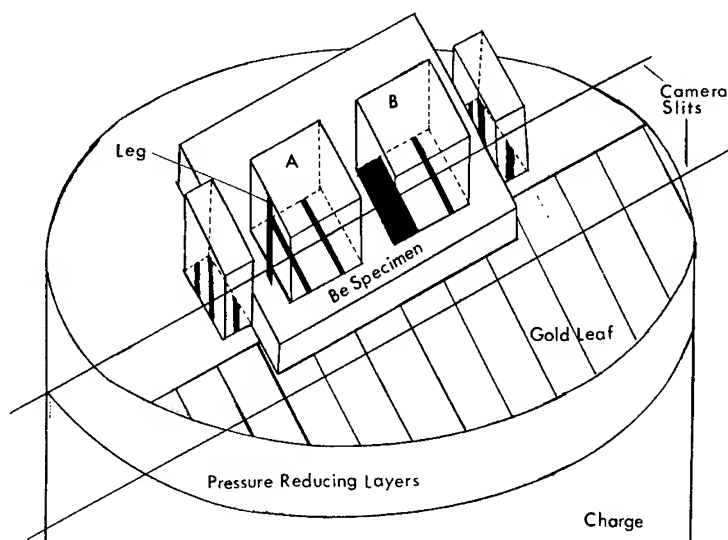


Fig. 1 - Experimental assembly

to scale the values to give true distance versus time and to differentiate successive elements which could be chosen to overlap. In the short flight shots, a linear least square regression was judged to give the most suitable estimate of velocity since the distance-time traces were close to linear.

### 3. RESULTS AND DISCUSSION

The Appendix shows the detailed results. In the table, the abbreviations used are:

OL = optical lever measurement on a wedge-shaped specimen.

TR = "total reflection" method on a flat plate specimen.

$\rho_0$  = initial density.

X = specimen thickness.

h = total distance over which measurements were made.

W = wave velocity, suffix denoting elastic or plastic.

$U_{FS}$  = free surface velocity, suffix denoting elastic or plastic.

$\sigma$  = standard deviation except where preceded by  $\pm$ . In this case it represents the spread of plastic wave velocities calculated from the

observed spread of wave arrival times at different positions on the specimen surface.

All the total reflection traces showed that a definite value of free surface velocity is associated with the arrival of the elastic wave, and if a ramp from zero exists, then it occurs within the first  $1/2 \mu\text{m}$  of travel. An example trace is shown in Fig. 2.

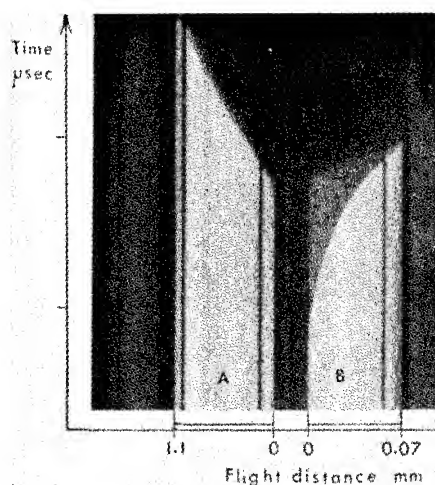


Fig. 2 - Photographic results, (A) glass block having large angle of contact with surface shows motion due to plastic wave, and (B) block at small angle magnifies details of surface motion due to elastic wave

Many of the shots were designed to monitor the initial surface motion over a restricted time interval less than  $\Delta t$  where  $\Delta t$  is the time taken for the first (hence fastest) elastic wave arriving at the free surface, to reflect back to the plastic wavefront and return again to the free surface (see Fig. 3(a)). More extended observations were made in some shots however and these traces show increases in free surface velocity at earlier times than would be expected if a purely two-wave structure were present, e.g., shot 2044 in Fig. 3(b).

Measurements of the mean velocity of the primary elastic wave (Fig. 4) and the associated surface velocity (Fig. 5) of the plate specimens have been combined in Fig. 6 to show values of stress versus density, using the relation

$$P_e = \rho_0 W_e u_e, \quad \text{where} \quad u_e = \frac{1}{2} (U_{FS})_e$$

derived from conservation of mass and momentum across the wavefront. This stress is the

elastic limit of the material if there is no change of velocity with thickness. The solid curves in Figs. 4, 5, and 6 are least square fits, and the broken lines in Fig. 6 represent the standard deviation about the curve.

In Fig. 7, the experimental plastic wave velocities are shown to be in quite good agreement with a purely hydrodynamic calculation (RICSHAW, Ref. 5) using a Gruneisen equation of state for beryllium in which the ratio of the Gruneisen parameter and specific volume is assumed constant and equal to the ratio of the values for solid material. RICSHAW assumes total pore collapse at negligible pressure. Although the calculation ignores any effect due to the known elastic behaviour, this measure of agreement suggests that pore compaction is complete in these plastic waves. The computed plastic wave pressures were 100 Kb in  $1.845 \text{ gm cm}^{-3}$  to 45 Kb in  $1.277 \text{ gm cm}^{-3}$  material. The broken curve in Fig. 7 is an empirical fit to the experimental points.

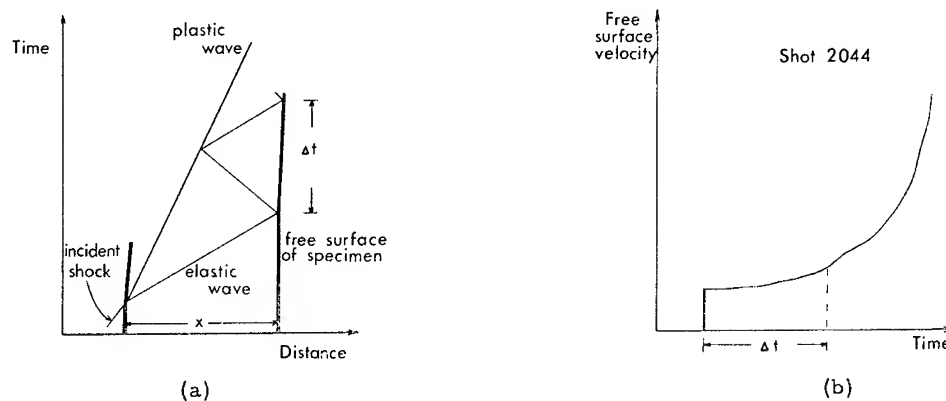


Figure 3

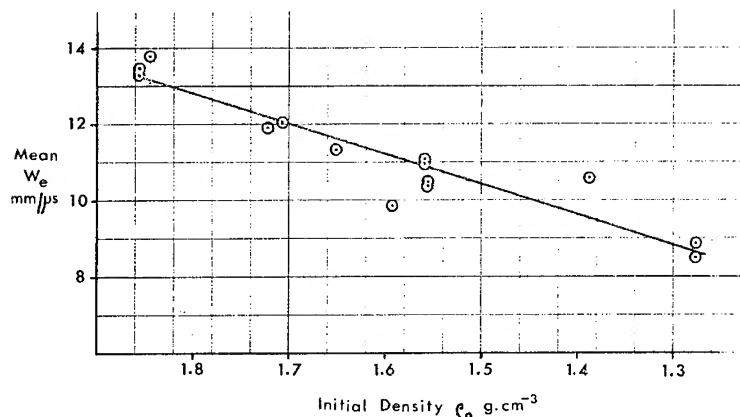


Fig. 4 - Elastic wave velocity

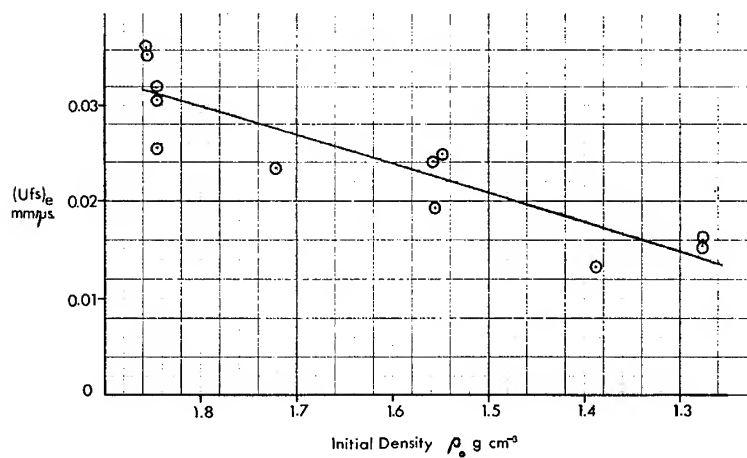


Fig. 5 - Free surface velocity due to elastic precursor

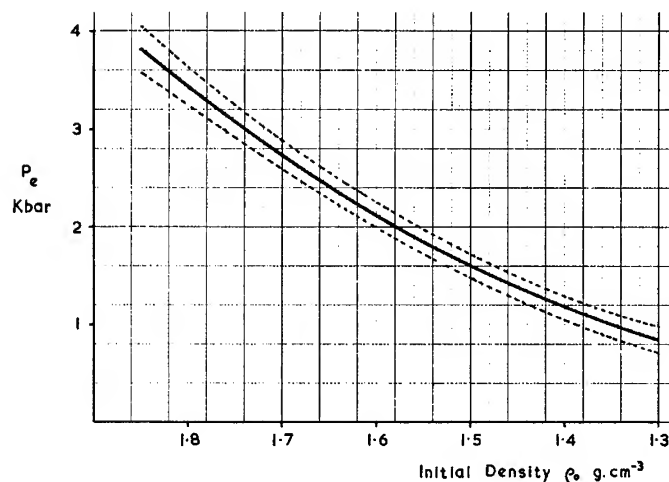


Fig. 6 - Elastic limit

### 3.1 Elastic Compression Curves (Fig. 8)

The longitudinal sound velocity  $W_e = (\text{modulus of elasticity}/\rho_0)^{1/2}$  where  $\rho_0$  = density.

Taking the  $P, v$  curve as linear up to the elastic limit the modulus of elasticity is

$$\frac{P}{(v_0 - v)/v_0}$$

where  $v$  is specific volume at  $P$ .

Hence

$$P = -\rho_0 W_e^2 \left( \frac{v}{v_0} - 1 \right).$$

Thus the slopes of the  $P, v/v_0$  lines are defined by  $-\rho_0 W_e^2$ , and a set of lines for densities 1.3 to 1.845 g cm $^{-3}$  have been drawn taking  $W_e$  from the fitted line in Fig. 4 with the slopes shown in Table 1. The lines are terminated at the appropriate value of  $P_e$  obtained from Fig. 6.

### 3.2 Plastic Compression Curves

The shapes of the  $P, v$  curves in the plastic region are not defined by this work but a rough estimate of their initial slopes has been made as follows:

We have determined the variation of  $W_p$  with  $\rho_0$  (Fig. 7) and the slopes of the Rayleigh



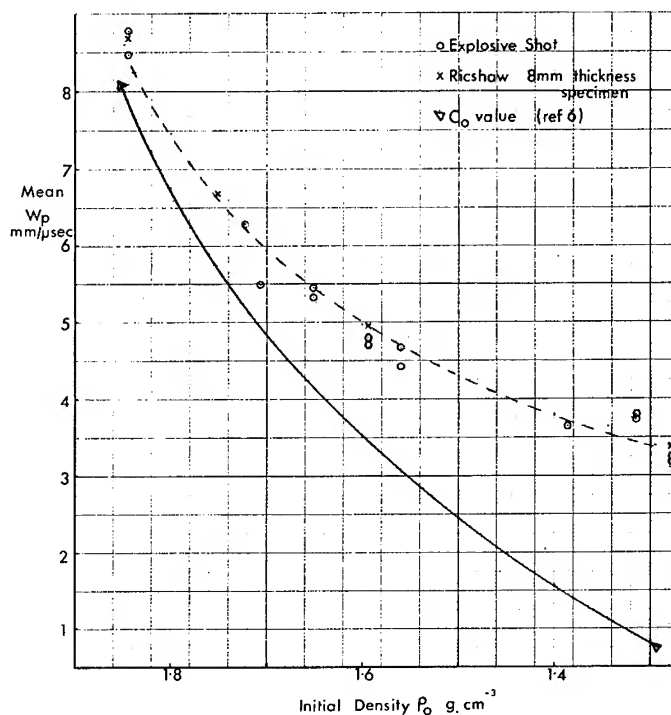
Fig. 7 - Plastic wave velocity  $W_p$ 

TABLE 1

$\rho_0$	1.845	1.8	1.7	1.6	1.5	1.4	1.3	gm cm <sup>-3</sup>
$\rho_0 W_e^2$	3.16	2.92	2.43	2.00	1.62	1.29	1.01	Mb cc/cc
	±0.12	±0.10	±0.07	±0.06	±0.05	±0.06	±0.07	

lines, EH in Fig. 9 may be shown to be  $-\rho_0 W_p^2$  approximately (since  $v_E \approx v_0$ ). If the initial slopes of the plastic curves at E are  $-\rho_0 W_0^2$ , then the value of  $W_0$  pertaining to solid beryllium is established from the empirical linear relation

$$W = W_0 + B u$$

where B is constant. Reference (6) quotes  $W_0 = 8.06$  mm/μsec for a density of  $1.851$  gm cm<sup>-3</sup> (due to McQueen and Marsh).

The same reference quotes a linear fit to  $W_u$  data (over a pressure range 70 to 180 Kbar) for  $1.295$  gm cm<sup>-3</sup> beryllium in which  $W_0 = 0.79$  mm/μsec.

These two values are shown in triangles in Fig. 7, and the solid curve has been constructed through them with reference to the experimental  $W_p$  curve and assuming that  $(W_p - W_0)$  increases linearly from  $\rho_0 = 1.851$  gm cm<sup>-3</sup> to  $\rho_0 = 1.295$

gm cm<sup>-3</sup>. The solid curve is proposed as an approximate estimate of the variation of  $W_0$  with density.

Implicit in this argument is the assumption that the porous  $W_u$  curves are linear. This has been demonstrated to be untrue in the case of porous copper (7), but it may be a better approximation than the "total compaction at negligible pressure" model which results in  $W_u$  curves passing through the origin.

A set of  $W_0$  values from Fig. 7 are shown in Table 2 and a selection is shown in Fig. 10 in comparison with the calculated curves. Also in the table are the estimated initial slopes of the plastic curves,  $\rho_0 W_0^2$ .

#### 4. CONCLUSIONS

An elastic precursor wave of finite initial amplitude was seen in all porosities examined.

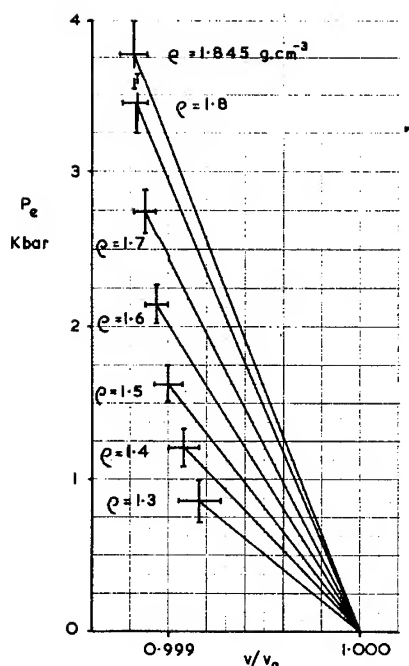


Fig. 8 - Compression of porous beryllium

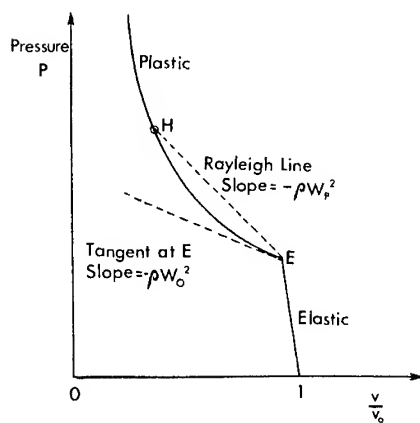


Figure 9

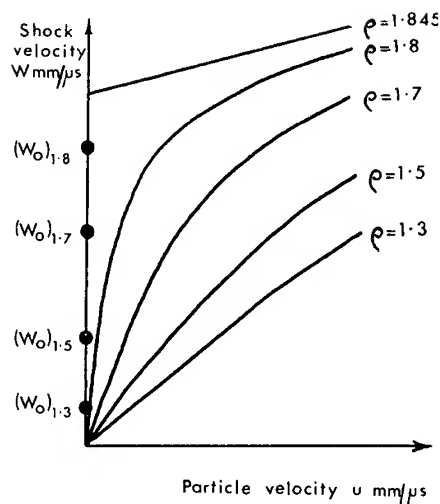


Fig. 10 -  $W_0$  values derived from Fig. 7 compared with total compaction theory curves

The variation with density, of its amplitude and velocity was measured using the optical techniques described.

Further precursor wave structure was evident in the traces and its presence in the sintered beryllium used, is not inconsistent with Boade's qualitative proposal of a "repacking" wave with which he explained the double precursor found in sintered copper and sintered tungsten foams. The observed elastic wave structure indicates that there is more detail in the  $P, v$  curves than is shown in the simplified diagrams here, with possibly a curvature of the "elastic" portion of the curves before the transition to plastic.

Measurements of the plastic wave show that it produced complete pore compaction in all densities of beryllium examined, but a tentative estimate has been made of the variations with density of the effective bulk sound velocity

TABLE 2

$\rho_0$	1.845	1.8	1.7	1.6	1.5	1.4	1.3	gm cm <sup>-3</sup>
$W_0$	7.88	6.76	4.86	3.51	2.45	1.58	0.83	mm/ $\mu$ sec
$\rho_0 W_0^2$	1.15	0.82	0.40	0.20	0.09	0.03	0.01	Mb cc/cc

and hence the initial slope of the plastic compression curve. These values are likely to be over-estimates owing to the non-linearity of the shock velocity versus particle velocity curves for porous media, and depend on a rather extended extrapolation of the Ref. (6) data.

#### 5. ACKNOWLEDGMENTS

We wish to thank Mr. A. Schofield for his support of this work, and to thank Mr. P. W. Wright, Mr. B. D. Lambourn and Dr. I. C. Skidmore for helpful discussions and criticism.

We also express our gratitude to Dr. A. J. Martin and his staff for the production and surface preparation of beryllium specimens.

#### 6. REFERENCES

1. R. R. Boade, "Dynamic compression of porous tungsten," *Jour. App. Phys.*, Vol. 40, No. 9; pp. 3781-3785 (Aug. 1969).
2. G. Eden, and P. W. Wright, "A technique for the precise measurement of the motion of a plane free surface", *Proc. 4th Symposium on Detonation, USNOL*, Oct. 1965, pp. 573-583.
3. G. R. Fowles, *Jour. App. Phys.*, Vol. 32, No. 8, p. 1475 (Aug. 1961).
4. C. Peyne, J. Pujol, and J. Thouvenin, "Experimental method for analysis of the structure of a shock wave in a solid", *Proc. 4th Symposium on Detonation, USNOL*, Oct. 1965, pp. 566-572.
5. N. E. Hoskin, and B. D. Lambourn, "The computation of general problems in one dimensional unsteady flow by the method of characteristics", *Proc. Conf. on Computational Physics, Culham*, July 1969, CLM-CP (1969).
6. Lawrence Radiation Laboratory Report UCRL-50108, *Compendium of Shock Wave Data*, Vol. 1, Sect. A-1, Ed. Van Thiel et al.
7. R. R. Boade, "Compression of porous copper by shock waves", *Jour. App. Phys.* Vol. 39, No. 12 (Nov. 1968).

## APPENDIX

Shot No.	Expt. Type	Material	$\rho_0$ (g cm <sup>-3</sup> )	X mm	h mm	MEAN $w_e$ (mm/ $\mu$ s)	$\sigma_{w_e}$ (mm/ $\mu$ s)	MEAN $w_p$ (mm/ $\mu$ s)	$\sigma_{w_p}$ (mm/ $\mu$ s)	$(U_{FS})_e$ (mm/ $\mu$ s)	$\sigma_{U_{FS}}$	$(U_{FS})_p$ (mm/ $\mu$ s)	$\sigma_{U_{FS}}$
47	OL	S200D	1.845	2 to 20		13.80		8.48		0.031	13%		
2025	OL	S200D	1.845	2 to 20		13.79	0.8%	8.78	0.5%	0.032	5%	0.986	3%
2042	TR	I400	1.850	10.29	0.012					0.0255			
2041	TR	I400		10.29	2.9 2.9							0.990 1.000	0.2% 0.8%
2044	TR	S200D	1.548	12.40	0.130					0.0249	~5%		
2056	OL	S200D	1.707	1 to 13		12.05	0.7%	5.49	0.4%				
2054	TR	S200D	1.722	12.60	0.010	11.91		6.31	±0.08	0.0235	0.2%		
2053	TR	S200D	1.387	12.70	0.010	10.58		3.64	±0.02	0.0131	1.2%		
2133	TR	S200D	1.277	12.60	0.017 0.017	8.87 8.50		3.22 3.17	±0.03 ±0.03	0.0155 0.0161	0.6% 0.6%		
2134	TR	S200D	1.314	4.95	0.025			3.79 3.74	±0.08 ±0.13				
2135	TR	I400	1.856	10.29	0.0094	13.44 13.27				0.0362 0.0356	0.8% 0.8%		
2160	TR	S200D	1.651	8.00	0.0097 2.480	11.32		5.45 5.33	±0.13				
2161	TR	S200D	1.593	7.98	0.074 1.120	9.86		4.69 4.79				1.089	1.1%
2219	TR	S200D	1.556	12.65	0.036 0.140	10.49 10.35		4.43	±1%	0.0193 0.0241	1.4% 1.6%		
2220	TR	S200D	1.559	4.80	0.019 0.058	10.94 11.09		4.69	±0.3%				

# NUMERICAL ANALYSIS OF A DIVERGING SHOCK WAVE IN PLEXIGLAS CYLINDERS

Minao Kamegai  
*Lawrence Radiation Laboratory, University of California  
Livermore, California*

and

John Erkman  
*U.S. Naval Ordnance Laboratory  
Silver Spring, Maryland*

## ABSTRACT

The Mie-Grüneisen type equation of state was derived for Plexiglas from the experimentally determined relation between shock velocity and particle velocity. The equation was used in the two dimensional elastic-plastic code, HEMP, to study a diverging shock wave in a Plexiglas cylinder. The agreement between the computation and experimental data is generally good. The curvature of the shock front in Plexiglas is simulated satisfactorily. Calculated stress versus time curves for different lengths of Plexiglas give some insight into the mechanics of gap testing of explosives.

## INTRODUCTION

This paper presents a numerical analysis made at Lawrence Radiation Laboratory, Livermore, for the dynamic behavior of Plexiglas (polymethylmethacrylate, PMMA). Experimental studies were performed at the Naval Ordnance Laboratory, Silver Spring, Maryland (1, 2, 3). A Mie-Grüneisen type equation of state is derived for PMMA in a form compatible with HEMP, the LRL elastic-plastic code (4). The data from which the equation of state is derived are a functional relation between the shock and the particle velocities measured at NOL.

The computed results are compared with data from the NOL reports. Attention is focused on the shock and free surface velocities along the axis, and the radius of curvature of the shock front. The interaction of the lateral rarefaction wave with the shock is also discussed.

## EXPERIMENTAL

### A. Observing Curvature of the Shock Fronts in PMMA

One of the NOL experimental assemblies is shown in Fig. 1. In these experiments and others described below, the material was shocked by detonating tetryl charges in contact with the specimen. The charges were two pellets each 5.08 cm in diam and 2.54 cm long, detonated at a point on the axis of symmetry. In the shock curvature experiments, the PMMA specimen was a rectangular block 5.08 cm sq by 12.7 cm long. The difference of curvature of the shock front in the rectangular column from that in a cylindrical column was taken into account. The square cross section was used because of difficulties in observing the shock wave in a cylinder.

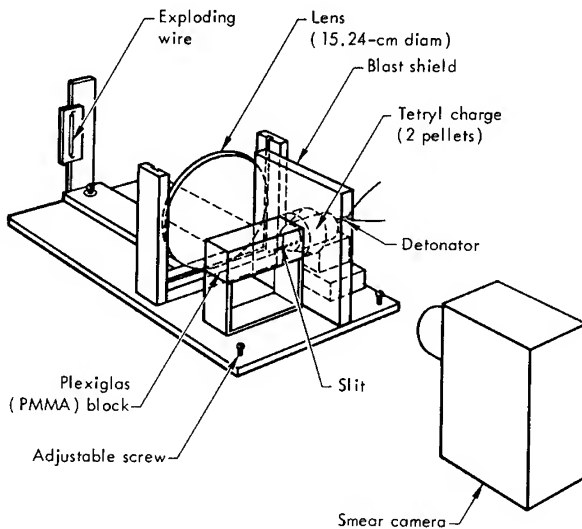


Fig. 1 - Experimental assembly for recording curvature of shock front

### B. Measuring the Shock Velocity

The shock velocity is measured by recording the progress of the front along the axis, using a streak camera. For this work, the diameter of the PMMA specimen cylinders was slightly greater than 5.08 cm. So that the shock could be viewed clearly against the back light, the lateral face of the cylinders was machined flat and polished so that two flat strips about 0.5 cm wide lay parallel to the axis, diametrically facing each other. The thickness of PMMA between the flat sections was 5.08 cm.

The camera records represented position versus time, so the experimental data had to be differentiated to get the shock velocity  $S$ . One reason for undertaking the computations reported here was to find out whether the  $S$  versus  $x$  curve is smooth. We wished to determine if the experimental data had been properly averaged so as to obtain the usual smooth gap-test calibration curves.

### C. Measuring the Free Surface Velocity

Free surface velocities were taken from experiments in which minute, thin plastic foils were projected off the free surface of PMMA cylinders (see Fig. 2). These cylinders were each 5.08 cm in diam; different lengths were used so that a curve of free surface velocity as a function of axial distance could be developed.

## EQUATION OF STATE

### A. Equation of State for PMMA

The data taken with smear cameras yielded the shock velocities and the free surface velocities. After the data points were smoothed, a functional relation between the shock velocities and the particle velocities was derived assuming that the particle velocity is half the free surface velocity. The relationship (5) was found to be

$$S = 0.587 \exp(-2.30u) + 2.45 + 1.67u \quad (1)$$

where  $S$  and  $u$  are the shock and particle velocities in mm/ $\mu$ sec, respectively.

Assuming the Hugoniot relations, the Mie-Grüneisen type equation of state for PMMA was derived from Eq. (1) as follows:

$$P = 0.09\mu + 0.001\mu^2 + 0.55\mu^3 + 0.441(E/V) \quad (2)$$

where  $\mu = (1/v) - 1$  is the volume compression,  $V = v/v_0$  is the ratio of the specific volumes, and  $E = e/v_0$  is the ratio of the specific energy to the specific volume at room temperature. The shear modulus of elasticity  $G$  and yield strength  $Y_0$  are  $G = 0.0143$  Mbar and  $Y_0 = 0.00142$  Mbar, respectively. The derivation of Eq. (2) is semiempirical because the first constant and Grüneisen coefficient are calculated from physical principles whereas the second and the third coefficients are empirically chosen.

Figures 3 and 4 demonstrate the accuracy of the equation of state. In Fig. 3, the shock and particle velocities are calculated from Eq. (2) according to the relationships

$$-\sigma = \rho_0 S u, \quad (3a)$$

$$V = 1 - \frac{u}{S}, \quad (3b)$$

$$-\sigma = P + (2/3) Y_0, \quad (3c)$$

where the stress ( $\sigma$ ) is positive in tension. The results are shown as a curve. The data points shown in this figure are taken from Eq. (1) and fall within 3% of the curve. Point A is the elastic limit of PMMA (explained below). Figure 4 shows a similar comparison between the Hugoniot curve as calculated from Eq. (2) and the points taken from Eq. (1) according to the relations in Eqs. (3). These points also fall within 3% of the curve below 0.3 Mbar.

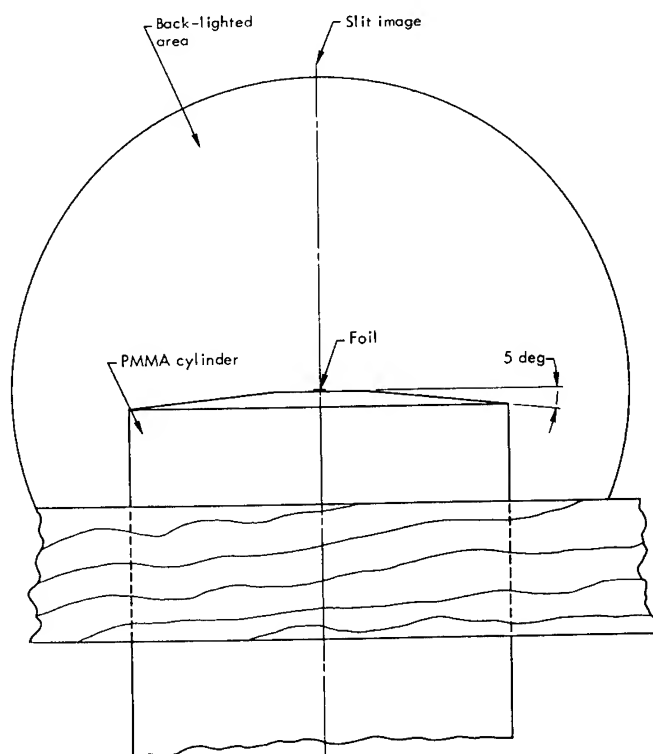


Fig. 2 - Typical smear camera setup for measuring the free surface velocity

The elastic limit is determined as follows. Equations (3) describe the plastic deformation which takes place above the elastic limit, whereas the elastic deformation which takes place below the elastic limit is described by a one-dimensional elastic relationship,

$$-\sigma = \left( K + \frac{4}{3} G \right) \left( \frac{1}{V} - 1 \right), \quad (4)$$

where  $K$  and  $G$  are the bulk modulus and shear modulus, respectively. Therefore, the intersection of these two curves is the elastic limit. The longitudinal sound velocity in PMMA yields

$$K + \frac{4}{3} G = 0.109 \text{ Mbar}.$$

In Fig. 5, the elastic limit is found at  $-\sigma_A = 5.45 \text{ kbar}$  and  $\mu = 0.05$

#### B. Equation of State for Tetryl

The equation of state for the detonation products of tetryl has not yet been studied to the extent as those for the more widely used explosives. For this reason, we used the gamma-law equation  $P = (\gamma - 1) E/V$  to

describe tetryl product gases. The tetryl was pressed to a density of  $1.51 \text{ gm/cc}$  and had a detonation velocity ( $D$ ) of  $0.72 \text{ cm}/\mu\text{sec}$ . The LRL Chemistry Department (6) determined the chemical energy,  $E_0$ , to be  $0.072 \text{ eu/cc}$  ( $\text{eu} = \text{Mbar} \times \text{cc} = 10^5 \text{ J}$ ). Solving for  $\gamma$  in the relation

$$\gamma^2 - 1 = \frac{\rho_0 D^2}{2 E_0}$$

yields  $\gamma = 2.54$ . This implies a Chapman-Jouguet pressure of  $0.221 \text{ Mbar}$  [ $P_{cj} = \rho_0 D^2 / (\gamma + 1)$ ], which is probably  $0.024 \text{ Mbar}$  too great. An alternate estimate, using results from the RUBY code, gives a value of  $2.98$  for  $\gamma$  and  $0.197 \text{ Mbar}$  for  $P_{cj}$ . The result of using the smaller value of  $\gamma$  is that such shock wave variables as stress, shock velocity, and particle velocity are probably too large.

#### COMPUTATIONS

Computations were performed with the HEMP code. This code is a two-dimensional Lagrangian code capable of handling problems in which the shear strength of the flowing material cannot be neglected. That is, it computes

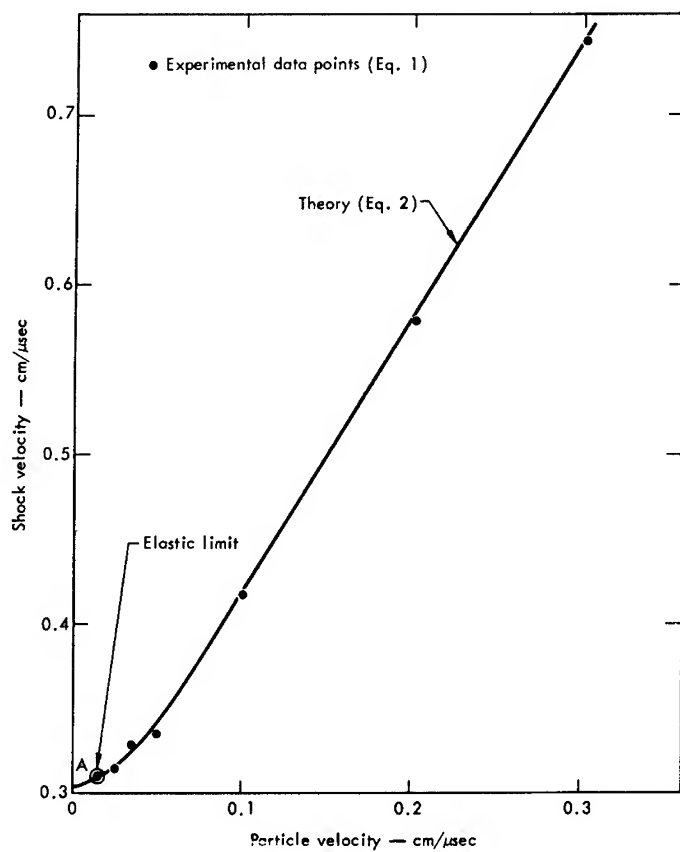


Fig. 3 - Shock velocity versus particle velocity

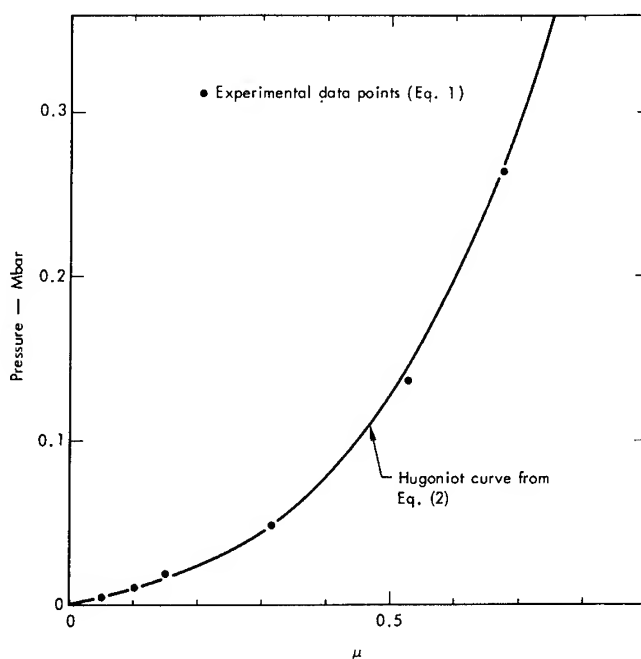


Fig. 4 - Equation of state for PMMA



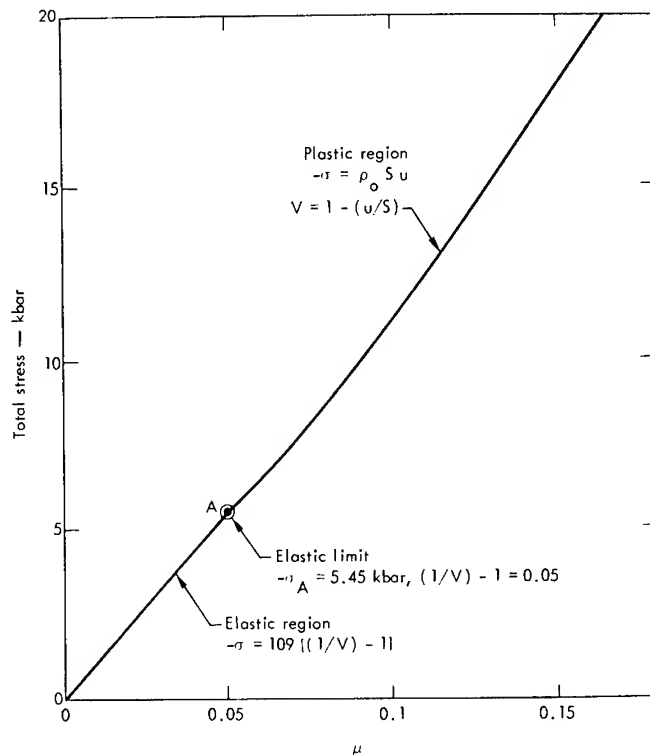


Fig. 5 - Stress curve derived from the measured shock and particle velocities

flow in elastic-plastic materials such as PMMA for which an elastic-plastic equation of state has been derived as above. The problem was set up as shown in Fig. 6, which gives the dimensions and the number of zones for each dimension. Each zone for this particular case is 0.127 cm sq. A zone size of 0.06 cm was used for computing the shape of the shock front. The problem is axially symmetric and has free surfaces as boundaries on three sides. The boundary between the explosive and the PMMA was treated so that the gases could slip with respect to the PMMA. No provision was made to simulate fracturing of the PMMA which, in these experiments, was observed to shatter completely near the explosive.

#### A. Shock Path

The computed position of the shock front is the point of the maximum  $Q$ , which is the well known artificial viscosity (4,7). Figure 7 shows shock position as a function of time. Also shown in this figure are data points obtained from five experiments done at NOL (2). These data are derived from the streak camera records in a straightforward manner. There are no difficult operations such as numerical or graphical differentiation. A real difference is evident between the experimental and computed results, meaning that the shock strengths by computation were too great. Hence we expect that for any given position the computed

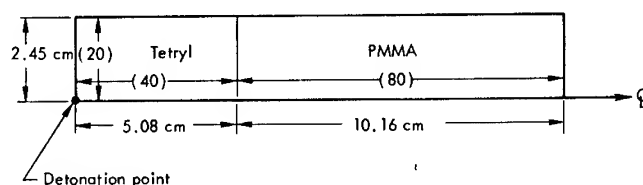


Fig. 6 - Geometry of the HEMP problem. The numbers in parentheses are zone numbers.

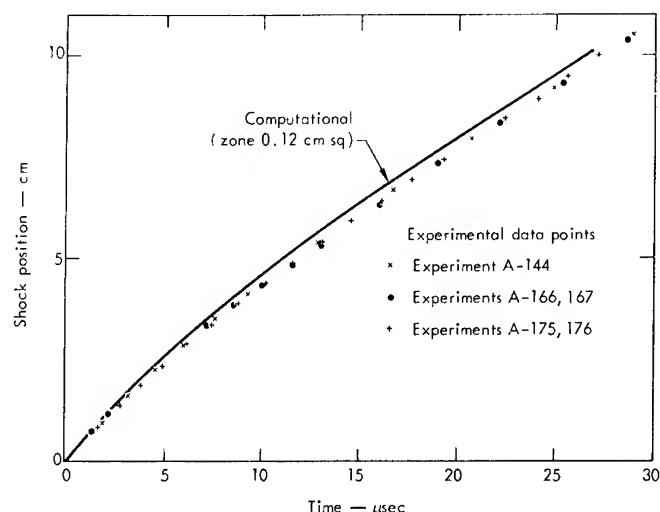


Fig. 7 - Shock position along the axis of a PMMA cylinder 5.08 cm in diam and 10.16 cm long

shock and particle velocities will be too large.

Since HEMP computes the shock position rather than the shock velocity, one has to differentiate Fig. 7 either graphically or numerically to get the shock velocity. An alternative approach would be to derive the shock velocities by Eq. (1) from the maximum particle velocities which HEMP calculates.

#### B. Particle and Free Surface Velocities

The particle velocity was recorded graphically and in tabular form. Figure 8 shows the peak particle velocity as a function of axial distance taken from the most recent NOL large scale gap test (LSGT) calibration (8). The curve was derived from both free surface velocities and shock velocities. Also shown in this figure are the computed maximum particle velocities and computed half-the-free-surface velocities at various points along the axis.

A broad "hump" appears in the experimental curve between 2.0 and 4.0 cm along the axis. The computation seems to confirm this result, implying that the  $s$  versus  $x$  curve should also show the hump as described in Ref. (2).

The disagreement between computational and experimental results is more than 10%. As discussed in the section on the tetryl equation of state, the Chapman-Jouguet pressure calculated from the gamma-law equation of state

may be too large. This probably explains the discrepancy between the computation and the experiment.

#### C. Radius of Curvature

Figure 9 shows five profiles of the shock front as computed by HEMP using finer zoning, i.e., 0.06-cm zones. Each curve is labeled with the elapsed time from initiation of detonation in the tetryl. The location of the front is found by searching for those zones having the greatest value of  $Q$ . For comparison, data points derived from NOL experiments are also plotted on Fig. 9. The agreement is good. The maximum difference is of the order of the dimension of a zone, 0.06 cm. Thus the numerical simulation reproduces the shape of the shock front better than it calculates the peak particle velocity.

By assuming that the shock wave is a spherical wave just as it enters the PMMA, the radius of curvature ( $r$ ) of the diverging spherical wave could be calculated for each profile, as shown on the bottom of Fig. 9. As the shock front advances in PMMA, a lateral rarefaction wave relieves the pressure. The point of deviation between the shock front and the diverging spherical wave is the front of the lateral rarefaction. The broken line in Fig. 9 follows the rarefaction fronts across the five profiles.

Measurements of the radius of curvature, made by a least square analysis of the photographic records, show a discontinuous decrease

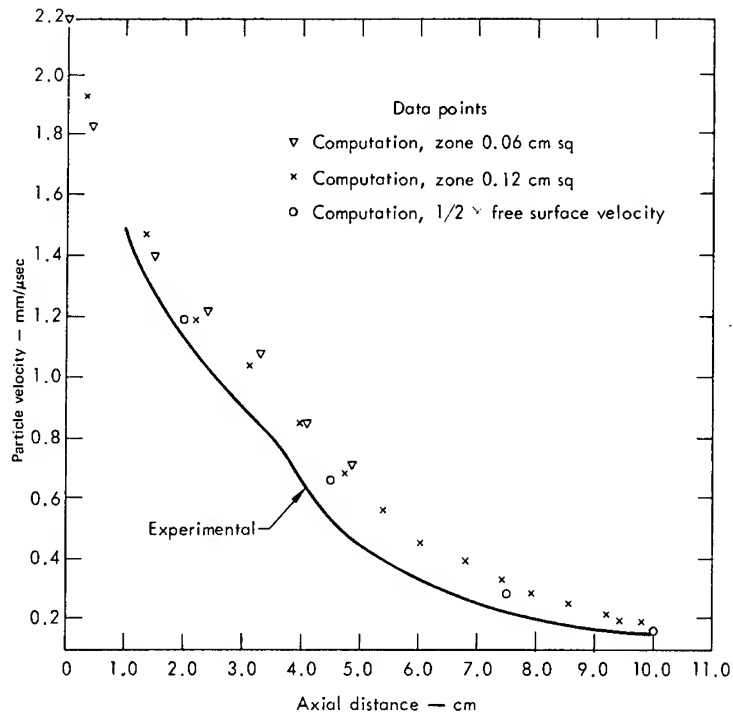


Fig. 8 - Particle velocity versus axial distance

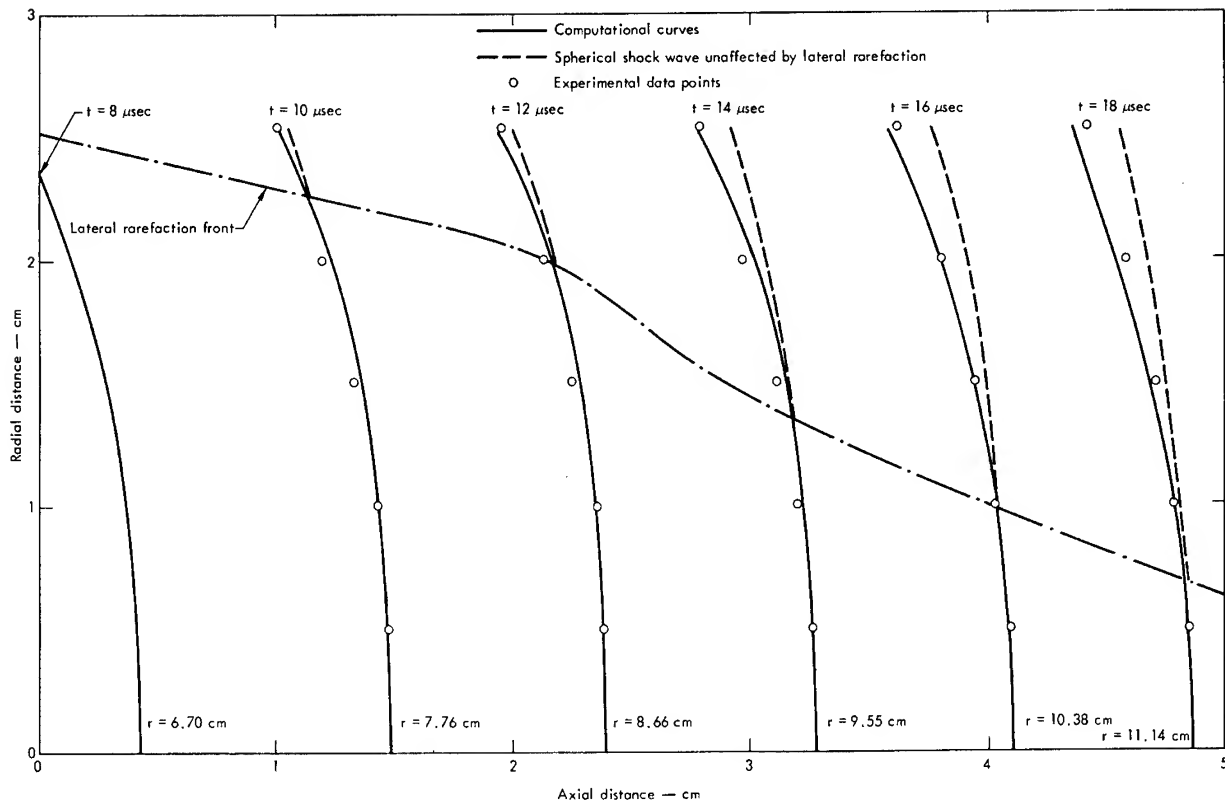


Fig. 9 - Shock profiles (time measured from detonation)

in the radius between 2 and 4 cm axial distance (1). Close examination of Fig. 9 reveals that the lateral rarefaction wave traveling along the shock front seemingly accelerates in this region, introducing more asphericity to the shock profile. Thus the radius of curvature measured by the least square analysis on the assumption that the shock front is a perfect sphere displays this apparent discontinuity.

## DISCUSSION AND CONCLUSIONS

It has been shown in the preceding discussion that simulation of the flow in a PMMA rod gives good results. This is inferred from comparing the shock path curves from experiments with that from the simulation. The computed particle velocity versus distance curve also agrees well with that obtained from experimental work. Finally, the curvature of the shock front is also reproduced by the simulation. The computed velocities and pressures are about 10% higher than the experimental values; this can be attributed to our selection of a  $\gamma$  value for tetryl giving a value for  $P_{ci}$  about 12% higher than better estimates (e.g., RUBY code computations). Hence we feel that a computer simulation of the LSGT is feasible.

Results of simulating the LSGT are useful because the process gives data which are either experimentally inaccessible or very difficult to obtain. For example, the simulation gives both particle velocity and pressure as functions of time for various points in the PMMA (see Figs. 10 and 11). For a point near the explosive, these curves display a sharp spike which decays significantly during some 0.5  $\mu\text{sec}$ . (See curves for  $x = 0$  or 0.03 cm and  $x = 0.44$  cm in Figs. 10 and 11.) For greater

values of  $x$ , the particle velocity curve becomes nearly flat (see  $x = 2.39$  cm curves) while the pressure curve is triangular. For  $x \geq 3.28$  cm, the rate of decay of  $u$  and  $P$  again becomes more rapid. Thus in the gap test, where different lengths of PMMA are used, the acceptor explosives are subjected not only to different peak pressures but to different rates of unloading.

The results of LSGT tests of several explosives are given in Table 1 (9). The critical pressure pulse required to initiate detonation in an explosive can be located in Fig. 11 by using the 50% gap thickness from Table 1 and the shock path curve (Fig. 7). In the LSGT, nitroguanidine responds to an intense, rapidly decaying shock. (Note that we always refer to the shock in the PMMA.) TATB responds to a less intense shock (59 kbar) which decays at a more moderate rate. Note also that the pressures given in Table 1 do not agree with those read from the peak pressure envelope of the curves in Fig. 11 because of the choice of equation-of-state parameters for tetryl (see above).

For such relatively insensitive explosives as TNT, the peak pressures are about 20 kbar and the rate of unloading  $\sim 17$  kbar/ $\mu\text{sec}$ . Note that the peak pressure, however, is still above that given by the LSGT calibration. The code rounds the shock front rather severely as  $x$  approaches 5 cm. Apparently finer zoning is required for more accurate computation of the rise time of the shock front.

The next step in simulating the LSGT is to compute the flow in the acceptor explosives. For this, we need an equation of state of the unreacted explosive, and values for at least some of the parameters that control the initiating

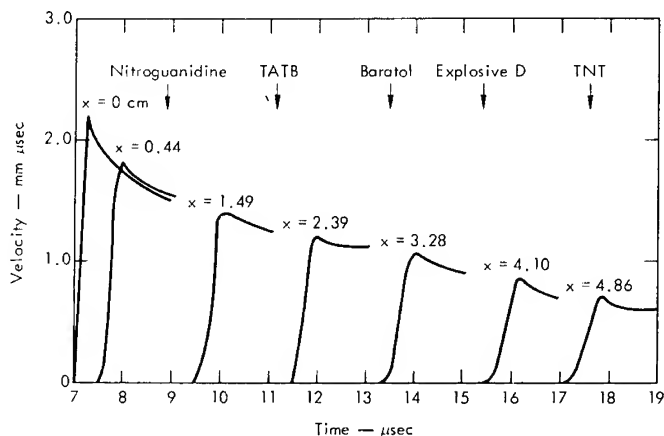


Fig. 10 - Particle velocity versus time after initiation

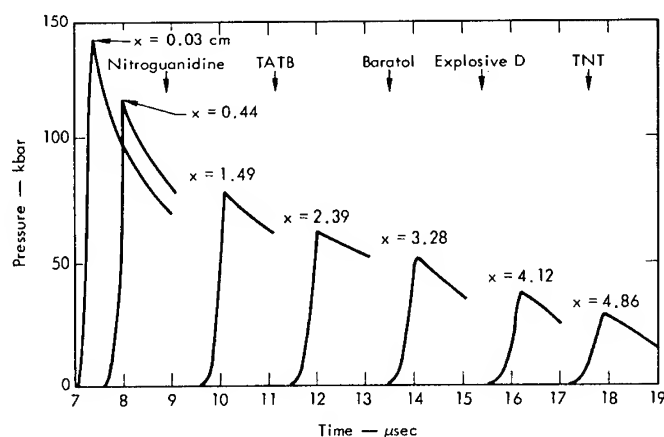


Fig. 11 - Pressure versus time after initiation

TABLE 1  
Large Scale Gap Test Results for Several Explosives

Explosive	Density— gm/cc	Theoretical Maximum Density— %	Gap Sensitivity (50% Point)		Method of Preparing Charges
			cm	kbar	
Nitroguanidine	1.64	92.1	0.81	93	Pressed in isostatic press
TATB	1.82	94.6	2.0	59	Pressed in isostatic press
Baratol	—	—	3.0	43	Cast
Explosive D	1.59	92.6	3.8	31	Pressed in hydraulic press
TNT	1.60	97.1	4.7	21	Pressed in isostatic press

process. This step is taken only after careful evaluation of probable values of the results has been completed.

#### ACKNOWLEDGMENTS

The authors wish to thank Mark Wilkins, Donna Price, Julius Enig, and Michael Guinan for their suggestions and comments. Gerald Richards was very helpful in interpreting the code. Beb Licuanan and Katherine Spence were the computer assistants.

#### REFERENCES

1. U.S. Naval Ordnance Laboratory, Technical Rept. NOLTR 64-66.
2. U.S. Naval Ordnance Laboratory, Technical Rept. NOLTR 65-43.
3. U.S. Naval Ordnance Laboratory, Technical Rept. NOLTR 67-10.
4. M. L. Wilkins, "Calculation of Elastic-Plastic Flow," Lawrence Radiation Laboratory, Livermore, Rept. UCRL-7322, Rev. 1.
5. J. W. Enig, NOL, private communication.
6. Edward Lee, Chemistry Department, Lawrence Radiation Laboratory, Livermore, private communication.
7. J. von Neumann and R. D. Richtmyer, J. Appl. Phys. 21, 232 (1950).
8. U.S. Naval Ordnance Laboratory, Technical Rept. NOLTR 66-87, p. 36.
9. I. Jaffe, G. E. Roberson, A. R. Clairmont, Jr., and D. Price, U.S. Naval Ordnance Laboratory, Technical Rept. NOLTR 65-177 (CONFIDENTIAL).

# A CODE METHOD FOR CALCULATING HYDRODYNAMIC MOTION IN HE DETONATIONS

Charles E. Needham  
*Air Force Weapons Laboratory*  
*Kirtland Air Force Base, New Mexico*

## ABSTRACT

A method is presented for calculating high explosive hydrodynamic motion and detonation. A two-dimensional Eulerian hydrodynamic code is used. The code allows for flow with large distortions and turbulence, permitting calculations normally difficult or impossible with the usual Lagrangian codes. A burn routine treats each zone individually. Detonation proceeds at a velocity determined by local conditions. It is immediately applicable to implosions, shaped charges, and complex interacting detonation fronts. The hydrodynamic code has proved accurate in predicting pressures, flow fields, and detonation velocities. Calculations of a center-detonated sphere demonstrated the code's symmetry. A second calculation demonstrated some of the code's capability. A "bomb-shaped" charge was two-point detonated producing a high-velocity jet where the two waves met. Calculation was continued until the peak air shock pressure was less than 30 psi. Results are compared with the same "bomb-shape" one-point detonated. This method provides all the parameters to accurately describe the hydrodynamic motion inside the explosive as well as in the surrounding media.

## INTRODUCTION

In recent years we who have been working with the SHELL code have been asked to provide predictions of airblast parameters for high explosive detonations. Until recently these requests were answered with the results obtained from two basic computer codes, SAP and SHELL.

SAP is a one-dimensional, Lagrangian, spherically symmetric, hydrodynamic computer code which we modified to allow high explosive "burn." SHELL is a two-dimensional, Eulerian, cylindrically symmetric hydrodynamic code. In all cases the burn was accomplished by SAP. If, after the burn was complete, two-dimensional effects were present (such as a reflecting ground plane) the SHELL code was used. The results of a SAP calculation were then converted to two-dimensions before two-dimensional effects were evident. The two-dimensional SAP results were then used as initial conditions for a SHELL calculation.

This procedure has provided experimenters with predictions for arrival times, overpressures, dynamic pressures, positive phase durations and impulses — in general, all measurable parameters. The results of such calculations have proven to be very accurate and for most experiments fall well within the error bars of the experimental data.

Recently we were asked to make predictions for the airblast from a bomb-shaped charge detonated simultaneously at both ends. The "burn" could not be done in one-dimension. This paper describes the method used to provide such predictions and presents some results of the calculations.

## THE HYDRODYNAMIC CODE

The basic SHELL code is a two-dimensional, cylindrically symmetric, Eulerian, hydrodynamic computer code. An Eulerian code allows flow with large distortions and turbulence thus

permitting calculations in situations which Lagrangian codes find difficult if not impossible. We considered this property to be most important in solving problems of the type mentioned in the introduction.

The partial differential equations for non-viscous, nonconducting compressible fluid flow are solved for each zone. The equations are

#### Mass

$$\left( \frac{\partial}{\partial t} + \mathbf{u} \cdot \nabla \right) \rho + \rho \nabla \cdot \mathbf{u} = 0$$

#### Momentum

$$\rho \left( \frac{\partial}{\partial t} + \mathbf{u} \cdot \nabla \right) \mathbf{u} + \nabla p + \rho \nabla \phi = 0$$

#### Energy

$$\rho \left( \frac{\partial}{\partial t} + \mathbf{u} \cdot \nabla \right) E + \nabla \cdot p \mathbf{u} + \rho \mathbf{u} \cdot \nabla \phi = 0$$

where

$\rho$  = density

$\mathbf{u}$  = velocity

$p$  = pressure

$E$  = specific total energy

$t$  = time

$\phi$  = potential of external field.

A time step ( $\Delta t$ ) is chosen and the cell parameters are updated to time ( $t + \Delta t$ ) in terms of the parameters at time  $t$ .

SHELL is a one-material code. In this form it has the capability of making pure hydrodynamic calculations for any material which can be treated as a compressible, inviscid fluid and for which a valid equation of state exists. The one-material version has been used for years in the study of air blast and pellet impact. The accuracy of the code is time tested and proven.

The basic one-material code is the heart of what we call the "SHELL family of fine codes." Some other members of the family are SHELL2, a two-material code; RADISH, a hydrocode with radiation diffusion; RADISH5, a five-material code with radiation diffusion; SPSHELL, a version written in polar coordinates; SHELLP, a version written for pure two-dimensional flow (no axis of symmetry).

A prerequisite for a code used to calculate HE "burn" is that it be able to handle several materials. RADISH5 was therefore chosen as a basis for the two-dimensional "burn" code. The radiation diffusion subroutine was removed in anticipation of a high explosive burn subroutine.

The hydrodynamic calculation is carried out in the following order: Subroutine CDT determines a time step based on

$$\Delta t < \frac{\Delta x_i}{2v_i}$$

where  $v_i$  is the maximum of material speed or sound speed and  $\Delta x_i$  is the minimum dimension of a zone.

Next, Subroutine PH1 considers the fluid at rest and determines only the pressure term contribution to the time derivative. The velocities are updated and the energy may be either updated or the change in energy stored for later reference.

Subroutine PH4 is an optional routine. It is either the radiation diffusion or "burn" routine. If used, the energy is appropriately updated, ignoring material motion.

Subroutine PH2 then transports mass. Momentum is conserved and energy, velocity and mass are updated in each cell. Total energy is conserved exactly. This completes one hydrodynamic cycle. Auxiliary routines are then called for editing and plotting before returning to CDT for the next cycle.

## THE "BURN" ROUTINE

Three main considerations made during the writing of the burn routine were its ease of use, compatibility with the already existing hydrocode, and application to the problems of interest.

The purpose of the calculation was to produce answers to the problems of the hydrodynamic motion of the detonation products and their effect on the surrounding media. The burn routine, therefore, is not concerned with the exact behavior at the detonation front nor with time-dependent chemistry of the explosive. Based on our experience with the one-dimensional burn routine, we established the following "ground rules."

1. The detonation front is a sharp line dividing the cell into burned and unburned explosive.

2. The detonation front proceeds through the unburned material at the sound speed of the material in the zone now being burned.

3. The energy released during detonation is simply the detonation energy times the amount of mass engulfed by the detonation front in one time step.

The above rules were sufficient in the one-dimensional case; however, two-dimensional effects present specific problems. In one-dimension the direction of the motion of the detonation front is obvious, either radially inward or outward. This problem was solved in two-dimensions by adding rule number four:

4. The detonation wave in a partially burned zone proceeds in the direction of the pressure gradient.

In two-dimensions we also have the problem of orientation of the detonation front within a zone. We found it impractical to keep track of possibly several detonation fronts in a single zone. To solve this problem we established rule number five.

5. No zone may ignite a neighboring zone until the first zone is completely burned.

One condition, which was not foreseen but which appeared in our second test problem, was the presence of a low-density region of high explosive at the surface of the charge. This condition is caused by the limited geometric resolution of an Eulerian code. The outer boundary of the charge did not coincide with zone boundaries; therefore, the density of the outer surface was taken as the mass-weighted average density of the high explosive and air. The artificially low density caused an artificially high surface sonic velocity. The result was that the detonation proceeded along the outer edge of the charge at several times the detonation velocity. It was therefore necessary to establish rule number six.

6. No zone may ignite a neighboring zone if its own density is below some arbitrary percentage of loading density.

A minor modification was also necessary in the mass transport routine, again due to the Eulerian description of the high explosive boundary. No burned explosive is allowed to leave a zone until all other materials have left.

With the above assumptions and rules the only information necessary to the burn routine is an equation of state and the detonation energy.

The routine treats each zone individually. Four passes are made through the entire grid each cycle. In the first pass, all energies are updated based on the results of PH1 and the ratio of burned high explosive to total high explosive is determined. If the ratio indicates the presence of either burned or unburned HE in an amount less than 1 part in  $10^4$  the small amount is zeroed and the energy properly balanced.

The second pass considers only those zones containing all burned explosive, with neighboring zones having unburned explosive but no burned explosive. In this case the detonation proceeds from the zone interface, perpendicular to the interface at the local sound speed.

The third pass through the grid ignores those zones considered in the second pass and only considers zones which are partially burned. When a partially burned zone is found, the two components of the pressure gradient across the cell are calculated (one radial, one axial). From these, the direction of the vector gradient is found. The detonation wave now proceeds at the speed of sound in the direction of the vector gradient, that is, along what I will call the sound vector.

The vector components of the now defined sound vector are taken in the direction of the two pressure gradient components. The detonation wave may now proceed along the pressure gradient components with a velocity equal to the corresponding sound vector component.

Defining the computational mesh such that  $X_i$ ,  $Y_j$  are the upper right hand corner of a zone having dimensions  $DX_i$ ,  $DY_j$  and density  $\rho_k$ , we may describe the amount of mass engulfed by the detonation wave in one time step.

First we must define the position of the detonation front in the zone. Assuming we are moving radially outward, the position of the detonation front (RZ) is defined by

$$RZ^2 = X_{i-1}^2 + \frac{TM - MU}{\pi \rho_k DY_j}$$

where TM is the total mass of the zone and MU is the mass of unburned explosive in the zone.

The mass of unburned explosive engulfed in a time step is then calculated as

$$\Delta M_k = \pi [(RZ + C_r \Delta t)^2 - RZ^2] \rho_k DY_j$$



where  $C_r$  is the radial component of the sound vector and  $\Delta t$  is the time step.

If the detonation wave crosses a zone boundary in a time step, the mass engulfed in the neighboring zone is calculated

$$\Delta M_{k+1} = \pi (RZ + C_r \Delta t)^2 - X_i^2 \rho_{k+1} DY_j.$$

Similar equations are used for axial motion of the detonation front.

The final pass through the grid converts the mass engulfed by the detonation wave in each zone from unburned explosive to burned explosive and deposits an amount of energy  $\Delta M_k E$ , where  $E$  is the amount of energy released per unit mass.

## CALCULATIONAL RESULTS

The calculations presented here used the LSZK equation of state for the detonation products in a TNT explosion. The SHELL code used a purely compressional equation of state for the unburned TNT. This is an analytical fit to the Hugoniot for solid explosives.

The first test problem was a 50-cm radius HE sphere loading density  $1.58 \text{ gm/cm}^3$  detonated at the center. Forty-six hundred and eight zones were in the computational mesh, each zone was 1.5 cm square. Thus, 1745 zones defined the sphere. This test problem served a dual purpose. The symmetry of the burn routine could be checked and the accuracy of the method could be found because analytical solutions are known for this configuration.

Figure 1 is an energy contour at a time of 70  $\mu\text{sec}$ . The detonation has been carried through approximately 30 zones. The outer series of contours demonstrates the limit of geometric resolution of the Eulerian grid. The input sphere was geometrically perfect. The stairsteps indicate the zone size. The inner contours show the symmetry of the detonation front relative to the surface of the sphere.

At this time the detonation front has reached a radius of approximately 47 cm with a detonation velocity of  $6.7 \times 10^5 \text{ cm/sec}$ . The analytic detonation velocity for the LSZK equation of state at this loading density is  $6.9 \times 10^5 \text{ cm/sec}$ . The difference between the calculated and analytic velocity is easily accounted for by the 1.5-cm zone size in the calculation and finite difference approximation made. Twice this error would not be considered serious. It can

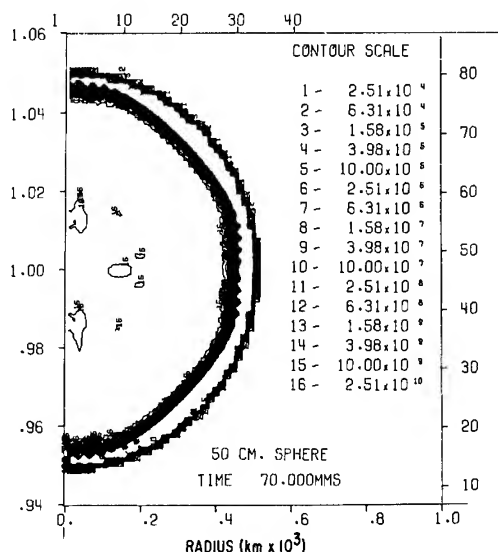


Fig. 1 - Energy contour

further be shown that this detonation velocity is constant over most of the radius. It took a few zones for the detonation to stabilize. The sawtooth effect on the detonation front is a result of the definition of the pressure gradient across a zone. This instability is bounded to a distance of less than one zone dimension. The burn method surpassed our expectations in accuracy of both geometric definition and hydrodynamic parameters. Figure 2 is a comparison with the analytical solution.

We then proceeded to make calculations for the specific case requested. "How would the airblast from a specific conventional bomb be modified if a second detonator were installed at the rear?" We chose the configuration such that the nose of the bomb was 1 meter above ground at the time of detonation. This placed the tail of the bomb 3.8 m above ground. Forty-six hundred and eight zones were used. Each zone was 4.5 cm in the axial direction by 1.5 cm in the radial direction. This asymmetry of the zones led to some asymmetry of the detonation front but was not considered serious.

A second calculation was made using the same configuration with only one detonator located at the tip of the bomb.

Comparison of the two calculations shows the detonation front from the tip is identical in both cases to a time of  $\sim 120 \mu\text{sec}$ . At this time the interaction of the two detonation fronts in the two-point calculation becomes important and considerably modifies the front.

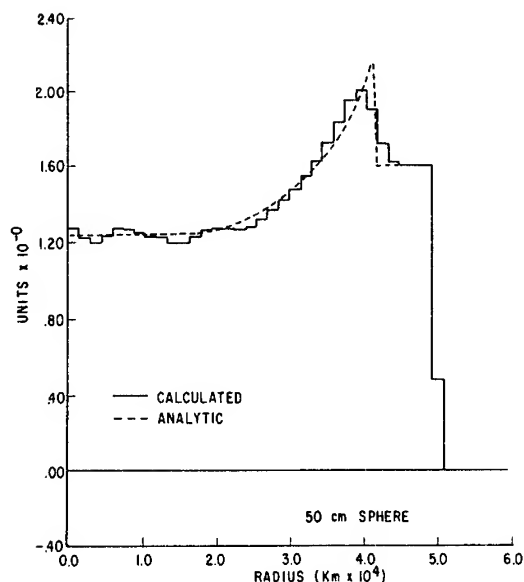


Fig. 2 - Density horizontal histogram

A jet forms at the plane of intersection of the detonation waves. The effect of this jet is found by comparing the peak pressure and dynamic pressure as a function of radius for the two calculations. Figure 3 is a comparison of the overpressure vs. distance curves for the two-point detonation and the one-point detonation at ground level. The overpressure remains at least a factor of two greater for the two-point detonation to a distance of about 10 meters. This represents the difference between 750 psi and 1500 psi.

#### POSSIBLE MODIFICATIONS

Of special interest in problems of this type is the effect of time-dependent chemistry behind the detonation front. A subroutine for the multimaterial code is now available for use which allows calculation of atmospheric time-dependent chemistry.

This routine can be modified to handle high-explosive time-dependent chemistry. Some work is now being done using a seven-species equilibrium chemistry routine.

Cased charges may also be calculated as long as the conditions are such that the case material may be treated as hydrodynamic, that is, as long as material strength is not important. Case fracturing can be included by employing relatively simple minimum density checks during the mass-transport phase of the calculation.

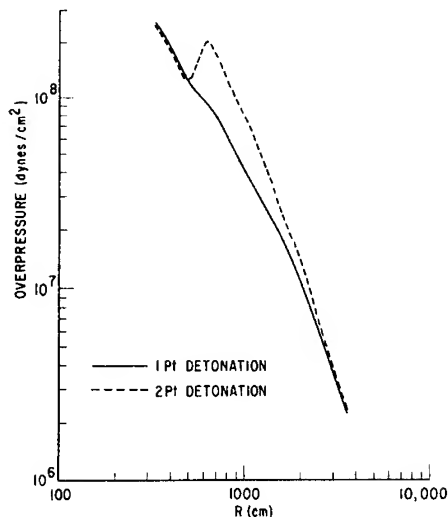


Fig. 3 - Overpressure vs ground range (at ground surface)

#### CONCLUSIONS

The development of the ability to calculate the phenomenology of complex interacting detonation waves provides, I believe, a significant advance in prediction and calculational technique.

This code provides a powerful tool for the study of the hydrodynamic aspects of detonation. The code has proven to be very accurate in the prediction of airblast from high-explosive detonations in several test series conducted both in the United States and Canada. I see no reason why this accuracy should be changed during the calculation of detonation.

It should be pointed out, however, that this code is expensive to run and may prove impractical for many budgets. The 5000-zone version of the code has a storage requirement of 240,000 octal locations and a running time of at least one hour on the CDC 6600 computer for the simplest of test problems. The one-point detonation presented here required approximately 5 hours to complete the burn and an additional 30 hours to carry the calculation to low overpressures.

In this particular instance, however, the cost of the full calculation was less than the cost of detonating one such actual device. The cost of field testing would then have to be included in addition. The calculation provides much more complete information than could be obtained from a single field test or even a series of tests.

# A REALISTIC APPROACH FOR DESCRIBING THE EXPLOSION-GENERATED AXI-SYMMETRIC WAVE PROPAGATING IN A HALF-SPACE

A. Sakurai  
*Waterways Experiment Station  
Vicksburg, Mississippi*

## ABSTRACT

In connection with the generally unsatisfactory situation of the present state-of-the-art for a surface burst problem, the particular sensitivity of the input to the solution of the problem is discussed and related to the singularity of the solution at the explosion source. In consequence of this, a realistic approach to the problem is considered by developing the approximate solution which has the singularity representing the characteristics of the source condition explicitly so that the above sensitive property can be handled properly. The approach is applied to the two cases of the acoustic and the elastic half-spaces, and their results are compared favorably with the test data for water and rock environments.

## INTRODUCTION

Consider here the problem of describing the shock wave generated by an explosion on or near an interface and its propagation into the lower half-space. The current standard theoretical approach to this problem is to simulate the process by a step-by-step numerical code calculation. The results are, however, generally not satisfactory (1, 2) as compared with its application to other problems such as airblast calculation. Quite often codes simply fail to give meaningful results because of instability. When they do give results, their solutions are often not only different from each other for the same physical problem, but also disagree with the test data.

This situation stems from the particular charge location, i.e., at the interface of two different media, which results in a sensitivity to the problem. The feature can be seen more clearly in the following example of water half-space, to which an analytical solution is available for the water shock induced by a spreading airblast loading on the surface (3), so that the procedure is free from the error of code simulation. Now, the water shock values computed

from this solution for the airblast input from an explosion above the surface show good agreement with the test data for various charge heights to small distances of a few charge radii (4). But, once the charge is partially in water, the test data show far larger shock values, in fact, ten times as large, compared with those computed, even if the measured surface pressure values from the test data are used for the surface airblast loading.

This singular nature at the surface is typical for a surface burst problem, and partly due to the direct wave from the direct impact but, as will be seen below, mostly caused by the airblast near the explosion source.

Mathematically, the phenomenon is related to the singularity of the solution at the explosion source. The solution given in the example above is designated only for the above-surface cases and lacks the singularity, and a solution without the singularity cannot describe the surface burst. On the other hand, any solution incorporating the singularity properly can possibly describe the dominant feature of the shock field outside the close-in range, as much as 90 percent as given above.

It is thus more realistic for the surface burst problem to utilize a solution including the singularity representing the characteristics of the source condition expressed explicitly so that its sensitivity can be properly handled to get a far-field solution that represents the one from the designated environment. Once the singularity is removed, it is not difficult to obtain an improvement by a straight computation.

Now, the mathematical problem of the explicit solution of a surface burst is very difficult even for the simplest models such as acoustic or linear elasticity, and the existing analytical solutions to this problem are either incomplete or unrealistic for the present purpose; thus, a more realistic and explicit solution, although approximate, is developed. The actual procedure for this is as follows. First, the nature of the source singularity is determined from the asymptotic expansion of the formal solution expressed in the Laplace-Hankel transforms, and then the approximated solution is constructed from the sum of the elementary solutions which have singularities at the origin and are matched to the above singularity.

In the following paragraphs, the method is applied to the two cases of acoustic and elastic half-spaces and their results are compared favorably with the test data for water and rock environments, respectively.

#### ACOUSTIC HALF-SPACE

Assume here that linear acoustic properties hold within the entire space. The assumption of acoustic property in the upper half-space sounds unrealistic and, in fact, is inadequate to describe the airblast field there. But it turns out to be sufficient for the purpose of providing the dominant feature in the lower half-space, as far as the solution has an appropriate singularity at the surface.

Using the cylindrical coordinate system  $(r, z, \theta)$  with  $z = 0$  the interface, the pressures  $p$  and  $p'$  in the lower and upper regions should satisfy

$$\Delta p = \frac{1}{C^2} \frac{\partial^2 p}{\partial t^2}, \quad \Delta p' = \frac{1}{C'^2} \frac{\partial^2 p'}{\partial t^2} \quad (1)$$

where

$$\Delta \equiv \frac{1}{r} \frac{\partial}{\partial r} r \frac{\partial}{\partial r} + \frac{\partial^2}{\partial z^2},$$

$$p \equiv p(r, z, t), \quad p' \equiv p'(r, z, t)$$

$t$  is the time and  $C, C'$  are the acoustic velocities in the lower and upper regions, respectively.  $p, p'$  must also satisfy the condition at the interface given as

$$p - p' = 0, \quad (2)$$

$$\frac{\partial}{\partial z} \left( \frac{p}{\rho_0} - \frac{p'}{\rho'_0} \right) = 0 \quad \text{for } z = 0, \quad r > 0$$

where  $\rho_0, \rho'_0$  are the densities in the lower and upper half-spaces.

A formal solution of Eqs. (1) and (2) with a source singularity at the origin  $(r, z = 0)$  can be given in the following way.

Express the solution  $p, p'$  of Eq. (1) in the general Laplace-Hankel transforms as

$$\left. \begin{aligned} p(r, z, t) &= L^{-1} \left[ \int_0^\infty b(\omega, s) J_0(\omega r) e^{-a z} \omega d\omega \right] \\ p'(r, z, t) &= L^{-1} \left[ \int_0^\infty b'(\omega, s) J_0(\omega r) e^{-a' z} \omega d\omega \right] \end{aligned} \right\} \quad (3)$$

where

$$a = \sqrt{\omega^2 + (s/C)^2}$$

$$a' = \sqrt{\omega^2 + (s/C')^2}$$

and  $L^{-1}$  represents the inverse Laplace transform with  $s$  its variable, and determine  $b, b'$  to satisfy Eq. (2) and have a source at the origin from

$$\left. \begin{aligned} b - b' &= \kappa(s) \\ \frac{a}{\rho_0} b - \frac{a'}{\rho'_0} b' &= \kappa'(s) \end{aligned} \right\} \quad (4)$$

where  $\kappa$  and  $\kappa'$  are functions of  $s$  only, to result in

$$b(\omega, s) = \left( \kappa - \frac{\rho'_0}{a'} \kappa' \right) \left( 1 - \frac{\rho'_0}{\rho_0} \frac{a}{a'} \right)^{-1}$$

which can be simplified, in practice, to

$$b(\omega, s) = \kappa - \frac{\rho'_0}{a'} \kappa'$$

because of the small value of the ratio  $\rho'_0/\rho_0$  for typical cases of application.

Thus, we get the formal solution  $p$  given as

$$p = L^{-1} \left[ \int_0^\infty \left( \kappa + \frac{\rho'_0}{a'} \kappa' \right) J_0(r\omega) e^{-az} \omega d\omega \right]. \quad (5)$$

The source functions  $\kappa$  and  $\kappa'$  in Eq. (4) are related to the total input force  $F_0(t)$  and acceleration  $W_0(t)$  at the center by

$$\left. \begin{aligned} \kappa(s) &= L(F_0), \quad F_0(t) = \int_0^\infty (p - p')_{z=0} r dr \\ \kappa'(s) &= -L \left\{ \int_0^\infty \left[ \frac{\partial}{\partial z} \left( \frac{p}{\rho_0} - \frac{p'}{\rho'_0} \right) \right]_{z=0} r dr \right\} \\ &= -L(W_0), \\ W_0(t) &= \int_0^\infty \frac{\partial}{\partial t} (V' - V)_{z=0} r dr \end{aligned} \right\} \quad (6)$$

where  $V, V'$  are the  $z$ -components of the material velocities.

It can be shown that

$$\begin{aligned} L^{-1} \left[ \int_0^\infty \kappa \cdot J_0(r\omega) e^{-az} \omega d\omega \right] &= \frac{z}{q^3} \\ &\times F_0 \left( t - \frac{q}{C} \right) \\ &\times H \left( t - \frac{q}{C} \right) \end{aligned}$$

where  $H$  is the Heaviside step function and  $q = \sqrt{r^2 + z^2}$ .

Accordingly, Eq. (5) is reduced to

$$\left. \begin{aligned} p &= \frac{z}{q^3} F_0 \left( t - \frac{q}{C} \right) H \left( t - \frac{q}{C} \right) + p_a \\ p_a &= L^{-1} \left[ -\rho'_0 \kappa' \int_0^\infty J_0(r\omega) \frac{e^{-az}}{a'} \omega d\omega \right] \end{aligned} \right\} \quad (7)$$

It is noted here that the first term  $p$  in Eq. (7) represents the "direct wave" caused by the direct impact of the source to the medium in the lower space, while the second term  $p_a$  is

interpreted as the "airblast induced wave" (5). Now, an explicit expression for  $p_a$  is derived in a manner as mentioned in the introduction above. By simply repeating the integration by parts, we get from Eq. (7)

$$\begin{aligned} (p_a)_{r=0} &= \frac{C'}{C} \rho'_0 W_0 \left( t - \frac{z}{C} \right) H \left( t - \frac{z}{C} \right) \cdot \frac{1}{z} \\ &+ C' \left( 1 - \frac{C'^2}{C^2} \right) H \left( t - \frac{z}{C} \right) \\ &\times \int_0^{t - \frac{z}{C}} \left( t - \frac{z}{C} - \eta \right) \rho'_0 W_0(\eta) d\eta \cdot \frac{1}{z^2} \\ &+ \dots \end{aligned} \quad (8)$$

Since  $p_a$  is a solution of the wave equation for  $p$  in Eq. (1), it can be expressed generally as the sum of the elementary solutions of the wave equation

$$p_a = \sum_{\substack{m, n=0, \\ 1, 2, \dots}} L_z^m \cdot L_r^n \cdot \frac{1}{q} f_{m,n} \left( t - \frac{q}{C} \right) \quad (9)$$

where

$$L_z \equiv \frac{\partial}{\partial z}, \quad L_r \equiv \frac{1}{r} \frac{\partial}{\partial r} r \frac{\partial}{\partial r}$$

and  $f_{m,n}$  are functions to be determined. Utilizing the symmetry property of  $p_a$  to the  $z = 0$  plane, Eq. (9) is reduced to

$$p_a = \frac{1}{q} f_{00} \left( t - \frac{q}{C} \right) + \frac{\partial^2}{\partial z^2} \cdot \frac{1}{q} f_{20} \left( t - \frac{q}{C} \right) + \dots \quad (10)$$

By comparing the terms in Eq. (10) with the same powers in  $z$  at  $r = 0$  of Eq. (8), the functions  $f_{00}, f_{20}, \dots$  are determined. They depend on how many terms are retained, and the second approximation using the first two terms gives

$$\begin{aligned} f_{00} &= \frac{C'}{C} \cdot \frac{1}{2} \left( 1 + \frac{C'^2}{C^2} \right) \rho'_0 W_0 \left( t - \frac{q}{C} \right) H \left( t - \frac{q}{C} \right) \\ f_{20} &= \frac{1}{2} C C' \left( 1 - \frac{C'^2}{C^2} \right) H \left( t - \frac{q}{C} \right) \\ &\times \int_0^{t - \frac{q}{C}} \left( t - \frac{q}{C} - \eta \right) \rho'_0 W_0(\eta) d\eta. \end{aligned} \quad (11)$$

With the explicit expression of  $p_a$  of Eqs. (10) and (11), Eq. (7) gives the pressure formula provided by the input functions  $F_0$  and  $W_0$ , which depend on the nature of the explosion. For the surface burst of a spherical HE charge, it is found (5) that they can be given by

$$F_0(t) = (\alpha a_0)^2 p_s e^{-t/D_s}, \quad (12)$$

$$\rho'_0 W_0(t) = K \frac{U'}{C} p'_s a_0 e^{-t/D'_s}$$

where  $a_0$  is the charge radius;  $p'_s$ ,  $U'$ ,  $D'_s$  are the initial shock pressure, velocity, and duration of the free airblast;  $p_s$ ,  $D_s$  are the corresponding values in the lower medium (free-water data); and  $\alpha$ ,  $K$  are the factors due to the deviation of the center of the charge from the interface. Thus, the pressure formula becomes for this case

$$p(r, z, t) = \bar{p}(r, z, t) H(y)$$

$$y = t - \frac{q}{C}$$

$$\begin{aligned} \bar{p}(r, z, t) = & p_s a_0^2 \frac{z}{q^3} e^{-y/D_s} \\ & + p'_s \frac{U'}{C} \frac{1}{2} \frac{a_0}{q} \left\{ \left[ 1 + \frac{C'^2}{C^2} \right. \right. \\ & + \left. \left( 1 - \frac{C'^2}{C^2} \right) \frac{z^2}{q^2} \right] e^{-y/D'_s} \\ & + \left( 1 - \frac{C'^2}{C^2} \right) \left( 3 \frac{z^2}{q^2} - 1 \right) \frac{CD'_s}{q} \\ & \times \left( \frac{y}{D'_s} - 1 + e^{-y/D'_s} \right) \frac{CD'_s}{q} \\ & \left. - 1 + e^{-y/D'_s} \right\} \end{aligned} \quad (13)$$

The pressure values for the water environments are computed from Eq. (13) using the values  $p_s = 4.6 \times 10^5$  psi,  $p'_s = 1.2 \times 10^4$  psi,  $D_s = 0.042 W^{1/3}$  msec,  $D'_s = 0.038 W^{1/3}$  msec,  $a_0 = 0.13 W^{1/3}$  ft,  $C = 4.9$  ft/msec,  $U'/C = 6.9$ ,  $C'/C = 0.23$ , and  $\alpha = K = 1$ , with  $W$  the charge weight in pounds, and they are compared with test data from detonations of various charge weights ranging from 5.5 to 10,000 pounds (5, 6).

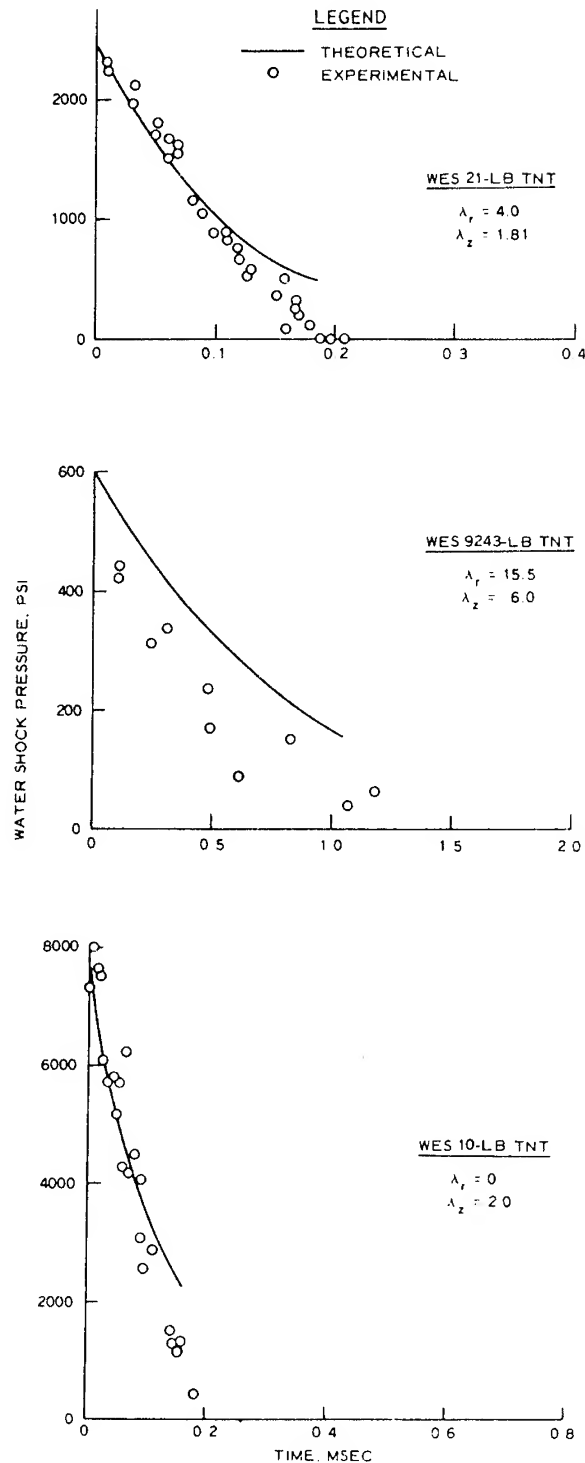


Fig. 1 - Water shock pressure-time history from Eq. (13) compared with test data

The agreement between the theoretical and test values is satisfactory as seen in Fig. 1.

As noted in the Introduction above, the direct wave was appeared in the first term in Eq. (13) has a significant contribution only for small  $q$  values, and otherwise the pressure values are dominated by the airblast induced term.

### ELASTIC HALF-SPACE

Consider here an elastic lower half-space and the shock field is described by the displacement potentials  $\phi$  and  $\psi$ , which are determined from the wave equations with the propagation velocities  $C_D$  and  $C_s$ , respectively. Upper medium is again assumed acoustic; then the formal solutions for  $\phi$  and  $\psi$ , satisfied by the boundary condition

$$\left. \begin{aligned} \sigma_{zr} &= 0 \\ \sigma_{zz} - p' &= 0 \\ \frac{\partial v}{\partial t} - \frac{\partial v'}{\partial t} &= 0 \end{aligned} \right\} \text{ for } z = 0, \quad r > 0 \quad (14)$$

with  $\sigma_{zr}$  and  $\sigma_{zz}$  the stress components, and having an input source at the origin, are determined in a similar manner as in the previous case.

$$\begin{aligned} \phi &= L^{-1} \left[ \int_0^\infty A \cdot J_0(r\omega) e^{-a_1 z} \omega d\omega \right] \\ \psi &= L^{-1} \left[ \int_0^\infty \frac{2a_1}{\omega^2 + a_2^2} A \cdot J_0(r\omega) e^{-a_2 z} \omega d\omega \right] \end{aligned} \quad (15)$$

where

$$a_1 = \sqrt{\omega^2 + (s/C_D)^2}, \quad a_2 = \sqrt{\omega^2 + (s/C_s)^2}$$

$$\begin{aligned} A &= \frac{1}{\rho_0 s^2} \left[ 1 + \frac{2C_s^2}{s^2} \omega^2 \left( 1 - \frac{2a_1 a_2}{\omega^2 + a_2^2} \right) \right]^{-1} \\ &\times \left[ \kappa(s) - \frac{\rho'_0}{a'} \kappa'(s) \right] \end{aligned}$$

and the smallness of the density ratio  $\rho'_0/\rho_0$  is also utilized to simplify  $A$ . The source functions  $\kappa$  and  $\kappa'$  are related to  $F_0(t)$  and  $W_0(t)$  as in Eq. (6), except for  $p$  replaced by  $\sigma_{zz}$  (c.f. Eq. (14)).

The formal solutions  $\phi, \psi$  given in Eq. (15) are now expanded, as in Eq. (8), in power series of  $1/z$  along the axis  $r = 0$ . It is convenient for this to divide  $\phi$  and  $\psi$  in two parts as

$$\phi = \phi_d + \phi_a, \quad \psi = \psi_d + \psi_a \quad (16)$$

where  $\phi_d, \psi_d$  are the terms with  $\kappa(s)$  and  $\phi_a, \psi_a$  for  $\kappa'(s)$  terms. Suffixes  $d$  and  $a$  stand for "direct" and "airblast" as in Eq. (7). Then we get

$$\begin{aligned} (\phi_a)_{r=0} &= -\frac{\rho'_0}{\rho_0} \frac{C'}{C_D} \cdot \frac{1}{z} \bar{W}_D^{(2)} \\ &\quad - \frac{\rho'_0}{\rho_0} \frac{C'}{2} \left[ 1 - \frac{C'^2}{C_D^2} - \frac{4C_s^2}{C_D^2} \right. \\ &\quad \times \left. \left( 1 - \frac{2C_s}{C_D} \right) \right] \frac{1}{z^2} \bar{W}_D^{(3)} + \dots \\ (\psi_a)_{r=0} &= -\frac{\rho'_0}{\rho_0} \frac{C_s}{C_D} \frac{C'}{z} \bar{W}_s^{(3)} \\ &\quad - \frac{\rho'_0}{\rho_0} \frac{C'}{C_D} \frac{C_s^2}{3} \left( \frac{C_D^2}{C_s^2} - \frac{C'^2}{C_s^2} - 7 + \frac{8C_s}{C_D} \right) \\ &\quad \times \frac{1}{z^2} \bar{W}_s^{(4)} + \dots \\ (\phi_d)_{r=0} &= \frac{1}{\rho_0 C_D} \frac{1}{z} \bar{F}_D^{(1)} \\ &\quad + \frac{1}{\rho_0} \left[ 1 - \frac{4C_s^2}{C_D^2} \left( 1 - \frac{2C_s}{C_D} \right) \right] \\ &\quad \times \frac{1}{z^2} \bar{F}_D^{(2)} + \dots \\ (\psi_d)_{r=0} &= \frac{2C_s}{\rho_0 C_D} \frac{1}{z} \bar{F}_s^{(2)} \\ &\quad + \frac{1}{\rho_0} \frac{C_s^2}{C_D} \left( \frac{C_D^2}{C_s^2} - 7 + \frac{8C_s}{C_D} \right) \\ &\quad \times \frac{1}{z^2} \bar{F}_s^{(3)} + \dots \end{aligned} \quad (17)$$

where

$$W^{(m)}(y) = H(y) \int_0^y (y-\eta)^{m-1} W_0(\eta) d\eta$$

$$F^{(m)}(y) = H(y) \int_0^y (y-\eta)^{m-1} F_0(\eta) d\eta$$

$$m = 1, 2, \dots$$

subscripts D, s stand for  $t - q/C_D$ ,  $t - q/C_s$ , respectively, submitted for the variable  $y$ , and the bar signifies the value at  $r = 0$ .

$\phi_a$ ,  $\phi_d$ ;  $\psi_a$ ,  $\psi_d$  in Eq. (16) are then postulated as Eq. (9) by utilizing elementary solutions of respective wave equations.

As a trial attempt, only their first terms are retained and are determined from Eq. (17) as

$$\begin{aligned} \phi_a &= -\frac{\rho'_0 C'}{\rho_0 C_D} W_D^{(2)} \cdot \frac{1}{q}, & \psi_a &= -\frac{\rho'_0 C_s}{\rho_0 C_D} C' W_s^{(3)} \cdot \frac{1}{q} \\ \phi_d &= \frac{1}{\rho_0 C_D} F_D^{(1)} \cdot \frac{1}{q}, & \psi_d &= \frac{2C_s}{\rho_0 C_D} F_s^{(2)} \cdot \frac{1}{q}. \end{aligned} \quad (18)$$

The horizontal and vertical displacements  $u$  and  $v$  are determined by

$$u = \frac{\partial \phi}{\partial r} + \frac{\partial^2 \psi}{\partial r \partial z}, \quad v = \frac{\partial \phi}{\partial z} - \frac{1}{r} \frac{\partial}{\partial r} \left( r \frac{\partial \psi}{\partial r} \right)$$

and they become very complicated even to the simplest approximation given by Eq. (18), but are simplified at  $z = 0$  to

$$\begin{aligned} (u)_{z=0} &= -\frac{1}{r} \cdot \frac{1}{\rho_0 C_D^2} \left[ F_D - C' \rho'_0 W_D^{(1)} \right] \\ &\quad - \frac{1}{r^2} \cdot \frac{1}{\rho_0 C_D} \left[ F_D^{(1)} - C' \rho'_0 W_D^{(2)} \right] \\ (v)_{z=0} &= -\frac{1}{r} \cdot \frac{2}{\rho_0 C_s C_D} \left[ F_s - C' \rho'_0 W_s^{(1)} \right] \\ &\quad - \frac{1}{r^2} \cdot \frac{2}{\rho_0 C_D} \left[ F_s^{(1)} - C' \rho'_0 W_s^{(2)} \right] \\ &\quad - \frac{1}{r^3} \cdot \frac{C_s}{\rho_0 C_D} \left[ 2F_s^{(2)} - C' \rho'_0 W_s^{(3)} \right]. \end{aligned} \quad (19)$$

Input functions  $F_0$  and  $W_0$  appropriate to ground shocks are found in the form (7)

$$F_0(t) = (\alpha a_0)^2 P_s \int_0^{t/D_s} e^{-\eta^2} d\eta \quad (20)$$

$$\rho'_0 W_0(t) = K a_0 \frac{U'}{C'} P_s e^{-t^2/D_s'^2}$$

where the parameters are all as defined in Eq. (12).

Horizontal acceleration  $(\ddot{u})_{z=0}$  from Eq. (19) with Eq. (20) is compared with experimental data (8) from detonation of HE on the rock surface. Only a tenth of the charge radius is in the ground in this case,  $a^2 = 0.2$ , and the  $K$  is the maximum value of 8. In Fig. 2 some typical  $\ddot{u}$  data are compared with the computed values. These show the basic consistency of the theory with the experimental data.

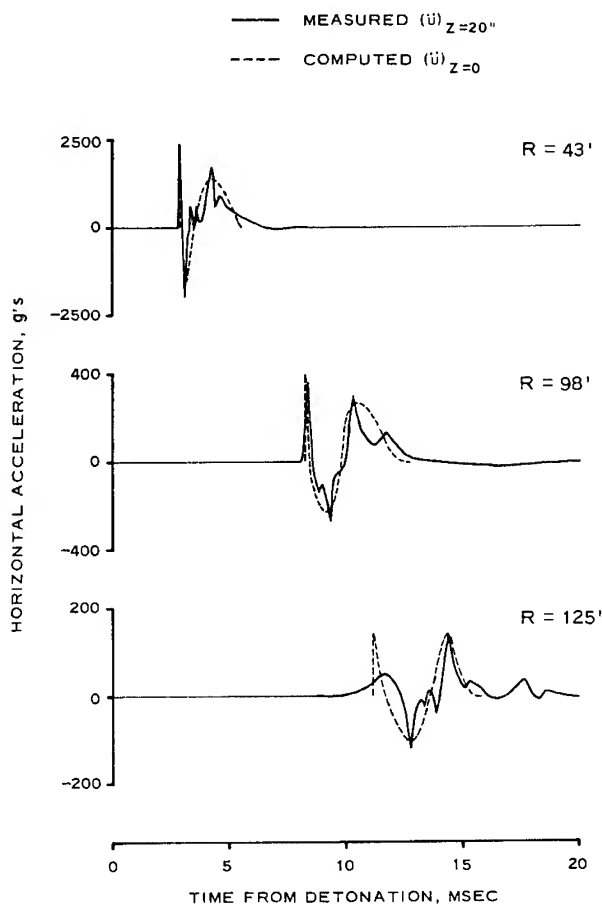


Fig. 2 - Comparison of calculated horizontal acceleration-time history with test data from MINE ORE Event, MINE SHAFT Series

## REFERENCES

1. H. F. Cooper, Jr., "Comparison Studies of Finite Difference Results for Explosions on the Surface of the Ground," Air Force Weapons Laboratory, Technical Report AFWL-TR-67-25, May 1967.
2. D. C. Gakenheimer, "Response of An Elastic Half Space to An Expanding Ring of



- Surface Pressure," RAND, Memorandum RM-6095-PR, August 1969.
3. A. Sakurai and J. M. Pinkston, "Water Shock Waves Resulting from Explosions above an Air-Water Interface, Report 1, Results of a Theoretical Investigation," U.S. Army Engineer Waterways Experiment Station Technical Report 1-771, April 1967.
  4. L. Miller, J. M. Pinkston, and J. N. Strange, "Water Shock Waves Resulting from Explosions above an Air-Water Interface, Report 2, Experimental Study," U.S. Army Engineer Waterways Experiment Station Technical Report TR 1-771, May 1970
  5. A. Sakurai, "Shock Waves Resulting from Explosions at an Air-Water Interface, Report 1, Analytical Study," U.S. Army Engineer Waterways Experiment Station Technical Report N-69-3, May 1969.
  6. L. Miller and J. M. Pinkston, "Shock Waves Resulting from Explosions at an Air-Water Interface, Report 2, Experimental Investigation, " U.S. Army Engineer Waterways Experiment Station Technical Report TR N-69-3, January 1971
  7. J. L. Drake and A. Sakurai, "Far Field Characteristics of Ground Shock Induced by Explosions," Army Science Conference Proceedings, June 1970.
  8. C. E. Joachim, "Mine Shaft Ground Motion Measurements: Events Mine Under and Mine Ore," U.S. Army Engineer Waterways Experiment Station, Technical Report (to be published).

# THE COMPUTATION OF GENERAL PROBLEMS IN ONE DIMENSIONAL UNSTEADY FLOW BY THE METHOD OF CHARACTERISTICS

B. D. Lambourn and N. E. Hoskin  
*Atomic Weapons Research Establishment  
Aldermaston, Berkshire, England*

## ABSTRACT

This paper describes the logical structure of a general purpose characteristic code RICSHAW which overcomes many of the difficulties that have previously discouraged the use of such codes. The code has the ability to consider multiple shocks, shock interactions and formation of shocks in compression waves in any number of regions using arbitrary equations of state. The relative advantages of characteristic and finite difference schemes are discussed and comparisons are given with calculations using a finite difference mesh code. It is shown that for similar usage of computer time the characteristic code gives smoother solutions, with much greater certainty of the position of shocks and other waves, and a physical insight into the wave phenomena that occur.

# EQUATION OF STATE OF DETONATION PRODUCTS

H. C. Hornig, E. L. Lee, and M. Finger  
Lawrence Radiation Laboratory, University of California  
Livermore, California 94550

and

J. E. Kurrle  
Mason & Hangar-Silas Mason Co., Inc., Burlington AEC Plant  
Burlington, Iowa 52601

## ABSTRACT

In previous papers we have described how isentropic expansions could be measured, and how an equation of state could be inferred if detonation velocity as a function of density were also known. The assumptions were: (1) that the fluid was essentially nonreactive once formed; (2) that the Grüneisen parameter,  $\frac{v}{C_v} \left( \frac{\partial P}{\partial T} \right)_v$ , was at most weakly temperature-dependent; and (3) that the C-J hypothesis holds.

This paper compares calculated results with experiments on PETN with the purpose of testing the assumptions made in the previous analysis. Recent  $P_{CJ}$  and detonation velocity measurements are reported for a density range  $0.25 < \rho_0 < 1.77$ .

## INTRODUCTION

Experimental determination of the equation of state of explosive detonation products has been the subject of many studies (1-9). These studies have provided in each case a proposed equation which contains various thermodynamic and hydrodynamic assumptions, and is more or less successful in describing the input data. In (9) we suggested the possibility of testing the assumptions by performing experiments which would provide independent data.

There are three assumptions contained in the equation of state given in (9). First, the Chapman-Jouguet (C-J) condition applies behind the detonation front. Next, the detonation products once formed are essentially nonreactive; and essentially the same products are formed from pentaerithritoltetranitrate (PETN) at various loading densities. This assumption implies that the heat (or energy  $E_0$ ) of detonation per gram is constant. Finally, we can neglect the dependence of the Grüneisen

parameter  $G = \frac{v}{C_v} \left( \frac{\partial P}{\partial T} \right)_v = v \left( \frac{\partial P}{\partial E} \right)_v$  on temperature; i.e.,  $G = G(V)$ .

The data used in (9) were the dependence of detonation velocity on density  $D(\rho_0)$ , and the isentropic pressures  $P_s(V)$ , which result from the detonation of PETN at its maximum loading density,  $\rho_0$  (max). To within the accuracy of the data the resulting equation of state is unique.

The equation given in (9) is

$$P = P_s + [G(V)/V] (E - E_s), \quad (1)$$

where

$$P_s = A \exp(-R_1 \cdot V) + B \exp(-R_2 \cdot V) + C/V^{(1+\omega)} \quad (2)$$

$$E_s = (A/R_1) \exp(-R_1 \cdot V) + (B/R_2) \exp(-R_2 \cdot V) + (C/\omega)(1/V^\omega) \quad (3)$$

This work was performed under the auspices of the U.S. Atomic Energy Commission.

and\*

$$G(V) = A_1 [1 + \tanh A_2 (A_3 - \rho/1.77)] \\ + B_1 [1 + \tanh B_2 (B_3 - \rho/1.77)] \quad (4) \\ + C_1 / \cosh [C_2 (C_3 - \rho/1.77)] + D_1$$

The coefficients for the above equations are given in Tables 1 and 2.

TABLE 1  
Coefficients for  $P_s(V)$

A	7.972
B	0.1943
C	0.00601
$R_1$	4.8
$R_2$	1.2
$\omega$	0.23

TABLE 2  
Coefficient for  $G(V)$

	1	2	3
A	0.11	15.0	1.35
B	0.21	4.5	0.71
C	0.09	7.5	0.25
D	0.40	—	—

We used the resulting equation to predict: (1) C-J pressure as a function of density,  $P_{CJ}(\rho_0)$ ; (2) expansion behavior of the detonation products of PETN at various densities,  $P_s(V)$  at  $\rho_0$ ; and (3)  $T_{CJ}(\rho_0)$ . We have obtained data for comparison with (1) and (2) but will restrict our attention to (1) in this paper.

## EXPERIMENTAL

PETN has a number of desirable properties for detonation studies: (1) it can be prepared in high purity; (2) it can be pressed into handleable charges over a wide density range (from  $\sim 0.8$  g/cc to crystal density, 1.77 g/cc) and gently pressed or shaken in place to densities as low as 0.25 g/cc; (3) because of the high oxygen content of PETN, its detonation products should be almost all gaseous; and (4) PETN shows negligible diameter effects in pieces of convenient size 1 to 2 in. in diameter. We used several sources of high purity PETN, but intermediate and low density charges were

best prepared from carefully recrystallized PETN with a surface area of 2 to 3.6 m<sup>2</sup>/g and particles of 1.5  $\mu$  in diameter by 2  $\mu$  in length. The PETN contained 1% of tripentaerithritol-octanitate (Tripeon) which acts as a mild binder. Charges 1 and 2 in. in diameter and measuring up to one diameter in length were pressed in dies with double acting rams.

The average density of each specimen was obtained from weight and volume measurements. The density uniformity along the axis of parts with density above 0.9 g/cc was monitored by a radiographic technique. Each radiograph was calibrated by placing beside the specimens a machined step tablet and a flat block, both of Plexiglas, closely matched to the specimen in x-ray absorption. We obtained a sensitivity of  $\sim 0.3\%$  in uniformity by measuring the film density with an accurate densitometer. A uniformity in density of 1 to 3% was obtained in most charges.

PETN detonation pressures were obtained by measuring the velocity of the shock transmitted by a plane detonation wave into polymethylmethacrylate (PMMA = Plexiglas) discs placed against the face of the charge (see Fig. 1). We observed the transit signals generated by the shock electric effect in the PMMA. The shock electric effect has been described by Hayes (17, 18).

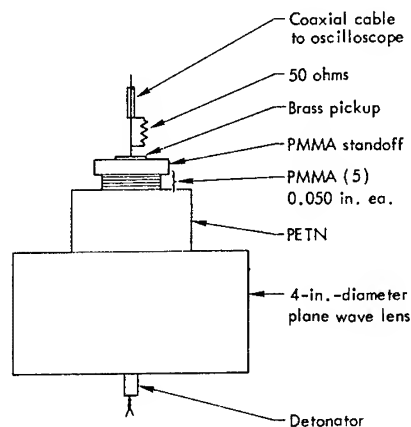


Fig. 1 - Experimental arrangement for  $P_{CJ}$  measurement by shock electric effect

Signals recorded with a high-speed oscilloscope provided accurate measurement of the shock arrival time at each interface of the stack of five accurately measured PMMA discs (1.27 mm thick). Time measurements were

\*The formula for  $G(V)$  was given incorrectly in (9).

made to a precision of a few nanoseconds. In the lowest density group (0.5 g/cc and less), the electrical signals were too weak for accurate measurement. For these specimens the C-J pressure was measured by either a quartz crystal (19), or a streak camera viewing the PMMA head-on (see Fig. 2). In the latter method the shock light did produce readable signals as the shock crossed each interface.

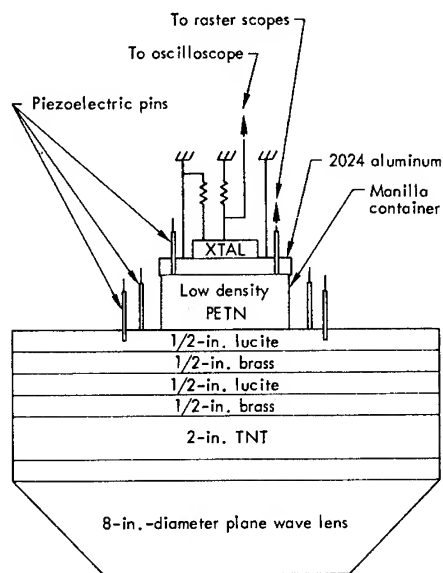


Fig. 2 - Experimental arrangement for  $P_{CJ}$  measurement by quartz crystals

Three driver systems were used to match the initiating pressure to the specimen. We tested for detonation stability by measuring detonation velocity and pressure as a function of sample length. A 4-in. diameter plane wave lens was used to initiate PETN charges down to a density of  $\sim 0.9$  g/cc. We observed slight overdrive in the first 0.5 in. of 0.9 g/cc PETN. At lower densities we observed excessive overdrive, and these pressure measurements were discarded.

For the lowest density charges (0.5 g/cc and less), special low-pressure initiating systems were used. This system had an input pressure to the PETN that just barely exceeded the threshold for initiation. Because of the low pressure of this initiating system, half the samples failed to detonate. Another driver system used with the lowest density charges consisted of a strongly attenuated 8-in.-diameter plane wave lens (Fig. 2). From a quartz crystal

experiment we estimate that a pressure of  $\sim 12$  kbar was transmitted to the PETN.

The distance-time ( $x-t$ ) data of the shock in the five PMMA discs were treated in the following way to yield the  $P_{CJ}$  in the PETN. Because of the gradual decay of the velocity of the shock as it passes through the PMMA, the initial shock velocity ( $U_{sor}$  at  $x=0$ ) was calculated by fitting the six  $x-t$  at points to the quadratic equation,

$$t = a + bx + cx^2 \quad (5)$$

The values of  $U_{sor}$  are listed in Table 3. Detonation pressures in the PETN were calculated using the impedance matching equation:

$$P_{CJ} = U_{por}(\rho_0 D + \rho_r U_{sor})/2 \quad (6)$$

where  $P_{CJ}$ ,  $\rho_0$ , and  $D$  are the pressure, density, and detonation velocity of the explosive sample; and  $\rho_r$ ,  $U_{por}$ , and  $U_{sor}$  are density, particle velocity, and shock velocity at  $x=0$  of the reference PMMA. The density of the PMMA used was 1.180 g/cc.

As described below,  $D$  was calculated from Eq. (7),  $U_{sor}$  was extrapolated from shock velocity measurements, and  $U_{por}$  was obtained from one of the three Hugoniot for PMMA given in Table 4. Selection of the Hugoniot depended on the value of  $U_{sor}$ .

For the shots with a quartz crystal detector, we used the calibration and quartz Hugoniot of Graham, Neilson, and Benedick (19) to convert the observed voltage into the shock parameters required in the impedance matching equation. The pressure data are listed in Table 3.

Detonation velocities were measured in several ways, but not all are equally valid. In each pressure experiment using the shock electric effect, a signal was automatically recorded as the shock front crossed the entrance and exit face of the PETN charge. This transit time gave an average detonation velocity which included the transient behavior near the initiated end. Indeed, with a 4-in.-diameter plane wave lens the 0.5 in. long charges showed underdrive at 1.76 g/cc and overdrive at 0.9 g/cc.

It was believed that these measurements did not yield sufficiently reliable detonation velocities. Therefore, a number of rate sticks were fired. In addition, measurements were made in the cylinder test (5) in which a 1-in. diameter column of PETN charges was confined in a copper tube with 0.1-in. wall. Piezoelectric

TABLE 3a  
PETN Experimental Detonation Pressures, This Work

Density (g/cc)	Dimensions of PETN Diameter × Length (in.)	Detonation Velocity* (mm/μsec)	Shock Velocity $U_{sor}$ (mm/μsec)	Detonation Pressure $P_{CJ}$ (kbar)
Shock Electric Effect Measurements				
1.764	2 × 0.5	8.28	7.01	338
1.763	1 × 0.5	8.27	6.98	333
1.763	1 × 0.5	8.27	6.98	334
1.763	1 × 1	8.27	7.04	340
1.763	2 × 0.5	8.27	7.01	338
1.763	2 × 1	8.27	7.03	340
1.762	2 × 1	8.27	6.99	335
1.762	2 × 1	8.27	7.07	343
1.758	1 × 1	8.26	6.98	333
1.71	1 × 1	8.11	6.86	311
1.71	1 × 1	8.11	6.81	307
1.71	1 × 1	8.10	6.83	309
1.70	1 × 1	8.08	6.84	308
1.70	1 × 1	8.06	6.83	306
1.69	1 × 1	8.03	6.83	304
1.60	1 × 1	7.76	6.57	266
1.60	1 × 1	7.74	6.60	266
1.59	1 × 1	7.71	6.52	259
1.53	1 × 1	7.49	6.21	225
1.46	1 × 1	7.22	5.99	198
1.45	1 × 1	7.18	6.16	208
1.44	1 × 1	7.14	6.05	199
1.38	1 × 1	6.91	5.79	173
1.23	1 × 1	6.38	5.45	136
1.23	1 × 1	6.37	5.42	134
1.23	1 × 1	6.37	5.47	137
1.23	1 × 1	6.37	5.56	142
1.23	1 × 1	6.36	5.54	141
1.23	1 × 1	6.36	5.56	142
0.99	1 × 0.5	5.48	4.91	87
0.95	1 × 0.5	5.33	4.93	85
0.93	1 × 1.5	5.27	4.68	73
0.93	1 × 1	5.26	4.77	77
0.93	1 × 1.5	5.25	4.61	70
0.89	1 × 1	5.10	4.70	71
0.88	1 × 1	5.06	4.63	68
Optical (Smear Camera) Measurements				
0.48	1.5 × 1	3.60	3.72	24
0.30	1.5 × 0.5	2.99	3.44	13
0.29	1.5 × 1	2.96	3.49	15
0.27	1.5 × 0.5	2.91	3.18	5
Quartz Crystal Measurements				
Density (g/cc)	Dimensions of PETN Diameter × Length (in.)	Detonation Velocity* (mm/μsec)	Pressure in Quartz (kbar)	Detonation Pressure $P_{CJ}$ (kbar)
0.25	1.75 × 1	2.83	16	8
0.25	1.75 × 1	2.83	13	7
0.25	1.75 × 1.5	2.83	12	6

\*Obtained from 3-segment "best fit" equations for Detonation Velocity (see text).

TABLE 3b  
PETN Experimental Detonation Pressures,  
Other Work

Density (g/cc)	Detonation Velocity (mm/ $\mu$ sec)	Detonation Pressure $P_{CJ}$ (kbar)	Ref.
1.77	8.50	340	(14)
1.77	8.31	320	(9)
1.67	7.97	300	(16)
1.66	8.10	246	(15)
1.65	7.92	305	(23)
1.51	7.42	187	(15)
0.95	5.30	64	(15)

pins accompanying the quartz crystal experiments also yielded velocity data at  $\rho = 0.25$  g/cc. Detonation velocities from our rate stick and cylinder test measurements and from other investigators are listed in Table 5. These data were fitted with three linear segments intersecting at  $\rho = 0.37$  and  $1.65$  g/cc. The resulting equations are:

$$D = 2.14 + 2.84 \rho, \quad \rho < 0.37, \text{ mm}/\mu\text{sec}$$

$$D = 3.19 + 3.70 (\rho - 0.37),$$

$$0.37 < \rho < 1.65, \text{ mm}/\mu\text{sec}$$

$$D = 7.92 + 3.05 (\rho - 1.65), \quad \rho > 1.65, \text{ mm}/\mu\text{sec} \quad (7)$$

In Fig. 3 we can see the relationship of the collected experimental  $D(\rho_0)$  data compared to the best fit Eq. (7) above. Detonation velocities

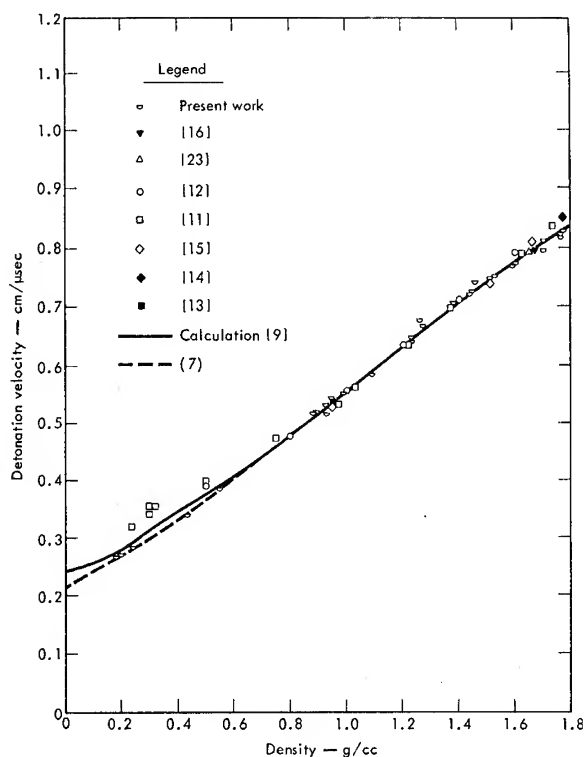


Fig. 3 - PETN detonation velocity vs density

calculated from the above best fit equation are listed in column 3 of Table 3 and were used in the calculation of detonation pressure.

We estimate the overall uncertainty in  $P_{CJ}$  to be about 5% except for  $\rho_0 < 0.5$ , where it may be as large as 20%.

TABLE 4  
PMMA Hugoniot\*

Source	Range			Equation
	P (kbar)	$U_p$ (mm/ $\mu$ sec)	$U_s$ (mm/ $\mu$ sec)	
(20) Barker, Hollenbach	0-31	0-0.72	2.7-3.6	$U_s = 2.745 + 3.537 U_p - 8.834 U_p^2 + 8.361 U_p^3$ $U_p = 36.70 - 34.155 U_s + 10.347 U_s^2 - 1.010 U_s^3$
(21) Compendium-2A	31-200	0.72-2.63	3.6-6.58	$U_s = 2.510 + 1.545 U_p$
(22) Compendium-3A	200-700	2.63-5.7	6.58-10	$U_s = 3.167 + 1.30 U_p$

\*PMMA density = 1.180 g/cc.

TABLE 5a  
PETN Experimental Detonation Velocities,  
This Work

Density (g/cc)	Detonation Velocity (mm/ $\mu$ sec)	Density (g/cc)	Detonation Velocity (mm/ $\mu$ sec)
Pin Switch Measurement			
1.773	8.30*	1.27	6.66†
1.765	8.28†	1.26	6.76†
1.765	8.16†	1.09	5.83†
1.765	8.24*	1.09	5.83†
1.763	8.27*	0.55	3.85*
1.762	8.25*	0.436	3.40*
1.762	8.26*	0.241	2.81*
1.51	7.44†	0.201	2.73*
1.51	7.49†	0.185	2.67*
Shock Electric Effect Measurement‡			
1.71	8.00	1.23	6.48
1.71	8.00	1.23	6.50
1.71	8.08	1.23	6.46
1.70	8.03	1.23	6.46
1.70	7.96	1.23	6.46
1.69	7.97	1.23	6.43
1.60	7.74	0.99	5.52
1.60	7.74	0.95	5.41
1.59	7.69	0.93	5.31
1.53	7.51	0.93	5.33
1.46	7.41	0.93	5.15
1.45	7.26	0.89	5.20
1.44	7.20	0.88	5.17
1.38	7.07		

\*Unconfined rate stick.

†Cylinder test.

‡All other data are detonation pressure experiments.

## RESULTS AND DISCUSSION

Figure 3 shows the  $D(\rho_0)$  data and the calculated curve produced by the equation of state (9). Since publication of our earlier paper more velocity data have been obtained requiring some adjustment of the  $D(\rho_0)$  fit. However, the resulting adjustment in our equation of state is not significant for the comparisons we shall make. For this reason, and for consistency, we have retained the coefficients published previously.

We show in Fig. 4 the dependence of  $P_{CJ}$  on density as measured here and elsewhere and the dependence as calculated in (9). The  $P_{CJ}$  for the basis isentrope ( $\rho_0 = 1.77$ ) should be revised from 320 to 340 kbars, a change which would remove the discrepancy in  $P_{CJ}(\rho_0)$  for

TABLE 5b  
PETN Experimental Detonation Velocities,  
Other Data

Density (g/cc)	Detonation Velocity (mm/ $\mu$ sec)	Ref.	Density (g/cc)	Detonation Velocity (mm/ $\mu$ sec)	Ref.
1.77	8.50	(14)	1.03	5.62	(11)
1.73	8.35	(11)	1.00	5.55	(12)
1.67	7.97	(16)	0.97	5.33	(11)
1.66	8.10	(15)	0.95	5.30	(15)
1.65	7.92	(23)	0.95	5.35	(13)
1.62	7.91	(11)	0.80	4.76	(12)
1.60	7.92	(12)	0.75	4.71	(11)
1.51	7.42	(15)	0.50	3.90	(12)
1.51	7.42	(11)	0.50	3.97	(11)
1.40	7.13	(12)	0.32	3.53	(11)
1.37	6.97	(11)	0.30	3.55	(11)
1.22	6.36	(11)	0.30	3.42	(11)
1.20	6.34	(12)	0.24	3.20	(11)

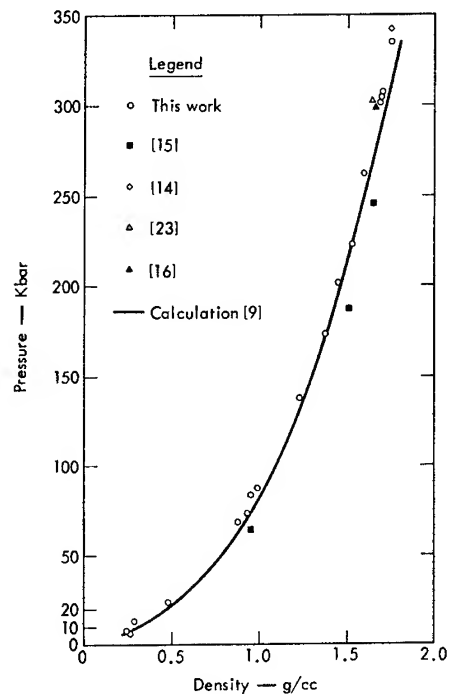


Fig. 4 - PETN detonation pressure vs density

$\rho_0 > 1.6$ , but as in the case of the  $D(\rho_0)$  dependence, we have retained the earlier value.

The region near the C-J plane has been investigated experimentally by Rivard and Venable



(10) for Composition B, who obtained results not inconsistent with the C-J hypothesis. Calculated values presented here based on the C-J hypothesis are in agreement with experiment. We can say at least that there is no contradiction to the C-J hypothesis based on our results.

The remaining two assumptions are not wholly separable, but a parameter study, shown in Figs. 5 and 6, gives some indication of their effect on  $P_{CJ}(\rho_0)$  and  $D(\rho_0)$ . Curve A is calculated for  $G' = 1.2 G$ . Curve B represents a situation where  $E_0$  decreases linearly with density from the normal value of 0.057 at  $\rho_0 = 1.77$  to 0.037 at  $\rho_0 = 0$ . The experimental data lie within these limits.

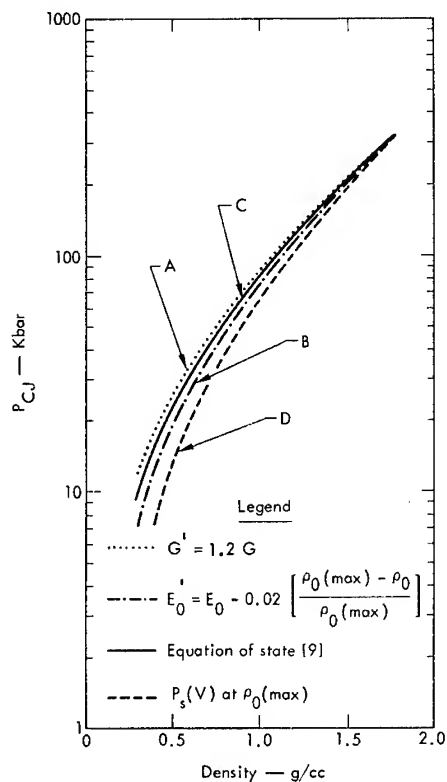


Fig. 5 - Effect of  $G$  and  $E_0$  on  $P_{CJ}(\rho_0)$  of PETN

As can be seen in Fig. 5, the difference between the basis isentrope  $P_s(V)$  at  $\rho_0 = 1.77$ , and  $P_{CJ}(\rho_0)$  is never more than 15 kbar. For  $\rho_0 < 0.6$ , of course, this difference is a major fraction of the total pressure.

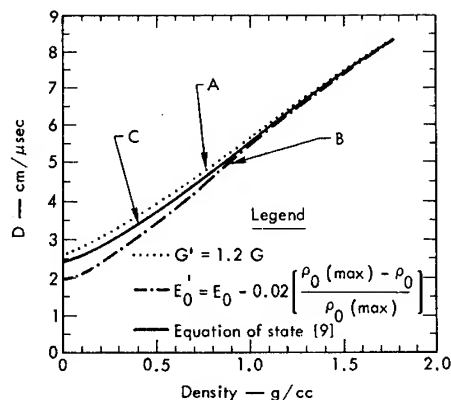


Fig. 6 - Effect of  $G$  and  $E_0$  on  $D(\rho_0)$  of PETN

## CONCLUSION

The  $P_{CJ}(\rho_0)$  dependence is not a severe test of the assumptions regarding  $G$  and  $E_0$ . However, the experimental confirmation of the  $P_{CJ}(\rho_0)$  dependence is encouraging and, moreover, essential to the interpretation of the more crucial experiments on  $P_s(V)$  at lower loading densities.

Refinement of the  $D(\rho_0)$  dependence, especially at low density, and confirmation of both  $P_{CJ}(\rho_0)$  and  $P_s(V)$  should make it possible to calculate reliable temperatures of the detonation products of PETN (using methods described in (9)). We intend to present the results of the expansion experiments at lower PETN densities and the temperature calculations in a future publication.

## ACKNOWLEDGMENTS

For their contributions to the experimental measurements, the authors are indebted to K. V. Fordyce, H. A. Golopol, L. R. Hawk, F. H. Helm, M. W. Jepson, E. J. Nidick, Capt. M. C. Purdy (USAF), and R. J. Wasley. We wish also to acknowledge the literature review performed by B. M. Hilliker and the many helpful discussions with J. W. Kury.

## REFERENCES

1. H. Jones and A. R. Miller, "The Detonation of Solid Explosives," Proc. Roy. Soc. London, Vol. A-194, p. 480 (1948).

2. H. Jones, Third Symposium on Combustion, Flame and Explosion Phenomena, p. 590, Williams and Wilkins (1949).
3. W. Fickett and W. W. Wood, "A Detonation-Product Equation of State Obtained from Hydrodynamic Data," *Phys. of Fluids*, Vol. 1, 528 (1958).
4. M. L. Wilkins, "The Equation of State of PBX 9404 and LX04-01," Lawrence Radiation Laboratory, Livermore, Rept. UCRL-7797 (1964).
5. J. W. Kury, H. C. Hornig, E. L. Lee, J. L. McDonnell, D. L. Ornellas, M. Finger, F. M. Strange, M. L. Wilkins, "Metal Acceleration by Chemical Explosives," Fourth Symposium on Detonation, p. 3, Office of Naval Research (1965).
6. N. M. Kuznetsov and K. K. Shvedov, "Equation of State of the Detonation Products of RDX," *Fizika Goreniya i Vzryva*, Vol. 2, No. 4, pp. 85-96 (1966).
7. N. M. Kuznetsov and K. K. Shvedov, "Isentropic Expansion of the Detonation Products of RDX," *Fizika Goreniya i Vzryva*, Vol. 3, No. 2, pp. 203-210, 1967. "Combustion, Explosion and Shock Waves," Vol. 3(2), p. 125 trans.
8. E. L. Lee, H. C. Hornig, and J. W. Kury, UCRL-50422, May 2, 1968.
9. E. L. Lee and H. C. Hornig, "Equation of State of Detonation Product Gases," Twelfth Symposium (International) on Combustion, p. 493 (1969).
10. W. C. Rivard and D. Venable, "A PHERMEX Study of the Flow Behind a Detonation Wave in Composition B," *Bull. Am. Phys. Soc. Series 11*, Vol. 14, 1094 (1969).
11. W. Friederich, "Über die Detonation der Sprengstoffe" (The detonation of explosives). *Z. ges. Schiess-Sprengstoffw.*, Vol. 28 (1933), pp. 2-6, 51-3, 80-3, 113-16. Translated from the German (September 1968) by J. Mulhaus.
12. E. A. Christian and H. G. Snay, "Analysis of Experimental Data on Detonation Velocities," NAVORD Rept. 1508 (1956).
13. M. A. Cook, R. T. Keyes, W. S. Partridge, W. O. Ursenbach, "Velocity-Diameter Curves, Velocity Transients and Reaction Rates in PETN, RDX, EDNA and Tetryl," *J. Am. Chem. Soc.*, Vol. 79, pp. 32-7 (1957).
14. Y. A. Apin and I. M. Voskoboynikov, *HMFT*, Vol. 117, No. 5 (1961).
15. A. N. Dremin and K. K. Shvedov, *Zh. Prikl. Mekh. Tekn. Fiz.*, Vol. 3, p. 154 (1964) (Translation).
16. W. Fickett, "Detonation Properties of Condensed Explosives Calculated with an Equation of State Based on Intermolecular Potentials," Los Alamos Scientific Laboratory Rept. LA 2712 (1962), p. 134.
17. B. Hayes, "The Detonation Electric Effect," *J. Appl. Phys.*, Vol. 38, pp. 507-511, Feb. 1967.
18. B. Hayes, "Electric Signals Generated by Shock and Detonation Waves," presented at the Western States Section of the Combustion Institute, Oct. 28, 1968.
19. R. A. Graham, F. W. Neilson and W. B. Benedick, "Piezoelectric Current from Shock-Loaded Quarts - A Submicrosecond Stress Gauge," *J. Appl. Phys.*, Vol. 36, May 1965, pp. 1775-1783.
20. L. M. Barker and R. E. Hollenbach, "Shock Wave Studies of PMMA, Fused Silica, Sapphire," Sandia Corp. Rept. SC-DC-70-4655 (submitted for Publication to the Journal of Applied Physics).
21. "Compendium of Shock Wave Data," UCRL-50108, Vol. II, Section C, General Editor, M. van Thiel, Lawrence Radiation Laboratory, June 1966, Equation 2A for Polymethylmethacrylate.
22. "Compendium of Shock Wave Data," UCRL-50108, Vol. II, Section C, General Editor, M. van Thiel, Lawrence Radiation Laboratory, June 1966, Equation 3A for Polymethylmethacrylate.
23. Private Communication, R. Craig, Los Alamos Scientific Laboratory.

## DISCUSSION

Charles L. Mader  
Los Alamos Scientific Laboratory  
Los Alamos, New Mexico

The authors of this paper have extended the experimental C-J pressure and velocity data for PETN down to 0.25 gm/cc. Such data are very useful for evaluating equations of state. IN LA-2900 the calculated C-J pressure and velocity is given for PETN from 1.77 to 1.0 gm/cc. For comparison with Hornig,

et al. data, we extended the calculations down to 0.25 gm/cc and the results are shown in Fig. 1 and 2. The BKW technique has been found to predict C-J pressures to within 20% and velocities within 10% for many high-density explosive systems as shown in LA-2613 and LA-2900. Within these usual limits the BKW calculated pressures and velocities are in agreement with the experimental data of Hornig, et al. for PETN from 0.25 to 1.77 gm/cc.

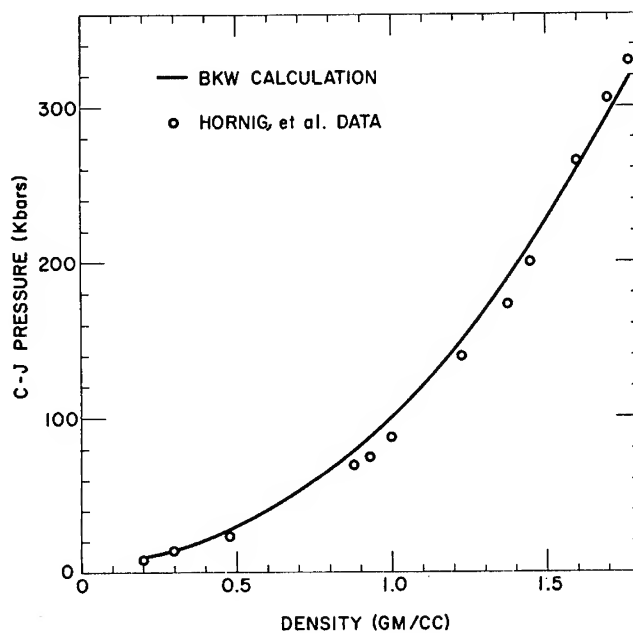


Figure 1

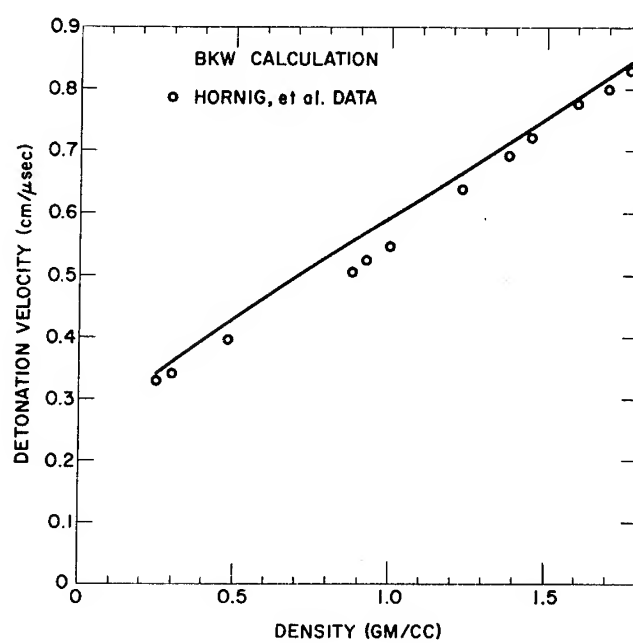


Figure 2

# OPTICAL PROPERTIES OF DETONATION WAVES (OPTICS OF EXPLOSIVES)

M. Busco  
*Ministero Difesa*  
*Roma, Italy*

## ABSTRACT

Detonation phenomena are considered, taking into account the geometric and kinematic characteristics of the detonation wave front. In unlimited isotropic explosive medium the detonation velocity is perpendicular to the wave front, this condition is sufficient to apply to detonation the abstract model of Geometrical Optics. A region having "optical behavior" is then defined for charges of limited dimensions; the longitudinal and transversal conditions are established. Several types of Detonation Wave Generators (D.W.G.), calculated applying the Fermat's principle, are considered. Definitions and codification of different families of D.W.G. are given.

## INTRODUCTION

The detonation phenomenon in condensed high-explosive media involves the propagation of a supersonic wave of compression, the detonation wave, which presents a locus of discontinuity (the wave front) for the state variables  $p$ ,  $v$ ,  $T$ , the particle velocity  $u$  and for many other thermodynamic and mechanical quantities.

The wave front is followed by a reaction zone in which the release of chemical energy is so rapid that the region of a complete (or nearly complete) reaction moves jointly with the wave. A mass of gas at high pressure and temperature travels in the same direction as the wave front which proceeds at detonation velocity  $v_D$ .

The wave front is represented by an ideal regular surface  $f$  which is just a geometric abstraction. In fact if the phenomenon is analyzed in a microscopic way (Fig. 1), subdividing the wave front in parts, each consisting of elementary fronts  $dS_i$  followed by gaseous flow, it is easy to visualize it as the various parts move at different variable speeds depending upon the size and orientation of explosive crystals (which have in general anisotropic properties) and on the size and distribution of particles and gaseous inclusions. For statistical and physical reasons the elementary surfaces  $dS_i$  are oscillating, during the propagation,

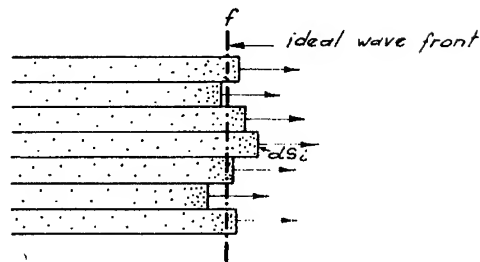


Fig. 1 - Detonation wave front

around a regular surface  $f$  which is the wave front considered in this paper. The finer the crystallization and the granulation, the more the elementary surfaces  $dS_i$  are fusing with the ideal wave front  $f$ .

For a full knowledge of detonation phenomenon, the form of the detonation wave front, the detonation velocity in every point of the front and, moreover, the quantities  $p$ ,  $v$ ,  $T$ ,  $u$ , the energies, momentum and detonation head must be known. The last quantities are difficult to obtain with accuracy due to the extreme conditions of detonation phenomena, but they can be considered by the thermohydrodynamic theory, and great strides have been made in the direction applying the modern computing techniques.

In this paper only the detonation wave front and its evolution in time is considered. This quantity does not represent a complete knowledge of detonation; nevertheless, it gives important information of the phenomenon and it can be easily calculated theoretically and measured experimentally without difficulty.

Simple analogy allows us to apply to the propagation of the detonation wave front the abstract scheme of geometrical optics, provided the explosive media are isotropic. One can realize immediately that in an unlimited homogeneous explosive medium a detonation wave front generated at an initiation point  $I$  is spherical and travels with detonation velocity perpendicular to the front at each point. If the wave encounters another explosive homogeneous medium having a different value of detonation velocity, the front refracts according to the laws of geometrical optics, since the detonation velocity is always perpendicular to the wave front.

Thus the propagation of a wave front in an isotropic medium (with a velocity perpendicular to the front) is a sufficient condition that allows us to apply to the phenomenon the abstract scheme of geometrical optics. In this way the electromagnetic waves, the mechanical waves and the detonation waves can be treated in the same manner.

Obviously the geometrical scheme represents a first approach (an approximation) to be improved by further physical considerations. This second aspect represents the physical optics.

#### GEOMETRICAL OPTICS: LONGITUDINAL AND TRANSVERSAL CONDITION

The applicability of the principles of geometrical optics has been admitted for isotropic unlimited explosive media. The validity of the geometrical optics scheme to finite explosive charges must be verified on the basis of physical experimentation. Reference is made to the most simple type of charge, the homogeneous unconfined cylindrical charge. These phenomena are considered in a simple way to achieve a model of general value.

In a cylindrical homogeneous charge of radius  $R_1$ , the detonation wave front is in general spherical in shape except at the very edge of the charge where slight edge effects may be observed. A spherical segment generated at the initiation point  $I$  is expanding linearly in

the interval  $(0 + X_{M1})$ . Experience shows the value of  $X_{M1}$  is approximately confined between  $4R_1$  and  $7R_1$  according to different types of explosives (1).

If  $x > X_{M1}$ , the radius of curvature of the wave front assumes a steady-state value  $r_{M1}$  and proceeds by translation. If a charge of radius  $R_2 > R_1$  is considered, a value  $X_{M2} > X_{M1}$  is obtained and consequently the maximum value of radius of curvature becomes  $r_{M2} > r_{M1}$ .

The phenomenon can be represented as in Fig. 2; in the shaded area  $A_1$ , the wave front has an "optical behaviour," in other words the wave front travels with detonation velocity  $V_D$  perpendicular to the front, for  $x > X_{M1}$  the wave front proceeds by translation and the velocity  $V_D$  appears perpendicular to the front only along the axis (the  $V_D$  is considered a function only of the type of explosive and its density which is constant in a homogeneous medium).

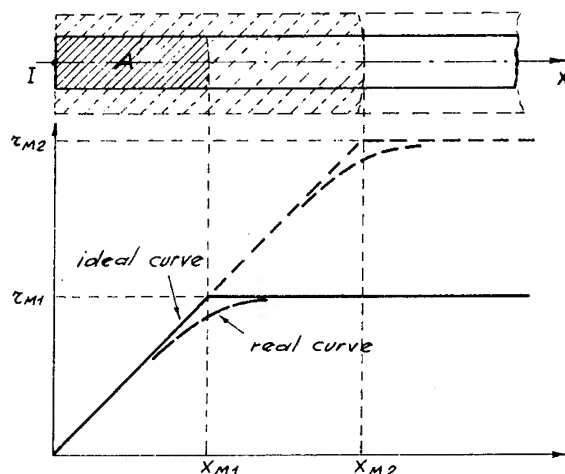


Fig. 2 - Radius of curvature versus distance

The "optical region" with respect to the initiation point  $I$ , for a cylindrical charge, is defined by the condition  $x < X_M$ , which is the longitudinal condition for homogeneous, cylindrical, unconfined charges.

It can be seen that for  $R \rightarrow \infty$ ;  $X_M \rightarrow \infty$ ,  $r_M \rightarrow \infty$ , the "optical behaviour" for the unlimited space is obtained.

The phenomenon examined is caused by lateral expansion and heat loss.

With the same reference to homogeneous unconfined cylindrical charge, other considerations (not specifically related to the optical behaviour of the wave front, but able to make a more general optical model) are taken into account. With reference to the experimental diagram given in Fig. 3, it can be seen that for a value of charge radius  $R < R_c$ , the propagation of detonation does not occur; the velocity  $V_D$  grows in the interval  $(R_c + R_M)$  and assumes a constant value for  $R > R_M$  (1).

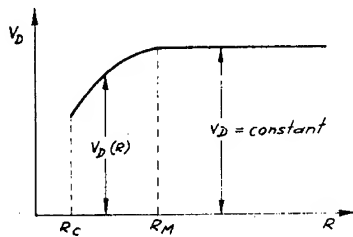


Fig. 3 - Detonation velocity vs. charge radius

The phenomenon is caused by rarefactions from the sides (release waves). It happens for practically all high explosives;  $R_M$  varies from some mm. to some cm. and depends on the type of explosive, its density and granulation. For those explosives where it is not possible to achieve a constant value of  $V_D$  (e.g.: A.N. explosives) a mean value of  $V_D$  in a given interval can be taken into account. To generalize the optical model, it is logical to consider charges in which  $V_D$  is defined only by the type of explosive and its density and not by charge dimensions; in other words charges having a radius  $R > R_M$  have to be considered.

Summarizing, in a homogeneous unconfined cylindrical charge, the "optical region," in which the velocity  $V_D$  depends only on the type of explosive and its density, is defined by the two conditions:

$$X < X_M; \quad R > R_M.$$

It is more difficult to establish the "optical region" for a charge more complicated than a cylindrical one.

General considerations are beyond the scope of this work; a method to determine the "optical region" for two charges composed of two explosive cylinders is given. With reference

to Fig. 4a, in which the axial section of a charge composed of two cylinders of the same homogeneous explosive having respectively a radius  $R_1$  and  $R_2 < R_1$  and length  $X_1$  and  $X_2$ , the "optical region" with respect the initiation point I (shaded area) includes all the charge if the following longitudinal condition and transversal condition are satisfied:

$$a) \quad X_1 < X_{M1}$$

$$X_1 + X_2 < X_{M2} \quad (X_{M2} < X_{M1})$$

$$b) \quad R_2 > R_M \quad (R_1 > R_2)$$

$X_{M1}$  and  $X_{M2}$ , for a given explosive, are functions of the radius of cylinder.

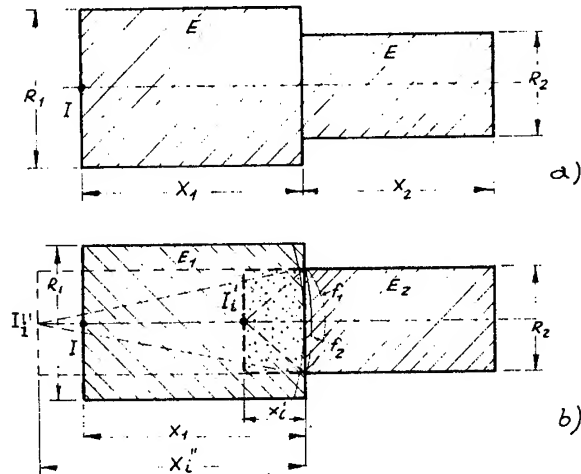


Fig. 4 - "Optical Region" in two types of explosive charge

The second type of charge is composed of a cylinder of homogeneous explosive  $E_1$  having radius  $R_1$ , length  $X_1$  and detonation velocity  $V_{D1}$  (at the end of which is the initiation point I) joined with another cylinder of homogeneous explosive  $E_2$  having radius  $R_2 < R_1$ , length  $X_2$  and detonation velocity  $V_{D2}$ .

To define the "optical region" with respect the initiation point I, for the first cylinder, the longitudinal condition  $X_1 < X_{M1}$  has to be satisfied.

For the second cylinder the verification must be done considering an ideal initiation point which can be at the right side of I ( $I_1$ ) or at the left side of I ( $I_1'$ ), respectively, if  $V_{D1} \leq V_{D2}$ .

The graphic demonstration of this fact is shown in Fig. 4b. If  $v_{D1} < v_{D2}$ , the wave front in the explosive  $E_2$  (near the separation surface) is spherical with a curvature radius  $r'_2 < r_1$ . Consequently, for the cylinder of explosive  $E_2$  one obtains the same geometrical results if the first cylinder is substituted with another cylindrical charge of explosive  $E_2$ , radius  $R_2$  and length  $X'_1$ .

The longitudinal condition for the equivalent charge becomes:

$$X'_{eq} = X'_1 + X_2 < X_{M2}.$$

If  $v_{D1} > v_{D2}$ , the ideal initiation point becomes  $I'_1$  and the longitudinal condition is

$$X''_{eq} = X''_1 + X_2 < X_{M2}.$$

To ascertain that detonation velocities have the values characteristic of explosives, the transversal conditions  $R_1 > R_{M1}$ ,  $R_2 > R_{M2}$  have to be verified.

All the systems considered are unconfined. Different considerations have to be made if the charges are covered with an inert lining.

#### DEFINITION OF BASIC CHARACTERISTICS OF DETONATION WAVE GENERATORS

In a region of an explosive medium in which the model of geometrical optics can be applied, it is quite easy to design any type of detonation wave generator (D.W.G.) applying the Huygens principle (graphic method) or the Fermat's principle (analytical method). Provided that only revolution and plane systems are taken into account, all the considerations can be related to the plane.

The Fermat's principle contains all the laws of geometrical optics; in the variational form it can be expressed in the following way: in an isotropic (plane) medium the path of a point of wave front, from the point  $P_1(x_1, y_2)$  to the point  $P_2(x_2, y_2)$ , is an extremal of the integral:

$$T = \int_{P_1}^{P_2} \frac{ds}{v_D(x, y)}$$

where

$T$  = time employed by the point  $P$  of wave front to go from  $P_1$  to  $P_2$

$s$  = arc length.

The extremal is an integral curve of the Euler differential equation

$$\frac{d}{dx} \frac{y'}{v_D(x, y) \sqrt{1 + (y')^2}} + \frac{\sqrt{1 + (y')^2}}{v_D^2(x, y)} \frac{\partial v_D(x, y)}{\partial y} = 0.$$

The constants of the general integral  $y(x, C_1, C_2)$  are generally determined by the conditions:

$$\begin{cases} y_1 = y(x_1, C_1, C_2) \\ y_2 = y(x_2, C_1, C_2) \end{cases}.$$

In many cases concerning homogeneous media, the Fermat's principle can be applied in a form of a simple algebraic equation with the minimum time condition. In such applications the Malus theorem of the normal congruence appears very useful.

Before the calculation of some detonation wave generators, it is worth while to give some definitions and information in order to establish a general classification of the D.W.G.

#### Types of D.W.G.

- The D.W.G. is an explosive system able to generate a detonation wave having an established wave front. The D.W.G. is defined by the code letter  $G_i$ , where  $i = 2$  or  $3$  according to space dimensions of the generator. The "wave generator" is equivalent to the expression "wave shaper" and "lens." Instead of "lens" it would be more appropriate to use the expression "wave transformer" (the word lens was adopted from the resemblance in shape of a double-convex lens to the seed of a lentil, said "lens" by Latins).

#### • D.W.G. Operating by Refraction or by Diffraction

The D.W.G. can operate by refraction or by diffraction; the code letter  $G_i$  is then followed by the letter  $R$  or  $D$  according to the particular operational mode. (See Fig. 5.)



## FAMILIES OF DETONATION WAVE GENERATORS

designed applying the Principles of Geometrical Optics. Codification of different types of Generators [in the bracket ( ) the Code Letter]

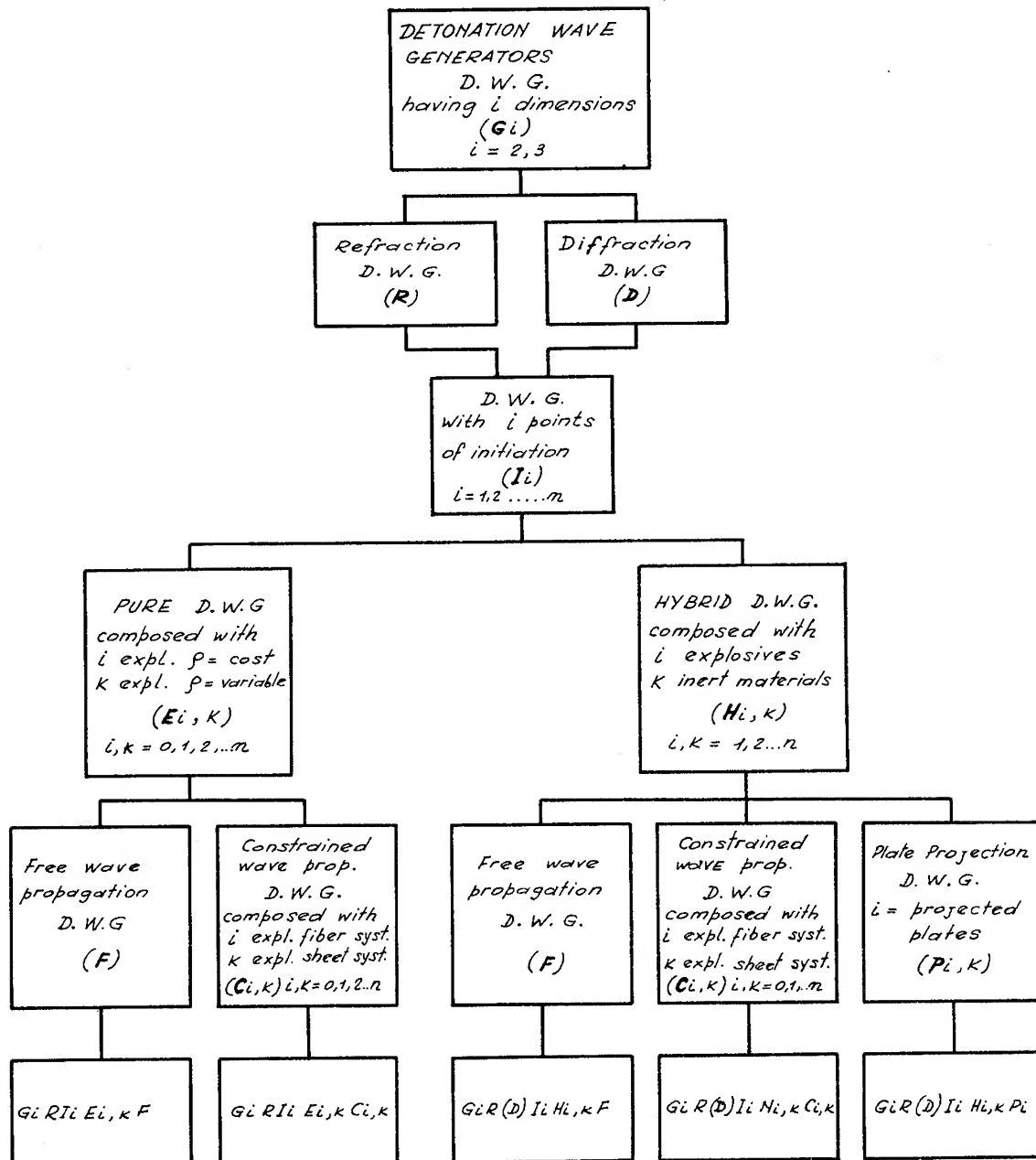


Figure 5

It is worth while to recall that in the case of detonation only one wave front exists (and not a train of wave fronts as in electromagnetic waves or in sound waves); consequently, the interference phenomena are not present. In the detonation the term diffraction means the action of wave front to surrounding an obstacle generally constituted by inert material.

● D.W.G. Provided with  $i$  Initiation Points

The initiation point is represented by a point  $I$ . A D.W.G. can be provided with a number of  $i$  initiation points,  $i = 1, 2, \dots, n$ . The code letter  $I_i$  designs this condition.

● Pure D.W.G.

A pure D.W.G. is constituted of only explosive media. The code letter is  $E_{i,k}$ ;  $i$  represents the number of homogeneous explosives ( $\rho$  constant) in the system,  $k$  represents the number of heterogeneous explosives ( $\rho$  variable) ( $i, k = 0, 1, 2, \dots, n$ ).

● Free Propagation Mode in D.W.G.

If the explosive components have the same number of space dimensions of the D.W.G., the detonation wave propagates in free mode; the letter  $F$  designates this condition.

● Constrained Propagation Mode in D.W.G.

If at least one explosive component has one dimension less than the dimensions of all the system, the D.W.G. is defined as constrained. This condition is indicated by a letter  $C_{i,k}$ ; where  $i$  is the number of different types of explosive fibers and  $k$  is the number of different types of explosive sheets.

In plane D.W.G. ( $G_2$ ),  $k = 0$ .

It is useful to recall the definition of explosive fiber and explosive sheet.

The explosive fiber can be represented by a line; in fact, its transversal dimensions are negligible with respect to the length. The wave front can be represented by a point constrained to follow the path having the form of the line. The explosive sheet can be represented by a plane (2-dimensional space). Its thickness is negligible with respect to the other two dimensions. If the homogeneous sheet explosive is a plane, the trajectories of the points of the wave front (rays) are straight lines (the space is Euclidean). If the homogeneous explosive sheet is not plane, the trajectories of the points of the wave front are the geodesics of the surface.

● Hybrid D.W.G.

A hybrid D.W.G. is an explosive system composed of explosives and inert media. The letter  $H_{i,k}$  designates this property, where  $i$  is the number of the explosive media of the system and  $k$  is the number of inert media ( $i, k = 1, 2, \dots, n$ ).

An inert material can have different functions:

● An inert element can delay propagation of the detonation wave and in that case a shock wave traveling on it at velocity lower than detonation velocity can initiate, under certain conditions, the explosive placed in the opposite side of the element.

If all the media have the same dimensions of the system, the propagation is free, and the D.W.G. are designed with the letter  $F$ .

The shock wave propagates by refraction in the inert material.

● The delay can be obtained in another manner, also, by projecting by a detonation of a charge a metallic plate against another explosive and initiating it.

The plate, traveling at a velocity lower than the detonation velocity of the explosive, is able to create in another explosive a wave front of particular shape.

These hybrid D.W.G. are designated by a letter  $P_{i,k}$ ;  $i$  is the number of the plates which can be equivalent to lines,  $k$  is the number of the plates which can be equivalent to surfaces.

● Finally the inert media can constitute barriers separating different explosive elements, as in the case of explosive fibers and explosive grids or nets. These D.W.G., in which the explosive components have smaller dimensions than those of the system, are constrained and are designated by a letter  $C_{i,k}$ ; where  $i$  is the number of explosive fiber systems (2) or explosive grid systems (3) and  $k$  is the number of explosive sheet systems. In the plane D.W.G. ( $G_2$ ),  $k = 0$ .

The D.W.G. operating by diffraction are practically all hybrid (the barrier is generally inert).

In the block diagram of Fig. 5, families of D.W.G. are shown.

It is worth while to give some example of D.W.G. design.

$$\frac{\sqrt{x^2 + y^2}}{V_{D1}} + \frac{x^* - x}{V_{D2}} = T$$

$$T = T_{\min} = \frac{x_0}{V_{D1}} + \frac{x^* - x_0}{V_{D2}}.$$

Fig. 6 - Straight line D.W.G.

Fig. 7 - Implosive D.W.G.

$$T = \frac{1}{v_{D1}} \int_{-\pi}^0 \sqrt{r^2 + \left(\frac{dr}{d\theta}\right)^2} d\theta + \frac{r}{v_{D2}}$$

$$= \frac{r_x}{v_{D2}} = \text{constant}.$$
$$\frac{dT}{d\theta} = 0 = \sqrt{r^2 + \left(\frac{dr}{d\theta}\right)^2} = \gamma \frac{dr}{d\theta}; \quad \gamma = \frac{v_{D1}}{v_{D2}} > 1$$
$$\frac{dr}{r} = \frac{d\theta}{\sqrt{\gamma^2 - 1}}$$
$$r = r_0 \frac{\theta}{e^{\sqrt{\gamma^2 - 1}}}.$$

● Discontinuous Straight Line D.W.G., Code G<sub>2</sub> R I<sub>1</sub> H<sub>1,1</sub> C<sub>2,0</sub>. With reference to Fig. 8,  $\mathcal{F}_I$  represents the initiating explosive fiber having a detonation velocity  $v_{D1}$ ; the other fibers  $\mathcal{F}_j$  have a detonation velocity  $v_{D2}$ .

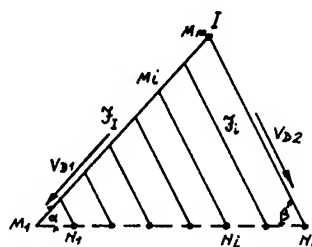
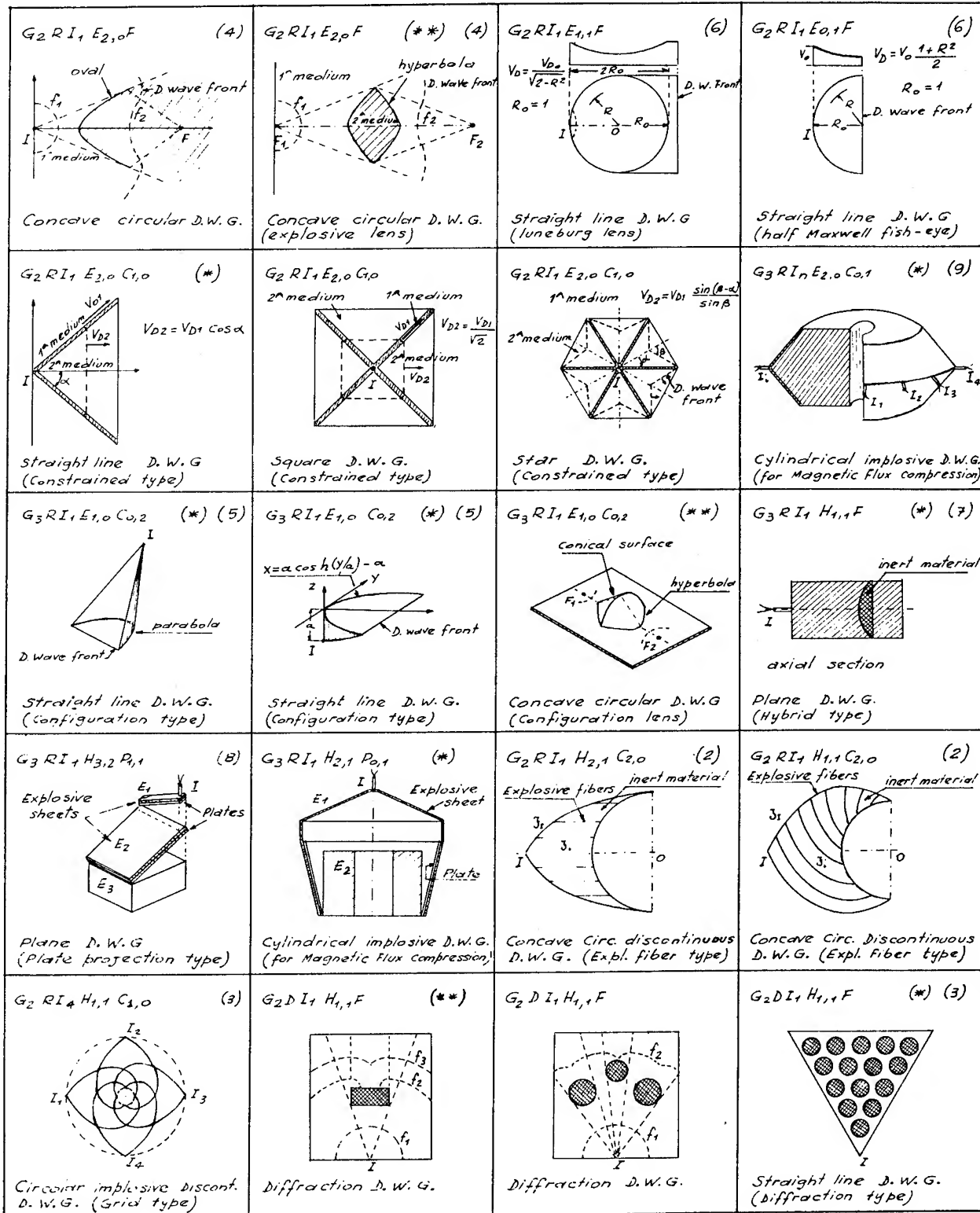


Fig. 8 - Straight line (dis-  
continuous) D.W.G. (Ex-  
plosive Fibers)

$$\frac{\overline{I M_i}}{V_{D1}} + \frac{\overline{M_i N_i}}{V_{D2}} = T; \quad T = \frac{\overline{I M_1}}{V_{D1}} = \frac{\overline{I N_n}}{V_{D2}}.$$



(\*) Experimentally tested

(\*\*) Experimentally tested by the author

Fig. 9 - Types of D.W.G.

Hence:

$$V_{D1} = \frac{\sin \beta}{\sin \alpha} V_{D2} .$$

For

$$\alpha = \beta , \quad V_{D1} = V_{D2} , \quad \overline{IM_1} = \overline{IN_n} .$$

In Fig. 9 several types of D.W.G. are given.

### PHYSICAL OPTICS

The described D.W.G. are designed applying the principles of geometrical optics.

Some of these D.W.G. have been successfully tested, nevertheless the design based on the geometric model gives results which can diverge in some cases from desired values. More precise calculations must be carried out on an experimental basis.

Briefly, some significant phenomena are taken into account.

#### • Detonation Velocity Transient

In the initiation point and in the surface separating two different explosive media, the detonation velocity  $V_D$  generally does not assume abruptly the steady-state value related to the explosive considered, but reaches the final value gradually with a transient that lasts for a given interval  $\Delta x$ . In Fig. 10 a section of cylindrical charge composed of two homogeneous explosives is shown. In the diagram below, the transients related to initiation point  $I$  and to separation surface  $S^*$  are indicated with a dotted line.

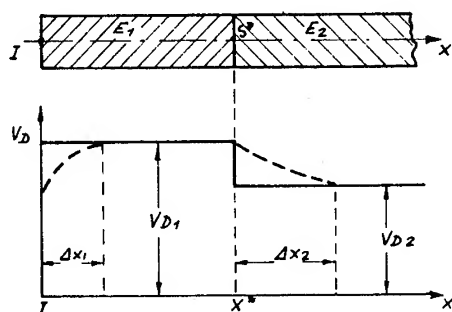


Fig. 10 - Detonation velocity transient

If the intervals  $\Delta x_1$  and  $\Delta x_2$  are small, the discontinuous line can be accepted in the calculation of D.W.G.; otherwise, the transient phenomena have to be taken into account.

Some transients can last for few mm; other transients can continue for a greater interval of space (several cm) as in A.N. explosives.

#### • Detonation Velocity Related to the Value of Curvature Radius of the Wave Front

The detonation velocity  $V_D$  is function of the radius of curvature  $r$  of the wave front. In the implosion for small  $r$ ,  $V_D$  can assume values much greater than the steady-state value. In some cases this fact must be taken into account.

#### • Mach Bridge

The interaction of two detonation waves at a certain angle  $\theta > \theta_c$  ( $\theta_c$  is a critical value related to a particular type of explosive) can generate a Mach Bridge, which is distortion of the wave front, traveling at a velocity greater than the steady-state value.

#### • Some phenomena occurring in Inert Media

Figure 11 is a hybrid system composed of two explosive cylinders with an inert cylinder interposed between them. The ideal diagrams  $t = t(x)$  and  $V_D = V_D(x)$  are given in continuous line, the real diagrams are shown in dotted line. The shock wave induced in the inert material  $M$  does not initiate the explosive  $E_2$  at the abscissa  $x_2$  but at certain distance  $\Delta x'$  from  $x_2$ . This phenomenon has to be considered in some cases in the design of D.W.G.

There are other considerations in the phenomena related with projection of plates, etc.

#### • Technological Qualities of the Explosive Media and of the Initiators

The characteristics of explosive charges (homogeneity, dimensional precision, perfect joint between different explosives and between explosives and inert media, etc.) are of greatest importance in the design of D.W.G. The quality of initiators (negligible time delay and jitter) is very significant especially in D.W.G. provided with several initiating points.

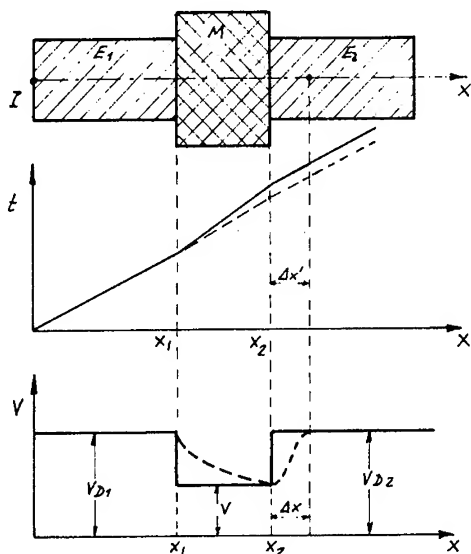


Fig. 11 - Detonation wave propagation in an hybrid explosive system

## CONCLUSION

The geometrical optics model applied to detonations represents a useful tool in the explosives field. The applicability of the geometrical optics model also implies the transposition of all which has been discovered in other fields (e.g.: in optics of light, in optics of microwaves, etc.) to the detonation problem. It is worth while to recall that this method allows the study of only the characteristics of the detonation wave front, which is only one part of the whole phenomenon. With reference to the model, a general classification of Detonation Wave Generators (D.W.G.) can be established; in this paper a systematic arrangement of the D.W.G. in families has been attempted.

Physical knowledge of the detonation phenomenon is necessary to get parameters to design high characteristics D.W.G.

## REFERENCES

1. M. A. Cook, The science of high explosives pp. 44 - 57, 99 - 106, Reinhold Publishing Co., New York, 1959.
2. M. Defourneaux, Guidage et mise en forme d'ondes de detonation le long de surfaces alternativement explosives et inertes. pp. 551 - 558 Symposium H.D.P.I.U.T.A.M. - Paris - Septembre 1967 - Ed. Dunod Paris, 1968.
3. D. L. Coursen, Explosive Device, United States Patent Office 2, 943, 571 Patented July 5, 1960.
4. M. Busco, Una nuova scienza: l'Ottica degli Esplosivi - Missili - Fasc. 4 - Luglio-Agosto 1963. Considerazioni generali sul fenomeno dell'implosione. Missili - Fasc. 6 - Novembre-Dicembre 1964.
5. J. O. Erkmann, Simultaneous Detonation Along a Line - The Review of Scientific Instruments, Vol. 30, Nr. 9, pp. 818-820 - Sept. 1959.
6. G. Toraldo Di Francia, A Family of Perfect Configuration Lenses of Revolution. Opt. Acta, Vol. 1, no. 4, pp. 157-163, Feb. 1955.
7. H. S. Yadav et al., Design of a Plane Wave Lens by Metal - Explosive Combination. Explosivstoffe, 10 - pp. 217-220, Oct. 1969.
8. R. Schall, Detonationsphysik from K. Vollrath and G. Thomer - Kurz zeitphysik, Springer-Verlag Wien, N.Y., pp. 859-862, 1967.
9. A. Brin et al., Magnetic Field Compression. Proceedings of the Conference on Megagauss Magnetic Field Generation by Explosives and Related Experiments, pp. 21-36 EUR. 2750 e., 1966.

# HYDRODYNAMIC BEHAVIOR AND EQUATION OF STATE OF DETONATION PRODUCTS BELOW THE CHAPMAN-JOUQUET STATE

L. A. Roslund and N. L. Coleburn  
U.S. Naval Ordnance Laboratory  
White Oak, Silver Spring, Maryland 20910

## ABSTRACT

The stability to detonation and expansion behavior of reaction products from an aluminized explosive, HBX-1, were studied. The detonation velocity-charge diameter and detonation velocity-loading density relationships were determined by streak camera techniques and electronic probe methods. These data gave reaction zone lengths which increase from 0.07 mm for an initial explosive density of 1.72 g/cm<sup>3</sup> to 1.5 mm at 1.3 g/cm<sup>3</sup>. With the pressure-particle velocity relation established from 338,000 bars to 15 bars, and conditions in the C-J state ( $P_{CJ} = 220.4$  bars) specified, the generalized hydrodynamic relations derived by Jones were used to evaluate the constants in an empirical equation of state and in the Wilkins equation of state as modified by Allan and Lambourn.

## INTRODUCTION

The detonation of an explosive produces flow in the surrounding medium which is directly affected by the way the available energy is released as the reaction products expand to low pressures. The energy released is from the work integral

$$A = \int_{V_0}^V P dV = Q - q \quad (1)$$

where  $A$  is the maximum available work in an adiabatic expansion of the detonation products from the initial explosive volume  $V_0 = (1/\rho_0)$  to the final specific volume  $V$ .  $Q$  is the heat of detonation and  $q$  is the heat retained by the detonation products at  $V$ .

Calculations of the maximum work from Eq. (1) are handicapped because little is known about the detonation reactions or the characteristics of the pressure-volume expansion adiabat. Many attempts have been made to develop more elaborate equations of state for the detonation reaction products. The results of Deal (1) and considerations by Fickett and Wood (2) seemed to support the view that for some

explosives a constant gamma adiabat may adequately describe the product gas expansion states. Energy transfer computations, using the constant gamma assumption, however indicate the assumption is incorrect since the results are in considerable disagreement with experimental measurements from metal acceleration experiments. Moreover the assumption is not expected to describe the expansion behavior of burnt gases from explosive compositions with substantial after-burning reactions.

In this work we studied the hydrodynamic behavior of the detonation products from an aluminized explosive, HBX-1, by making measurements of the pressure-particle velocity relationship for its C-J adiabat. With these data we have described the expansion behavior from 338,000 bars to 15 bars, using an empirical equation of state and a characteristic form of the Wilkins equation of state as modified by Allan and Lambourn (3). The characteristic equation has the form

$$P = \begin{cases} B \exp(-kV) + WG_1 V^{-(1+W)} & V \leq V_C \\ G_2(V + V^*)^{-1} & V > V_C \end{cases} \quad (2)$$

where  $V_C$  is a critical volume which specifies the properties of the adiabat. In regions of high pressure with volumes less than  $V_C$  the data are best fitted by the first equation and in regions of expansion for volumes greater than  $V_C$  the data obey the second equation.  $B$ ,  $k$ ,  $G_1$ ,  $W$ ,  $G_2$ , and  $V^*$  are constants. The following sections describe how the experimental determinations of the hydrodynamic properties are used in evaluating the equation-of-state constants. These properties are the change in the infinite diameter value of the detonation velocity with loading density, the properties of the C-J state, and experimental P-u data for an expansion from the C-J state. The expansion adiabat derived from these data is compared with the constant gamma adiabat, and the variation of

$$\gamma = - \left( \frac{\partial \ln P}{\partial \ln V} \right)_s$$

with volume is calculated.

## EXPERIMENTAL ARRANGEMENTS AND RESULTS

### A. Charge Preparation

The explosive configuration used in the experiments was a cylindrical charge of pressed HBX-1; RDX/TNT/Aluminum/WAX (40/38.1/17.1/4.8), by weight, which was initiated by a plane-wave explosive system. The pressed charges\* were prepared by mixing granular RDX and TNT into an aluminum/wax mixture, 18 parts to 5 parts by weight. This mixture was formed by stirring aluminum and Stanolind wax in carbon tetrachloride and then evaporating the solvent. Seventy percent of the HBX-1 by weight consisted of material (aluminum, RDX, and TNT) with particle sizes between 44 microns and 180 microns. Charges with particle sizes in this range were formed at the desired charge density in a hydrostatic press and then machined to the appropriate dimensions.

### B. Detonation Velocity Measurements and Results

Detonation velocities and the critical diameter of HBX-1 were measured as a function of charge density using smear camera and "raster oscilloscope" pin techniques. In the smear

camera measurements, unconfined HBX-1 at loading densities ranging from about 1.33 g/cm<sup>3</sup> (75% TMD\*) to about 1.74 g/cm<sup>3</sup> (98% TMD) was detonated in a "stacked" cylinder configuration. This configuration consisted of five explosive cylinders of different diameters but of the same loading density. The cylinders were stacked in order of decreasing diameters; 5.08-cm, 2.54-cm, 1.27-cm, 0.635-cm, and 0.476-cm. The cylinder heights corresponding to these diameters were 10.2-cm, 10.2-cm, 5.08-cm, 3.81-cm, and 3.81-cm, respectively. The stacked cylinders were fired by the detonation of a tetryl booster 5.08-cm diameter by 2.54-cm high. The tetryl was initiated by a 5.08-cm diameter pentolite-baratol plane-wave booster. Techniques described in (4) were used to give narrow, bright light pips which facilitated the analysis of the detonation trace in the smear camera records. The failure diameter for each charge density was estimated by examining the smear camera record for the diameter at which the detonation wave failed to propagate with a steady velocity. Single charges each 37-cm long, 5.08-cm diameter and 2.54-cm diameter also were fired simultaneously with the stacked cylinder array and the detonation velocities were measured using electronic probes and a raster-type oscilloscope. In these measurements the circuit consisted of a single strip of copper running the length of the charge, separated by an air gap from a series of electrically-charged precisely spaced copper strips which served as probe contacts to be consecutively shorted by the passage of the shock.

The camera data (which was less precise) generally showed agreement with the probe data to better than 0.5%. The electronic measurements were precise to better than  $\pm 0.2\%$ . With this precision in the velocity measurements, the greatest source of error in the experiments probably is the density variation within the test explosive.

Examination of the detonation traces from the stacked cylinder array showed that detonation did not propagate into the 0.476-cm diameter charges. The critical minimum diameter for HBX-1 is about 0.6-cm. From the measurements, we determined a critical density (between 1.602 g/cm<sup>3</sup> and 1.530 g/cm<sup>3</sup>) below which detonation will not propagate in pressed HBX-1 at about 0.6-cm diameter. We infer that detonation cannot occur in smaller diameters at densities lower than this critical density (5). Moreover, we found a sharply different sensitivity between pressed and cast HBX-1. For

\*Cast charges also were fired to compare their diameter effect with pressed charges at the highest experimental density, about 1.74 g/cm<sup>3</sup>.

\*Theoretical maximum density, 1.76 g/cm<sup>3</sup>.



example, charges of 0.635-cm diameter pressed to 1.72 g/cm<sup>3</sup> detonated; cast charges of the same density and diameter failed.

The detonation velocities for charges loaded at various densities in the different charge diameters are plotted in Fig. 1. Linear least square lines are drawn through the data. The effect of charge diameter on the velocities is greatest at lower loading densities. We extrapolated the curves relating the measured detonation velocity to the reciprocal of the charge diameter for different loading densities. For charge diameters  $\geq 1.27$  cm the curves appeared linear. The extrapolation gave the velocities for the infinite diameter or ideal curve which is represented by

$$D_{\infty} = -0.063 + 4.305 \rho \quad (3)$$

The curved front theory (6) relates charge diameter  $d$ , and reaction zone length  $a$ ,

$$D = D_{\infty}(1 - a/d) \quad (4)$$

Assuming the equation only applies to charge diameters  $> 1.27$  cm, we computed values of the reaction zone lengths which are plotted as functions of density in Fig. 2. The result is a

smooth decrease of the reaction zone length with increasing density. This is attributed to the increased surface exposed to ignition by the decrease in grain size achieved by the crushing action of compaction to higher density and hence an increased burning rate with the increased pressure in the reaction zone.

Wood and Kirkwood (7) give a relation between reaction zone length and curvature of the detonation front

$$a = (S/3.5)(1 - D/D_{\infty}) \quad (5)$$

where  $S$  is the radius of curvature of the detonation front. Extensive studies of the shape of the wave by Cook et al (8) show the front is spherical. Hence maximum curvature is likely at the critical diameter, i.e.,

$$S = \frac{1}{2} d_c \quad (6)$$

At the critical diameter, 0.635 cm, and critical density, about 1.60 g/cm<sup>3</sup>, the critical detonation velocity is 5380 m/sec, and  $D_{\infty} = 6820$  m/sec. These data give a reaction zone length of 0.19 mm as compared to 0.40 mm from the curved front theory.

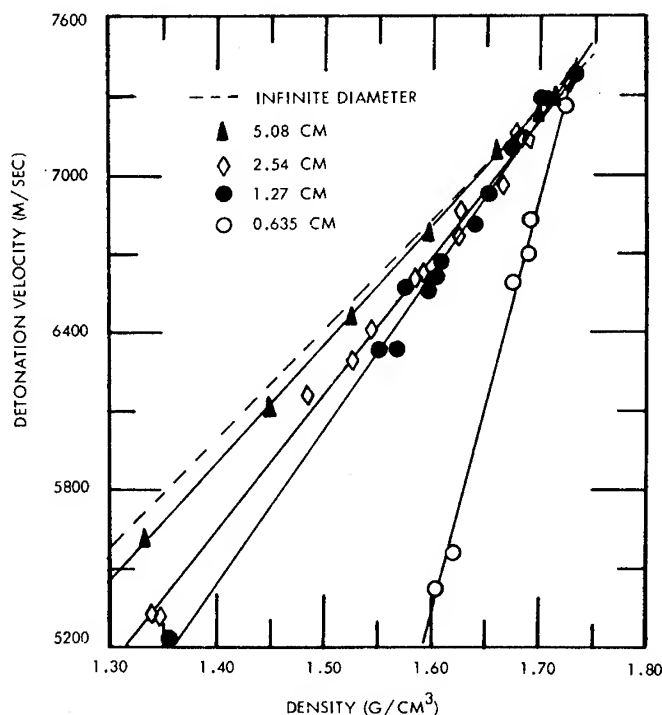


Fig. 1 - Detonation velocity vs charge density for several charge diameters of pressed HBX-1

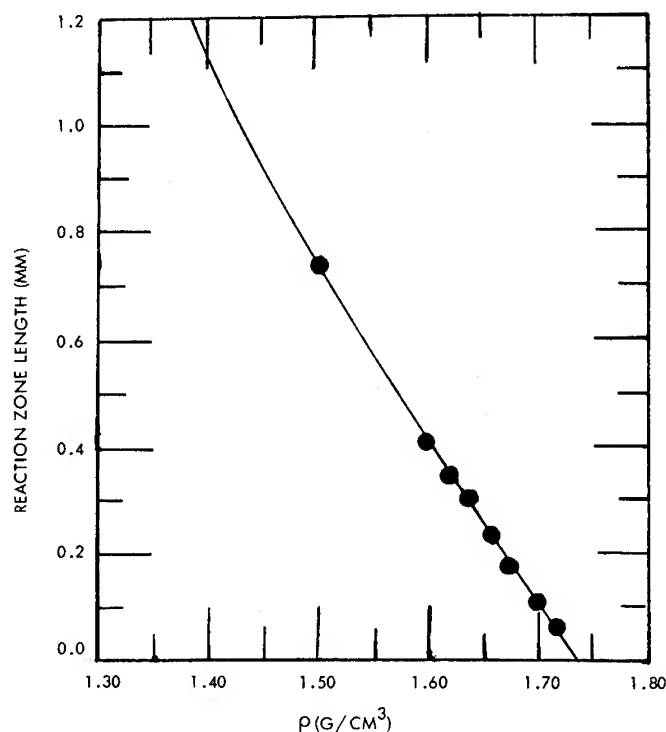


Fig. 2 - Reaction zone length vs density of HBX-1

### C. Shock Impedance Measurements of the Chapman-Jouguet State

The pressure and specific volume of the explosion products centered at the C-J state were determined from shock wave velocity or free-surface velocity measurements. Shock waves were transmitted into several materials of various specified thicknesses in contact with detonating HBX-1 and the above parameters were measured. To denote the attenuation and narrow limits of the Von Neumann spike region (9), the data from these experiments were linearly extrapolated to values for zero thickness.

In these shock wave measurements the charge configuration consisted of a 12.7-cm diameter, 6.4-cm high cylinder of HBX-1, initiated on one end face by an explosive plane-wave lens of the same diameter. The other face of the cylinder was held in close contact with the inert material using a thin silicone grease film to eliminate air gaps. Measurements of the free-surface velocities and shock wave velocities were made for various plate and wedge thicknesses of aluminum, brass, Plexiglas, water, and polyurethane which were shocked by detonating HBX-1 in the above charge geometry.

A reflected-light smear-camera technique described previously (10) was used for these measurements.

The C-J isentropic behavior from about 20 kbars to 15 bars was determined from optical measurements of the initial velocities of shock waves produced by detonating HBX-1 in air and argon initially at compressed or reduced pressure states. These experiments were done in an expendable, gas-tight chamber which could be filled with compressed gas at 1000 psi or evacuated to about 0.01 bar. Figure 3 shows the experimental arrangement. The chamber consisted of a 7.62-cm inside diameter, 26-cm long cast iron pipe tee, with 0.5-cm thick walls. The opposite ends of the pressure chamber tee were fitted with 2.54-cm thick Plexiglas windows to allow viewing of the charge configuration with a rotating-mirror smear camera. The bottom end of the chamber was covered by a brass plate designed to give an air-tight seal and also to transfer detonation from a detonator outside the chamber to a plane-wave initiator inside the chamber.

The charges fired in the chamber were 5.08-cm diameter cylinders, 16.5-cm long and

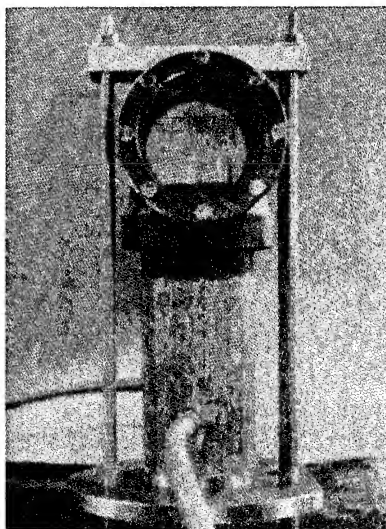


Fig. 3 - Test chamber for shock measurements in gases

were confined in copper cylinders with 0.64-cm thick walls. This confinement sufficiently reduces the diameter effect on HBX-1 so that the shock velocity data are considered applicable to an ideal charge. For viewing purposes, one end face of the explosive protruded about 1.27 cm from the copper cylinder. The other end face of the HBX-1 was initiated by an explosive train consisting of a 2.54-cm long, 5.08-cm diameter pentolite pellet, a pentolite-baratol plane-wave generator and an SE-1 detonator.

The slit of the smear camera was aligned to view the shock wave emerging from the protruding face of the charge for a distance of one charge radius, about 2.54 cm. Figure 4 shows the shock wave trace emerging from a detonating charge in air initially at  $.00355 \text{ g/cm}^3$  (3 bars). The camera writing speed was  $3.8 \text{ mm}/\mu\text{sec}$ . The shock wave velocity was determined from the distance vs. transit time readings of the trace. Vertical distance on the film was converted to laboratory coordinates using magnification reference markers positioned inside the test chamber.

In the region 1 mm to 6 mm from the charge surface, the trace readings gave velocities which were characteristically high and not reproducible. This we attribute to "fog over" from intense shock light on the record, or possible blow-off of luminous detonating particles from the charge surface. The region 6 mm to 20 mm from the charge gave trace readings which were essentially linear. Slope measurements were made in this region to obtain the initial gas shock velocities.

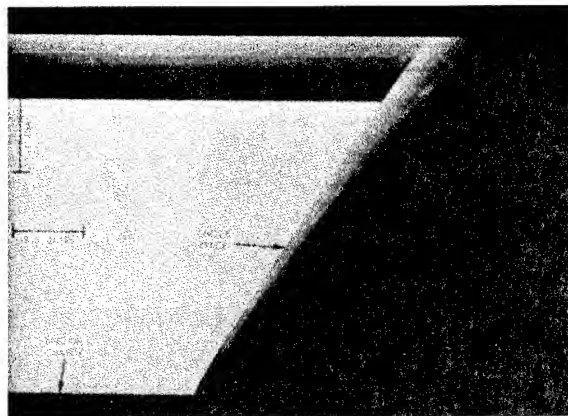


Fig. 4 - Smear camera record of shock wave propagation from the end of an HBX-1 cylinder

For the shock pressures and particle velocities corresponding to our measured air shock velocities we used the data in (11). Since our measured shock velocities in argon are in the range of the shock Hugoniot of argon determined by Christian, Duff, and Yarger (12), we used their relation for the particle velocities in Table 1. We obtained good support for these data from the calculations by Bond (13) of the shock Hugoniots of argon for several initial pressures.

#### EXPERIMENTAL DATA ANALYSIS

We obtained the data in Table 1 from the measured shock wave velocities and free-surface velocities corresponding to zero thickness of the various solid materials and their known shock Hugoniots. Since the pressures and particle velocities are continuous across the reaction products-material interface, the P-u data correspond to points on the detonation products Hugoniot above the C-J state and on the expansion adiabat below the C-J state. The P-u data are plotted in Fig. 5.

To establish the C-J state we assumed that the aluminum and wax in HBX-1 are chemically and physically inert in the detonation front (14). The detonation parameters then are functions of the nominal density,  $\rho_0$  of the explosive components in the charge, i.e., the ratio (weight of explosive)/(volume available to the explosive reaction products). For HBX-1 with the experimental charge density of  $1.712 \text{ g/cm}^3$ , we obtain  $\rho_0 = 1.624 \text{ g/cm}^3$ .

TABLE 1  
Pressure-Particle Velocity Measurements

Material	$\rho_0$ (g/cm <sup>3</sup> )	$P_0$ (bars)	P (kbars)	u (cm/ $\mu$ sec)
Brass	8.40	—	338	0.0800
Aluminum	2.74	—	270	0.1370
Plexiglas	1.18	—	181.0	0.2430
Water	1.00	—	156.4	0.2620
Polyurethane	0.188	—	37.9	0.3250
Argon	$7.05 \times 10^{-2}$	40.8	16.9	0.4500
Argon	$4.7 \times 10^{-2}$	27.0	11.8	0.4620
Argon	$3.09 \times 10^{-2}$	17.9	7.92	0.4660
Argon	$1.55 \times 10^{-2}$	9.0	4.70	0.5100
Argon	$1.02 \times 10^{-2}$	6.0	3.39	0.5370
Air	$7.10 \times 10^{-3}$	6.0	2.54	0.5700
Air	$3.55 \times 10^{-3}$	3.0	1.41	0.6020
Air	$3.55 \times 10^{-3}$	3.0	1.46	0.6130
Air	$3.43 \times 10^{-3}$	3.0	1.30	0.5870
Air	$1.27 \times 10^{-3}$	1.0	0.670	0.6970
Air	$1.27 \times 10^{-3}$	1.0	0.670	0.6920
Air	$8.9 \times 10^{-4}$	0.7	0.510	0.7280
Air	$6.3 \times 10^{-4}$	0.5	0.370	0.7270
Air	$6.3 \times 10^{-4}$	0.5	0.370	0.7300
Air	$3.7 \times 10^{-4}$	0.3	0.260	0.8050
Air	$3.6 \times 10^{-4}$	0.3	0.230	0.7640
Air	$12.6 \times 10^{-5}$	0.1	0.101	0.8600
Air	$12.6 \times 10^{-5}$	0.1	0.101	0.8600
Air	$8.86 \times 10^{-5}$	0.07	0.069	0.8480
Air	$8.01 \times 10^{-5}$	0.07	0.069	0.8900
Air	$1.23 \times 10^{-5}$	0.01	0.015	1.0540
Air	$1.23 \times 10^{-5}$	0.01	0.015	1.0700
Air	$1.23 \times 10^{-5}$	0.01	0.016	1.1040

The C-J state was established according to the impedance match conditions by drawing the straight line with slope  $\rho_0 D = P/u$  from the origin to intersect the curve given by an exponential fit to the P-u data above 10 kbar. With  $D = 7307$  m/sec we obtain  $P_{CJ} = 220.4$  kbars,  $u_{CJ} = 1858$  m/sec. Then using the detonation theory, at the C-J point

$$D = u_{CJ} + C \quad (7)$$

where C is the velocity of sound at the C-J point. The isentropic exponent

$$\gamma_{CJ} = (\rho_0 D^2 / P_{CJ}) - 1 \quad (8)$$

Also

$$\rho_{CJ} / \rho_0 = \frac{D}{D - u_{CJ}} \quad (9)$$

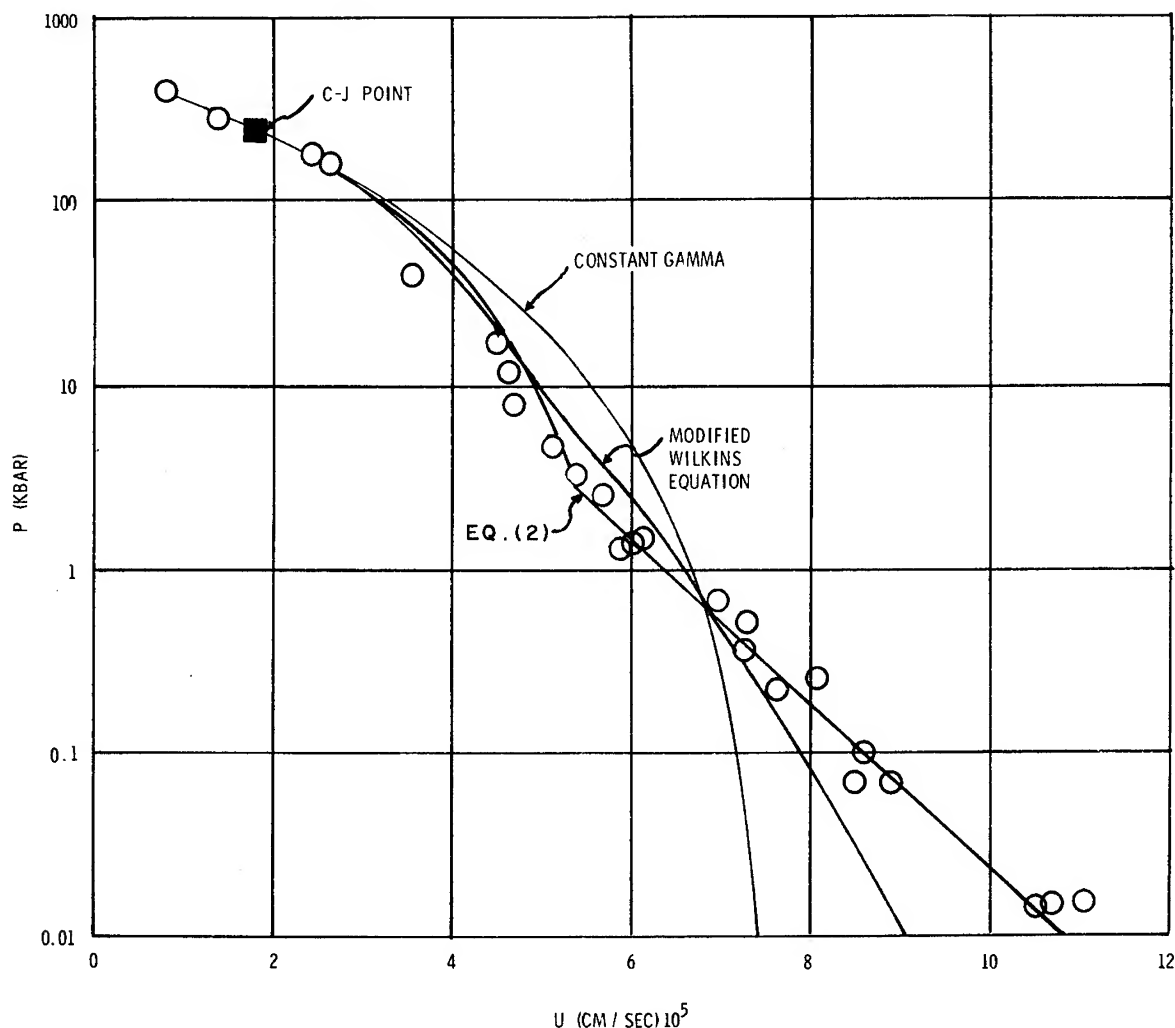


Fig. 5 - Experimental P-u data and equation-of-state results for pressed HBX-1

and for the experimental C-J point,  $\rho_{CJ} = 2.178$  g/cm<sup>3</sup> and  $\gamma = 2.934$ .

The constants in the characteristic equation of state, Eq. (2), were evaluated from the experimental data, following the generalized formulation of the detonation theory by Jones (15). Jones defines the quantity  $\alpha$ , from the detonation products Hugoniot by

$$\frac{\partial (E - Q)_P}{\partial V} = \frac{P}{\alpha} \quad (10)$$

We assume no radial expansion at the C-J plane, therefore  $\alpha$  is evaluated from the infinite diameter detonation velocity-loading density relation, Eq. (3).  $\gamma_{CJ}$  is the initial value of the isentropic exponent in

$$\gamma = - \left( \frac{\partial \log P}{\partial \log V} \right)_s \quad (11)$$

and

$$\alpha = (\gamma_{CJ} + 1) \left/ \left( 1 + \frac{\rho_0 dD}{Dd \rho_0} \right) \right. - 2 \quad (12)$$

The constant  $W$  in the equation of state

$$P = B \exp(-kV) + WG_1 V^{-(1+W)}$$

for  $V \leq V_C$  was found from

$$W = \alpha \gamma_{CJ} / (\alpha + 1) \quad (13)$$

B and  $G_1$  were determined from Eq. (2) and Eq. (11) using the C-J values of  $P$ ,  $v$ , and  $\gamma$ . Differentiation of Eq. (2) with respect to  $v$  gives

$$-\frac{dP}{dV} = kB \exp(-kV) + W(1+W)G_1 v^{-(2+W)} \quad (14)$$

Also, Eq. (11) gives

$$-\frac{dP}{dV} = \frac{\gamma P}{V} \quad (15)$$

With  $\rho = v^{-1}$  and the C-J values one then obtains

$$G_1 = \frac{P_{CJ}(\gamma_{CJ}\rho_{CJ}^{-k})\rho_{CJ}^{-(1+W)}}{W[(1+W)\rho_{CJ}^{-k}]} \quad (16)$$

$$B = [P_{CJ} - W G_1 \rho_{CJ}^{(1+W)}] \exp(k/\rho_{CJ}) \quad (17)$$

Then a value of  $k$  was chosen to give the best fit to the experimental  $P$ - $u$  adiabat in the region  $v < v_C$ . To calculate the  $P$ - $u$  adiabat from the characteristic equation we used the Riemann relation

$$u - u_1 = \int_{\rho_1}^{\rho} c \frac{d\rho}{\rho} \quad (18)$$

where  $c$  is the velocity of sound;  $u_1$  and  $\rho_1$  are the particle velocity and density for our known state, in this case the C-J state. For the adiabat,  $c$  is given by

$$c = \left(\frac{\partial P}{\partial \rho}\right)_s^{1/2} = v \left(-\frac{\partial P}{\partial v}\right)_s^{1/2} \quad (19)$$

In the region where  $v > v_C$  the characteristic equation is  $P = G_2/(v + v^*)$ . This follows since in Fig. 5, the experimental  $P$ - $u$  data in the lower region are related best by

$$\log P = Mu + A \quad (20)$$

Differentiation of Eq. (18) and Eq. (20) gives, with Eq. (19),

$$\left(\frac{du}{dV}\right)^2 = -\frac{dP}{dV} \quad (21)$$

$$\frac{dP}{du} = MP \quad (22)$$

$$\left(\frac{du}{dV}\right)\left(\frac{dV}{dP}\right) = \frac{1}{MP} \quad (23)$$

$$\left(\frac{1}{MP}\right)^2 \left(\frac{dP}{dV}\right)^2 = -\frac{dP}{dV} \quad (24)$$

$$-\frac{dP}{P^2} = M^2 dV \quad (25)$$

Since the reference state is now the critical point with the characteristic values  $P_C$  and  $v_C$ , we have

$$-\int_{P_C}^P \frac{dP}{P^2} = \int_{v_C}^v M^2 dV \quad (26)$$

$$\frac{1}{P} - \frac{1}{P_C} = M^2(v - v_C) \quad (27)$$

$$P[v - v_C + 1/(P_C M^2)] = 1/M^2 \quad (28)$$

With

$$v^* = -v_C + 1/(P_C M^2) \quad \text{and} \quad G_2 = 1/M^2, \quad (29)$$

then

$$P(v + v^*) = G_2 \quad (30)$$

$v_C$  is evaluated by iteration, using Eq. (18) to calculate the  $P$ - $u$  adiabat from Eq. (2) and then comparing the results with the experimental data of Fig. 5.  $P_C$  is calculated from the characteristic equation using  $v = v_C$ . Equation (29) gives the value of  $v_C^*$ .

## DISCUSSION

The equation-of-state constants for HBX-1 are listed in Table 2. The small values of  $\alpha$  and  $W$  are typical of explosive compositions with large amounts of solid or non-ideal detonation products, as indicated by the relatively large values of  $dD/d\rho_0$ . For pure explosives,  $\alpha$  varies from about 0.2 to 0.8, depending on the loading density, and  $dD/d\rho_0$  ranges from about 3000-3500 m/sec/g/cm<sup>3</sup>.

The "best fit" to the experimental  $P$ - $u$  data for  $v < v_C$  is obtained with the parameter  $k = 6.450$  g/cm<sup>3</sup>;  $B = 4.187$  Mbar and  $G_1 = 0.00397$  Mbar in the characteristic equation. The experimental  $P$ - $u$  relation for  $v > v_C$  gives  $M = -10.4589$   $\mu$ sec/cm,  $G_2 = 9.142 \times 10^9$  (cm/sec)<sup>2</sup>. The solid line in Fig. 5 is obtained when  $v_C = 1.15$  cm<sup>3</sup>/g; then  $P_C = 3.645$  kbar and  $v^* = 1.358$  cm<sup>3</sup>/g.

If the complete  $P$ - $u$  adiabat is calculated using the modified Wilkins equation for  $v > v_C$ ,

TABLE 2  
Equation-of-State Constants  
for HBX-1

$$\begin{aligned}\rho &= 1.712 \text{ g/cm}^3 \\ \rho_0 &= 1.624 \text{ g/cm}^3 \\ D &= 7.307 \text{ mm}/\mu\text{sec} \\ \gamma_{CJ} &= 2.934 \\ P_{CJ} &= 220.4 \text{ kbars} \\ u_{CJ} &= 1.858 \text{ mm}/\mu\text{sec} \\ \rho_{CJ} &= 2.178 \text{ g/cm}^3 \\ \frac{dD}{d\rho_0} &= 3800 \text{ m/sec/g/cm}^3 \\ \alpha &= 0.1325 \\ W &= 0.3432 \\ v_C &= 1.15 \text{ cm}^3/\text{g} \\ P_C &= 3.645 \text{ kbars} \\ k &= 6.450 \text{ g/cm}^3 \\ B &= 4.187 \text{ Mbars} \\ G_1 &= 0.00397 \text{ Mbar} \\ G_2 &= 9.142 \times 10^9 \text{ (cm/sec)}^2 \\ v^* &= 1.358 \text{ cm}^3/\text{g} \\ M &= -10.4589 \text{ } \mu\text{sec/cm}\end{aligned}$$

the curve deviates from the experimental data as shown in Fig. 5. Also plotted in Fig. 5 is the constant  $\gamma$  adiabat  $P$ - $u$  curve. The experimental  $P$ - $u$  data from 20 kbars to 1 kbar are well below this curve. This covers the range of the compressed gas experiments. We note an abrupt upward trend in the particle velocity data at about 10 kbars. The trend is considered real and not a result of experimental error. At points below 1 kbar the experimental data shift significantly away from the constant  $\gamma$  curve. These data result from the detonation products expanding into a rarefied atmosphere, i.e., the initial conditions of the reduced pressure experiments.

The pressure-volume adiabats for the characteristic equations of state (Eq. (2)), the modified Wilkins equation, and the constant gamma "straight line" assumption are shown in Fig. 6. The adiabat derived from the experimental data dips below the constant gamma curve near the C-J point and then crosses over both the constant gamma and modified Wilkins equation of state curves below 3 kbars. The inflection in our experimental data beginning at about 3.0 kbars produces the sharp break in the adiabat at  $v = 1.15 \text{ cm}^3/\text{g}$ . The variation of

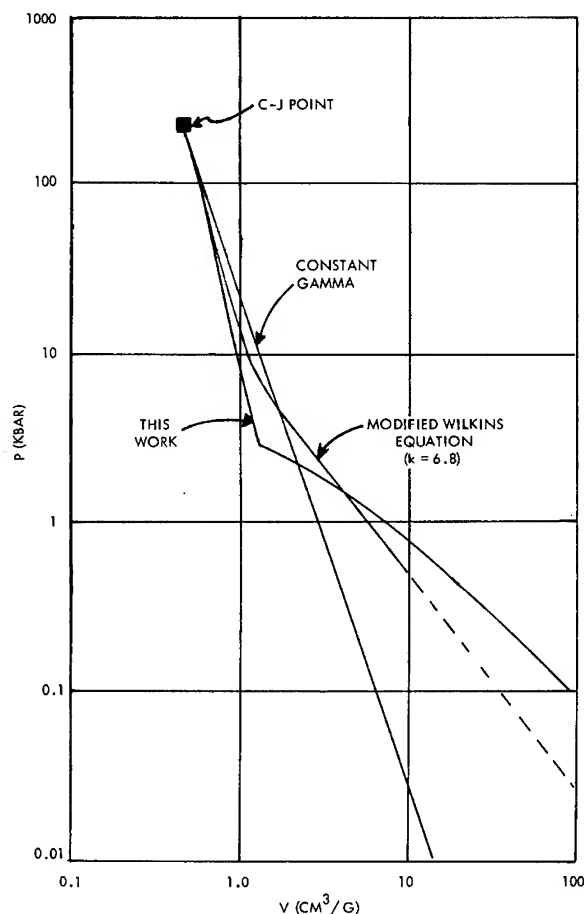


Fig. 6 - Pressure-volume adiabats for HBX-1

$$\gamma = - \left( \frac{\partial \ln P}{\partial \ln v} \right)_s$$

with volume for the modified Wilkins equation of state is shown in Fig. 7. We note that  $\gamma$  first increases from its C-J value of 2.934, to about 3.9, and finally decreases to 1.343. This final value is compatible with the value of  $W$  in the equation of state, i.e., the limiting value,  $\gamma = 1 + W$ . It is in the range of expected values for real gases at low pressures as calculated from the ratio of specific heats,  $C_p/C_v$  about 1.2 to 1.5. Also in Fig. 7,  $\gamma$  derived from the experimental adiabat is shown. The use of the characteristic equation,

$$P(V + v^*) = G_2$$

for  $v > 1.15 \text{ cm}^3/\text{g}$  produces a discontinuity in

$$- \left( \frac{\partial \log P}{\partial \log v} \right)_s$$

as indicated by the broken line in Fig. 7.

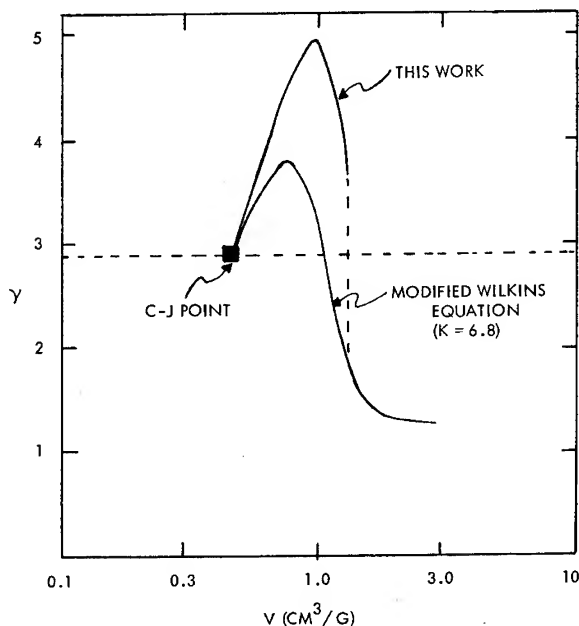


Fig. 7 - Variation of  $\gamma = -(\partial \log P / \partial \log V)_S$  with volume of reaction products from HBX-1

## REFERENCES

1. W. E. Deal, "Measurements of the Reflected Shock Hugoniot and Isentrope for Explosive Reaction Products", *Phys. of Fluids*, **1**, 523 (1958).
2. W. Fickett and W. W. Wood, "Detonation-Product Equation of State Obtained from Hydrodynamic Data", *Phys. of Fluids*, **1**, 528 (1958).
3. J. W. S. Allan and B. D. Lambourn, "An Equation-of-State of Detonation Products at Pressures Below 30 kbars", 4th Symp. on Det., 52 (1965).
4. T. P. Liddiard and B. E. Drimmer, *J. Soc. Motion Picture & Tele. Engrs.* **70**, 106 (1961).
5. D. Price, "Contrasting Patterns in the Behavior of High Explosives", 11th Symp. on Comb., 1967, The Combustion Inst., Pitts., Pa.
6. H. Eyring, R. E. Powell, G. H. Duffey, and R. B. Parlin, "The Stability of Detonation", *Chem. Rev.* **45**, 69 (1949).
7. W. W. Wood and J. G. Kirkwood, "Diameter Effect in Condensed Explosives. The Relation Between Velocity and Radius of Curvature of the Detonation Wave", *J. Chem. Phys.*, **22**, 1920-24 (1954).
8. M. A. Cook, G. S. Horsky, R. T. Keyes, W. A. Partridge, and W. O. Ursenback, "Detonation Wave Fronts in Ideal and Non-ideal Detonation", *J. Appl. Phys.*, **27**, 269 (1956).
9. R. E. Duff and E. Houston, *J. Chem. Phys.*, **23**, 1268 (1955), report the spike region is about 1 mm in aluminum impacted by Composition B with a reaction zone thickness of 0.13 mm.
10. See N. L. Coleburn, "The Compressibility of Pyrolytic Graphite", *J. Chem. Phys.*, **40**, 71 (1964). Also N. L. Coleburn and T. P. Liddiard, "The Unreacted Shock Hugoniot of Several Explosives", *Ibid*, **44**, 1929 (1966).
11. J. Hilsenrath and M. Klein, "Table of Thermodynamic Properties of Air in Chemical Equilibrium Including Second Virial Corrections from 1500°K to 15,000°K", AEDC-TDR-63-16 (August 1963); and, "Tables of Thermal Properties of Air", NBS Circ, 564, Wash., D.C. (1953).
12. R. H. Christian, R. E. Duff, and F. Yarger, "Shock Hugoniot of Argon", *J. Chem. Phys.*, **23**, 2042 (1955).
13. J. W. Bond, Jr., Los Alamos Rept. LA-1693 (unpublished). J. W. Bond, Jr., "Structure of Shock Front in Argon", *Phys. Rev.*, **105**, 1683 (1957).
14. This assumption is supported for high charge densities by the experimental data of A. N. Dremin, P. F. Pokhill, M. I. Arifov, *AKAD. NAUK. (DOKL.)*, **131**, 5 (1960), (in Russian).
15. H. Jones, 3rd Symp. on Comb., Flame, and Explosion Phenomenon, Williams and Wilkins, Balto., Md., P. 590 (1949).



# SHOCKED STATES OF FOUR OVERDRIVEN EXPLOSIVES

J. H. Kineke, Jr., and C. E. West, Jr.  
USA Ballistic Research Laboratories  
Aberdeen Proving Ground, Maryland

## ABSTRACT

Shock propagation observations have been made for four explosives at shock pressures greater than the detonation pressure. The transmission of steady-state shock waves with pressures up to six times the detonation pressure in 76/24 Baratol and three times the detonation pressure in cast TNT, Composition B, and PB-HMX-9404 was observed with a rotating mirror streak camera. Specimen discs were shocked by the impact of molybdenum plates accelerated by explosive plane wave generators. For each explosive, a linear relation between shock propagation rate and material velocity in the shock front was found, which extrapolated to pressures in excess of observed C-J pressures. Comparison is made with Skidmore and Hart's description of overdriven states.

## INTRODUCTION

When an explosive is subjected to shock pressures in excess of the Chapman-Jouguet pressure, a transient condition described as overdriven detonation results. The impact of a flying plate of molybdenum at moderately high velocity on a buffer plate of the same material will generate a strong shock wave in the buffer plate. The impingement of this strong shock on the interface between the buffer and an explosive specimen can produce the severe conditions necessary for the generation in the explosive of a shock whose propagation rate and pressure are initially in excess of those characteristic of the C-J state. By measurement of the initial propagation rate of the overdriven shock and the state of the buffer material, together with the known properties of the buffer, the pressure and density initially reached in the explosive can be calculated.

## DESCRIPTION OF EXPERIMENTS

In the course of an experiment a plane flat-topped shock wave is generated in a molybdenum buffer plate by the impact of a molybdenum flyer plate, accelerated by an explosive plane wave lens and explosive disc across an air gap. The conceptual plan for the experiments is shown in Fig. 1. The state of the shocked buffer

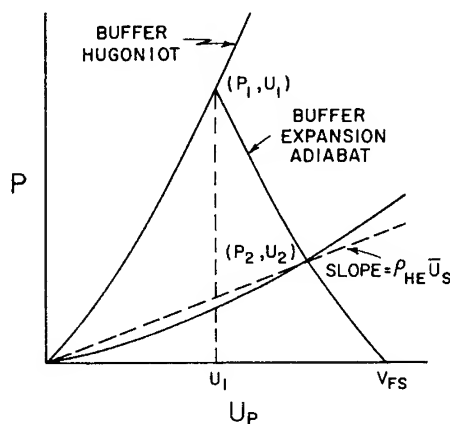


Fig. 1 - Conceptual plan for experiments

material is  $(P_1, u_1)$  on the known shock Hugoniot of molybdenum. When the shock reaches the surface of the buffer, an adiabatic expansion takes place. That area of the buffer not impeded by a specimen suffers a drop to zero pressure, and will be accelerated to the particle velocity at the foot of the adiabat,  $v_{fs}$ . That area of the buffer over which lies an explosive specimen will drop to some intermediate state  $(P_2, u_2)$ . Meanwhile, a shock is produced in the explosive specimen, which, because

pressure and material velocity must be continuous at the interface, is characterized by the same state ( $P_2, u_2$ ). An auxiliary experiment, to be reported later, was used to demonstrate that the expansion adiabat of molybdenum, used for the buffer plate, in the pressure range up to 2.0 megabars, can be approximated by the reflection of the shock Hugoniot about the point ( $P_1, u_1$ ). Then  $v_{fs}$ , which is measured directly, is  $2u_1$ . An amalgam of shock velocity  $U_h$  - material velocity  $u_p$  data for Mo (1), (2), (3), yielded the relation:

$$U_h = c_o + S u_p \quad (1)$$

where  $c_o = 0.5143 \text{ cm}/\mu\text{sec}$  and  $S = 1.2547$ . Then the expansion adiabat from a particular state of Mo can be written:

$$P_A = \rho_{Mo} [c_o + S(v_{fs} - U_p)](v_{fs} - U_p) \quad (2)$$

The pressure of the transmitted shock in the explosive specimen is:

$$P = \rho_{HE} U_s u_2 \quad (3)$$

where  $\rho_{HE}$  is the unshocked density of the explosive and  $U_s$  is the shock propagation rate in the specimen at the interface between the buffer and the specimen. Equating eqs. (2) and (3) at the point ( $P_2, u_2$ ), and solving for  $u_2$ , which hereafter is referred to as  $U_p$ :

$$U_p = \left[ n - (n^2 - m)^{1/2} \right] / 2 \rho_{Mo} S \quad (4)$$

where:

$$n = \rho_{HE} U_s + \rho_{Mo} (c_o + 2 S v_{fs})$$

and:

$$m = 4 \rho_{Mo}^2 S v_{fs} (c_o + S v_{fs})$$

The pressure and density ratio in the shock front are then calculated, using  $U_s$  and  $U_p$  and the continuity of mass and momentum relations.

Polished specimens of explosive, mounted on the surface of the buffer, were observed with a rotating mirror streak camera, writing at  $15 \text{ mm}/\mu\text{sec}$ , to measure the transit time. Specimens, generally four per shot, ranged in thickness from .05 cm to .2 cm, the thickness and flatness held to  $\pm .0002 \text{ cm}$  over the .625 cm diameter.

Instantaneous velocity as a function of distance from the buffer-specimen interface could be obtained by numerical differentiation of the specimen thickness-transit time data and

extrapolated to the buffer-specimen interface. The doubtfulness of extrapolated differentiated data was avoided because of the observed constancy of average shock velocity. In Fig. 2, for four typical experiments, measured average shock velocity is plotted as a function of specimen thickness. In every case where readable data could be obtained from more than one explosive specimen, the same result was obtained, that is, the average shock velocity, within experimental accuracy, appeared to be constant initially for a given experiment. Thus, it could be concluded that a steady-state shock, uninfluenced by a rarefaction from the rear of the flyer had, in fact, been observed. Therefore,

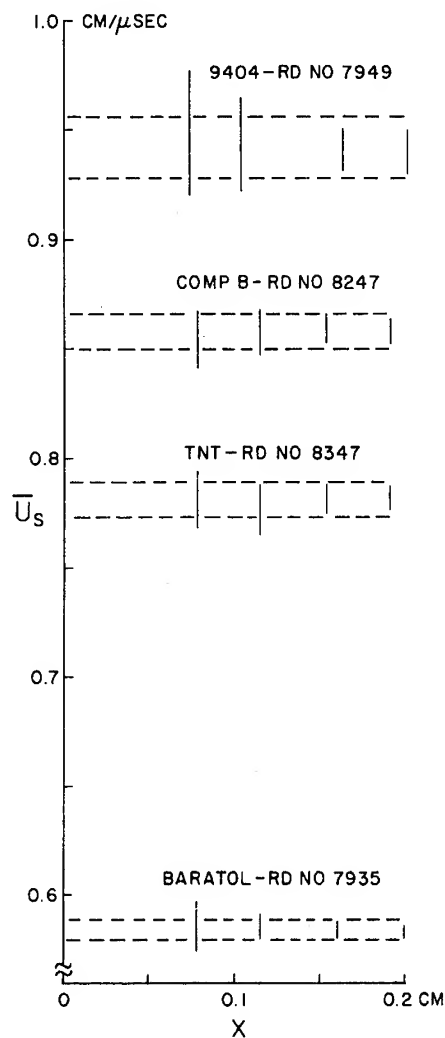


Fig. 2 - Representative observations of shock velocity as a function of specimen thickness. Vertical bars indicate uncertainty in each measurement. Limits of uncertainty of weighted means are defined by the dashed lines.

extrapolation of shock velocity to the interface between specimen and buffer ( $x = 0$ ) consisted merely of determining the weighted average of several observations.

Average shock velocities for each experiment were calculated by weighting each observation inversely with its uncertainty  $\sigma_i$ . Thus:

$$U_s = \sum \left[ U_{si} / \left( \sigma_i \sum_{j=1}^n 1/\sigma_j \right) \right], \quad (5)$$

where  $n$  is the number of readable specimens. Uncertainties in  $U_s$  were between 0.7% and 2.4%.

## RESULTS

The measured shock velocities in the specimens and the measured free surface velocities of the buffer plates are tabulated, with their uncertainties, in Tables 1-4. Mean calculated material velocities, density ratios, and pressures are also shown, with the uncertainties having been suppressed, but readily obtainable from  $U_s$  and  $V_{fs}$ .

Shock velocity as a function of material velocity is plotted in Figs. 3 and 4, together with C-J points determined by Jameson (4), (5). Also plotted are four points for Composition B,

TABLE 1  
Shock States—76/24 Baratol

Rd	$V_{fs}$ cm/ $\mu$ sec	$U_s$ cm/ $\mu$ sec	$U_p$ cm/ $\mu$ sec	$\rho_o/\rho$	P Mbar
7940	.252 $\pm$ .001	.580 $\pm$ .006	.200	.655	.301
8168	.252 $\pm$ .001	.583 $\pm$ .010	.201	.655	.303
7935	.259 $\pm$ .003	.584 $\pm$ .005	.206	.647	.312
8169	.263 $\pm$ .001	.593 $\pm$ .007	.209	.647	.321
8170	.269 $\pm$ .001	.600 $\pm$ .008	.213	.644	.331
8238	.287 $\pm$ .001	.609 $\pm$ .009	.227	.627	.358
8239	.299 $\pm$ .001	.623 $\pm$ .007	.236	.621	.380
7934	.308 $\pm$ .003	.641 $\pm$ .006	.242	.623	.401
7933	.332 $\pm$ .003	.668 $\pm$ .009	.259	.612	.450
7941	.353 $\pm$ .004	.678 $\pm$ .007	.275	.594	.482
8179	.362 $\pm$ .002	.685 $\pm$ .007	.282	.588	.499
8025	.397 $\pm$ .004	.729 $\pm$ .011	.307	.579	.579
8027	.404 $\pm$ .003	.735 $\pm$ .012	.312	.576	.595
7962	.412 $\pm$ .004	.736 $\pm$ .009	.317	.568	.606
8024	.422 $\pm$ .002	.737 $\pm$ .014	.326	.558	.621
7733	.430 $\pm$ .006	.755 $\pm$ .008	.331	.562	.643
7930	.458 $\pm$ .003	.780 $\pm$ .010	.351	.551	.707
7931	.488 $\pm$ .005	.799 $\pm$ .009	.373	.534	.770
7929	.489 $\pm$ .007	.806 $\pm$ .010	.373	.538	.780
8171	.512 $\pm$ .002	.829 $\pm$ .010	.390	.530	.835
8172	.516 $\pm$ .002	.832 $\pm$ .010	.393	.528	.844
8180	.517 $\pm$ .002	.838 $\pm$ .007	.392	.532	.851
7717	.519 $\pm$ .002	.846 $\pm$ .019	.394	.534	.859
8181	.522 $\pm$ .003	.850 $\pm$ .014	.396	.534	.869
8182	.592 $\pm$ .005	.892 $\pm$ .010	.446	.500	1.030

TABLE 2  
Shock States—Cast TNT

Rd	$V_{fs}$ cm/ $\mu$ sec	$U_s$ cm/ $\mu$ sec	$U_p$ cm/ $\mu$ sec	$\rho_o/\rho$	P Mbar
8259	.327 $\pm$ .001	.716 $\pm$ .006	.274	.617	.312
8026	.347 $\pm$ .001	.738 $\pm$ .007	.290	.607	.339
8006	.376 $\pm$ .002	.759 $\pm$ .006	.313	.588	.378
8008	.391 $\pm$ .004	.785 $\pm$ .010	.324	.587	.405
8347	.402 $\pm$ .001	.781 $\pm$ .008	.334	.572	.414
8356	.418 $\pm$ .002	.788 $\pm$ .009	.347	.560	.434
8260	.421 $\pm$ .002	.799 $\pm$ .007	.349	.563	.443
8261	.438 $\pm$ .002	.806 $\pm$ .008	.363	.550	.464
8262	.451 $\pm$ .002	.817 $\pm$ .007	.373	.543	.483
8009	.452 $\pm$ .003	.823 $\pm$ .012	.373	.546	.489
8013	.454 $\pm$ .003	.820 $\pm$ .011	.376	.542	.491
8264	.468 $\pm$ .005	.831 $\pm$ .008	.387	.535	.510
8263	.473 $\pm$ .002	.833 $\pm$ .008	.391	.531	.517
8266	.499 $\pm$ .003	.853 $\pm$ .009	.412	.517	.557
8265	.515 $\pm$ .003	.873 $\pm$ .011	.423	.515	.586
8331	.528 $\pm$ .003	.886 $\pm$ .010	.433	.511	.609
8014	.534 $\pm$ .003	.905 $\pm$ .015	.437	.517	.628
8338	.537 $\pm$ .002	.899 $\pm$ .009	.439	.511	.628

determined by Skidmore and Hart (6). Since each of the four sets of data seem reasonably well described by a straight line, each point was weighted inversely as the product of its horizontal and (almost) vertical uncertainties, and each set fitted to an equation of the form:

$$U_s = a + b U_p \quad (6)$$

The coefficients  $a$  and  $b$  are tabulated in Table 5. Each straight line has been extrapolated to the C-J propagation rate, with similar results. In each case, the extrapolation yielded a material velocity in excess of that for the C-J state, by 14% for Baratol, to 36% for TNT.

Pressures and density ratios, calculated with eq. (4) and the continuity relations, were weighted and fitted to second degree polynomials of the form:

$$P = c + d(\rho_o/\rho) + e(\rho_o/\rho)^2 \quad (7)$$

The coefficients are listed in Table 5 and the fitted curves shown in Fig. 5. Any statement concerning extrapolation of the data through the C-J point in this plane becomes highly ambiguous.

#### DISCUSSION OF RESULTS

Results of experiments with Composition B similar to those described here were presented by Skidmore and Hart (6). Their datum points are plotted in Fig. 3 and agree quite well with the current data.

Skidmore and Hart also described a model for the overdriven states measured. It was assumed that the experiments measured the state of the products of overdriven detonation, which obeyed a polytropic gas equation of state:

$$E = PV/(\gamma - 1) \quad (8)$$

A further assumption made had the energy released by the reaction,  $Q$ , identical for the C-J

TABLE 3  
Shock States—Composition B

Rd	$V_{fs}$ cm/ $\mu$ sec	$U_s$ cm/ $\mu$ sec	$U_p$ cm/ $\mu$ sec	$\rho_o/\rho$	P Mbar
8359	.331 $\pm$ .002	.814 $\pm$ .017	.269	.669	.368
8243	.344 $\pm$ .002	.818 $\pm$ .007	.280	.657	.385
7996	.369 $\pm$ .001	.839 $\pm$ .008	.300	.643	.423
7997	.391 $\pm$ .002	.855 $\pm$ .010	.317	.629	.455
7990	.395 $\pm$ .002	.864 $\pm$ .013	.320	.629	.463
8244	.400 $\pm$ .002	.857 $\pm$ .007	.324	.622	.467
8247	.402 $\pm$ .002	.858 $\pm$ .008	.326	.620	.470
8245	.408 $\pm$ .001	.870 $\pm$ .009	.330	.621	.482
8246	.432 $\pm$ .002	.889 $\pm$ .016	.349	.608	.518
7989	.449 $\pm$ .002	.904 $\pm$ .012	.362	.599	.549
8248	.451 $\pm$ .003	.892 $\pm$ .013	.364	.592	.546
7998	.455 $\pm$ .003	.901 $\pm$ .012	.367	.592	.555
7999	.483 $\pm$ .004	.922 $\pm$ .013	.390	.577	.604
8249	.501 $\pm$ .002	.942 $\pm$ .010	.403	.573	.636
7988	.506 $\pm$ .003	.947 $\pm$ .016	.407	.571	.644
8357	.525 $\pm$ .005	.960 $\pm$ .017	.422	.561	.679
8358	.534 $\pm$ .003	.963 $\pm$ .014	.428	.555	.693
7991	.554 $\pm$ .003	.993 $\pm$ .015	.443	.554	.739

state and the overdriven states. These assumptions, together with the Rankine-Hugoniot relations, permitted derivation of a relationship between propagation rate  $U_s$  of the overdriven state and the pressure  $P$  of that state, involving as parameters the propagation rate  $U_{cj}$  and pressure  $P_{cj}$  of the C-J state:

$$U_s = U_{cj} [(2 - P_{cj}/P) P_{cj}/P]^{-1/2} \quad (9)$$

Equation (9) is independent of the value of  $\gamma$  because of the form of equation of state chosen.

A comparison of Skidmore and Hart's model with the present experiments is shown in Figs. 6 and 7. The agreement they found for Composition B is verified for pressures up to about 0.6 megabar, with some divergence of the data from equation (9) above that pressure. Some modicum of agreement also exists for 76/24 Baratol. On the other hand, substantial disagreement, throughout the pressure range, is evident for both PB-HMX-9404 and cast TNT.

Skidmore and Hart also examined experimentally the states of reflected shocks in Composition B from an overdriven state at .42 megabar. These states had been found to be consistent with their theoretical formulation, for  $\gamma = 2.85$ , which value of  $\gamma$  was computed from:

$$\gamma = (U_{cj} - U_{p(cj)})/U_{p(cj)} \quad (10)$$

While reflected shock experiments are not reported in the present work, it was felt appropriate to calculate  $\gamma$  for the sets of overdriven states here. These were computed by linear regressions of the form:

$$\ln P = \ln C + \gamma \ln (\rho/\rho_o) \quad (11)$$

A fit of this form is less than optimum, since undue weight is given to points at the lower end of the range. Nevertheless, some indication of the value of  $\gamma$  required to fit the data is provided. These computed  $\gamma$ 's are listed in Table 6, together with those of Jameson for the C-J

TABLE 4  
Shock States—PB-HMX-9404

Rd	$V_{fs}$ cm/ $\mu$ sec	$U_s$ cm/ $\mu$ sec	$U_p$ cm/ $\mu$ sec	$\rho_o/\rho$	P Mbar
8109	.334 $\pm$ .002	.901 $\pm$ .011	.263	.708	.435
7952	.350 $\pm$ .002	.907 $\pm$ .012	.277	.696	.460
8110	.355 $\pm$ .002	.912 $\pm$ .010	.279	.694	.470
7951	.361 $\pm$ .001	.917 $\pm$ .008	.284	.690	.480
7950	.391 $\pm$ .002	.931 $\pm$ .014	.308	.669	.527
7834	.397 $\pm$ .003	.924 $\pm$ .018	.312	.662	.532
8113	.412 $\pm$ .002	.941 $\pm$ .008	.324	.656	.562
7949	.413 $\pm$ .002	.942 $\pm$ .014	.325	.655	.563
8112	.429 $\pm$ .002	.949 $\pm$ .013	.337	.645	.589
7835	.429 $\pm$ .002	.943 $\pm$ .021	.337	.642	.587
7943	.445 $\pm$ .003	.970 $\pm$ .013	.349	.640	.623
7942	.464 $\pm$ .002	.983 $\pm$ .015	.363	.630	.658
8116	.479 $\pm$ .002	.981 $\pm$ .012	.375	.617	.678
8117	.480 $\pm$ .002	.978 $\pm$ .011	.376	.615	.678
8234	.492 $\pm$ .002	.989 $\pm$ .007	.386	.610	.699
8233	.499 $\pm$ .003	.996 $\pm$ .009	.391	.607	.711
8135	.503 $\pm$ .003	.998 $\pm$ .011	.394	.606	.723
8131	.507 $\pm$ .002	1.001 $\pm$ .013	.397	.603	.732
8236	.553 $\pm$ .003	1.019 $\pm$ .012	.432	.576	.813
7855	.559 $\pm$ .006	1.023 $\pm$ .024	.436	.573	.823
8137	.578 $\pm$ .003	1.036 $\pm$ .011	.452	.563	.863

TABLE 5  
Empirical Coefficients

Explosive	$\rho_o$	a	b	c	d	e	Range
	gm/cm <sup>3</sup>	cm/ $\mu$ sec		Mbar	Mbar	Mbar	Mbar
76/24 Baratol	2.587 $\pm$ .010	.3159	1.3198	9.799	-27.103	19.242	.30 < P < 1.03
Cast TNT	1.588 $\pm$ .003	.4313	1.0442	5.183	-14.149	10.150	.31 < P < .63
Composition B	1.678 $\pm$ .006	.5357	1.0047	6.653	-17.140	11.576	.36 < P < .74
PB-HMX-9404	1.839 $\pm$ .004	.7077	0.7290	4.713	- 9.925	5.487	.43 < P < .87

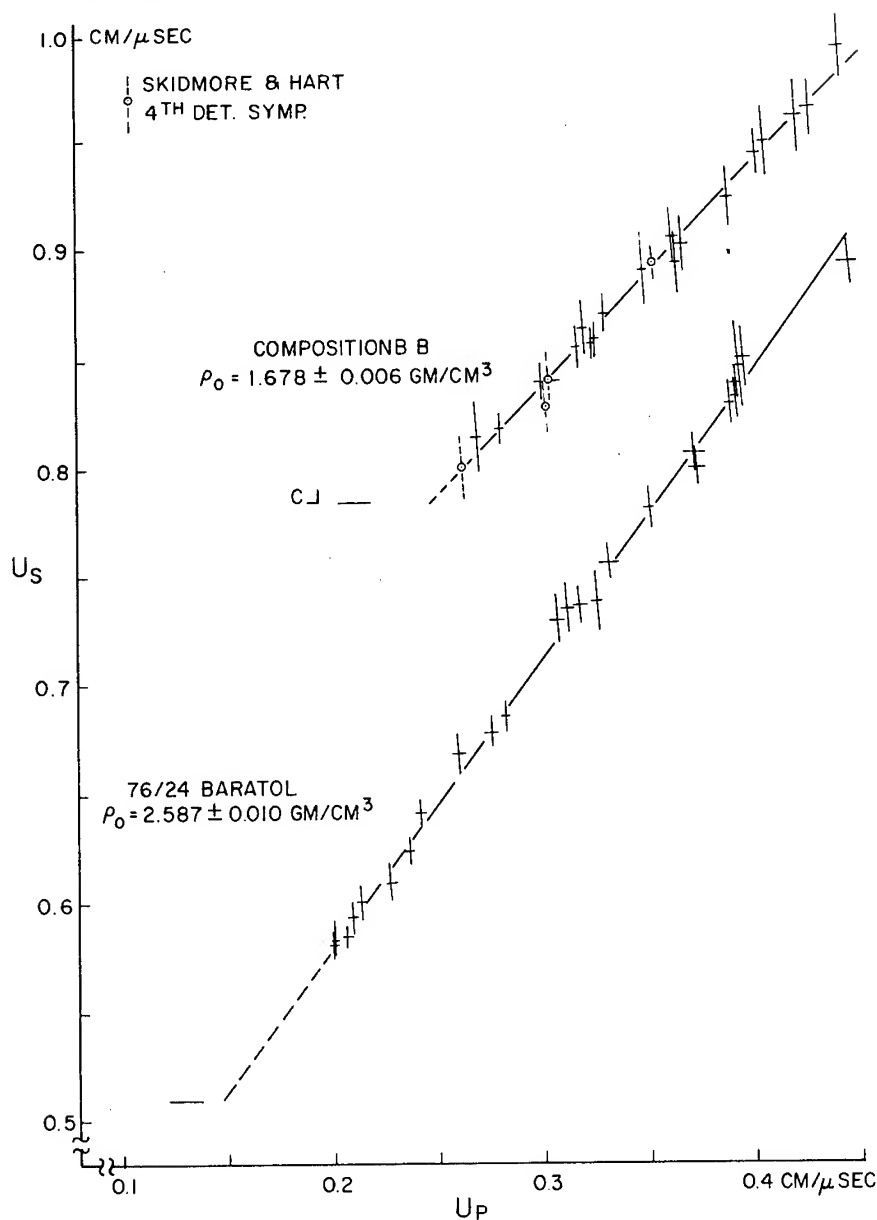


Fig. 3 - Shock velocity -- material velocity data for Composition B and 76/24 Baratol

state. In three of the explosives the  $PV^\gamma$  formulation reasonably well described the data, for the  $\gamma$  evoked by the fit. In the fourth explosive, Composition B, the fit was extremely tenuous, suggesting the inappropriateness of a fit of the form of equation (11). Despite the fact that suitable fits to equation (11) were obtained for three of the explosives, the computed values of  $\gamma$  for the overdriven states of all four explosives bear little relation to those of the C-J states, being little less than and greater than those of the C-J states by ten to sixty percent.

The foregoing discussion evinces the following speculative comments. Some doubt is placed on the validity of the model described by equation (9), because of the inadequacy of the fits in Figs. 6 and 7. Yet, no definite insufficiency can be attributed to the assumptions made.

The assumption that the energy released by the reaction is identical for the C-J state and the overdriven state might be borne out by the fact that an overdriven detonation, if

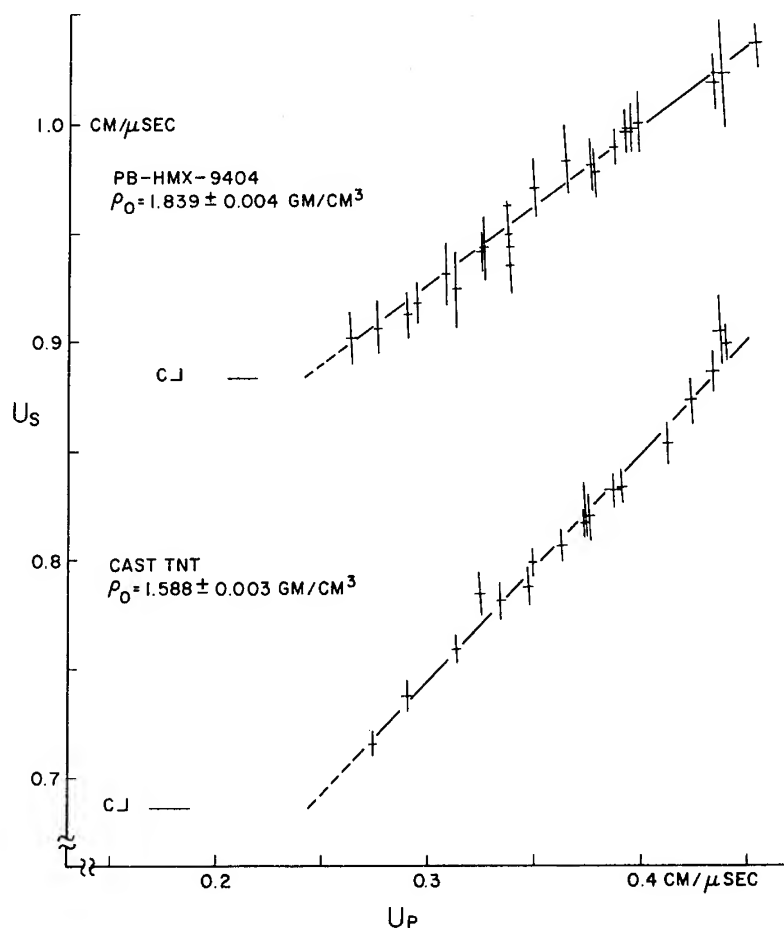


Fig. 4 - Shock velocity -- material velocity data for PB-HMX-9404 and cast TNT

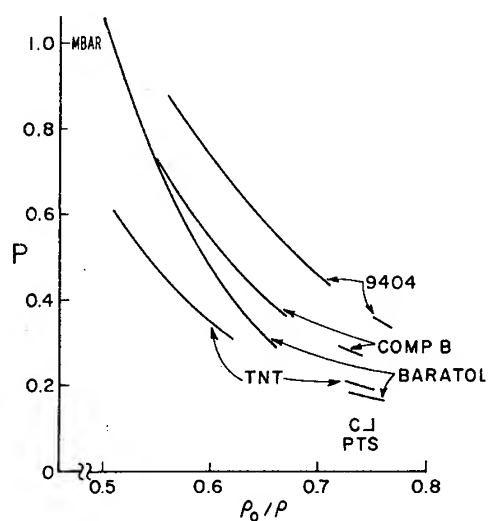


Fig. 5 - Pressure-density ratio regressions for four explosives, from Table 5

TABLE 6  
Polytropic Exponents

Explosive	$\gamma$	
	C-J	Overdriven
Composition B	$2.71 \pm .13$	$2.98 \pm .30$
Cast TNT	$2.84 \pm .20$	$3.43 \pm .13$
76/24 Baratol	$2.95 \pm .23$	$4.79 \pm .12$
PB-HMX-9404	$3.17 \pm .12$	$2.92 \pm .09$

propagated sufficiently far, will decay into the usual steady-state detonation. This statement is supported by preliminary experiments, not formally reported at this time, on the attenuation of overdriven detonation in 76/24 Baratol and PB-HMX-9404, with extended charges. Initial propagation rates were consistent with those measured in thin specimens, and, within



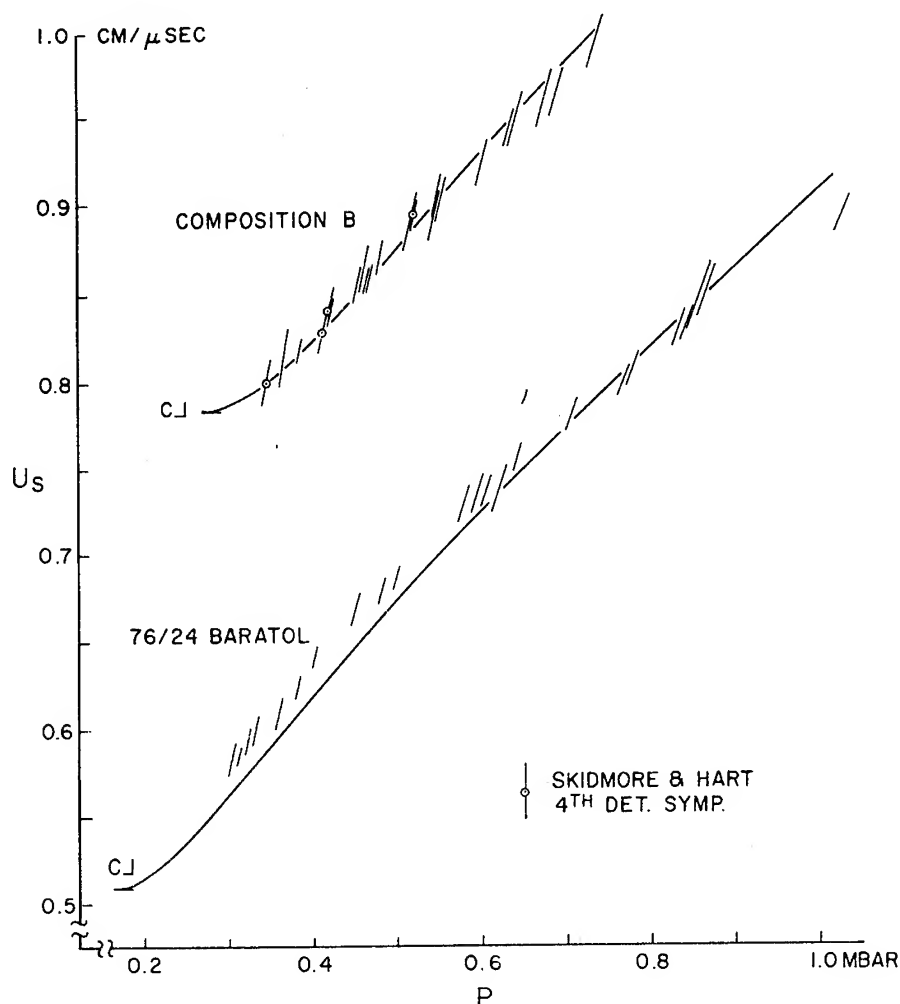


Fig. 6 - Shock velocity data as a function of pressure, for Composition B and 76/24 Baratol, compared to C-J points and equation (9)

experimental uncertainty, were constant. Decay of propagation rate commenced at distances in the explosive samples of five to twenty flyer thicknesses. Between 100 and 200 flyer thicknesses from the buffer-explosive interface, the propagation rate had dropped to the steady-state rates; 0.51 cm/μsec for Baratol and 0.88 cm/μsec for 9404. These preliminary observations that overdriven detonations decay to C-J rates indicate that the ultimate products of an overdriven detonation, in the pressure range investigated, are probably the same as those for a C-J detonation. Therefore, no unique modification of the series of decomposition processes in the detonation, resulting in a change of  $Q$  and a steady unsupported detonation whose propagation rate is greater than the C-J rate, takes place.

The assumption that a polytropic equation of state describes the C-J state would not appear to be unreasonable. However, the succession of states extending from slightly above to several times the C-J pressure can be fitted uniquely to a polytropic equation of state, but the  $\gamma$ 's obtained seem to bear little relation to the C-J  $\gamma$ . Thus, it probably should be concluded that use of a polytropic form for the present experiments is inappropriate and the computed  $\gamma$ 's obtained are fortuitous.

With the assumptions of Skidmore and Hart's model not vigorously eroded, a reasonable speculation is that data described in these experiments is not representative of the products of detonation at the C-J plane. Rather, these data are representative of the unreacted

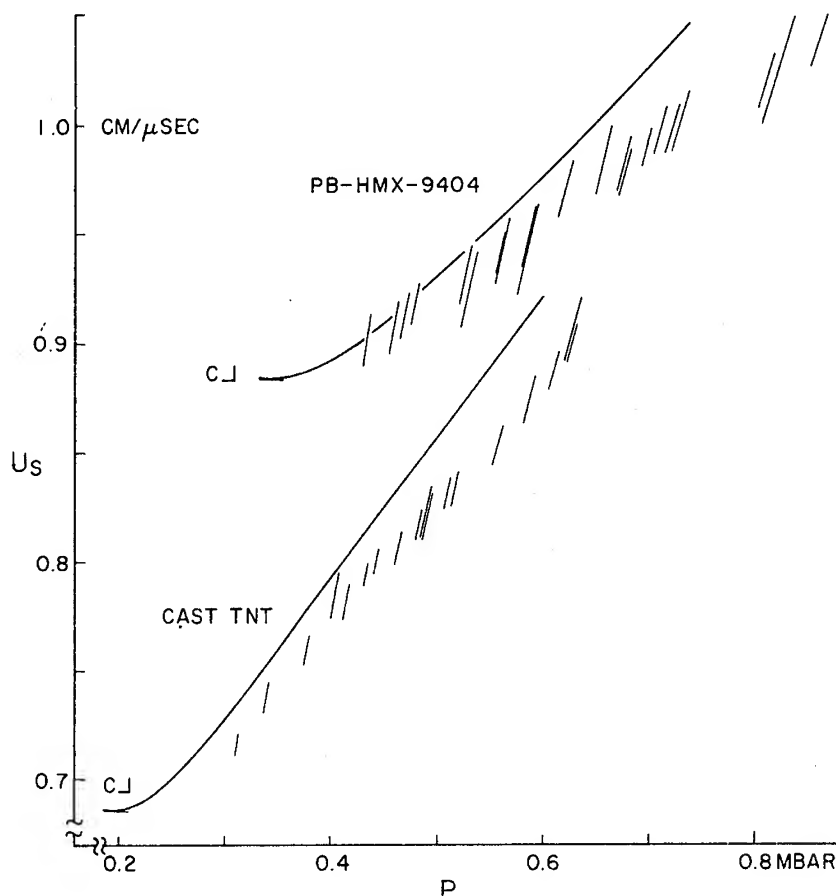


Fig. 7 - Shock velocity data as a function of pressure, for PB-HMX-9404 and cast TNT, compared to C-J points and equation (9)

Hugoniots of the explosives investigated. This statement would seem to be supported by the facts that any judicious extrapolation of the data in Figs. 3 and 4 always arrives at a pressure higher than the C-J pressure, and that the initial propagation rate for overdriven states deviates undetectably from constancy, and so is probably not fed by a reaction.

#### ACKNOWLEDGMENTS

The authors express their thanks to Mr. Dan Wanner for performing many of the measurements, Mr. John K. Kelly for developing the several computer programs used in data reduction and fitting, and Dr. Robert R. Karpp for contributing useful comments.

#### REFERENCES

1. J. M. Walsh, M. H. Rice, R. G. McQueen, and F. L. Yarger, "Shock Wave Compressions of Twenty-Seven Metals", *Phys. Rev.* Vol. 108, 1957, pp. 196-216.
2. R. G. McQueen and S. P. Marsh, "Equation of State for Nineteen Metallic Elements from Shock-Wave Measurements to Two Megabars", *J. Appl. Phys.*, Vol. 31, No. 7, 1960, pp. 1253-1269.
3. K. K. Krupnikov, A. A. Bakanova, M. I. Brazhnik, and R. F. Trunin, "An Investigation of the Shock Compressibility of Titanium, Molybdenum, Tantalum, and Iron",

- Sov. Phys. - Doklady, Vol. 8, 1963, pp. 203-208.
4. R. L. Jameson and A. Hawkins, "Shock Velocity Measurements in Inert Monitors Placed on Several Explosives". This symposium. (Composition B, PB-HMX-9404, cast TNT.)
  5. R. L. Jameson, BRL, private communication. (76/24 Baratol)
  6. I. C. Skidmore and S. Hart, "The Equation of State of Detonation Products Behind Overdriven Detonation Waves in Composition B", Fourth Symposium on Detonation, NOL, 1965, pp. 47-51.

**Session VII**  
**EXPERIMENTS ON SHOCKS AND FLOWS**

Chairman: Y. Manheimer-Timnat  
*Israel Institute of Technology*

# VAPORIZING OF URANIUM AFTER SHOCK LOADING

Ph. de Beaumont  
*Commissariat à l'Energie Atomique - Paris*  
and

J. Leygonie  
*Centre d'Etudes de Gramat - Lot*

## ABSTRACT

An explosive device based on the principle of a conical implosion achieves generating, in uranium and copper samples, plane and steady shock waves, the strength of which approaches 15 Mbars in uranium. Both the shock velocity and free-surface velocity in air have been measured simultaneously. Different equations of state have been tried, to interpret the experimental results of uranium; only an equation of state of liquid type restore these results along with those previously obtained up to 2 Mbars. Furthermore, the free-surface velocity observed for 15 Mbars in uranium implies a complete vaporizing during the expansion.

## INTRODUCTION

The state of matter is adequately known in the range of pressures close to 1 Mbar where it is sufficient to have a good potential (crystalline metal) and use the Mie-Grüneisen relation between thermal pressure and energy. In the range of very high temperatures, the equations of state of Thomas-Fermi are then very appropriate.

Here, it has been tried to reach experimentally an intermediate domain of pressure and temperature. The experiment consists of focusing a conical fronted shock into a plane Mach-bridge of high strength (more than 15 Mbars); the theory shows that the simple description, by Mie-Grüneisen, of thermic terms is no more valid, and therefore it is not possible yet to use Thomas-Fermi's equations. The state of matter will be described with an equation of liquid state, thus allowing for continuous change from solid phase to gaseous phase which has been encountered when loading uranium and then expanding it into the atmosphere.

## EXPERIMENTAL DEVICE

The device in question is a conical implosion generator represented on Fig. 1.

The impact of the conical tamper of copper (2-mm width) on a target of same material generates a converging conical shock wave resulting in a Mach bridge on the axis. The diameter of the Mach bridge is close to 10 mm in the plane of the support of the sample, thus making it possible to measure dynamic pressures of 11 Mbars in copper. A modified version measures up to 18 Mbars, but it was not necessary to use it to get a complete vaporizing of uranium after shock loading. The sample is a pellet 2 mm high and 6 mm in diameter, smaller than the diameter of the Mach bridge which behaves as an isolated plane wave with regard to the sample.

A large number of shots were accomplished in different samples of solids and transparent liquids of variable width in order to check the steadiness of shock waves generated by Mach bridges. The measured defects of steadiness, on samples varying from 1 to 3 mm in width, were never over  $\pm 1.8\%$  on shock velocities, which is within the range of accuracy of the measurement itself. Then the steadiness defects are not noticeable.

## METHOD OF MEASUREMENTS AND RESULTS OBTAINED

The measurements were carried out by optical methods, i.e., using a high-resolution

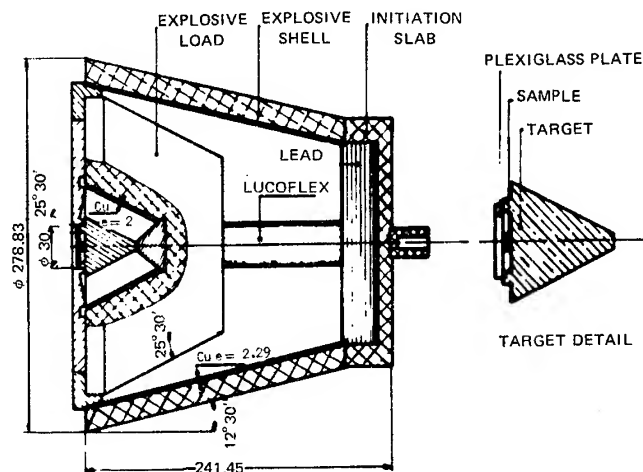


Fig. 1 - Conical implosion generator  
(strength = 11 Mbars)

streak camera with a rotating mirror. Film analysis requires several machines; a tele-reader, a micrometric microscope, a micro-densitometer, and an isodensity recorder.

The streak camera records the diameter of the sample through a plate of plexiglass placed at a determined distance from the free surface. The following events are recorded on the film, in order:

- Shock emergence on the plane bearing the sample,
- Shock emergence on the free surface of the sample,
- Phenomena associated with the impact of the sample on the plexiglass plate.

The film analysis procedure will be examined in the next paragraphs.

Fifteen shots were achieved for each metal. A certain number of shots had to be rejected for the following reasons:

- Incorrect centering of the Mach bridge on the sample,
- Perturbation of the plexiglass plate before impact by lateral jets, most of the time because of incorrect centering.

The value given for the couple  $U$ , shock velocity  $U_s$ , free-surface velocity, is the mean of the nonrejected shots:

	$U = 11,790 \text{ m/s}$
for uranium	$U_s = 16,500 \text{ m/s}$
	$U = 15,850 \text{ m/s}$
for copper	$U_s = 20,640 \text{ m/s}$

The scattering of experimental results around the mean value for uranium is

$$\frac{\Delta U}{U} = \pm 2.5\%; \quad \frac{\Delta U_s}{U_s} = \pm 1.5\%$$

and for copper

$$\frac{\Delta U}{U} = \pm 2.9\%; \quad \frac{\Delta U_s}{U_s} = \pm 1.7\%$$

The reason for this scattering, essentially due to difficulties in analyzing records, is given in the following paragraphs.

#### ANALYSIS OF EXPERIMENTAL RESULTS

##### Measure of $U$ (Shock Velocity)

The method of measurement is shown in Fig. 2 on a streak camera record.

The Mach bridge occurring in the plane of the sample is limited by diameter  $AD$ . The major part of the trail is obscured by the pellet.

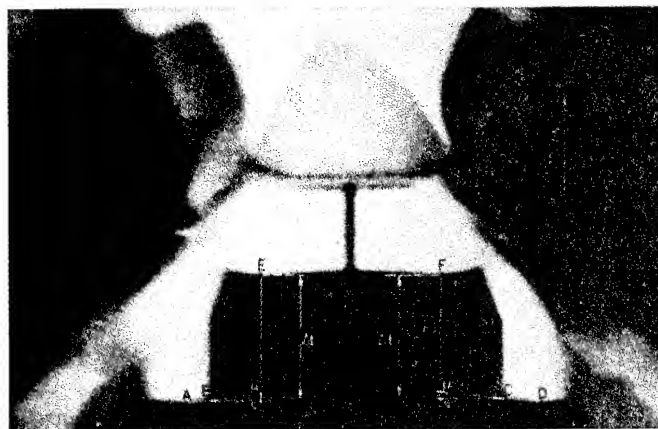


Fig. 2 - Streak camera record

The wave is slightly concave, with a mean rise of 16 ns, varying  $\pm 6$  ns from one shot to the other.  $U$  is measured straight above E and F, the points limiting the zone being undisturbed by the lateral expansion at the time of shock emergence. The middle of segment  $\mu\nu$  is considered as the most probable instant for shock emergence straight above E and F. This method of interpolation has been checked by means of a number of shots in transparent samples, for which the time interval obtained from interpolation can be compared to the real time interval. It is verified that the maximum range of error is  $\pm 4$  ns. For a sample 2 mm high, the measured time interval varies from 200 ns to 100 ns when  $U$  varies from 10,000 m/s to 20,000 m/s, so that error  $\Delta U/U$  varies from  $\pm 4/200$  to  $\pm 4/100$ , i.e., from  $\pm 2\%$  to  $\pm 4\%$ .

The analysis gives the following results for  $U$  (m/s):

Uranium		Copper	
Shot No.	$U$ (m/s)	Shot No.	$U$ (m/s)
3224	11,680	3191	15,870
3231	11,710	3192	15,380
3233	11,760	3200	16,240
3234	11,890	3211	16,270
3236	12,000	3212	15,360
3238	11,990	3603	15,450
3599	11,650	3607	16,080
3600	11,610	3617	15,870
3601	12,150	3622	16,190
3618	11,490		
3620	12,000		
3621	11,670		

i.e., for uranium:

$$U_{\text{mean}} = 11,790 \text{ m/s}$$

$$\Delta t_{\text{mean}} = 170 \text{ ns}$$

$$\frac{\Delta U}{U} (\text{theory}) = \pm \frac{4}{170} = \pm 2.35\%$$

$$\frac{\Delta U}{U} (\text{exp}) = \pm 2.5\%$$

for copper:

$$U_{\text{mean}} = 15,850 \text{ m/s}$$

$$\Delta t_{\text{mean}} = 126 \text{ ns}$$

$$\frac{\Delta U}{U} (\text{theory}) = \pm \frac{4}{126} = \pm 3.18\%$$

$$\frac{\Delta U}{U} (\text{exp}) = \pm 2.9\%$$

The agreement between theoretical and experimental  $\Delta U/U$  is good. Notice that the trails characterizing the arrival and emergence of shock in pellets are defined on the film as beginnings of very impressed zones. They do not correspond to the exact time of arrival of these events, because of light diffusion on both sides of the camera streak under high luminosity. Therefore, for  $U$  the phenomenon is identical on both sides of the measured time interval, this not being the case for  $U_s$ , the free-surface velocity.

Measure of  $U_s$

The phenomena occurring at the free-surface departure and at the impact on the

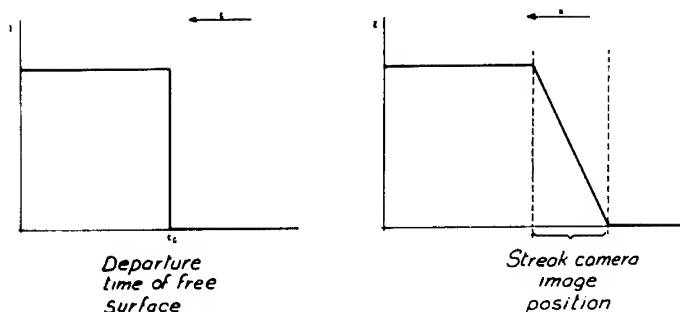


Fig. 3 - Intensity and illumination

plexiglass plate are essentially different and need be analysed separately.

At the free-surface departure, a high-strength shock is sent into the air. The saturation rise time of luminosity is physically negligible. This shock being very intense, the mean-free path of photons in the equilibrium zone is of the order of  $5 \mu\text{s}$  in visible light; i.e., a rise time, at the shock velocity of  $23 \mu/\text{ns}$ , of  $5/23 = 0.2 \text{ ns}$ .

On the contrary, light diffusion in the emulsion and the width of the streak yield to a smooth rise of blackening on the film.

The intensity of radiation has the shape shown on Fig. 3a. The illumination on the film, as a consequence, has the shape of Fig. 3b.

This illumination is diffused according to the formula

$$E'(x) = \int_{-\infty}^{+\infty} E(\xi) \cdot A(|x - \xi|) d\xi$$

if  $A(|x - \xi|)$  is the step response of the emulsion, which is taken as:

$$A(|x - \xi|) = e^{-|x - \xi|/r_0}$$

with  $r_0 = 40 \mu$ , for Tri-X 400 ASA film, used in dynamic conditions.

The film blackening is given by

$$d(x) = c + \gamma \log E'(x)$$

with  $\gamma \approx 1$ . Finally, Fig. 4a shows the blackening curve computed for free-surface departure, as well as the streak position at same time; Fig. 4b shows the curve experimentally obtained with a microdensitometer giving a magnification of 1000.

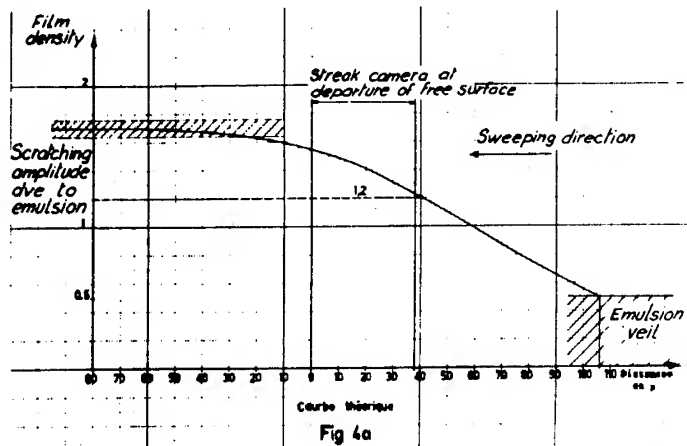


Fig. 4a - Theoretical blackening



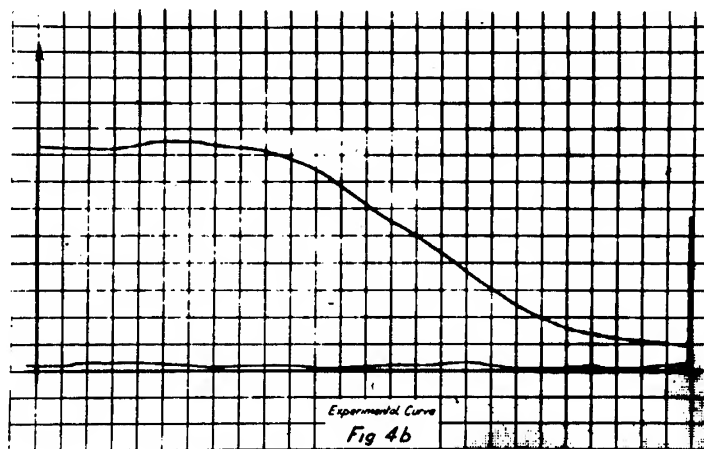


Fig. 4b - Experimental blackening

Agreement is excellent, and the streak position is, so far, well determined with respect to the rise front.

At the time when the free surface impacts the plexiglass plate, the luminous phenomena appearing are complex, as shown by recording (Fig. 5a) and related microdensitogram (Fig. 5b).

These phenomena can be explained in the following way: in the case of copper, the free surface moves with velocity of 20,650 m/s and the shock wave created in air moves with velocity of 23,250 m/s, which brings the air to a temperature of 45,000°K. The luminous

emission radiating from the front is very important, the maximum being for  $h\nu = 11$  eV.

The effect of radiation flux on the plexiglass plate varies largely with respect to time; in fact, the width of the cold air gap between the plate and shock front in air dwindles rapidly, which allows more and more UV photons of high energy to reach the plate; they will be absorbed in a layer a few  $\mu$  wide which will be more and more disturbed, partly from vaporizing; so the interface will be more and more opaque to visible radiation. This effect, then, is responsible for the record  $\Omega$  to 0 on the densitogram of Fig. 5b.

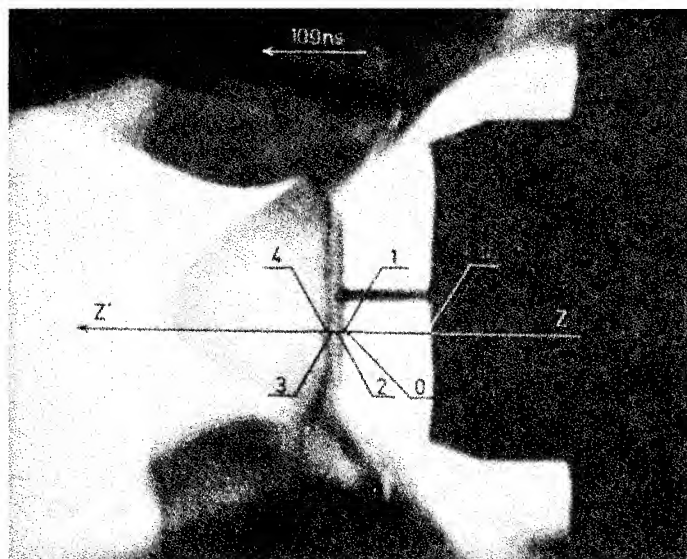


Fig. 5a - Streak camera record for copper

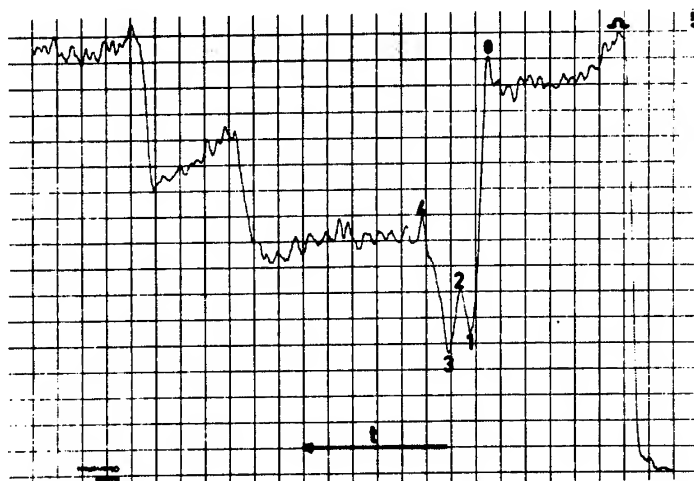


Fig. 5b - Microdensitogram of previous record (z z', Fig. 5a).

At 0, air shock reaches the plate and is reflected, bringing the air temperature from  $45,000^\circ\text{K}$  to  $70,000^\circ\text{K}$ , multiplying by 1.7 the visible radiation intensity, and increasing the blackening by 0.23 d. The blackening peak is widened by diffusion. The peak is followed by a rapid absorption of light according to branch 0 to 1 which is imputed once more to an interface effect, but of different nature than the previous one—compression up to 20 kb, corresponding to the reflected air shock on one hand, direct thermic conduction at the interface on the other hand. The result is "metallisation" of a very thin layer of increasing width. Opacity increases regularly, excluding any other phenomena during the 8 ns necessary for the return travel of the air shock from plate to free-surface and back. However, according to the reflexion on the plate of the second air shock, the increase of pressure and temperature is terribly rapid. It takes only 3 ns to rise from 20 kb to 1.5 Mb. The luminous intensity rises very rapidly to point 2 (Fig. 5b) of densitogram, corresponding to the impact time of the free surface, i.e., at time of maximum compression of air at the interface. The middle of the streak is at 2 at impact time, because this point is at the top of a diffusion peak. From the impact time, a mechanical shock of 1.5-Mb intensity is generated in plexiglass, of which the coefficient of absorption  $k'\nu$  in the visible is largely increased under such a compression. If  $I_2$  is the air luminosity at the interface at impact time  $t_2$ ,  $U_V$  the shock velocity in plexiglass,  $u_V$  the particle velocity in plexiglass, equal to interface velocity,  $t$  time, then the luminosity at time  $t$  is given by:

$$I_2 \exp [-k'\nu(U_V - u_V)(t - t_2)] .$$

It is necessary to add the self-luminosity of plexiglass brought, by shock, to a high temperature close to  $10,000^\circ\text{K}$ . This luminosity at time  $T$  will be given by:

$$I_c(T)\{1 - \exp [-k'\nu(U_V - u_V)(t - t_2)]\}$$

where  $I_c(T)$  is the luminosity of a black body at temperature  $T$ . On the whole, from instant  $t_2$  (point 2, Fig. 5b), the luminosity is given by:

$$I(t) = I_2 \exp [-k'\nu(U_V - u_V)(t - t_2)] + I_c(T)\{1 - \exp [-k'\nu(U_V - u_V)(t - t_2)]\} .$$

Such a function presents the characteristic shape of branch 2, 3, and 4, with following stage of Fig. 5b.

Between 2 and 3, term  $I_2$  is preponderant but dwindles. At 3, term  $I_c$  is of same order as  $I_2$ . Between 3 and 4, term  $I_c$  is preponderant and increases. In 4 we have

$$(U_V - u_V)(t_4 - t_2) \approx \frac{1}{k'\nu} ,$$

the term  $I_c$  alone is noticeable and remains constant later on. Light from the interface does not get across the plexiglass any more; the shocked layer of plexiglass is optically thin for its own radiation and emits as a black body.

As a consequence of the previous analysis, the position of the middle of the streak is well determined on the densitogram at impact time

of free surface. If it is equally known at departure due to a diffusion correction, the free-surface velocity is precisely measured, even for a flight time as short as 100 ns. Experiment confirms this fact as shown by the small scattering of results of the following table:

Uranium		Copper	
Shot No.	$U_s$ (m/s)	Shot No.	$U_s$ (m/s)
3235	16,300	3191	20,480
3236	16,300	3192	20,300
3238	16,900	3211	20,800
		3212	21,000

For uranium,

$$\left(\frac{\Delta U_s}{U_s}\right)_{exp} = \pm 1.5\%$$

For copper,

$$\left(\frac{\Delta U_s}{U_s}\right)_{exp} = \pm 1.7\%$$

One notices the small number of analysed recordings: this is due to the difficulty of achieving an undisturbed recording for the plexiglass plate; it comes either from lateral precursors in the case of a slightly eccentric wave, or from front precursors in case of a sample the surface of which is not microscopically perfect.

It is also possible to get an approximate measurement of air shock velocity with point 0.

In copper this gives (for  $U_s = 20,640$  m/s  $\pm 1.7\%$ ):

$$U_{air,exp} = 22\,910 \text{ m/s} \pm 2.6\%$$

Theoretical calculations taking into account dissociation and ionisation give for the same value of  $U_s$ , the value:

$$U_{air,theory} = 23\,250 \text{ m/s}$$

which differs from  $U_{air,exp}$  only by  $\pm 1.47\%$ ; the agreement is satisfactory.

In uranium, a certain number of shots lead to parasitic phenomena, illustrated in Fig. 6a and 6b.

There is no intermediate increase in light between luminosity fall 0 to 1 and saturation rise 1 to 2 from emission coming from the plexiglass plate. On the contrary, a rather important increase of luminosity is observed at 0. We impute it to the presence of thin particles ejected from the free surface at time of emergence of shock, due to the bad state of the surface. These particles would be oxidized at time of reflection of shock in air, increasing the luminosity level that obscures events behind it. These shots have been excluded automatically from analysis.

Finally, it will be shown later that the free surfaces vaporize at the emergence of the shock. This would cause considerable difficulty measuring their velocities if expansion occurred in a vacuum, because in that case densities would be close to zero, though velocities are equal to the maximum speed of free expansion

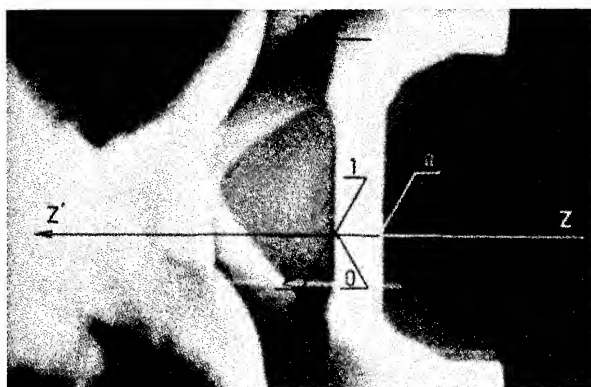


Fig. 6a - Streak camera record for a uranium shot for which direct free-surface measurement is not possible

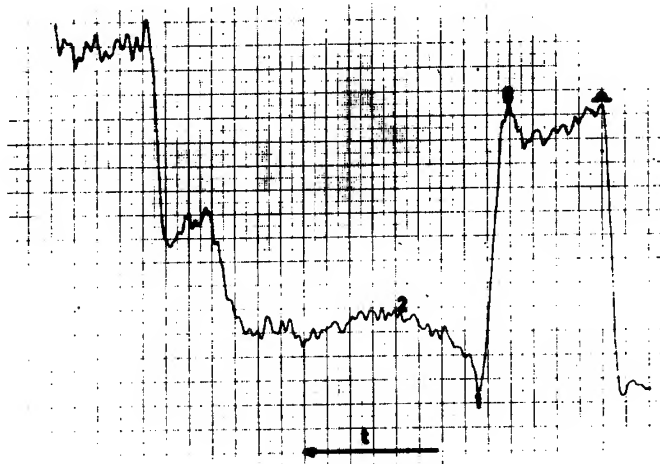


Fig. 6b - Microdensitogram of previous record (z z', Fig. 6a)

(adiabat). But as the experiment is done in air at standard conditions, the air shock applies a pressure of a few kilobars against free surfaces, sufficient to give vapor a density of about a few grams per  $\text{cm}^3$  depending on the metal, thus allowing a measurement of velocity as precise as with solid samples.

$$\frac{\rho}{\rho_0} = \frac{\gamma + 1}{\gamma - 1} = 6. \quad (3)$$

Knowing that  $u_{\text{air}} = U_S$  and eliminating  $U$  between (1) and (2), we obtain:

$$P_{\text{air}} \doteq 3.3 \text{ kbar}.$$

#### INTERPRETATION TRIAL WITH MIE-GRÜNEISEN EQUATION OF STATE

##### Preliminary Calculations

In order to give rough estimates of pressure and density obtained in this experiment, we use the relation  $U_S = 2u$  (where  $u$  is the particle velocity behind the shock) which is valid only for weak shocks (isentropic) with expansion in vacuum. The conservation equations

$$\rho_0 U = \rho(U - u), \quad (\text{continuity}) \quad (1)$$

$$P = \rho_0 U u, \quad (\text{momentum}) \quad (2)$$

used with experimental values  $U = 11,790 \text{ m/s}$  and  $U_S = 16,500 \text{ m/s}$ , give  $P = 18.5 \text{ Mbar}$  and  $\rho = 63 \text{ g/cm}^3$ .

If the expansion takes place in air shocked by emergence of shock from uranium sample, an estimate of air shock pressure ( $P_{\text{air}}$ ), neglecting dissociation and ionisation, taking  $\gamma = 1.4$  and using the strong shock approximation, can be given by:

This magnitude will be sufficient to estimate the expansion amplitude on the isentropic curves computed later on.

##### Mie-Grüneisen Equation

The specific equation used was set up by Gasnier with respect to Viard et al. (Ref. 1) results for shock pressure inferior to 2 Mbar.

$$P = P_K(V) + \frac{\gamma(V)}{V} C_V T, \quad (4)$$

for pressure, and

$$E = E_K(V) + C_V T + \frac{1}{2} \delta T^2, \quad (5)$$

for internal energy.

The first terms of (4) and (5) represent the internal potential of metallic crystal, the following terms are for temperature ( $\gamma$  being the Grüneisen parameter),  $(1/2) \delta T^2$  for free electrons energy.

The Pack, Evans and James (P.E.J.) potential, is here used



# INTERPRETATION WITH AN EQUATION OF LIQUID STATE

## Structure of the Equation

We shall justify later on the following equation:

$$P = P_K(V) + \frac{3\gamma(V) + Z'(T,V)}{1 + Z'(T,V)} \frac{C_V T}{3V} + \frac{1}{4} \frac{1}{V_0} \delta_0 \left( \frac{V_0}{V} \right)^{1/2} T^2 \quad (11)$$

for pressure, and

$$E = E_K(V) + \frac{1}{2} \frac{2 + Z'(T,V)}{1 + Z'(T,V)} C_V T + \frac{1}{2} \delta_0 \left( \frac{V}{V_0} \right)^{1/2} T^2 \quad (12)$$

for energy.

This describes more accurately than the Mie-Grüneisen equation the thermic terms of a crystal and the free electrons of a metal.

A similar type of equation is to be found in Kormer (Ref. 2) and Gasnier (Ref. 3), the latter deriving it from the partition function of a mixture of free particles and harmonic oscillators.

Z being the proportion of free particles in specific volume V, and 1 - Z the proportion of harmonic oscillators, the free energy of the mixture is:

$$F = E_K(V) - \frac{R}{A} T \log (ZVT^{3/2}B) Z \left( \frac{1-Z}{x^3} \right)^{1-Z} \quad (13)$$

with

R = ideal gas constant

A = atomic weight

$$B = \left( \frac{2\pi Ak}{\hbar h^2} \right)^{3/2} \frac{1}{N}$$

k and h = Boltzmann and Planck constants

$\hbar$  = Avogadro number

N = total particle density

$$x = \frac{\theta}{T}$$

$\theta$  = Debye temperature.

Z is such that free energy is minimum, i.e.,

$$\left( \frac{\partial F}{\partial Z} \right)_{V,T} = 0,$$

which yields

$$\frac{Z}{1-Z} = \frac{T^{3/2}}{B V \theta^3} = Z' \quad (14)$$

thus defining  $Z'$ .

The expression of Grüneisen's parameter:

$$\gamma(V) = - \left( \frac{\partial \log \theta}{\partial \log V} \right)_T$$

together with Dugdale and MacDonald's formula (7) lead to the expression of:

$$\theta(V) = Cst V^{1/3} \left[ - \frac{d}{dV} (P_K V^{2/3}) \right]^{1/2}$$

Cst such that  $\theta = \theta_0$  for  $V = V_0$ .

The thermodynamic identities:

$$P = - \left( \frac{\partial F}{\partial V} \right)_{T,Z}$$

and

$$E = -T^2 \left[ \frac{\partial}{\partial T} \left( \frac{F}{T} \right) \right]_{V,Z}$$

lead to Eqs. (11) and (12) above.

The electronic terms identical to those of Kormer (Ref. 2) use the heat capacity coefficient of free electrons:

$$\delta_0 = \frac{1}{2} \frac{\pi^2}{A} \frac{VR}{T_F} \quad (15)$$

with v, valency;  $T_F$ , Fermi's temperature calculated in Ref. 4, gives  $\delta_0 = 55$  (C.G.S.) for uranium.

The internal potential we take is the one of P.E.J. as above, giving for Debye temperature a suitable shape (monotone, decreasing function of specific volume).

## Isentropic Curve Equation

The differential relation  $dE + PdV = TdS = 0$  gives:

$$\left\{ \frac{3\gamma(V) + Z'(T,V) \frac{C_V}{3} \frac{T}{V} - \frac{\frac{\partial Z'}{\partial V}(T,V)}{[1 + Z'(T,V)]^2} \frac{C_V}{2} T + \frac{1}{2} \delta_0 V_0^{-1/2} V^{-1/2} T^2 \right\} dV + \left\{ \frac{2 + Z'(T,V) \frac{C_V}{2}}{1 + Z'(T,V)} - \frac{\frac{\partial Z'}{\partial T}(T,V)}{[1 + Z'(T,V)]^2} \frac{C_V}{2} T + \delta_0 V_0^{-1/2} V^{1/2} T \right\} dT = 0$$

with

$$\frac{\partial Z'}{\partial T} = \frac{3}{2} \frac{Z'(T,V)}{T}$$

$$\frac{\partial Z'}{\partial V}(T,V) = -Z'(T,V) \cdot \left( V^{-1} + 3\theta^{-1} \frac{d\theta}{dV} \right)$$

$$\frac{d\theta}{dV} = -\frac{\beta}{6} \frac{\theta_0}{V_0} x^{-2/3} e^{\frac{\beta}{2}(1-x^{1/3})}$$

## Calculations and Results

Using the same method as above, we determined a set of parameters  $\alpha$ ,  $\beta$ , and  $\theta_0$  such that:

- Shock states previously experimented up to 2 Mbars be respected
- Shock velocity of present experiment be verified
- Free-surface velocity of present experiment be reached as close as possible.

The values of parameters are as below (C.G.S.):

$$\alpha = 0.25 \times 10^{12}$$

$$\beta = 13.1$$

$$\theta_0 = 20^\circ \text{K}$$

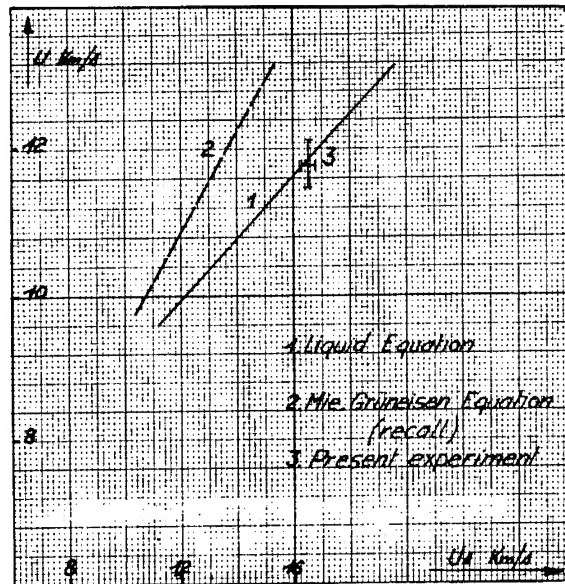


Fig. 8 - Shock and free surface velocities (liquid equation)

and yield for  $U = 11.79 \text{ km/s}$ ,  $U_s = 16.30 \text{ km/s}$  (Fig. 8) which is satisfactory.

The shock state reached in this experience on uranium is located at coordinates:

$$P = 15.1 \text{ Mbar}, \rho = 44.2 \text{ g/cm}^3.$$

The vaporizing rate,  $Z$ , reached at shock is 77.5% and along expansion path exceeds rapidly 99% (Fig. 9).

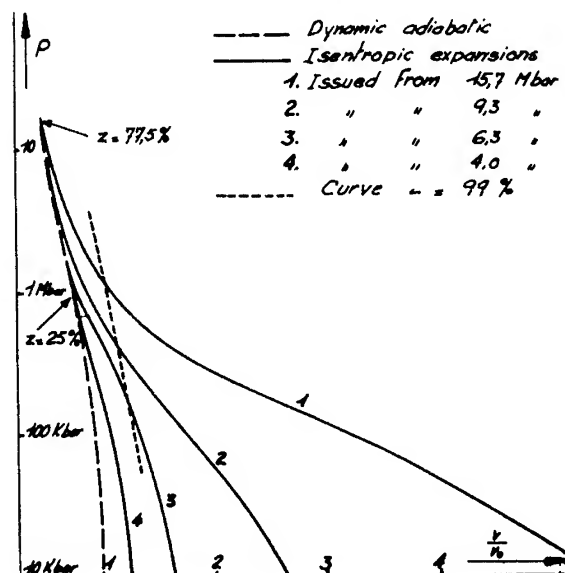


Fig. 9 - Vaporizing rate  $Z$

Final density obtained during expansion is close to  $4 \text{ g/cm}^3$ ; uranium is vaporized, but its density keeps to a level whose measurement of free-surface velocity is possible.

## CONCLUSION

This equation enables us to describe matter states for pressures as high as tens of Mbars and temperatures reaching a hundred thousands degrees.

This equation has, besides, the interest of describing states obtained at lower strength shocks, because it fits together with Mie-Grüneisen's equation ( $Z=0$ ).

One notices, moreover, the flexibility of this equation by observing (Fig. 9) the deformation of isentropic curves with respect to the region of shock states; isentropic curve 4 presents the steep aspect of isentropic expansion of solid state, the others (3, 2, and 1) spread themselves more and more towards the saturation curve, reaching progressively regions of state plane where dense vapors and gases exist.

It is shown (Fig. 10) that it is possible to distinguish the shock states leading by expansion to dense or less dense states, by means of the isentropic curve ending at critical point (Ref. 5); shock states resulting in expansion below critical isentropic lead to dense states (solid or liquid), the ones in expansions above critical isentropic lead to less dense states (liquid or gas). The phase change which should occur in the saturation curve does not occur because of too fast an expansion, as emphasized by Zel'dovich (Ref. 6).

We had the pleasure to hear recently that, in an underground experiment, shock states close to 30 Mbar had been realised in iron and lead; Al'tshuler (Ref. 7) interpreted them also with an equation of this type.

## REFERENCES

1. J. Viard, Les ondes de détonation, C.N.R.S., Gif-sur-Yvette 1961, Editions du Centre
2. Kormer et al., Dynamic compression (Sov. Phys., JETP, Vol. 15, No. 3, Sept. 1962).
3. R. Gasnier, Symposium H.D.P., I.U.T.A.M., Paris Sept. 1967, Dunod, Paris, Gordon and Breach, New York, p. 131.
4. Kittel, Introduction à la physique de l'état solide, Dunod, Paris, 1958, pp. 252-4.
5. Skidmore, Morris, Thermodynamics of nuclear materials, IAEA, Vienne 1962, pp. 173-216.
6. Zel'dovich and Raizer, Physics of shock waves, Academic Press 1967, p. 766.
7. Al'tshuler et al., Soviet Physics JETP, 27, 3, Sept. 1968, pp. 420-2.

Note by editor: See also J. Leygonie and J.-Cl. Bergon, p. 529 of Ref. 3 cited above.

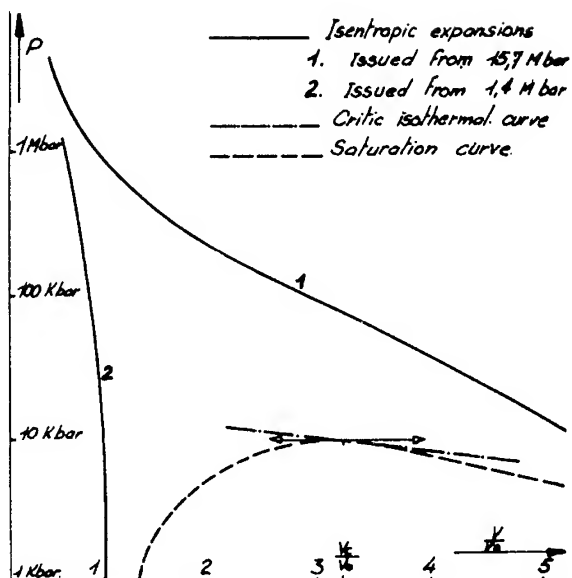


Fig. 10 - Saturation curve

National de la Recherche Scientifique, 15  
quai Anatole France - Paris 7 eme, 1962,  
p. 383.



## OBSERVATIONS OF DETONATION IN A HIGH VACUUM

J. E. Hay, W. C. Peters, and R. W. Watson  
*Safety Research Center, Bureau of Mines*  
*U.S. Department of the Interior, Pittsburgh, Pennsylvania*

### ABSTRACT

High-speed framing camera and time-resolved spectrographic observations have been made of the detonation of a number of solid explosives in a high vacuum ( $10^{-6}$  torr). The salient feature of the results is the high velocity attained by the leading products emitted from the end of the charges—about 20 km/sec—with all explosives which contain hydrogen. Time-resolved spectra have been obtained of the light emitted when the products stagnate on an acrylic plastic plate. A pink luminosity, involving the hydrogen alpha line, is produced by the leading products on impact. Early development of other hydrogen Balmer lines and subsequent development of sodium lines and lithium lines in doped charges were also observed. The early appearance of hydrogen spectra as compared to sodium and lithium spectra is attributed to relative diffusion of species having different molecular weights in the edge of the products cloud. With PETN and HN, opaque whitish jets or plumes of colored gas are occasionally observed off the end of the charges; these are interpreted as unreacted explosive and intermediate products respectively.

Order-of-magnitude computations have shown that agreement with the measured velocities of the leading products (20 km/sec) can be obtained by invoking ambipolar diffusion of electrons and ions in the expanding products cloud.

### INTRODUCTION

Detonation of solid explosives in a vacuum has been an object of study for many years from both an experimental (1-4) and theoretical viewpoint. The salient feature of these results has been the observation of high velocities of the ejecta from the end of the charge—velocities of the order of 20 km/sec. To the authors' knowledge, these velocities have not been satisfactorily accounted for theoretically, a situation which poses an interesting problem in plasma dynamics. Even more interesting from the standpoint of detonation physics and chemistry is the possibility that removal of the ambient air allows direct observation of the properties of the detonation and its products for the following reasons: (1) spectroscopic studies will not be hampered by emission or absorption by the ambient atmosphere; (2) rapid, free expansion in at least the leading edge of the products cloud may freeze the course of chemical reaction, allowing the study of intermediate species by mass spectrometric means, molecular beam

experiments, etc.; (3) the low densities attained in the leading edge of the products cloud may enable molecular flow to occur with the possibility of species separation by various mechanisms. The observations reported herein result from attempts to lay a groundwork for the design of experiments to study the properties, structure and kinetics of detonation in a high vacuum.

These observations are of two types: (1) a broad phenomenological study of the gross properties of detonation in a high vacuum; and (2) some time-resolved spectrographic studies of the light emitted when the leading edge of the expanding products cloud stagnates against a rigid surface in a high vacuum.

### EXPERIMENTAL APPARATUS AND TECHNIQUE

A schematic of the time-resolved spectroscopy experimental setup is shown in Fig. 1 with

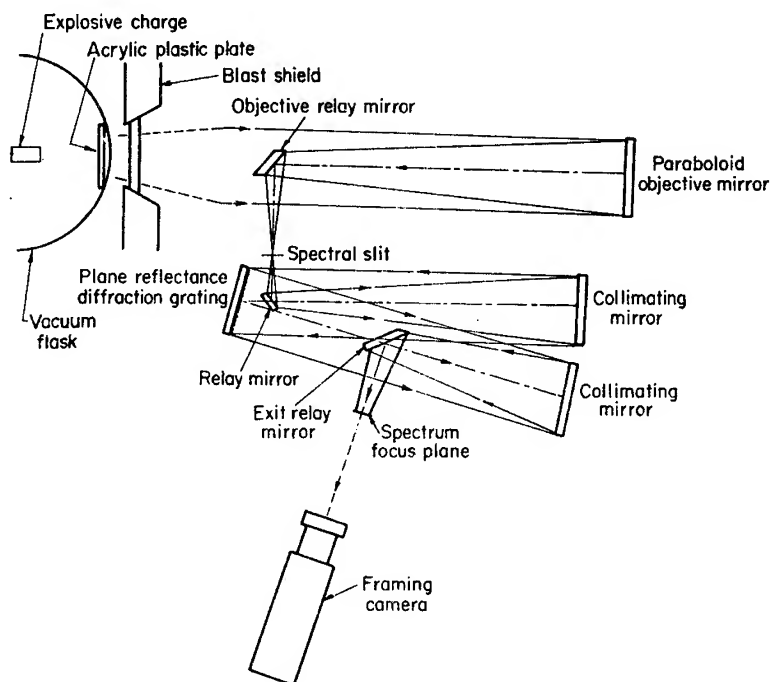


Fig. 1 - A schematic of the experimental arrangement used for time-resolved spectroscopy studies of explosives detonated in a vacuum

emphasis on the internal optics of the main component, a Beckman Whitley D-2 Spectrographic Dispersion Unit. Insufficient light intensity was a major problem, so it should be noted that this dispersion unit is constructed entirely of reflection optics, thus eliminating the attenuation of light due to multiple lenses. The objective mirror has a magnification of .10 and aperture ratio of  $f/4.2$  for an object distance of 500 cm. The collimating mirror is a 16-inch focal length,  $f/4$  parabolic mirror mounted in a temperature-compensated positioning assembly to assure a high degree of collimation necessary for high spectral resolution. The dispersion device is a plane reflectance grating ruled in an area 102 mm by 128 mm for the dispersion and blaze wavelength required. The entrance slit is variable from .02 to 3.0 mm, calibrated.

For most of the work reported here, a 300 grooves/mm grating blazed for 5000 Å was used; this had a minimum efficiency of 50% at 5086 Å, 63% at 4800 Å, and 65% at 4358 Å. The dispersion obtained using this grating was  $\approx 85$  Å/mm with a field of 2090 Å.

A 22-liter vacuum flask containing a 1.9-by 7.6-cm cylindrical charge of PETN was positioned as close as practical (to conserve light

intensity) to the viewing port of a blast chamber. A 7.6-by 7.6-by 0.16-cm acrylic plastic plate was used as the stagnation surface for two reasons: (1) to facilitate focusing the spectrograph on the surface towards the charge, and (2) to eliminate contamination of the spectra by alkaline metal lines from the glass wall of the flask. The stagnation plate was positioned parallel to the face of the explosive charge and 17.8 cm away. The spectrograph was focused on a fiducial mark which was scratched on the surface of the plate and aligned with the axis of the charge. The charge was detonated with an M-36 military detonator. The charge length was sufficient to assure a steady-state detonation when the front reached the face.

The data reported below were taken with a Cordin model 10-010 framing camera as the time-resolving element. A maximum time resolution of 1  $\mu$ sec was set by the maximum usable speed (1 megafame/sec) of the framing camera. Low light levels and short exposure times required the use of extremely fast (ASA 8000) recording film. The total recording time at maximum usable framing camera speed was 25  $\mu$ sec. Relative exposure density measurements were made from the film using a Joyce-Loebl microdensitometer.

## RESULTS

### A. Gross Features

In the initial framing camera experiments, the experimental arrangement was essentially the same as that described for the spectrographic work, except that the charges were initiated by an Army Engineer Special Detonator. The explosives fired in these experiments included cast Composition B, pentolite, pressed tetryl, lead azide (LA), RDX, PETN, and hydrazine nitrate (HN). The last three explosives named plus TNT are a series designed to span a wide range of chemical compositions: TNT for high carbon content, RDX for high nitrogen, PETN for high oxygen, and HN because it is carbon-free. Preliminary results indicated that, as other investigators (1-2) observed, the leading products appear to travel at velocities of the order of 20 km/sec. The leading products were found to produce a characteristic pinkish luminosity reminiscent of an electric discharge in hydrogen when they impinge on a solid surface. No visible evidence of high velocity products was found with LA; this explosive is the only one studied which contains neither hydrogen nor carbon. Thus, it seemed likely that the high velocity products contain hydrogen.

In almost every case, a diffuse black cloud of detonation products expands from the original charge position with a much lower velocity, generally from 6 to 12 km/sec (except for LA in which case the expansion velocity is an order of magnitude less). The density of this cloud varies with the explosive and appears greatest with Composition B and tetryl, less so with RDX and pentolite, and still less so in the case of PETN and HN. The opaque products cloud is attributed mainly to free carbon in the case of the high-carbon-content explosives; for those explosives which contain little carbon the cloud concentrates toward the rear of the original charge position and is tentatively attributed mainly to vaporized copper and other opaque products from the detonator.

With cylindrical PETN charges, a particularly interesting phenomenon occurs. A small cloud of intense blue products forms just off the end of the charge immediately after the arrival of the detonation front. The high density of the products comprising this cloud is evidenced by optical distortion of a background grid when viewed through the cloud. The region of perceptible refraction extends beyond the region of perceptible blue color. Presumably a high density gas cloud is always present off the end of the charge immediately following the

arrival of detonation, but is obscured by the opacity of the products formed by the high-carbon explosives. The nature of the blue gas is unknown but it is conceivable that, at the very high pressures which must prevail in this region, the dissociation of normally unstable species such as  $\text{NO}_3$  (which is blue) would be suppressed.

In two firings with relatively low-density pressed PETN ( $1.2 \text{ g/cm}^3$ ) a whitish material, presumably unreacted PETN, was ejected from the end of the charge with a velocity of several kilometers per second (the exact velocity is difficult to estimate because of the diffuse leading edge of the ejected material). This would seem to indicate that when the detonation front reflects from the free surface as a rarefaction the incipient reaction just behind the detonation front is quenched.

With HN charges, a small brownish cloud forms in a manner similar to the blue cloud with PETN, although in this case the high density of the cloud is not as apparent. Since HN is rich in oxygen and nitrogen, it is believed that this brown gas is nitrogen dioxide.

In all cases, except LA and HN, a blue luminescence is produced at the vessel walls, apparently due to the impingement of products with velocities of about 12 km/sec. The product which causes this luminosity may be carbon dioxide since it seems most intense with PETN and does not occur with the explosives which do not contain carbon.

### B. Time-Resolved Spectra

All time-resolved spectral information reported in this paper is based on film records analyzed with a microdensitometer. Microdensitometer traces of time-resolved spectra of the first ejecta from a PETN charge striking an acrylic plastic plate in a vacuum of  $5 \times 10^{-6}$  torr are shown in Fig. 2(a). Traces corresponding to the first 5  $\mu\text{sec}$  after arrival at the plate are reproduced. The salient features in the wavelength range 5000 Å to 7000 Å are:

1. Only the hydrogen  $\alpha$ -line (6563 Å) is observed during the first 2  $\mu\text{sec}$  after arrival of the first ejecta at the wall.
2. After 3  $\mu\text{sec}$  the sodium D-line (5890 Å) appears; this line increases in intensity at later times.
3. Coincident with the increase in intensity of the sodium line is a decrease in intensity of

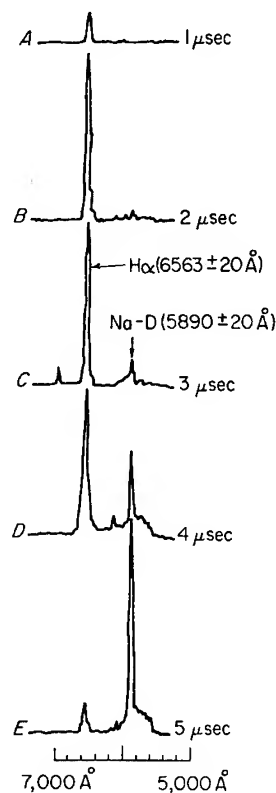


Fig. 2(a) - Microdensitometer traces of time-resolved emission spectra of PETN detonation ejecta impinging a solid surface in a vacuum, wavelength range 5000 Å to 7000 Å

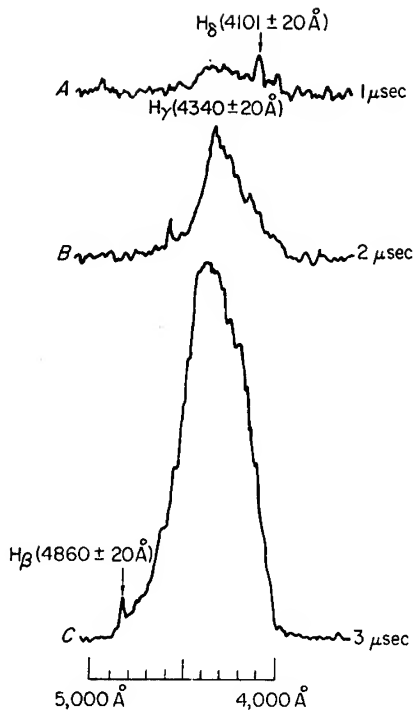


Fig. 2(b) - Microdensitometer traces of time-resolved emission spectra of PETN detonation ejecta impinging a solid surface in a vacuum, wavelength range 4000 Å to 5000 Å

the hydrogen  $\alpha$ -line (see Fig. 4). Traces obtained in the 4000 Å to 5000 Å wavelength region are reproduced in Fig. 2(b). The hydrogen  $\beta$ ,  $\gamma$ , and  $\delta$  lines are observed but with poor signal-to-noise ratio. The reason for the broad peak centered at approximately 4400 Å after 3  $\mu$ sec is not completely understood at this time; however, part of it is tentatively attributed to variation in the efficiency of the grating with wavelength. These features support the theory that spatial separation of the detonation product species is observed.

To assure that the observed hydrogen lines are from the explosive and not from hydrogen contained in the several monolayers of water which would remain on the stagnation plate at this vacuum, the plate was heated to  $>200^\circ\text{C}$  under a vacuum of  $10^{-6}$  torr and essentially the same results were obtained. At this temperature and pressure, it is doubtful that enough water remains on the plate surface to yield the hydrogen line intensity observed.

Since, in the first experiments performed, the products were simply allowed to stagnate against the glass wall of the vacuum vessel, the appearance of sodium emission lines was attributed to the sodium in the glass. When an acrylic stagnation plate was substituted, and the sodium lines continued to be observed despite precautions to avoid contamination of the explosive charge and apparatus (by fingerprints, etc.), it was concluded that the sodium is present in the explosive as a residue from the washing stage of the manufacturing process. To verify that the observed sodium line was from the charge, a PETN charge was doped with lithium and the results shown in Fig. 3 obtained. Again, spatial separation of the hydrogen and lithium was observed, but the time lag is reduced corresponding to the smaller mass difference ( $M_{\text{Na}} = 23$  amu;  $M_{\text{Li}} = 7$  amu;  $M_{\text{H}} = 1$  amu).

The relative intensities of H- $\alpha$  and sodium D-lines are plotted in Fig. 4 as a function of

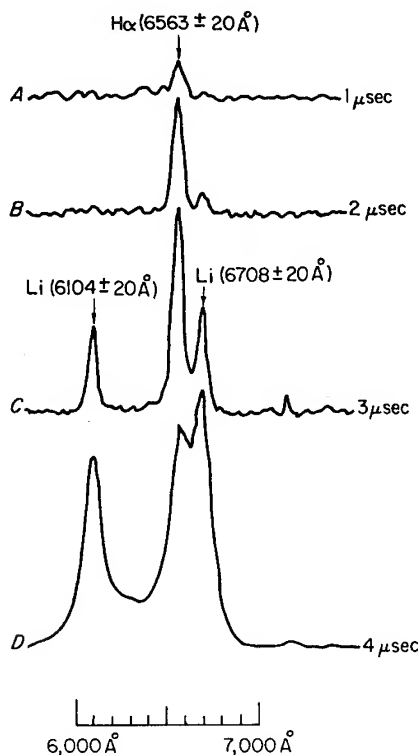


Fig. 3 - Microdensitometer traces of the time-resolved spectra obtained using a lithium-doped PETN charge (zero time is the arrival time at the stagnation plate)

time (zero time is the time at which the detonation just reaches the end of the charge as determined from framing camera pictures). The H- $\alpha$  line peaks between 13  $\mu$ sec and 15  $\mu$ sec and the sodium D-line peaks between 18  $\mu$ sec and 19  $\mu$ sec. This corresponds to a velocity difference of roughly 4 mm/ $\mu$ sec. Similar peak arrival times could not be obtained from the lithium-doped charge data because the lithium lines were buried in continuum radiation before they peaked.

## DISCUSSION

A computer program was formulated which describes the expansion of a cloud of detonation products according to the Richtmyer hydrodynamic flow formulation (5). The program is similar to that of Lutzky (6). The principal differences are in the initial conditions.

Calculations were performed for RDX at an initial density of 1.77 g/cm<sup>3</sup>. The initial velocity and pressure were chosen according to the following reasoning. The region under

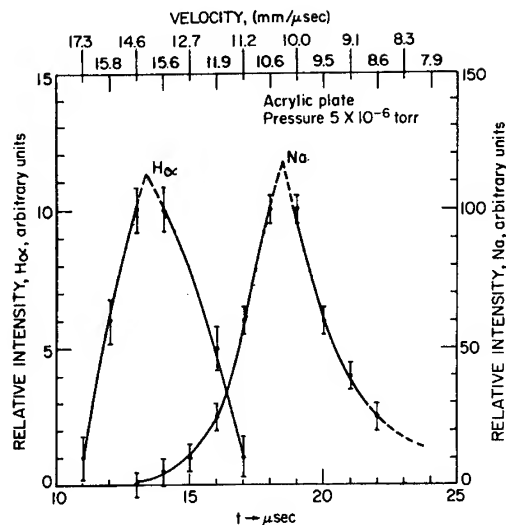


Fig. 4 - Relative intensities of the hydrogen  $\alpha$  and sodium D-lines as a function of time (zero time is the time at which the detonation front just reaches the end of the PETN charge)

consideration is a lamina of essentially infinitesimal thickness at the end of the charge. If the reaction induction time is finite, the first event which occurs when the detonation front arrives at the free surface is that this lamina is accelerated to a velocity twice the particle velocity in the detonation and the pressure in the lamina falls to zero. Thus, when the explosive reacts, it does so at its normal density rather than the density to which it is compressed in the detonation zone, generating products at a pressure estimated as  $[\gamma/(\gamma + 1)]^\gamma$  times the C-J pressure. The initial velocity and pressure were thus chosen to be 4.4 mm/ $\mu$ sec and 143 kilobars respectively. The gamma for the product gases was taken as 2.77.

The principal result of the calculations is that the leading edge of the expanding cloud reaches a terminal speed of 6.6 mm/ $\mu$ sec at the end of 300 nanoseconds, reaching 95% of that value within 50 nanoseconds. The pressure in the leading lamina is down by a factor of  $2 \times 10^5$  from its initial value, after 300 nanoseconds. The internal energy is down by a factor of  $3 \times 10^3$ . This latter result implies a very low temperature in the leading lamina (measured in its own rest frame) for all reasonable estimates of the initial temperature. The calculated terminal speed of the leading edge is in good agreement with measurements made on the microsecond framing-camera photographs of the speed of the visible grey-black

cloud of detonation products. However, it is about one-third the value needed to account for the time of appearance of the "pink glow" emission.

Possible ways to account for the high speed of the emission which causes the pink glow are:

1. The mechanism of ambipolar diffusion can be invoked to double the speed of the ionized portion of the cloud. In ambipolar diffusion, a pressure gradient in the plasma at the surface of the explosive will tend to accelerate the electron gas at several thousand times the rate for ions. Any tendency for the electrons to move ahead of the ions, however, is quickly balanced by an electric field caused by the separation of charges. The electrons, being highly mobile in comparison to the ions, will quickly achieve a near equilibrium between the influences of the pressure gradient and electric field. However, the same electric field acts on the ions but in the same direction as the pressure gradient. This subjects the ions to a total force away from the surface double that on a neutral species. An order of magnitude calculation shows that a charge separation of even a tenth of a percent creates an electric field which would produce forces on the charged particles many orders of magnitude greater than the pressure gradient. The difference in arrival times of various species (hydrogen, lithium, sodium) in the pink glow is presumably due to the fact that the same pressure and electric field act on both light and heavy species in the detonation "plasma," accelerating the lightest species the most.

2. The mechanism proposed by Johansson and Selberg (3) which invokes elastic collision between heavy molecules in the detonation products and lighter molecules in the ambient gas. Although this is an attractive hypothesis, it appears doubtful that the lighter molecules actually come from the ambient gas for two reasons: (a) the intensity of the light emitted when these molecules impinge on a surface ought to increase as the number of available molecules increases; however, over a million-fold increase in ambient pressure ( $10^{-7}$  to  $10^{-1}$  torr) no obvious increase in luminosity was observed; (b) velocities of the sodium atoms or ions, which certainly do not originate in the ambient gas, are very nearly as high as those of the hydrogen atoms, molecules or ions.

## CONCLUSIONS

Experimental results appear to verify the assumption of the possibility of molecular

species separation in the leading edge of the detonation products cloud in a high vacuum. Although the details of the expansion process have not been fully resolved, there is preliminary evidence that time-resolved spectroscopic measurements of the products are feasible and may be used to infer the composition and thermodynamic state of the products generated in the reaction zone.

## ACKNOWLEDGMENT

This work was supported by the Ballistic Research Laboratories, U.S. Army Aberdeen Research and Development Center, under Authorization No. 8946.

## NOTE

Reference to specific equipment is made to facilitate understanding and does not imply endorsement by the Bureau of Mines.

## REFERENCES

1. C. H. Johansson and S. Ljungberg, "Influence of Air Pressure on the Velocity of Ejected Explosion Gases," *Arkiv för Fysik*, **6**, pp. 369-373, 1952.
2. U. Ericsson, "Explosive Shock Travel Times at Different Ambient Densities," *Appl. Sci. Res., Section A*, **5**, pp. 309-320, 1955.
3. C. H. Johansson and H. L. Selberg, "Transient High Temperature Gas Layers in Detonation," *Proc. 4th Int'l. Conf. Ionization Phenomena in Gases*, Uppsala, Aug. 17-21, 1959, IVD 1114, 1960.
4. N. Lundborg, "Front and Mass Velocity at Detonation in Evacuated Chambers," *Arkiv för Fysik*, **25**, pp. 541-543, 1964.
5. R. D. Richtmyer, "Difference Methods for Initial Value Problems," p. 200, *Inter-science Publishers, Inc.*, New York, N.Y., 1957.
6. M. Lurzky, "Explosions in Vacuum," U.S. Naval Ordnance Laboratory Report NOLTR 62-19, Nov. 1962.

## DISCUSSION

Y. MANHEIMER-TIMNAT

Technion Israel Institute of Technology  
Haifa, Israel

The blue light observed in the PETN experiments could come from the blue continuum

observed for instance in shock tube experiments where excited  $\text{CO}_2$  is formed by reaction between CO and O. It might be of interest to compare results from detonation products composition calculations with the observed blue light emission.

## PLANE SPALLING OF COPPER

F. David, J. Vacellier, F. Prouteau, J. Legrand, R. Chéret  
*Commissariat à l'énergie Atomique*  
*Centre d'études de Vaujours*  
*93 Sevran (France)*

### ABSTRACT

A plane shock wave is induced in a pure copper sample in such a way that spalling occurs. On examination of the recovered spalls and of the free-surface velocity measurements, one is led to assume that spalling originates from a progressive decohesion of the grains. A rising-fracture-strength  $R^*$  is defined and related to the first decrease of the free-surface velocity; an almost linear relation appears to exist between  $R^*$  and the pressure  $p$  of the emergent shock. One-dimensional calculations based upon the experimental law  $R^*(p)$ , a simplified expression of the cohesion stress, an empirical law of growing of the cracks, are in reasonable agreement with the experimental results.

### INTRODUCTION

All the here-mentioned experiments deal with O.F.H.C. electrolytically prepared copper samples, annealed at 600°C and  $10^{-5}$  torr for four hours. The mean grain diameter is approximately 0.3 mm.

In order to achieve a good approximation of a one-dimensional flow, the thickness  $X_0$  of the sample is chosen so as to remain a fraction of the diameter  $\phi$  ( $5 \leq X_0 \text{ mm} \leq 40$ ,  $\phi = 150 \text{ mm}$ ). A plane shock wave is induced in the sample, either by an explosive donor charge with the same diameter, or by a 3-mm-thick flying plate ( $2.7 < V_{\text{mm}}/\mu\text{s} < 3.5$ ). In both cases an expansion wave follows the incident shock. As soon as the latter arrives at the free surface, another expansion wave propagates backwards in the sample. It is well known that the region where the two expansion waves interfere undergoes stresses which may involve spalling.

### EXPERIMENTS

#### Recovering of the Spalls

In order to get free of the effects of lateral expansion, the target is composed of a ring which confines a pastille whose diameter is 30 mm. When a spall appears, it flies some

time in the air, next penetrates through a layer of bicarbonate powder initially placed at the surface of a water tank, and finally comes to a standstill at the bottom of the tank. Figure 1 shows spalls thus recovered.

#### Microscopic Examination of the Spalls

A careful microscopic examination of a diametral cross section of a recovered spall reveals the existence of distortions and cracks. These perturbations generally follow the outline of the grains along directions which, on the average, are normal to the flow; they appear at some distance from the free surface, looking



Figure 1



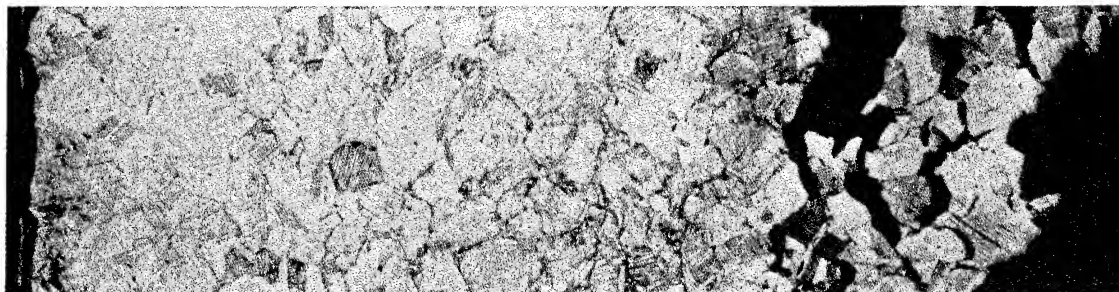


Figure 2

more and more like cracks as the distance to the free surface increases, so much so that cohesion between grains nearly disappears near the spalling surface. It may be emphasized that the same features are also found in shocked but not spalled samples. Figure 2 illustrates the above-described microstructure.

#### Free-Surface Velocity Measurements

Eden and Wright's technique (1) is used to determine the free-surface velocity of the sample. As shown in Fig. 3, the light emitted by an argon flash is totally reflected by the faces  $F$ ,  $F'$ , and  $F''$  of a prism, then sent back towards a 50- $\mu\text{m}$  streak camera. The movement of the free surface  $S$  of the sample progressively removes the total reflection on the face  $F$ . Let  $\alpha$  be the angle between  $F$  and  $S$ ; let  $\beta$  be the angle on the film between the time axis and the limiting line of the illuminated zone: let  $v$  and  $\gamma$  be respectively the inscription speed and the magnifying power of the camera. The free surface speed  $u$  is given by:

$$u = \frac{v}{\gamma} \sin \alpha \operatorname{tg} \beta.$$

When  $u$  undergoes a variation  $\Delta u$ , a variation

$$\Delta \beta = \sin 2\beta \frac{\Delta u}{2u}$$

is recorded on the film. The best precision is obtained when  $\beta = \pi/4$ ; this condition is achieved by a proper choice of  $v$ . As for  $\alpha$ , it must be neither too small, since a planar defect  $\delta\alpha$  of  $S$  involves an apparent variation  $\delta u = u \cdot \cot \alpha \cdot \delta\alpha$  of  $u$ , nor too large, since a disturbing jet appears between  $F$  and  $S$  for large values of  $\alpha$ .

In order to correct the measurements for a possible rotation of the free surface, two

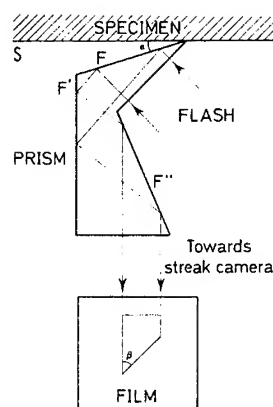


Figure 3

prisms are disposed symmetrically about the axis of the target (this involves a sample 80 mm in diameter). When working under these conditions, one achieves a continuous measurement of  $u$  with 2% experimental error.

Table 1 summarizes the main results of the measurements;  $p$  is the pressure of the emerging shock,  $u_0$  is the initial free-surface velocity;  $\Delta u$  is the first decrease of  $u$ , i.e., from the moment when the shock emerges until the first noticeable acceleration;  $\Delta t$  is the corresponding time interval. Every mentioned value is averaged over two or three shots.

#### INTERPRETATION

##### Spalling Mechanism

It is well known (2 to 13) that a calculation may be achieved where spalling merely consists in splitting the sample in conformity with the experimentally determined thickness of the first spall. Among the information given by such a calculation is the above-defined time interval  $\Delta t$ . Whatever the chosen equation of

TABLE 1

SCHEME OF EXPERIMENT		$X_0$ (mm)	$u_0$ (mm/ $\mu$ s)	$p$ (kb)	$\Delta u$ (mm/ $\mu$ s)	$\Delta t$ ( $\mu$ s)
IMPACT  OF  COPPER  PLATE	VELOCITY # 3.5 mm/ $\mu$ s	20	3.20	905	0.52	0.9
		25	2.80	750	0.45	0.8
		30	2.53	660	0.38	0.8
		35	2.235	500	0.25	0.7
		40	1.19	455	0.22	0.6
	VELOCITY # 2.7 mm/ $\mu$ s	25	2.30	580	0.25	1
		30	2.15	530	0.23	0.9
		35	1.95	470	0.20	0.8
		40	1.85	440	0.12	0.8
	DETONATION OF A CHARGE IN CONTACT WITH SAMPLE (Detonation velocity = 8 mm/ $\mu$ s)		10	1.82	430	0.12
20			1.70	395	0.10	0.6
Detonation velocity = 6.2 mm/ $\mu$ s		5	1.22	265	0.12	1.2
		20	1.05	220	0.10	1

state of the sample is, the calculated value of  $\Delta t$  is three or four times the experimental value. This fact and the cracked structure of the recovered spalls evidence that spalling cannot be accounted for by assuming a simple and instantaneous splitting. More precisely they suggest that it originates from a progressive decohesion of the sample which takes place at the grain interfaces as soon as they undergo what may be called the "rising fracture stress"  $R^*$ . While the cracks propagate, following the outline of the grains along directions which in the average are normal to the flow, compression waves are emitted which slacken the decohesion of the material and, at last, cause the free surface to accelerate.

#### The $R^*(p)$ Curve

When time elapses, a slice of the sample undergoes increasing stress when in the region where the two expansion waves interfere, then decreasing stress because of the compression waves reflected from the free surface (cf. Fig. 4). In other terms the stress reaches its maximum value on the last characteristic  $\Gamma^-$  of the reflected expansion wave. Therefore the first crack appears at some point A of  $\Gamma^-$ .

The rightward-bound compression wave reaches the free surface at some point B and causes it to accelerate, which is noticeable on the continuous record of  $u$ . About the characteristics OA and AB, one may write:

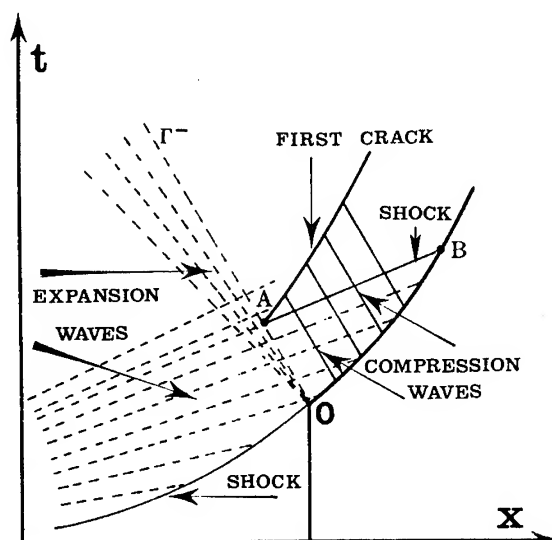


Figure 4

$$R^* = \int_0^A \rho a \, du = \int_A^B \rho a \, du \quad (2)$$

Under the reasonable assumption that  $\rho a$  is constant in the OAB region of the flow, Eqs. (2) yield:

$$R^*/\rho_0 a_0 = u_0 - u_A = u_A - u_B \quad (3)$$

Consequently,  $R^*$  may be expressed in terms of the above-defined  $\Delta u$  by:

$$R^* = \rho_0 a_0 \frac{\Delta u}{2} \quad (4)$$

It appears from the  $\Delta u$  measurements that  $R^*$  varies almost linearly with  $p$ , as is shown on Fig. 5.

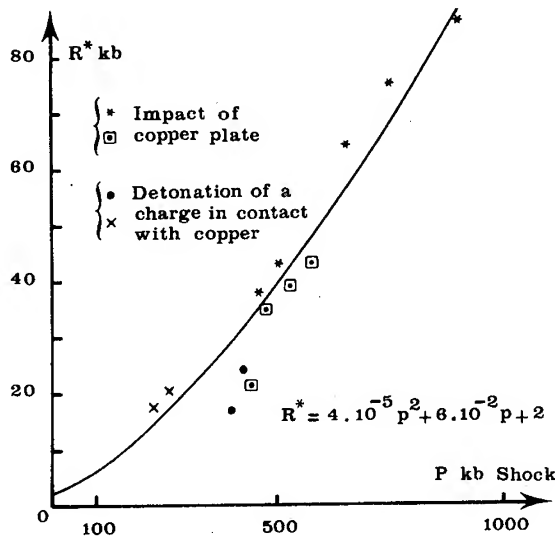


Fig. 5 - Experimental relation  $R^*(p)$

## NUMERICAL CALCULATIONS

### Simulation of the Spalling Mechanism

The distortions and cracks are located on geometric planes  $P$  normal to the flow, and spaced by the mean diameter  $\delta$  of the grains (cf. Fig. 6). A splitting occurs on a plane  $P$  as soon as the stress reaches  $R^*$ . On the two lips of the crack, a so-called cohesion stress  $\sigma_c$  is maintained. In order to estimate  $\sigma_c$ , it is assumed that one decohesion locus appears on each interface of plane  $P$  at the instant  $t^*$  when the stress equals  $R^*$  (cf. Fig. 7) and that  $\sigma_c$  is in direct ratio to the contact area.

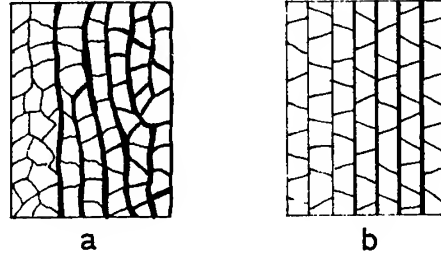


Fig. 6 - (a) Features of distortion zones; (b) schematic structure

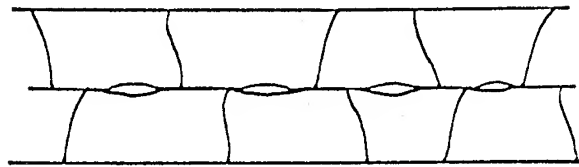


Fig. 7 - Decohesion points hypothesis

### Numerical Calculations

The above simulation has been fitted to numerical calculations in the following way. The space interval of the Lagrangian grid is chosen so as to be  $\delta/3$ . Thus every third plane of the grid is a plane  $P$ .

One assumes that  $\sigma_c$  is in direct ratio with the contact area. Consequently, at times  $t \geq t^*$ ,  $\sigma_c$  is given by:

$$\sigma_c = R^* \left[ 1 - \left( \int_{t^*}^t \frac{2c \, dt}{\delta} \right)^2 \right] \quad (5)$$

where  $c$  is the cracking speed.

As for the cracking speed  $c$ , the following empirical law is used

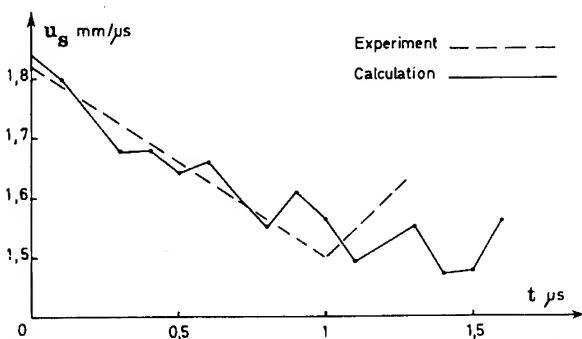
$$C = \begin{cases} 0 & \text{if } \sigma \leq \sigma_c \\ \frac{\bar{a}}{2} \operatorname{th}^{3/2} \left( \frac{\bar{\sigma}}{\sigma_c} - 1 \right) & \text{if } \sigma > \sigma_c \end{cases}$$

where  $\bar{\sigma}$  is the average of the stress values in the two neighbouring meshes, and  $\bar{a}$  is the similar average of the sound velocity values.

The calculated and recovered spalls are compared in Table 2. The calculated and measured free-surface velocity are compared on Fig. 8, whereas Fig. 9 gives an example of calculated flow.

TABLE 2

Scheme of Experiment		$x_0$ (mm)	Spall's Thickness (mm)	
			Experiment	Calculation
Detonation of a charge in contact with sample	$D = 6,2 \text{ mm}/\mu\text{s}$	5	No spalling	No spalling
		10	No spalling	No spalling
		20	No spalling	No spalling
	$D = 8 \text{ mm}/\mu\text{s}$	5	No spalling	No spalling
		10	No spalling	No spalling
		15	No spalling	No spalling
		20	6.5; 13.5	5.4; 14.6
		25	6; 4; 15	5.1; 4.5; 15.4
		30	6.5; 11.5; 12	7.1; 5.2; 17.7

Fig. 8 - Free-surface velocity: charge in contact with sample ( $x_0 = 10 \text{ mm}$ )

## CONCLUSION

The experimental program which has been carried out has defined more clearly features that are characteristic of spalling. The numerical simulation of the mechanism is somewhat less satisfactory, insofar as experiments and calculations agree only for thin targets ( $x_0 \leq 30 \text{ mm}$ ). However, it is most probable that the agreement should be widely improved by using less empirical cracking speed and cohesion stress.

## REFERENCES

1. G. Eden and P. Wright, A technique for the precise measurement of the motion
2. J. S. Rinehart, Some quantitative data bearing on the scabbing of metals under

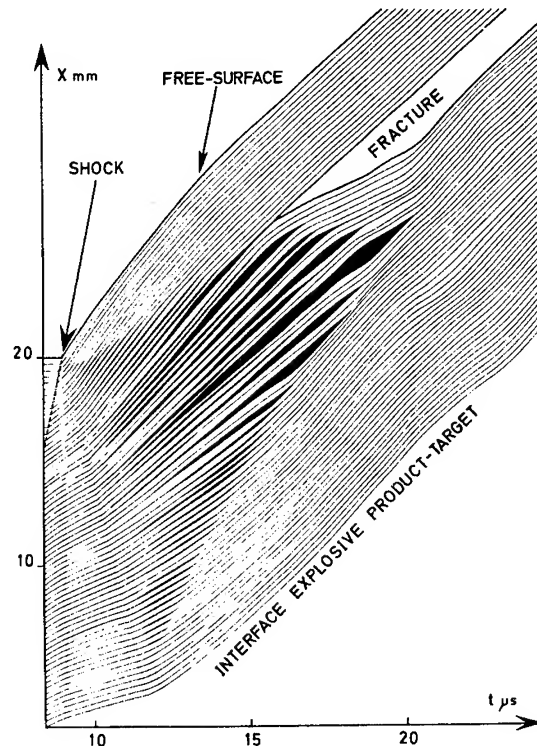


Figure 9

of a plane-free surface. The 4th Symposium on detonation. U.S.N.O.L. 1965.

- explosive attack. *J. of Applied Phys.*, Vol. 22, No. 5, 1951.
3. J. S. Rinehart, Scabbing of metals under explosive attack: multiple scabbing. *J. of Applied Phys.*, Vol. 23, No. 11, 1952.
  4. R. G. McQueen and S. P. Marsh, Ultimate Yield Strength of Copper. *J. of Applied Phys.*, Vol. 33, No. 2, 1952.
  5. M. L. Wilkins, Calculs de l'écaillage dans les métaux. Les ondes de détonation. C.N.R.S., 1962.
  6. J. H. Smith, Three low-pressure spall thresholds in copper. S.C. 4747 (RR) 1963.
  7. R. Curran, Non hydrodynamic attenuation of shock waves in aluminium. *J. of Applied Phys.*, Vol. 34, No. 3, 1963.
  8. P. Beatrix, Expériences d'écaillage dans l'aluminium et interprétation des résultats. *Annales de Phys.*, T.8., 1963.
  9. C. L. Mader, Spalling calculations. G MX 2 - Los Alamos Scientific Laboratory, 1965.
  10. B. D. Lambourn and J. E. Hartlem, The calculation of the hydrodynamic behaviour of plane one-dimensional explosive/metal system. The 4th Symposium on detonation. U.S.N.O.L., 1965.
  11. I. C. Skidmore, An introduction to shock waves in solids. *Applied Materials Research*, July 1965.
  12. J. Vacellier, G. Verdes, and J. Legrand, Conditions d'écaillage de l'uranium et d'un alliage uranium Molybdène. Symposium H.P.D.-I.U.T.A.M., 1967.
  13. B. R. Breed, C. L. Mader, and D. Venable, Technique for the determination of dynamic tensile strength characteristics. *J. of Applied Physics*, Vol. 38, No. 8, 1967.

## SPALLING UNDER OBLIQUE IMPACT

I. C. Skidmore and J. W. Lethaby  
*Atomic Weapons Research Establishment*  
*Aldermaston, Reading, England*

### ABSTRACT

A light gas gun has been used to project 6.67 cm diameter  $\times$  0.635 cm thick brass discs at similar target discs 8.89 cm diameter  $\times$  1.27 cm thick with the angle between the colliding surfaces increasing from zero in  $0.5^\circ$  steps. The impact velocity was maintained constant giving rise to a 23 kb tension compared with the incipient dynamic fracture stress of 14 kb deduced separately. Sectioning the recovered target discs showed that as the angle increased the fracture zone was displaced away from the first impact point and contracted until at  $2^\circ$  it disappeared. The measured fracture locations are in agreement with a simple analytic description of fracture being suppressed by lateral rarefactions limiting the zone where, with respect to the impact point, steady two-dimensional flow conditions are maintained. Two-dimensional hydrodynamic computer code calculations justify the analysis and also illustrate some secondary features of the fracture pattern.

### 1. INTRODUCTION

Plate impact systems have been commonly used in spallation studies for over ten years. Their attraction is that ideally they can provide a uniaxial strain configuration which is the easiest non-steady flow situation to treat theoretically. However, since experimental arrangements must always have limited lateral dimensions and may show deviations from planarity it is important to assess their effect on the uniaxial flow field to validate any interpretation based on one-dimensional theory. The experiments reported here were aimed at examining an aspect of this problem.

Our early work on spalling in plate collision experiments (1) gave dynamic fracture strengths a factor of three or more greater than values reported round about the same time by other laboratories using the same approach (2). On the other hand our results were not too dissimilar from values derived from experiments on plates under detonation wave attack (3) and hence the discrepancy aroused little comment. However, recent attempts to elucidate the time dependent nature of spalling have resurrected the problem in order to separate the consequences of more sophisticated

spallation studies from extraneous experimental influences.

It was observed in our early experiments that the projectile plate acceleration system of explosive plus metal attenuator gave rise to considerable plate curvature. This suggested that the wave pattern generated by such an impact deviated considerably from the simple uniaxial flow assumption of the theoretical analysis. Hence a study was initiated to examine the effect of controlled oblique impacts on spallation behaviour. The material chosen was 60/40 brass since it provides easily discernible fracture patterns. The basic geometry examined was the impact of a 0.635 cm thick projectile plate on a 1.27 cm thick target. In our original work with these dimensions the dynamic fracture strength quoted was 65 kb. This should be compared with a value of 14 kb from the present work.

In the first experiments a large projectile plate was accelerated by a tangentially incident detonation wave to impact target plates 5 cm square, inclined at various angles of incidence, here referred to as the angle between the colliding surfaces. The impact velocity was sufficient to generate a 40 kb tension and it was

observed that no spalling occurred in plates inclined at angles greater than  $2^\circ$ .

These experiments suffered from a lack of precision due to the variability of the explosive driving system and hence did not provide a fine control over the impact angle. This disadvantage has been overcome more recently by using a light gas gun to accelerate the projectile plate to impact a target plate mounted obliquely at the muzzle. These experiments are described in section 2 and the results interpreted in section 3.

## 2. EXPERIMENTAL METHOD

The light gas gun is a single stage device consisting of a 3 m long barrel with a 7 cm bore mounted directly onto a pressure vessel accepting working pressures of up to 200 bars. The projectile carrier is a hollow plastic cylinder 7 cm long with a wall thickness of 3 mm surrounded by two inset PTFE runners. It is enclosed at one end by a metal disc and PTFE washer which before firing provides a gas tight seal between the pressure chamber and the barrel. The carrier is restrained by a tie rod incorporating an electrically fired explosive release bolt. The system enables the initial gas pressure to be accurately predetermined thus giving good control and reproducibility over muzzle velocity. Using helium as the driver gas the gun is capable typically of

accelerating a 0.5 kgm projectile to a muzzle velocity of about  $700 \text{ m sec}^{-1}$ . The barrel is normally evacuated to a pressure of about  $10^{-5}$  bars to avoid building up an air cushion between projectile and target.

The muzzle arrangement in the present experiments is shown in Fig. 1. The projectile disc had a diameter of 6.67 cm and was mounted on a polyurethane foam plug of density  $0.3 \text{ gm cm}^{-3}$  which fitted within the carrier. This foam plug distributes the accelerating forces over the projectile plate surface thereby avoiding distortion. It has a negligible impedance compared to brass so that the interface with the projectile plate may be regarded as a free surface.

The target disc was 8.89 cm in diameter and was mounted on a short detachable end section of the barrel. It was supported on three legs,  $120^\circ$  apart, two of which were set at the same height and the third adjusted to give the required angle of incidence. This angle was measured to within  $0.015^\circ$  with a clinometer. Sixteen low mass electrical probes were inserted through the disc on a concentric 6.35 cm diameter circle and set at a constant distance from the surface to give an oscillographic recording of the projectile arrival time so enabling the true angle of incidence to be determined.

The brass samples were to British Standard 251 having a density of  $8.44 \text{ gm cm}^{-3}$  and

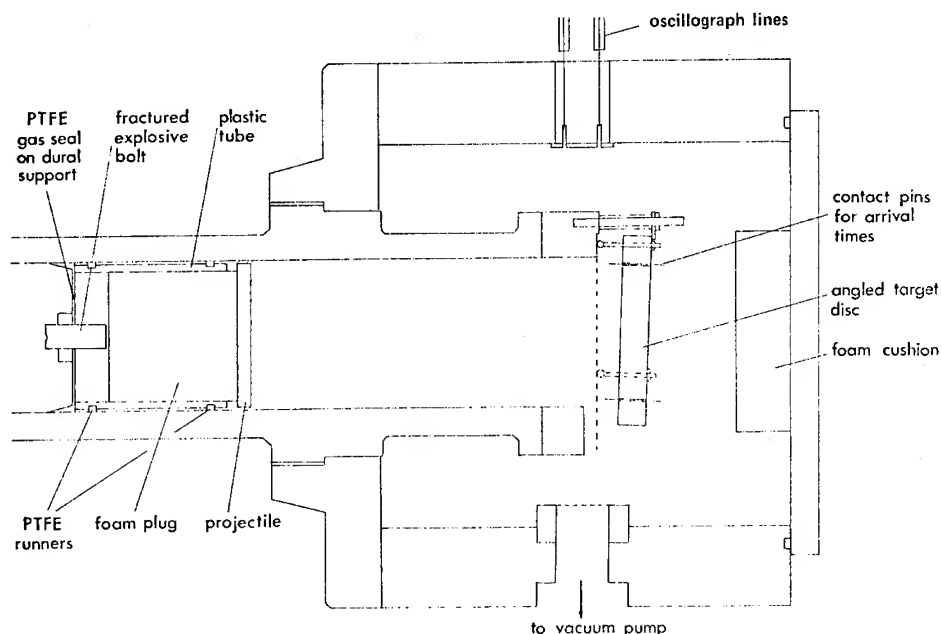


Fig. 1 - Experimental arrangement at gas gun muzzle

with a nominal composition Cu 62.5/Zn 35.5/Sn 1.25, the remainder being impurities.

In a separate series of experiments the critical impact velocity for incipient fracture was determined as  $90 \text{ m sec}^{-1}$ . The impact velocity selected for the oblique impacts was about 50% higher to show a well-defined fracture at normal incidence. The angle of incidence was increased in  $0.5^\circ$  steps until fracture was no longer apparent. The impact velocity given by the pressure calibration of the gun was  $148 \pm 4 \text{ m sec}^{-1}$ , except at normal incidence where the experiment formed part of another series and gave  $142 \pm 4 \text{ m sec}^{-1}$ . The actual angles of incidence as determined by the probes are recorded in Table 1 and considered to be accurate within 5%.

Recovered target discs were sectioned along the diameter through the first impact point, the surface polished and then etched in dilute nitric acid to reveal the fracture pattern. The results are shown in Fig. 2. As the angle of incidence increases the originally well-defined symmetric fracture is displaced away from the initial impact point and reduces in size and severity until by  $2^\circ$  it has disappeared. A secondary inclined fracture near the region where impact ceases is evident from  $1^\circ$  onwards and is the only fracture remaining at  $2^\circ$ .

### 3. INTERPRETATION OF RESULTS

The impact velocity used here generates shock waves which, at normal incidence, after

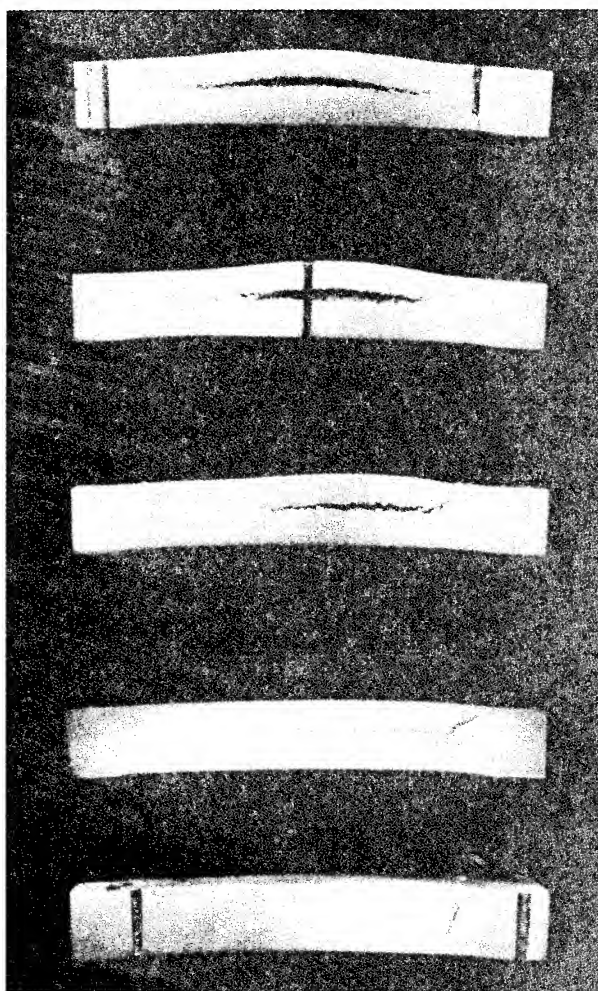


Fig. 2 - Fracture patterns in targets impacted at different angles of incidence



reflection and interaction produce a tension of 23 kb compared with the critical tension of 14 kb required to cause incipient fracture under these conditions. The variation in angle of incidence of up to  $2^\circ$  only has a small effect on the impact pressure so the changes in the observed fracture pattern must be due to effects modifying the primary wave interaction process. These must be caused by the stress relieving waves penetrating laterally from outside the impact area.

The basic phenomena can be illustrated by a simple linearised hydrodynamic model in which all waves are propagated at bulk sound velocity  $C$ . This is much larger than the impact velocity  $V$  so that particle velocity may be neglected in comparison with the propagation velocity. The model is justified by noting that the stress of 23 kb is about ten times larger than the Hugoniot elastic limit for this type of brass so that elasto-plastic wave structures should not deviate too much from the hydrodynamic prediction while at the same time the stress is sufficiently small to cause little dispersion.

The basic wave pattern is illustrated in Fig. 3. The target plate of thickness  $a$  is struck by a projectile plate of diameter  $d$  and thickness  $b$  inclined at an angle  $\theta$  to the target surface. Impact first occurs at time  $t = 0$  at the point  $O_1$  and the impact point travels along the surface with a phase velocity  $C_i$  until the impact ends at the point  $O_2$  at time  $t' = d/C_i$ . At some earlier time the impact point is at  $A$  where, if  $\theta$  is less than some critical value  $\theta_c$ , shock fronts  $AB$  and  $AC$  are generated in the target and projectile respectively inclined at an angle  $\phi$  to the interface. These reflect from the free surfaces as rarefaction fronts  $BD$  and  $CD$  and the interaction at  $D$  generates the tension which causes fracture. The fracture is assumed to occur instantaneously implying that any time dependency of the fracture process is ignored. At time zero a rarefaction wave  $R_1$  originates at the point  $O_1$  and proceeds to diverge outwards with velocity

$C$  while at time  $t'$  a similar rarefaction  $R_2$  originates from  $O_2$ . If the regular interaction point  $D$  lies within the range of influence of the two rarefactions  $R_1$  and  $R_2$  then the regular tensile interaction process is modified with consequent effects on the fracture pattern.

If, with respect to the impact point, a steady two-dimensional flow pattern is established then the phase velocity of the impact point is given by

$$C_i = V \operatorname{cosec} \theta = C \operatorname{cosec} \phi.$$

Thus

$$\sin \phi = \sin \theta \operatorname{cosec} \theta_c$$

where

$$\sin \theta_c = \frac{V}{C}$$

and when  $\sin \theta > \sin \theta_c$  this relation cannot be satisfied and a steady flow pattern is no longer possible. This is because  $C_i$  becomes subsonic and the rarefaction  $R_1$  is always in advance of the impact point  $A$ . Thus steady flow at  $A$ , and hence at  $D$ , can only be initiated at angles less than  $\theta_c$ . However, since the interaction at  $D$  is displaced in space and time from  $A$ , the effect of rarefactions  $R_1$  and  $R_2$  in suppressing the steady tensile interaction defines a smaller limiting angle  $\theta_o$ , depending on the dimensions of the system.

In the coordinate system shown in Fig. 3 the fracture plane is  $y_o = a - b$ . The interaction  $D$  first occurs at position  $x_o = (a + b) \tan \phi$  at time  $t_o$  where  $Ct_o = (a + b) \sec \phi$ . The point  $D$  then moves according to

$$x = x_o + C_i (t - t_o)$$

or

$$Ct = x \sin \phi + (a + b) \cos \phi. \quad (1)$$

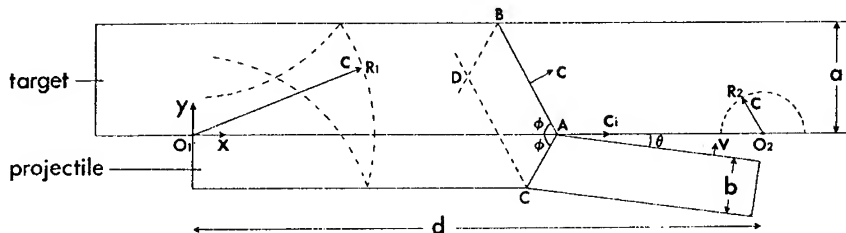


Fig. 3 - Schematic illustration of wave front patterns in impacting plates

The rarefaction  $R_1$  moves along  $y_0$  according to

$$(Ct)^2 = x^2 + (a-b)^2 \quad (2)$$

and similarly for the rarefaction  $R_2$

$$(Ct - d \sin \phi)^2 = (d-x)^2 + (a-b)^2 \quad (3)$$

The interaction point D coincides with the rarefaction front  $R_1$  at  $x_1$ ,  $t_1$  given by the solutions of Eqs. (1) and (2), i.e.,

$$x_1 = (a+b) \tan \phi + 2(ab)^{1/2} \sec \phi \quad (4)$$

$$Ct_1 = (a+b) \sec \phi + 2(ab)^{1/2} \tan \phi.$$

Thus when  $t < t_1$  the rarefaction front envelops the interaction point and the steady tensile interaction occurs only for  $x > x_1$ .

Similarly the interaction point D coincides with the rarefaction front  $R_2$  at  $x_2$ ,  $t_2$  given by the solution of Eqs. (1) and (3), i.e.,

$$x_2 = (a+b) \tan \phi - 2(ab)^{1/2} \sec \phi + d \quad (5)$$

$$Ct_2 = (a+b) \sec \phi - 2(ab)^{1/2} \tan \phi + d \sin \phi.$$

When  $t > t_2$  the rarefaction  $R_2$  has enveloped the point D so the steady tensile interaction is confined to  $x < x_2$ .

The critical angles  $\phi_0$ , and  $\theta_0$  beyond which no regular tensile interaction occurs are given by putting  $x_1 = x_2$  which from Eqs. (4) and (5) gives

$$\cos \phi_0 = \frac{4(ab)^{1/2}}{d}$$

and

$$\sin \theta_0 = \frac{V}{C} \sin \phi_0 = \sin \theta_c \left( 1 - \frac{16ab}{d^2} \right)^{1/2}.$$

If the impact velocity were equal to the critical impact velocity  $V_c$  required to initiate incipient fracture in this geometry then the fracture plane would be confined between the limits  $x_1$  and  $x_2$ . However, when  $V > V_c$  the stress may not be relieved sufficiently outside this zone to suppress fracture and the fracture can extend further, say between limits  $x'_1$  and  $x'_2$ . We make the simple assumption that at fracture time the stress in the fracture plane varies linearly from its constant value between  $x_1$  and  $x_2$  to zero at  $x = 0$  and  $x = d$  respectively. Then

$$x'_1 = \alpha x_1, \quad x'_2 = d(1-\alpha) + \alpha x_2$$

where

$$\alpha = V_c/V.$$

This defines a slightly larger angle of incidence  $\theta'_0$  at which fracture is suppressed, found by putting  $x'_1 = x'_2$  to give

TABLE 1  
Comparison of Calculated Results with Experiment  
(For definition of symbols see Fig. 3 and text)

$a = 1.27 \text{ cm}$ $b = 0.635 \text{ cm}$ $d = 6.67 \text{ cm}$ $V = 148 \text{ m sec}^{-1}$ $C = 3790 \text{ m sec}^{-1}$ $V_c = 90 \text{ m sec}^{-1}$						$\theta_c = 2.23^\circ$ $\theta_0 = 1.88^\circ$ $\theta'_0 = 2.12^\circ$		
Calculated						Experiment		
$\theta$ (deg)	$\phi$ (deg)	$x_1$ (cm)	$x_2$ (cm)	$x'_1$ (cm)	$x'_2$ (cm)	$\theta$ (deg)	$x'_1$ (cm)	$x'_2$ (cm)
0	0	1.80	4.87	1.09	5.58	0.0	0.9	5.7
0.5	12.92	2.28	5.26	1.39	5.81	0.52	1.3	5.8
1.0	26.55	2.96	5.61	1.80	6.03	1.00	1.8	6.0
1.5	42.10	4.14	5.97	2.52	6.24	1.52	2.5	6.1
1.88	57.30	6.31	6.31	3.84	6.45			
2.0	63.35	7.80	6.46	4.74	6.54	2.07	-	-
2.12	70.90	10.97	6.67	6.67	6.67			

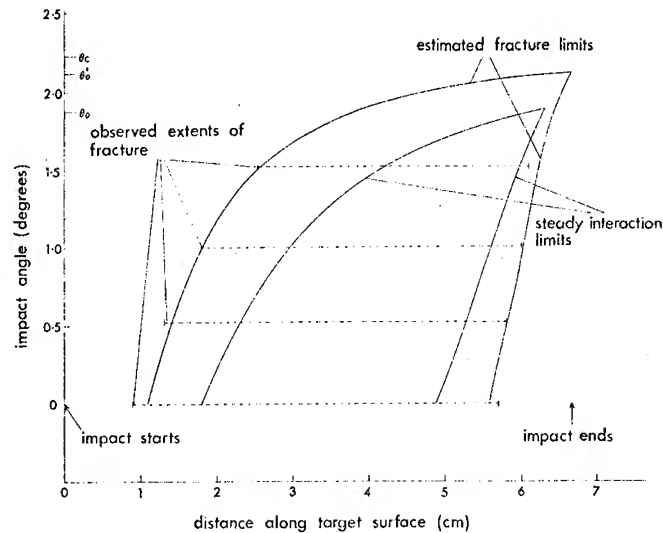


Fig. 4 - Comparison of observed and estimated fracture zone limits as a function of angle of incidence

$$\sin \theta'_0 = \sin \theta_c \left( 1 - \frac{16 ab \alpha^2}{d^2} \right)^{1/2}$$

Calculated results are compared with experiment in Table 1 and the form of the variation of fracture location with angle of incidence is illustrated in Fig. 4. It is seen that the estimated fracture limits agree with observation to better than 2 mm which considering the uncertainties in this type of measurement must be regarded as very satisfactory. Theory suggests that a small fracture should have been observed at an angle of incidence of  $2^\circ$  whereas nothing was detected visually. However, this is the situation where the two rarefaction waves  $R_1$  and  $R_2$  overlap and the assumptions of the simple model, including ignoring the time dependency of the fracture process, become less justifiable.

The shape of the secondary fracture in the region where impact terminates suggests that it is caused by the interaction of rarefaction BD and  $R_2$  in Fig. 3. This would generate a fracture surface in the form of a shallow parabola with its directrix inclined at an angle  $\phi$  to the target surface. Comparison of the values of  $\phi$  given in Table 1 with the inclination of the secondary fractures evident in Fig. 2 gives reasonable confirmation of their suggested cause.

Two-dimensional Lagrangian mesh computer code studies have been made of the problem and confirm the general characteristics of the simple model proposed here. Because of mesh

size limitations and the use of an artificial viscosity to enable shocks to be described the resolution of wave fronts, other than the primary shocks, is poor. However, the computed pressure distributions are indicative of their effect. In particular the tension distribution in the fracture plane outside the steady interaction region is not strictly linear, but the particular assumption of linearity in the analytic approach gives a close approximation to the computed tension in the region of interest. Thus the scheme for predicting fracture limits has some justification when impact velocities are not greatly in excess of critical.

The overall effect of side rarefactions is to relieve tension by lateral flow. In detail however, the interaction of rarefaction  $R_1$  or  $R_2$  in Fig. 3 with the steady tensile interaction D would be expected to locally enhance the tension. This in fact is demonstrated by the computational studies. Figure 5(a) shows the computed tension contours in the target at about  $6.8 \mu\text{sec}$  after a  $140 \text{ m sec}^{-1}$  velocity impact at normal incidence. In the centre of the target the flow remains uniaxial though the tension is slightly less than expected due to artificial viscous smearing. About midway between the axis and the location corresponding to the edge of the projectile the tension increases over a length of about 1 cm in the fracture plane. The consequences of this sort of effect can be seen in specimens impacted at near the critical velocity for incipient spalling when, in section, nominally symmetric fractures are produced off axis. Figure 5(b) shows the effect in a

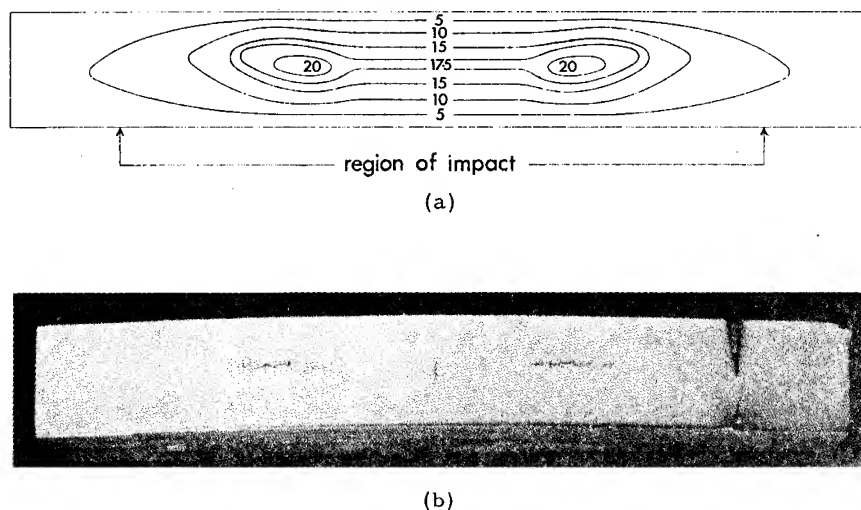


Fig. 5 - Comparison of (a) computed tension contours (in kilobars) for a  $140 \text{ m sec}^{-1}$  impact at normal incidence with (b) observed fracture patterns for an  $86 \text{ m sec}^{-1}$  impact

brass target identical with those used previously impacted at  $86 \text{ m sec}^{-1}$  at normal incidence.

The same type of simple wave analysis may be applied to situations in which the projectile plate is curved. For the configuration discussed above it can be shown that to obtain a quasi one-dimensional incipient spalling interaction on the axis of the target the radius of curvature of the projectile plate must be greater than about 50 cm. In our earliest experiments the radius of curvature was in fact about 10 cm. Thus a uniaxial flow interpretation was not appropriate and it is not surprising that the critical velocity for incipient fracture then obtained was about five times the value now resulting from good plane impacts.

In this investigation we have shown how lateral rarefactions have a marked effect on the flow patterns generated by slightly oblique impacts at the low velocities appropriate to spallation thresholds. This has been effectively demonstrated in a particular configuration by observing the degeneration and final inhibition of spall fracture as the angle of incidence increases from 0 to  $2^\circ$ . A simple sonic model

has been used to predict the fracture location in these experiments and shows satisfactory agreement with observations. However, the treatment is questionable in regions where the flow is affected by lateral rarefactions and the real value of the approach is in assessing the validity of applying a one-dimensional interpretation to particular experimental situations.

#### REFERENCES

1. I. C. Skidmore, "An introduction to shock waves in solids," Applied Materials Research, Vol. 4, pp. 131-147, July 1965.
2. B. M. Butcher, L. M. Barker, D. E. Munson, and C. D. Lundergan, "Influence of stress history on time-dependent spall in metals," A.I.A.A. Journal, Vol. 2, pp. 977-990, June 1964.
3. B. R. Breed, C. L. Mader, and D. Venable, "Technique for the determination of dynamic tensile strength characteristics," J. App. Phys., Vol. 38, No. 8, July 1967.

# INTERACTIONS OF SPHERICAL SHOCK WAVES IN WATER

N. L. Coleburn and L. A. Roslund  
U.S. Naval Ordnance Laboratory  
White Oak, Silver Spring, Maryland

## ABSTRACT

High-speed framing camera techniques were used to study underwater shock wave interactions and the associated spherical flow from simultaneous detonation of twin, separated explosive spheres. Critical angles for Mach wave formation varied from  $36^\circ$  to  $41^\circ$  for incident pressures between 6.5 kbar and 1.62 kbar. Predicted critical points for the onset of Mach formation were calculated using oblique shock reflection theory and an energy-dependent form of the Hugoniot equation-of-state for water.

## INTRODUCTION

The oblique interaction of two identical gas shocks has undergone extensive theoretical analysis (1,2). Also, the interactions of twin shocks in several specific fluids including water were subjected to theoretical study by Seeger and Polachek (3). However, in the latter case there are few examples of accurate experimentation to provide justification for the theory (4). In this paper we present the results of an experimental and theoretical study of the flow from colliding shock waves produced by the underwater detonation of two identical explosive spheres. The experimental study used high-speed shadowgraph photography; the calculations include the latest equation-of-state data for water (5).

In Fig. 1 equal intersecting shock waves from two simultaneous detonations meet and reflect on the plane of symmetry as a rigid wall. The theoretical problem of describing the shock configuration reduces to that of a single spherical decaying shock incident upon a rigid boundary. The parameters of the resulting reflected wave can be calculated by applying oblique shock reflection theory (6) to the propagation of the incident shock wave.

In the experiments the pressures of the reflected shock waves exceed the incident values at the points of interaction on the symmetry plane. These waves leave the collision plane and move as two new shocks receding from each other into fluid under compression.

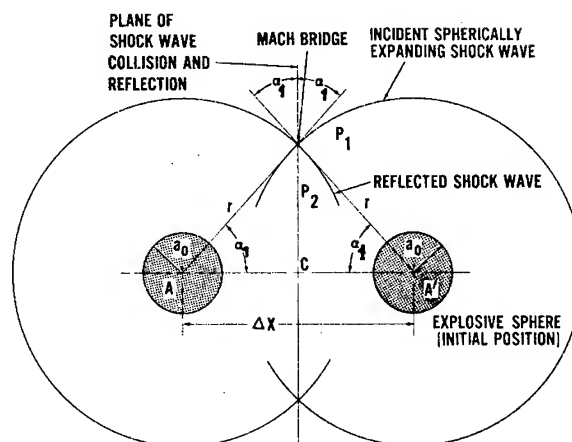


Fig. 1 - The separated charge arrangement and a sketch of shock wave positions at the point of Mach wave formation

Along the collision plane the constraints which characterize the flow, at first, allow regular reflection. However, differences from regular reflection occur as the angle between the shock front and the collision plane is increased or as the shock strength is increased. When the boundary conditions can no longer be satisfied by regular reflection, a Mach wave is formed. In air the collision of very weak spherical shocks generated by the breaking of glass spheres has been studied optically by Glass and Heuckroth (7). They and other investigators have produced photographs revealing Mach

regions. However, we are not aware of any experimental studies by optical methods to measure the pressure of other properties of this flow in water (8). In this work we used high-speed framing camera shadowgraph to record details of the shock interactions for incident shock pressures between 6.5 kbar and 1.62 kbar. The reflected shock pressures were deduced from the flow velocities and the Hugoniot equation-of-state of water (9). Then, the theoretical minimum critical angles and pressures for Mach wave formation were compared with the experimentally measured angles and pressures.

## EXPERIMENTAL

The explosive spheres in the separated charge arrangement, Fig. 1, were cast pentolite (10), 6.33-cm diameter, each weighing 225 grams. They were centrally initiated by 0.48-cm diameter, 1.27-cm long electric detonator's fired simultaneously ( $\pm 0.15 \mu\text{sec}$ ). The separation distance in terms of charge radii between the sphere centers,  $\Delta x$ , was varied to change the incident shock wave pressures and thus the interaction pressures at the plane of collision. (See Table 1 for notation.) The incident angle,  $\alpha_1$  is the angle through which each shock wave strikes the collision plane. At the first point of collision, point C on Fig. 1,  $\alpha_1$  is zero and the flow is governed by relations which apply to normal incidence and normal reflection. As the two incident shock waves expand,  $\alpha_1$  increases until it reaches the critical value where a Mach wave is formed. Beyond this point the Mach bridge is retained as a part of the expanding shock wave structure. The shock wave shadowgraph measurements were made using a focal-plane shutter rotating-mirror framing camera (11). Figure 2 shows the experimental arrangement. The explosive spheres were suspended in the center of the bombproof aquarium, which consisted of a 60-cm cube having two sides made of 1.27-cm thick Plexiglas. Two argon-filled exploding bombs (12), 60-cm long, provided short duration high-intensity backlighting for the experiments. Each bomb was capped on one end with a transparent shield and on the other end by a 5.1-cm diameter, 5.1-cm long pentolite cylinder. The bomb interiors contained strips of sheet explosive attached to the pentolite cylinder. The strong shocks of  $\sim 250$  kbar from the detonation of the pentolite cylinder and the sheet explosive produced highly luminous shock light in the argon of  $\sim 300 \mu\text{sec}$  duration. This light was reflected into the aquarium by white cardboard to provide diffuse back illumination of the shock events occurring in the water.

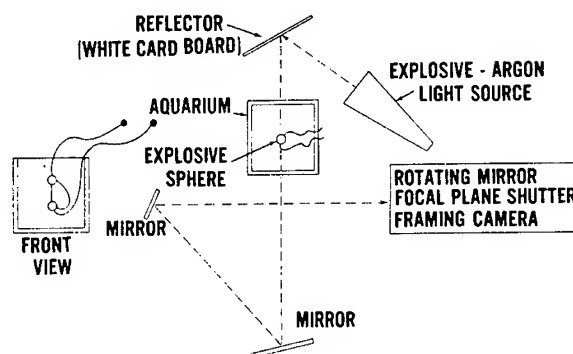


Fig. 2 - Experimental arrangement for shadowgraph measurements

Figure 3 is a sequence of shadowgraph which show the underwater shock wave interactions from two simultaneously detonated pentolite spheres. The spheres were suspended 17.8-cm apart center to center ( $\Delta x = 5.6$ ). The distance between each pair of magnification markers on the bottom and right-hand side of each frame is 5.08 cm. The camera framing rate was 125,000 frames per second. This rate corresponds to  $1.8 \mu\text{sec}$  between the time adjacent frames. Figure 3 consists of a selected group of frames  $3.6 \mu\text{sec}$  apart (13).

At  $\sim 8 \mu\text{sec}$  after initiation (during the recording of frame 1B of Fig. 3) the detonation waves reach the explosive water interface. The wave arrivals are detected by growth in size and the difference in contrast of the spheres from their original appearances in the first frame. In frame 1C the initial appearances of the underwater shock waves are noted. Each shock wave surges outward at initial velocity  $\sim 6000$  m/sec with a peak pressure that exceeds 120 kbar. The opaque gaseous products also expand but at a slower rate than the outward motion of the shock waves. This result is confirmed in Fig. 4 which compares the propagation rates of shock waves and product gas bubbles from the underwater detonation of pentolite spheres.

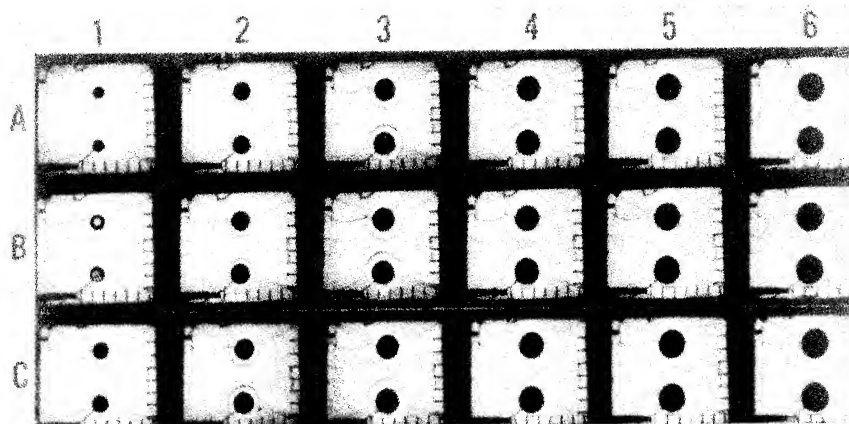
The two spherically expanding shock waves collide at  $\sim 36.3 \mu\text{sec}$  after detonation in frame 4C of Fig. 3. The velocity of each shock wave at the time of collision is  $2.25 \text{ mm}/\mu\text{sec}$  and the peak pressure is 8.0 kbar. Immediately after collision, a region of regular reflection is produced on the plane of symmetry between the spheres. The first appearance of the Mach interaction occurs about  $18 \mu\text{sec}$  after the head-on collision. Figure 5 is a sketch of wave front propagations observed in Fig. 3 showing

TABLE 1  
Notation

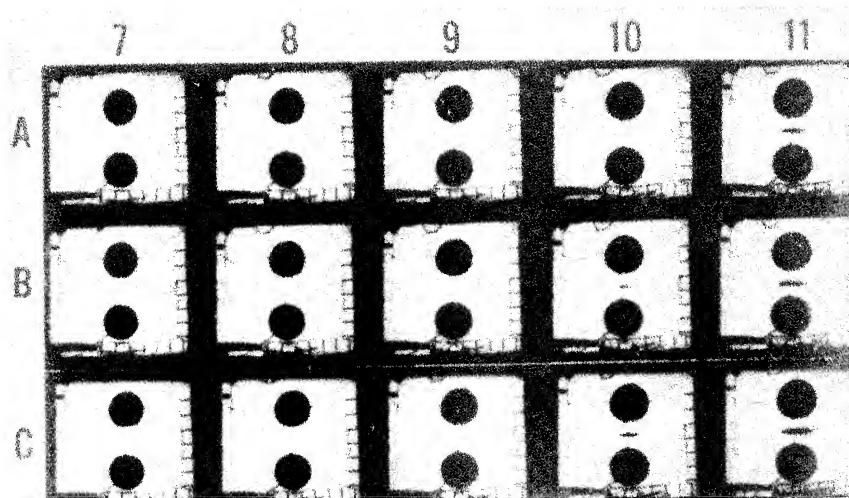
$P$	= pressure
$k$	= constant
$U_s$	= shock velocity
$u_p$	= particle velocity
$E$	= internal energy
$f$	= equation of state function
$\Delta X$	= center-to-center distance between spheres in terms of radius of the spheres
$R_0$	= radius of a sphere, weight $W_1$ , twice the weight of a single sphere
$R$	= radius of the shock wave at any point on the plane of symmetry or radius of the collision circle on the plane of symmetry
Subscript 0 refers to fluid at rest, ambient condition	
Subscript 1 refers to the incident shock wave	
Subscript 2 refers to the reflected shock wave	
Subscript M refers to Mach reflection	
$S$	= incident shock
$S'$	= reflected shock
$\alpha_1$	= angle of shock incidence
$\alpha_2$	= angle of shock reflection
$\alpha_M$	= angle $\alpha_1$ at the point where Mach reflection begins
$q$	= velocity flow vector
$N$	= normal component of velocity vector
$L$	= tangential component of velocity vector
$\rho$	= density
$\delta$	= angle of flow divergence

the occurrence and position of the Mach wave formation. At this point the angle  $\alpha_1$  is  $37^\circ$ . The bridge of the Mach wave increases in size as the wave moves outward. We note, e.g., in Fig. 3 frame 12C, when the interaction front is 20-cm from the line joining the centers of the explosive spheres, the Mach bridge is 4-cm wide.

As events progress, each of the two intersecting underwater shock waves collides with the product gas bubble from the other sphere. These collisions result in two backward-facing rarefaction waves which propagate to the point of the initial interaction. The collision of the rarefaction waves produces a region of



(a)



(b)

Fig. 3 - Framing camera shadowgraphs of shock wave interaction from separated twin explosive spheres, 3.6  $\mu\text{sec}$  between time-adjacent frames

cavitation. This result is characterized in Fig. 3 by the growth of the black spot of bubbles in the central region between the slowly advancing product gas bubbles. In our interaction experiments, the collision of underwater rarefaction waves of equal strength generally produced a cavitation region which grew as a symmetrical disc, reaching its maximum size in  $\sim 40 \mu\text{sec}$ .

The velocities of the underwater shock waves were obtained from the slopes of the distance-time curves (Fig. 5). The shock wave velocities were converted to their corresponding peak pressures by a seventh-power polynomial treatment of equation-of-state data for water (14). Figure 6 gives the peak pressure

curves for the interaction wave as it advances along the plane of symmetry between the two separated spheres. These data are compared to the measurements for a single two-pound pentolite sphere. (In this comparison the radial distances,  $R/R_0$ , refer to the radius of a single pentolite sphere equal in weight to the total weight of the two separated spheres.) The curve for the single sphere represents data from more than twenty experiments in which optical measurements were made of shock wave propagation from 453-gram and 1800-gram pentolite spheres (15). The measurements are probably accurate to  $\sim 2\%$ . At  $R/R_0 = 1$ , the initial shock wave peak pressure is 120 kbar in the water at the surface of a centrally detonated,



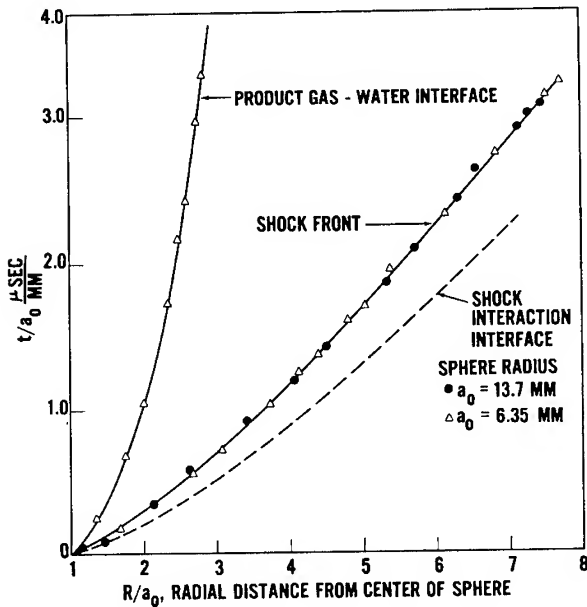


Fig. 4 - Underwater shock propagation time vs distance from initial detonation break out on the surface of pentolite spheres

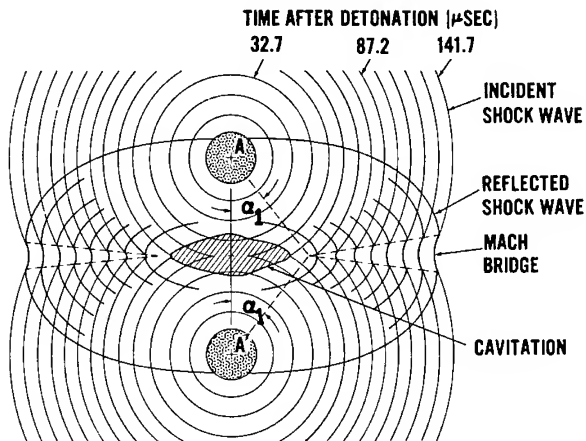


Fig. 5 - Time profiles of the collision of two equal spherically expanding underwater shock waves showing Mach wave formation (10.9  $\mu$ sec between successive wave fronts)

single pentolite sphere (15). We note in Fig. 6 that at  $R/R_0 = 2$  the pressure decays to 17.5 kbar, a value which is ~10% to 50% smaller than the peak pressure from the interaction of two separated spheres. This over-pressure is increased as the initial collision pressure is decreased throughout the range of our experiments. For example, at  $R/R_0 = 5$  the interaction

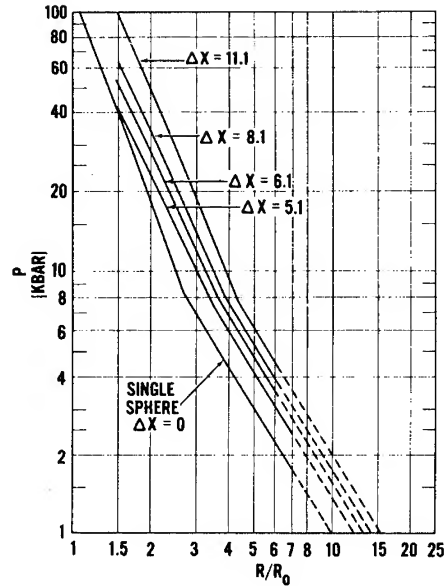


Fig. 6 - Underwater shock wave pressure-distance curves from a single pentolite sphere, weight  $w_1$ , and from twin pentolite spheres, total weight  $w_1$ .  $\Delta X$  is the separation distance between twin spheres

peak pressure is 6.1 kbar from twin explosive spheres, each weighing 225 grams and separated by 11.1 radii (26.7 cm between centers) and 4.1 kbar for charges separated by 5.1 radii (16.2 cm between charge centers). For comparison a 453-gram pentolite sphere will give a peak pressure of 2.98 kbar at  $R/R_0 = 5$ .

In the calculations we considered the flow in the immediate vicinity of the point A, Fig. 7, when the incident shock, S, strikes the rigid wall, obliquely through angle  $\alpha_1$  and is reflected as S' which leaves the wall through angle  $\alpha_2$ . The coordinates are chosen with respect to an observer moving along the wall with the point A. The incident and reflected shocks divide the medium into three regions (0), (1), and (2). The velocities in each region are assumed constant and the velocity vectors, N and L are normal and tangent respectively to the appropriate shock. The initial flow,  $q_0$ , is diverted through angle  $\delta_1$  by the incident shock and through  $\delta_2$  by the reflected shock. These angles are equal since the initial flow and the final flow are parallel to the wall. Also, we assume the incident shock is planar at the boundary wall; tangential flow across either of the shock waves is prohibited. Therefore

$$L_0 = L_1, \quad (1)$$

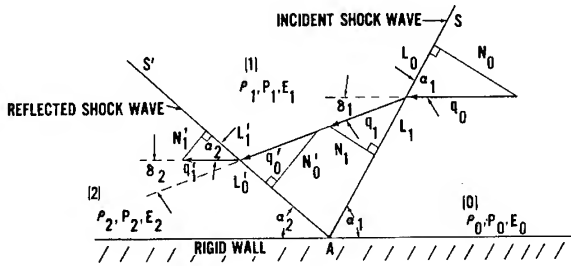


Fig. 7 - Geometry of oblique shock wave reflection off a rigid wall

and

$$L'_0 = L'_1 \quad (2)$$

(Though our experiments show this incident shock is actually a spherically diverging and decaying wave, the error introduced by the one-dimensional approach is relatively small.) Conservation of mass and momentum across each shock is expressed as

$$\rho_0 N_0 = \rho_1 N_1 \quad \text{for } S \quad (3)$$

$$\rho_1 N'_0 = \rho_2 N'_1 \quad \text{for } S' \quad (4)$$

$$\rho_0 N_0^2 = \rho_1 N_1^2 + P_1 \quad \text{for } S \quad (5)$$

$$\rho_1 N'^2_0 + P_1 = \rho_2 N'^2_1 + P_2 \quad \text{for } S' \quad (6)$$

Using the method of Courant and Friedrichs (1), we combine Eqs. (1)-(6) to relate the pressure and density in the three regions to the velocity vectors, i.e.,

$$\frac{P_1 - P_0}{\rho_0} = \vec{q}_0 \cdot (\vec{q}_0 - \vec{q}_1) \quad (7)$$

$$\frac{P_2 - P_1}{\rho_1} = \vec{q}_1 \cdot (\vec{q}_1 - \vec{q}_2) \quad (8)$$

$$\frac{P_0 - P_1}{\rho_1} = \vec{q}_1 \cdot (\vec{q}_1 - \vec{q}_0) \quad (9)$$

$$\frac{P_1 - P_2}{\rho_2} = \vec{q}_2 \cdot (\vec{q}_2 - \vec{q}_1) \quad (10)$$

Since the rigid boundary requires that the flow behind the reflected shock be parallel to the incident flow, the direction of the vectors  $\vec{q}_0$  and  $\vec{q}_2$  are such that

$$\vec{q}_0 \times \vec{q}_2 = 0 \quad (11)$$

Therefore, the angle  $\delta_1$  equals  $\delta_2$ , which we express as

$$\frac{\vec{q}_0 \cdot \vec{q}_1}{q_0 q_1} = k \frac{\vec{q}_1 \cdot \vec{q}_2}{q_1 q_2} \quad (12)$$

where  $k = 1$ . (This is  $\cos \delta_1 = \cos \delta_2$ .) If  $k$  has any value other than unity, the final flow is inclined to the original flow.

Equations (7)-(12) were combined by Erkmann (16) to relate  $\rho_2$ ,  $P_2$ , and  $q_0$ , assuming  $P_0$  is zero. The relation is

$$\frac{P_1 - P_2}{\rho_2} = \frac{(k \rho_0 q_0)^2 \left( q_0^2 - \frac{P_1}{\rho_0} - \frac{P_2}{\rho_1} \right)^2}{(\rho_0 q_0^2 - P_1)^2} - \left( q_0^2 - \frac{P_1}{\rho_0} - \frac{P_2}{\rho_1} \right) \quad (13)$$

With  $k = 1$ , Eq. (13) is a fourth degree equation in  $q_0$  having one positive real root in the region of interest. This region is between the value of  $\rho_0/\rho_2$  for the reflection of a normally incident shock and the value of  $\rho_0/\rho_2$  for which regular reflection of oblique shocks is no longer possible. Equation (13) solved simultaneously with the equation of state gives the reflected shock states before Mach wave formation.

For conditions across the incident wave front, we used the conservation equations and the Rice-Walsh equation (9) relating the shock velocity ( $U_s$ ) and particle velocity ( $u_p$ ) of water,

$$U_s = 0.1483 + 1.099 \ln (1 + u_p/0.519) \quad (14)$$

We obtained the density, pressure, and internal energy behind the reflected wave by reapplying the conservation equations and incorporating the energy-dependent equation of state derived by Walker and Sternberg (5),

$$P = \frac{f_1}{V} + \frac{f_2}{V^3} + \frac{f_3}{V^5} + \frac{f_4}{V^7} \quad (15)$$

where  $f_1$ ,  $f_2$ ,  $f_3$ , and  $f_4$  are polynomials in the internal energy fitted to experimental data. Equations (13) and (15) were solved simultaneously by iteration to obtain the shock parameters associated with the reflected wave.

The head-on collision between two equal shocks was treated with the same approach as

the oblique shock but with simplification since  $\alpha_1$  is zero. For this case the pressures and densities behind the reflected and incident shock fronts are related by

$$P_2 \left( \frac{\rho_0}{\rho_1} - \frac{\rho_0}{\rho_2} \right) = P_1 \left( 1 - \frac{\rho_0}{\rho_2} \right). \quad (16)$$

Equations (16) and (15) were solved simultaneously for the densities and pressures in the reflected shock states resulting from normally incident shocks.

### THEORETICAL RESULTS AND COMPARISONS WITH EXPERIMENT

Reflected shock pressures and reflected shock angles were calculated for the decaying incident shocks of five experimental separated charge arrangements. The incident shock angles were incrementally increased from zero (normal incidence) to the point where regular reflection no longer occurs and a Mach wave is formed. The incremental increases of incident angles were accompanied by incident pressure increases. The relation between incident angle and incident pressure was obtained from the experimental pressure-distance measurements for a single sphere, Fig. 6.

Figures 8 and 9 were calculated assuming non-decaying incident waves with incident pressures of 10.3 kbar to 1.0 kbar and non-decaying incident waves with incident pressure values that were measured in five separated charge configurations. Figure 8 shows the reflection angle as a function of the incident angle. We note the critical angle for Mach wave formation increases as the incident pressure decreases, ranging from 31 degrees for a 10.3 kbar shock to 50 degrees for 1.0 kbar shock. Experimentally, increases in charge separation  $\Delta X$ , cause decreases in the incident pressure at the reflection plane thus increasing the magnitude of the critical angle. We found, however, at Mach formation that the incident and reflected angles were related by  $\alpha_2 = 45^\circ + \alpha_1/2$ .

Figure 9 shows the ratio of reflected pressure to the incident pressure as a function of the incident angle. At the occurrence of Mach wave formation the pressure ratio ranges from 4.3 for the 10.3 kbar incident shock to 3.3 for the 1.0 kbar shock. The calculated data for the five experimental, separated charge arrangements are within this range. In Fig. 9 at  $\alpha_1 = 0^\circ$  the pressure ratios describe normal reflection, i.e., the head-on collision of two

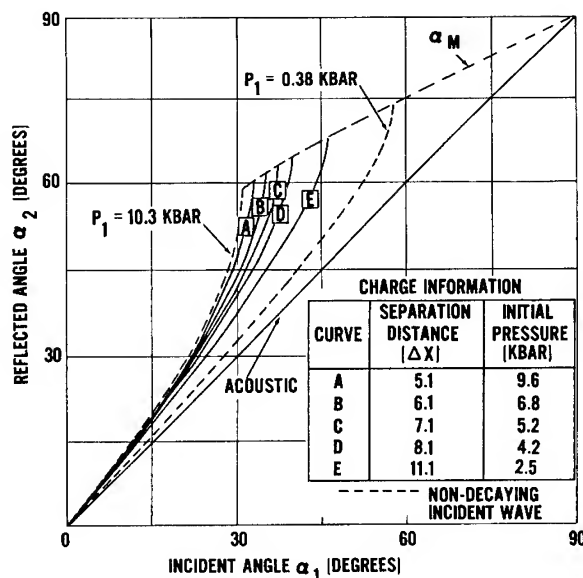


Fig. 8 - Reflected angle as a function of the incident angle for five separated charge arrangements

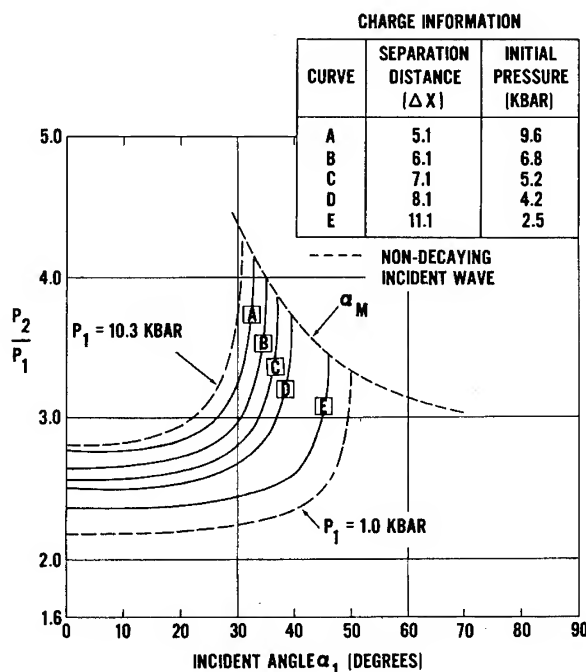


Fig. 9 - The ratio of reflected pressure to incident pressure as a function of the incident angle for five separated charge arrangements

equal shocks. For this occurrence we find that the reflected wave is 2.82 times as strong, i.e.,

$P_2 = 29.0$  kbar from the normally incident wave of 10.3 kbar. The pressure ratios decrease as the incident pressure decreases and gradually approaches the acoustic value.

In Table 2 we list the experimental and theoretical critical incident shock angles that generated Mach waves in the five different charge separations of the above experiments. For these  $\Delta X$  values the corresponding reflected shock pressures and angles of shock reflection also were calculated. The experimental data show an essentially constant critical angle  $\sim 37^\circ$  for  $\Delta X$  between 5.1 and 8.1. Both the calculations and the experiments show an increase in  $\alpha_M$  between  $\Delta X = 8.1$  and  $\Delta X = 11.1$ . The calculated and experimental values for the critical incident shock pressures which generated the Mach waves are in reasonably good agreement. The differences increase as  $\Delta X$  increases.

TABLE 2

Comparison of Theoretical and Experimental Shock Wave Parameters for Mach Wave Formation in Water

Theoretical Values			Experimental Values	
$\Delta X$	$P_1$ (kbar)	$\alpha_M$ (deg)	$P_1$ (kbar)	$\alpha_M$ (deg)
5.1	6.79	32.98	6.50	36
6.1	4.81	35.13	4.60	37
7.1	3.58	37.38	3.63	37
8.1	2.71	39.77	2.95	37
11.1	1.43	45.96	1.62	41

We attribute the differences between the calculated and the experimentally determined  $\alpha_M$  values partially to the fact that the theory cannot consider the effects of rarefaction waves which alter the strength and perhaps the direction of the experimental interacting shocks. Also, the shock wave at the reflection plane, though assumed to be planar is in fact not planar as the experiments show.

## REFERENCES

1. R. Courant and K. O. Friedrichs, "Supersonic Flow and Shockwaves," Interscience, 1948.
2. W. Bleakney and A. H. Taub, Rev. Mod. Phys., 21, 584 (1949).
3. R. J. Seeger and H. Polachek, J. Appl. Phys., 22, 640 (1951).
4. Summaries of related investigations are provided by R. H. Cole, "Underwater Explosions," Princeton University Press (1948). Also A. H. Shapiro, "The Dynamics and Thermodynamics of Compressible Fluid Flows," Vol. I, Ronald Press (1953).
5. W. A. Walker and H. M. Sternberg, "Proceedings of the 4th Symposium (international) on Detonation," (ACR-126, U.S. Gov't Printing Office, Wash., D.C.) 27-38 (1965).
6. J. Von Neumann, "Oblique Reflection of Shocks," BuOrd Explosives Res. Rept. No. 12 (1943).
7. I. I. Glass and L. E. Heuckroth, Phys. Fluids, 2, 542 (1959).
8. Since our work was completed, Glass and Heuckroth have reported a study of very weak underwater explosions generated by breaking glass spheres. See L. E. Heuckroth and I. I. Glass, Phys. Fluids, 11, 2095 (1968).
9. M. H. Rice and J. M. Walsh, J. Chem. Phys., 26, 824 (1957).
10. An explosive mixture of pentaryltetranitrate (PETN) and trinitrotoluene (TNT), each 50% by weight.
11. See S. J. Jacobs, J. D. McLanahan and E. C. Whitman, J. SMPTE, 72 (1962).
12. Z. Pressman, "Proceedings of the 5th International Congress on High-Speed Photography," edited by J. S. Courtney-Pratt, p. 56, Soc. Motion Picture and Television Engineers, New York (1962).
13. The camera uses a slotted rotating mirror which transfers the images to two film tracks. Figure 3 is a result of photographs made on 70-mm film in one of these tracks.
14. M. H. Rice and J. M. Walsh, op. cit., P. W. Bridgman, J. Chem. Phys., 3, 597 (1935). W. T. Holser and G. C. Kennedy, Am. Jour. Sci., 256, 744 (1958).
15. N. L. Coleburn, B. E. Drimmer, Bull. Am. Phys. Soc., 7, 20 (1962).
16. J. O. Erkman, Stanford Research Institute, Poulter Labs. Tech. Rept. 003-55 (1955). Also see J. O. Erkman, Phys. Fluids, 1, 535 (1958).

# THE SPEED OF PROPAGATION OF RELEASE WAVES IN POLYMETHYL METHACRYLATE

Karl W. Schuler  
Sandia Laboratories  
Albuquerque, New Mexico

## ABSTRACT

A constitutive equation determined from observations of compressive waves in polymethyl methacrylate (PMMA) is used to calculate the speeds of acceleration waves, and the results are compared with experimentally measured release wave speeds. Below about 6 kbar, the calculations and measurements are in good agreement, while above this stress they diverge.

## INTRODUCTION

Experimental observations have disclosed that a nonlinear viscoelastic constitutive equation is required to describe stress wave propagation in polymeric materials. These experiments used laser interferometry [1,2] to observe the detailed structure of finite amplitude waves produced during plate impacts [3,4]. The experiments were designed to include the observation of release waves which result from the reflection of the compressive wave from the free surface of the flyer plate. This experimental configuration is shown schematically in the  $X-t$  diagram of Fig. 1. This study presents measurements of the speed of release wave fronts made in a series of experiments of this type which were conducted on polymethyl methacrylate (PMMA). These wave fronts are modeled as acceleration waves which, in the context of singular surfaces, are fronts across which the acceleration undergoes a discontinuity. Calculations of acceleration wave speeds based on the constitutive equation for a finite linear viscoelastic fluid [5] are compared with experimental results.

First, for completeness, well-known results on acceleration wave propagation are reviewed [6], and a general expression for acceleration wave speeds in terms of the response functions of a finite linear viscoelastic fluid is calculated. This expression shows that

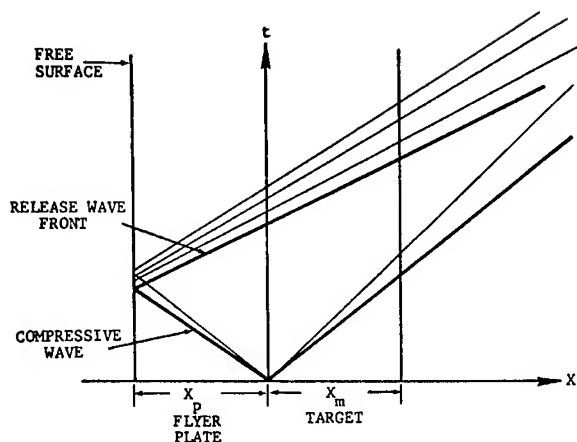


Fig. 1 - Schematic  $X-t$  diagram of plate impact experiment

the acceleration wave speed depends on the deformation history. By considering two limiting cases, the extent of this history dependence is evaluated. Then, the manner in which the response functions of the constitutive equation are determined from the experimental data is reviewed. Finally, curves showing the acceleration wave speeds which correspond to the limiting histories are presented. The predicted acceleration wave speeds are used as a check on the consistency of the steady wave analysis

which was employed in the data reduction. A comparison of the experimental data with the calculated acceleration wave speed concludes the study.

## ACCELERATION WAVES

The experiments were designed so that observations of both the compressive and release waves were completed before the arrival of disturbances from the lateral surfaces of the plates. Since the material is assumed to be isotropic, the motion during the time of observation is that of one-dimensional strain. Thus,

$$x = x(X, t) \quad (1)$$

gives the spatial position at time  $t$  of the material particle whose position in a fixed reference configuration was  $X$ . The velocity,  $v$ , of the particle is given by

$$v = \frac{\partial x}{\partial t}(X, t) \quad (2)$$

and the ratio of the density,  $\rho$ , to that of the reference configuration,  $\rho_0$ , is given by

$$\frac{\rho_0}{\rho} = \frac{\partial x(X, t)}{\partial X} \quad (3)$$

An acceleration wave is defined as a singular surface moving with respect to the material and across which  $x$ ,  $v$ , and  $\rho$  are continuous while the derivatives of  $v$  and  $\rho$  suffer jump discontinuities. Thus studies of acceleration waves may be viewed as the study of the propagation of weak (nonshock) disturbances. And, indeed, the relationship between acceleration waves and ultrasonic sinusoidal progressive waves has been indicated by Coleman and Gurtin [7].

If at time  $t$  the acceleration wave is located at the material point  $Y(t)$ , then the intrinsic velocity of the wave is given by

$$U = \frac{d}{dt} Y(t) \quad (4)$$

If  $f^+$  and  $f^-$  represent the magnitude of  $f(x, t)$  immediately ahead of and behind the wave, respectively, then

$$[f] = f^- - f^+$$

indicates the magnitude of the jump in  $f$  across the wave. With the above notation, Maxwell's theorem [6] asserts that if  $f(X, t)$  is

a continuous function of  $X, t$  whose derivatives suffer jump discontinuities at the wave front but are continuous everywhere else, then

$$\left[ \frac{\partial f}{\partial t} \right] = -U \left[ \frac{\partial f}{\partial X} \right] \quad (5)$$

From (2), (3), and (5), it is easily shown that

$$\left[ \frac{\partial v}{\partial t} \right] = U \frac{\rho_0}{\rho^2} \left[ \frac{\partial \rho}{\partial t} \right] \quad (6)$$

From the balance of linear momentum it follows that

$$\left[ \frac{\partial T}{\partial x} \right] = -\rho_0 \left[ \frac{\partial v}{\partial t} \right] \quad (7)$$

where the stress,  $T$ , has been regarded as positive in compression. Because the stress is continuous across an acceleration wave, it is possible, by using (5), to rewrite (7) as

$$\left[ \frac{\partial T}{\partial t} \right] = \rho_0 U \left[ \frac{\partial v}{\partial t} \right] \quad (8)$$

Finally, (6) and (8) may be solved for  $U^2$  yielding

$$U^2 = \left( \frac{\rho}{\rho_0} \right)^2 \frac{\left[ \frac{\partial T}{\partial t} \right]}{\left[ \frac{\partial \rho}{\partial t} \right]} \quad (9)$$

It was shown by Schuler [3] that for uniaxial strain the constitutive equation of a finite linear viscoelastic fluid reduces to

$$T = p(\rho) + \int_{-\infty}^t K(\rho(t); t - \tau) \times \left[ \left( \frac{\rho(t)}{\rho(\tau)} \right)^2 - 1 \right] d\tau \quad (10)$$

where  $p(\rho)$  and  $K(\rho; t - \tau)$  are material functions. Evaluating

$$\left[ \frac{\partial T}{\partial t} \right]$$

from (10) and substituting into (8), it follows that the speed of an acceleration wave in a finite linear viscoelastic fluid is given by

$$U^2 = \left( \frac{\rho}{\rho_0} \right)^2 \left\{ \frac{dp}{d\rho} + 2 \int_{-\infty}^t K \frac{\rho(\tau)}{\rho^2(\tau)} d\tau + \int_{-\infty}^t \frac{\partial K}{\partial \rho} \left[ \left( \frac{\rho(\tau)}{\rho(\tau)} \right)^2 - 1 \right] d\tau \right\}. \quad (11)$$

It is clear from (11) that the acceleration wave speed in these materials is dependent on the history of the deformation.

Ideally, in order to compare the predictions of (11) with the experimental observation of release waves, the following procedure should be followed: (a) determine the history of the deformation at particles through which the release wave passes; (b) use (11) to determine  $U$  as a function of time at each particle, and (c), use (4) to determine the material trajectory of the release wave front. Clearly, this procedure will be difficult. For example, the deformation history experienced by a particle located at the free surface of the flyer plate consists of a sudden jump in strain caused by the arrival of the shock. Hence the acceleration wave speed at this particle can be found from (11) by using the jump history:

$$\rho(\tau) = \begin{cases} \hat{\rho}, & \tau = t \\ \rho_0, & -\infty < \tau < t. \end{cases} \quad (12)$$

In contrast to what occurs at this position, a particle located at the impact surface has a relatively long time to reach equilibrium prior to the arrival of the release wave. If this particle does reach equilibrium, the appropriate history to employ in (11) is the rest history, i.e.,

$$\rho(\tau) = \hat{\rho}, \quad -\infty < \tau \leq t. \quad (13)$$

At other particles in the path of the release wave, it is not clear what might be a reasonable history to assume.

However, since (12) and (13) represent extremes, consideration of these two histories should provide bounds on the variation of the acceleration wave speed. Additional motivation for the consideration of the histories given by (12) and (13) arises from noting that the thickness of the flyer plate is the essential feature in determining the history seen by a particle in the path of the release wave. If the flyer is very thin, then the release wave passes through a region which is far from equilibrium in that it has just experienced a jump in strain caused by the passage of a shock wave. On the other

hand, if the flyer plate is very thick, then the release wave travels through a region which for the most part has reached equilibrium.

It is easily shown that for the jump history, (12), the wave speed predicted by (11) is

$$U^2 = \left( \frac{\hat{\rho}}{\rho_0} \right)^2 \frac{d}{d\rho} \times \left[ p + \left( \left( \frac{\rho}{\rho_0} \right)^2 - 1 \right) \phi(0, \hat{\rho}) \right], \quad (14)$$

while that corresponding to the rest history, (13), is given by

$$U^2 = \left( \frac{\hat{\rho}}{\rho_0} \right)^2 \left( \frac{dp}{d\rho} + \frac{2}{\rho} \phi(0, \hat{\rho}) \right). \quad (15)$$

where, in both (14) and (15), the quantity  $\phi(t - \tau; \rho)$ , the stress relaxation function, is given by

$$\phi(t - \tau; \rho) = \int_{t-\tau}^{\infty} K(\xi; \rho) d\xi. \quad (16)$$

Hereafter  $U_1$  and  $U_2$  will denote the velocities given by (14) and (15), respectively.

From (14) and (15) it is clear that the functions  $p$  and  $\phi$  as functions of  $\rho$  must be specified. This has been done for PMMA by observing compressive wave propagation. In the next section these results are reviewed.

## DETERMINATION OF MATERIAL PARAMETERS

Detailed measurements of the compressive wave propagating in polymethyl methacrylate (PMMA)\* were carried out by using a velocity interferometer to observe the motion of a mirror which was imbedded in the target plate. The location of the mirror,  $x_M$  in Fig. 1, was varied from 6 to 37 mm; this variation allowed observation of the way in which the wave structure changed with propagation distance. A typical particle velocity history is shown in

\*The polymethyl methacrylate used in these experiments was plexiglas produced by Rohm & Haas Company. For a more complete description of these experiments see [3,4].

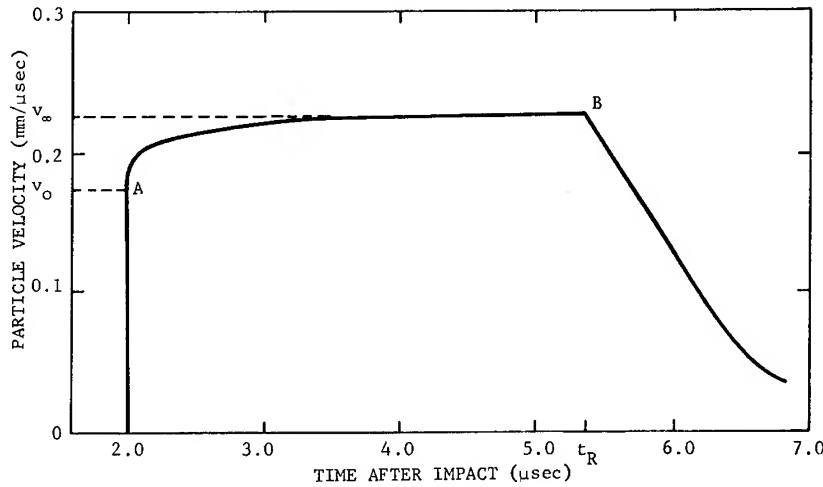


Fig. 2 - Particle velocity history observed in PMMA 6.359 mm from the impact surface (flyer plate impacted at .450 mm/μsec and was 6.568-mm thick)

Fig. 2. Here, point A will be termed the head of the compressive wave, point B the tail. It was found from these observations that the compressive wave profile was steady (did not change shape) for experiments in which the stresses were below about 6 kbar. For experiments in which the stress exceeded this level, a spreading of the compressive wavefront was observed. However, at large distance from the impact surface, the amount of this spreading was seen to decrease; this suggests that wave profiles obtained from large mirror distances could be considered steady.

From the constitutive equation (10), it is easily shown that the stress developed when the material is subjected to the jump history (12) is given by

$$T = p(\hat{\rho}) + \phi(0; \hat{\rho}) \left[ \left( \frac{\rho}{\rho_0} \right)^2 - 1 \right] \quad (17)$$

where  $\phi(0; \hat{\rho})$  is given by (16). This stress-density function will be termed the instantaneous stress-density function,  $T_I$ . Similarly, it can be shown that the stress developed when the material is subjected to the rest history (13) is given by

$$T = p(\hat{\rho}) \quad (18)$$

This function will be termed the equilibrium stress-density function,  $T_E$ . Thus if  $T_I$  and  $T_E$  can be determined, it follows from (17) and (18) that  $p(\rho)$  and  $\phi(0; \rho)$  can be found.

Substituting (17) into (14) shows that the wave speed  $U_1$  is given by

$$U_1 = \frac{\rho}{\rho_0} \sqrt{\frac{dT_I}{d\rho}} \quad (19)$$

which is the result one would expect if the material were elastic and loaded and unloaded along  $T_I$ . In a similar way,  $U_2$  can be related to the slope of the instantaneous stress-density curve which passes through a point on the equilibrium stress-density curve. Of course, the instantaneous stress-density curve centered on some point of  $T_E$  differs from (17) which is the instantaneous stress-density curve centered at  $\rho_0$ .

If the wave is a steady wave, propagating with velocity  $U_s$ , it can be shown [3] that the balance of mass and momentum require that

$$T = \rho_0 U_s v \quad (20)$$

$$1 - \frac{\rho_0}{\rho} = \frac{v}{U_s}$$

hold at each point of the wave.\* Thus, measurement of the particle velocity,  $v$ , and steady wave velocity,  $U_s$ , determines the stress and the density. In particular, the particle velocity

\*If the wave is not steady, then Eq. (20) still holds at the shock front, with  $U_s$  equal to the shock velocity; hence, the determination of  $T_I$  is independent of the steady wave assumption.



jump at the shock,  $v_0$ , and the maximum particle velocity,  $v_\infty$ , at the tail of the wave can be used to find  $T_I$  and  $T_E$  respectively.

In keeping with conventional shock wave practice,  $T_I$  is given parametrically by a " $U_s$ - $u_p$ " curve. For PMMA, it was found that the steady wave velocity (shock velocity) could be well fitted by the following function of particle velocity jump at the shock

$$U_s = 2.763 + 3.626 v_0 - 5.644 v_0^2. \quad (21)$$

For  $T_E$ , it was found that

$$p(\rho) = 89.28 \epsilon + 699.41 \epsilon^2 - 3688.7 \epsilon^3, \quad (22)$$

where

$$\epsilon = (1 - (\rho_0/\rho)) = v_\infty/U_s,$$

provided the best fit to the experimental data. The data points through which (22) was fitted consisted of all data points obtained in experiments conducted at stress levels below 6 kbar. From those experiments conducted above this stress level, only those in which observations were made at a large distance from the impact surface (37 mm) were used.

#### CALCULATION AND A DISCUSSION OF THE SPEEDS $U_1$ , $U_2$

From the results of (12)-(21), the wave speeds  $U_1$  and  $U_2$  were calculated as functions of strain,  $\epsilon$ . The results of these calculations are shown in Fig. 3. It is seen that  $U_1$ , the speed corresponding to the jump history, is greater than  $U_2$ , the speed corresponding to the rest history. Both speeds pass through a maximum which occurs at a strain of about 6%. This maximum is a reflection of the fact that both the instantaneous and equilibrium stress-density curves have an inflection point at a strain of about 6%.

Before comparing these results to the experimental data, the consistency of the steady wave assumption with these results is investigated. Intuitively, a steady wave in a viscoelastic material results from a balance being achieved between the tendency of the wave to decay due to dissipation and to grow due to nonlinear stress-strain behavior. Hence, in order to have a steady wave, each part of the wave must tend to overtake the part ahead of it; i.e., the local acceleration wave speed should not decrease from the head to the tail of the wave. This criterion is essentially the

sufficiency requirement used by Greenberg [8] to prove the existence of steady waves in viscoelastic materials.

For a given wave velocity, the curves labeled I and II on Fig. 3 give the strain at the head and the tail of a steady wave, respectively. Thus, for a steady wave propagating at 3.1 mm/ $\mu$ sec, the strain at the head of the wave (i.e., just behind the shock) is given by point (A), while the strain at the tail of the wave is given by point (B). These curves were calculated from (20) along with either (21) or (22).

But  $U_1$  and  $U_2$  are the acceleration wave speeds at the head and the tail respectively of a steady wave. Thus, for a steady wave traveling at about 3.1 mm/ $\mu$ sec, point (C) gives the acceleration wave speed at the head of the steady wave, while point (D) gives the acceleration wave speed at the tail.

Note that, for a steady wave speed of 3.1 mm/ $\mu$ sec, the acceleration wave speeds at the head and tail of the wave, i.e., at points (C) and (D), are almost identical. For steady waves traveling slower than 3.1 mm/ $\mu$ sec, the acceleration wave speed at the tail of the wave, point (E), is greater than that at the head, point (F), while the reverse is true for waves traveling faster than this velocity. Thus, based on the sufficiency criterion outlined above, it can be concluded that the existence of a steady wave traveling faster than 3.1 mm/ $\mu$ sec is not consistent with the constitutive equation.\* This steady wave speed corresponds to a stress level of about 6 kbar. Thus the assumptions made in the previous section must be modified to allow for nonsteady waves above 6 kbar and a new determination of  $T_E$  must be made. Barker and Hollenbach [4] considered the compressive waveform as a simple centered wave and applied an incremental analysis to determine the stress and strain at the tail of the wave. The results of their calculations for experiments in which the stress levels exceed 6 kbar are shown in Table 1. In addition, the stress-strain points which result from the steady wave analysis for experiments below 6 kbar are shown.

\*In general, examination of the acceleration wave speeds at the head and the tail is not a complete check of sufficiency because the criterion is a monotone increase in acceleration wave speed from head to tail. However, for the case considered here, further calculations based on Eq. (11) and the history encountered in a steady wave have demonstrated this monotonicity.

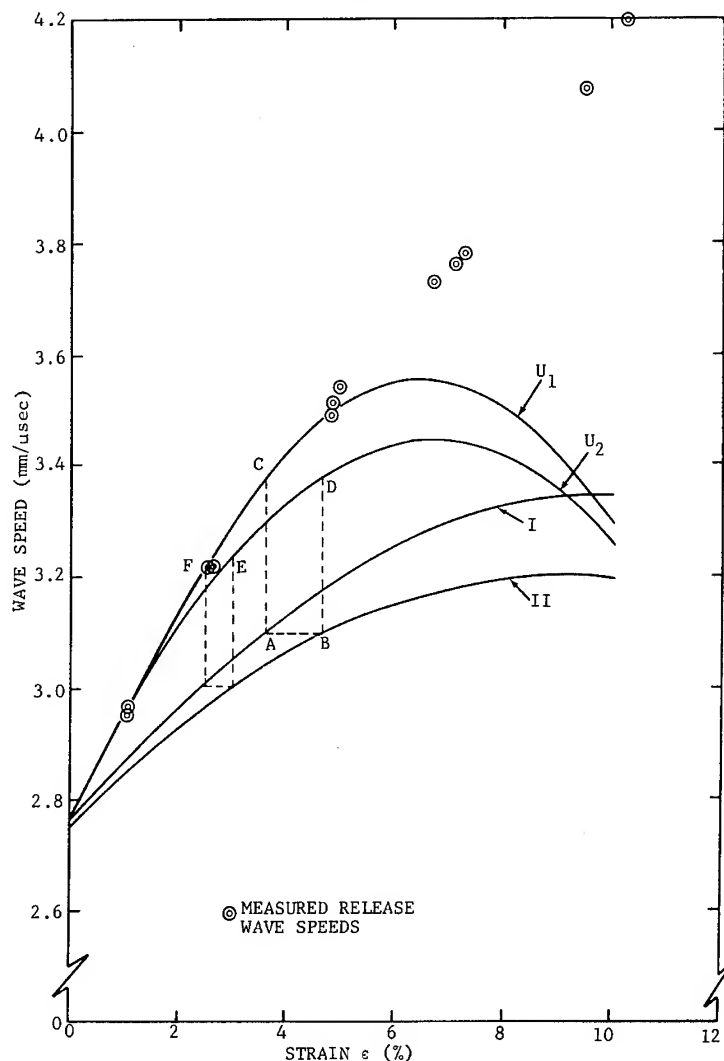


Fig. 3 - Plots of measured release wave speed and calculated acceleration wave speed

From a  $T_E$  curve fitted to the stress-strain points of Table 1, a new calculation of  $U_2$  may be made; however, for clarity, this curve has been omitted from Fig. 3. Of course, the determination of  $U_1$ , which by Eq. (19) is related to the slope of  $T_I$ , is unaffected by these considerations.

The release wave speeds shown in Table 1 are average speeds calculated from

$$U_R = \frac{X_m + X_p}{t_a - \frac{X_p}{U_s}}$$

where,  $X_p$  is thickness of the flyer,  $t_a$  the time after impact at which the release wave

arrives, and  $U_s$  is the measured shock speed. For a given impact condition, no significant variation of release wave speed was observed over the range of propagation distances (typically from 6 to 42 mm). The measured release wave speed and corresponding equilibrium strain values are plotted in Fig. 3.

From Fig. 3 it is seen that below a strain of  $\approx 6\%$ , which corresponds to a stress level of  $\approx 6$  kbar, excellent agreement exists between the calculations of the speed  $U_1$  and the measured release speeds. Over this same range, the speed  $U_2$  tends to fall below the experimental points. Since the calculations of both  $U_1$  and  $U_2$  involve derivatives of fitted curves it is felt that this agreement is remarkably good. Further confirmation of the adequacy of

TABLE 1

Shot Designation <sup>a</sup>	Equilibrium Values <sup>b</sup>		Measured Release Wave Speed (mm/ $\mu$ sec)
	Stress (kbar)	Strain (%)	
312, 313	1.03	1.08	2.97
2109	1.04	1.09	2.97
2105	1.03	1.08	2.95
314, 315	2.66	2.55	3.22
2110	2.66	2.54	3.22
2112	2.71	2.61	3.22
2115	2.68	2.53	3.23
316, 317	5.71	4.93	3.54
2113	5.53	4.82	3.51
2116	5.49	4.80	3.49
2106R1	8.36	7.22	3.78
2107R1	8.25	7.09	3.76
2107R2	7.85	6.66	3.73
318, 319	11.99	10.24	4.19
2108	10.98	9.47	4.07

<sup>a</sup>Shots in the 300 series are due to Barker and Hollenbach [4].

<sup>b</sup>For shots 2106R1, 2107R1, 2107R2, 318, 319, and 2108 values were computed from a centered wave analysis; for all others, a steady wave analysis was used.

the constitutive model for stresses below  $\approx 6$  kbar has been obtained from numerical calculations using the Wondy finite difference code [9].

It is interesting to compare the speed  $U_1$  and  $U_2$  with the speed corresponding to a hydrodynamic model with a Hugoniot given by (22). Based on this Hugoniot, a release wave speed of 3.34 mm/ $\mu$ sec is calculated for a strain level of 6%. This prediction is considerably lower than either  $U_1$  (3.55 mm/ $\mu$ sec) or  $U_2$  (3.44 mm/ $\mu$ sec) evaluated at the same strain. Hence, a hydrodynamic model would be inadequate at predicting such phenomena as thin pulse attenuation in these materials.

For strains larger than  $\approx 6\%$  (stress greater than  $\approx 6$  kbar), a marked discrepancy exists between the measured release wave speeds and the prediction based on either  $U_1$  or  $U_2$ . This discrepancy and the inflection points which occur in both the  $T_E$  and  $T_I$  curves

indicate that above  $\approx 6$  kbar a new form of constitutive equation is required. Barker has indicated that the material behavior at these inflection points displays some of the features of elastic plastic phenomena. This and other models which incorporate stronger dependence on the strain history are presently under investigation.

## CONCLUSIONS

Measurements have been made on the speed of propagation of release wave fronts in PMMA. These measurements show that the release wave speed increases with increasing strain ahead of the front. The release waves were modeled as acceleration waves propagating in a finite linear viscoelastic fluid, the parameters of which were determined from the behavior of the compressive wave. It was concluded that below 6 kbar this model adequately describes the experimental results. Above 6 kbar, the proposed model predicted a wave speed which decreased with increasing strain ahead of the wave. It appears that a more complex dependence on the history of the deformation must be included in the constitutive model in order to account for the observations above 6 kbar.

## ACKNOWLEDGMENTS

The author is indebted to L. M. Barker and R. E. Hollenbach for allowing their data to be included here and to Dr. P. J. Chen for his helpful discussions and suggestions on acceleration wave propagation.

## REFERENCES

1. L. M. Barker and R. E. Hollenbach, "Interferometer Technique for Measuring the Dynamic Mechanical Properties of Materials," *Rev. of Sci. Inst.*, Vol. 36, No. 11, p. 1617, Nov. 1965.
2. L. M. Barker, "The Fine Structure of Compressive and Release Wave Shapes in Aluminum Measured by the Velocity Interferometer Technique," *Behavior of Dense Media Under High Dynamic Pressures Symposium*, H. D. D. Gordon Breach, New York, 1968.
3. K. W. Schuler, "Propagation of Steady Shock Waves in Polymethyl Methacrylate," *J. Mech. Phys. Solids*, Vol. 18, No. 4, p. 277, Sept. 1970.

4. L. M. Barker and R. E. Hollenbach, "Shock Wave Studies of PMMA, Fused Silica, and Sapphire," *J. Appl. Phys.*, Vol. 41, No. 10, p. 4208, Sept. 1970.
5. Bernard D. Coleman and Walter Noll, "Foundations of Linear Viscoelasticity," *Rev. Mod. Phys.*, Vol. 33, No. 2, 239-249, April 1961.
6. Bernard D. Coleman, Morton E. Gurtin and Ismael Herrera R., "I. The Velocity of One-Dimensional Shock and Acceleration Waves," *Arch. Rational Mech. Anal.*, Vol. 19, 1965.
7. Bernard D. Coleman and Morton E. Gurtin, "II. On the Growth and Decay of One-Dimensional Acceleration Waves," *Arch. Rat. Mech. Anal.*, Vol. 19, 1965.
8. James M. Greenberg, "Existence of Steady Waves for a Class of Nonlinear Dissipative Materials," *Quart. Appl. Math.*, Vol. 26, No. 1, 1968.
9. K. W. Schuler and R. J. Lawrence, "A Non-linear Viscoelastic Subroutine for One-Dimensional Lagrangian Wave Propagation Codes," in preparation.

## ARTIFICIAL VISCOSITY METHOD CALCULATION OF AN UNDERWATER DETONATION

H. M. Sternberg and W. A. Walker  
*Naval Ordnance Laboratory*  
*White Oak, Silver Spring, Maryland*

### ABSTRACT

The flow following the detonation of a centrally initiated pentolite sphere underwater at sea level is calculated by the artificial viscosity method up to the time the main shock in the water is 100 charge radii from the center. Calculated pressure vs distance, pressure vs time and particle velocity vs distance are presented. Improvements in the artificial viscosity method computation used by the authors for underwater detonations in a previous paper are described. These deal with the form of the artificial viscosity function, fine-zoning at the shock front, and initial conditions.

---

An expanded version of this paper has been published under the title "Calculated Flow and Energy Distribution Following Underwater Detonation of a Pentolite Sphere" in *The Physics of Fluids*, Vol. 14, No. 9, pp. 1869-1878, September 1971.

# SPHERICAL EXPLOSIONS IN WATER

L. W. Hantel and W. C. Davis  
*University of California, Los Alamos Scientific Laboratory*  
*Los Alamos, New Mexico 87544*

## ABSTRACT

Calibration data are presented for the shock wave in water driven by a centrally-initiated sphere of explosive. The measured quantity is the shock position as a function of time; a simple function is fit by a least-squares technique to the data. The derivative of the fit function gives shock velocity, which is used with the known shock Hugoniot function for water to get shock pressure. The useful range of pressure in the water is from 150 to 5 kbar, with an uncertainty less than  $\pm 5\%$ . For spheres of 3", 4-1/2", and 6" diameter, no departure from simple scaling is found. The calibrated system is intended as a generator of a reproducible pressure pulse for use in explosive sensitivity tests, gauge calibration, etc.

## INTRODUCTION

The behavior of shock waves driven by centrally-initiated spherical explosive charges has been of interest for many years. In particular, considerable work to calibrate these shock waves for use as known pressure pulses has been done at the Naval Ordnance Laboratory. In 1949 Eyster, Smith, and Walton (1) described an underwater gap test designed to measure the critical initiation pressure of an explosive. In this test, centrally-initiated spherical charges were used to generate spherically diverging water shocks, which were then allowed to impinge upon cylindrical acceptor charges located at various distances from the surface of the sphere. Liddiard (2) used this same technique to study the initiation of burning resulting from low amplitude mechanical shocks. Interest in the interaction of spherical shocks in water prompted Coleburn and Roslund (3) to study shock wave interactions resulting from the simultaneous detonation of two spherical charges of explosive under water.

The water shock resulting from the central initiation of a sphere of explosive radiates outward more or less spherically depending on the simultaneity of the break-out times around the sphere. The amplitude of the shock decreases with increasing distance from the sphere surface, giving a convenient method for subjecting objects to shocks of different intensities by

placing them at different distances from the sphere. However, for quantitative use of the method one must determine the relationship between the shock pressure and distance from the sphere. If the relationship between the radial distance the shock wave has traveled and time,  $R = R(t)$ , can be established, it can be differentiated to give the shock velocity  $U$ . Using the equation of state data of Rice and Walsh (4) one can then determine the pressure as a function of distance. In many past experiments the  $R-t$  data have been obtained through the use of framing cameras. Generally, the camera records a limited number of distance-time data points for any given shot. Then a polynomial is fit to the data to give the form

$$R = A_0 + A_1 t + A_2 t^2 + A_3 t^3 + \dots + A_n t^n \quad (1)$$

In a limited number of experiments at LASL, Smith and Hantel (5) found the framing-camera-polynomial-fit method unsatisfactory. In these experiments the expansion of various diameter 9205\* spheres was recorded using a Beckman and Whitley Model 189 framing camera. Polynomials of various degrees were fit to the resulting  $R-t$  data and differentiated to give the shock velocity. This approach was not

\*92/6/2 - RDX/polystyrene/dioctyl phthalate,  
 $\rho = 1.686 \text{ gm/cc}$ .

satisfactory because it gave inconsistent velocities in the low pressure range. This was traced to the polynomial fits, which oscillated in this range, giving oscillating values for the derivative. Also, the limited number of frames available per shot did not yield enough data points of sufficient resolution to give a reasonable fit for any one shot, thus making shot-to-shot comparisons difficult.

This paper gives the results of an experiment designed to eliminate these problems. Instead of a framing camera, a rotating-mirror streak camera was used to record the expansion of the sphere, which results in a much larger number of data points and improved resolution. In addition, a more realistic equation with a basis in spherical detonation theory was used to fit the  $R-t$  data. The aims of this experiment were threefold: first, to collect data for calibration of an underwater gap test; second, to see if the data from spheres of different radii would scale; third, to obtain  $R-t$  data of sufficient quality to serve as a basis for extending the theory of spherical detonation.

## EXPERIMENTAL

Although the main difficulties in the earlier experiments were thought to be camera resolution and the small number of data points, it was decided that development of a good spherical initiator would be desirable. An initiator was developed which consisted of 2 gr/ft MDF XTX,\* and 9404.† Figure 1 is a schematic of the initiator. If one excludes a region from the point where the MDF enters the 9404 ball down to a latitude of  $45^\circ$ , the breakout times measured on four different spheres were simultaneous to within 0.08 sec. Generally the lower hemisphere was simultaneous to within less than  $0.03 \mu\text{sec}$ . On the six centrally initiated 9205 spheres fired, arrival times measured in the area covered by the smear camera were simultaneous to within  $0.09 \mu\text{sec}$ .

Once the initiator had been developed we decided on a six-shot series with the 9205 spheres. The series consisted of two shots each with 3"-, 4.5"-, and 6"-diameter spheres. Figure 2 shows a completed sphere assembly with the initiator in place. The spheres were fired inside  $2' \times 2' \times 2'$  Plexiglas boxes containing tap water at  $25^\circ\text{C}$ . The slit on the smear camera was orientated so that the expansion of the

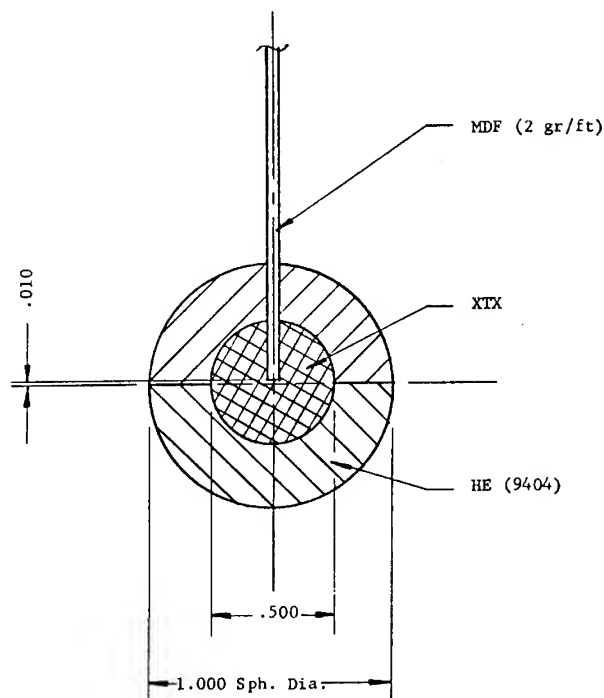


Fig. 1 - Spherical initiator

water shock on both the right and left sides of the sphere would be recorded simultaneously. The system was backlit with an argon flash collimated by a Fresnel lens to give shadow-graph lighting. The resolution was better than 1 mm at the object with a magnification of  $1/30$ .

The films were read on a Bensen-Lehner comparator, and the data were converted to mm and  $\mu\text{sec}$  by the PFIEFE (6) code, which is a standard code used to reduce cylinder-test data (7). Approximately 240 data points were obtained for each sphere.

## DATA ANALYSIS

One of the objects of these experiments was to develop an equation that describes the motion of the shock front as a function of time. The equation chosen is

$$R = 1 + (At^2 + Bt + C)(t - 1) + D(t - 1)^{3/2} \quad (2)$$

This equation is in reduced form, with

$$t = \frac{t_o + a/D}{a/D}$$

and

\*80/20 - PETN/Sylgard 182,  $\rho = 1.533 \text{ gm/cc}$ .

†94/3/3 - HMX/nitrocellulose/chloroethyl phosphate,  $\rho = 1.845 \text{ gm/cc}$ .

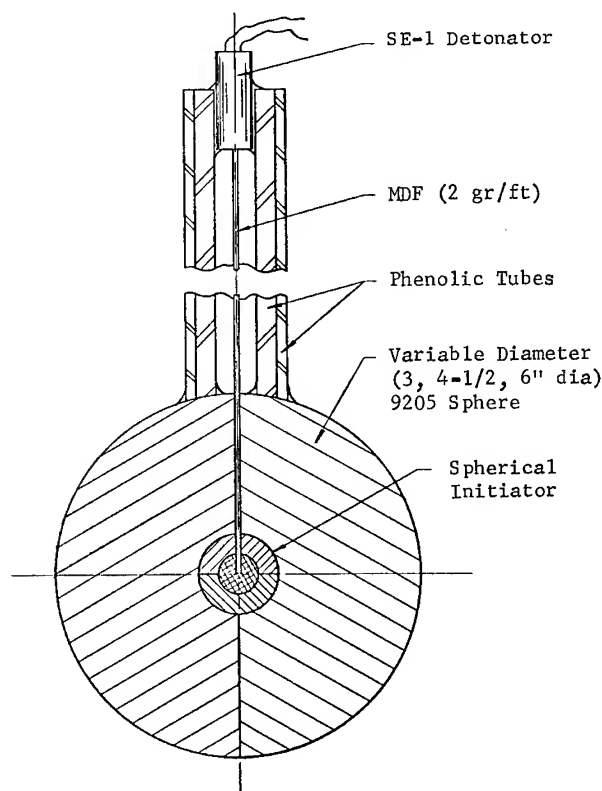


Fig. 2 - Spherical charge with initiator

$$R = \frac{R_o + a}{a}$$

where

$t_o$  = observed time from breakout.

$a$  = sphere radius.

$D$  = detonation velocity for 9205  
(8.17 mm/ $\mu$ sec).

$R_o$  = observed distance of shock front  
from sphere surface.

The purpose of the reduced form is to make direct comparisons between spheres of different diameters possible. The basis in theory for the above equation is that Taylor's (8) theory of spherical detonation implies that the second derivative of  $R(t)$  should become infinite, as  $t_o^{-1/2}$ , as  $t_o$  approaches 0. This requirement is satisfied by the  $(t-1)^{3/2}$  term, the rest of the function being a simple polynomial. The above equation was fit to the individual data sets (two for each sphere, one left and one right) by the method of least squares using

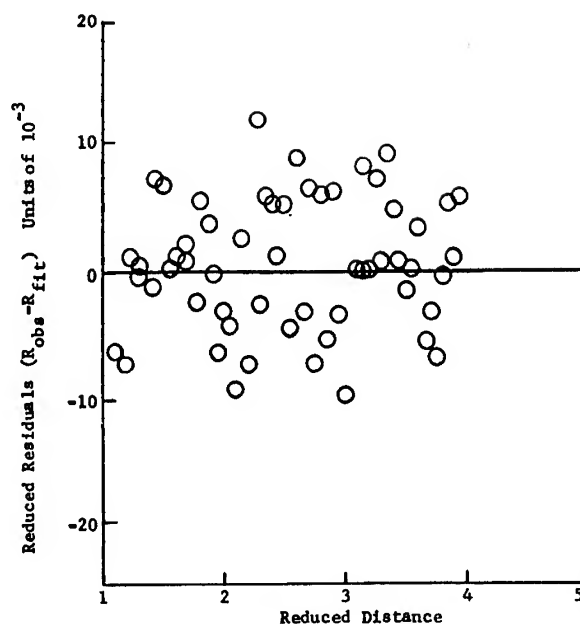


Fig. 3 - Residual plot, shot B7101, 4.5" sphere

$$R = 1 + (7.300 \times 10^{-1} + 5.118 \times 10^{-2} t - 7.130 \times 10^{-4} t^2) (t-1) - 2.800 \times 10^{-1} (t-1)^{3/2}$$

the EILEEN (9) code. Figure 3 is a plot of the residuals ( $R_{\text{observed}} - R_{\text{fit}}$ ) for one of the 4.5" diameter 9205 spheres. This plot is typical of all the shots fired. These residuals represent position errors up to about 0.5 mm, the total distance under observation being 500 mm.

Another of the aims of this experiment was to see if the data from spheres of different diameters would scale. Figure 4 is a plot of data points from all six spheres in reduced variables. It is obvious that the data do scale quite nicely. The next step was to use the EILEEN code to fit the above equation to the data from all six spheres lumped together as one data set. The equation resulting from this fit is:

$$R = 1 + (7.303 \times 10^{-1} + 4.928 \times 10^{-2} t - 5.948 \times 10^{-4} t^2) (t-1) - 2.777 \times 10^{-1} (t-1)^{3/2} \quad (3)$$

The residual plots for the individual spheres resulting from comparison of this calculated  $R$  and the observed  $R$  for each sphere do not show the randomness of Fig. 3, but show a small but definite shot-to-shot difference. The experimental difference in shock position from shot



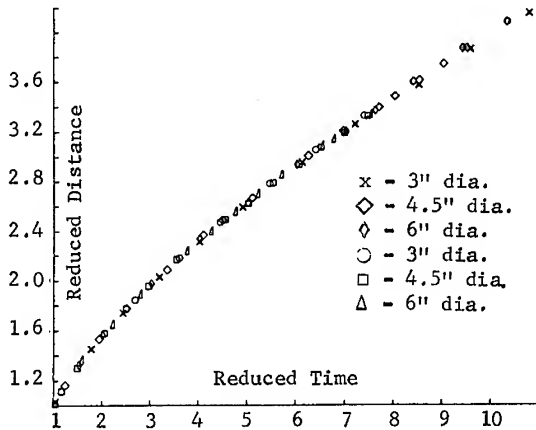


Fig. 4 - Reduced distance vs reduced time. Data for all six spheres.

to shot is in the neighborhood of 1 mm. Probably the largest uncertainty, which may be responsible for most of the difference, is in the determination of effective camera magnification.

The next point of interest is the calculated shock velocity and resulting pressure-distance plots. The expression for the "reduced shock velocity" is obtained by differentiating the  $R = R(t)$  equation with respect to time,

$$\begin{aligned} \frac{dR}{dt} = U_{red} = & 6.810 \times 10^{-1} + 9.975 \times 10^{-2}t \\ & - 1.784 \times 10^{-3}t^2 \\ & - 4.166 \times 10^{-1}(t-1)^{1/2}. \end{aligned} \quad (4)$$

The shock velocity in mm/ $\mu$ sec is then obtained by multiplying  $U_{red}$  by  $D$  (8.17 mm/ $\mu$ sec). A plot of shock velocity vs reduced radius is shown in Fig. 5. The pressure is determined from the conservation of momentum equation

$$P = \rho_o U u. \quad (5)$$

The relationship between  $U$  and  $u$  used in this calculation is (4,10)

$$U = 1.647 + 1.921 u - 0.096 u^2. \quad (6)$$

The density  $\rho_o$  is that of water before being shocked. A plot of pressure vs reduced radius is shown in Fig. 6. It should be pointed out that this relationship between  $U$  and  $u$  is not really known to be satisfactory. It was obtained from data taken at higher pressures than our experiment, and there are no data in our lower pressure range. Additional Hugoniot data for

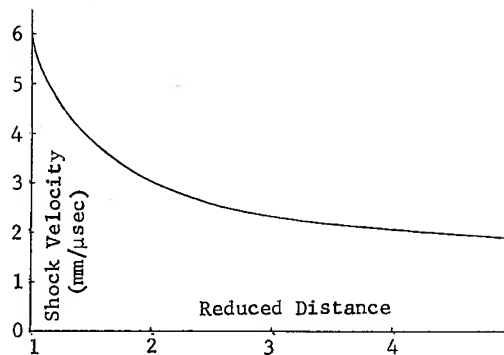


Fig. 5 - Shock velocity vs reduced distance. Calculated from fit to all six spheres.

water in the low pressure region would be of considerable interest for this and other problems.

A test of the appropriateness of the equation chosen to fit the data is provided by considering the initial velocity of the water shock. The equation is chosen to make the deceleration of the shock infinite at the initial point. If nature departed very much from this idealization, the apparent explosive pressure which would give the shock velocity in water implied by the fit would be far from that of the real

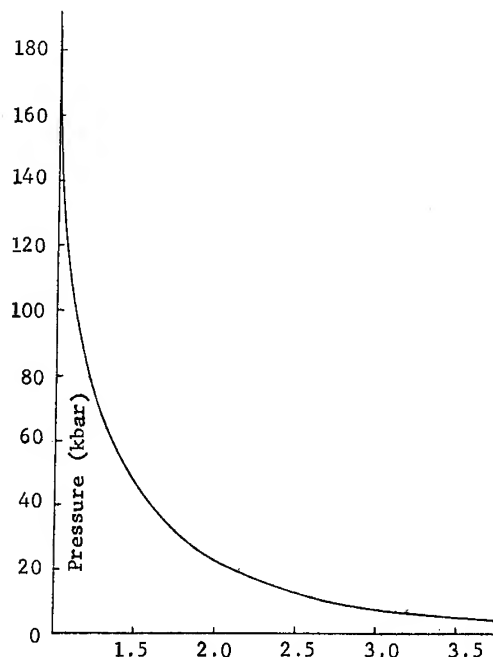


Fig. 6 - Pressure vs reduced distance. Calculated from fit to all six spheres.

explosive. The fit gives an initial velocity of 6.36 mm/ $\mu$ sec, which corresponds to a pressure of 182 kbar in the water. Making the match in the  $P-u$  plane, one finds the explosive pressure necessary to drive this shock is about 285 kbar. Extensive experimental data for 9205 are not available, but a few shots by B. G. Craig (11) give a pressure of  $275 \pm 15$  kbar, and a BKW calculation (12) by C. L. Mader (13) gives 288 kbar. The agreement is very good, and this implies that the form chosen for the fit is appropriate and that the detonation behaves much like Taylor's model (8).

Effective use of the data presented in this paper requires not only knowledge of the peak pressure at any time  $t$ , but also an indication of how the pressure changes with distance behind the shock front. The pressure gradient behind the shock front can be calculated from the rate of change of pressure at the shock front. Using the flow equations, the total derivatives of pressure and particle velocity along the shock path, the Hugoniot relationship, and the conservation of mass equation, it can be shown that

$$\left(\frac{\partial P}{\partial r}\right)_t = -\left(\frac{\rho_o U}{\eta}\right) \left\{ \frac{2u}{r} + \frac{1}{\rho c^2} \left(\frac{dP}{dt}\right)_s \right. \\ \left. \times \left[ 1 + \frac{\rho_o U}{M^2} \left(\frac{du}{dP}\right)_H \right] \right\} \quad (7)$$

where  $\eta = 1 - M^2$  and  $M = (U - u)/c$ .

In this expression  $(\partial P/\partial r)_t$  is the pressure gradient behind the shock at an instant of time,  $\rho_o$  is the initial density of the water, and  $\rho$  is the density of water at the shock pressure.  $U$  is the instantaneous shock velocity,  $u$  is the particle velocity,  $r$  is the distance from the center of the spherical coordinate system, and  $c$  is the sound velocity in the water at the shock pressure.  $(dP/dt)_s$  is the rate of change of pressure at the shock. This can be obtained from the pressure-time relationship (obtained by combining Eqs. (4), (5), and (6)).  $(du/dP)_H$  is the derivative of the particle velocity with respect to pressure along the shock Hugoniot curve (obtained by combining Eqs. (5) and (6)). The sound velocity can be found from a table given by Rice and Walsh (4).

## SUMMARY

With this set of experiments a good calibration of the underwater gap test has been obtained. The water shock pressure is known

to about 5% throughout the range from 150 to 5 kbar, and the system can be used without any further development. A good fit to all the data has been found, and the remaining uncertainties in the calibration result from real shot-to-shot differences and experimental errors.

No departure from scaling can be seen in the results. The size range, only a factor of two, is not large enough to make this a sensitive test of scaling, but the data are good enough that an effect of a few percent would be detected. We are confident that the reduced fit can be used for other sizes near the experimental range.

In a spherical explosion there is a second shock which arises when the rarefaction from the explosive surface propagates back through the burned products and reflects at the center. This second shock propagates outward and eventually overtakes the first shock. Berger and Holt (14) did some calculations for a PETN sphere exploded in sea water, and found the overtake to occur at about seven radii. Our experimental range does not go this far, and we saw no evidence of the second shock. The effects of the initiator have not been calculated, but it seems certain that it perturbs the flow to some extent. No evidence of any effects have been seen.

## ACKNOWLEDGMENTS

It is a pleasure to acknowledge the assistance furnished by many members of the Los Alamos Scientific Laboratory, especially of groups GMX-2, GMX-3, GMX-6, GMX-8, GMX-10, and J-11, without whose help these experiments could not have been done. This work was done under the auspices of the U.S. Atomic Energy Commission.

## REFERENCES

1. E. H. Eyster, L. C. Smith, and S. R. Walton, "The Sensitivity of High Explosives to Pure Shock," U.S. Naval Ordnance Laboratory memorandum 10,336 (1949).
2. T. P. Liddiard, Jr., "The Initiation of Burning in High Explosives by Shock Waves," Proceedings Fourth Symposium (International) on Detonation, U.S. Naval Ordnance Laboratory, White Oak, Silver Spring, Maryland (1965) 487-495.
3. N. L. Coleburn, L. A. Roslund, "Collision of Spherical Shock Waves in Water," U.S.

- Naval Ordnance Laboratory, White Oak  
Silver Spring, Maryland, NOLTR-68-110  
(1968).
4. M. H. Rice and J. M. Walsh, *J. Chem. Phys.* 26, 824 (1957).
  5. L. C. Smith and L. W. Hantel, unpublished work.
  6. The PFIEFE code was written by L. Gritz, LASL group GMX-3, for use on the CDC 6600 computers, to convert x-y input data to time-distance data.
  7. J. W. Kury, H. C. Hornig, et al, "Metal Acceleration by Chemical Explosives," *Proceedings Fourth Symposium (International) on Detonation*, U.S. Naval Ordnance Laboratory, White Oak, Silver Spring, Maryland (1965) 3-13.
  8. R. Courant, K. O. Friedrichs, Supersonic Flow and Shock Waves, Interscience Publishers, Inc., New York, 1948, pp. 424-433.
  9. The EILEEN code is a least-squares fitting routine written by E. G. Hantel, LASL group J-11, for use on the IBM 7030 computer. In this program all data points are considered to be of equal weight.
  10. LASL group GMX-6, "Selected Hugoniot," LA-4167-MS, Los Alamos Scientific Laboratory, 1969.
  11. B. G. Craig, private communication.
  12. C. L. Mader, "Detonation Properties of Condensed Explosives Computed Using Becker-Kistiakowsky-Wilson Equation of State," LA-2900, Los Alamos Scientific Laboratory (1963).
  13. C. L. Mader, private communication.
  14. S. A. Berger and M. Holt, *Phys. Fluids* 5, 426 (1962).

# LIST OF ATTENDEES

Dr. M. Taylor Abegg  
Sandia Corporation  
Sandia Base  
Albuquerque, New Mexico 87115

Dr. David D. Abernathy  
Naval Weapons Laboratory  
Dahlgren, Virginia 22448

Dr. James E. Ablard  
Naval Ordnance Laboratory  
White Oak  
Silver Spring, Maryland 20910

Dr. G. R. Abrahamson  
Stanford Research Institute  
Menlo Park, California 93025

Mr. I. B. Akst  
Mason and Hanger  
Silas Mason Co., Inc.  
P. O. Box 647  
Amarillo, Texas 79105

Mr. Robert C. Allen  
Teledyne McCormick Selph  
Hollister Airport  
Hollister, California 95023

Dr. W. H. Andersen  
Shock Hydrodynamics  
15010 Ventura Boulevard  
Sherman Oaks, California 91403

Dr. Charles K. Arpke  
Air Force Armament Laboratory  
AFATL (ADLR)  
Eglin AFB, Florida 32542

Mr. W. W. Atkins  
Naval Research Laboratory  
4555 Overlook Avenue  
Washington, D. C. 20390

Mr. James L. Austing  
Illinois Institute of Technology  
Research Institute  
10 West 35th Street  
Chicago, Illinois 60616

Dr. Arthur E. Axworthy  
Rocketdyne  
6633 Canoga Avenue  
Canoga Park, California 91304

Mr. J. R. Baker  
Naval Research Laboratory  
4555 Overlook Avenue  
Washington, D. C. 20390

Mr. Harold M. Barnett  
Sandia Laboratories  
Albuquerque, New Mexico 87115

Mr. Norman Barr  
U. S. Blasting Materials  
Gulf Oil Company  
P. O. Box 419  
Eudora, Kansas 66025

Dr. William B. Benedick  
Sandia Laboratories  
P. O. Box 5800  
Albuquerque, New Mexico 87115

Dr. Raymond L. Beauregard  
Naval Ordnance Systems Command  
(ORD-033)  
Department of the Navy  
Washington, D. C. 20360

Dr. H. Bernier  
Commissariat a L'Energie Atomique  
Boite Postale No. 7  
93 Sevrans, France

Dr. James H. Blackburn  
Honeywell, Inc.  
600 Second Street North  
Hopkins, Minnesota 55343

Mr. P. G. W. Brink  
Embassy of South Africa  
3051 Massachusetts Avenue, N. W.  
Washington, D. C. 20008

Dr. Christian Brochet  
Laboratoire d'Energetique  
Universite de Poitiers  
E.N.S.M.A. - rue Guillaume VII  
86 Poitiers, France

Dr. Jacques Brossard  
Laboratoire d'Energetique  
E.N.S.M.A. - rue Guillaume VII  
86 Poitiers, France

Mr. Nathan C. Brown  
Valpey - Fisher Corporation  
1015 First Street  
Holliston, Massachusetts 01746

Professor Lloyd Brownell  
U. S. Army (Frankford)  
1118 McMurray Street  
Richland, Washington 99352

Dr. James A. Burgess  
E.R.D.E., Ministry of Technology  
Powdermill Lane  
Waltham Abbey  
Essex, England

Dr. Marcello Busco  
Ministero Difesa  
Viale Universita, 4  
Roma, Italy

Dr. Jacques Calzia  
Poudrerie & Laboratoires  
De Sevrans  
Boite Postale No. 4  
93 Sevrans, France

Dr. Arthur W. Campbell  
Los Alamos Scientific Laboratory  
Los Alamos, New Mexico 87544

Dr. C. E. Canada  
Mason and Hanger  
Silas Mason Co., Inc.  
P. O. Box 647  
Amarillo, Texas 79105

Dr. Richard T. Castle  
Battelle Memorial Institute  
505 King Avenue  
Columbus, Ohio 43201

Dr. Angelo A. Catani  
General Electric Co.  
ASRO Building 9, Room 52  
Court Street  
Syracuse, New York 13201

Dr. R. F. Chaiken  
U. S. Bureau of Mines  
4800 Forbes Avenue  
Pittsburgh, Pennsylvania 15213

Dr. M. Munawar Chaudhri  
Cavendish Laboratory  
Surface Physics  
Cambridge University  
Free School Lane  
Cambridge, England

Dr. R. Cheret  
Commissariat a L'Energie Atomique  
Boite Postale No. 7  
93 Sevrans, France

Mr. K. L. Christensen  
McDonnell Douglas Astronautics Co.  
Western Division  
5301 Bolsa Avenue  
Huntington Beach, California 92647

Mr. John C. Christian  
The Marquardt Company  
16555 Saticoy Street  
Van Nuys, California 91409

Dr. George B. Clark  
Director, Rock Mechanics & Explosives  
Research Center  
University of Missouri  
Rolla, Missouri 65401

Dr. R. B. Clay  
IRECO Chemicals  
726 Kennecott Building  
Salt Lake City, Utah 84111

Mr. Arthur Cohen  
U. S. Army Ballistic Research  
Laboratories  
Aberdeen Proving Ground, Maryland 21005

Mr. Richard W. Collett  
Engineering Sciences Laboratory  
Picatinny Arsenal  
Dover, New Jersey 07801

Mr. N. L. Coleburn  
Naval Ordnance Laboratory  
White Oak  
Silver Spring, Maryland 20910

Mr. Jerald E. Colvin  
Mason and Hanger  
Silas Mason Co., Inc.  
Burlington AEC Plant  
Burlington, Iowa 52601

Dr. Robert L. Conger  
Naval Weapons Center  
Corona Laboratories  
Corona, California 91720

Dr. M. Cowperthwaite  
Stanford Research Institute  
Menlo Park, California 94025

Mr. Bobby G. Craig  
Los Alamos Scientific Laboratory  
Los Alamos, New Mexico 87544

Dr. C. James Dahn  
Illinois Institute of Technology  
Research Institute  
10 West 35th Street  
Chicago, Illinois 60616

Dr. Charles B. Dale  
Naval Ordnance Station  
Indian Head, Maryland 20640

Dr. Heinz Damm  
German Embassy  
4645 Reservoir Road, N.W.  
Washington, D.C. 20007

Dr. D. E. Davenport  
Singer-Link  
1077 Arques Avenue  
Sunnyvale, California 95286

Dr. William C. Davis  
Los Alamos Scientific Laboratory  
Los Alamos, New Mexico 87544

Dr. John W. Dawson  
U. S. Army Research Office  
Box CM, Duke Station  
Durham, North Carolina 27706

Dr. W. E. Deal  
Los Alamos Scientific Laboratory  
Los Alamos, New Mexico 87544

Mr. P. de Beaumont  
Commissariat a l'Energie Atomique  
Boite Postale No. 27  
Villeneuve St. Georges  
France

Mr. M. Defourneaux  
Institute Franco-Allemand de Recherches  
12 rue de l'Industrie  
68 St. Louis, France

Dr. James Densmore  
Reynolds Industries Inc.  
P. O. Box 850  
Marina Del Rey, California 90291

Dr. Werner Diepold  
Berghausen  
Karlsruhe, Germany

Mr. Walter H. Dittrich  
AFATL (ADLRW)  
Eglin AFB, Florida 32542

Dr. Gus Dorrough, Jr.  
Lawrence Livermore Laboratory  
University of California  
Livermore, California 94551

Professor Anatoly N. Dremin  
Institute of Chemical Physics  
USSR Academie of Sciences  
Chernogolovka  
Moscow Region, 142432  
USSR

Dr. Russell E. Duff  
Systems, Science and Software  
P. O. Box 1620  
La Jolla, California 92037

Mr. Godfrey Eden  
U.K.A.E.A.  
Atomic Weapons Research  
Establishment  
Aldermaston, Reading  
Berkshire, England

Mr. George Edwards  
(ORD-054111)  
Naval Ordnance Systems Command  
Washington, D. C. 20360

Mr. L. J. Edwards  
AFRPL, Edwards AFB  
Edwards, California 93523

Mr. Clyde W. Eilo  
Hercules, Inc.  
910 Market Street  
Wilmington, Delaware 19899

Dr. Walter Engel  
Berghausen  
Karlsruhe, Germany

Mr. Julius W. Enig  
Naval Ordnance Laboratory  
Silver Spring, Maryland 20910

Mr. Avner Erez  
Israel Ministry of Defence  
Scientific Department  
P. O. Box 7063  
Tel-Aviv, Israel

Mr. John O. Erkman  
Naval Ordnance Laboratory  
White Oak  
Silver Spring, Maryland 20910

Dr. John H. Evans, Jr.  
Atlas Chemical Industry, Inc.  
Valley Forge Industrial Park  
Valley Forge, Pennsylvania 19481

Dr. Marjorie W. Evans  
Evans Associates  
14511 De Bell  
Los Altos, California 94022

Dr. Harry D. Fair, Jr.  
FRL Picatinny Arsenal Explosives  
Laboratory  
Building 407  
Dover, New Jersey 07801

Dr. Errol L. Falconer  
Canadian Industries Ltd.  
Explosives Research Lab.  
McMasterville  
Quebec, Canada

Dr. Mae I. Fauth  
Naval Ordnance Station  
Indian Head, Maryland 20640

Dr. Claude Fauquignon  
Commissariat a l'Energie  
Atomique  
Boite Postale No. 7  
Sevran, France

Dr. John E. Field  
Cavendish Laboratory  
Cambridge University  
Free School Lane  
Cambridge, England

Mr. Milton Finger  
Lawrence Livermore Laboratory  
University of California  
P. O. Box 808  
Livermore, California 94550

Mr. Amnon Fisher  
Israel Ministry of Defence  
Scientific Department  
P. O. Box 7063  
Tel-Aviv, Israel

Mr. Elbert E. Fisher  
Honeywell, Inc.  
2345 Walnut Street  
Roseville, Minnesota 55113

Dr. Robert F. Flagg  
Director, R&D Division  
Holey, Inc.  
2751 San Juan Road  
Hollister, California 95023

Dr. Isaias Flit  
Peruvian Navy  
31 Bay State Road  
Boston, Massachusetts 02215

Mr. Duane A. Fojt  
Naval Weapons Center, Code 4541  
China Lake, California 93555

Dr. David R. Forshey  
U. S. Bureau of Mines  
4800 Forbes Avenue  
Pittsburgh, Pennsylvania 15213

Dr. H. M. Freiwald  
Ministry of Defense  
51 Bonn  
Postfach, Germany

Mr. Nilson H. Froula  
Systems Science and Software  
P. O. Box 1620  
La Jolla, California 92037

Mr. David R. Garfinkle  
Shock Hydrodynamics Inc.  
15010 Ventura Boulevard  
Sherman Oaks, California 91403

Dr. W. Geiger  
Battelle-Institut  
AM Roemerhof 35  
6 Frankfurt/Main, Germany

Mr. William A. Gey  
Naval Weapons Center  
Box 5362  
China Lake, California 93555

Dr. Stephen P. Gill  
Physics International Co.  
2700 Merced Street  
San Leandro, California 94577

Dr. David Good  
Explosives Corporation of America  
Issaquah, Washington 98027

Mr. LeRoy Green  
Lawrence Livermore Laboratory  
University of California  
P. O. Box 808  
Livermore, California 94550

Mr. Gordon A. Greene  
Naval Weapons Center  
Code 4541  
China Lake, California 93555

Professor T. K. Groves  
University of Calgary  
Explosives and High Pressure  
Laboratory  
1312-16 Avenue, N. W. Calgary  
Calgary, Alberta, Canada

Dr. Harold J. Gryting  
Naval Weapons Center  
Code 45402  
China Lake, California 93555

Mr. Richard Guariente  
Lawrence Livermore Laboratory  
University of California  
Livermore, California 94550

Mr. William H. Gust  
Lawrence Livermore Laboratory  
University of California  
P. O. Box 808  
Livermore, California 94550

Mr. Wilfred S. Hall  
British Defense Staff  
British Embassy  
3100 Mass. Avenue, N. W.  
Washington, D. C. 20008

Mr. Lawrence W. Hantel  
Los Alamos Scientific Laboratory  
P. O. Box 1663  
Los Alamos, New Mexico 87544

Mr. Jere G. Harlan  
Sandia Corporation  
Sandia Base  
Albuquerque, New Mexico 87115

Mr. George E. Hauver  
U. S. Army Ballistic Research  
Laboratories  
Aberdeen Proving Ground  
Maryland 21005

Mr. Edmund Hay  
U. S. Bureau of Mines  
4800 Forbes Avenue  
Pittsburgh, Pennsylvania 15213

Mr. Bernard Hayes  
Los Alamos Scientific Laboratory  
P. O. Box 1663 (GMX-8)  
Los Alamos, New Mexico 87544

Dr. Manfred Held  
Fa Messerschmitt-Bolkow Blohm  
8898 Schrobenuhausen  
Hagenauer Forst  
Germany

Mr. Joseph Herszkowitz  
Explosives Laboratory FRL  
Picatinny Arsenal  
Dover, New Jersey 07801

Dr. John A. Hicks  
E.R.D.E., Ministry of Technology  
Powdermill Lane  
Waltham Abbey  
Essex, England

Dr. Tsutomu Hikita  
Faculty of Engineering  
University of Tokyo  
Bunkyo-Ku  
Tokyo, Japan

Dr. R. Lenton Hill, Jr.  
Air Force Armament Laboratory  
Eglin Air Force Base, Florida 32542

Mr. William F. Holden  
Naval Ordnance Station  
Indian Head, Maryland 20640

Mr. Howard Hornig  
Lawrence Livermore Laboratory  
University of California  
Livermore, California 94550

Dr. Philip M. Howe  
U. S. Army Ballistic Research  
Laboratory  
Aberdeen Proving Ground, Maryland 21005

Mr. George E. Ingram  
Shock Wave Physics  
Division 5133  
Sandia Laboratories  
P. O. Box 5800  
Albuquerque, New Mexico 87115

Dr. O. R. Irwin  
Aerojet-General Corp.  
Downey, California 90241

Dr. Sigmund J. Jacobs  
Naval Ordnance Laboratory  
White Oak  
Silver Spring, Maryland 20910

Professor Jean Jacquesson  
E.N.S.M.A., Université de Poitiers  
rue Guillaume VII  
86 Poitiers, France

Mr. J. S. De Jager  
Embassy of South Africa  
3051 Massachusetts Avenue, N. W.  
Washington, D. C. 20008

Mr. Edward James, Jr.  
Lawrence Livermore Laboratory  
University of California  
Livermore, California 94500

Mr. Robert L. Jameson  
U. S. Army Ballistic Research Lab.  
Aberdeen Proving Ground, Maryland 21005

Dr. James O. Johnson  
Los Alamos Scientific Laboratory  
P. O. Box 1663  
Los Alamos, New Mexico 87544

Mr. Roger G. Johnson  
Honeywell, Inc.  
2345 Walnut Street  
St. Paul, Minnesota 55113

Dr. Jerry Jones  
Naval Weapons Center  
Code 5053  
Corona, California 91720

Dr. Taylor B. Joyner  
Naval Weapons Center  
Code 6056  
China Lake, California 93555

Mr. Irving Kabik  
Naval Ordnance Laboratory  
White Oak  
Silver Spring, Maryland 20910

Dr. Minao Kamegai  
Lawrence Livermore Laboratory  
P. O. Box 808  
Livermore, California 94550

Mr. M. Kamel  
University of California, Berkeley  
1937 Elinera Drive  
Pleasant Hill, California 94523

Major James M. Karth  
U. S. Air Force  
AFATL (ADLRW)  
Eglin AFB, Florida 32542

Mr. Bennett W. Kelley  
Honeywell, Inc.  
2600 Ridgway Parkway  
Minneapolis, Minnesota 55413

Mr. J. E. Kennedy  
Sandia Laboratories  
P. O. Box 5800  
Albuquerque, New Mexico 87115

Mr. James D. Kershner  
52 La Paloma Drive  
White Rock, New Mexico 87544

Mr. Bruce Kirk  
McDonnell Douglas Astronautics Co.  
P. O. Box 516  
St. Louis, Missouri 63166

Mr. Gershow Kover  
c/o Government of Israel  
Mr. Z. Yarom  
850 Third Avenue  
New York, New York 10022

Mr. P. E. Kramer  
Mason and Hanger  
Silas Mason Co., Inc.  
P. O. Box 647  
Amarillo, Texas 79105

Mr. P. S. Kujawa  
U. S. Bureau of Mines  
630 Sansome #1429  
San Francisco, California 94111

Mr. James E. Kurrle  
Mason and Hanger  
Silas Mason Co., Inc.  
P. O. Box 561  
Burlington, Iowa 52601

Dr. John W. Kury  
Lawrence Livermore Laboratory  
University of California  
Livermore, California 94550

Mr. Andre Kusubov  
Lawrence Livermore Laboratory  
University of California  
P. O. Box 808  
Livermore, California 94550

Dr. Chase L. Leavitt  
Reynolds Industries Inc.  
P. O. Box 850  
Marina Del Rey, California 90291

Mr. Edward L. Lee  
Lawrence Livermore Laboratory  
University of California  
Livermore, California 94550

Dr. D. J. Lewis  
ICI Limited  
Mond Division R & D Department  
P. O. Box 7  
Norwich, Cheshire, England

Mr. Thomas P. Liddiard  
Naval Ordnance Laboratory  
White Oak  
Silver Spring, Maryland 20910

Dr. C. D. Lind  
Naval Weapons Center  
Code 4541  
China Lake, California 93555

Mr. Lars Lindner  
Research Institute of Swedish  
National Defence  
Box 416  
17204 Sundbyberg 4, Sweden

Dr. Carl F. Lucy  
Ordnance Research Inc.  
P. O. Box 1426  
Ft. Walton Beach, Florida 32548

Dr. Herbert J. MacDonald  
Physics International Co.  
2700 Merced Street  
San Leandro, California 94577

Mr. William McBride  
Explosive Engineering Research Dept.  
Naval Weapons Station  
Yorktown, Virginia 23491

Dr. Clinton D. McLaughlin  
U. S. Naval Torpedo Station  
Keyport, Washington 98345

Mr. Charles L. Mader  
Los Alamos Scientific Laboratory  
P. O. Box 1663  
Los Alamos, New Mexico 87544

Dr. Sidney J. Magram  
Office Chief Research and Development  
HDQTRS, Department of the Army  
Washington, D. C. 20310

Dr. H. Dean Mallory  
Detonation Physics Division  
Naval Weapons Center (603)  
China Lake, California 93555

Professor Y. Manheimer-Timnat  
Technion, Israel Institute of Technology  
Haifa, Israel

Professor N. Manson  
Universite de Poitiers  
ENSMA rue Guillaume VII  
Poitiers, France

Dr. Rudolph J. Marcus  
Office of Naval Research  
Branch Office  
1030 East Green Street  
Pasadena, California 91024

Mr. Walter L. Marshall  
Mason and Hanger  
Silas Mason Co., Inc.  
P. O. Box 561  
Burlington, Iowa 52601

Dr. W. W. Marshall  
U.K.A.E.A.  
Atomic Weapons Research  
Establishment  
Aldermaston, Reading  
Berkshire, England

Dr. Joseph F. Masi  
Air Force Office of Scientific  
Research (SREP)  
1400 Wilson Blvd.  
Arlington, Virginia 22209

Mr. Aldo Mazzella  
Physics International Co.  
2700 Merced Street  
San Leandro, California 94577

Dr. Vincent J. Menichelli  
Jet Propulsion Laboratory  
4800 Oak Grove Drive  
Pasadena, California 91103

Mr. Fred L. Menz  
Naval Weapons Center  
Corona, California 91720

Dr. Andre Migault  
Laboratoire Metallurgie  
Universite de Poitiers  
ENSMA - rue Guillaume VII  
Poitiers, France

Mr. Bobbie M. Miles  
Mason and Hanger  
Silas Mason Co., Inc.  
P. O. Box 561  
Burlington, Iowa 52601

Mr. A. Miron  
Government of Israel  
850 Third Avenue  
Suite 607  
New York, New York 10022

Dr. John J. Molloy  
Ensign Bickford Co.  
660 Hopmeadow Street  
Simsbury, Connecticut 06070

Dr. Otto J. Molnar  
Council for Scientific and  
Industrial Research  
P. O. Box 14  
Dynamit Factory C. P.  
Republic of South Africa

Mr. E. T. Moore, Jr.  
Shock Dynamics Department  
Physics International Co.  
2700 Merced Street  
San Leandro, California 94577

Dr. Reynaldo Morales  
Los Alamos Scientific Laboratory  
2339-B 35th Street  
Los Alamos, New Mexico 87544

Dr. Douglas M. Mumma  
Physics International Co.  
2700 Merced Street  
San Leandro, California 94577

Dr. Arthur J. Murphy  
Jet Propulsion Laboratory  
4800 Oak Grove Drive  
Pasadena, California 91103

Mrs. Hyla S. Napadensky  
Illinois Institute of Technology  
Research Institute  
10 West 35th Street  
Chicago, Illinois 60616

Mr. Charles E. Needham  
USAF-AFWL, Kirtland AFB  
Albuquerque, New Mexico 87117

Dr. Charles J. O'Brien  
Aerojet Liquid Rocket Company  
P. O. Box 13222  
Sacramento, California 95813

Professor A. K. Oppenheim  
University of California, Berkeley  
Berkeley, California 94720

Mr. Donald Ornellas  
Lawrence Livermore Laboratory  
University of California  
Livermore, California 94550

Mr. A. K. Osterkamp  
Singer-Link  
1077 E. Arques Avenue  
Sunnyvale, California 94086

Mr. Reginald F. Page  
Bell Telephone Laboratories  
Whippany Road  
Whippany, New Jersey 07951

Dr. Daniel K. Parks  
Falcon Research & Development Co.  
1441 Ogden Street  
Denver, Colorado 80218

Mr. Dale Partridge  
Gulf Oil Company  
U. S. Blasting Materials  
P. O. Box 8200  
Kansas City, Missouri 64105

Mr. Wayne L. Patrick  
Mason and Hanger  
Silas Mason Co., Inc.  
Burlington AEC Plant  
Burlington, Iowa 52601

Dr. James B. Patton  
Physics International Co.  
2700 Merced Street  
San Leandro, California 94577

Dr. Eugenio Pelizza  
Ministero Difesa  
Mariperman - S. Bartolomeo  
La Spezia, Italia

Dr. Russel G. Perkins  
Armed Services Explosives Safety Board  
Room G-B 270, Forrestal Building  
Washington, D. C. 20314

Dr. Algot Persson  
Swedish Detonic Research Foundation  
Vinterviken  
Stockholm, Sweden

Dr. P. A. Persson  
Swedish Detonic Research Foundation  
Vinterviken  
Stockholm, Sweden

Mr. Stig Petersson  
AB Bofors  
S-690  
20 Bofors, Sweden

Mr. Richard A. Plauson  
Naval Weapons Center  
Code 4541  
China Lake, California 93555

Mr. A. Popolato  
Los Alamos Scientific Laboratory  
P. O. Box 1663  
Los Alamos, New Mexico 87544

Mr. Francis B. Porzel  
Naval Ordnance Laboratory  
White Oak  
Silver Spring, Maryland 20910

Dr. Lester A. Potteiger  
Naval Weapons Laboratory  
Dahlgren, Virginia 22448

Dr. Donna Price  
Naval Ordnance Laboratory  
Code 231  
White Oak  
Silver Spring, Maryland 20910

CDR Henri E. Rambonnet  
Royal Netherlands Navy  
Royal Netherlands Embassy  
4200 Linneer Avenue, N. W.  
Washington, D. C. 20008

Professor Alan Randolph  
Los Alamos Scientific Laboratory  
Los Alamos, New Mexico 87544

Dr. Neil R. Richardson  
Technical Ordnance, Inc.  
6420 Goodrich Avenue  
Minneapolis, Minnesota 55426

Mr. J. K. Rigdon  
Mason and Hanger  
Silas Mason Co., Inc.  
P. O. Box 647  
Amarillo, Texas 79105

Dr. William C. Rivard  
Los Alamos Scientific Laboratory  
P. O. Box 1663  
Los Alamos, New Mexico 87544

Mr. Glenn L. Roark  
McDonnell Douglas Astronautics Company  
5301 Bolsa Avenue  
Huntington Beach, California 92647

Dr. Ralph Roberts  
Power Program, Code 473  
Office of Naval Research  
800 N. Quincy Street  
Arlington, Virginia 22217

Professor Ronald R. Rollins  
University of Missouri - Rolla  
104 Buehler Bldg.  
Rolla, Missouri 65401

Dr. Julius Roth  
Stanford Research Institute  
Menlo Park, California 94025

Mr. Norman L. Rump  
U. S. Naval Weapons Center  
China Lake, California 93555

Dr. Leon W. Saffian  
Picatinny Arsenal  
Dover, New Jersey 07054

Dr. A. Sakurai  
Waterways Experiment Station  
Vicksburg, Mississippi 39180

Mr. Jacob Savitt  
Explosiform, Inc.  
P. O. Box 36  
Belvedere, California 94920

Professor Karl Scheller  
ARL (Chemistry Research  
Laboratory)  
ARL (ARC)  
Wright Patterson AFB, Ohio 45433

Dr. L. B. Seely  
Menlo College  
1407 Portola Road  
Menlo Park, California 94025

Dr. Robert Shaw  
Stanford Research Institute  
333 Ravenswood Avenue  
Menlo Park, California 94025

Dr. James H. Shea  
Physics International Company  
2700 Merced Street  
San Leandro, California 94577

Mr. James B. Shore  
Schlumberger Well Services  
P. O. Box 2175  
Houston, Texas 77001

Dr. I. C. Skidmore  
AWRE/UKAEA  
Aldermaston, Reading  
England

Dr. Louis C. Smith  
Los Alamos Scientific Laboratory  
P. O. Box 1663  
Los Alamos, New Mexico 87544

Dr. James J. Smolen  
Schlumber Well Services  
P. O. Box 2175  
Houston, Texas 77001

CDR Gordon Spergel  
Canadian Armed Forces  
458 Tillbury Avenue  
Ottawa, Ontario  
Canada

Dr. Dante Stirpe  
Los Alamos Scientific  
Laboratories  
GMX-7  
Los Alamos, New Mexico 87544

Mr. Richard H. Stresau  
R. Stresau Laboratory, Inc.  
Star Route  
Spooner, Wisconsin 54801

Professor M. Summerfield  
Princeton University  
Princeton, New Jersey 08540

Dr. John P. Sumner  
Honeywell, Inc.  
600 Second Street North  
Hopkins, Minnesota 55343

Mr. Leroy J. Syrop  
Del Mar Engineering Labs  
6901 W. Imperial Highway  
Los Angeles, California 90045

Mr. Boyd C. Taylor  
U. S. Army Ballistics Research Lab.  
Attn: AMXRD - BTL  
Aberdeen Proving Ground  
Maryland 21005

Dr. J. W. Taylor  
Department of Fuel Science  
University of Leeds  
Leeds, England

Dr. Melvin T. Thieme  
Los Alamos Scientific Laboratories  
Los Alamos, New Mexico 87544

Dr. Rodney S. Thurston  
Los Alamos Scientific Laboratory  
5 Dakota Lane  
Los Alamos, New Mexico 87544

Dr. William M. Truesdell  
Boston Naval Shipyard, Code 2390  
Boston, Massachusetts 42129

Mr. T. J. Tucker  
Sandia Corporation  
Sandia Base  
Albuquerque, New Mexico 87115

Mr. Allen J. Tulis  
Illinois Institute of Technology  
Research Institute  
10 W. 35th Street  
Chicago, Illinois 60616

Mr. Chug Tuttle  
Gulf Oil Company  
U. S. Blasting Materials  
P. O. Box 8200  
Kansas City, Missouri 64105

Dr. Paul A. Urtiew  
Lawrence Livermore Laboratory  
P. O. Box 808  
Livermore, California 94550

Dr. Robert W. Van Dolah  
U. S. Bureau of Mines  
4800 Forbes Avenue  
Pittsburgh, Pennsylvania 15213

Dr. Mathias van Thiel  
Lawrence Livermore Laboratory  
P. O. Box 808  
Livermore, California 94550

Dr. Veyrie  
Commissariat a L'Energie Atomique  
Boite Postale No. 7  
93 Sevran, France

Dr. W. E. Voreck  
Picatinny Arsenal  
EL Building 407  
Dover, New Jersey 07871

Dr. Jerry Wackerle  
Los Alamos Scientific Laboratory  
P. O. Box 1663  
Los Alamos, New Mexico 87544

Mr. Franklin Walker  
Lawrence Livermore Laboratory  
University of California  
Livermore, California 94550



Mr. G. R. Walker  
Defence Research Establishment  
Valcartier  
P. O. Box 880, Courcellette  
Quebec, Canada

Mr. Robert K. Warner  
Harry Diamond Laboratories  
Connecticut & Van Ness Street, N.W.  
Washington, D. C. 20438

Mr. Richard Wasley  
Lawrence Livermore Laboratory  
University of California  
Livermore, California 94550

Mr. Richard W. Watson  
U. S. Bureau of Mines  
4800 Forbes Avenue  
Pittsburgh, Pennsylvania 15213

Dr. Gerhard Weinert  
Test Station  
Berliner Street 115  
233 Eckerforde, Germany

Dr. L. F. Welanetz  
Applied Physics Laboratory  
8621 Georgia Avenue  
Silver Spring, Maryland 20910

Mr. D. M. Welsh  
Canadian Safety Fuse Co., LTD  
Brownsburg, Quebec, Canada

Dr. Alexander B. Wenzel  
Southwest Research Institute  
P. O. Drawer 28510  
San Antonio, Texas 78228

Dr. Kevin J. White  
U. S. Army Ballistic Research Lab.  
Aberdeen Proving Ground, Maryland 21005

Mr. John C. Whitson  
Naval Weapons Center  
Code 4541  
China Lake, California 93555

Dr. Mark L. Wilkins  
Lawrence Livermore Laboratory  
P. O. Box 808  
Livermore, California 94550

Dr. Bernard T. Wolfson  
Air Force Office of Scientific  
Research (HQS)  
1400 Wilson Blvd.  
Arlington, Virginia 22209

Mr. Avi Yarom  
Government of Israel  
850 Third Avenue  
New York, New York 10022

Dr. Thomas A. Zaker  
Armed Services Explosives Safety  
Board  
5 Tifton Court  
Potomac, Maryland 20854

Dr. F. Van Zeggeren  
C. I. L.  
McMasterville  
Quebec, Canada

Dr. Martin F. Zimmer  
Air Force Armament Laboratory  
AFATL (ADLRW)  
Eglin AFB, Florida 32542

# AUTHOR INDEX

(D) indicates discussion.

Akst, I. B., 59  
Andersen, W. H., 67, 77(D)  
Austing, James L., 47, 151(D)  
Avrami, Louis, 351

Beaumont, Ph. de, 547  
Beedham, K., 279  
Berke, Joseph G., 89, 237  
Bjarnholt, Gert, 115  
Boyle, V. M., 251  
Brochet, C., 41  
Brossard, J., 41  
Busco, M., 513

Calzia, J., 231  
Carabin, H., 231  
Chaudhri, M. M., 301  
Chéret, R., 31, 41, 46(D), 425(D), 567  
Coleburn, N. L., 523, 581  
Conger, Robert L., 11(D), 151(D)  
Cowperthwaite, M., 39(D), 427  
Craig, B. G., 29(D), 188(D), 205(D),  
230(D), 257(D), 321

David, F., 567  
Davis, W. C., 3, 13, 75(D), 599  
Défourneaux, M., 457  
Desoyer, J. S., 403  
Dremin, A. N., 86(D), 399  
Duff, R., 21(D), 188(D), 275(D)  
Dyer, A. S., 279, 291

Eden, G., 467  
Edwards, David J., 413  
Eichler, T. V., 313  
Enig, Julius W., 99  
Erkman, John, 477  
Ervin, L. H., 251  
Evans, Marjorie, 89

Fauquignon, C., 361  
Fickett, W., 3  
Field, J. E., 301  
Finger, M., 137, 151(D), 503  
Fritz, J. N., 447  
Fujiwara, S., 267

Graham, R. A., 369  
Gryting, H. J., 150(D), 168(D)

Hallouin, M., 403  
Hantel, L. W., 599  
Hauver, G. E., 387  
Hawkins, A., 23  
Hay, J. E., 81, 559  
Hayes, B., 447  
Held, M., 29(D)  
Hikita, T., 167(D)  
Holmes, W. I., 279  
Hornig, H. C., 137, 503  
Hoskin, N. E., 501

Ingram, G. E., 369

Jacobs, Sigmund J., 413  
Jacques, L., 457  
Jacquesson, J., 403  
Jameson, R. L., 23, 29(D)  
Johnson, Charles D., 47  
Jung, R. G., 191

Kamegai, Minao, 477  
Kamel, Mostafa M., 114(D)  
Kennedy, J. E., 435  
Kineke, J. H., Jr., 533  
Kot, C. A., 313  
Kurrle, J. E., 503  
Kury, J. W., 137  
Kusakabe, M., 267  
Kusubov, A. S., 105  
Kwak, D., 119

Lambourn, B. D., 501  
Lee, E. L., 137, 150(D), 331, 503  
Legrand, J., 567  
Leopold, Howard S., 339  
Lethaby, J. W., 573  
Leygonie, J., 547

Mader, Charles L., 11(D), 150(D), 177  
189(D), 511(D)  
Manheimer-Timnat, Y., 46(D), 565(D)  
Manson, N., 41  
Marshall, E. F., 321  
Marshall, W. W., 185, 188(D), 247  
Mazzella, A., 351  
Moore, E. T., 151(D)  
Morvan, J., 429  
Mottet, A. L., Jr., 67

Napadensky, H. S., 313  
Needham, Charles E., 487

Oppenheim, A. K., 119

Persson, Per-Anders, 115, 118(D), 153,  
167(D)

Peters, W. C., 559  
Petrone, Francis J., 99  
Price, Donna, 207  
Prouteau, F., 567  
Pujols, H., 429

Randall, R. R., 67  
Ribovich, J., 81  
Rigdon, J. K., 59  
Rivard, W. C., 3, 11(D)  
Romain, J. P., 403  
Roslund, L. A., 523, 581  
Roth, Julius, 219

Sakurai, A., 493  
Sanborn, R. H., 331  
Savitt, Jacob, 189(D)  
Schuler, Karl W., 589  
Scott, Calvin L., 259  
Seely, L. B., 89, 237  
Shaw, Robert, 89, 237  
Shea, J. H., 351  
Sjölin, T., 153  
Skidmore, I. C., 573

Smith, C. P. M., 467  
Smolen, J. J., 119  
Smothers, W. G., 251  
Sternberg, H. M., 597  
Stresau, R., 266(D)  
Stromberg, H. D., 331

Taylor, John Watson, 291, 311  
Tegg, Derek, 89, 237  
Trott, B. D., 191, 205(D)  
Tulis, Allen J., 47

Urtiew, P. A., 105, 114(D), 118(D), 119

Vacellier, J., 567  
Van Dolah, R. W., 81  
Venable, D., 3, 13  
Verdès, G., 31, 41

Wackerle, G., 188(D)  
Walker, F. E., 114(D), 167(D)  
Walker, W. A., 597  
Watson, R. W., 81, 169, 559  
West, C. E., Jr., 533  
Williams, R. F., 427

Yakushev, V. V., 399

Zaker, T. A., 313  
Zernow, L., 67